PE&A 94PJ20
November 15, 1996

DESCRIPTION AND VALIDATION OF THE STOCHASTIC GROUND MOTION MODEL

Principal Investigator
W. Silva

Coordinating Authors
W. Silva, N. Abrahamson, G. Toro, C. Costantino

November 1996

PACIFIC ENGINEERING AND ANALYSIS
311 POMONA AVENUE
EL CERRITO, CALIFORNIA 94530

Prepared for the
ENGINEERING RESEARCH AND APPLICATIONS DIVISION
DEPARTMENT OF NUCLEAR ENERGY
BROOKHAVEN NATIONAL LABORATORY, ASSOCIATED UNIVERSITIES, INC.
UPTON, NEW YORK 11973

CONTRACT NO. 770573

BNL Project Manager
Kamal Bandyopadhyay

ACKNOWLEDGMENTS

The need for a description and thorough validation of the stochastic ground motion model as implemented at DOE sites was recognized by Jeffrey Kimball. The authors are grateful for this interest and support.

CONTENTS

CONTENTS (cont.)

CONTENTS (cont.)

CONTENTS (cont.)

CONTENTS (cont.)

CONTENTS (cont.)

Section Page

TABLES

TABLES (cont.)

TABLES (cont.)

CHAPTER 1

INTRODUCTION

1.1 PURPOSE OF STUDY

Both the point- and finite-source stochastic ground motion models represent recent and promising developments in the quantification of strong ground motions for engineering design. The models as presented in this study combine appropriate elements of seismological source and wave propagation physics with a conventional geotechnical approach to evaluating the effects of nonlinear site response on strong ground motions. In this context, the models represent an attempt to bring together, perhaps for the first time, simultaneous consideration of earthquake source, path, and site processes.

Because of the recent nature of the model's development and its combined seismological and geotechnical aspects, as well as implementation at several DOE sites, a thorough evaluation and description of the model is warranted. Beginning with the inception of the initial stochastic point-source model in 1981 (Hanks and McGuire, 1981) and later extensions to include equivalent-linear site response and the finite-fault, numerous descriptions and validations have appeared in the literature as well as technical reports. This body of work contains descriptions and demonstrations of the general reliability of the models as well as careful validations. It provided the necessary confidence for use of the models in applications to design ground motions and is discussed in Chapter 2.

The overall purpose of the current work is to present a complete description of the models and

to perform a careful and thorough validation using a very extensive set of data. Having both the descriptions and validations in a single report is a convenient resource for those who wish to examine the models' components as well as evaluate strengths and weaknesses.

The validation and comparison exercises presented are entirely in terms of 5% damped pseudo absolute response spectra. This representation of strong ground motions is the most appropriate, currently acceptable, and least ambiguous approach to defining seismic hazard through design ground motions. The point-source model has been used to produce time histories for some time (Boore, 1983; Silva and Lee, 1987) and the finite-source model was selected by SCEC (Southern California Earthquake Center) to participate in supplying earthquake time histories for scenario earthquakes in Los Angeles. The comparison exercises could have been expanded to include time history comparisons for each earthquake at each site. However, since the stochastic point- and finite-source models are implemented primarily to provide response spectral estimates, the validation and comparison exercises concentrate exclusively on this component of the models.

In the current (and near future) approach to developing time history representations of the seismic hazard at a site for structural and soils analyses, spectral matching techniques are employed to scale time histories to a target response spectral representation. The time histories are generally selected to be consistent with the earthquakes, propagation paths, and site conditions which control or dominate the spectral representation. The time histories are either matched individually to the target response spectrum or, more properly, their ensemble average response spectrum matches the target so that each time history can reflect more natural variations in energy content with frequency. An approach that has been successfully implemented in

practice is the use of the stochastic models to help develop the design response spectrum and then employ suites of time histories from finite-fault simulations as input to spectral matching, if a sufficient number of suitable recorded motions are not available.

1.2 MODEL BACKGROUND

The stochastic ground motion model as implemented in the validation and comparison exercises had its inception with the early observation by Hanks (1979) that RMS (root mean square) accelerations at close distances could be interpreted as band-limited, finite duration white noise with a source spectrum consistent with the omega-square model of (Aki, 1967; and Brune, 1970, 1971). This early point-source model was later extended to estimate peak accelerations by applying random vibration theory (RVT) to relate peak time domain values to RMS accelerations (Hanks and McGuire, 1981). Hanks and McGuire (1981) further validated the model with existing strong motion data ($M \geq 4$) over the distance range of about 10 to 100 km. Their results showed that the simple point-source model, using a Fourier amplitude spectrum which is constant between the earthquake source corner frequency (Brune 1970, 1971) and a high-frequency cutoff due to propagation path/site damping, predicted peak acceleration values to within 50% or less. This is a remarkably close agreement since typical empirical relations have a standard deviation on peak acceleration of about 0.4 (natural log) which is a 40% factor (σ of 1.4).

The two corner frequencies (source and path/site) give rise to the band-limited characterization of the model with the strong motion or faulting duration defined as the inverse of the magnitude dependent source corner frequency (Chapter 2). The only free parameters in the Hanks/McGuire

model are the two corner frequencies and distance (1/R geometrical attenuation). Due to the assumed constant Fourier acceleration spectrum, the model can easily be integrated for the a_{RMS}:

$$a_{RMS} = 0.85 \frac{(2\pi)^2}{106} \frac{\Delta\sigma}{\rho R} \sqrt{\frac{f_{max}}{f_0}} \quad (1\text{-}1).$$

Assuming the acceleration time history is white Gausion noise, the RVT estimate of peak acceleration is given by

$$a_{max} = a_{RMS} \sqrt{2 \ln\left(\frac{2 f_{max}}{f_0}\right)} \quad (1\text{-}2).$$

The source corner frequency (f_0) is determined by the magnitude using Brune scaling (Chapter 2) and is the low frequency limit, while the high frequency limit, f_{max}, is taken as the highest frequency passed through the recording instrument. The stress drop $\Delta\sigma$ is constant and, for this first model, a value of 100 bars provided the best fit to the RMS and peak value data.

The model for a_{RMS} (Equation 1-1) is the simplest possible physically correct expression for ground motions. Equation 2-2 for PGA results from simply applying RVT to the A_{RMS} equation assuming the time domain duration is given by f_0^{-1}. This remarkably simple analytical expression correctly predicted the magnitude and distance dependencies of peak ground accelerations and showed that high frequency strong ground motion increases with magnitude only because the faulting duration increases. Larger earthquakes have larger high frequency

*Numerical coefficients for the point-source model are discussed fully in Chapter 2.

motions not because of any fundamental difference in source processes but simply because they last longer. This is a direct result of the stochastic assumption, the longer the source radiates, the higher the probability of observing larger motions.

The extension of this simple point-source model to response spectral ordinates as well as peak particle velocity resulted from the work of Boore (1983) and Boore and Joyner (1984). This work (Boore, 1983) also validated the model over a wide magnitude range ($0.4 \leq M \leq 7.7$) and wide frequency range (up to 400 Hz).

Methods for the generation of complete time histories using the point-source model was presented in Boore (1983) and by Silva and Lee (1987). The latter work also presented an implementation of the model to developing spectrum compatible time histories. Later, the model was extended to include crustal amplification effects (Boore, 1986; Silva and Lee, 1987), and validated with strong motion data and at long periods using amplitude and dominant period data recorded by the World Wide Standardized Seismographic Network for magnitudes up to 9.5 (Boore, 1986).

More recent extensions of the point-source model include an RVT equivalent-linear site response (Chapter 2) as well as accommodating crustal wave propagation (Ou and Herrmann, 1990; Chapter 2).

The development of the finite-fault version began in the late 1980's as a natural extension to the point-source model. Due to the success of the point-source model to accurately reflect average

source/site geometries, it was a natural next step to distribute the point-sources spatially and temporally and simply add them up to model the effects of source finiteness. The concept was not new (Chapter 2), the summing of recordings of small earthquake to simulate a large earthquake was suggested in 1978 (Hartzell, 1978) and forms the basis for several simulation approaches currently in use (Chapter 2). In the case of the finite-fault model implemented here, the simple point-source model motions are summed. This simple approach does not rely upon appropriate recordings and appeared to produce motions with an accuracy comparable to the more computational rigorous semi-empirical methods (Schneider et al., 1993; EPRI, 1995; SCEC, 1996; USGS, 1996).

1.3 APPLICATIONS OF THE MODEL

The point- and finite-source models may be implemented in two general ways: 1) to directly simulate motions for a particular deterministic source/path/site scenario and, 2) to simulate motions over a magnitude, distance, and site category grid. In the later application the synthetic data are then used as input to regression analyses resulting in region- and site-specific attenuation relations for use in either deterministic or probabilistic seismic hazard evaluations.

An additional important application of both the point- and finite-source models is the assessment of parameter sensitivity. Due in large part to the simplicity of the models, parametric analyses are straightforward and may be rapidly done by varying either a single parameter such as stress drop (EPRI, 1993) or groups of parameters (Silva, 1992; Roblee et al., 1996).

Variations of group of parameters can provide very useful insights as to whether the source or site is a controlling factor over a specific frequency range. If, for example, variation in slip

model and nucleation point results in a much greater variation in response spectral estimates than variations in site shear-wave velocity and G/G_{max} and hysteretic damping curves, then little is gained in extensive site investigations and laboratory dynamic testing (Roblee et al., 1996).

For these parametric assessments, parameters values are generally randomly selected using a Monte Carlo approach with the distributions and uncertainties constrained by observations (Chapter 3; Silva, 1992; EPRI, 1993; Roblee et al., 1996). The standard deviation of the resulting response spectra provides a statistically significant assessment or ranking of parameter sensitivities (Silva, 1992). Applying this approach to the entire set of unconstrained parameters (Chapter 5.15) results in an estimate of the parametric uncertainty appropriate to a particular design scenario combining the parametric uncertainty with the modeling uncertainty (Chapter 5) produces an estimate of the total uncertainty for the model prediction. This total uncertainty can then be used in probabilistic seismic hazard analyses as well as in estimating different fractiles for deterministic applications (Silva, 1992; EPRI, 1993).

1.4 DESCRIPTION OF VALIDATION STUDY

The validation study consists of both quantative and qualitative analyses. The quantative analyses (Chapter 5) involve modeling 15 earthquakes at over 500 sites (Table 5.2). In this application the modeling uncertainty is estimated as a chi-square on the average horizontal component response spectra for each earthquake as well as over all earthquakes (Chapter 5.15).

The point-source modeling includes initial inversions of Fourier amplitude spectra for stress drop, crustal damping (Q(f)), and site kappa values followed by forward modeling of response

spectra. In the finite-source modeling, available slip models are used along with the Q(f) models derived from the point-source inversions.

In order to extend the magnitude and distance range of the validations, qualitative comparisons are done between the point-source model predictions and a new empirical attenuation relation (Chapter 6). The empirical relation (Appendix A) was developed to specifically include the recent significant earthquakes which are treated in the quantative modeling exercises (Loma Prieta, Landers, and Northridge). This qualitative validation is done in two phases, initially involving an inversion of the spectra from the empirical relation for model parameters (Chapter 6.2) followed by a comparison of predicted response spectra using the derived parameters. The inversion involves a range in magnitudes (M 5.5 to M 7.5) to assess stress drop dependencies while the comparison concentrates on M 6.5, the approximate centroid of the empirical data distribution (Appendix A).

An additional and related validation more closely tied to recorded motions is a comparison of response spectral shapes (Sa/PGA). In this comparison exercise, point-source model shapes are compared to statistical shapes computed from recordings in magnitude bins over the range of about M 5.0 to M 7.4 (Chapter 7). This analysis provides a comparison of the magnitude scaling of the model directly to the recorded motions as well as an evaluation of the model's ability to accommodate site effects.

The combinations of the quantative validation exercises, using 15 well recorded earthquakes (plus 3 aftershocks), with the qualitative comparison exercises comprising a total of 503 sites

represents a comprehensive evaluation intended to clearly illustrate both the model's strengths and weaknessness.

CHAPTER 2

STOCHASTIC GROUND MOTION MODEL DESCRIPTION

2.1 BACKGROUND

In the context of strong ground motion, the term "stochastic" can be a fearful concept to some and may be interpreted to represent a fundamentally wrong or inappropriate model (abiet the many examples demonstrating that it works well; Boore, 1983, 1986). To allay any initial misgivings which may arise largely through ignorance and bias, a brief discussion of exactly what is stochastic in the stochastic ground motion model seems prudent.

The stochastic point-source model may be termed a spectral model in that it fundamentally describes the Fourier amplitude spectral density at the surface of a half-space (Hanks and McGuire, 1981). The model uses a Brune (1970, 1971) omega-square (Section 2.1) source description of the source Fourier amplitude spectral density which is easily the most widely used and qualitatively validated source description available. Seismic sources ranging from $M = -6$ (hydrofracture) to $M = 8$ have been interpreted in terms of the Brune omega-square model over the last 30 years with the general conclusion that it provides a reasonable and consistent representation of crustal sources, particularly for tectonically active regions such as plate margins. A unique phase spectrum can be associated with the Brune source spectrum to produce a complex spectrum and propagated using either exact or approximate (1-2- or 3-D) wave propagation algorithms to produce single or multiple component time histories. In this context the model is not stochastic, it is decidedly deterministic and as exact and rigorous as one chooses. A two-dimensional array of such point-source may be appropriately located on a fault

surface (area) and fired with suitable delays to simulate rupture propagation on an extended rupture plane (Section 2.2). As with the single point-source, any degree of rigor may be used in the wave propagation algorithm to produce multiple component or average horizontal component time histories. The result is a kinematic** finite-source model which has as its basis a source time history defined as a Brune pulse whose Fourier amplitude spectrum follows an omega-square model. This finite-fault model would be very similar to that used in published inversions for slip models (Chapter 4) if the 1-D propagation was treated using a reflectivity algorithm. This algorithm is a complete solution to the wave equation from static offsets to an arbitrarily selected high frequency cutoff (generally 1-2 Hz).

If one were to use recordings of small earthquakes made at a site of interest and whose sources are distributed along the expected rupture surface to model the wave propagation, the result would be an empirical Green function method (Hartzell, 1978). Proceeding further, if one simply had well distributed recordings at close distances to a small earthquake and the recordings are corrected back to the source by removing wave propagation effects using a simple approximation (say 1/R plus a constant for crustal amplification and radiation pattern), an empirical source function is obtained. This can be used to replace the Brune pulse to introduce some natural (although source, path, and site specific) variation into the dislocation time history. If this is coupled to an approximate wave propagation algorithm (asymptotic ray theory) which includes the direct rays and those which have undergone a single reflection, the result is the

**Kinematic source model is one whose slip (displacement) is defined (imposed) while in a dynamic source model forces (stress) is defined (see Aki and Richards 1980 for a complete description).

empirical source function method (EPRI, 1993). Combing the reflectivity propagation (which is generally limited to frequencies $\leq$ 1-2 Hz due to computational demands) with the empirical source function approach (appropriate for frequencies $\geq$ 1 Hz; EPRI, 1993) results in a broad band simulation procedure which is strictly deterministic at low frequencies (where an analytical source function is used) and incorporates some natural variation at high frequencies through the use of an empirical source function (Sommerville, 1995).

All of these techniques are fundamentally similar, well founded in seismic source and wave propagation physics, and importantly, they are all approximate. Simply put, all models are wrong and the single essential element in selecting a model is to incorporate the appropriate degree of rigor through extensive validation exercises. It is generally felt that more complicated models produce more accurate results, however, the implications of more sophisticated models with the increased number of parameters is often overlooked. This is not too serious a consequence in modeling past earthquakes since a reasonable range in parameter space can be explored to give the "best" results. However for future predictions, this increased rigor may carry undesirable baggage in parametric variability (Roblee et al., 1996). The effects of lack of knowledge (epistemic uncertainty; EPRI, 1993) regarding parameter values for future occurrences results in uncertainty or variability in ground motion predictions. It may easily be the case that a very simple model, such as a point-source, can have comparable, or even smaller, total variability (modeling plus parametric) to a much more rigorous model (EPRI, 1993). What is desired in a model is sufficient sophistication such that it captures the dominant and stable features of source, distance, and site dependencies observed in strong ground motions. It is these considerations which led to the development of the stochastic point- and finite-source

models and, in part, leads to the stochastic element of the models.

The stochastic nature or component of the point- and finite-source models is simply an assumption made about the character of ground motion time histories which permits stable estimates of peak parameters (e.g. acceleration, velocity, strain, stress, oscillator response) to be made without computing detailed time histories (Hanks and McGuire, 1981; Boore, 1983). This process uses random vibration theory to relate a time domain peak value to the time history root-mean-square (RMS) value (Boore, 1983). The assumption of the character of the time history for this process to strictly apply is that it be normally distributed random noise and stationary (its statistics do not change with time) over its duration. A visual examination of any time history quickly reveals that this is clearly not the case: time histories (acceleration, velocity, stress, strain, oscillator) start, build up, and then diminish in time. However poor the assumption of stationary Gaussian noise may appear, the net result is that the assumption is weak enough to permit the approach to work surprisingly well, as numerous comparisons with recorded motions and both qualitative and quantative validations have shown (Hanks and McGuire, 1981; Boore, 1983, 1986; McGuire et al., 1984; Boore and Atkinson, 1987, Silva and Lee, 1987; Toro and McGuire, 1987; Silva et al., 1990; EPRI, 1993; Schneider et al., 1993; Silva and Darragh, 1995). Corrections to RVT are available to accommodate different distributions as well as non-stationarity and are usually applied in the estimation of peak oscillator response in calculating response spectra (Boore and Joyner, 1984; Toro, 1985).

2.2 POINT-SOURCE MODEL

The conventional stochastic ground motion model uses an ω-square source model (Brune, 1970,

1971) with a single corner frequency and a constant stress drop (Boore, 1983; Atkinson, 1984). Random vibration theory is used to relate RMS (root-mean-square) values to peak values of acceleration (Boore, 1983), and oscillator response (Boore and Joyner, 1984; Toro, 1985; Silva and Lee, 1987) computed from the power spectra to expected peak time domain values (Boore, 1983).

The shape of the acceleration spectral density, a(f), is given by

$$a(f) = C \frac{f^2}{1+(\frac{f}{f_C})^2} \frac{M_0}{R} P(f) A(f) e^{-\frac{\pi f R}{\beta_0 Q(f)}} \qquad (2\text{-}1)$$

where

$C = (\frac{1}{\rho_0 \beta_0^3}) \cdot (2) \cdot (0.55) \cdot (\frac{1}{\sqrt{2}}) \cdot \pi.$

M_0 = seismic moment,

R = hypocentral distance,

β_0 = shear-wave velocity at the source,

ρ_0 = density at the source

Q(f) = frequency dependent quality factor (crustal damping),

A(f) = amplification,

P(f) = high-frequency truncation filter,

f_C = source corner frequency.

C is a constant which contains source region density (ρ_0) and shear-wave velocity terms and accounts for the free-surface effect (factor of 2), the source radiation pattern averaged over a sphere (0.55) (Boore, 1986), and the partition of energy into two horizontal components ($1/\sqrt{2}$).

Source scaling is provided by specifying two independent parameters, the seismic moment (M_0) and the high-frequency stress parameter or stress drop ($\Delta\sigma$). The seismic moment is related to magnitude through the definition of moment magnitude **M** by the relation

$$\log M_0 = 1.5\,\mathbf{M} + 16.05 \qquad \text{(Hanks and Kanamori, 1979)} \qquad (2\text{-}2).$$

The stress drop ($\Delta\sigma$) relates the corner frequency f_c to M_0 through the relation

$$f_c = \beta\,(\Delta\sigma/8.44\,M_0)^{1/3} \qquad \text{(Brune; 1970, 1971)} \qquad (2\text{-}3).$$

The stress drop is sometimes referred to as the stress parameter (Boore, 1983) since it directly scales the Fourier amplitude spectrum for frequencies above the corner frequency (Silva, 1991; Silva and Darragh 1995). High (> 1 Hz) frequency model predictions are then very sensitive to this parameter (Silva, 1991; EPRI, 1993) and the interpretation of it being a stress drop or simply a scaling parameter depends upon how well real earthquake sources (on average) obey the omega-square scaling (Equation 2-3) and how well they are fit by the single-corner-frequency model. The parameter is a physical parameter if the model is considered to generally work well and its values have physical interpretations in source processes. Otherwise, it simply a high frequency scaling factor.

The spectral shape of the single-corner-frequency ω-square source model is then described by the two free parameters M_0 and $\Delta\sigma$. The corner frequency increases with the shear-wave velocity and with increasing stress drop, both of which may be region dependent.

The amplification accounts for the increase in wave amplitude as seismic energy travels through lower- velocity crustal materials from the source to the surface. The amplification depends on average crustal and near surface shear-wave velocity and density.

The P(f) filter is an attempt to model the observation that acceleration spectral density appears to fall off rapidly beyond some region-dependent maximum frequency. This observed phenomenon truncates the high frequency portion of the spectrum and is responsible for the band-limited nature of the stochastic model. The band limits being the source corner frequency at low frequency and the high frequency spectral attenuation. This spectral fall-off has been attributed to near-site attenuation (Hanks, 1982; Anderson and Hough, 1984) or to source processes (Papageorgiou and Aki, 1983) or perhaps to both effects. In the Anderson and Hough (1984) attenuation model, adopted here, the form of the P(f) filter is taken as

$$P(f) = e^{-\pi\kappa(r)f} \qquad (2\text{-}4).$$

Kappa (r) (κ(r) in Equation 2-4) is a site and distance dependent parameter that represents the effect of intrinsic attenuation upon the wavefield as it propagates through the crust from source to receiver. Kappa (r) depends on epicentral distance (r) and on both the shear-wave velocity (β_R) and quality factor (Q_S) averaged over a depth of H beneath the site (Hough et al., 1988;).

At zero epicentral distance kappa (κ) is given by

$$\kappa = \frac{H}{\overline{\beta_R}\ \overline{Q_S}} \qquad (2\text{-}5).$$

The bar in Equation 2-5 represents an average of these quantities over a depth H. The value of kappa at zero epicentral distance is attributed to attenuation in the very shallow crust directly below the site (Hough and Anderson. 1988; Silva and Darragh, 1995). The intrinsic attenuation along this part of the path is not thought to be frequency dependent and is modeled as a frequency independent, but site dependent, constant value of kappa (Hough et al., 1988; Rovelli et al., 1988). This zero epicentral distance kappa is the model implemented in this study.

The crustal path attenuation from the source to just below the site is modeled with the frequency-dependent quality factors Q(f).

The Fourier amplitude spectrum, a(f), given by Equation 2-1 represents the stochastic ground motion model employing a Brune source spectrum that is characterized by a single corner frequency. It is appropriate for a point-source and models direct shear-waves in a homogeneous half-space (with effects of a velocity gradient through the A(f) filter, Equation 2-1). For horizontal motions, vertically propagating shear-waves are assumed. Validations using incident inclined SH-waves with raytracing to find appropriate incidence angles leaving the source showed little reduction in uncertainty. For vertical motions P/SV propagators are used coupled with raytracting to model incident inclined plane waves (EPRI, 1993).

At zero epicentral distance kappa (κ) is given by

$$\kappa = \frac{H}{\overline{\beta_R}\,\overline{Q_S}} \qquad (2\text{-}5).$$

The bar in Equation 2-5 represents an average of these quantities over a depth H. The value of kappa at zero epicentral distance is attributed to attenuation in the very shallow crust directly below the site (Hough and Anderson. 1988; Silva and Darragh, 1995). The intrinsic attenuation along this part of the path is not thought to be frequency dependent and is modeled as a frequency independent, but site dependent, constant value of kappa (Hough et al., 1988; Rovelli et al., 1988). This zero epicentral distance kappa is the model implemented in this study.

The crustal path attenuation from the source to just below the site is modeled with the frequency-dependent quality factors Q(f).

The Fourier amplitude spectrum, a(f), given by Equation 2-1 represents the stochastic ground motion model employing a Brune source spectrum that is characterized by a single corner frequency. It is appropriate for a point-source and models direct shear-waves in a homogeneous half-space (with effects of a velocity gradient through the A(f) filter, Equation 2-1). For horizontal motions, vertically propagating shear-waves are assumed. Validations using incident inclined SH-waves with raytracing to find appropriate incidence angles leaving the source showed little reduction in uncertainty. For vertical motions P/SV propagators are used coupled with raytracting to model incident inclined plane waves (EPRI, 1993).

Equation 2-1 represents an elegant ground motion model that accommodates source and wave propagation physics as well as propagation path and site effects with an attractive simplicity. The model is appropriate to an engineering characterization of ground motion since it captures the general features of strong ground motion in terms of peak acceleration and spectral composition with a minimum of free parameters (Boore, 1983; McGuire et al., 1984; Boore, 1986; Silva and Green, 1988; Silva et al., 1988; Schneider et al., 1993). An additional important aspect of the stochastic model employing a simple source description is that the region dependent parameters can be evaluated by observations of small local or regional earthquakes. Region specific seismic hazard evaluations can then be made for areas with sparse strong motion data with relatively simple spectral analyses of weak motion (Silva, 1992).

In order to compute peak time-domain values, i.e. peak acceleration and oscillator response, RVT is used to relate RMS computations to peak value estimates. Boore (1983) and Boore and Joyner (1984) contain an excellent development of the RVT methodology as applied to the stochastic ground motion model. The procedure, in general, involves computing the RMS value by integrating the power spectrum from zero frequency to the Nyquist frequency and applying Parsevall's relation. Extreme value theory is then used to estimate the expected ratio of the peak value to the RMS value of a specified duration of the stochastic time history. The duration is generally taken as the inverse of the corner frequency (Boore, 1983).

Factors that effect strong ground motions such as surface topography, finite and propagating seismic sources, laterally varying near-surface velocity and Q gradients, and random inhomogeneities along the propagation path are not included in the model. While some or all

of these factors are generally present in any observation of ground motion and may exert controlling influences in some cases, the simple and elegant stochastic point-source model appears to be robust in predicting median or average properties of ground motion (Boore 1983, 1986; Schneider et al., 1993; Silva, 1993). For this reason it represents a powerful predictive and interpretative tool for engineering characterization of strong ground motion.

2.3 FINITE-SOURCE MODEL GROUND MOTION MODEL

In the near-source region of large earthquakes, aspects of a finite-source including rupture propagation, directivity, and source-receiver geometry can be significant and may be incorporated into strong ground motion predictions. To accommodate these effects, a methodology that combines the aspects of finite-earthquake-source modeling techniques (Hartzell, 1978; Irikura 1983) with the stochastic point-source ground motion model has been developed to produce response spectra as well as time histories appropriate for engineering design (Silva et al., 1990; Silva and Stark, 1992). The approach is very similar to the empirical Green function methodology introduced by Hartzell (1978) and Irikura (1983). In this case however, the stochastic point-source is substituted for the empirical Green function and peak amplitudes; PGA, PGV, and response spectra (when time histories are not produced) are estimated using random process theory.

Use of the stochastic point-source as a Green function is motivated by its demonstrated success in modeling ground motions in general and particularly strong ground motions (Boore, 1983, 1986; Silva and Stark, 1992; Schneider et al., 1993; Silva and Darragh, 1995) and the desire to have a model that is truly site and region specific. The model can accommodate a region

specific Q(f), Green function sources of arbitrary moment or stress drop, and site specific kappa values. The necessity of regional and site specific recordings or the modification of possibly inappropriate empirical Green functions is eliminated.

For the finite-source characterization, a rectangular fault is discretized to provide the locations of NS subfaults of moment M_0^s. The empirical relationship

$$A = M - 4.0 \qquad (2\text{-}6).$$

is used to assign areas to both the target earthquake (if its rupture surface is not fixed) as well as to the subfaults and implies a constant static stress drop of about 30 bars. This relation results from regressing log area on M using the data of Wells and Coppersmith (1994) with the M coefficient fixed at unity. The subevent magnitude M_s is generally taken in the range of 5.0-6.5 depending upon the size of the target event. M_s 5.0 is used for crustal earthquakes with M in the range of 5.5 to 8.0 and M_s 6.4 is used for large subduction earthquakes with $M > 7.5$. The value of NS is determined as the ratio of the target event area to the subfault area. To constrain the proper moment, the total number of events summed (N) is given by the ratio of the target event moment to the subevent moment. The subevent and target event rise times are determined by the equation

$$\log \tau = 0.33 \log M_0 - 8.54 \qquad (2\text{-}7)$$

which results from a fit to the rise times used in the finite-fault modeling exercises in Chapter 5. Slip on each subfault is assumed to continue for a time τ. The ratio of target-to-subevent rise times is given by

$$\frac{\tau}{\tau^s} = 10^{0.5\,(M - M^s)} \qquad (2\text{-}8)$$

and determines the number of subevents to sum in each subfault. This approach is generally referred to as the constant-rise-time model and results in variable slip velocity for nonuniform slip distributions. Alternatively, one can assume a constant slip velocity resulting in a variable-rise-time model for heterogenous slip distributions.

Recent modeling of the Landers (Wald and Heaton, 1994b), Kobe (Wald, 1996) and Northridge (Hartzell et al. 1996) earthquakes suggests that a mixture of both may be present. Longer rise times seem to be associated with areas of larger slip with the ratio of slip-to-rise time (slip velocity) being depth dependent. Lower slip velocities (longer rise times) are associated with shallow slip resulting in relatively less short period seismic radiation. This result may explain the general observation that shallow slip is largely aseismic. The significant contributions to strong ground motions appear to originate at depths exceeding about 4 km (Campbell, 1993; Boore et al., 1994) as the fictitious depth term in the empirical attenuation relation presented in Appendix A suggests. Finite-fault models generally predict unrealistically large strong ground motions for large shallow (near surface) slip using rise times or slip velocities associated with deeper (> 4 km) zones of slip. This is an important and unresolved issue in finite-fault modeling and initial attempts using depth dependent rise times as well as depth dependent slip

velocities in the validation exercises for the earthquakes with shallow slip (Landers and Imperial Valley) had mixed success. A more thorough analysis is necessary, ideally using several well validated models, before this issue can be satisfactorily resolved. As a result, the simple constant rise time model was retained in the validation exercises since it generally performed better than the constant slip velocity model. Reducing the subevent stress drop to 5 bars in the Brune subevent source spectrum for earthquakes with shallow slip provided good results (Chapter 5) and allowed the validations to include shallow slip earthquakes.

To introduce heterogeneity of the earthquake source process into the stochastic finite-fault model, the location of the sub-events within each subfault (Hartzell, 1978) are randomized as well as the subevent rise time. The stress drop of the stochastic point-source Green function is taken as 30 bars, consistent with the static value based on the M 5.0 subevent area using the equation

$$\Delta\sigma = \frac{7}{16}\left(\frac{M_e}{R_e^3}\right) \qquad \text{(Brune, 1970, 1971)} \qquad (2\text{-}8)$$

where R_e is the equivalent circular radius of the rectangular sub-event.

Different values of slip are assigned to each subfault as relative weights so that asperities or non-uniform slip can be incorporated into the methodology. The rupture velocity is taken as depth independent at a value of 0.8 times the shear-wave velocity generally at the half-depth of the slip surface. A random component (20%) is added to the rupture velocity. The radiation pattern is computed for each subfault, a random component added, and the RMS applied to the motions computed at the site.

The ground-motion time history at the receiver is computed by summing the contributions from each subfault associated with the closest Green function, transforming to the frequency domain, and convolving with the Green function spectrum (Equation 2-1). The locations of the Green functions are generally taken at center of each subfault for small subfaults or at a maximum separation of about 5 to 10 km for large subfaults. As a final step, the individual contributions associated with each Green function are summed in the frequency domain multiplied by the RMS radiation pattern, and the resultant power spectrum at the site is computed. The appropriate duration used in the RVT computations for PGA, PGV, and oscillator response is computed by transforming the summed Fourier spectrum into the time domain and computing the 5 to 75% arias intensity (Ou and Herrmann, 1990).

As with the point-source model, crustal response effects are accommodated through the amplification factor (A(f)) or by using vertically propagating shear waves through a vertically heterogenous crustal structure. Propagation path damping, through the Q(f) model, is incorporated from each fault element to the site. Near-surface crustal damping is incorporated through the kappa operator (Equation 2-1). To model crustal propagation path effects, the method of Ou and Herrmann (1990) can be applied from each subfault to the site.

Time histories may be computed in the process as well by simply adding a phase spectrum appropriate to the subevent earthquake. The phase spectrum can be extracted from a recording made at close distance to an earthquake of a size comparable to that of the subevent (generally M 5.0 to 6.5). Interestingly, the phase spectrum need not be from a recording in the region of interest. A recording in WNA can effectively be used to simulate motions appropriate to ENA

(Silva et al., 1989). Transforming the Fourier spectrum computed at the site into the time domain results in a computed time history which includes all of the aspects of rupture propagation, source finiteness, as well as propagation path and site effects.

For fixed fault size, mechanism, and moment, the specific source parameters for the finite-fault are slip distribution, location of nucleation point, and site azimuth. The propagation path and site parameters remain identical for both the point- and finite-source models.

2.4 SITE EFFECTS MODEL

To model soil and soft rock response, an RVT-based equivalent-linear approach is used by propagating either the point- or finite-source outcrop power spectral density through a one-dimensional column. RVT is used to predict peak time domain values of shear-strain based upon the shear-strain power spectrum. In this sense, the procedure is analogous to the program SHAKE (Schnabel et al., 1972) except that peak shear strains in SHAKE are measured in the time domain. The purely frequency domain approach obviates a time domain control motion and, perhaps just as significantly, eliminates the need for a suite of analyses based on different input motions. This arises because each time domain analysis may be viewed as one realization of a random process. In this case, several realizations of the random process must be sampled to have a statistically stable estimate of site response. The realizations are usually performed by employing different control motions whose response spectrum matches a specified target. In the frequency-domain approach, the estimates of peak shear strains as well as oscillator response are, as a result of the RVT, fundamentally probabilistic in nature. Stable estimates of site response can then be rapidly computed permitting statistically significant estimates of

uncertainties based on parametric variations.

The parameters that influence computed response include the shear-wave velocity profile and the strain dependencies of both the shear modulus and shear-wave damping.

CHAPTER 3

GENERIC SITE CONDITIONS AND CRUSTAL MODEL

3.1 SITE AND CRUSTAL MODELS

For the point- and finite-source validation exercises, both generic site categories and representative shear-wave velocity profiles as well as a generic crustal model are necessary. The desire is to produce generic site category profiles and a generic crustal model which are consistent with the strong motion data used in the empirical regressions (Appendix A). The site category profiles are placed on top of the generic crustal model for the point-source simulation comparisons to the empirical attenuation (Chapter 5) and statistical response spectral shapes (Chapter 6). For the point- and finite-source individual earthquake validation exercises (Chapter 4), the generic category profiles are places on top of the local/regional crustal models used in determining the slip models.

3.2 GENERIC SITE CATEGORIES

The development of appropriate generic site conditions for site classification is always a perplexing problem. Ideally one desires a quantative basis such as an average shear-wave velocity (with bounds) over some depth interval (Boore et al., 1993) with the velocity average and bounds as well as depth carefully chosen to distinguish significant and stable differences in site response over a frequency range of engineering interest. While this can be done with some effort, it then leaves the issue of requiring accurate measures of shear-wave velocities. For applications to engineered structures where seismic safety is an issue, this is generally not a significant problem as the site licensing agency will usually mandate such measurements.

However, for the analysis of recorded motions, the requirement of accurate shear-wave velocity measurements at recording sites is a significant issue. Most strong motion recording sites do not have reliable shear-wave velocity profiles thereby greatly reducing the number of available sites for regressions analyses or validation exercises. One is faced with the problem of a more rigorous and accurate site classification scheme at the cost of less well constrained (resolved) empirical regression parameters as well as more poorly constrained modeling uncertainty and bias, all due to fewer available sites.

As a result of these considerations, a more qualitative site classification scheme has been implemented to provide two categories: generic soft rock and deep soil. These broad categories provides consistency between the new empirical attenuation relation developed (Appendix A) and generic site conditions for the sixteen validation earthquakes (Chapter 4). The new categories also permit use of the maximum number of sites for both the empirical regressions and validation exercises as well as recognize that typical rock site conditions in WNA is not represented by a shear-wave velocity of 2,500 ft/sec at the surface.

3.1.1 Soft Rock

The soft rock category is a combination of the Geomatrix categories A and B (rock and shallow/stiff soil, Table 3.1) while deep soil is a combination of the Geomatrix C and D categories (deep narrow and wide valleys).

Geomatrix categories A and B were combined based on an examination of a median, shear-wave velocity profile computed from measured profiles categorized as A (Figure 3.1a). The profile

for category A in Figure 3.1a shows low shear-wave velocities near the surface with a steep shallow gradient which is not unlike the profile for category B (shallow/stiff soil), in view of their variabilities. These profiles suggest that combining the two is a reasonable representation of typical California soft rock site conditions and the combined profile is shown in Figure 3.2. The smoothed version represents the base case soft rock category. Comparing this combined profile (Geomatrix A and B) with the median profiles computed at sites with measured shear-wave velocities and categorized using the USGS criterion (Table 3.1, Figure 3.3) shows a similarity with USGS category B (soft rock/stiff soil). The USGS category A (hard rock) is very poorly represented in the strong motion data base and is likely relatively rare in California except at exposures of unweathered to slightly weathered crystalline rocks.

3.1.2 Deep Soil

For the deep soil category, the Geomatrix categories C and D (Figure 3.1b) are similar, again in view of their variabilities, with the narrow valley deep soil showing a slightly steeper gradient and stiffer conditions, possibly due to depositional environment and perhaps shallower average depths.*** As with the rock/shallow soil category, the Geomatrix deep soils (C and D) were combined to produce a single deep soil category with the profile shown in Figure 3.4. The generic deep soil profile may be characterized as cohesionless soils comprised of sands, gravels, and low PI clays. As with the soft rock profile (Figure 3.2), the smoothed version represents the base case profile for the analyses.

***It is important to note that the profiles are analyzed to their maximum depth so the velocities near the bottom of shallow soil sites may reflect weathered rock.

The soft sites, characterized by Geomatrix E and USGS D categories, are not considered in this work. These sites generally represent conditions which contain substantial cohesive soils such as San Francisco Bay muds and clays and it is not clear that they can be treated in a generic sense. Additionally, as with the hard rock sites (USGS A and Geomatrix Category A), two few recordings are available either to constrain empirical regressions or develops meaningful statistics for validation exercises.

3.3 PROFILE RANDOMIZATION

In order to accommodate both epistemic and aleatory uncertainty in a realistic manner into the category profiles, a profile randomization scheme (Appendix C) was implemented in the comparisons to empirical attenuation and statistical response spectral shapes. In this approach, both shear-wave velocities and layer thicknesses are varied using category specific correlation models based on an analysis of variance of a total of over 500 measured shear-wave velocity profiles (Appendix C). The algorithm starts with a given profile (base case or best estimate) such as soft rock (Figure 3.2, smoothed) or deep soil (Figure 3.4 smoothed) and generates a suite of random profiles about the input profile (base case or best estimate) with correlation statistics appropriate to the category (or combination of categories).

At the specified base of the profile, generally taken as the first competent layer, the velocity is varied according to a lognormal distribution with a standard error**** (natural log) of 0.3 (EPRI,

****In the context of these analyses, competent material refers to rock or sediment (geologic description) with a shear-wave velocity of at least 3,000 ft/sec and is therefore expected to remain predominately linear under moderate to high loading conditions (50-70%g).

1993) and is constrained to have a higher velocity than the layer above.

In addition to velocity and layer thickness randomization, depth to competent material is also varied for the deep soil category. This variation is necessary to accommodate the different soil profile depths at the strong motions recording sites. While the actual statistics of this variation awaits accurate velocity measurements at recording sites, a reasonable assumption is that an average deep soil site is deep ($\geq$ 100 ft) and the question becomes one of determining an average reasonable depth. To address this question, two considerations present themselves: the bandwidth of interest, the lower end of which approximately determines the base case soil column depth and the comfort level (maximum depth) in application of the vertically propagating shear-wave model and nonlinear dynamic soil properties.

For the first consideration, the bandwidth of interest is approximately 50-0.5 Hz which translates to a base-case soil column depth of about 500-1,000 ft, depending upon loading conditions. For the depth of a 1-D analysis, the recent EPRI (1993) work in modeling motions at three test sites using equivalent-linear and three nonlinear codes showed close agreement with recorded motions to depths of about 700 ft using laboratory derived dynamic material properties. It is not unreasonable to assume the modeling to be a realistic representation of ground motions to a depth of about 1,000 ft and, at this point, verify this assumption in the validation and comparison exercises.

In addition to an appropriate average depth for generic profiles, there is another important issue associated with accommodating profile variation in randomization. In general, a site specific

soil profile does not display a largely monatomic velocity increase with depth (except perhaps for till and loess sites) and the presence of these variations or notches (low velocity zones) has the effect of reducing the short period motions (particularly as the level of loading increases) compared to a smooth profile with equivalent travel times. As a result, the median response spectra computed over a number of analyses using random profiles (generally 30-50; EPRI, 1993) is generally lower than the spectrum computed using the base case (or median) profile. To illustrate this, Figure 3.5 shows the spectra computed for a M 6.5 earthquake at a distance of 15 km using a 500 ft deep base case soil profile as well as the median and $\pm$ 1σ spectra using 30 random profiles varying in depth from 100-1,000 ft. Figure 3.6 shows the median and $\pm$ 1σ profiles from the randomization as well as the base case deep soil input profile (Figure 3.4). Figure 3.6 suggests that the profile randomization scheme is providing a reasonable representation of the actual profile variation and Figure 3.5 shows a difference of about 10-20% between the median and base case responses.

This difference is an important issue in the validation exercises (the comparison exercises, Chapters 5 and 6, use randomized profiles) since only the base case profiles are used. This suggests that the short period motions from the simulations should overpredict on average, resulting in a stable negative bias. Ideally, to obtain an unbiased estimate of the modeling uncertainty and bias, perhaps the best fitting single profile response should be taken at each site. However with 588 sites this would necessities over 17,000 additional runs as well as developing an acceptable and stable selection criterion.

The case for the generic rock site is shown in Figure 3.7 for the same magnitude and distance. In this case, the generic rock profile (Figure 3.8) is varied to a depth of about 100 ft, the maximum depth constraining the correlation model for this category (rock sites are typically not drilled to greater depths). As with the deep soil, a significant difference exists between the median response spectrum and the spectrum computed using the base case profile (Figure 3.8). The difference is greater for the rock profile because the absolute velocity variation is greater for rock than soil. That is, the COV for shear-wave velocity is about 0.4 for both rock and soil near the surface and decreases slightly with depth (Appendix C) resulting in about the same relative variation for both rock and deep soil sites (lognormal distribution). However, at equivalent depths, the median shear-wave velocity is much greater at rock than at soil sites resulting in a greater absolute variation in velocity at rock sites. This difference in absolute variation in shear-wave velocities between rock and deep soil sites is consistent with the observed higher variation in strong ground motions at rock sites relative to deep soil sites.

In general, the difference between the median response and response of the base case profile increases with loading level due to nonlinear material properties (rock and soil). As the control motion increases in amplitude, the equivalent-linear analysis increases the strains in the low-velocity notches thereby decreasing the velocity and increasing the damping at each iteration. The effort is to filter the energy through scattering as well as damping. It is likely that a nonlinear analysis would not develop as much reduction in shear-modulus and increase in damping in the low velocity zones as the equivalent-linear strain compatible values resulting in less of a difference between median response and base case response as loading levels increase.

At some point (in loading level and profile stiffness space) the equivalent-linear approach must be considered as a poor, rather that good, approximation to nonlinear response and probably yield lower motions (at short periods) than a nonlinear analysis using comparable dynamic material properties. The recent EPRI (1993) work showed that for a deep stiff soil site with pronounced low velocity zones (Gilroy 2), similar on average to our generic deep soil, the equivalent-linear provided very similar results to three different nonlinear codes as well as to recorded motions for control motions up to about 50%g. In the validation exercises (Chapter 4), control motions likely exceeded 50%g in some cases (such as the Northridge earthquake) and the equivalent-linear approach appears to perform satisfactorily. However, it must be kept in mind that in both the comparison and validation exercises, modulus reduction as and damping curves were either developed (generic rock and soil, Peninsular Ranges, and Imperial Valley) or assessed (North Coast, Mojave, and all others) in the context of equivalent-linear analyses. Because of the differences in response between equivalent-linear and nonlinear analyses at high loading levels for profile with notches, these dynamic material properties may be most appropriate in the context of equivalent-linear analyses. What is required is a careful and consistent evaluation of the differences in response between the two approaches in terms of loading levels, profile characteristics, and dynamic material properties.

3.4 GENERIC CRUSTAL MODEL

In the comparison exercises where point-source model predictions are compared to empirical results and to statistical response spectral shapes, an appropriate generic crustal model is needed beneath the generic rock and soil site profiles. Because raytracing is not used in these comparisons, as there is no apparent flattening in the empirical attenuation with distance

(Chapter 5 and Appendix A), the requirements for a generic crustal model are greatly relaxed. In this context, the only purpose of the crustal model is to provide representative amplification for vertically propagating shear-waves from the source region (taken as 6-8 km depending on magnitude, Chapters 5 and 6) to the base of the generic site profiles in a manner which is appropriate for the majority of data in the strong motion data base (Appendix B). To generate a generic crustal model, models from the regions listed in Table 3.2a were simply averaged. Since the generic crustal model is intended to represent hard (California) rock site conditions, Peninsular Range models (e.g. Northridge; Chapter 5) are not included as they generally reflect some influence of the deep Los Angeles basin. To show the shallow gradient more clearly, the generic crustal model extended to three different depths is shown in Figures 3.9 to 3.11. For the shallow portion of the generic crustal model ($\approx$ top 100m), the soft rock gradient (Figure 3.2) was used to reduce the velocities to 1km/sec. This is reasonable since regional models are generally poorly constrained, particularly for shear-waves, in the top 1 km or so. Both the soft rock and deep soil (Figure 3.6) profiles are placed at a depth corresponding to 1 km/sec (about 30m) to produce the generic rock and soil crustal models. Figures 3.9 to 3.10 actually show the soft rock crustal model. The generic California rock has a shear-wave velocity over the top 30m of 1 km/sec. The generic crustal model is taken to be representative of hard (California) rock conditions at the surface and appropriate to produce outcropping control motions for the soft rock and deep soil site profiles and is listed in Table 3.2b.

Table 3.1 Strong motion Recording Site Classifications

GEOMATRIX SITE CLASSIFICATION

Geotechnical subsurface characteristics (Robert Youngs, personal communications)

A = Rock. Instrument on rock (V_s > 600 mps or < 5m of soil over rock.

B = Shallow (stiff) soil. Instrument on/in soil profile up to 20m thick overlying rock.

C = Deep narrow soil. Instrument on/in soil profile at least 20m thick overlying rock, in a narrow canyon or valley no more than several km wide.

D = Deep broad soil. Instrument on/in a soil profile at least 20m thick overlying rock, in a broad valley.

E = Soft deep soil. Instrument on/in deep soil profile with average V_s < 150 mps.

USGS SITE CLASSIFICATION SCHEMES (Boore et al., 1994)

Average shear-wave velocity to a depth of 30m is:

A = > 750 m/s

B = 360 - 750

C = 180 - 360

D = < 180 m/s

Table 3.2a Regional Crustal Models Used In Developing The Generic Crustal Model

Earthquake	Model Source
Loma Prieta	Wald (1991)
Coyote Lake	Liu and Helmberger (1983)
Morgan Hill	Hartzell and Heaton (1986)
Landers	Wald and Heaton (1994b)
North Palm Springs	Hartzell (1989)
Cape Mendocino	Graves (1994)
Coalinga	Eaton (1990)

Table 3.2b Generic Crustal Model

Thickness (m)	V_s (km/sec)	Density (cgs)
1.52	243.83	2.00
2.44	304.79	2.00
2.13	365.74	2.00
3.05	426.70	2.00
4.27	533.37	2.00
3.35	630.90	2.00
4.27	716.25	2.00
5.79	838.16	2.00
6.71	966.17	2.00
33.00	1000.00	2.02
40.00	1190.00	2.08
65.00	1360.00	2.12
100.00	1530.00	2.17
115.00	1720.00	2.23
160.00	1890.00	2.28
237.00	2070.00	2.33
228.00	2300.00	2.40
550.00	2550.00	2.47
800.00	2760.00	2.53
1100.00	2970.00	2.59
1550.00	3150.00	2.64
2400.00	3320.00	2.69
6100.00	3500.00	2.75
7500.00	3700.00	2.80
9000.00	4000.00	2.89
20000.00	4250.00	2.96

CHAPTER 4

REGIONAL INVERSIONS

4.1 GEOGRAPHIC PROVINCES

To determine whether regional differences in path (Q(f)) and site (kappa) parameters are resolvable within California, earthquakes which were located within the geographic provinces of Wesnousky (1986) (Figure 4.1) were combined in the inversions. In these regional inversions only events which had recordings spanning a range in distance sufficient to constrain Q(f) and kappa (10 to beyond 50 km) were used in the regional inversions. For the remaining earthquakes (Chapter 5), the region specific Q(f) was fixed and inversions performed only for stress drop and kappa values.

The geographic provinces for which sufficient data were available are the North Coast, Mojave, and Peninsular Ranges. The earthquakes and sites taken to be generally consistent with these provinces are: the Loma Prieta, Coyote Lake, and Morgan Hill for the North Coast; Landers and North Palm Springs for Mojave; and the Whittier Narrows, Northridge, and San Fernando earthquakes for the Peninsular Ranges. While some of the sites do span provinces (the Landers earthquake has sites in Los Angeles, Chapter 5) which is undesirable, large source-to-site distances are required to result in reasonably unique Q(f) models. The basic assumption is that a sufficient amount of the path lies within the desired province to have a dominate affect on the inversions.

4.2 INVERSION METHOD

In the inversion scheme, earthquake source, path and site parameters are obtained by using a nonlinear least-squares inversion of Fourier amplitude spectra for the point-source model parameters (Chapter 2). The bandwidth for each amplitude spectrum computed from recordings was judgmentally selected based upon visual examination. In no cases did the bandwidth extend beyond the filter corner frequencies (Appendix B). The inversion scheme treats multiple earthquakes and sites simultaneously with the common crustal path damping parameter Q(f). The parameter covariance matrix is examined to determine which parameters which may be resolved for each data set. Asymptotic standard errors are computed at the final iteration. The five parameters which may be determined include: kappa (site-specific attenuation), Q_0 and η (frequency-dependent path Q model), M, and corner frequency. The procedure uses the Levenberg-Marquardt algorithm (Press et al., 1986). Crustal and soil profile amplification is accommodated in the inversion scheme by incorporating the appropriate mean transfer functions in the model spectra (Chapters 5 and 6).

To reduce the non-uniqueness inherent in inversion schemes, a suite of starting models is employed. The final set of parameters is selected based upon a visual inspection of the model fit to the Fourier amplitude spectrum, the chi-square values, and the parameter covariance matrix.

The stress drop is calculated from the moment and corner frequency using the relation

$$f_C = \bar{\beta}_0 \left(\frac{\Delta \sigma}{8.44 \cdot M_0}\right)^{\frac{1}{3}} \qquad (4\text{-}1)$$

In the final inversions the magnitude (M) was fixed at the values assigned in the strong motion catalogue (Appendix B). These are the "consensus" values and are usually long period moment estimates. The inversion process generally results in lower magnitudes, partially due to the use of only strong motion data (limited low frequency range) and because of the low frequency overprediction of the single-corner-frequency point-source model at close distances (Chapter 6). Use of the inversion magnitudes would significantly reduce the uncertainty and bias estimates, but it would also affect the stress drop estimates (Equation 4-1). To use the stress drops, model uncertainty, and bias estimates in forward predictions, the magnitude will generally be specified (constrained) through fault length, area, and/or slip rate. These magnitudes imply the "consensus" or very long period values so it is more appropriate to fix the magnitudes and accept the higher variability and bias estimates. Alternatively an empirical relationship could be established between the two sets of magnitudes (consensus and inversion) and that relation used in future model predictions. The issue then becomes one of how well constrained the relation is for large magnitude ($M > 7$) and how to directly incorporate its uncertainty into the predictions (rather than implicitly through the increased variability and bias estimates).

The inversions are done on log amplitude spectra since strong ground motion data appear to be log normally distributed. This is consistent with the model being represented as a product (rather than sum) of models (Equation 2.1). The inversion bandwidth is magnitude dependent, extending to longer periods with increasing magnitudes. The low frequency limit is site dependent as well and may be seen in the Fourier amplitude spectra (model and data) plotted in Chapters 4 and 5). A high frequency limit was set at 20 Hz (noise contamination permitting)

to reduce the tendency toward high frequency weighting when using linear frequencies (the density of points increases with frequency). Tests were done using spectra smoothed over a constant log frequency window to provide exactly equal weighting. However, this procedure resulted in poorer fits (for fixed M) possibly due to the models' tendency to overpredict low frequency amplitudes at close distances. In view of this it was decided that it is probably more appropriate to weight the fit where the model performs best (also the frequency range of most interest). After much experimentation, an upper limit of 20 Hz combined with linear frequency appeared to represent a reasonable compromise for implicit weighting.

4.2.1 Point-Source Distance

The selection of an appropriate point-source distance for implementation at large and close distances to extended sources is a perplexing issue (EPRI, 1993). Probably no single distance metric is appropriate in all instances and one is left with the usual choice of reducing modeling variability with a sophisticated distance measure (e.g. for sites over a dipping fault like the Cape Mendocino, Northridge, and Tabas earthquakes) at the expense of increased parametric variability in predicting motions for future earthquakes. For example, if a point-source distance is defined for sites over a dipping fault such that depth to the fault plane is included, modeling variability may be reduced by accommodating some variation in predicted motions as the site location moves over the rupture. On the other hand, in predicting motions for similar circumstances, if the fault dip is not well known, its effect must be treated through parametric variations.

In keeping with the model's simplicity, the point-source distance metric for these validation

exercises has been selected to be the closest horizontal distance to the surface projection of the rupture surface and to a depth of the largest asperity in the particular earthquake slip model. Hypocentral depth is used for small earthquakes (several aftershocks). For WNA this average depth is about 8 km and in implementing the point-source model in predicting motions, this depth must be treated parametrically and can dominate the parametric variability at very close distances. It should be added that the finite-source model faces a more severe issue as one can not know beforehand the location(s), along dip and strike, of the large asperities which can control motions at close distances. For the finite-source model, randomization in slip distribution is the point-source equivalent to depth randomization (Silva, 1992).

4.3 INVERSION RESULTS

In order to constrain the inversions for the Q(f) model, initial regional inversions were done using all the stations for each region but with only two sites: rock and soil. The inversion code permits multiple stations treated as the same site. Distinct kappa values are determined for each site and multiple stations (at varying distances) may be specified as belonging to a single site (or category). The results are shown in Table 4.1 and indicate significant regional differences in Q(f) and kappa values between the North Coast and the two southern California provinces, the Peninsular Ranges and Mojave. The North Coast appears to exhibit more deep crustal damping (lower Q(f) models) as well as shallow crust and soil (higher kappa values). The Mojave is least attenuating, particularly in rock kappa values, and this is reflected in the generally higher shallow crustal shear-wave velocities (Chapter 5). The η values are quite distinct between northern and southern California but there is significant coupling between Q_0 and η, probably

resulting in highly non-unique results. As a result, η was fixed at 0.6 (Boore, 1983) and the resulting Q_0 values are considered the most reliable. For the combined inversion Q_0 is high, close to 300, but not as high as the value of about 500 obtained in the inversions of the empirical attenuation relation (Chapter 6, Table 6.1). The average Q_0 for the North Coast and Peninsular Ranges is about 200, close to the traditional value of 150 (Boore, 1986; Nuttli, 1986).

The Peninsular Range and North Coast rock kappa values, 0.05 sec and 0.06 sec respectively, are in reasonable agreement with the 0.03 sec and 0.06 sec values obtained by Silva and Darragh (1995) in fitting response spectral shapes to a limited number of sites for the San Fernando and Loma Prieta earthquakes.

For the Mojave Province, the kappa resulting from the regional inversion with η fixed at 0.6 is 0.03 sec for rock sites, the same value obtained from fits to response spectral shapes to the Landers rock site data (Silva and Darragh, 1995). This lower kappa value is significant (0.03 sec verses 0.05 to 0.06 sec for the Peninsular Range and North Coast Provinces) and results in important differences in rock site spectra between the low and high kappa regions.

4.3.1 Peninsular Range

The Whittier Narrows (M 6.0), Northridge (M 6.7), and San Fernando (M 6.6) earthquakes comprise the Peninsular Range set. The Q(f) model is fixed at 264 $f^{0.06}$ (Table 4.1), a value intermediate between the North Coast and Mojave regions. The Whittier Narrow earthquake has the highest stress drop, about 90 bars, followed by Northridge at 60 bars and San Fernando

at about 40 bars. The average kappa value for soil (0.056 sec) is very similar to that for the Mojave province, probably due to the large number of common stations (25, Table 4.5). This value of 0.056 sec for soil is significantly lower than the 0.083 sec for soil sites of the North Coast. This difference is significant and may be a result of the soils of the Los Angeles basin (Peninsular Range Province) having more linear dynamic material properties than those of the North Coast. This observation persists in the point- and finite-source modeling exercises (Chapter 5) manifesting itself in the requirement of more linear modulus reduction and damping curves for Peninsular Range earthquakes than for the other provinces.

The rock average kappa is 0.048 sec, a bit lower than the 0.053 sec for the North Coast rock sites suggesting similar shallow (1 to 2 km) crustal damping for both regions.

It is interesting to compare the kappa values for the same sites resulting from the two inversions. For the Mojave province, the common Los Angeles soil sites are at distances exceeding over a hundred km (Table 4.4) while for the Peninsular Ranges inversions, distances are generally less than about 50 km (Table 4.2). For fixed Q(f), the inversion process will place any significant model departures into kappa estimates. That is, if the geometrical attenuation or Q(f) models are inappropriate, there would be a large difference in the kappa values determined for the same stations using separate inversions and earthquakes, particularly with the common stations located at very different distances. Table 4.5 shows the 25 common stations with their separately determined kappa values. The ratios are generally close to 1 with a median of 1.1 reflecting about a 10% difference in average kappa values. This is considered very close to 1 and lends confidence that the simple model is capturing the essential elements of the data and that the

parameter values, stress drop, kappa, and Q(f) are reasonably well determined and reliable.

Figure Set 4.2 shows the Fourier amplitude spectra; initial model, final model, and data (vector sum of the horizontal components dived by $\sqrt{2}$).

4.3.2 North Coast

Table 4.3 shows the results for the North Coast province: the Loma Prieta, Coyote Lake, and Morgan Hill earthquakes. The regional Q_0 and η fixed at 176 $f^{0.6}$ from the two site inversions (Table 4.1). Floating η gives 348 $f^{0.32}$ (Table 4.1) but results in significant coupling between Q_0, η, and f_c (corner frequency). As a result, it is felt that the best constrained (and most unique) set of parameters are for η fixed. The stress drops range from about 50 bars for the M 6.5 Morgan Hill earthquake to about 70 bars for both the Loma Prieta and Coyote Lake earthquakes. Averaging (lognormal) the kappa values over the sites results in 0.053 sec for rock, 0.083 sec for soil, and 0.064 sec overall. This compares favorably with the 2 site (rock and soil) inversions listed in Table 4.1. The Fourier amplitude spectra are shown in Figure Set 4.3.

4.3.3 Mojave

This province contains two earthquakes, the M 7.2 Landers with a stress drop of about 40 bars and the M 6 North Palm Springs with a 60 bar stress drop (Table 4.4). The Q(f) model is fixed at 371 $f^{0.6}$ (Table 4.1) and the average kappa values are 0.025 sec for rock, 0.058 sec for soil, and 0.050 sec overall. The low rock kappa is consistent with the high upper crustal shear-wave

velocities, compared to the other regions (Chapter 5), and may be the reason for the lower soil kappa values as well (lower damping in the underlying rock). These results are consistent with the 2-site inversions listed in Table 4.1. Spectra plots are shown in Figure Set 4.4.

Table 4.1 Regional Inversions Determination of Crustal Q Models and Average Kappa Values

Region	Number of Stations*	Q_o	η	κ (sec) Rock	κ (sec) Soil
Peninsular Range (Northridge, San Fernando, and Whittier Narrows)	221	174	0.77	0.053	0.058
		264	0.60**	0.051	0.056
		1286	0.00**	0.047	0.052
North Coast (Loma Prieta, Coyote Lake, and Morgan Hill)	92	348	0.32	0.056	0.069
		176	0.60**	0.059	0.072
		814	0.00**	0.053	0.066
Mojave (Landers and North Palm Springs)	86	186	0.64	0.030	0.052
		371	0.60**	0.030	0.056
		1678	0.00**	0.023	0.049
Combined***	399	346	0.53	0.050	0.059
		291	0.60**	0.051	0.060
		1518	0.00**	0.047	0.056

*Note: number of sites for each inversion is 2 (rock and soil)
**Values held fixed
***Shear-wave velocity = 3.50 km/sec, density = 2.7 cgs, crossover distance = 60 km
Starting values $Q_o = 150$, $\eta = 0.60$, $\kappa = 0.040$ sec

Table 4.2 Regional Inversion Determination of Stress Drops and Kappa Values: Peninsular Range

Regional $Q_o^* = 264$, $\eta^* = 0.60$; (Table 4.1)						
Earthquake		M^*		$\Delta\sigma$ (bars)	$ASE_{\Delta\sigma}$ (bars)	
1. Whittier Narrows		6.0		95.7	0.9	
2. Northridge		6.7		62.9	0.6	
3. San Fernando		6.6		36.1	0.6	
Site	Name	Number	Earthquake	κ (sec)	Category	R (km)
1	WHD	USGS 289	1	0.034	D	15.4
2	FAI	USC 90066	1, 2	0.064	D	15.5,46.0
3	ALH	CDMG 24461	1	0.042	D	15.5
4	SMA	CDMG 24401	1	0.052	D	15.6
5	OBR	CDMG 24400	1, 2	0.036	D	15.8,37.2
6	ATH	CDMG 80053	1	0.067	D	16.2
7	CAM	USC 90093	1, 2	0.064	D	16.3,42.7
8	JAB	USC 90094	1	0.042	D	16.6
9	FIG	USC 90032	1	0.058	C	16.6
10	VER	USC 90025	1, 2	0.066	D	17.5,35.2
11	CYP	USC 90033	1, 2	0.063	C	17.6,31.0
12	COM	USC 90073	1	0.054	C	17.7
13	OLD	USC 90095	1	0.051	C	17.7
14	ALT	CDMG 24402	1	0.048	D	18.0
15	BAD	USC 90070	1	0.077	D	18.1
16	NOR	USGS 634	1	0.057	D	18.5
17	RIM	USC 90072	1	0.077	D	18.5
18	DWN	CDMG 14368	1, 2	0.050	D	18.8,45.0
19	BRC	USC 90074	1, 2	0.068	C	18.8,59.3
20	FLT	USC 90034	1, 2	0.058	D	19.0,28.0
21	GR2	USC 90022	1, 2	0.049	D	20.0,31.8

Table 4.2 (Cont.) Regional Inversion Determination of Stress Drops and Kappa Values: Peninsular Range

Site	Name	Number	Earthquake	κ (sec)	Category	R (km)
22	GRA	USC 90068	1	0.066	C	20.7
23	CAS	USC 90078	1	0.041	D	20.9
24	OAK	USC 90065	1	0.060	D	20.9
25	70S	USC 90023	1	0.061	D	21.1
26	116	CDMG 14403	1, 2	0.047	D	21.3,38.8
27	MTW	CDMG 24399	1, 2	0.034	A	21.6,37.4
28	PAL	USC 90063	1, 2	0.039	C	21.6,24.4
29	WST	USC 90021	1, 2	0.051	D	21.8,25.9
30	OR2	USC 90080	1	0.054	D	21.9
31	FLO020	USC 90087	1	0.073	D	22.3
32	BRD	USGS 951	1	0.054	D	22.4
33	ING	CDMG 14196	1, 2	0.044	D	23.6,39.7
34	DEL	USC 90084	1, 2	0.051	D	23.9,55.1
35	HOL	CDMG 24303	1, 2	0.045	D	24.7,22.6
36	NYA	USC 90060	1, 2	0.056	C	25.1,21.1
37	SAT	USC 90091	1, 2	0.057	D	25.2,11.0
38	BLD	CDMG 24157	1, 2	0.041	B	25.4,26.8
39	CER	CDMG 14242	1	0.052	D	25.6
40	BUE	USC 90012	1, 2	0.052	D	25.7,60.6
41	CBN	USGS 108	1	0.043	A	25.8
42	BAL	USC 90088	1	0.072	D	26.9
43	WAT	USC 90081	1	0.061	D	26.9
44	OSA	USC 90045	1	0.062	D	27.8
45	TUJ	USC 90061	1, 2	0.045	C	27.8,22.2
46	WON	USC 90017	1, 2	0.057	A	28.1,18.8

Table 4.2 (Cont.) Regional Inversion Determination of Stress Drops and Kappa Values: Peninsular Range

Site	Name	Number	Earthquake	κ (sec)	Category	R (km)
47	PMN	CDMG 23525	1	0.058	D	29.5
48	GLE	USC 90058	1	0.067	C	29.7
49	CTS	CDMG 24390	1	0.065	D	30.0
50	CAT	USC 90040	1	0.058	D	30.0
51	CTN	CDMG 24389	1	0.044	D	30.1
52	MU2	USC 90014	1	0.059	C	30.2
53	REC	CDMG 14241	1	0.065	D	30.4
54	CEN	USC 90054	1, 2	0.050	D	30.8,24.5
55	LUC	USC 90044	1	0.086	C	31.1
56	C02	USC 90010	1	0.039	D	31.2
57	MAN090	USC 90046	1	0.061	C	31.2
58	COL	USC 90009	1	0.053	C	32.5
59	MUL	USC 90013	1, 2	0.071	C	33.0,14.6
60	HAR	CDMG 14395	1	0.067	D	33.5
61	RO3	USC 90006	1	0.050	D	34.3
62	RO2	USC 90007	1	0.055	D	34.7
63	KAG	USC 90005	1	0.038	D	35.7
64	EUC	USC 90002	1	0.058	D	36.2
65	ARL	CDMG 24087	1, 2	0.058	D	36.3,11.5
66	SEA	USC 90082	1, 2	0.061	D	37.0,63.2
67	FEA	CDMG 13122	1	0.069	C	37.1
68	SAY	USC 90001	1	0.066	D	40.3
69	HNT	CDMG 13197	1	0.054	D	40.8
70	STA	USC 90003	1	0.053	D	41.3
71	SYL	CDMG 24514	1, 2	0.063	D	41.9,11.2

Table 4.2 (Cont.) Regional Inversion Determination of Stress Drops and Kappa Values: Peninsular Range

Site	Name	Number	Earthquake	κ (sec)	Category	R (km)
72	LOS	USC 90057	1, 2	0.059	D	48.0,15.9
73	TOP	USC 90053	1	0.046	D	48.6
74	VAS	CDMG 24047	1, 2	0.037	A	49.8,25.6
75	NWH	CDMG 24279	1, 2	0.071	D	52.3,11.5
76	CSR,ORR,CRR	CDMG 24278	1, 2, 3	0.047	B	72.2,22.8,20.1
77	NHO	USC 90069	1, 2	0.057	B	16.1,49.0
78	VIR	USC 90052	1	0.060	B	55.2
79	CSH	CDMG 24277	1	0.066	B	64.9
80	GRV	USGS 709	1	0.031	B	15.6
81	CHA,CHL	USC 90015	1, 2	0.071	B	35.6,15.9
82	FAR	USC 90016	1, 2	0.063	B	31.9,17.2
83	MAL	CDMG 24396	1, 2	0.055	B	63.0,31.4
84	PAC,KAG	CDMG 24088	1, 2	0.067	B	35.0,12.3
85	JOS	USC 90077	1, 2	0.039	B	17.0,49.3
86	SER	USC 90090	1, 2	0.057	B	32.4,77.0
87	SOR	USC 90071	1, 2	0.066	B	16.7,52.7
88	RIV	CDMG 13123	1, 2	0.036	B	56.8,99.4
89	SCS	DWP 74	2	0.062	D	11.0
90	JEN	USGS 0655	2	0.088	D	11.0
91	CNP	USC 90053	2	0.069	D	11.1
92	PUL	CDMG 24207	2	0.029	A	12.1
93	ROS	USC 90006	2	0.072	D	12.4
94	CCN	CDMG 24389	2	0.055	D	19.7
95	MRP	CDMG 24283	2	0.076	D	20.8
96	STM	CDMG 24538	2	0.040	D	22.2

Table 4.2 (Cont.) Regional Inversion Determination of Stress Drops and Kappa Values: Peninsular Range

Site	Name	Number	Earthquake	κ (sec)	Category	R (km)
97	H12	CDMG 24607	2	0.054	C	23.4
98	LH9, L09	USGS 127	2, 3	0.044	A	27.1,18.4
99	PIC	CDMG 24612	2	0.057	D	30.1
100	SMR	CDMG 24401	2	0.047	D	35.4
101	ELI	CDMG 24575	2	0.062	D	37.9
102	ANA	CDMG 24576	2	0.071	D	39.4
103	LIT	CDMG 23595	2	0.064	A	47.8
104	NEE	CDMG 24586	2	0.093	D	52.6
105	LBC	CDMG 14560	2	0.071	D	56.2
106	WRI	CDMG 23574	2	0.038	D	72.5
107	CUC	CDMG 23598	2	0.060	A	80.8
108	PHE	CDMG 23597	2	0.053	D	86.7
109	BER	CDMG 23672	2	0.051	D	103.8
110	SBE	CDMG 23542	2	0.039	D	108.8
111	HEM	CDMG 13660	2	0.046	D	144.7
112	CDF	CDMG 12673	2	0.046	D	147.6
113	SPV	USGS 0637	2	0.061	D**	11.0
114	KAT	USC 90055	2	0.056	C	11.0
115	RRS	DWP 77	2	0.046	D**	11.0
116	CLD	USC 90009	2	0.067	C	13.6
117	SCR	MWD 78	2	0.048	B**	15.8
118	MU2	USC 90014	2	0.045	C	16.6
119	GLE	USC 90058	2	0.087	C	16.7
120	TPF	USGS 5081	2	0.056	D**	17.0
121	WIL	USC 90018	2	0.066	D	21.0

Table 4.2 (Cont.) Regional Inversion Determination of Stress Drops and Kappa Values: Peninsular Range

Site	Name	Number	Earthquake	κ (sec)	Category	R (km)
122	STN	USC 90091	2	0.051	D	24.3
123	W15	USC 90020	2	0.061	C	28.0
124	SAR	USC 90047	2	0.065	D	28.3
125	VRM	USC 90096	2	0.054	D	29.8
126	BIR	USC 90079	2	0.064	D	36.8
127	MAN	USC 90046	2	0.060	C	36.9
128	LH1	CDMG 24271	2	0.082	C	37.1
129	SMV	USC 90095	2	0.051	C	37.5
130	LV5	CDMG 24055	2	0.059	C	39.1
131	LV6	CDMG 24309	2	0.054	D	39.3
132	PTM	CDMG 25148	2	0.050	A	40.3
133	ARC	USC 90099	2	0.067	D	41.0
134	PLM	CDMG 24521	2	0.080	C	42.9
135	RAN	CDMG 14404	2	0.069	A	51.1
136	WAI	USC 90083	2	0.065	D	53.7
137	SSE	USC 90082	2	0.053	D	55.9
138	GAR	USC 90085	2	0.055	D	65.0
139	WWJ	CDMG 23590	2	0.092	A	65.6
140	HUN	CDMG 13197	2	0.065	D	76.0
141	PAC	CDMG 24207	2	0.058	B	12.1
142	SC2	LA 00	2	0.048	B**	15.3
143	L04	USGS 126	3	0.034	A	20.5
144	L01	CDMG 125	3	0.064	C	23.1
145	PDL	USGS 262	3	0.050	D	24.9
146	FSD	CDMG 285	3	0.036	A	25.0

Table 4.2 (Cont.) Regional Inversion Determination of Stress Drops and Kappa Values: Peninsular Range

Site	Name	Number	Earthquake	κ (sec)	Category	R (km)
147	PSL	USGS 266	3	0.046	A	26.0
148	FTR	CDMG 121	3	0.052	A	26.4
149	PEL	USGS 135	3	0.030	D	27.9
150	PAS	CDMG 80053	3	0.052	D	29.6
151	SAD	LAFC 104	3	0.020	A	33.3
152	WND	ACOE 289	3	0.049	D	42.5
153	OPP	CDWR 994	3	0.061	C	43.8
154	PUD	CDMG 278	3	0.052	D	55.3
155	PVE	2	3	0.072	C	59.6
156	SOD	ACOE 287	3	0.029	A	62.7
157	TLI	USGS 130	3	0.088	D	63.3
158	CND	ACOE 108	3	0.033	A	65.0
159	PHN	CDMG 272	3	0.072	D	69.9
160	WRP	CDWR 1102	3	0.043	D	77.9
161	CSM	CDWR 111	3	0.049	A	89.8
162	BFA	USGS 1004	3	0.132	D	111.3
163	SJC	USGS 465	3	0.041	C	111.5
164	SBF	USGS 282	3	0.069	D	123.6
165	ISD	ACOE 1035	3	0.076	A	129.5
166	H05	CDMG 12331	3	0.024	D	141.1
167	AZP	CIT 103	3	0.033	C	175.0
168	SDC	USGS 314	3	0.056	D	211.0
169	BSF	USGS 105	3	0.047	C	215.9
170	L12	CDMG 128	3	0.038	B	15.3
171	PCD	CDMG 279	3	0.021	B	8.3

Table 4.2 (Cont.) Regional Inversion Determination of Stress Drops and Kappa Values: Peninsular Range

Site	Name	Number	Earthquake	κ (sec)	Category	R (km)
172	SON	SCE 280	3	0.053	B	128.1
173	MA1	CDWR 1041	3	0.075	B	109.7
174	MA2	CDWR 1042	3	0.069	B	108.3
175	MA3	CDWR 1043	3	0.063	B	108.7
176	C08	USGS 1015	3	0.057	B	218.5
177	PPP	CDWR 269	3	0.025	B	35.9
178	WTW	USGS 290	3	0.039	B	61.3
179	FTJ	USGS 998	3	0.055	B	59.2

AVG (all) = 0.054
AVG (rock) = 0.048
AVG (soil) = 0.056

*Parameters held fixed
**Provisional category assignment
Starting values: $\Delta\sigma$ = 100 bars, κ = 0.040 sec
Shear-wave velocity = 3.5 km/sec, density = 2.7 cgs, crossover distance = 65 km

Table 4.3 Regional Inversion Determination of Stress Drops and Kappa Values: North Coast

Regional $Q_o^* = 176$, $\eta^* = 0.60$; (Table 4.1)						
Earthquake		M^*		$\Delta\sigma$ (bars)	$ASE_{\Delta\sigma}$ (bars)	
1. Loma Prieta		6.9		73.7	1.0	
2. Coyote Lake		5.7		70.1	1.7	
3. Morgan Hill		6.2		49.0	0.8	
Site	Name	Number	Earthquake	κ (sec)	Category	R (km)
1	CLS	CDMG 57007	1, 3	0.069	B	12.0,24.7
2	LGP	UCSC 16	1	0.044	A	12.0
3	BRN	UCSC 13	1	0.039	A	12.6
4	STG	CDMG 58065	1	0.063	D	14.3
5	G01	CDMG 47379	1, 2, 3	0.048	A	14.8,13.3,16.9
6	WVC	CDMG 58235	1	0.083	D	14.8
7	GOF	CDMG 57476	1	0.090	D	15.8
8	G02	CDMG 47380	1, 2, 3	0.059	D	15.8,12.0,15.9
9	WAH	UCSC 14	1	0.033	D	16.3
10	G03	CDMG 47381	1, 2, 3	0.060	D	17.0,10.7,15.3
11	LOB	CDMG 58135	1, 3	0.043	A	17.1,46.1
12	UC2	UCSC 15	1	0.031	B	17.3
13	G04	CDMG 57382	1, 2, 3	0.078	D	18.4,9.5,13.7
14	G06	CDMG 57383	1, 2, 3	0.063	B	21.6,8.1,12.7
15	AND	USGS 1652	1, 3	0.062	D	23.4,8.6
16	ANA	USGS 1652	1	0.084	A	23.4
17	CYC	CDMG 57217	1, 2, 3	0.054	A	23.4,9.2,8.0
18	CLD	CDMG 57504	1	0.074	D	23.8
19	AGW	CDMG 57066	1, 3	0.084	D	26.8,25.8
20	SVL	USGS 1695	1	0.074	D	27.0
21	HDA	USGS 1656	1, 3	0.085	D	27.0,27.6
22	HCA	USGS 1028	1, 3	0.091	D	29.5,31.7

Table 4.3 (Cont.) Regional Inversion Determination of Stress Drops and Kappa Values: North Coast

Site	Name	Number	Earthquake	κ (sec)	Category	R (km)
23	HSP	CDMG 47524	1	0.086	D	29.9
24	SAL	CDMG 47179	1	0.077	D	30.8
25	SGI	USGS 1032	1	0.072	A	31.5
26	HVR	CDMG 57191	1, 2, 3	0.083	C	32.6,33.6,8.7
27	SLC	USGS 1601	1	0.061	A	32.9
28	PAE	CDMG 58264	1	0.082	D	33.1
29	SG3	CDMG 47189	1	0.089	B	35.6
30	MCH	CDMG 47377	1	0.062	A	41.4
31	A07	CDMG 58378	1	0.064	A	43.7
32	A09	USGS 1161	1	0.068	A	43.7
33	A10	CDMG 58373	1	0.086	A	43.8
34	BES	CDMG 58262	1	0.074	A	45.8
35	A3E	CDMG 58219	1	0.051	A	53.9
36	A2E	CDMG 58393	1	0.048	D	54.0
37	HWB	CDMG 58498	1	0.039	D	55.5
38	SSF	CDMG 58539	1	0.041	A	64.3
39	DMH	CDMG 58130	1	0.056	B	72.5
40	TIB	CDMG 58224	1	0.051	D	73.3
41	PJH	CDMG 58338	1	0.058	A	74.3
42	RIN	CDMG 58151	1	0.035	A	75.2
43	YBI	CDMG 58163	1	0.058	A	76.3
44	PHT	CDMG 58131	1	0.074	A	77.1
45	TLH	CDMG 58133	1	0.068	A	77.5
46	PRS	CDMG 58222	1	0.051	A	78.5
47	CFH	CDMG 58132	1	0.067	A	79.8
48	BRK	CDMG 58471	1	0.080	A	80.2
49	GGB	USGS 1678	1	0.056	A	80.9

Table 4.3 (Cont.) Regional Inversion Determination of Stress Drops and Kappa Values: North Coast

Site	Name	Number	Earthquake	κ (sec)	Category	R (km)
50	PTB	CDMG 58043	1	0.070	A	84.6
* 51	MSJ,FMS	CDMG 1377	1, 3	0.068	D	41.2,32.3
52	GMR	CDMG 57425	1, 3	0.055	B	25.3,14.5
53	GIL	CDMG 47379	1, 3	0.055	A	15.0,16.8
54	SJB	CDMG 1377	2, 3	0.087	D	20.0,29.8
55	SJ3	CDMG 1492	2	0.064	D	21.1
56	SJ5	CDMG 1492	2	0.066	D	27.6
57	HD1	USGS 1656	3	0.075	D	27.6
58	HD3	USGS 1656	3	0.083	D	27.6
59	HD4	USGS 1656	3	0.083	D	27.6
60	HD5	USGS 1656	3	0.081	D	27.6
61	WSE270	CDMG 58235	3	0.078	D	29.2
62	WVE000	CDMG 58235	3	0.076	D	29.2
63	WNE270	CDMG 58235	3	0.082	D	29.2
64	SJR	USGS 1655	3	0.066	D	34.1
65	SJL	USGS 1655	3	0.064	D	34.1
66	A1E	USGS/CDMG 1180	3	0.073	D	52.4
67	LBN	CDMG 56012	3	0.084	D	63.7
68	SFO	CDMG 58223	3	0.051	D	71.5

AVG (all) = 0.064
AVG (rock) = 0.053
AVG (soil) = 0.083

*Parameters held fixed
Starting values: $\Delta\sigma$ = 100 bars, κ = 0.040 sec
Shear-wave velocity = 3.4 km/sec, density = 2.7 cgs, crossover distance = 50 km

Table 4.4 Regional Inversion Determination of Stress Drops and Kappa Values: Mojave

Regional $Q_o^* = 371$, $\eta^* = 0.60$; (Table 4.1)						
Earthquake		M^*		$\Delta\sigma$ (bars)	$ASE_{\Delta\sigma}$ (bars)	
1. Landers		7.19		40.7	0.5	
2. North Palm Springs		6.00		62.8	1.1	
Site	Name	Number	Earthquake	κ (sec)	Category	R (km)
1	LUC	SCE 24	1	0.028	A	8.3
2	CLW	SCE 23	1	0.062	D	20.9
3	DES,DSP	CDMG 12149	1, 2	0.057	D	18.4, 10.0
4	YER	CDMG 22074	1	0.067	D	24.6
5	BAR	CDMG 23559	1	0.070	D	35.5
6	PAL,PSA	CDMG 12025	1, 2	0.046	D	31.2, 14.4
7	29P	CDMG 22161	1	0.037	A	40.3
8	SIL,H10	CDMG 12206	1, 2	0.042	A	48.5, 18.8
9	IND	CDMG 12026	1	0.056	D	49.4
10	JOS	CDMG 22170	1	0.092	C	13.4
11	HEM	CDMG 12331	1	0.039	D	65.6
12	FTI	CDMG 24577	1	0.040	D	63.5
13	FHS,NPS	USGS 5070	1, 2	0.052	D	22.6, 10.0
14	MVH	USGS 5071	1, 2	0.075	C	16.3, 10.3
15	BAK	CDMG 32075	1	0.038	D	89.1
16	BAL	USC 90088	1	0.064	D	144.9
17	ARC	USC 90099	1	0.070	D	138.0
18	CAM	USC 90093	1	0.064	D	136.0
19	JAB	USC 90094	1	0.059	D	155.0
20	TUJ	USC 90061	1	0.055	C	144.9
21	BOR	CDMG 33083	1	0.058	D	90.3
22	FLO	USC 90087	1	0.063	D	138.6

Table 4.4 (Cont.) Regional Inversion Determination of Stress Drops and Kappa Values: Mojave

Site	Name	Number	Earthquake	κ (sec)	Category	R (km)
23	PLM	USC 90086	1	0.062	D	150.3
24	BUE	USC 90012	1	0.058	D	158.8
25	DEV	USC 90004	1	0.065	D	173.2
26	BAD	USC 90070	1	0.068	D	128.8
27	DWN	CDMG 14368	1	0.060	D	158.2
28	FAI	USC 90066	1	0.067	D	136.6
29	FEA	CDMG 13122	1	0.063	C	121.9
30	EUC	USC 90002	1	0.060	D	146.5
31	LPL	USC 90063	1	0.061	C	148.9
32	OAK	USC 90065	1	0.057	D	123.4
33	COL	USC 90073	1	0.061	C	137.0
34	WAI	USC 90083	1	0.055	D	153.5
35	ING	CDMG 14196	1	0.062	D	168.0
36	116	CDMG 14403	1	0.063	D	165.1
37	VER	USC 90025	1	0.064	D	158.5
38	FLE	USC 90034	1	0.068	D	153.8
39	FIG	USC 90032	1	0.062	C	149.5
40	WES	USC 90021	1	0.063	D	159.9
41	OBR	CDMG 24400	1	0.053	D	150.5
42	SGR	USC 90022	1	0.061	D	162.3
43	W15	USC 90020	1	0.062	C	161.8
44	W70	USC 90023	1	0.064	D	164.7
45	NYK	USC 90060	1	0.068	C	149.2
46	BRI	USC 90074	1	0.068	C	143.8
47	RIM	USC 90072	1	0.071	D	132.8

Table 4.4 (Cont.) Regional Inversion Determination of Stress Drops and Kappa Values: Mojave

Site	Name	Number	Earthquake	κ (sec)	Category	R (km)
48	AMO	USC 90084	1	0.057	D	158.2
49	STC	USC 90003	1	0.063	D	173.2
50	POM	CDMG 23525	1	0.053	D	118.3
51	ROS	USC 90006	1	0.061	D	164.4
52	GLE	USC 90058	1	0.064	C	152.3
53	SYC	USC 90089	1	0.061	D	136.2
54	CAS	USC 90078	1	0.053	D	162.0
55	ORN	USC 90080	1	0.055	D	161.6
56	PUE,PLC	USC 90072	1, 2	0.015	B	90.0, 67.8
57	RIV,RVA	CDMG 13123	1, 2	0.027	B	89.2, 57.1
58	WWT	USGS 5072	2	0.044	C	10.0
59	CAB	USGS 5073	2	0.047	D	11.9
60	FVR	USGS 5069	2	0.056	C	16.2
61	JST	CDMG 22170	2	0.076	C	24.3
62	H08	CDMG 12204	2	0.040	C	24.5
63	H06	CDMG 12202	2	0.046	D	32.5
64	LDR	CDMG 22T13	2	0.044	D	32.9
65	H05	CDMG 12331	2	0.034	D	35.2
66	INO	USGS 5067	2	0.039	D	36.8
67	SNY	USGS 5038	2	0.038	D	37.2
68	H04	CDMG 13201	2	0.037	D	38.5
69	A01	USGS 5224	2	0.025	A	39.4
70	ARS	USGS 5230	2	0.024	A	39.8
71	INI	CDMG 726	2	0.038	D	42.8
72	AZF	USGS 5160	2	0.037	C	43.2

Table 4.4 (Cont.) Regional Inversion Determination of Stress Drops and Kappa Values: Mojave

Site	Name	Number	Earthquake	κ (sec)	Category	R (km)
73	H02	CDMG 13199	2	0.020	A	49.0
74	CLI	CDOT 754	2	0.067	D	51.4
75	ATL	USGS 5231	2	0.033	A	51.5
76	H01	CDMG 13198	2	0.026	A	54.7
77	LMR	CDMG 707	2	0.010	A	65.1
78	HES	CDMG 23321	2	0.043	D	70.3
79	RNC	CDMG 5253	2	0.037	D	96.8

AVG (all) = 0.050
AVG (rock) = 0.025
AVG (soil) = 0.058

*Parameters held fixed
Starting values: $\Delta\sigma$ 100 = bars, κ = 0.040 sec
Shear-wave velocity = 3.7 km/sec, density = 2.5 cgs, crossover distance = 65 km

Table 4.5 Common Sites for Mojave and Peninsular Range Inversions

Name	Number	κ (sec) Mojave	κ (sec) Peninsular	Kappa Ratio (Mojave/Peninsular)
BAL	USC 90088	0.065	0.072	0.9
CAM	USC 90093	0.064	0.064	1.0
FAI	USC 90066	0.067	0.065	1.0
JAB	USC 90094	0.060	0.040	1.5
VER	USC 90025	0.064	0.066	1.0
BAD	USC 90070	0.068	0.076	0.9
RIM	USC 90072	0.072	0.076	1.0
CAS	USC 90078	0.053	0.040	1.3
OAK	USC 90065	0.058	0.058	1.0
BUE	USC 90012	0.058	0.053	1.1
BAL	USC 90088	0.065	0.071	0.9
TUJ	USC 90061	0.055	0.045	1.2
GLE	USC 90058	0.065	0.066	1.0
COL	USC 90073	0.062	0.052	1.2
EUC	USC 90002	0.060	0.057	1.1
ROS	USC 90006	0.062	0.066	0.9
GLE	USC 90058	0.065	0.084	0.8
W15	USC 90020	0.062	0.062	1.0
WAI	USC 90083	0.056	0.068	0.8
116	CDMG 14196	0.063	0.048	1.3
OBR	CDMG 24400	0.053	0.036	1.5
DWN	CDMG 14368	0.061	0.050	1.2
116	CDMG 14403	0.063	0.048	1.3
ING	CDMG 14196	0.062	0.044	1.4
FEA	CDMG 13122	0.063	0.068	0.9

AVG (log) = 1.1

CHAPTER 5

MODEL VALIDATION

5.1 PARTITION AND ASSESSMENT OF GROUND MOTION VARIABILITY

An essential requirement of any numerical modeling approach, particularly one which is implemented in the process of defining design ground motions, is a quantative assessment of prediction accuracy. A desirable approach to achieving this goal is in a manner which lends itself to characterizing the variability associated with model predictions. For a ground motion model, prediction variability is comprised of two components: modeling variability and parametric variability. Modeling variability is a measure of how well the model works (how accurately it predicts ground motions) when specific parameter values are known. Modeling variability is measured by misfits of model predictions to recorded motions through validation exercises and is due to unaccounted for components in the source, path, and site models (i.e. a point-source cannot model the effects of directivity and linear site response cannot accommodate nonlinear effects). Parametric variability results from a viable range of values for model parameters (i.e. slip distribution, soil profile, G/G_{max} and damping curves). It is the sensitivity of a model to a viable range of values for model parameters. The total variability, modeling plus parametric, represents the variance associated with the ground motion prediction and, because it is a necessary component in estimating fractile levels, may be regarded as important as median predictions.

Both the modeling and parametric variabilities may have components of randomness and uncertainty. Table 5.1 summarizes the four components of total variability in the context of

ground motion predictions. Uncertainty is that portion of both modeling and parametric variability which, in principle, can be reduced as additional information becomes available, whereas randomness represents the intrinsic or irreducible component of variability for a given model or parameter. Randomness is that component of variability which is intrinsic or irreducible for a given model. The uncertainty component reflects a lack of knowledge and may be reduced as more data are analyzed. For example, in the point-source model, stress drop is generally taken to be independent of source mechanism as well as tectonic region and is found to have a standard error of about 0.7 (natural log) (EPRI, 1993). This variation or uncertainty plus randomness in $\Delta\sigma$ results in a variability in ground motion predictions for future earthquakes. If, for example, it is found that normal faulting earthquakes have generally lower stress drops than strike-slip which are, in turn, lower than reverse mechanism earthquakes, perhaps much of the variability in $\Delta\sigma$ may be reduced. In extensional regimes, where normal faulting earthquakes are most likely to occur, this new information may provide a reduction in variability (uncertainty component) for stress drop, say to 0.3 or 0.4 resulting in less ground motion variation due to a lack of knowledge of the mean stress drop. There is, however, a component of this stress drop variability which can never be reduced in the context of the Brune model. This is simply due to the heterogeneity of the earthquake dynamics which is not accounted for in the model and results in the randomness component of parametric variability in stress drop. A more sophisticated model may be able to accommodate or model more accurately source dynamics but, perhaps, at the expense of a larger number of parameters and increased parametric uncertainty (i.e. the finite-fault with slip model and nucleation point as unknown parameters for future earthquakes). That is, more complex models typically seek to

reduce modeling randomness by more closely modeling physical phenomena. However, such models often require more comprehensive sets of observed data to constrain additional model parameters, which generally leads to increased parametric variability. If the increased parametric variability is primarily in the form of uncertainty, it is possible to reduce total variability, but only at the additional expense of constraining the additional parameters. Therefore, existing knowledge and/or available resources may limit the ability of more complex models to reduce total variability.

The distinction of randomness and uncertainty is model driven and somewhat arbitrary. The allocation is only important in the context of probabilistic seismic hazard analyses as uncertainty is treated as alternative hypotheses in logic trees while randomness is integrated over in the hazard calculation (Cornell, 1968). For example, the uncertainty component in stress drop may be treated by using an N-point approximation to the stress drop distribution and assigning a branch in a logic tree for each stress drop and associated weight. A reasonable three point approximation to a normal distribution is given by weights of 0.2, 0.6, 0.2 for expected 5%, mean, and 95% values of stress drop respectively. If the distribution of uncertainty in stress drop was such that the 5%, mean, and 95% values were 50, 100, and 200 bars respectively, the stress drop branch on a logic tree would have 50, and 200 bars with weights of 0.2 and 100 bars with a weight of 0.6. The randomness component in stress drop variability would then be formally integrated over in the hazard calculation.

5.1.1 Assessment of Modeling Variability

Modeling variability (uncertainty plus randomness) is usually evaluated by comparing response

spectra computed from recordings to predicted spectra and is a direct assessment of model accuracy. The modeling variability is defined as the standard error of the residuals of the log of the average horizontal component (or vertical component) response spectra. The residual is defined as the difference of the logarithms of the observed average 5% damped acceleration response spectra and the predicted response spectra. At each period, the residuals are squared, and summed over the total number of sites for one or all earthquakes modeled. Dividing the resultant sum by the number of sites results in an estimate of the model variance. Any model bias (average offset) that exists may be estimated in the process (Abrahamson et al., 1990; EPRI 1993) and used to correct (lower) the variance (and to adjust the median as well). In this approach, the modeling variability can be separated into randomness and uncertainty where the bias corrected variability represents randomness and the total variability represents randomness plus uncertainty. The uncertainty is captured in the model bias as this may be reduced in the future by refining the model. The remaining variability (randomness) remains irreducible for this model. In computing the variance and bias estimates only the frequency range between processing filters at each site (minimum of the 2 components) is used. The causal butterworth filter corners are listed for each site (and component) in the Strong Motion Catalogue (Appendix B).

5.1.2 Assessment of Parametric Variability

Parametric variability, or the variation in ground motion predictions due to uncertainty and randomness in model parameters is difficult to assess. Formally, it is straight-forward in that a Monte Carlo approach may be used with each parameter randomly sampled about its mean (median) value either individually for sensitivity analyses (Silva, 1992; Roblee et al., 1996) or

in combination to estimate the total parametric variability (Silva, 1992; EPRI, 1993). In reality, however, there are two complicating factors.

The first factor involves the specific parameters kept fixed with all earthquakes, paths, and sites when computing the modeling variability. These parameters are then implicity included in modeling variability provided the data sample a sufficiently wide range in source, path, and site conditions. The parameters which are varied during the assessment of modeling variation should have a degree of uncertainty and randomness associated with them for the next earthquake. Any ground motion prediction should then have a variation reflecting this lack of knowledge and randomness in the free parameters.

An important adjunct to fixed and free parameters is the issue of parameters which may vary but by fixed rules. For example, source rise time (Chapter 2, Equation 2-7) is magnitude dependent and in the stochastic finite-source model is specified by an empirical relation. In evaluating the modeling variability with different magnitude earthquakes, rise time is varied, but because it follows a strict rule, any variability associated with rise time variation is counted in modeling variability. This is strictly true only if the sample of earthquakes has adequately spanned the space of magnitude, source mechanism, and other factors which may affect rise time. Also, the earthquake to be modeled must be within that validation space. As a result, the validation or assessment of model variation should be done on as large a number of earthquakes of varying sizes and mechanisms as possible.

The second, more obvious factor in assessing parametric variability is a knowledge of the

appropriate distributions for the parameters (assuming correct values for median or mean estimates are known). In general, for the stochastic models, median parameter values and uncertainties are based, to the extent possible, on evaluating the parameters derived from previous earthquakes (Silva, 1992; EPRI, 1993).

The parametric variability is site, path, and source dependent and must be evaluated for each application (Roblee et al., 1996). For example, at large source-to-site distances, crustal path damping may control short-period motions. At close distances to a large fault, both the site and finite-source (asperity location and nucleation point) may dominate, and depending upon site characteristics, the source or site may control different frequency ranges (Silva, 1992; Roblee et al., 1996).

In combining modeling and parametric variations, independence is assumed (covariance is zero) and the variances are simply added to give the total variability.

$$_{ln}\sigma^2_T = {}_{ln}\sigma^2_M + {}_{ln}\sigma^2_P \text{*****} \qquad (5\text{-}1),$$

where

$_{ln}\sigma^2_M$ = modeling variation,

$_{ln}\sigma^2_P$ = parametric variation.

5.1.3 Validation Earthquakes

*****Strong ground motions are generally considered to be log normally distributed.

The validation exercises include all earthquakes with derived slip models (with the exception of the Kobe earthquake), a total of 14. The Little Skull Mountain earthquake, which occurred on the Nevada Test Site, and which does not have a slip model was added because of interest to DOE. A general slip model is derived for this earthquake as the best fitting of a suite of randomly generated models (Chapter 5). Also the largest aftershock (M 5.2) of the 1979 M 6.5 Imperial Valley earthquake was added to provide a linear response constraint to the development of modulus reduction and hysteretic damping curves for Imperial Valley soils (Chapter 5). The total number of earthquakes modeled then is 16 at 502 sites covering the fault distance range of about 1 km to nearly 200 km for WNA data and from about 5 km out to about 450 km for ENA data (Nahanni and Saguenay earthquakes). Table 5.2 lists the earthquakes modeled, magnitudes, fault distance ranges, and number of sites. In the following sections, the earthquakes are treated in Geologic Province groups and then in chronological order for those events which occurred outside the three provinces.

To refine the M_0 verses rise time relation based on the modeling results, rise times are varied about the original empirical relation

$$\log \tau = 0.33 \log M_0 - 8.62 \qquad (5\text{-}2)$$

and the best fitting rise times selected based on a visual examination of the bias estimates. The empirical rise time relation was based on a fit to the rise time data of Heaton (1990) with the slope constrained to 0.33 (similarity constraint; Hartzell, 1978). The selection of best fitting rise

times permits a reassessment of the empirical relation in the context of the stochastic finite-fault model. This approach is not intended to be exhaustive but to determine whether or not any bias exists in the empirical relation and to provide a reasonable basis for incorporating any adjustments. Naturally, if a significant difference is encountered then either rise time must be treated parametrically and randomly varied in prediction exercises or the validations redone with the revised rise time scaling relation.

5.2 PENINSULAR RANGE EARTHQUAKES

The Peninsular Range earthquakes include the M 6.7 Northridge, M 6.6 San Fernando, and M 6.0 Whittier Narrows. The Northridge earthquake is treated first as it has the largest number of sites (Table 5.2) and widest range in levels of motion. The point-source stress drop and kappa values determined from the regional inversion are listed in Table 4.2. The regional Q(f) model determined in the regional 2-site (rock and soil) inversion is 264 $f^{0.6}$ (Chapter 4, Table 4.1).

5.2.1 1994 Northridge Earthquake

For the 1994 M 6.7 Northridge earthquake, a total of 94 sites are modeled: 71 soil and 23 rock. The fault distance range is about 7 km (sites over the rupture surface) to nearly 150 km (Table 5.2). The sites extend from the San Fernando Valley into the Los Angeles Basin to the south and to the San Andreas fault to the north and east (Figure 5.1). The crustal model is from Wald and Heaton (1994) and is listed in Table 5.3. To model rock and soil sites, the generic rock or soil profile (Chapter 3) is simply placed on top of the regional crustal model. The shallow

generic rock profile is truncated at velocities exceeding 1.0 km/sec, the velocity of the top layer of the Wald and Heaton (1994) Northridge crust (Table 5.3).

Both the rock and soil sites are allowed to exhibit material nonlinearity to depths of 500 ft (Table 5.4). For the rock sites, the generic soft rock G/G_{max} and hysteretic material damping curves (Chapter 6) are used. These curves were based on modifications to laboratory test results (Appendix D) required to model the rock site empirical attenuation (Appendix A and Chapter 6). For the soil sites, finite-source modeling (section following point-source results) using both the EPRI cohesionless soil curves (Chapter 6) and the generic deep soil (Chapter 6) curves showed more satisfactory results using the generic deep soil curves. As a result, the soft soil curves are adopted as being appropriate for Peninsular Range or Los Angeles area cohesionless soils.

The kappa values for the rock beneath the nonlinear zones at both rock and soil sites is taken as 0.03 sec (Table 5.3). This value was selected to give a total kappa (including nonlinear zone small strain damping) of about 0.04 sec, a value consistent with the empirical inversions (Table 6.1).

The finite-source model parameters are listed in Table 5.4. The rise time of 1.30 sec represents a best fit over a limited set of trial values and was selected based on a visual examination of the model bias, model variability, and response spectral fits. The static stress drop, based on the area, is about 39 bars and the point-source stress drop resulting from the inversions (Table 4.4) is 62.9 bars. The point-source depth is taken as 11 km, the depth of the largest asperity in the

Wald and Heaton (1994) slip model (Figure 5.2).

5.2.1.1 Point-Source Inversions For Stress Drop and Kappa Values

The Northridge earthquake is included in the Peninsular Range Province set along with the Whittier Narrows and San Fernando earthquakes. The Fourier amplitude spectra for both the recordings and the model predictions, are shown in Figure Set 4.2 and the site specific kappa values are listed in Table 4.2. For the Peninsular Range sites, the average rock kappa value is 0.048 sec and the corresponding soil kappa value is 0.056 sec.

5.2.1.2 Point-Source Modeling Results

The point-source model bias and variability estimates computed over all the 94 sites are shown in Figure 5.3. The bias is generally near zero between about 1 to 20 Hz and shows a slight underprediction at higher frequencies (equivalent to peak acceleration). The strong negative bias at low frequencies ($<$ 1 Hz) is a manifestation of the general tendency for the point-source to overpredict over the low frequency range at large magnitudes (Chapter 6). The dip in the bias estimates near 10 Hz is where the 5% damped pseudo absolute response spectral acceleration is beginning to saturate to peak ground acceleration. The response spectra are generally decreasing with increasing frequency (Figure 5.6) and reach full saturation around 30 Hz where the bias estimates become constant with increasing frequency. Over this relatively constant portion, the bias plots reflect the behavior of peak ground acceleration which is actually controlled by lower frequencies, in the 2 to 6 Hz range, where the spectral acceleration peaks.

The model variability (uncertainty plus randomness) is about 0.5 about 1 Hz and rises

significantly below 1 Hz reflecting the stable point-source low frequency overprediction. The bias corrected variability (randomness) is significantly lower over this frequency range due to the large statistically significant negative bias estimates. The randomness estimates provide a minimum estimate of model variability and represent the reduction in variability (total-randomness) achievable with the model provided the ground motion estimates are corrected for the low frequency overprediction.

To separate site effects, Figures 5.4 and 5.5 show analogous plots for soil and rock sites respectively. For the 71 soil sites, Figure 5.4 shows similar results to the combined estimates due to the greater number of soil sites (71 soil verses 23 rock sites). For the rock sites, Figure 5.5 shows a broad peak of about 0.4 (factor of about 1.5) at intermediate frequencies (about 2-3 Hz) and a general underprediction of about 0.25 (natural log) at high frequencies. Approximately 25% of this positive bias is due to just two sites with very high motions: PUL (Pacoima Upper Left) and ORR (Castaic Old Ridge Route). Figure set 5.6 shows the 5% damped pseudo absolute response spectra, data (log average of 2 horizontal components) and model predictions, with PUL on the bottom of the first page and ORR on the third page. The recorded motions exceed the model predictions by a factor of over 3 at some periods (less than about 2 sec). The recorded motions are very high at these sites for the San Fernando earthquake as well suggesting strong site effects.

Further examination of Figure set 5.6 shows the fundamental cause of the broad peak near 3 Hz and trough at 10 Hz in the rock site bias plot (Figure 5.5). A typical example is site KAG (page 2, Figure set 5.6) which shows the model spectra with a peak near 0.1 sec while the recorded

motions have a spectral peak near 0.3 to 0.4 sec. Much of the difference is due to the previously discussed issue between the median spectrum computed over a range in random profiles and the spectrum computed from a smooth median profile (Chapter 3). The effects of randomizing a profile to produce realistic profile samples with accompanying low and high velocity layers is to reduce the average short period motions and increase intermediate period motions (with respect to the period range of profile influence). This observation was demonstrated in Figure 3.7 which is reproduced here as Figure 5.7. The figure shows the shift in spectral peak to longer periods (from near 0.12 Hz to 0.2 Hz) between the spectrum computed from the smooth base case profile and the median spectrum computed over 30 spectra from randomized profiles. Figure 5.8 (same as Figure 3.5) shows an analogous plot for deep soil illustrating a similar although much less pronounced behavior. The difference is significant; particularly for rock sites, and suggests that an appropriate approach to estimating model bias and variability for use in future predictions is to either use a median prediction at each site or select the best fitting spectrum out of the random selection of site profiles. This would be of interest to try but time has precluded the attempt for this report. As a result, the bias and randomness estimates, particularly for rock sites, must be viewed in the context that they likely represent upper bounds and use of median predictions would generally both smooth and improve the bias estimates.

5.2.1.3 Finite-Source Modeling Results

Figure 5.9 shows the model bias and variability estimates over the total 94 sites for the stochastic finite-source model. The bias is generally small over the effective structural frequency range of about 0.2 to 100 Hz (peak acceleration is at about 30 Hz). At low frequency ($\leq$ 1 Hz)

there is a significant departure from the point-source large negative bias (Figure 5.3) suggesting the appropriateness of the finite-source model as a broad-band methodology.

Not surprisingly (Silva, 1992), for frequencies above 1 Hz, there is little difference in the bias estimates for the point- and finite-source models: both are considered good. Comparing the variability estimates, Figure 5.9 for the finite-source and Figure 5.3 for the point-source, very similar results are obtained, again for frequencies of 1 Hz and above. The bias corrected estimates are nearly identical for the two models ranging from about 0.5 at 100 Hz to about 0.75 at 0.2 Hz (lowest reliable frequency).

Although the present analysis considers many more sites and over a much larger distance range the bias and variability estimates are comparable to those using the much more computationally demanding broad-band simulation procedure which includes near-field terms and a much more rigorous were propagation model (Sommerville et al., 1995). These results are interesting in that the point- and finite-source modeling includes rock, basin edge, and deep basin sites ranging in distance from over the source rupture out to nearly 150 km. This suggests that the simple point-source model (if corrected for low frequency bias), with a very simple 1/R ($1/\sqrt{R}$ for R > twice crustal thickness), predicts broad-band strong ground motions at an average site with an accuracy comparable to much more sophisticated approaches such as the stochastic finite-source and the broad-band simulation procedure. The stochastic finite-source model bias and variability (Figure 5.9) indicates that simple assumptions in the context of source finiteness (Chapter 2) results in a surprisingly accurate and broad-band simulation methodology (Silva, 1992). Additionally, for both the point- and finite-source models, the simple assumption of

vertically propagating shear-waves appears to capture reasonably well strong motion site effects for sites located above the source out to distances of over 100 km.

To separate out soil and rock sites, Figures 5.10 and 5.11 show model bias and variability plots for the two recording site conditions. As with the point-source, due to the large number of soil sites (71 soil, 23 rock), the soil only and combined results are very similar. The soil sites (Figure 5.10) show slightly more negative bias and lower variability indicating the opposite condition must apply to the rock sites (Figure 5.11). This is definitely the case as Figure 5.11 shows, displaying a similar trend in the high frequencies (> 1 Hz) as the point-source rock results (Figure 5.5). As with the point-source, the broad peak near 2 to 3 Hz and trough at 10 Hz is largely attributable to the amplification of the smooth base-case rock profile.

For a qualitative appraisal of the response spectral predictions, Figure 5.12 shows the individual site spectra. Consistent with the bias estimates, the overall fit is generally good over the rather wide distance range. Site CDF, at 147 km is in the Mojave Province and is quite high for the Imperial Valley earthquake as well, perhaps suggesting strong localized effects. For the rock sites, Figure 5.12 shows features similar to the point-source, overprediction around 0.1 sec and underprediction near 0.5 sec, reflecting the rock site bias estimates.

To examine any systematic distance bias and to determine appropriate G/G_{max} and hysteretic damping curves, separate variability and bias estimates were computed for "near source" sites located within about 30 km fault distance. The "near source" criterion of 30 km was selected such that a minimum of 10 rock and 10 soil sites would be included (enough for meaningful

5.13 shows the combined sites variability and bias plots for sites within about 30 km (48 sites). The figure shows a more negative high frequency bias and lower variability, particularly for frequencies below about 2 Hz, than is shown for all the sites in Figure 5.9. The more distant sites are modeled less accurately than the close-in sites. To see if this is restricted to rock or soil site conditions, Figures 5.14 and 5.15 show the estimates for soil and rock respectively. Comparing Figures 5.14 for the close-in soil sites and Figure 5.10 for all soil sites, the bias estimates below 1 to 2 Hz are similar while the low frequency variability of the close-in soil sites is lower. Comparing the corresponding figures for the rock sites, Figure 5.11 for all rock sites and Figure 5.15 for the close-in rock sites reveals the same general trend: the low frequency bias is about the same while the variability is reduced for the close-in sites.

In general, the low frequency bias is similar between close-in and all the sites for both rock and soil sites. However, the low frequency variability decreases for the close-in sites suggesting the model is not capturing the greater variability in the more distant sites. This may be a wave propagation effect as the sites move out of the San Fernando basin across changes in crustal structure (Magistrale et al., 1992). It would be of interest to see if empirical Green functions could reduce this "distant site" model variability as these are the conditions under which this approach appears most appealing.

At high frequencies, above about 3 Hz, the "close-in" sites show more negative bias and lower variability (Figures 5.9 and 5.13). This is largely dominated by the soil sites since neither the bias nor the variability estimates change significantly between all the "close-in" sites and the soil "close-in" sites (Figures 5.13 and 5.14).

5.2.1.3.2 Assessment of G/G_{max} and Hysteretic Damping Curves. To assess the appropriate degree of soil nonlinearity in terms of implementing either the EPRI (1993) or the generic deep soil G/G_{max} and hysteretic damping curves for the Peninsular Range soil sites, the finite-fault modeling was repeated using the EPRI (Chapter 6) curves. Figure 5.16a shows the bias and randomness estimates for all 71 soil sites computed using the EPRI curves. Comparing this figure with Figure 5.10 (Figure 5.16b) for the deep soil curves it is apparent that the degree of nonlinearity is discernable for frequencies exceeding about 8 Hz where the bias and randomness estimates differ significantly. The more positive bias estimates resulting from the more nonlinear EPRI curves reflect lower high frequency motions. To concentrate on the higher levels of loading at the "close-in" sites, Figure 5.17a shows the estimates for the soil sites within about 30 km of the rupture. The bias is near zero from 0.2 to 100 Hz. Comparing that figure to Figure 5.14 (Figure 5.17b) illustrating the results using the generic deep soil curves, which shows a negative high frequency (> 1 Hz) bias or overprediction, the conclusion might be reached that the EPRI curves are the more appropriate set. However, these equivalent-linear site response analyses were done with a simple smooth generic profile which results in greater high frequency motions than a median spectrum computed over a suite of random profiles (Chapter 3).

Referring back to Figure 5.8, where this issue is illustrated, the spectrum computed for the generic smooth profile exceeds the median spectrum by about 10% on average for periods shorter than about 1 sec and about 20% for periods shorter than about 0.3 sec. The implication is straightforward in that if at each site, a median spectrum based on equivalent-linear analyses

of a suite of random profiles were used as the site spectral estimate, the high frequency motions would be lower. Unfortunately, the difference in spectral level between the spectrum computed for a smooth base-case profile and a median (or mean) spectrum depends on the level of control motion. The difference increases with loading level due to the nonlinearity of the soil (Chapter 3 and Roblee et al., 1996). As a result, it is not possible to quantify or refine the G/G_{max} and hysteretic damping curves unless the profiles are randomized at each site and the median spectrum is used in the bias estimates. Qualitatively it may be concluded that the high frequency negative bias obtained using the more linear generic soil curves, reflecting about a 20% overprediction, suggests that the generic deep soil curves are the more appropriate of the two sets. Figure 5.8 indicates that if median spectra had been computed at each site using the generic deep soil curves the negative high frequency bias estimates shown in Figure 5.14 would be reduced to near zero, like those in Figure 5.17.

5.2.1.3.3 Assessment of Nonlinear Site Response. Because the bias analyses provided sufficient resolution to discriminate between the EPRI and generic deep soil G/G_{max} and hysteretic damping curves, it is of interest to determine if a similar analysis could reject the hypothesis of linear soil site response. To provide linear site response bias estimates, the finite-source simulation was repeated constraining the number of equivalent-linear iterations to 1. This effectively sets G/G_{max} to 1 and the damping to that at a cyclic shear strain of 10^{-4}%. The resulting kappa value is 0.04 sec (Table 5.4) which is the value determined in the inversions of the empirical attenuation relations for soil sites at small strains (Table 6.1).

The results of the linear site response analyses are compared to the equivalent-linear analyses using the best fitting generic soil curves in Figure 5.18. The bias estimates are for the "close-in" sites and the large significant high frequency negative bias for the linear analyses is quite apparent. The abrupt departure between the linear and nonlinear bias estimates at 3 Hz suggests that for this suite of sites considered and under these loading conditions, nonlinear site response is an important consideration for frequencies exceeding about 3 Hz. Alternatively, the assumed linear kappa value of 0.04 sec may be in considerable error, by at least 100%. This does seen unlikely but remains an unresolved issue until enough small earthquakes (aftershocks) are recorded at these sites to provide estimates of small strain kappa values.

In support of the rejection of the linearity hypothesis, Figure 5.19 shows a corresponding plot for soil sites beyond about 30 km fault distance. Interestingly the bias estimates are nearly identical up to about 3 to 4 Hz where the linear response estimates begin to fall below those of the nonlinear response. The maximum difference is about 0.1 at 10 Hz reflecting about 10% larger motions for the linear analyses. The difference is likely not statistically significant and neither model can be rejected based on these results. However, if the kappa values were increased by a significant amount, even by only 50%, the high frequency linear bias estimates would decrease significantly (nearly the same percentage as the kappa increase; Silva, 1992) resulting in strongly positive bias estimates. We are left then with explaining the high kappa values close to the source yet average soil kappa values at similarly classified sites beyond 30 km. It does appear that the rejection of linearity for the "close-in" sites is the most physically consistent hypothesis.

Parenthetically, these results suggest an envelope of clear detectibility of soil nonlinearity for generic Peninsular Range soils. Magnitudes significantly above about 6.5, distances within about 30 km (expected rock outcrop peak acceleration above about 20%g), frequencies above about 3 Hz, and, for statistical stability, at least 20 stations.

This represents a set of rather stringent conditions and it is not surprising why the debate between engineers and seismologists over nonlinear soil response raged for so long.

5.2.2 1971 San Fernando Earthquake

A total of 39 sites, 21 rock and 18 soil, are modeled for the M 6.6, 1971 San Fernando earthquake over the fault distance range of about 3 to 218 km (Table 5.2). The site distribution is shown in Figure 5.20. Because only a homogeneous half-space crustal model was used in determining the source model (Heaton, 1982), the Northridge crustal model of Wald and Heaton (1994) was adopted (Table 5.3). The simple half-space model used by Heaton (1982) was justified in that only close-in sites were used which are dominated by energy propagating upward from the source. The main issue is the lack of amplification in the half-space model which may have been mapped into the source (slip) model. This is likely the case as the finite-source model shows a significant broad-band negative bias. The use of an appropriate crustal shear-wave velocity gradient in the source inversion would likely result in a broader and perhaps deeper shallow asperity.

As with the Northridge earthquake, rock and soil sites have potential nonlinear zones to 500 ft and use the same kappa values and G/G_{max} and hysteretic damping curves (Table 5.5).

The finite-source parameters are listed in Table 5.5. The best fitting rise time is 1.25 sec and the static stress drop 34.3 bars. The point-source stress drop is 36.1 bars (Table 4.4), about the same as that of the static value. The point-source depth is taken as 8 km, midpoint between the shallow and deep asperities of the Heaton (1982) slip model.

The slip model used (Figure 5.21) was generated as the combination of the two Heaton (1982) rupture models on subparallel faults San Fernando and Sierra Madre, onto the larger and deeper Sierra Madre Fault. This was necessary since the current stochastic finite-fault model cannot accommodate articulated rupture planes. As a result, some of the fault distances for the closest sites may be inappropriate. However, judging from the fit of response spectra, the effect does not appear to be a controlling factor. It may have a much greater influence in a time domain comparison of the arrival times of significant phases which likely led to the two rupture surfaces.

5.2.2.1 Point-Source Inversions For Stress Drop and Kappa Values

The San Fernando earthquake is included in the Peninsular Range Province set along with the Northridge and Whittier Narrows earthquakes. The Fourier amplitude spectra for both the recordings and the model predictions, are shown in Figure Set 4.2 and the site specific kappa values are listed in Table 4.2. For the Peninsular Range sites, the average rock kappa value is 0.048 sec and the corresponding soil kappa value is 0.056 sec.

5.2.2.2 Point-Source Modeling Results

Bias and variability estimates are shown in Figure 5.22 computed over all 39 sites for the point-source using a stress drop of 36.1 bars. The bias shows the typical negative low frequency

point-source overprediction. Reprocessing by PE&A has extended the useable bandwidth from about 0.3 to 30 Hz (plots are on structural frequency for response spectra) over this distance range so the reliability of the estimates decreases significantly below about 0.3 Hz. At higher frequency the bias is positive indicating a slight underprediction. The variability plot shows values larger than for the Northridge earthquake, about 0.6 from about 0.4 to 100 Hz.

Bias and variability plots for the 18 soil and 21 rock sites separately are shown in Figures 23 and 24 respectively. For the soil sites, the high frequency (> 1 Hz) bias is about zero and increases to about 0.25 for rock sites (Figure 5.24). Apparently the slight underprediction over all sites (Figure 5.22) is being driven by the rock sites. Interestingly the randomness plots are similar, around 0.6. Considering the distance range, about 3 to 200 km, the level of randomness and generally small bias values is very encouraging for this complicated source.

Examining the spectral plots in Figure set 5.25, it appears that a significant contribution to the rock site underprediction may be due to sites PCD (Pacoima) and ORR (Castaic). This was the case with the Northridge earthquake as well and indicates the possibility of strong local effects at these sites.

5.2.2.3 Finite-Source Modeling Results

The bias and randomness plots for the finite-source are shown in Figure 5.26 for all the sites. The bias is nearly constant at about -0.25 and decreases to nearly -0.4 around 0.5 Hz. The low frequency overprediction of about 1.4 is similar for the soil and rock sites (Figures 5.27 and 5.28) and is probably related to the use of a homogenous half-space in deriving the slip model(s)

(Heaton, 1982). Since a combination of integrated velocity and displacement strong motion records were used as the near-source constraints on the slip model(s), the dominant periods are long and generally greater than about 1 to 2 sec and probably do not exceed 10 sec (Appendix B). The crustal amplification for the generic rock and soil models at a period of 5 sec is about 1.3 and 1.4 respectively (Figures 6.4 and 6.5), in general agreement with the finite-source low frequency negative bias. Use of a crustal model in deriving the San Fernando earthquake slip model(s) should result in a smaller (near zero) bias perhaps by adjusting parameters such as rise time, asperity sharpness (stress drop), and asperity depth. The finite-fault variability estimates are larger than those of the point-source possibly reflecting the issue of the crustal gradient. Not unrelated, this larger finite-fault variability may be an indication that subparallel rupture surfaces or a fault plane articulated with depth (Heaton and Helmberger, 1979) are required to better fit the strong motion data.

The response spectra, data and model predictions for the finite-fault are shown in Figure Set 5.29. In general the model captures the overall spectra reasonably well.

5.2.3 1987 Whittier Narrows Earthquake

The M 6.0 Whittier Narrows earthquake modeling and inversions has the 2nd largest number of sites of all the earthquakes considered, at total of 88. Of the 88 sites modeled, only 18 are rock leaving 70 soil sites. Unfortunately, there are simply not very many rock sites available for this earthquake. The fault distance range is about 10 to 80 km due to deep source (Hartzell and Iida, 1990) and Figure 5.30 shows the site distribution. The Wald and Heaton (1994) crustal model is used (Table 5.3) since it is very similar to the model used in the inversions for slip

distribution (Hartzell and Iida, 1990). Rock and soil sites are produced by placing the generic profiles on top of the crustal model and are potentially nonlinear to a depth of 500 ft (Table 5.6), exactly the same as for the Northridge and San Fernando earthquakes. Generic rock and generic deep soil G/G_{max}, and hysteretic damping curves (Table 5.6) are used consistent with the results of the Northridge earthquake for the Peninsular Range soils.

The source parameters are listed in Table 5.6. The point-source and finite-source stress drops are 95.7 and 27.3 bars respectively and the point-source depth is 15 km, the depth to the largest asperity. The best fitting rise time is 0.25 sec and the slip model (Figure 5.31) is from Hartzell and Iida (1990). It should be noted that Hartzell and Iida did not use any data in their slip model inversions at epicentral distances exceeding about 15 km as they wished to minimize wave propagation effects. This appears to have an impact on the current finite-fault modeling as the distant sites (beyond about 30 km fault distance) are not fit as nearly well as the closer sites.

5.2.3.1 Point-Source Inversions for Stress Drop and Kappa Values

The Whittier Narrows earthquake is included in the Peninsular Range inversions (Chapter 4). The Fourier amplitude spectra are shown in Figure Set 4.2 and the site specific kappa values are listed in Table 4.2.

5.2.3.2 Point-Source Modeling Results

For all 88 sites, the model bias and variability plots are shown in Figure 5.32. The bias is essentially zero for frequencies above 1 Hz. The point-source low frequency overprediction is quite strong for this earthquake, about 0.6 from near 1 Hz to about 0.3 Hz, the approximate low

frequency range of the data. The bias corrected variability (randomness) averages about 0.6 while the uncorrected values rise sharply below 1 Hz. Overall the simple point-source appears to capture ground motions quite well for frequencies above 1 Hz.

For the soil and rock sites, Figures 5.33 and 5.34 show the corresponding analyses. Figure 5.33, for soil sites, shows a slight high frequency overprediction while Figure 5.34 shows the opposite for the rock sites. As with the San Fernando earthquake (unlike the Northridge), the variability for the soil sites is lower than for the rock sites.

To examine directly the fits to the response spectra, Figure Set 5.35 shows the model and data 5% damped response spectra. As with the other earthquakes, the simple point-source model generally performs well in matching the overall level of the recorded motions. Notable exceptions are the 4 most distant sites, all rock, which show large short period underpredictions. Site CSR is Castaic Old Ridge Route which showed a substantial underprediction for the Northridge and San Fernando earthquakes as well.

5.2.3.3 Finite-Source Modeling Results

For the finite-source model, the bias and randomness plots are shown in Figures 5.36, 5.37 and 5.38 for all 88 sites, 71 soil, and 17 rock sites respectively. Over all the sites the bias is small and shows a distinct overprediction, or valley, near 0.8 Hz. From Figure 5.32, for the point-source, it appears this is present there as well and may be associated with resonances in the shear-wave velocity profiles. Using the median (or mean) spectrum from randomized profiles (Appendix C) would eliminate any profile resonances and result in much smoother bias and

variability estimates.

The bias plot for the soil sites (Figure 5.37) is similar to all the sites (Figure 5.36) due to the larger number of soil sites (71 soil verses 17 rock). The slightly more negative high frequency bias for soil sites suggests that the rock sites are substantially underpredicted. For the soil sites, the variability is about 0.5 at high frequencies and shows the usual low frequency increase at low frequency. The effects of the profile resonances are clearly seen in the randomness plots as low frequency peaks.

For the 17 rock sites, Figure 5.38 shows the bias and variability plots illustrating a significant broad-band underprediction and much larger variability. To examine whether this underprediction is distant dependent, Figure 5.39 and 5.40 show the bias and randomness plots for soil and rock sites respectively at fault distances less than about 30 hrs. For the soil sites, the close-in results (Figure 5.39) suggest a slightly larger overprediction and about the same level of variability as all soil sites (Figure 5.37). However for rock sites, Figure 5.40 shows a near zero bias and significantly lower variability than for all the rock sites (Figure 5.38). Apparently the more distant ($\geq$ 30 km) rock sites are significantly underpredicted and show considerable unmodeled variation. This result is similar to the Northridge earthquake but in that case the distant ($\geq$ 30 km) soil and rock sites showed higher variability.

To examine this rock site underprediction ($\geq$ 30 km) more closely, Figure Set 5.41 shows the response spectra for each site. In general the predictions are in agreement with the recorded motions with some very good matches and with several sites showing significant departures.

The most distant rock sites, VAS, VIR, RIV, MAL, CSH, and CSR illustrate the higher frequency underprediction with CSR (Castaic Old Ridge Route) the major contributor. The less severe tendency for the distant soil sites to be underpredicted is illustrated in the spectra plots as well. The point-source (Figure Set 5.35) does a much better job (except for CSR) using simple $1/\sqrt{R}$ geometric attenuation. It would be of interest to see if Hartzell and Iida would have similar results or if the inclusion of sites beyond 15 km epicentral distance would have resulted in changes to their slip model.

For 88 sites ranging in fault distance from about 10 to 80 km, both the point- and finite-source models predict the motions very well as the all-site bias and variability plots suggest. This is encouraging since the slip model was determined from data recorded at sites within 15 km epicentral distance.

5.3 NORTH COAST EARTHQUAKES

In this North Coast Province group, the Loma Prieta earthquake is treated first as it has by far the largest number of sites spanning the greatest distance range. The Loma Prieta presentation is followed chronologically by the 1979 M 5.7 Coyote Lake and 1984 M 6.2 Morgan Hill earthquakes. The site kappa values and stress drops determined in the point-source inversion (Chapter 4) are listed in Table 4.3. The regional Q(f) models and average kappa values from the regional inversions are 176 $f^{0.6}$ and 0.053 sec and 0.083 sec for rock and soil sites respectively and are listed in Table 4.1

5.3.1 Loma Prieta Earthquake

For the 1984 M 6.9 earthquake, a total of 53 sites covering the fault distance range of about 5 to 90 km (Table 5.2) are modeled. The sites are comprised of 33 rock and 20 soil. Most of the rock sites are located beyond about 30 km (20) while most of the soil sites (17) are "close-in" or within about 30 km of the source.

The site distribution is shown in Figure 5.42. The soft Geomatrix side E (Bay mud) sites are not modeled at this time as there are too few recordings to constrain an attenuation relation for the comparison exercises. Also the additional effort in developing a generic profile, producing amplification factors, and assessing appropriate G/G_{max} and hysteretic damping curves is not warranted in validating the model. The presumption being that there is nothing unusual about the response of soft sites that would violate the appropriateness of the site response model, particularly under the moderate levels of loading during the Loma Prieta earthquake. Additionally, the soft sites Treasure Island and Lotung (Taiwan) were successfully modeled in the EPRI (1993) assessment of equivalent-linear verses nonlinear site response analyses.

The crustal model is from Wald et al. (1991) and is listed in Table 5.7 and is the same crustal model used in determining the slip distribution. To model rock and soil sites, the generic rock or soil profile (Chapter 3) is simply placed on top of the regional crustal model. The shallow generic rock profile is truncated at velocities exceeding 1.0 km/sec, the velocity of the top layer of the crustal model (Table 5.7).

Both the rock and soil sites are allowed to exhibit material nonlinearity to depths of 500 ft (Table 5.8). For the rock sites, the generic soft rock G/G_{max} and hysteretic material damping curves

(Chapter 6) are used. These curves were based on modifications to laboratory test results (Appendix D) required to model the rock site empirical attenuation (Appendix A and Chapter 6). For the soil sites, both the EPRI cohesionless soil and deep generic soil curves (Chapter 6) and used to provide an assessment of which set is more appropriate for North Coast soils. In the initial analyses the EPRI curves are used.

The kappa values for the rock beneath the nonlinear zones at both rock and soil sites is taken as 0.03 sec (Table 5.8). This value was selected to give a total kappa (including nonlinear zone small strain damping) of about 0.04 sec, a value consistent with the empirical inversions at low levels of loading (Table 6.1).

The finite-source model parameters are shown in Table 5.8. The rise time of 1.60 sec represents a best fit over a limited set of trial values and was selected based on a visual examination of the model bias, model variability, and response spectral fits. The static stress drop, based on the area, is about 33 bars and the point-source stress drop resulting from the inversions (Table 4.3) is 73.7 bars. The point-source depth is taken as 12 km, the depth of the largest asperity in the Wald et al. (1991) slip model (Figure 5.43).

5.3.1.1 Point-Source Inversions For Stress Drop and Kappa Values

The Loma Prieta earthquake is included in the North Coast Province set along with the Coyote Lake and Morgan Hill earthquakes. The Fourier amplitude spectra for both the recordings and the model predictions, are shown in Figure Set 4.3 and the site specific kappa values are listed in Table 4.4. For the North Coast sites, the average rock kappa value is 0.053 sec and the

corresponding soil kappa value is 0.083 sec. The average North Coast soil kappa value is significantly higher than the corresponding Peninsular Range value of 0.058 sec. Since the average rock site kappa values are nearly the same for both provinces (0.056 sec for the Peninsular Range), this suggests that the North Coast soil sites have either intrinsically higher material damping or are exhibiting a higher degree of material nonlinearity.

5.3.1.2 Point-Source Modeling Results

The point-source model bias and variability estimates computed over all the 53 sites are shown in Figure 5.44. The bias is generally near zero (within the $\pm$ 90% confidence limits) between about 1 to 20 Hz and shows a slight underprediction at higher frequencies (equivalent to peak acceleration). The trend in the negative bias at low frequencies ($<$ 1 Hz) is a manifestation of the general tendency for the point-source to overpredict over the low frequency range at large magnitudes (Chapter 6).

The model variability (uncertainty plus randomness) is about 0.6 above 2 Hz and rises significantly below 2 Hz, reflecting unmodeled low frequency site variations as the bias is near zero.

To separate site effects, Figures 5.45 and 5.46 show analogous plots for soil and rock sites respectively. For the 20 soil sites, Figure 5.45 shows a lower, near constant bias for frequencies above about 1 Hz. For the rock sites, Figure 5.46 shows a broad peak of about 0.3 (factor of about 1.4) at intermediate frequencies (about 1 to 5 Hz) and a general underprediction of about 0.2 (natural log) at very high frequencies. It appears that much of this positive bias may be due

to just 5 sites with very high motions: PRS, CFH, BRK, CGB, and PTB, all rock sites and at distances beyond about 70 km. Figure set 5.47 shows the 5% damped pseudo absolute response spectra, data (log average of 2 horizontal components) and model predictions, with the most distant sites on the last page. The recorded motions exceed the model predictions by a factor of over 3 at some periods. These recorded motions are very high at these sites but other nearby rock sites, such as YBI, PHT, and TLH, reflect closer to expected levels (about 0.05g) suggesting strong site effects. Similar results are also observed in the finite-source analyses which incorporates crustal propagation effects (Chapter 2). This suggests that the underprediction at the distant rock sites is not a result of the simple point-source $1/\sqrt{R}$ geometrical attenuation at these distances.

In general however, the point-source performs well with a low bias and small randomness (Figure 5.44) over this wide distance range.

5.3.1.3 Finite-Source Modeling Results

Figure 5.48 shows the model bias and variability estimates over the total 53 sites for the stochastic finite-source model. The bias is generally small over the frequency range of about 0.3 to 100 Hz (peak acceleration is at about 30 Hz). Near 1 Hz there is a small underprediction and an overprediction near 10 Hz. At higher frequency the bias is near zero.

Not surprisingly (Silva, 1992; Schneider et al., 1993), for frequencies above about 0.5 Hz, the difference in the bias estimates for the point- and finite-source models is small: both are considered good. Comparing the variability estimates, Figure 5.48 for the finite-source and

Figure 5.44 for the point-source, very similar results are obtained, again for frequencies of about 0.5 Hz and above. The bias corrected estimates are nearly identical for the two models ranging from about 0.5 at 100 Hz to about 0.75 at 0.2 Hz (lowest reliable frequency), very similar to the results obtained for the Northridge earthquake analyses.

To separate out soil and rock sites, Figures 5.49 and 5.50 show model bias and variability plots for the two recording site conditions: soil and rock. As with the point-source, due to the larger number of rock sites (33 rock verses 20 soil), the rock only and combined results are very similar. The soil sites show a near zero bias from about 0.3 Hz to 100 Hz while the rock sites show the low frequency underprediction and high frequency (10 Hz) overprediction seen in the results for all the sites (Figure 5.48). The variability for soil is low, about 0.4 from high frequency to near 2 Hz where it increases to about 0.75 with decreasing frequency. For rock sites, Figure 5.50 shows higher levels above 2 Hz and similar values as soil for frequencies below 2 Hz, not unlike the point-source results. In general however, the finite-source rock motions are larger than those of the point-source for frequencies above about 5 Hz.

For a qualitative appraisal of the response spectral predictions, Figure Set 5.51 shows the individual site spectra. Consistent with the bias estimates, the overall fit is generally good over the rather wide distance range. As with the point-source spectra, the most distant 5 rock sites (last page) show large underpredictions. Since the finite-source model incorporates crustal wave propagation effects (Ou and Herrmann, 1990), these large motions may be due to some localized effects.

To examine any systematic distance bias and to determine appropriate G/G_{max} and hysteretic damping curves, separate variability and bias estimates were computed for "near source" sites located within about 30 km fault distance. As with the Northridge earthquake, the "near source" criterion of 30 km was selected such that a minimum of 10 rock and 10 soil sites would be included (enough for meaningful comparative statistics) and that rock outcrop peak accelerations would generally be above 15 to 20%g. The last criterion was to ensure an expectation of discernable nonlinear soil site response with the EPRI (1993) (Chapter 6) modulus reduction and damping curves in the context of the generic deep soil shear-wave velocity profile.

Naturally these sites do not cover the entire province and soil conditions can vary dramatically within any province but this restricted set of stations represent those with high enough loading conditions to permit a possibility of discriminating between the EPRI and generic deep soil sets of curves (Chapter 2).

Since the empirical attenuation relations for soil, which are dominated by Peninsular Range soils (Appendix A), show significantly less nonlinearity than the EPRI curves suggest (Chapter 6) and the deep soil generic curves (Chapter 6) were derived based on the empirical soil attenuation, it is desirable to see if the modeling can resolve the appropriate degree of model nonlinearity. It was hoped that these "near source" criteria would enable selecting between either the EPRI (1993) curves or the generic deep soil curves (Chapter 6) as being more appropriate for North Coast soils.

It should be emphasized that we are treating generic conditions with the assumption that the soil

sites are, on average, similar to the generic deep soil profile and that a shear-wave velocity of about 3,000 ft/sec (bedrock) is reached, on average, at a depth of about 500 ft.

5.3.1.3.1 Assessment of Distance Bias. To consider first any significant distance bias, Figure 5.52 shows the combined sites variability and bias plots for sites within about 30 km (30 sites). The figure shows a more negative high frequency bias and lower variability than is shown for all the sites in Figure 5.48. The more distant sites are modeled less accurately than the close-in sites. To see if this is restricted to rock or soil site conditions, Figures 5.53 and 5.54 show the close-in estimates for soil and rock respectively. Comparing Figures 5.53 for the close-in soil sites and Figure 5.49 for all soil sites, the bias estimates below are similar while the variability of the close-in soil sites is generally lower. Comparing the corresponding figures for the rock sites, Figure 5.50 for all-rock sites and Figure 5.54 for the close-in rock sites show a more negative bias for the close-in rock sites (as expected) while the variability is about the same.

In general, the bias and variability estimates for the "close-in" sites is similar to all the sites. For the soil sites, the close-in sites reflect a lower variability than all the soil sites while the converse is true for the rock sites. For rock sites, the "close-in" bias shows a high-frequency overprediction for frequencies above about 4 Hz that is stronger than all rock sites due to the large underprediction at the most distant rock sites.

The "close-in" soil sites (Figure 5.53) show a slightly negative bias and low high-frequency variability indicating they are modeled reasonably well and may provide sufficient resolution to

distinguish G/G_{max} and hysteretic curves as well as to test the hypothesis of soil site linearity. The slight high frequency negative bias would be reduced through the use of a median model spectrum.

5.3.1.3.2 Assessment of G/G_{max} and Hysteretic Damping Curves. To assess the appropriate degree of soil nonlinearity in terms of implementing either the EPRI (1993) or the generic deep soil G/G_{max} and hysteretic damping curves for the North Coast soil sites, the finite-fault modeling was repeated using the deep soil (Chapter 6) curves. Figure 5.55a shows the bias and randomness estimates for all 30 soil sites computed using the generic deep soil curves. Comparing this figure with Figure 5.49 (Figure 5.55b) for the deep soil curves it is apparent that the degree of nonlinearity is discernable for frequencies exceeding about 8 Hz where the bias and randomness estimates show a significant difference. The more negative bias estimates resulting from the more linear deep soil curves reflect larger high frequency motions. To concentrate on the higher levels of loading at the "close-in" sites, Figures 5.56a and b show the estimates for the soil sites within about 30 km of the rupture. The bias is strongly negative for frequencies above about 6 Hz. The results using the EPRI curves (Figure 5.53), which show a slightly negative high frequency (> 1 Hz) bias or overprediction, appear to be more consistent with observed motions. Using a median spectrum computed over a suite of random profiles (Chapter 3) would result in somewhat lower high frequency motions reducing the negative bias by about 0.1 to 0.2 log (natural) units.

Referring back to Figure 5.8, where this issue is illustrated, the spectrum computed for the

generic smooth profile exceeds the median spectrum by about 10% on average for periods shorter than about 1 sec and about 20% for periods shorter than about 0.3 sec. The implication is straightforward in that if at each site, a median spectrum based on equivalent-linear analyses of a suite of random profiles were used as the site spectral estimate, the high frequency motions would be lower. Unfortunately, the difference in spectral level between the spectrum computed for a smooth base-case profile and a median (or mean) spectrum depends on the level of control motion. The difference increases with loading level due to the nonlinearity of the soil (Chapter 3 and Roblee et al., 1996). As a result, it is not possible to quantify or refine the G/G_{max} and hysteretic damping curves unless the profiles are randomized at each site and the median spectrum is used in the bias estimates. Qualitatively it may be concluded that the high frequency negative bias obtained using the more linear generic soil curves, reflecting about a 50% overprediction at 10 Hz, suggests that the EPRI curves are the more appropriate of the two sets. Figure 5.8 indicates that if median spectra had been computed at each site using the generic deep soil curves the negative high frequency bias estimates shown in Figure 5.53 would be reduced to near zero, or slightly positive.

5.3.1.3.3 Assessment of Nonlinear Site Response. Because the bias analyses provided sufficient resolution to discriminate between the EPRI and generic deep soil G/G_{max} and hysteretic damping curves, it is of interest to determine if a similar analysis could reject the hypothesis of linear soil site response. To provide linear site response bias estimates, the finite-source simulation was repeated constraining the number of equivalent-linear iterations to 1 as in the similar Northridge linear analyses. The resulting kappa value is 0.04 sec (Table 5.8)

which is the value determined in the inversions of the empirical attenuation relations for soil sites at small strains (Table 6.1).

The results of the linear site response analyses are compared to the equivalent-linear analyses using the best fitting EPRI curves in Figure 5.57. The bias estimates are for the "close-in" sites and the large high frequency negative bias resulting from the linear analyses is quite apparent. The abrupt departure between the linear and nonlinear bias estimates at about 3 Hz, the same frequency as in the Northridge analyses, suggests that for this suite of sites and under these loading conditions, nonlinear site response is an important consideration for frequencies exceeding about 3 Hz. Alternatively, the assumed linear kappa value of 0.04 sec may be in considerable error, by at least 100%. This seems unlikely but remains an unresolved issue until enough small earthquakes (aftershocks) are recorded at these sites to provide estimates of small strain kappa values.

Unfortunately, beyond 30 km, only 3 soil sites are available and the resulting bias estimates are too poorly constrained (90% confidence level is a factor of 2) to draw any substantial inferences about the appropriateness of the small strain kappa value of 0.04 sec. The bias estimates are high but they reflect a broad band underprediction of about 0.4 ($\pm$ 1) for frequencies above about 0.7 Hz. This is apparent in the response spectra plots for soil sites A2E, HWB, and TIB with TIB dominating the broad band underprediction. Since kappa would affect frequencies exceeding about 3 Hz (for kappa values around 0.04 sec), it is not likely that the small strain soil kappa value of 0.04 sec is seriously in error and the hypothesis of linear soil response may be rejected, although somewhat less convincingly than for the Northridge analysis.

As for the Northridge analyses, these results suggest an envelope of clear detectibility of soil nonlinearity for generic Peninsular Range and North Coast soils. Magnitudes significantly above about 6.5, distances within about 30 km (expected rock outcrop peak acceleration above about 20%g), frequencies above about 3 Hz, and, for statistical stability, at least 20 stations.

5.3.2 1979 Coyote Lake Earthquake

A total of 7 soil and 3 rock sites are modeled for the M 5.7 Coyote Lake earthquake. The sites range in distance from about 3 to 30 km (Table 5.2) and are on the westerly site of the rupture. Figure 5.58 shows the site locations with the linear string of sites comprising the Gilroy array. The low number of sites is a consequence of the small magnitude. All 10 sites in the strong motion database (Appendix B) were included in the inversions and forward modeling as they represent the "free field" sites which recorded useable data over a reasonable bandwidth.

The crustal model is from Liu and Helmberger (1983) and is listed in Table 5.9. It is the same model as used in the inversions for the slip model (Liu and Helmberger, 1983). As in the previous cases, the generic rock and soil shear-wave velocity profiles are placed on top of the regional crustal model. The kappa values beneath the shallow rock and deep soil profiles are 0.03 sec resulting in a total kappa value of 0.04 sec for both rock and soil sites (Table 5.10).

For both rock and soil sites, nonlinear zones extend to 500 ft and the soft rock and EPRI G/G_{max} and hysteretic damping curves are used for rock and soil sites respectively (Table 5.10).

The point- and finite-source model parameters are listed in Table 5.10. The best fitting rise time

is 0.36 sec and the static stress drop is 14.6 bars. The rupture surface is 10.0 x 7.6 km, 76 km^2 and is on the borderline for finite-fault modeling with M 5.0 subevents: only 9 subfaults are required. The slip model is shown in Figure 5.59.

The point-source depth is taken as 8 km and the stress drop resulting from the inversions is 70.1 bars (Table 4.3).

5.3.2.1 Point-source Inversions for Stress Drop and Kappa Values.

The Coyote Lake earthquake is included in the North Coast Province inversions (Chapter 4) along with the Loma Prieta and Morgan Hill earthquakes. The Fourier amplitude spectra are shown in Figure Set 4.3 and the site specific kappa values are listed in Table 4.3.

5.3.2.2 Point-Source Modeling Results

For all 10 sites (7 soil and 3 rock) the model bias and variability plots are shown in Figure 5.60. The bias is low, near zero, for frequencies above about 0.4 Hz, the approximate lowest frequency for which the analyses are reliable. The variability is also very low above 20 Hz (about 0.25) and rises to about 0.4 below 20 Hz. With only 7 soil and 3 rock sites, separate bias and randomness estimates are too poorly constrained to be reliable and are not shown. In general the soil sites follow closely the all sites, while the rock sites show the typical high frequency negative bias and generally higher randomness.

The response spectra plots are shown in Figure 5.61 and reflect a generally good match. Clearly

the soil sites are modeled more closely than the rock sites which show the short period overprediction. However, the effects of using the median spectrum in lieu of a single run with the base case profile is much more severe than for soil sites (Chapter 3) and would substantially reduce the rock site overprediction.

5.3.2.3 Finite-Source Modeling Results

Figure 5.62 shows the model bias and variability estimates for the finite-source model. The model bias is slightly more negative than for the point-source at high frequency (above about 4 Hz) and the ± 90% confidence limits are wider suggesting higher variability. This is shown in the variability plot which suggests that the point-source captures the site-to-site variations more accurately than does the finite-source, particularly for frequencies above about 1 Hz. These results are also clearly seen in the spectra plots (Figure 5.63) which indicates that the point-source model provides more accurate ground motion estimates for this earthquake than does the finite-source model. Too few subevents are being summed using an M 5.0 subevent to smooth out summation periodicities. Either using a smaller subevent or modifying the subevent rise time distribution would be necessary to improve the finite-source model's predictions. Neither approach is warranted as the results are considered acceptable.

5.3.3 1984 Morgan Hill Earthquake

A total of 21 soil and 8 rock sites are modeled for the M 6.2 Morgan Hill earthquake. The sites range in fault distance from about 1 to 70 km (Table 5.2). Figure 5.64 shows the site locations with the linear string of sites comprising the Gilroy array. The sites extend from San Jose (SJR)

up to the San Francisco International Airport (SFO).

The crustal model is from (Hartzell and Heaton, 1986) and is listed in Table 5.11. It is the same model as used in the inversions for the slip model (Hartzell and Heaton, 1986). As in the previous cases, the generic rock and soil shear-wave velocity profiles are placed on top of the regional crustal model. The kappa values beneath the shallow rock and deep soil profiles are 0.03 sec resulting in a total kappa value of 0.04 sec for both rock and soil sites (Table 5.12).

For both rock and soil sites, nonlinear zones extend to 500 ft and the soft rock and EPRI G/G_{max} and hysteretic damping curves are used for rock and soil sites respectively (Table 5.12).

The point- and finite-source model parameters are listed in Table 5.12. The best fitting rise time is 0.70 sec and the static stress drop is 10 bars. The rupture surface is 27.0 km long and 11.5 km wide and the slip model is shown in Figure 5.65.

The point-source depth is taken as 8 km and the stress drop resulting from the inversions is 49 bars (Table 4.3).

5.3.3.1 Point-source Inversions for Stress Drop and Kappa Values.

The Morgan Hill earthquake is included in the North Coast Province inversions along with the Loma Prieta and Coyote Lake earthquakes (Chapter 4). The Fourier amplitude spectra are shown in Figure Set 4.3 and the site specific kappa values are listed in Table 4.3.

5.3.3.2 Point-Source Modeling Results

For all 29 sites (21 soil and 8 rock) the model bias and variability estimates are shown in Figure 5.66. The bias is low and slightly negative for frequencies near 1 Hz and above and shows the typical point-source low frequency overprediction down to about 0.5 Hz, the lowest frequency of reliable analyses. The variability is higher at high frequency (near 0.5) than for the Coyote Lake earthquake and about the same for frequencies below 10 Hz.

The soil and rock site results are shown in Figures 5.67 and 5.68 respectively with the soil (21 sites) generally reflecting the all-sites results. As is usually the case, the rock (8 sites) bias estimates are more negative at high frequency (around 10 Hz) and the variability is higher than the soil.

The response spectra plots are shown in Figure Set 5.69 and reflect a reasonably good match. The soil sites are generally modeled more closely than the rock sites which show a more broad band overprediction. However, the effects of using the median spectrum in lieu of a single run with the base case profile is much more severe than for soil sites (Chapter 3) and would substantially reduce the rock site overprediction.

5.3.3.3 Finite-Source Modeling Results

Figure 5.70 shows the bias and variability estimates for the finite-source model computed over all the sites. In general, it is similar to the point-source results (Figure 5.66) but with slightly larger high frequency ($\geq$ 10 Hz) motions. The high frequency variability is lower than the point-source results but rises steeply at low frequency where peaks appear at 0.5 and at 0.9 Hz.

The peaks also occur in the point-source variability estimates (Figure 5.66) but are much less pronounced.

The soil site results are plotted in Figure 5.71 and are very similar to the all-site results due to the larger number of soil sites (21 soil verses 8 rock). The rock site bias and variability estimates, Figure 5.72, are very similar to the point-source bias results (Figure 5.68) but show a lower high frequency variability, similar to the soil site results. For this earthquake, the finite-source model is capturing additional high frequency site-to-site variability which the point-source model is neglecting.

Interestingly, the 0.5 and 0.8 Hz peak are strong in both the rock site and soil site variability estimates for the finite-source as well as in the point-source rock site results but are subdued in the point-source soil site variability estimates. The cause of these peaks is likely related to profile resonances that may be enhanced by peaks in the finite-source spectrum. If they are related to the finite-fault, site azimuth could play a role enhancing differing spectral components due to rupture propagation effects or directivity.

The effects of the profiles can be seen in the point-source spectra plots (Figure Set 5.69) for rock and soil sites. Soil site G02 (Gilroy Array N0. 2) and adjacent rock site G01 (Gilroy Array No. 1) show clear 1 sec and 2 sec profile resonances. The corresponding plot for the finite-source (Figure Set 5.73) shows an enhanced 1 sec resonance at site G02 as well as an enhanced 2 sec resonance at site G01. Both of the sites are at essentially the same azimuth, south of the rupture surface (Figure 5.64) with the rupture propagating toward them (Hartzell and Heaton,

1986). This may be a case where rupture directivity has enhanced profile resonances and clearly illustrates the need to randomize the profiles and use median spectral estimates. This would smooth out the profile resonances and provide for more robust bias and variability estimates.

5.4 MOJAVE EARTHQUAKES

The Mojave Province includes the **M** 7.2 Landers, and the **M** 6.0 North Palm Springs earthquakes. The Landers earthquake is treated first as it has the largest number of sites (Table 5.2) and widest range in levels of motion. The point-source stress drop and kappa values determined from the regional inversion are listed in Table 4.4. The regional Q(f) model determined in the regional 2-site (rock and soil) inversion is 371 $f^{0.6}$ (Chapter 4, Table 4.1).

5.4.1 1992 Landers Earthquake

For the 1992 **M** 7.2 Landers earthquake, a total of 57 sites are modeled: 52 soil and 5 rock. The fault distance range is about 1 km to nearly 180 km (Table 5.2). The sites extend from the Mojave desert into the Los Angeles Basin to the west (Figure 5.74). The crustal model is from Wald and Heaton (1994b) and is listed in Table 5.13. To model rock and soil sites, the generic rock or soil profile (Chapter 3) is simply placed on top of the regional crustal model. The shallow generic rock profile is truncated at velocities exceeding 1.98 km/sec, the velocity of the top layer of the Wald and Heaton (1994b) Northridge crust (Table 5.13).

Both the rock and soil sites are allowed to exhibit material nonlinearity to depths of 500 ft (Table 5.14). For the rock sites, the generic soft rock G/G_{max} and hysteretic material damping curves

(Chapter 6) are used. These curves were based on modifications to laboratory test results (Appendix D) required to model the rock site empirical attenuation (Appendix A and Chapter 6). For the soil sites, the EPRI cohesionless soil curves (Chapter 6) are used as not enough soil sites are available with sufficiently high motions to discriminate between EPRI and the generic deep soil curves. For the Peninsular range soil sites, the generic deep soil curves are used along with the Northridge crustal model (Table 5.3).

The high shear-wave velocity of the top layer of the Mojave crustal model, 1.98 km/sec, is significantly higher than either the North Coast or Peninsular Range Provinces (1.0 km/sec) and is more like CEUS conditions than WUS (EPRI, 1993). Silva and Darragh (1995) obtained an average kappa value of 0.03 sec by fitting response spectral shapes for the three Mojave rock sites LUC, 29P, SIL (Table 4.4). This values is in agreement with the 0.03 sec value obtained in the regional inversions (Table 4.1) and reflects the dependence of kappa on shallow (1 to 2 km) crustal rock properties: harder rocks are associated with lower kappa values (lower damping) than soft rock site conditions (Silva and Darragh, 1995). As a result, the kappa values for the rock beneath the nonlinear zones (500 ft, Table 5.14) at both rock and Mojave soil sites is taken as 0.025 sec. This gives a total kappa value of 0.03 sec for Mojave rock and soil sites. For Peninsular Range soil sites the rock kappa value is 0.03 sec for total small strain kappa of 0.04 sec (Table 5.4).

The finite-source model parameters are listed Table 5.14. The rise time of 1.80 sec represents a best fit over a limited set of trial values and was selected based on a visual examination of the model bias, model variability, and response spectral fits. The static stress drop, based on the

area, is about 15 bars and the point-source stress drop resulting from the inversions (Table 4.4) is 40.7 bars. The point-source depth is taken as 8 km, the depth of the largest asperity in the Wald and Heaton (1994b) slip model (Figure 5.75).

5.4.1.1 Point-Source Inversions For Stress Drop and Kappa Values

The Landers earthquake is included in the Mojave Province set along with the North Palm Springs earthquake. The Fourier amplitude spectra for both the recordings and the model predictions are shown in Figure Set 4.4 and the site specific kappa values are listed in Table 4.4. For the Mojave sites, the average rock kappa value is 0.025 sec with the average value for soil of 0.050 sec.

5.4.1.2 Point-Source Modeling Results

For the point-source model, the bias and variability plots are shown in Figure 5.76 for all the sites. Over most of the frequency range, the bias reflects a general underprediction, particularly at low frequency (around 1 Hz). The peaks and troughs are related to the profile resonances with a trough in bias reflecting a profile resonance peak. The variability is generally low, below 0.5, above 1 Hz and shows the typical increase at low frequency due to unmodeled site variations. In general, Figure 5.76 shows that the point-source is capable of surprisingly accurate ground motion predictions for an M 7.2 extended rupture and for distances out to nearly 200 km (Table 5.2).

Because there are only 5 rock sites (3 within about 90 km, Figure 5.79) out of 57 total sites separate plots are not shown for rock site and soil sites analyses. In general, the rock sites show

a broadband negative bias that is controlled by 2 sites 29P and SIL (Figure 5.79).

To examine more closely the positive bias (underprediction) shown over all the sites (Figure 5.76), separate bias and variability estimates are shown computed for the Peninsular Range sites and Mojave sites alone. Figure 5.77 shows the results for the Peninsular Range sites, beginning with site POM at about 120 km (Figure 5.79). The figure shows a much more positive bias, except around 3 to 20 Hz where the bias is considered low. The increase in bias estimates at very high frequency, above 20 Hz actually reflects peak ground acceleration and is controlled by much lower frequencies; in the range where the response spectral accelerations peak over these distances, 100 to 200 km. The model bias then shows a large low frequency ($\leq$ 3 Hz) underprediction averaging about 0.5, a factor of about 1.6. This low frequency underprediction is apparent in the spectral plots, Figure 5.79, especially for the very distant sites beyond about 150 km. This feature is very similar to the intermediate period underprediction seen in the point-source model comparisons to empirical attenuations for M 7.5 at distances 100 and 200 km (Chapter 6, Figure Sets 6.10 and 6.11). Since the Peninsular Range sites are all soil (Figure 5.09), basin effects are suspected but, in the comparison to the empirical attenuation (Chapter 6), the same underprediction was present for <u>both</u> rock and soil sites. It is obviously an aspect of wave propagation not accounted for in the point-source model and may be related to intermediate to short period surface wave development or 2-D effects in crossing province boundaries with very different crustal structures.

To complete the picture, Figure 5.78 shows the analyses for the Mojave Province sites only. The distance range is about 1 to 100 km, site POM (Figure 5.79) is the first soil site in the

Peninsular Range province, and the bias estimates are near zero above 1 Hz and show the typical point-source overprediction below 1 Hz. The variability is low, about 0.5 above 0.5 Hz, suggesting that the model is performing quite well on average out to 100 km. These results are in general agreement with the empirical comparisons which indicate that the distance underprediction is magnitude dependent, increasing with increasing magnitude.

While not many data constrain the empirical attenuation relation for distances beyond 100 km for M larger than 7, the Landers results along with the empirical comparisons (Chapter 6) suggest caution in applying the point-source model for M larger than about 7¼ and for distances greater than 100 km. For these cases there is a reasonably high likelihood that the predictions could be low for frequencies below about 3 Hz, unless a high stress drop was used as compensation. This is of little consequence for WNA where the hazard is dominated by much closer sources but could be an issue in CEUS. If the underprediction is related to wave propagation effects not accommodated in the currently implemented point-source model, the same conditions may or may not apply in typical CEUS crustal structures. This is an important issue to resolve and the next section on the finite-fault model results will produce some useful insights.

Figure Set 5.79 shows the spectra plots and indicates that the point-source simulations do very well within about 100 km and begin to seriously underpredict (at low frequency) beyond. Interestingly, site LUC, at a fault distance of about 1 km from an 80 km long rupture (Table 5.14) is modeled very well by the simple point-source for periods as long as to 10 sec (The

Lucern recordings have been processed to retain appropriate long period energy; Bill Iwan, personal communication).

5.4.1.3 Finite-Source Modeling Results

For all 57 sites, the bias and variability estimates are shown in Figure 5.80. Overall the bias is lower than for the point-source (Figure 5.76) with a broad positive peak in the 1 to 3 Hz range. The bias corrected variability is also lower throughout most of the frequency range suggesting the finite-source is capturing more site-to-site variations in the recorded motions.

To examine the Peninsular Range site only, Figure 5.81 can be compared to the point-source results shown in Figure 5.77. For the finite-source, the bias is much lower, particularly at low frequency ($\leq$ 1 Hz) where the bias has decreased by 100%, from about 0.6 to around 0.3 (the profile resonances in the bias estimates would be smoothed out using a median response spectrum for each site). The randomness has also decreased substantially however the bias corrected estimates are essentially the same indicating that the source finiteness is not capturing more site-to-site variation but is simply producing larger motions beyond 100 km an average. These results are in agreement with the discussion on Attenuation With Distance in Chapter 6. The effects of source finiteness has a strong impact on the attenuation of motion with distance or far field slope (fall off beyond 1 source depth). Large source areas have a smaller slope simply due to the effects of finiteness. This feature is demonstrated in Chapter 6 and is consistent with the strong motion data. It is quite apparent in the Landers analyses for sites beyond about 100 km.

Returning to the point- and finite-source bias estimates for the Peninsular Range sites (Figures 5.77 and 5.81), although the underprediction has been substantially reduced with the finite-source, a significant positive bias (about 0.3) exists for frequencies below about 3 Hz. To see if this is also the case for the closer sites ($\leq$ 100 km), Figure 5.82 shows the bias and variability estimates computed over the 18 Mojave Province sites. The bias results are very similar to the point-source (Figure 5.78) and show a near zero bias above 1 Hz and a sharp fall off to overprediction below. Above about 5 Hz, the finite-source randomness is much lower than the point-source indicating that within 100 km, the finiteness is capturing aspects of site-to-site variation unmodeled in the point-source simulations.

The low frequency negative bias in both the point- and finite-source simulation results is intriguing. It is expected in the point-source and was present to a much lesser extent in the Northridge earthquake analyses (Figure 5.9). It may simply be related to including low velocity materials above the crustal models. The finite-fault low-frequency decrease in bias begins around 1 Hz, the approximate high frequency limit in the inversions for slip which use the crustal models without surficial materials. Neglect of the soil column amplification (the inversions are generally dominated by soil sites) results in a factor of about 2 over rock at 1 Hz (Figures 6.4 and 6.5). It would be of interest to use the stochastic finite-fault model, which incorporates site effects and material nonlinearity in slip model inversions. The result would likely reduce the low frequency bias by perhaps broadening the asperities.

The finite-source plots are shown in Figure 5.83 and generally reflect a good overall fit to the recorded motions. The distant motions, beyond about 100 km (Peninsular Range soil sites begin

with site POM) show the tendency to underpredict for periods longer than about 0.3 sec, the trend clearly seen in the bias estimates at about 3 Hz and below (Figure 5.81). This tendency is not nearly as severe as in the point-source spectra plots (Figure 5.79) and, with the bias estimates, indicates that source finiteness has not completely resolved the issue of low frequency underprediction beyond 100 km (the Peninsular Range sites). The underprediction may be generic or related to a region specific 2-D crustal path effect in propagating from the Mojave crust to the Northridge crust. The relatively broad band nature of the underprediction, below about 4 Hz and with a broad peak in the 1 to 3 Hz range, does not suggest basin effects. Also the comparisons to the empirical attenuation (Chapter 6) showed the point-source underprediction for M 7.5 at 100 and 200 km occurred for both rock and soil sites.

The underprediction issue for both the point- and finite-source models is potentially important for ground motion predictions for large magnitude earthquakes at distances exceeding about 100 km, and for frequencies below about 3 to 4 Hz.

5.4.2 1986 North Palm Springs Earthquake

The M 6.0 North Palm Springs earthquake modeling includes a total of 29 sites, 20 soil and 9 rock (Table 5.2). The distance range is about 1 to 90 km. Figure 5.84 shows the site map with the majority of stations located to the southwest of the rupture. The crustal model is from Hartzell (1989) and is listed in Table 5.15. As usual, the generic rock and soil profiles are placed on top of the regional crustal model. The shallow generic rock profile is truncated at a velocity of 1.7 km/sec, the velocity of the top layer of the Hartzell (1989) crustal model.

Both rock and soil sites are allowed to have nonlinear response to depths of 500 ft. For rock sites the G/G_{max} and hysteretic damping curves for generic rock (Chapter 6) are used while the EPRI curves are used for the cohesionless soils as with the Landers earthquake, a kappa value of 0.025 sec is used for the rock beneath the profiles to give a total small-strain kappa value of 0.03 sec for both rock and soil sites (Table 5.16).

The finite-source model parameters are listed in Table 5.16. The rise time of 0.45 sec represents a best fit over a suite of several trial values. The rupture area is large, 22 km by 15 km, giving a static stress drop of only 4.5 bars. The point-source stress drop is 62.8 bars (Table 5.16). Because the fault dips 46° to the northeast stations WWT and NPS are located over the rupture surface.

The slip model used is based on the use of aftershocks as Green functions and results basically in a single large asperity at a depth of about 10 km (Hartzell, 1989). The best fitting slip model resulting from the use of synthetic Green function contains a number of distributed asperities, some shallow, and results in a large high frequency ($\geq$ 1 Hz) underprediction by about 80%. Since the slip model inversions are for frequencies less than 1 Hz, this large difference in the high frequency motions between the two slip models was not apparent to Hartzell (1989). Because the slip model resulting from the empirical Green function inversions provided the closer high frequency fit, it was adopted for the analyses. Additionally, the current analyses incorporate shallow rock and soil shear-wave velocities while the synthetic Green functions were computed for the basic crustal model with a surface velocity of 1.7 km/sec. As a result, the use of the slip model based on the empirical Green functions is considered more consistent with the

current analyses. As the Landers earthquake analyses indicated, it would be of considerable interest to determine slip models for these earthquakes using the broadband stochastic finite-fault which accommodates nonlinear site effects in an inversion mode.

5.4.2.1 Point-Source Inversions For Stress Drop and Kappa Values

The North Palm Spring earthquake is included in the Mojave Province set along with the Landers earthquake. The Fourier amplitude spectra for both the recordings and the model predictions, are shown in Figure Set 4.4 and the site specific kappa values are listed in Table 4.4. For the Mojave sites, the average rock kappa value is 0.025 sec and the corresponding soil kappa value is 0.058 sec.

5.4.2.2 Point-Source Modeling results

Bias and variability estimates are shown in Figure 5.86 computed over all 29 sites for the point-source using a stress drop of 62.8 bars. The bias shows the typical negative low frequency point-source overprediction with the low frequency limit for reliable analyses at about 0.5 Hz. At higher frequency, the bias is positive indicating a slight underprediction. The variability plot shows values larger than for the Landers earthquake, about 0.5 from about 2 to 100 Hz.

For the 20 soil and 9 rock sites, Figures 5.87 and 5.88 show the corresponding analyses. As expected, due to the larger number of soil sites, the soil site results are very similar to all the sites. The rock sites however show a high frequency underprediction or negative bias of nearly 0.4 (factor of 1.4) above about 6 Hz. The rock site variability is higher than for the soil, which is not unexpected, and is quite poor below about 4 Hz.

The response spectra plots, Figure 5.89 also show the generally poor results at the rock sites while most of the soil sites are modeled reasonably well. Results of similar quality were obtained by Hartzell (1989) who attributes the difficulty in modeling this earthquake to the "extremely complex and varied geology".

5.4.2.3 Finite-Fault Modeling Results

Figure 5.90 shows the bias and variability estimates for the finite-source model over all the sites. The overall bias is positive above about 0.5 Hz and the point-source low frequency overprediction is not present. The variability is high however, about 0.6 throughout much of the reliable frequency range. The randomness is also high reflecting unmodeled site-to-site variation that is larger than the point-source for frequencies exceeding about 1 Hz (Figure 5.86).

For the soil and rock sites separately, Figures 5.9 and 5.92 show the bias and variability estimates. As with the point-source results, the soil is near zero and the rock shows a strong underprediction at high frequencies.

The spectra plots, Figure Set 5.93, reflect the generally acceptable fit to the soil sites and rather poor results for the rock sites. Even the results for the soil sites are perplexing. For example sites NPS and MVF are both soil, nearly over the rupture surface (Figure 5.84), and at about 10 km fault distance (Appendix B) yet there is a difference of at least 3 in recorded peak accelerations. Site NPS look more like a rock spectrum and MVF has very large 2 sec motions that the finite-fault modeling is not capturing. Based on both the point- and finite-source modeling results, it is comforting that a highly regarded colleague (Hartzell, 1989) experienced

similar difficulties with this earthquake.

5.5 1978 TABAS EARTHQUAKE

Data from only 4 sites are available for the M 7.4 Tabas earthquake: 3 rock and 1 soil. The fault distance range is about 3 to 90 km Table (5.2) and the site distribution is shown in Figure 5.94. The crustal model is listed in Table 5.17. The model is from Hartzell and Mendoza (1991) and is about 45 km thick, much thicker than typical California models (Chapter 3, and Table 5.3). It also has a high velocity surface layer (1.65 km/sec). Both aspects make it more like typical ENA crustal models than WNA (EPRI, 1993) and low kappa values (Silva and Darragh, 1995) might be expected to result from the inversions.

For both the rock and soil models, the generic shallow shear-wave profiles were placed on top of the Hartzell and Mendoza (1991) crust. Because the inversions did not show low ENA type kappa values for the rock sites (Table 5.18), a standard WNA value of 0.03 sec was used for the rock beneath the soil profiles (Table 5.19). Although the shear-wave velocity of the top crustal layer is about 5,400 ft/sec (Table 5.17) and would be expected to reflect a lower kappa value, the results from the inversions and modeling, limited by only 4 sites (3 close-in), suggest nominal WNA conditions. In this context, the Q_0 was fixed at 291, the value resulting from the combined WNA inversions (Table 4.1).

As with the previous earthquakes, nonlinear zones extend to 500 ft for both rock and soil sites (Table 5.19). The G/G_{max} and hysteretic damping curves are the same for the soft rock sites but the EPRI curves are used for the soil site (BOS) as well as all non-Peninsular Range cohesionless

soil sites (the Imperial Valley, Section 5.6, required more linear curves than the generic deep soil). In this case, with only one soil site and with relatively low motions, either set of curves would provide about the same results. Unless the ground motion data clearly demand more linear response such as in the Northridge earthquake, the EPRI curves are preferred, since they are based on laboratory testing (Chapter 6) and provide good results with the North Coast Loma Prieta earthquake (Section 5.3).

The finite-fault parameters are listed in Table 5.19. The slip model is from Hartzell and Mendoza (1991) and is shown in Figure 5.95. The rupture surface strikes 33° and dips 25° to the NE with a rake of 114°. The rise time is 3.53 sec based on several trial values and the subevent stress drop is fixed at 5 bars. The low subevent stress drop (nominally about 30 bars using the rupture area verses magnitude relation in Chapter 2) was found to be necessary for earthquakes with significant amounts of shallow slip (Chapter 2). The nominal 30 bar subevent stress drop results in short period motions a factor of 2 to 3 too large. The 5 bar value is based on an extensive modeling exercise for the Landers earthquake examining the effects of slip and depth dependent rise times as well as slip velocities. The simple, non-physical, lowering of the subevent corner frequency produced the best overall results but leaves the issue of how to model short period motions from shallow slip physically unresolved.

The static stress drop is 12.3 bars and the point-source stress drop is 21.5 bars (Table 5.19).

5.5.1 Point-Source Inversions for Stress Drop and Kappa Values

As with the Province inversions (Chapter 4), smooth transfer functions are incorporated for the

rock and soil sites. The rock sites include the generic shallow soft rock profile and the soil sites the generic deep soil (Chapter 3): both overlie the Hartzell and Mendoza (1991) crust (Table 5.17).

Results of the 4 station inversions are shown in Table 5.18. The average kappa value is 0.046 sec with the average of the 3 rock sites of 0.040 typical WNA values. The kappa values are a bit higher but in general agreement with those of Shoja-Taheri and Anderson (1988). The higher values obtained in this work reflects the inclusion of crustal and site amplification. The stress drop is low, about 22 bars (Table 5.18). If the rock sites are very hard, as the crustal model suggests, not using a transfer function which includes the shallow soft rock profile would result in lower kappa values and a higher stress drop. There are simply too few data (sites) and poorly known site conditions to resolve this issue.

The fits to the Fourier amplitude spectra are shown in Figure 5.96 and are good at high frequency (> 3 Hz) for the 3 close-in sites. The distant site (FER) appears to have a strong amplification from about 1 to 10 Hz. The fits at low frequency are poor and using the log average spectra (equal weighing with frequency, Chapter 4) does not offer any improvement: the stress drop decreases to 14 bars and the average kappa decreases to 0.031 sec.

The slip model is largely driven by teleseismic data as only 3 strong motion sites were used in the slip model inversion (Hartzell and Mendoza, 1991). The large misfit seen in the point-source Fourier amplitude spectrum (Figure 5.96) at site TAB is also poorly fit in the Hartzel and Mendoza inversion and in the modeling of Saikia (1994) as well. Because of the few close-in

data (3 sites) and poorly known site conditions as well as crustal structure, the slip model may simply be poorly known.

5.5.2 Point-Source Modeling Results

Figure 5.97 shows the point-source bias and randomness plots. With only 4 sites, little information is contained in the estimates as the range in the ± 90% confidence limits suggest. The bias is essentially zero but again showing the low frequency (< 1 Hz) point-source overprediction. The model variability is high and somewhat uniform at about 0.8.

The response spectra are shown in the next figure (Figure 5.98) and appear to capture the spectral shapes reasonably well. Perhaps a more refined distance measure accommodating the effects of sites located over dipping faults would improve the fit (reduce the variability, Chapter 4).

5.5.3 Finite-Source Modeling Results

The bias and variability estimates for the finite-source are similar to the point-source and are shown in Figure 5.35. The finite-source bias is more positive than the point-source for frequencies above 1 Hz and remains high at low frequencies reflecting a broad-band underprediction. The variability is the same as well, about 0.8, over most of the frequency range.

The response spectra are shown in Figure 5.100 and indicate a generally good fit except at site TAB. Eliminating this site results in a near zero bias from 0.1 to 100 Hz and significantly

reduces the variability. The large underprediction at this site drives the bias and variability estimates and suggest, due to its wideband nature, a generic problem with the slip model, station location, or instrument.

Except for site TAB both the point- and finite-source models perform reasonably well. The point-source overpredicts at the three sites which the finite-source models very well. This is probably due to too high a stress drop resulting from the inversions as the single site, TAB with high recorded motions, would have a large effect representing 25% of the data.

5.6 IMPERIAL VALLEY EARTHQUAKES

The analyses for the 1979 Imperial Valley earthquakes include the M 6.4 mainshock and the M 5.3 (Liu and Helmberger, 1985) aftershock. For the mainshock 33 soil and 2 rock sites are modeled, covering the distance range of about 1 to 50 km (Tables 5.2 and 5.22). The aftershock includes 16 soil sites (no rock site data are available) over the fault (hypocentral) distance range of about 12 to 52 km (Tables 5.2 and 5.23). For the mainshock, the site location map is shown in Figure 5.101.

The crustal model is from Liu and Helmberger (1980) with the top 98m replaced by a smoothed version of the El Centro profile (Bycroft, 1980). The shallow profile is based on downhole borehole measurements taken at the old El Centro strong motion site (new E09) and is listed in Table 5.20. The top 500 ft of the profile is shown in Figure 5.102 and the entire crustal model is shown in Figure 5.103. The crustal model (except for the top 93m) is the same model used

in the Liu and Helmberger (1985) study of the M 5.3 aftershock and is very similar to the crustal model used by Hartzell and Heaton (1983) in their inversions for the M 6.4 mainshock slip model. For rock sites, the shallow generic rock profile replaces the top 2.4 km of the generic Imperial Valley profile where the shear-wave velocity reaches 1.0 km/sec (Figure 5.103). This velocity occurs at a depth of about 100 ft (34m) in the generic rock profile (Figure 3.2)

In a similar manner as the other analyses, nonlinearity is permitted to depths of 500 ft in both the rock and soil profiles (Table 5.21). For the soil site, the shear-wave velocity at 500 ft is only 1,312 ft/sec (Table 5.21, Figure 5.102) and, with this stiffness, considerable nonlinear response would be expected at even greater depths under the 1979 M 6.4 loading conditions (over 50%g at some soil sites). It is assumed that the soils at greater depths are too dense to exhibit significant nonlinearity and are constrained to have linear response.

For the rock sites, the generic soft rock G/G_{max} and hysteretic curves are used. For the soil sites, analyses with the EPRI and generic deep soil curves showed too much nonlinear response and a separate set of curves are developed. Since the Imperial Valley soils generally consist of clays with classifications ranging from CL to CH and silty dense sands to at least 400 ft (NUREG, CR-1643), it is not surprising that the curves for cohesionless soils appear to be inappropriate. What is surprising however, is the small degree of nonlinearity shown in the soils, substantially less than the cohesive soil curves of Vucetic and Dobry (1991) would predict for this PI range, about 10 to 40% (Turner and Stokoe, 1982). Unless some modification of the

Vucetic and Dobry (1991) curves were made for the effects of confining pressure, use of their curves, as well as the EPRI and generic deep soil curves, greatly overdamp the motions.

The kappa values beneath the nonlinear zones is taken as 0.02 sec. This gives a total small strain kappa value of 0.03 sec for both the rock and soil sites. The soil site kappa value of 0.03 sec is based on Durward et al. (1996) who found a kappa value of 0.03 sec at low levels of ground motion by analyzing 24 earthquakes recorded at and near the El Centro array in the Empirical Valley.

For the rock site, the total kappa value is also 0.03 sec using a kappa of 0.02 sec for the materials below about 500 ft where the shear-wave velocity is 3,773 ft/sec in the Liu and Helmberger (1985) crust. The kappa values of 0.02 sec and 0.03 sec are not constrained by any local or regional data and a total kappa value of 0.04 to 0.05 sec would be more consistent with the empirical inversions as well as Peninsular Range rock sites. However, it is a bit difficult to imagine a kappa of 0.03 to 0.04 sec to be associated with rock with shear-wave velocities close to 4,000 ft/sec and higher while 0.02 sec is constrained for soil materials with velocities of 1,300 ft/sec: both at depths of about 500 ft. Since there are only 2 rock sites, the issue is not significant and assuming 0.02 sec results in the same low strain total kappa value of 0.03 sec for both rock and soil sites.

The finite-source model parameters are listed in Table 5.21 and the Hartzell and Heaton (1983) slip model is shown in Figure 5.104. The slip model largely consists of a single dominant asperity at a depth of about 8 km located almost directly beneath site EMO (Meloland Overpass,

Figure 5.101). The slip model has a considerable amount of shallow slip resulting in the use of a subevent stress drop of 5 bars. This is consistent with the Landers and Tabas earthquakes and is necessary to keep from dramatically overpredicting the high frequency ($\geq$ 1 Hz) motions. The rise time of 0.73 sec is a best fit over a limited number of trial values. The static stress drop is 12.6 bars and the point-source value from the inversion is 23.2 bars (Table 5.22). The point-source depth is taken as 8 km for the mainshock and 9.5 km for the aftershock (Liu and Helmberger, 1985).

5.6.1 Point-Source Inversions for Stress Drop and Kappa Values

In the inversions for stress drop and kappa values, smooth mean transfer functions are used to incorporate amplification appropriate for the Imperial Valley soil and rock sites. Magnitudes are held fixed (Chapter 4). The Q(f) model is also fixed at the Peninsular Range value of 264 for an η fixed at 0.6 (Table 4.1), as the distance range is too small to constrain the Q(f) models.

The point-source inversion results, stress drop and kappa values, are listed in Tables 5.22 and 5.23 for the mainshock and aftershock respectively.

Due to nonlinear site effects, the inversions consider the mainshock and aftershock in separate analyses as the same kappa value at a common site may not be appropriate for both earthquakes. This effect can be seen in the kappa values for the 2 common sites which experienced the highest motions during the mainshock: sites E07 and E06. The sites straddle the Imperial fault (Figure 5.101) and have average kappa values of about 0.07 sec for the mainshock (Table 5.22) and

about 0.04 sec for the aftershock (Table 5.23), a significant difference.

The stress drops are low, about 23 and 29 bars with the aftershock value slightly larger than the mainshock stress drop. Interestingly, the shallow slip events which require low subevent stress drops (Landers and Tabas) seem to have low point-source stress drops as well. The average kappa values over all the soil sites are 0.050 sec for the mainshock and a slightly lower value of 0.042 sec for the aftershock.

The fits to the Fourier amplitude spectra for the mainshock and aftershock are shown in Figure Sets 5.105 and 5.106 over the frequency range used in the inversions. For the mainshock, Figure Set 5.105, the overall fits are reasonably good over most of the bandwidths with some features of interest in the close-in sites. The closest sites, EMO, E07, and E06 show a large low frequency (0.3 Hz) peak which is absent in the two following close-in sites AEP and AGD. The close-in sites which do not have the low-frequency peak are to the south of the northward propagating rupture while sites EMO, E07, and E06 are in the direction of rupture propagation. The low frequency peak is the result of rupture directivity and is quite strong for these sites adjacent to the rupture surface. As the El Centro array sites move outward, away from the rupture, the peak diminishes slowly until beyond about 15 km where it diminishes rapidly (sites E02 and E12). A similar trend is not seen in the high frequencies suggesting that directivity is predominately a low frequency phenomenon (Silva, 1992). While nonlinearity would reduce the effects of directivity at high frequencies (Bill Joyner, personal communication), the surprisingly low degree of nonlinear response at these sites (except for sites EMO and E07) indicates that soil nonlinearity may not be reducing high frequency directivity effects to a significant degree.

Similar plots for the aftershock are shown in Figure Set 5.106. As with the mainshock, the fits are generally good with most of the reliable data at frequencies of 1 Hz and above. For both earthquakes, site DTA (DLT in the mainshock) are poorly fit. The model severely underpredicts the motions over a wide bandwidth resulting in anomalously low kappa values. In the forward modeling with both the finite (mainshock only) and point-sources the fit is equally poor. The reason for these underpredictions is not known.

5.6.2 Point-Source Modeling Results

5.6.2.1 M 5.3 Aftershock

Figure 5.107 shows the model bias and variability estimates computed over all 16 sites for the aftershock. The bias is near zero above 1 Hz (the low frequency limit of reliable analyses) to about 10 Hz and positive (about 0.2) above. The variability is nearly constant at about 0.5 from about 1 Hz to 100 Hz. This is not considered high as small magnitude earthquakes show more site-to-site variability than do large ($M \geq 6.5$) earthquakes (Appendix A).

The response spectra plot are shown in Figure Set 5.108 and reflect a generally good fit out to about 1 sec. The high frequency underprediction is largely driven by site DLT, which shows a peak acceleration underprediction of more than a factor of 3.

5.6.2.2 M 6.4 Mainshock

For the mainshock, Figure 5.109 shows the point-source model bias and variability plots computed over all 35 sites. The bias is small from about 0.2 Hz (the lower limit of the data)

to 100 Hz. The variability is also low for a small magnitude and is fairly uniform at about 0.5 over most of the frequency range.

Considering just the 33 soil sites, Figure 5.110 shown the corresponding bias and variability estimates. The bias is less positive and the variability has dropped slightly indicating a general improvement. The 2 rock sites (CPR and SOP) are poorly fit with large underpredictions, which can be seen the response spectra plots in Figure Set 5.111. For the soil sites, the predicted spectra provide a reasonably good match to the recorded motions with the exception of site DTA, which also shows a large and broadband underprediction.

Sites EMO and E07, the first 2 plots in Figure Set 5.111, show a mismatch in the spectral peaks between the simulations and recorded motions indicating too little nonlinear response in the equivalent linear analyses. These 2 sites appear to have undergone the greatest degree of nonlinearity and the derived G/G_{max} and hysteretic damping curves are probably too linear for these sites. However, for the remaining sites, the computed motions appear to capture the shapes and overall levels of the recorded motions reasonably well. The spectral peaks in the other close-in sites (E06, AEP, AGR, and E05) are near 0.2 sec in both the recorded and simulated motions.

A constraint on the possible nonlinearity is also possible by comparing the peak response in the aftershock spectra to those of the mainshock. At sites E06 and E07 for the aftershock (Figure Set 5.111) the peak spectral amplification is in the 0.2 to 0.3 sec range and shifts to about 0.6 to 0.8 sec during the mainshock for the 2 closest sites: EMO and E07 (examining the spectral

peak computed using the mainshock coda should show the peak shift back to shorter periods, Silva et al., 1986). At sites E06, E07, and E08 the peak response shows little or no shift between mainshock and aftershock indicating little increase in nonlinearity between the mainshock and aftershock. Profile randomization and use of the median spectrum will result in a shift of the peak response to longer periods (Figure 3.5) but not to the extent required to match the recorded motions of the mainshock shown in Figure Set 5.111. The result being that sites EMO and E07 appear to require more nonlinear curves than the remaining El Centro sites and there is little to suggest that they were subjected to significantly larger motions than sites E06 or E08, only 1 to 3 km more distant (Figure 5.10).

5.6.2.2.1 Development G/G_{max} and Hysteretic Damping Curves The sites of the El Centro array (including sites EMO and HVP) with peak accelerations ranging from about 12%g to 50%g are used to develop a set of G/G_{max} and hysteretic damping curves that are consistent with the assumed generic Imperial Valley profile and recorded motions.

The Imperial Valley earthquake effective source zone consists of a single large asperity located nearly directly below the El Centro array. Possibly because of this, the point-source model produces more accurate modeling results (lower bias and variability) than the finite-source model, particularly over the El Centro array. As a result, it is used to generate the control motions in the development of the modulus reduction and damping curves.

To assess the degree of nonlinear response across the 15 sites of the study array as well as the

effects of the EPRI and generic deep soil curves on the simulated motions, Figure 5.112 shows bias estimates for the suite of analyses. In the context of the assumptions in the analyses, the EPRI and generic deep soil curves show considerably more nonlinear response than appears appropriate and the linear analysis, with a constant kappa value of 0.03 shows sec a negative bias for frequencies above about 5 Hz. There is a strong contribution to this overprediction by sites EMO and E07 and the bias estimates indicate that most of the sites exhibited small degrees of nonlinear response.

A series of analyses using various suites of curves resulted in a depth dependent set with separate curves for 0 to 300 ft and beyond 300 ft. The curves are shown in Figure 5.113 and are intended to provide the best overall fit to the study site data. They result in a slightly positive bias (Figure 5.112) which would increase only slightly with randomization as the generic profile COV of about 0.4 (Appendix C) would be reduced to about 0.2 reflecting deep sites located in the same depositional environment.

Recent application of the profile correlation model to over 100 measured shear-wave velocity profiles at the Department of Energy Savannah River Site has shown a significant reduction in the profile shear-wave velocity COV over the generic value of about 0.4. This occurs for sites located kilometers apart and appears to be a result of similar depositional environment. There is another reduction in COV in going from the km scale to footprint scale (tens to hundreds of feet) which is much less dramatic. These results are important and show two step reductions in deep soil profile variability: a factor of 100% in going from generic (all North America) to km scale separation within the same depositional environment and another, smaller reduction

over scales of tens to hundreds of feet (Gabe Toro, personal communication).

As a result of the reduced COV expected for the Imperial Valley study sites, the slightly positive bias resulting from the Imperial Valley analyses with the curves is considered acceptable. The curves are likely too linear for sites EMO and E07 but appear to be appropriate for the other 13 sites (Figure 5.111).

The variability estimates over the study sites (Figure 5.112) is low, less than about 0.4 over the frequency range of reliable data (above about 0.2 Hz). In general the point-source model performed quite well for both the mainshock and aftershock at most of the sites.

5.6.3 Finite-Source Modeling Results

Figure 5.114 shows the bias and variability estimates for the finite-source model computed over all 35 sites. The bias is positive (about 0.2) at 2 Hz and above and the variability is uniformly high (0.6 to 0.7) over the entire bandwidth. Both the bias and variability estimates for the finite- source are larger than the point-source (Figure 5.109) indicating it is doing a poorer job of fitting the data.

As with the point-source model results, the rock sites (CPR and SUP) are underpredicted by a considerable degree and the bias and variability estimates improve slightly considering only the soil sites (Figure 5.115). In general, the point-source results are significantly better than the finite-source results and the reason for this difference is apparent in the plot of the response spectra, Figure Set 5.116. For sites in the direction of rupture EMO, E07, E06, E05, E08, etc.

both the point- and finite-source models give comparable results (Figure Sets 5.115 and 5.111). However for the sites which are located in the opposite azimuth, such as AEP, AGR, BCR, SHP, etc., the finite-source model shows consistently lower short period motions than the point-source simulations with a large underprediction of the recorded motions at short periods ($\leq$ 1 sec). Since the slip models are determined at periods exceeding about 1 sec this observation brings up the important issue that the sources of short period ($\leq$ 1 sec) radiation may not, under all circumstances, coincide with the sources of long period ($\geq$ 1 sec) radiation. Inversions for slip models using a broadband finite-fault source model with nonlinear site effects may reveal non-coincident sources of short and long period energy. The Imperial Valley modeling results suggest that the sites located to the southeast of the asperity may require additional source(s) of short period energy located at closer distances.

5.7 1985 NAHANNI EARTHQUAKE

The M 6.8 December 23, 1985 Nahanni earthquake occurred in western Canada but is considered to have important features in common with ENA earthquakes: thrust mechanism with regional compressive stresses, area of low seismicity rates, and a high velocity crust (Hartzell et al., 1994). As a result, the Nahanni earthquakes are generally considered to be ENA analogues and representative of source, path, and site characteristics to be expected in geographical ENA. Because of this, low kappa values are expected (Silva and Darragh, 1995) and the Q(f) model determined in the Saguenay inversion (Section 5.9) is used.

Only 3 sites, all hard rock, recorded this earthquake and all are within about 16 km of the rupture surface (Table 5.2). Figure 5.117 shows the site map with sites S1 and S2 located over

the fault rupture. The rupture surface dips 25° to the southwest and the top edge is at a depth of 4 km (Hartzell et al., 1994). The slip model is shown in Figure 5.118 and consists of 2 large asperities at depths of about 4 and 8 km (the hypocenter). Consistent with the modeling results for other earthquakes with significant shallow slip; Landers, Tabas, and Imperial Valley, the subevent stress drop is taken as 5 bars.

The crustal and source models are from Hartzell et al. (1994). The crustal model is listed in Table 5.24 and the source parameters are listed in Table 5.25. Because the sites are all hard rock and an appropriate shallow rock profile is unavailable, linear site response analyses are done in the modeling using the site specific kappa values resulting from the point-source inversion (Table 5.26).

The source rise time is 1.15 sec and both the static and point-source stress drops are about 13 bars (Table 5.25). The low stress drops are consistent with those of the other earthquakes with significant shallow slip, generally less than about 20 bars. Since 2 of the 3 sites are over the rupture surface, the point-source depth is taken as 4 km, the depth of the shallowest asperity.

5.7.1 Point-Source Inversions for Stress Drop and Kappa Values

As with the previous inversions, a smooth transfer function is used to accommodate the amplification of the Hartzell et al. (1994) crustal model (Table 5.24) from 8 km (depth of largest asperity, Figure 5.119) to the surface. The Q(f) model is fixed at 317 $f^{0.6}$, the best fit values from the Saguenay earthquake inversion (Section 5.9).

The results of the inversion are shown in Table 5.26. The point-source stress drop is low, 13.4 bars, and the kappa values average 0.016 sec, consistent with the average value of 0.012 sec found by Silva and Darragh (1995) for the same sites from eyeball fits using templates of response spectral shapes.

For this earthquake, because of the low kappa values and short distances, the bandwidth is extended to 50 Hz in the inversions. Results using a constant log (df) (frequency spacing) to produce even weighing across the bandwidth (Chapter 4) resulted in a lower stress drop (about a factor of 2), lower kappa values, and a poorer fit. The fits to the Fourier amplitude spectra are shown in Figure 5.119 over the frequency range used in the inversion. As usual, the point-source model is high relative to the recorded motions at low frequency and in general agreement at intermediate to high frequency. The large underprediction at site 1, averaging over a factor of 2 around 3 Hz is due in large part to the inclusion of the "moose kick" which occurred about 9 seconds into the record. This arrival, at just over 1g, is not present at the other 2 sites and is believed to have a very localized source beneath or adjacent to site 1. Similar difficulty was experienced by Hartzell et al. (1994) in modeling the records at this site.

5.7.2 Point-Source Modeling Results

For the point-source model, the spectra plots are shown in Figure 5.120. Sites 2 and 3 show reasonable agreement to the recorded motions but are high at long period and underpredict at short period. Site 1 shows the large underprediction present in the Fourier amplitude spectra.

The bias and variability estimates (Figure 5.121) are unconstrained but reflect the generally fair

fits obtained over all three sites.

5.7.3 Finite-Source Modeling Results

For the finite-source model, spectra and bias and variability plots are shown in Figures 5.122 and 5.123. The results are similar to those of the point-source, with a slight improvement at sites 1 and 3 but a broadband overprediction at site 2. The bias is lower at high frequencies but because neither the bias nor variability estimates are constrained, the difference between the point- and finite-source model is not resolvable.

In general, for both models, the fits may be considered fair, a similar conclusion reached by Hartzell et al. (1994) from their waveform modeling results.

5.8 1987 SUPERSTITION HILLS(B) EARTHQUAKE

The 1987 Superstition Hills earthquake modeled is event (B) which is the larger of the two earthquakes that occurred on November 24, 1987. The magnitude, **M** 6.7, is based on teleseismic observations and is incompatible with the strong motion data. Both the waveform modeling of Wald et al. (1990) and the current inversions find **M** 6.4 to be more consistent with the strong motion data.

A total of 12 sites (1 rock), all the available strong motion data (appendix B), are used in the inversion and forward modeling. Figure 5.124 shows the site map with the general area located in the northern Imperial Valley just south of the Salton Sea and north of the El Centro array.

As a result of the close proximity to the site area of the 1979 Imperial Valley earthquake, the same soil and rock profiles are used (Table 5.20). In addition, because the Superstition Hills site area reflects depositional environment similar to the El Centro array area, the Imperial Valley G/G_{max} and hysteretic curves (Figure 5.113) are used.

The slip model is from Wald et al. (1990) and is shown in Figure 5.125. The mechanism is vertical strike-slip and the top edge of the rupture is at a depth of 0.5 km. As with the Imperial Valley slip model (Figure 5.104), there is considerable shallow slip and a subevent stress drop of 5 bars is used. The rise time is 0.74 sec (Table 5.27) and is a best fit over a suite of trial values.

The point- and finite-source stress drops are 43.4 bars and 31.2 bars respectively. The static stress drop of 31.2 bars is the highest of the shallow slip events: Landers, Tabas, Imperial Valley, and Nahanni. The point-source depth is 9.0 km, the depth of the largest asperity in the Wald et al. (1990) slip model (Figure 5.125).

5.8.1 Point-Source Inversions for Stress Drop and Kappa Values

In the Superstition Hills earthquake inversions, the same rock and soil site transfer functions are used as for the Imperial Valley analyses. The inversion results are listed in Table 5.28. The stress drops are shown for M 6.4 and 6.7 with the preferred M 6.4 kappa values. The M 6.4 stress drop is 43.4 bars and the average soil kappa value is 0.051 sec, in agreement with the soil site average of 0.050 sec for the Imperial Valley mainshock (Table 5.22). The single rock site has a kappa value of 0.028 sec, slightly lower than the 0.034 value obtained for the same site

in the Imperial Valley inversion results.

The fits to the Fourier amplitude spectra are shown in Figure Set 5.126. Except for the rock site SSM, the point-source spectra provide a generally good match to the vector sum (divided by $\sqrt{2}$) spectra of the recorded motions.

5.8.2 Point-Source Modeling Results

Figure 5.127 shows the estimates of the model bias and variability for the point-source over all 11 sites. The bias is slightly negative (overprediction) and uniform from about 0.3 Hz (lower limit of reliable analyses) to 100 Hz. The variability is low over the same frequency range averaging about 0.4. In general the model is doing very well with a tendency to overpredict on average. These results are reflected in the response spectra plots shown in Figure 5.128. The overprediction is easily seen and is largest at site BRW. Except for the rock site, SSM, the model is capturing the overall levels and shapes reasonably well. Site PTS, the first plot in Figure 5.128, is almost directly over the fault (Figure 5.124) and shows a small short period overprediction. This is analogous to sites EMO and E07 (Figure Set 5.111) for the Imperial Valley earthquake. All three sites show similar levels of recorded motions and approximately the same degree of overprediction. This supports the conclusion that the Imperial Valley curves (Figure 5.113) are somewhat too linear at the cyclic shear strains generated at these sites but are appropriate for the other sites. A set of curves more appropriate for these three sites may reflect much sharper curvature at effective strains around 0.1%, the average strains generated over the top 50 ft at these sites. More analyses are required to refine the Imperial Valley curves and the current results are considered as acceptable.

5.8.3 Finite-Source Modeling Results

For the finite-source model, the bias and variability estimates are shown in Figure 5.129. For this earthquake, both the bias and variability estimates are quite similar for the point- and finite-source models. The bias is low, slightly negative and the variability is reasonably uniform at about 0.4 over most of the bandwidth. On average there is little statistical difference in the accuracy of the two models for this earthquake.

The corresponding response spectra plots are shown in Figure 5.130 and are similar to the point-source results (Figure 5.128).

In general both the point- and finite-source models provide a good fit to the recorded motions for this earthquake with the exception of the single rock site SSM.

5.9 1988 SAGUENAY EARTHQUAKE

The M 5.8 Saguenay earthquake occurred in the Quebec Province of Canada, well within geographic ENA. The earthquake represents the largest and most widely recorded event to occur in the ENA tectonic environment. Because of its relatively large high frequency motions, this earthquake has generated considerable uncertainty in quantifying strong ground motions in ENA (EPRI, 1993). The source spectrum of this earthquake is incompatible with the simple Brune single corner frequency omega-square source spectrum (Chapter 2), having a larger high frequency (frequencies above the corner frequency) spectral level relative to the low frequency spectra level than the simple Brune model predicts. To match the high frequency spectral level,

a large point-source stress drop is required (Ou and Herrmann, 1990; Somerville et al., 1990; EPRI, 1993). With a simple Brune source this results is large overprediction of the low frequencies and has resulted in the application of the two-corner spectral model to ENA (Atkinson, 1993). However, although the two-corner source spectral model matches the shape of the Saguenay ground motion spectra much better than the single-corner Brune model, it still dramatically underpredicts the absolute levels of the Saguenay data. To match the Saguenay mainshock high frequency spectral levels, the two-corner source model requires much higher frequency levels than the rest of the ENA recorded motions upon which model is based. The case is clear that the recorded high frequency motions from the 1988 Saguenay mainshock require special consideration regardless of how they are modeled. As a result, both the point-source and finite-source models for this earthquake show significant and unique departures from all of the other earthquakes modeled in this study.

For the Saguenay earthquake, 22 sites (all rock) are modeled covering the fault distance range of 47 to 460 km (Table 5.2). The site location map is shown in Figure 5.131 and spans a wide area as the most distant site (WBOZ) is at over 400 km epicentral distance.

The slip model is from Hartzell et al. (1994) and is plotted in Figure 5.132. It consists of a single asperity with a concentrated high slip region at a depth of about 26 km. The top edge of the rupture surface is at a depth of 22 km and dips eastwardly at 65°.

The crustal model is from Hartzell et al. (1994) and is listed in Table 5.29. Because all the sites are hard rock and an appropriate shallow generic profile is unknown, only the basic crustal

model is used along with linear site response analyses fixing the kappa values to those determined from the inversions (Table 5.31).

The source parameters are listed in Table 5.30. The point-source stress drop is very high, 572 bars, and the static stress drop is about 14 bars. The point-source depth is about 26 km, the center of the high slip region the single asperity (Figure 5.132). The subevent stress drop is 200 bars and the rise time is 0.46 sec. Both values represent a best fit over a very limited set of trial values.

5.9.1 Point-Source Inversion for Stress Drop, Kappa and Q(f)

To accommodate crustal amplification from a depth of 25 km to the surface, a smooth crustal transfer function is used in the inversions. The inversion results are listed in Table 5.31 with a stress drop of 572.2 bars and an average kappa value of 0.023 sec, significantly lower than the WNA average of about 0.04 sec (Chapter 6) and in general accord with the value of 0.016 sec from the Nahanni inversion. Interestingly, the kappa values at the GSC sites, which are located within and on the edge of the Grenville Province, are significantly lower than the ECTN values. The ECTN sites listed in Table 5.31 are all located in the Appalachian thrust belt, a region of crustal transition and the kappa values may reflect softer shallow (1 to 2 km) crustal rocks.

To obtain a Q(f) model appropriate for the region, the distant ECTN sites were added. Since these stations have only a vertical component, a constant H/V factor of 1.4 has been used to approximately convert them to an average horizontal component. Use of a more accurate

empirical frequency dependent H/V relation (Atkinson and Boore, 1994) is complicated by the choice of appropriate crustal amplification factors to apply to the corrected horizontal components. As a result, the simple constant factor is used. The resulting Q(f) model is 317 $f^{0.86}$. Interestingly, the Q_o value of 317 is very similar to WNA values for η fixed at 0.6 (Table 4.1). The main difference is in the stronger frequency dependence for the Saguenay data. At 10 Hz the Saguenay Q is approximately double (factor of 1.8) the WNA assuming the same Q_o value. At 1 Hz these results suggest that, apart from crustal propagation effects, WNA and ENA motions should attenuate in about the same manner.

The fits to the Fourier amplitude spectra over the bandwidths used at each site are plotted in Figure Set 5.133. The high frequency spectral levels are fit fairly well with the 572 bar stress drop, except for the most distant site at 460 km. The consequence of boosting the high frequencies with a single corner frequency is shown in the large low frequency overprediction at most of the sites.

5.8.2 Point-Source Modeling Results

The point-source bias and variability plots are shown in Figure 5.134. For frequencies at 1 Hz and above, the range of reliable analyses, the bias increases from a strong overprediction (a factor of about 1.5) to a constant of about 0.2 (a 20% underprediction) at 10 Hz. The variability is high ranging from about 0.5 at high frequency ($\geq$ 10 Hz) and increases to about 0.75 around 1 Hz. These high values are to be expected as the distance ranges out to nearly 500 km and 9 of the 22 sites are vertical components (Table 5.31), corrected to horizontal using a constant

factor. Taking these factors into consideration, the bias and variability plots are considered to reflect generally good results for the point-source model.

The response spectra plots are shown in Figure Set 5.135 and reflect a fair fit at high frequency and the low frequency overprediction, especially for the closer sites.

5.9.3 Finite-Source Modeling Results

For the finite-source model, the bias and variability estimates are shown in Figure 5.136. For both the bias and variability, the results are very similar to the point-source with the finite-source variability slightly larger.

The response spectra are shown in Figure Set 5.137 and are similar to the point-source results as well. At the two closest sites, 516 and 517, the finite-source levels near 1 Hz are too high. Overall, the motions are predicted fairly well, except at site WBO, the most distant site, which shown a very significant broadband underprediction.

The 200 bars subevent stress drop is a necessary ingredient in the finite-fault modeling. This value raises the spectral levels by a factor of about 2 for frequencies higher than the subevent corner, around 1 Hz. Interestingly, the 200 bar subevent stress drop results in a corner frequency of about 2 Hz, similar to that obtained by Somerville et al. (1990) for their empirical source function. They found that enriched high frequency energy was needed to match the strong motion amplitudes and used the closest strong motion recording to obtain a source function with appropriate spectral levels.

These results are all consistent and indicate that the Saguenay mainshock source is significantly different in spectral composition than any of the earthquakes modeled here. Special consideration must be taken with either point- or finite-source models to match both the high and low frequency spectral levels of this earthquake. In general, both the point- and finite-source models are considered to provide a fair fit to the recorded motions with both models showing too high low frequency motions, particularly for the closer stations.

5.10 1992 Little Skull Mountain Earthquake

The M 5.7 Little Skull Mountain earthquake occurred on the nuclear test facility (NTS) near Las Vegas, Nevada within the southern Great Basin tectonic region. In addition to the mainshock, the two largest aftershocks are used in the inversions to help constrain the kappa values at the common sites.

A total of 8 sites (all rock) are used in the inversions and forward modeling exercise. The mainshock was recorded at all 8 sites, spanning the distance range of 15 to 98 km (Table 5.2). The M 4.5 aftershock was recorded at 5 sites and the smaller M 4.2 aftershock at just 3 sites (Table 5.34). Only the mainshock is modeled and the site map is shown in Figure 5.138. The crustal model is based on a regional earthquake location model refined at the near surface by shallow geophysical data. The crustal model is listed in Table 5.32 and consists of a shallow stiff Tuff layer 40m thick overlying much more competent materials. The shallow Tuff, with shear-wave velocities around 2,000 ft/sec, would be expected to exhibit some nonlinear response at high levels of loading ($\geq$ 30%g). For the Little Skull Mountain earthquake, the highest peak

acceleration is about 20%g, as a result linear analyses are used with the inversion kappa values (Table 5.34).

The source parameters are listed in Table 5.33. The point-source and finite-source stress drops are 63.7 bars and 21.9 bars respectively. The point-source depth is taken at the hypocentral depth, 12 km. The rupture surface is about 7 x 7 km^2 and is based on the aftershock zone. The top edge of the rupture surface is at a depth of 5.8 km and dips 70° to the southeast. The slip distribution is shown in Figure 5.139 and was selected as the best fit from a suite of 30 randomly generated slip models (Silva, 1992). The best fit rise time is 0.38 sec and the subevent stress drop is 30 bars.

5.10.1 Point-Source Inversions for Stress Drop, Kappa, and Q(f)

As with the other inversions, a smooth transfer function is used to include the amplification from the source at 12 km to the surface. Results of the inversion are listed in Table 5.34 for the mainshock and two aftershocks. The mainshock stress drop is 63.6 bars with the aftershocks having significantly lower values. The Q(f) model is 256 $f^{0.47}$ which is lower than the WNA model of 291 $f^{0.6}$ resulting from the combined inversion of the Peninsular Range, North Coast, and Mojave earthquakes (Table 4.1). The kappa values average 0.023 sec, a value significantly below the WNA kappa of 0.04 sec resulting from the inversions of the empirical attenuation (Chapter 6). Apparently the shallow crustal rocks of the region are less attenuating those of tectomically more active California.

The Fourier amplitude spectra plots are shown in Figure Set 5.140 for the mainshock and the two

two aftershocks. At high frequencies, the fits are good while the model is high at intermediate frequencies. The spectral sag in the mainshock motions is interesting. It may be related to source finiteness (cancellation) as its frequency varies with station azimuth. However, it is quite strong at 100 km, 10 source dimensions away. It is clear that it is not a crustal or site resonance as none of the higher modes appear to be present. It would be interesting to see the results from a formal inversion for a slip model using these data.

5.10.2 Point-Source Modeling Results

Figure 5.141 shows the mainshock bias and variability estimates computed over the 8 sites. The ± 90% confidence limits are wide due to the small number of sites. The bias shows the typical low frequency point-source overprediction ranging from about -1 at 0.5 Hz (the lower limit of reliable analyses is about 0.2 Hz) and increasing to near zero around 5 Hz. The variability is low above 10 Hz and about 0.5 from about 2 to 10 Hz. Below 2 Hz, it is very high but the randomness (bias corrected variability) remains nearly uniform: most of the sites have a large misfit from 0.2 to 2 Hz which is constant in sign. This is easily seen in the response spectra plots shown in Figure Set 5.142. The point-source model is doing generally well at short period ($\leq$ 0.5 sec), overpredicting at longer periods, and converging to the recorded motions at long periods ($>$ 1 sec) as the high-pass filter corners are approached.

5.10.3 Finite-Source Modeling Results

As previously discussed, since a slip model was not available for this earthquake a suite of random models were generated using a method which preserves asperity characteristics such as size, number, and location. To calibrate the method, asperity characteristics were measured for

10 slip models determined by waveform modeling (published slip models) and a statistical model developed which preserves the observed statistical properties. The method was tested by generating suites of random slip models for the Loma Prieta and Whittier Narrows earthquakes and computing bias and variability estimates using the ensemble average spectra at each site. The resulting bias and variability estimates were compared to estimates computed using the published slip models based on waveform modeling. In general the bias and variability estimates computed using the simulated slip models were comparable to or lower than those computed using the "real" slip models. As a result it is believed that the slip model simulation procedure produces reasonable representations of actual slip models derived from inversions of recorded motions.

To select the best random slip model, simulations were performed for each slip model and the one which produced the lowest overall bias and uncertainty estimates was selected. The resulting estimates are shown in Figure 5.143. The bias is near zero at 3 hz above and shows an increasing overprediction to about 1 Hz where it increases with decreasing frequency. The $\pm$ 90% confidence are wide, wider than for the point-source suggesting higher variability. This is indeed the case and the finite-source variability is generally larger than that of the point-source above about 1 Hz.

The response spectra plots for the finite-source simulations are shown in Figure 5.144 and show about the same level of fit at high frequencies but with smaller low frequency motions. These results are surprisingly good considering the slip model was randomly selected. It would be of interest to perform a formal inversion for the best fitting slip distribution using the stochastic

finite-fault model to determine how much the fit is improved and over what frequency range.

5.11 1992 Cape Mendocino Earthquake

The M 6.8 Cape Mendocino earthquake occurred near the town of Petrolia in Northern California and may represent the largest event associated with the Cassadia subduction zone with instrumental recordings. The teleseismic M 7.1, which is based on very long period data ($\geq$ 45 sec) is incompatible with the 20 sec body waves (Hagerty and Schwartz, 1996) as well as the strong motion data. The lower M 6.8 was determined by Hagerty and Schwartz (1996) and is the preferred value in the strong motion inversions as well. To reduce the strong coupling between magnitude and corner frequency in the inversions, magnitude is held fixed at M 6.7 in the inversion for stress drop and kappa values.

A total of 5 sites (1 rock) were used in the inversions and forward modeling (Table 5.37). The fault distance range is 8 to 45 km (Table 5.2) and the site map is shown in Figure 5.145. Sites CMP and PET are located over the rupture surface. The crustal model is from Graves (1994) and the generic shallow rock and soil profiles are placed on top of the regional crustal model. Nonlinear zones for both rock and soil sites extend to 500 ft with a total low strain kappa of 0.04 sec (Table 5.36) for both site conditions. For the rock sites, the generic soft rock G/G_{max} and hysteretic damping curves are used. Since too few soil site recordings are available to reliably discriminate between the EPRI and generic deep soil curves, the EPRI curves assumed to be appropriate for the soil sites. The source parameters are listed in Table 5.36. The slip model is from Graves (1994) and is shown in Figure 5.146. It consists predominately of a

single large asperity at a down dip depth of about 20 km (9.6 km depth). The rupture surface dips 140 to the northeast with the top edge at a depth of 4.2 km. The rise time is 1.40 sec and the subevent stress drop is 30 bars. The point-source and finite-source stress drops are 27.2 bars and 13.2 bars respectively (Table 5.36).

5.11.1 Point-Source Inversions for Stress Drop and Kappa Values

As in the other inversions, smooth mean transfer functions appropriate for rock and soil sites are used. The Q(f) model is fixed at the North Coast value (176 $f^{0.6}$, Table 4.1) and the inversion results are listed in Table 5.37. The point-source stress drop is 27.2 bars and the average soil kappa value is 0.068 sec. The rock site, CPM, has a low kappa for California rock, 0.026, suggesting reasonably hard rock conditions. This low kappa value may have contributed to the unusually high short period motions which exceeded 1g at this site.

The Fourier amplitude spectra are shown in Figure 5.147 and reflect a generally good fit over most of the frequency ranges. Sites CPM and EUR show an underpredictions below about 3 Hz to about 0.2 Hz. The broad peak at site CPM (Cape Mendocino) from about 3 to 8 Hz is likely driving the high levels of the short period response spectra seen at this site. Taking the peak Fourier amplitude spectra as about 130 cm/sec^2 at the 7 Hz peak, and assuming the bandwidth is 2 Hz around the peak, results in a time domain estimate of 0.93g: close to the average of about 1.2g for the horizontal components. Interestingly, this peak is present to a lesser extent at all the close-in sites, PET, FOR, and RIO and decreases in prominence with distance very rapidly. This observation suggests that it is source related and perhaps enhanced by local site conditions at the Cape Mendocino site. Overall, fits to the Fourier amplitude spectra are

considered good.

5.11.2 Point-Source Modeling Results

With only 5 sites, the bias and variability estimates are poorly constrained. This is reflected in the large range in the ± 90% confidence limits shown in Figure 5.147. The bias estimates indicate a general and large underprediction at high frequencies beginning at about 1 Hz. The variability is high, nearly 0.75, above 1 Hz, indicating a generally poor fit. This is seen in the response spectra plots shown in Figure 5.148. Basically none of the sites are fit very well, possibly due to the point-source distance definition (Chapter 4) being poor in cases where the sites are over or near the edges of shallow dipping rupture surfaces.

5.11.3 Finite-Source Modeling Results

Significantly better results are seen in the finite-source modeling as Figure 5.149 illustrates. The bias is small at 0.5 Hz and above and the variability has decreased to about 0.5 over the same frequency range. The response spectra fits, Figure 5.150, reflect the improvement and show reasonably good fits at sites CPM, EUR, PET, and RIO. A lower kappa value (0.025 sec) at site CPM would increase the spectral levels below 0.1 sec by about 20 to 30%, nearly the level of the recorded motions. Apparently the anomalously large motions at CPM are largely being captured by the source finiteness coupled with hard rock site conditions. A more refined slip model would hopefully improve the fit at site FOR. Overall the fit with the finite-source simulations is clearly superior to that of the point-source and suggests that for sites located over or adjacent to shallow dipping ruptures, the current point-source distance metric warrants improvement.

5.12 Model Bias and Variability Estimates

The bias and variability estimates computed over all the earthquakes (16) and sites (503) reflect the magnitude range M 5.3 (Imperial Valley aftershock) to M 7.4 and a site distance range of 1 to 218 km (460 km for CEUS). This represents a comprehensive data set and is expected to provide a statistically robust assessment of both the point- and finite-source models.

5.12.1 Point-Source Model

Final model bias and variability estimates for the point-source model are shown in Figures 5.152, 5.153, and 5.154 for all, soil, and rock sites respectively. Over all the sites (Figure 5.152) the bias is slightly positive for frequencies greater than about 10 Hz and is near zero from about 10 Hz to 1 Hz. Below 1 Hz, the stable point-source overprediction is reflected in the negative bias. The analyses are considered reliable down to about 0.3 Hz where the point-source shows about a 40% overprediction.

The model variability is low, about 0.5 above about 3 to 4 Hz and increases with decreasing frequency to near 1 at 0.3 Hz. Above 1 Hz, there is little difference between the total variability (uncertainty plus randomness) and randomness (bias corrected variability, Section 5.1.1) reflecting the near zero bias estimates. Below 1 Hz there is considerable uncertainty contributing to the total variability suggesting that the model can be measurably improved as its predictions tend to be consistently high at very low frequencies ($\leq$ 1 Hz). This stable misfit may be interpreted as the presence of a second corner frequency for WNA sources (Atkinson and Silva, 1996).

For the soil sites, Figure 5.153 shows a slight improvement at 1 Hz and above in both the bias and variability estimates. This indicates that the rock sites must reflect the converse and Figure 5.154 does show larger bias and variability estimates than the results for all the sites. Soil sites are modeled more accurately than rock sites. This suggests that strong ground motions at rock sites are more variable than motions at soil sites and the model is not capturing the increased site-to-site variation. The larger rock site bias above 10 Hz suggests a small stable underprediction possibly due to the use of a single smooth rock profile rather than randomizing the profile and using a mean spectrum. This is consistent with the trend seen in the individual earthquake analyses: soil sites are modeled more accurately than rock sites.

For the finite-fault, Figures 5.155, 5.156, and 5.157 show the corresponding bias and variability estimates. For all the sites, the finite-source model provides slightly smaller bias estimates and, surprisingly, slightly higher variability for frequencies exceeding about 5 Hz. The low frequency ($\leq$ 1 Hz) point-source overprediction is not present in the finite-source results, indicating that it is giving accurate predictions over a broad frequency range, from about 0.3 Hz (the lowest frequency of reliable analyses) to the highest frequency of the analyses. For the soil and rock sites, a trend similar to the point-source results is present: the bias is larger and the variability is higher for rock site conditions than for soil site conditions.

In general, for frequencies of about 1 Hz and above the point-source and finite-source give comparable results: the bias estimates are small (near zero) and the variabilities range from about 0.5 to 0.6. These estimates are low considering the analyses are based on a data set comprised of earthquakes with **M** less than **M** 6.5 (288 of 513 sites) and high frequency ground motion

variance decreases with increasing magnitude, particularly above M 6.5 (Youngs et al., 1995; Appendix A). Additionally, for the vast majority of sites, generic site conditions were used (inversion kappa values were used for only the Saguenay and Nahanni analyses, 25 rock sites). As a result, the model variability (mean = 0) contains the total uncertainty and randomness contribution for the site. The parametric variability due to uncertainty and randomness in site parameters: shear-wave velocity, profile depth, G/G_{max} and hysteretic damping curves need not be added to the model variability estimates. It is useful to perform parametric variations to assess site parameter sensitivities, but only source and path damping Q(f) parametric variabilities require assessment on a site specific basis and added to the model variability. The source uncertainty and randomness components include point-source stress drop and finite-source slip model and nucleation point variations (Silva, 1992).

As an additional assessment of the stochastic models, bias and variability estimates were made over all earthquakes (except Saguenay since it was not used in the regressions) and sites using the empirical attenuation relation. For all the sites, the estimates are shown in Figure 5.158. Interestingly, the point-source overprediction below about 1 Hz is present in the empirical relation perhaps suggesting the model functional form for spectral shape requires refinement. Comparing these results to the point- and finite-source results (Figures 5.152 and 5.155) shows comparable bias and variability estimates. Over all the sites, the numerical models perform about as well as the well constrained empirical model (removing the Saguenay earthquake slightly improves the model results).

Considering just soil sites, Figure 5.159 shows similar bias estimates as the models (Figures

5.153 and 5.156) but the model variability is slightly lower. The models, point- and finite-source, are slightly more accurate than the empirical relation. For the rock sites, Figure 5.160, model simulations are comparable to the empirical relation, except the point-source and finite-source models (Figures 5.154 and 5.155) show a slight positive bias at 3 Hz and above 20 Hz. In general, both the point- and finite-source models produce ground motion estimates that are as accurate as the empirical model when averaged over all sites. It is likely that there is a distance bias and the models perform better than the empirical at close distances and worse at large distances (particularly the point-source model). These results are very encouraging and provide an addition qualitative validation of the point- and finite-source models. Praranthetically this approach provides a rational basis for evaluating empirical attenuation models.

5.13 Revised Rise Time Seismic Moment Relation

To complete the finite-fault analyses, the revised rise time verses seismic moment relation is shown in Figure 5.161. It reflects slightly longer (12%) rise times than the empirical relation

$$\log(\tau) = 0.33 \log(M_o) - 8.62 \qquad (5\text{-}3)$$

which was based on rise times determined by waveform modeling (Heaton, 1990). The revised relation is given by

$$\log(\tau) = 0.33 \log(M_o) - 8.54 \qquad (5\text{-}4)$$

and is an eyeball fit to the best fit rise times resulting from the finite-fault modeling (Figure 5.158, Table 5.38). The 12% increase is not considered to indicate a significant difference from the empirical relation since uncertainty in rise times determined by waveform modeling is generally considered high. The revised relation results in slightly lower motions (about 5 to 10%) and provides slightly better bias estimates. As a result, it is retained as a refinement of the finite-source model.

Because the finite-source bias estimates were based on the best fitting rise times with Equation 5-3 providing starting values, new bias estimates should be computed using the revised rise time/moment scaling relation (Equation 5-4). However, because the best fitting rise times are very close to the revised model (within about $\pm$ 10%), the impacts on the bias estimates would be very small.

5.14 Point-Source Stress Drop Summary and Generic WNA Parameters

Table 5.39 lists the point-source stress drops determined for each earthquake. The average (log) for WNA earthquakes (including Tabas) is about 47 bars. This value is consistent with the 59 bar average over mechanism and magnitude (M 5.5 to M 7.5) determined in the inversions of the empirical attenuation relation (Chapter 6, Table 6.1). Based on these results, a reasonable value for a magnitude and mechanism independent stress drop for applications to WNA is 60 bars. The additional WNA parameters, Q(f) and kappa, are listed in Table 4.1 by geologic province or combined provinces for region independent applications. For generic applications a rock kappa value of 0.04 sec is recommended since the Mojave Province (kappa = 0.030 sec) is significantly underrepresented in rock sites (Chapter 5). For soil sites, Chapter 6 will show

that kappa does depend on level of control motion (expected rock outcrop) and an appropriate constant value requires assessment of desired levels of conservatism. In general, a soil kappa of 0.06 sec represents a reasonable value for generic applications. It is important to emphasize, however, that all of these parameters; stress drop, kappa, and Q(f), must be used in a manner consistent with the crustal and soil/rock amplification factors used in the inversions. For example, the kappa of 0.06 sec must be used with soil amplification appropriate for soil sites ranging in depth from 100 ft to 1,000 ft and is most appropriate for deep soils. In all cases, rock or soil sites, crustal amplification must also be included for these parameter values to result in realistic ground motion levels.

Table 5.1 Contributions to Total Variability in Ground Motion Models

	Modeling Variability	Parametric Variability
Uncertainty *(also Epistemic Uncertainty)*	Modeling Uncertainty: Variability in predicted motions resulting from particular model assumptions, simplifications and/or fixed parameter values. *Can be reduced by adjusting or "calibrating" model to better fit observed earthquake response.*	Parametric Uncertainty: Variability in predicted motions resulting from incomplete data needed to characterize parameters. *Can be reduced by collection of additional information which better constrains parameters*
Randomness *(also Aleatory Uncertainty)*	Modeling Randomness: Variability in predicted motions resulting from discrepancies between model and actual complex physical processes. *Cannot be reduced for a given model form.*	Parametric Randomness: Variability in predicted motions resulting from inherent randomness of parameter values. *Cannot be reduced a priori* by collection of additional information.*

*Some parameters (e.g. source characteristics) may be well defined after an earthquakes.

Table 5.2 Earthquakes Modeled

Earthquake	Date	M	Fault Distance Ranges(km)	Rock Sites	Soil Sites	Total Sites
San Fernando	1971	6.6	3 - 218	21	18	39
Tabas	1978	7.4	3 - 90	3	1	4
Coyote Lake	1979	5.7	3 - 30	3	7	10
Imperial Valley	1979	6.4	1 - 50	2	33	35
Imperial Valley(AS)	1979	5.3	12 - 52	0	16	16
Morgan Hill	1984	6.2	1 - 70	8	21	29
Nahanni	1985	6.8	6 - 16	3	0	3
North Palm Springs	1986	6.0	1 - 90	9	20	29
Whittier Narrows	1987	6.0	10 - 80	18	70	88
Superstition Hills(B)	1987	6.4* (6.7)	1 - 28	1	11	12
Saguenay	1988	5.8	47 - 460	22	0	22
Loma Prieta	1989	6.9	5 - 90	33	20	53
Little Skull Mtn.	1992	5.7 (4.4,4.2)**	15 - 98	8	0	8
Landers	1992	7.2	1 - 177	5	52	57
Cape Mendocino	1992	6.8	8 - 45	1	4	5
Northridge	1994	6.7	7 - 147	23	71	94
			Total	159	344	503

*Preferred Value (see Chapter 5)
**Aftershocks

Table 5.3 Northridge Crustal Model (from Wald and Heaton, 1994)

Thickness (km)	V_s (km/sec)	Density (cgs)
0.5	1.0	2.1
1.5	2.0	2.3
2.5	3.2	2.5
23.0	3.6	2.6
5.0	3.9	2.9
	4.5	3.0

Table 5.4 Northridge Earthquake Source, Path, and Site Parameters

M = 6.7
$\Delta\sigma$ bars = 62.9* (point), 39.2 (finite)**
Q_0 = 264, η = 0.60 (Table 4.1)
Point Source Depth = 11 km
Crustal Model: Wald and Heaton (1994)
Rock Site Parameters
Nonlinear Zone: 500 ft
κ = 0.03 sec: rock below nonlinear zone, V_s = 3,281 ft/sec
κ = 0.04 sec: total, small strain
G/G_{max} and Hysteretic Curves: generic soft rock, Chapter 6
Soil Site Parameters
Nonlinear Zone: 500 ft
κ rock = 0.03 sec: below nonlinear zone, V_s = 3,281 ft/sec
κ rock = 0.04 sec: total, small strain
G/G_{max} and Hysteretic Curves: generic deep soil, Chapter 6
Finite Fault Parameters
Fault Length = 18.0 km, Fault Width = 21.9 km (Wald and Heaton, 1994)
M (subevent) = 5.0
Subfault Length = 3.6 km, Subfault Width = 2.6 km
Number of Subfaults = 40
Rise Time = 1.30 sec, Subevent Rise Time = 0.15 sec, Subevent Stress Drop = 30 bars
Slip Model: Wald and Heaton (1994)
Site Distances and Kappa Values, See Table 4.2

*Table 4.2

** $\Delta\sigma = \frac{7}{16} M_0 / (A/\pi)^{\frac{3}{2}}$

Table 5.5 San Fernando Earthquake Source, Path, and Site Parameters

M = 6.6
$\Delta\sigma$ bars = 36.1* (point), 34.3 (finite)**
Q_0 = 264, η = 0.60 (Table 4.1)
Point Source Depth = 8 km
Crustal Model: Wald and Heaton (1994) Northridge
Rock Site Parameters
Nonlinear Zone: 500 ft
κ = 0.03 sec: rock below nonlinear zone, V_s = 3,281 ft/sec
κ = 0.04 sec: total, small strain
G/G_{max} and Hysteretic Curves: generic soft rock, Chapter 6
Soil Site Parameters
Nonlinear Zone: 500 ft
κ rock = 0.03 sec: below nonlinear zone, V_s = 3,281 ft/sec
κ rock = 0.04 sec: total, small strain
G/G_{max} and Hysteretic Curves: generic deep soil, Chapter 6
Finite Fault Parameters
Fault Length = 18.0 km, Fault Width = 19.0 km (Heaton, 1982)
M (subevent) = 5.0
Subfault Length = 3.0 km, Subfault Width = 3.2 km
Number of Subfaults = 36
Rise Time = 1.25 sec, Subevent Rise Time = 0.15 sec, Subevent Stress Drop = 30 bars
Slip Model: Modified Heaton (1982)
Site Distances and Kappa Values, See Table 4.2

*Table 4.2

** $\Delta\sigma = \frac{7}{16} M_0/(A/\pi)^{\frac{3}{2}}$

Table 5.6 Whittier Narrows Earthquake Source, Path, and Site Parameters

M = 6.0
$\Delta\sigma$ bars = 95.7* (point), 27.3 (finite)**
Q_0 = 264, η = 0.60 (Table 4.1)
Point Source Depth = 15 km
Crustal Model: Wald and Heaton (1994) Northridge
Rock Site Parameters
Nonlinear Zone: 500 ft
κ = 0.03 sec: rock below nonlinear zone, V_s = 3,281 ft/sec
κ = 0.04 sec: total, small strain
G/G_{max} and Hysteretic Curves: generic soft rock, Chapter 6
Soil Site Parameters
Nonlinear Zone: 500 ft
κ rock = 0.03 sec: below nonlinear zone, V_s = 3,281 ft/sec
κ rock = 0.04 sec: total, small strain
G/G_{max} and Hysteretic Curves: generic deep soil, Chapter 6
Finite Fault Parameters
Fault Length = 10.0 km, Fault Width = 10.0 km (Hartzell and Iida, 1990)
M (subevent) = 5.0
Subfault Length = 3.3 km, Subfault Width = 2.5 km
Number of Subfaults = 12
Rise Time = 0.50 sec, Subevent Rise Time = 0.15 sec, Subevent Stress Drop = 30 bars
Slip Model: Hartzell and Iida (1990)
Site Distances and Kappa Values, See Table 4.2

*Table 4.2

** $\Delta\sigma = \frac{7}{16} M_0/(A/\pi)^{\frac{3}{2}}$

Table 5.7 Loma Prieta Crustal Model (from Wald et al., 1991)

Thickness (km)	V_s (km/sec)	Density (cgs)
0.1	1.00	2.00
0.4	1.95	2.30
0.5	2.48	2.35
2.0	2.77	2.35
2.0	3.10	2.35
2.0	3.31	2.45
2.0	3.55	2.58
4.0	3.61	2.62
5.0	3.62	2.63
7.0	3.85	2.77
	4.62	3.28

Table 5.8 Loma Prieta Earthquake Source, Path, and Site Parameters

M = 6.9
$\Delta\sigma$ bars = 73.7* (point), 33.0 (finite)**
Q_0 = 176, η = 0.60 (Table 4.1)
Point Source Depth = 12 km
Crustal Model: Wald et al. (1991)
Rock Site Parameters
Nonlinear Zone: 500 ft
κ = 0.03 sec: rock below nonlinear zone, V_s = 3,281 ft/sec
κ = 0.04 sec: total, small strain
G/G_{max} and Hysteretic Curves: generic soft rock, Chapter 6
Soil Site Parameters
Nonlinear Zone: 500 ft
κ rock = 0.03 sec: below nonlinear zone, V_s = 3,281 ft/sec
κ rock = 0.04 sec: total, small strain
G/G_{max} and Hysteretic Curves: EPRI, Chapter 6
Finite Fault Parameters
Fault Length = 40.0 km, Fault Width = 17.5 km (Wald et al., 1991)
M (subevent) = 5.0
Subfault Length = 3.3 km, Subfault Width = 2.5 km
Number of Subfaults = 84
Rise Time = 1.60 sec, Subevent Rise Time = 0.15 sec, Subevent Stress Drop = 30 bars
Slip Model: Wald et al. (1991)
Site Distances and Kappa Values, See Table 4.3

*Table 4.3

** $\Delta\sigma = \frac{7}{16} M_0/(A/\pi)^{\frac{3}{2}}$

Table 5.9 Coyote Lake Crustal Model (from Liu and Helmberger, 1983)

Thickness (km)	V_s (km/sec)	Density (cgs)
0.5	1.5	2.40
2.5	2.8	2.70
9.0	3.3	2.78
	3.9	3.80

Table 5.10 Coyote Lake Earthquake Source, Path, and Site Parameters

M = 5.7
$\Delta\sigma$ bars = 70.1* (point), 14.6 (finite)**
Q_0 = 176, η = 0.60 (Table 4.1)
Point Source Depth = 8 km
Crustal Model: Liu and Helmberger (1983)
Rock Site Parameters
Nonlinear Zone: 500 ft
κ = 0.03 sec: rock below nonlinear zone, V_s = 4,900 ft/sec
κ = 0.04 sec: total, small strain
G/G_{max} and Hysteretic Curves: generic soft rock, Chapter 6
Soil Site Parameters
Nonlinear Zone: 500 ft
κ rock = 0.03 sec: below nonlinear zone, V_s = 4,900 ft/sec
κ rock = 0.04 sec: total, small strain
G/G_{max} and Hysteretic Curves: EPRI, Chapter 6
Finite Fault Parameters
Fault Length = 10.0 km, Fault Width = 7.6 km Liu and Helmberger (1983)
M (subevent) = 5.0
Subfault Length = 3.3 km, Subfault Width = 2.5 km
Number of Subfaults = 9
Rise Time = 0.36 sec, Subevent Rise Time = 0.15 sec, Subevent Stress Drop = 30 bars
Slip Model: Liu and Helmberger (1983)
Site Distances and Kappa Values, See Table 4.2

*Table 4.3

** $\Delta\sigma = \frac{7}{16} M_0 / (A/\pi)^{\frac{3}{2}}$

Table 5.11 Morgan Hill Crustal Model (from Hartzell and Heaton, 1986)

Thickness (km)	V_s (km/sec)	Density (cgs)
0.7	1.55	2.22
2.3	2.60	2.45
2.0	2.94	2.55
4.0	3.26	2.65
4.5	3.46	2.70
3.1	3.92	2.82
6.4	3.17	2.60
	4.38	2.90

Table 5.12 Morgan Hill Earthquake Source, Path, and Site Parameters

M = 6.2
$\Delta\sigma$ bars = 49.0* (point), 10.0 (finite)**
Q_0 = 176, η = 0.60 (Table 4.1)
Point Source Depth = 8 km
Crustal Model: Hartzell and Heaton (1986)
Rock Site Parameters
Nonlinear Zone: 500 ft
κ = 0.03 sec: rock below nonlinear zone, V_s = 5,086 ft/sec
κ = 0.04 sec: total, small strain
G/G_{max} and Hysteretic Curves: generic soft rock, Chapter 6
Soil Site Parameters
Nonlinear Zone: 500 ft
κ rock = 0.03 sec: below nonlinear zone, V_s = 5,086 ft/sec
κ rock = 0.04 sec: total, small strain
G/G_{max} and Hysteretic Curves: EPRI, Chapter 6
Finite Fault Parameters
Fault Length = 27.0 km, Fault Width = 11.5 km (Hartzell and Heaton, 1986)
M (subevent) = 5.0
Subfault Length = 3.4 km, Subfault Width = 2.9 km
Number of Subfaults = 32
Rise Time = 0.70 sec, Subevent Rise Time = 0.15 sec, Subevent Stress Drop = 30 bars
Slip Model: Hartzell and Heaton (1986)
Site Distances and Kappa Values, See Table 4.3

*Table 4.3

** $\Delta\sigma = \frac{7}{16} M_0/(A/\pi)^{\frac{3}{2}}$

Table 5.13 Landers Crustal Model (from Wald and Heaton, 1994b)

Thickness (km)	V_s (km/sec)	Density (cgs)
1.5	1.98	2.30
2.5	3.15	2.60
22.0	3.52	2.70
5.0	3.83	2.87
	4.50	3.10

Table 5.14 Landers Earthquake Source, Path, and Site Parameters

M = 7.2
$\Delta\sigma$ bars = 40.7* (point), 15.4 (finite)**
Q_0 = 371, η = 0.60 (Table 4.1)
Point Source Depth = 8 km
Crustal Model: Wald and Heaton (1994b) Landers
Rock Site Parameters
Nonlinear Zone: 500 ft
κ = 0.02 sec: rock below nonlinear zone, V_s = 6,496 ft/sec
κ = 0.03 sec: total, small strain
G/G_{max} and Hysteretic Curves: generic soft rock, Chapter 6
Soil Site Parameters
Nonlinear Zone: 500 ft
κ rock = 0.02*** sec: below nonlinear zone, V_s = 6,496 ft/sec
κ rock = 0.03 sec: total, small strain
G/G_{max} and Hysteretic Curves: EPRI, Mojave soil, generic deep soil, Peninsular Range soil, Chapter 6
Finite Fault Parameters
Fault Length = 78.0 km, Fault Width = 15.0 km
M (subevent) = 5.0
Subfault Length = 3.1 km, Subfault Width = 3.0 km
Number of Subfaults = 125
Rise Time = 1.80 sec, Subevent Rise Time = 0.15 sec, Subevent Stress Drop = 5 bars
Slip Model: Wald and Heaton (1994b)
Site Distances and Kappa Values*

*Table 4.4

** $\Delta\sigma = \frac{7}{16} M_0 / (A/\pi)^{\frac{3}{2}}$

***For sites located in the Peninsular Range a kappa value of 0.03 sec is used

Table 5.15 North Palm Springs Crustal Model (Hartzell, 1989)

Thickness (km)	V_s (km/sec)	Density (cgs)
1.6	1.70	2.28
3.9	3.04	2.58
31.5	3.79	2.80
	4.50	2.95

Table 5.16 North Palm Springs Earthquake Source, Path, and Site Parameters

M = 6.0
$\Delta\sigma$ bars = 62.8* (point), 4.5 (finite)**
Q_0 = 371, η = 0.60 (Table 4.1)
Point Source Depth = 10 km
Crustal Model: Hartzell (1989)
Rock Site Parameters
Nonlinear Zone: 500 ft
κ = 0.02 sec: rock below nonlinear zone, V_s = 5,778 ft/sec
κ = 0.03 sec: total, small strain
G/G_{max} and Hysteretic Curves: generic soft rock, Chapter 6
Soil Site Parameters
Nonlinear Zone: 500 ft
κ rock = 0.02 sec: below nonlinear zone, V_s = 5,778 ft/sec
κ rock = 0.03 sec: total, small strain
G/G_{max} and Hysteretic Curves: EPRI, Chapter 6
Finite Fault Parameters
Fault Length = 22.0 km, Fault Width = 15.2 km (Hartzell, 1989)
M (subevent) = 5.0
Subfault Length = 3.1 km, Subfault Width = 3.0 km
Number of Subfaults = 35
Rise Time = 0.45 sec, Subevent Rise Time = 0.15 sec, Subevent Stress Drop = 30 bars
Slip Model: Hartzell (1989)
Site Distances and Kappa Values*

*Table 4.4

** $\Delta\sigma = \frac{7}{16} M_0/(A/\pi)^{\frac{3}{2}}$

Table 5.17 Tabas Crustal Model (Hartzell and Mendoza, 1991)

Thickness (km)	V_s (km/sec)	Density (cgs)
0.8	1.65	2.3
1.2	2.40	2.4
5.5	2.90	2.4
6.8	3.15	2.5
8.5	3.45	2.5
22.5	3.75	2.7
	4.60	3.1

Table 5.18 Single Earthquake Inversion Tabas

Regional Q_o^*, η^* = 291.0, 0.60 (Table 4.1)

M^* = 7.4

$\Delta\sigma$ (bars) = 21.5 ± 1.1

Site	Name	Number	κ (sec)	Category	R (km)
1	DAY	9102	0.062	A	8.0
2	TAB	9101	0.045	B	8.1
3	BOS	70	0.082	C	17.0
4	FER	71	0.019	A	83.9

AVG (all) = 0.046
AVG (rock) = 0.040

*Parameters held fixed: Q_0 from combined WNA inversion (Table 4.1)
Starting values: $\Delta\sigma$ = 100 bars, κ = 0.040 sec
Shear-wave velocity = 3.2 km/sec, density = 2.5 cgs, crossover distance = 90 km

Table 5.19 Tabas Earthquake Source, Path, and Site Parameters

M = 7.4
$\Delta\sigma$ bars = 21.5* (point), 12.3 (finite)**
Q_0 = 291, η = 0.60 (Table 4.1, Combined Provinces)
Point Source Depth = 8 km
Crustal Model: Hartzell and Mendoza (1991)
Rock Site Parameters
Nonlinear Zone: 500 ft
κ = 0.03 sec: rock below nonlinear zone, V_s = 5,414 ft/sec
κ = 0.04 sec: total, small strain
G/G_{max} and Hysteretic Curves: generic soft rock, Chapter 6
Soil Site Parameters
Nonlinear Zone: 500 ft
κ rock = 0.03 sec: below nonlinear zone, V_s = 5,414 ft/sec
κ rock = 0.04 sec: total, small strain
G/G_{max} and Hysteretic Curves: EPRI, Chapter 6
Finite Fault Parameters
Fault Length = 95.0 km, Fault Width = 45.0 km (Hartzell and Mendoza, 1991)
M (subevent) = 5.0
Subfault Length = 3.2 km, Subfault Width = 3.0 km
Number of Subfaults = 450
Rise Time = 3.53 sec, Subevent Rise Time = 0.15 sec, Subevent Stress Drop = 5 bars
Slip Model: Hartzell and Mendoza (1991)
Site Distances and Kappa Values*

*Table 5.18

** $\Delta\sigma = \frac{7}{16}\,\pi\, M_0 / (A/\pi)^{\frac{3}{2}}$

Table 5.20 Imperial Valley Crustal Model (from Liu and Helmberger, 1985; top 98m based on Bycroft, 1980)

Thickness (m)	V_s (m/sec)	Density (cgs)
1.524	121.92	1.52
1.129	137.16	1.52
1.129	137.16	1.52
1.829	152.40	1.52
1.890	152.40	1.52
2.286	176.79	1.52
2.286	176.79	1.52
2.286	198.12	1.52
2.286	198.12	1.52
2.286	220.98	1.52
2.286	220.98	1.52
2.591	236.22	1.52
2.591	236.22	1.52
2.412	259.08	1.52
2.413	259.08	1.52
2.412	271.28	1.52
2.413	271.28	1.52
2.615	288.75	1.52
2.615	288.75	1.52
2.615	303.48	1.52
2.615	303.48	1.52
2.615	313.89	1.52
2.615	313.89	1.52
2.857	327.30	1.52

Table 5.20 (Cont.) Imperial Valley Crustal Model (from Liu and Helmberger, 1985; top 98m based on Bycroft, 1980)

Thickness (m)	V_s (m/sec)	Density (cgs)
2.858	327.30	1.52
2.857	338.27	1.52
2.858	338.27	1.52
2.857	349.25	1.52
2.858	349.25	1.52
3.048	363.88	1.52
3.048	363.88	1.52
3.048	373.73	1.52
3.048	373.73	1.52
3.048	386.73	1.52
3.048	386.73	1.52
3.230	395.73	1.52
3.230	395.73	1.52
3.230	400.00	1.52
3.230	400.00	1.52
4.765	400.00	1.52
5.250	400.00	1.52
5.250	400.00	1.52
5.250	400.00	1.52
5.250	400.00	1.52
5.250	400.00	1.52
5.250	400.00	1.52
5.250	400.00	1.52

Table 5.20 (Cont.) Imperial Valley Crustal Model (from Liu and Helmberger, 1985; top 98m based on Bycroft, 1980)

Thickness (m)	V_s (m/sec)	Density (cgs)
5.250	400.00	1.52
5.250	400.00	1.52
5.250	400.00	1.52
26.25	400.00	1.52
26.25	400.00	1.52
26.25	500.00	1.56
26.25	500.00	1.56
26.25	500.00	1.56
26.25	500.00	1.56
26.25	600.00	1.61
78.75	600.00	1.61
105.00	700.00	1.74
105.00	800.00	1.85
105.00	900.00	1.89
105.00	1000.00	1.94
105.00	1150.00	2.03
105.00	1300.00	2.15
339.00	1500.00	2.26
480.00	1640.00	2.36
160.00	1740.00	2.39
160.00	1910.00	2.44
160.00	2080.00	2.48
160.00	2150.00	2.50

Table 5.20 (Cont.) Imperial Valley Crustal Model (from Liu and Helmberger, 1985; top 98m based on Bycroft, 1980)

Thickness (m)	V_s (m/sec)	Density (cgs)
640.00	2220.00	2.52
160.00	2300.00	2.55
160.00	2500.00	2.60
160.00	2710.00	2.63
2271.00	2750.00	2.65
5000.00	3180.00	2.75
10000.00	4100.00	2.80
0.00	4500.00	3.20

Table 5.21 Imperial Valley Earthquakes Source, Path, and Site Parameters

M = 6.4 (5.3 Aftershock)
$\Delta\sigma$ bars = 23.2* (point), 12.6 (finite)** (28.7*, Aftershock)
Q_0 = 264, η = 0.60 (Table 4.1, Peninsular Range)
Point Source Depth = 8 km (9.6 km, Aftershock)
Crustal Model: Liu and Helmberger (1985)
Rock Site Parameters
Nonlinear Zone: 500 ft
κ = 0.02 sec: material below nonlinear zone, V_s = 1,312 ft/sec
κ = 0.03 sec: total, small strain
G/G_{max} and Hysteretic Curves: generic soft rock, Chapter 6
Soil Site Parameters
Nonlinear Zone: 500 ft
κ rock = 0.02 sec: below nonlinear zone, V_s = 3,773 ft/sec
κ rock = 0.03 sec: total, small strain
G/G_{max} and Hysteretic Curves: Imperial Valley
Finite Fault Parameters
Fault Length = 42.0 km, Fault Width = 10.0 km (Hartzell and Heaton, 1983)
M (subevent) = 5.0
Subfault Length = 3.0 km, Subfault Width = 2.5 km
Number of Subfaults = 56
Rise Time = 0.73 sec, Subevent Rise Time = 0.15 sec, Subevent Stress Drop = 5 bars
Slip Model: Hartzell and Heaton (1983)
Site Distances and Kappa Values*

*Table 5.22 (5.23, Aftershock)

** $\Delta\sigma = \frac{7}{16} M_0 / (A/\pi)^{\frac{3}{2}}$

Table 5.22 Single Earthquake Inversion Imperial Valley

Regional Q_o^*, η^* = 264, 0.60 (Table 4.1, Peninsular Range)

M^* = 6.4

$\Delta\sigma$ (bars) = 23.2 ± 0.4

Site	Name	Number	κ (sec)	Category	R (km)
1	H-EMO	CDMG 5155	0.088	D	8.0
2	H-E07	USGS 5028	0.082	D	8.0
3	H-E06	USGS 5158	0.053	D	8.1
4	H-AEP	UCSD 6616	0.047	D	8.3
5	H-AG	UCSD 6618	0.046	D	8.5
6	H-E05	USGS 952	0.052	D	8.8
7	H-E08	USGS 5159	0.040	D	9.0
8	H-BCR	USGS 5054	0.036	D	9.1
9	H-EDA	USGS 5165	0.061	D	9.6
10	H-E04	USGS 955	0.057	D	10.6
11	H-SHP	UCSD 6619	0.032	C	10.8
12	H-ELC	CDMG 5154	0.067	D	11.0
13	H-HVP	USGS 5055	0.058	D	11.5
14	H-E10	USGS 412	0.057	D	11.8
15	H-BRA	USGS 5060	0.059	D	12.1
16	H-CXO	USGS 5053	0.056	D	12.3
17	H-QKP	UCSD 6617	0.043	D	13.2
18	H-E11	USGS 5058	0.053	D	14.9
19	H-E03	USGS 5057	0.047	D	15.1
20	H-PTS	USGS 5051	0.072	D	15.1

Table 5.22 (Cont.) Single Earthquake Inversion Imperial Valley

Site	Name	Number	κ (sec)	Category	R (km)
21	H-WSM	CDMG 5169	0.083	D	15.9
22	H-E02	USGS 5155	0.044	D	17.1
23	H-CH	UCSD 6621	0.039	D	17.2
24	H-E12	USGS 931	0.048	D	19.6
25	H-CP	UCSD 6604	0.019	A	21.8
26	H-E01	USGS 5056	0.031	D	22.9
27	H-E13	USGS 5059	0.044	D	23.5
28	H-CMP	UCSD 6622	0.039	D	24.2
29	H-CAL	USGS 5061	0.066	D	24.8
30	H-SUP	USGS 286	0.034	A	25.9
31	H-DTA	UCSD 6605	0.014	D	30.9
32	H-PLS	USGS 5052	0.059	D	32.5
33	H-NIL	CDMG 724	0.056	D	36.4
34	H-VCT	UCSD 6610	0.024	D	41.2
35	H-CC4	USGS 5066	0.090	D	49.3

AVG (all) = 0.048
AVG (rock) = 0.025
AVG (soil) = 0.050

*Parameters held fixed
Starting values: $\Delta\sigma$ = 100 bars, κ = 0.040 sec
Shear-wave velocity = 3.4 km/sec, density = 2.8 cgs, crossover distance = 40 km

Table 5.23 Single Earthquake Inversion Imperial Valley AS

Regional Q_o^*, η^* = 264, 0.60 (Table 4.1, Peninsular Range)

M^* = 5.3

$\Delta\sigma$ (bars) = 28.7 ± 0.8

Site	Name	Number	κ (sec)	Category	R (km)
1	A-HVP	USGS 5055	0.053	D	11.4
2	A-E06	CDMG 942	0.041	D	13.2
3	A-E07	USGS 5028	0.045	D	13.4
4	A-E05	USGS 952	0.033	D	13.6
5	A-E04	USGS 955	0.037	D	13.9
6	A-EDA	USGS 5165	0.044	D	14.1
7	A-E08	CDMG 958	0.036	D	14.3
8	A-BCR	USGS 5054	0.058	D	15.4
9	A-CXO	USGS 5053	0.057	D	16.1
10	A-E10	USGS 412	0.047	D	16.2
11	A-E03	USGS 5057	0.058	D	17.0
12	A-E11	USGS 5058	0.048	D	18.5
13	A-E02	USGS 5155	0.050	D	19.3
14	A-E01	USGS 5056	0.046	D	25.0
15	A-BRA	USGS 5060	0.044	D	27.0
16	A-DLT	---- 6605	0.010	D	52.0

AVG = 0.042

*Parameters held fixed
Starting values: $\Delta\sigma$ = 100 bars, κ = 0.040 sec
Shear-wave velocity = 3.4 km/sec, density = 2.8 cgs, crossover distance = 40 km

Table 5.24 Nahanni Crustal Model (from Hartzell et al., 1994)

Thickness (km)	V_s (km/sec)	Density (cgs)
0.32	2.60	1.85
0.80	2.80	2.05
0.50	3.10	2.20
2.00	3.25	2.35
31.38	3.57	2.60
	4.70	3.30

Table 5.25 Nahanni Earthquake Source, Path, and Site Parameters

M = 6.8
$\Delta\sigma$ bars = 13.4* (point), 13.5 (finite)**
Q_0 = 317, η = 0.86 (Table 5.31, Saguenay)
Point Source Depth = 4 km
Crustal Model: Hartzell et al. (1994)
Rock Site Parameters
Nonlinear Zone: Hard Rock, Linear Analysis
κ = Site Specific From Inversion (Table 5.26), V_s = 8,531 ft/sec
Soil Site Parameters
No soil sites
Finite Fault Parameters
Fault Length = 48.0 km, Fault Width = 21.0 km, (Hartzell et al., 1994)
M (subevent) = 5.0
Subfault Length = 2.8 km, Subfault Width = 3.5 km
Number of Subfaults = 102
Rise Time = 1.15 sec, Subevent Rise Time = 0.15 sec, Subevent Stress Drop = 5 bars
Slip Model: Hartzell et al. (1994)
Site Distances and Kappa Values*

*Table 5.26

** $\Delta\sigma = \frac{7}{16} M_0 / (A/\pi)^{\frac{3}{2}}$

Table 5.26 Single Earthquake Inversion Nahanni

Regional Q_o^*, η^* = 317, 0.86 (Table 5.31 Saguenay)

M^* = 6.8

$\Delta\sigma$ (bars) = 13.4 ± 0.5

Site	Name	Number	κ (sec)	Category	R (km)
1	S1	6097	0.021	A	4.0
2	S2	6098	0.020	A	4.0
3	S3	6099	0.010	A	13.5

AVG = 0.016

*Parameters held fixed
Starting values: $\Delta\sigma$ = 100 bars, κ = 0.006 sec
Shear-wave velocity = 3.6 km/sec, density = 2.6 cgs, crossover distance = 70 km

Table 5.27 Superstition Hills (B) Earthquakes Source, Path, and Site Parameters

M = 6.4
$\Delta\sigma$ bars = 43.4* (point), 31.2 (finite)**
Q_0 = 264*, η = 0.06* (Table 4.1, Peninsular Range)
Point Source Depth = 9 km
Crustal Model: Imperial Valley (Table 5.20)
Rock Site Parameters
Nonlinear Zone: 500 ft
κ = 0.02 sec: material below nonlinear zone, V_s = 1,312 ft/sec
κ = 0.03 sec: total, small strain
G/G_{max} and Hysteretic Curves: generic soft rock, Chapter 6
Soil Site Parameters
Nonlinear Zone: 500 ft
κ rock = 0.02 sec: below nonlinear zone, V_s = 3,773 ft/sec
κ rock = 0.03 sec: total, small strain
G/G_{max} and Hysteretic Curves: Imperial Valley
Finite Fault Parameters
Fault Length = 20.0 km, Fault Width = 11.5 km (Wald et al., 1990)
M (subevent) = 5.0
Subfault Length = 3.3 km, Subfault Width = 2.9 km
Number of Subfaults = 24
Rise Time = 0.74 sec, Subevent Rise Time = 0.15 sec, Subevent Stress Drop = 5 bars
Slip Model: Wald et al. (1990)
Site Distances and Kappa Values*

*Table 5.28

** $\Delta\sigma = \frac{7}{16} M_0 / (A/\pi)^{\frac{3}{2}}$

Table 5.28 Single Earthquake Inversion Superstition Hills

Regional Q_o^*, η^* = 264, 0.60 (Table 4.1, Peninsular Range) M^* = 6.4 (6.7) $\Delta\sigma$ (bars) = 43.4 (26.6) ± 1.4 (0.9)					
Site	Name	Number	κ (sec)	Category	R (km)
1	ICC	CDMG 01335	0.054	D	18.6
2	WSM	CDMG 11369	0.043	D	20.2
3	IVW	USGS 5210	0.037	D	25.4
4	POE**	POE Rd	0.036	D	15.3
5	SLT	USGS 5062	0.059	D	28.5
6	SSM	USGS 286	0.028	B	9.96
7	PTS	USGS 5051	0.070	D	9.01
8	KRN**	Kornblown Rd	0.059	D	21.6
9	BRW	USGS 5060	0.053	D	20.3
10	CAL	USGS 5061	0.042	D	29.7
11	PLC	USGS 5052	0.060	D	22.8

AVG (soil) = 0.051

*Parametersheld fixed
The M 6.7 is based on the teleseismic moment
The M 6.4 is consistent with the strong motion data (Wald et al., 1990)
Starting values: $\Delta\sigma$ = 100 bars, κ = 0.040 sec
Shear-wave velocity = 3.4 km/sec, density = 2.6 cgs, crossover distance = 40 km
**Temporary stations

Table 5.29 Saguenay Crustal Model (Hartzell et al., 1994)

Thickness (km)	V_s (km/sec)	Density (cgs)
1.44	2.6	2.30
6.00	3.4	2.50
12.00	3.5	2.67
14.00	3.7	2.85
10.00	4.0	3.02
	4.7	3.35

Table 5.30 Saguenay Earthquake Source, Path, and Site Parameters

M = 5.8
$\Delta\sigma$ bars = 572.2* (point), 13.7 (finite)**
Q_0 = 317, η = 0.86 (Table 5.31)
Point Source Depth = 25.7 km
Crustal Model: Hartzell et al. (1994)
Rock Site Parameters
Nonlinear Zone: Hard Rock, Linear Analysis
κ = Site Specific From Inversion (Table 5.31), V_s = 8,531 ft/sec
Soil Site Parameters
No soil sites
Finite Fault Parameters
Fault Length = 10.0 km, Fault Width = 10.0 km, (Hartzell et al., 1994)
M (subevent) = 5.0
Subfault Length = 3.3 km, Subfault Width = 2.5 km
Number of Subfaults = 12
Rise Time = 0.46 sec, Subevent Rise Time = 0.15 sec, Subevent Stress Drop = 200 bars
Slip Model: Hartzell et al. (1994)
Site Distances and Kappa Values*

*Table 5.31

** $\Delta\sigma = \frac{7}{16} M_0 / (A/\pi)^{\frac{3}{2}}$

Table 5.31 Single Earthquake Inversion Saguenay

Regional Q_o η = 317, 0.86
M* = 5.8
$\Delta\sigma$ (bars) = 572.2 ± 25.4

Site	Name	Number	κ (sec)	Category	R (km)
1	S16	GSC	0.009	A	46.8
2	S17	GSC	0.005	A	64.9
3	S20	GSC	0.004	A	87.9
4	S08	GSC	0.012	A	90.2
5	1125A54	ECTN	0.030	A	91.4
6	1125A61	ECTN	0.026	A	91.9
7	1125A64	ECTN	0.028	A	99.1
8	S01	GSC	0.008	A	110.6
9	1125A16	ECTN	0.034	A	110.7
10	S10	GSC	0.027	A	110.8
11	1125A21	ECTN	0.029	A	117.4
12	S09	GSC	0.028	A	118.9
13	1125A11	ECTN	0.042	A	119.1
14	1125EBNZ**	ECTN	0.040	A	224.1
15	1125SBQZ**	ECTN	0.040	A	306.4
16	1125GSQZ**	ECTN	0.046	A	314.6
17	1125TRQZ**	ECTN	0.017	A	327.8
18	1125MNTZ**	ECTN	0.032	A	341.1
19	1125KLNZ**	ECTN	0.060	A	381.8
20	1125GRQZ**	ECTN	0.026	A	385.5
21	1125OTTZ**	ECTN	0.036	A	452.8
22	1125WBOZ**	ECTN	0.032	A	460.1

AVG = 0.023

*Parameters held fixed

**ECTN vertical component, H/V of 1.4 used to convert vertical records to horizontal.

Starting values: $\Delta\sigma$ = 300 bars, κ = 0.008 sec

Shear-wave velocity = 3.7 km/sec, density = 2.8 cgs, crossover distance = 87 km

Table 5.32 Little Skull Mountain Crustal Model

Thickness (km)	V_s (km/sec)	Density (cgs)
0.040	0.6	1.70
0.040	1.2	2.00
0.140	1.5	2.30
0.600	2.1	2.40
0.780	1.9	2.40
1.500	2.9	2.40
2.200	3.4	2.50
10.700	3.5	2.75
16.000	3.8	2.90
	4.6	3.30

Table 5.33 Little Skull Mountain Earthquake Source, Path, and Site Parameters

M = 5.6
$\Delta\sigma$ bars = 63.7* (point), 21.9 (finite)**
Q_0 = 256*, η = 0.47*
Point Source Depth = 12 km
Crustal Model: Modified Regional
Rock Site Parameters
Nonlinear Zone: Rock, Linear Analysis (Low Levels of Motion ≤ 20%g)
κ = Site Specific From Inversion (Table 5.34), V_s = 1,969 ft/sec
Soil Site Parameters
No soil sites
Finite Fault Parameters
Fault Length = 7.0 km, Fault Width = 6.6 km, (Aftershock zone)
M (subevent) = 5.0
Subfault Length = 2.3 km, Subfault Width = 3.3 km
Number of Subfaults = 6
Rise Time = 0.38 sec, Subevent Rise Time = 0.15 sec, Subevent Stress Drop = 30 bars
Slip Model: Derived
Site Distances and Kappa Values*

*Table 5.34

** $\Delta\sigma = \frac{7}{16} M_0/(A/\pi)^{\frac{3}{2}}$

Table 5.34 Single Earthquake Inversion Little Skull Mountain

Regional Q_o, η = 256, 0.47

M* = 5.7, 4.4, 4.2

$\Delta\sigma$ (bars) = 63.7, 33.7, 45.6 ± 1.9, 1.2, 2.0

Site	Name	Number	κ (sec)	Category	R (km)
1	LAT		0.036		17.5, 17.5,17.5
2	NTS		0.031		26.8, 26.8, ----
3	BEA		0.004		46.8, 46.8,98.8
4	PA2		0.031		58.5, ----, ----
5	PA1		0.031		63.9, ----, ----
6	LVC		0.017		98.7, ----, ----
7	LVA		0.028		98.2, 98.2, ----
8	DVS		0.032		98.8, 98.8,98.8

AVG = 0.023

*Parameters held fixed

Starting values: $\Delta\sigma$ = 100 bars, κ = 0.040 sec

Shear-wave velocity = 3.5 km/sec, density = 2.7 cgs, crossover distance = 64 km

Table 5.35 Cape Mendocino Crustal Model (from Graves, 1994)

Thickness (km)	V_s (km/sec)	Density (cgs)
0.2	1.5	1.5
4.8	2.3	1.8
9.5	3.2	2.3
15.3	3.9	2.8
	4.7	3.3

Table 5.36 Cape Mendocino Earthquake Source, Path, and Site Parameters

M = 6.8
$\Delta\sigma$ bars = 27.2* (point), 13.2 (finite)**
Q_0 = 176*, η = 0.06 (Table 4.1, North Coast)
Point Source Depth = 9.6 km
Crustal Model: Graves (1994)
Rock Site Parameters
Nonlinear Zone: 500 ft
κ = 0.03 sec: rock below nonlinear zone, V_s = 4,922 ft/sec
κ = 0.04 sec: total, small strain
G/G_{max} and Hysteretic Curves: generic soft rock, Chapter 6
Soil Site Parameters
Nonlinear Zone: 500 ft
κ rock = 0.03 sec: below nonlinear zone, V_s = 4,922 ft/sec
κ rock = 0.04 sec: total, small strain
G/G_{max} and Hysteretic Curves: generic deep soil, Chapter 6
Finite Fault Parameters
Fault Length = 32.0 km, Fault Width = 32.0 km (Graves, 1994)
M (subevent) = 5.0
Subfault Length = 3.2 km, Subfault Width = 2.9 km
Number of Subfaults = 110
Rise Time = 1.40 sec, Subevent Rise Time = 0.15 sec, Subevent Stress Drop = 30 bars
Slip Model: Graves (1994)
Site Distances and Kappa Values, See Table 5.35

*Table 4.1

** $\Delta\sigma = \frac{7}{16} M_0 / (A/\pi)^{\frac{3}{2}}$

Table 5.37 Single Earthquake Inversion Cape Mendocino

Regional Q_o^*, η^* = 176, 0.60 (Table 4.1, North Coast)

M^* = 6.8

$\Delta\sigma$ (bars) = 27.2 ± 1.3

Site	Name	Number	κ (sec)	Category	R (km)
1	CPM	CDMG 89005	0.026	A	9.6
2	PET	CDMG 89156	0.042	D	9.6
3	FOR	CDMG 89486	0.103	D	10.6
4	RIO	CDMG 89324	0.064	C	10.8
5	EUR	CDMG 89509	0.076	D	29.9

AVG (soil) = 0.068

*Parameters held fixed

Starting values: $\Delta\sigma$ = 100 bars, κ = 0.040 sec

Shear-wave velocity = 3.2 km/sec, density = 2.3 cgs, crossover distance = 60 km

Table 5.38 Rise Time Summary

Earthquake	Date	M	Seismic Moment x 10^{25} (dyne-cm)	Rise Time (sec)
San Fernando	1971	6.6	8.91	1.25
Tabas, Iran	1978	7.4	141.00	2.35
Coyote Lake	1979	5.7	0.40	0.36
Imperial Valley	1979	6.4	4.47	0.73
Morgan Hill	1984	6.2	2.24	0.70
Nahanni	1985	6.8	17.80	1.15
North Palm Springs	1986	6.0	1.12	0.45
Whittier Narrows	1987	6.0	1.12	0.50
Superstition Hills(B)	1987	6.4	4.47	0.74
Saguenay	1988	5.8	0.56	0.46
Loma Prieta	1989	6.9	25.10	1.50
Little Skull Mtn.	1992	5.7	0.40	0.38
Landers	1992	7.2	70.80	1.78
Cape Mendocino	1992	6.8	17.80	1.40
Northridge	1994	6.7	12.60	1.40

Table 5.39 Stress Drop Summary

Earthquake	Date	M	Stress Drop Inversion (bars)	Stress Drop SE (bars)	N
San Fernando	1971	6.6	36.1	1	39
Tabas, Iran	1978	7.4	21.5	1	4
Coyote Lake	1979	5.7	70.1	2	10
Imperial Valley	1979	6.4	23.2	1	35
Imperial Valley(AS)	1979	5.3	28.7	1	16
Morgan Hill	1984	6.2	49.0	1	29
Nahanni	1985	6.8	13.4	1	3
North Palm Springs	1986	6.0	62.8	1	29
Whittier Narrows	1987	6.0	95.7	1	88
Superstition Hills(B)	1987	6.4.(6.7)	43.4 (26.6)	1	12
Saguenay	1988	5.8	572.2	22	22
Loma Prieta	1989	6.9	73.7	1	53
Little Skull Mtn.	1992	5.7	63.7	2	8
A		4.4	340	1	5
B		4.2	46.0	2	3
Landers	1992	7.2	40.7	1	57
Cape Mendocino	1992	6.8	27.2	1	5
Northridge	1994	6.7	62.9	1	94

WNA AVG* = 46.9

Excludes* Saguenay, Nahanni, and aftershocks

CHAPTER 6

POINT-SOURCE MODEL VALIDATION

COMPARISON TO EMPIRICAL ATTENUATION

6.1 ATTENUATION WITH DISTANCE

For the empirical WNA strong motion database, significant uncertainty exists in the appropriate form of attenuation with distance. At issue is whether or not a flattening or change in slope at intermediate distance (40-80 km) is required to optimally fit the data. Extensive modeling of crustal propagation effects in the EPRI (1993) study suggested that if the source depth is unknown and if accommodation is made for realistic variations in crustal structure (velocity and Q(f)), the issue of non-monotonic attenuation becomes ambiguous. This result was confirmed with an initial analysis of residuals in developing the empirical attenuation model in Appendix A. Interestingly, the ambiguity was somewhat resolved when the empirical data suggested a magnitude dependent attenuation (Idriss, 1993) which was also supported by stochastic finite-fault modeling for magnitudes from M 5.5 to M 7.5. The finite-fault modeling also shed light on why simple 1/R (or near 1/R) attenuation works as well as it does for both empirical and simple analytical models (like the stochastic point-source).

For a layered crustal model with velocity generally increasing with depth, wave propagation modeling which includes direct as well as multiply and post-critically reflected waves, predicts, for a point-source, rapid attenuation ($> 1/R$), followed by a flattening, and then an increased falloff with distance. Finite-source modeling using distributed point-sources, each with 1/R

geometrical attenuation shows an attenuation less than 1/R with the slope inversely proportional to the source size (fault area). This is simply an artifact of source finiteness and 1/R (for an elastic system) is not approached until beyond at least one source dimension (length, for a vertical strike slip rupture). Each element falls off with 1/R but the sum falls off at less than 1/R. If, on the other hand, each element uses attenuation for direct plus multiply and post-critically reflected waves, the sum falls off like 1/R, flattens, and again falls off. This effect is demonstrated in Figure 6.1 which shows predicted peak acceleration values verses distance for an M 6.5 vertical strike slip earthquake using the empirical relation (Appendix A), a point-source with a crossover from 1/R to $1/\sqrt{R}$ at 50 km, and finite-fault simulations for rock site conditions. The finite-fault simulations use both 1/R geometrical attenuation as well as direct plus reflected waves (Ou and Hermann, 1990) appropriate for the Loma Prieta crustal model (Chapter 4).

The finite-fault motions are generated using the area verses magnitude relation of Equation 2-6 and a vertical strike slip fault. Motions are simulated at 12 site locations equally spaced along one side of the fault and at each end. Each site location is at the same fault distance with simulations at fault horizontal distances of 1, 3, 5, 10, 15, 20, 30, 50, 70, 100, 200, and 400 km. Source variation is accommodated by averaging over 11 random slip models each with a randomly selected nucleation point located within a nucleation zone. The nucleation zone is defined as the lower half of the rupture surface and not within 10% of the ends (Silva, 1992). At each site, 11 motions (response spectra) are averaged and at each distance the 12 sites at the same fault distance are averaged. For the 12 distances, 1,584 finite-fault runs are required. The Q(f) model is for the North Coast ($176\ f^{0.6}$, Table 4.1) and the kappa value is 0.038 sec resulting

from inversions of the empirical attenuation relation (Chapter 6). The point-source stress drop is 59 bars, also a result of the empirical inversions for M 5.5 to M 7.5 and over all source mechanism (Table 6.1).

The point-source simulations shown in Figure 6.1 (dashed line) compare favorably with the empirical predictions at 10 km and beyond suggesting that a simple form of geometrical attenuation is compatible with the strong motion database (see residual plots in Appendix A). The point-source underprediction within 10 km reflects the inversion results for strike slip mechanism showing a higher stress drop for M 6.5 than for M 5.5, opposite the trend for oblique and reverse mechanism (Table 6.1). Comparing the finite-fault simulations using 1/R geometrical attenuation (x's) with the direct plus reflected waves attenuation (open circles) in Figure 6.1, the more rigorous attenuation is higher in close with a transition around 5 km and a significant difference out to about 70 km, beyond which the post-critical reflections begin to dominate. The 1/R attenuation finite-fault simulations are consistent with the 1/R point-source and empirical predictions out to about 10 km but show a large overprediction beyond, out to about 80 km. The finiteness of the source results in a net attenuation rate that is less than that of its individual elements: when the elements fall off faster than 1/R, as wave propagation physics predicts for direct rays, the summed result falls off closer to 1/R. At the distance range where the post-critical reflections arrive (50-80 km) the attenuation rate flattens and then falls off again, but at less than 1/R. The distance range of a change in slope or flattening depends upon source depth and crustal structure (depth to Moho; EPRI, 1993) and averaging over both results in a generally smooth attenuation for distances within about 50 km with a slope greater

than 1 for small magnitude ($\approx$ M 5.5) and decreases (becomes flatter) as magnitude increases (Appendix A).

To see this magnitude dependent attenuation rate, Figure 6.2 shows PGA attenuation for M 7.5 and M 5.5 earthquakes using the empirical attenuation model (Appendix A) and both the point- and finite-source models. The point-source model uses a constant (magnitude independent) stress drop of 59 bars. In this case, the finite-fault simulations are averages for three California crustal models representing the North Coast, Peninsular Ranges, and Mojave regions. The magnitude dependent attenuation rates are quite distinct for both the empirical and finite-fault simulations. The M 7.5 point-source simulations would be consistent with the empirical estimates within about 100 km if a lower stress drop were used (Table 6.1) and underpredict beyond about 100 km. Interestingly, source finiteness is more on issue for the point-source at large distances than at close distances, contrary to cherished beliefs. The smaller magnitude dependence in the attenuation rate shown in the point-source simulations is due to the distance dependent duration term (Hermann, 1985) which has a larger relative effect as the source duration decreases (smaller M, Chapter 2).

Of significance in the finite-source simulations is the effect of averaging crustal models on the range of post-critical arrivals. The range is spread out, showing a smoother transition or change in rate. Additionally, the effects of the post-critical reflections are much less pronounced for the large magnitude (M 7.5) than the small magnitude (M 5.5) simulations, which may be regarded as nearly a point-source. These results suggest that: 1) a magnitude dependent

attenuation rate is physically reasonable and appropriate to incorporate in empirical regression models (as well as point-source simulations); 2) deriving attenuation models from small (M < 5.5) strong motion data may result in underpridictions for large M at large distances; 3) not accommodating a magnitude dependent attenuation rate may result in an interpretion of a flat zone or change in slope at intermediate to far distance ranges (50 to 100 km) in the WNA strong motion data set; 4) variations in crustal model (and finiteness for large earthquakes) smears the effects of post-critical reflections resulting in a geometrical attenuation which may be adequately modeled by a point-source with 1/R out to a transition distance (50 to 70 km) and $1/\sqrt{R}$ beyond.

6.2 INVERSIONS OF EMPIRICAL ATTENUATION

In order to provide the appropriate point-source model parameters for comparisons to the empirical attenuation model of Appendix (A), inversions of Equation (1) (point-source Fourier amplitude spectral density model) were performed. The analyses consisted of inversions for stress drop, kappa values (rock and soil), and Q(f) for three earthquakes (M 5.5, 6.5, and 7.5) at 7 rupture distances: 1, 5, 10, 20, 50, 100, and 200 km. For the point-source distances, considering a vertical strike-slip fault, epicentral distance was taken as rupture distance and source depth was assumed to be magnitude dependent. Based on California seismicity, a point-source depth of 6 km was used for M 5.5 and 8 km for M 6.5 and M 7.5. To produce Fourier amplitude spectral densities for the inversions, the 5% damped response spectra computed using the empirical attenuation model (Appendix A) were matched using RVT (Silva, 1987). In this process, smooth Fourier amplitude spectral densities are generated whose RVT based response spectrum matches the target spectrum. The results, target and spectral match, for the strike-slip

case are shown in Figure Set 6.3 for rock and Figure Set 6.3b for soil. There is a very close match over the entire frequency range (0.02 Hz to 100 Hz, 28 frequencies) and the results are similar for the other cases.

6.2.1 Transfer Functions

To provide appropriate amplification for the generic rock and soil crustal models, linear elastic mean transfer functions (8 km to the surface) were computed for the base case profiles (Figures 3.6 and 3.8) using the profile randomization scheme (Appendix C). The soil profile depth was randomized (uniform distribution) between 100 ft and 1,000 ft (mean 550 ft) and the rock profile was randomized to 100 ft (Chapter 3). The mean (normal distribution) and $\pm$ 1 σ transfer functions are shown in Figure 6.4 for rock and in Figure 6.5 for soil. The smoothed (by eye) mean transfer functions are plotted in Figure 6.6. The main difference between rock and soil amplification is from about 0.2 Hz to about 10 Hz and reflects the deeper low velocities in the soil profile. At high frequencies ($\geq$ 10 Hz), the rock and soil amplifications are nearly the same (around 4) reflecting similar shear-wave velocities near the surface (Chapter 3).

6.2.2 Inversion Results

The use of a linear transfer function is suitable for the rock site regressions since the empirical attenuation of Appendix A was constrained to be linear. However, for soil, this is not the case and the empirical attenuation relation clearly shows that soil amplification depends upon expected rock peak acceleration levels (Appendix A). To accommodate nonlinearity, at least in damping, the inversions for soil kappa values were done in distance bins or ranges reflecting different

levels of expected rock peak acceleration values. The distance ranges were selected to approximately double in rock peak acceleration beginning with ≤ 5% PGA (linear). Five ranges in expected rock PGA (distance) were used: ≤ 5%, 5 to 10%, 10 to 20%, 20 to 40%, and > 40%. The distance ranges depend upon magnitude and were selected from the 7 (epicentral) distances ranging from 1 to 200 km.

The inversions were done for varying mechanism (strike slip, oblique slip, and reverse) and results are shown in Table 6.1 along with the starting values. In the first set of inversions, parameters were determined for each mechanism separately (three inversions). As with a similar previous analysis using the Sadigh at al., (1989) empirical attenuation for rock (Silva and Darragh, 1995), stress drop generally decreases with increasing magnitude. This is likely due to the tendency of the omega-square model to overpredict at low frequencies, particularly for larger magnitudes (M > 6.0) (Silva and Darragh, 1995; Chapter 5) and suggests a breakdown of self-similarity. This feature has recently been better quantified in a direct empirical analysis of WNA Fourier amplitude spectra (Atkinson and Silva, 1996). In this case the low frequency overprediction was interpreted as evidence of the need of to introduce a second corner frequency into the model (Atkinson and Silva, 1996). The stress drop also varies with mechanism with the average increasing from 48 bars for strike-slip to 55 bars for oblique-slip and 63 bars for reverse mechanism earthquakes. This reflects the generally higher observed motions for reverse mechanism earthquakes compared to strike-slip mechanisms (Appendix A).

The Q(f) models (Table 6.1) were determined separately for each mechanism to check parameter coupling (generally the off diagonal terms in the parameter correlation matrix are less than about

0.5). The Q(f) models are generally similar for each mechanism suggesting the stress drops and Q(f) models are stable and reasonably unique. Because the coupling of Q_o and η is very high (cross-correlations around 0.95) over this limited distance range (1 to 200 km), inversions for Q_o were done for η constrained to 0.6, a typical WNA value (Boore, 1983), and to zero (constant Q model). The resulting Q(f) models are about 600 for $\eta = 0.6$ and about 2,000 for $\eta = 0.0$. These are quite high with more typical WNA values (Chapter 4) being around 100 to 200 for η of 0.6 (Boore, 1983) and just under 1,000 for $\eta = 0$ (Fletcher and Boatwright, 1991). These high Q(f) models are probably a result of the magnitude dependent attenuation rate (Chapter 6.1) built into the empirical model (Appendix A) but not yet incorporated into the point-source model.

The kappa values resulting from the individual mechanism inversions are also quite stable in that they show a weak dependence on mechanism. For rock sites, kappa is about 0.04 sec, in agreement with the work of Silva and Darragh (1995) using response spectral shapes and with the inversions on the Sadigh empirical attenuation relation for rock sites (Silva and Darragh, 1995). For soil sites, the kappa values increase from about 0.04 sec (close to the rock values) for very low expected rock peak accelerations ($\leq$ 5%g) to around 0.06 for high rock peak accelerations ($\geq$ 40%g). Soil site kappa values increase about 50% for about a 10-fold increase in loading conditions. Although this nonlinear response is clear, it is much weaker than typical current generic modulus reduction and damping curves for cohesionless soils (EPRI, 1993) would predict in the context of the generic deep soil profile (Chapter 3).

The combined inversion parameters shown in Table 6.1 result from a single inversion using the "data" from the three mechanisms. In this case, the inversion is for nine earthquakes, three magnitudes and three mechanism, resulting in nine stress drops but with a single Q(f) model and a single rock and soil site (each at 7 distances). In general the results are very similar to the individual mechanism inversions and are taken to represent the best constrained parameter values. The average stress drop (over mechanism) ranges from about 80 bars for M 5.5 to 36 bars for M 7.5. The largest change, nearly a factor of 2, occurs at large magnitude: M 6.5 to M 7.5. The change in stress drop with mechanism is about a factor of 2 going from about 40 bars for strike-slip mechanisms to nearly 80 bars for reverse faults. The overall average stress drop is about 60 bars. This is less than the 100 bar average found in a similar inversion of 25 WNA mainshocks (EPRI, 1993). The 60 bar average is also less that the approximately 90 bar average (M 5.0 to M 7.5) found in inverting the Sadigh et al. (1989) empirical rock attenuation model (Silva and Darragh, 1995). In both of these cases, the rock sites did not include the shallow steep velocity gradient (Figure 3.2) and had maximum amplification factors of around 2.5. This is significantly less than the 4.0 (Figure 6.6) resulting from the steep shallow gradient of the soft rock profile.

Additionally, the current inversions use mean amplification factors whereas the earlier studies used median factors. The mean factors are thought to be more appropriate in the context of RVT. This follows from the relationship of the discrete power spectrum to the RMS for normally distributed white noise. The equivalence of the power spectrum sum to the RMS is based on the sum of the expected values of the squared absolute Fourier components (Aki and

Richards, 1980). In this context then, the appropriate Fourier amplitude spectrum to use in computing the power spectrum is an estimate of the mean. The difference between the mean and median transfer functions for the profile correlation model (Appendix C) is about 20% and both are plotted in Figure 6.7 for the deep soil profile.

The use of the larger mean transfer function is an additional factor contributing to the lower stress drops since the high frequencies in the point-source model scale directly with stress drop (Boore, 1983). A 20% increase in stress drop results in nearly a 20% increase in Fourier spectral amplitudes for frequencies higher than the corner frequency (Silva, 1990). The combination of significantly larger rock site amplification factors and the use of mean, rather than median, amplification results in higher short period model predictions for the same stress drop. Conversely, in the inversion process, a lower stress drop is required to maintain equivalent levels of high frequency motion.

The Q(f) model shown in Table 6.1 for the combined inversion is very similar to those resulting from the individual mechanisms. Again the Q(f) model is quite high possibly reflecting the magnitude independent attenuation rate. The corresponding kappa values are also similar, near 0.04 sec for rock and linear soil and about 0.06 sec for soil subjected to high levels of loading (rock outcrop about 40 to 70%g).

As an example, the Fourier amplitude spectra (initial model, final model, and those derived from empirical attenuation) are shown in Figure Set 6.8 for rock and in Figure Set 6.9 for soil for the strike slip inversion. The overall fit for rock is generally good, particularly for M 5.5 and M

6.5. The low frequency overprediction at close distances is evident in the M 6.5 and more pronounced in the M 7.5 spectra. For M 7.5, at larger distances, the model underpredicts from about 0.3 to 3 Hz and is low by about a factor of 2 at 200 km around 0.6 Hz. The same trend occurs in the soil spectra (Figure Set 6.9) where the fit is generally better than for rock. The fit to the soil spectra is considered excellent overall but the large magnitude underprediction at distance is nearly as large as the rock results. If this occurred only in the soil spectra then one would suspect basin effects, however, a very similar and even larger trend is seen in the rock site results. Along with the excellent match for M 6.5, this result suggests that basin effects are not a dominate feature at large distances from significant earthquakes and that vertically propagating shear-waves (up to 1,000 ft) generally does well at accommodating the dominate and stable features of strong ground motions at rock and soil sites. The M 7.5 bias may be an artifact of the magnitude dependent attenuation rate not accommodated in the model, coupled with the need for a second corner frequency (Atkinson and Silva, 1996).

To examine the corresponding response spectra, Figure Sets 6.10 and 6.11 show 5% damped pseudo absolute acceleration spectra for the final model and the empirical attenuation relation. The fit is generally good and follows that of the Fourier amplitude spectra. The underprediction at close distance (1 km) and at large distance for M 7.5 is more broadband due to the smoothing inherent in the 5% damping (particularly at higher frequencies). The generally favorable agreement with the empirical model suggests that the simple point-source captures the dominate features in strong ground motions in terms of magnitude dependency, distance attenuation, and site effects over the frequency range of 0.2 to 50 Hz. Refinements or corrections to the point-

source model include a possible double corner and magnitude dependent attenuation rate (both of which are accommodated in the stochastic finite-fault model; Atkinson and Silva, 1996). The inclusion of these refinements into the point-source model would likely improve the model at very close distances but the cause of the M 7.5 large distance underprediction centered at 0.6 Hz remains unclear.

6.2.3 Generic Modulus Reduction and Damping Curves

Initial comparisons of model spectra to the empirical attenuation spectra using the recently developed EPRI (1993) modulus reduction and damping curves for cohesionless soils as well as a set of curves for soft rock (Appendix D) showed too much damping and too great a shift of the spectral peak (5% damped spectral acceleration) to longer periods as loading level increased. As a result, a revised set of both rock and soil curves was developed which produced response spectra (absolute level and shape) generally consistent with the empirical model predictions.

6.2.3.1 G/G_{max} and Hysteretic Curves for Soil

In developing the revised set of soil curves, the original shapes were maintained and the depth dependencies varied with all other parameters held fixed. The depth dependency (effects of initial confining pressure) of the EPRI (1993) soil curves is based upon the expected behavior of the reference strains with depth (Hardin and Drnevich, 1972; EPRI, 1993). The reference strain is a parameter in the EPRI (1993) hyperbolic model which controls the reduction of the secant modulus with increasing strain. It is a function of both the shear strength (τ_{max}) and low-strain shear modulus (G_{max})

$$\gamma_r = \tau_{max}/G_{max} \qquad (6\text{-}1),$$

and appears in the initial loading backbone curve as

$$\tau = \tau_{max} \frac{\frac{\gamma}{\gamma_r}}{1 + \frac{\gamma}{\gamma_r}} \qquad (6\text{-}2),$$

with the resulting secant modulus given by

$$\frac{G}{G_{max}} = \frac{1}{1 + \frac{\gamma}{\gamma_r}} \qquad (6\text{-}3).$$

The reference strain then controls the "linearity" of the secant modulus with higher values shifting the curves to higher strains (EPRI, 1993). In addition to confining pressure (depth), the reference strain is also affected by material soil properties and reflects low-strain shear strength. As a result, gravelly soils have low reference strains and more plastic clays have higher values. The reference strains used in the EPRI (1993) curves (Figure 6.12) were selected to be appropriate for soils comprised of gravels, sands, and low PI silts and clays and are primarily based on the results of laboratory testing as well as published curves (EPRI, 1993).

The more linear curves (Figure 6.13) which are compatible with the empirical attenuation relation (Appendix A), may be a result of the relatively large contribution to the strong motion database of the very linear Imperial Valley soils (Chapter 5.5) and the older more fine grained and more linear (Pleistocene) soils of the Los Angeles basin. The EPRI soil curves are likely more appropriate younger and perhaps more coarse grained materials and appear to work well for the North Coast earthquakes and sites (Chapter 5; EPRI, 1993). The revised curves are the

EPRI curves of 51 ft to 150 ft for 0 ft to 50 ft and the EPRI 501 ft to 1,000 ft for soil depths greater than 50 ft.

6.2.3.2 G/G_{max} and Hysteretic Damping Curves for Rock

For the rock G/G_{max} and hysteretic damping curves, initial attempts in the comparison exercises with the average curves in Appendix D showed results similar to the EPRI (1993) soil curves: too much damping and too large a spectral shift to longer periods at higher loading conditions. Since the empirical rock attenuation relations in Appendix A are essentially linear (constrained), this result is not surprising. Because there are few data recorded at rock sites at high levels of loading and the available data may be dominated by very hard rock at shallow depth (e.g.: Pacoima, San Fernando and Northridge earthquakes; Lucern, Landers earthquake) the rock attenuation relation is not well constrained at close distances for large magnitude ($M \geq 6.5$) earthquakes, particularly at short periods. Based on the shallow materials at typical soft rock sites (Chapter 3), with shear-wave velocities of 1,000 to 2,000 ft/sec and consisting essentially of weathered zones of poorly cemented granular soils, some nonlinear response may be expected. The derived set of rock curved (Figure 6.14) is an attempt to reconcile the results of laboratory testing (Appendix D) and trends in the data suggested by the rock attenuation relation (Appendix A). The curves for deeper material (> 20 ft) are essentially the Comanche Peak claystones (Appendix D) extrapolated to higher strains. Dr. Robert Pyke (personal communication) assisted in the extrapolation using the EPRI (1993) soil model based on reference strains.

It is important to emphasize that the derived modulus reduction and damping curves for soft rock and deep soil must be viewed in the context of the entire model: single-corner-frequency omega-square source spectra, point-source, 1/R ($1/\sqrt{R}$, R > 60 km) geometrical attenuation, vertically propagating shear-waves (source-to-surface), equivalent-linear, and the use of RVT to estimate peak oscillator response. While all of these approximations may be a scary thought to the timid, it should be kept in mind that all of the components have been separately validated. The accuracy with which the sum models observations is a measure of the degree to which each approximation or component accommodates the dominant and stable features of strong ground motions.

6.3 COMPARISON EXERCISES

The comparison exercises will consist of qualitative evaluations of 5% damped response spectra computed for the empirical and point-source models for a M 6.5 earthquake at both generic site conditions: soft rock and deep soil (Chapter 3). M 6.5 was selected because this magnitude represents the approximate centroid of the strong motion data, resulting in the most well constrained ground motion predictions, certainly for distances ranging from about 5 to 10 km to about 70 km (depending on site conditions).

For the empirical predictions, a vertical strike-slip earthquake is assumed and 5% damped response spectra computed at rupture distances of 0, 7, 15, 30, 60, 100, and 200 km for both soft rock and deep soil conditions. The distances were selected to approximately double the expected rock PGA values beginning at about 5%g at 60 km. The comparisons at 100 and 200

km were added since the empirical model is considered well enough constrained to 200 km (Appendix A). To generate the point-source model predictions, the inversion parameters for a strike slip earthquake (Table 6.1) were used. The stress drop is 59 bars and the Q(f) model used is 291 $f^{0.6}$ resulting from the combined regional inversions (Table 4.1). This lower Q(f) model is thought to be more "realistic" in that it is derived directly from the strong motion data and is the recommended model for use in California. The empirical relation for M 6.5 is likely model driven for distances exceeding about 60 to 75 km.

6.3.1 Soft Rock Comparisons

For the soft rock generic site, the material is considered to be potentially nonlinear to a depth of 500 ft where the shear-wave velocity is about 4,400 ft/sec. Over this depth range the damping curves (Figure 6.14) control the material damping while a kappa value of 0.02 sec is used to model the remainder of the shallow crust (1 to 2 km). The resulting total low-strain kappa is about 0.03 sec and increases to about 0.04 sec for the closest distance (0 km) with a corresponding peak acceleration value of about 0.50g. This is in general agreement with the inversion results of a rock kappa of about 0.037 sec (Table 6.1), independent of level of motion.

Beginning at 200 km, the rock comparisons are shown in Figure Set 6.15. For the model, median and $\pm$ 1 sigma spectra representing site variations are shown along with the median empirical spectra. The rock profiles are varied to a depth of 100 ft (Chapter 3) which corresponds to a maximum period of about 1 sec. The variation in model spectra due to a variation in material properties starts at about 1 sec and increases with decreasing period to a

maximum at around 0.2 to 0.3 sec. In general the model captures the absolute empirical spectra reasonably well at all distances. The short period underprediction at large distance (100 and 200 km) is likely due to the lower Q(f) model used (Q_o = 291, Table 4.1 compared to Q_o = 521, Table 6.1). At closer distances ($\leq$ 30 km) the model overpredicts slightly but generally reflects the empirical attenuation rate as distance decreases. At the two shortest distances (7 and 0 km), the expected empirical rock peak accelerations are about 0.4 and 0.7g and the model is developing high enough strains to increase damping and soften the profiles. At the closest distance, the model significantly underpredicts the empirical relation at short periods ($\leq$ 0.2 sec) and "saturates" to a peak acceleration of about 0.5g. It is difficult to assess which (or either) of the models is correct as few rock recordings are available at such close distances and several reflect hard rock conditions (e.g. Pacoima and Lucerne). For the median soft rock profile (Figure 3.2) it is difficult to imagine linearity under such high loading conditions suggesting that the empirical rock relation might be somewhat high at short periods and at very close distances.

6.3.2 Deep Soil Comparison

The kappa value assumed for the rock beneath the soil is taken as 0.034 sec to give a total small strain kappa (rock plus soil) of 0.04 sec. This corresponds to the value of about 0.04 sec for soil obtained in the inversions (Table 6.1). At the highest level of loading, corresponding to D = 0 and a rock outcrop peak acceleration of about 0.50g, the total kappa increases to about 0.07 sec, consistent with the value of about 0.06 sec in the inversions (Table 6.1).

For the deep soil comparisons, Figure Set 6.16 shows the stochastic point-source and empirical model predictions starting at 200 km and decreasing to 0 km. As for the rock site comparisons,

the fits are closer for distances less than 100 km and are generally a bit closer than the results for the rock case. In general the model displays the appropriate distance attenuation and shift in the spectral peak (maximum spectral amplification) to longer period as loading level increases. This general trend in nonlinearity is modeled reasonably well even up to the highest loading at D = 0. The median point-source spectra are generally within about 20% of the empirical model throughout the entire bandwidth and for the entire range in level of loading (distance). This is quite remarkable considering the simplicity of the model and suggests that the vertically propagating shear-wave model is an adequate representation of site effects for distances out to 200 km and over the period range of 0.01 to 5.0 sec. Additionally, simple geometric attenuation (1/R, $1/\sqrt{R}$) appears to capture the general trends in empirical strong motion attenuation over the distance range of primary interest to engineering design: 0 to 100 km.

The simple point-source magnitude dependency of response spectra is also in general accord with the empirical attenuation relation. This aspect is presented in Chapter 7 on comparisons to response spectral shapes.

In addition to the qualitative comparisons, both variability and bias estimates are computed as well. These estimates are computed separately for rock and soil site conditions. Because the number of sites is small (7 distances, 2 site categories) the estimates have considerable uncertainty and are intended only as a further qualitative assessment of the model relative to a single attenuation relation. Figures 6.17 and 6.18 show the results for soil and rock sites respectively. For both site conditions, the bias is generally small (near zero) from 0.2 Hz (lowest frequency in the empirical attenuation relation) up to 100 Hz. The variability estimates

are also very low, less than about 0.25 over most of the frequency range. The point-source model is providing ground motion estimates in good agreement with those of the empirical attenuation relation. A more statistically significant comparison would involve multiple magnitudes (at least 3) as well as multiple empirical relations to accommodate epistemic uncertainty, particularly over magnitudes, distances, and site conditions poorly constrained by data. However, combining results of empirical attenuations relations is not unambiguous in that consistent distance and site definitions are rarely used.

Table 6.1 Inversion of Empirical Attenuation Relations Determination of Stress Drops, Q Models, and Average Kappa Values

Inversions With Individual Mechanisms						
Strike Slip			Oblique		Reverse	
M	$\Delta\sigma$ (bars)		M	$\Delta\sigma$ (bars)	M	$\Delta\sigma$ (bars)
5.5	47		5.5	66	5.5	94
6.5	61		6.5	60	6.5	60
7.5	36		7.5	36	7.5	36
	Avg = 48			Avg = 54		Avg = 63
Q_o	η		Q_o	η	Q_o	η
911	0.31		1147	0.25	1563	0.16
546	0.60*		612	0.60*	696	0.60*
2054	0.00*		2457	0.00*	2361	0.00*
κ (sec) rock	κ (sec) soil	PGA(%g) rock outcrop	κ (sec) rock	κ (sec) soil	κ (sec) rock	κ (sec) soil
0.041	0.042	$\leq$ 5	0.038	0.040	0.035	0.039
	0.048	5 - 10		0.046		0.044
	0.051	10 - 20		0.049		0.048
	0.060	20 - 40		0.057		0.054
	0.067	> 40		0.063		0.059
Inversion With Combined Mechanisms						
M	$\Delta\sigma$ (bars)					
	SS	OB	RV	AVG		
5.5	43	67	130	80		
6.5	56	61	66	61		
7.5	33	36	39	36		
Avg = 44		55	78	59		

Table 6.1 (cont.) Inversion of Empirical Attenuation Relations
Determination of Stress Drops, Q Models, and Average Kappa Values

Q_o	η
1167	0.25
621	0.60*
2219	0.00*

κ (sec) rock	κ (sec) soil	PGA(%g) rock outcrop
0.038	0.041	≤ 5
	0.047	5 - 10
	0.050	10 - 20
	0.057	20 - 40
	0.063	> 40

*Values held fixed
Shear-wave velocity = 3.50 km/sec, density = 2.7 cgs, crossover distance = 60 km
Starting values $Q^* = 150$, $\eta = 0.60$, $\Delta\sigma = 50$ bars, $\kappa = 0.20$ sec
Note: $\Delta\sigma$ and kappa values for η fixed at 0.60. Fault distance range is to 200 km with 7 distances for each magnitude. Point source depth is 6 km for M 5.5 and 8 km for M 6.5 and M 7.5

CHAPTER 7

POINT-SOURCE MODEL VALIDATION

COMPARISON TO STATISTICAL SPECTRAL SHAPES

7.1 STATISTICAL SHAPES

Local geologic conditions have long been recognized to have a strong effect upon strong ground motions (Hayashi et al., 1971; Mohraz, 1976; Seed et al., 1976). For example, Figure 7.1 shows average spectral amplifications (response spectral acceleration divided by peak acceleration) computed from recordings made on rock and soil sites at close distances to earthquakes in the magnitude range of about 6 to 7. The differences in spectral shapes are significant and depend strongly upon the general site classifications. These variations in spectral content represent average site dependent ground motion characteristics and result from vertical variations in soil material properties (1-D effects). Due primarily to the limited number of records from earthquakes of different magnitudes, spectral content in terms of response spectral shapes, was interpreted not to depend upon magnitude nor distance, being primarily affected by the stiffness and depth of the local soil profile. With an increase in the strong motion data base, it has become apparent that spectral shapes depend strongly upon magnitude as well as site conditions (Joyner and Boore, 1982, Idriss, 1985; Silva and Green, 1989; Boore et al., 1994; Silva and Darragh, 1995) and that site effects extend to rock sites as well (Boatwright and Astrue, 1983; Campbell 1981, 1985, 1988; Cranswick et al., 1985; Silva and Darragh, 1995).

Examples of differences in spectral content largely attributable to one-dimensional site effects at rock sites can be seen in comparisons of spectral amplifications computed from motions

recorded in both active and stable tectonic regions (Silva and Darragh, 1995). Figures 7.2 and 7.3 show average spectral shapes computed from recordings made on rock at close distances to large and small earthquakes. For both magnitudes (moment magnitude M 6.4 and 4.0), the motions recorded in eastern North America (ENA), a stable tectonic region, show a dramatic shift in the maximum spectral amplifications toward shorter periods compared to the western North American (WNA) motions. These differences in spectral content are significant and are interpreted as primarily resulting from differences in the shear-wave velocity and damping in the rocks directly beneath the site (Boore and Atkison, 1987; Toro and McGuire, 1987; Silva and Green, 1989; Silva and Darragh, 1995). Also evident in Figures 7.2 and 7.3 are the strong magnitude dependency of the response spectral shapes. The smaller earthquakes show a much narrower bandwidth. This is a consequence of lower corner frequencies for smaller magnitude earthquakes (Boore, 1983; Silva and Green, 1989; Silva, 1991; Silva and Darragh, 1995).

The differences in spectral content due to soil site effects, as shown in Figure 7.1, and due to path or rock site effects, as shown in Figure 7.2 and 7.3, are dramatic and illustrate the degree to which one-dimensional site conditions (vertical variations in dynamic material properties) control strong ground motions.

The strong magnitude and site dependencies of spectral shapes provide a good qualitative basis for evaluating the performance of a strong motion model. If a simple model can, in some measure, reflect dependencies similar to those shown in well constrained statistical shapes, additional confidence is gained in implementing the model for magnitudes and site conditions (and period ranges) which are poorly constrained by data. The validations with response spectral

shapes permits direct comparisons with recorded motions over a wide magnitude range. As a result, any model deficiencies (biases) can be more carefully examined.

To compute the statistical shapes, magnitude bins were selected at 1/2 magnitude units from M 5.5 to M 7.5 (Table 7.1). This provided as wide a range as was possible yet retaining enough data within each bin to constrain the shapes. To better constrain the shapes a 0.1 unit overlap was used so that the same spectra may be included in adjacent bins. A 0.1 unit is considered an acceptable compromise for stability. As usual, the data set is sparse for M 7.5 (M > 7.2), particularly for rock sites (8 spectra, Table 7.1).

The distance range of 0 to 50 km was selected to minimize distance effects on the shapes. Within about 50 km in WNA, spectral shapes depend weakly on distance (Silva and Green, 1989; Appendix A). It is believed that sufficient validations of distance effects are contained in Chapters 4, 5, and 6 on regional inversions, point- and finite-source validations, and comparisons to empirical attenuation, respectively.

7.1.1 Soft Rock

The statistical shapes computed from recordings in the catalog (Appendix B) with sites classified as either Geomatrix A or B are shown in Figure Set 7.4 for M 5.0 to M 7.5 (Table 7.1). The spectra are 5% damping median and $\pm$ 1σ values. The dramatic increase in variability at long periods is due to the decrease in the number of spectral ordinates. The record specific processing (Appendix A) results in varying high-pass filters corner frequencies which are taken

as truncation points in computing the fractile levels. As the magnitude increases, the medians (and fractiles) become more stable to longer periods until very large magnitude where there are few data (Figure Set 7.4, M 7.5). For M 5.0 and M 5.5, the shape is well constrained out to about 1 to 2 sec only while for M 6.0 and above, the shapes are likely reliable out to about 8 sec. For M 7.5, there is a dramatic change in shape with the peak shifting to shorter periods than M 7.0. This shift has no doubt contributed to the "linearity" of the empirical rock attenuation relation (Appendix A) and may be manifestation of a combination of harder rock (kappa = 0.02 sec rather than 0.04 sec, Chapter 4.3.2) with the emergence of a double-corner source spectrum (Atkinson and Silva, 1996). With only two earthquakes (Tabas, 1 site and Landers, 3 sites) comprising only 4 sites, it is not possible to draw firm conclusions. However, it is clear that a kappa value closer to 0.02 sec (Mojave, Chapter 4) rather than 0.04 sec would be more appropriate. Apart from this departure, the magnitude dependencies shown in Figure 7.5 are clear with the spectral peak shifting to longer periods and the spectrum broadening as magnitude increases (Darragh et al., 1990).

7.1.2 Deep Soil

For deep soil, Geomatrix categories C and D (Chapter 3), the corresponding statistical spectra (median and $\pm$ 1σ) are shown in Figure Set 7.6. As with the rock statistical spectra, the long period stability increases with increasing magnitude however, there are easily twice the records in each magnitude bin. Interestingly, the M 7.5 shape, with more earthquakes (and sites) does not show the same short-period shift in maximum spectral amplification as the rock spectra. This is an important issue to resolve for large magnitude earthquakes and, pending more data,

requires more extensive finite-fault modeling. Figure 7.7 shows the median statistical spectra for each magnitude bin illustrating the strong magnitude dependence of the shapes.

It is important to emphasize that the variability in shape (standard error) has contributions from ranges in magnitude, distance, and mechanism as well as within class site variations and should be much larger than the site variation shown by the model shapes in the next section.

7.2 MODEL SHAPES

The shapes predicted by the point-source model are computed using the generic rock and soil profiles (Chapter 3) for the mean distances and magnitude bins listed in Table 7.1. The profiles (rock and soil) are randomized (30 realizations) so the variability in the computed shapes is an estimate of the site contribution alone. For the soil site, depth to bedrock is randomized (uniform distribution) from 100 ft to 1,000 ft for an average depth of 550 ft. A constant stress drop of 59 bars is used reflecting the average value over magnitude and mechanism obtained in the inversion of the empirical attenuation relations (Table 6.1). The use of a constant stress drop is not a significant issue since spectral shapes depend weakly on stress drop, showing a maximum variation of about 30% for a 100% (factor of 2) change in stress drop (Silva and Darragh, 1995). Additionally, the maximum sensitivity occurs at the longest period which is 10 seconds in this case.

For the empirical shapes, a vertical strike slip earthquake is assumed and the relations in Appendix A are used to computed (Sa/A_{max}) for the same magnitudes and distances as in the model shapes.

7.3 COMPARISON OF MODEL SPECTRAL SHAPES TO STATISTICAL AND EMPIRICAL SHAPES

To provide a qualitative comparison of model shapes to the statistical shapes (Figure Set 7.4) as well as to shapes predicted by the empirical attenuation relations, Figures Set 7.8 shows all three for rock sites. Each figure represents a single magnitude bin (M 5.0 to M 7.5) and the $\pm$ 1σ bounds are shown for the statistical spectra with the median shown for the model spectra. In general, there is close agreement among all three sets of spectra over the entire bandwidth and range in magnitudes. The point-source over-prediction at long periods appears around M 6.5 to M 7.0 with the spectral sag and shift in peak to shorter periods being very apparent for M 7.5. Figure 7.9 shows the magnitude scaling predicted by the model (median spectra).

For soil sites, the corresponding plots are shown in Figure Set 7.10 for the same magnitude bins. In this case, the statistical spectra are smoother because of the greater number of sites (Table 7.1). The agreement between all three sets of spectra is perhaps a bit better than the rock spectra and is generally considered good. As with the rock sites, the magnitude dependency is summarized in a single plot (Figure 7.11). For both the rock and soil sites, the model spectral shapes provide about as good a fit to the statistical shapes as do those computed using the empirical attenuation relation (Appendix A). The main exception is the large-magnitude long-period overprediction of the point-source model. It should be pointed out however, for applications to engineered structures, a tendency to overpredict is not considered a highly undesirable feature.

To illustrate the site dependencies, Figure Set 7.12 shows statistical (median) rock and soil spectral shapes for each magnitude bin. Analogous plots for model shapes are shown in Figure Set 7.13. The site effects are clearly evident with higher short period motions for rock sites, a magnitude dependent crossover, and higher long period motions for soil (Seed et al., 1976; Silva, 1991).

To complete the model shapes, the median and $\pm$ 1σ shapes are shown in Figure Set 7.14 for rock and 7.15 for soil. The uncertainty reflects both epistemic and aleatory components for the site only (Chapter 7.2) and is significantly smaller than that shown for the statistical shapes (Figure Set 7.4 and Figure Set 7.6). The variability in the statistical shapes contains within-bin magnitude and distance differences as well as source (stress drop) and propagation path variations.

Table 7.1 Statistical Response Spectral Shapes Magnitudes and Distances

Soft Rock				
M (Range,Mean,Bin)	Number of Spectra	Number of Earthquakes	D (Range, Mean) (km)	Expected Rock PGA (Strike Slip)
4.7 - 5.3, 5.0, 5.0	90	15	0 - 50, 13.5	0.062
5.2 - 5.8, 5.5, 5.5	108	18	0 - 50, 16.9	0.077
5.7 - 6.3, 6.0, 6.0	146	21	0 - 50, 22.1	0.095
6.2 - 6.8, 6.5, 6.5	148	12	0 - 50, 27.1	0.120
6.7 - 7.3, 6.8, 7.0	104	7	0 - 50, 26.0	0.154
7.2 + , 7.4, 7.5	8	8	0 - 50, 15.8	0.295
Deep Soil				
4.7 - 5.3, 5.1, 5.0	145	22	0 - 50, 15.8	0.060
5.2 - 5.8, 5.4, 5.5	159	35	0 - 50, 18.3	0.079
5.7 - 6.3, 6.0, 6.0	337	25	0 - 50, 23.2	0.096
6.2 - 6.8, 6.5, 6.5	342	17	0 - 50, 27.3	0.122
6.7 - 7.3, 6.9, 7.0	219	8	0 - 50, 28.3	0.140
7.2 + , 7.3, 7.5	50	4	0 - 50, 34.0	0.145

CHAPTER 8

SUMMARY AND CONCLUSIONS

"All models are wrong, some are simply more useful than others." This perspective is largely ignored by those who develop and use ground motion models and embraced by all others. It is, of course, accurate and the objective of this project was to present a comprehensive assessment of how useful the stochastic point- and finite-source models are in predicting strong ground motions for engineering design. Since both the point- and finite-source ground motion models combine seismological source and wave propagation physics with a conventional geotechnical approach to accommodating nonlinear site response, a complete description of the models and their backgrounds was presented.

To provide a quantative assessment of the predictive ability of the models in terms of estimating model bias and variability, a total of 16 earthquakes were modeled at 503 sites over the fault distance range of about 1 to 177 km (460 km for CEUS). Point-source inversions of the earthquakes were performed to provide stress drop and regional Q(f) models to be used in forward simulations. These results showed regional differences in Q(f) models as well as rock and soil site kappa values. The Mojave geologic Province is characterized by the lowest crustal damping ($Q(f) = 371\ f^{0.6}$) and lowest rock site kappa (0.030 sec). The North Coast Province has the highest crustal damping ($Q(f) = 176\ f^{0.6}$) and rock site kappa (0.059 sec). For the Peninsular Range earthquakes, crustal damping and rock site kappa are intermediate, $Q(f) = 264\ f^{0.6}$ and 0.051 sec. At soil sites, a significant difference is seen in the kappa values between the

Peninsular Range and the North Coast sites, 0.056 sec compared to 0.072 sec. The smaller kappa value for the Peninsular Range sites is reflected in nonlinear site response requiring significantly more linear G/G_{max} and hysteretic damping curves.

Model bias and variabilities were estimated for the 15 study earthquakes over all 503 sites for both the point- and finite-source models. In general the bias estimates were low and the variabilities small, with the best results for the most well recorded earthquakes (perhaps due to better determined slip models). There were exceptions, and in these cases both the point- and finite-source models provided poor results (e.g. North Palm Springs earthquake). For earthquakes with significant amounts of shallow slip (within 2 km of the surface), the subevent stress drop had to be significantly reduced, from the 30 bar nominal value to 5 bars. With a 30 bar subevent stress drop, high frequency ground motions ($\geq$ 1 Hz) are overpredicted by factors of 2 to 3. This result was pervasive and occurred for all events with significant shallow slip: Nahanni, Landers, Tabas, Imperial Valley, and Superstition Hills(B) earthquakes. Interestingly, for the Saguenay earthquake, a subevent stress drop of 100 bars was required to model the high frequency ground motions.

For three earthquakes, ground motions were sufficiently high and bias estimates were sufficiently small and well determined to permit resolution of nonlinear site response as well as the development of region specific G/G_{max} and hysteretic damping curves. For the cohesionless soils of the North Coast Province, the Loma Prieta analyses demonstrated the appropriateness of the EPRI (1993) curves. For similar soil conditions in the Peninsular Range Province, the Northridge analyses showed the EPRI (1993) curves resulted in too high a degree

of nonlinear soil response and a more linear set of curves was developed. For the soils of the Imperial Valley, comprised of silts, clays, and silty clays, the analyses of the 1979 mainshock and aftershock showed very little nonlinear response at all but two sites (Meloland and EC7) and a third set of curves was developed for these soils. These analyses suggested an envelope of clear detectability for nonlinear site response: **M** $\geq$ 6.5, distances within about 30 km, frequencies above 3 Hz, and, for statistical stability, at least 20 stations.

The final bias and variability estimates computed for all the earthquakes and over all the sites showed near zero bias for frequencies of about 1 Hz and above for both the point- and finite-source models. The point-source model shows a stable and significant negative bias (overprediction) from about 1 Hz to 0.3 Hz (the approximate low frequency limit of the analyses). Over this frequency range the finite-source bias remains near zero indicating broad band applicability.

The variability estimates are generally uniform at about 0.5 to 0.6 at 1 Hz and above. This is considered low as the majority of the data are for **M** less than **M** 6.5 and the sites range in distance out to 177 km (460 km for the Saguenay earthquake). Also, site specific kappa values are used at only 25 of the 503 sites. As a result, the model variability includes parametric uncertainty and randomness in site specific soil column shear-wave velocities, depth to bedrock, and G/G_{max} and hysteretic damping curves.

The final variability estimates also showed that soil sites are modeled more accurately than rock sites, a result generally reflected in the estimates for each earthquake. This indicates that

ground motions at rock sites show more site-to-site variability than soil sites and the models are not accommodating this feature.

To further validate the point-source model as well as the equivalent-linear one-dimensional site response model, comparisons of simulations were made to spectral estimates from an empirical attenuation relation developed for this project (Appendix A). The new empirical relation was based on a largely reprocessed strong motion database (Appendix B) which incorporates the most recent WNA earthquakes (Loma Prieta, Landers, and Northridge) and for site conditions (soft rock and deep soil) consistent with the generic profiles used in the 1-D site response model. A significant feature of the empirical attenuation relation is a magnitude dependent attenuation rate. This feature was accommodated in the functional form of the empirical relation when finite-fault modeling for **M** 5.5 and **M** 7.5 earthquakes clearly showed its presence. A consequence of this result is that the point-source model, if it does not accommodate a magnitude dependent geometrical attenuation or higher stress drop, may underpredict motions for large magnitudes at distances exceeding about 100 km. The point-source approximation to an extended source breaks down at large distances rather than at close distances, a result contrary to cherished beliefs.

Comparisons of point-source simulations using the inversion parameters to the empirical model spectra at large distances for **M** 6.5 and **M** 7.5 showed the point-source model to underpredict at intermediate frequencies (about 0.3 to 3.0 Hz). The underprediction is significant at distances exceeding about 100 km and for $\mathbf{M} \geq 6.5$. It is not interpreted as potential basin effects since

the underprediction occurs for both soft rock and deep soil site conditions. These results were also seen in the Landers earthquake analysis at rock and soil sites in the Los Angeles basin. Finite-fault simulations reduced the underprediction by 50%, supporting the magnitude dependent attenuation rate being due to source finiteness and suggesting that the remaining 50% may be due to wave propagation effects in crossing crustal structure boundaries.

Point-source inversions on the empirical attenuation relation resulted in magnitude and mechanism dependent stress drops, a rock site kappa value of 0.038 sec, and soil site kappa values which increased from about 0.04 sec to about 0.06 as the expected rock outcrop peak ground acceleration increased from about 5%g to over 40%g. Only a 50% increase for nearly a 1,000% increase in control motions. These soil site results suggested more linear response than typical G/G_{max} and hysteretic damping curves (EPRI, 1993). Comparisons of point-source simulations for **M** 6.5 to the empirical attenuation spectra at varying site distances (control motions) showed the Peninsular Range curves produced the degree of nonlinear response appropriate to that shown in the empirical attenuation relation. This result is consistent with the Peninsular Range (and very linear Imperial Valley) soils comprising a significant number of the soil sites in the strong motion database. The magnitude dependence of point-source stress drop is strong, dropping significantly with increasing magnitude, suggesting a breakdown of similarity.

To validate the magnitude and site dependency of response spectral shapes, the stochastic point-source model was compared to statistical shapes computed from the strong motion database as well as shapes from the empirical attenuation relation for magnitude bins centered on **M** 5.5,

6.0, 6.5, 7.0, and 7.5. Both soft rock and deep soil comparisons were made. The results showed that the point-source model, using vertically propagating shear-waves and equivalent-linear site response provided about as good a match to the statistical shapes as did the empirical model. The main exception being a large magnitude, long period overprediction present in both the point-source and empirical shape estimates. The point-source model generally captures the appropriate magnitude dependency shown in the statistical and empirical shapes and vertically propagating shear-waves using equivalent-linear site response captures the site dependency. These results indicate that the point-source (as well as finite-source) model can be used to develop response spectral shapes for source, path, and site conditions which are not well represented with ground motion recordings.

In general, this project has demonstrated that the stochastic point- and finite-source models produce accurate predictions of strong ground motions over the distance range of 0 to 100 km and for magnitudes **M** 5.0 to **M** 7.5. The point-source seriously underpredicts at intermediate periods for **M** $\geq$ 6.5 and for distances greater than about 100 km. A higher stress drop can be used but will result in overpredictions at short distances for large magnitude. Additionally, the point-source model overpredicts for frequencies below about 1 Hz, particularly for **M** $\geq$ 6.5. The stochastic finite-source model appears to be broadband, producing near zero bias from about 0.3 Hz (the lower limit of reliable analyses) to the high frequency limit of the data (100 Hz for response spectra, about 25 Hz for Fourier spectra).

The vertically propagating shear-wave model, used from the source region (2 to 15 km

depending upon earthquake) to the surface and for equivalent-linear site response at both soft rock and deep soil sites appears to capture the significant and stable features of crustal amplification and site response reflected in both strong motion recordings and the empirical attenuation relation. This is a notable result, as the distances ranged out to 177 km (over 400 km for CEUS) and soil column thickness of up to 1,000 ft (nominally 500 ft). The message is clear; simple and physically correct assumptions about source, path, and site processes capture the observed variations in strong ground motions with sufficient accuracy to provide reliable guidance in defining design ground motions. This work has quantified that accuracy for the point- and finite-source stochastic ground motion models.

CHAPTER 9

REFERENCES

Abrahamson, N.A., Somerville, P.G., Cornell, C.A. (1990). "Uncertainty in numerical strong motion predictions" *Proc. Fourth U.S. Nat. Conf. Earth. Engin.*, Palm Springs, CA., 1, 407-416.

Aki, K. and P. G. Richards. (1980). *"Quantitative siesmology."* W. H. Freeman and Co., San Francisco, California.

Aki, K. (1967). "Scaling law of seismic spectrum." *J. Geophys. Res.*, 73, 1217-1231.

Anderson, J. G. and S. E. Hough (1984). "A Model for the Shape of the Fourier Amplitude Spectrum of Acceleration at High Frequencies." *Bulletin of the Seismological Society of America,* 74(5), 1969-1993.

Atkinson, G.M and W.J. Silva (1996). "An empirical study of earthquake source spectra for California earthquakes." Submitted to the *Bull. Seism. Soc. Am.*

Atkinson, G.M. (1984). "Attenuation of strong ground motion in Canada from a random vibrations approach." *Bull. Seism. Soc. Am.*, 74(5), 2629-2653.

Atkinson, G.M. (1993). "Source spectra for earthquakes in eastern North America." *Bull. Seism. Soc. Am.*, 83(6), 1778-1798.

Boatwright, J., and Astrue, M. (1983). "Analysis of the aftershocks of the New Brunswick earthquake." *Workshop on Site-Specific Effects of Soil and Rock on Ground Motion and the Implications for Earthquake-Resistant Design.* USGS Open-File Rept. 83-245.

Boore, D.M., W.B. Joyner, and T.E. Fumal (1994). "Estimation of response spectra and peak accelerations from western North American earthquakes: and interim report. Part 2. *U.S. Geological Survey Open-File Rept.* 94-127.

Boore, D.M., W.B. Joyner, and T.E. Fumal (1993). "Estimation of response spectra and peak acceleration from western North American earthquakes: An interim report." *USGS* Open-File Rept. 93-509.

Boore, D.M., and Atkinson, G.M. (1987). "Stochastic prediction of ground motion and spectral response parameters at hard-rock sites in eastern North America." *Bull. Seism. Soc. Am.*, 77(2), 440-467.

Boore, D.M. (1986). "Short-period P- and S-wave radiation from large earthquakes: implications for spectral scaling relations." *Bull. Seism. Soc. Am.*, 76(1) 43-64.

Boore, D.M. and Joyner, W.B. (1984). "A note on the use of random vibration theory to predict peak amplitudes of transient signals." *Bull. Seism. Soc. Am.*, 74, 2035-2039.

Boore, D.M. (1983). "Stochastic simulation of high-frequency ground motions based on seismological models of the radiated spectra." *Bull. Seism. Soc. Am.*, 73(6), 1865-1894.

Brune, J.N. (1971). "Correction." *J. Geophys. Res.* 76, 5002.

Brune, J.N. (1970). "Tectonic stress and the spectra of seismic shear waves from earthquakes." *J. Geophys. Res.* 75, 4997-5009.

Bycroft, G. N. (1980). "El Centro California differential ground motion array." U.S. Geological Survey, *Open-file report 80-919.*

Campbell, K.W. (1993) "Empirical prediction of near-source ground motion from large earthquakes." in V.K. Gaur, ed., *Proceedings, Intern'l Workshop on Earthquake Hazard and Large Dams in the Himalya.* INTACH, New Delhi, p. 93-103.

Campbell, K.W. (1988). "Predicting strong ground motion in Utah." *Evaluation of Regional and Urban Earthquake Hazards and Risk in Utah,* edited by W.W. Hays and P.L. Gori, USGS Prof. Paper.

Campbell, K.W. (1985). "Strong motion attenuation relations: a ten-year perspective." *Earthquake Spectra* 1, 759-804.

Campbell, K.W. (1981). "Near-source attenuation of peak horizontal acceleration." *Bull. Seism. Soc. Am.*, 71(6), 2039-2070.

Cornell, C.A. (1968). "Engineering seismic risk analysis." *Bull. Seism. Soc. Am.*, 58, 1583-1606.

Cranswick, E., Wetmiller, R., and Boatwright, J. (1985). "High-frequency observations and source parameters of microearthquakes recorded at hard-rock sites." *Bull. Seism. Soc. Am.*, 75(6), 1535-1567.

Darragh, R. B., J. W. Silva, J. C. Stepp, and J. F. Schneider (1990). "Maximum spectral amplification and high-frequency truncation filters in the band limited white noise ground motion model at rock sites." in *Proc. of Fourth U.S. National Conference on Earthquake Engineering, Plam Springs, California, EERI*, 1, 437-446.

Durward, J.A., D.M. Boore and W.B. Joyner (1996). "The amplitude dependence of high-frequency spectral decay: Constraint on soil non-linearity." *in Proc. International Workshop on SHE Response Subjected to Strong Earthquake Motions.* Yokosuka, Japan.

Electric Power Research Institute (1995). *Proceedings: Modeling earthquake ground motion at close distances.* Palo Alto, Calif: Electric Power Research Institute, EPRI TR-104975.

Electric Power Research Institute (1993). "Guidelines for determining design basis ground motions." Palo Alto, Calif: Electric Power Research Institute, vol. 1-5, EPRI TR-102293.
vol. 1: Methodology and guidelines for estimating earthquake ground motion in eastern North America.
vol. 2: Appendices for ground motion estimation.
vol. 3: Appendices for field investigations.
vol. 4: Appendices for laboratory investigations.
vol. 5: Quantification of seismic source effects.

Fletcher, J.B., and Boatwright, J. (1991). Source parameters of Loma Prieta aftershocks and wave propagation characteristics along the San Francisco Peninsula from a joint inversion of digital seismograms. *Bull. Seism. Soc. Am.*, 81(5):1783-1812.

Graves, R.W. (1994). "Simulating the 3D basin response in The Portland and Puget Sound Regions from large subduction zone earthquakes." *USGS* Award: 1434-93-G-2327, Annual Technical Report.

Hanks, T.C. and Boore, D.M. (1984). "Moment-magnitude relations in theory and practice." *J. Geophys. Res.*, 89(B7), 6229-6235.

Hanks, T.C. (1982). "f_{max}." *Bull. Seism. Soc. Am.*, 72, 1867-1879.

Hanks, T.C., and McGuire, R.K. (1981). "The character of high-frequency strong ground motion." *Bull. Seism. Soc. Am.*, 71(6), 2071-2095.

Hanks, T.C. (1979). "b values and $\omega^{-\gamma}$ seismic source models: implications for tectonic stress variations along active crustal fault zones and the estimation of high frequency strong ground motion." *J. Geophys. Res.*, 84(B5), 2235-2241.

Hanks, T.C., and Kanamori, H. (1979). "A moment magnitude scale." *J. Geophys. Res.*, 84, 2348-2350.

Hardin, B. O.; Drnevich, V. P. (1972). "Shear Modulus and Damping in Soils: Design Equations and Curves," **Journal of the Soil Mechanics and Foundations Division,** ASCE, 98(GT7), 667-692.

Hagerty, M.T. and S.Y. Schwartz (1996). "The 1992 Cape Mendocino earthquake: Broadband determination of source parameters." *J. Geophys. Res.*, 101(B7), 16,043-16,058).

Hartzell, S., P. Liu and C. Mendoza (1996). "The 1994 Northridge, California, earthquake: Investigation of rupture velocity, risetime, and high-frequency radiation." *J. Geophys. Res.* 101(B9), 20,091-20,108.

Hartzell, S., C. Langer and C. Mendoza (1994). "Rupture histories of eastern North American earthquakes." *Bull. Seism. Soc. Am.*, 84(6), 1703-1724.

Hartzell, S., C. Langer and C. Mendoza (1991). "Application of an iterative least-squares waveform inversion of strong-motion and teleseismic records to the 1978 Tabas, Iran." *Bull. Seism. Soc. Am.*, 81(2), 305-331.

Hartzell, S.H. and Iida, M. (1990). "Source complexity of the 1987 Whittier Narrows, California, earthquake from the inversion of strong motion records." *J. Geophys. Res.* 95(B8), 12475-12485.

Hartzell, S.H. (1989). "Comparison of seismic waveform inversion results for the rupture history of a finite fault: application to the 1986 North Palm Springs, California, earthquake." *J. Geophys. Res.*, 94(B6), 7515-7534.

Hartzell, S.H., and Heaton, T.H. (1986). "Rupture history of the 1984 Morgan Hill, California, earthquake from the inversion of strong motion records." *Bull. Seism. Soc. Am.*, 76(3), 649-674.

Hartzell, S.H. and T.H. Heaton (1983). "Inversion of strong ground motion and teleseismic waveform data for the fault rupture history of the 1979 Imperial Valley, California, earthquake." *Bull. Seism. Soc. Am.*, 73(6), 1553-1583.

Hartzell, S.H. (1978). "Earthquake aftershocks as Green's functions." *Geophys. Res. Letters*, 5, 1-4.

Hayashi, S., Tsuchida, H., and Kurata, E. (1971). "Average response spectra for various subsoil conditions." *Third Joint Meeting, US-Japan Panel on Wind and Seismic Effects*, UJNR, Tokyo.

Heaton, T.H. (1990). "Evidence for and implications of self-healing pulses of slip in earthquake rupture". *Phys. Earth Planetary Int.*, 64, 1-20.

Heaton, T.H. (1982). "The 1971 San Fernando earthquake: a double event?" *Bull. Seism. Soc. Am.*, 72, 2037-2062.

Heaton, T.H., and Helmberger, D.V. (1979). "Generalized ray models of the San Fernando earthquake." *Bull. Seism. Soc. Am.*, 69(5), 1311-1341.

Herrmann, R.B. (1985). "An extension of random vibration theory estimates of strong ground motion to large distance." *Bull. Seism. Soc. Am.*, 75, 1447-1453.

Hough, S.E., Anderson, J.G., Brune, J., Vernon III, F., Berger, J., Fletcher, J., Haar, L., Hanks, T., and Baker, L. (1988). "Attenuation near Anza, California." *Bull. Seism. Soc. Am.*, 78(2), 672-691.

Hough, S. E. and J. G. Anderson (1988). "High-Frequency Spectra Observed at Anza, California: Implications for Q Structure." *Bull. Seism. Soc. Am.*, 78(2), 692-707.

Idriss, I.M. (1993). "Procedures for selecting earthquake ground motions at rock sites." *National Institute of Standards and Technology*. NIST GCR 93-625.

Idriss, I.M. (1985). "Evaluating seismic risk in engineering practice." *Proc. Eleventh Internat. Conf. on Soil Mech. and Foundation Eng.*, San Francisco, edited by A.A. Balkema, Rotterdam, 1, 255-320.

Irikura, K. (1983). "Semi-empirical estimation of strong ground motions during large earthquakes." *Bull. Disaster Prevention Res. Inst.*, Kyoto Univ., 33, 63-104.

Joyner, H.B. and D.M. Boore (1982) "Prediction of earthquake response spectra." *USGS*, Open-File Rept. 82-977.

Liu, H-L, and Helmberger, D.V. (1985). "The 23:19 aftershock of the 15 October 1979 Imperial Valley Earthquake: More evidence for an asperity." *Bull. Seism. Soc. Am.*, 75(3), 689-708.

Liu, H-L, and Helmberger, D.V. (1983). "The near-source ground motion of the 6 August 1979 Coyote Lake, California, earthquake." *Bull. Seism. Soc. Am.*, 73(1), 201-218.

Magistrale, H., H. Kanamori, and C. Jones (1992). "Forward and inverse three-dimensional P-wave velocity models of the southern California crust." *J. Geophys. Res.*, 97, 14,115-14,136.

McGuire, R. K., A. M. Becker, and N. C. Donovan (1984). "Spectral Estimates of Seismic Shear Waves." *Bull. Seism. Soc. Am.*, 74(4), 1427-1440.

Mohraz, B. (1976). "A study of earthquake response spectra for different geological conditions." *Bull. Seism. Soc. Am.*, 66(3) 915-935.

Nuttli, O.W. (1986). "Yield estimates of Nevada test site explosions obtained from seismic Lg wave." *J. Geophys. Res.*, 91: 2137-2151.

Ou, G.B. and R. B. Herrmann (1990). "Estimation theory for strong ground motion." *Seism. Res. Letters.* 61.

Papageorgiou, A.S., and Aki, K. (1983a). "A specific barrier model for the quantitative description of inhomogeneous faulting and the prediction of strong ground motion, part I, Description of the model." *Bull. Seism. Soc. Am.*, 73(4), 693-722.

Press, W.H., Flannery, B.P., Teukolsky, S.A., Vetterling, W.T. (1986). *"Numerical Recipes."* Cambridge Univ. Press, Cambridge.

Roblee, C.J., W.J. Silva, G.R. Toro and N. Abrahamson (1996). "Variability in site-specific seismic ground-motion design predictions." in press.

Rovelli, A., Bonamassa, O. Cocco, M., Di Bona, M. and Mazza, S. (1988). "Scaling laws and spectral parameters of the ground motion in active extensional areas in Italy." *Bull. Seism. Soc. Am.*, 78(2), 530-560.

Sadigh, R., Chang, C.Y., Makdizi, F., Egan, J. (1989). "Attenuation relations for horizontal peak acceleration and response spectra for rock sites." *Seism. Res. Letters.* 60(1):19.

Saikia, C. K. (1994). "Modeling of strong ground motions from the 16 September 1978 Tabas, Iran, earthquake." ***Bull. Seism. Soc. Am.***, 84(1), 31-46.

Schnabel, P.B., Lysmer, J., and Seed, H.B. (1972). *SHAKE: a Computer Program for Earthquake Response Analysis of Horizontally Layered Sites.* Earthq. Engin. Res. Center, Univ. of Calif. at Berkeley, EERC 72-12.

Schneider, J.F., W.J. Silva, and C.L. Stark (1993). "Ground motion model for the 1989 M 6.9 Loma Prieta earthquake including effects of source, path and site." *Earthquake Spectra*, 9(2), 251-287.

Schneider, J. F., W.J. Silva, S-J. Chiou, and J. C. Stepp (1991). "Estimation of Ground Motion at Close Distances Using the Band-Limited-White-Noise Model." *Proceedings of the Fourth International Conference on Seismic Zonation*, II, 187-194.

SCEC (1996) "Southern California Earthquake

Seed, H.B., Ugas, C. and Lysmer, J. (1976). "Site-dependent spectra for earthquake-resistant design." *Bull. Seism. Soc. Am.*, 66, 221-243.

Shoja-Taheri, J. and Anderson, J. G. (1988). "The 1978 Tabas, Iran, earthquake: an

interpretation of the strong motion records." ***Bull. Seism. Soc. Am.***, 78(1), 142-171.

Silva, W.J., and Darragh, R. (1995). "Engineering characterization of earthquake strong ground motion recorded at rock sites." Palo Alto, Calif:Electric Power Research Institute, TR-102261.

Silva, W.J. and Stark, C.L. (1993) "Source, path, and site ground motion model for the 1989 M 6.9 Loma Prieta earthquake." CDMG draft final report.

Silva, W.J. (1992). "Factors controlling strong ground motions and their associated uncertainties." *Dynamic Analysis and Design Considerations for High Level Nuclear Waste Repositories, ASCE* 132-161.

Silva, W.J. (1991). "Global characteristics and site geometry." Chapter 6 in *Proceedings: NSF/EPRI Workshop on Dynamic Soil Properties and Site Characterization.* Palo Alto, Calif.: Electric Power Research Institute, NP-7337.

Silva, W. J., R. Darragh, C. Stark, I. Wong, J. C. Stepp, J. Schneider, and S-J. Chiou (1990). "A Methodology to Estimate Design Response Spectra in the Near-Source Region of Large Earthquakes Using the Band-Limited-White-Noise Ground Motion Model". *Procee. of the Fourth U.S. Conf. on Earthquake Engineering,* Palm Springs, California. 1, 487-494.

Silva, W.J., Darragh, R.B., Green, R.K., and Turcotte, F.T. (1989). *Estimated Ground Motions for a new madrid Event.* U.S. Army Engineer Waterways Experiment Station, Wash., DC, Misc. Paper GL-89-17.

Silva, W.J., and Green, R.K. (1989). "Magnitude and distance scaling of response spectral shapes for rock sites with applications to North American tectonic environment." *Earthquake Spectra,* 5(3), 591-624.

Silva, W. J. and Turcotte, T. (1989). "Korean Seismic Signatures." Waterways Experiment Station Corps of Engineers Department of the Army. Vicksburg, Mississippi. Final Report, vol. I.

Silva, W. J. and R. K. Green (1988). "Magnitude and Distance Scaling of Response Spectral Shapes for Rock Sites with Applications to North American Environments." In *Proceedings: Workshop on Estimation of Ground Motion in the Eastern United States,* EPRI NP-5875, Electric Power Research Institute.

Silva, W. J., R. B. Darragh, R. K. Green, and F. T. Turcotte (1988). "Spectral Characteristics of Small Magnitude Earthquakes with Application to Western and Eastern North American Tectonic Environments." Report to U.S. Army Corps of Engineers Waterways Experiment Station, Vicksburg, Mississippi.

Silva, W.J. (1986). *"Soil response to earthquake ground motion."* Report prepared for Electric Power Research Institute, EPRI Research Project RP 2556-07.

Silva, W.J. and Lee, K. (1987). *"WES RASCAL code for synthesizing earthquake ground motions."* State-of-the-Art for Assessing Earthquake Hazards in the United States, Report 24, U.S. Army Engineers Waterways Experiment Station, Miscellaneous Paper S-73-1.

Somerville, P.G., Graves, R. and Saikia, C. (1995). "TECHNICAL REPORT: Characterization of ground motions during the Northridge earthquake of January 17, 1994." *Structural Engineers Association of California (SEAOC).* Report No. SAC-95-03.

Somerville, P.G., McLaren, J. P., Saikia, C. K., and Helmberger, D.V. (1990). "The 25 November 1988 Saguenay, Quebec, Earthquake: Source Parameters and the Attenuation of Strong Ground Motion." *Bull. Seism. Soc. Am.*, 80(5), 1118-1143.

Toro, G. R. and R. K. McGuire (1987). "An Investigation into Earthquake Ground Motion Characteristics in Eastern North America." *Bull. Seism. Soc. Am.*, 77(2), 468-489.

Toro, G. R. (1985). "Stochastic Model Estimates of Strong Ground Motion." In *Seismic Hazard Methodology for Nuclear Facilities in the Eastern United States*, Appendix B, R. K. McGuire, ed., Electric Power Research Institute, Project P101-29.

USGS (1996). Ground Motion Modeling. Yucca Mountain Report.

Turner, E. and Stokoe II, K.H. (1982). "Static and dynamic properties of clayey soils subjected to 1979 Imperial Valley Earthquake." Geotech. Engin. Dept., The University of Texas at Austin, Austin, Texas. Geotechnical Engineering Report GR82-26.

Youngs, R.R., N. Abrahamson, F.I. Makdisi and K. Sadigh (1995). "Magnitude-dependent variance of peak ground acceleration." *Bull. Seism. Soc. Am.*, 85(4), 1161-1176.

Wald, D.J. (1996). "Slip history of the 1995 Kobe, Japan, earthquake determined from strong motion, teleseismic, and geodetic data.". *J. of Physics of the Earth,* in press.

Wald, D.J., Heaton, T.H. (1994a). "A dislocation model of the 1994 Northridge, California, earthquake determined from strong ground motions." *U.S. Geological Survey,* Open-File Rpt. 94-278.

Wald, D.J., Heaton, T.H. (1994b). "Spatial and temporal distribution of slip for the 1992 Landers, California, earthquake." *Bull. Seism. Soc. Amer.*, 84(3), 668-691.

Wald, D.J., T.H. Heaton (1993). "Spatial and Temporal Distribution of Slip for the 1992 Landers, California Earthquake." *Bull. Seism. Soc. Amer.*

Wald, D.J., D.V. Helmberger, and T.R. Heaton (1991). "Rupture model of the 1989 Loma Prieta Earthquake from the inversion of strong motion and broadband teleseismic data." *Bull. Seism. Soc. Amer.*, 81(5), 1540-1572.

Wald, D.J., D.V. Helmberger and S.H. Hartzell (1990). "Rupture process of the 1987 Superstition Hills earthquake from the inversion of strong-motion data." *Bull. Seism. Soc. Amer.*, 80(5), 1079-1098.

Wells, D.L., Coppersmith, K.J. (1994). "New empirical relationships among magnitude, rupture length, rupture width, rupture area, and surface displacement." *Bull. Seism. Soc. Am.* 84(4), 974-1002.

Wesnousky, S. G. (1986). "Earthquakes, quaternary faults, and seismic hazard in California." *J. Geophys. Research,* 91(B12), 12,587-12,631.

Vucetic, M.; Dobry, R. (1991). "Effects of Soil Plasticity on Cyclic Response," Journal of Geotechnical Engineering, ASCE, 117(1), 89-107.

Chapter 2 Figure Captions

Figure 2.1. Stochastic Finite-Fault Ground Motion Model.

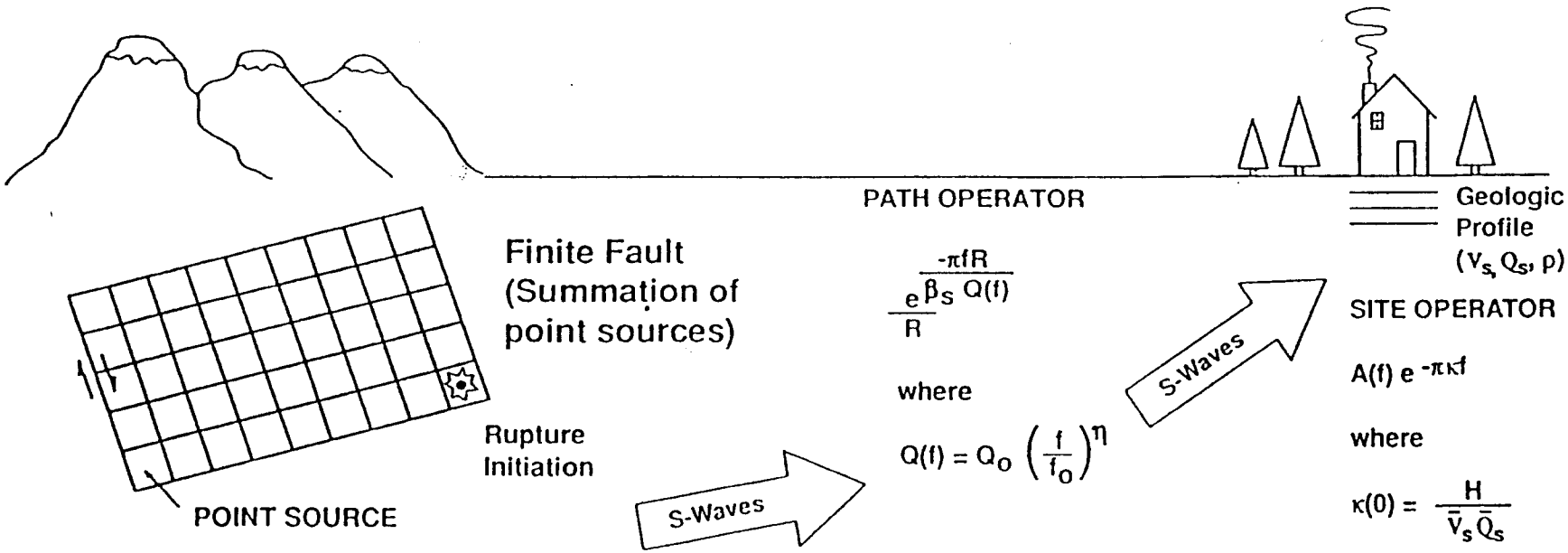
PATH OPERATOR
Geologic Profile
(V_s, Q_s, ρ)
Finite Fault (Summation of point sources)
$\frac{e^{\frac{-\pi f R}{\beta_S Q(f)}}}{R}$
where
$Q(f) = Q_o \left(\frac{f}{f_o}\right)^{\eta}$
S-Waves
SITE OPERATOR
$A(f)\, e^{-\pi \kappa f}$
where
$\kappa(0) = \frac{H}{\bar{V}_s \bar{Q}_s}$
Rupture Initiation
POINT SOURCE
$\frac{M_o f^2}{1+(f/f_c)^2}$
where
$f_c = \beta_S \left(\frac{\Delta\sigma}{8.44\, M_o}\right)^{\frac{1}{3}}$
S-Waves

Figure 2.1

Chapter 3 Figure Captions

Figure 3.1a. Median and $\pm$ 1 σ shear-wave velocity profiles for Geomatrix site categories A and B (Table 3.1).

Figure 3.1b. Median and $\pm$ 1 σ shear-wave velocity profiles for Geomatrix site categories C and D (Table 3.1).

Figure 3.2. Median and $\pm$ 1 σ shear-wave velocity profiles for soft rock (Geomatrix A and B) (solid lines) and smooth base case soft rock profile (dashed line).

Figure 3.3. Median shear-wave velocity profiles for USGS site classes A, B, and C (Table 3.1).

Figure 3.4. Median and $\pm$ 1 σ shear-wave velocity profiles for deep soil (Geomatrix C and D) (solid lines) and smooth base case deep soil profile (dashed line).

Figure 3.5. Median and $\pm$ 1 σ 5% damped pseudo absolute acceleration response spectra computed from 30 randomly generated deep soil profiles using the correlation model of Appendix C and with depth varying from 100 to 1,000 ft (solid line). The dashed line is the response spectrum computed using the base case deep soil profile (Figure 3.4).

Figure 3.6. Median and $\pm$ 1 σ shear-wave velocity profiles computed from 30 random profiles (solid lines) along with base case deep soil input profile.

Figure 3.7. Median and $\pm$ 1 σ 5% damped pseudo absolute acceleration response spectra computed from 30 randomly generated soft rock profiles using correlation model of Appendix C (solid lines). The dashed line is the response spectrum computed using the base case soft rock profile (Figure 3.2).

Figure 3.8. Median and $\pm$ 1 σ shear-wave velocity profiles for soft rock (Geomatrix A and B) (solid lines) and smooth base case soft rock profile (dashed lines).

Figure 3.9. Median and $\pm$ 1 σ crustal shear-wave velocity profiles computed from the crustal models listed in Table 3.2a (solid lines). Smooth base case model with soft rock shallow profile (Figure 3.2) on top (dashed lines). Top 1 km.

Figure 3.10. Median and $\pm$ 1 σ crustal shear-wave velocity profiles computed from the crustal models listed in Table 3.2a (solid lines). Smooth base case model (dashed lines). Top 10 km.

Figure 3.11. Median and $\pm$ 1 σ crustal shear-wave velocity profiles computed from the crustal models listed in Table 3.2a (solid lines). Smooth base case model (dashed lines). Top 40 km.

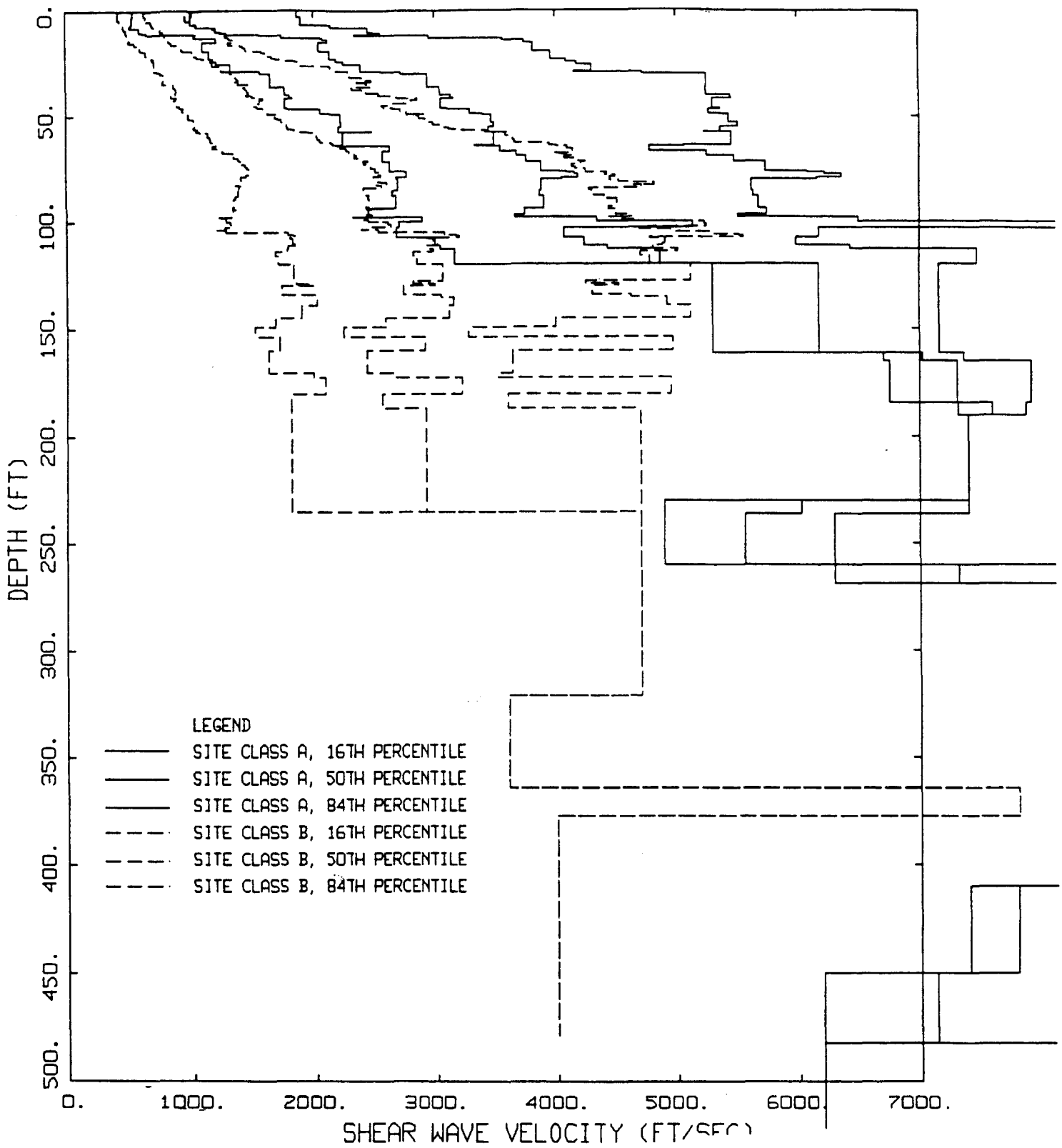

Figure 3.1a

GEOMATRIX SITE CLASSES
VELOCITY AVERAGE

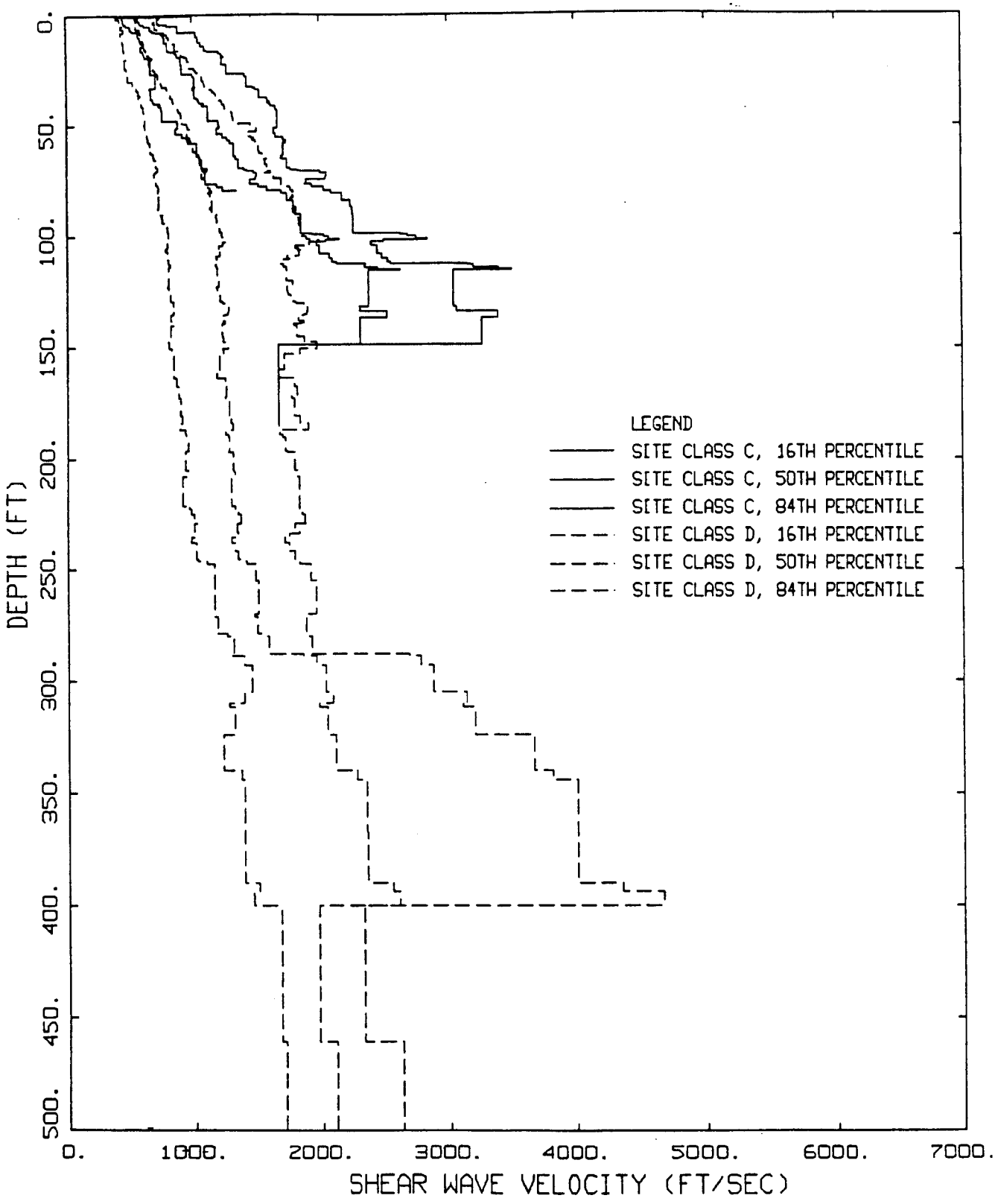

Figure 3.1b

GEOMATRIX SITE CLASSES
VELOCITY AVERAGE

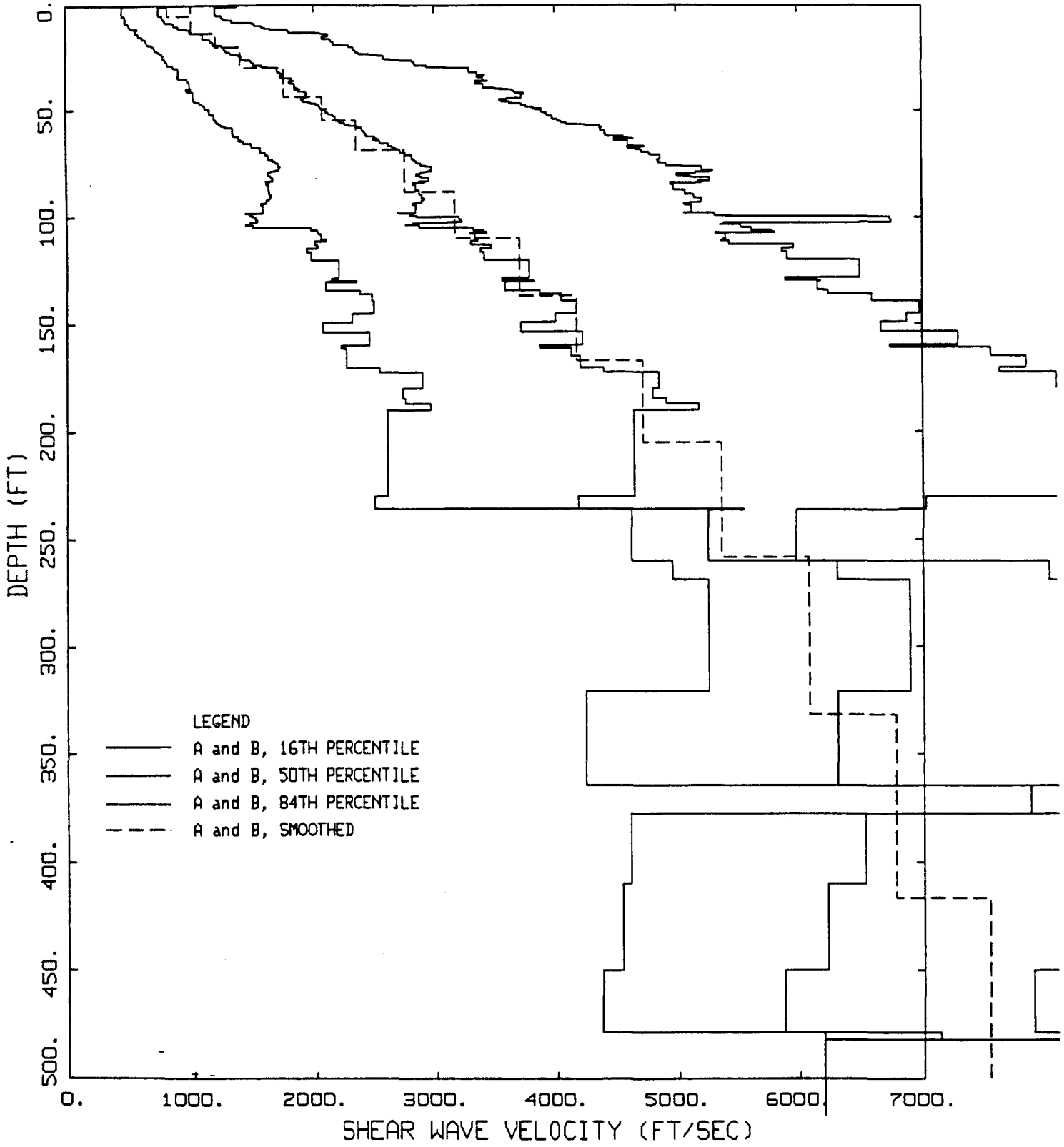

Figure 3.2

GEOMATRIX CLASS A & B

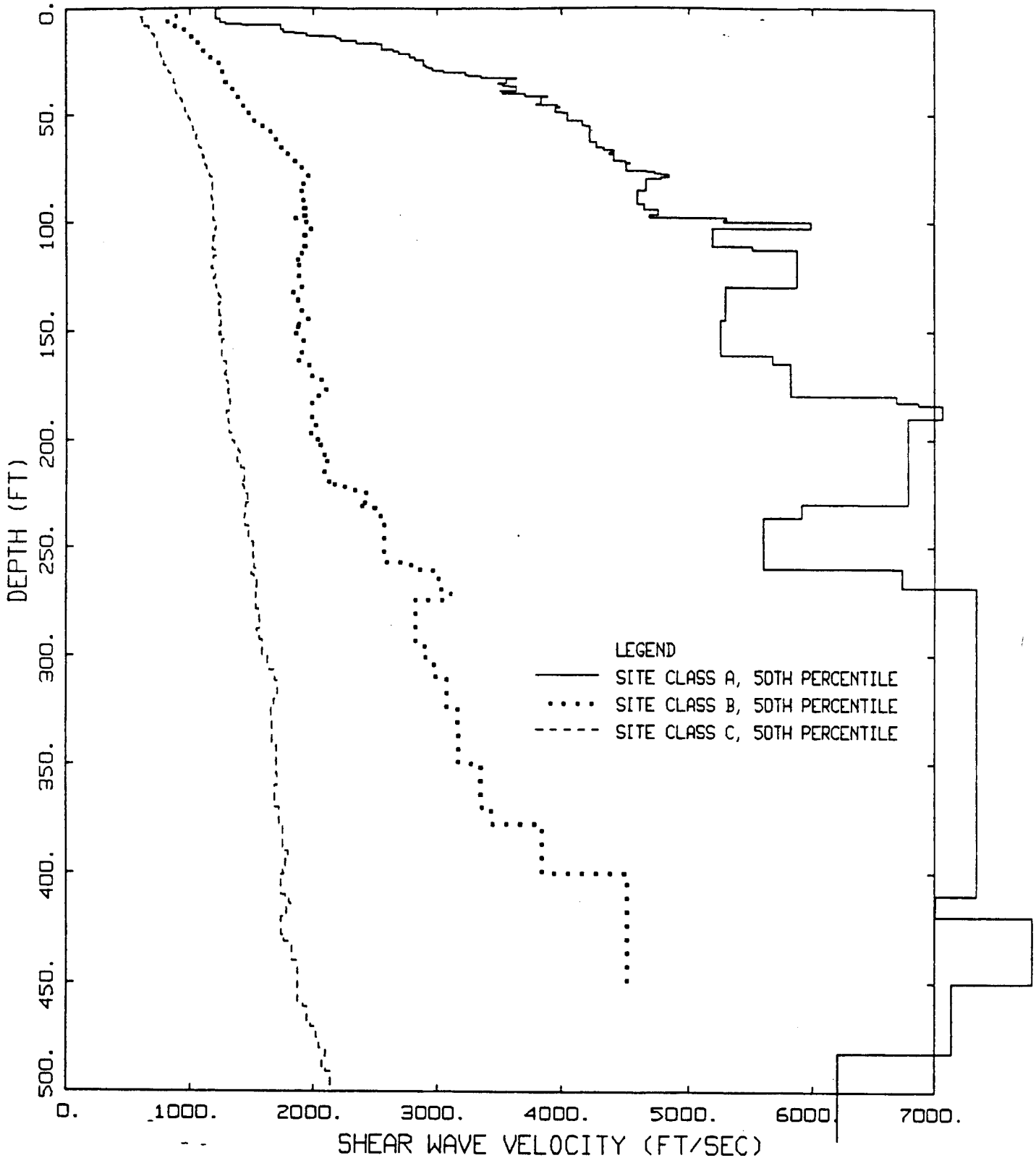

USGS SITE CLASSES
VELOCITY AVERAGE

Figure 3.3

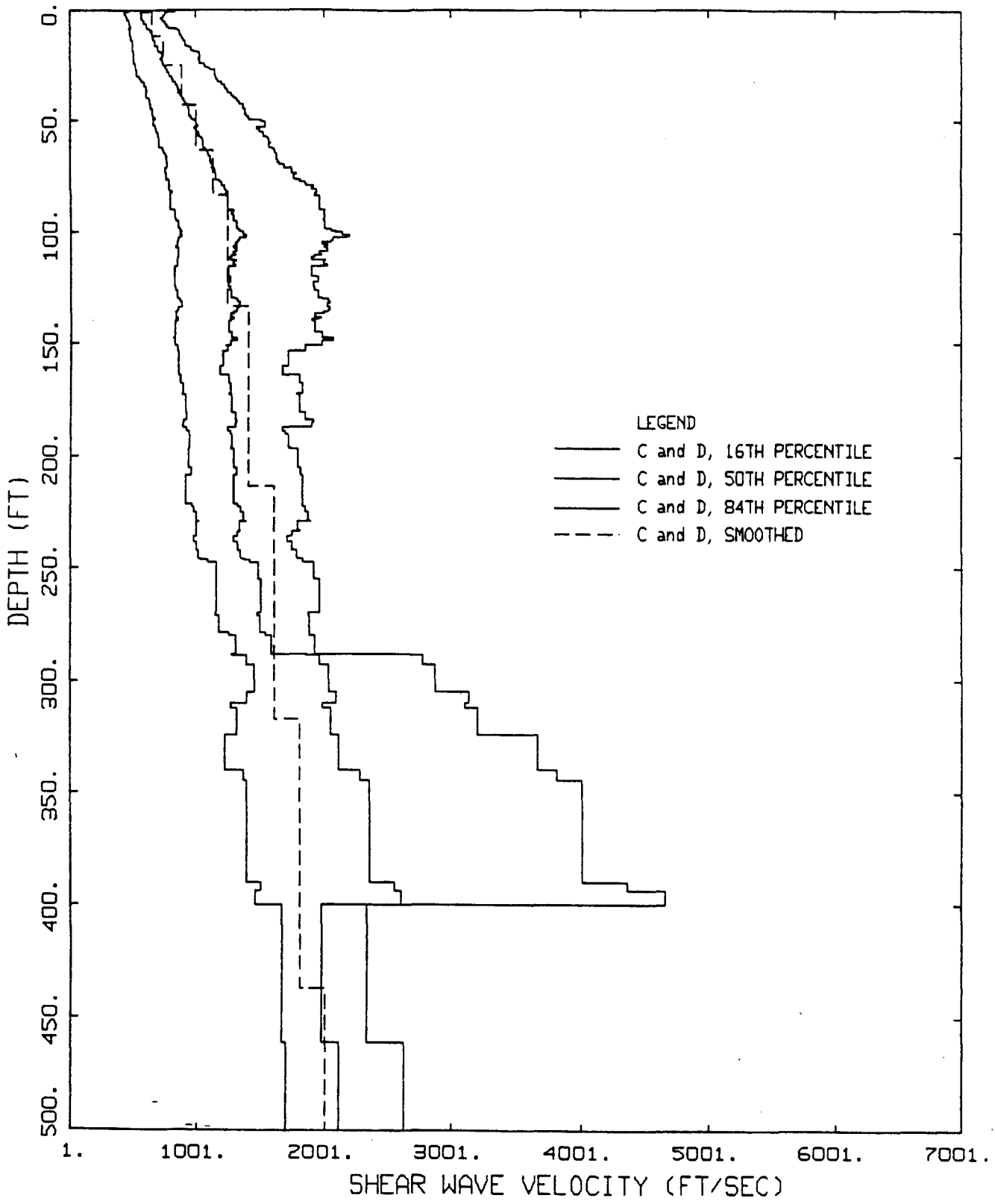

Figure 3.4

GEOMATRIX SITE CLASS C & D

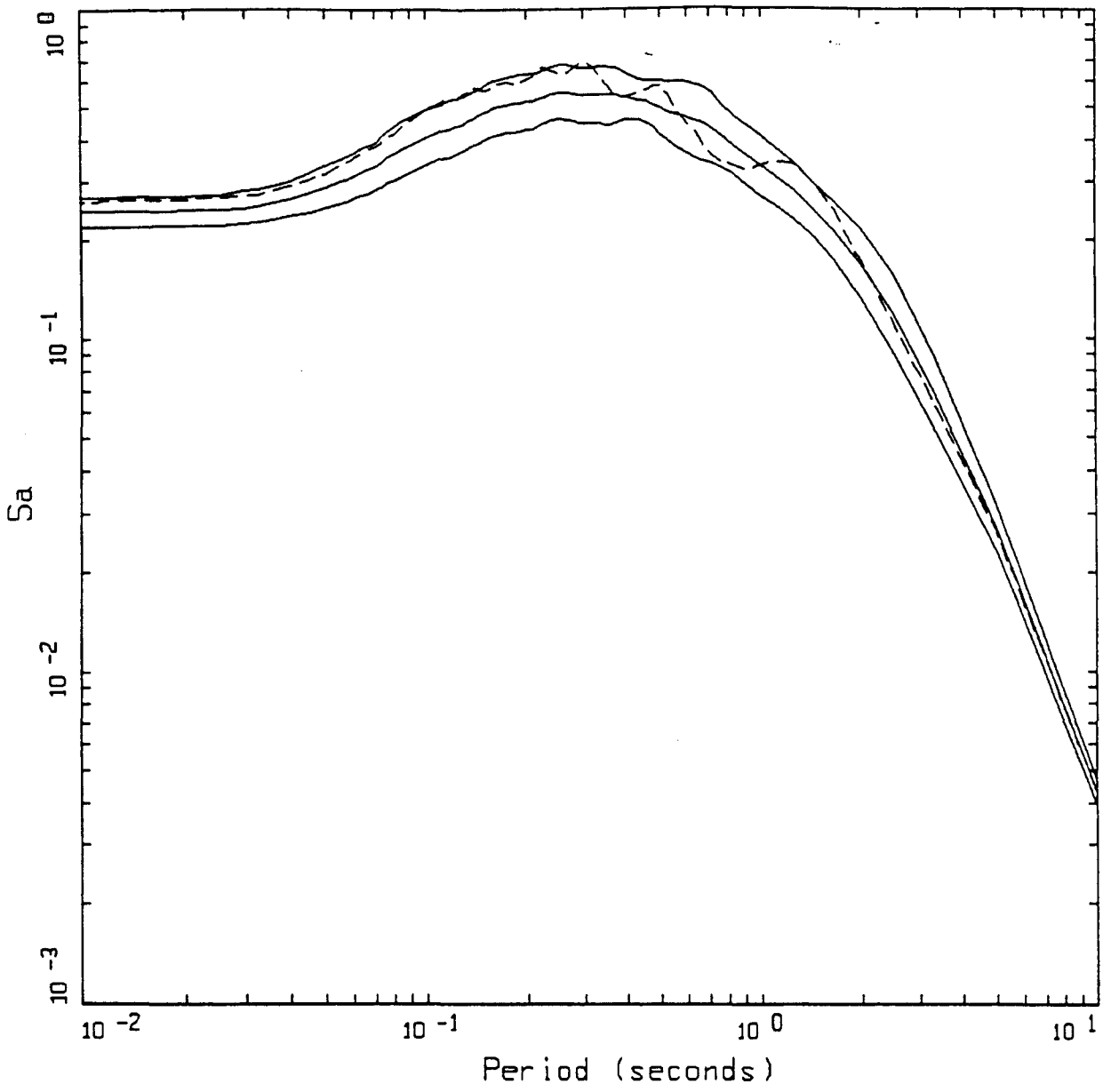

AVERAGE HORIZONTAL SOIL SPECTRA
M=6.5, D=15 KM, STRESS DROP = 59 BARS

LEGEND
84TH PERCENTILE
50TH PERCENTILE
16TH PERCENTILE
BASE CASE

Figure 3.5

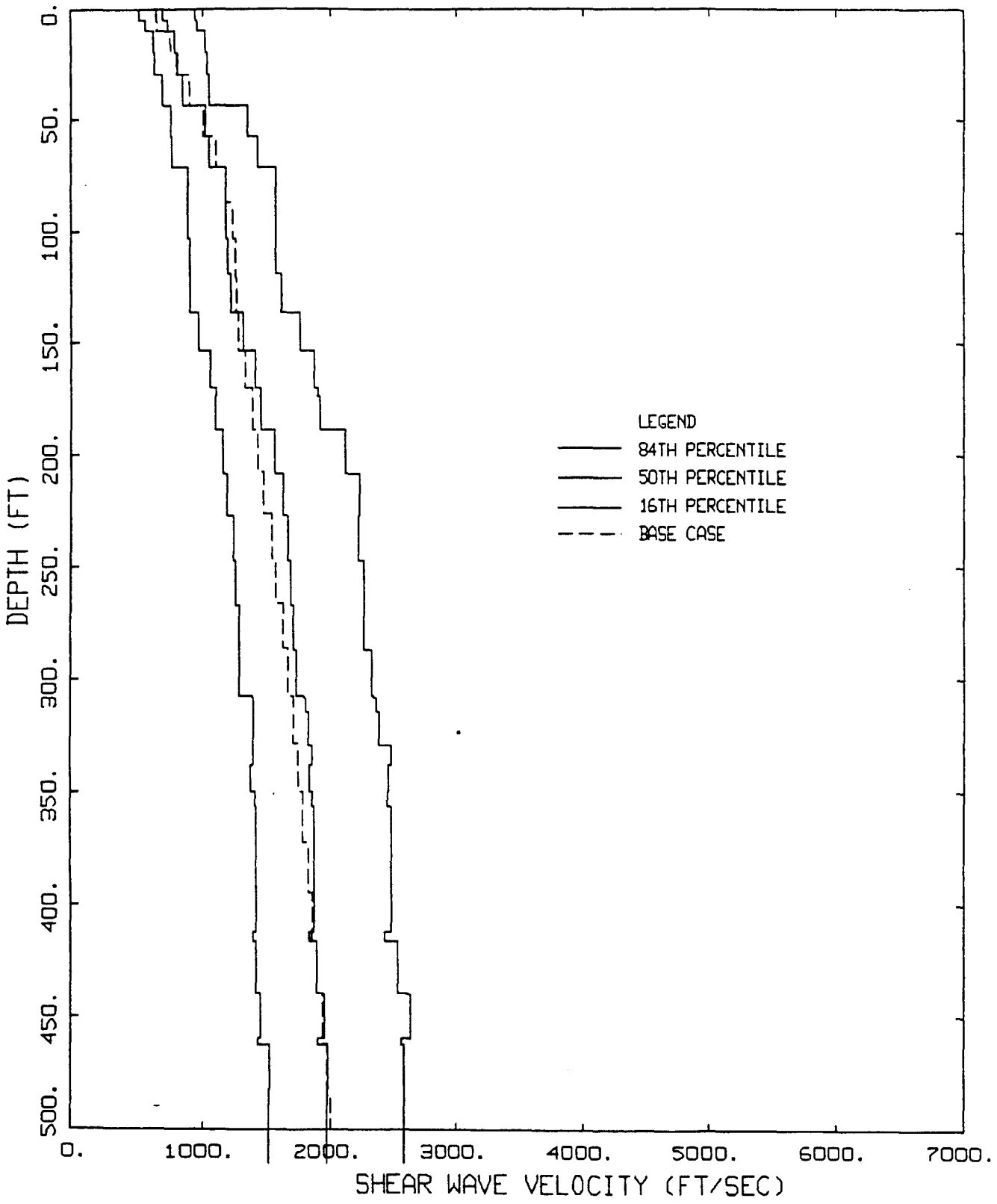

Figure 3.6

BROOKHAVEN CRUSTAL PROFILES
VELOCITY AVERAGE, SOIL

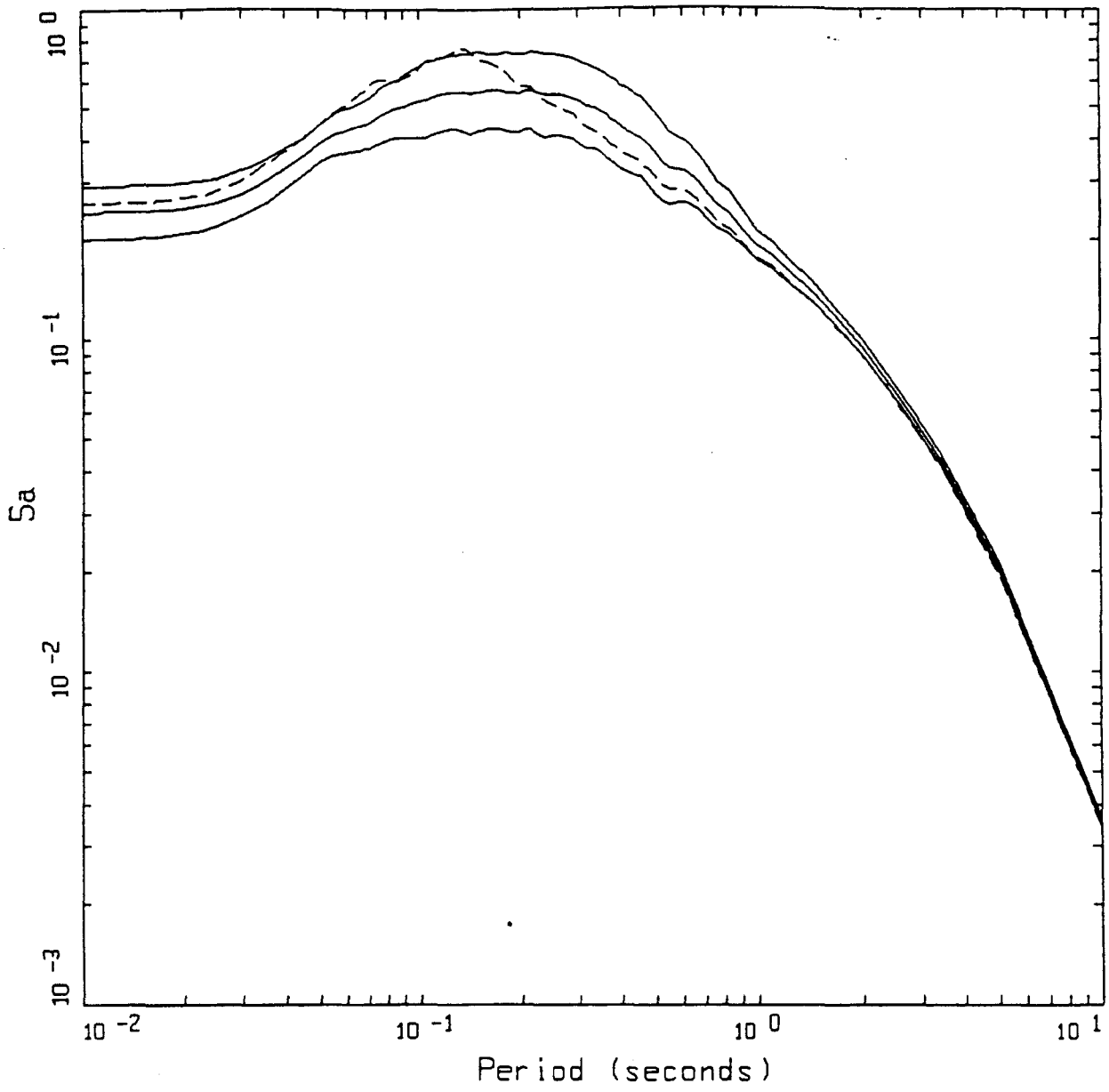

AVERAGE HORIZONTAL SPECTRA, ROCK
M=6.5, D=15 KM, STRESS DROP = 59 BARS

LEGEND
84TH PERCENTILE
50TH PERCENTILE
16TH PERCENTILE
BASE CASE

Figure 3.7

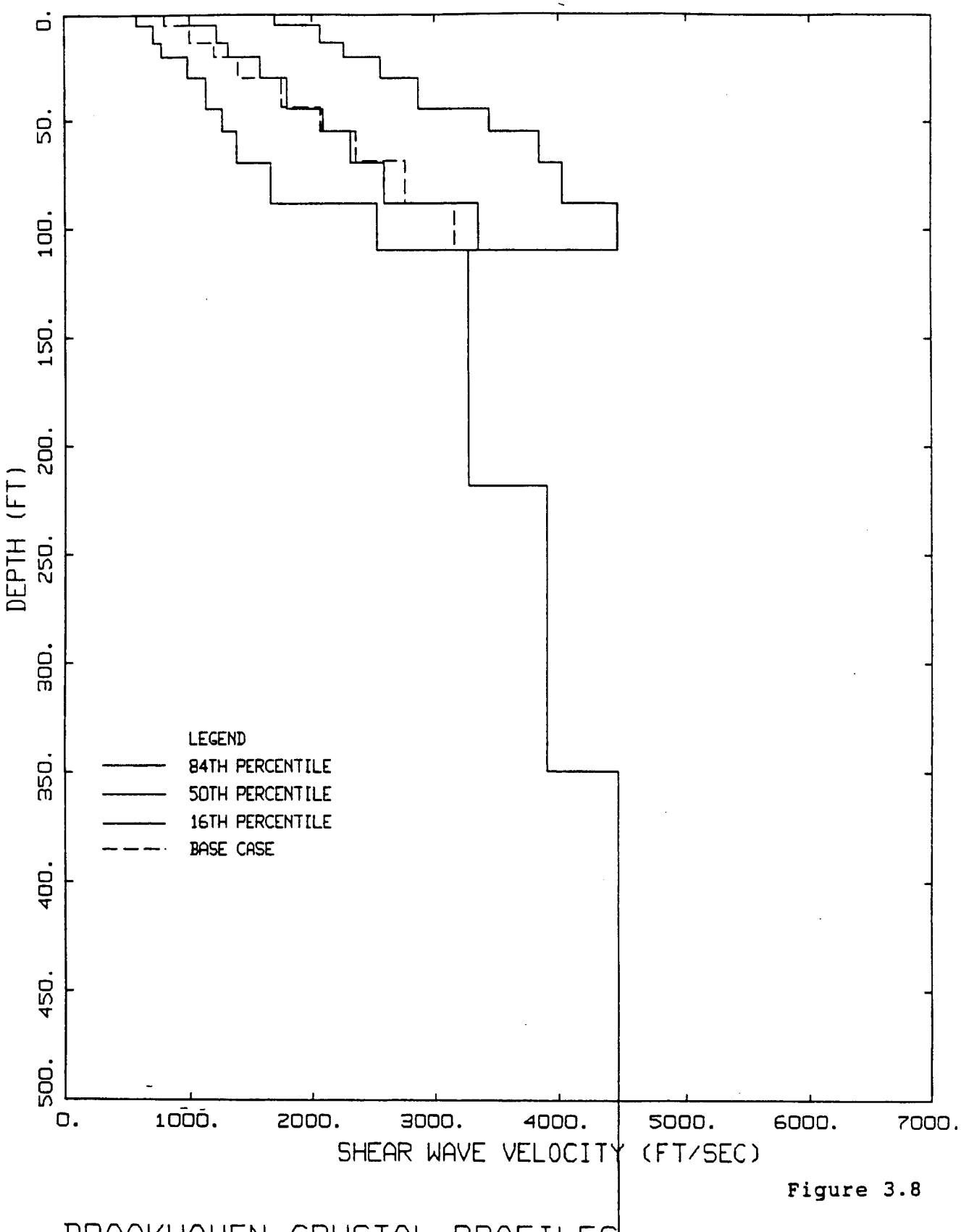

Figure 3.8

BROOKHAVEN CRUSTAL PROFILES
VELOCITY AVERAGE, ROCK

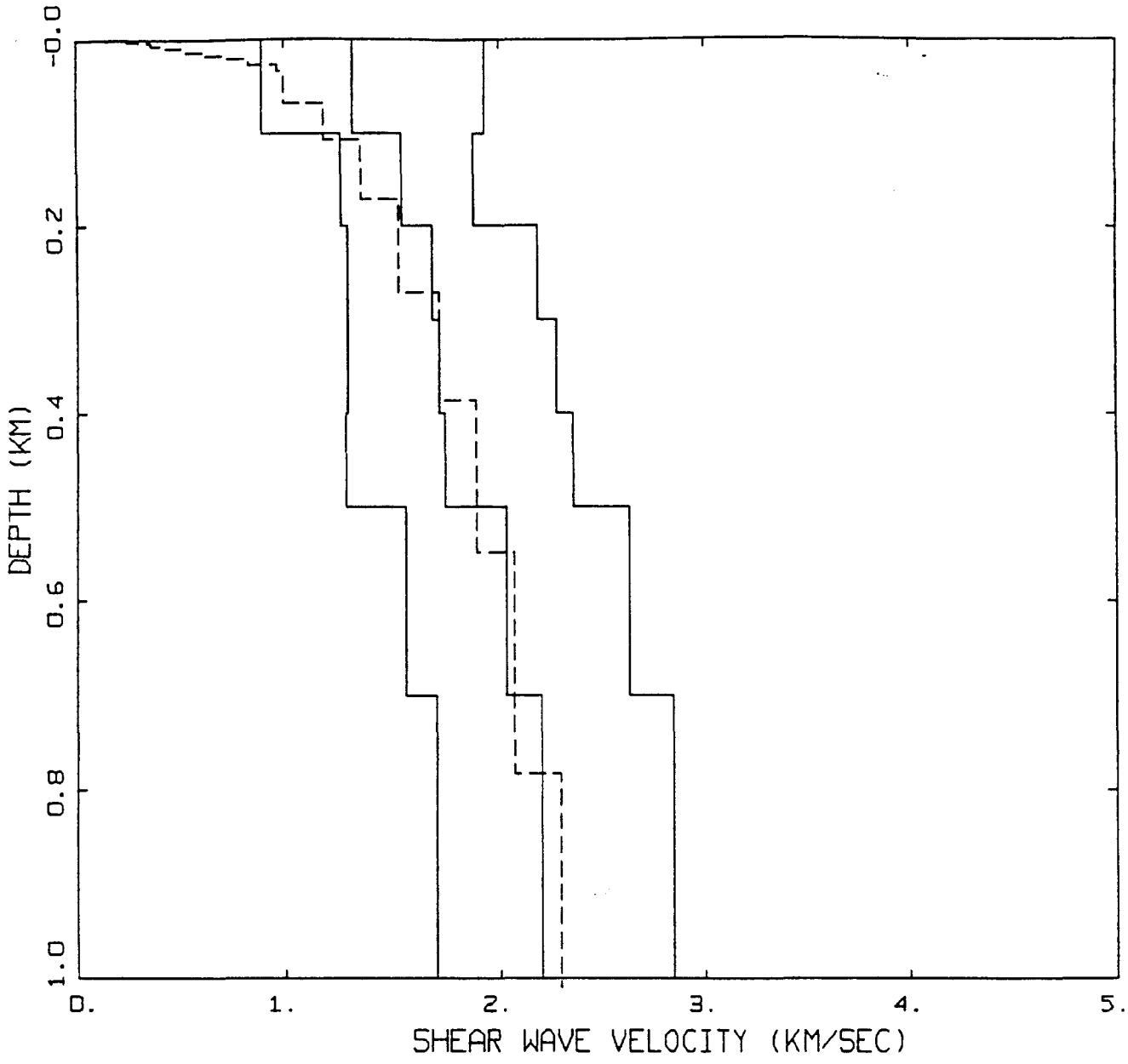

GENERIC CALIFORNIA CRUST
VELOCITY AVERAGE

LEGEND
84TH PERCENTILE
50TH PERCENTILE
16TH PERCENTILE
MODEL

Figure 3.9

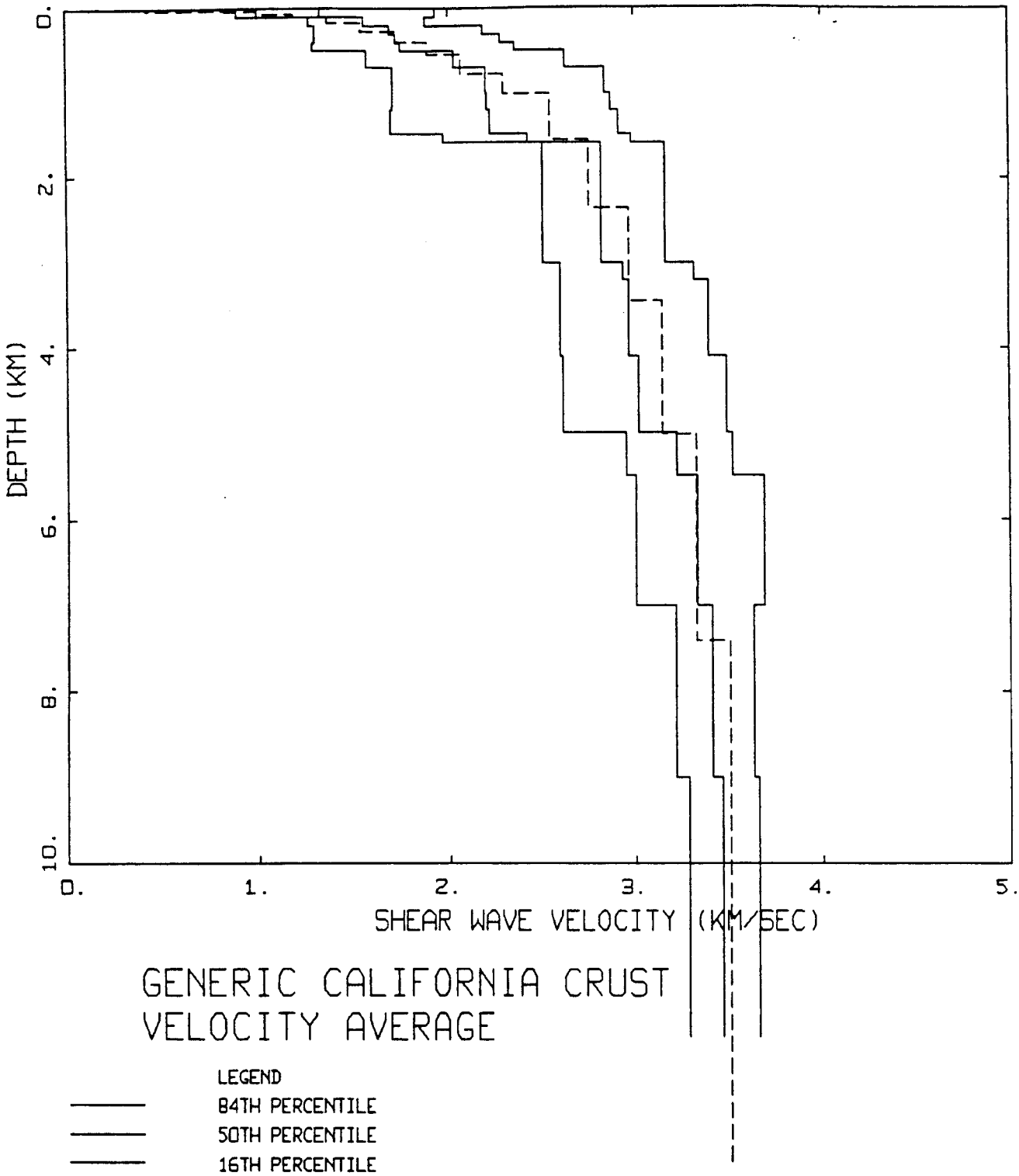
DEPTH (KM)
0.
2.
4.
6.
8.
10.
0.
1.
2.
3.
4.
5.
SHEAR WAVE VELOCITY (KM/SEC)
GENERIC CALIFORNIA CRUST
VELOCITY AVERAGE
LEGEND
84TH PERCENTILE
50TH PERCENTILE
16TH PERCENTILE
MODEL

Figure 3.10

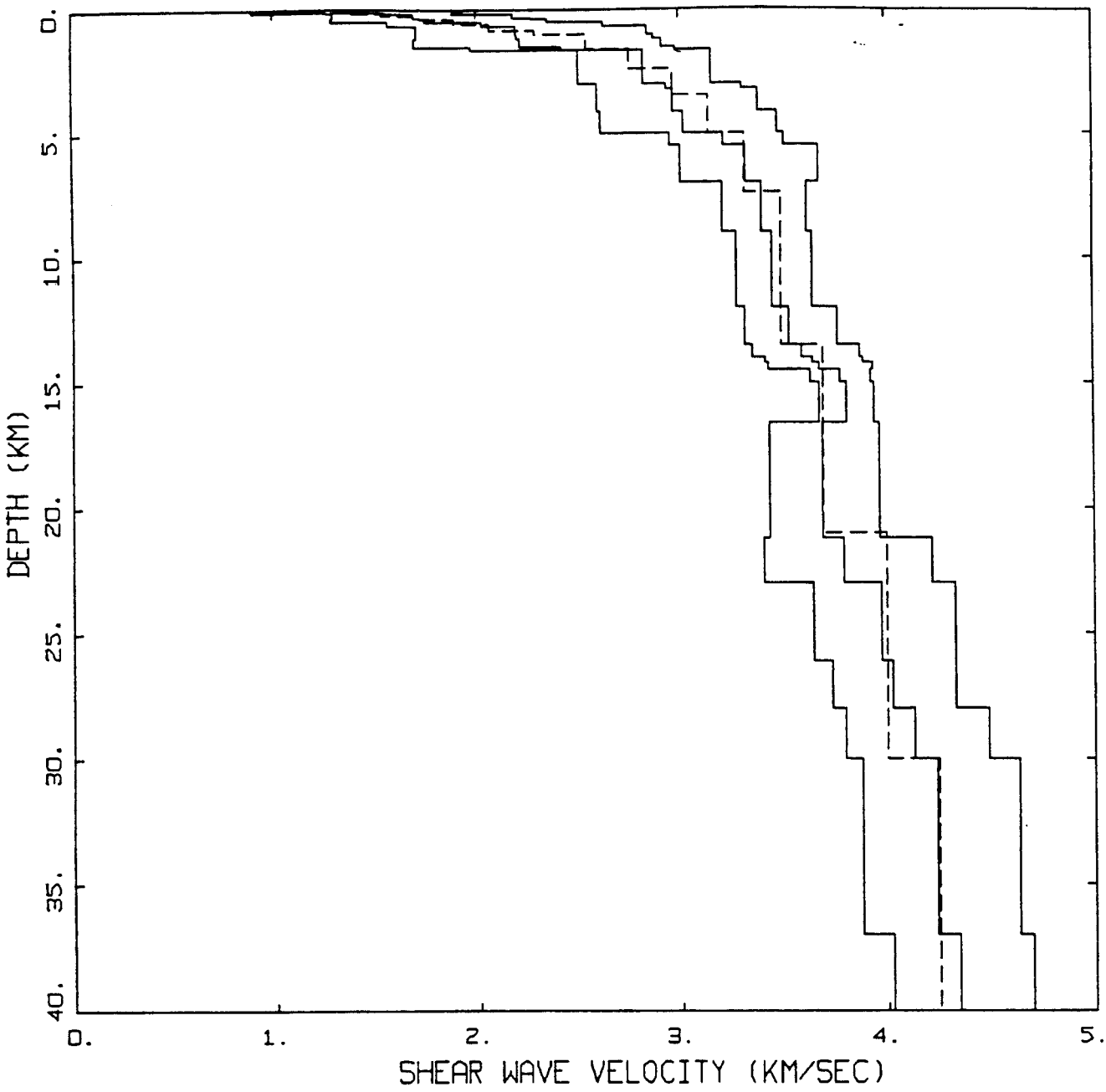

GENERIC CALIFORNIA CRUST
VELOCITY AVERAGE

LEGEND
84TH PERCENTILE
50TH PERCENTILE
16TH PERCENTILE
MODEL

Figure 3.11

Chapter 4 Figure Captions

Figure 4.1. Geographic provinces of California (Wesnousky, 1986).

Figure Set 4.2. Comparison of Fourier amplitude spectra for the Peninsular Range earthquakes (Northridge, Whittier Narrows, and San Fernando). Solid lines: recorded motion horizontal components vector sum divided by $\sqrt{2}$ (2 Hz wide triangular smoothing window). Dashed lines: initial model calculations. Dash-dotted lines: final model calculations.

Figure Set 4.3. Comparison of Fourier amplitude spectra for the North Coast earthquakes (Loma Prieta, Coyote Lake and Morgan Hill). Solid lines: recorded motion horizontal components vector sum divided by $\sqrt{2}$ (2 Hz wide triangular smoothing window). Dashed lines: initial model calculations. Dash-dotted lines: final model calculations.

Figure Set 4.4. Comparison of Fourier amplitude spectra for the Mojave earthquakes (Landers and North Palm Springs). Solid lines: recorded motion horizontal components vector sum divided by $\sqrt{2}$ (2 Hz wide triangular smoothing window). Dashed lines: initial model calculations. Dash-dotted lines: final model calculations.


MODOC
PLATEAU
NORTH
COAST
SIERRA
NEVADA
GREAT
VALLEY
GREAT
BASIN
CENTRAL
COAST
MOJAVE
DESERT
TRANSVERSE
RANGE
PENINSULAR
RANGE
SALTON
TROUGH

Figure 4.1

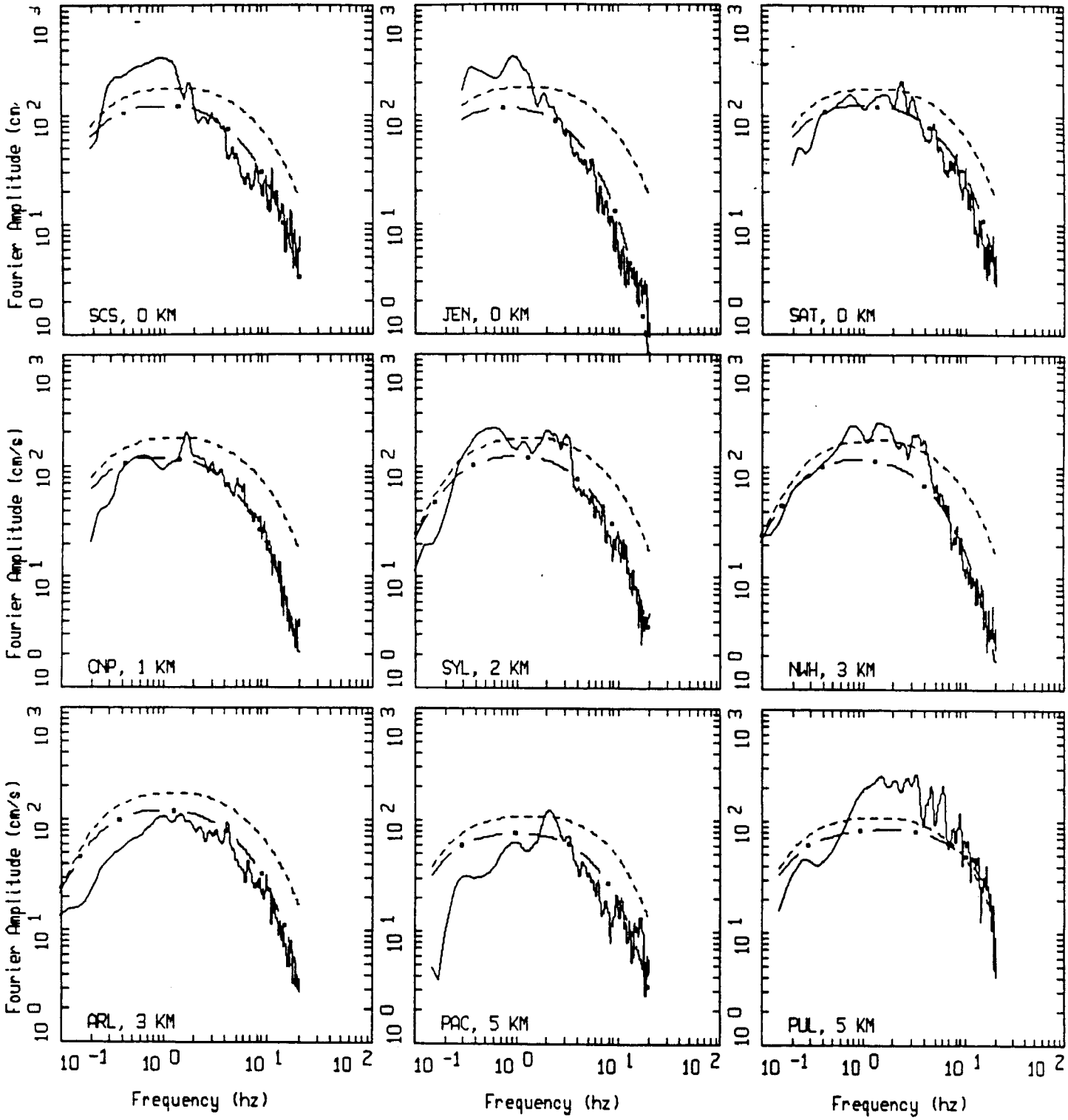

NORTHRIDGE-EARTHQUAKE, M=6.7, PAGE 1 OF 11.

Figure Set 4.2

LEGEND

DATA

INITIAL MODEL

FINAL MODEL

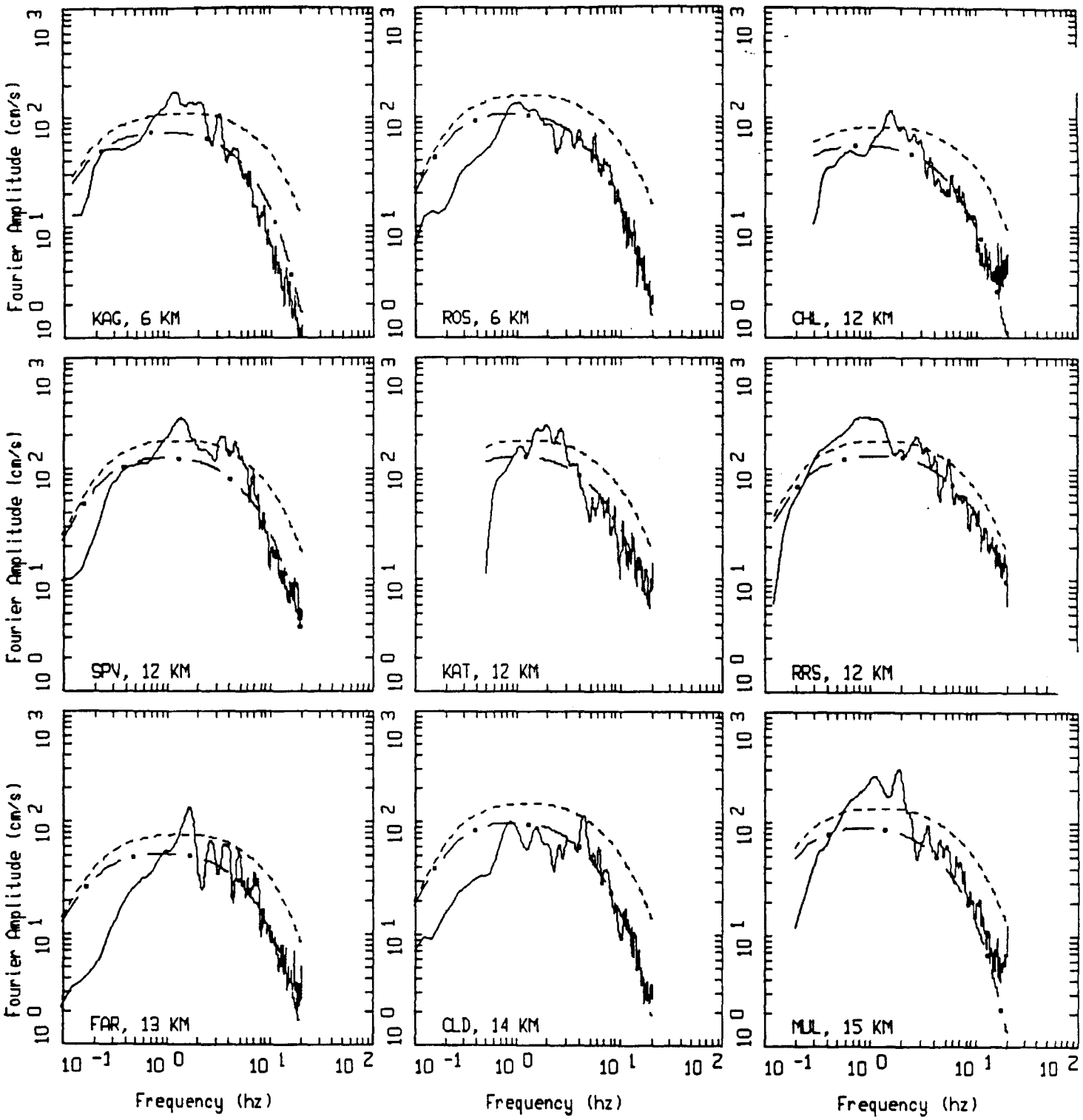

NORTHRIDGE EARTHQUAKE, M=6.7, PAGE 2 OF 11.

LEGEND

——— DATA

- - - - - INITIAL MODEL

—•— FINAL MODEL

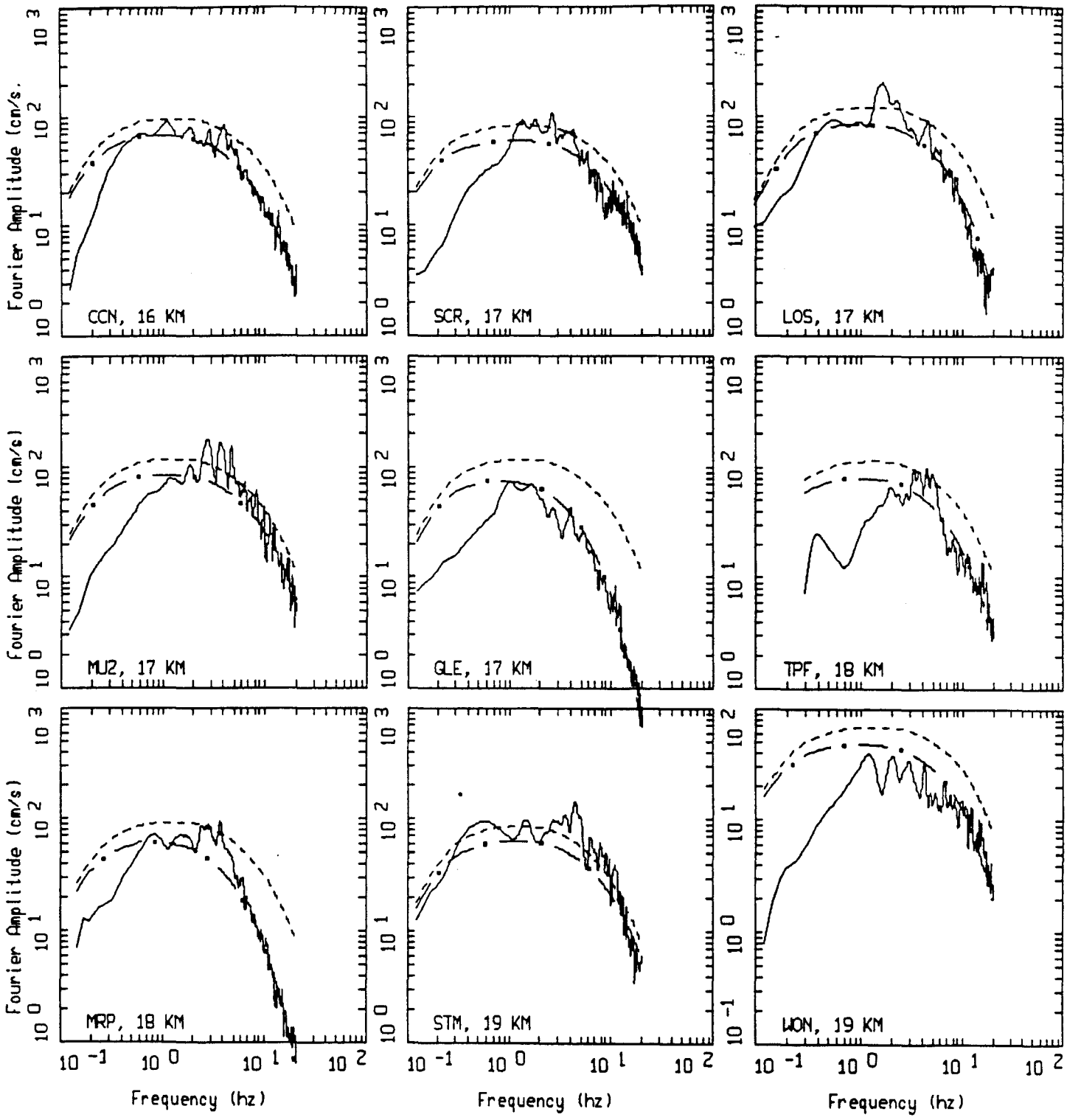

LEGEND

——— DATA

- - - - - INITIAL MODEL

—•— FINAL MODEL

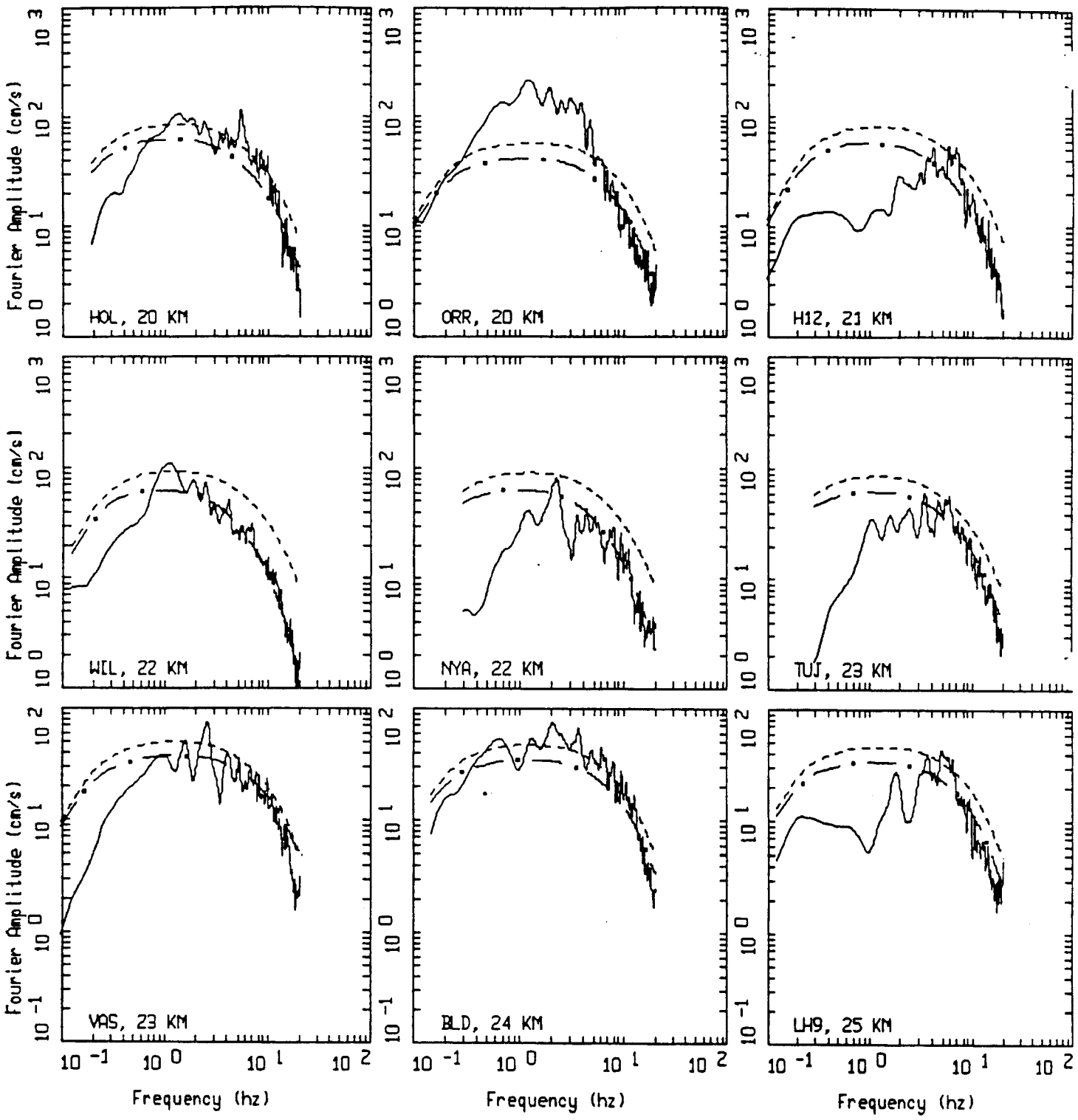

NORTHRIDGE EARTHQUAKE, M=6.7, PAGE 4 OF 11.

LEGEND

——— DATA

- - - - - INITIAL MODEL

—•— FINAL MODEL

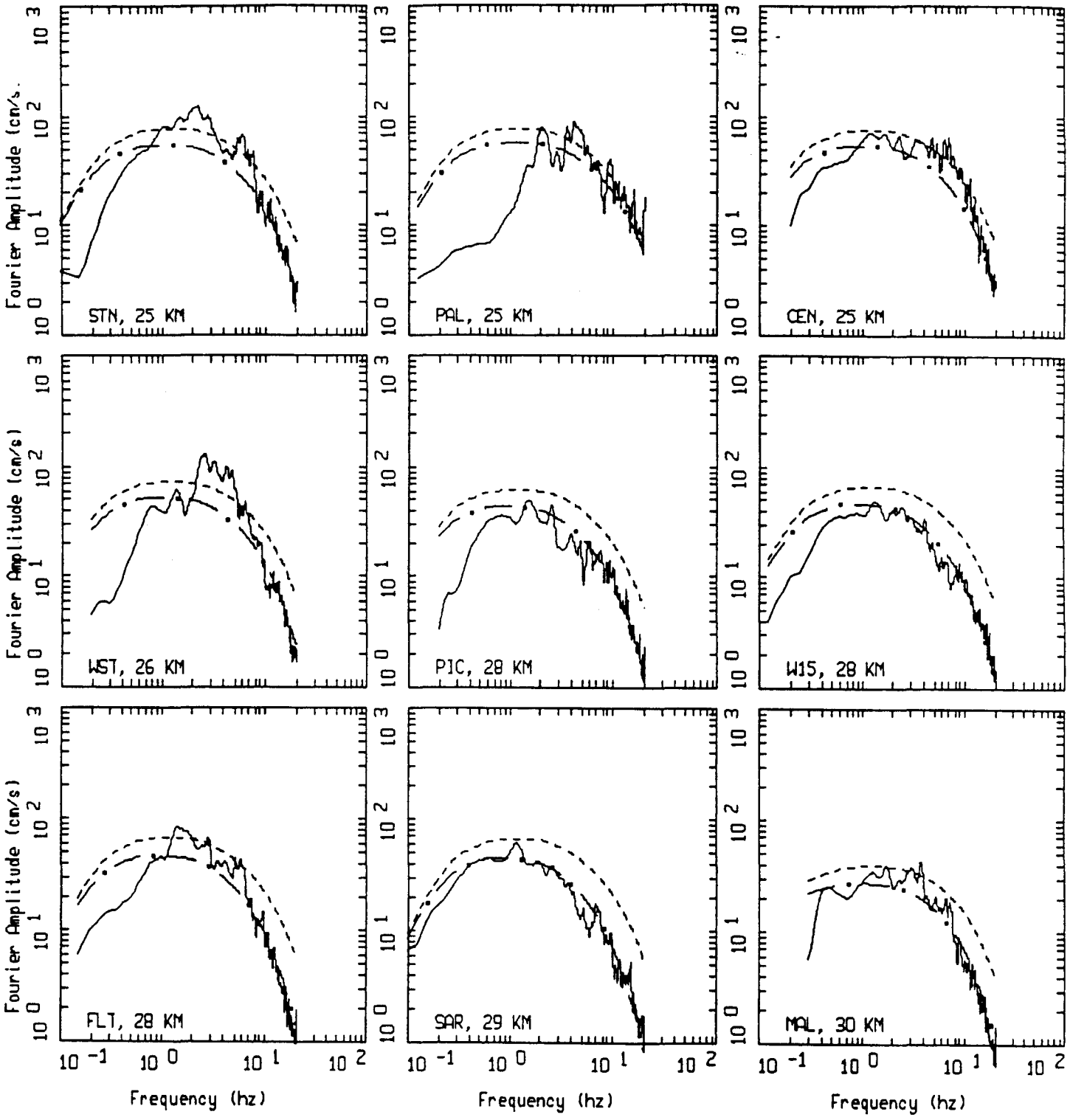

LEGEND

——— DATA

- - - - - INITIAL MODEL

— • — FINAL MODEL

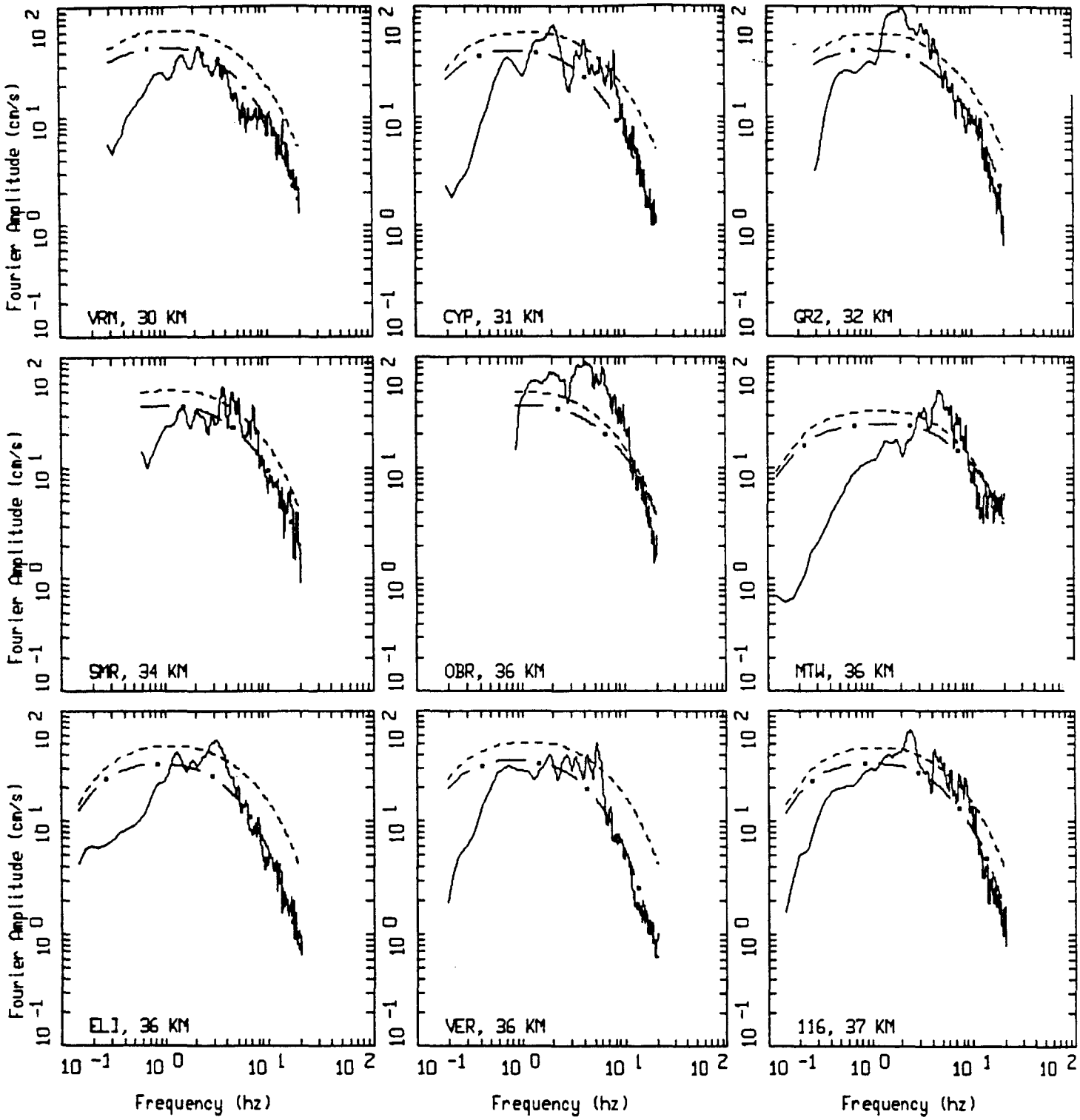

LEGEND

——— DATA

- - - - - INITIAL MODEL

—•— FINAL MODEL

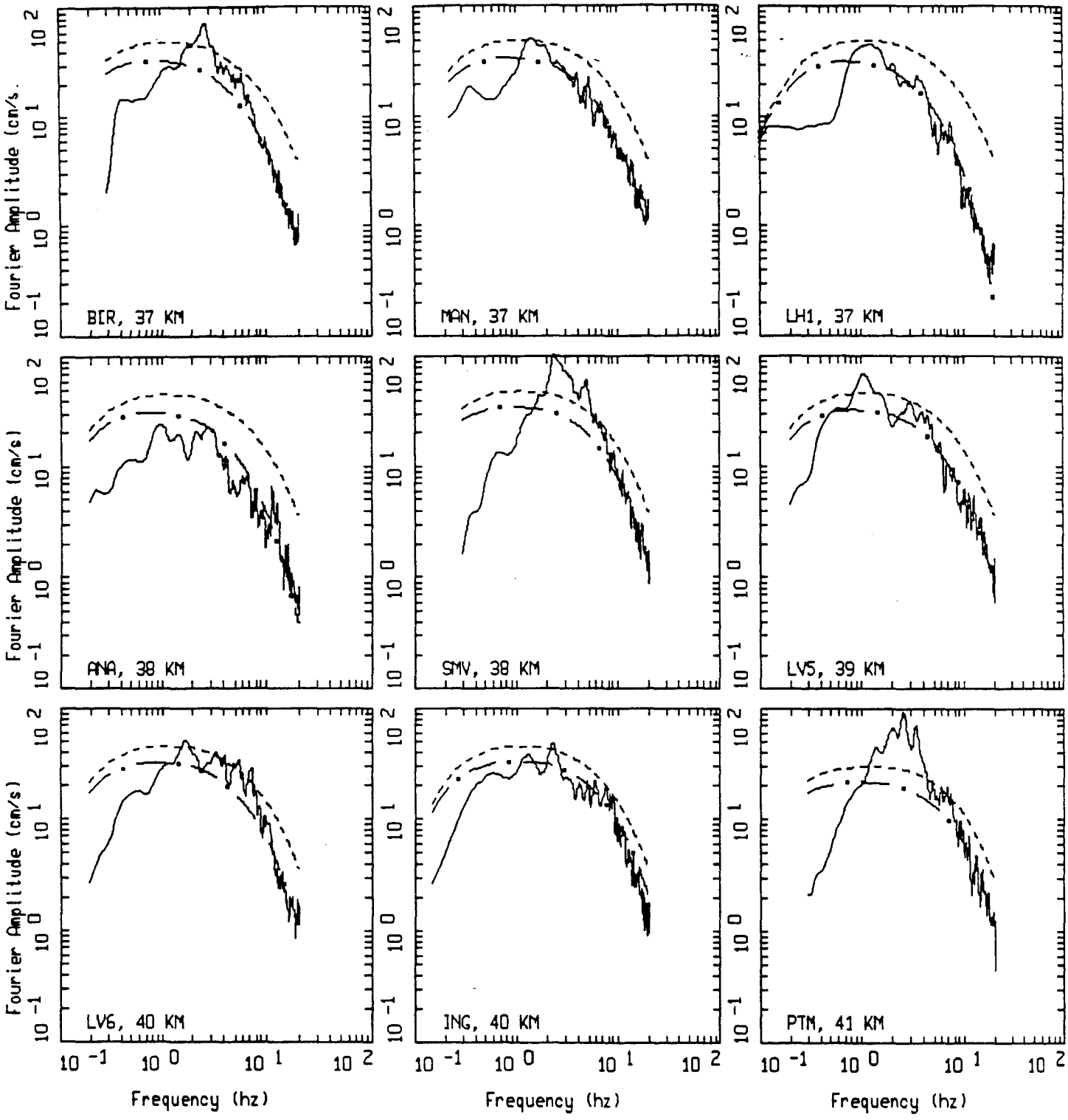

NORTHRIDGE EARTHQUAKE, M=6.7, PAGE 7 OF 11.

LEGEND

——— DATA

- - - - - INITIAL MODEL

— • — FINAL MODEL

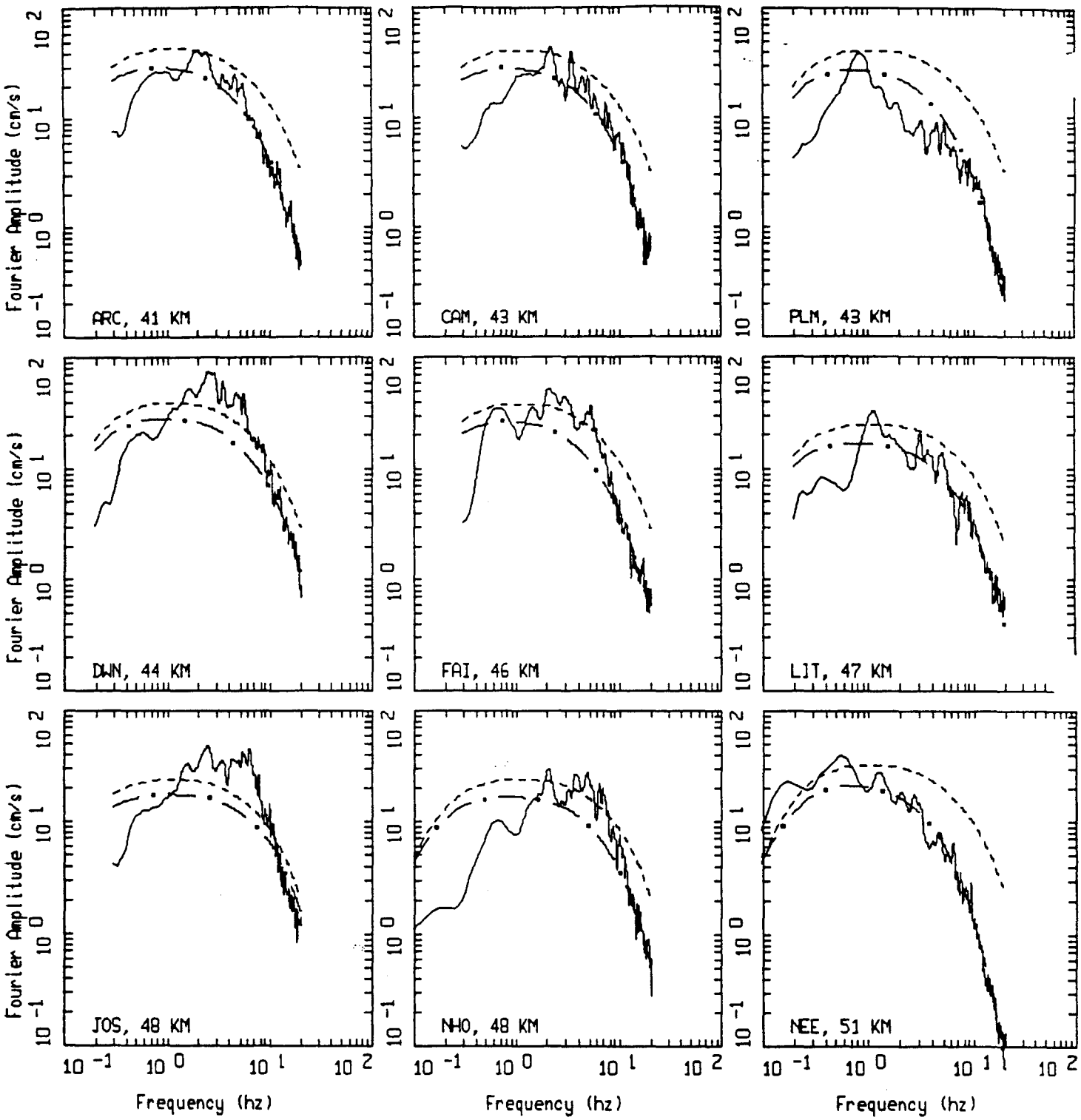

NORTHRIDGE EARTHQUAKE, M=6.7, PAGE 8 OF 11.

LEGEND

——— DATA

- - - - - INITIAL MODEL

—•— FINAL MODEL

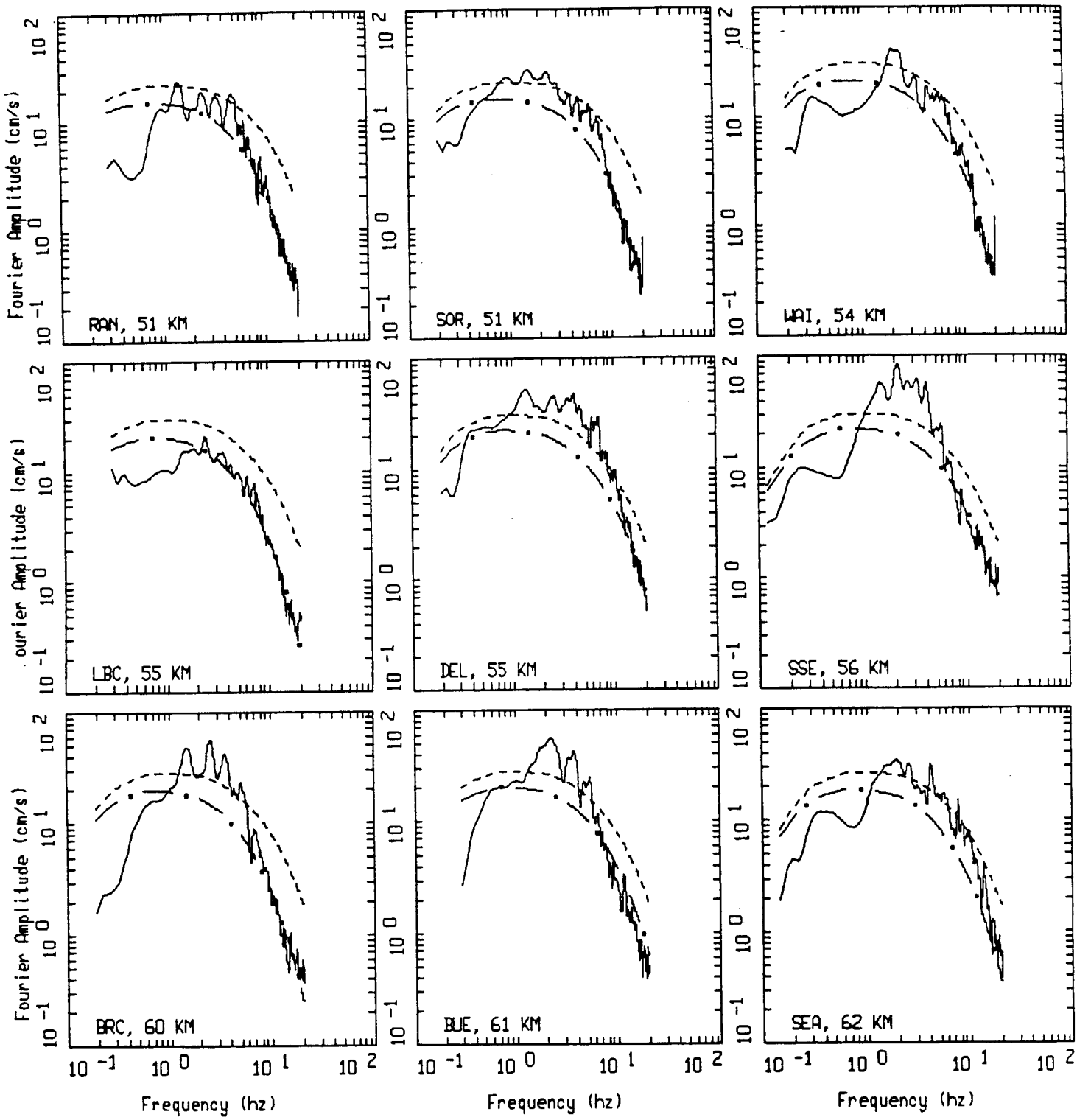

LEGEND

——— DATA

- - - - - INITIAL MODEL

—•— FINAL MODEL

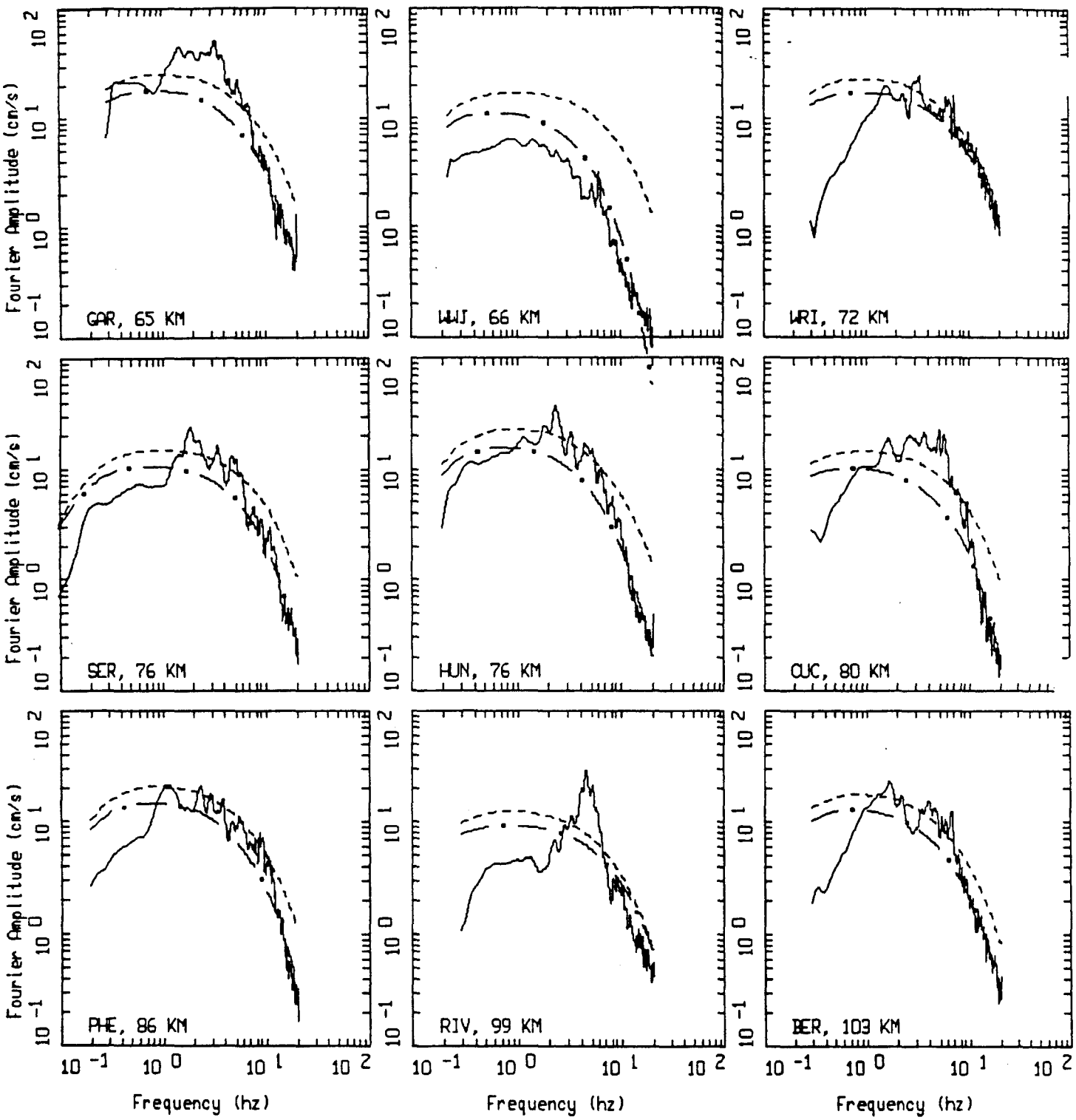

LEGEND

——— DATA

- - - - - INITIAL MODEL

—•— FINAL MODEL

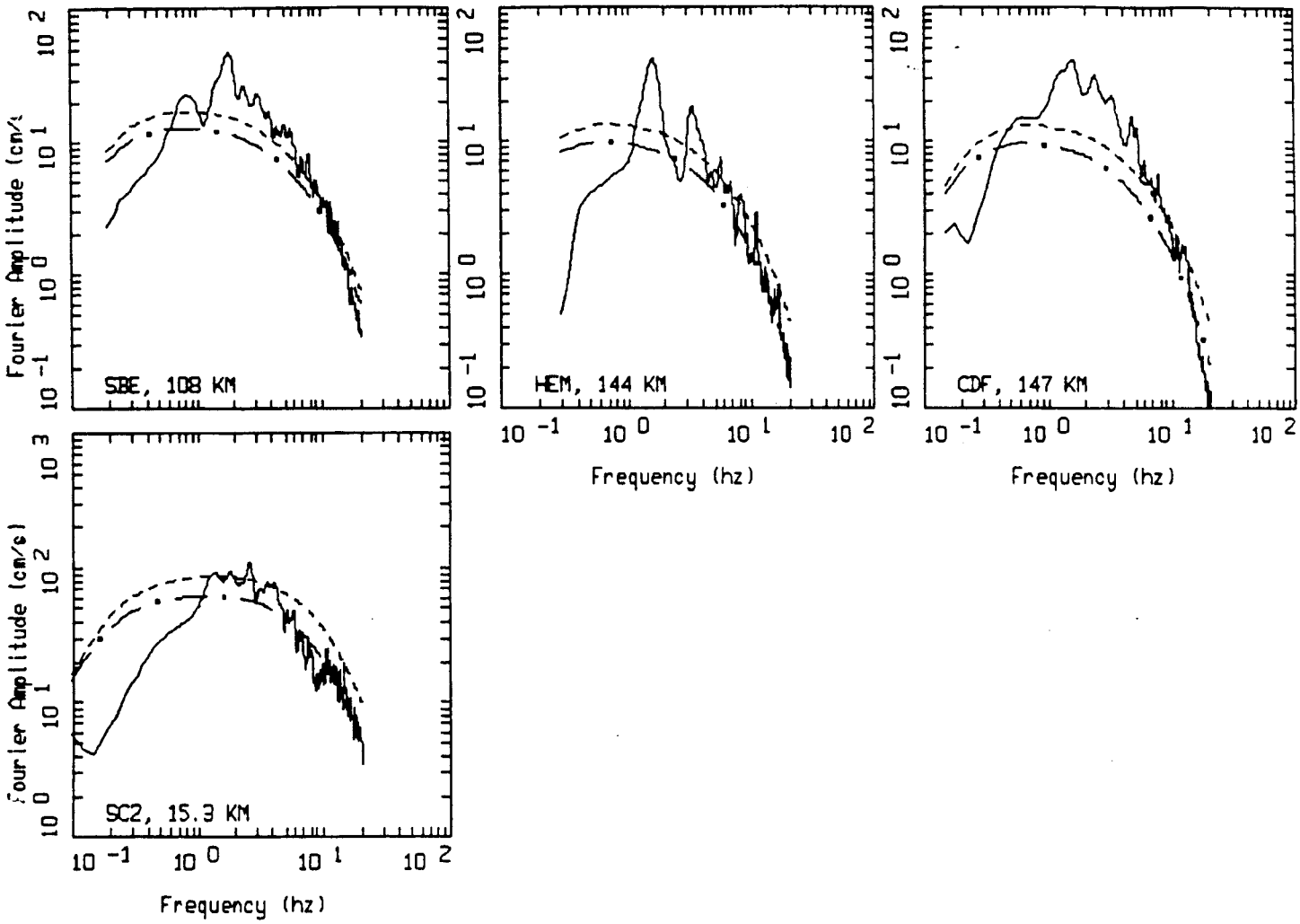

LEGEND

——— DATA

- - - - - INITIAL MODEL

— • — FINAL MODEL

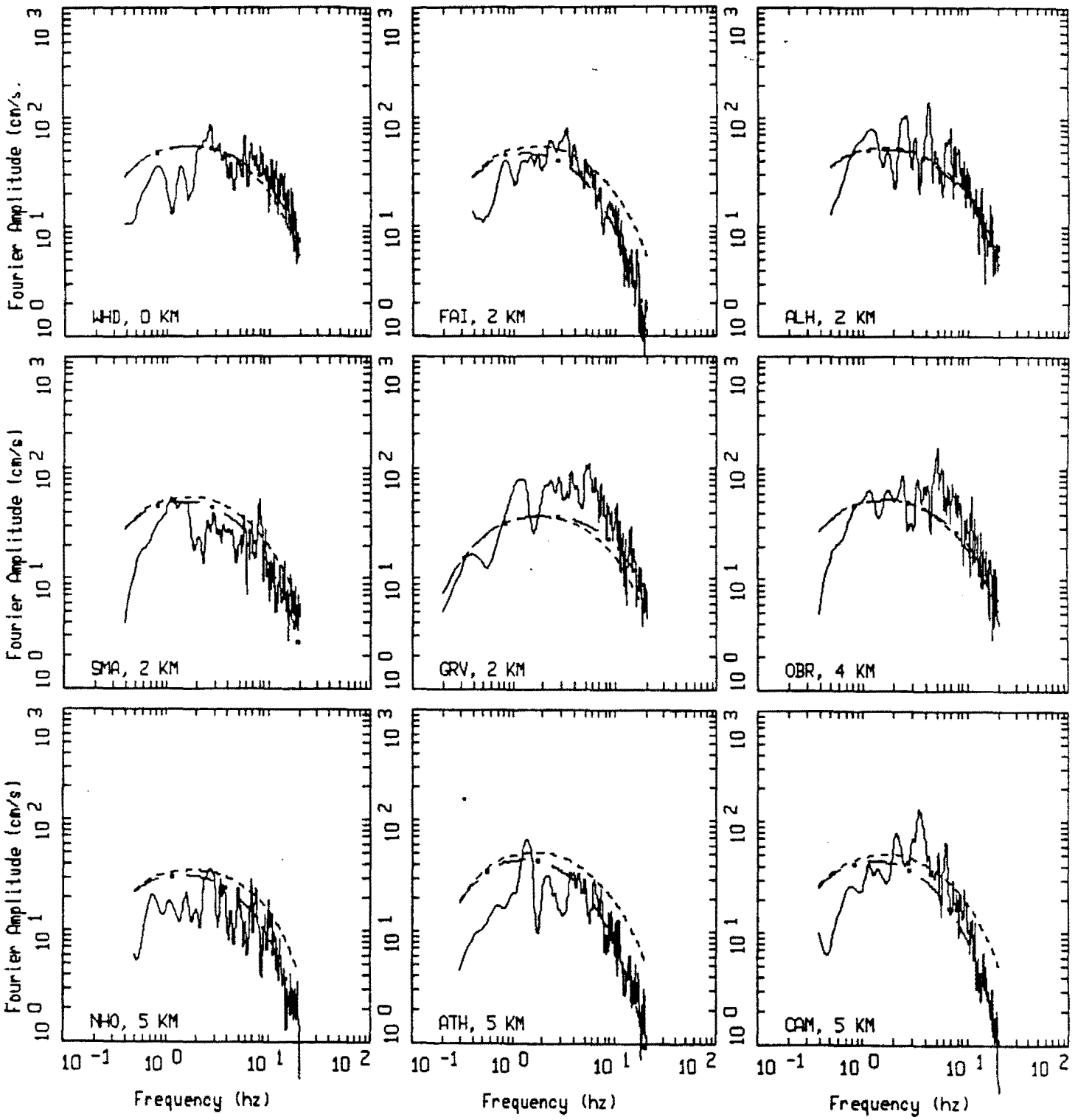

WHITTIER NARROWS EARTHQUAKE, M=6.0, PAGE 1 OF 10.

Figure Set 4.2

LEGEND

——— DATA

- - - - - INITIAL MODEL

— • — FINAL MODEL

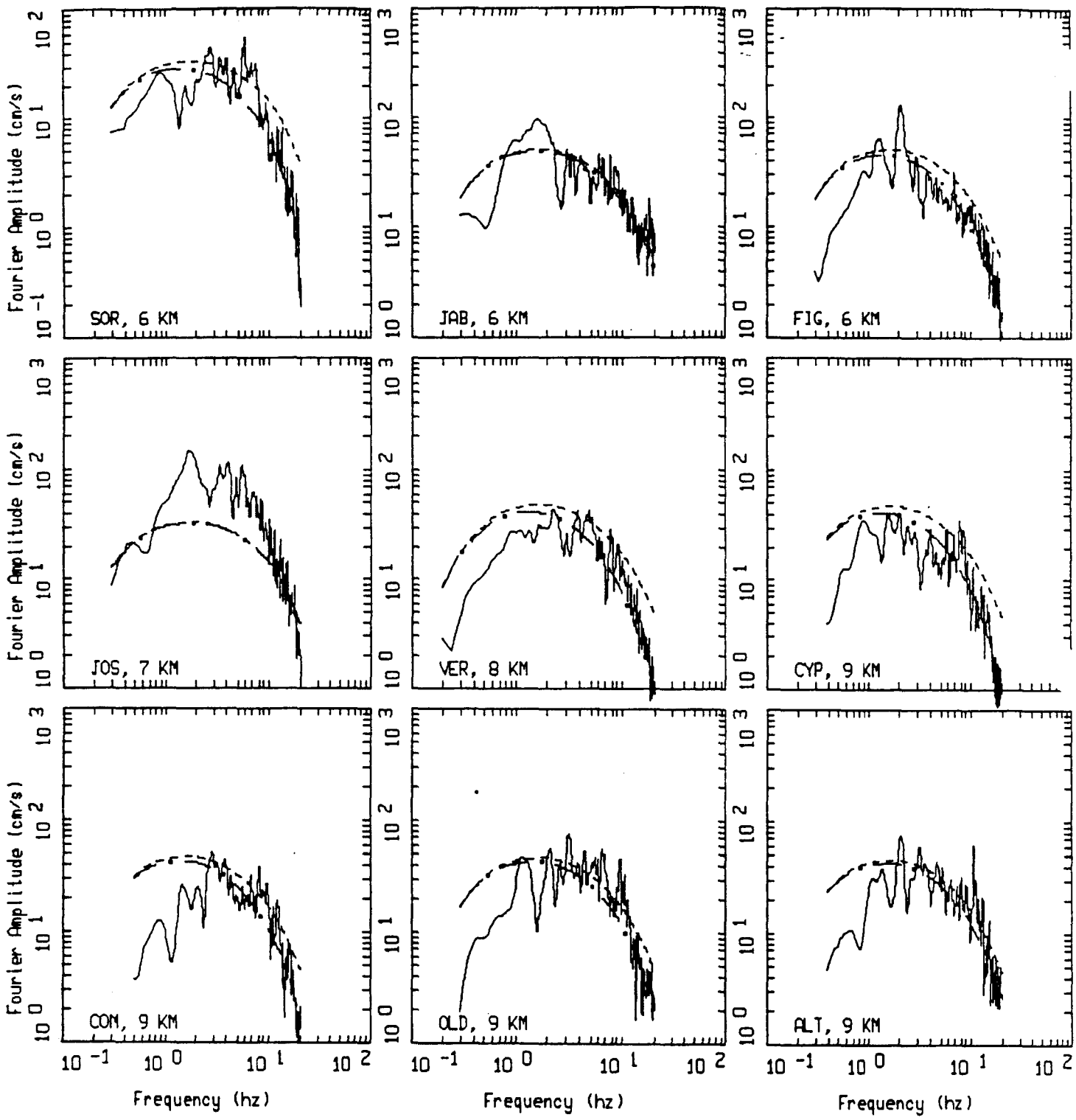

WHITTIER NARROWS EARTHQUAKE, M=6.0, PAGE 2 OF 10.

LEGEND

——— DATA

- - - - - INITIAL MODEL

—— • —— FINAL MODEL

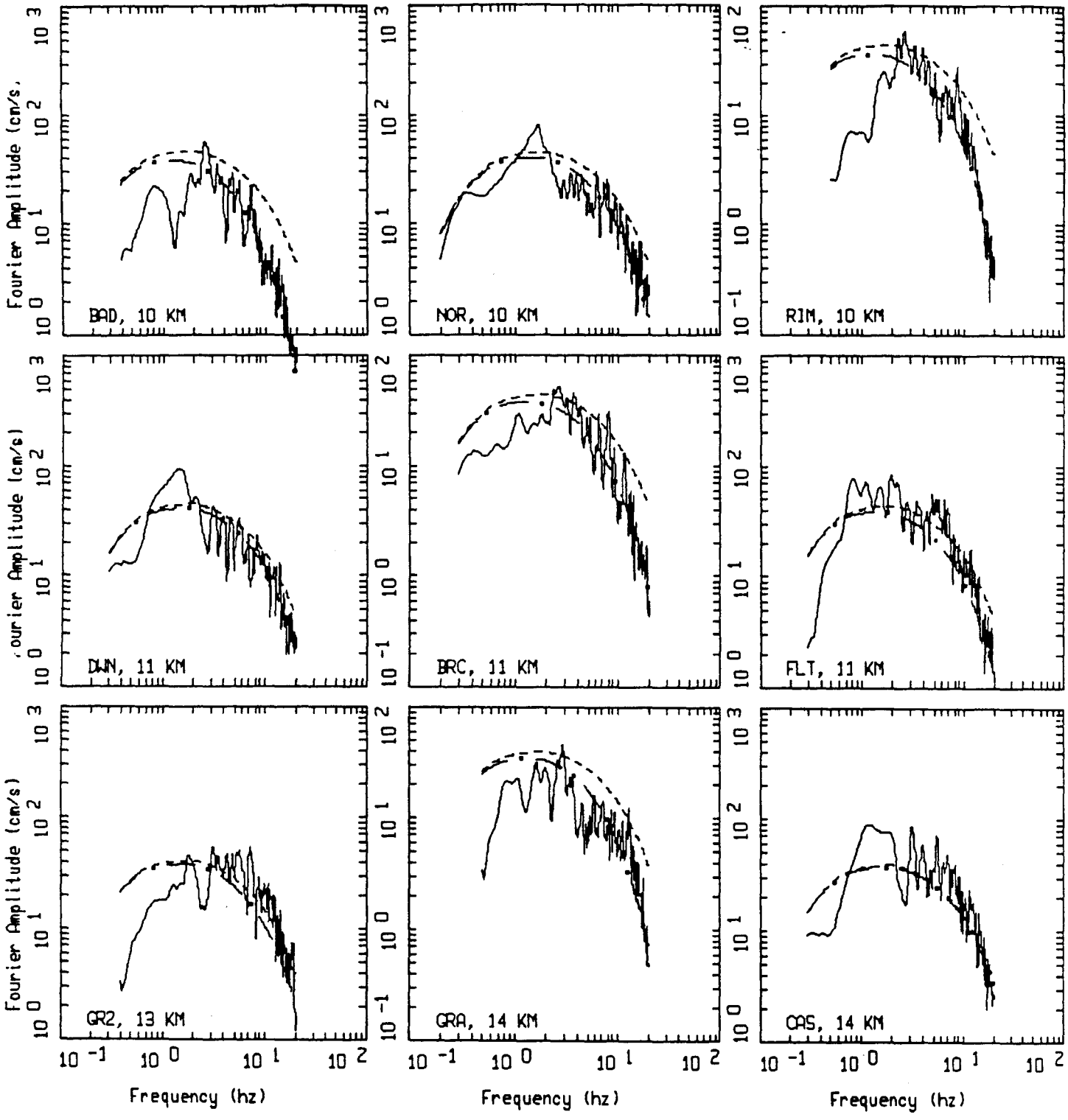

WHITTIER NARROWS EARTHQUAKE, M=6.0, PAGE 3 OF 10.

LEGEND

——— DATA

- - - - - INITIAL MODEL

—•— FINAL MODEL

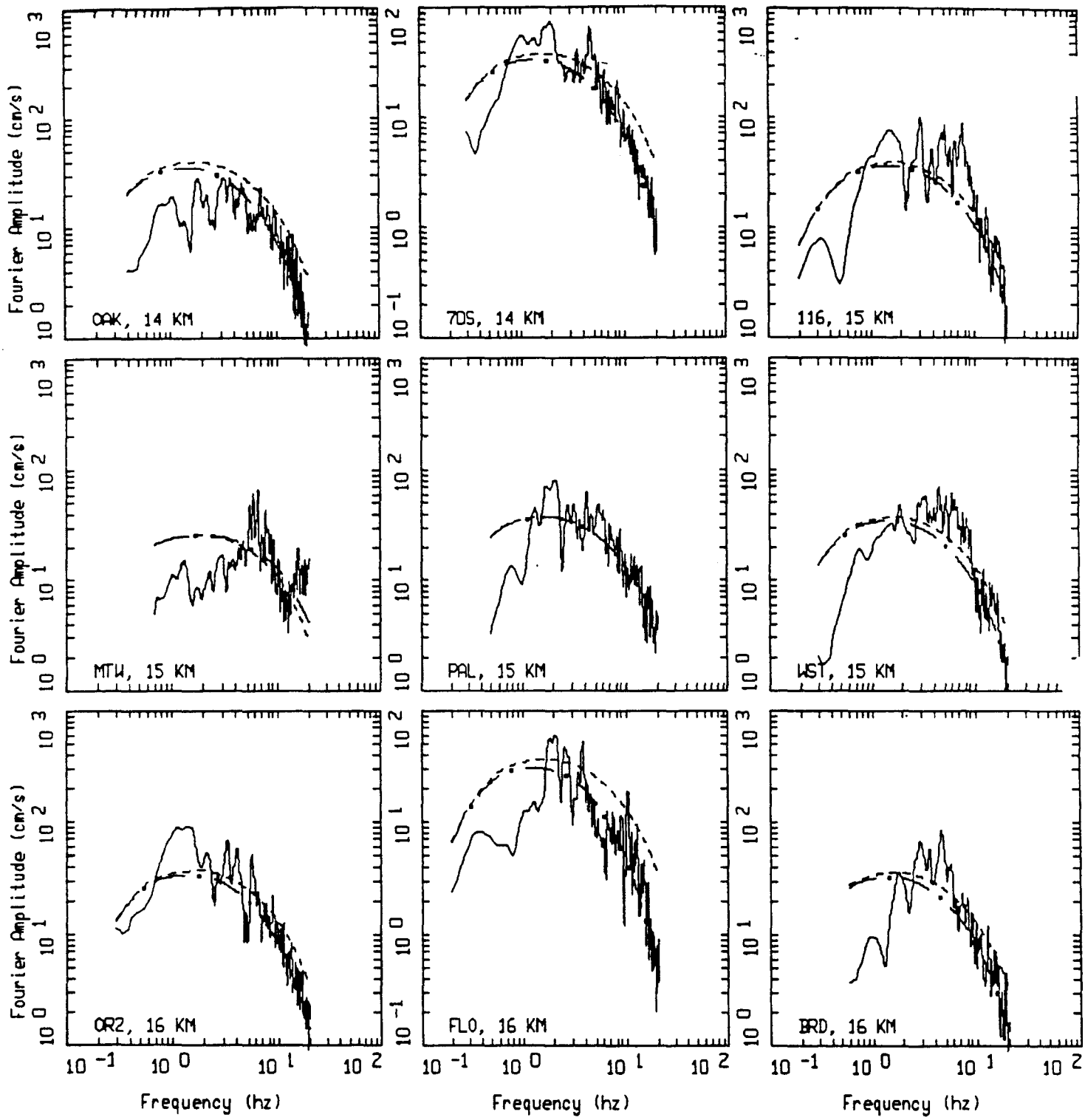

LEGEND

——— DATA

- - - - - INITIAL MODEL

—— • —— FINAL MODEL

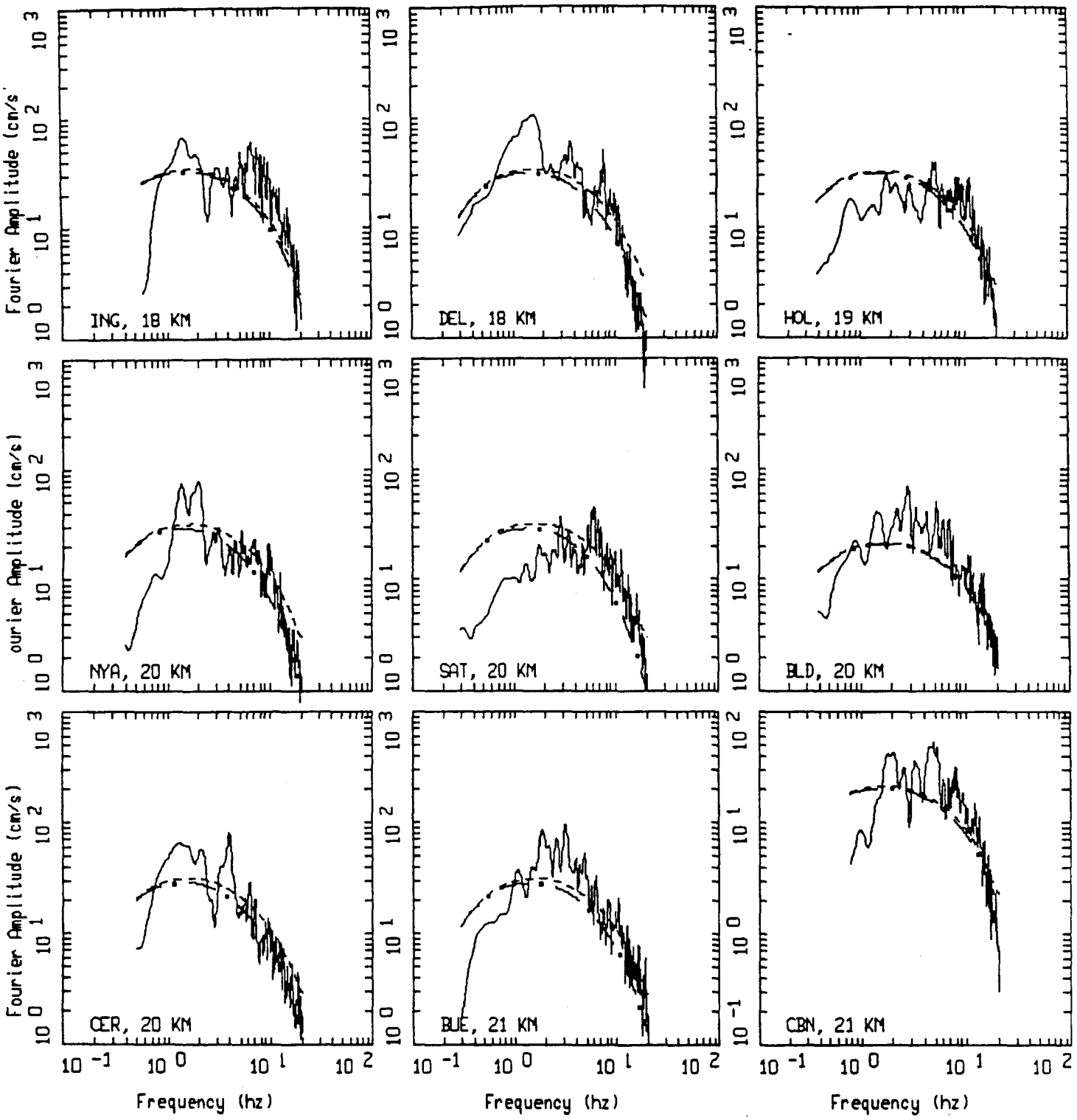

WHITTIER NARROWS EARTHQUAKE, M=6.0, PAGE 5 OF 10.

LEGEND

——— DATA

- - - - - INITIAL MODEL

—— • —— FINAL MODEL

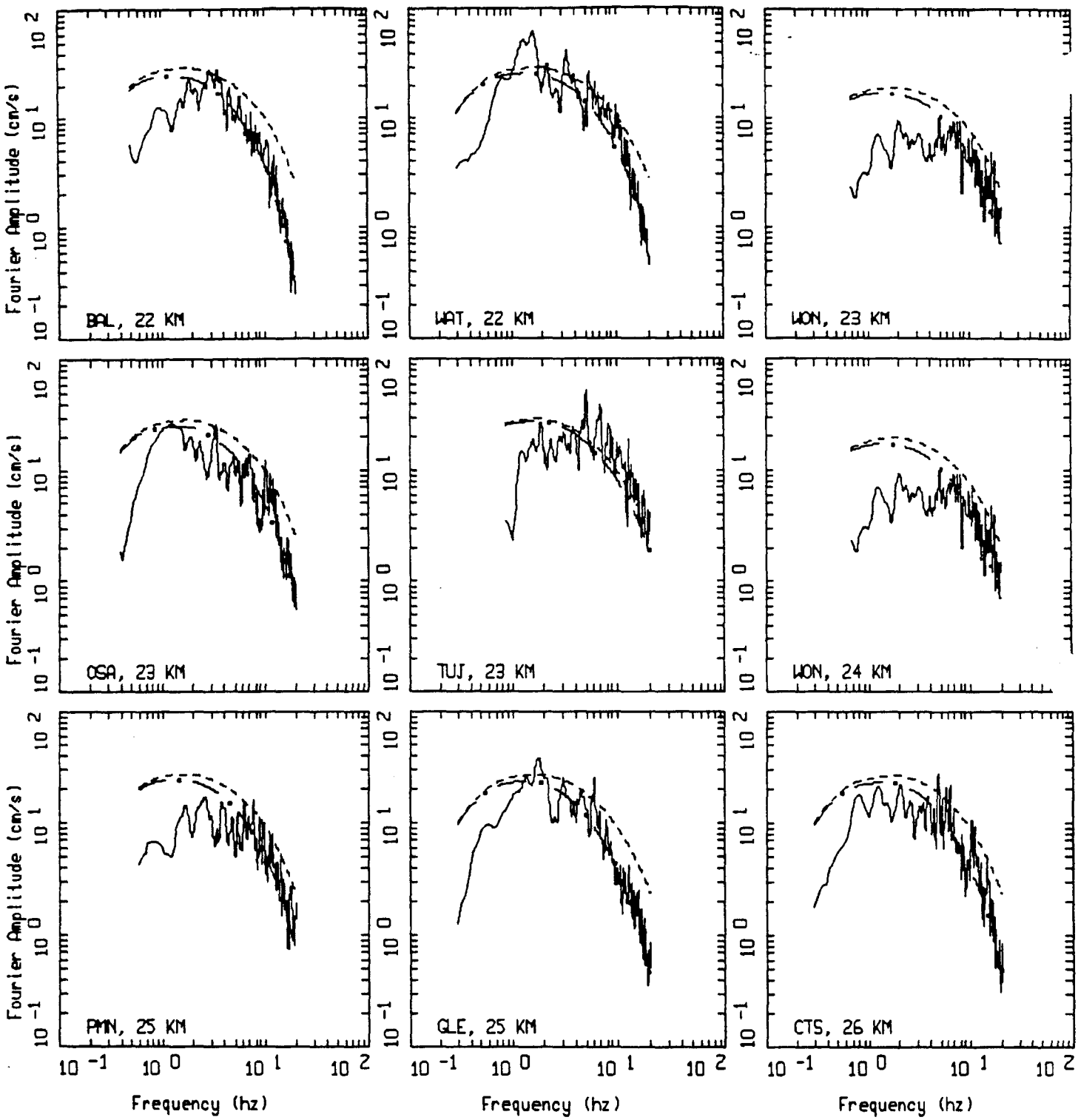

WHITTIER NARROWS EARTHQUAKE, M=6.0, PAGE 6 OF 10.

LEGEND

——— DATA

- - - - - INITIAL MODEL

— • — FINAL MODEL

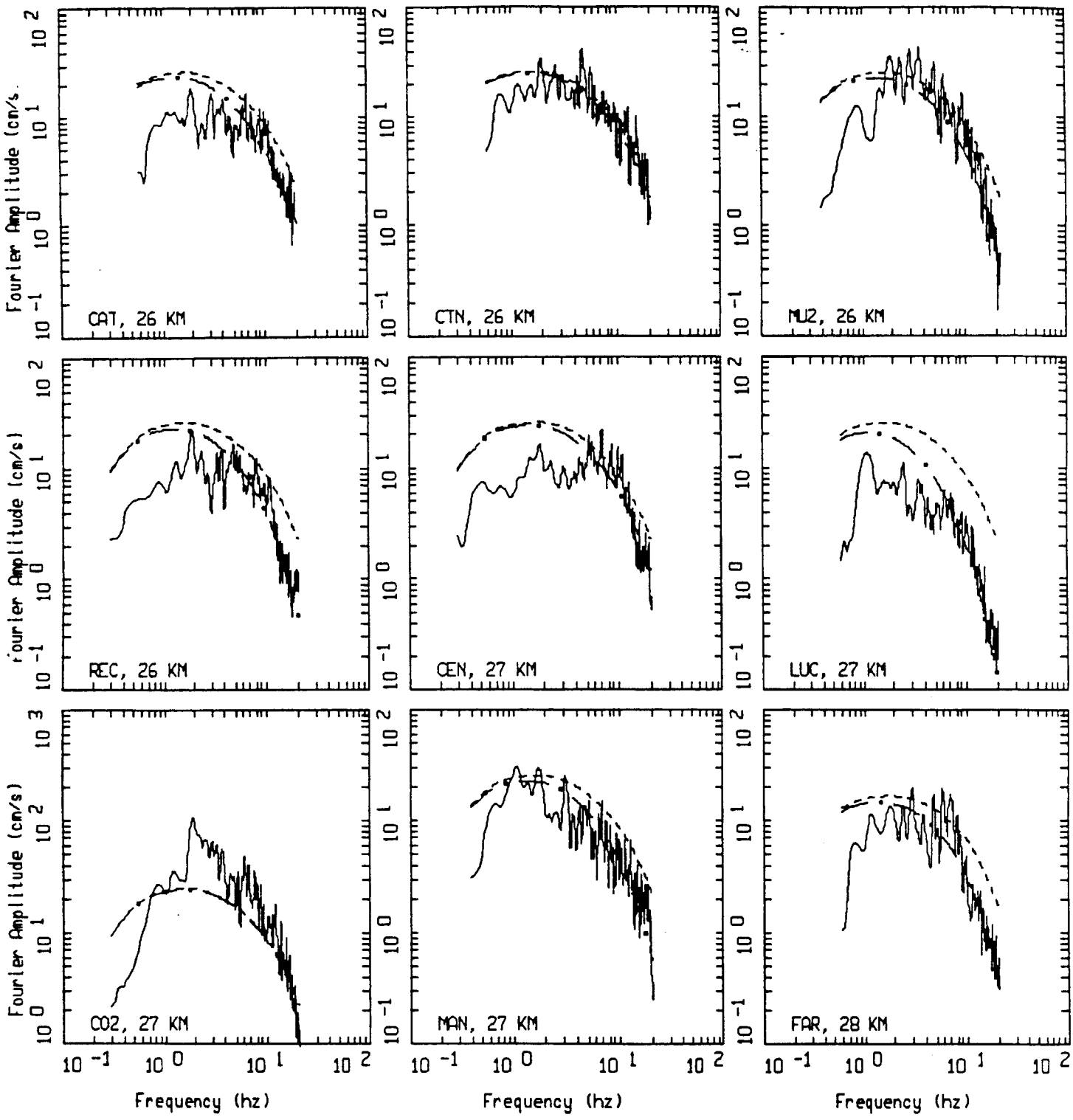

WHITTIER NARROWS EARTHQUAKE, M=6.0, PAGE 7 OF 10.

LEGEND

——— DATA

- - - - - INITIAL MODEL

—— • —— FINAL MODEL

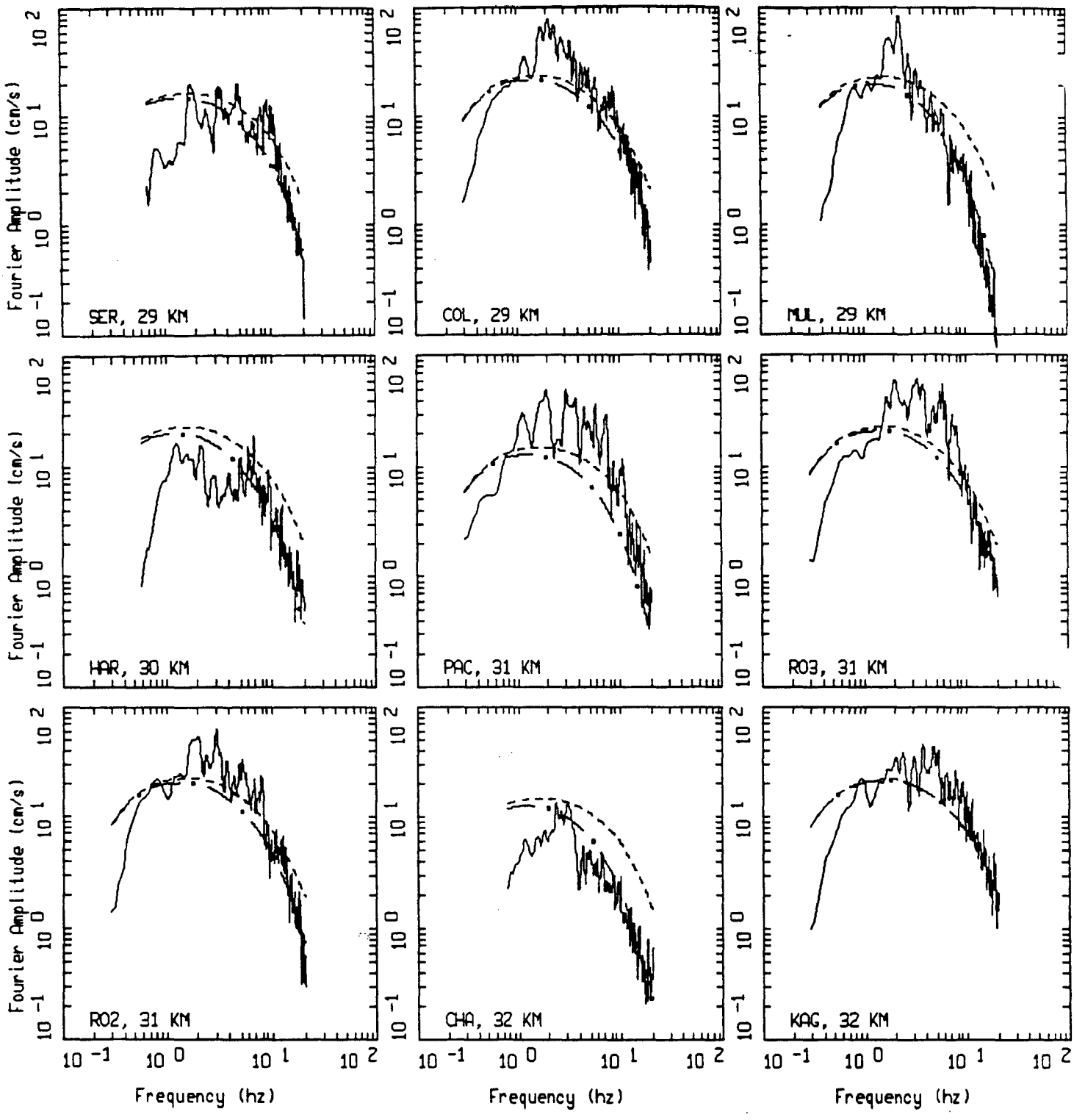

WHITTIER NARROWS EARTHQUAKE, M=6.0, PAGE 8 OF 10.

LEGEND

——— DATA

- - - - - INITIAL MODEL

— • — FINAL MODEL

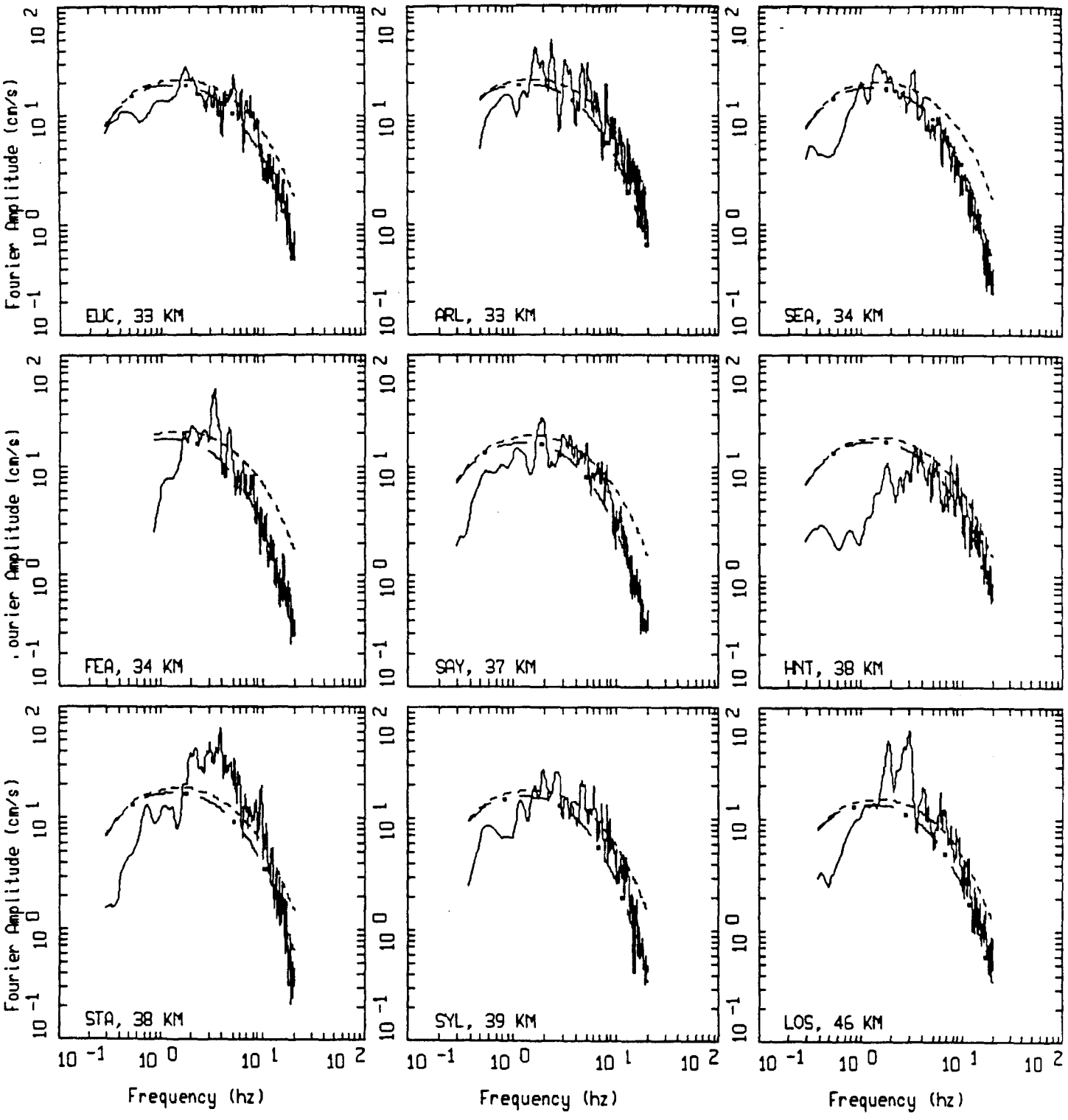

WHITTIER NARROWS EARTHQUAKE, M=6.0, PAGE 9 OF 10.

LEGEND

——— DATA

- - - - - INITIAL MODEL

— • — FINAL MODEL

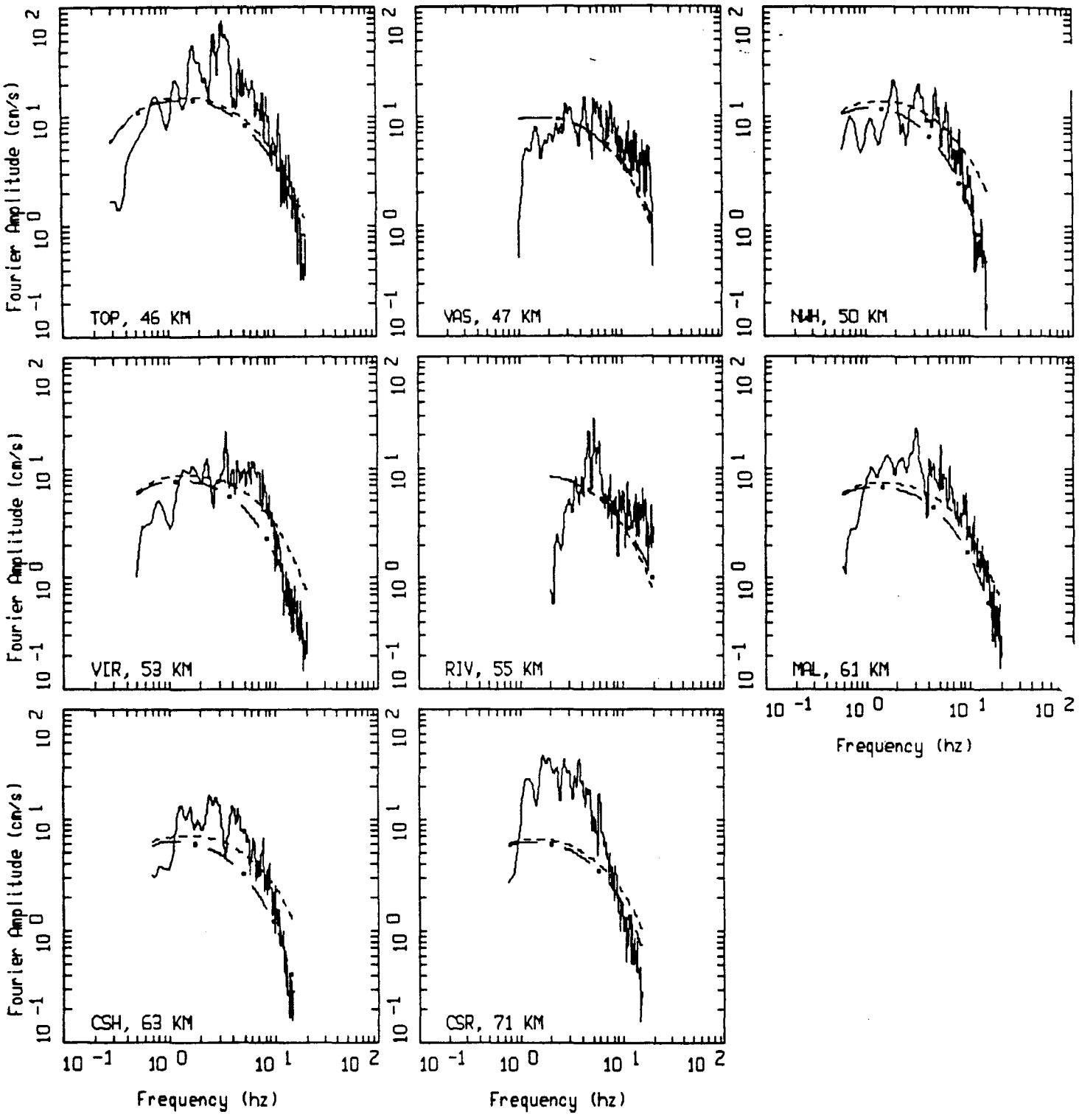

WHITTIER NARROWS EARTHQUAKE, M=6.0, PAGE 10 OF 10.

LEGEND

——— DATA

- - - - - INITIAL MODEL

— • — FINAL MODEL

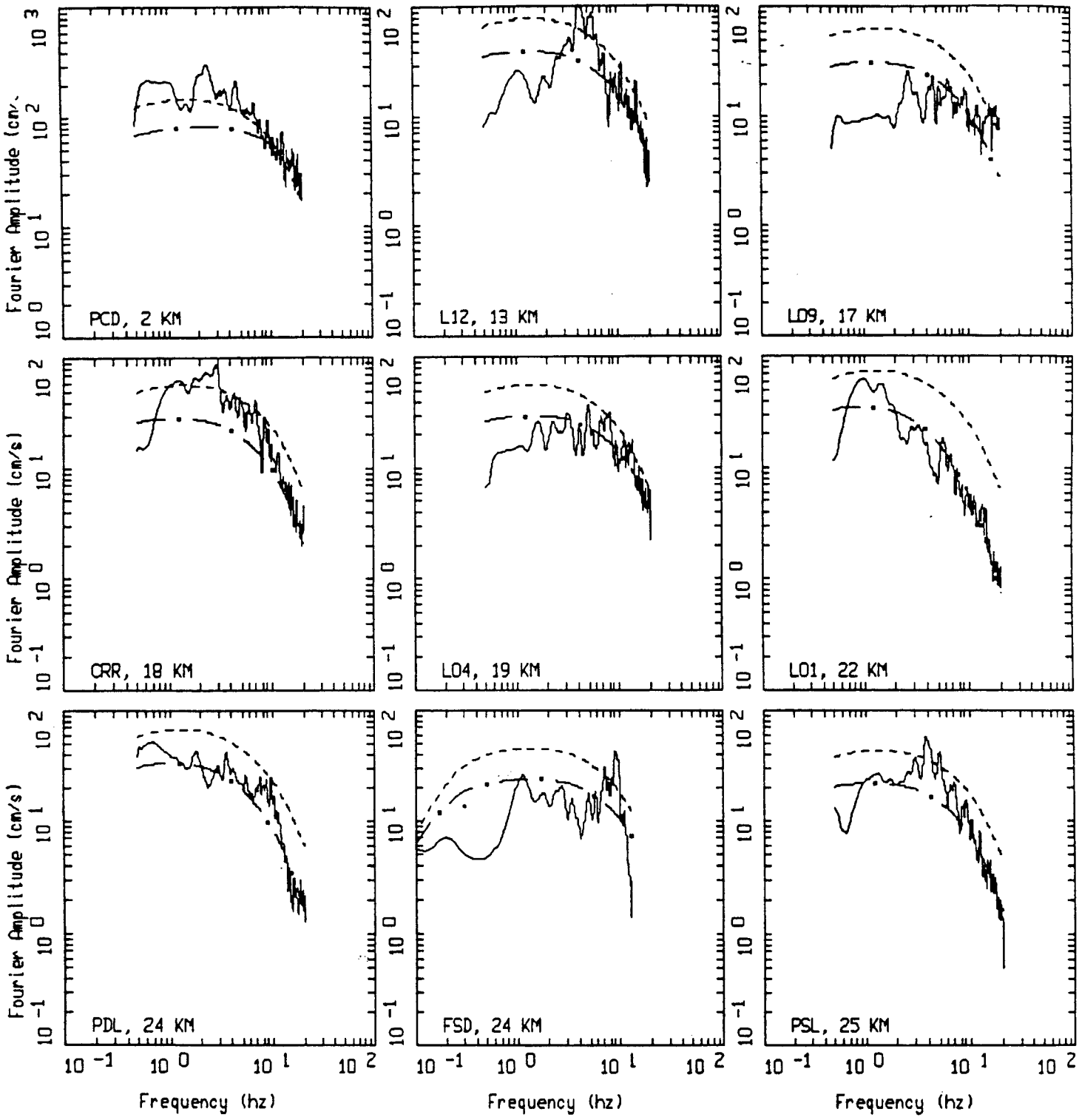

SAN FERNANDO EARTHQUAKE, M=6.6, PAGE 1 OF 5.

Figure Set 4.2

LEGEND

——— DATA

- - - - - INITIAL MODEL

— • — FINAL MODEL

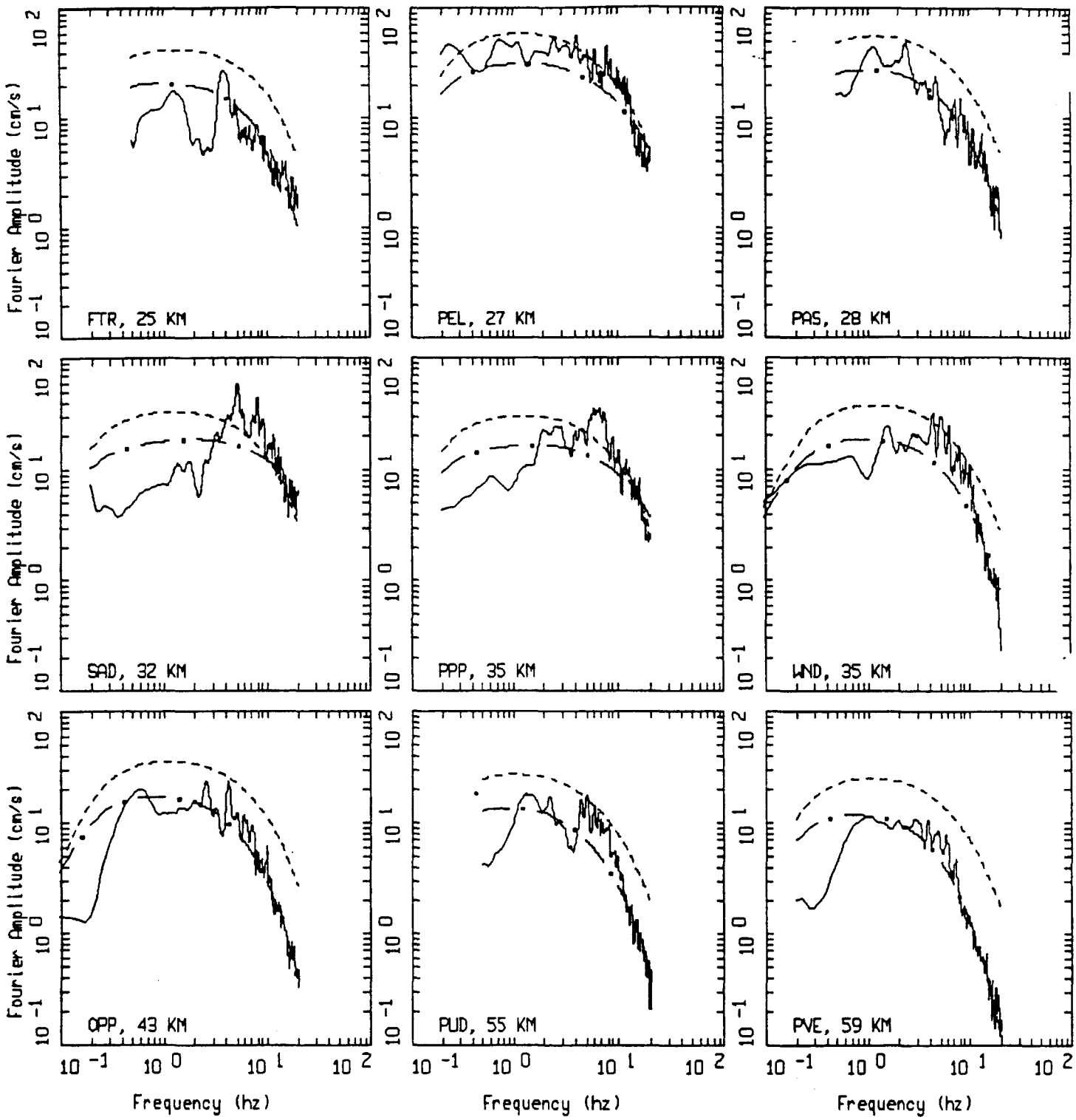

SAN FERNANDO_EARTHQUAKE, M=6.6, PAGE 2 OF 5.

LEGEND

——— DATA

- - - - - INITIAL MODEL

—•— FINAL MODEL

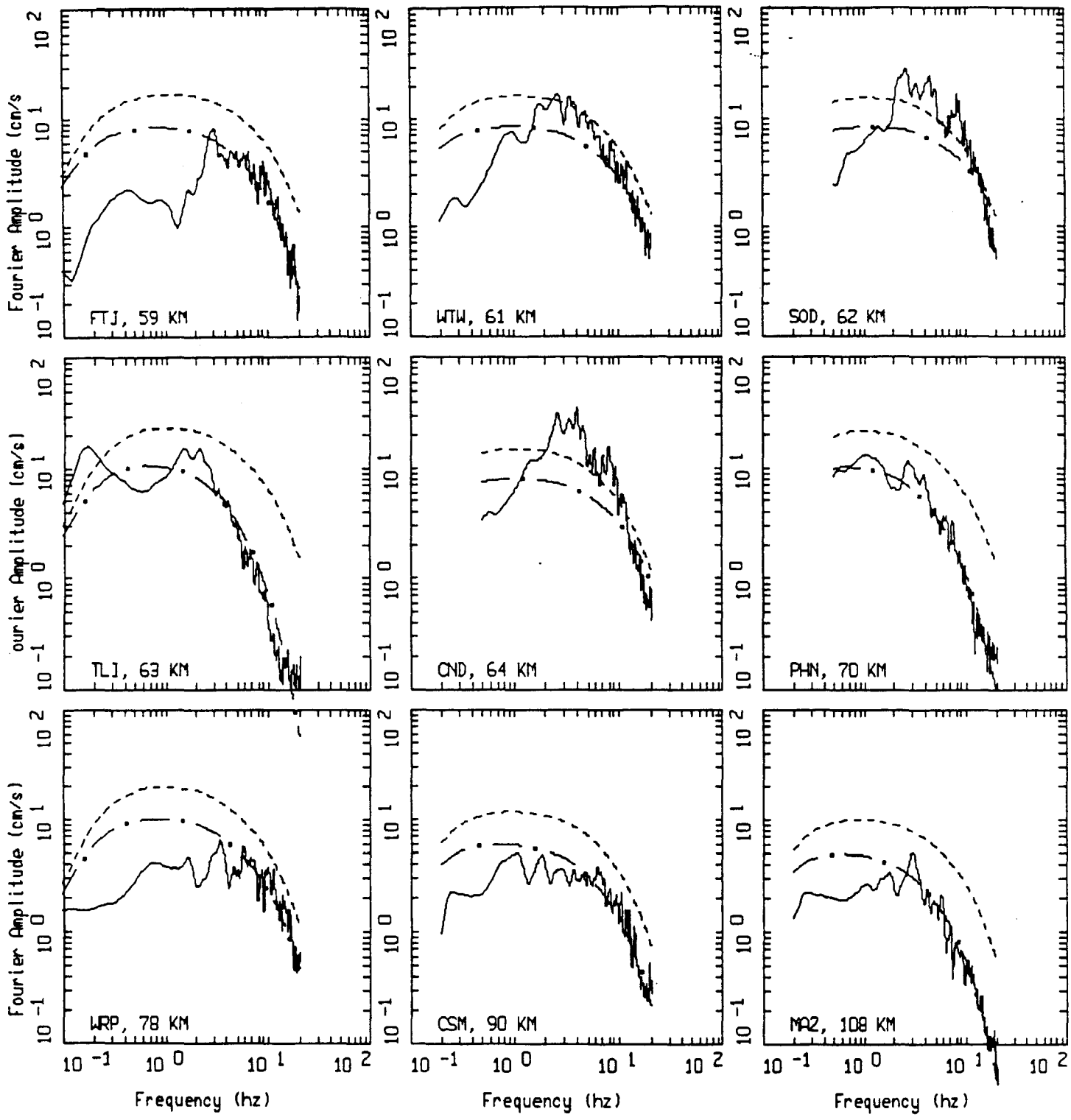

SAN FERNANDO_EARTHQUAKE, M=6.6, PAGE 3 OF 5.

LEGEND

DATA

INITIAL MODEL

FINAL MODEL

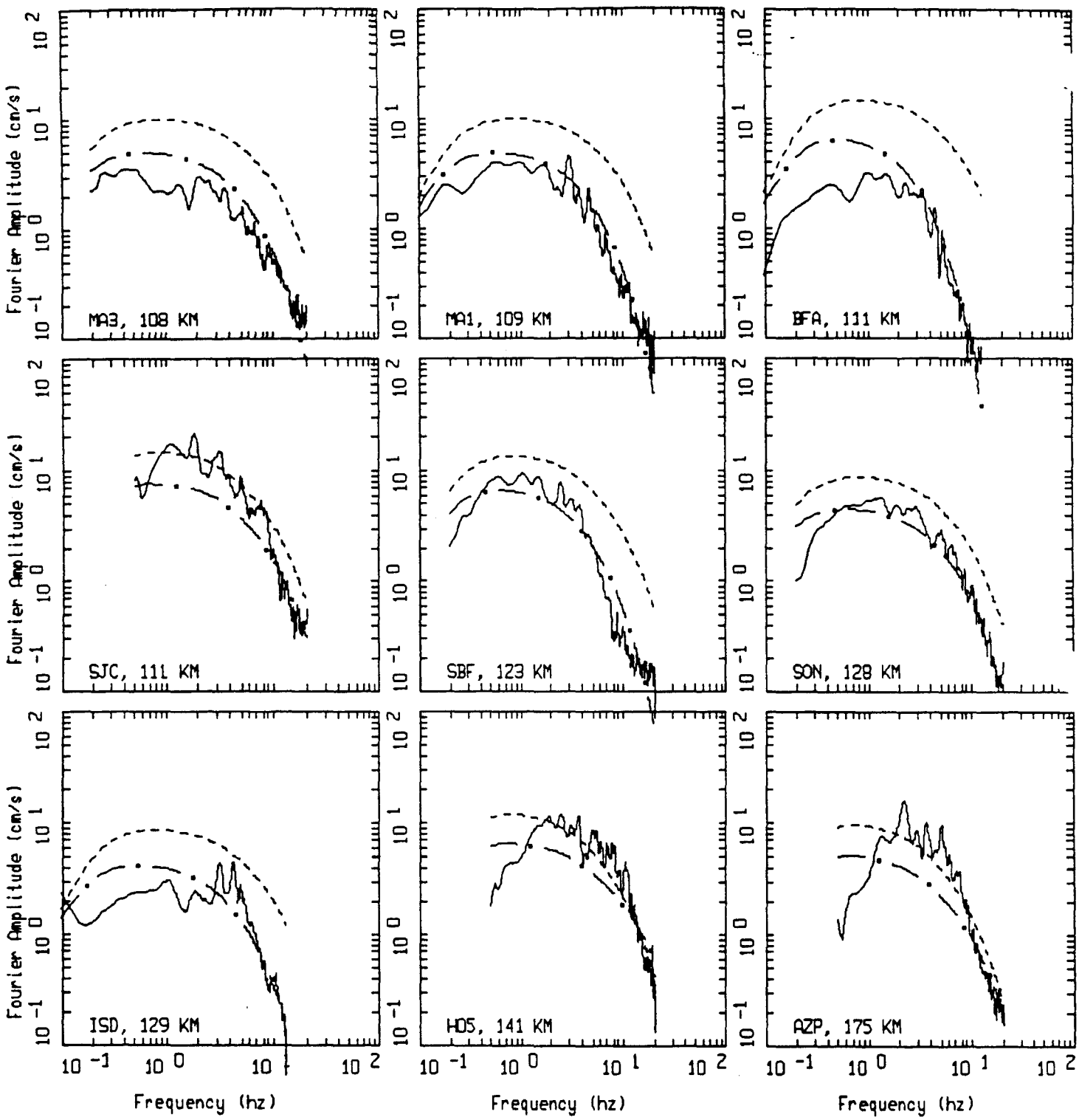

SAN FERNANDO_EARTHQUAKE, M=6.6, PAGE 4 OF 5.

LEGEND

——— DATA

- - - - - INITIAL MODEL

—•— FINAL MODEL

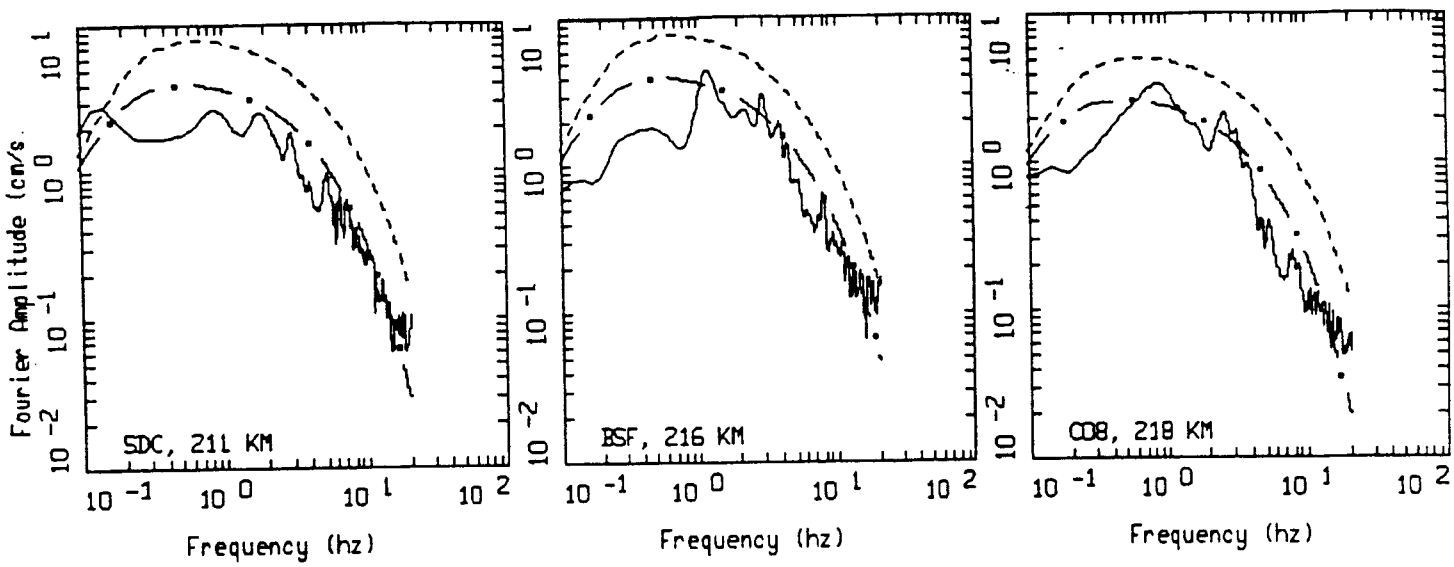

SAN FERNANDO EARTHQUAKE, M=6.6, PAGE 5 OF 5.

LEGEND

——— DATA

- - - - - INITIAL MODEL

—— • —— FINAL MODEL

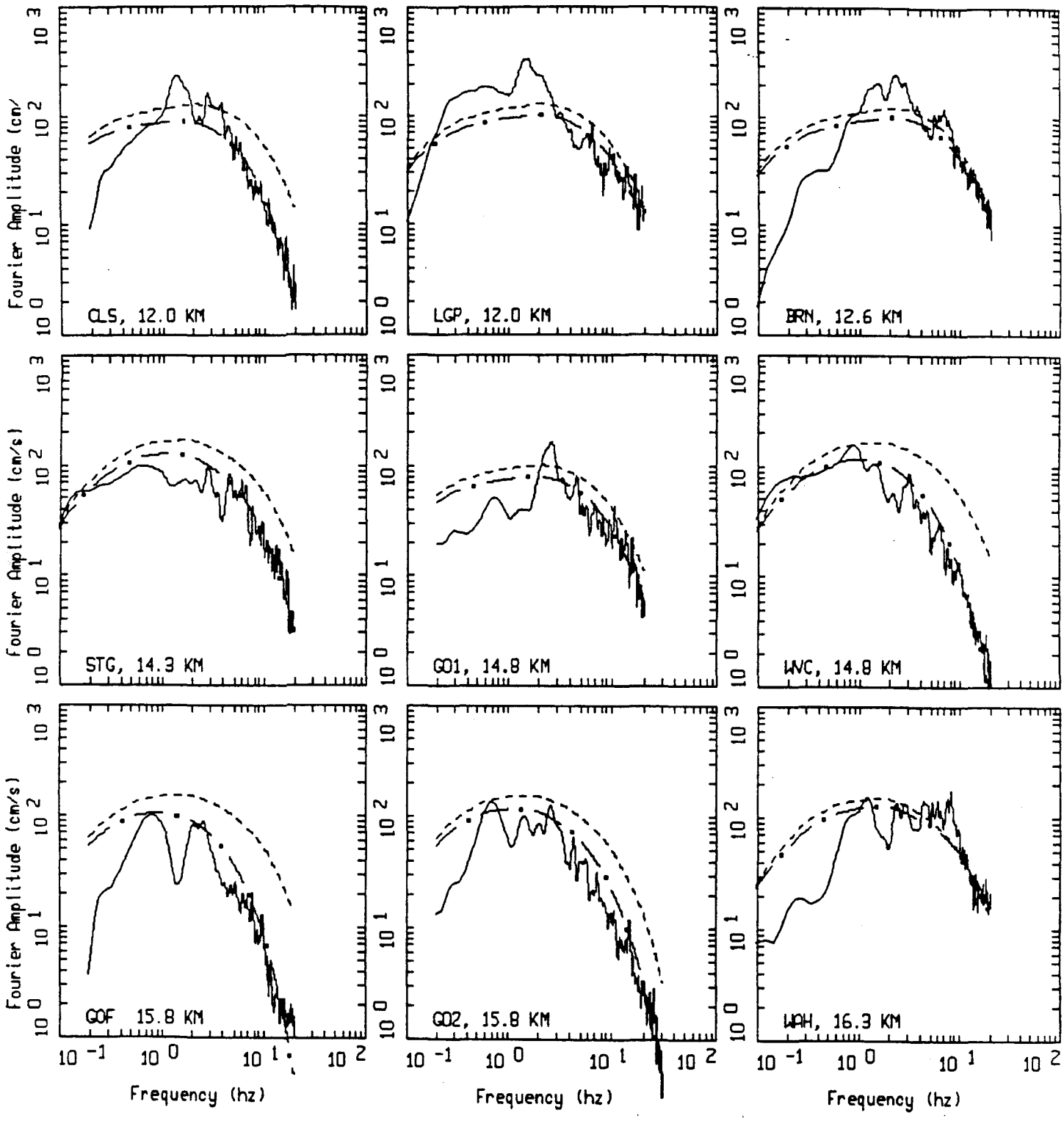

LOMA PRIETA EARTHQUAKE, M=6.9, PAGE 1 OF 6.

Figure Set 4.3

LEGEND

——— DATA

- - - - - INITIAL MODEL

— • — FINAL MODEL

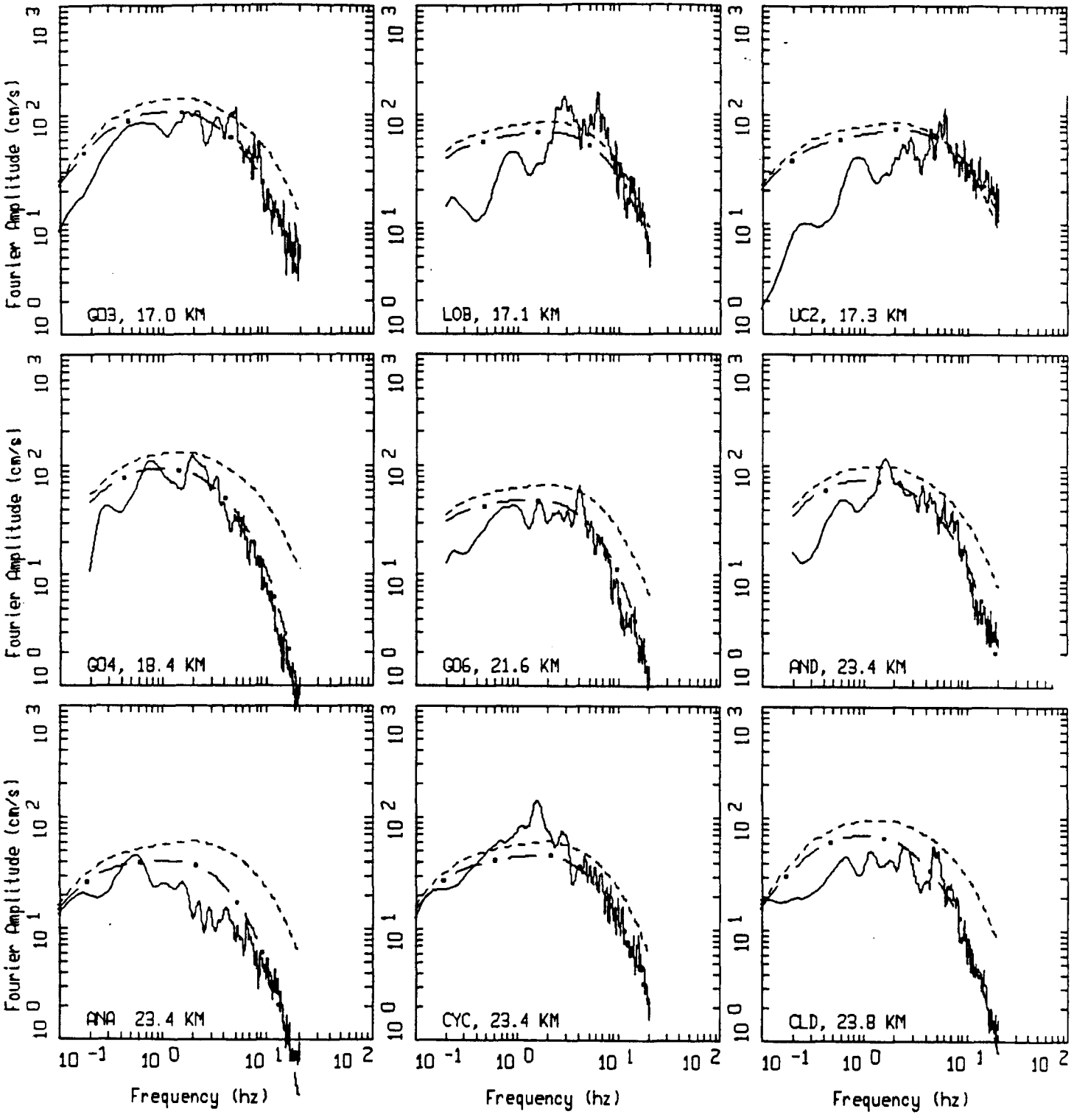

LOMA PRIETA EARTHQUAKE, M=6.9, PAGE 2 OF 6.

LEGEND

——— DATA

- - - - - INITIAL MODEL

— • — FINAL MODEL

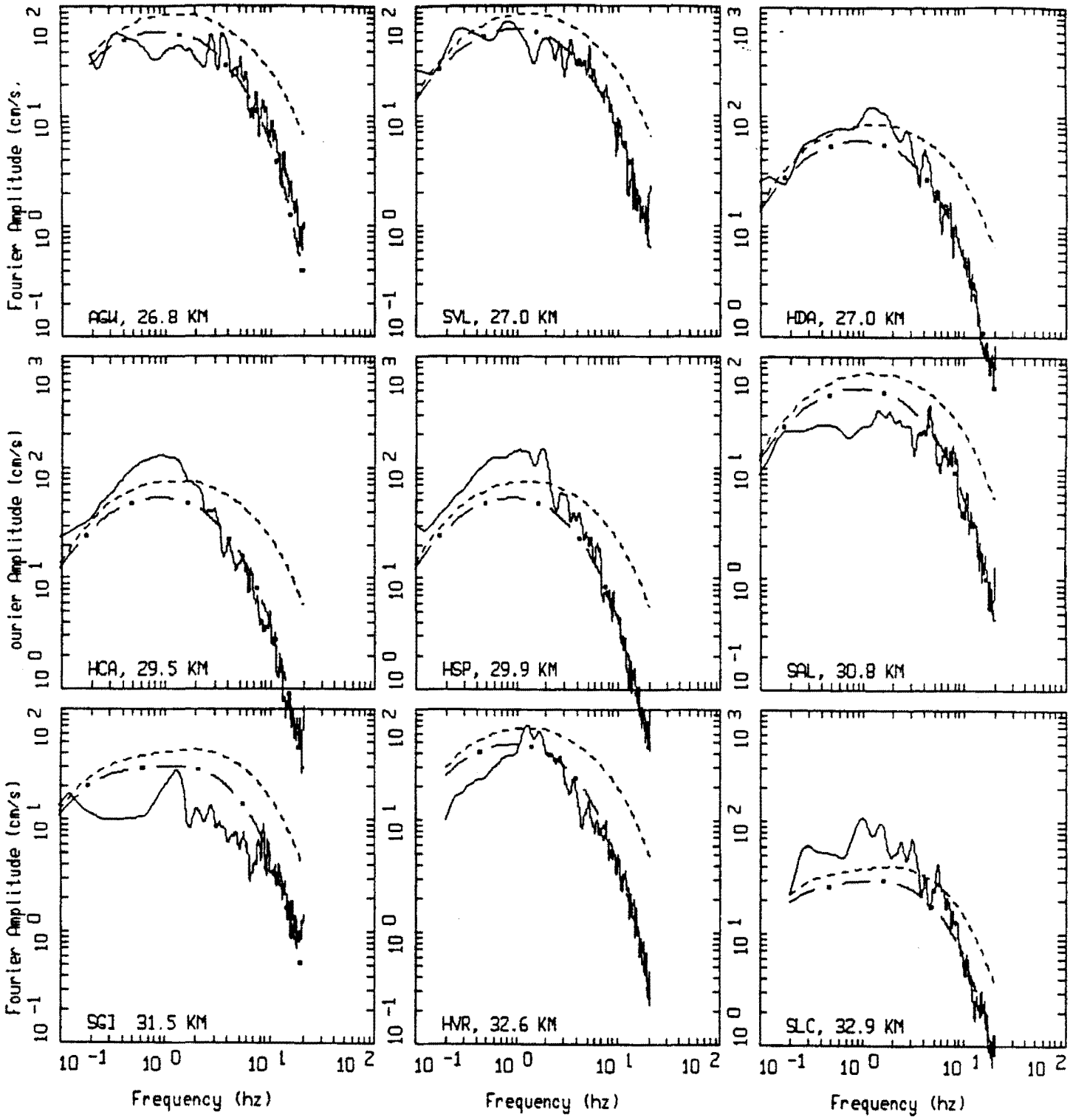

LOMA PRIETA EARTHQUAKE, M=6.9, PAGE 3 OF 6.

LEGEND

DATA

INITIAL MODEL

FINAL MODEL

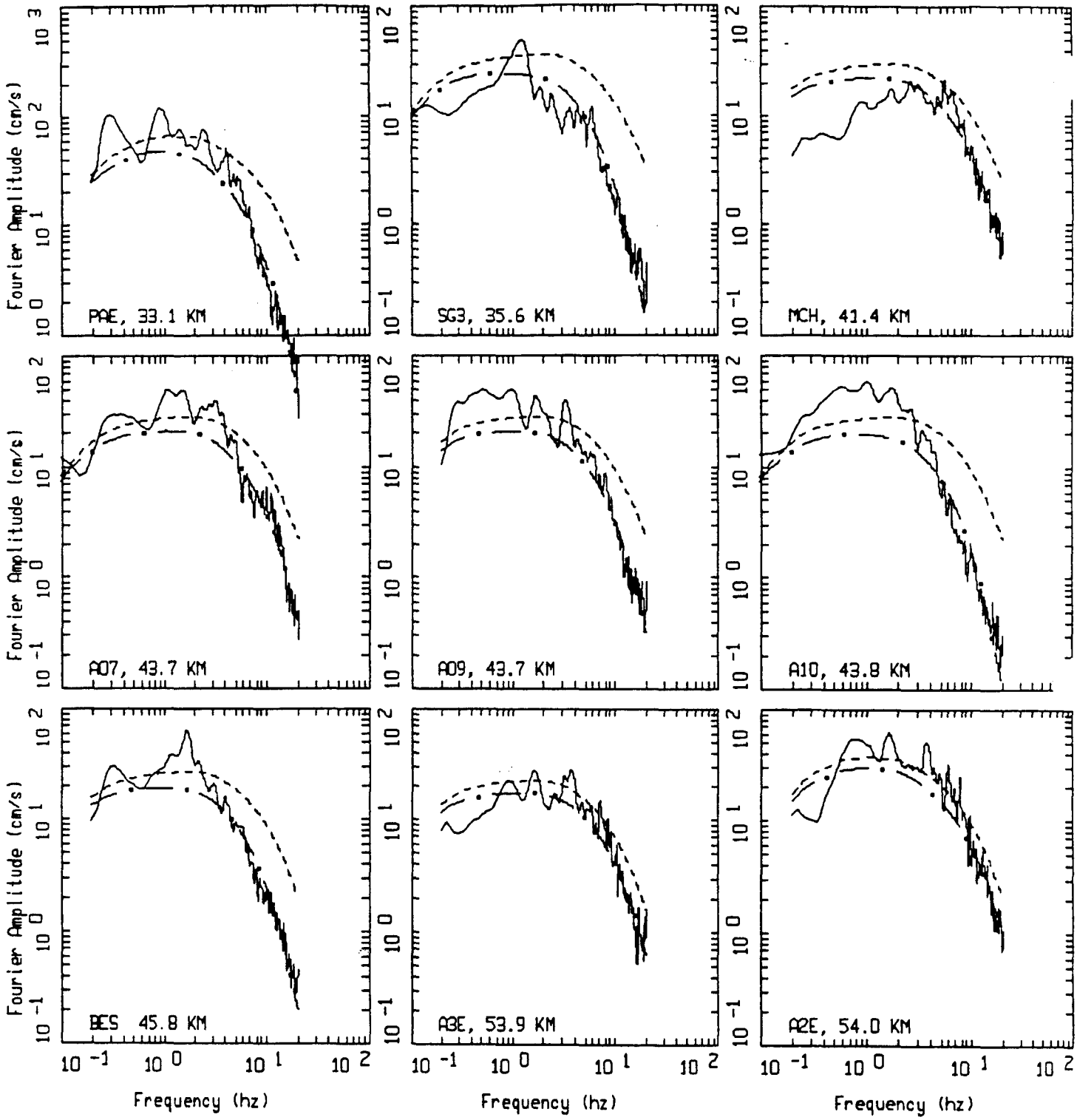

LOMA PRIETA EARTHQUAKE, M=6.9, PAGE 4 OF 6.

LEGEND

DATA

INITIAL MODEL

FINAL MODEL

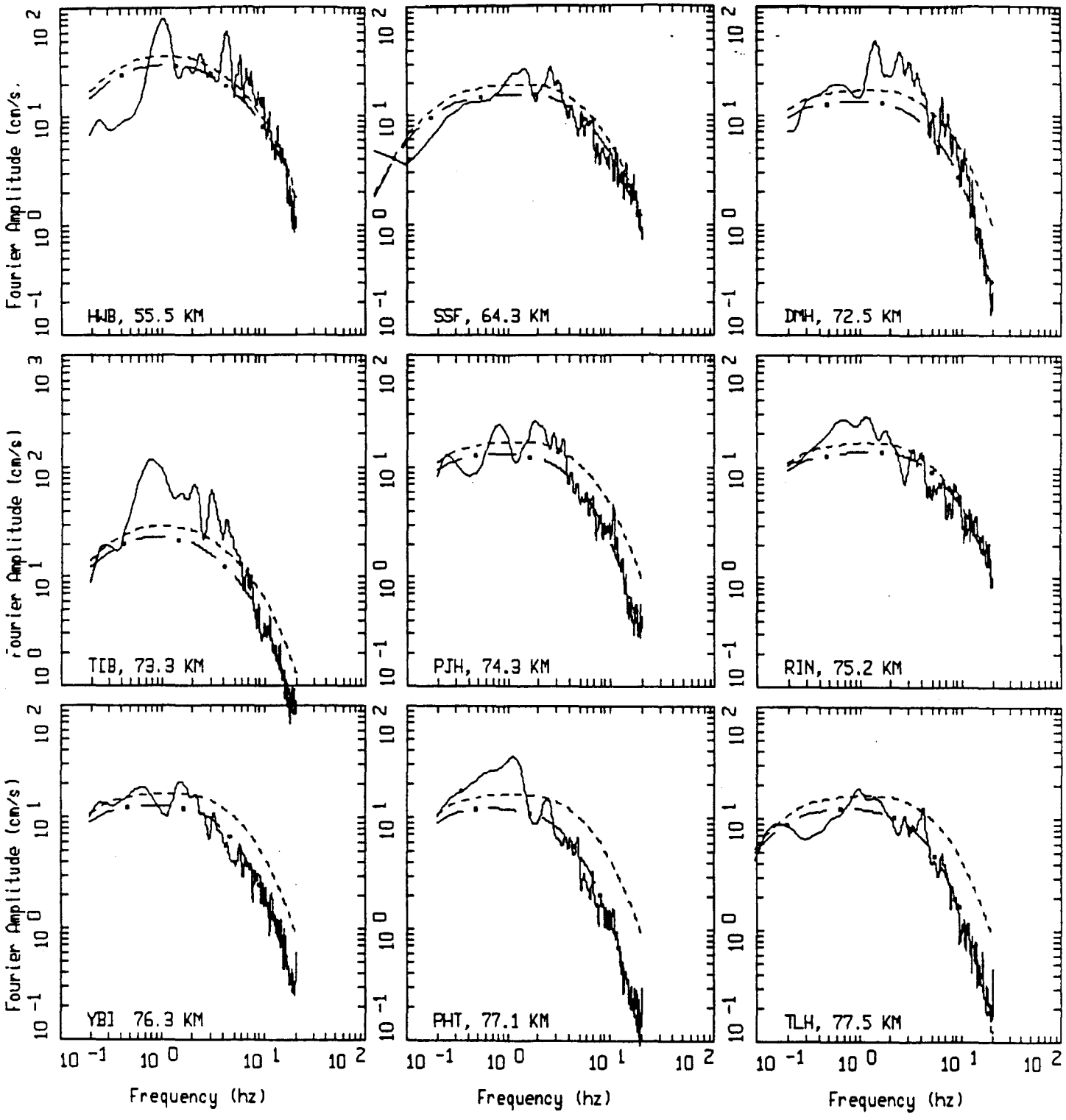

LOMA PRIETA EARTHQUAKE, M=6.9, PAGE 5 OF 6.

LEGEND

——— DATA

- - - - - INITIAL MODEL

—•— FINAL MODEL

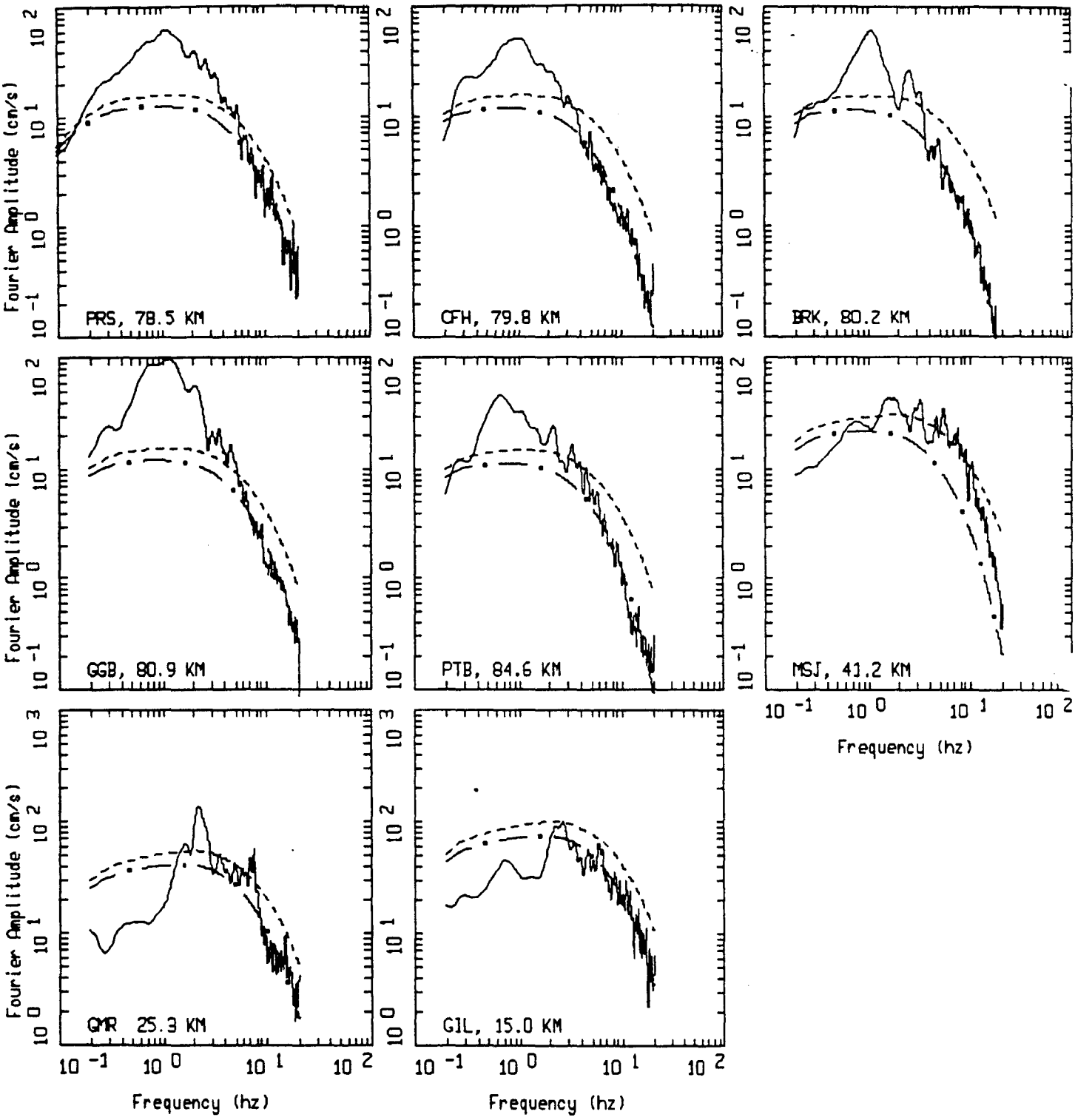

LOMA PRIETA EARTHQUAKE, M=6.9, PAGE 6 OF 6.

LEGEND

DATA

INITIAL MODEL

FINAL MODEL

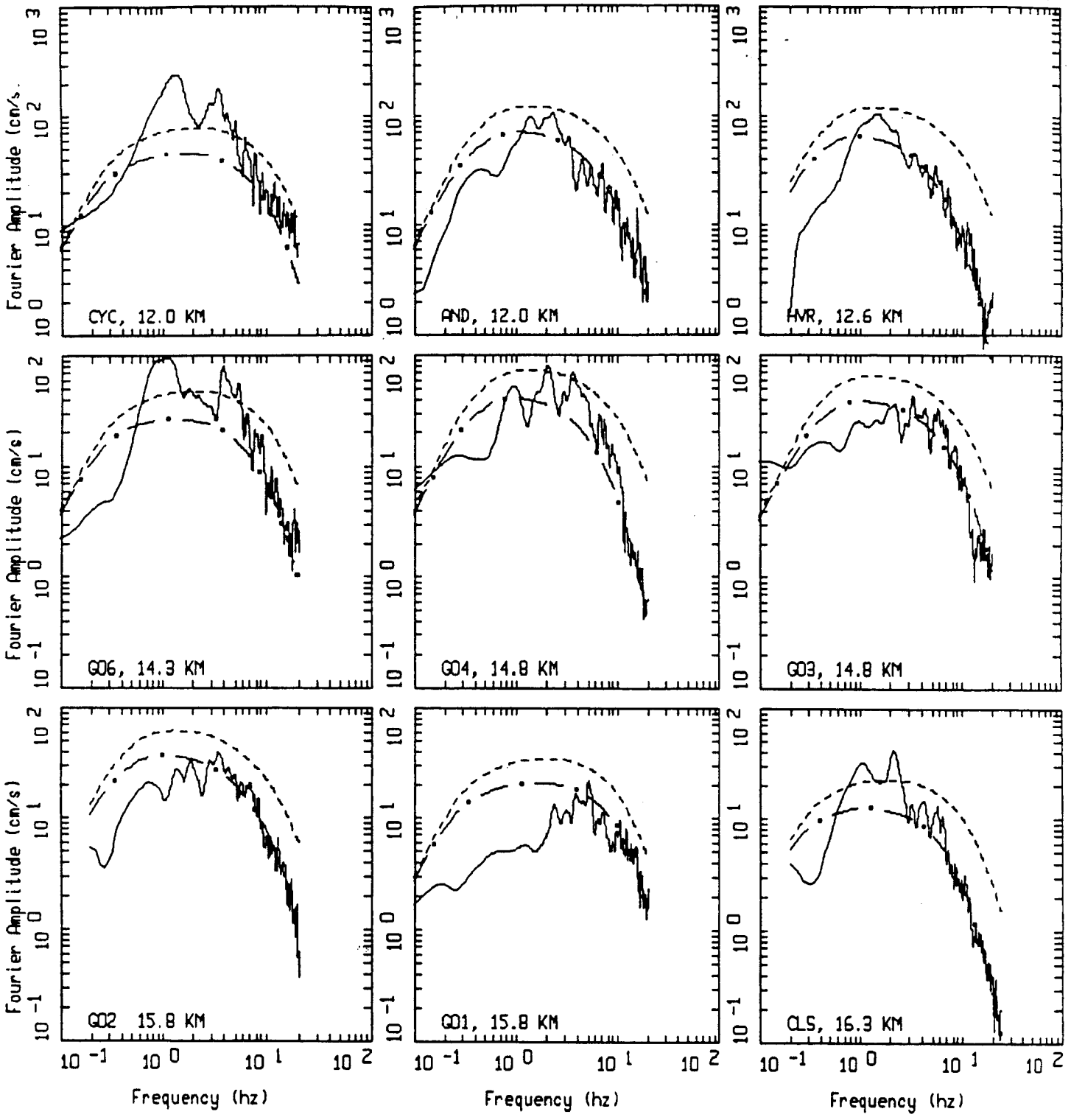

MORGAN HILL EARTHQUAKE, M=6.2, PAGE 1 OF 4.

Figure Set 4.3

LEGEND

DATA

INITIAL MODEL

FINAL MODEL

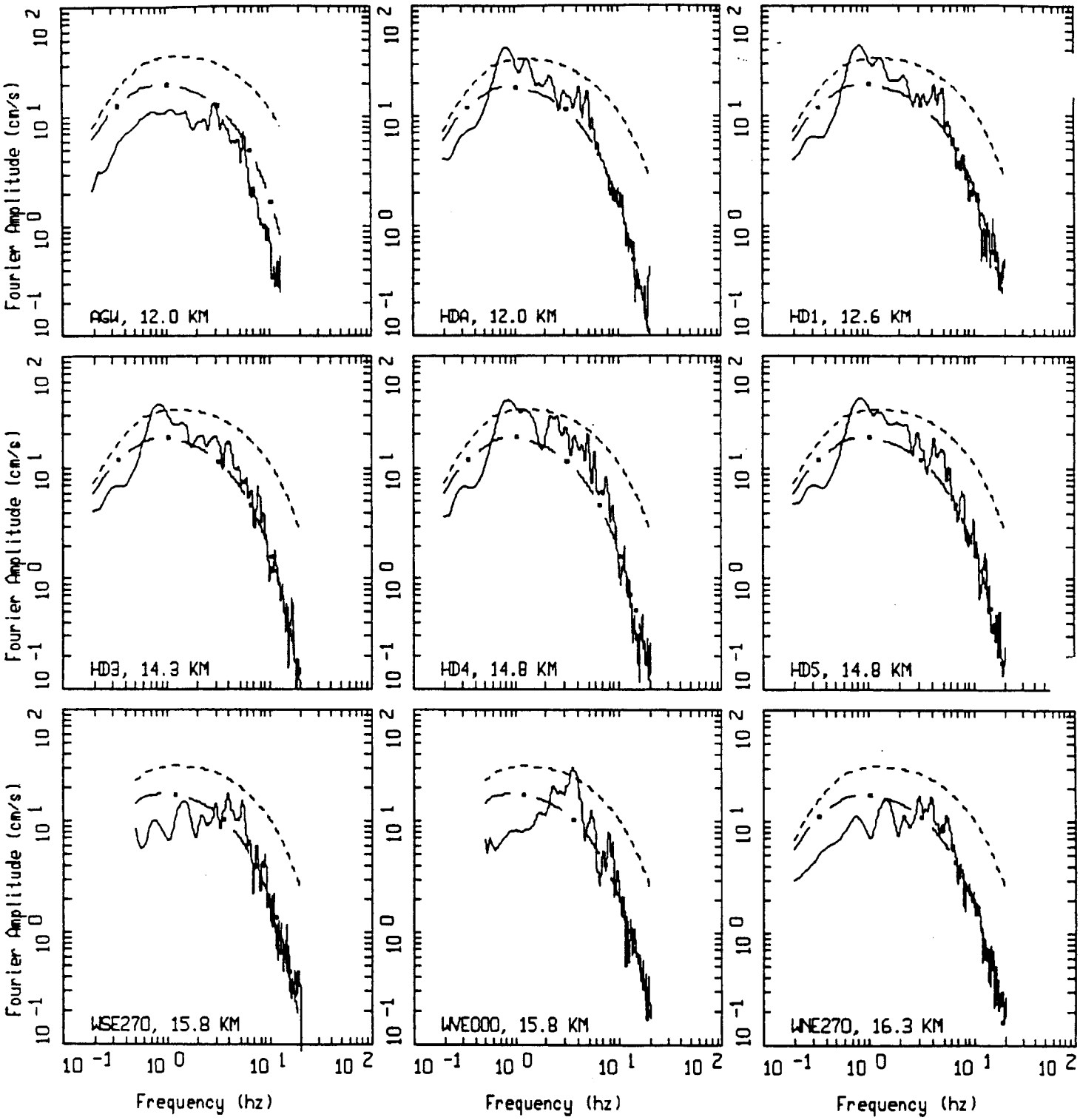

MORGAN HILL EARTHQUAKE, M=6.2, PAGE 2 OF 4.

LEGEND

——— DATA

- - - - - INITIAL MODEL

—•— FINAL MODEL

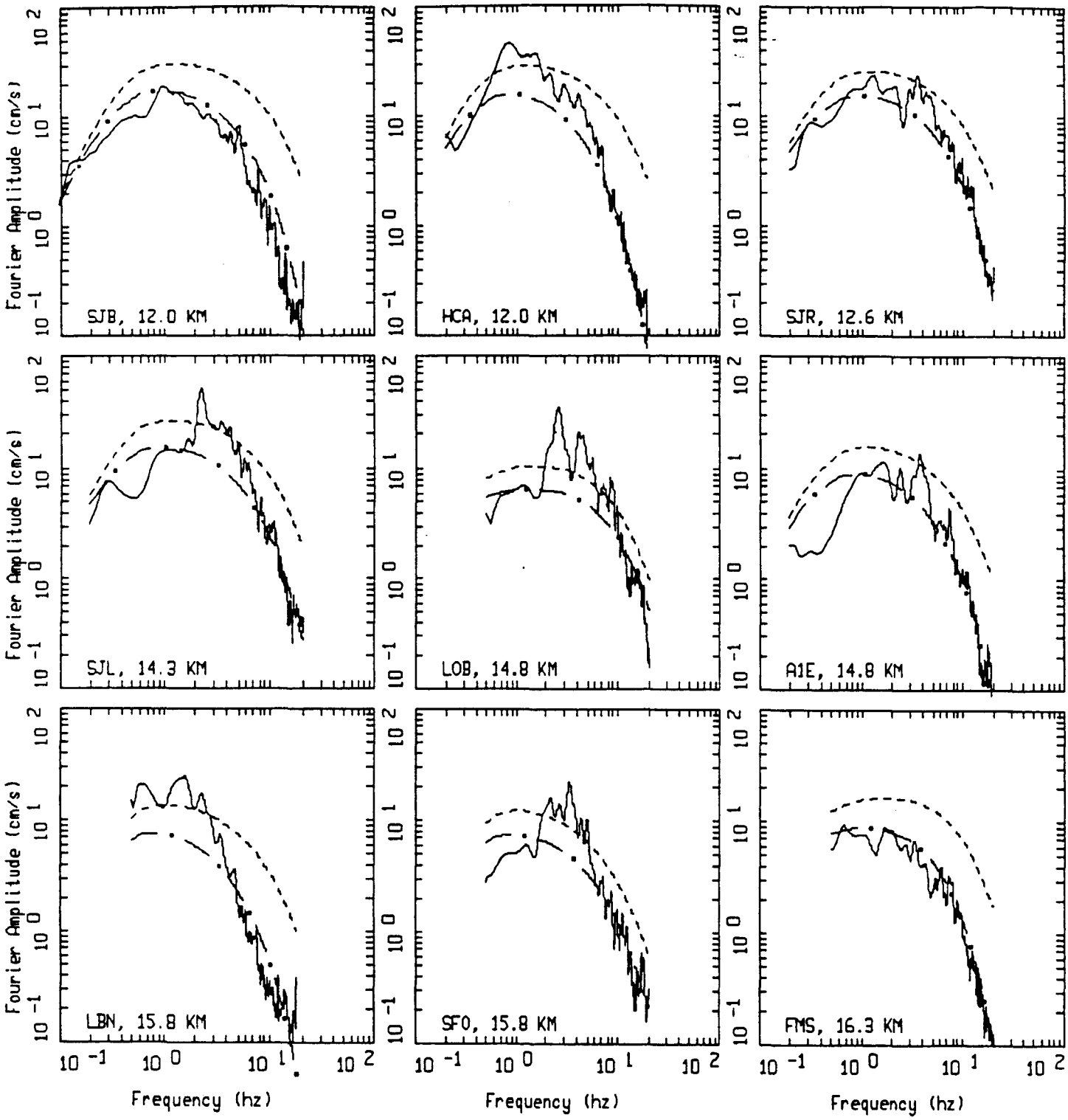

MORGAN HILL EARTHQUAKE, M=6.2, PAGE 3 OF 4.

LEGEND

——— DATA

- - - - - INITIAL MODEL

— • — FINAL MODEL

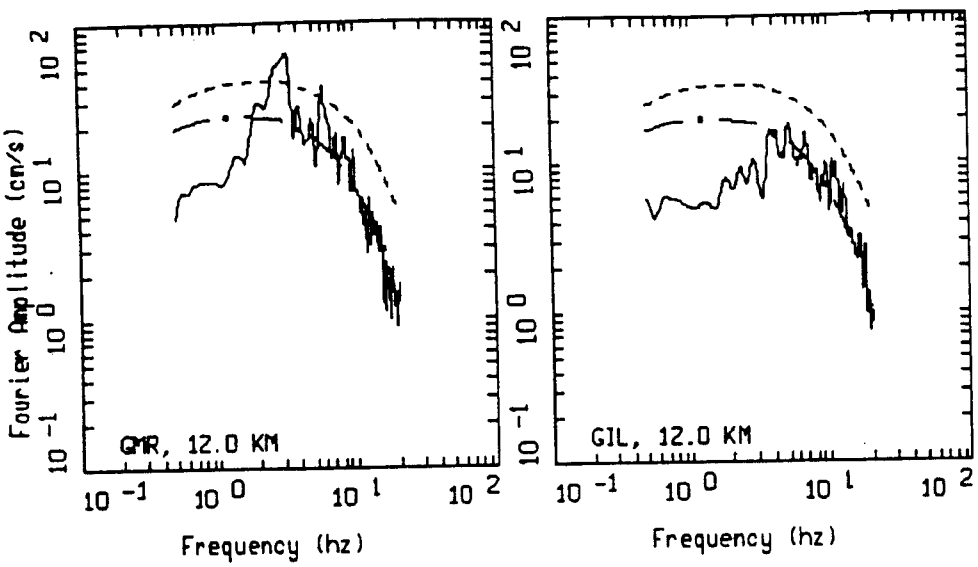

LEGEND

——— DATA

- - - - - INITIAL MODEL

—•— FINAL MODEL

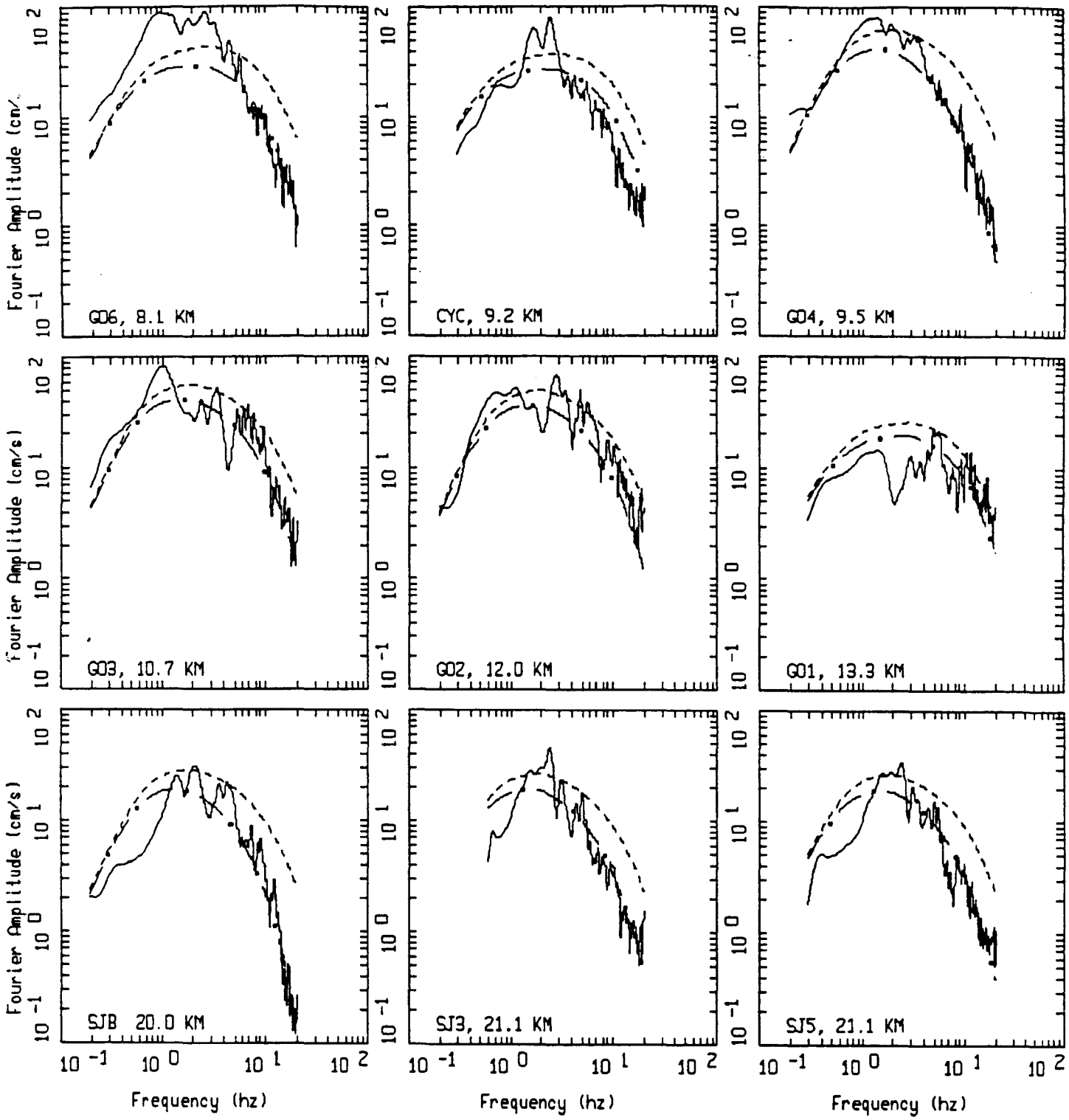

COYOTE LAKE EARTHQUAKE, M=5.7, PAGE 1 OF 2.

Figure Set 4.3

LEGEND

——— DATA

- - - - - INITIAL MODEL

—•— FINAL MODEL

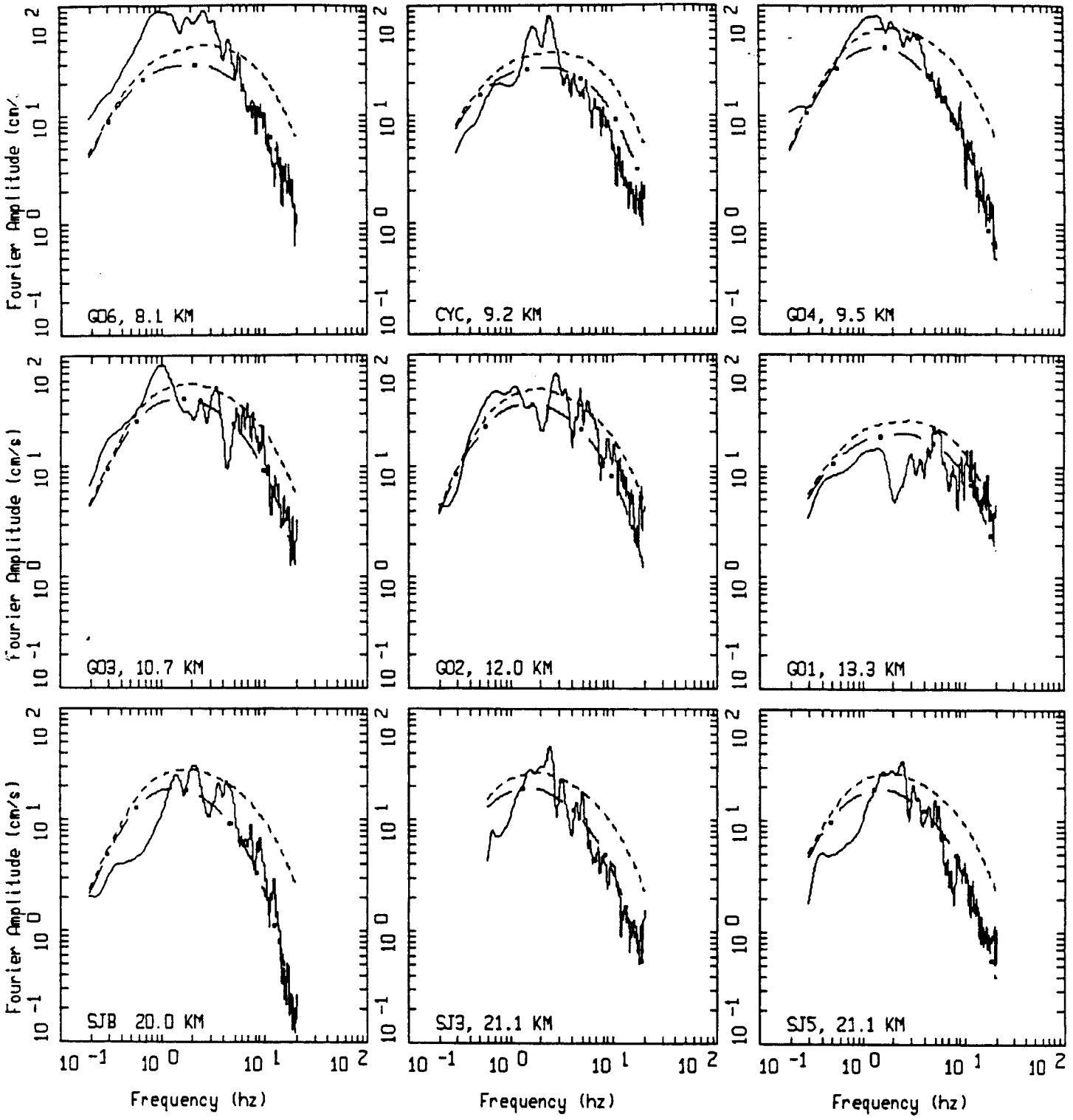

COYOTE LAKE EARTHQUAKE, M=5.7, PAGE 1 OF 2.

Figure Set 4.3

LEGEND

——— DATA

- - - - - INITIAL MODEL

—•— FINAL MODEL

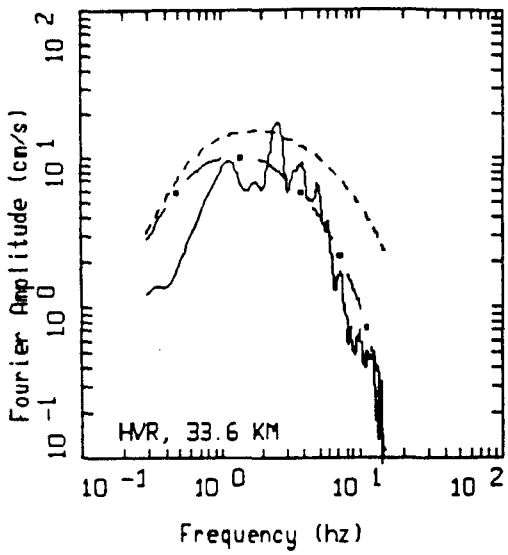

COYOTE LAKE EARTHQUAKE, M=5.7, PAGE 2 OF 2.

LEGEND

——— DATA

- - - - - INITIAL MODEL

—— • —— FINAL MODEL

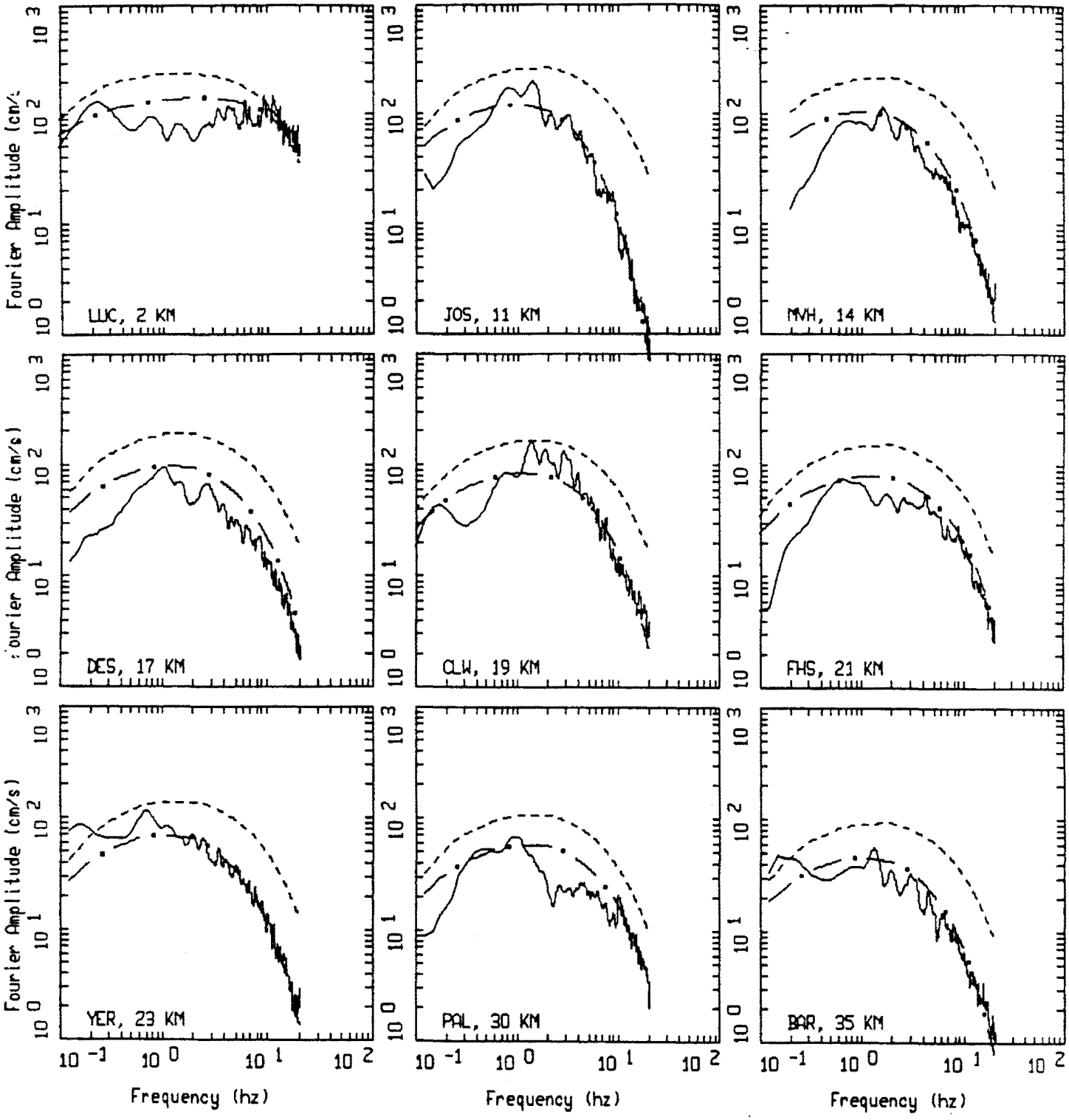

LANDERS EARTHQUAKE, M=6.0, PAGE 1 OF 7.

Figure Set 4.4

LEGEND

——— DATA

- - - - - INITIAL MODEL

— • — FINAL MODEL

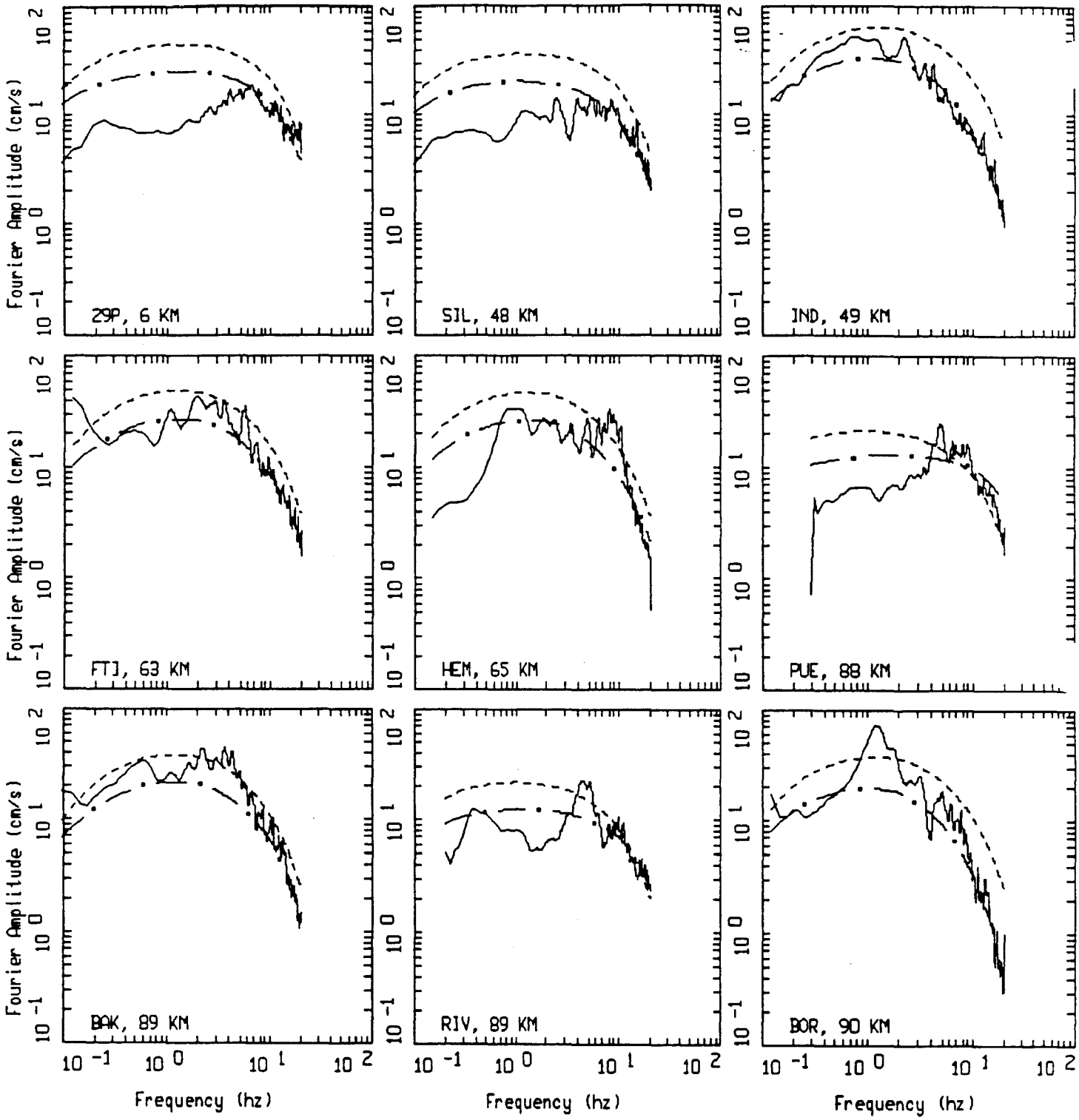

LANDERS EARTHQUAKE, M=6.0, PAGE 2 OF 7.

LEGEND

DATA

INITIAL MODEL

FINAL MODEL

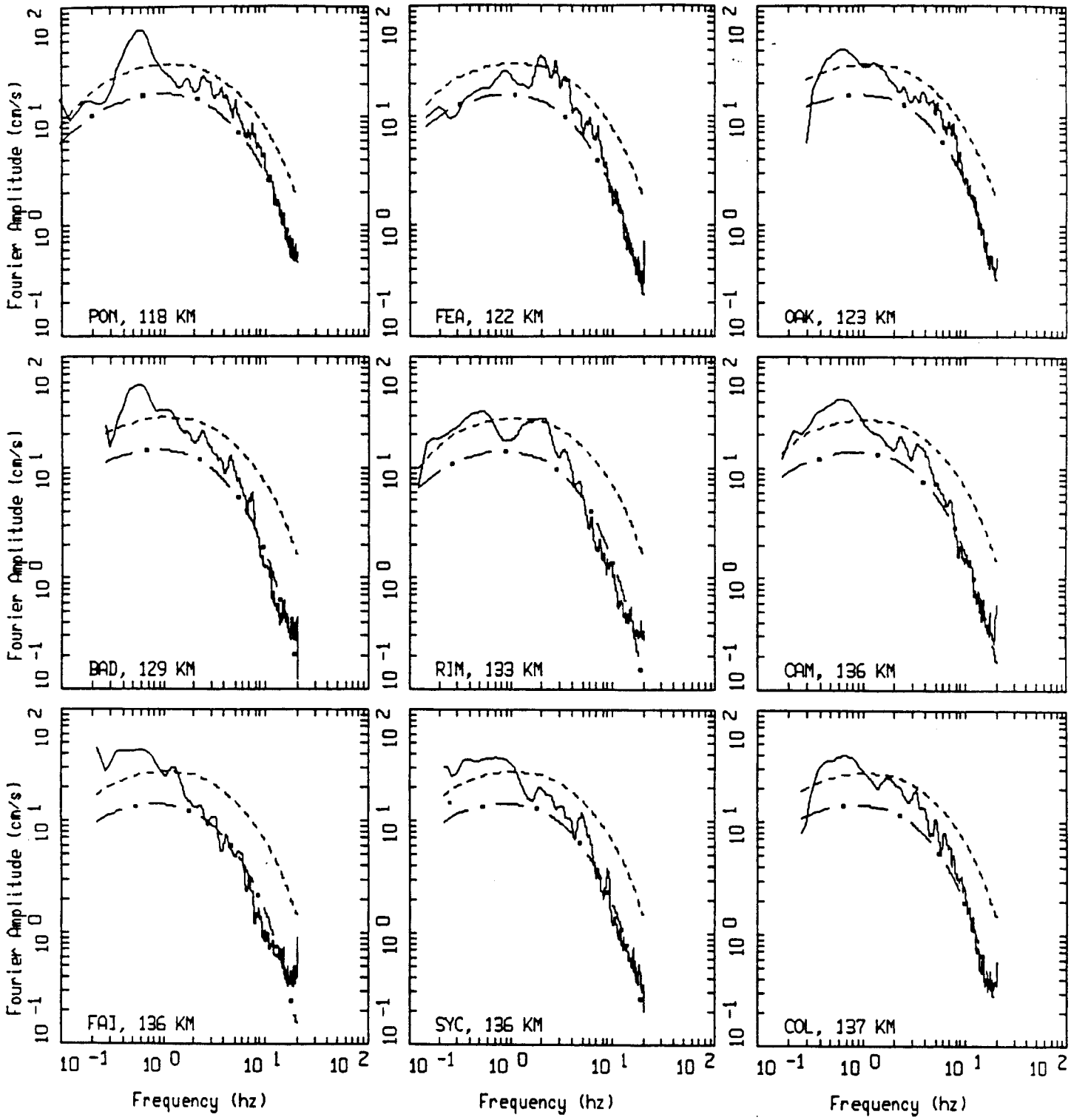

LANDERS EARTHQUAKE, M=6.0, PAGE 3 OF 7.

LEGEND

——— DATA

- - - - - INITIAL MODEL

— • — FINAL MODEL

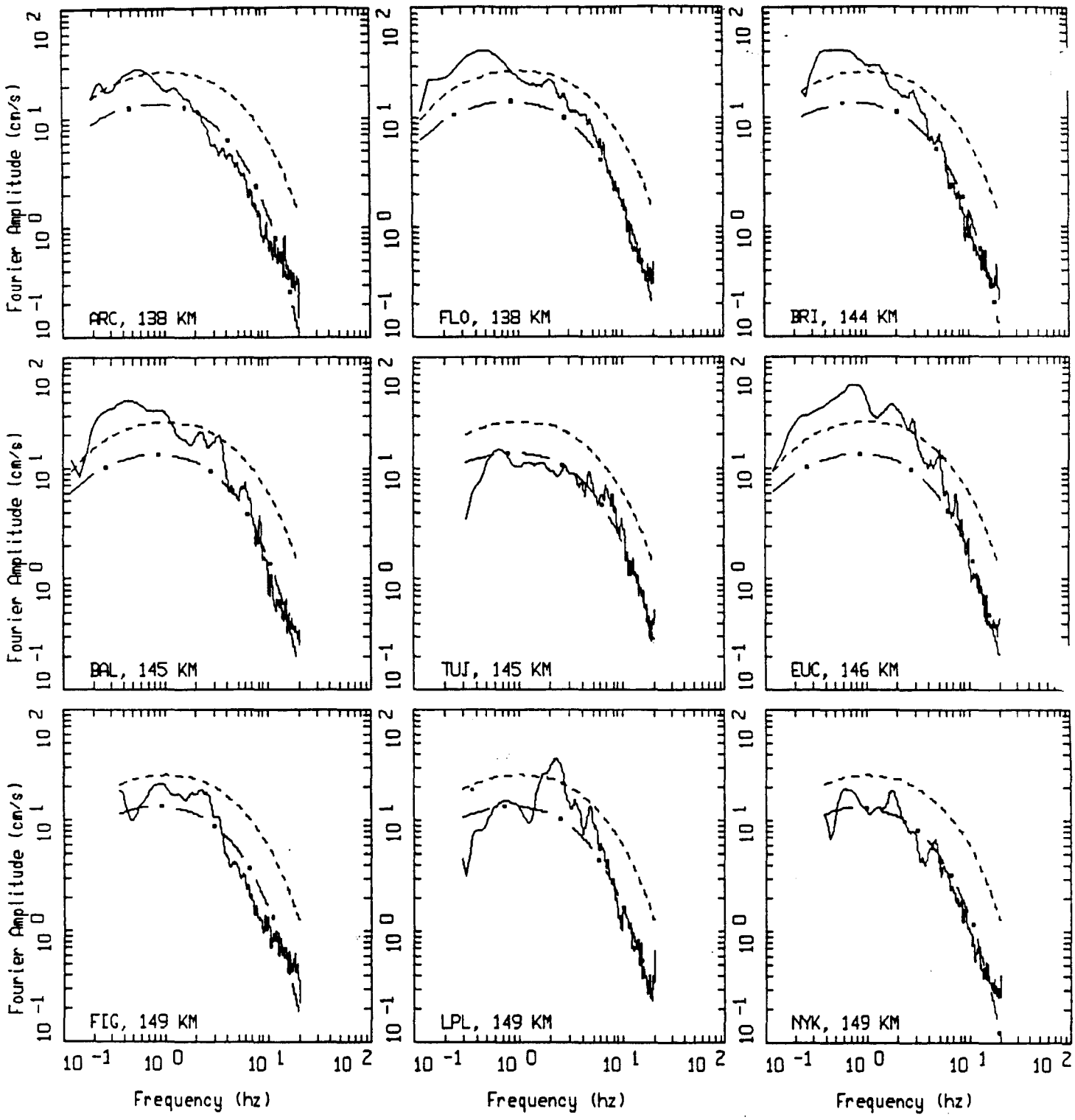

LANDERS EARTHQUAKE, M=6.0, PAGE 4 OF 7.

LEGEND

DATA

INITIAL MODEL

FINAL MODEL

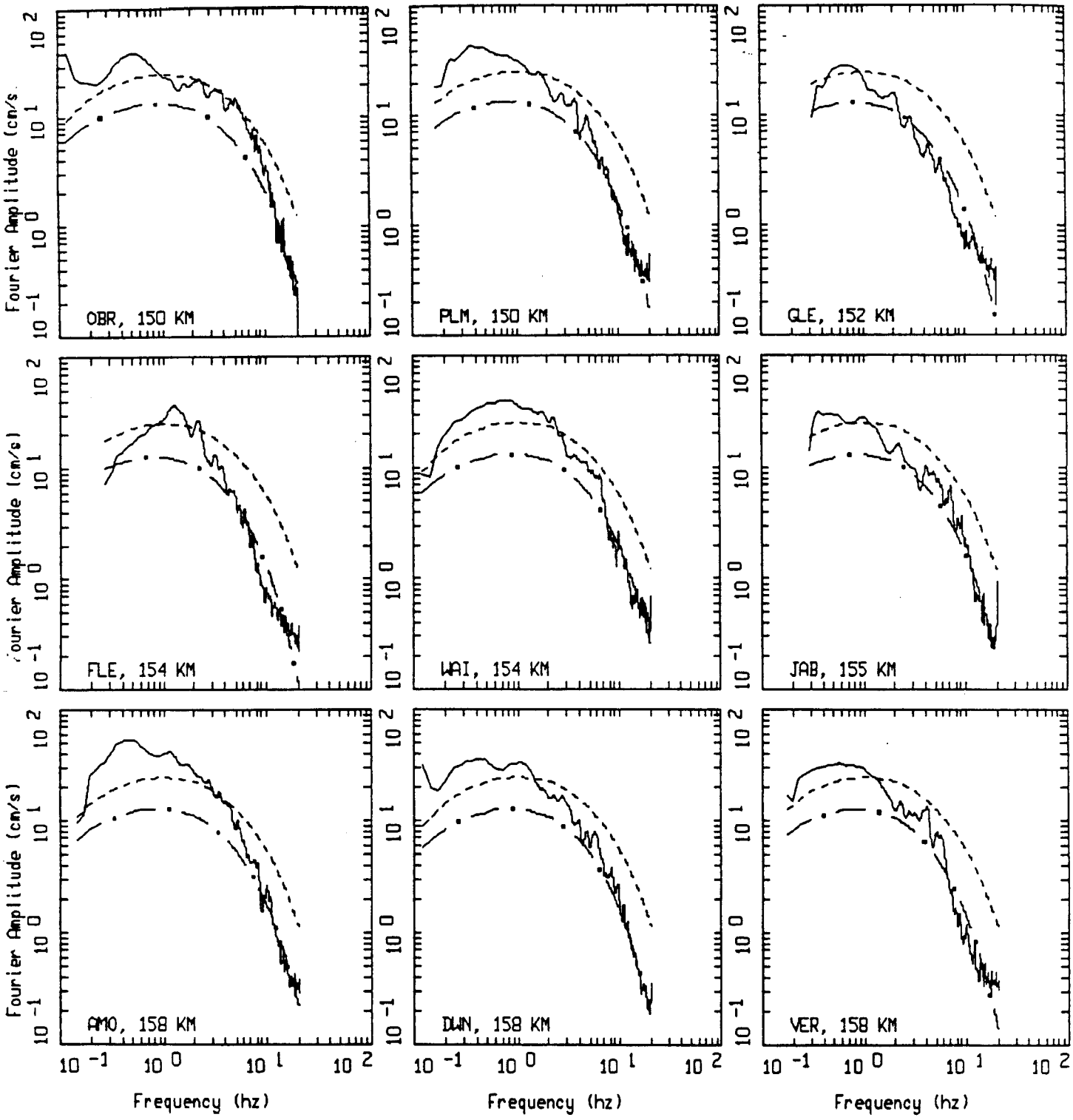

LANDERS EARTHQUAKE, M=6.0, PAGE 5 OF 7.

LEGEND

DATA

INITIAL MODEL

FINAL MODEL

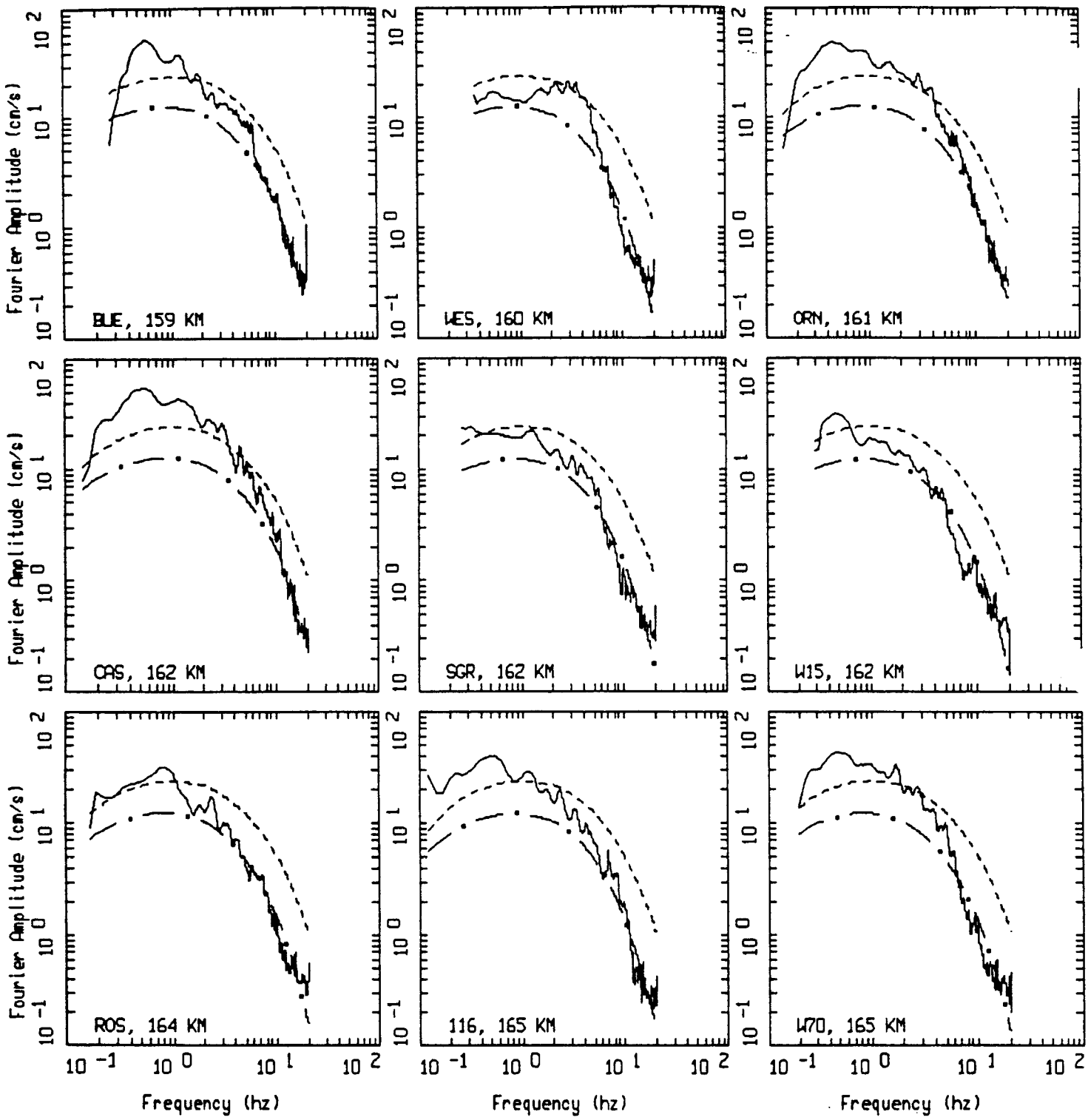

LANDERS EARTHQUAKE, M=6.0, PAGE 6 OF 7.

LEGEND

DATA

INITIAL MODEL

FINAL MODEL

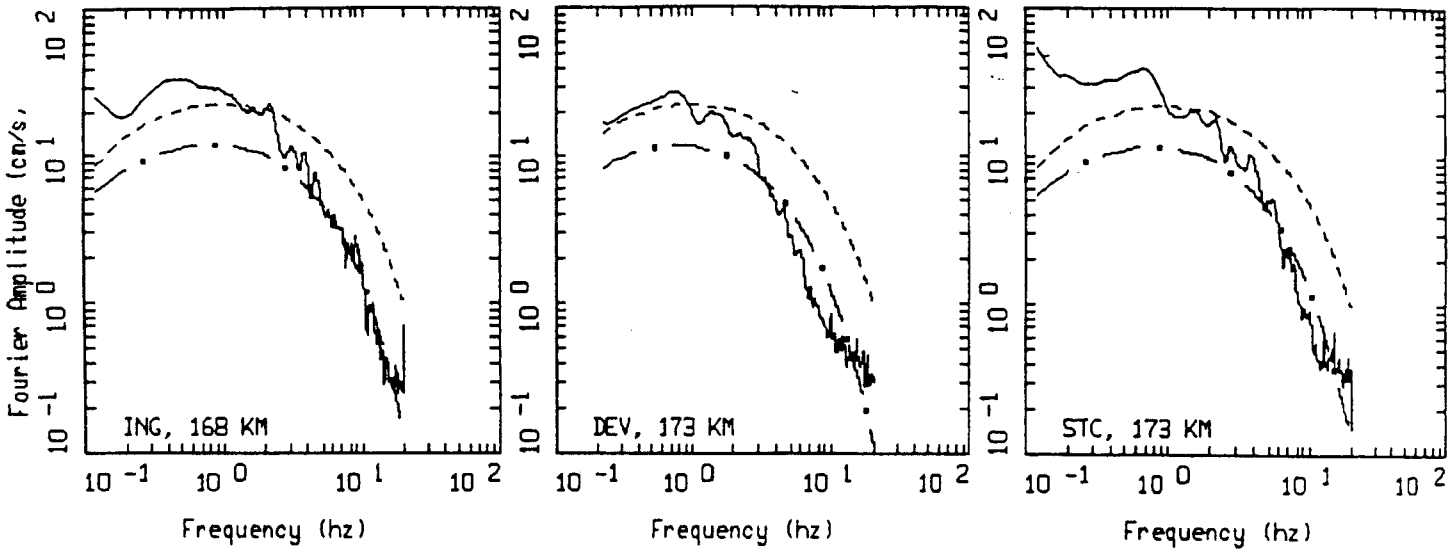

LANDERS EARTHQUAKE, M=6.0, PAGE 7 OF 7.

LEGEND

——— DATA

- - - - - INITIAL MODEL

— • — FINAL MODEL

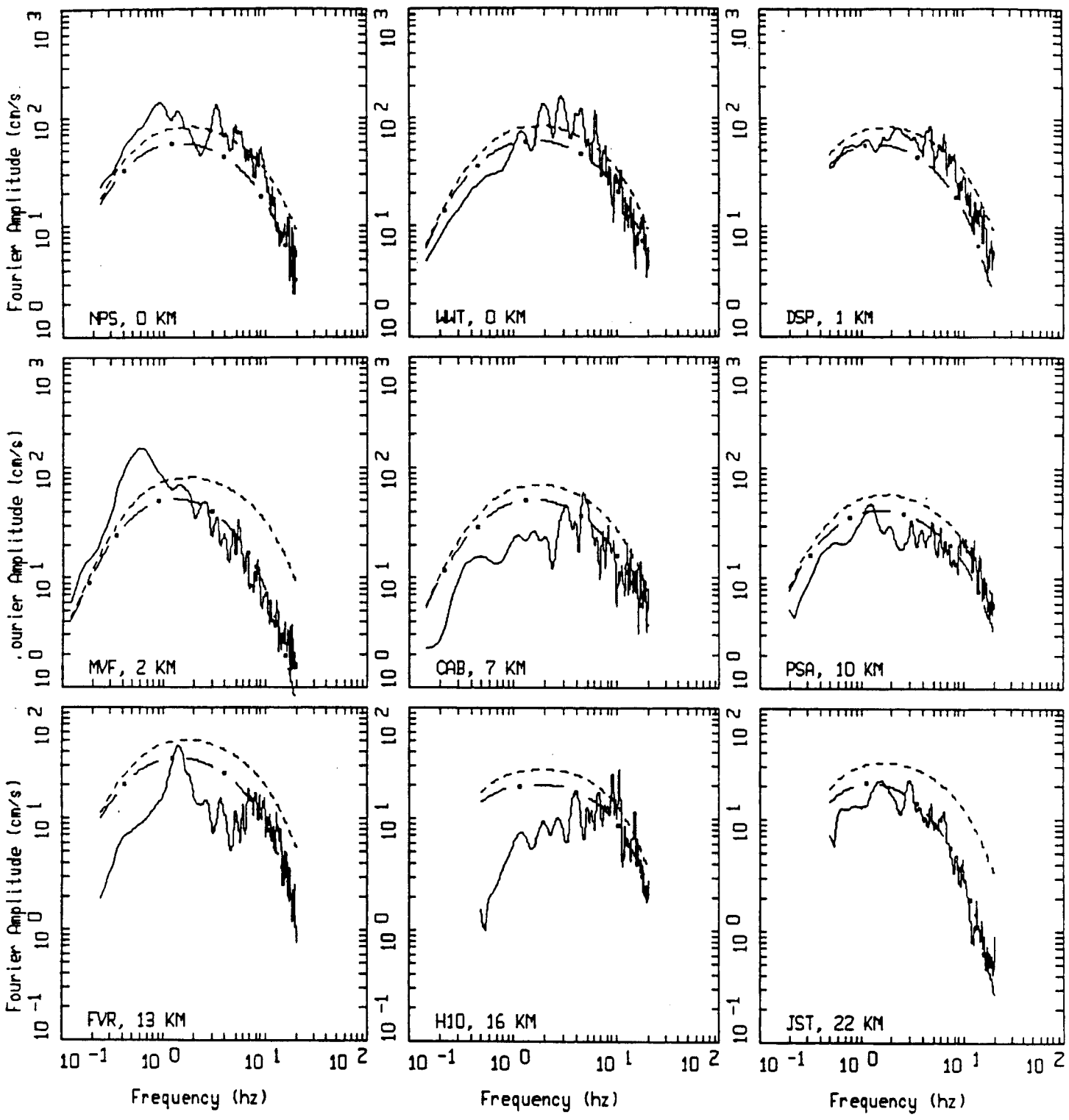

N PALM SPRINGS EARTHQUAKE, M=6.0, PAGE 1 OF 4.

Figure Set 4.4

LEGEND

——— DATA

- - - - - INITIAL MODEL

— • — FINAL MODEL

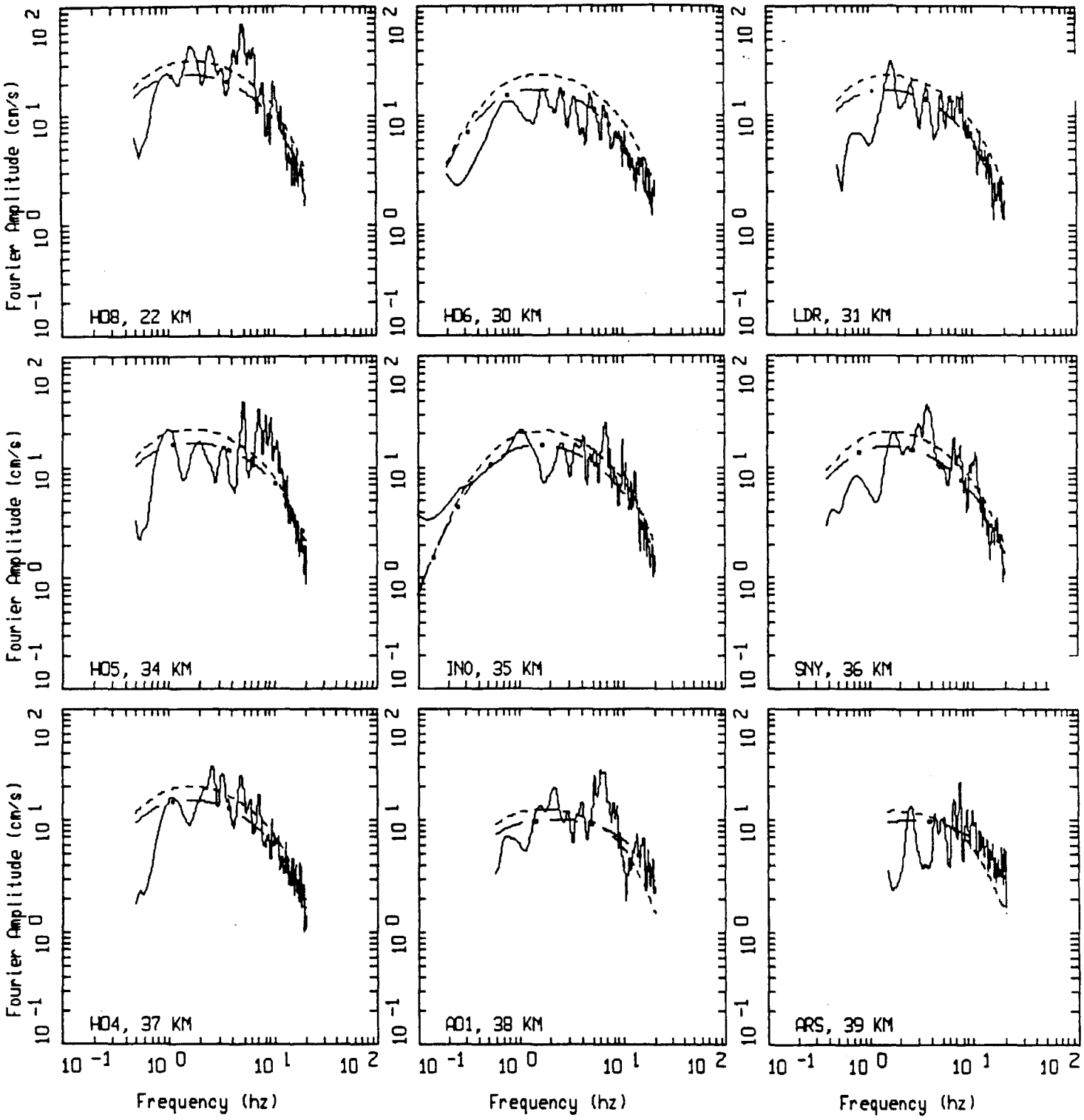

N PALM SPRINGS EARTHQUAKE, M=6.0, PAGE 2 OF 4.

LEGEND

——— DATA

- - - - - INITIAL MODEL

— • — FINAL MODEL

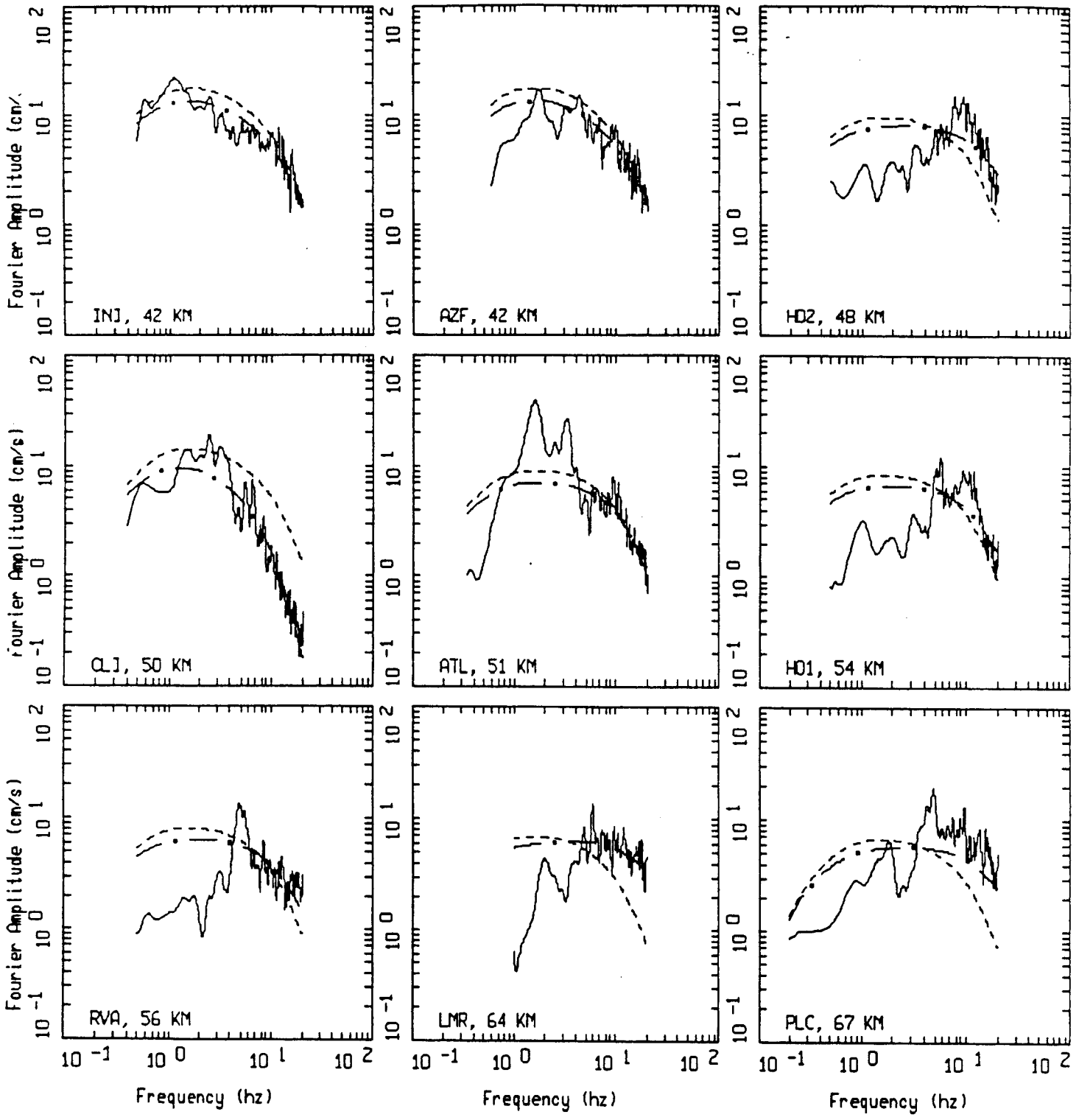

N PALM SPRINGS EARTHQUAKE, M=6.0, PAGE 3 OF 4.

LEGEND

DATA

INITIAL MODEL

FINAL MODEL

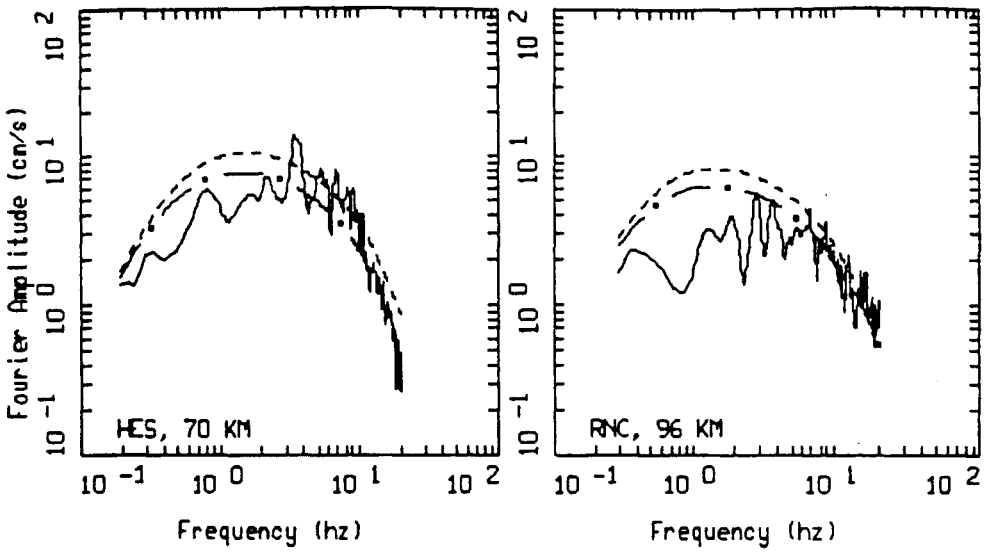

N PALM SPRINGS EARTHQUAKE, M=6.0, PAGE 4 OF 4.

LEGEND

——— DATA

- - - - - INITIAL MODEL

—— • —— FINAL MODEL

Chapter 5 Figure Captions

Figure 5.1. Site location map for the Northridge earthquake.

Figure 5.2. Slip model for the Northridge earthquake (from Wald and Heaton, 1994a).

Figure 5.3. Model bias and variability estimates for the Northridge earthquake computed over all 94 sites for the point-source model.

Figure 5.4. Model bias and variability estimates for the Northridge earthquake computed over all 71 soil sites for the point-source model.

Figure 5.5. Model bias and variability estimates for the Northridge earthquake computed over all 23 rock sites for the point-source model.

Figure Set 5.6. Comparison of average horizontal component 5% damped pseudo relative absolute response spectra: recorded motions (solid lines), point-source simulations (dashed lines).

Figure 5.7. Median and $\pm$ 1 σ 5% damped pseudo absolute acceleration response spectra computed from 30 randomly generated soft rock profiles using correlation model of Appendix C (solid lines) to a depth of 100 ft. The dashed line is the response spectrum computed using the base case soft rock profile (Figure 3.2). Same as Figure 3.7.

Figure 5.8. Median and $\pm$ 1 σ 5% damped pseudo absolute acceleration response spectra computed from 30 randomly generated deep soil profiles using the correlation model of Appendix C and with depth varying from 100 to 1,000 ft (solid line). The dashed line is the response spectrum computed using the base case deep soil profile (Figure 3.4). Same as Figure 3.5.

Figure 5.9. Model bias and variability estimates for the Northridge earthquake computed over all 94 sites for the finite-source model.

Figure 5.10. Model bias and variability estimates for the Northridge earthquake computed over all 71 soil sites for the finite-source model.

Figure 5.11. Model bias and variability estimates for the Northridge earthquake computed over all 23 rock sites for the finite-source model.

Figure Set 5.12. Comparison of average horizontal component 5% damped pseudo relative absolute response spectra: recorded motions (solid lines), finite-source simulations (dashed lines).

Figure 5.13. Model bias and variability estimates for the Northridge earthquake computed over all 48 sites within 30 km for the finite-source model.

Chapter 5 Figure Captions

Figure 5.14. Model bias and variability estimates for the Northridge earthquake computed over all 36 soil sites within 30 km for the finite-source model.

Figure 5.15. Model bias and variability estimates for the Northridge earthquake computed over all 12 rock sites within 30 km for the finite-source model.

Figure 5.16a. Model bias and variability estimates for the Northridge earthquake computed over all 71 soil sites for the finite-source model. EPRI G/G_{max} and hysteretic damping curves.

Figure 5.16b. Comparison of bias estimates for the Northridge earthquake computed over all 71 soil sites: Solid lines, generic deep soil G/G_{max} and hysteretic damping curves. Dotted lines, EPRI G/G_{max} and hysteretic damping curves.

Figure 5.17a. Model bias and variability estimates for the Northridge earthquake computed over all 36 soil sites within 30 km for the finite-source model. EPRI G/G_{max} hysteretic damping curves.

Figure 5.17b. Comparison of bias estimates for the Northridge earthquake computed over all 36 soil sites within 30 km: Solid lines, generic deep soil G/G_{max} and hysteretic damping curves. Dotted lines, EPRI G/G_{max} and hysteretic damping curves.

Chapter 5 Figure Captions

Figure 5.18. Comparison of bias estimates for the Northridge earthquake computed over all 36 soil sites within 30 km: Solid lines, generic deep soil G/G_{max} and hysteretic damping curves. Dotted lines, linear site response using fixed small strain properties.

Figure 5.19. Comparison of bias estimates for the Northridge earthquake computed over all 35 soil sites beyond 30 km: Solid lines, generic deep soil G/G_{max} and hysteretic damping curves. Dotted lines, linear site response using fixed small strain properties.

Figure 5.20. Site location map for the San Fernando earthquake.

Figure 5.21. Slip model for the San Fernando earthquake (from Heaton, 1982).

Figure 5.22. Model bias and variability estimates for the San Fernando earthquake computed over all 39 sites for the point-source model.

Figure 5.23. Model bias and variability estimates for the San Fernando earthquake computed over all 18 soil sites for the point-source model.

Figure 5.24. Model bias and variability estimates for the San Fernando earthquake computed over all 21-rock sites for the point-source model.

Figure Set 5.25. Comparison of average horizontal component 5% damped pseudo relative absolute response spectra: recorded motions (solid lines), point-source simulations (dashed lines).

Figure 5.26. Model bias and variability estimates for the San Fernando earthquake computed over all 39 sites for the Finite-source model.

Figure 5.27. Model bias and variability estimates for the San Fernando earthquake computed over all 18 soil sites for the finite-source model.

Figure 5.28. Model bias and variability estimates for the San Fernando earthquake computed over all 21 rock sites for the finite-source model.

Figure Set 5.29. Comparison of average horizontal component 5% damped pseudo relative absolute response spectra: recorded motions (solid lines), finite-source simulations (dashed lines).

Figure 5.30. Site location map for the Whittier Narrows earthquake.

Figure 5.31. Slip model for the Whittier Narrows earthquake (from Hartzell and Iida, 1990).

Figure 5.32. Model bias and variability estimates for the Whittier Narrows earthquake computed over all 88 sites for the point-source model.

Figure 5.33. Model bias and variability estimates for the Whittier Narrows earthquake computed over all 70 soil sites for the point-source model.

Figure 5.34. Model bias and variability estimates for the Whittier Narrows earthquake computed over all 18 rock sites for the point-source model.

Figure Set 5.35. Comparison of average horizontal component 5% damped pseudo relative absolute response spectra: recorded motions (solid lines), point-source simulations (dashed lines).

Figure 5.36. Model bias and variability estimates for the Whittier Narrows earthquake computed over all 88 sites for the finite-source model.

Figure 5.37. Model bias and variability estimates for the Whittier Narrows earthquake computed over all 70 soil sites for the finite-source model.

Figure 5.38. Model bias and variability estimates for the Whittier Narrows earthquake computed over all 17 rock sites for the finite-source model.

Figure 5.39. Model bias and variability estimates for the Whittier Narrows earthquake computed over all 53 soil sites within 30 km for the finite-source model.

Figure 5.40. Model bias and variability estimates for the Whittier Narrows earthquake computed over all 10 rock sites within 30 km for the finite-source model.

Figure Set 5.41. Comparison of average horizontal component 5% damped pseudo relative absolute response spectra: recorded motions (solid lines), finite-source simulations (dashed lines).

Figure 5.42. Site location map for the Loma Prieta earthquake.

Figure 5.43. Slip model for the Loma Prieta earthquake (from Wald et al., 1991).

Figure 5.44. Model bias and variability estimates for the Loma Prieta earthquake computed over all 53 sites for the point-source model.

Figure 5.45. Model bias and variability estimates for the Loma Prieta earthquake computed over all 20 soil sites for the point-source model.

Chapter 5 Figure Captions

Figure 5.46. Model bias and variability estimates for the Loma Prieta earthquake computed over all 33 rock sites for the point-source model.

Figure Set 5.47. Comparison of average horizontal component 5% damped pseudo relative absolute response spectra: recorded motions (solid lines), point-source simulations (dashed lines).

Figure 5.48. Model bias and variability estimates for the Loma Prieta earthquake computed over all 53 sites for the finite-source model.

Figure 5.49. Model bias and variability estimates for the Loma Prieta earthquake computed over all 20 soil sites for the finite-source model.

Figure 5.50. Model bias and variability estimates for the Loma Prieta earthquake computed over all 33 rock sites for the finite-source model.

Figure Set 5.51. Comparison of average horizontal component 5% damped pseudo relative absolute response spectra: recorded motions (solid lines), finite-source simulations (dashed lines).

Figure 5.52. Model bias and variability estimates for the Loma Prieta earthquake computed over all 30 sites within 30 km for the finite-source model.

Chapter 5 Figure Captions

Figure 5.53. Model bias and variability estimates for the Loma Prieta earthquake computed over all 17 soil sites within 30 km for the finite-source model.

Figure 5.54. Model bias and variability estimates for the Loma Prieta earthquake computed over all 13 rock sites within 30 km for the finite-source model.

Figure 5.55a. Model bias and variability estimates for the Loma Prieta earthquake computed over all 20 soil sites for the finite-source model. Generic deep soil G/G_{max} and hysteretic damping curves.

Figure 5.55b. Comparison of bias estimates for the Loma Prieta earthquake computed over all 20 soil sites: Solid lines, EPRI G/G_{max} and hysteretic damping curves. Dotted lines, generic deep soil G/G_{max} and hysteretic damping curves.

Figure 5.56a. Model bias and variability estimates for the Loma Prieta earthquake computed over all 17 soil sites within 30 km for the finite-source model. Generic deep soil G/G_{max} hysteretic damping curves.

Chapter 5 Figure Captions

Figure 5.56b. Comparison of bias estimates for the Loma Prieta earthquake computed over all 17 soil sites within 30 km: Solid lines, EPRI soil G/G_{max} and hysteretic damping curves. Dotted lines, generic deep soil G/G_{max} and hysteretic damping curves.

Figure 5.57. Model bias and variability estimates for the Loma Prieta earthquake computed over all 17 soil sites within 30 km for the finite-source model. Linear site response using fixed small strain properties.

Figure 5.58. Site location map for the Coyote Lake earthquake.

Figure 5.59. Slip model for the Coyote Lake earthquake (from Liu and Helmberger, 1983).

Figure 5.60. Model bias and variability estimates for the Coyote Lake earthquake computed over all 10 sites for the point-source model.

Figure 5.61. Comparison of average horizontal component 5% damped pseudo relative absolute response spectra: recorded motions (solid lines), point-source simulations (dashed lines).

Figure 5.62. Model bias and variability estimates for the Coyote Lake earthquake computed over all 10 sites for the finite-source model.

Figure 5.63. Comparison of average horizontal component 5% damped pseudo relative absolute response spectra: recorded motions (solid lines), finite-source simulations (dashed lines).

Figure 5.64. Site location map for the Morgan Hill earthquake.

Figure 5.65. Slip model for the Morgan Hill earthquake (from Hartzell and Heaton, 1986).

Figure 5.66. Model bias and variability estimates for the Morgan Hill earthquake computed over all 29 sites for the point-source model.

Figure 5.67. Model bias and variability estimates for the Morgan Hill earthquake computed over all 21 soil sites for the point-source model.

Figure 5.68. Model bias and variability estimates for the Morgan Hill earthquake computed over all 8 rock sites for the point-source model.

Figure Set 5.69. Comparison of average horizontal component 5% damped pseudo relative absolute response spectra: recorded motions (solid lines), point-source simulations (dashed lines).

Figure 5.70. Model bias and variability estimates for the Morgan Hill earthquake computed over all 29 sites for the finite-source model.

Figure 5.71. Model bias and variability estimates for the Morgan Hill earthquake computed over all 21 soil sites for the point-source model.

Figure 5.72. Model bias and variability estimates for the Morgan Hill earthquake computed over all 8 rock sites for the point-source model.

Figure Set 5.73. Comparison of average horizontal component 5% damped pseudo relative absolute response spectra: recorded motions (solid lines), finite-source simulations (dashed lines).

Figure 5.74. Site location map for the Landers earthquake.

Figure 5.75. Slip model for the Landers earthquake (from Wald and Heaton, 1994b).

Figure 5.76. Model bias and variability estimates for the Landers earthquake computed over all 57 sites for the point-source model.

Figure 5.77. Model bias and variability estimates for the Landers earthquake computed over all 39 sites located in the Los Angeles area for the point-source model.

Figure 5.78. Model bias and variability estimates for the Landers earthquake computed over all 18 sites located in the Mojave geologic province for the point-source model.

Figure Set 5.79. Comparison of average horizontal component 5% damped pseudo relative absolute response spectra: recorded motions (solid lines), point-source simulations (dashed lines).

Figure 5.80. Model bias and variability estimates for the Landers earthquake computed over all 57 sites for the finite-source model.

Figure 5.81. Model bias and variability estimates for the Landers earthquake computed over all 39 sites located in the Los Angeles area for the finite-source model.

Figure 5.82. Model bias and variability estimates for the Landers earthquake computed over all 18 sites located in the Mojave geologic province for the finite-source model.

Figure Set 5.83. Comparison of average horizontal component 5% damped pseudo relative absolute response spectra: recorded motions (solid lines), finite-source simulations (dashed lines).

Figure 5.84. Site location map for the North Palm Springs earthquake.

Figure 5.85. Slip model for the North Palm Springs earthquake (from Hartzell, 1989).

Figure 5.86. Model bias and variability estimates for the North Palm Springs earthquake computed over all 29 sites for the point-source model.

Figure 5.87. Model bias and variability estimates for the North Palm Springs earthquake computed over all 20 soil sites for the point-source model.

Figure 5.88. Model bias and variability estimates for the North Palm Springs earthquake computed over all 9 rock sites for the point-source model.

Figure Set 5.89. Comparison of average horizontal component 5% damped pseudo relative absolute response spectra: recorded motions (solid lines), point-source simulations (dashed lines).

Figure 5.90. Model bias and variability estimates for the North Palm Springs earthquake computed over all 29 sites for the finite-source model.

Figure 5.91. Model bias and variability estimates for the North Palm Springs earthquake computed over all 20 soil sites for the point-source model.

Figure 5.92. Model bias and variability estimates for the North Palm Springs earthquake computed over all 9 rock sites for the finite-source model.

Figure Set 5.93. Comparison of average horizontal component 5% damped pseudo relative absolute response spectra: recorded motions (solid lines), finite-source simulations (dashed lines).

Figure 5.94. Site location map for the Tabas earthquake.

Figure 5.95. Slip model for the Tabas earthquake (from Hartzell and Mendoza, 1991).

Figure 5.96. Comparison of Fourier amplitude spectra for the Tabas earthquake. Solid lines: recorded motion horizontal components vector sum divided by $\sqrt{2}$ (2 Hz wide triangular smoothing window). Dashed lines: initial model calculations. Dash-dotted lines: final model calculations.

Figure 5.97. Model bias and variability estimates for the Tabas earthquake computed over all 4 sites for the point-source model.

Figure 5.98. Comparison of average horizontal component 5% damped pseudo relative absolute response spectra: recorded motions (solid lines), point-source simulations (dashed lines).

Figure 5.99. Model bias and variability estimates for the Tabas earthquake computed over all 4 sites for the finite-source model.

Figure 5.100. Comparison of average horizontal component 5% damped pseudo relative absolute response spectra: recorded motions (solid lines), finite-source simulations (dashed lines).

Figure 5.101. Site location map for the Imperial Valley earthquake.

Figure 5.102. Top 500 ft of the generic Imperial Valley shear-wave velocity profile.

Figure 5.103. Generic Imperial Valley crustal model (from Liu and Helmberger, 1985).

Figure 5.104. Slip model for the Imperial Valley earthquake (from Hartzell and Heaton, 1983).

Figure Set 5.105. Comparison of Fourier amplitude spectra for the Imperial Valley mainshock. Solid lines: recorded motion horizontal components vector sum divided by $\sqrt{2}$ (2 Hz wide triangular smoothing window). Dashed lines: initial model calculations. Dash-dotted lines: final model calculations.

Figure Set 5.106. Comparison of Fourier amplitude spectra for the Imperial Valley aftershock. Solid lines: recorded motion horizontal components vector sum divided by $\sqrt{2}$ (2 Hz wide triangular smoothing window). Dashed lines: initial model calculations. Dash-dotted lines: final model calculations.

Figure 5.107. Model bias and variability estimates for the Imperial Valley aftershock earthquake computed over all 16 sites for the point-source model.

Figure Set 5.108. Comparison of average horizontal component 5% damped pseudo relative absolute response spectra: recorded motions (solid lines), point-source simulations (dashed lines).

Figure 5.109. Model bias and variability estimates for the Imperial Valley mainshock earthquake computed over all 35 sites for the point-source model.

Figure 5.110. Model bias and variability estimates for the Imperial Valley mainshock earthquake computed over all 33 soil sites for the point-source model.

Figure Set 5.111. Comparison of average horizontal component 5% damped pseudo relative absolute response spectra: recorded motions (solid lines), point-source simulations (dashed lines).

Figure 5.112. Comparison of bias estimates for the Imperial Valley mainshock earthquake computed over all 15 sites located the El Centro area within 15 km using 3 suites of G/G_{max} and hysteretic damping curves as well as linear site response analyses using fixed small strain material properties.

Figure 5.113. Generic G/G_{max} and hysteretic damping curves for Imperial Valley soils.

Figure 5.114. Model bias and variability estimates for the Imperial Valley mainshock earthquake computed over all 35 sites for the finite-source model.

Figure 5.115. Model bias and variability estimates for the Imperial Valley mainshock earthquake computed over all 33 soil sites for the finite-source model.

Figure Set 5.116. Comparison of average horizontal component 5% damped pseudo relative absolute response spectra: recorded motions (solid lines), finite-source simulations (dashed lines).

Figure 5.117. Site location map for the Nahanni earthquake.

Figure 5.118. Slip model for the Nahanni earthquake (from Hartzell et al., 1994).

Figure 5.119. Comparison of Fourier amplitude spectra for the Nahanni earthquake. Solid lines: recorded motion horizontal components vector sum divided by $\sqrt{2}$ (2 Hz wide triangular smoothing window). Dashed lines: initial model calculations. Dash-dotted lines: final model calculations.

Figure 5.120. Comparison of average horizontal component 5% damped pseudo relative absolute response spectra: recorded motions (solid lines), point-source simulations (dashed lines).

Figure 5.121. Model bias and variability estimates for the Nahanni earthquake computed over all 3 sites for the point-source model.

Figure 5.122. Comparison of average horizontal component 5% damped pseudo relative absolute response spectra: recorded motions (solid lines), finite-source simulations (dashed lines).

Figure 5.123. Model bias and variability estimates for the Nahanni earthquake computed over all 3 sites for the finite-source model.

Figure 5.124. Site location map for the Superstition Hills earthquake.

Figure 5.125. Slip model for the Superstition Hills earthquake (from Wald et al., 1990).

Figure Set 5.126. Comparison of Fourier amplitude spectra for the Superstition Hills(B) earthquake. Solid lines: recorded motion horizontal components vector sum divided by $\sqrt{2}$ (2 Hz wide triangular smoothing window). Dashed lines: initial model calculations. Dash-dotted lines: final model calculations.

Figure 5.127. Model bias and variability estimates for the Superstition Hills(B) earthquake computed over all 11 sites for the point-source model.

Figure 5.128. Comparison of average horizontal component 5% damped pseudo relative absolute response spectra: recorded motions (solid lines), point-source simulations (dashed lines).

Figure 5.129. Model bias and variability estimates for the Superstition Hills(B) earthquake computed over all 11 sites for the finite-source model.

Figure 5.130. Comparison of average horizontal component 5% damped pseudo relative absolute response spectra: recorded motions (solid lines), finite-source simulations (dashed lines).

Figure 5.131. Site location map for the Saguenay earthquake.

Figure 5.132. Slip model for the Tabas earthquake (from Hartzell et al., 1994).

Figure Set 5.133. Comparison of Fourier amplitude spectra for the Saguenay earthquake. Solid lines: recorded motion horizontal components vector sum divided by $\sqrt{2}$ (2 Hz wide triangular smoothing window). Dashed lines: initial model calculations. Dash-dotted lines: final model calculations.

Figure 5.134. Model bias and variability estimates for the Saguenay earthquake computed over all 22 sites for the point-source model.

Figure 5.135. Comparison of average horizontal component 5% damped pseudo relative absolute response spectra: recorded motions (solid lines), point-source simulations (dashed lines).

Figure 5.136. Model bias and variability estimates for the Saguenay earthquake computed over all 22 sites for the finite-source model.

Figure 5.137. Comparison of average horizontal component 5% damped pseudo relative absolute response spectra: recorded motions (solid lines), finite-source simulations (dashed lines).

Figure 5.138. Site location map for the Little Skull Mountain earthquake.

Figure 5.139. Slip model for the Little Skull Mountain earthquake. Best fit model from a random suite of slip distributions.

Figure set 5.140. Comparison of Fourier amplitude spectra for the Little Skull Mountain earthquake. Solid lines: recorded motion horizontal components vector sum divided by $\sqrt{2}$ (2 Hz wide triangular smoothing window). Dashed lines: initial model calculations. Dash-dotted lines: final model calculations.

Figure 5.141. Model bias and variability estimates for the Little Skull Mountain earthquake computed over all 8 sites for the point-source model.

Figure 5.142. Comparison of average horizontal component 5% damped pseudo relative absolute response spectra: recorded motions (solid lines), point-source simulations (dashed lines).

Figure 5.143. Model bias and variability estimates for the Little Skull Mountain earthquake computed over all 8 sites for the finite-source model.

Figure 5.144. Comparison of average horizontal component 5% damped pseudo relative absolute response spectra: recorded motions (solid lines), finite-source simulations (dashed lines).

Figure 5.145. Site location map for the Cape Mendocino earthquake.

Figure 5.146. Slip model for the Cape Mendocino earthquake (from Graves, 1994).

Figure 5.147. Comparison of Fourier amplitude spectra for the Cape Mendocino earthquake. Solid lines: recorded motion horizontal components vector sum divided by $\sqrt{2}$ (2 Hz wide triangular smoothing window). Dashed lines: initial model calculations. Dash-dotted lines: final model calculations.

Figure 5.148. Model bias and variability estimates for the Cape Mendocino earthquake computed over all 5 sites for the point-source model.

Figure 5.149. Comparison of average horizontal component 5% damped pseudo relative absolute response spectra: recorded motions (solid lines), point-source simulations (dashed lines).

Figure 5.150. Model bias and variability estimates for the Cape Mendocino earthquake computed over all 5 sites for the finite-source model.

Figure 5.151. Comparison of average horizontal component 5% damped pseudo relative absolute response spectra: recorded motions (solid lines), finite-source simulations (dashed lines).

Figure 5.152. Model bias and variability estimates for all earthquakes computed over all 503 sites for the point-source model.

Figure 5.153. Model bias and variability estimates for all earthquakes computed over all 344 soil sites for the point-source model.

Figure 5.154. Model bias and variability estimates for all earthquakes computed over all 159 rock sites for the point-source model.

Figure 5.155. Model bias and variability estimates for all earthquakes computed over all 487 sites for the finite-source model.

Figure 5.156. Model bias and variability estimates for all earthquakes computed over all 328 soil sites for the finite-source model.

Figure 5.157. Model bias and variability estimates for all earthquakes computed over all 159 rock sites for the finite-source model.

Figure 5.158. Model bias and variability estimates for all earthquakes computed over all 481 sites for the empirical model.

Figure 5.159. Model bias and variability estimates for all earthquakes computed over all 344 soil sites for the empirical model.

Figure 5.160. Model bias and variability estimates for all earthquakes computed over all 137 rock sites for the empirical model.

Figure 5.161. Best fitting rise times for the 15 earthquakes modeled using the stochastic finite-source ground motion model.

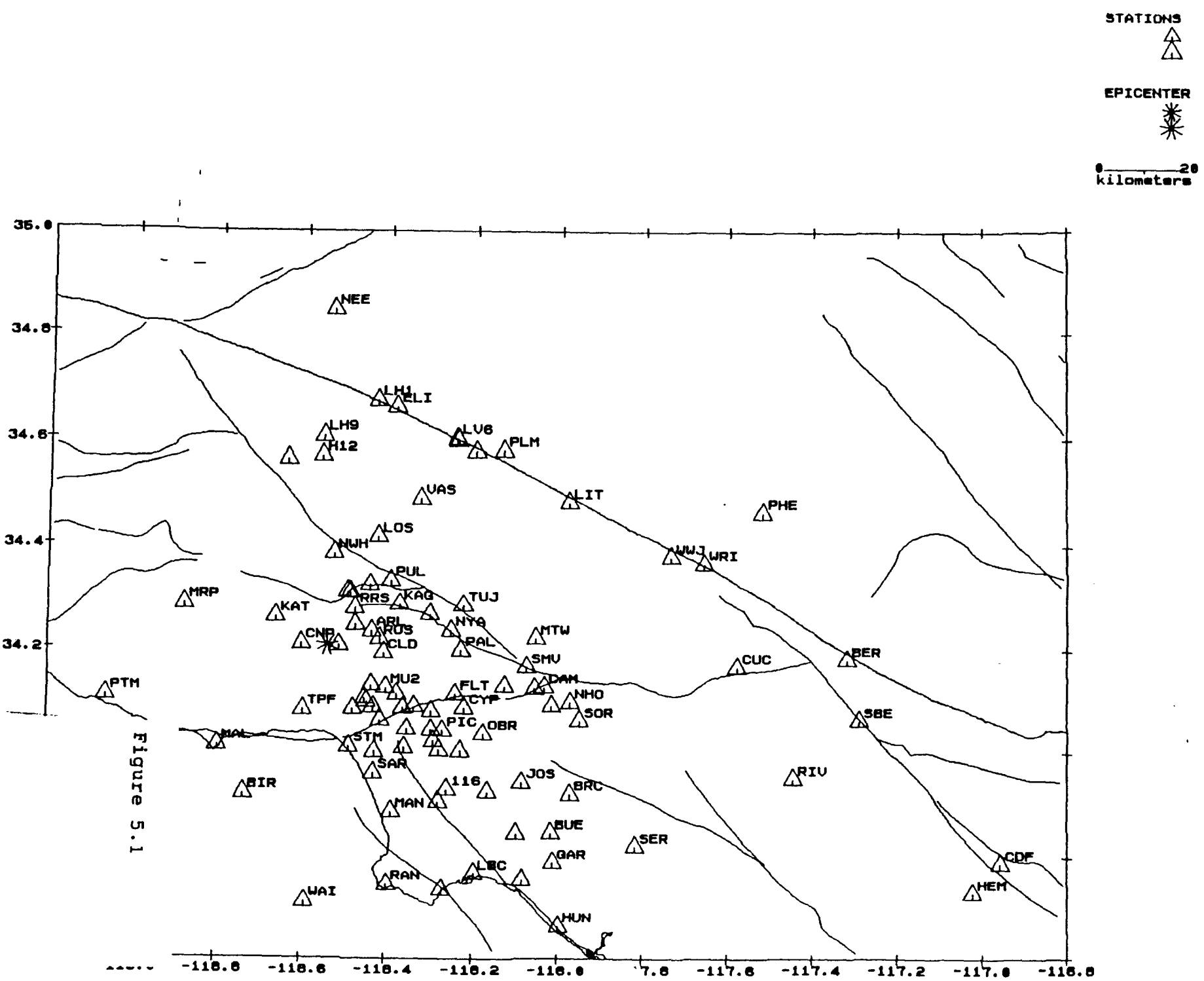

Figure 5.1

EQ3D-V4.00 FILE: SITES4.HP2 EPICENT.HP2
. SCA:1050000 MFAC:1.0 XFAC:1.0 Nm=95 Nx=0

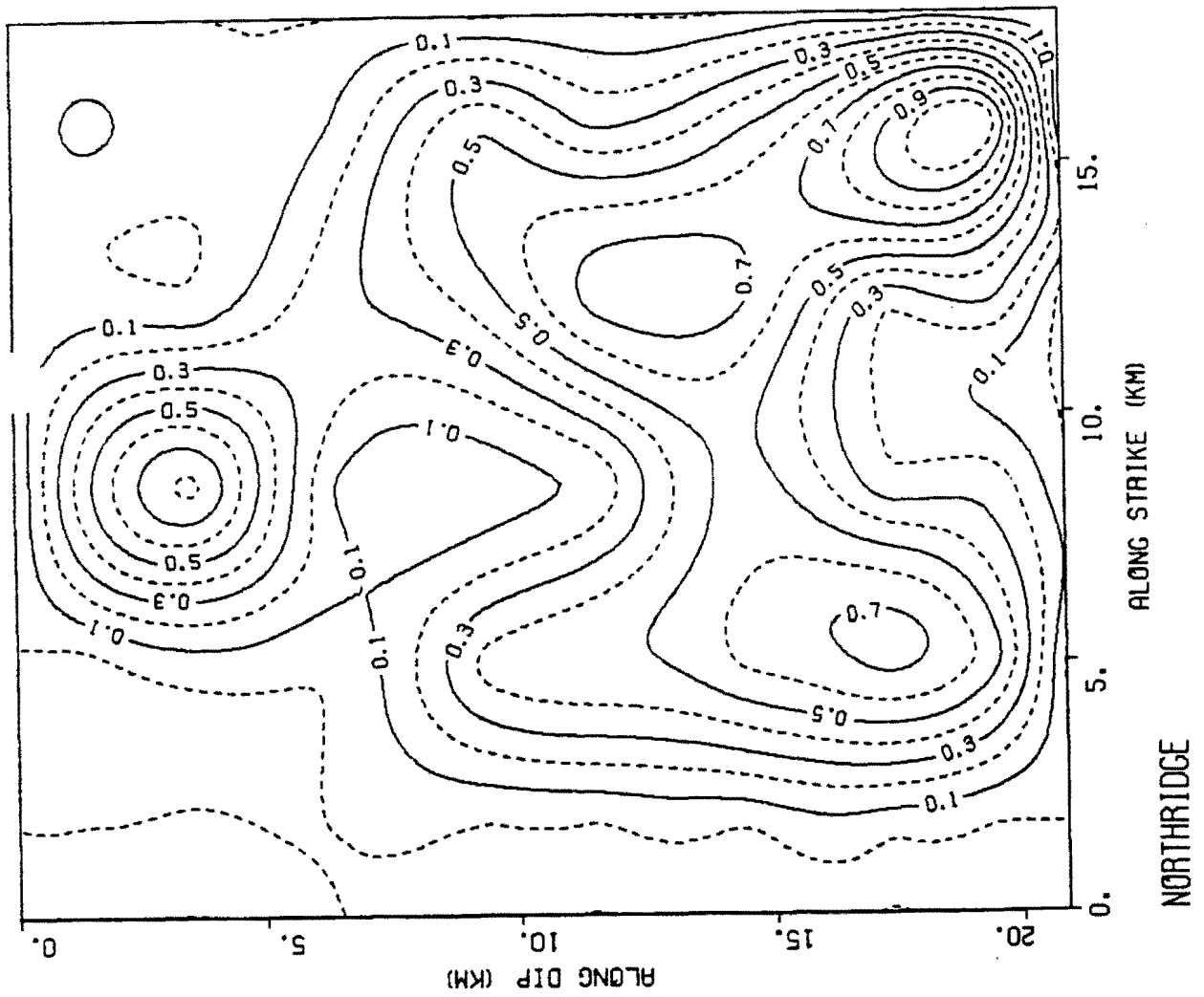
NORTHRIDGE
ALONG STRIKE (KM)
ALONG DIP (KM)
0.
5.
10.
15.
20.
0.1
0.3
0.5
0.7
0.9
1.0

Figure 5.2

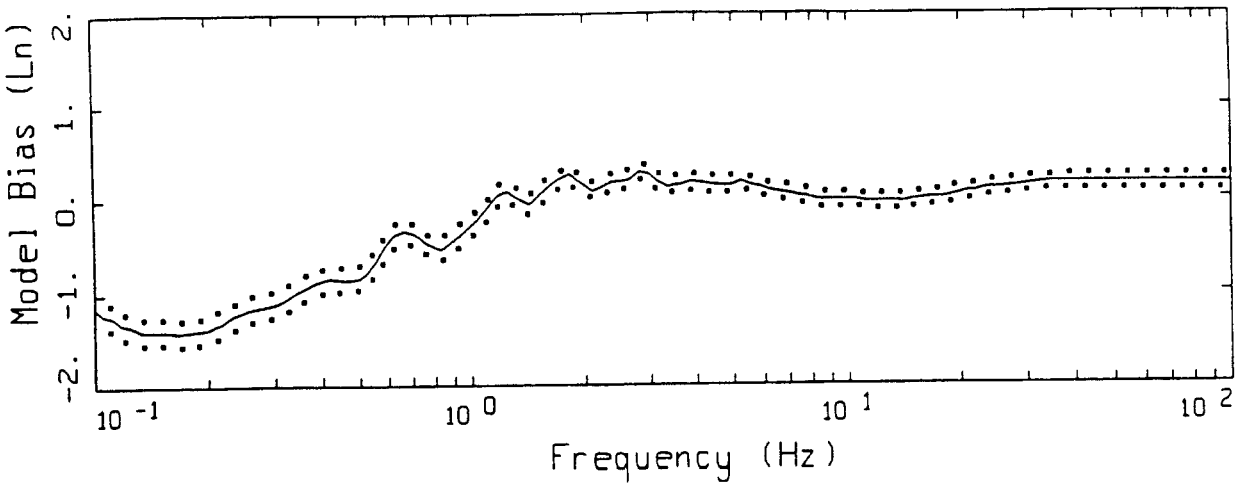

LEGEND
MODELING BIAS
90% CONFIDENCE INTERVAL OF MODELING BIAS
90% CONFIDENCE INTERVAL OF MODELING BIAS

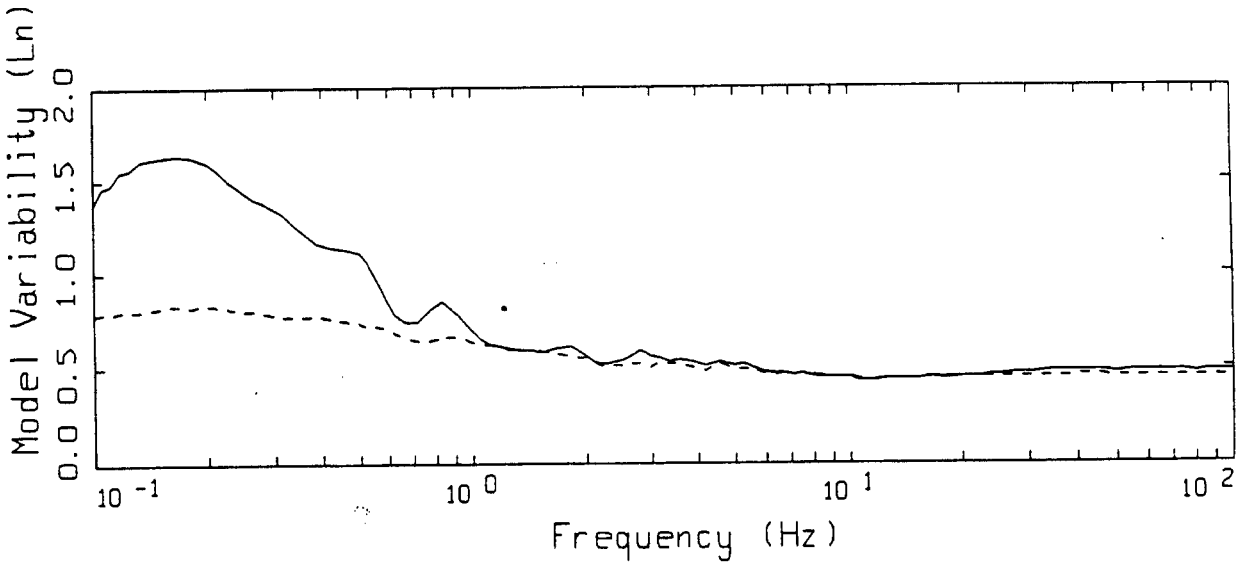

LEGEND
MEAN=0.0
BIAS CORRECTED

NORTHRIDGE POINT-SOURCE
NONLINEAR, ALL 94 SITES

Figure 5.3

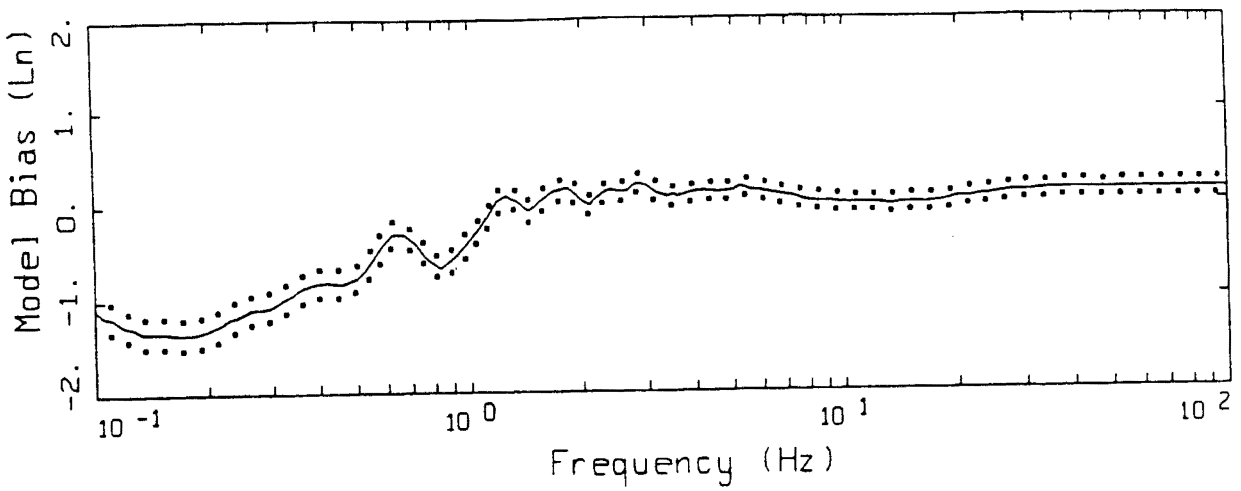

LEGEND
MODELING BIAS
90% CONFIDENCE INTERVAL OF MODELING BIAS
90% CONFIDENCE INTERVAL OF MODELING BIAS

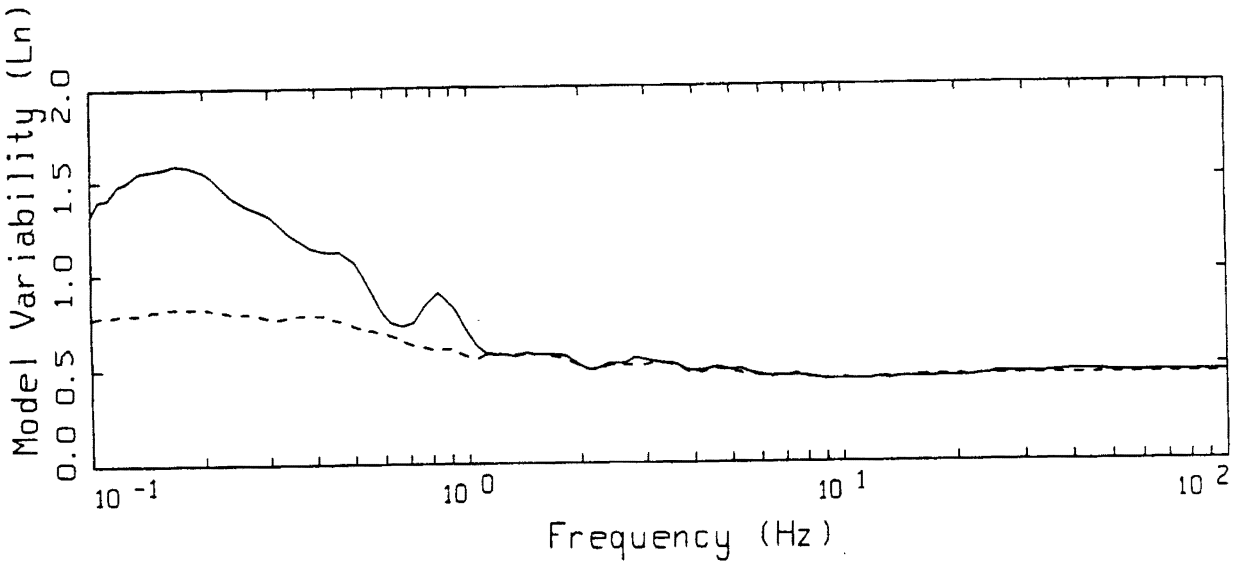

LEGEND
MEAN=0.0
BIAS CORRECTED

NORTHRIDGE POINT-SOURCE
NONLINEAR, 71 SOIL SITES

Figure 5.4

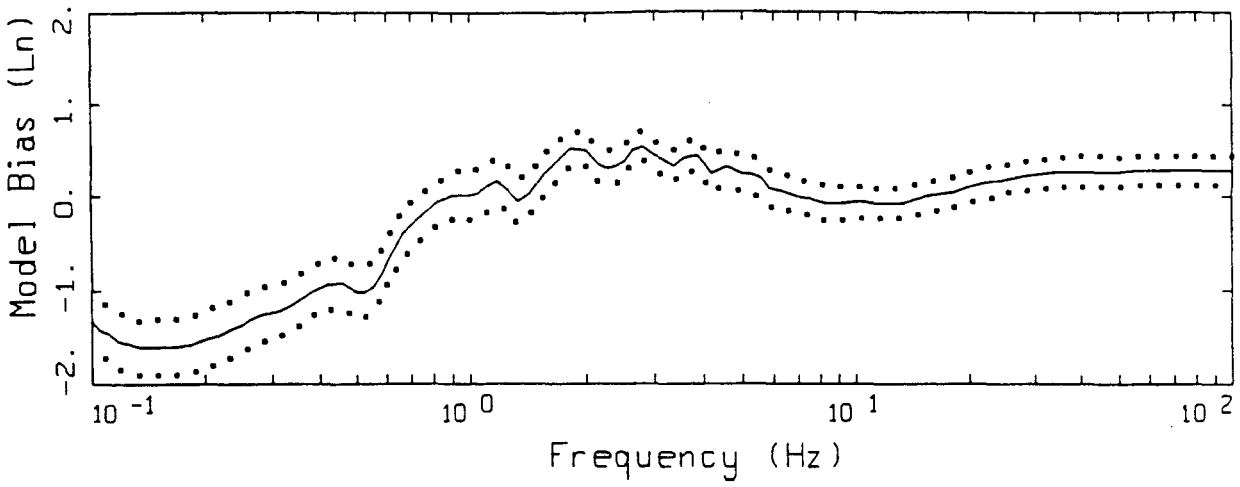

LEGEND
MODELING BIAS
90% CONFIDENCE INTERVAL OF MODELING BIAS
90% CONFIDENCE INTERVAL OF MODELING BIAS

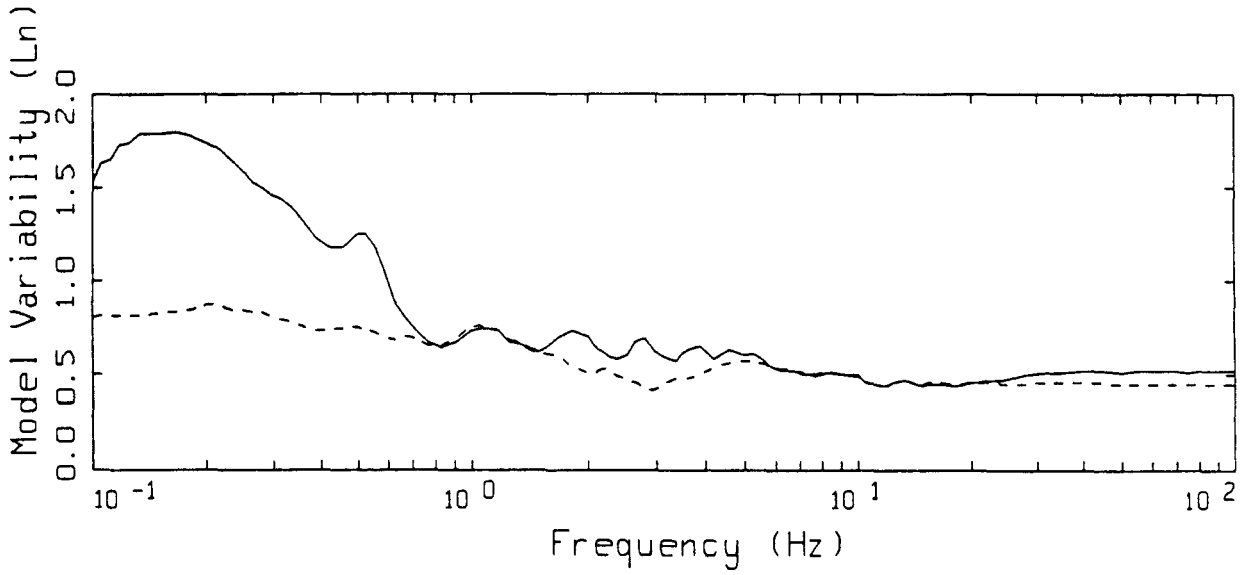

LEGEND
MEAN=0.0
BIAS CORRECTED

NORTHRIDGE POINT-SOURCE
NONLINEAR, 23 ROCK SITES

Figure 5.5

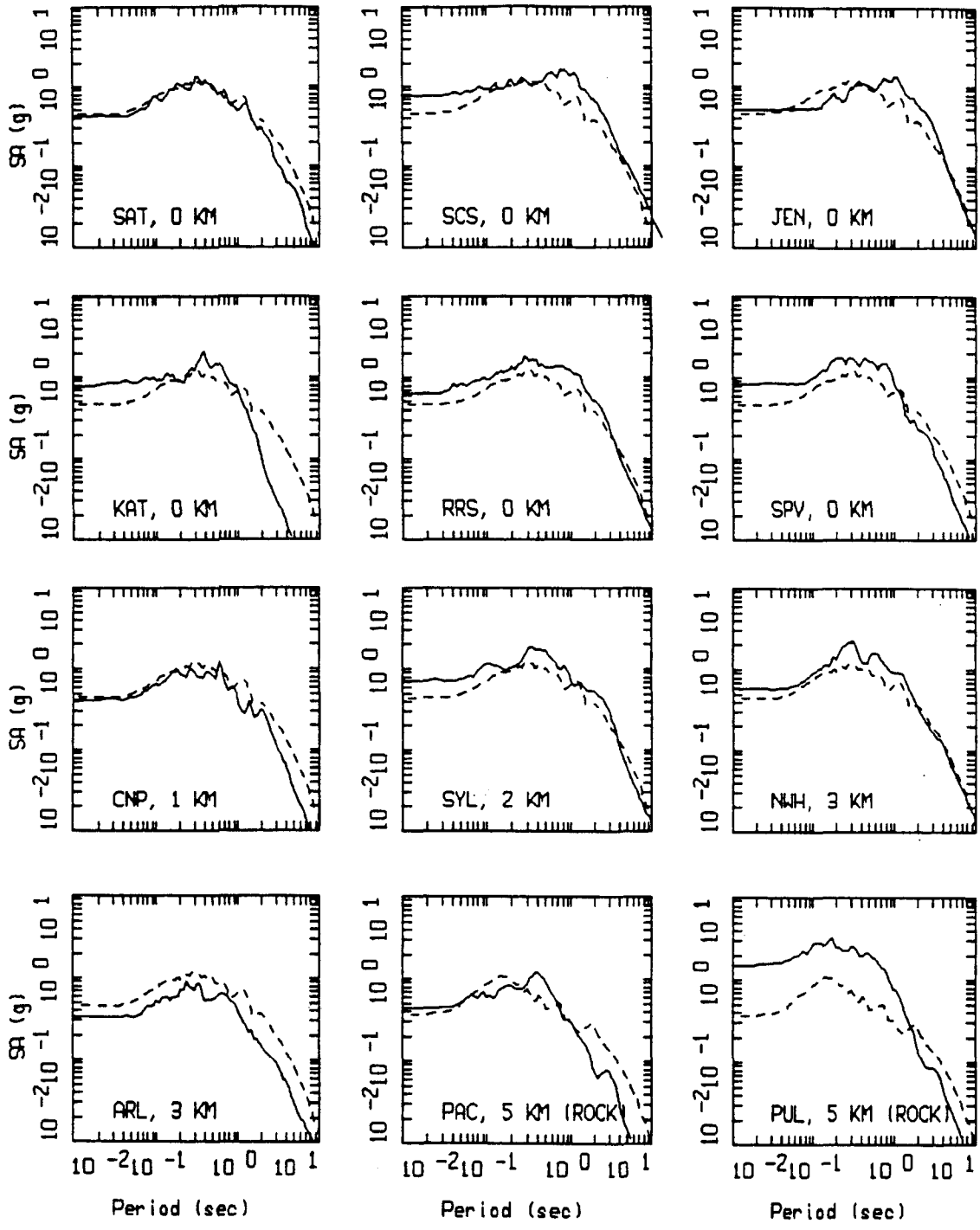

NORTHRIDGE, POINT SOURCE MODELING, PAGE 1 OF 8.
NONLINEAR PROFILES.

LEGEND
——— DATA
----- MODEL

Figure Set 5.6

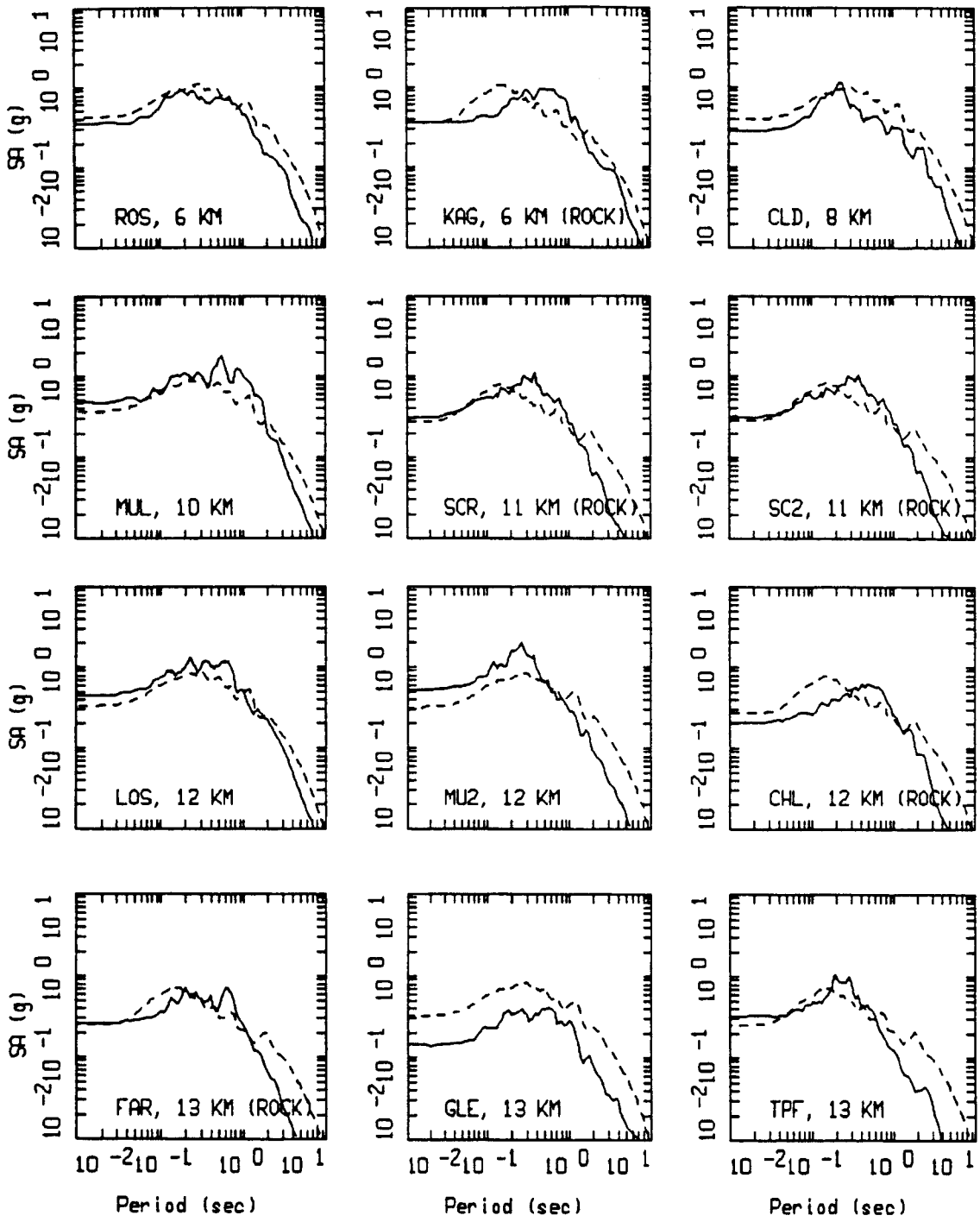

NORTHRIDGE, POINT SOURCE MODELING, PAGE 2 OF 8.
NONLINEAR PROFILES.

LEGEND
——— DATA
- - - - - MODEL

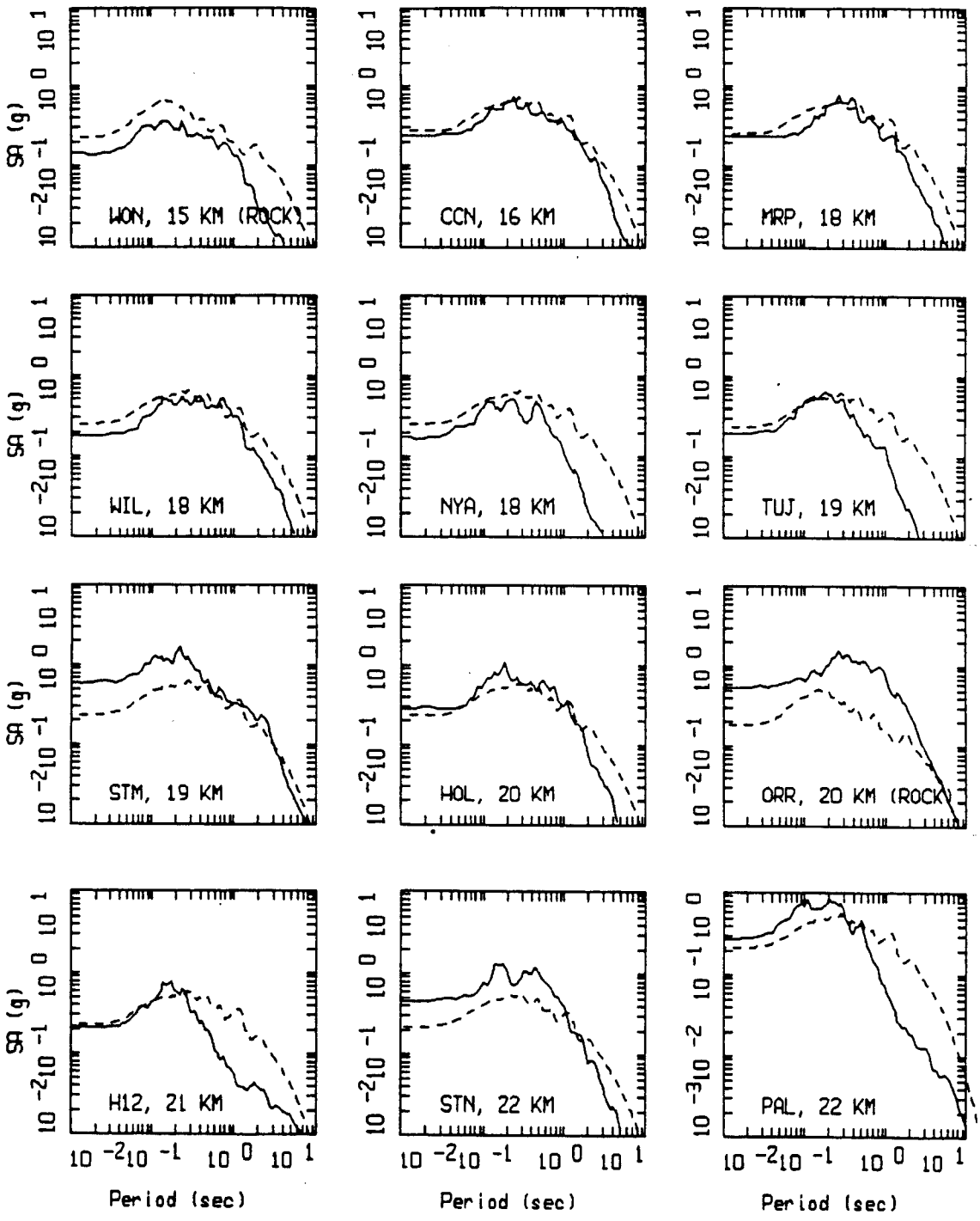

NORTHRIDGE, POINT SOURCE MODELING, PAGE 3 OF 8.
NONLINEAR PROFILES.

LEGEND

——— DATA

- - - - - MODEL

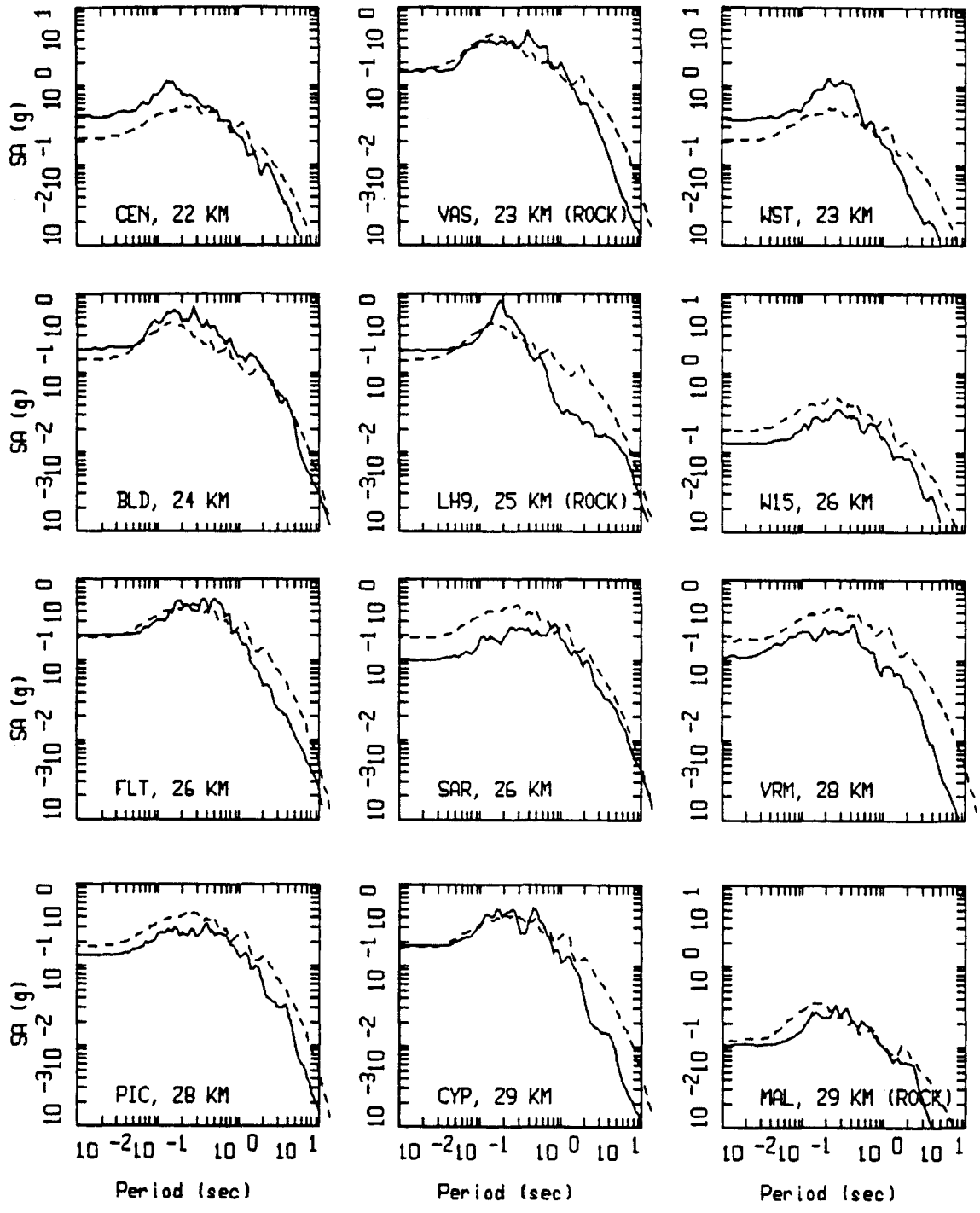

NORTHRIDGE, POINT SOURCE MODELING, PAGE 4 OF 8.
NONLINEAR PROFILES.

LEGEND

——— DATA

- - - - - MODEL

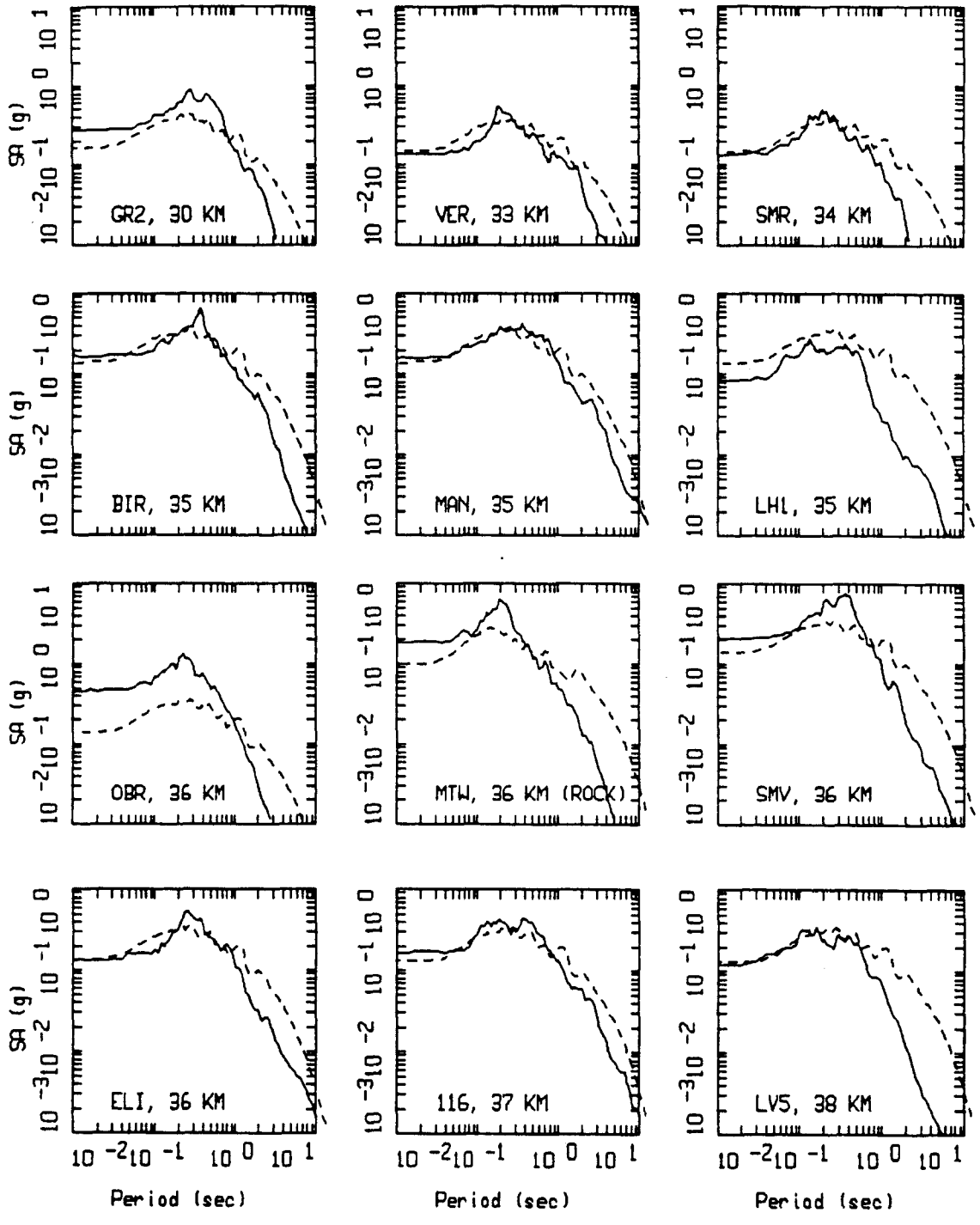

NORTHRIDGE, POINT SOURCE MODELING, PAGE 5 OF 8.
NONLINEAR PROFILES.

LEGEND

——— DATA

----- MODEL

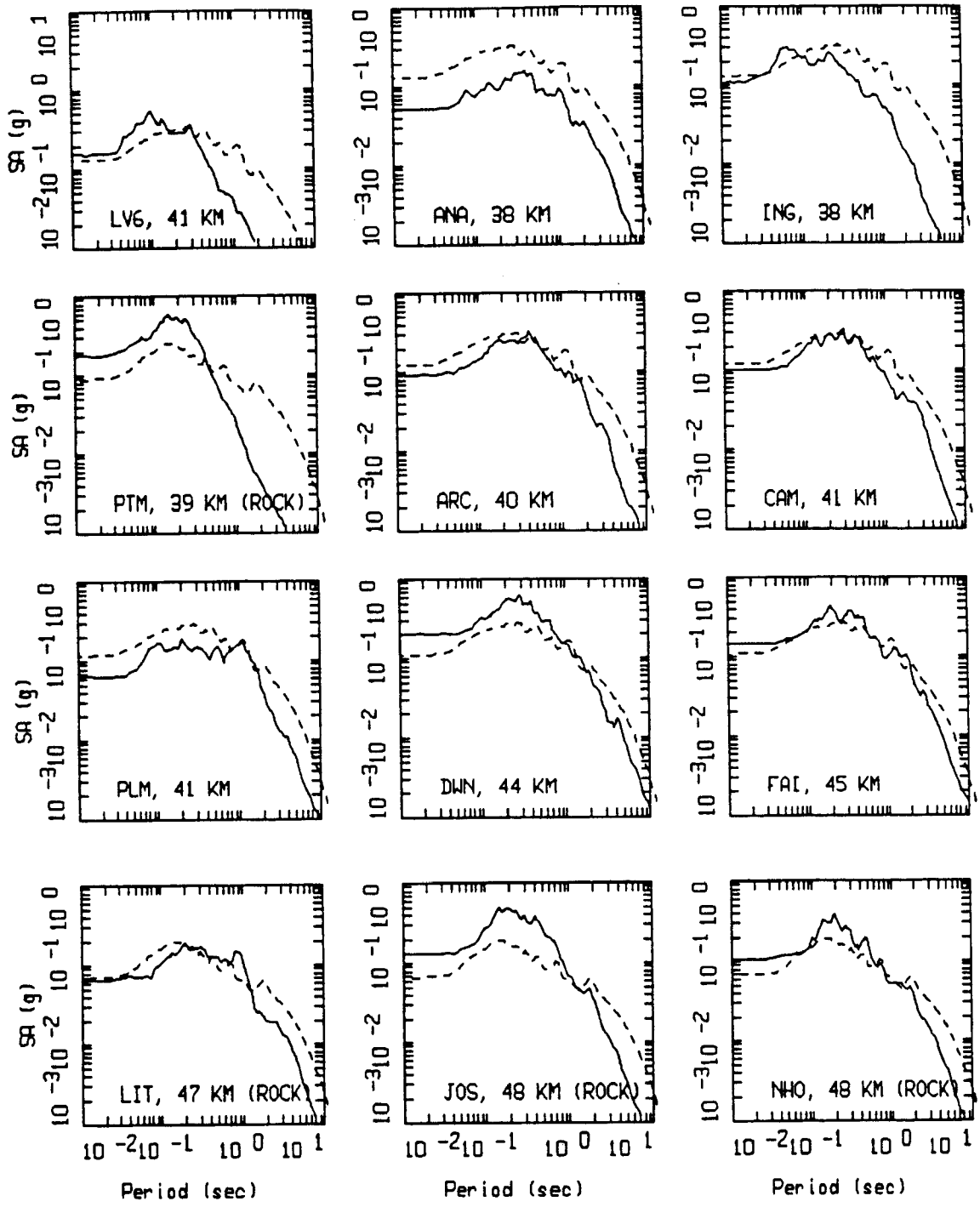

NORTHRIDGE, POINT SOURCE MODELING, PAGE 6 OF 8.

NONLINEAR PROFILES.

LEGEND

——— DATA

----- MODEL

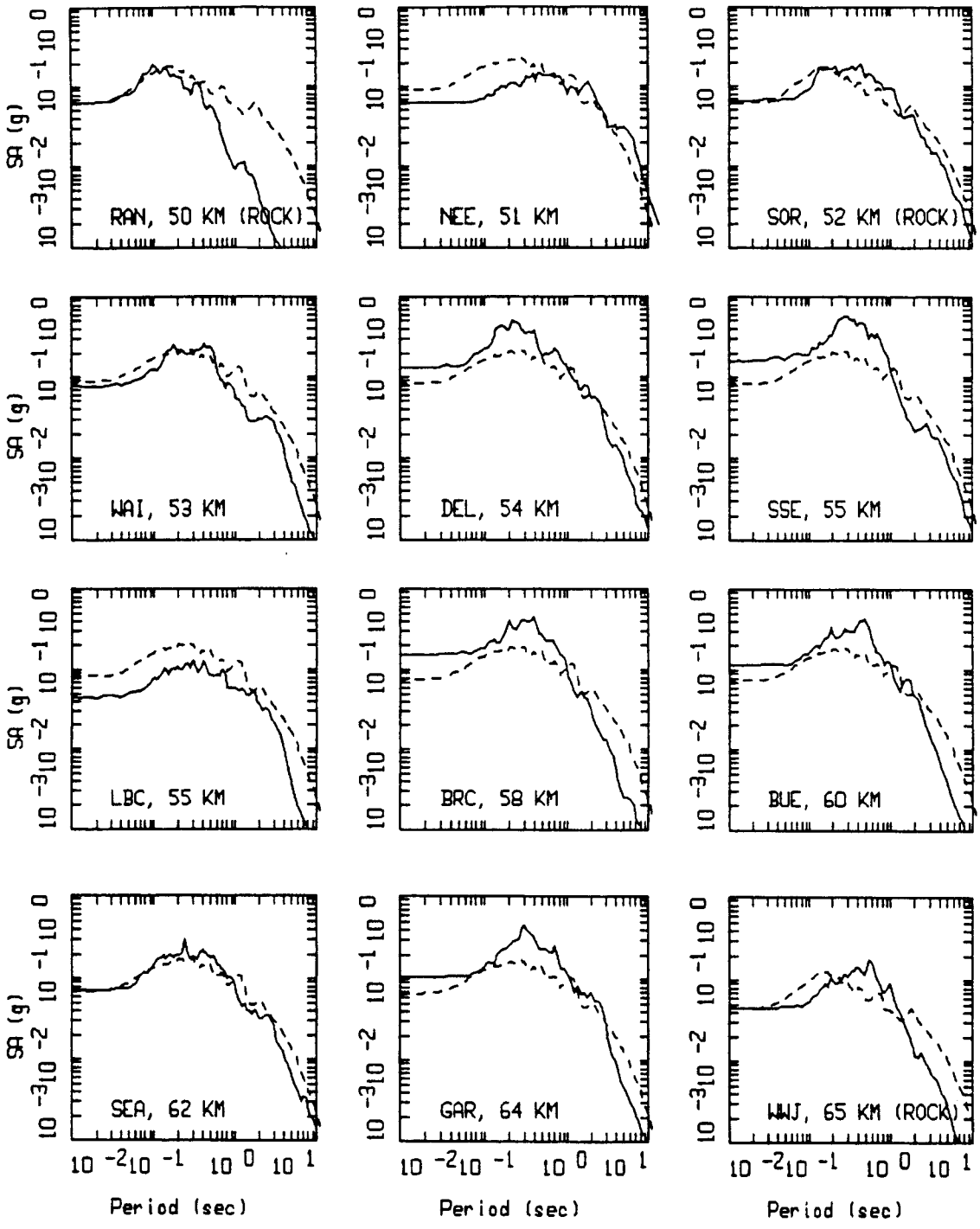

NORTHRIDGE, POINT SOURCE MODELING, PAGE 7 OF 8.
NONLINEAR PROFILES.

LEGEND

——— DATA

- - - - - MODEL

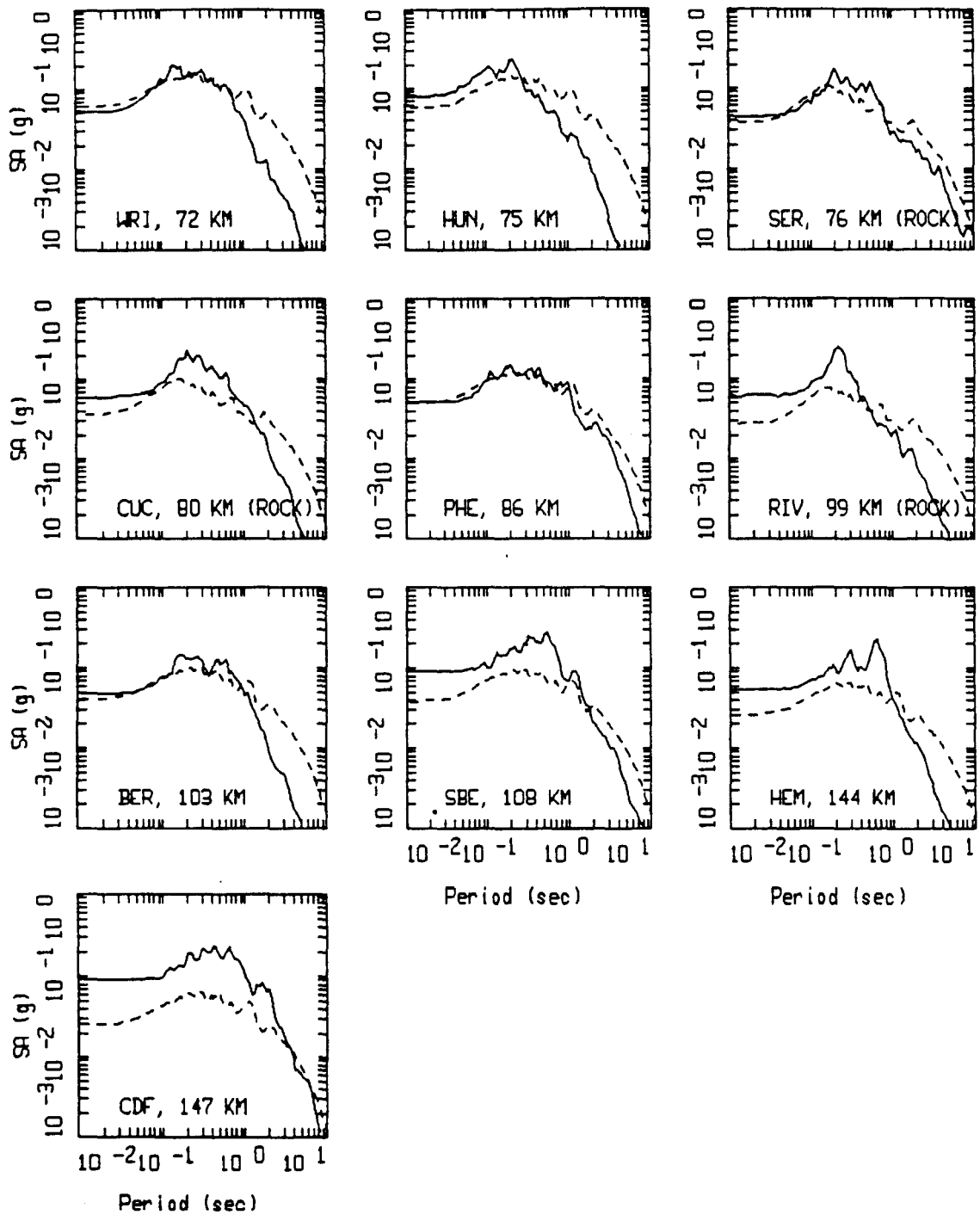

NORTHRIDGE, POINT SOURCE MODELING, PAGE 8 OF 8.
NONLINEAR PROFILES.

LEGEND

——— DATA

- - - - - MODEL

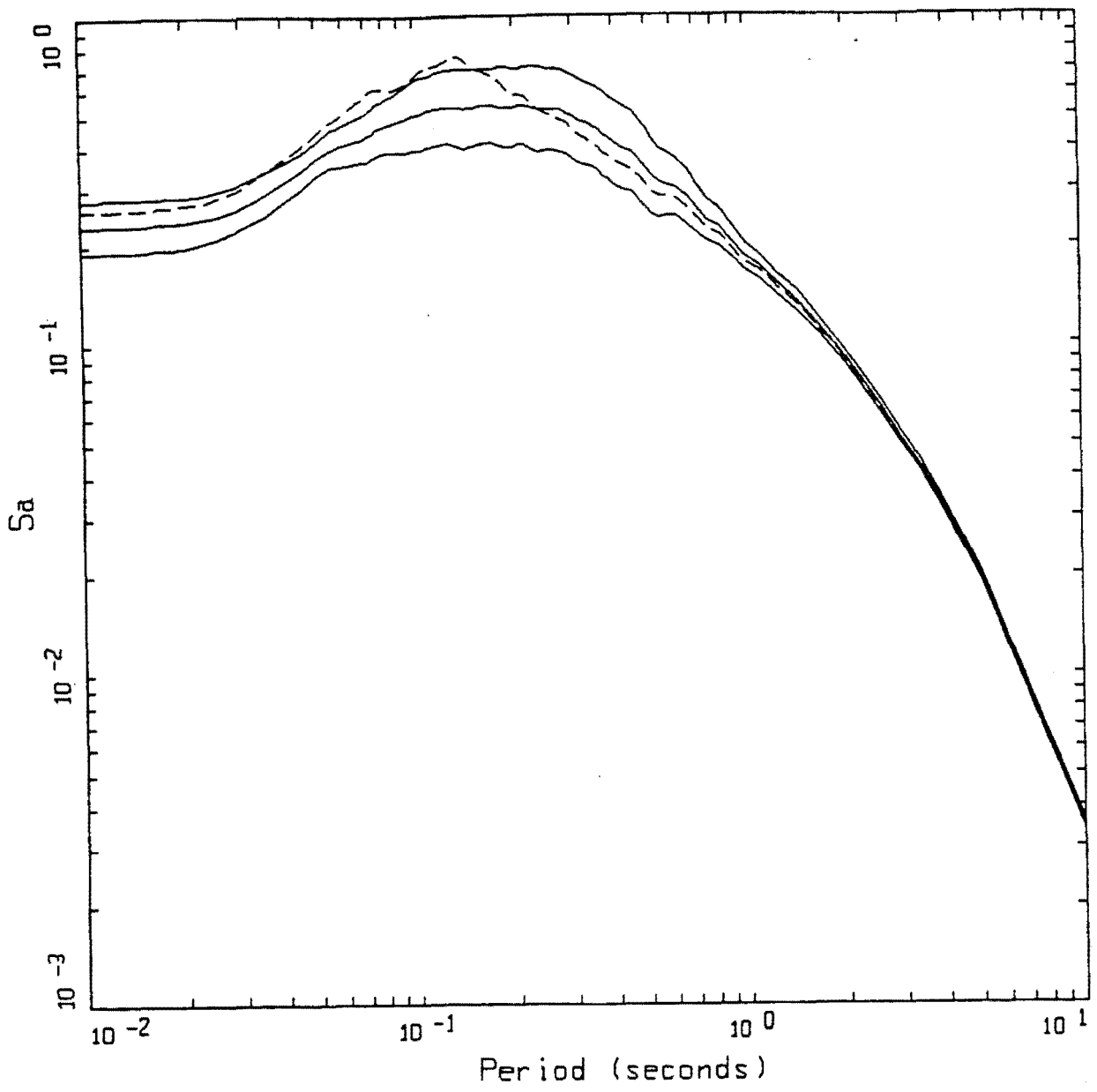

AVERAGE HORIZONTAL SPECTRA, ROCK
M=6.5, D=15 KM, STRESS DROP = 59 BARS

LEGEND
- BASE CASE
- 84TH PERCENTILE
- 50TH PERCENTILE
- 16TH PERCENTILE

Figure 5.7

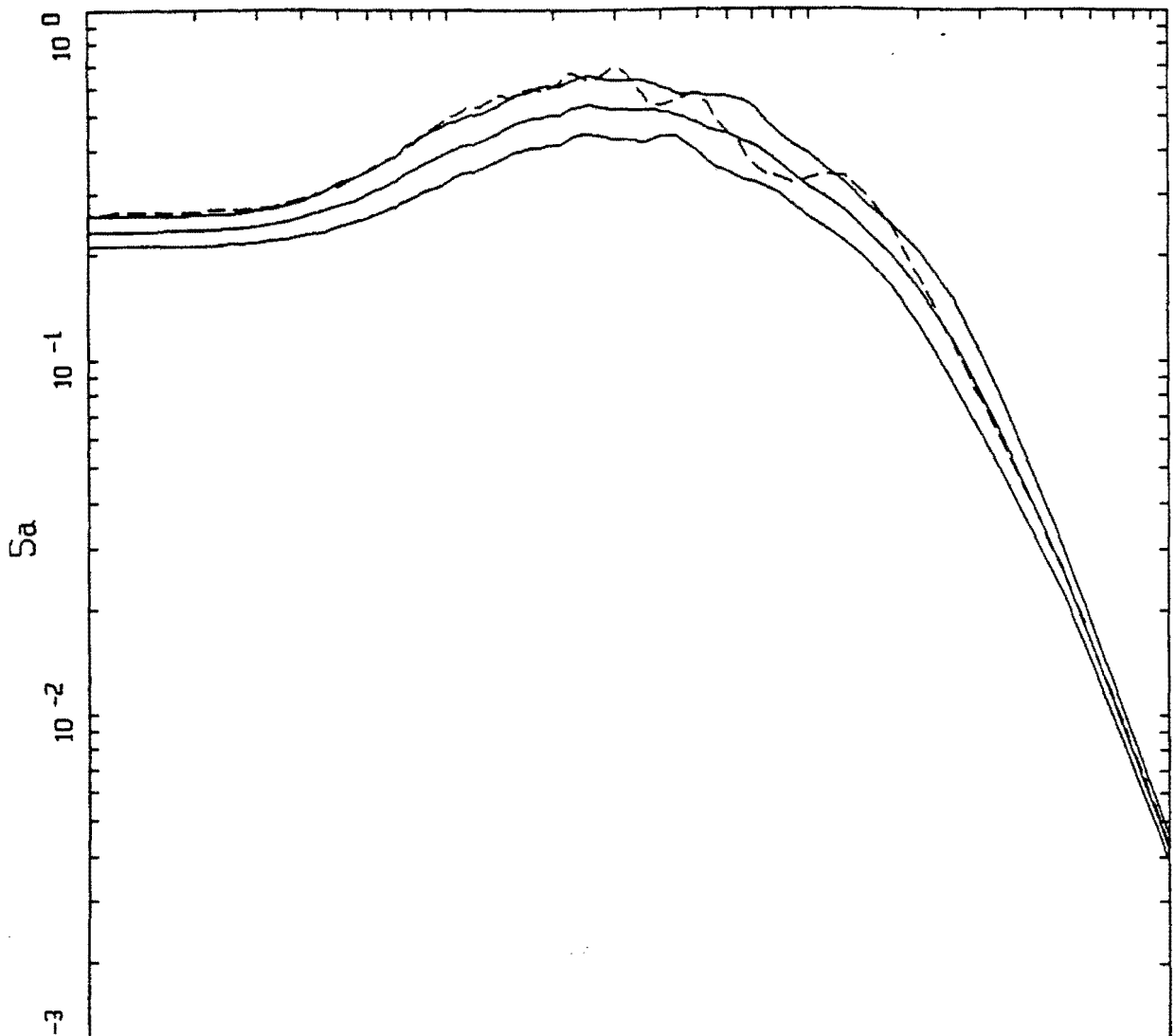

AVERAGE HORIZONTAL SOIL SPECTRA
M=6.5, D=15 KM, STRESS DROP = 59 BARS

LEGEND
- BASE CASE
- 84TH PERCENTILE
- 50TH PERCENTILE
- 16TH PERCENTILE

Figure 5.8

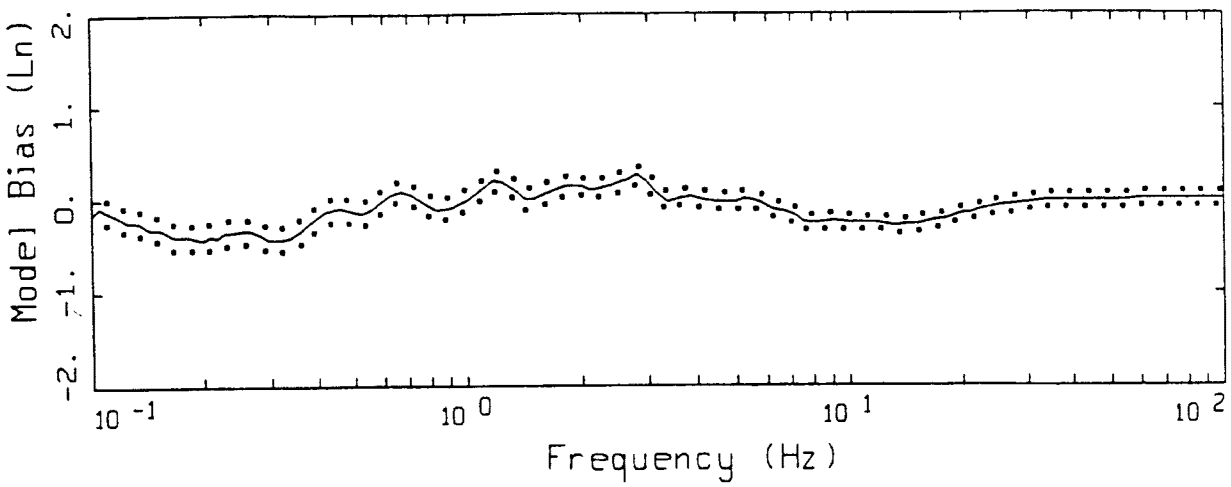

LEGEND
MODELING BIAS
90% CONFIDENCE INTERVAL OF MODELING BIAS
90% CONFIDENCE INTERVAL OF MODELING BIAS

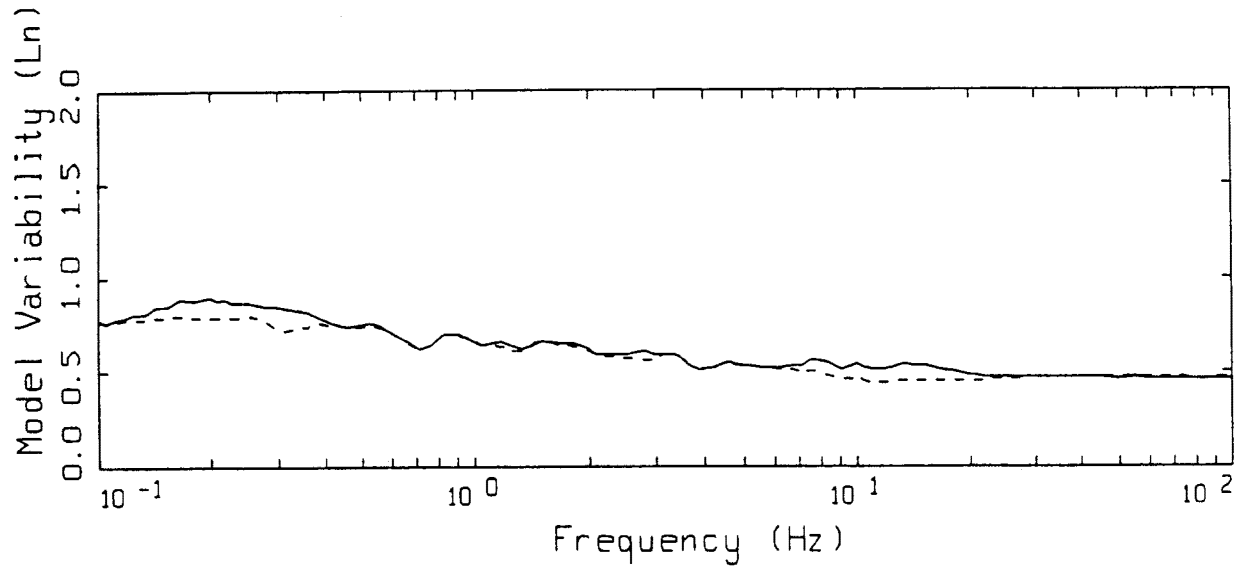

LEGEND
MEAN=0.0
BIAS CORRECTED

NORTHRIDGE FINITE-SOURCE
NONLINEAR, ALL 94 SITES

Figure 5.9

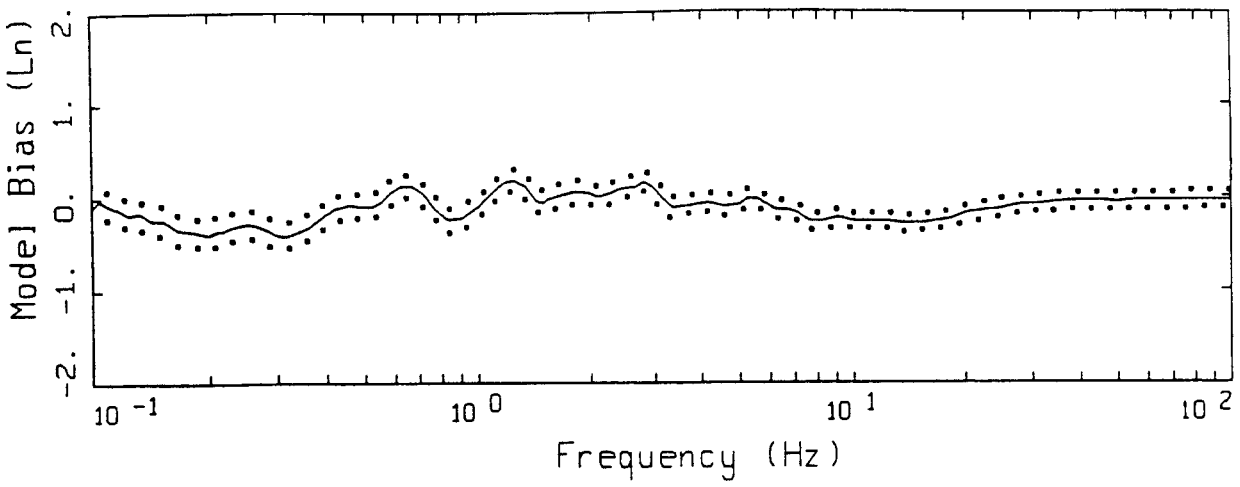

LEGEND
MODELING BIAS
90% CONFIDENCE INTERVAL OF MODELING BIAS
90% CONFIDENCE INTERVAL OF MODELING BIAS

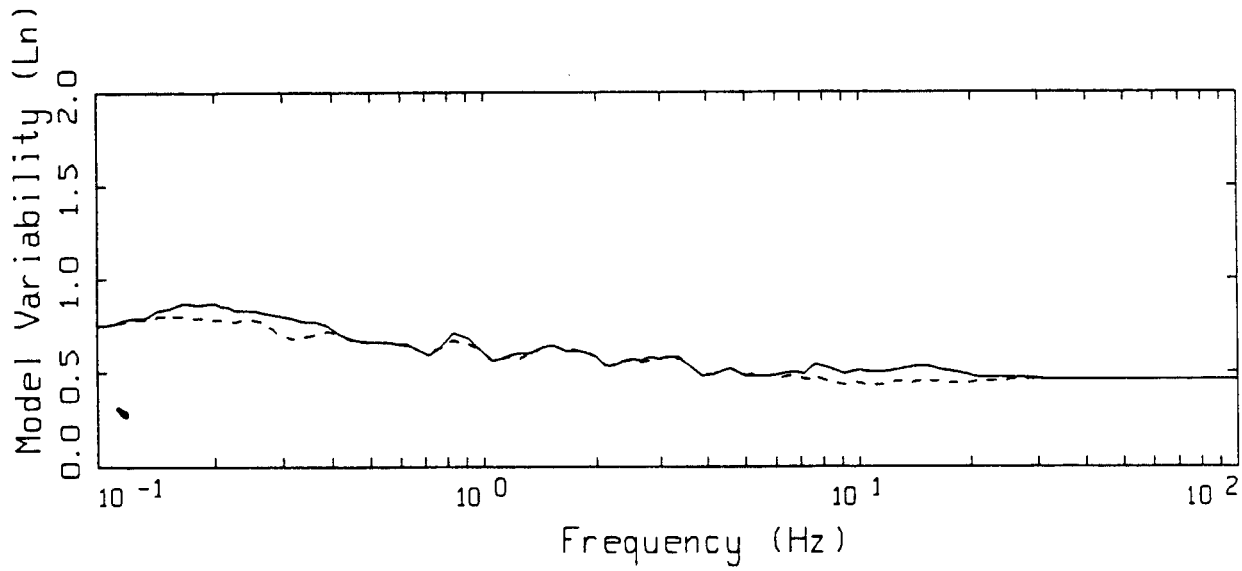

LEGEND
MEAN=0.0
BIAS CORRECTED

NORTHRIDGE FINITE-SOURCE
NONLINEAR, 71 SOIL SITES

Figure 5.10

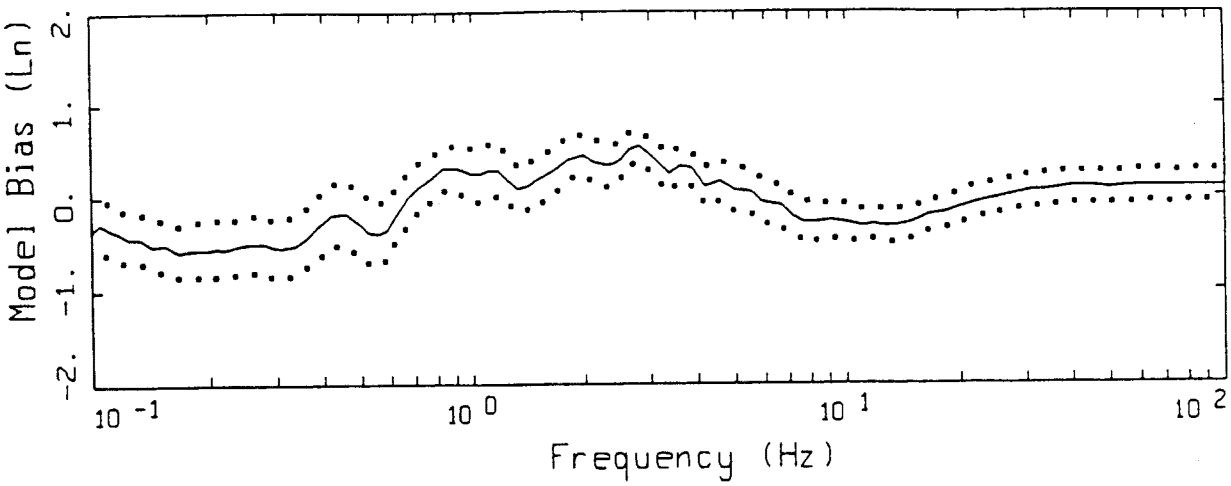

LEGEND
MODELING BIAS
90% CONFIDENCE INTERVAL OF MODELING BIAS
90% CONFIDENCE INTERVAL OF MODELING BIAS

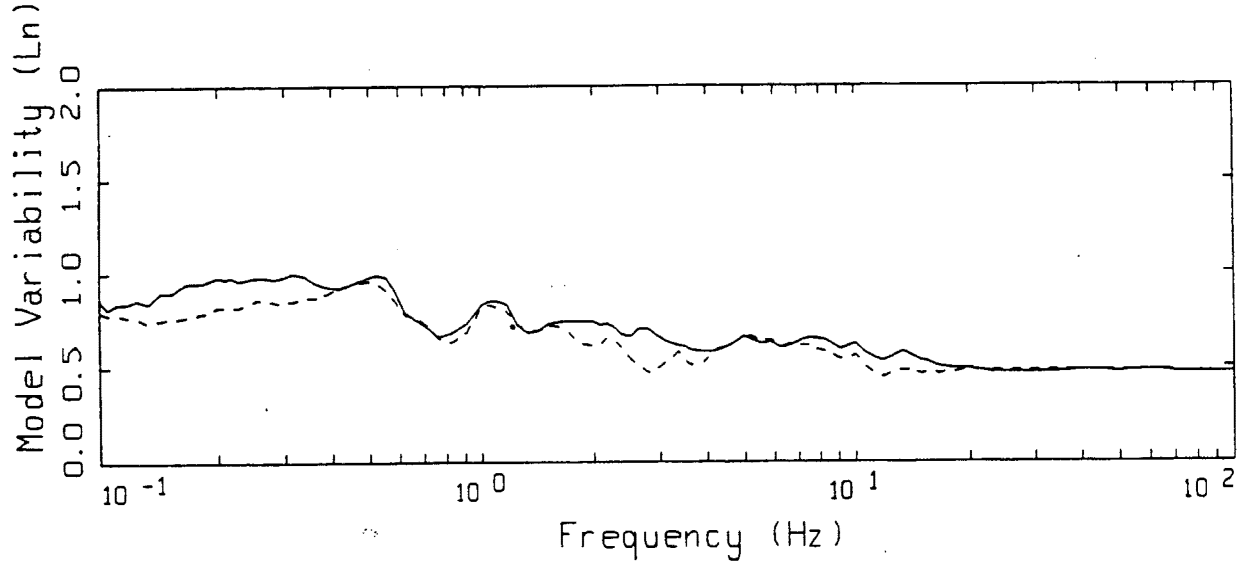

LEGEND
MEAN=0.0
BIAS CORRECTED

NORTHRIDGE FINITE-SOURCE
NONLINEAR, 23 ROCK SITES

Figure 5.11

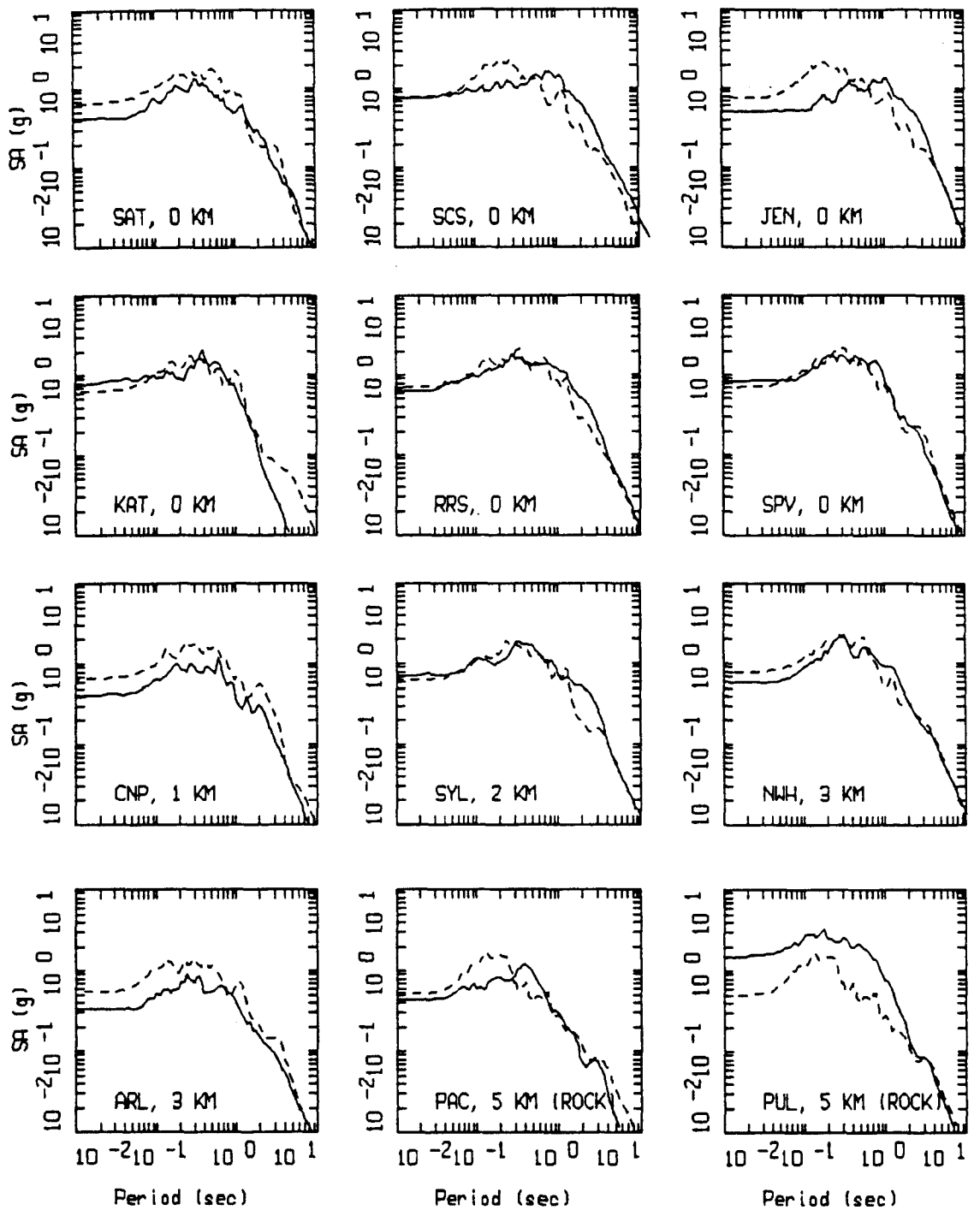

NORTHRIDGE, FINITE SOURCE MODELING, PAGE 1 OF 8.
NONLINEAR PROFILES.

Figure Set 5.12

LEGEND
——— DATA
- - - - - MODEL

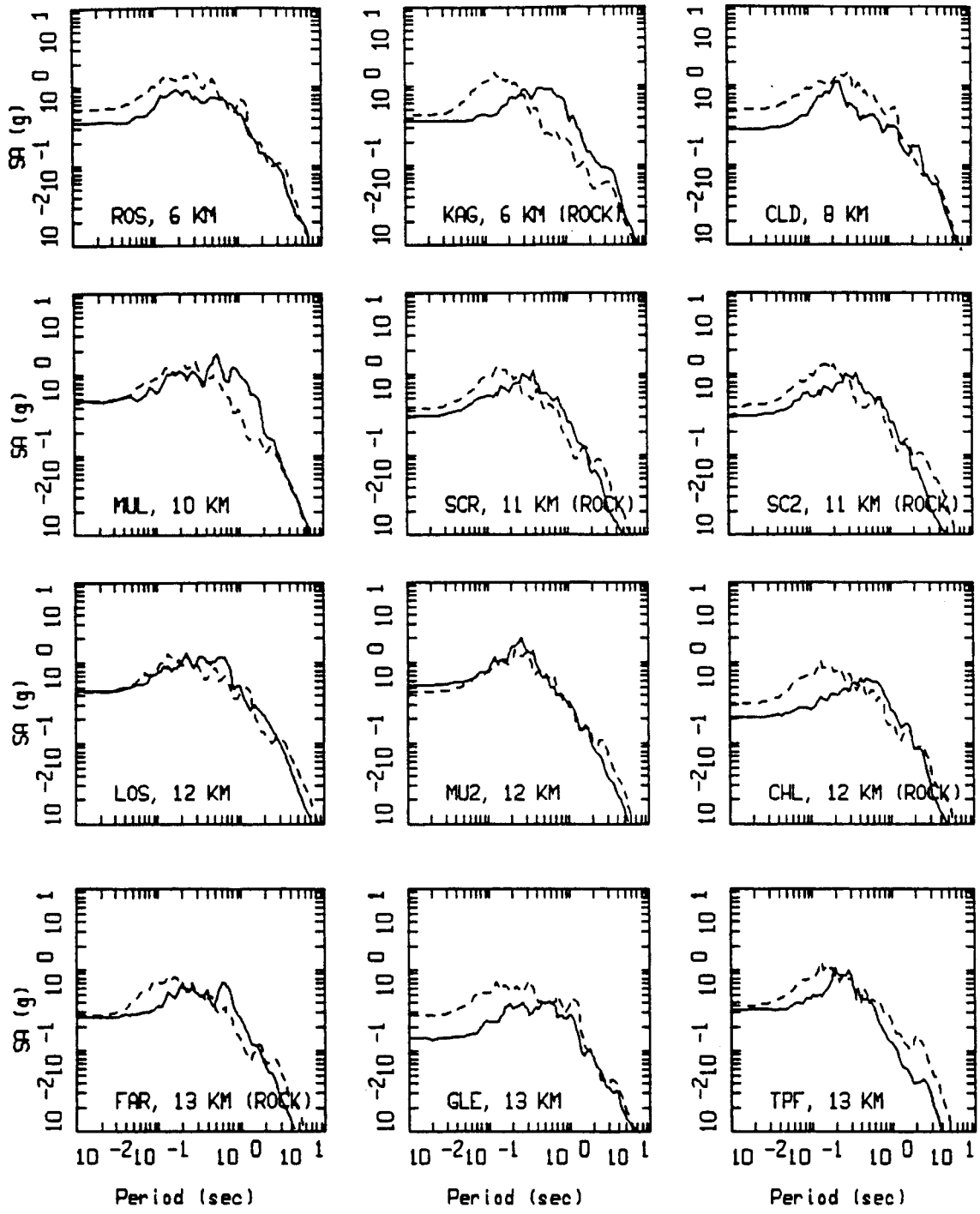

NORTHRIDGE, FINITE SOURCE MODELING, PAGE 2 OF 8.
NONLINEAR PROFILES.

LEGEND

——— DATA

- - - - - MODEL

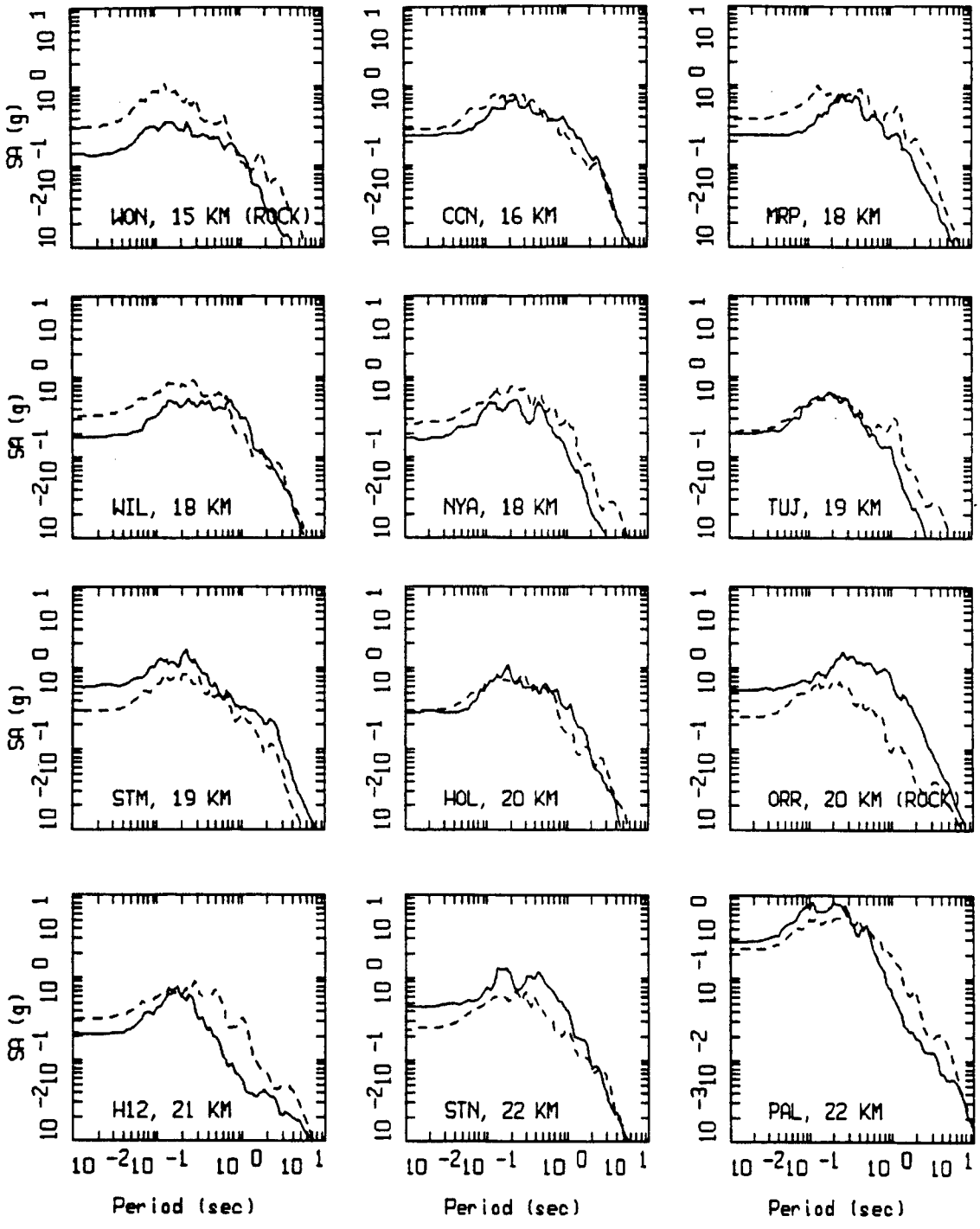

NORTHRIDGE, FINITE SOURCE MODELING, PAGE 3 OF 8.
NONLINEAR PROFILES.

LEGEND

——— DATA

- - - - - MODEL

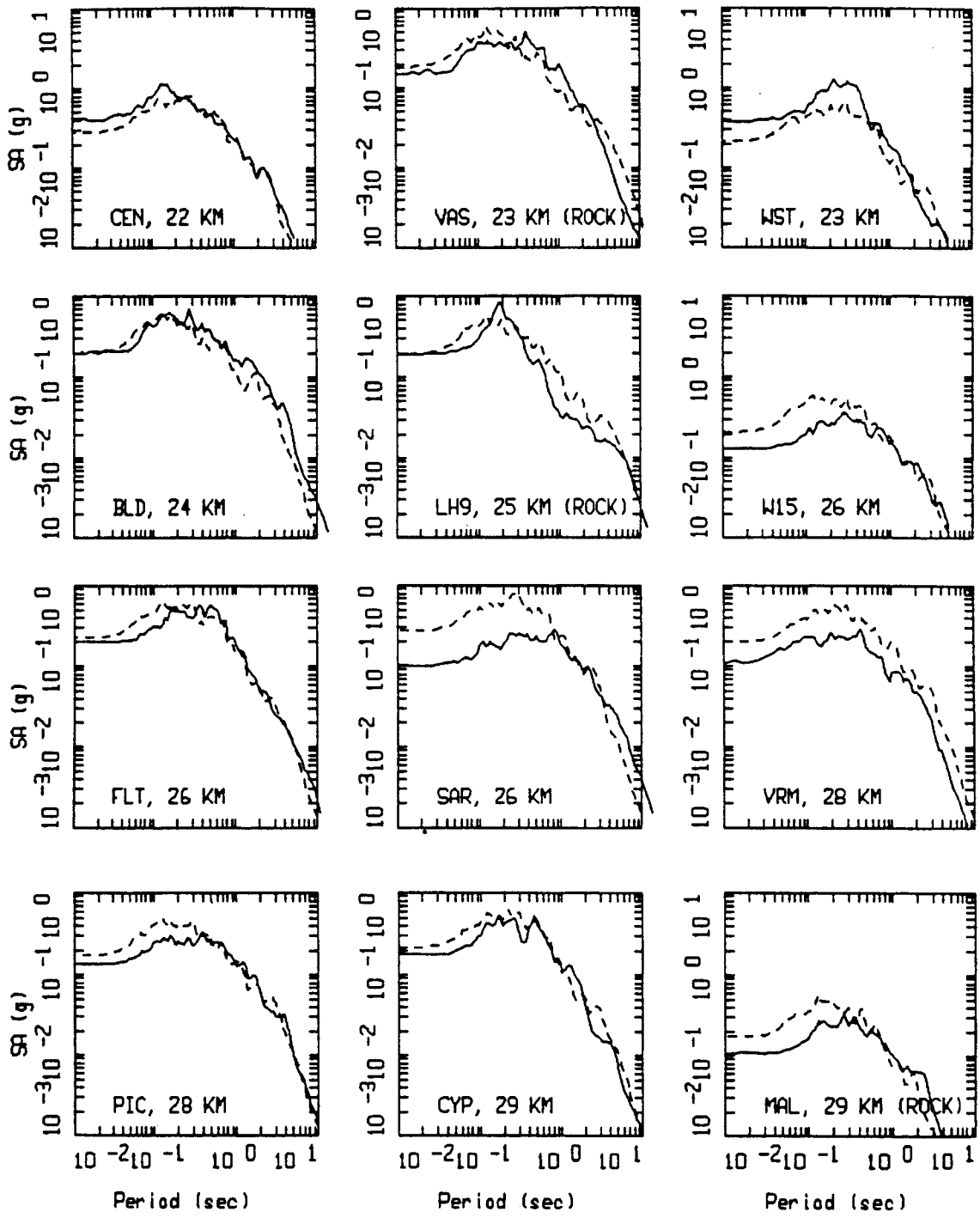

NORTHRIDGE, FINITE SOURCE MODELING, PAGE 4 OF 8.
NONLINEAR PROFILES.

LEGEND
——— DATA
----- MODEL

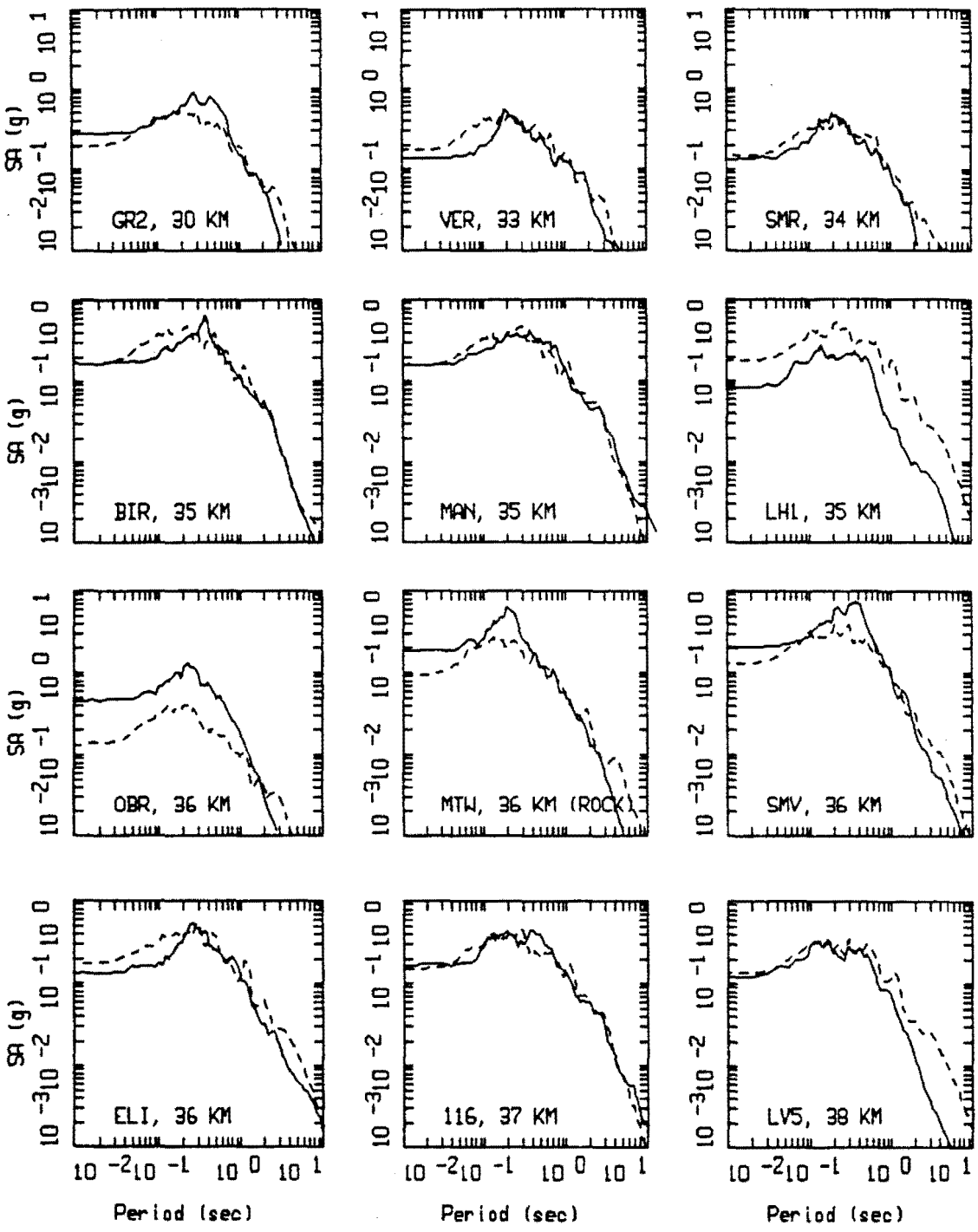

NORTHRIDGE, FINITE SOURCE MODELING, PAGE 5 OF 8.

NONLINEAR PROFILES.

LEGEND

——— DATA

- - - - - MODEL

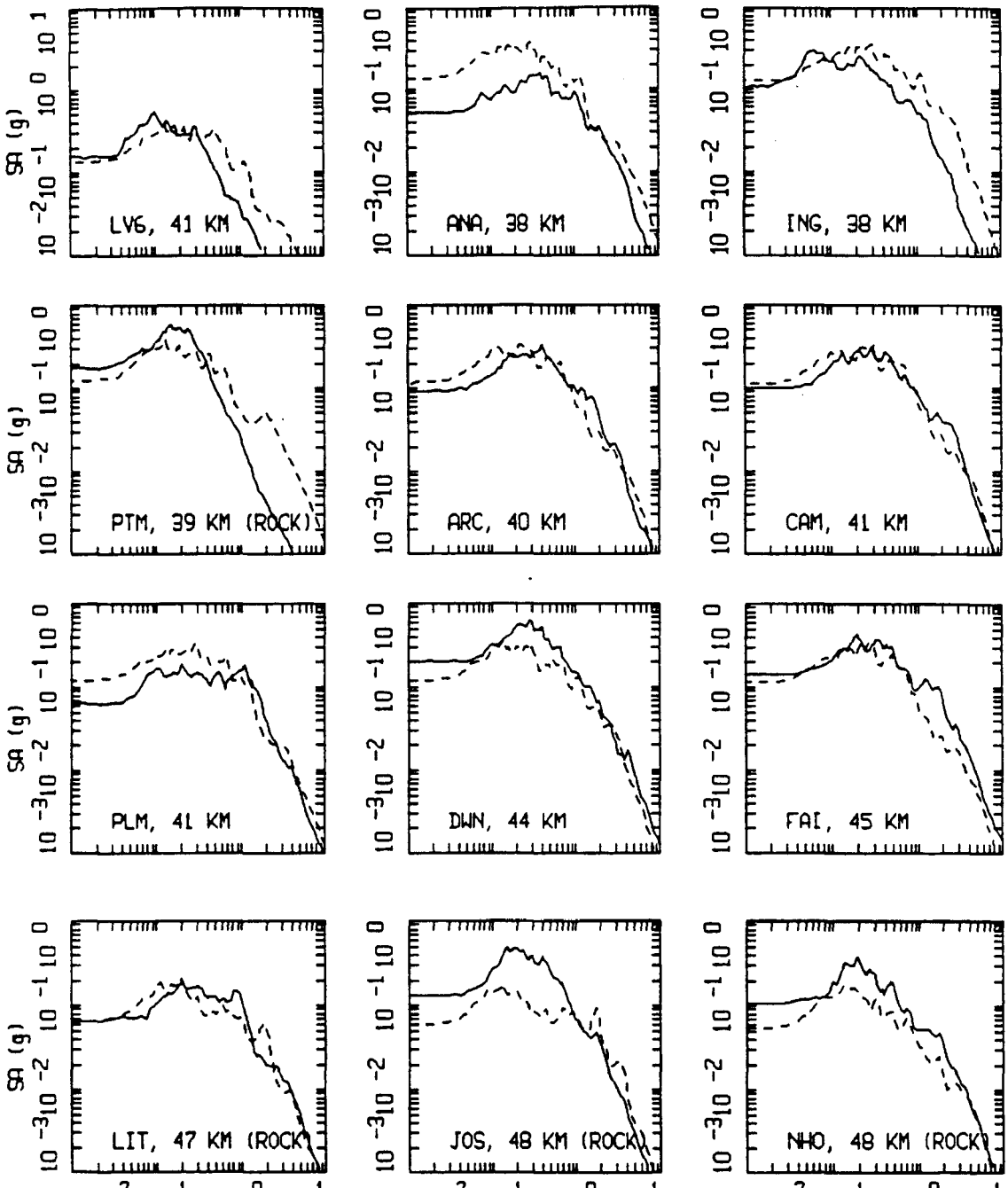

NORTHRIDGE, FINITE SOURCE MODELING, PAGE 6 OF 8.
NONLINEAR PROFILES.

LEGEND

——— DATA

- - - - - MODEL

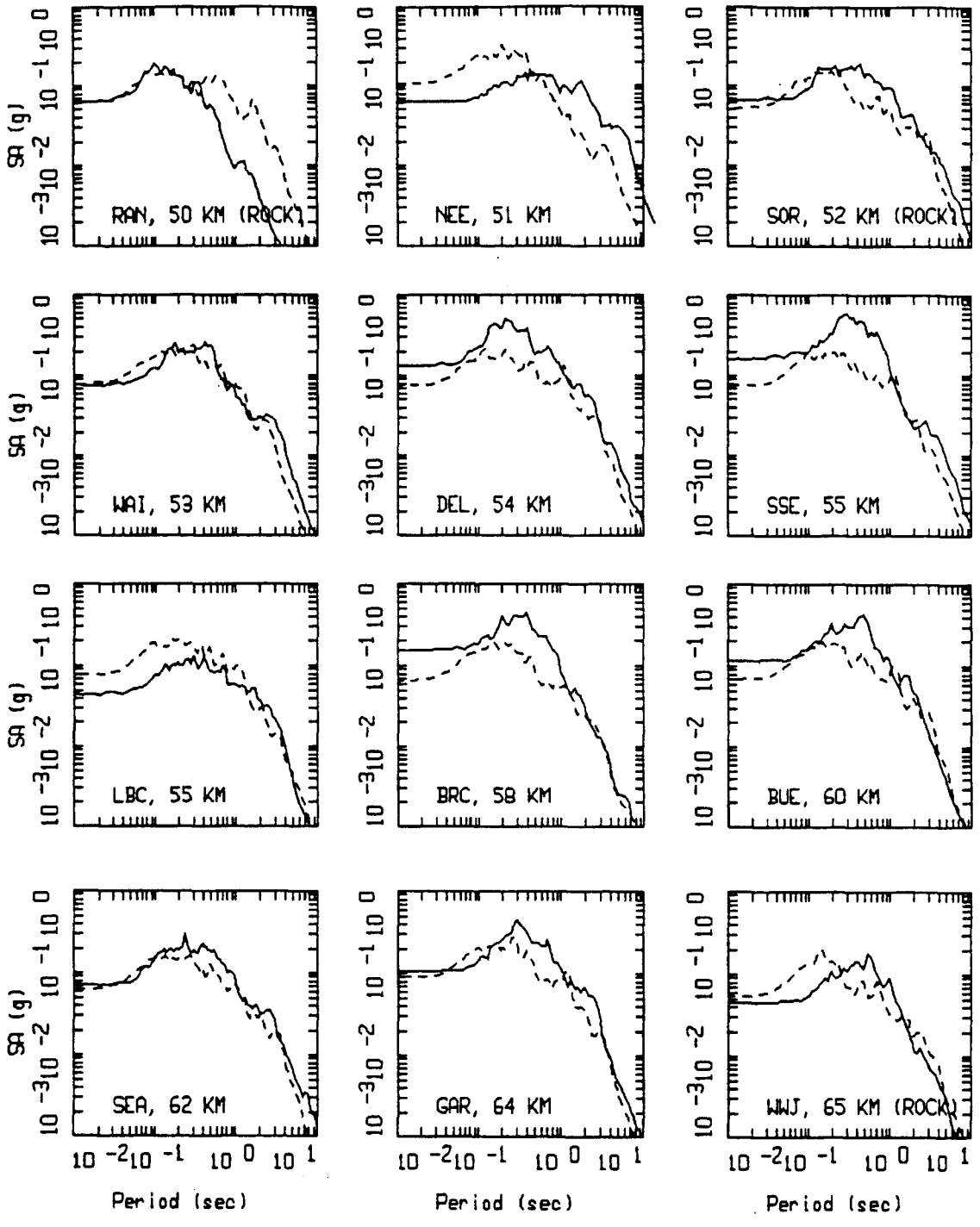

NORTHRIDGE, FINITE SOURCE MODELING, PAGE 7 OF 8.
NONLINEAR PROFILES.

LEGEND

——— DATA

- - - - - MODEL

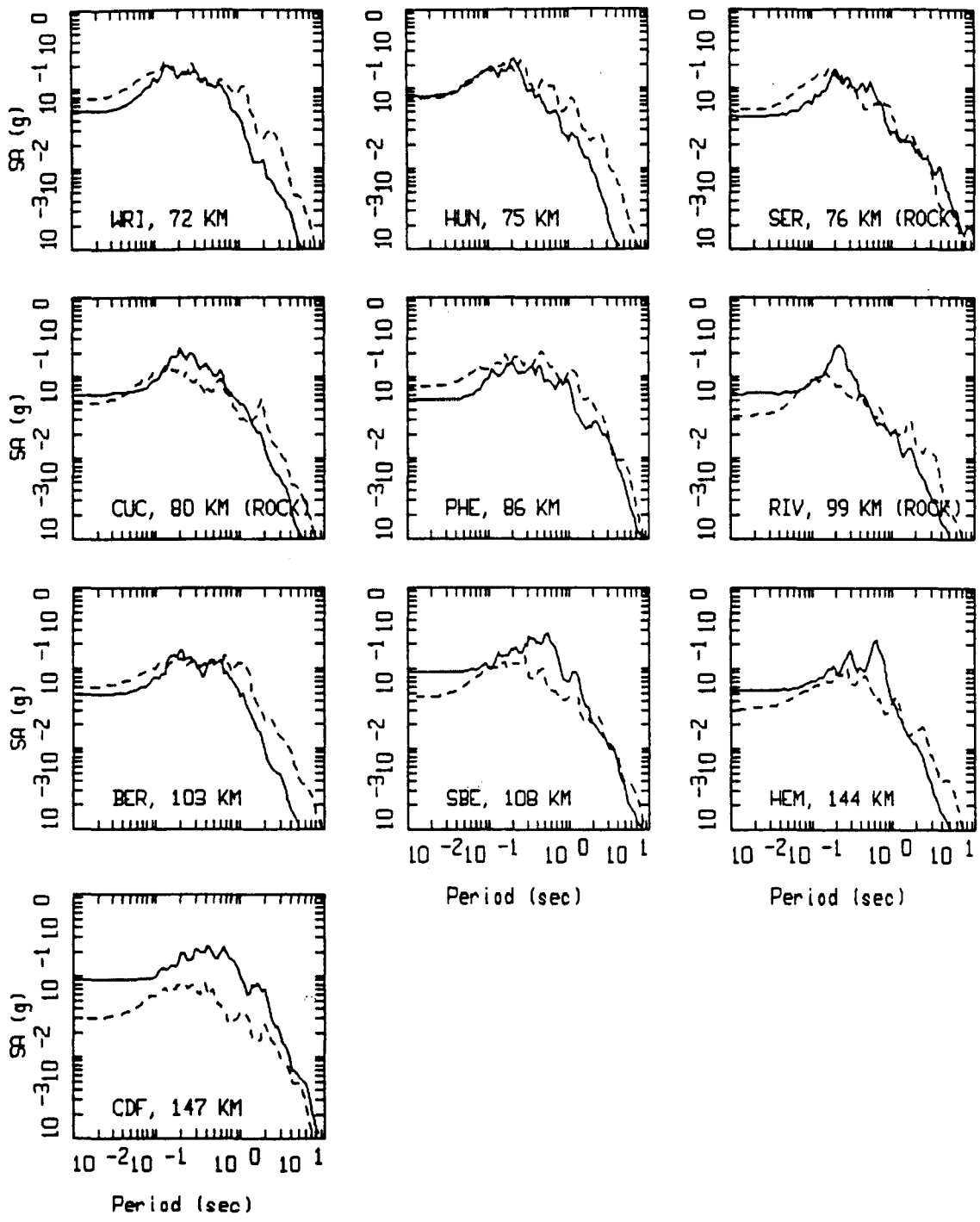

NORTHRIDGE, FINITE SOURCE MODELING, PAGE 8 OF 8.
NONLINEAR PROFILES.

LEGEND

——— DATA

----- MODEL

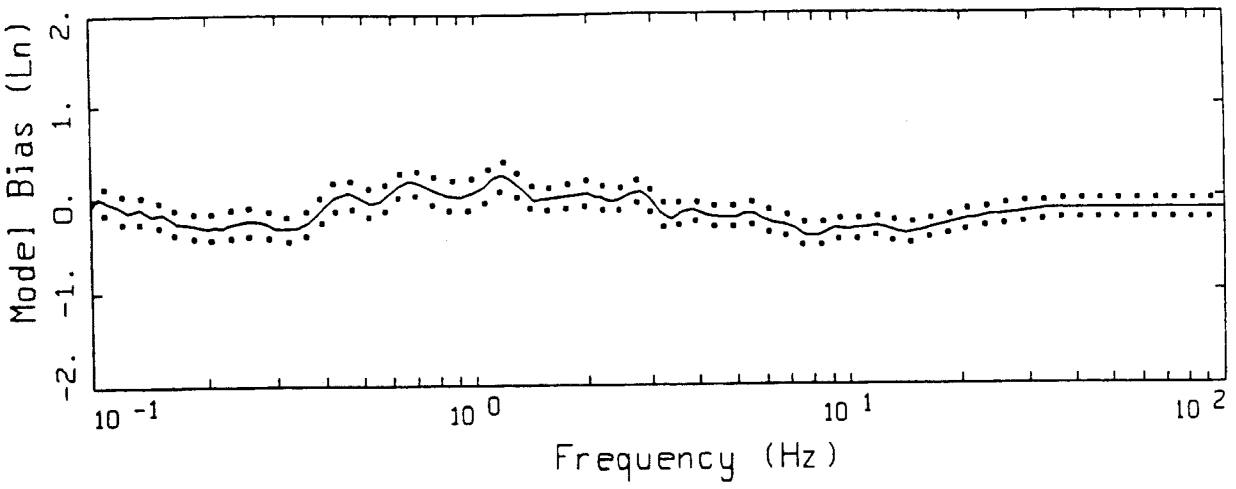

LEGEND
MODELING BIAS
90% CONFIDENCE INTERVAL OF MODELING BIAS
90% CONFIDENCE INTERVAL OF MODELING BIAS

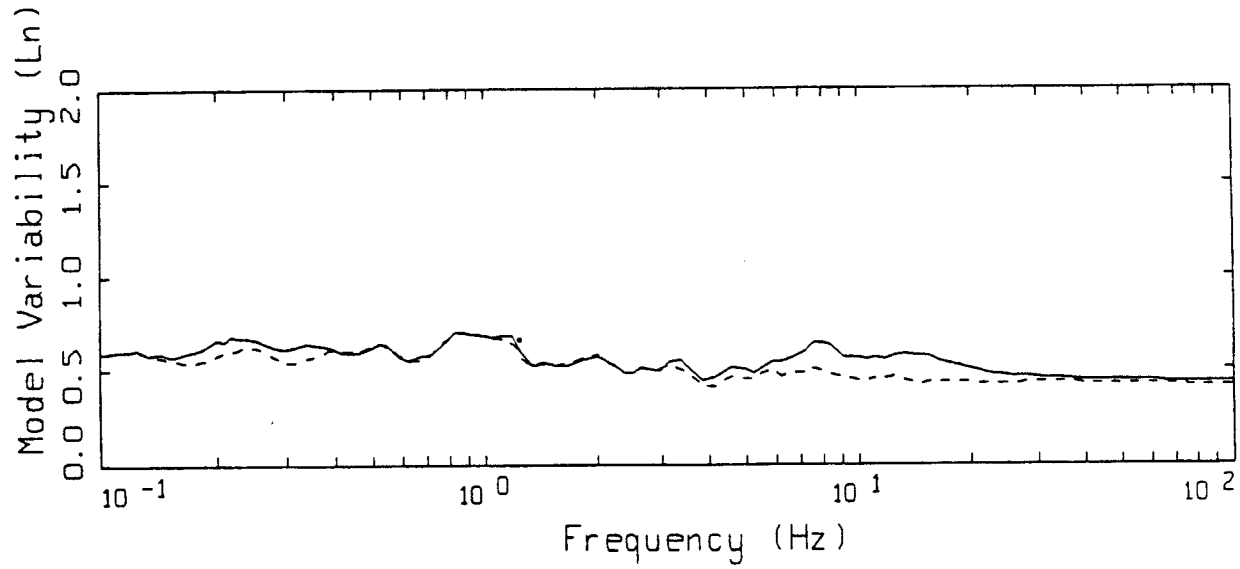

LEGEND
MEAN=0.0
BIAS CORRECTED

NORTHRIDGE FINITE-SOURCE
NONLINEAR, ALL 48 SITES TO 30 KM

Figure 5.13

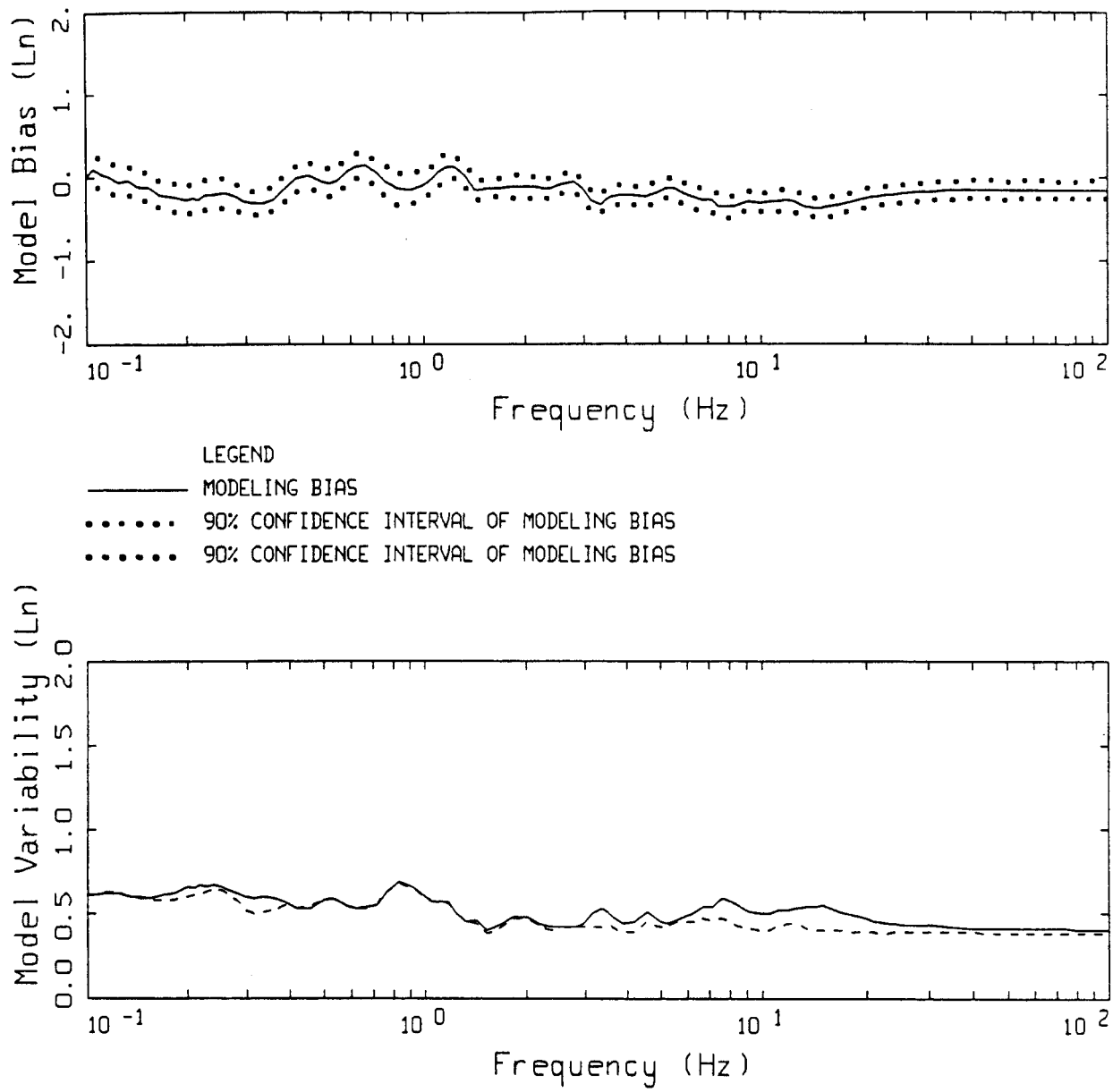
Model Bias (Ln)
2.
1.
0.
-1.
-2.
10 -1
10 0
10 1
10 2
Frequency (Hz)
LEGEND
MODELING BIAS
90% CONFIDENCE INTERVAL OF MODELING BIAS
90% CONFIDENCE INTERVAL OF MODELING BIAS
Model Variability (Ln)
0.0 0.5 1.0 1.5 2.0
10 -1
10 0
10 1
10 2
Frequency (Hz)
LEGEND
MEAN=0.0
BIAS CORRECTED
NORTHRIDGE FINITE-SOURCE
NONLINEAR, 36 SOIL SITES TO 30 KM

Figure 5.14

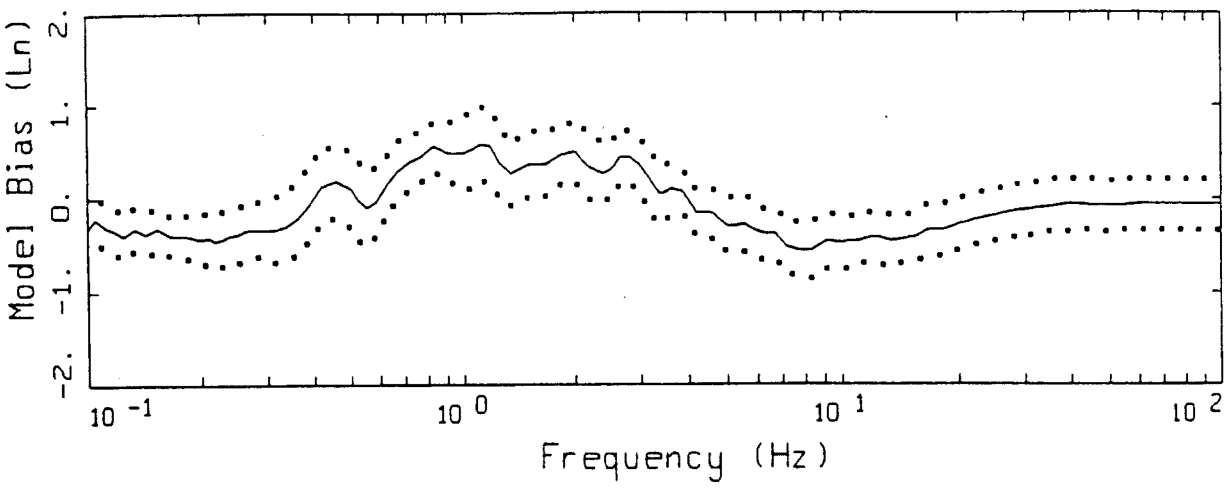

LEGEND
MODELING BIAS
90% CONFIDENCE INTERVAL OF MODELING BIAS
90% CONFIDENCE INTERVAL OF MODELING BIAS

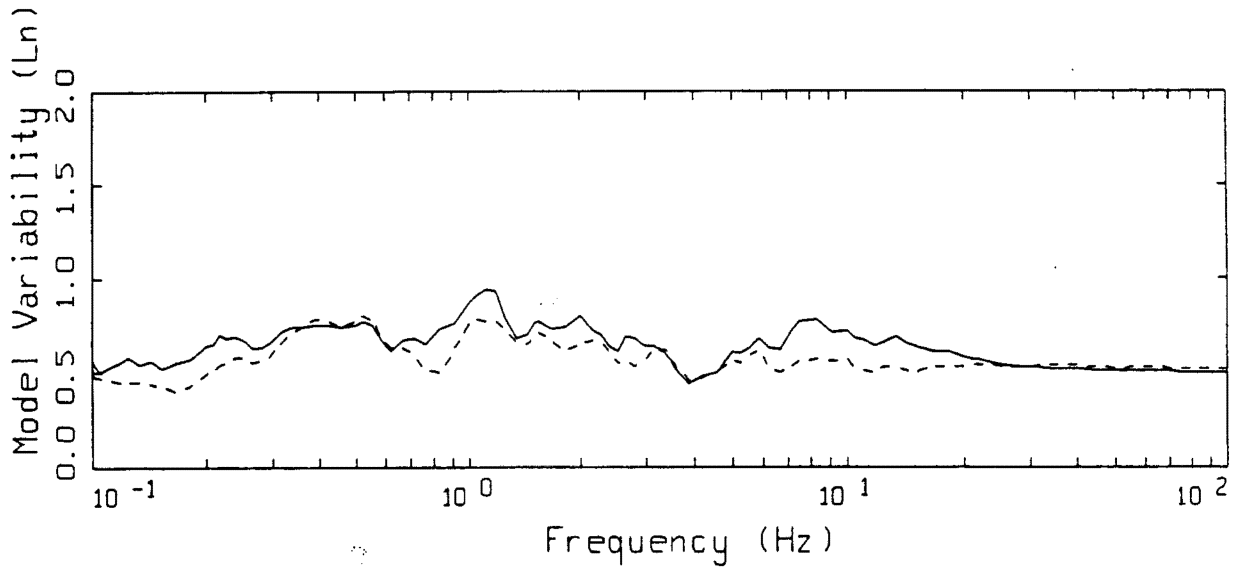

LEGEND
MEAN=0.0
BIAS CORRECTED

NORTHRIDGE FINITE-SOURCE
NONLINEAR, 12 ROCK SITES TO 30 KM

Figure 5.15

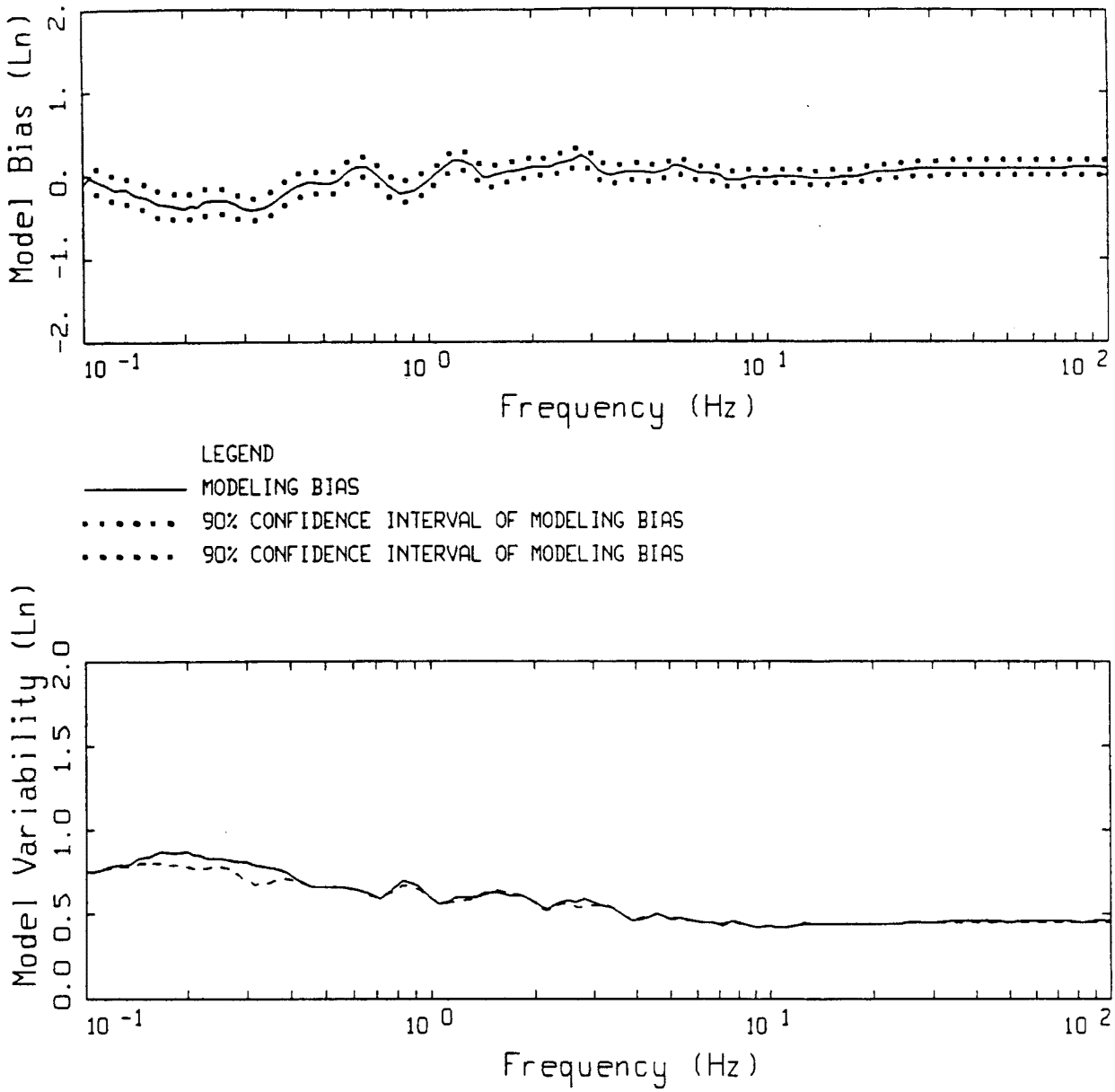
Model Bias (Ln)
2.
1.
0.
-1.
-2.
10 -1
10 0
10 1
10 2
Frequency (Hz)
LEGEND
MODELING BIAS
90% CONFIDENCE INTERVAL OF MODELING BIAS
90% CONFIDENCE INTERVAL OF MODELING BIAS
Model Variability (Ln)
0.0 0.5 1.0 1.5 2.0
10 -1
10 0
10 1
10 2
Frequency (Hz)
LEGEND
MEAN=0.0
BIAS CORRECTED
NORTHRIDGE FINITE-SOURCE
NONLINEAR, 71 SOIL SITES

Figure 5.16a

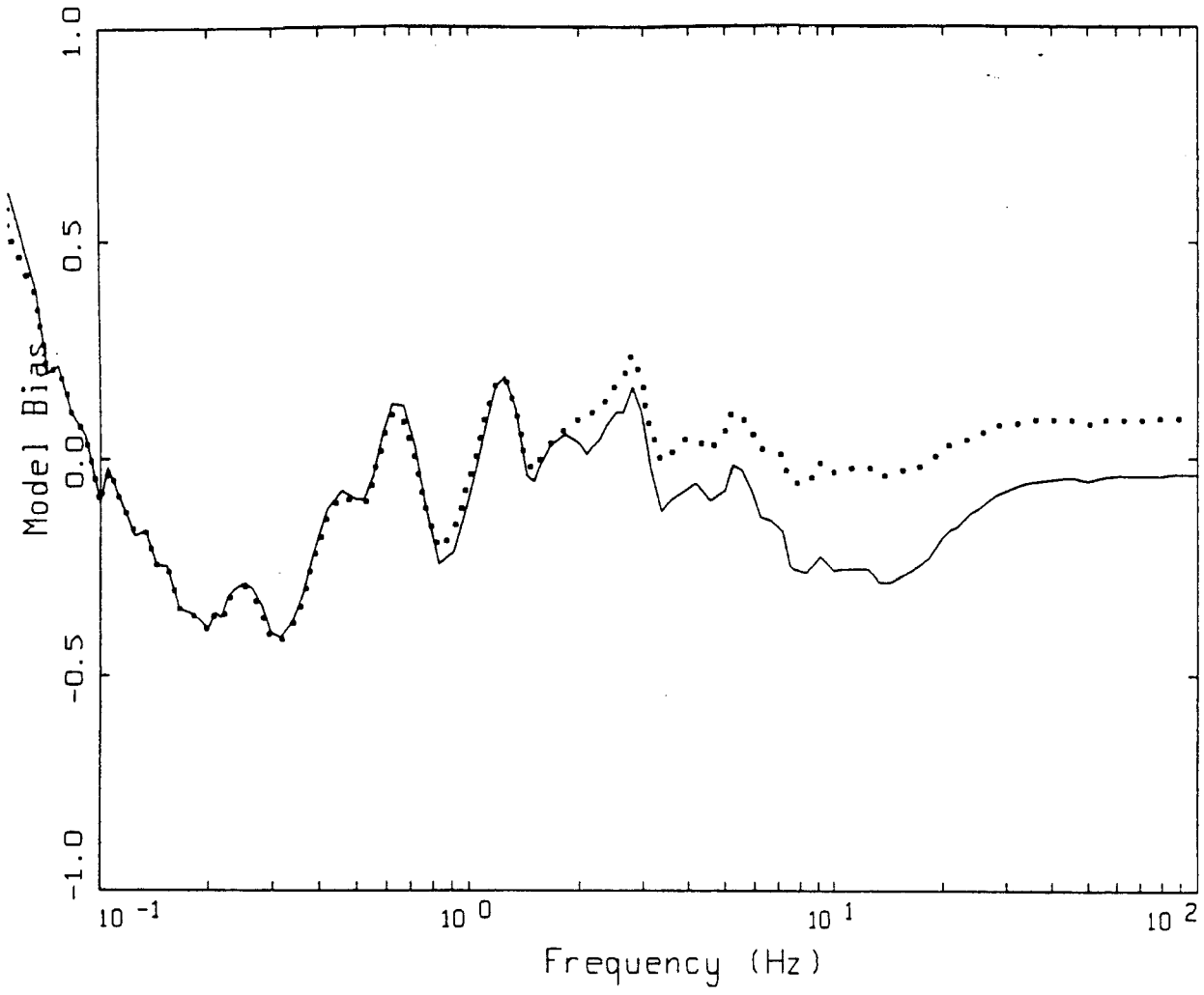

NORTHRIDGE FINITE SOURCE, MODELING BIAS
NONLINEAR PROFILES, 71 SOIL SITES

LEGEND

——— MODELING BIAS, DEEP SOIL CURVES

• • • • MODELING BIAS, EPRI CURVES

Figure 5.16b

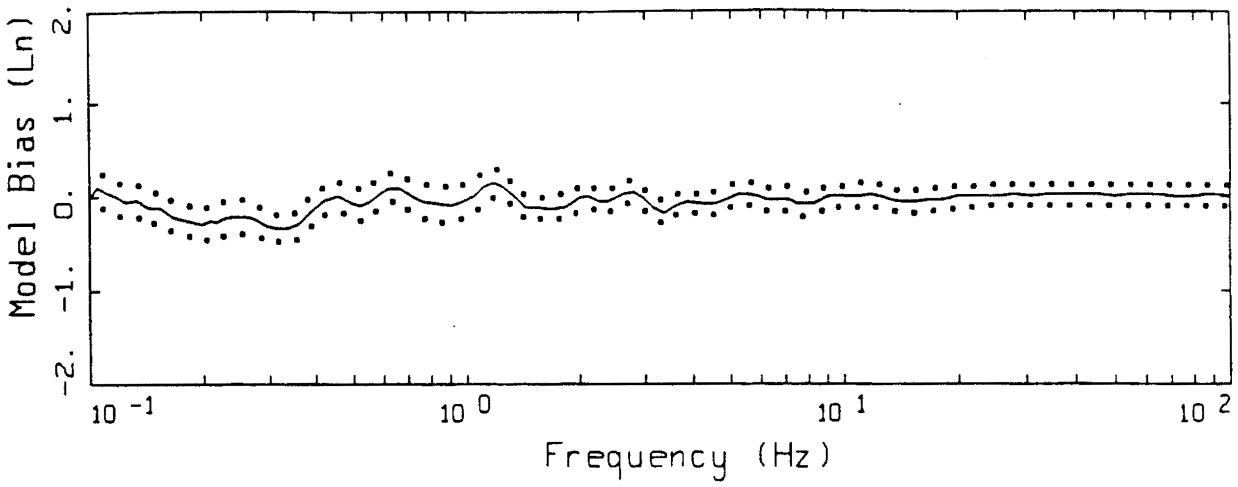

LEGEND
MODELING BIAS
90% CONFIDENCE INTERVAL OF MODELING BIAS
90% CONFIDENCE INTERVAL OF MODELING BIAS

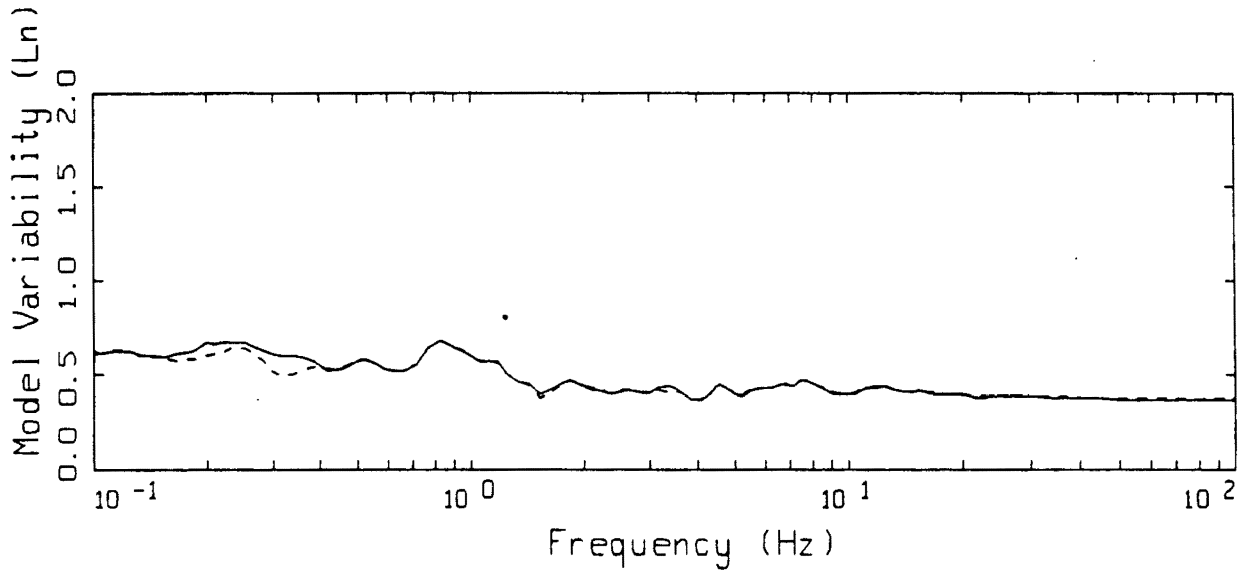

LEGEND
MEAN=0.0
BIAS CORRECTED

NORTHRIDGE FINITE-SOURCE
NONLINEAR, 36 SOIL SITES TO 30 KM

Figure 5.17a

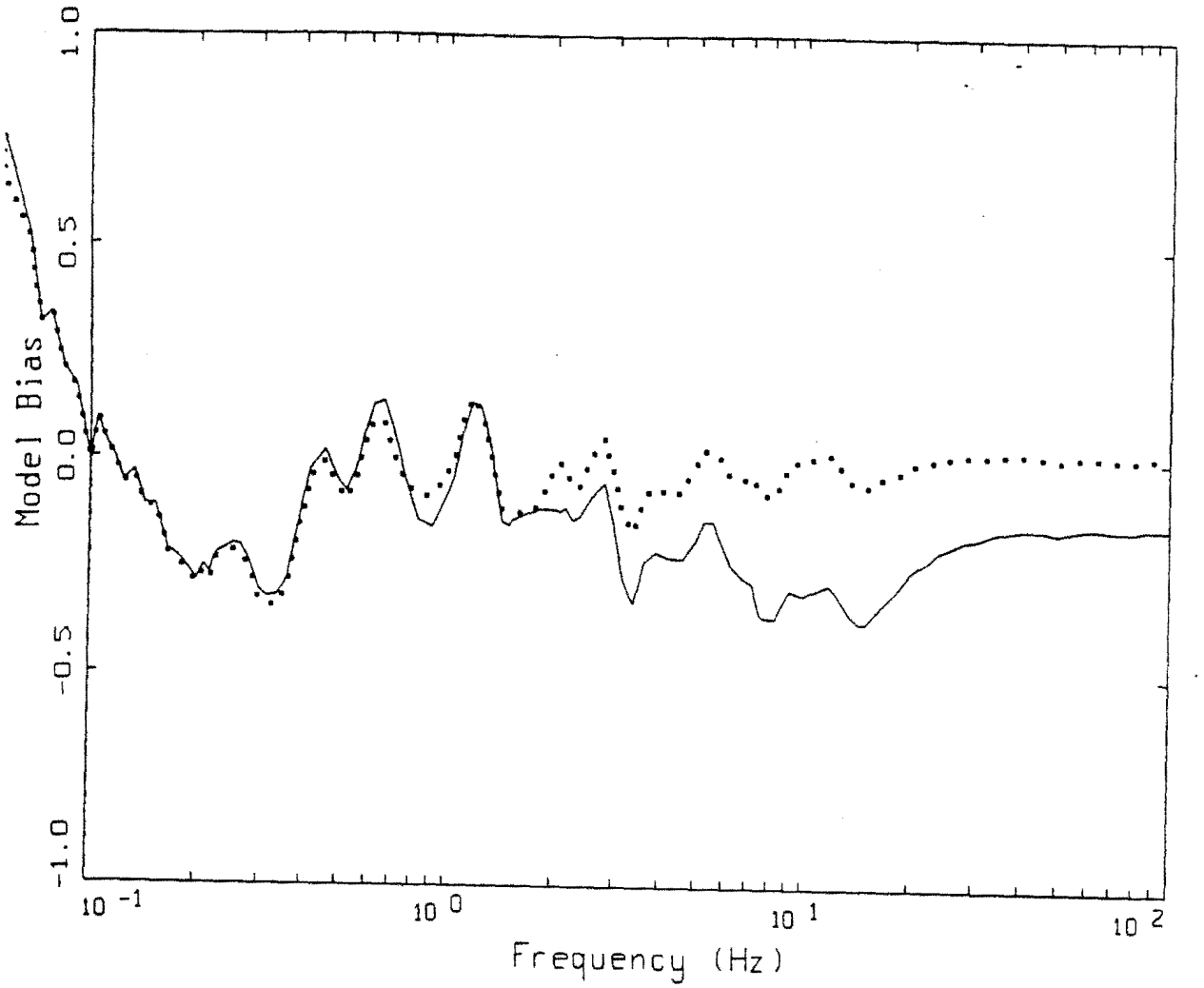

NORTHRIDGE FINITE SOURCE, MODELING BIAS
NONLINEAR PROFILES, 36 SOIL SITES TO 30 KM

LEGEND

——— MODELING BIAS, DEEP SOIL CURVES

• • • • MODELING BIAS, EPRI CURVES

Figure 5.17b

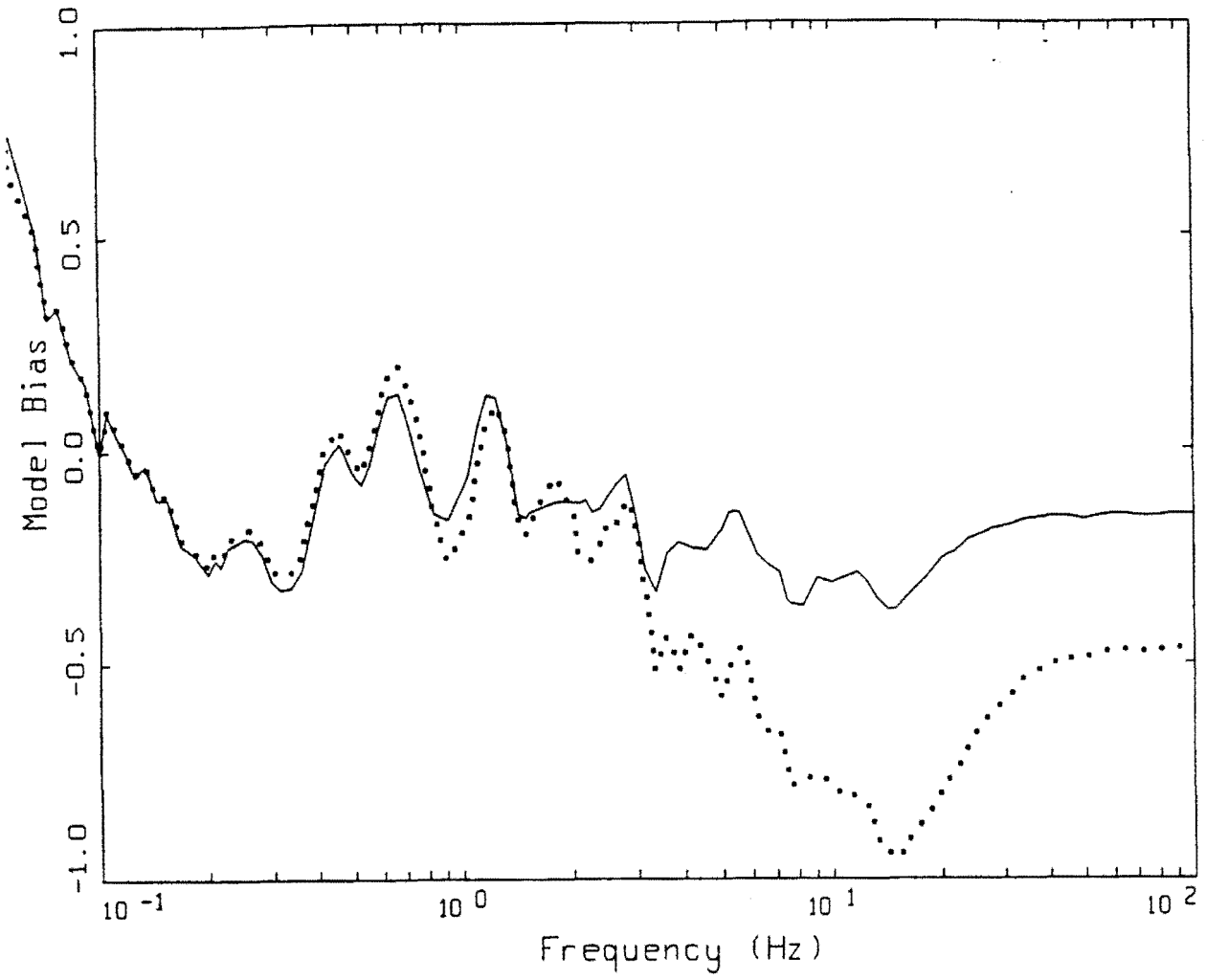

NORTHRIDGE FINITE SOURCE, MODELING BIAS
LINEAR AND NONLINEAR PROFILES, 36 SOIL SITES TO 30 KM

LEGEND

——— MODELING BIAS, NONLINEAR SOIL RESPONSE

• • • • MODELING BIAS, LINEAR SOIL RESPONSE

Figure 5.18

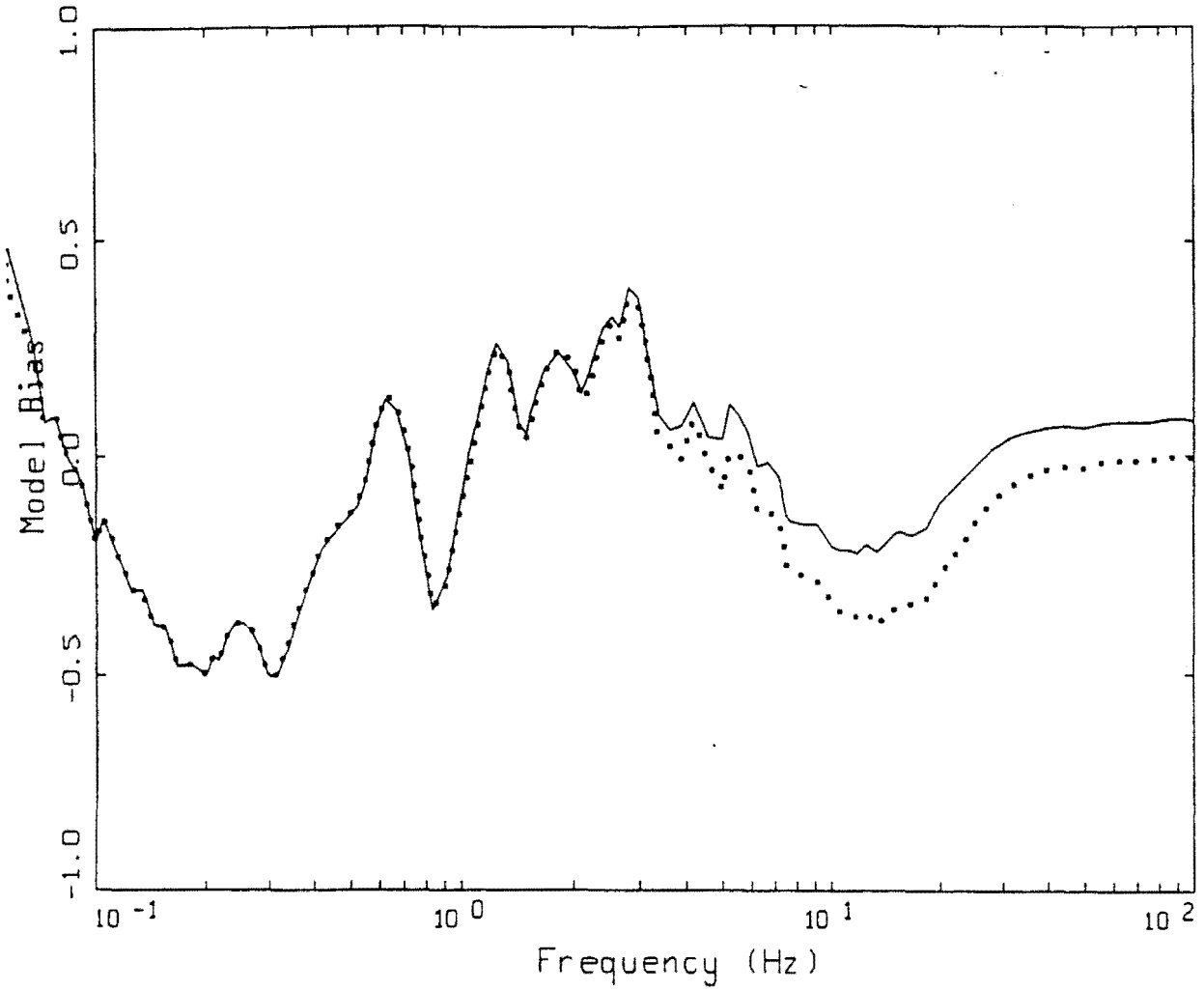

NORTHRIDGE FINITE SOURCE, MODELING BIAS
LINEAR AND NONLINEAR PROFILES, 35 SOIL SITES GT 30 KM

LEGEND

——— MODELING BIAS, NONLINEAR SOIL RESPONSE

• • • • MODELING BIAS, LINEAR SOIL RESPONSE

Figure 5.19

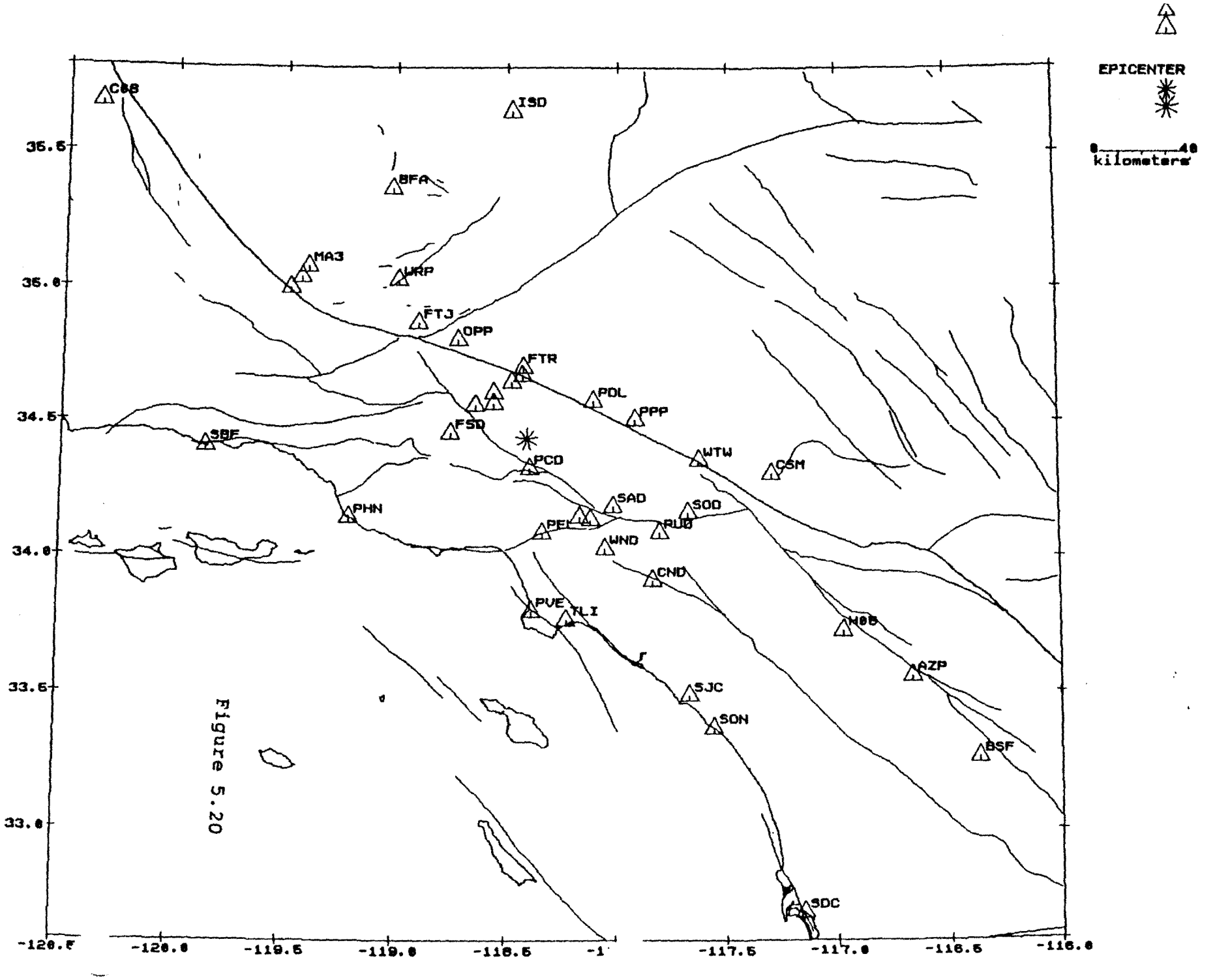

Figure 5.20

EQ3D-V4.00 FILE: SITES.HP2 EPICENT.HP2
. SCA:2000000 MFAC:1.0 XFAC:1.0 Nm=40 Nx=0

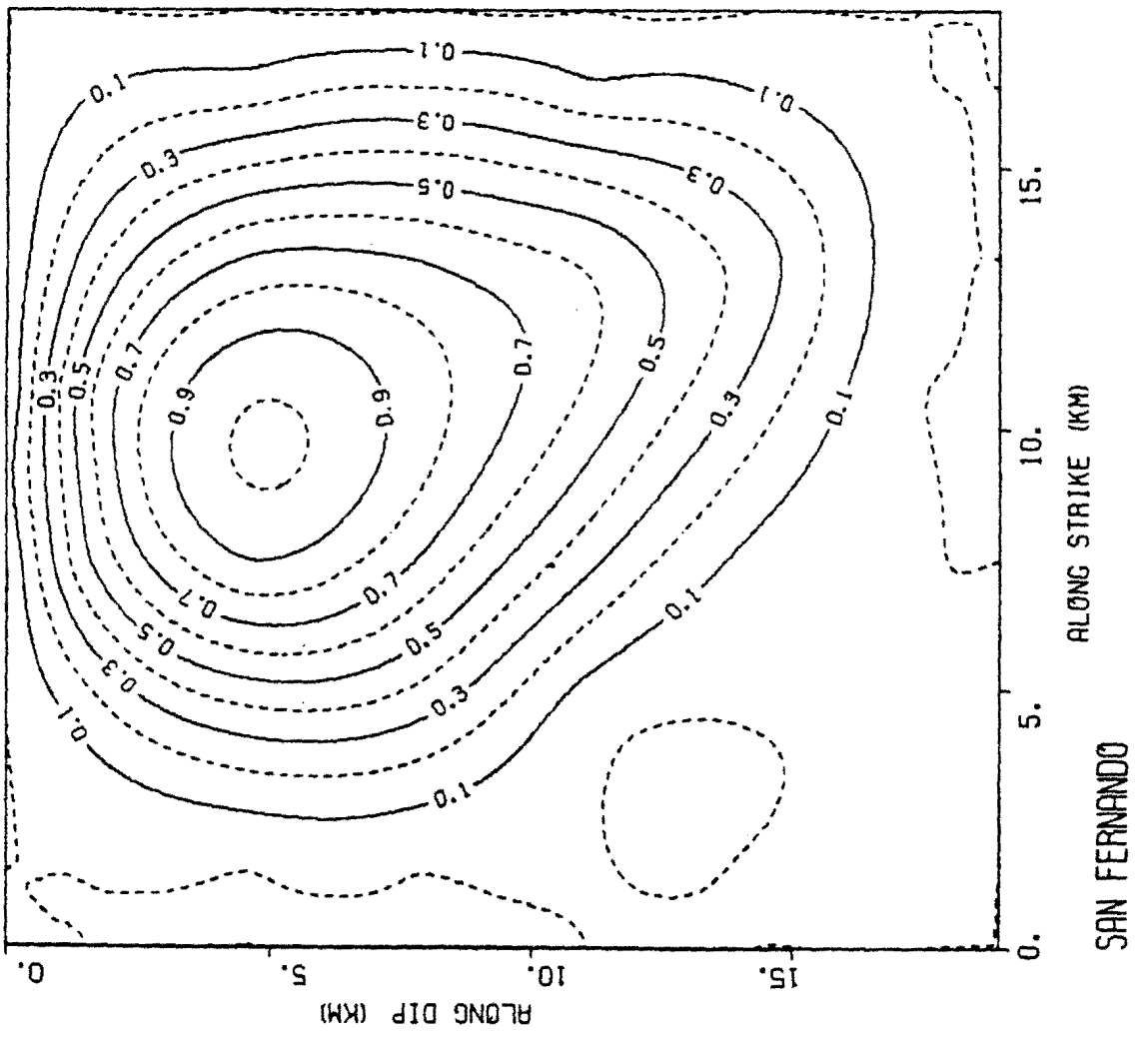
0.1
0.3
0.5
0.7
0.9
0.
5.
10.
15.
ALONG DIP (KM)
0.
5.
10.
15.
ALONG STRIKE (KM)
SAN FERNANDO

Figure 5.21

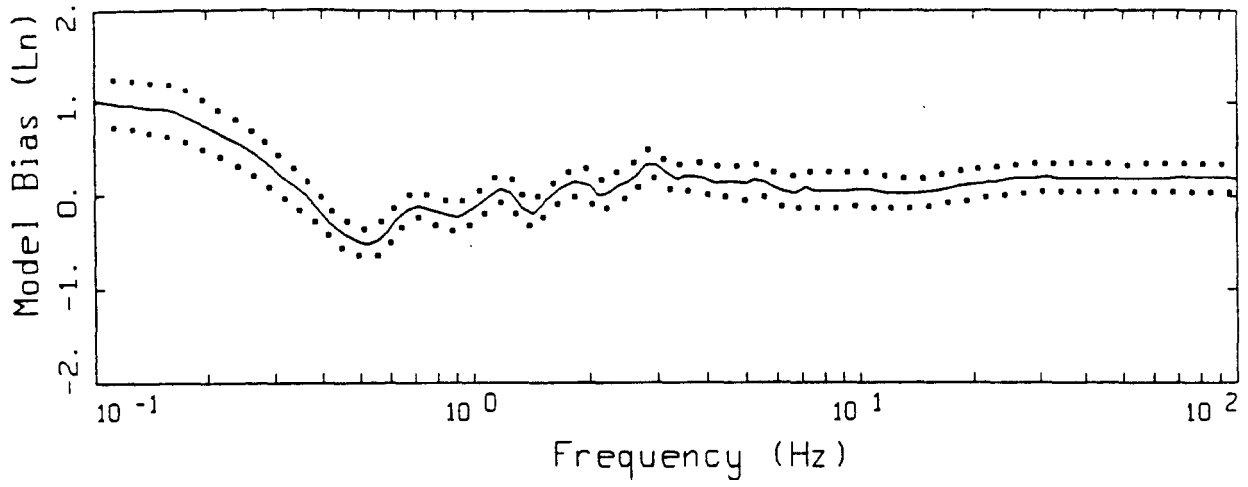

LEGEND
MODELING BIAS
90% CONFIDENCE INTERVAL OF MODELING BIAS
90% CONFIDENCE INTERVAL OF MODELING BIAS

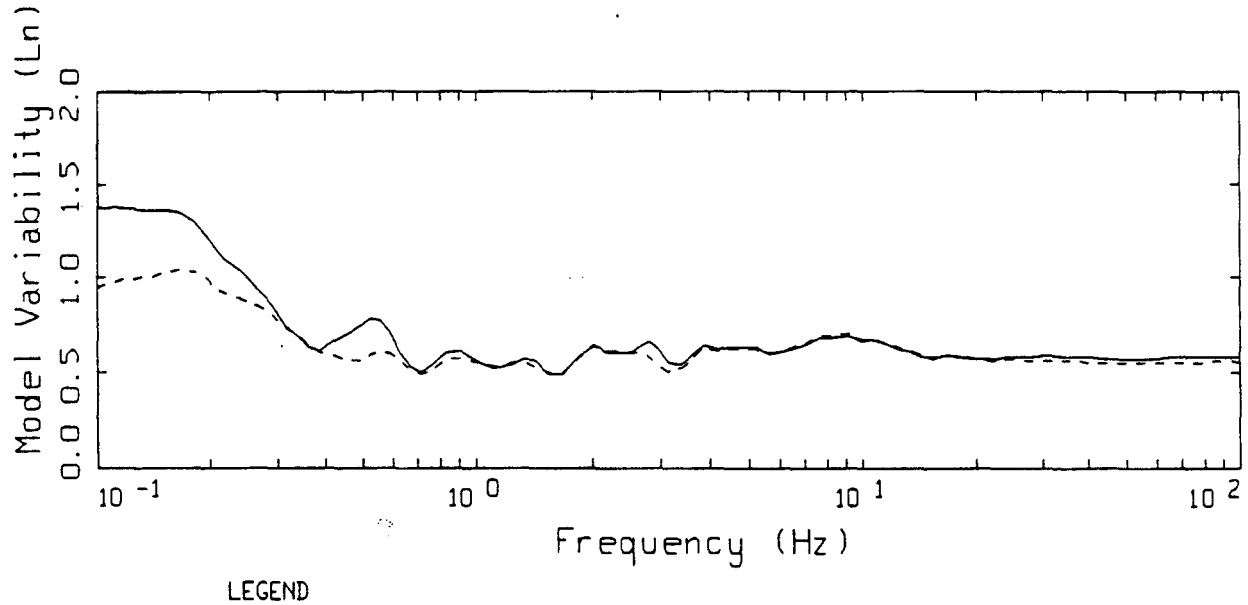

LEGEND
MEAN=0.0
BIAS CORRECTED

SAN FERNANDO POINT-SOURCE
NONLINEAR, ALL 39 SITES

Figure 5.22

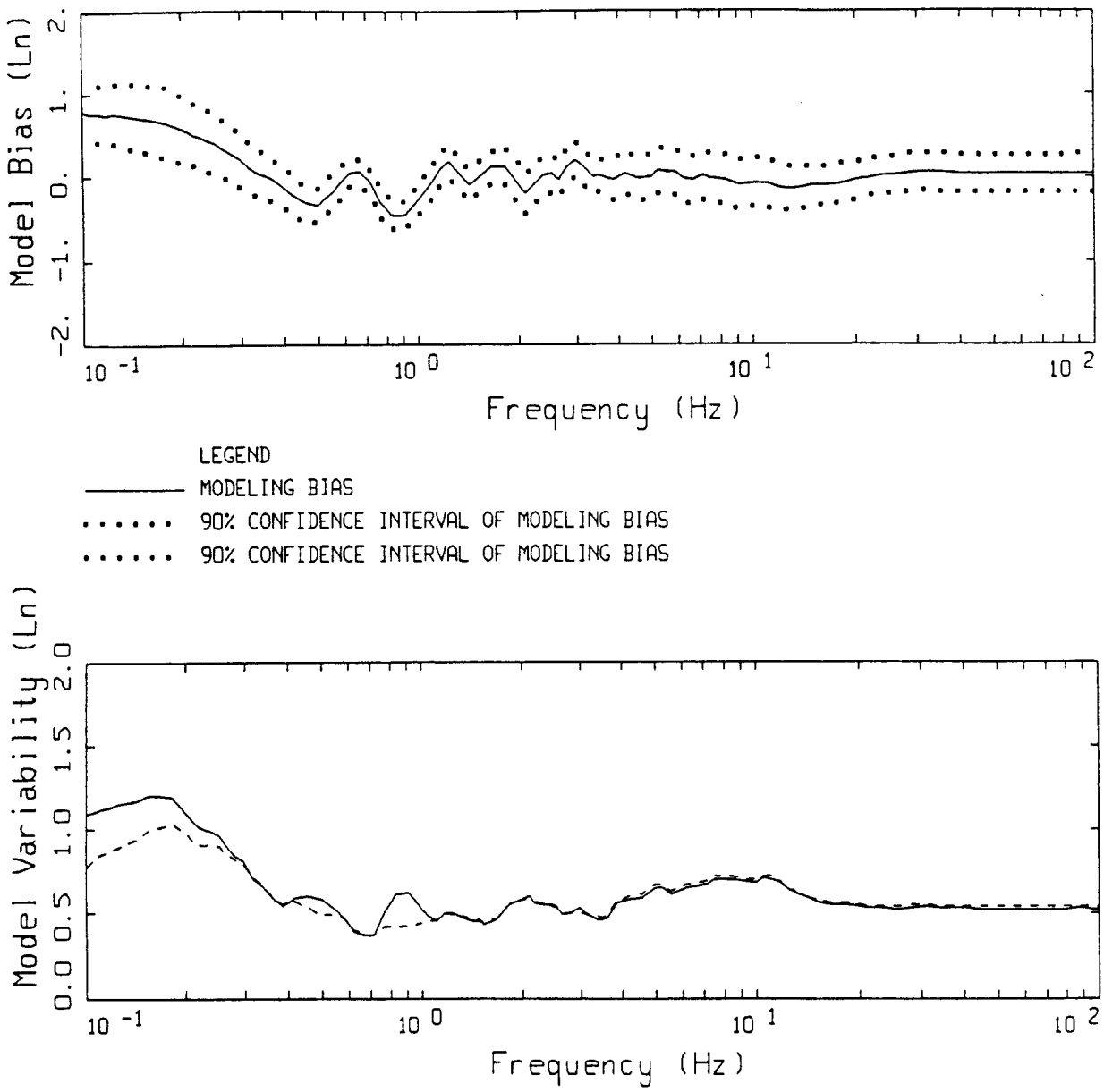

SAN FERNANDO POINT-SOURCE
NONLINEAR, 18 SOIL SITES

Figure 5.23

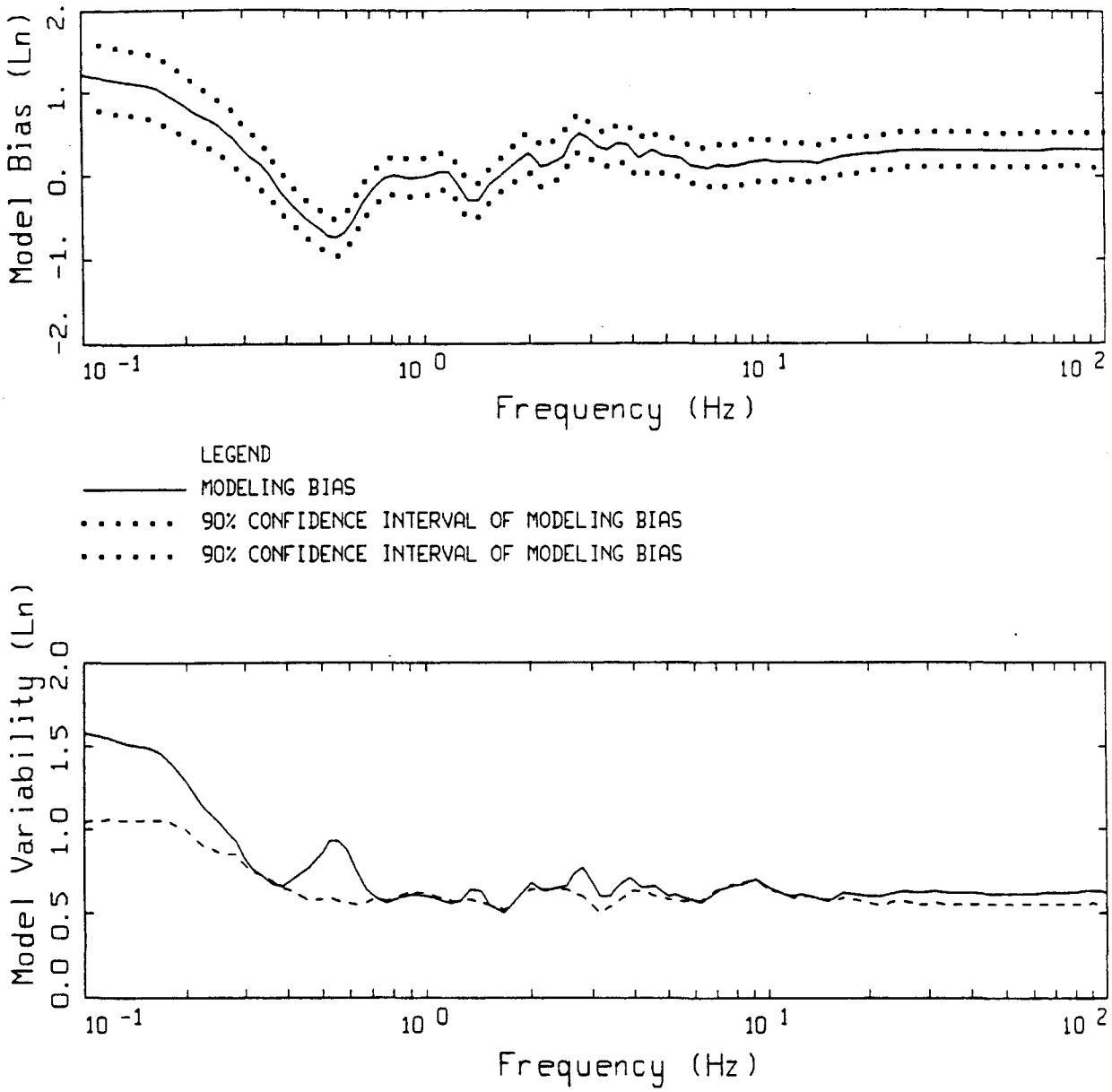
Model Bias (Ln)
2.
1.
0.
-1.
-2.
10 -1
10 0
10 1
10 2
Frequency (Hz)
LEGEND
MODELING BIAS
90% CONFIDENCE INTERVAL OF MODELING BIAS
90% CONFIDENCE INTERVAL OF MODELING BIAS
Model Variability (Ln)
0.0 0.5 1.0 1.5 2.0
10 -1
10 0
10 1
10 2
Frequency (Hz)
LEGEND
MEAN=0.0
BIAS CORRECTED
SAN FERNANDO POINT-SOURCE
NONLINEAR, 21 ROCK SITES

Figure 5.24

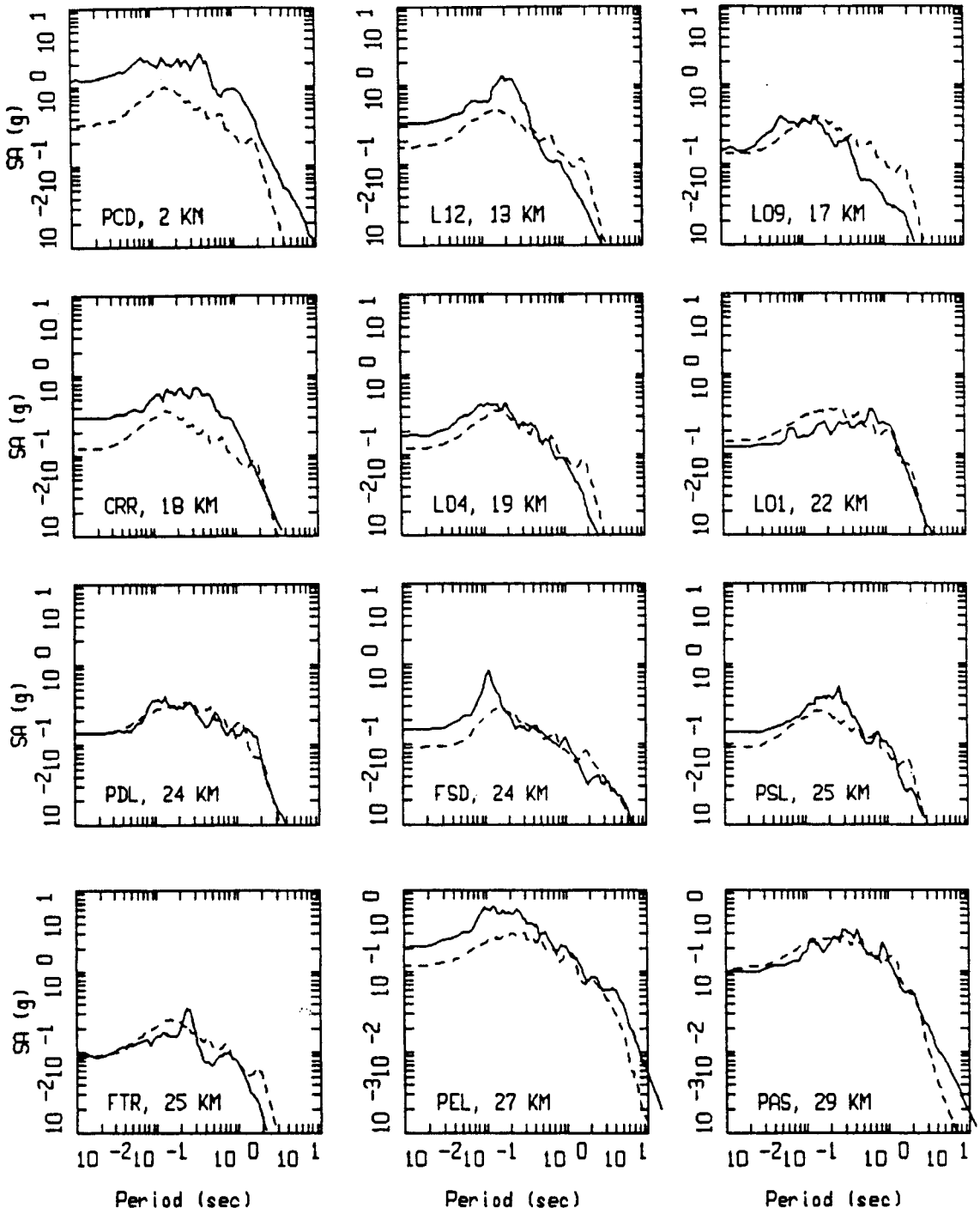

SAN FERNANDO, POINT-SOURCE MODELING, PAGE 1 OF 4.
NONLINEAR.

Figure Set 5.25

LEGEND

——— DATA

----- MODEL

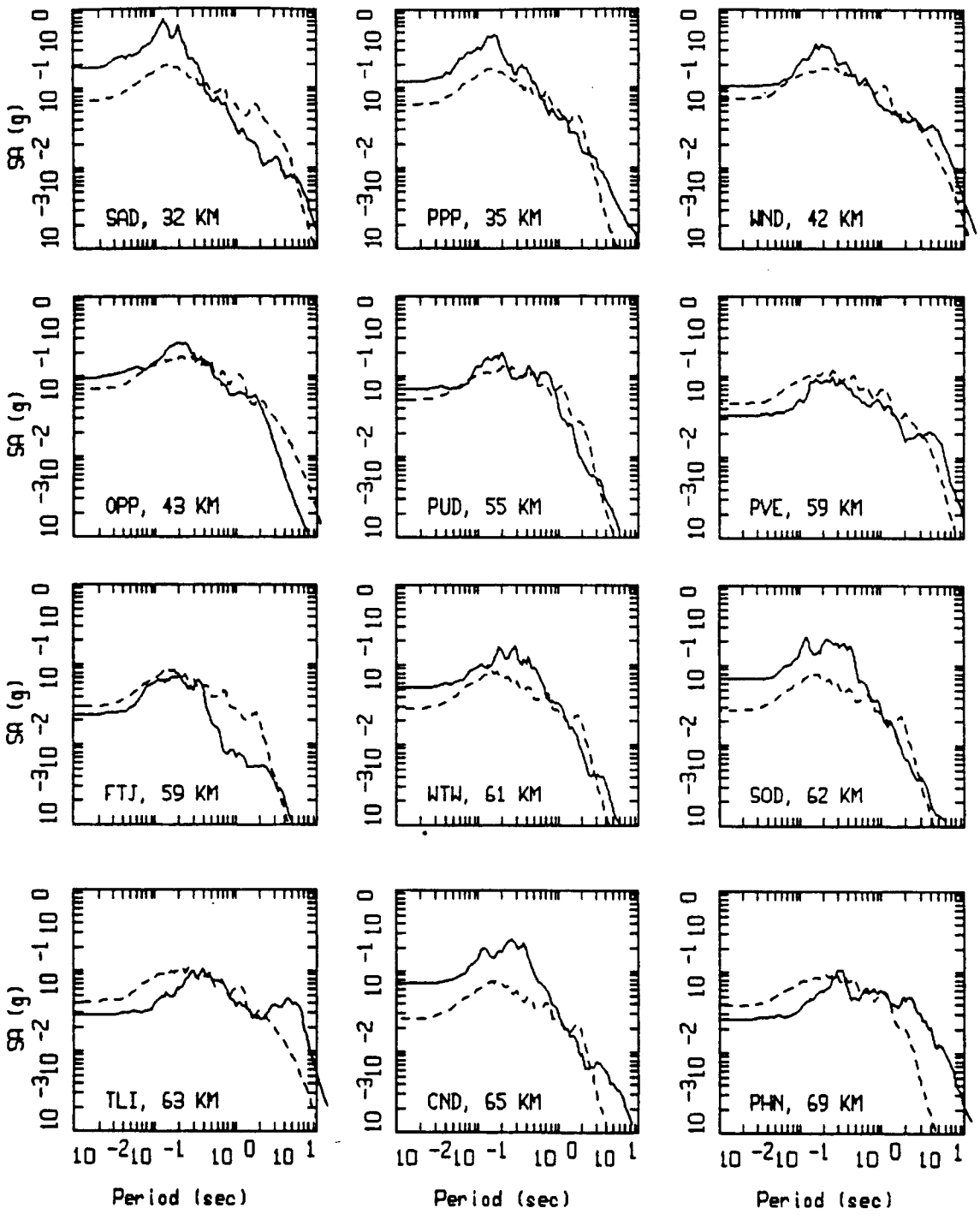

SAN FERNANDO, POINT-SOURCE MODELING, PAGE 2 OF 4.
NONLINEAR.

LEGEND

——— DATA

- - - - - MODEL

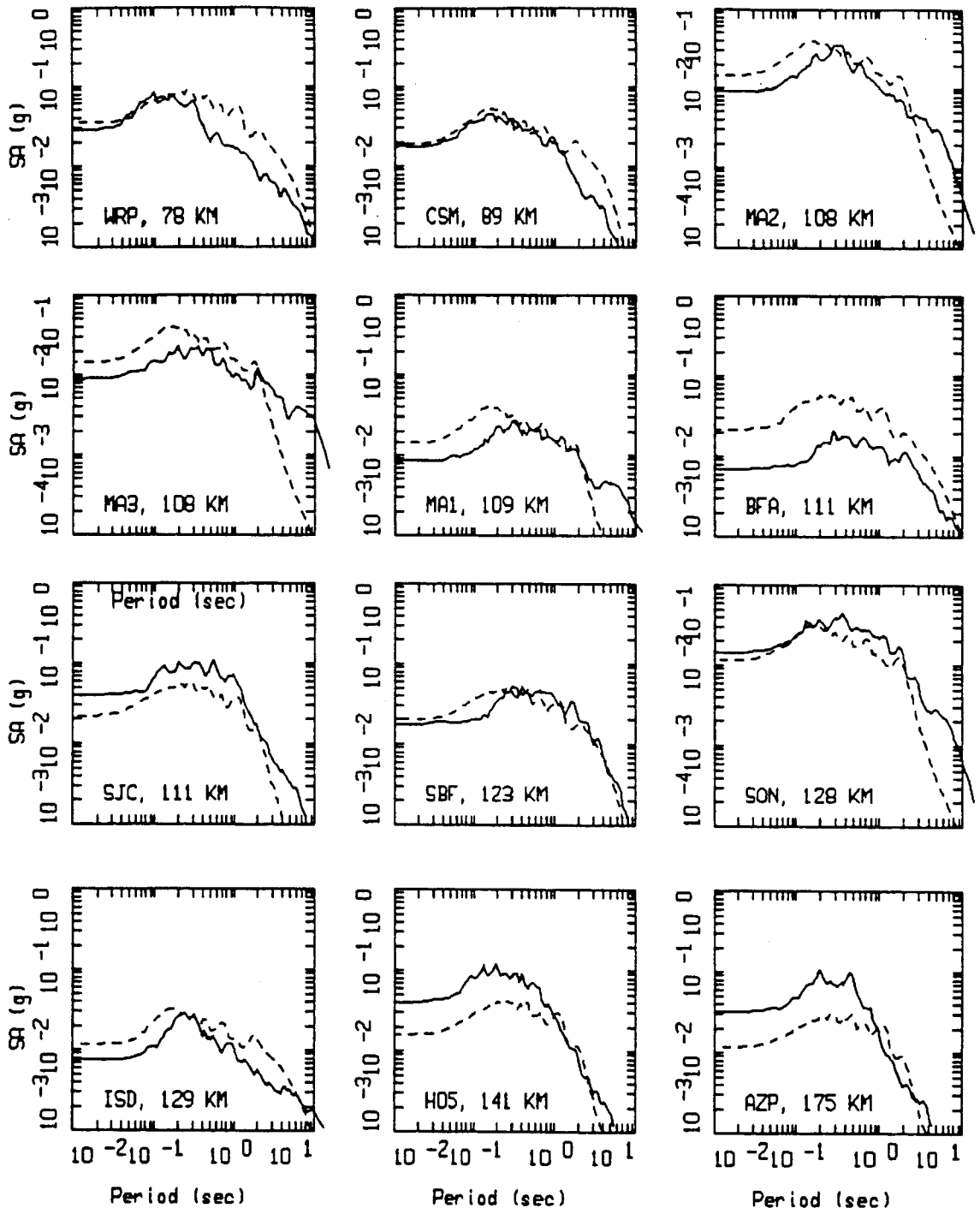

SAN FERNANDO, POINT-SOURCE MODELING, PAGE 3 OF 4.
NONLINEAR.

LEGEND

——— DATA

- - - - - MODEL

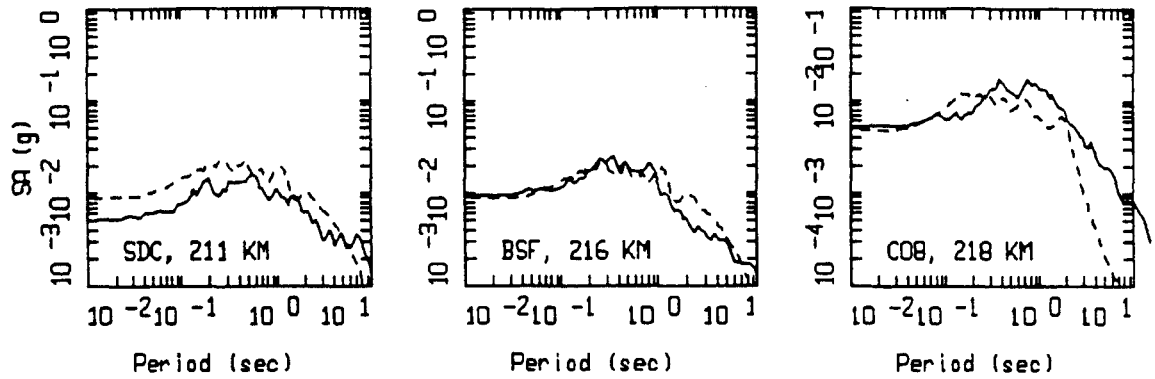

SAN FERNANDO, POINT-SOURCE MODELING, PAGE 4 OF 4.
NONLINEAR.

LEGEND

——— DATA

- - - - - MODEL

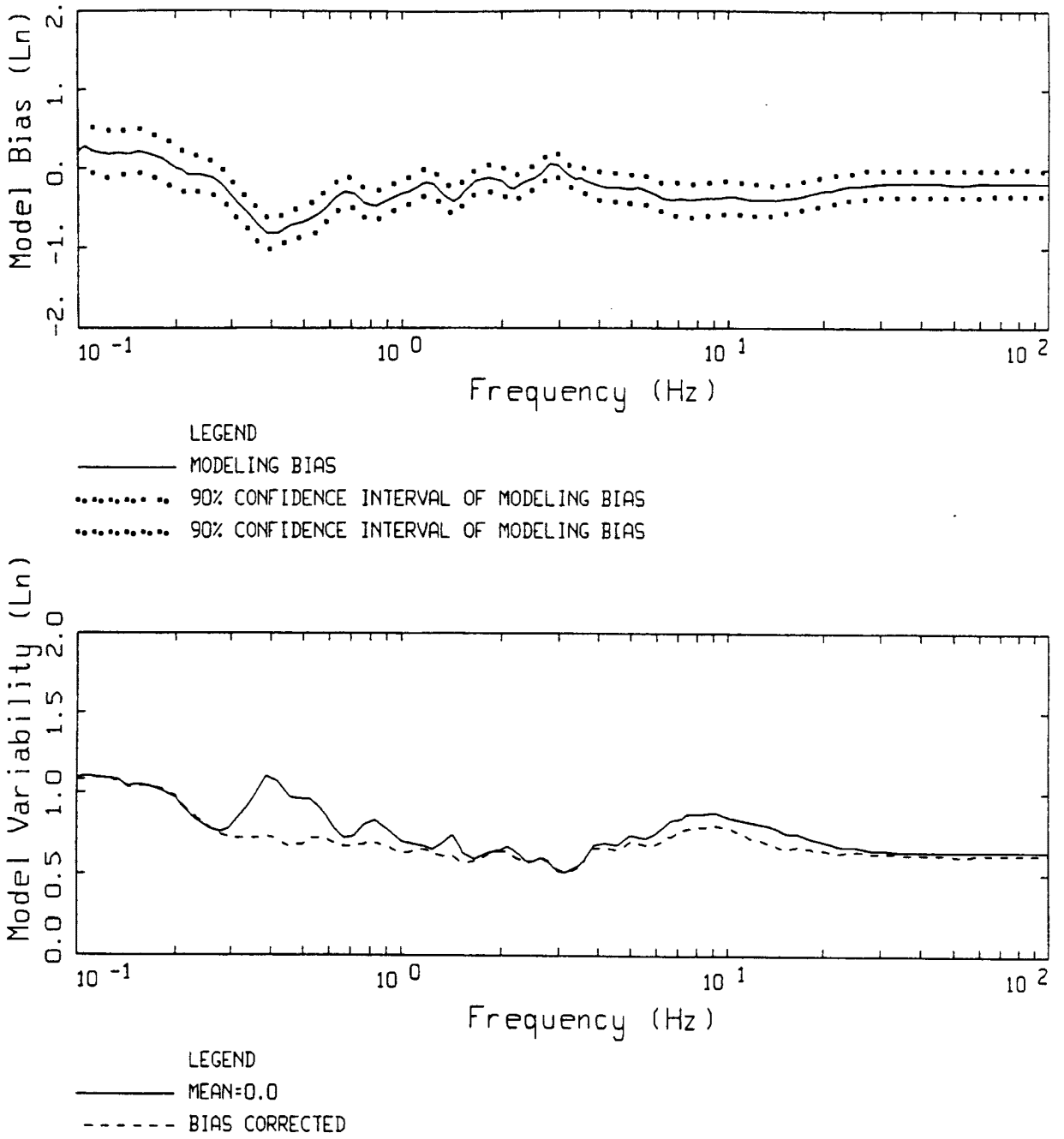

SAN FERNANDO FINITE-SOURCE
NONLINEAR, ALL 39 SITES

Figure 5.26

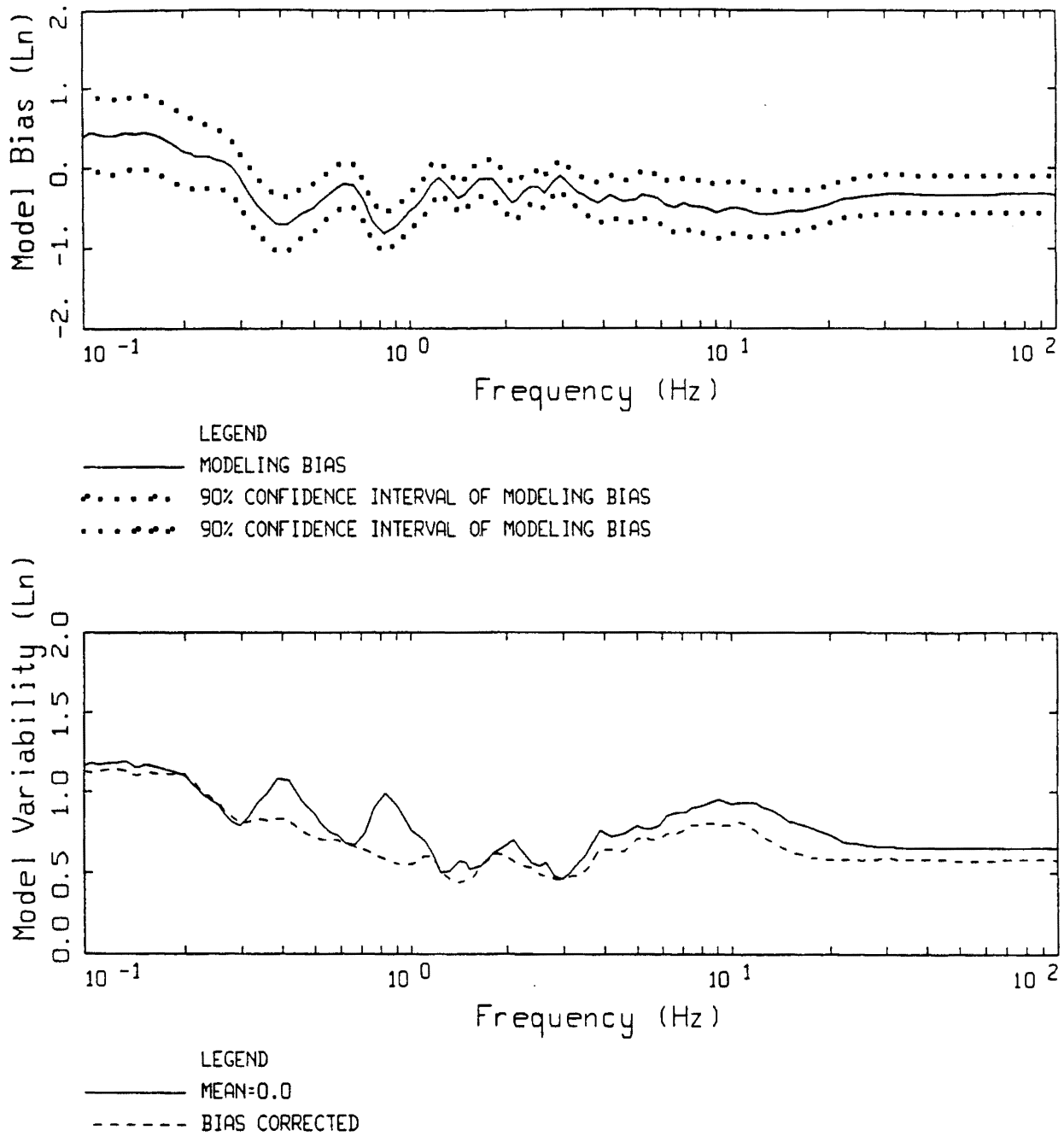

SAN FERNANDO FINITE-SOURCE
NONLINEAR, 18 SOIL SITES

Figure 5.27

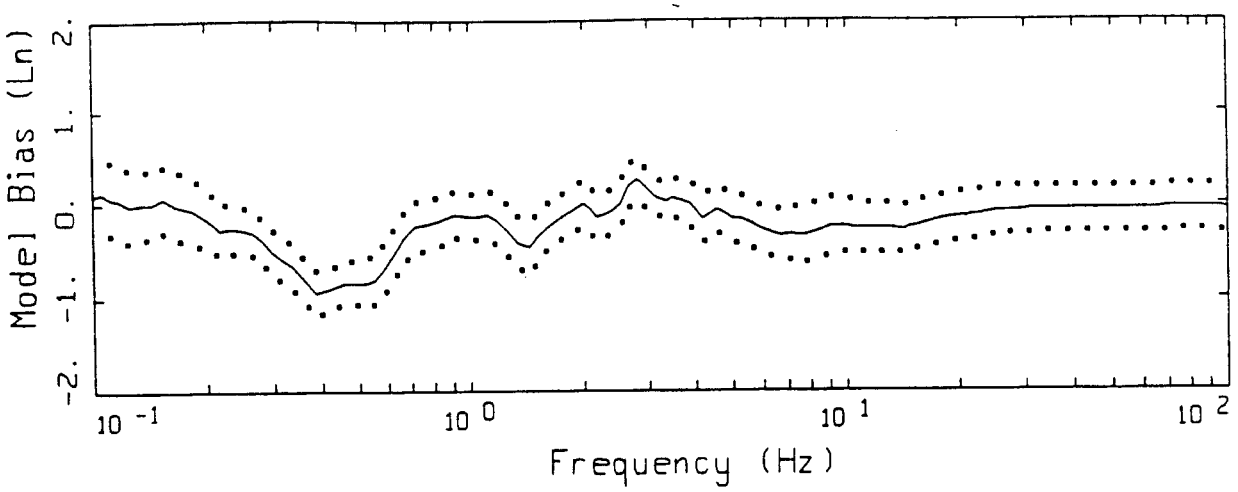

LEGEND
MODELING BIAS
90% CONFIDENCE INTERVAL OF MODELING BIAS
90% CONFIDENCE INTERVAL OF MODELING BIAS

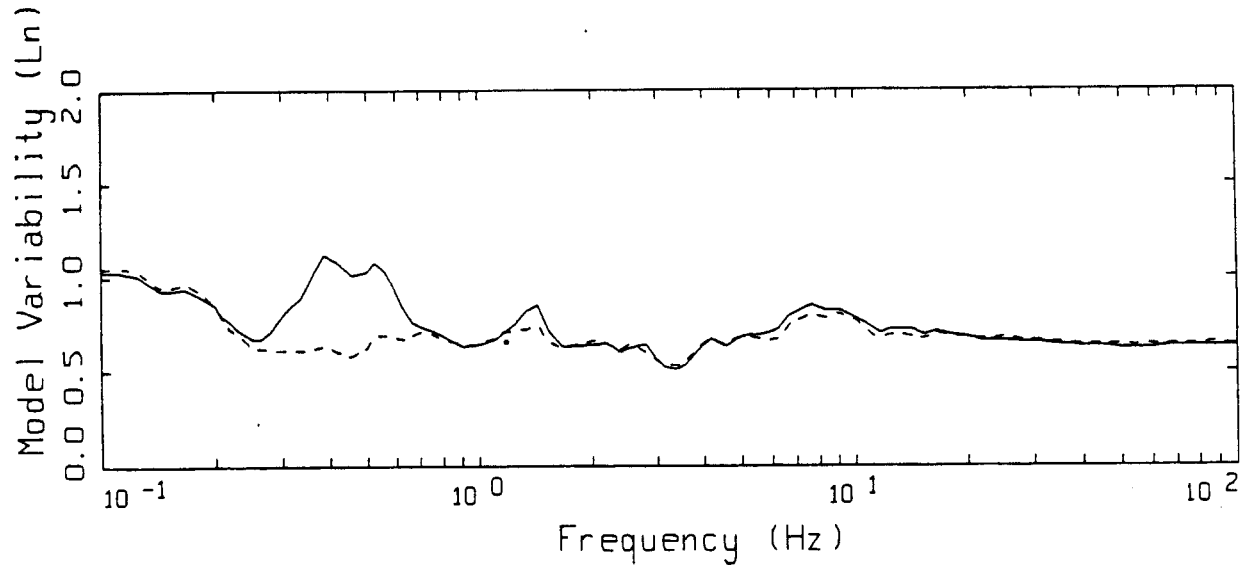

LEGEND
MEAN=0.0
BIAS CORRECTED

SAN FERNANDO FINITE-SOURCE
NONLINEAR, 21 ROCK SITES

Figure 5.28

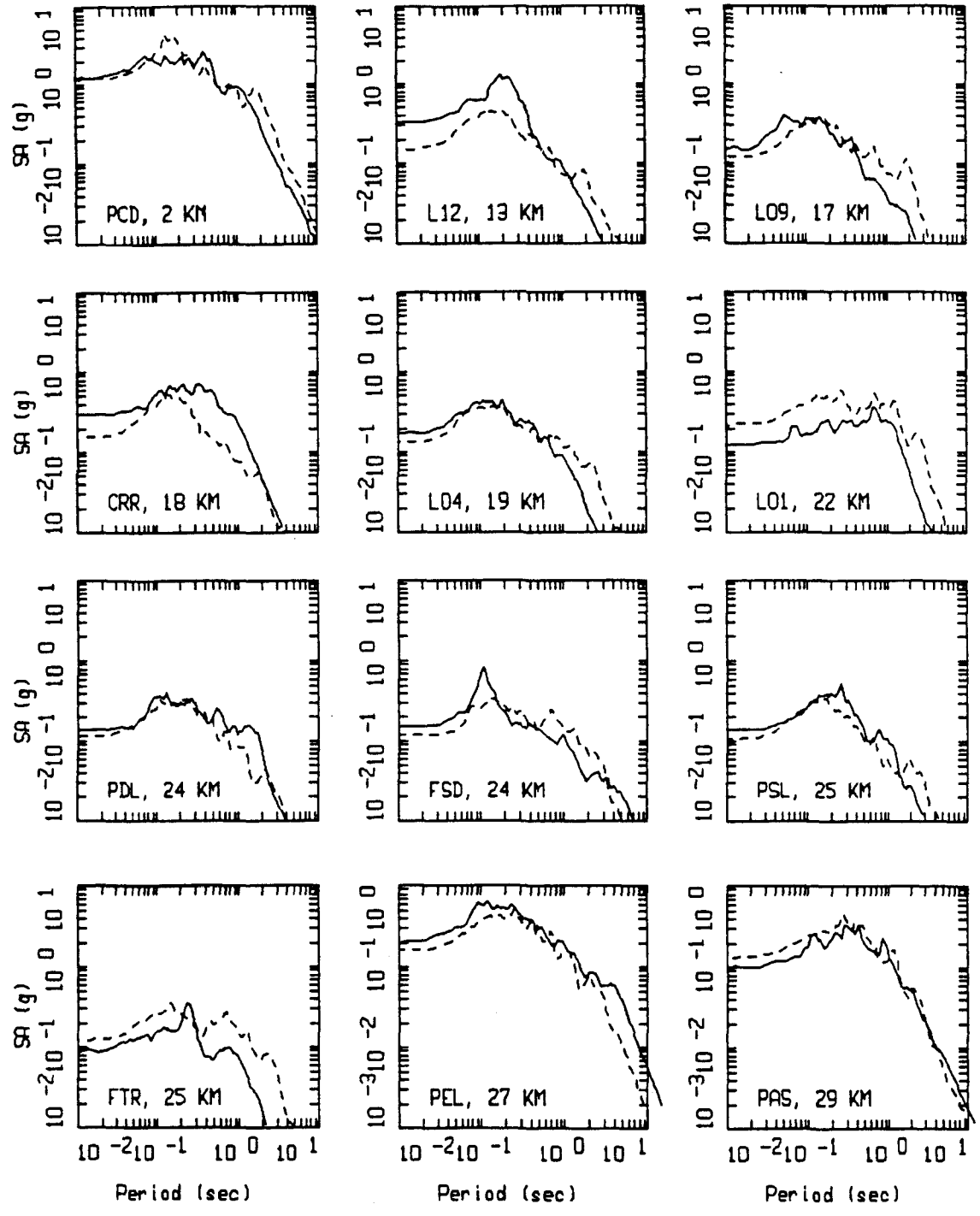

SAN FERNANDO, FINITE SOURCE MODELING, PAGE 1 OF 4.
NONLINEAR.

Figure Set 5.29

LEGEND

——— DATA

----- MODEL

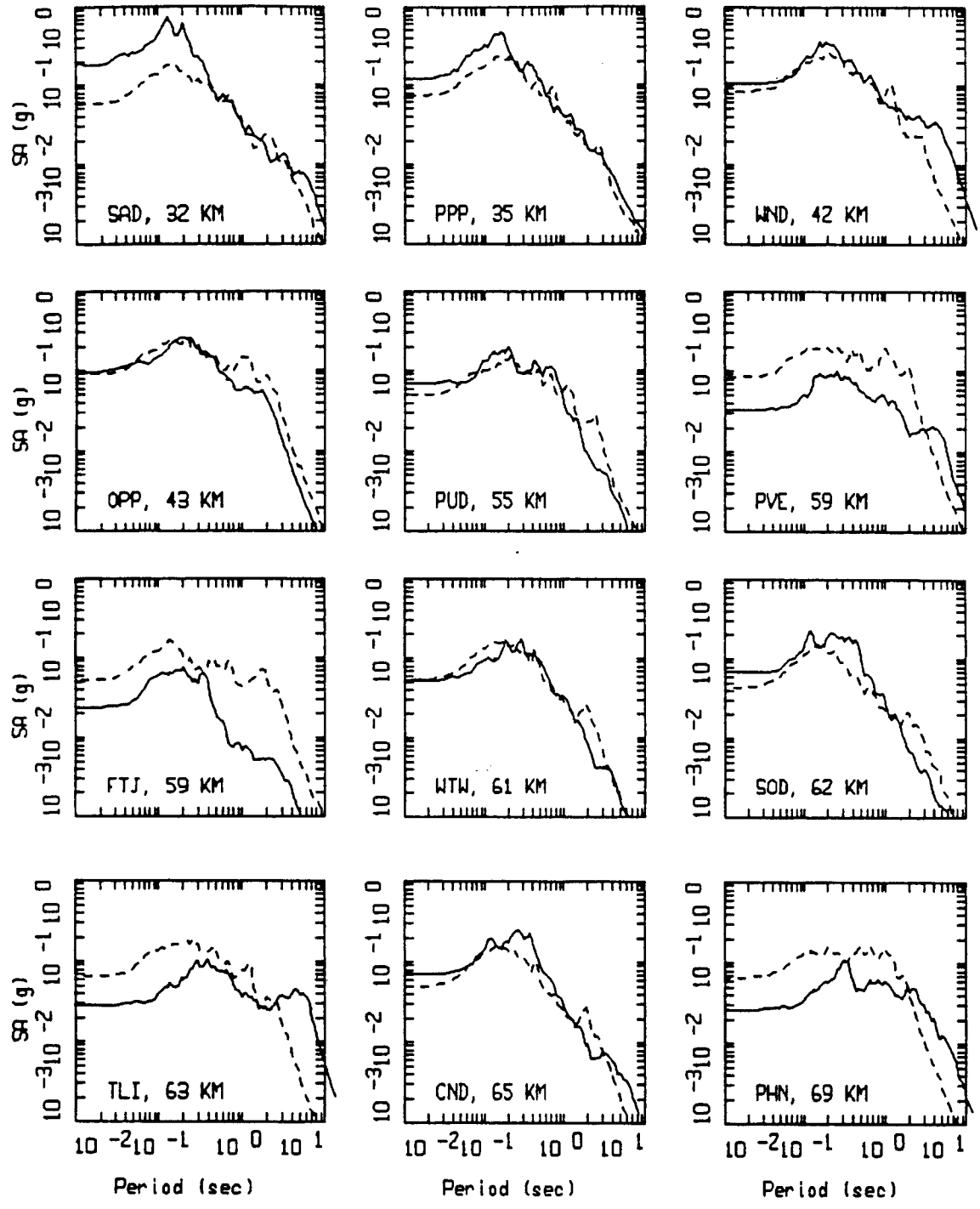

SAN_FERNANDO, FINITE SOURCE MODELING, PAGE 2 OF 4.
NONLINEAR.

LEGEND

——— DATA

- - - - - MODEL

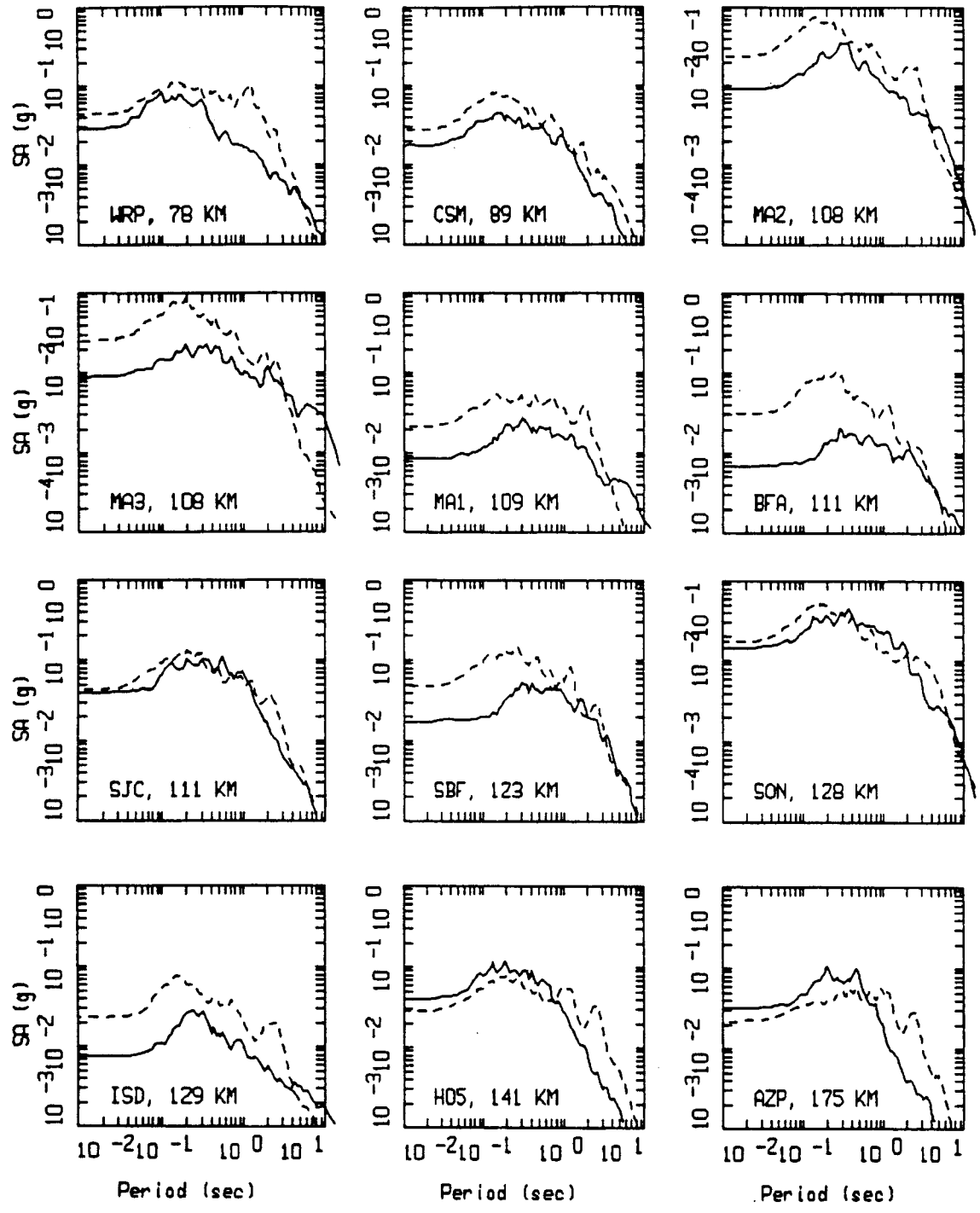

SAN FERNANDO, FINITE SOURCE MODELING, PAGE 3 OF 4.
NONLINEAR.

LEGEND

——— DATA

- - - - - MODEL

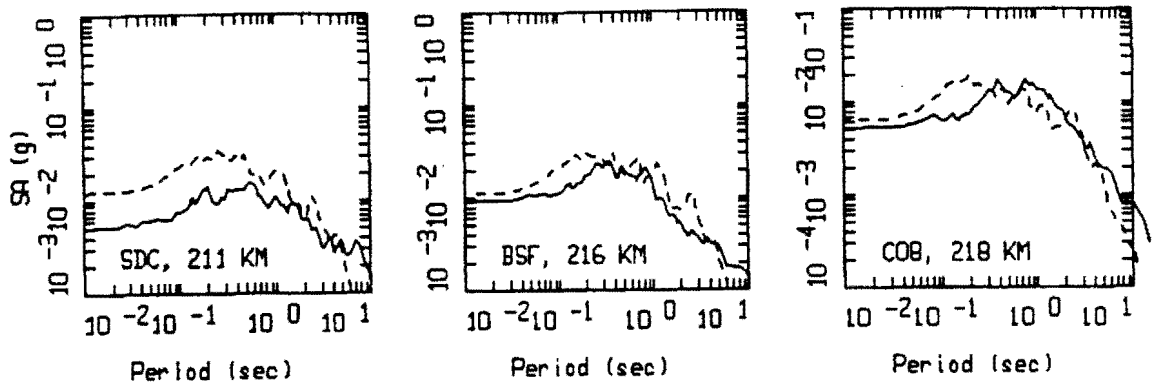

SAN FERNANDO, FINITE SOURCE MODELING, PAGE 4 OF 4.
NONLINEAR.

LEGEND
——— DATA
- - - - - MODEL

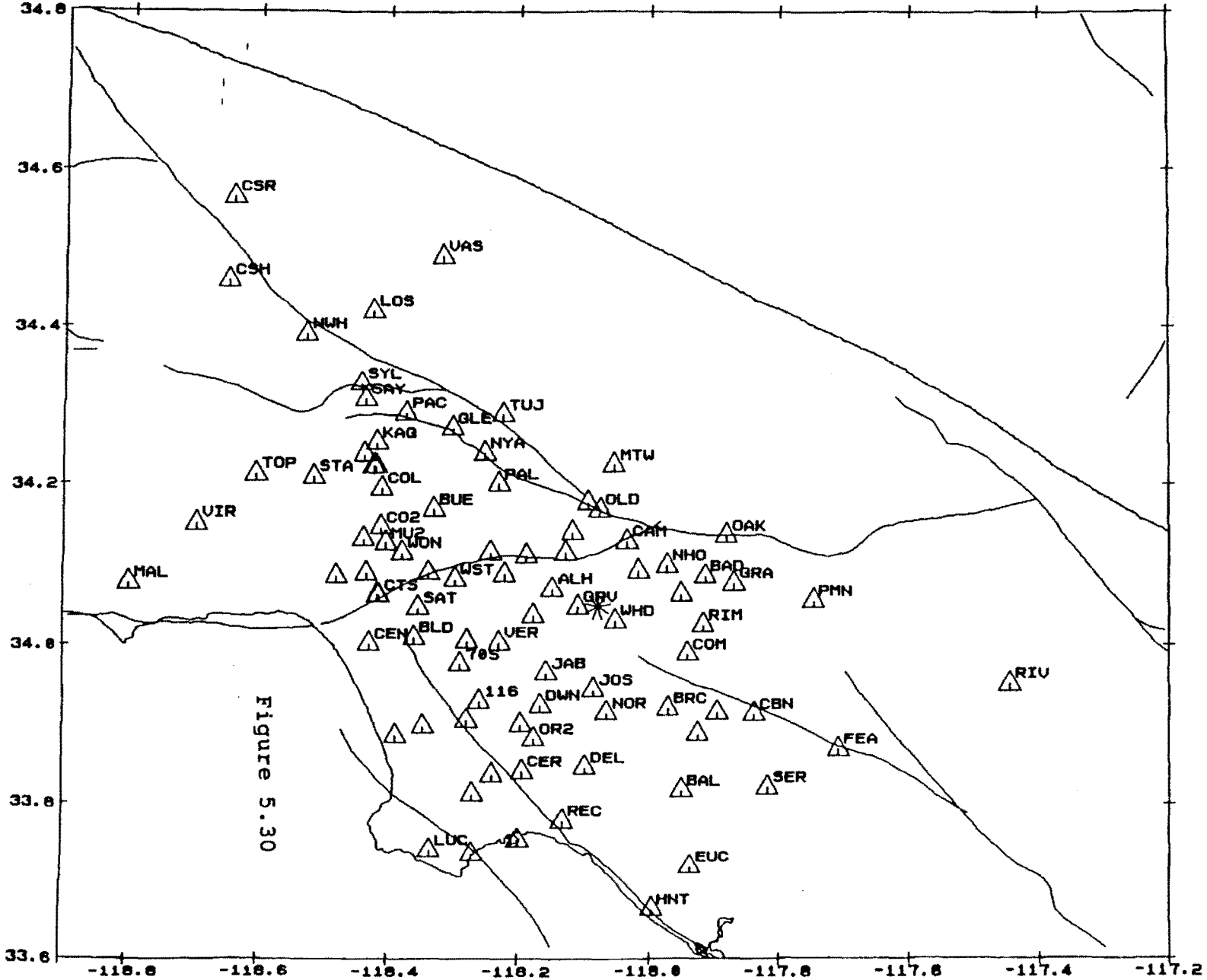

Figure 5.30

EQ3D-v4.00 FILE: SITES.HP2 EPICENT.HP2
. SCA:000000 MFAC:1.0 XFAC:1.0 Nm=89 Nx=0

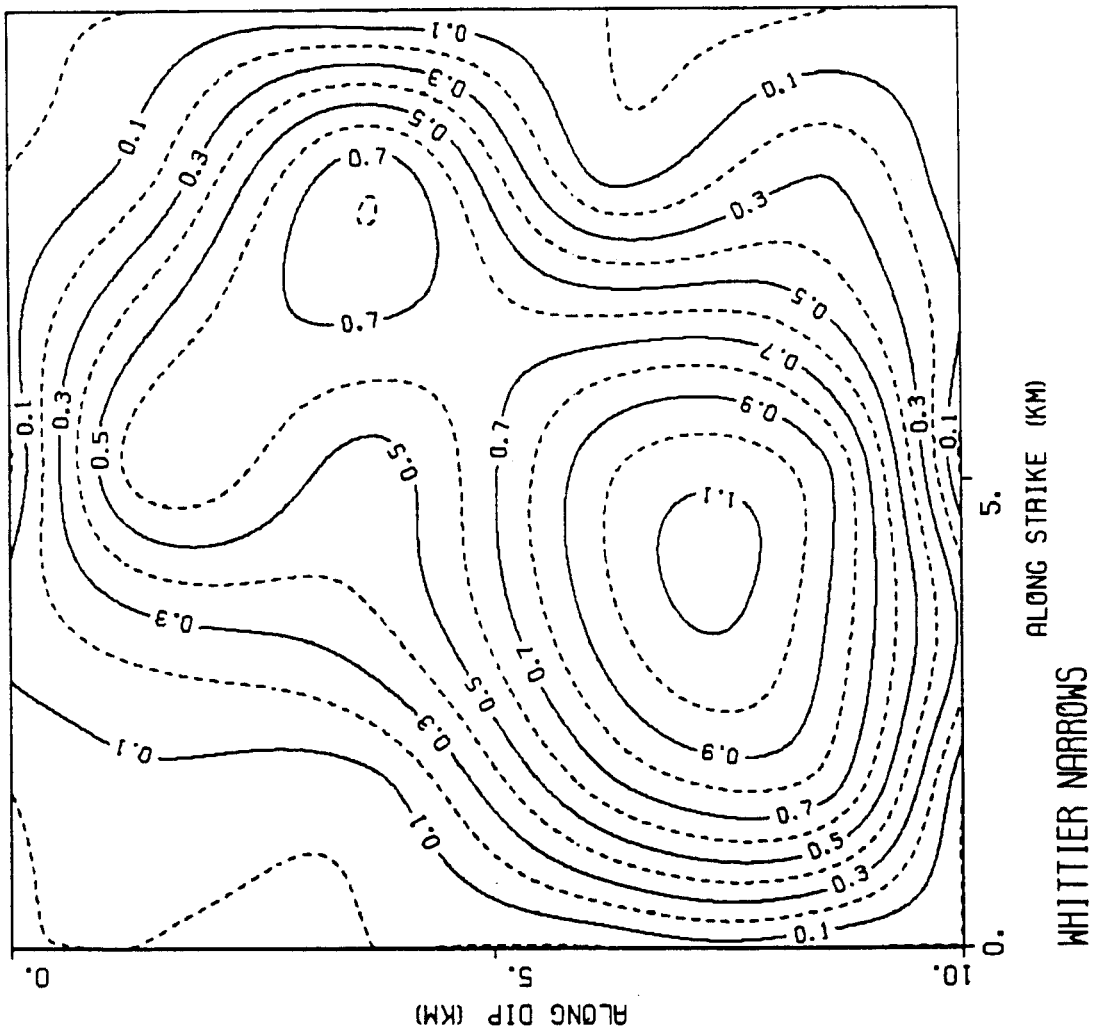
WHITTIER NARROWS
ALONG STRIKE (KM)
ALONG DIP (KM)
0.
5.
10.
0.1
0.3
0.5
0.7
0.9
1.1

Figure 5.31

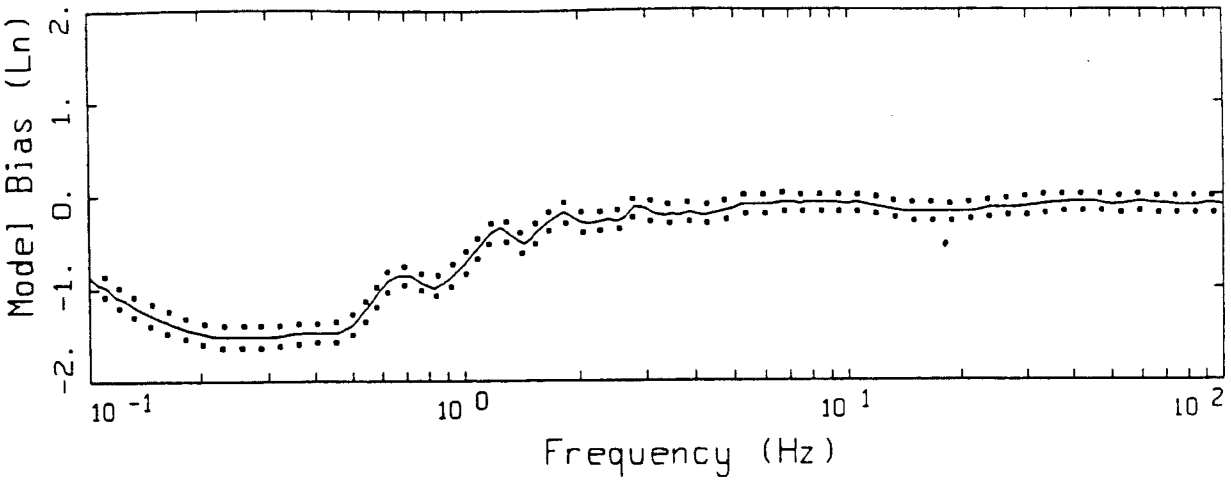

LEGEND
MODELING BIAS
90% CONFIDENCE INTERVAL OF MODELING BIAS
90% CONFIDENCE INTERVAL OF MODELING BIAS

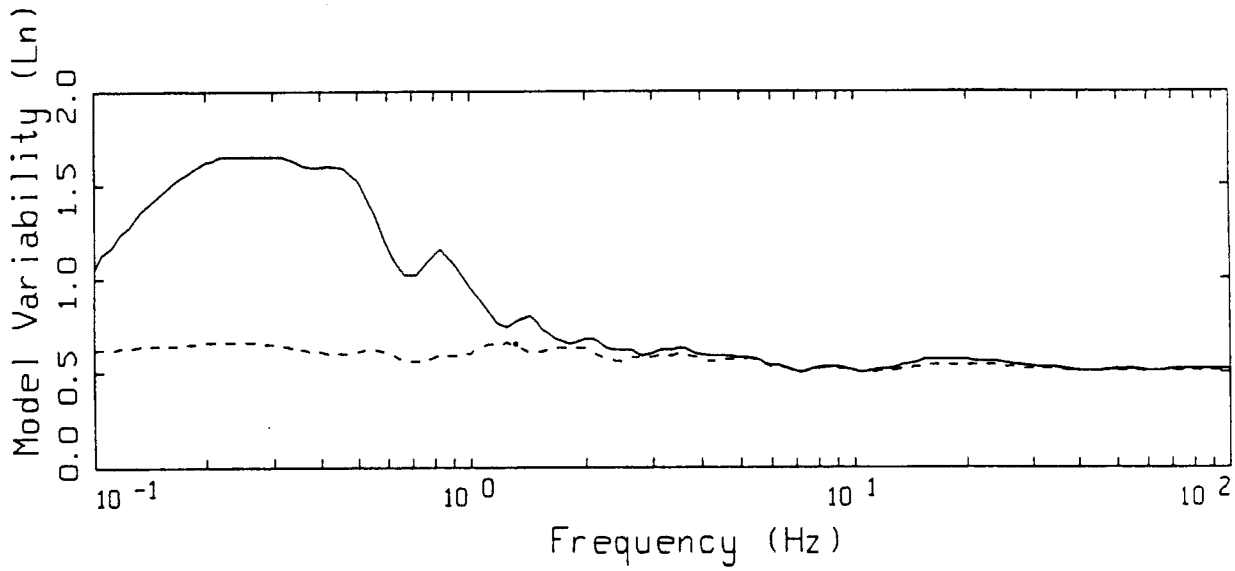

LEGEND
MEAN=0.0
BIAS CORRECTED

WHITTIER NARROWS POINT-SOURCE
NONLINEAR, ALL 88 SITES

Figure 5.32

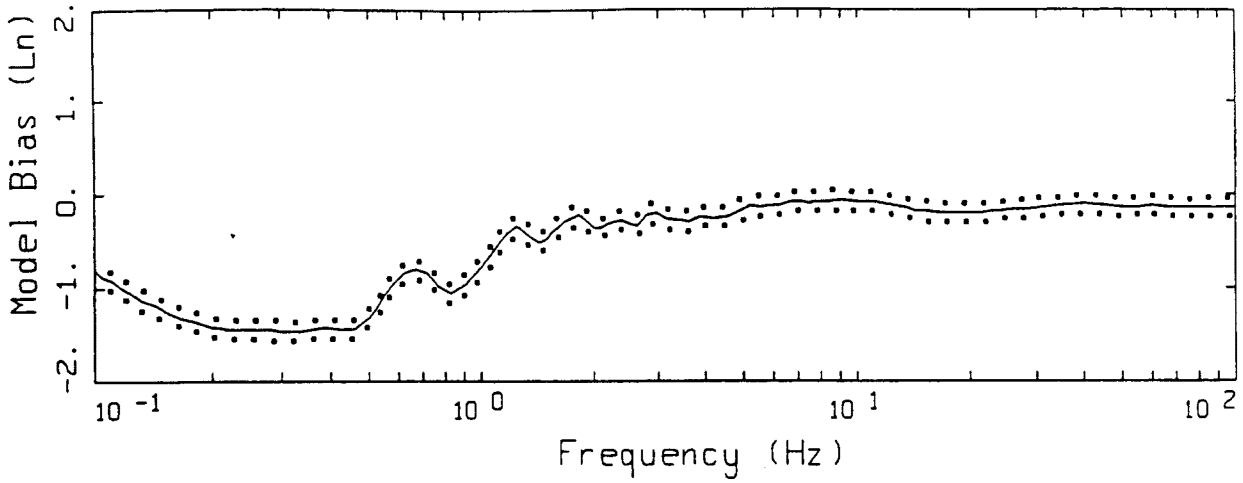

LEGEND
MODELING BIAS
90% CONFIDENCE INTERVAL OF MODELING BIAS
90% CONFIDENCE INTERVAL OF MODELING BIAS

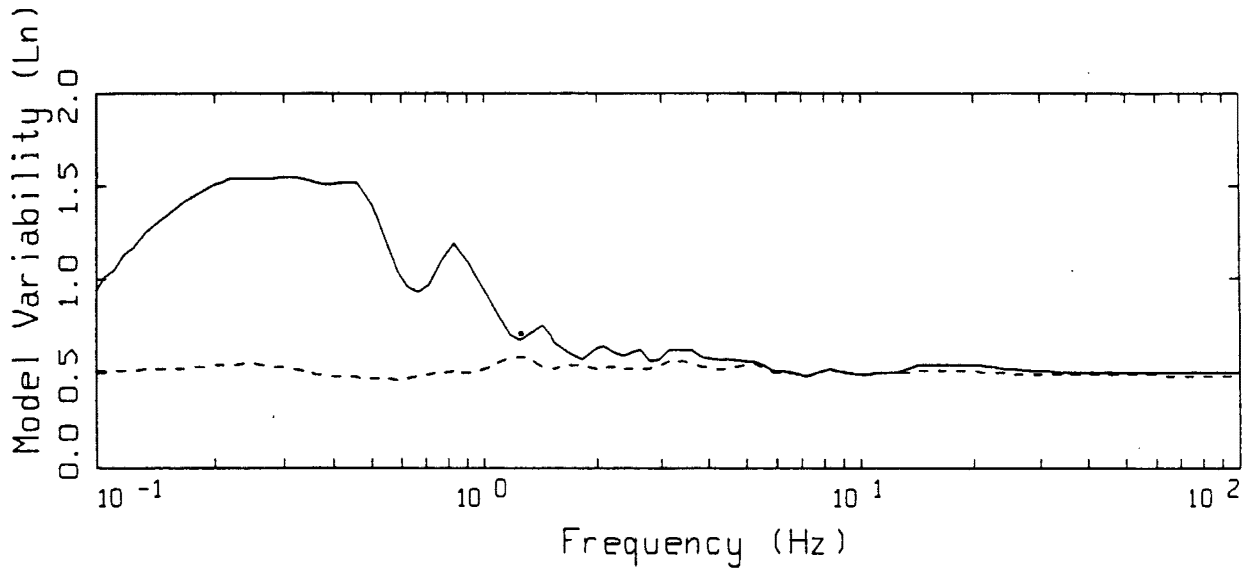

LEGEND
MEAN=0.0
BIAS CORRECTED

WHITTIER NARROWS POINT-SOURCE
NONLINEAR, 70 SOIL SITES

Figure 5.33

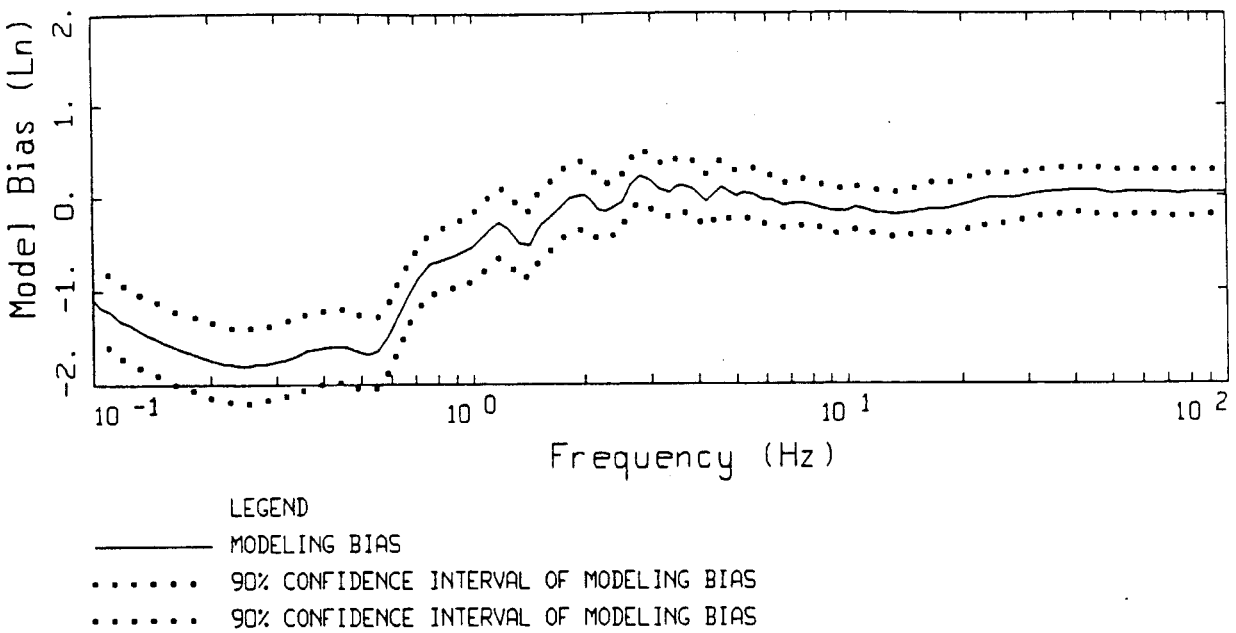

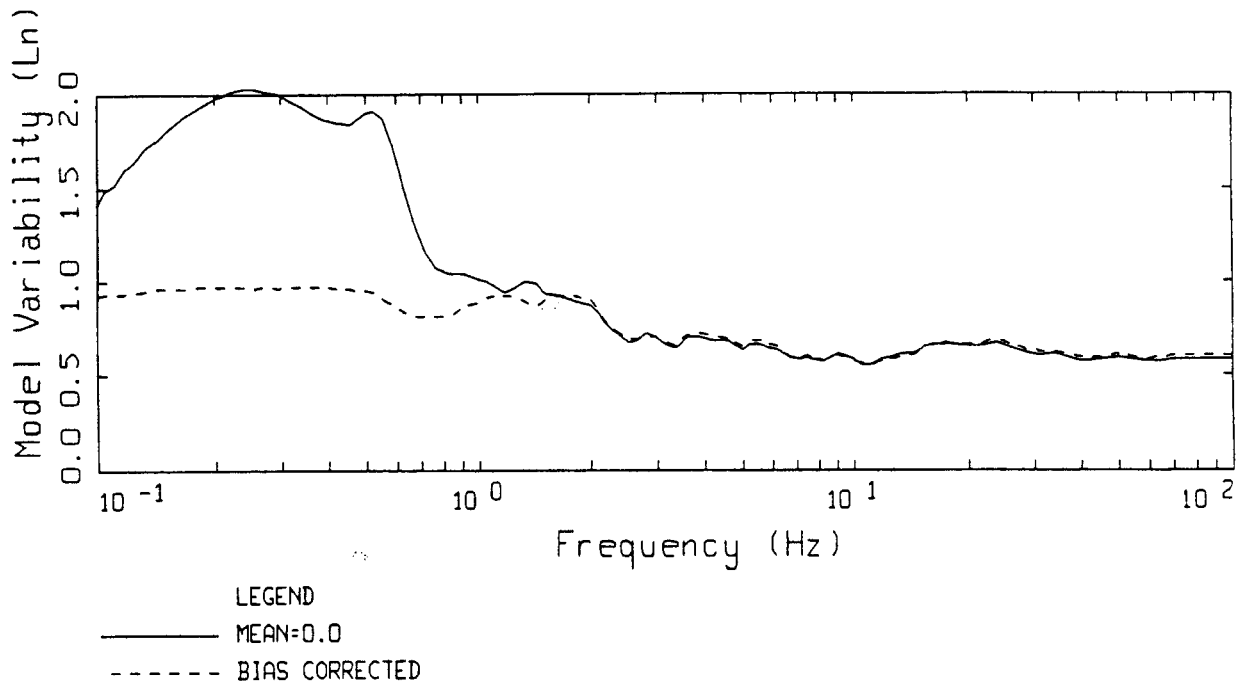

WHITTIER NARROWS POINT-SOURCE
NONLINEAR, 18 ROCK SITES

Figure 5.34

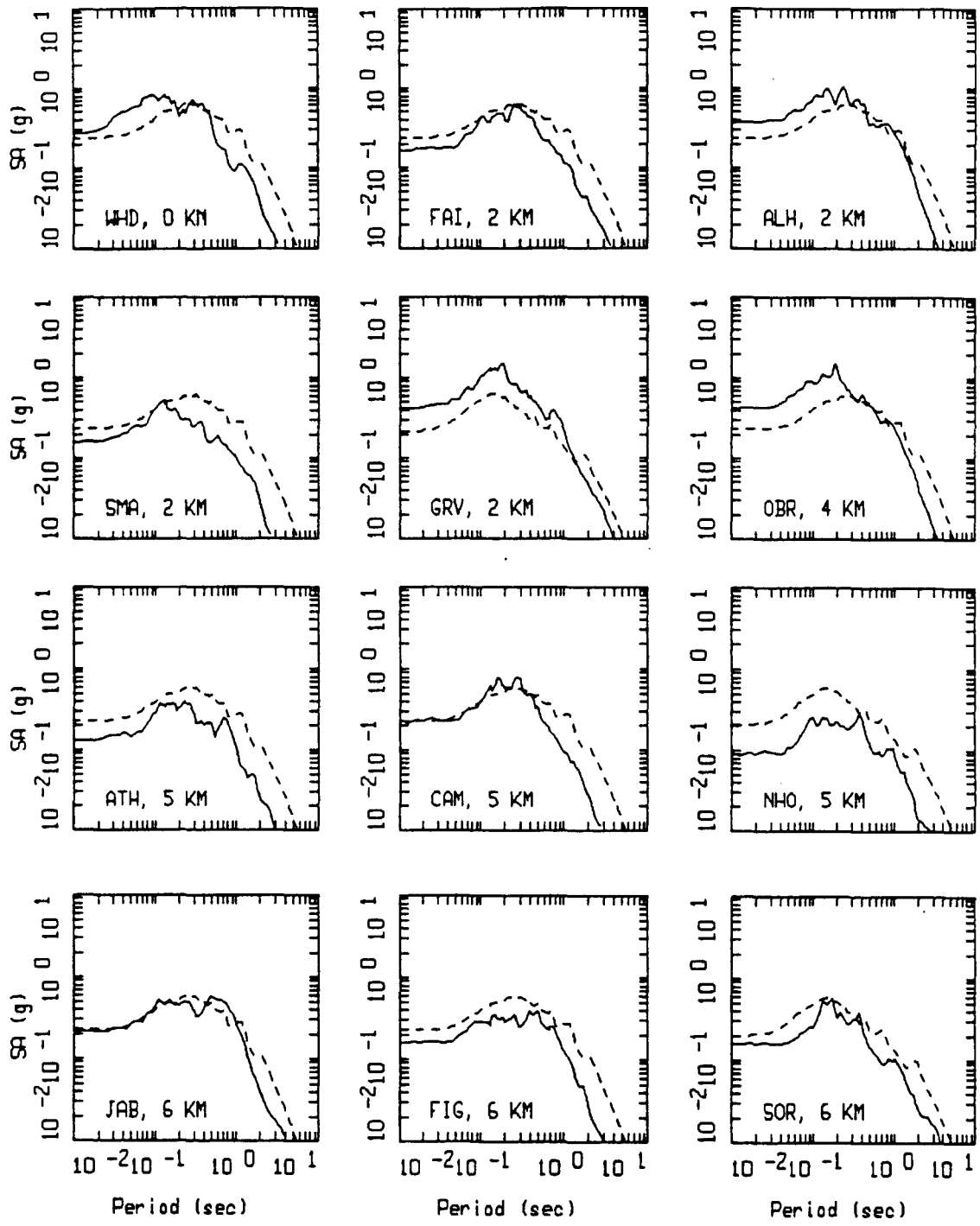

WHITTIER NARROWS, POINT-SOURCE MODELING, PAGE 1 OF 8.
NONLINEAR.

Figure Set 5.35

LEGEND

——— AVG OF TWO HORIZONTAL SPECTRA

- - - - - MODEL

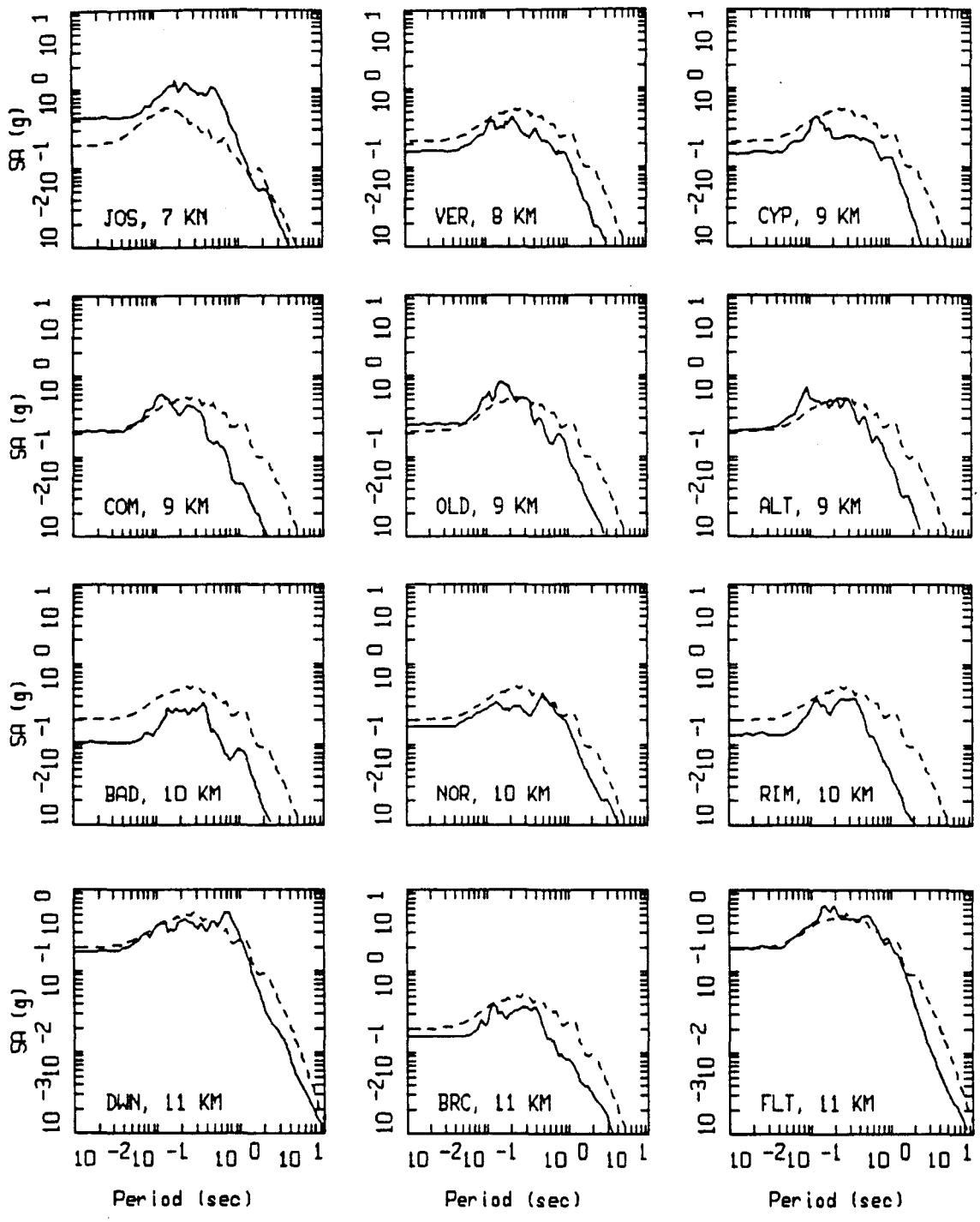

WHITTIER NARROWS, POINT-SOURCE MODELING, PAGE 2 OF 8.
NONLINEAR.

LEGEND

——— AVG OF TWO HORIZONTAL SPECTRA

- - - - - MODEL

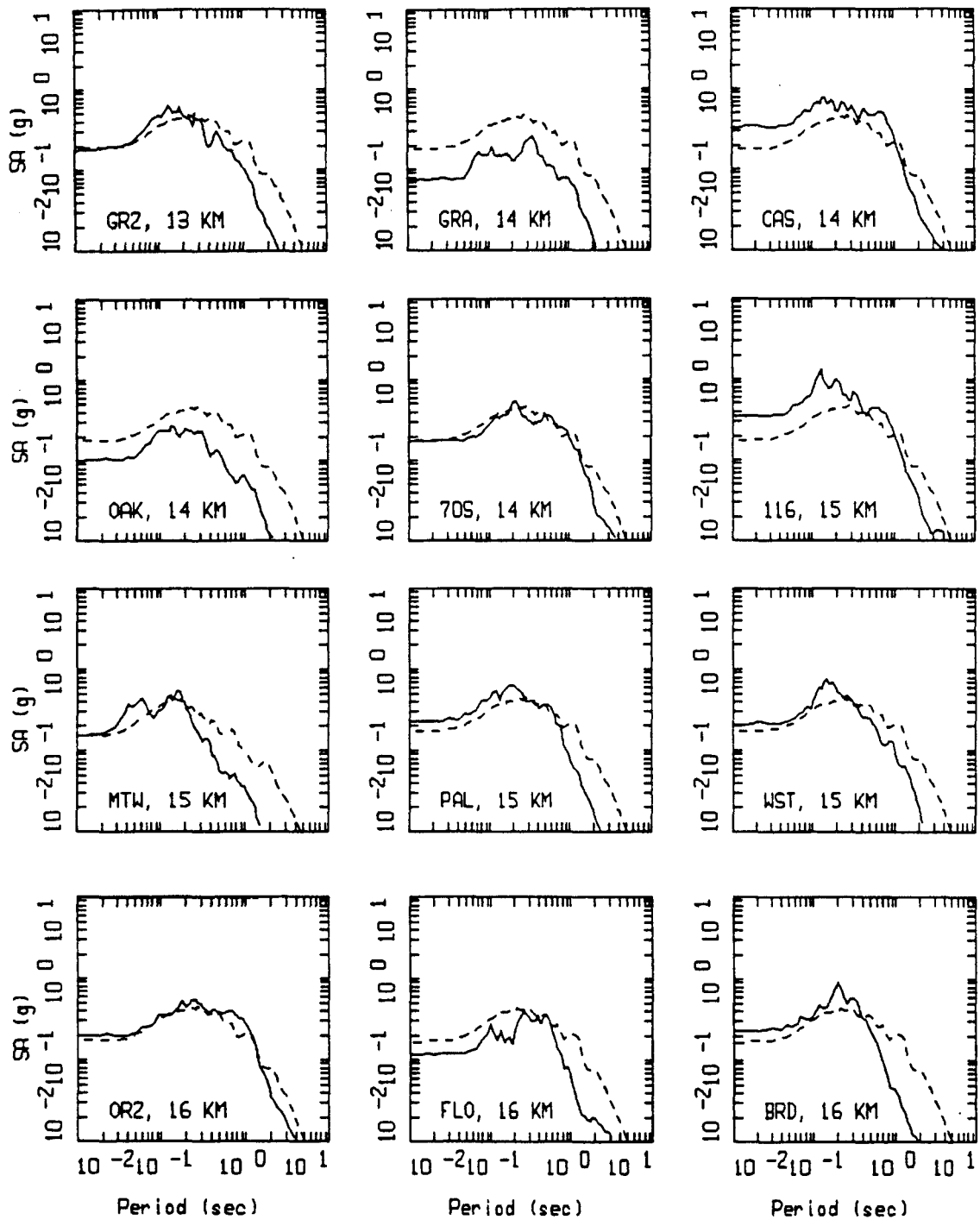

WHITTIER NARROWS, POINT-SOURCE MODELING, PAGE 3 OF 8.
NONLINEAR.

LEGEND

——— AVG OF TWO HORIZONTAL SPECTRA

- - - - - MODEL

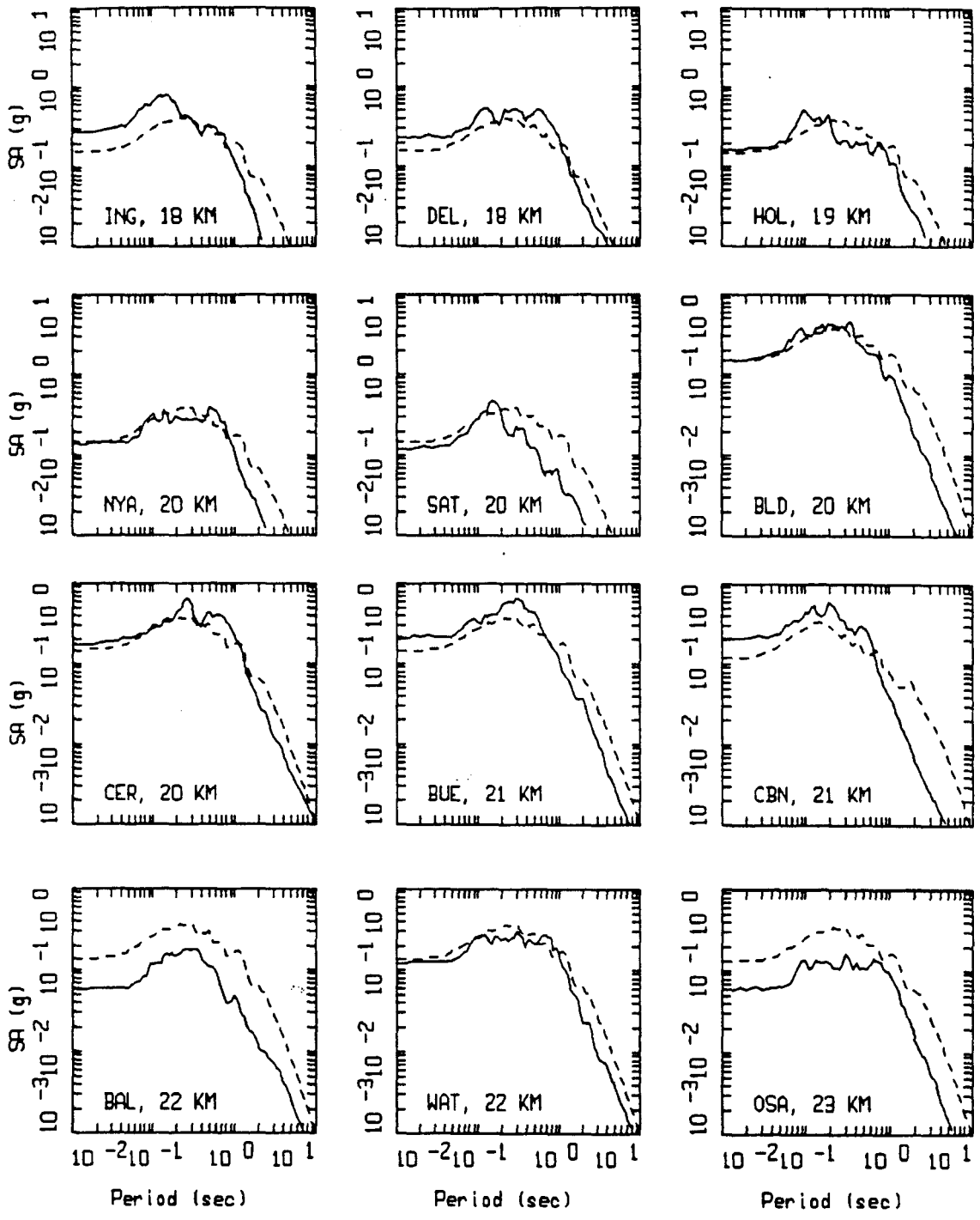

WHITTIER NARROWS, POINT-SOURCE MODELING, PAGE 4 OF 8.
NONLINEAR.

LEGEND

——— AVG OF TWO HORIZONTAL SPECTRA

----- MODEL

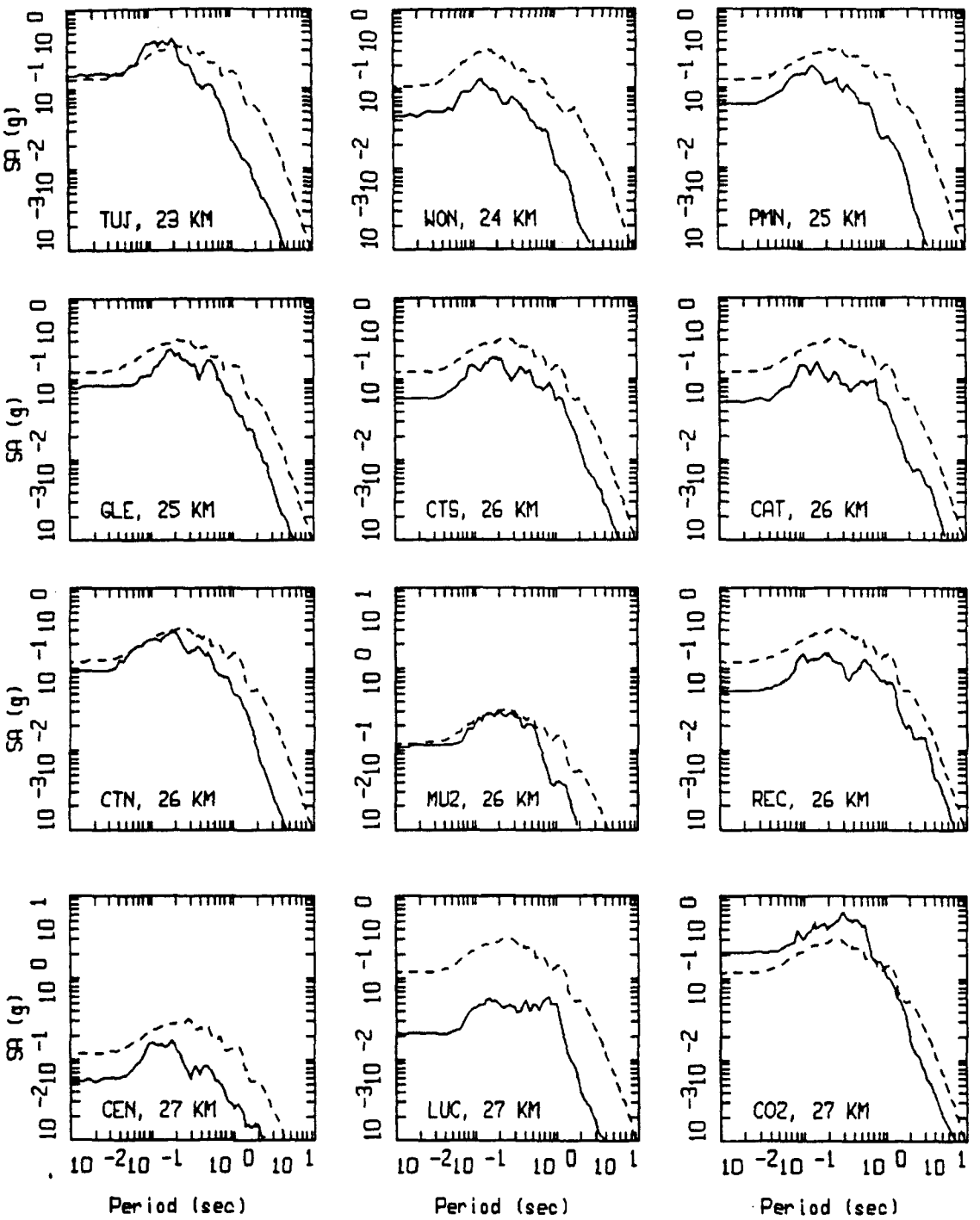

WHITTIER NARROWS, POINT-SOURCE MODELING, PAGE 5 OF 8.
NONLINEAR.

LEGEND

——— AVG OF TWO HORIZONTAL SPECTRA

- - - - - MODEL

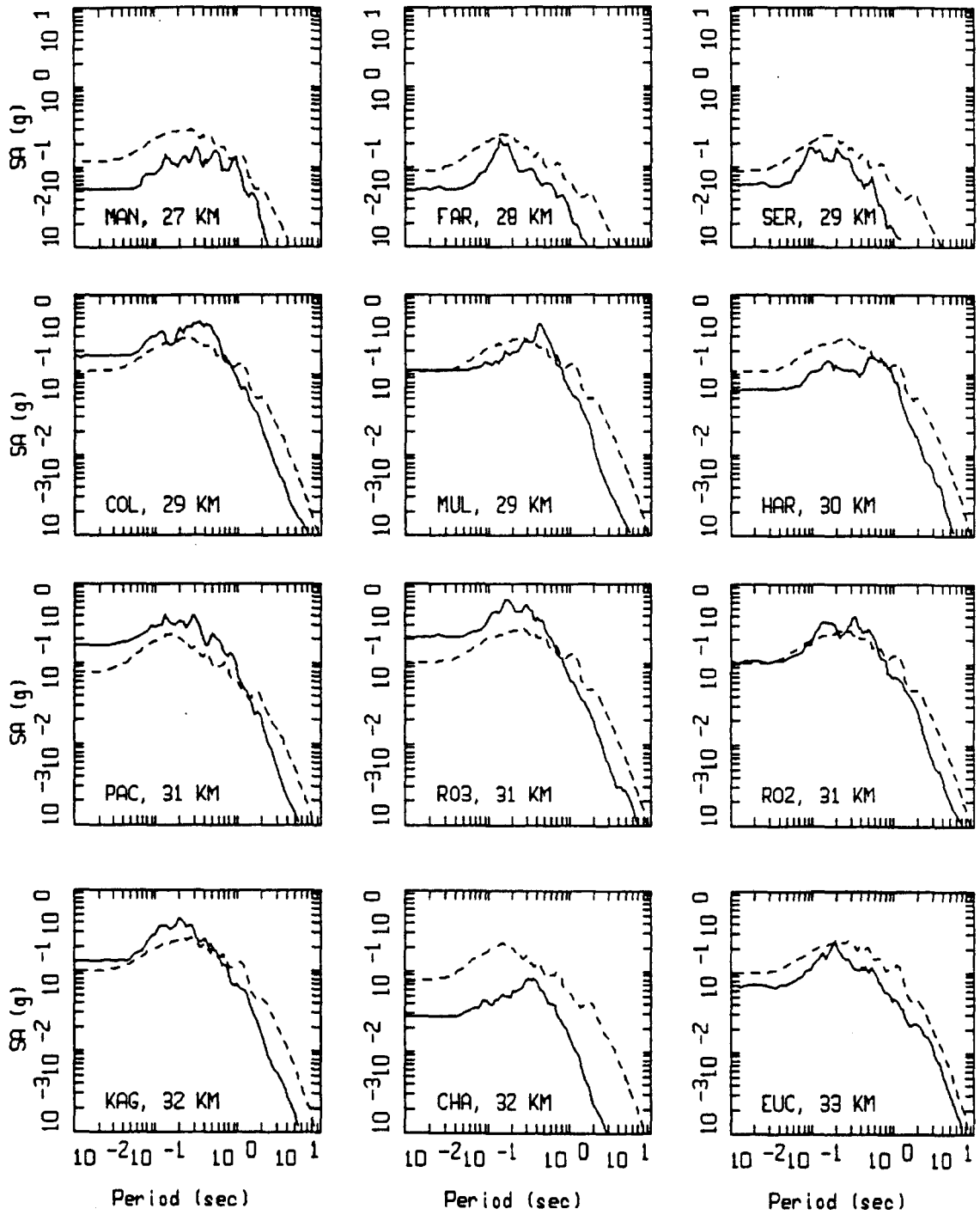

WHITTIER NARROWS, POINT-SOURCE MODELING, PAGE 6 OF 8.
NONLINEAR.

LEGEND

——— AVG OF TWO HORIZONTAL SPECTRA

- - - - - MODEL

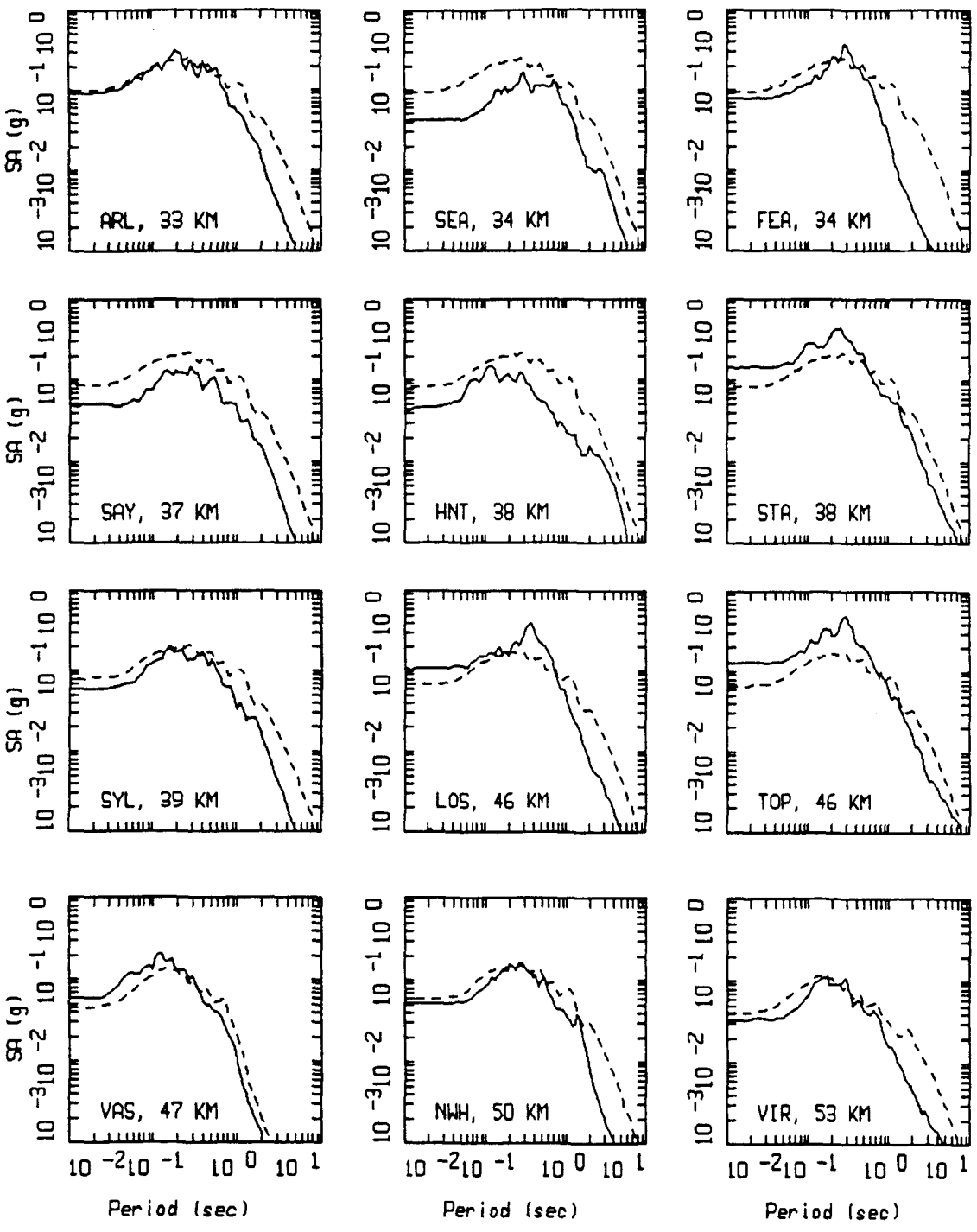

WHITTIER NARROWS, POINT-SOURCE MODELING, PAGE 7 OF 8.
NONLINEAR.

LEGEND

——— AVG OF TWO HORIZONTAL SPECTRA

----- MODEL

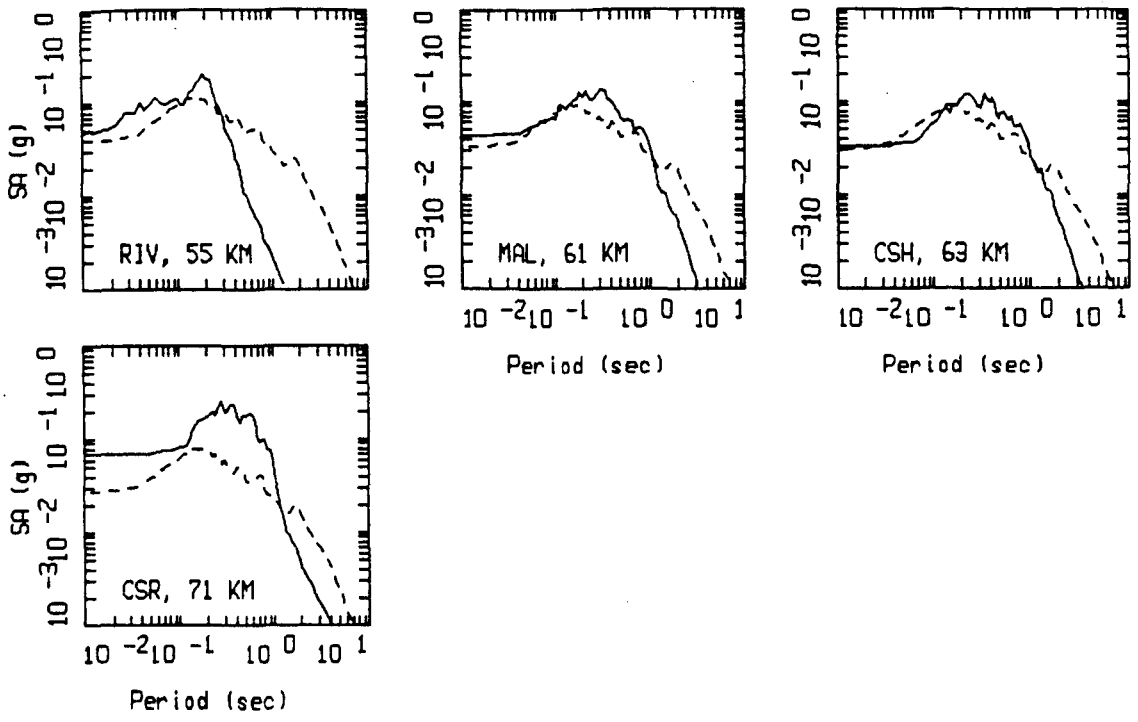

WHITTIER NARROWS, POINT-SOURCE MODELING, PAGE 8 OF 8.
NONLINEAR.

LEGEND

——— AVG OF TWO HORIZONTAL SPECTRA

----- MODEL

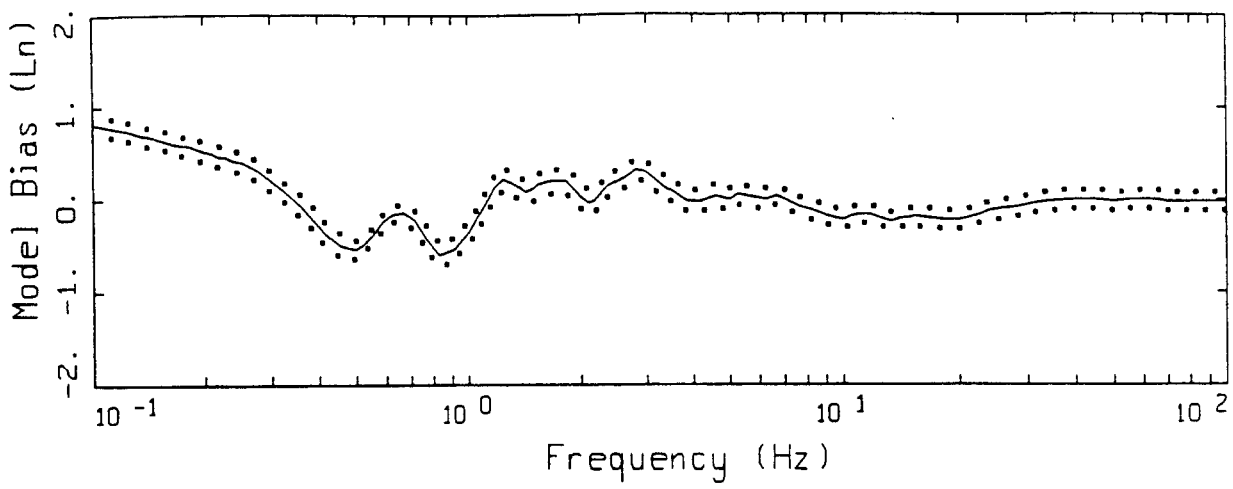

LEGEND
MODELING BIAS
90% CONFIDENCE INTERVAL OF MODELING BIAS
90% CONFIDENCE INTERVAL OF MODELING BIAS

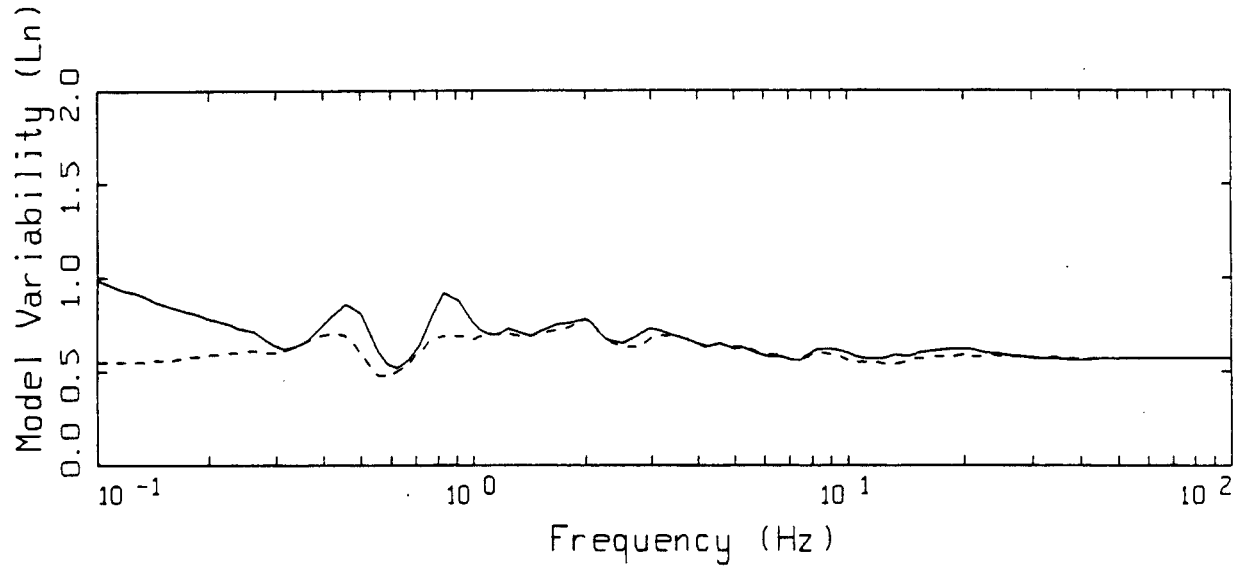

LEGEND
MEAN=0.0
BIAS CORRECTED

WHITTIER NARROWS FINITE-SOURCE
NONLINEAR, ALL 88 SITES

Figure 5.36

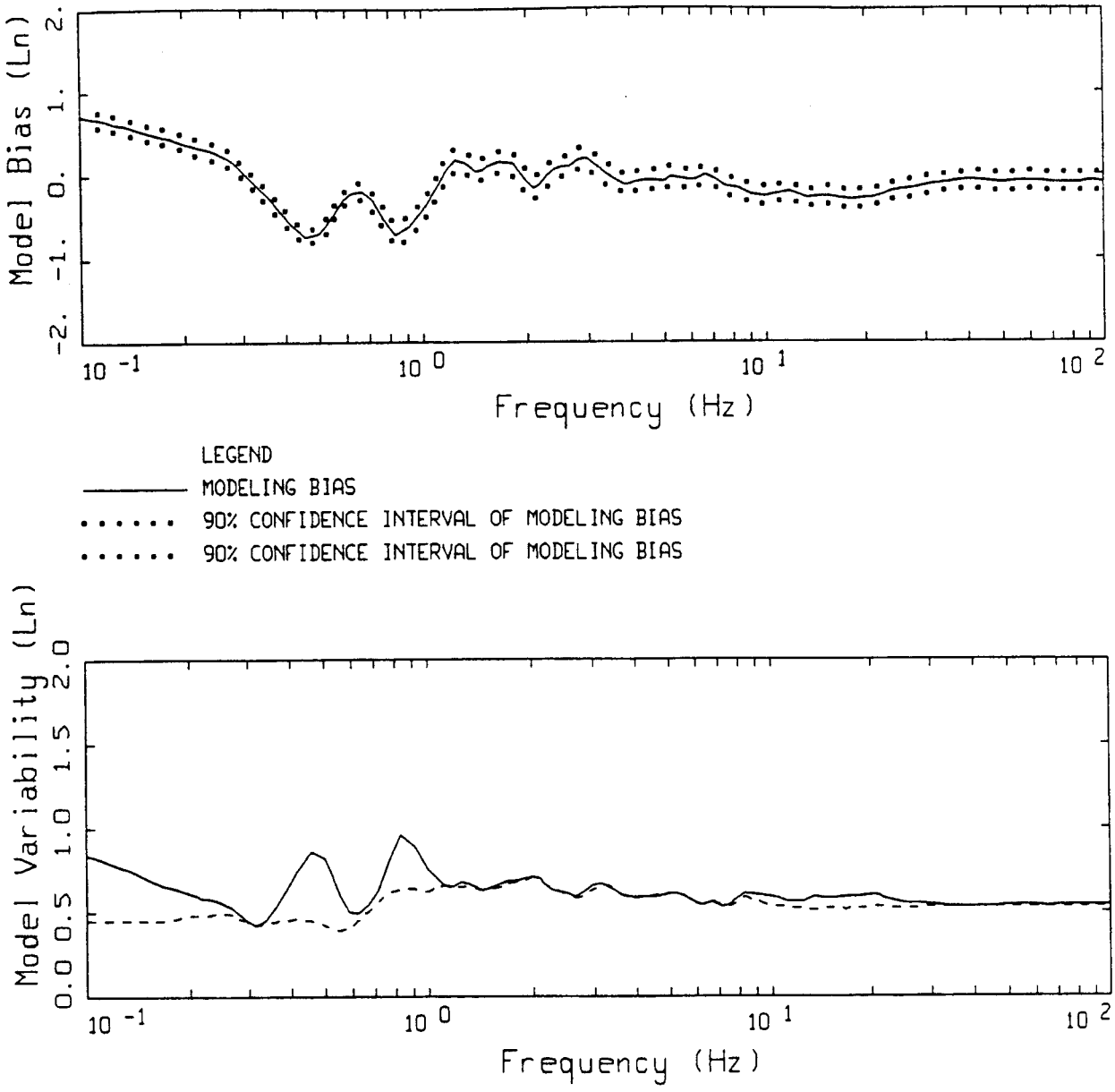

WHITTIER NARROWS FINITE-SOURCE
NONLINEAR, 70 SOIL SITES

Figure 5.37

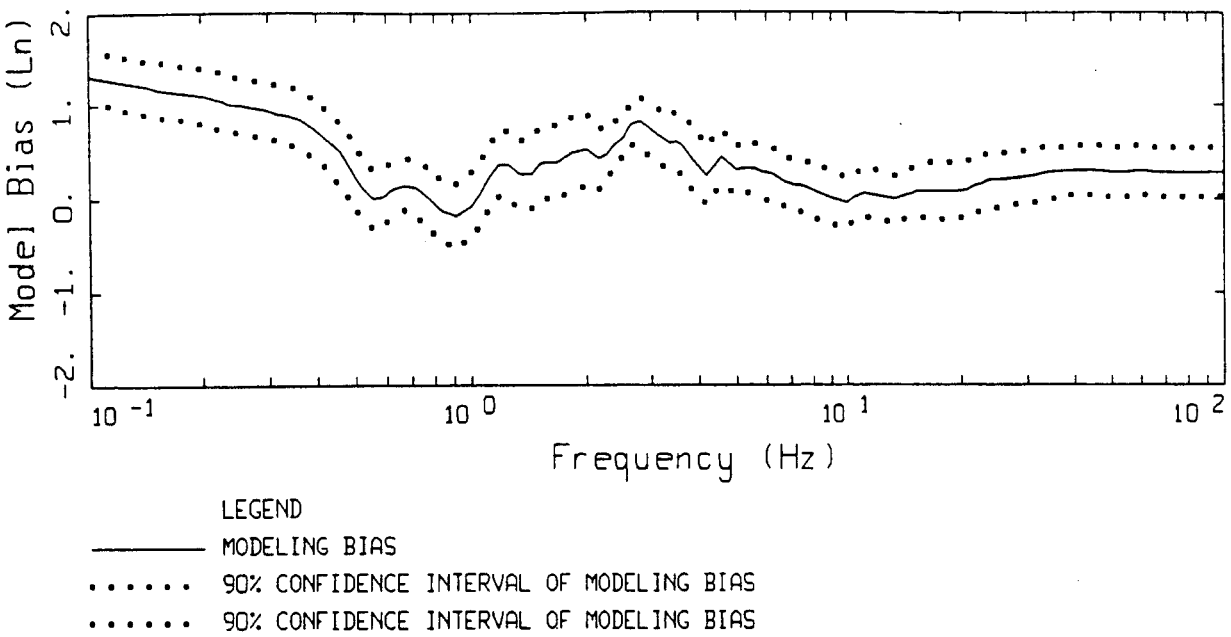

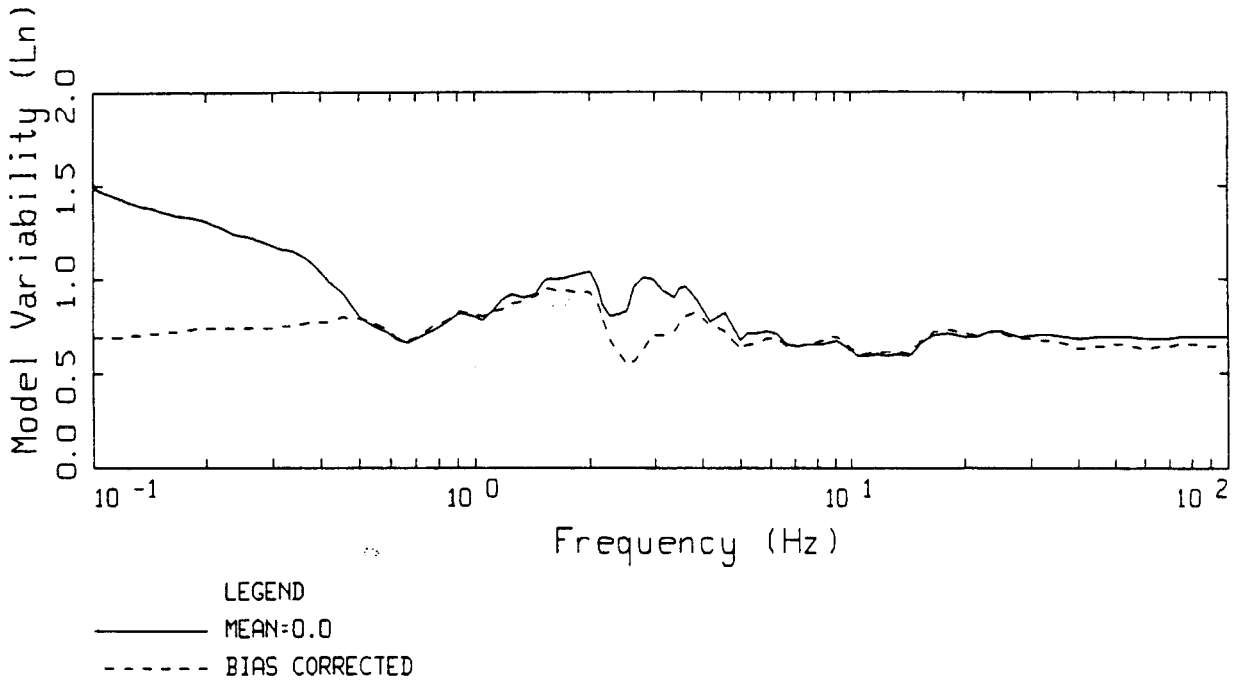

WHITTIER NARROWS FINITE-SOURCE
NONLINEAR, 17 ROCK SITES

Figure 5.38

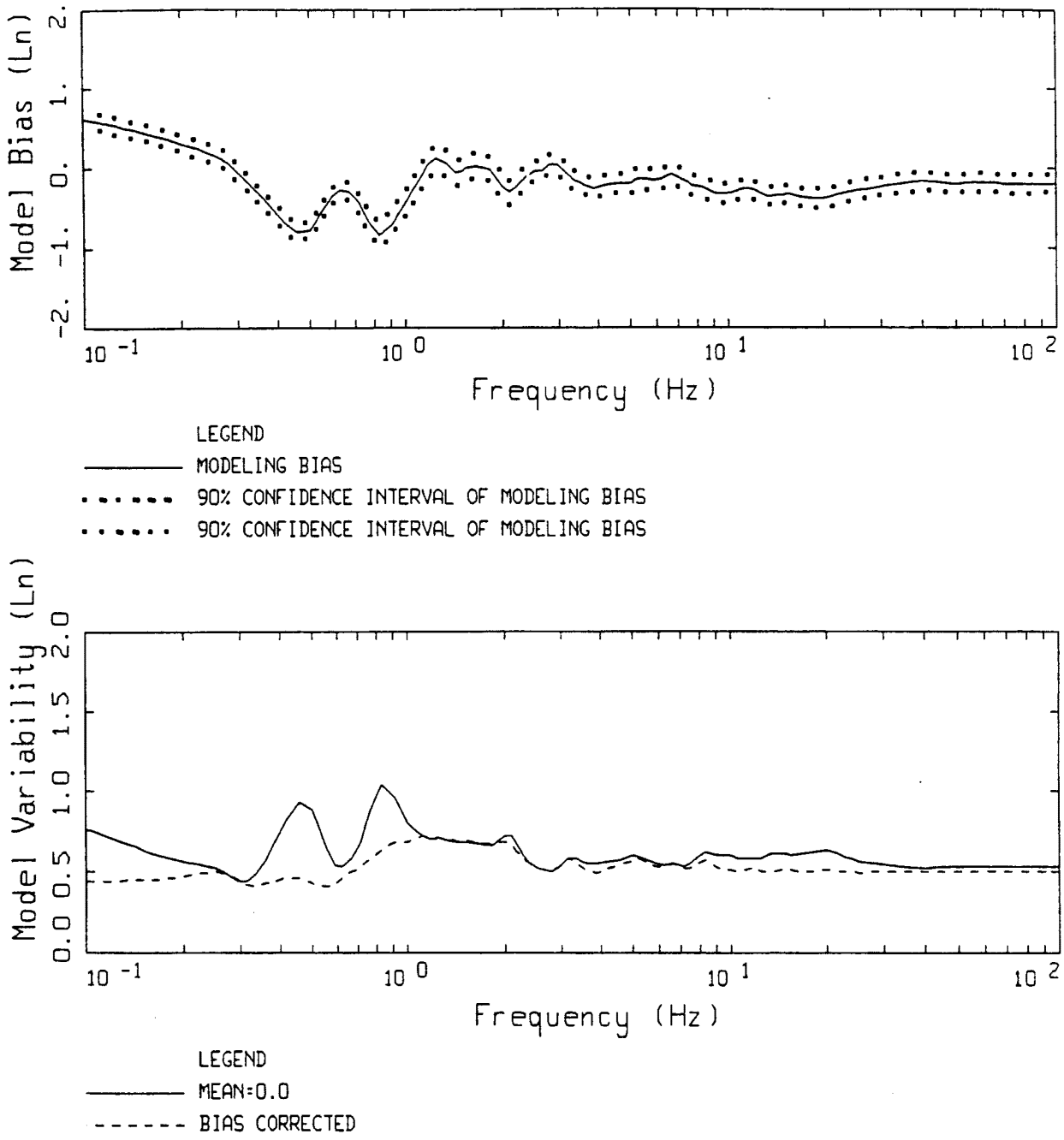

WHITTIER NARROWS FINITE-SOURCE
NONLINEAR, 53 SOIL SITES TO 30 KM

Figure 5.39

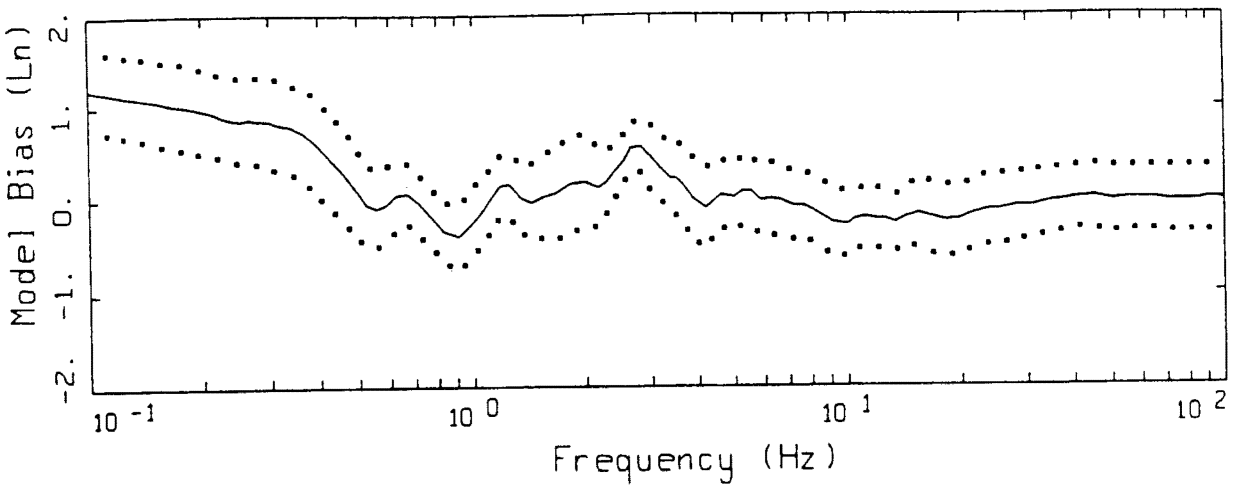

LEGEND
MODELING BIAS
90% CONFIDENCE INTERVAL OF MODELING BIAS
90% CONFIDENCE INTERVAL OF MODELING BIAS

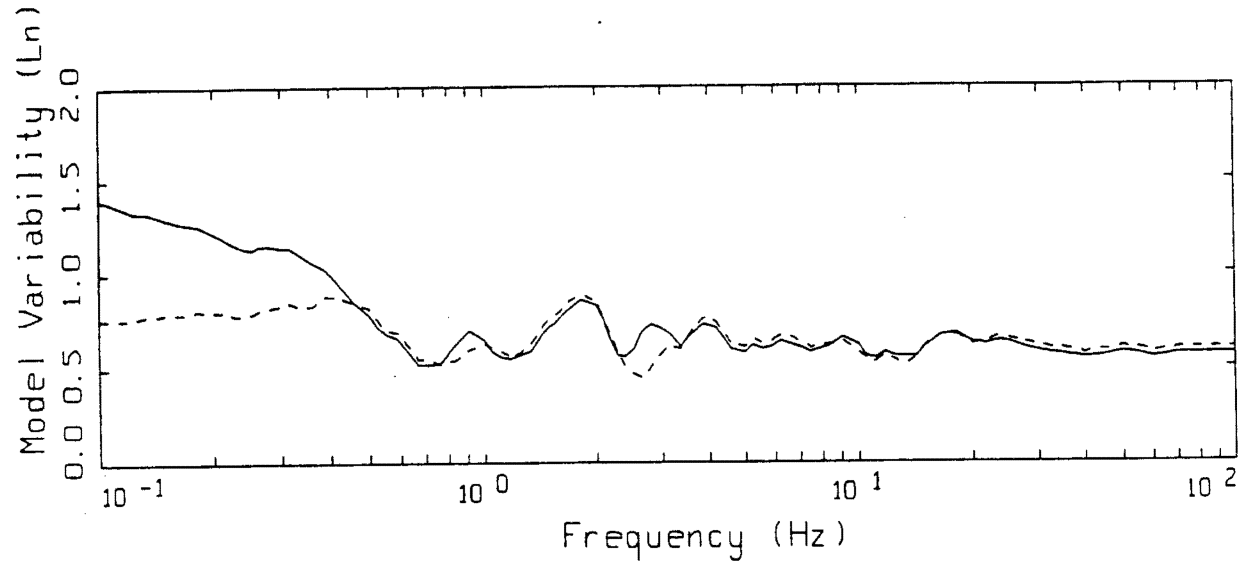

LEGEND
MEAN=0.0
BIAS CORRECTED

WHITTIER NARROWS FINITE-SOURCE
NONLINEAR, 10 ROCK SITES TO 30 KM

Figure 5.40

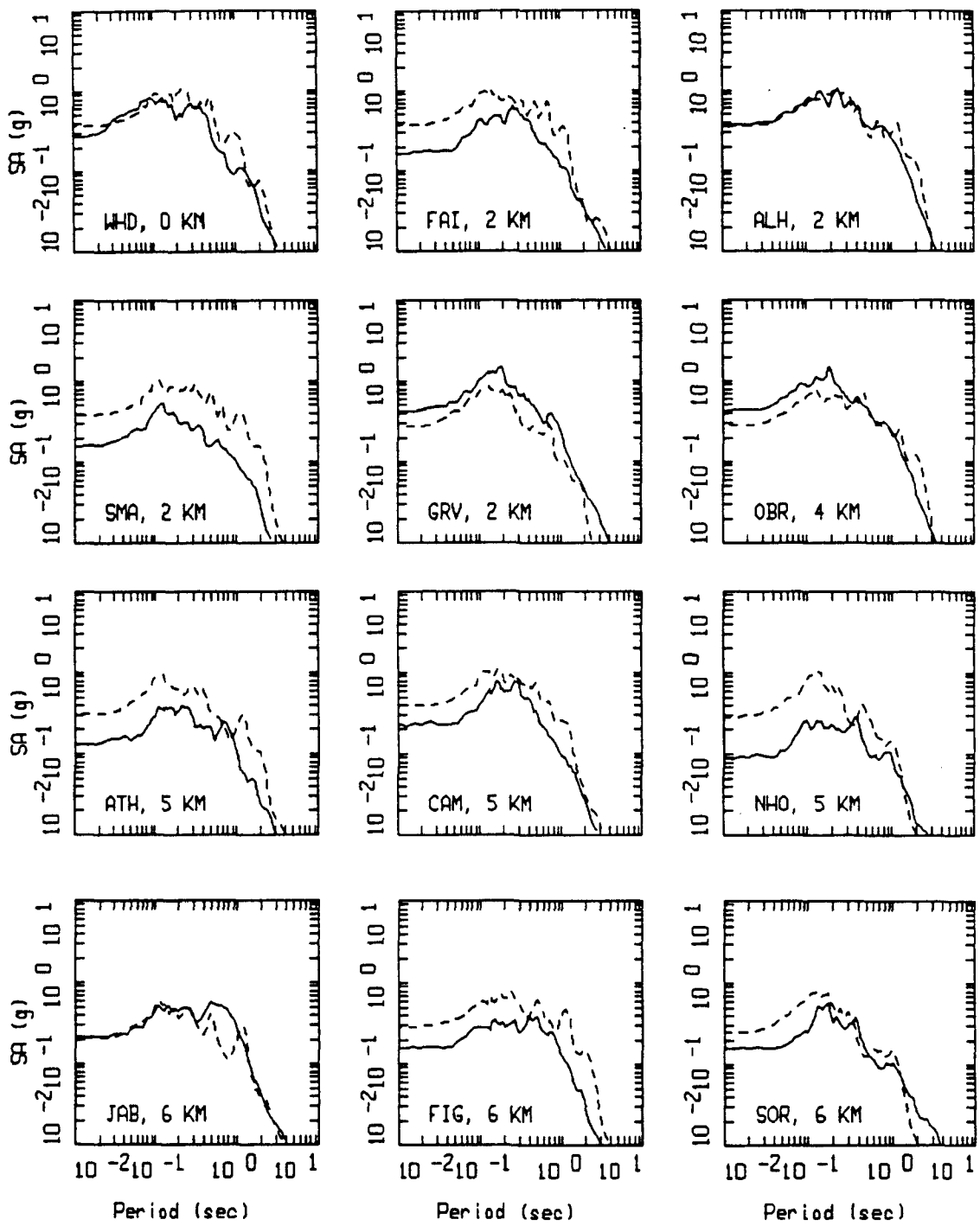

WHITTIER NARROWS, FINITE-SOURCE MODELING, PAGE 1 OF 8.
NONLINEAR.

Figure Set 5.41

LEGEND

——— AVG OF TWO HORIZONTAL SPECTRA

----- MODEL

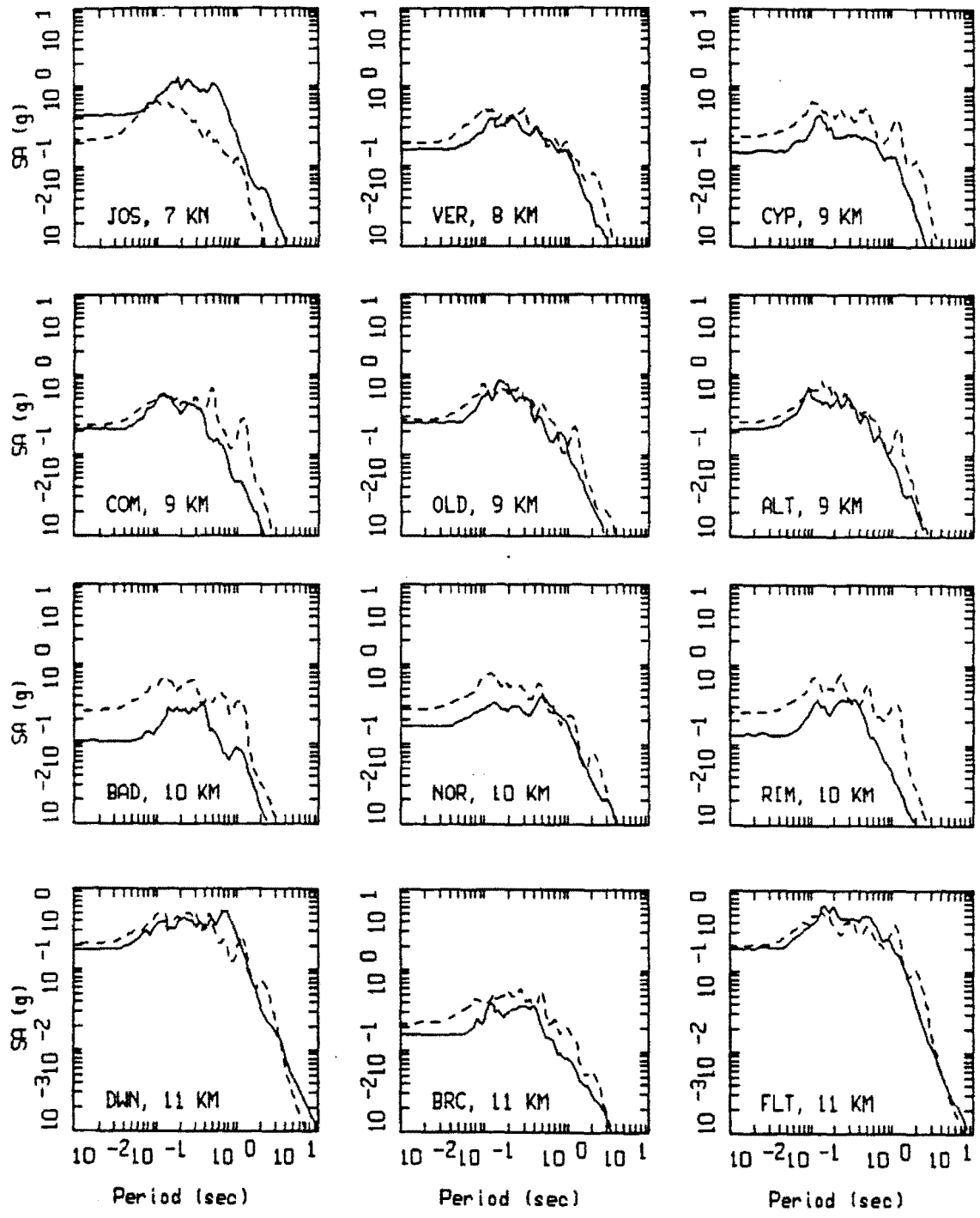

WHITTIER NARROWS, FINITE-SOURCE MODELING, PAGE 2 OF 8.
NONLINEAR.

LEGEND

——— AVG OF TWO HORIZONTAL SPECTRA

- - - - - MODEL

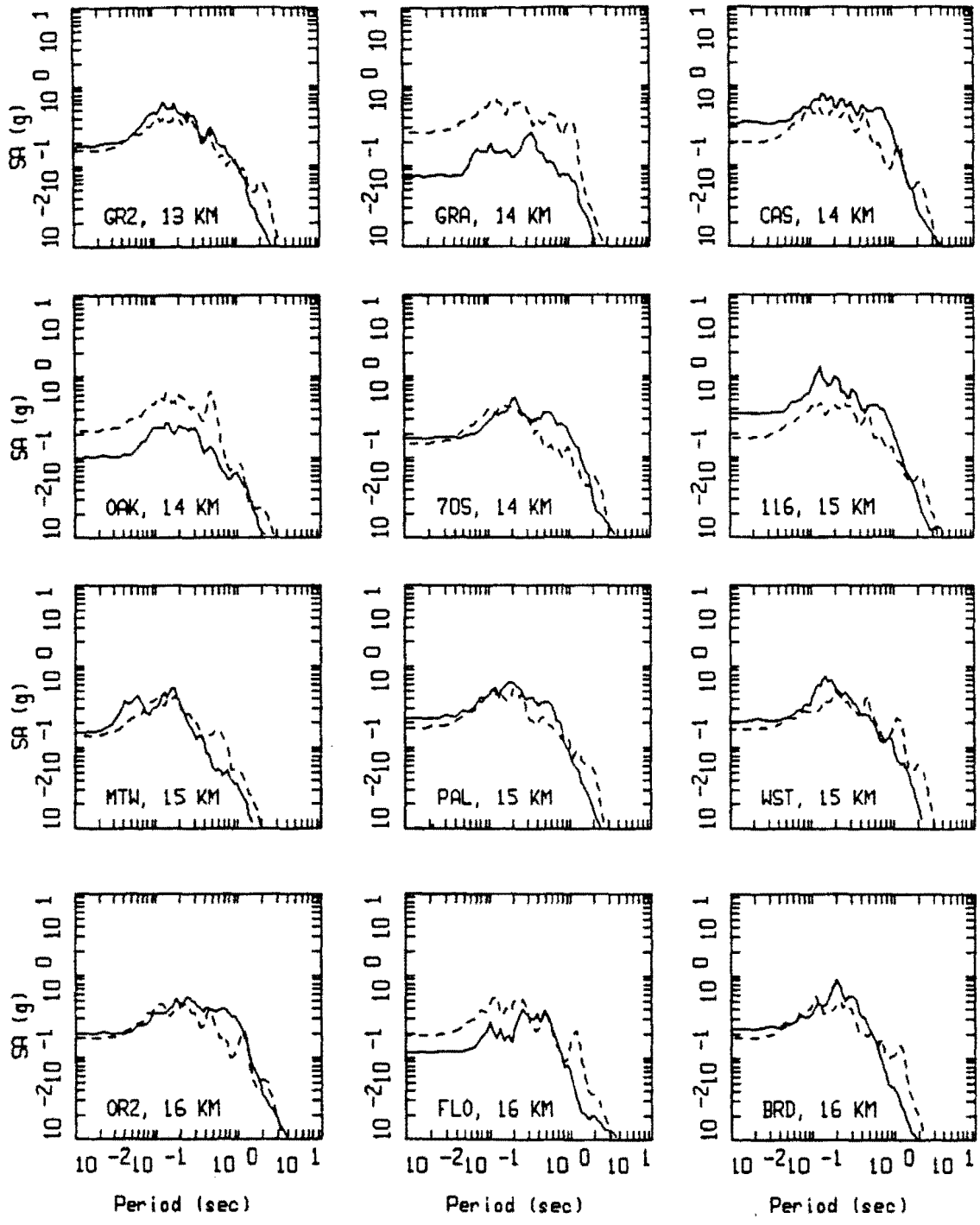

WHITTIER NARROWS, FINITE-SOURCE MODELING, PAGE 3 OF 8.
NONLINEAR.

LEGEND

——— AVG OF TWO HORIZONTAL SPECTRA

----- MODEL

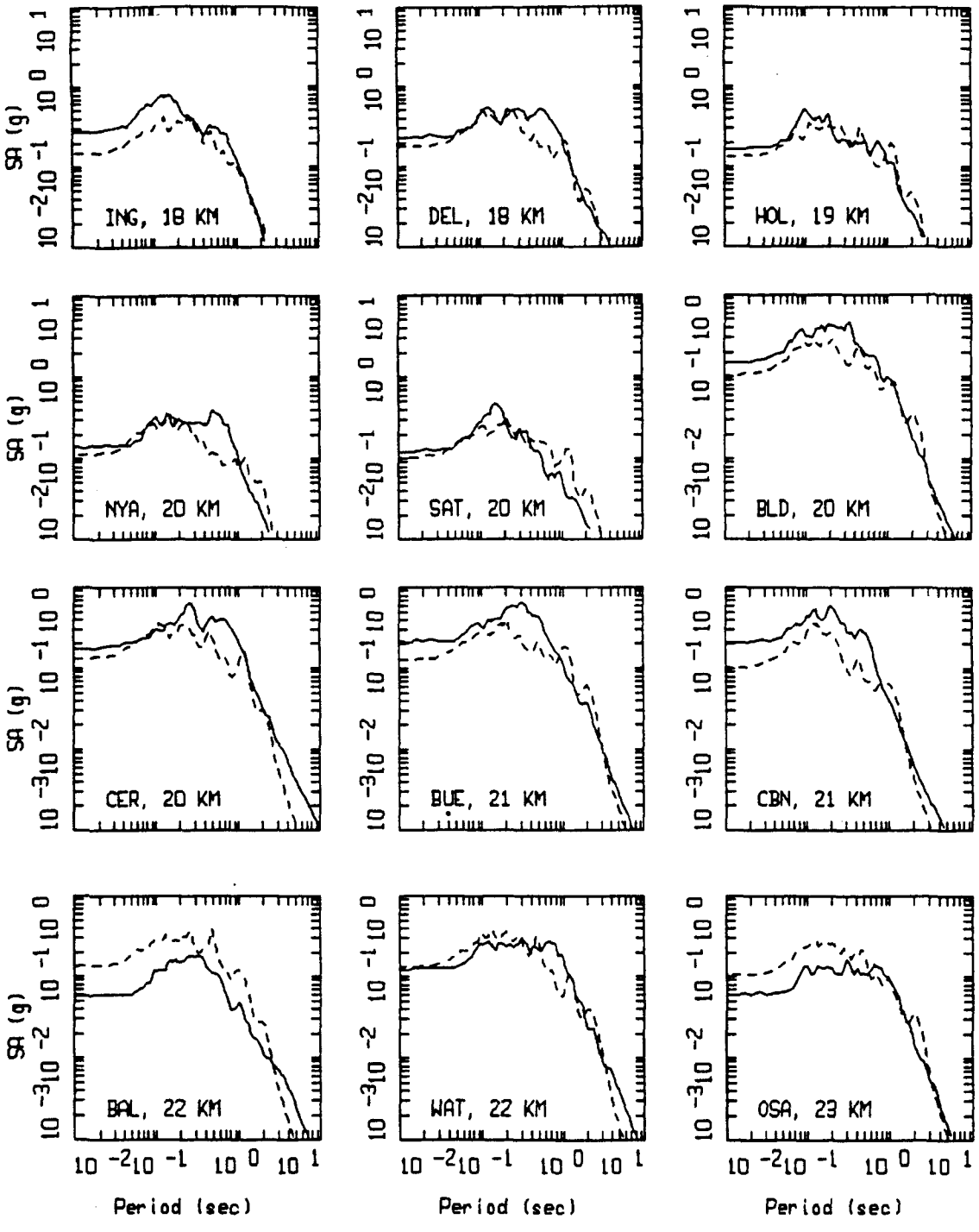

WHITTIER NARROWS, FINITE-SOURCE MODELING, PAGE 4 OF 8.
NONLINEAR.

LEGEND

——— AVG OF TWO HORIZONTAL SPECTRA

- - - - - MODEL

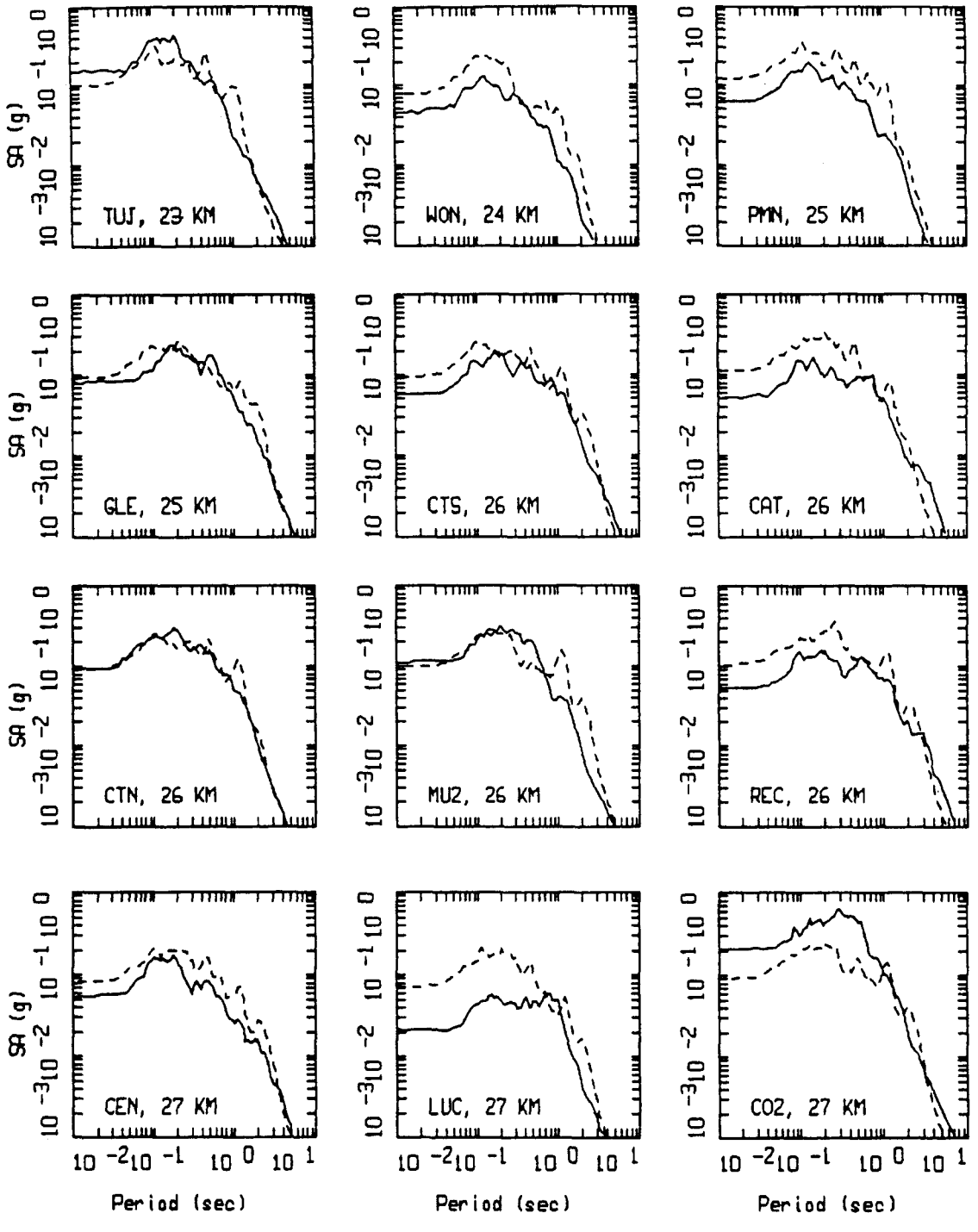

WHITTIER NARROWS, FINITE-SOURCE MODELING, PAGE 5 OF 8.
NONLINEAR.

LEGEND

——— AVG OF TWO HORIZONTAL SPECTRA

- - - - - MODEL

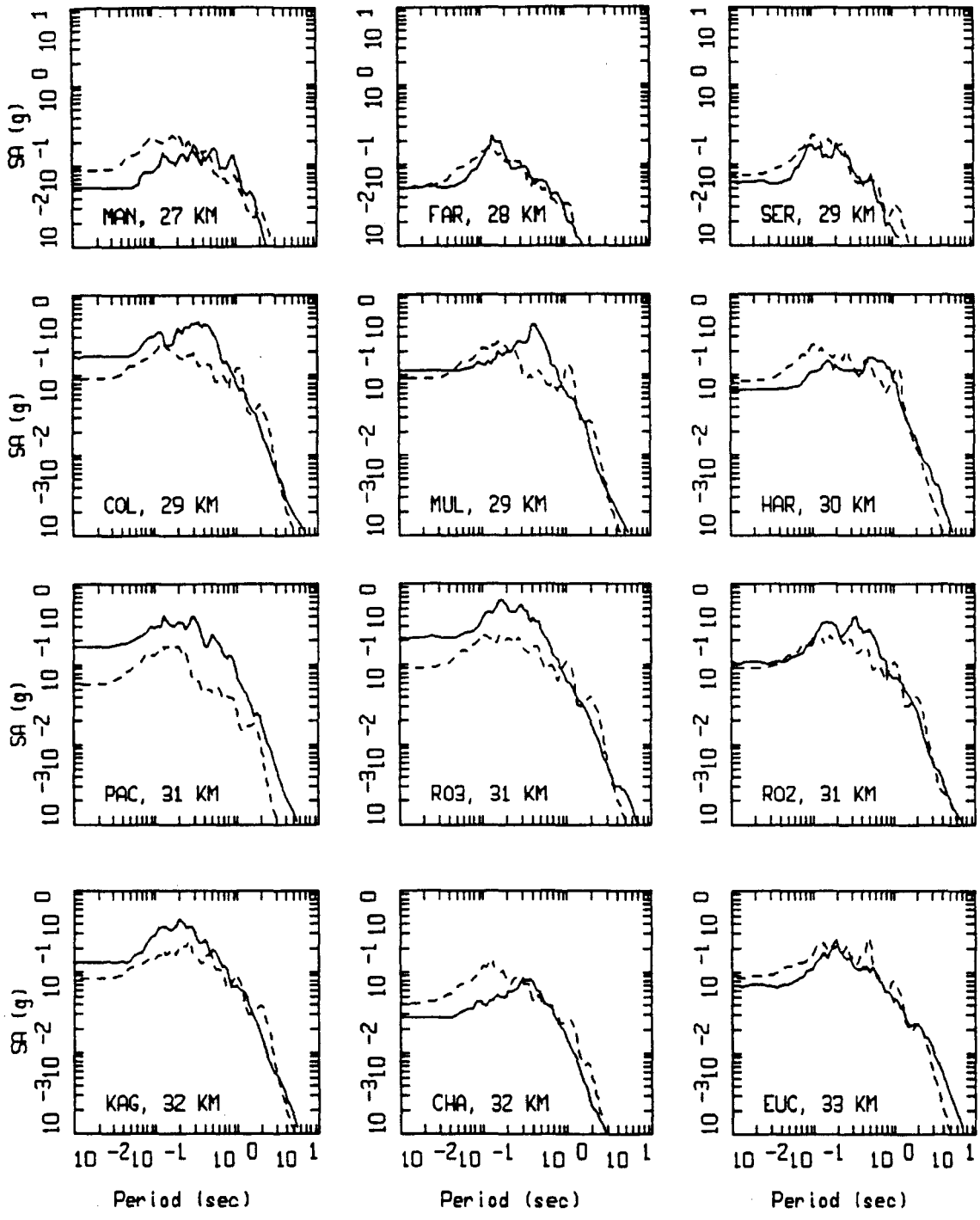

WHITTIER NARROWS, FINITE-SOURCE MODELING, PAGE 6 OF 8.
NONLINEAR.

LEGEND

——— AVG OF TWO HORIZONTAL SPECTRA

- - - - - MODEL

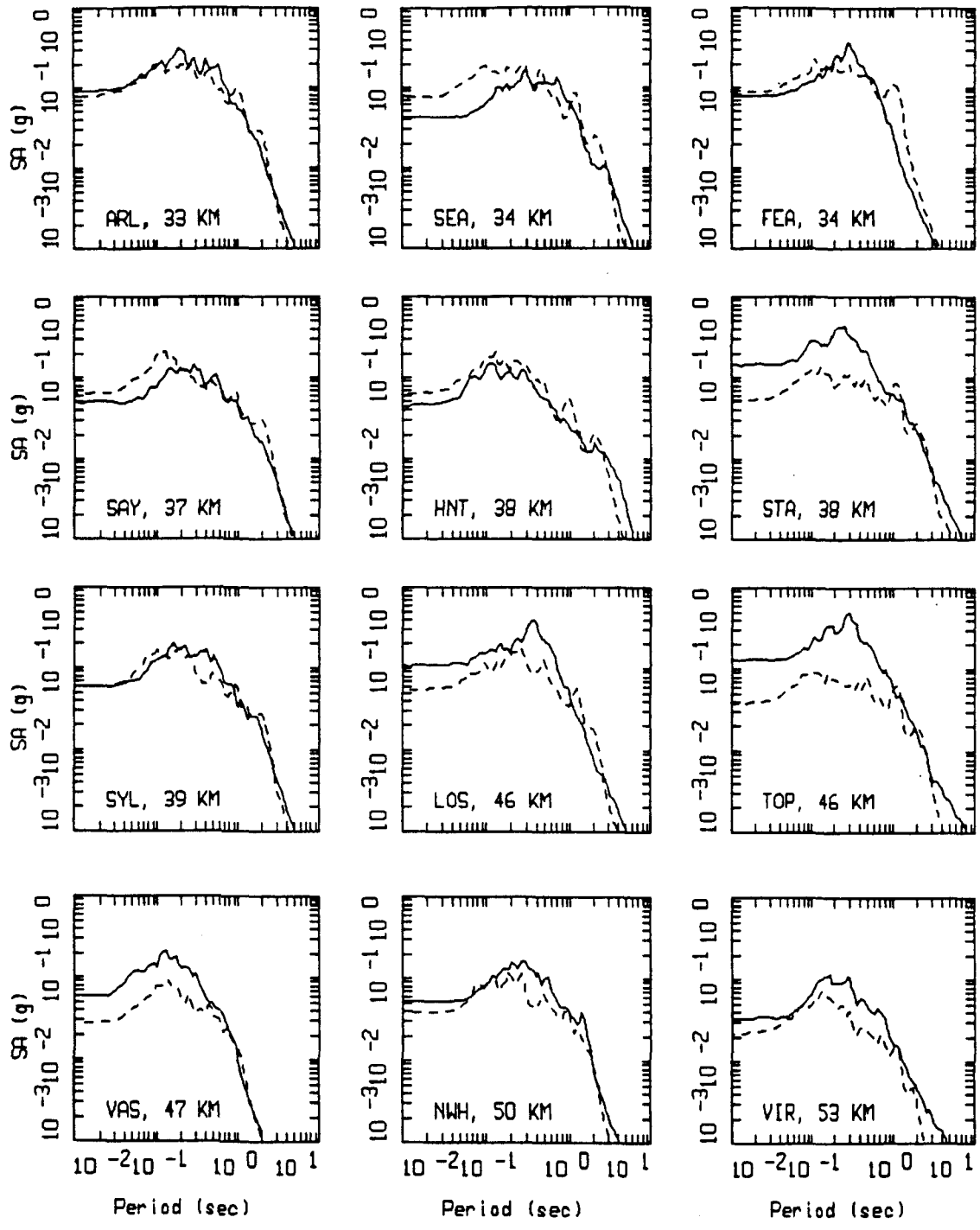

WHITTIER NARROWS, FINITE-SOURCE MODELING, PAGE 7 OF 8.
NONLINEAR.

LEGEND

——— AVG OF TWO HORIZONTAL SPECTRA

- - - - - MODEL

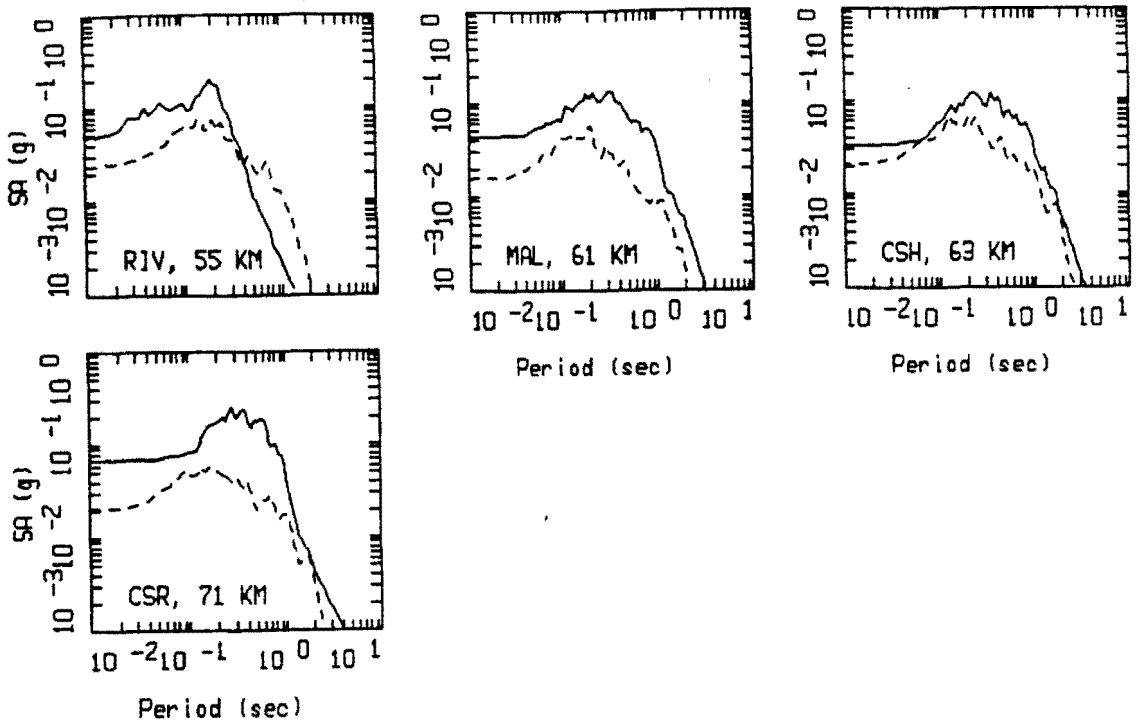

WHITTIER NARROWS, FINITE-SOURCE MODELING, PAGE 8 OF 8.

NONLINEAR.

LEGEND

——— AVG OF TWO HORIZONTAL SPECTRA

- - - - - MODEL

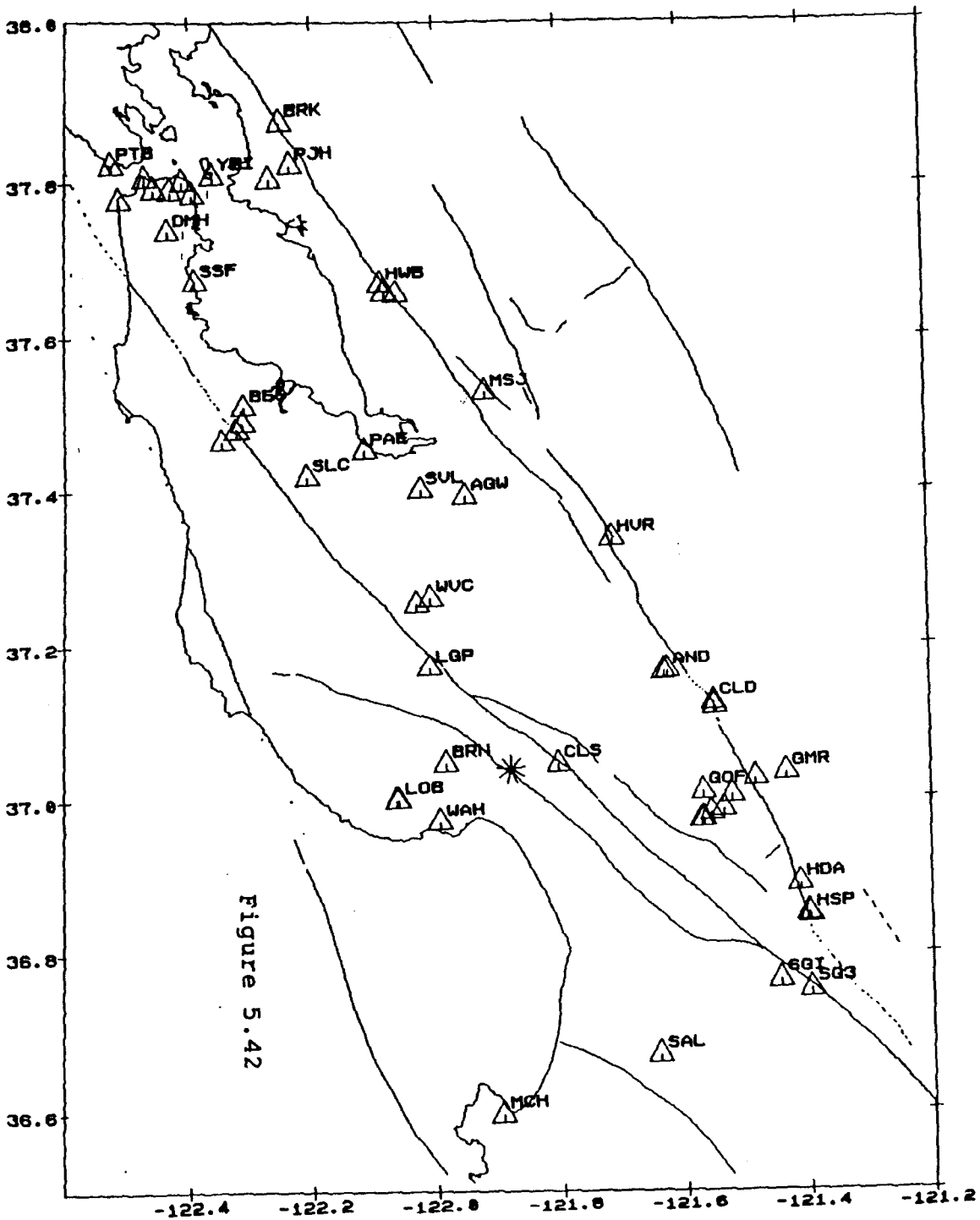

Figure 5.42

STATI

EPICENTER

0 20
kilometers

EQ3D-v4.00 FILE: SITES.HP2 EPICENT.HP2
. SCA:900000 MFAC:1.0 XFAC:1.0 Nm=54 Nx=0

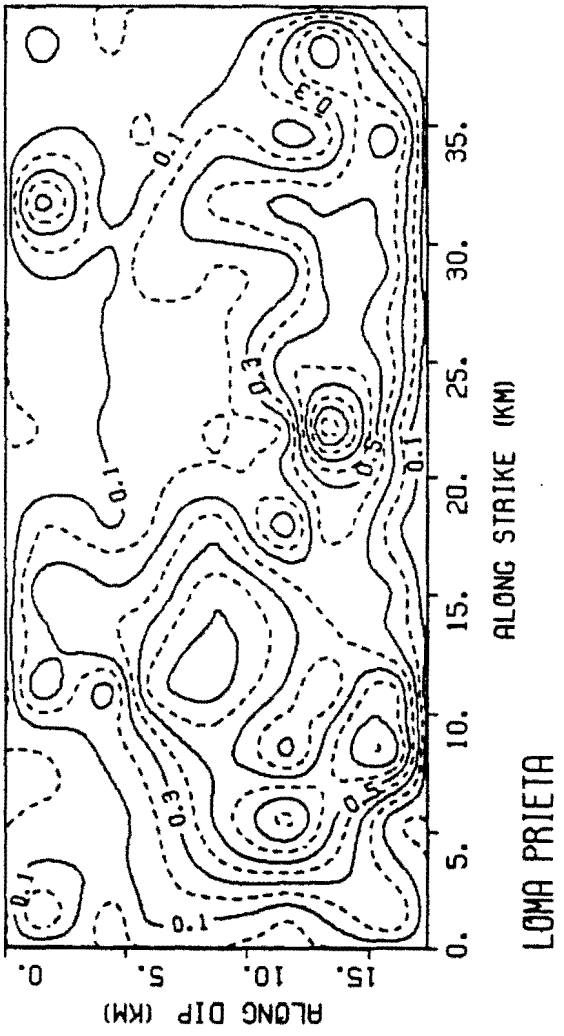
LOMA PRIETA
ALONG STRIKE (KM)
0.
5.
10.
15.
20.
25.
30.
35.
ALONG DIP (KM)
0.
5.
10.
15.
0.1
0.3
0.5

Figure 5.43

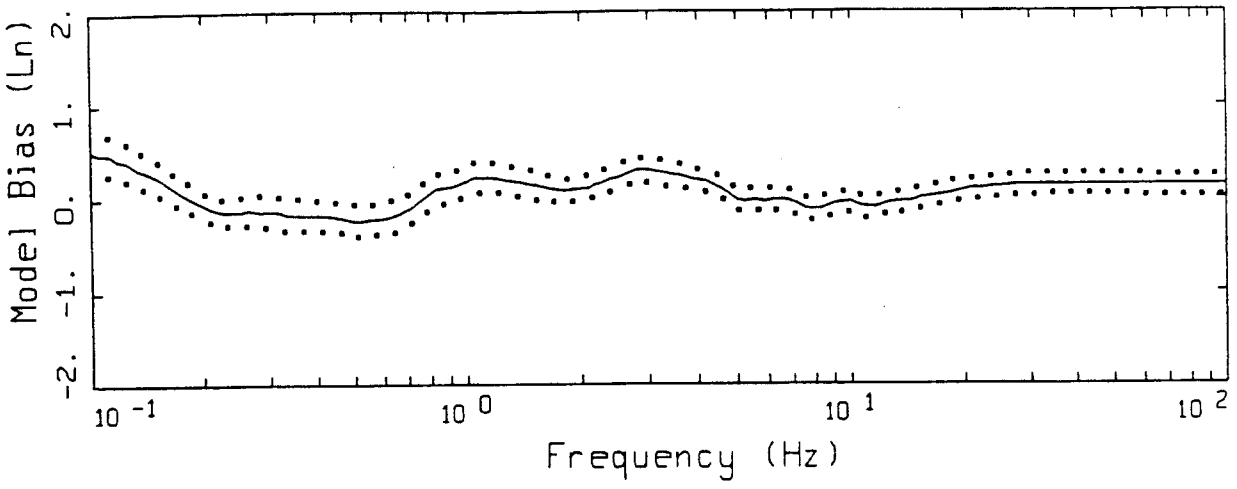

LEGEND
MODELING BIAS
90% CONFIDENCE INTERVAL OF MODELING BIAS
90% CONFIDENCE INTERVAL OF MODELING BIAS

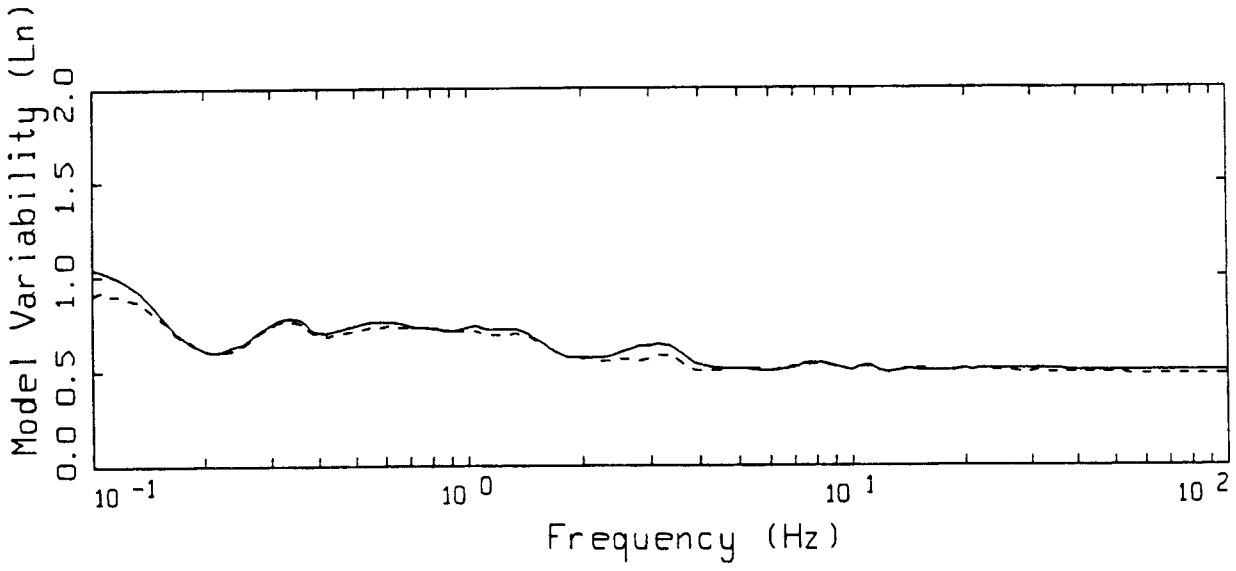

LEGEND
MEAN=0.0
BIAS CORRECTED

LOMA PRIETA POINT-SOURCE
NONLINEAR, ALL 53 SITES

Figure 5.44

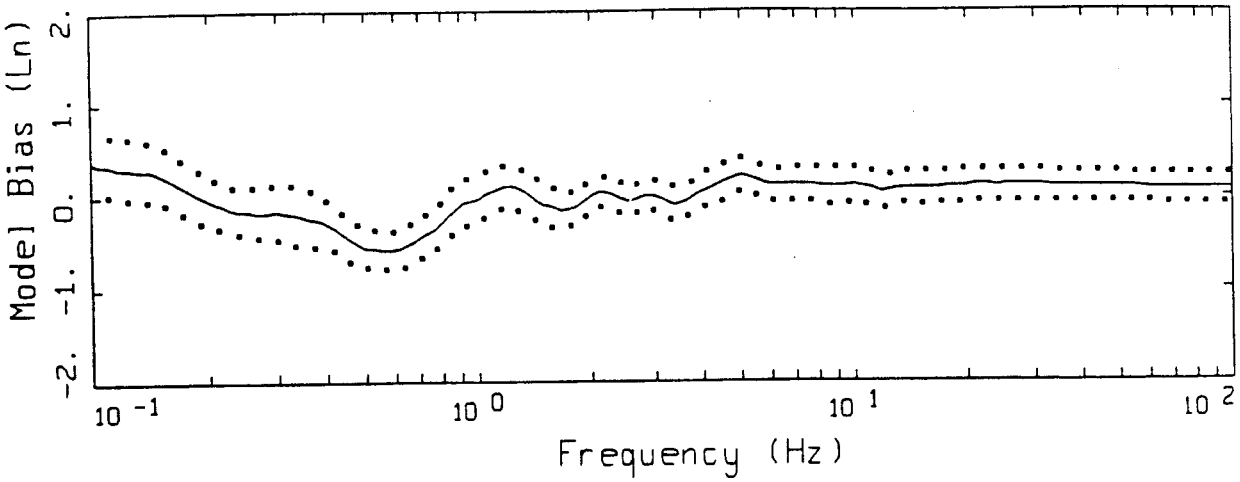

LEGEND
MODELING BIAS
90% CONFIDENCE INTERVAL OF MODELING BIAS
90% CONFIDENCE INTERVAL OF MODELING BIAS

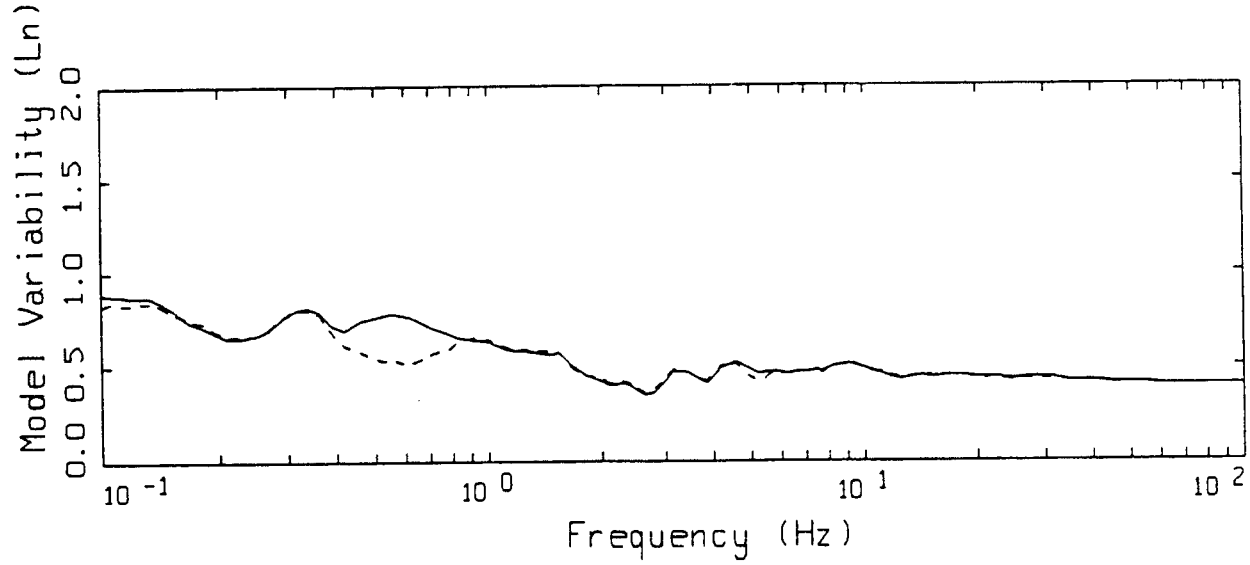

LEGEND
MEAN=0.0
BIAS CORRECTED

LOMA PRIETA POINT-SOURCE
NONLINEAR, 20 SOIL SITES

Figure 5.45

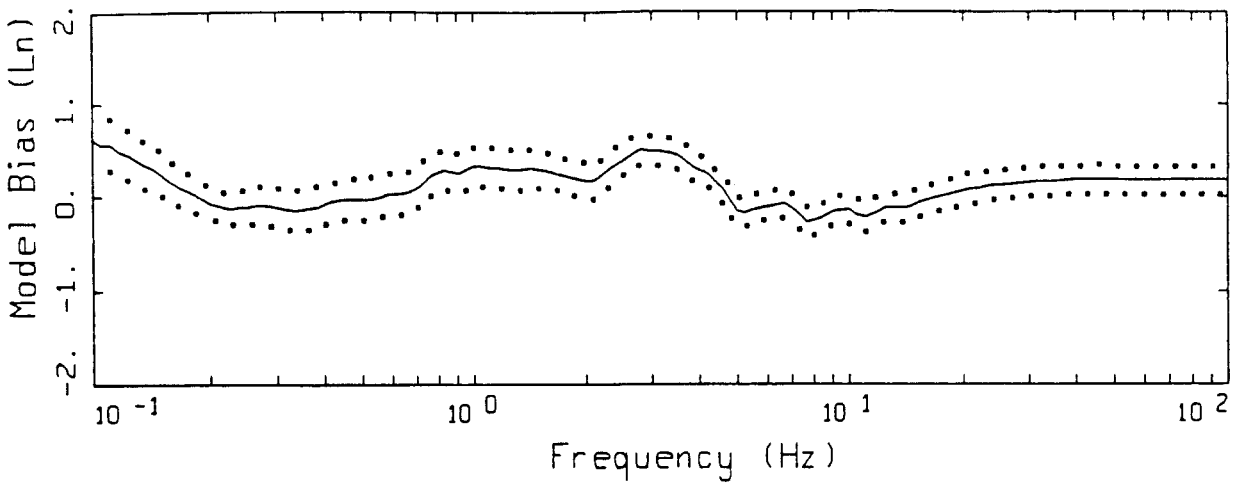

LEGEND
MODELING BIAS
90% CONFIDENCE INTERVAL OF MODELING BIAS
90% CONFIDENCE INTERVAL OF MODELING BIAS

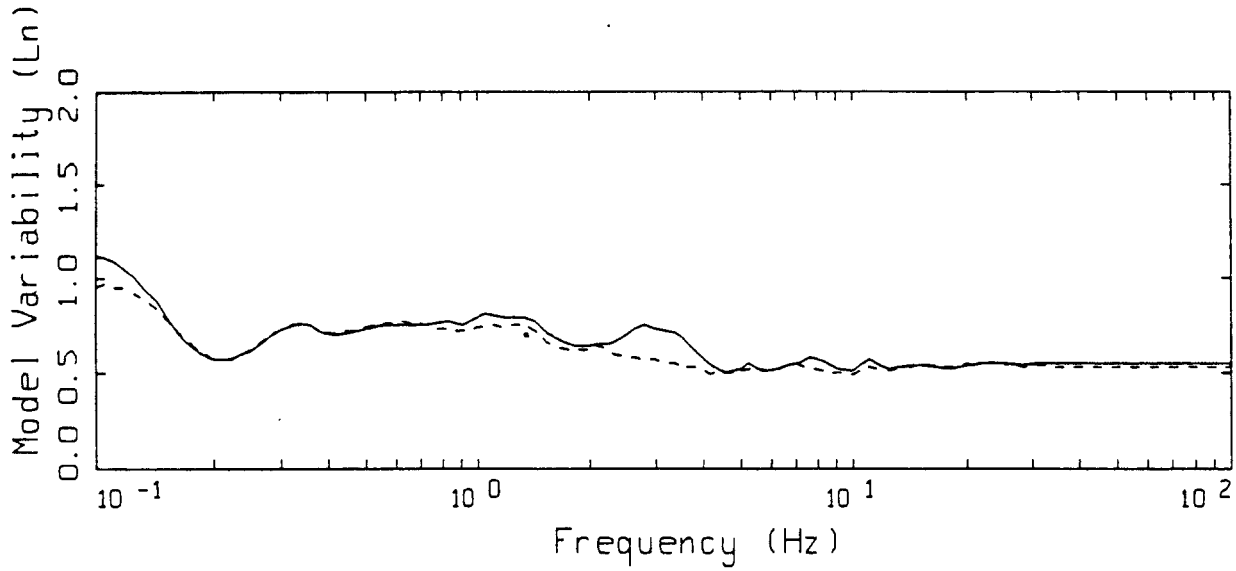

LEGEND
MEAN=0.0
BIAS CORRECTED

LOMA PRIETA POINT-SOURCE
NONLINEAR, 33 ROCK SITES

Figure 5.46

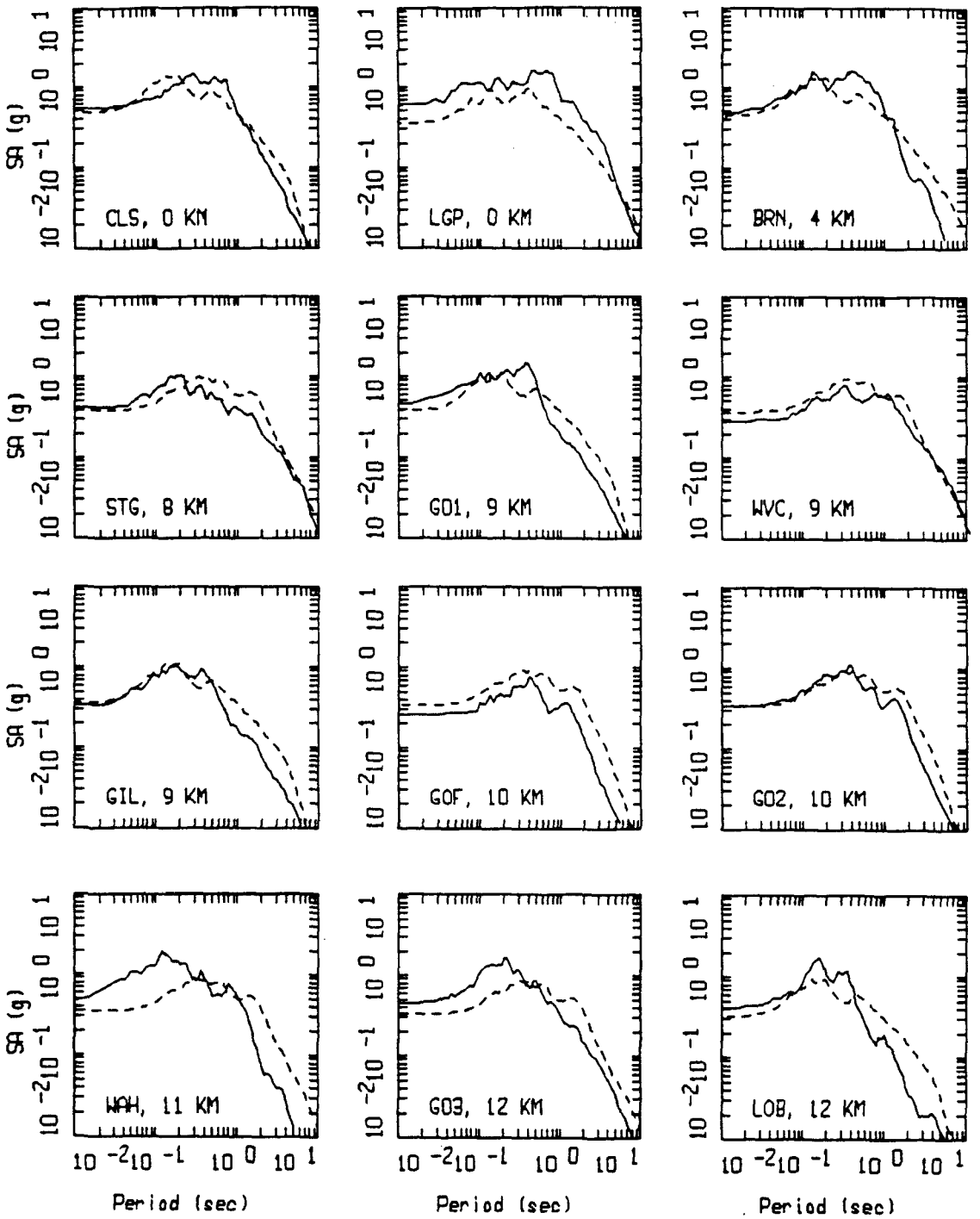

LOMA PRIETA, POINT SOURCE MODELING, PAGE 1 OF 5.
NONLINEAR.

Figure Set 5.47

LEGEND

——— DATA

----- MODEL

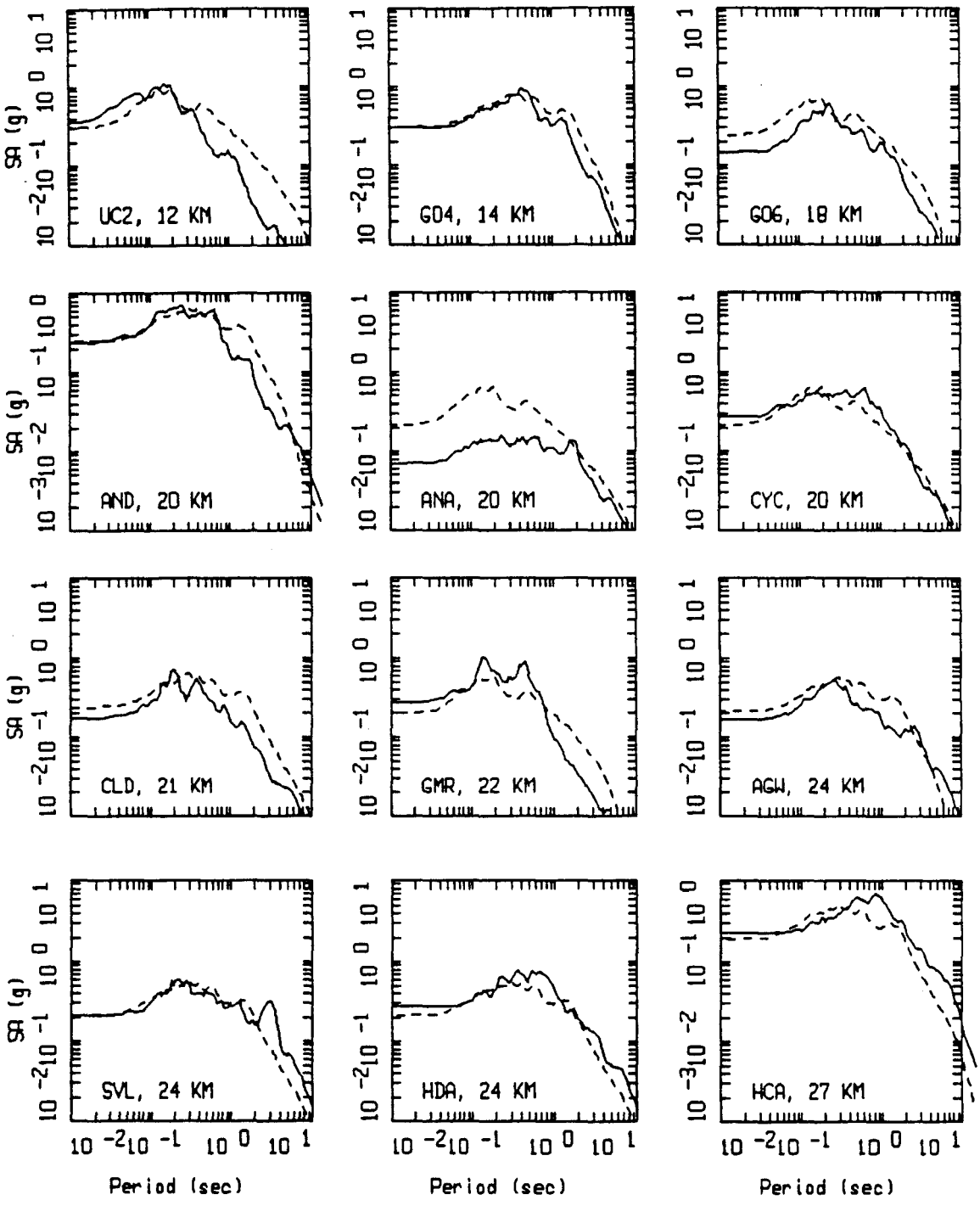

LOMA PRIETA, POINT SOURCE MODELING, PAGE 2 OF 5.
NONLINEAR.

LEGEND

——— DATA

----- MODEL

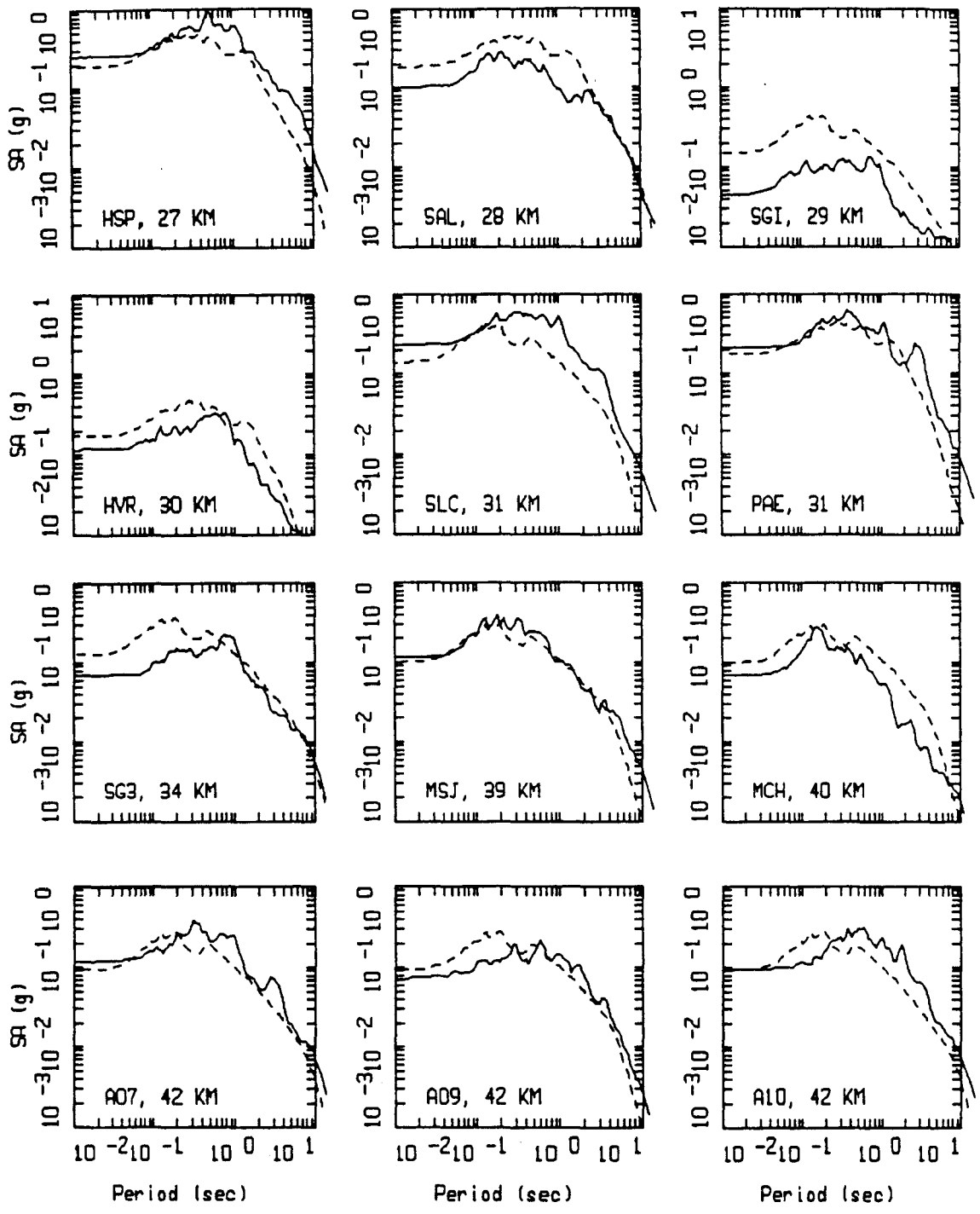

LOMA PRIETA, POINT SOURCE MODELING, PAGE 3 OF 5.
NONLINEAR.

LEGEND

——— DATA

----- MODEL

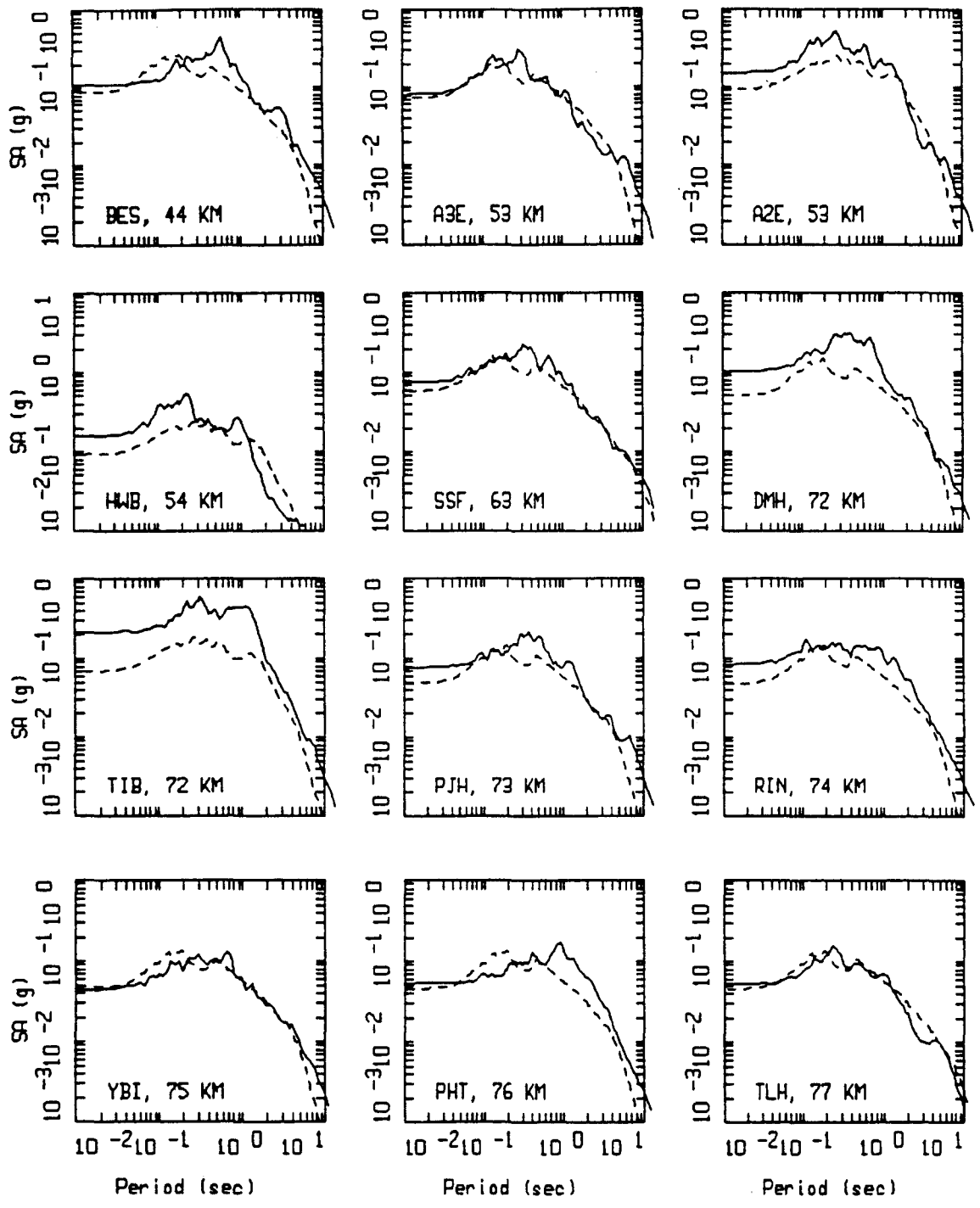

LOMA PRIETA, POINT SOURCE MODELING, PAGE 4 OF 5.
NONLINEAR.

LEGEND

——— DATA

----- MODEL

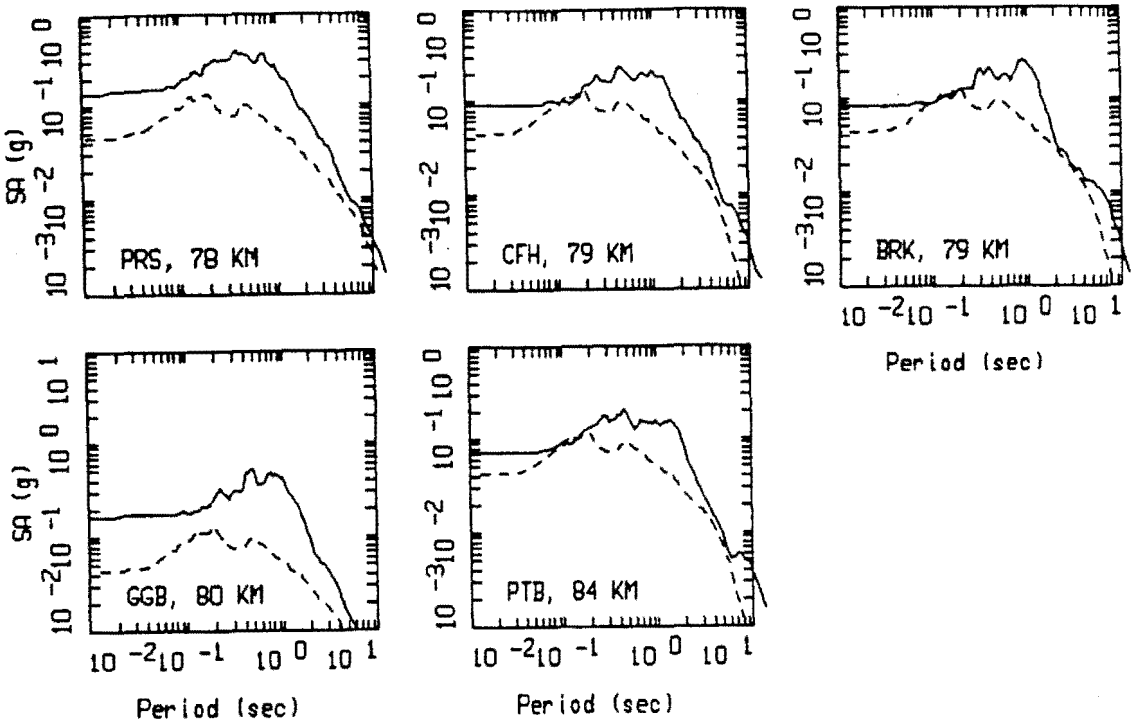

LOMA PRIETA, POINT SOURCE MODELING, PAGE 5 OF 5.
NONLINEAR.

LEGEND

——— DATA

- - - - - MODEL

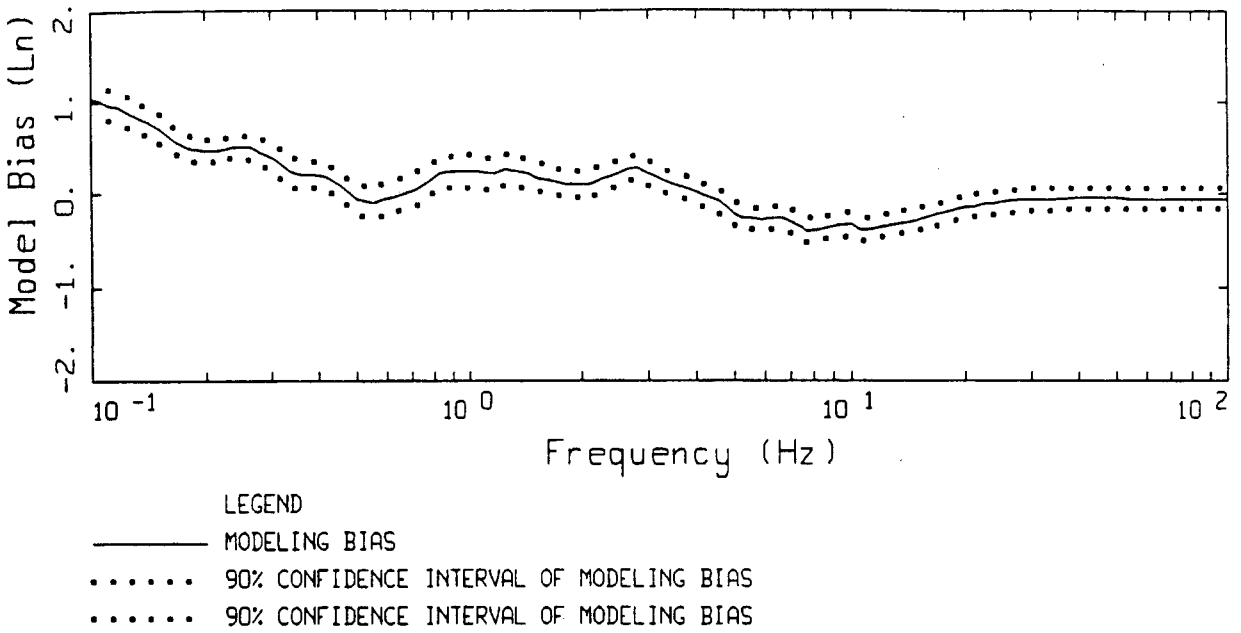

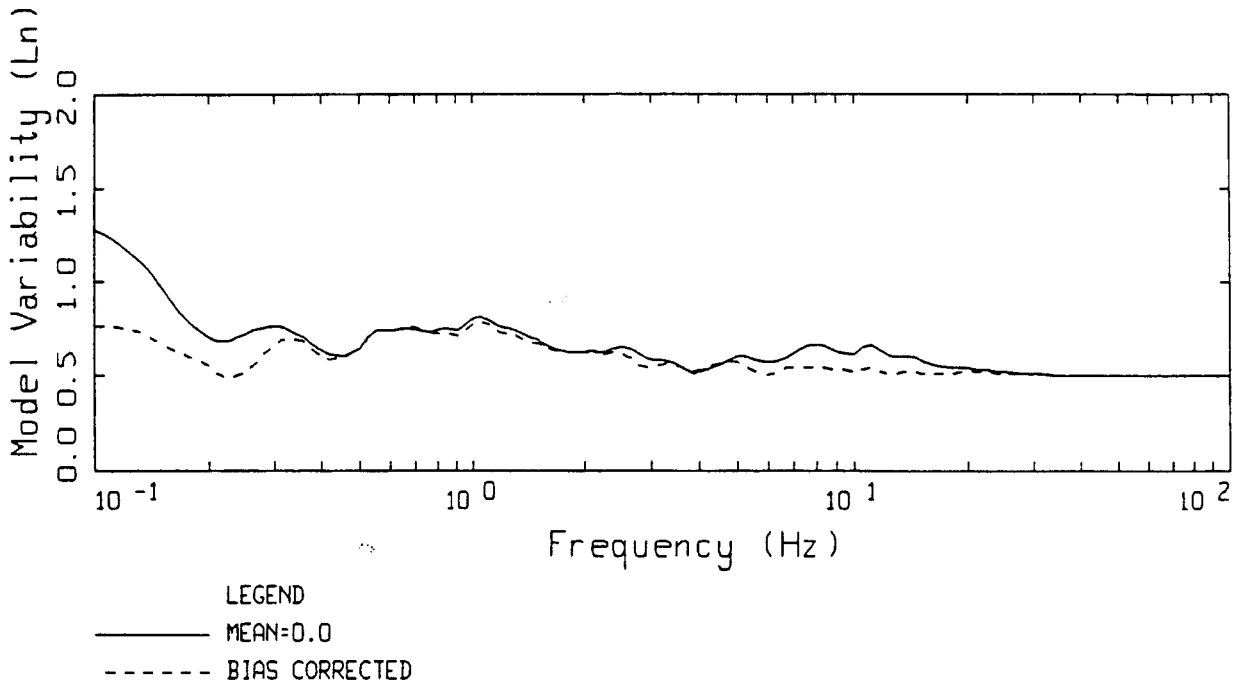

LOMA PRIETA FINITE-SOURCE
NONLINEAR, ALL 53 SITES

Figure 5.48

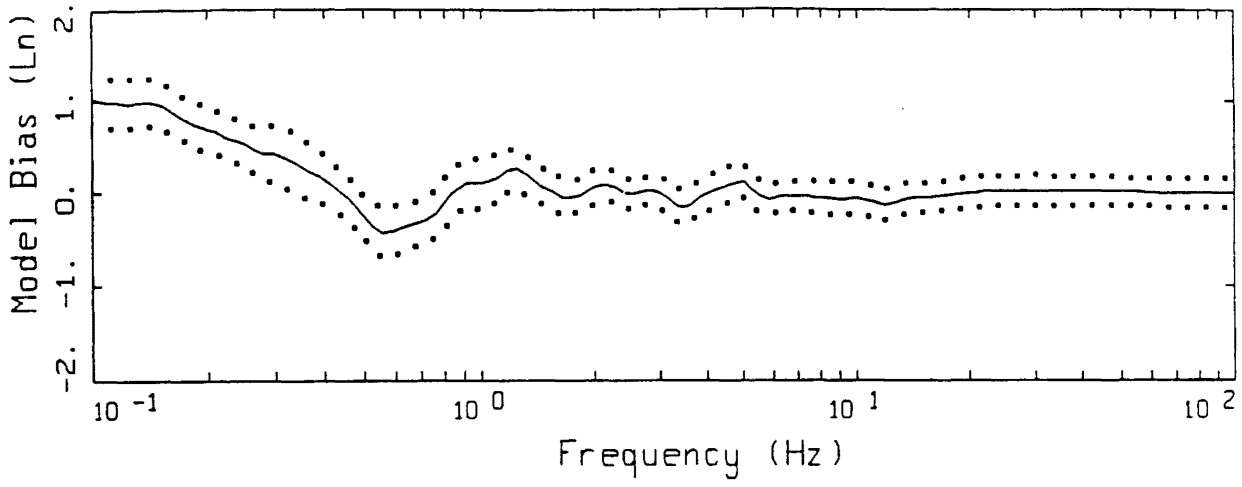

LEGEND
MODELING BIAS
90% CONFIDENCE INTERVAL OF MODELING BIAS
90% CONFIDENCE INTERVAL OF MODELING BIAS

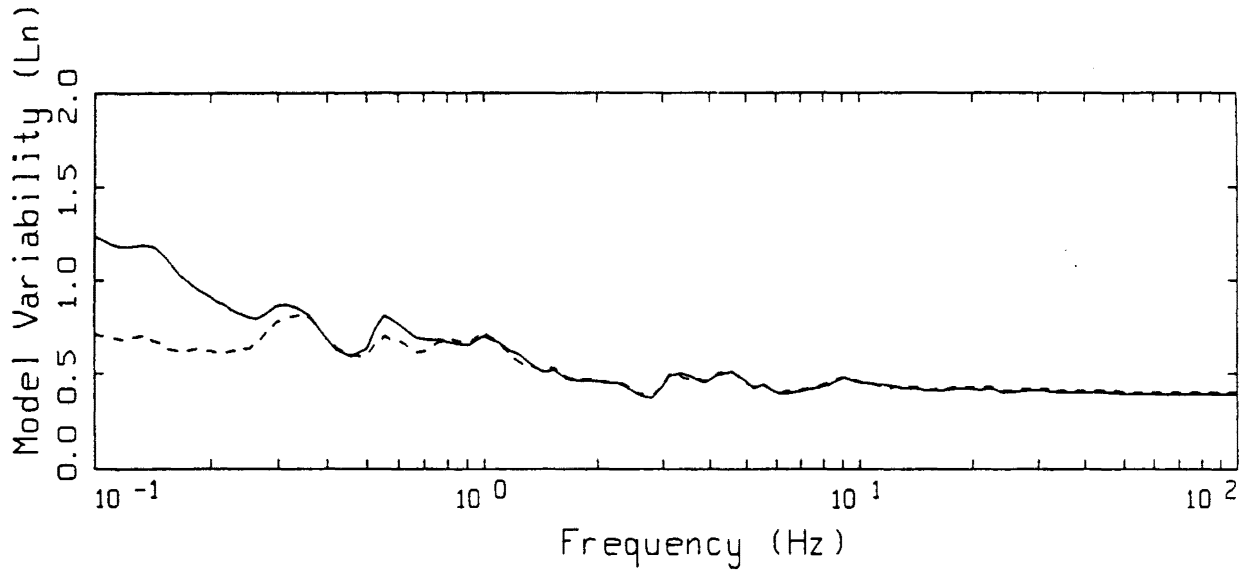

LEGEND
MEAN=0.0
BIAS CORRECTED

LOMA PRIETA FINITE-SOURCE
NONLINEAR, 20 SOIL SITES

Figure 5.49

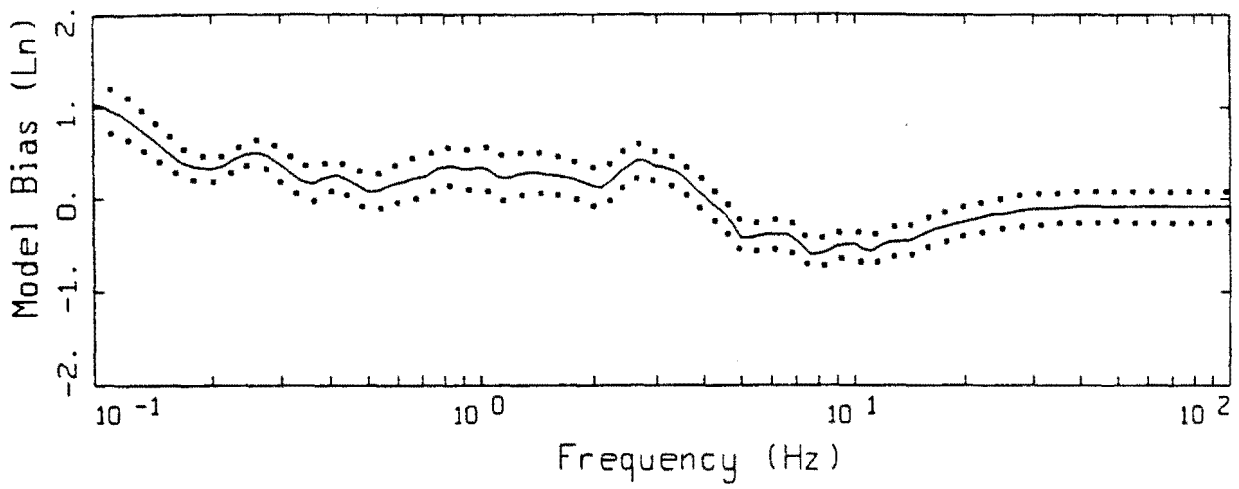

LEGEND
MODELING BIAS
90% CONFIDENCE INTERVAL OF MODELING BIAS
90% CONFIDENCE INTERVAL OF MODELING BIAS

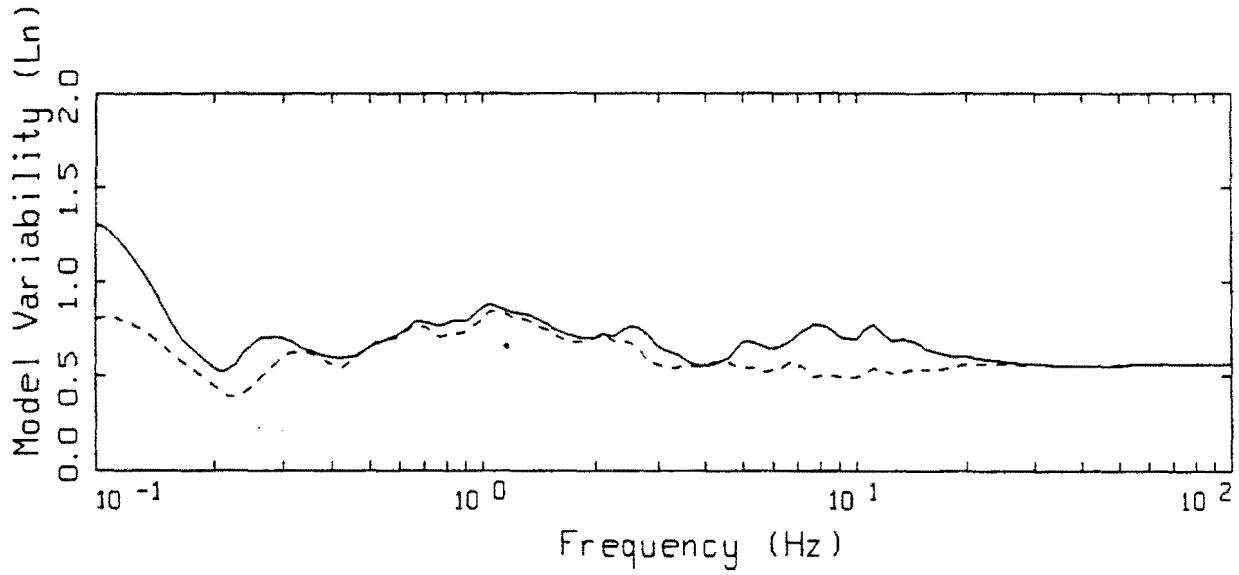

LEGEND
MEAN=0.0
BIAS CORRECTED

LOMA PRIETA FINITE-SOURCE
NONLINEAR, 33 ROCK SITES

Figure 5.50

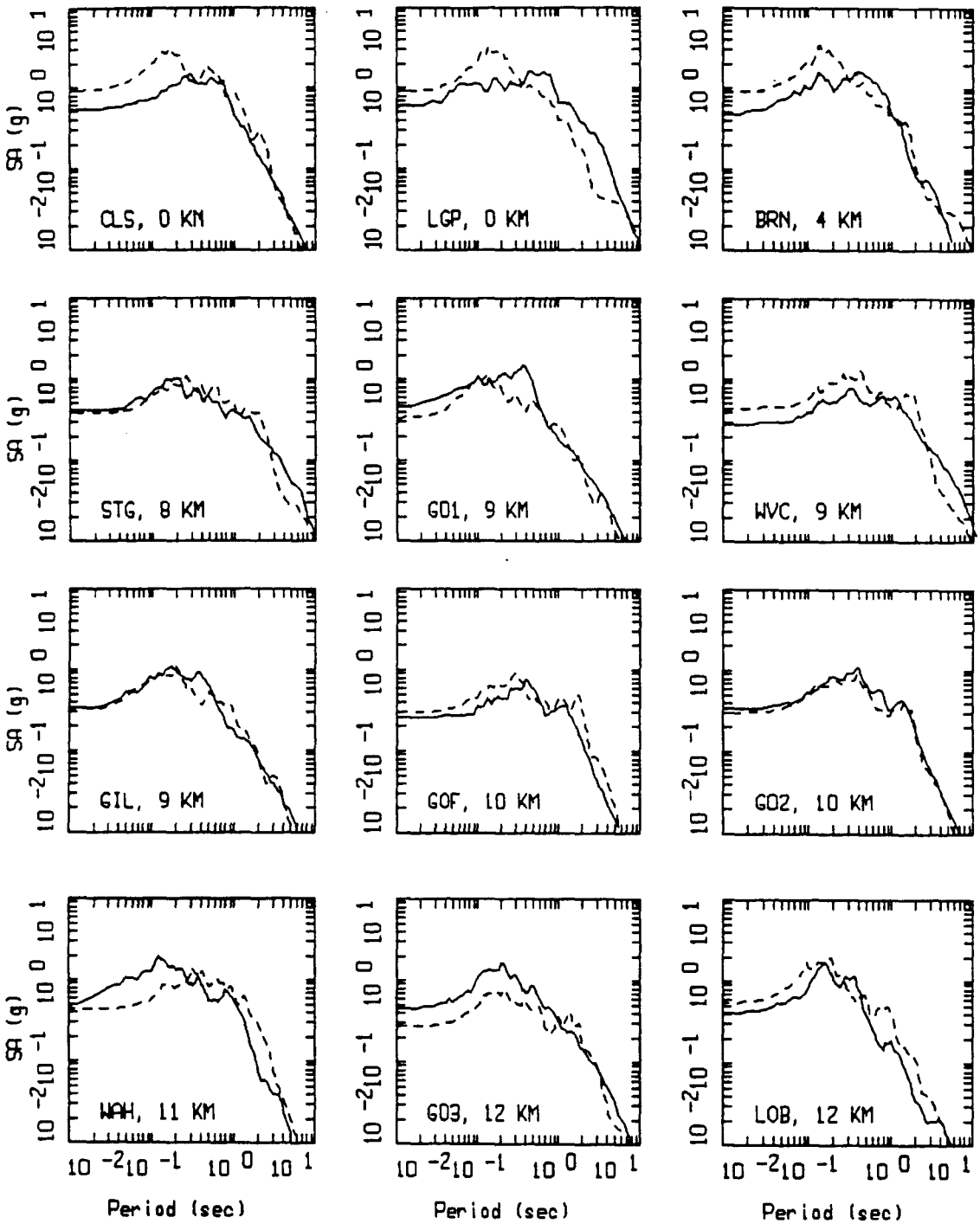

LOMA PRIETA, FINITE SOURCE MODELING, PAGE 1 OF 5.
NONLINEAR.

Figure Set 5.51

LEGEND

——— DATA

----- MODEL

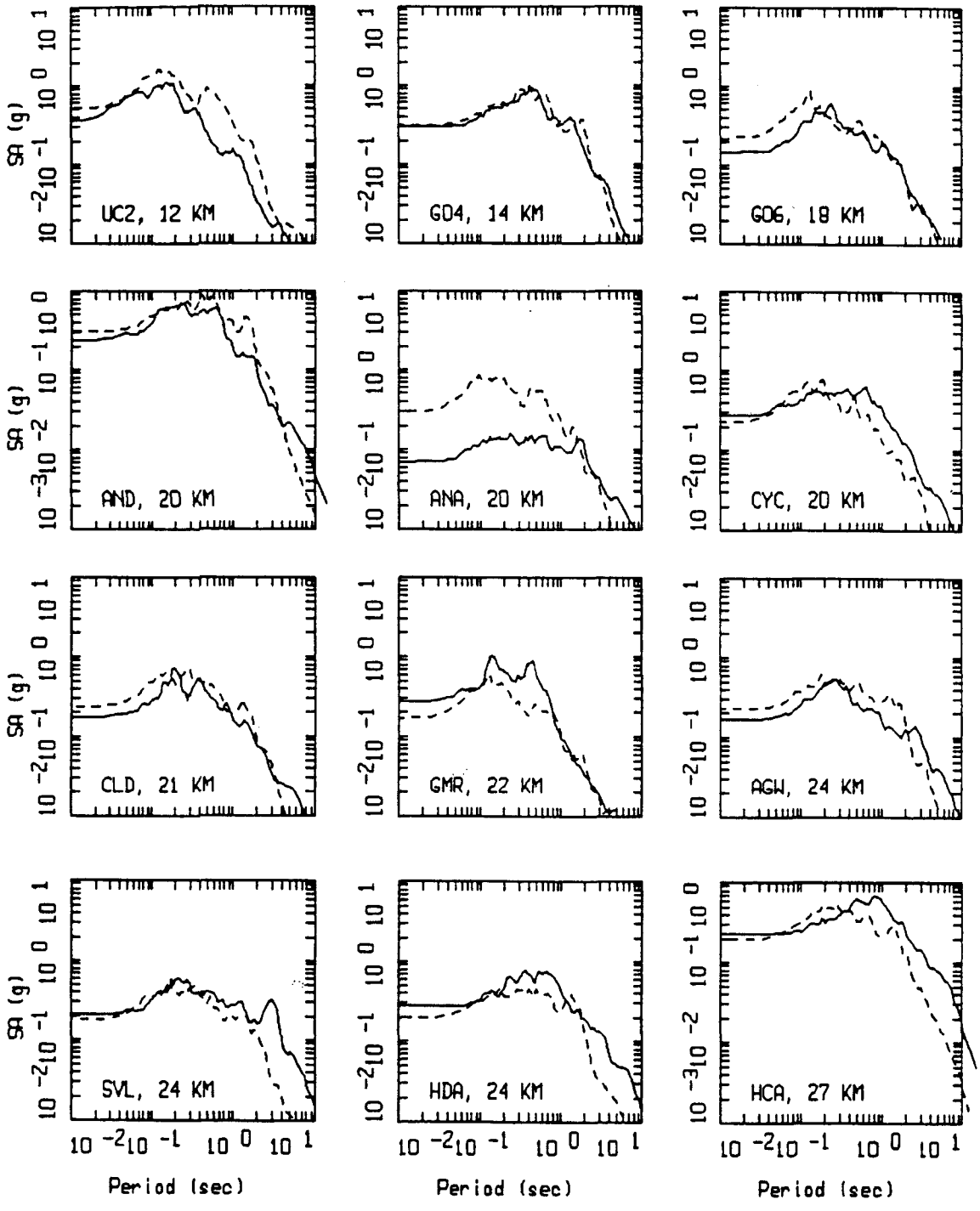

LOMA PRIETA, FINITE SOURCE MODELING, PAGE 2 OF 5.
NONLINEAR.

LEGEND

——— DATA

- - - - - MODEL

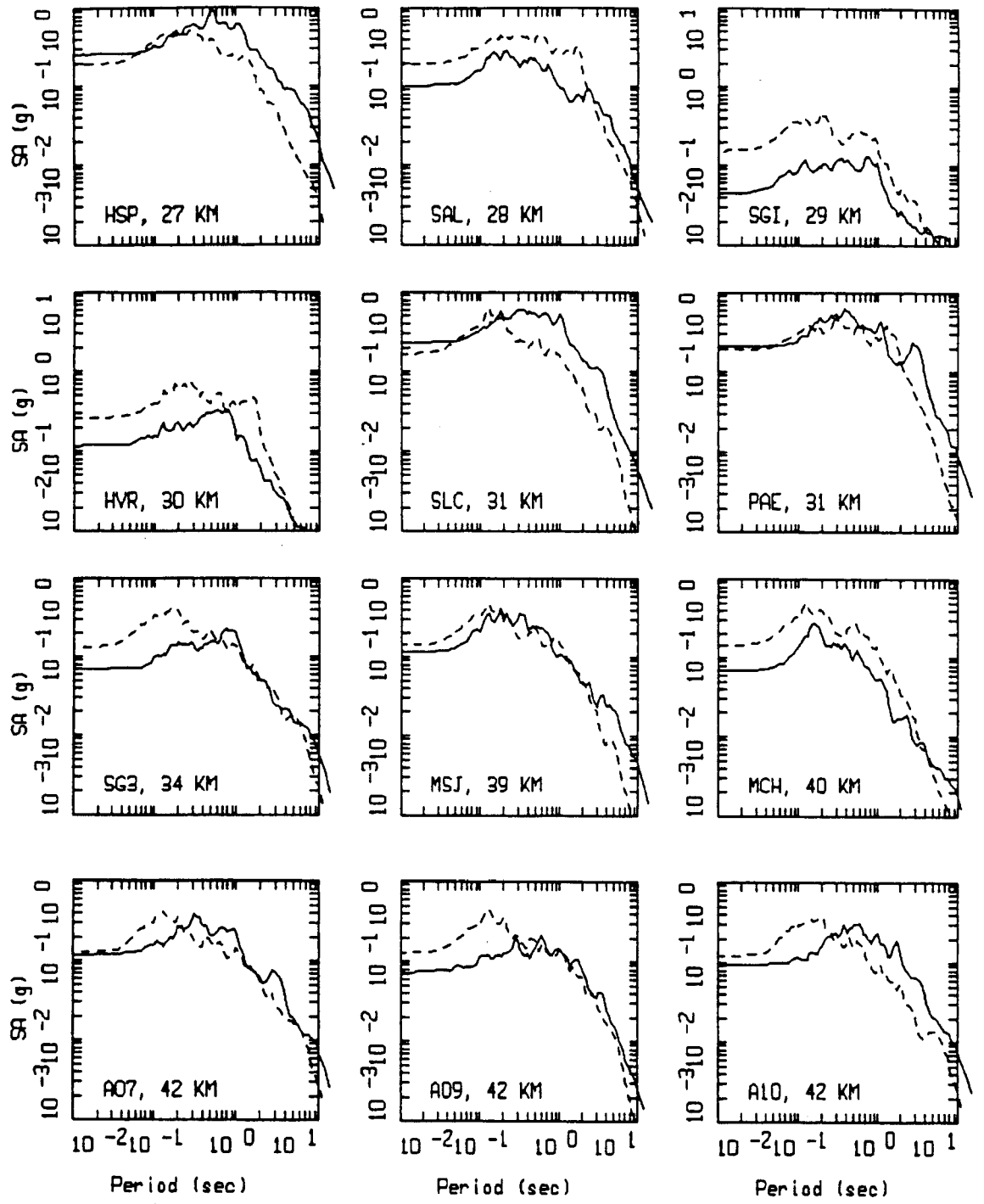

LOMA PRIETA, FINITE SOURCE MODELING, PAGE 3 OF 5.
NONLINEAR.

LEGEND

——— DATA

- - - - - MODEL

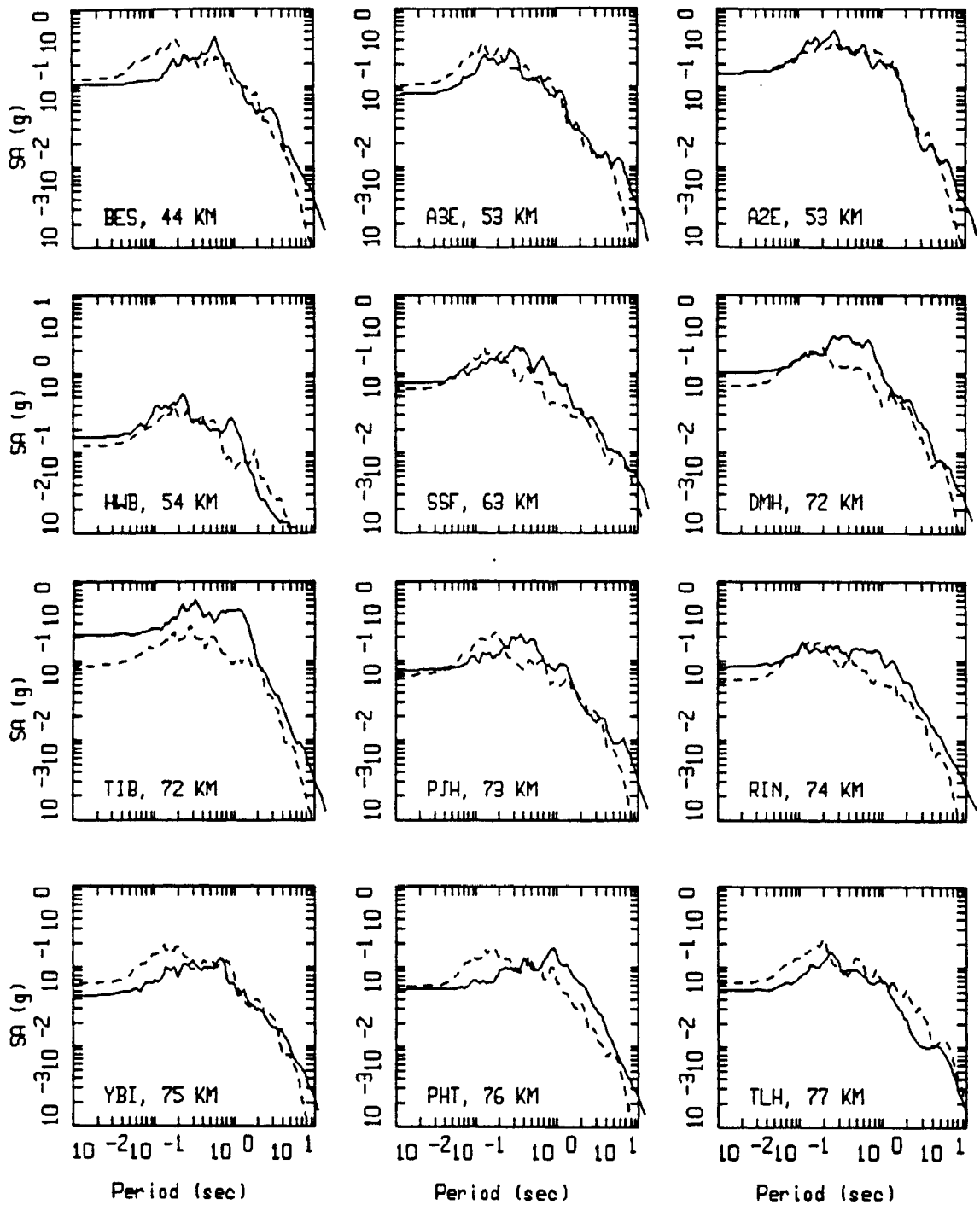

LOMA PRIETA, FINITE SOURCE MODELING, PAGE 4 OF 5.
NONLINEAR.

LEGEND

——— DATA

- - - - - MODEL

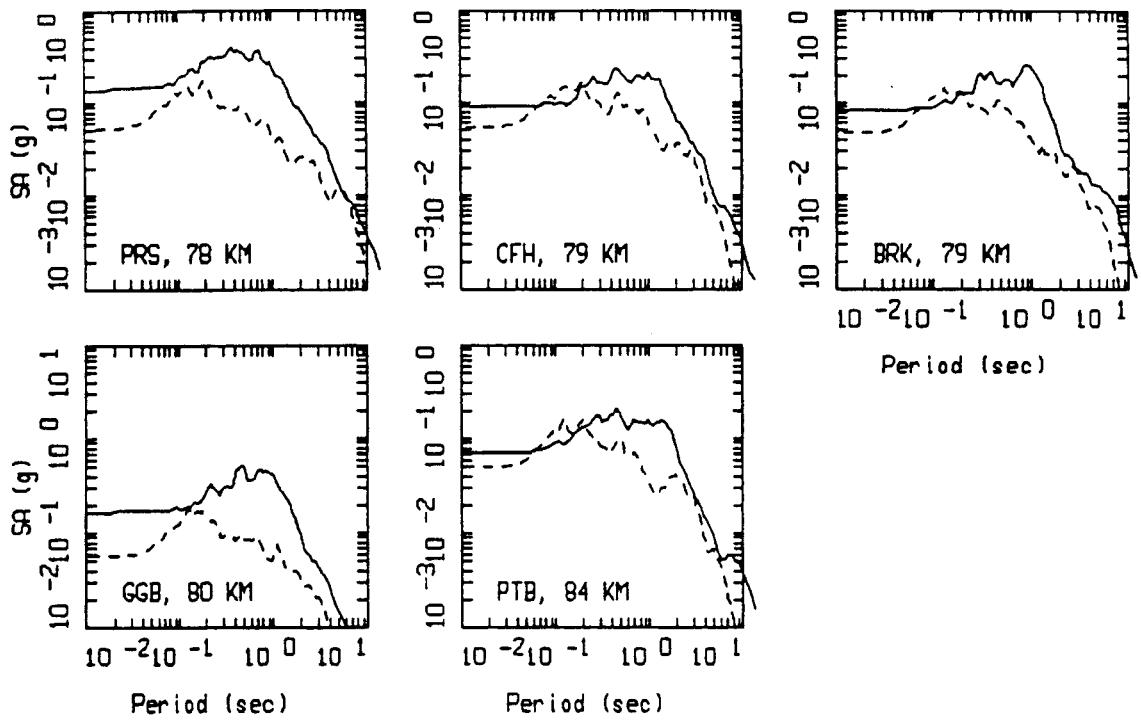

LOMA PRIETA, FINITE SOURCE MODELING, PAGE 5 OF 5.
NONLINEAR.

LEGEND

——— DATA

----- MODEL

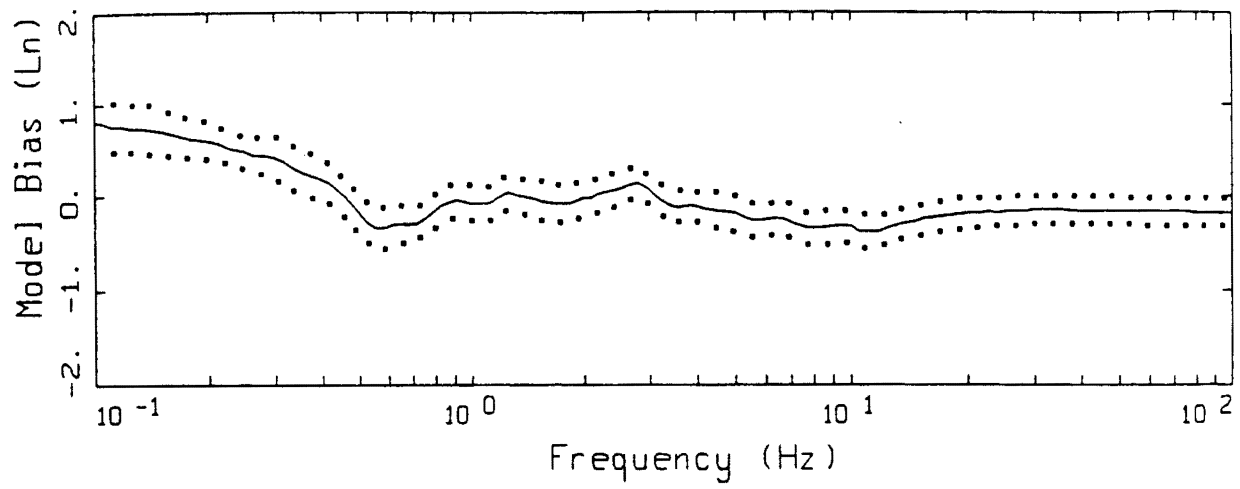

LEGEND
MODELING BIAS
90% CONFIDENCE INTERVAL OF MODELING BIAS
90% CONFIDENCE INTERVAL OF MODELING BIAS

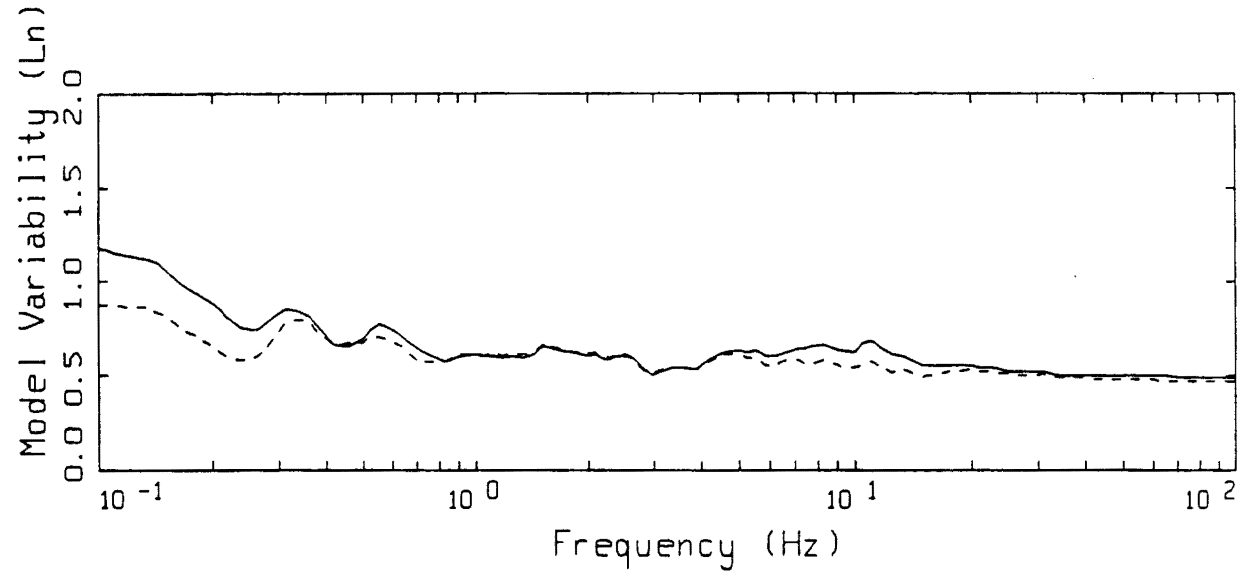

LEGEND
MEAN=0.0
BIAS CORRECTED

LOMA PRIETA FINITE-SOURCE
NONLINEAR, ALL 30 SITES TO 30 KM

Figure 5.52

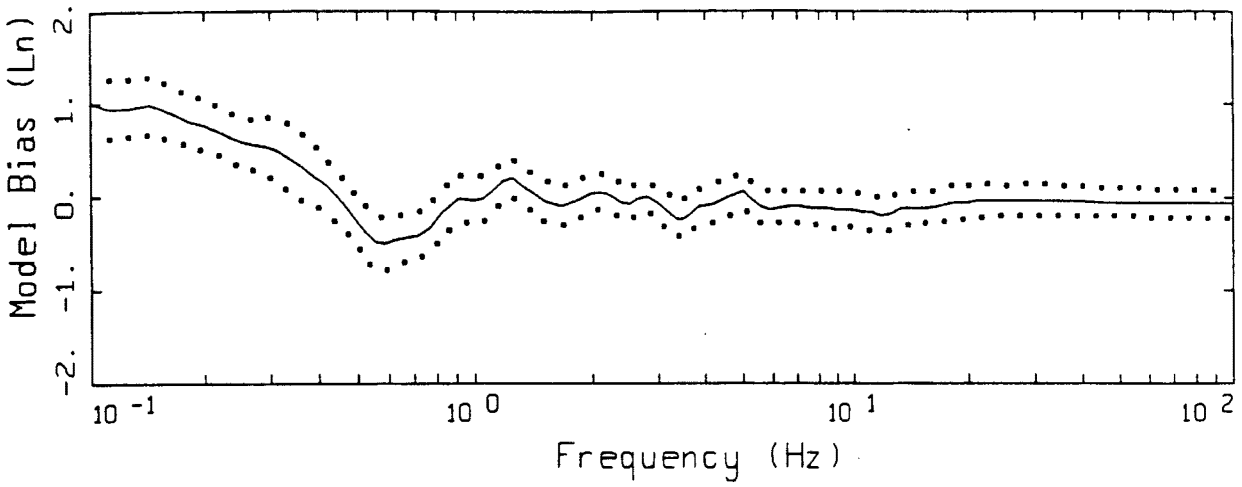

LEGEND
MODELING BIAS
90% CONFIDENCE INTERVAL OF MODELING BIAS
90% CONFIDENCE INTERVAL OF MODELING BIAS

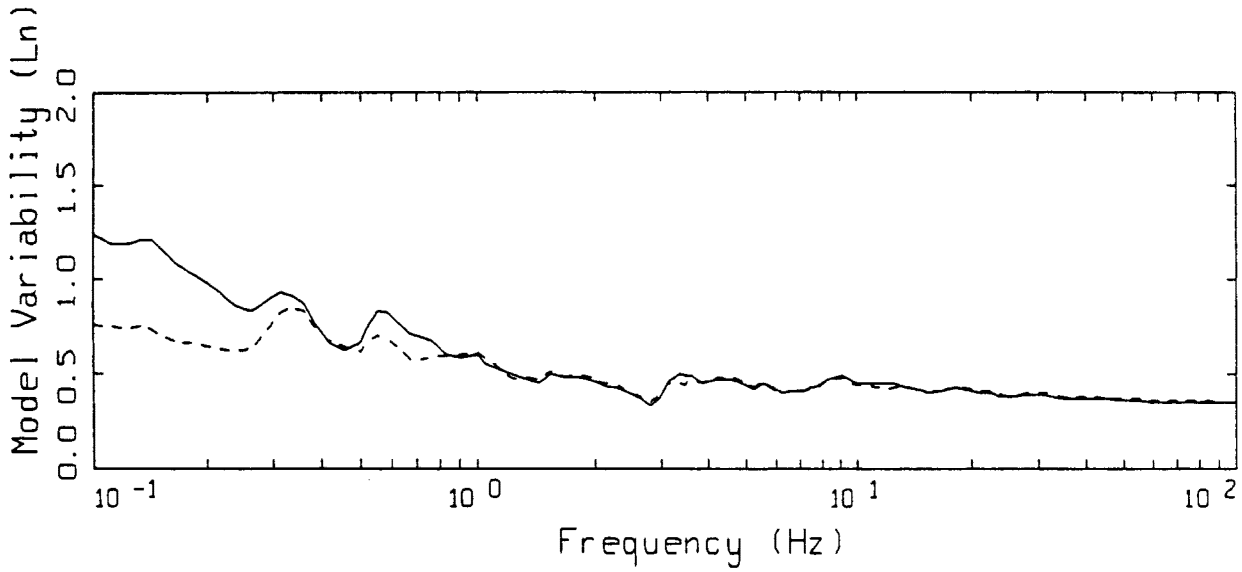

LEGEND
MEAN=0.0
BIAS CORRECTED

LOMA PRIETA FINITE-SOURCE
NONLINEAR, 17 SOIL SITES TO 30 KM

Figure 5.53

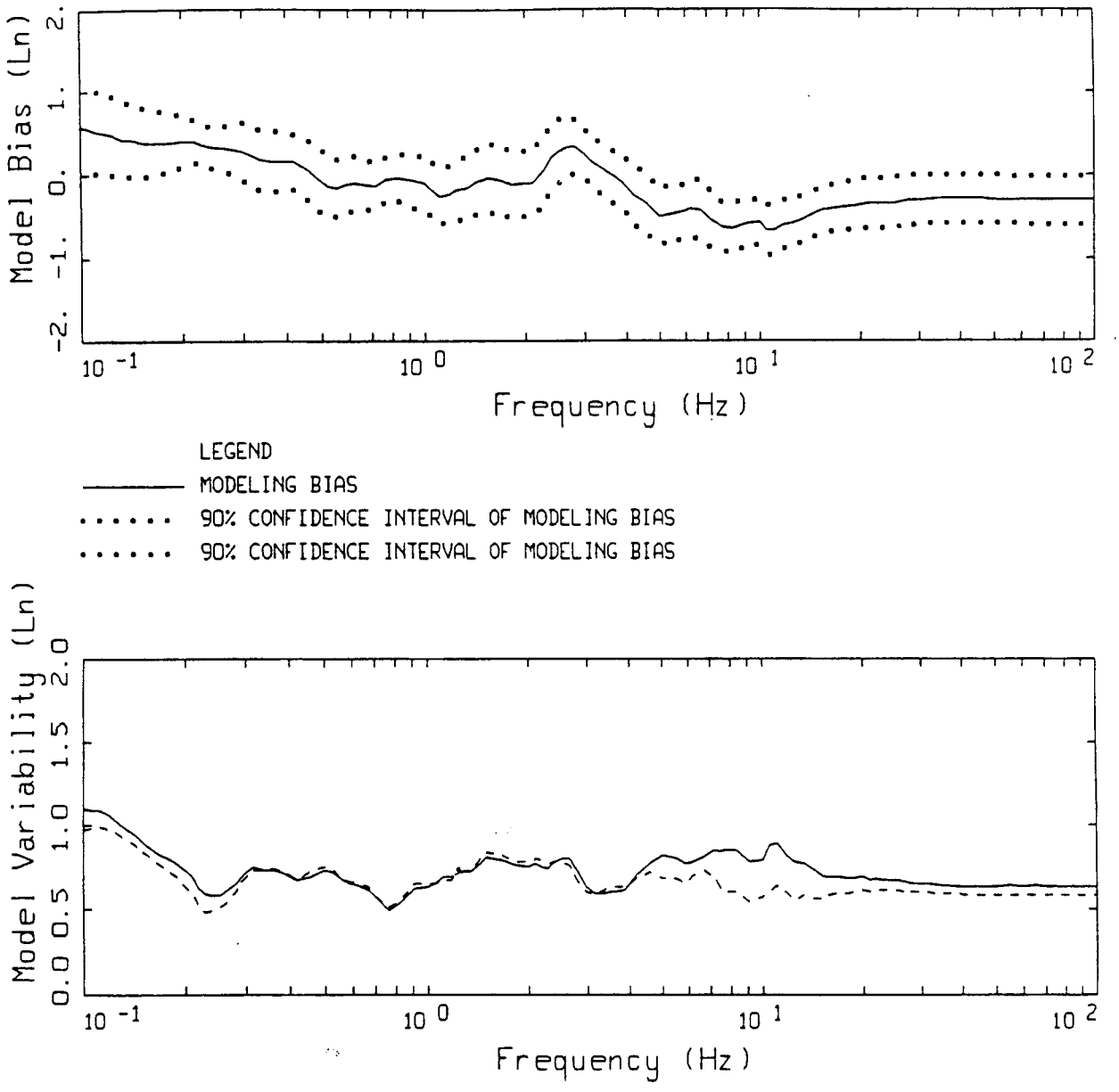

LOMA PRIETA FINITE-SOURCE
NONLINEAR, 13 ROCK SITES TO 30 KM

Figure 5.54

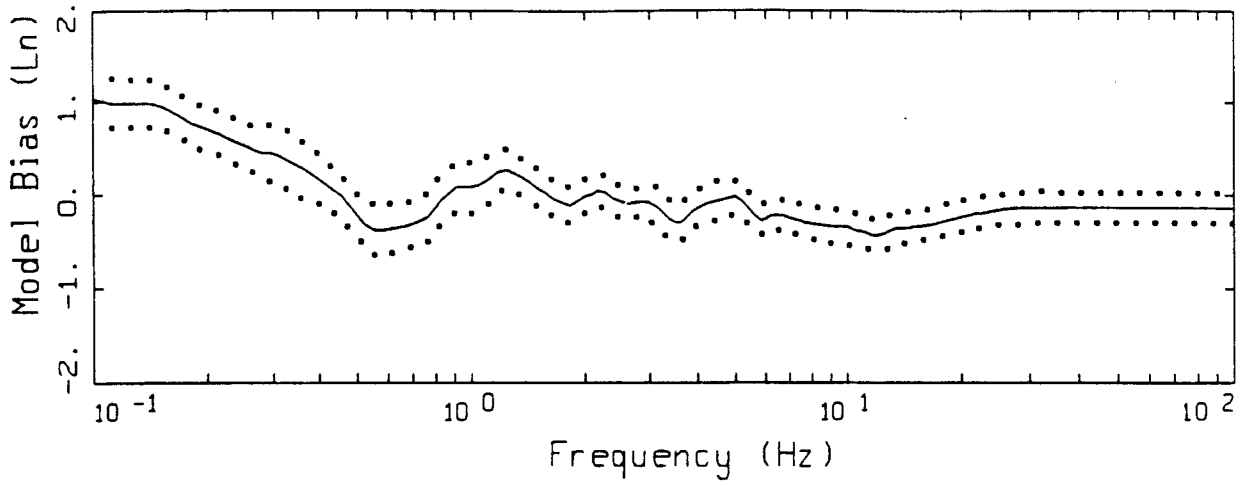

LEGEND
MODELING BIAS
90% CONFIDENCE INTERVAL OF MODELING BIAS
90% CONFIDENCE INTERVAL OF MODELING BIAS

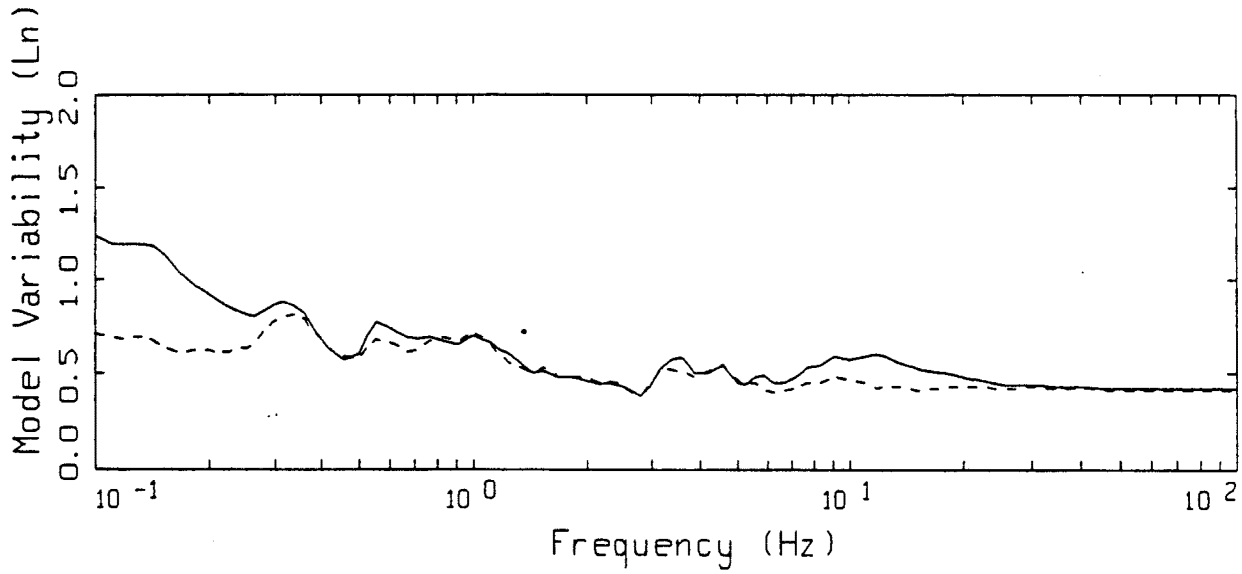

LEGEND
MEAN=0.0
BIAS CORRECTED

LOMA PRIETA FINITE-SOURCE
NONLINEAR, 20 SOIL SITES

Figure 5.55a

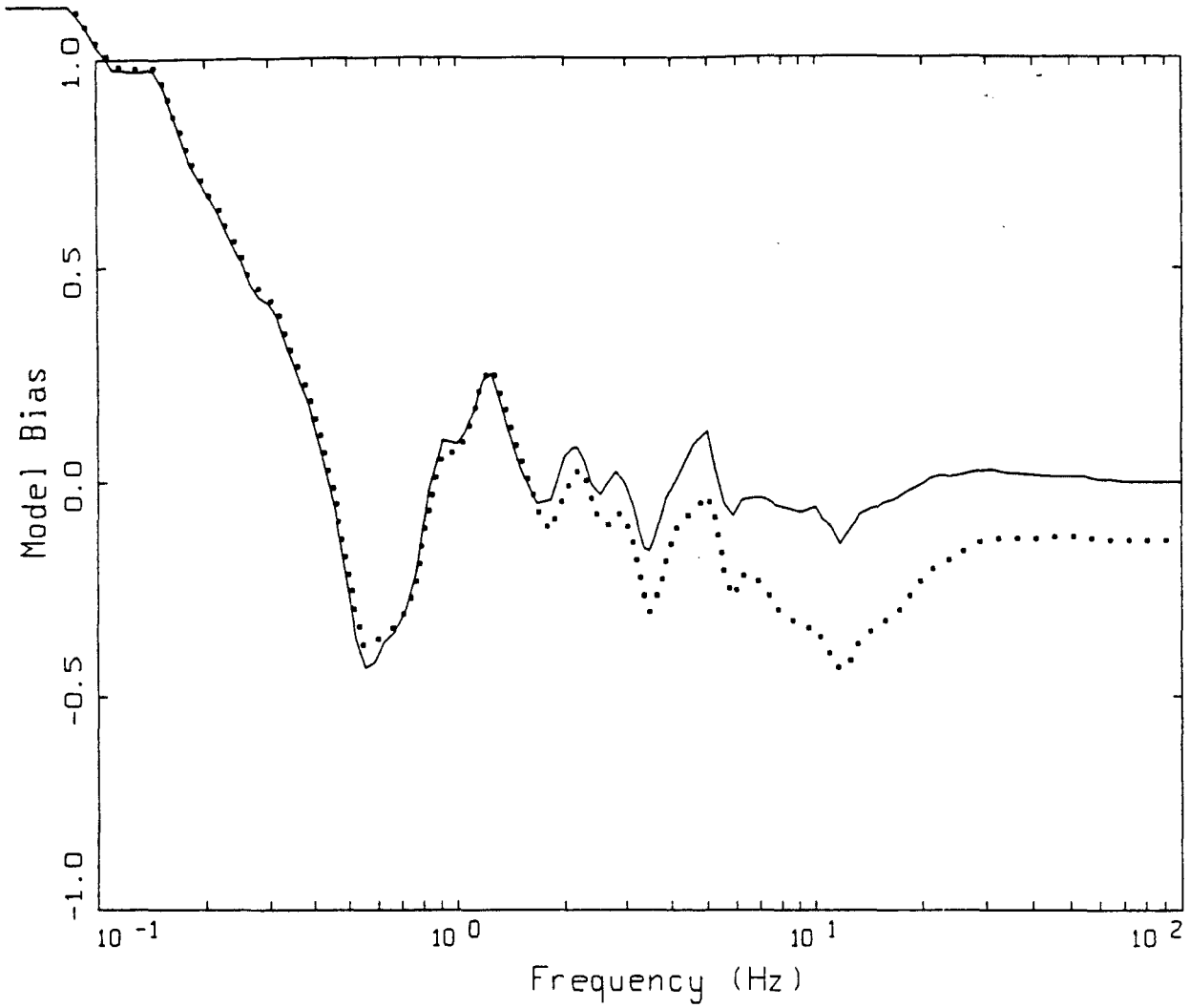

LOMA PRIETA FINITE SOURCE, MODELING BIAS
NONLINEAR PROFILES, 20 SOIL SITES

LEGEND

——— MODELING BIAS, EPRI CURVES

• • • • MODELING BIAS, DEEP SOIL CURVES

Figure 5.55b

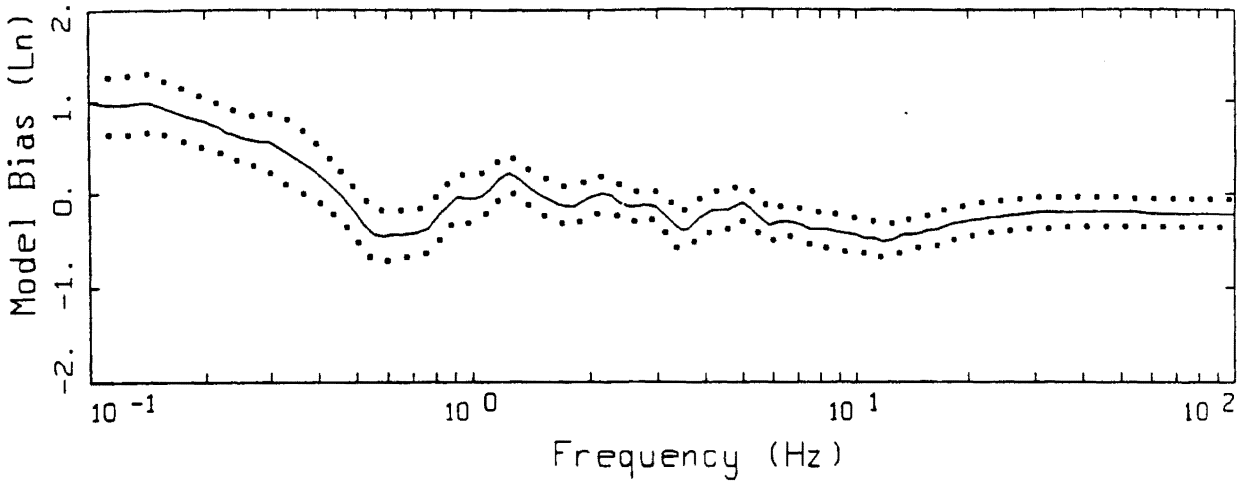

LEGEND
MODELING BIAS
90% CONFIDENCE INTERVAL OF MODELING BIAS
90% CONFIDENCE INTERVAL OF MODELING BIAS

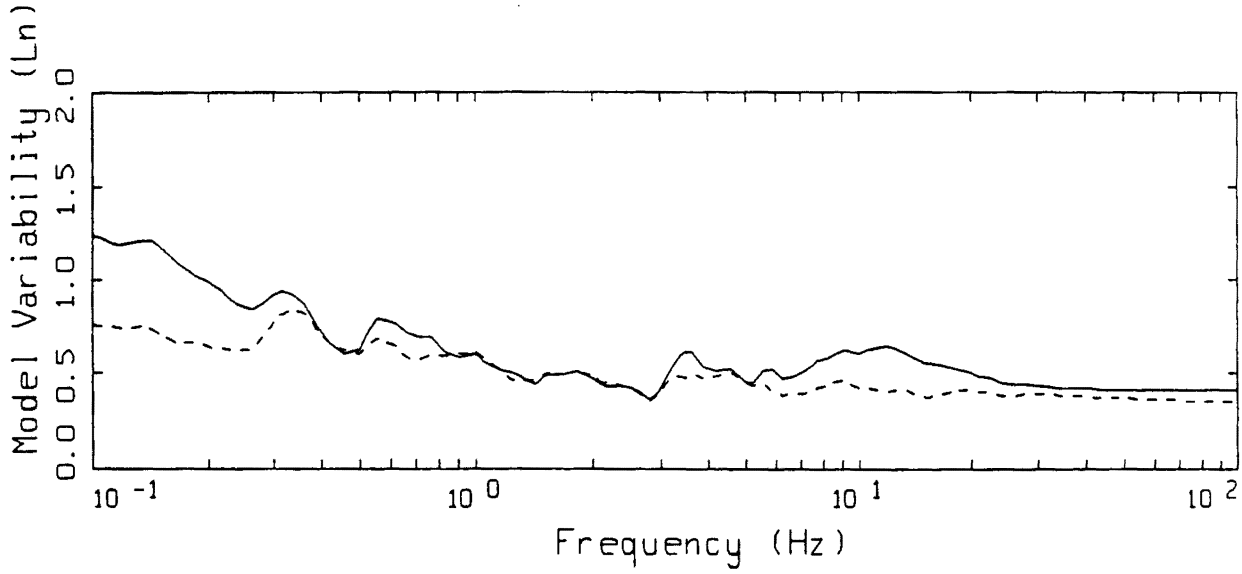

LEGEND
MEAN=0.0
BIAS CORRECTED

LOMA PRIETA FINITE-SOURCE
NONLINEAR, 17 SOIL SITES TO 30 KM

Figure 5.56a

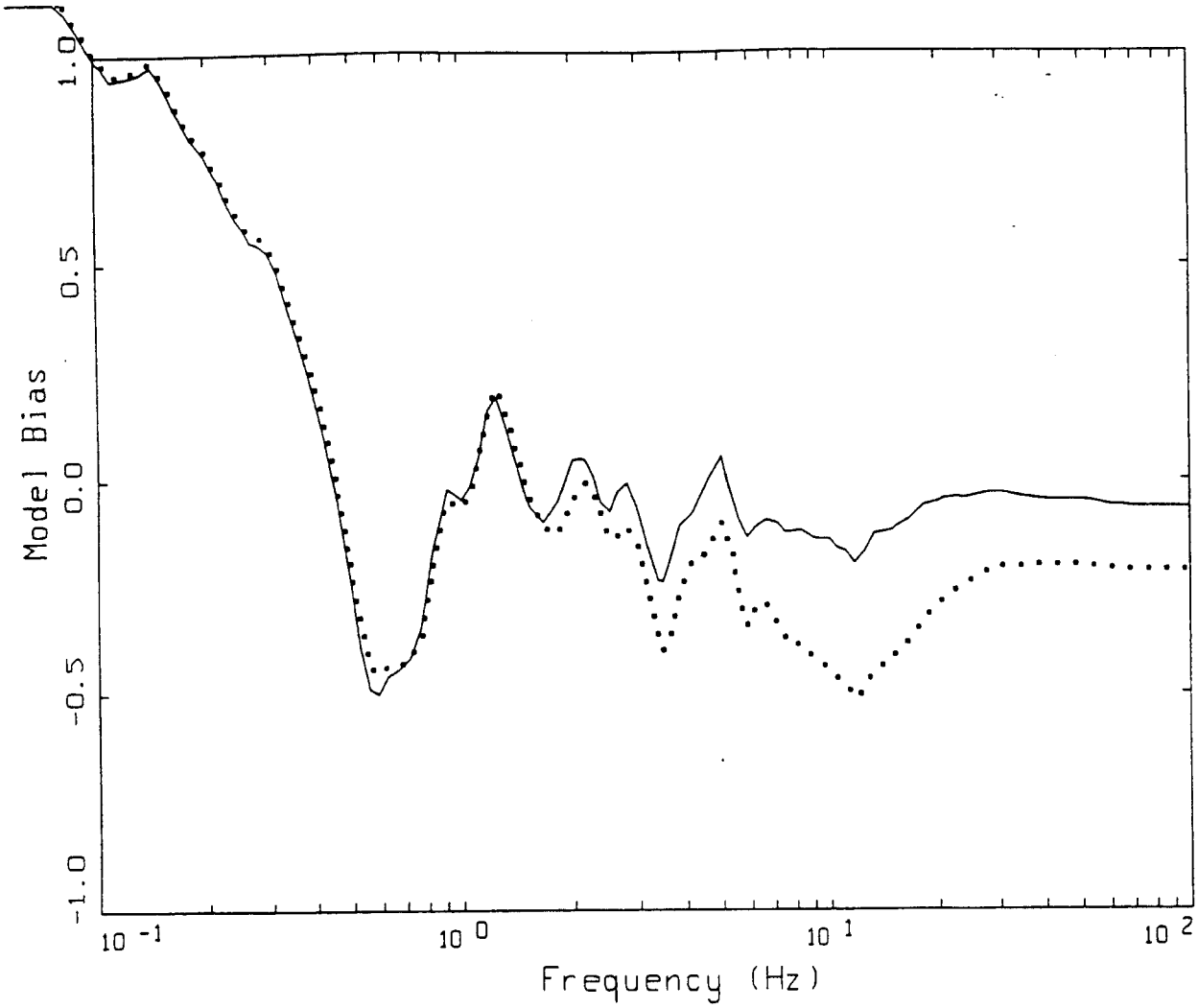

LOMA PRIETA FINITE SOURCE, MODELING BIAS
NONLINEAR PROFILES, 17 SOIL SITES TO 30 KM

LEGEND

——— MODELING BIAS, EPRI CURVES

• • • • MODELING BIAS, DEEP SOIL CURVES

Figure 5.56b

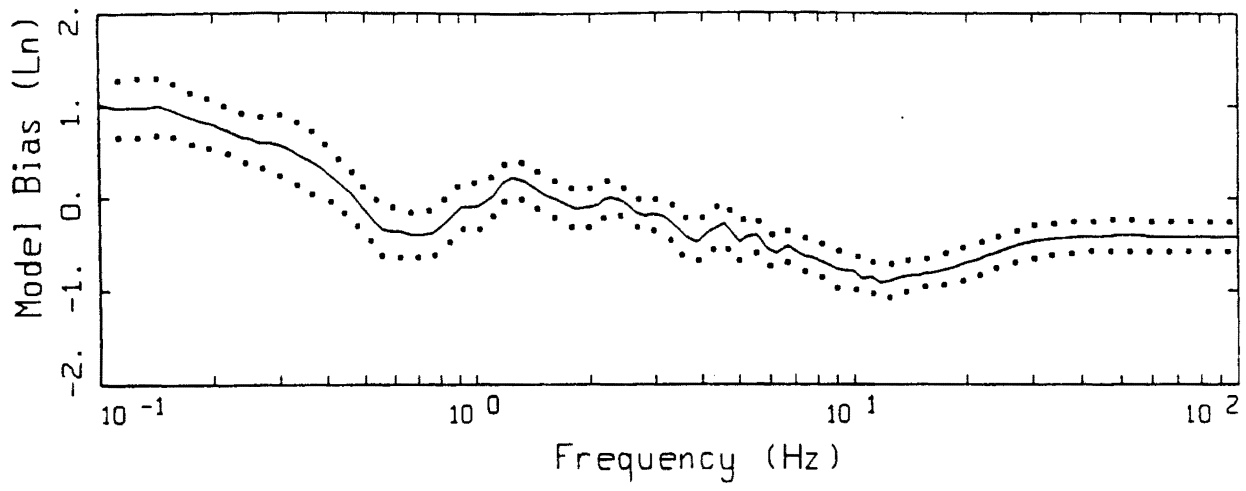

LEGEND
MODELING BIAS
90% CONFIDENCE INTERVAL OF MODELING BIAS
90% CONFIDENCE INTERVAL OF MODELING BIAS

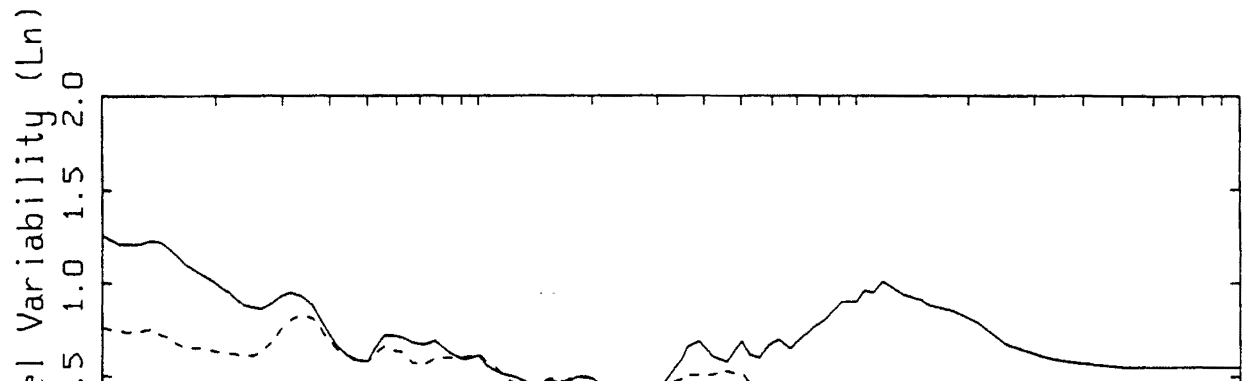

LEGEND
MEAN=0.0
BIAS CORRECTED

LOMA PRIETA FINITE-SOURCE
LINEAR, 17 SOIL SITES TO 30 KM

Figure 5.57

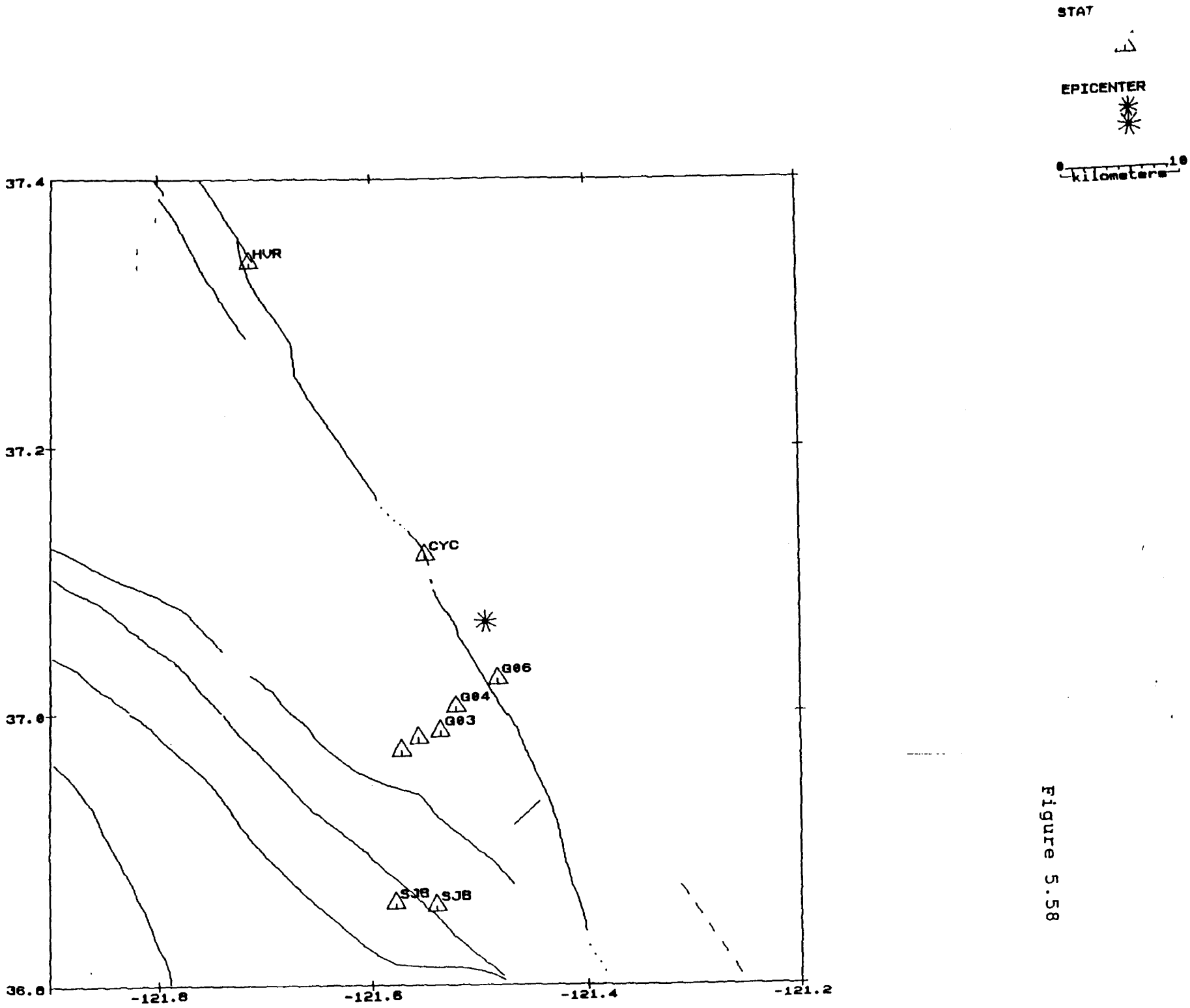
STAT
EPICENTER
0
10
kilometers
37.4
37.2
37.0
36.8
-121.8
-121.6
-121.4
-121.2
HVR
CYC
G06
G04
G03
SJB
SJB
EQ3D-v4.00 FILE: SITES.HP2 EPICENT.HP2
SCA:400000 MFAC:1.0 XFAC:1.0 Nm=11 Nx=0

Figure 5.58

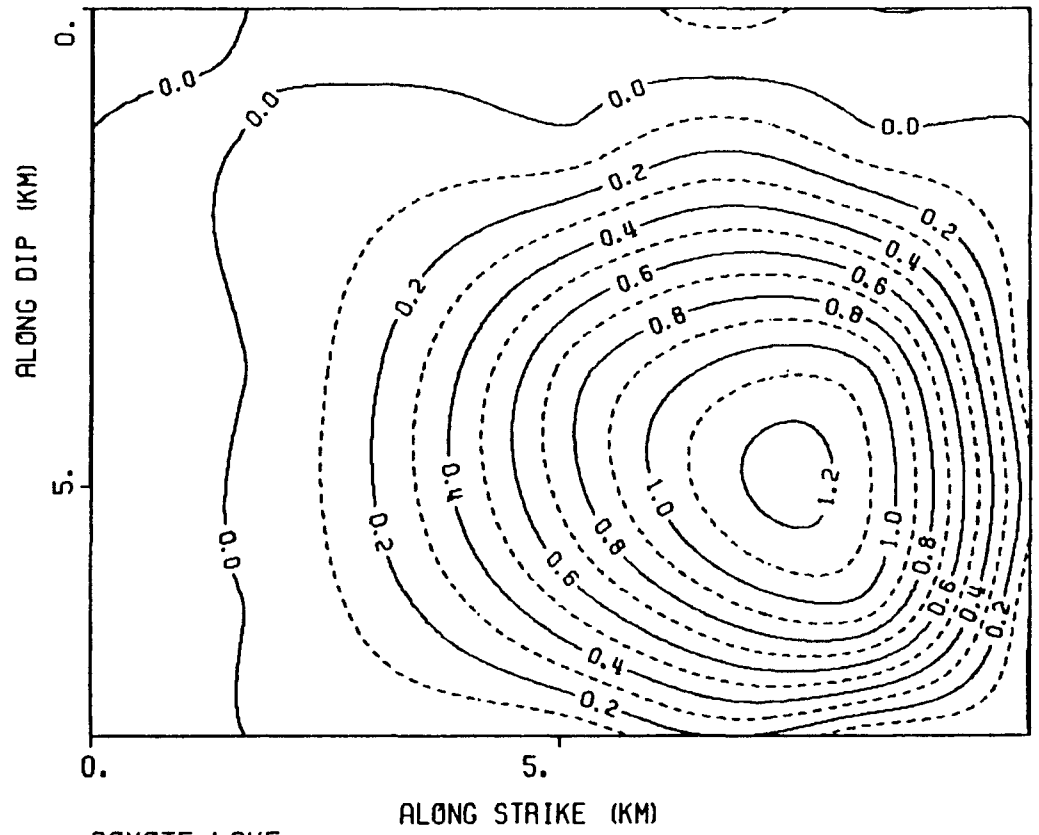
0.
5.
ALONG DIP (KM)
0.
5.
ALONG STRIKE (KM)
0.0
0.2
0.4
0.6
0.8
1.0
1.2
COYOTE LAKE

Figure 5.59

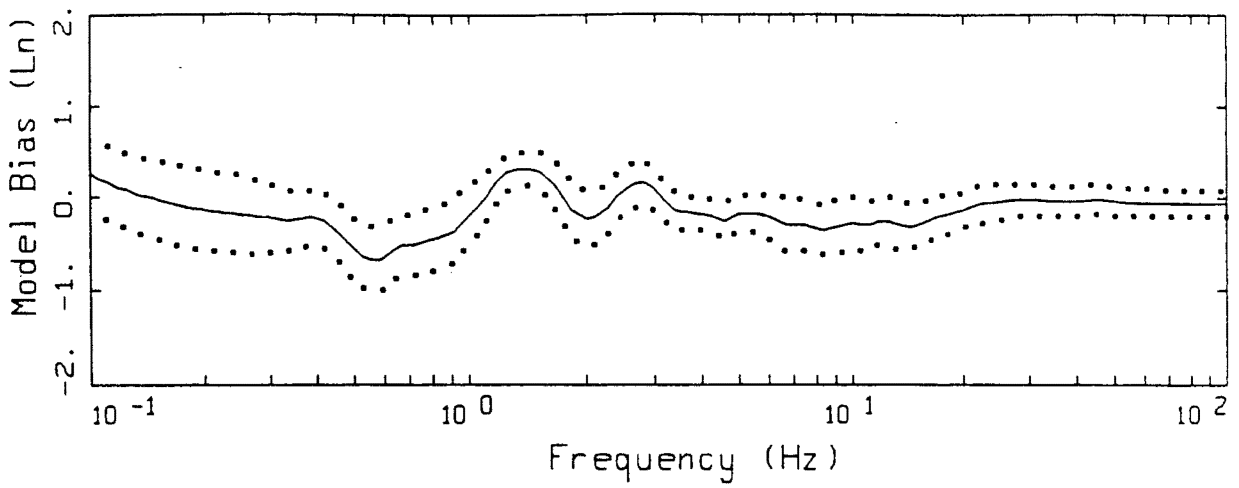

LEGEND
MODELING BIAS
90% CONFIDENCE INTERVAL OF MODELING BIAS
90% CONFIDENCE INTERVAL OF MODELING BIAS

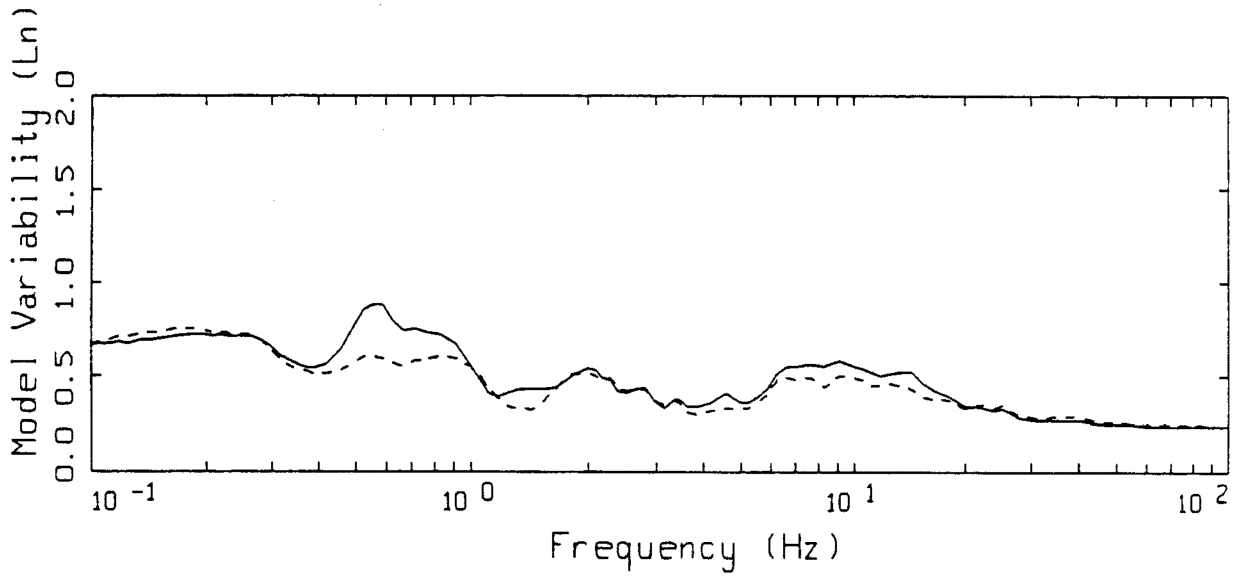

LEGEND
MEAN=0.0
BIAS CORRECTED

COYOTE LAKE POINT-SOURCE
NONLINEAR, ALL 10 SITES

Figure 5.60

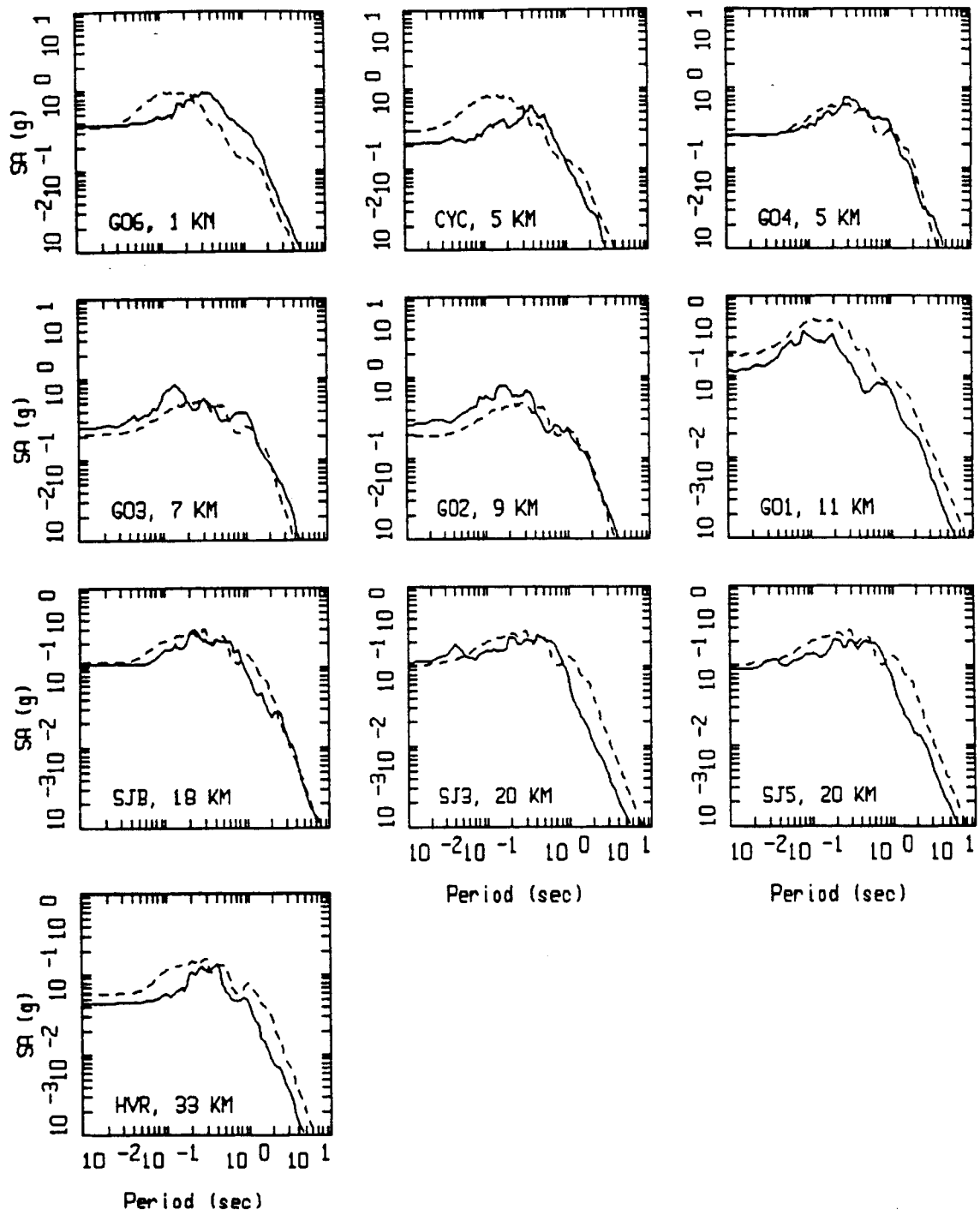

COYOTE LAKE, POINT SOURCE MODELING, PAGE 1 OF 1.
NONLINEAR.

LEGEND
——— DATA
----- MODEL

Figure 5.61

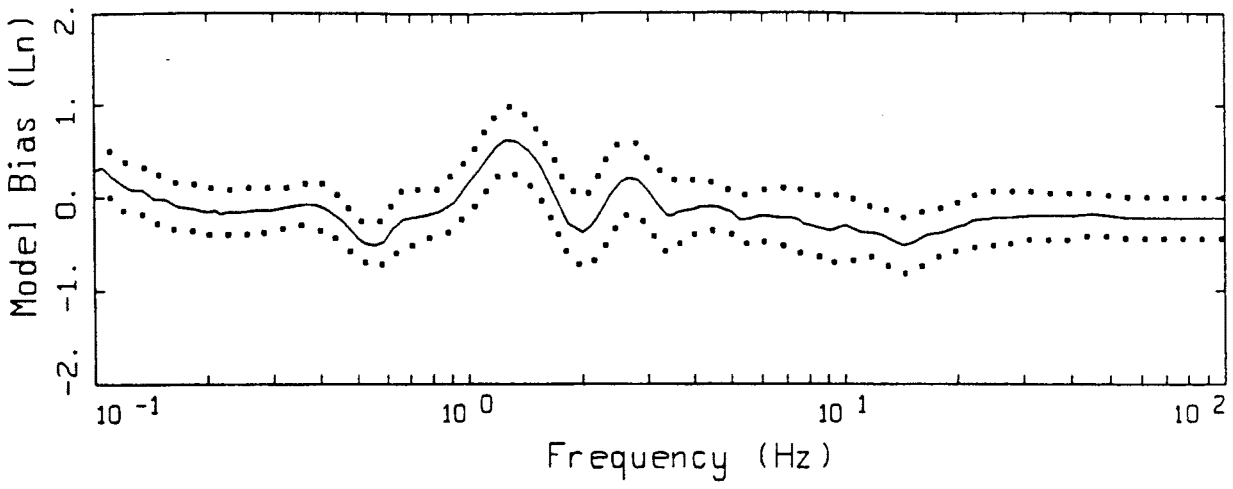

LEGEND
MODELING BIAS
90% CONFIDENCE INTERVAL OF MODELING BIAS
90% CONFIDENCE INTERVAL OF MODELING BIAS

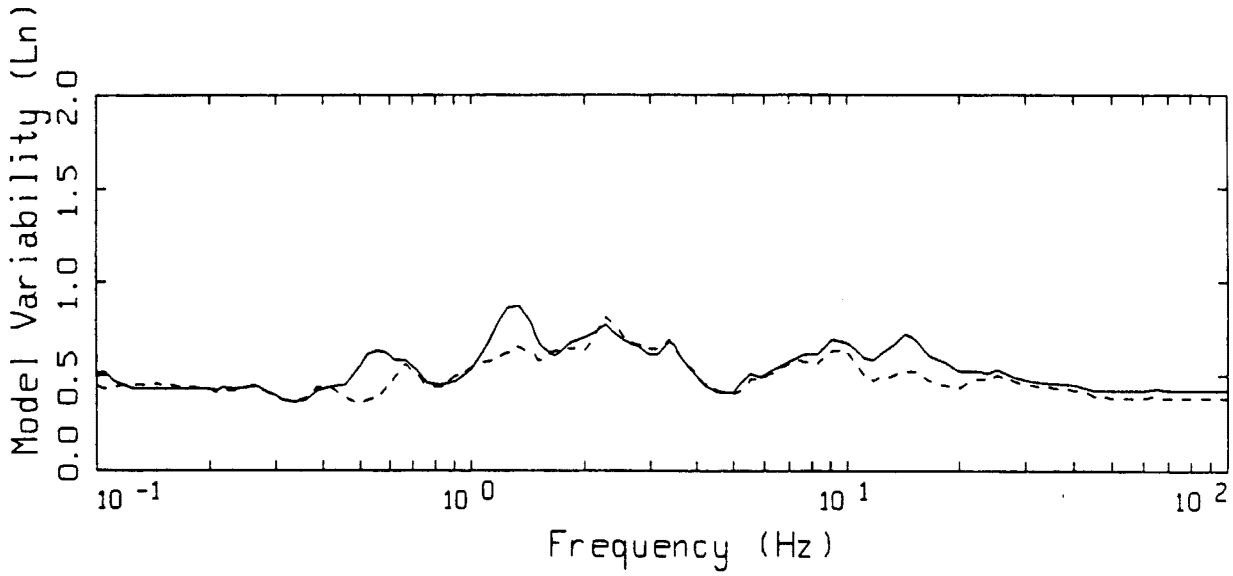

LEGEND
MEAN=0.0
BIAS CORRECTED

COYOTE LAKE FINITE-SOURCE
NONLINEAR, ALL 10 SITES

Figure 5,62

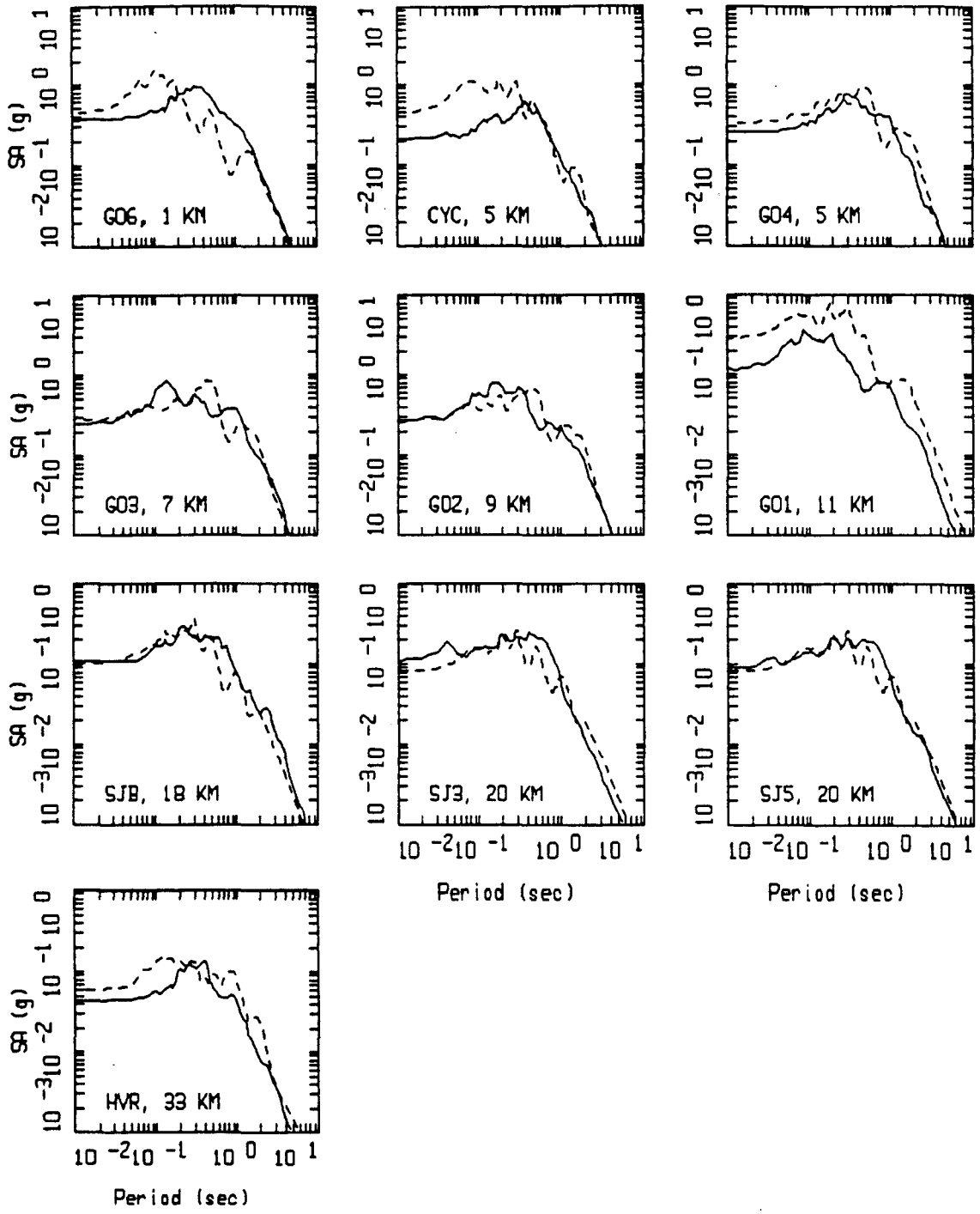

COYOTE LAKE, FINITE SOURCE MODELING, PAGE 1 OF 1.
NONLINEAR.

Figure 5.63

LEGEND

——— DATA

----- MODEL

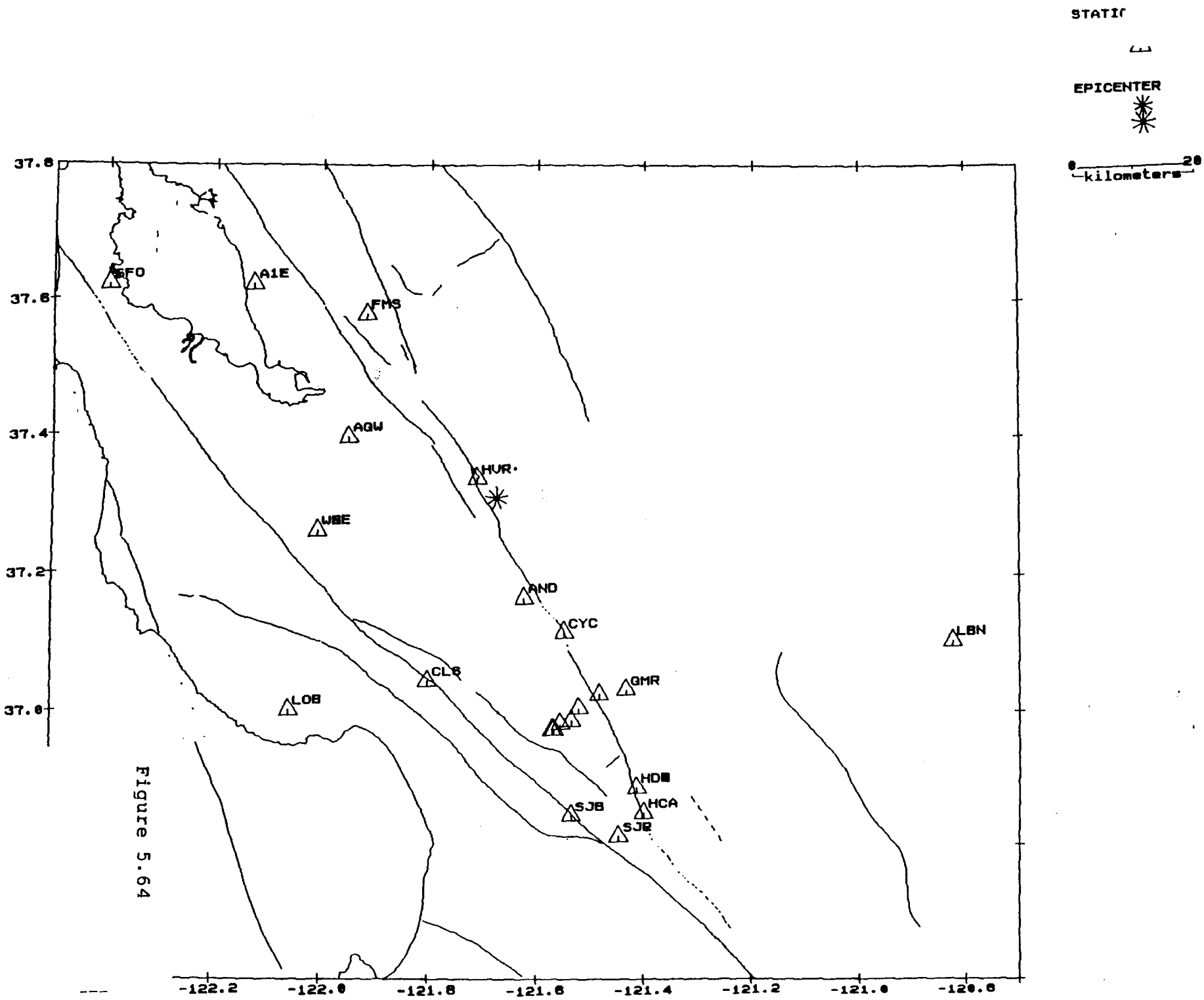
STATIC
EPICENTER
0
20
kilometers
37.8
37.6
37.4
37.2
37.0
SFO
A1E
FMS
AGW
HVR
WBE
AND
CYC
LBN
CLE
GMR
LOB
HDB
HCA
SJB
SJB
-122.2
-122.0
-121.8
-121.6
-121.4
-121.2
-121.0
-120.8
EQ3D-V4.00 FILE: SITES.MP2 EPICENT.MP2
SCA:000000 MFAC:1.0 XFAC:1.0 Nm=30 Nx=0

Figure 5.64

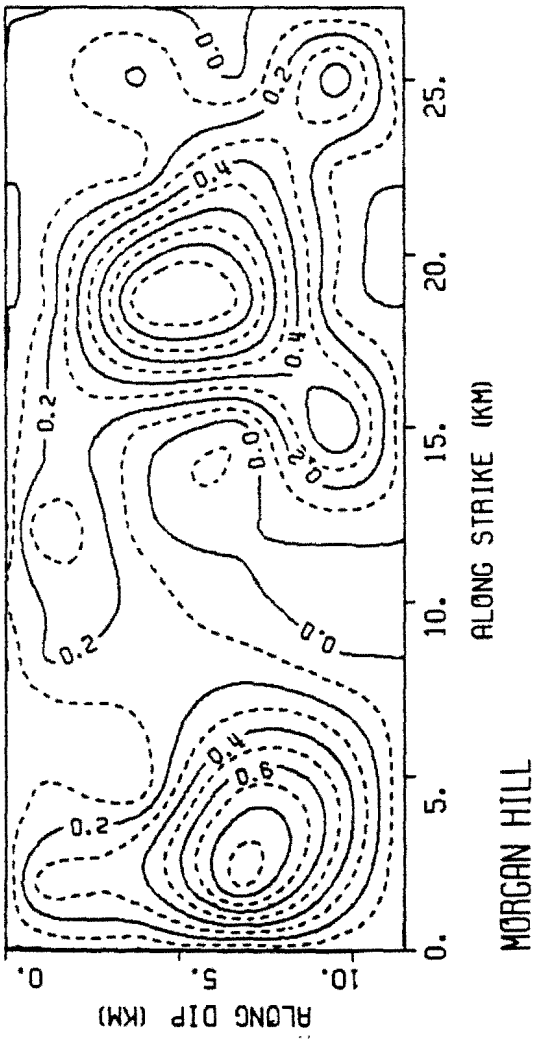
MORGAN HILL
ALONG STRIKE (KM)
ALONG DIP (KM)
0.
5.
10.
15.
20.
25.
0.0
0.2
0.4
0.6

Figure 5.65

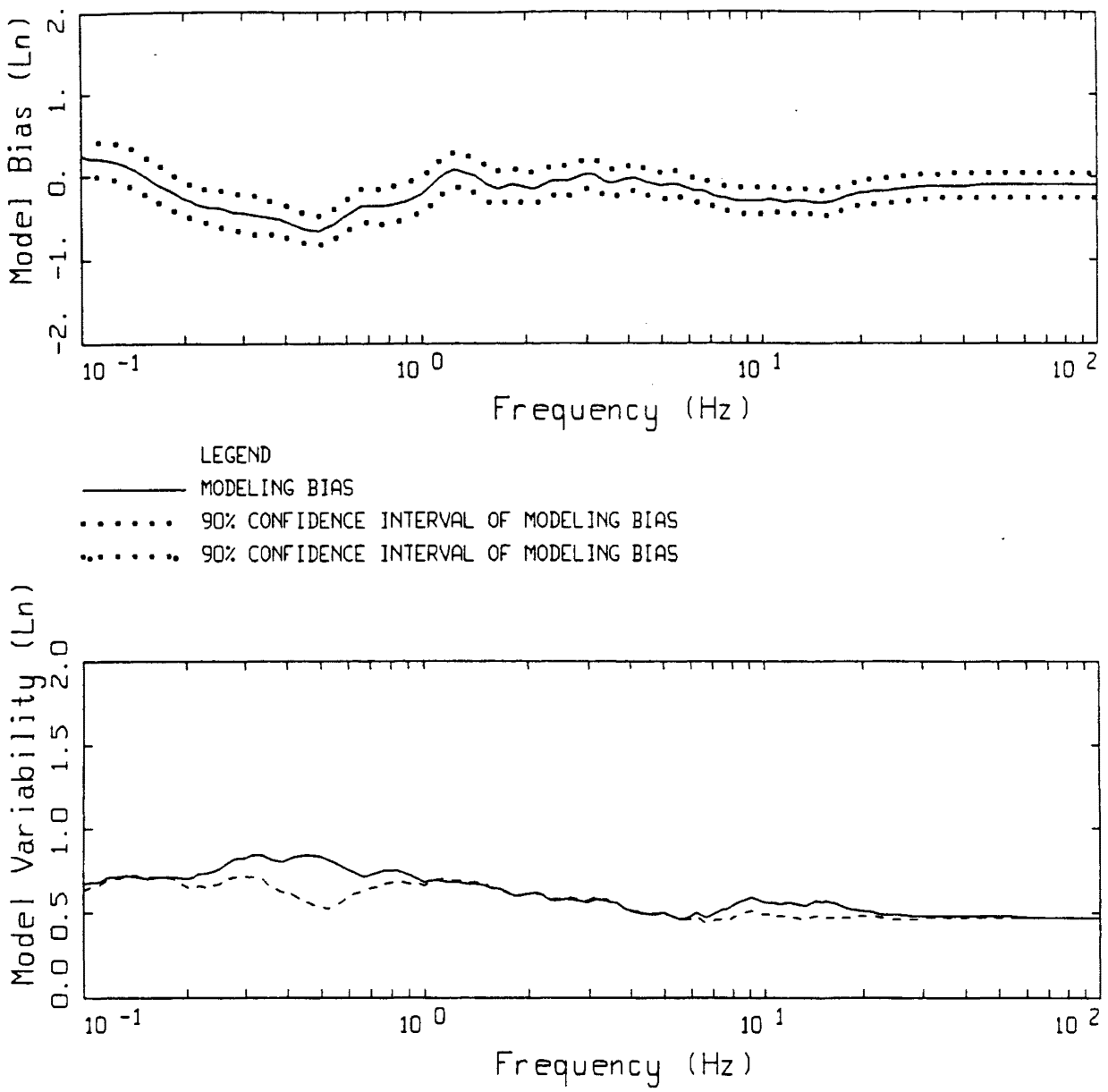
Model Bias (Ln)
2.
1.
0.
-1.
-2.
10 -1
10 0
10 1
10 2
Frequency (Hz)
LEGEND
MODELING BIAS
90% CONFIDENCE INTERVAL OF MODELING BIAS
90% CONFIDENCE INTERVAL OF MODELING BIAS
Model Variability (Ln)
0.0 0.5 1.0 1.5 2.0
10 -1
10 0
10 1
10 2
Frequency (Hz)
LEGEND
MEAN=0.0
BIAS CORRECTED
MORGAN HILL POINT-SOURCE
NONLINEAR, ALL 29 SITES

Figure 5.66

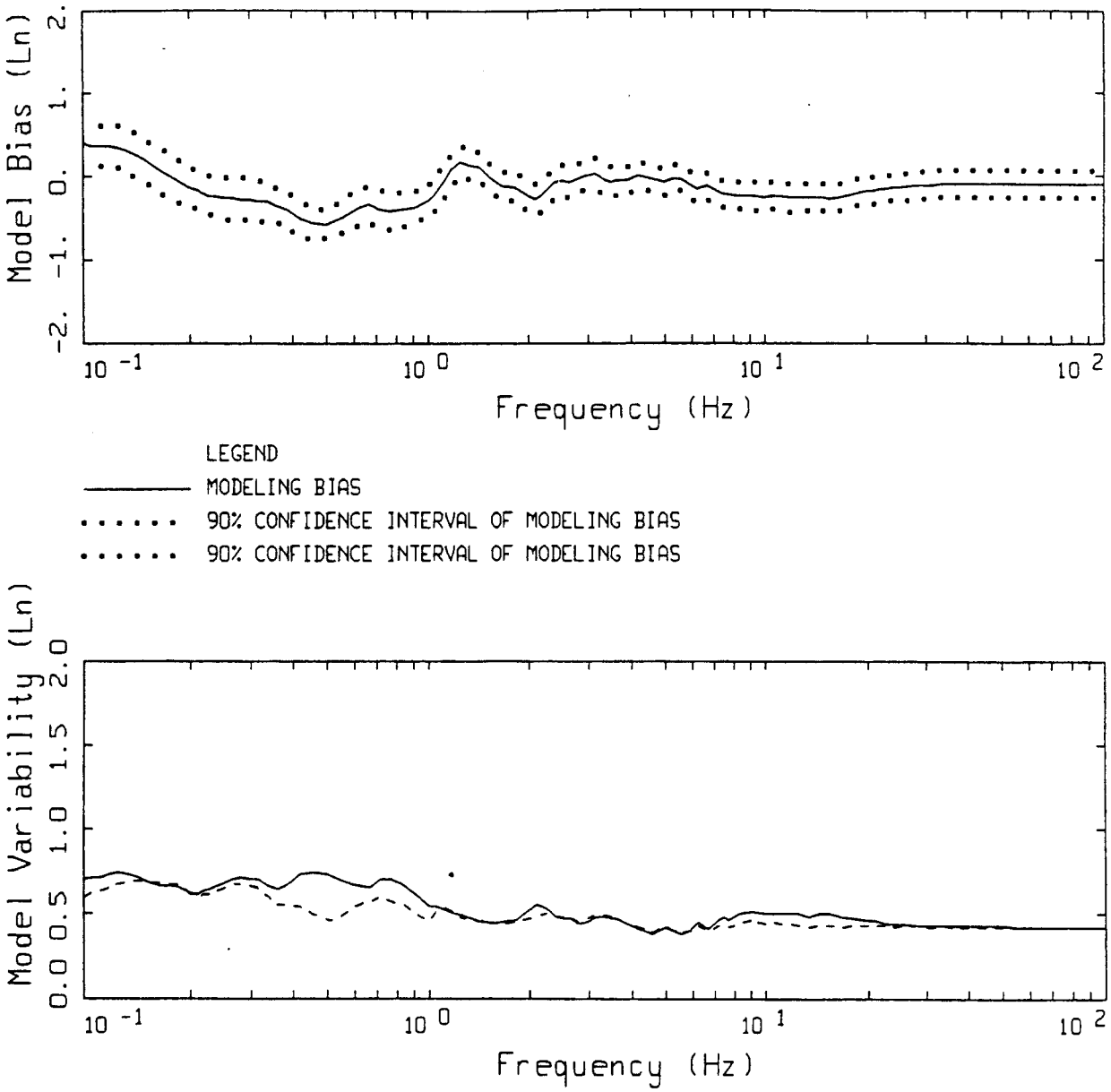
Model Bias (Ln)
2.
1.
0.
-1.
-2.
10 -1
10 0
10 1
10 2
Frequency (Hz)
LEGEND
MODELING BIAS
90% CONFIDENCE INTERVAL OF MODELING BIAS
90% CONFIDENCE INTERVAL OF MODELING BIAS
Model Variability (Ln)
0.0 0.5 1.0 1.5 2.0
10 -1
10 0
10 1
10 2
Frequency (Hz)
LEGEND
MEAN=0.0
BIAS CORRECTED
MORGAN HILL POINT-SOURCE
NONLINEAR, 21 SOIL SITES

Figure 5.67

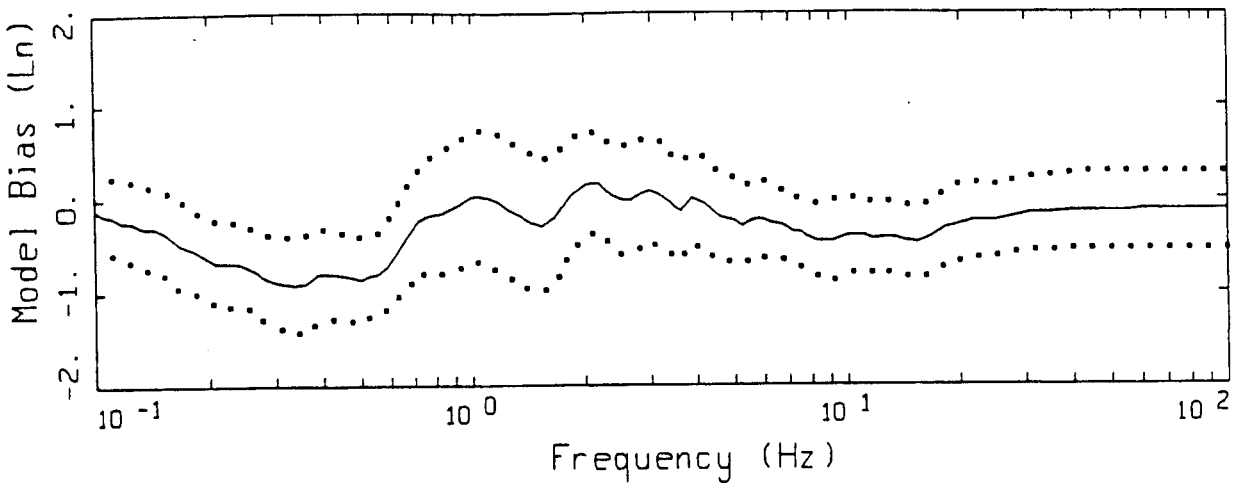

LEGEND
MODELING BIAS
90% CONFIDENCE INTERVAL OF MODELING BIAS
90% CONFIDENCE INTERVAL OF MODELING BIAS

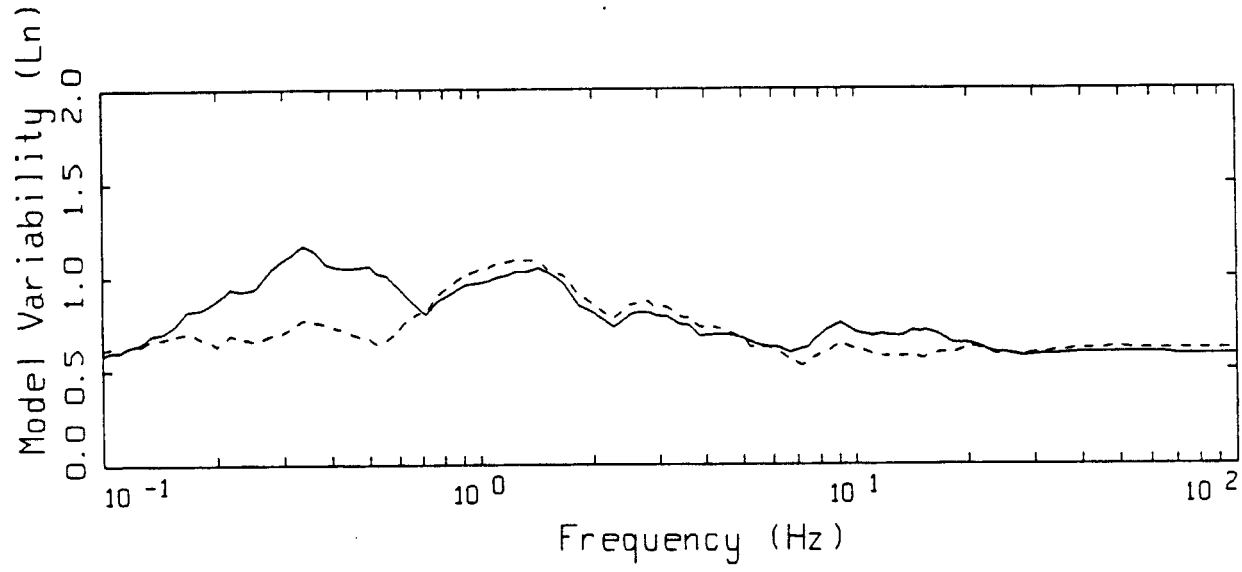

LEGEND
MEAN=0.0
BIAS CORRECTED

MORGAN HILL POINT-SOURCE
NONLINEAR, 8 ROCK SITES

Figure 5.68

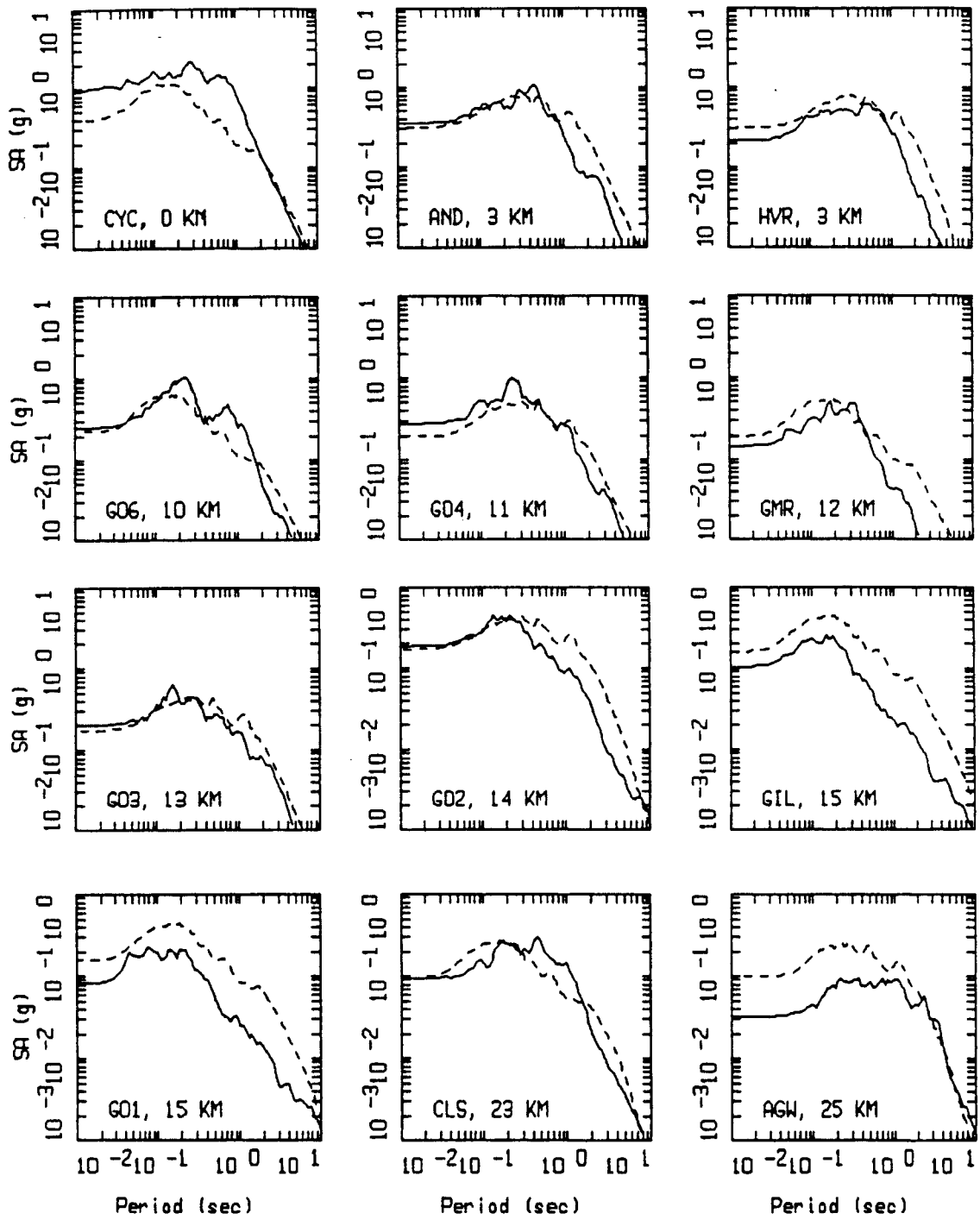

MORGAN HILL, POINT SOURCE MODELING, PAGE 1 OF 3.
NONLINEAR.

Figure Set 5.69

LEGEND

——— DATA

----- MODEL

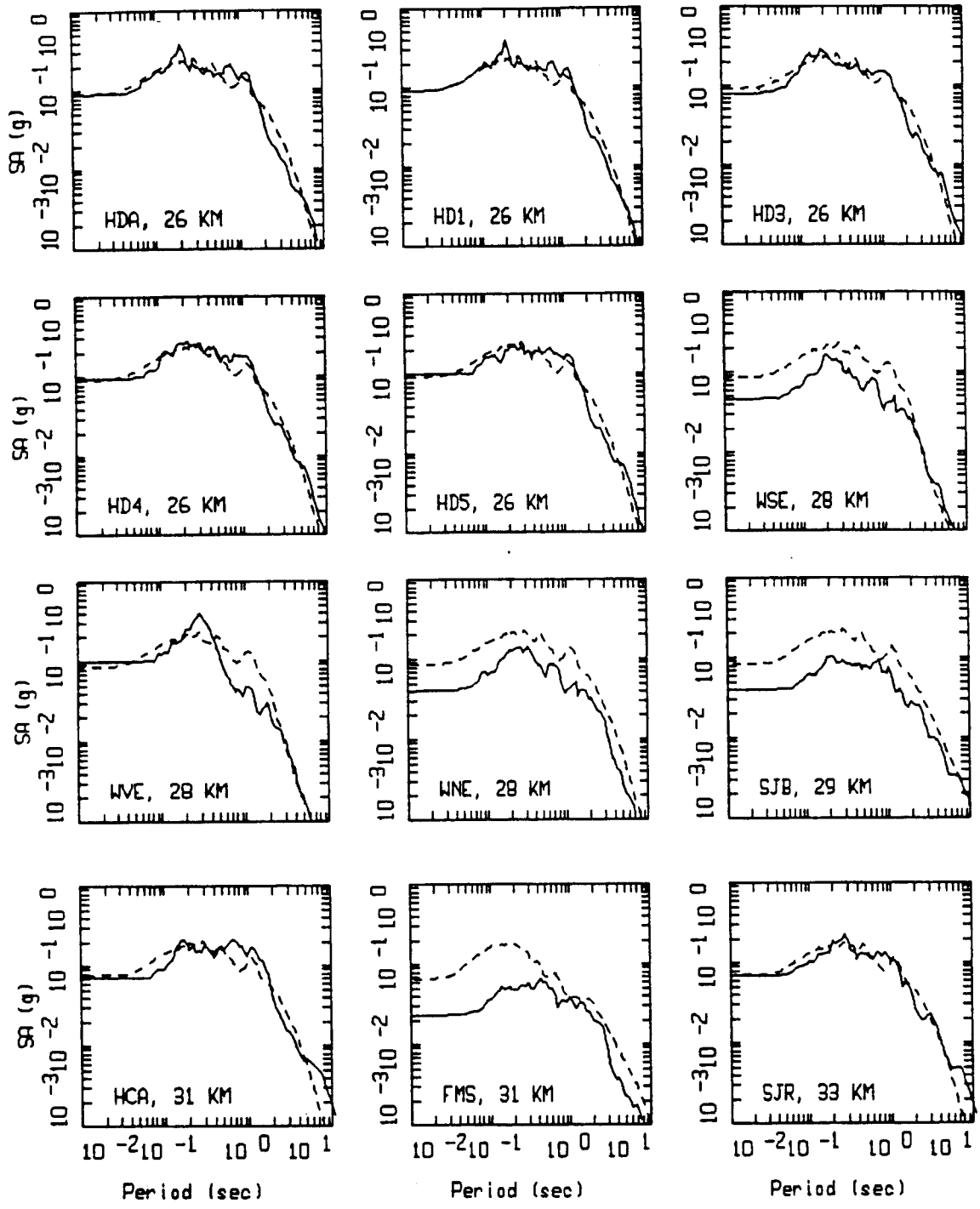

MORGAN HILL, POINT SOURCE MODELING, PAGE 2 OF 3.
NONLINEAR.

LEGEND
——— DATA
- - - - - MODEL

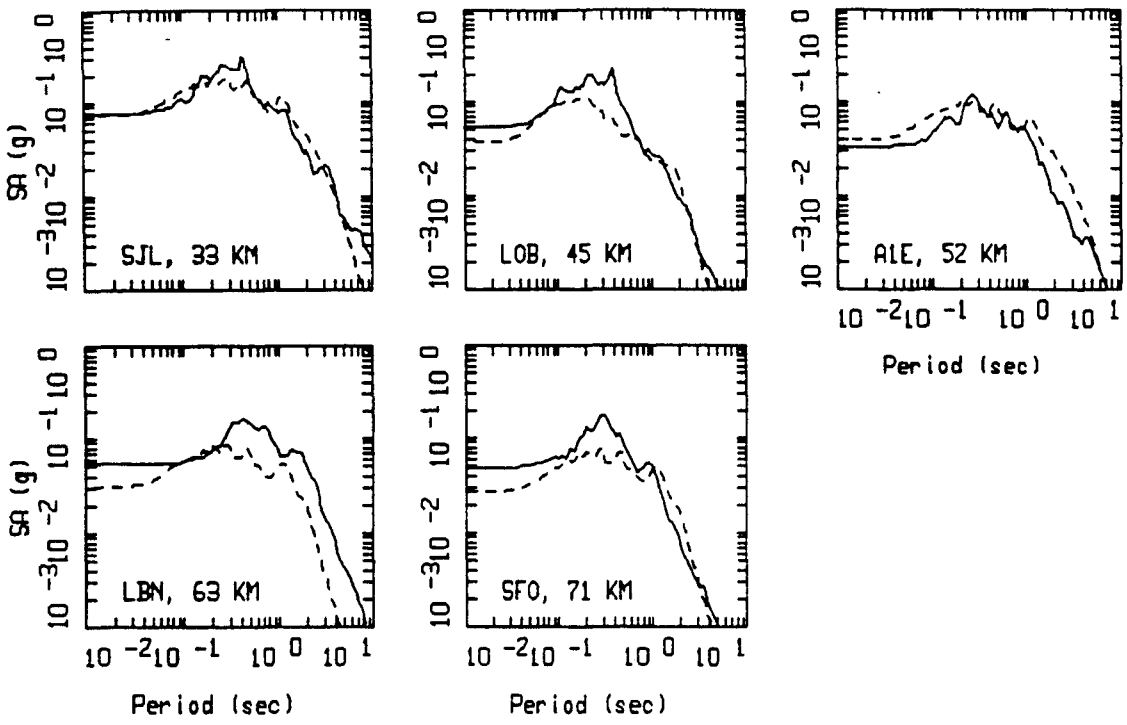

MORGAN HILL, POINT SOURCE MODELING, PAGE 3 OF 3.
NONLINEAR.

LEGEND
——— DATA
- - - - - MODEL

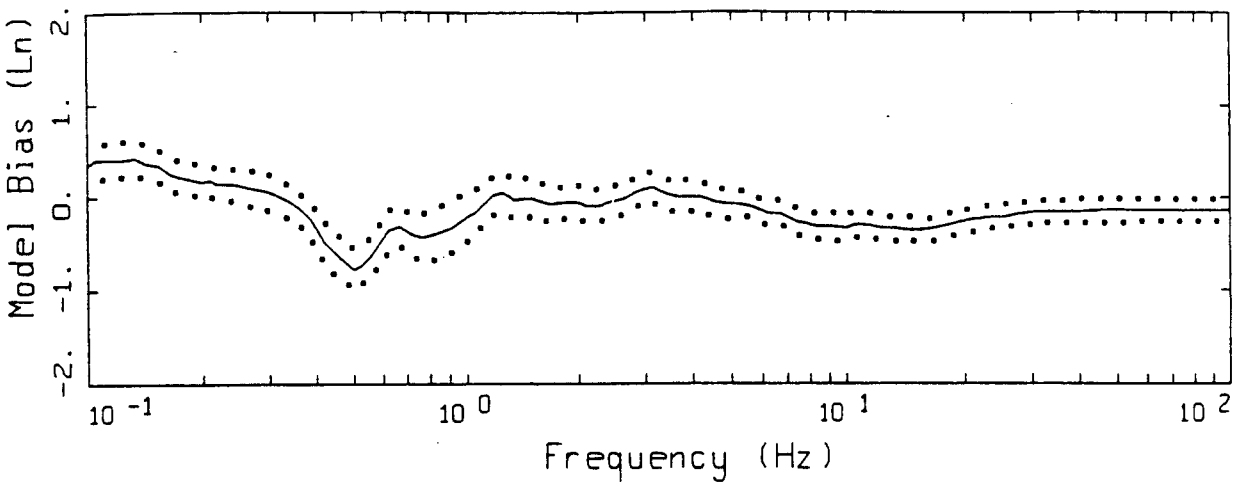

LEGEND
MODELING BIAS
90% CONFIDENCE INTERVAL OF MODELING BIAS
90% CONFIDENCE INTERVAL OF MODELING BIAS

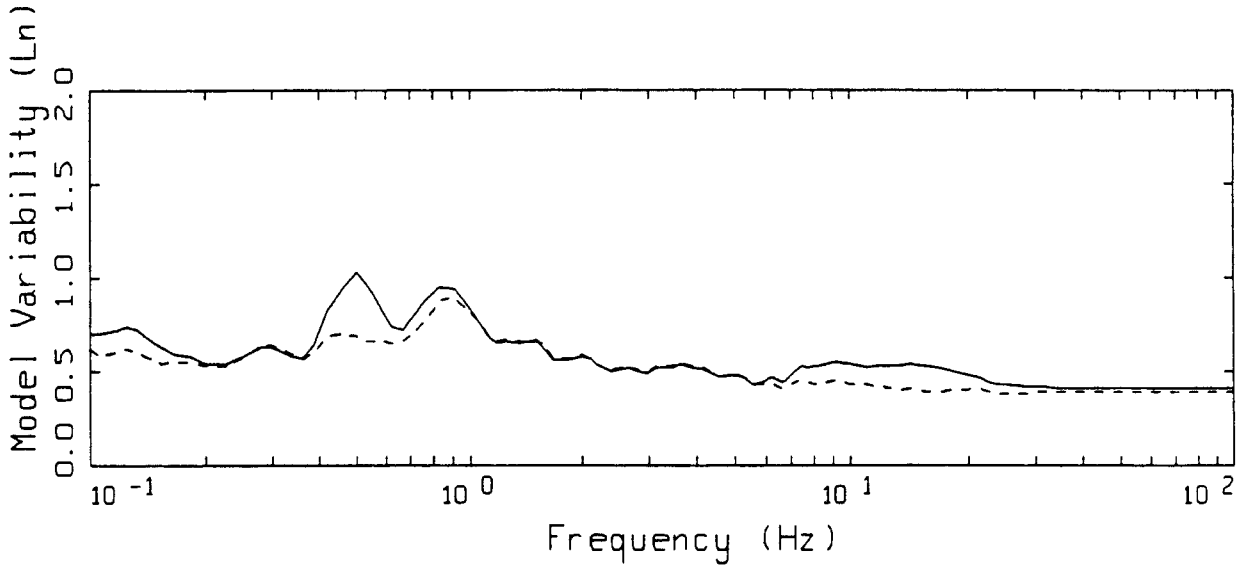

LEGEND
MEAN=0.0
BIAS CORRECTED

MORGAN HILL FINITE-SOURCE
NONLINEAR, ALL 29 SITES

Figure 5.70

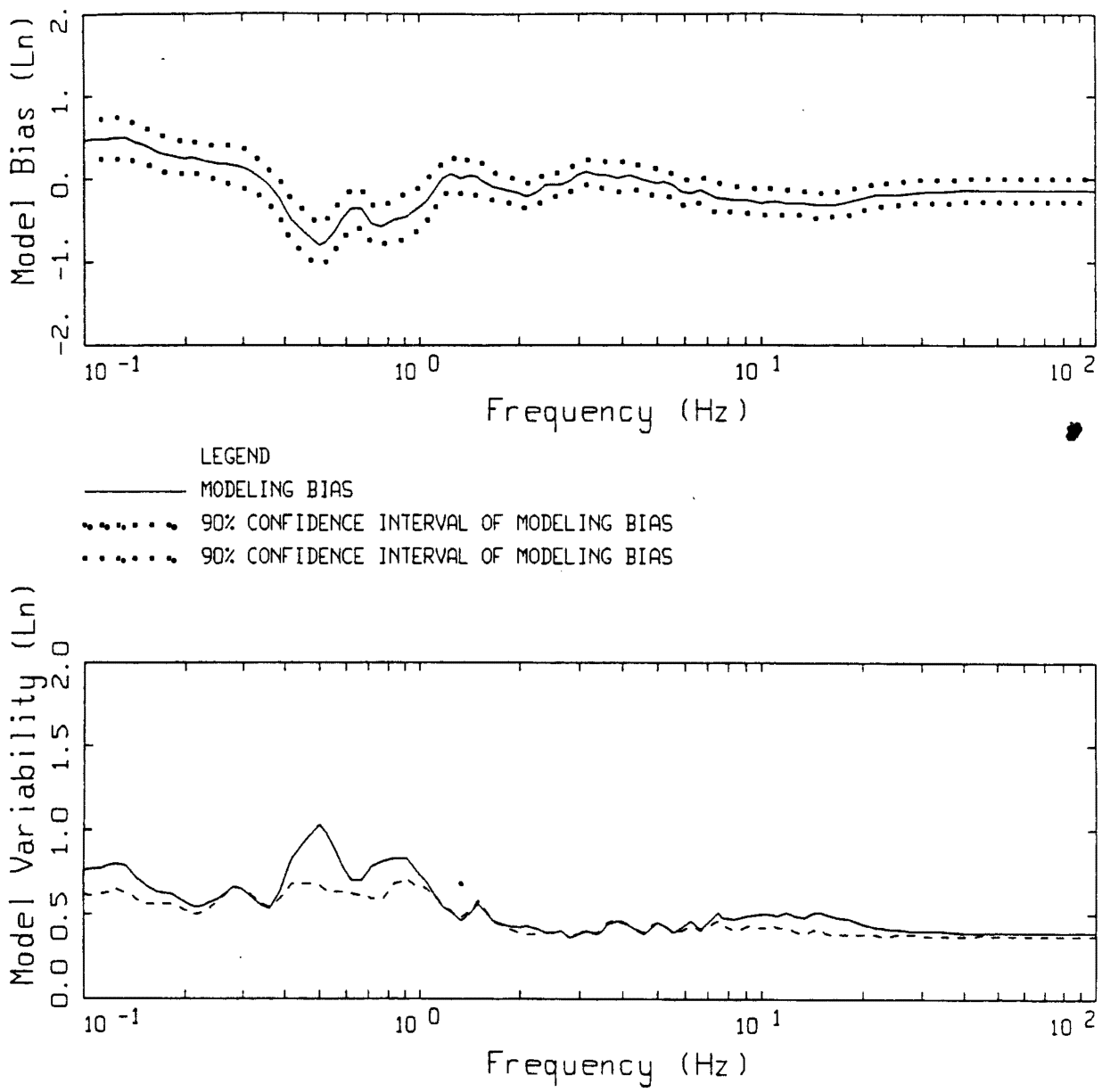

MORGAN HILL FINITE-SOURCE
NONLINEAR, 21 SOIL SITES

Figure 5.71

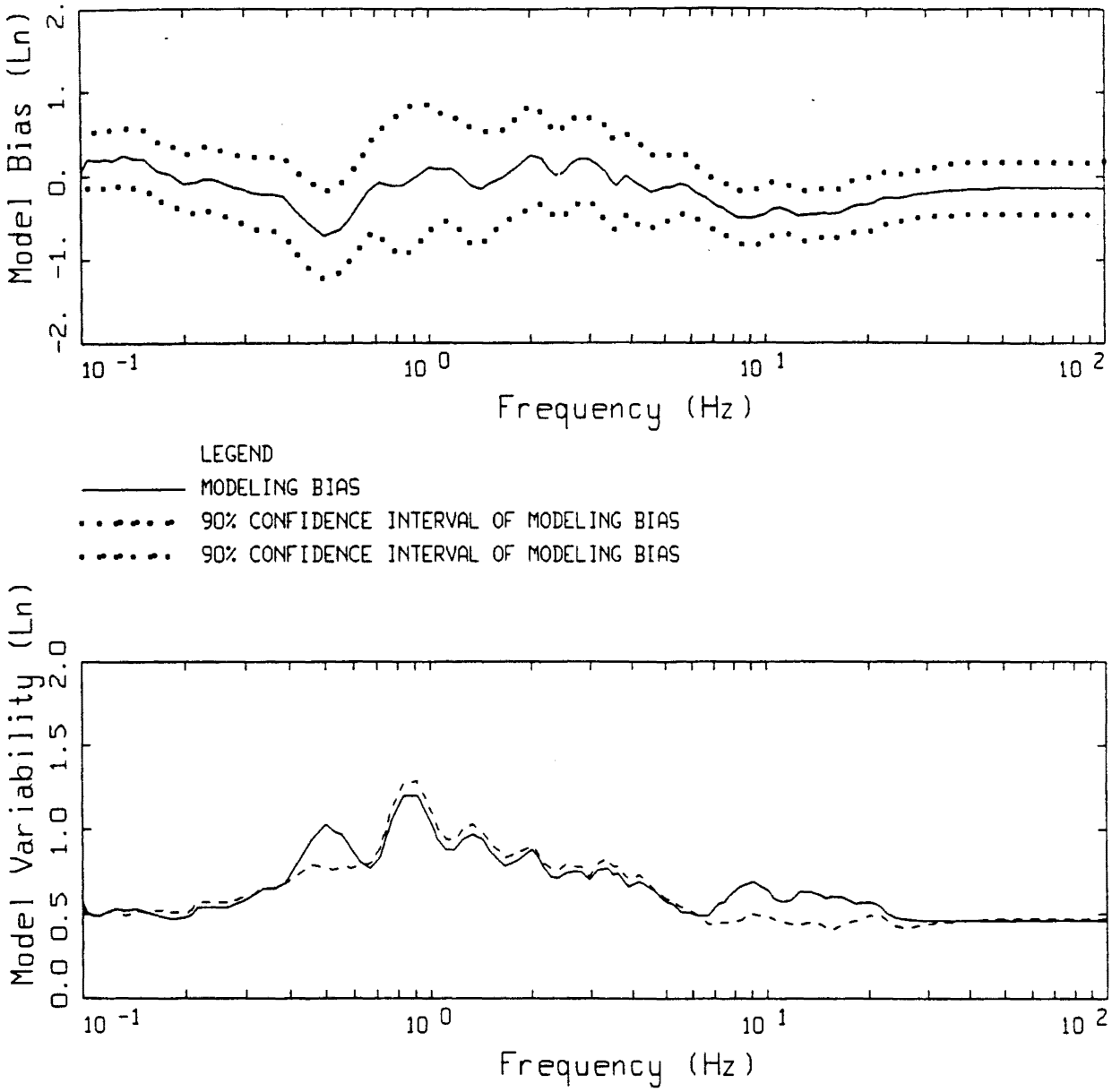
Model Bias (Ln)
2.
1.
0.
-1.
-2.
10 -1
10 0
10 1
10 2
Frequency (Hz)
LEGEND
MODELING BIAS
90% CONFIDENCE INTERVAL OF MODELING BIAS
90% CONFIDENCE INTERVAL OF MODELING BIAS
Model Variability (Ln)
0.0 0.5 1.0 1.5 2.0
10 -1
10 0
10 1
10 2
Frequency (Hz)
LEGEND
MEAN=0.0
BIAS CORRECTED
MORGAN HILL FINITE-SOURCE
NONLINEAR, 8 ROCK SITES

Figure 5.72

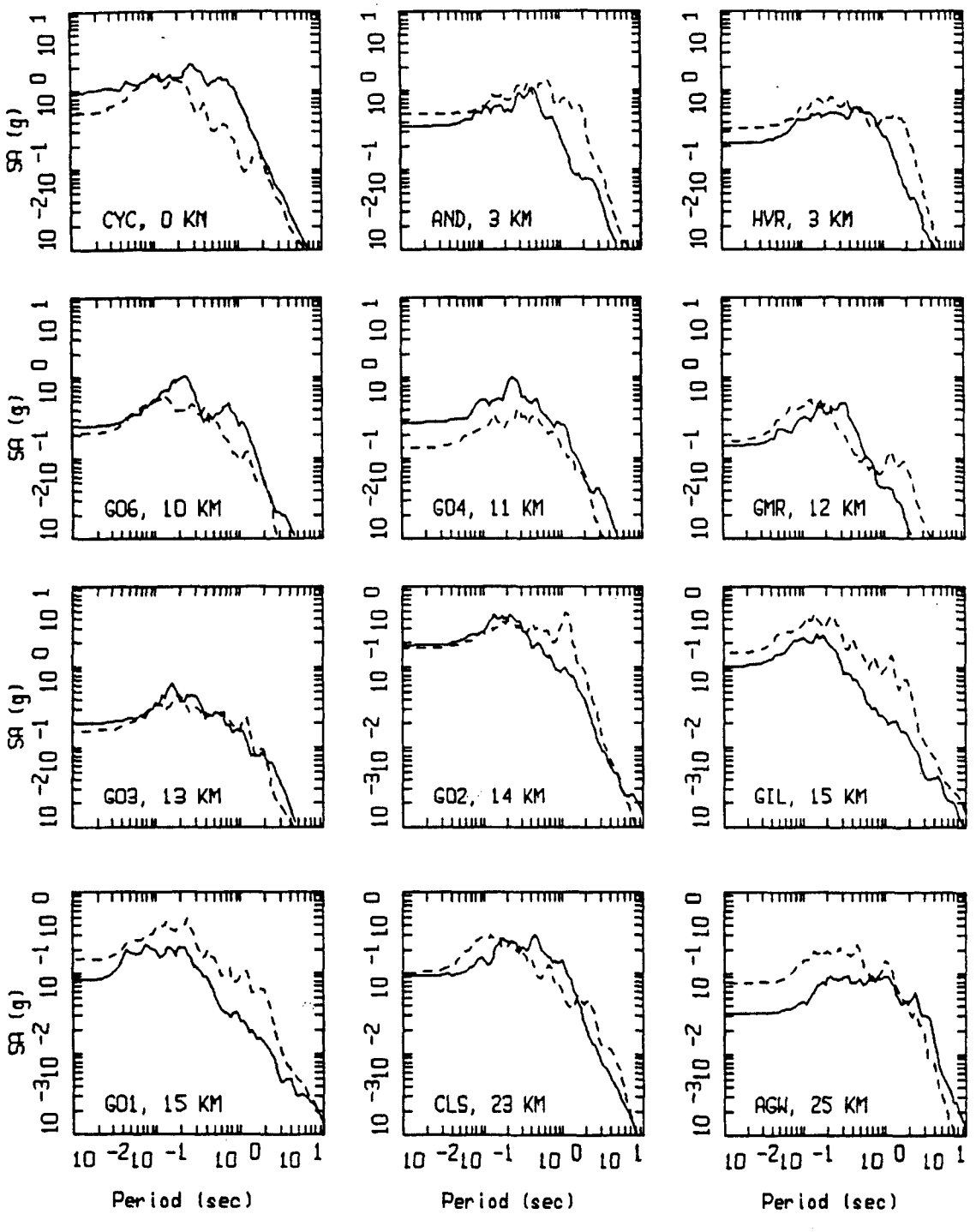

MORGAN HILL, FINITE SOURCE MODELING, PAGE 1 OF 3.
NONLINEAR.

LEGEND
——— DATA
----- MODEL

Figure Set 5.73

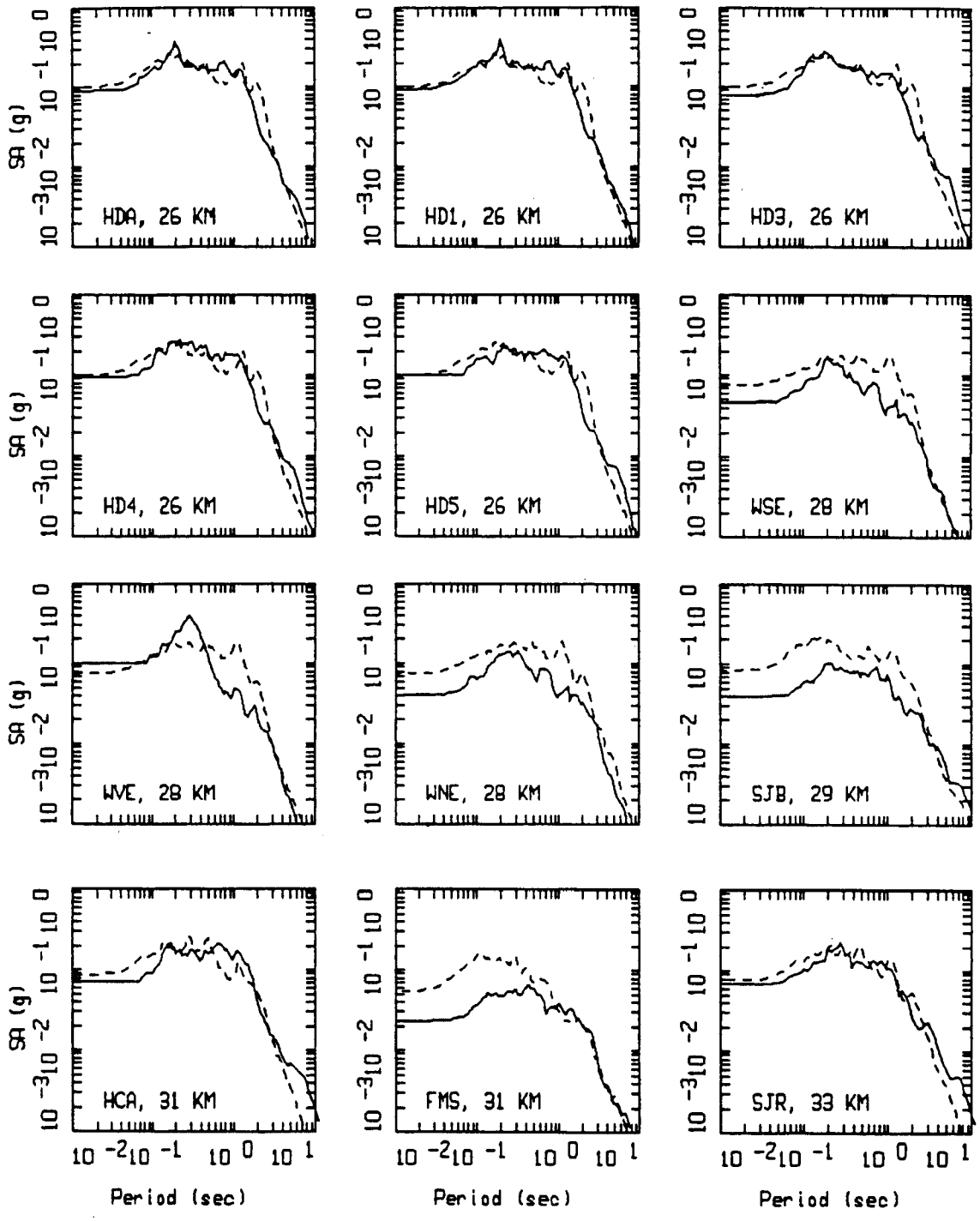

MORGAN HILL, FINITE SOURCE MODELING, PAGE 2 OF 3.
NONLINEAR.

LEGEND

——— DATA

- - - - - MODEL

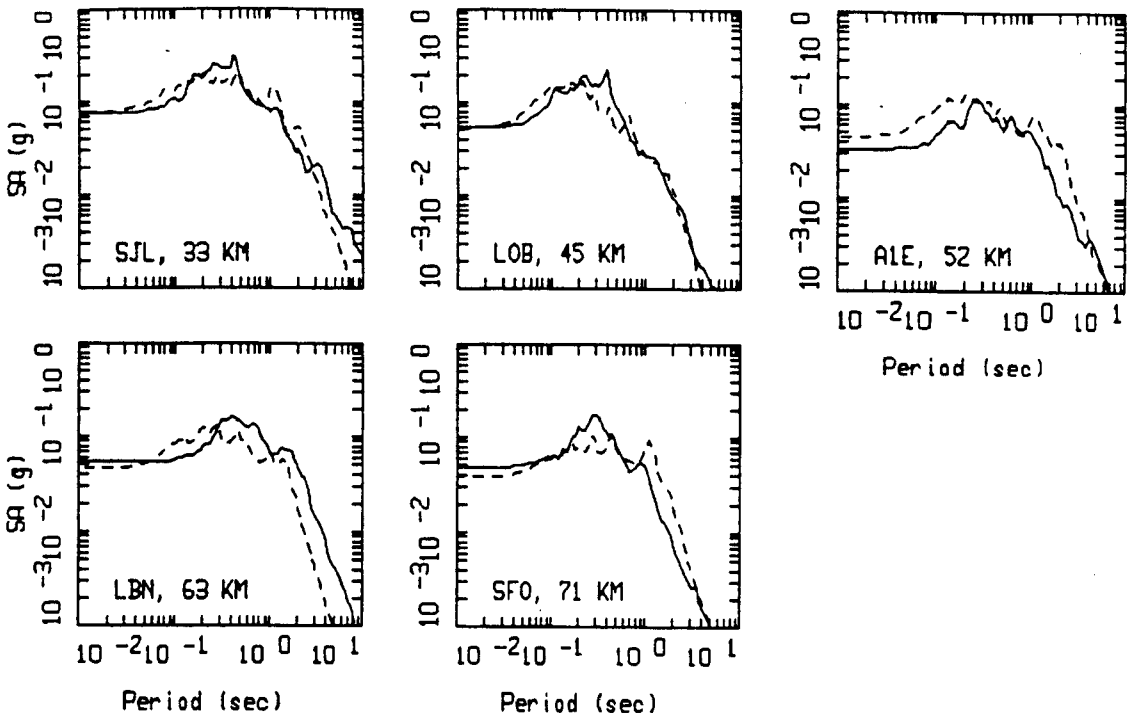

MORGAN HILL, FINITE SOURCE MODELING, PAGE 3 OF 3.
NONLINEAR.

LEGEND
——— DATA
----- MODEL

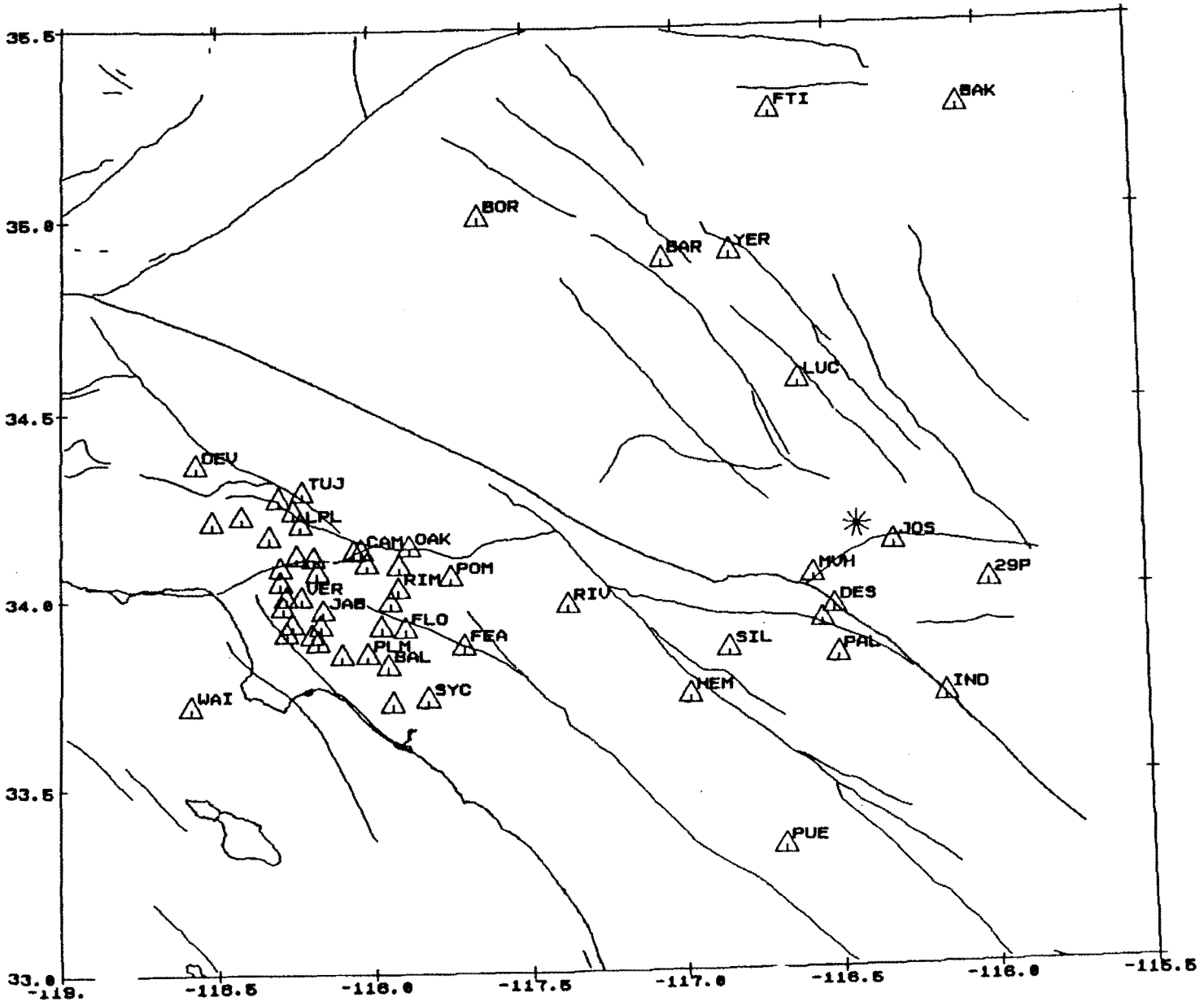

Figure 5.74

EQ3D-v4.00 FILE: SITES.HP2 EPICENT.HP2
. SCA:1000000 MFAC:1.0 XFAC:1.0 Nm=57 Nx=0

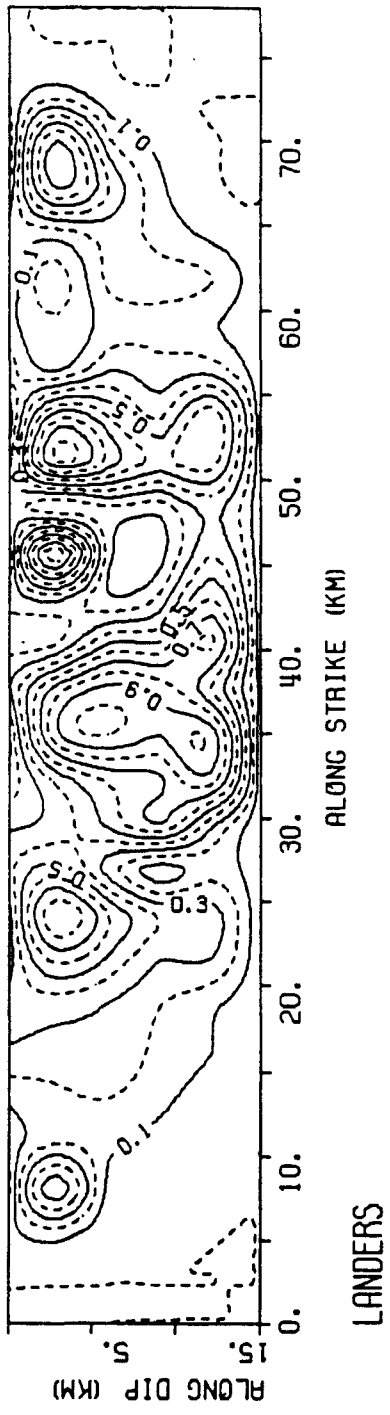
LANDERS
ALONG STRIKE (KM)
ALONG DIP (KM)
0.
10.
20.
30.
40.
50.
60.
70.
15.
5.
1.0
0.1
0.5
0.3
6.0

Figure 5.75

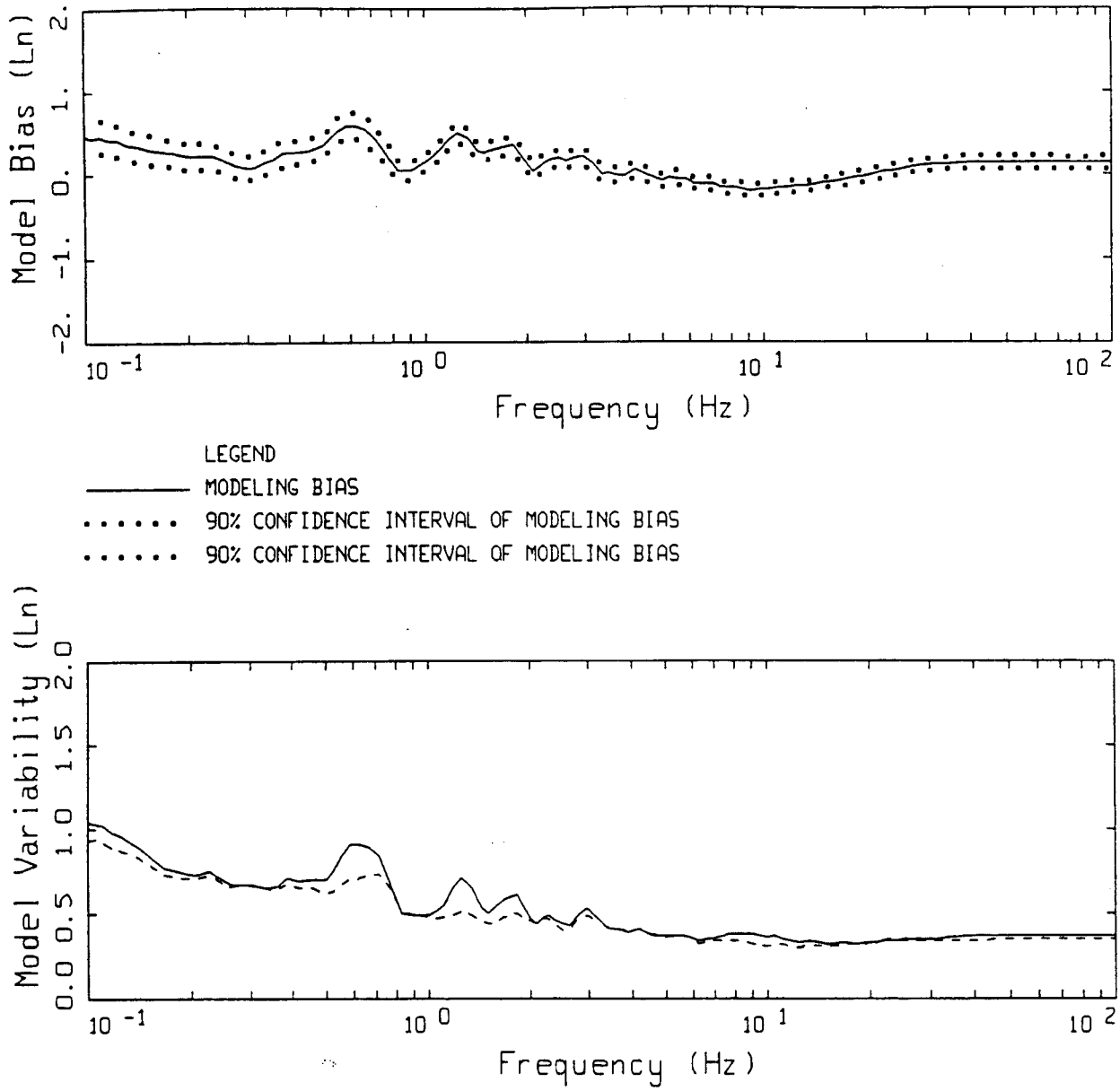
Model Bias (Ln)
2.
1.
0.
-1.
-2.
10 -1
10 0
10 1
10 2
Frequency (Hz)
LEGEND
MODELING BIAS
90% CONFIDENCE INTERVAL OF MODELING BIAS
90% CONFIDENCE INTERVAL OF MODELING BIAS
Model Variability (Ln)
0.0 0.5 1.0 1.5 2.0
10 -1
10 0
10 1
10 2
Frequency (Hz)
LEGEND
MEAN=0.0
BIAS CORRECTED
LANERS POINT-SOURCE
NONLINEAR, ALL 57 SITES

Figure 5.76

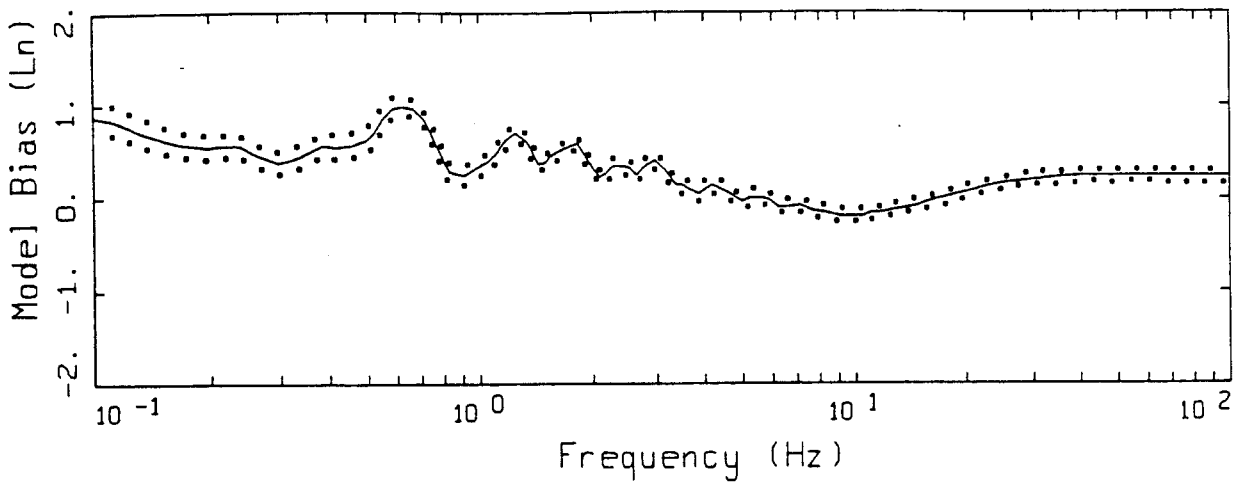

LEGEND
MODELING BIAS
90% CONFIDENCE INTERVAL OF MODELING BIAS
90% CONFIDENCE INTERVAL OF MODELING BIAS

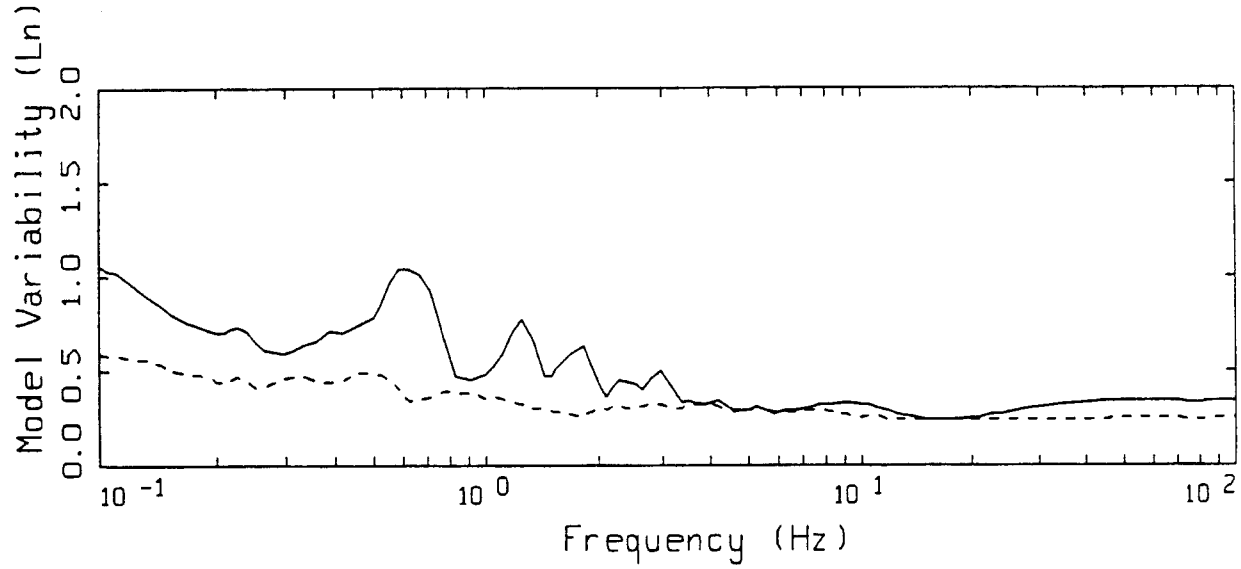

LEGEND
MEAN=0.0
BIAS CORRECTED

LANDERS POINT-SOURCE
NONLINEAR, ALL LA 39 SITES

Figure 5.77

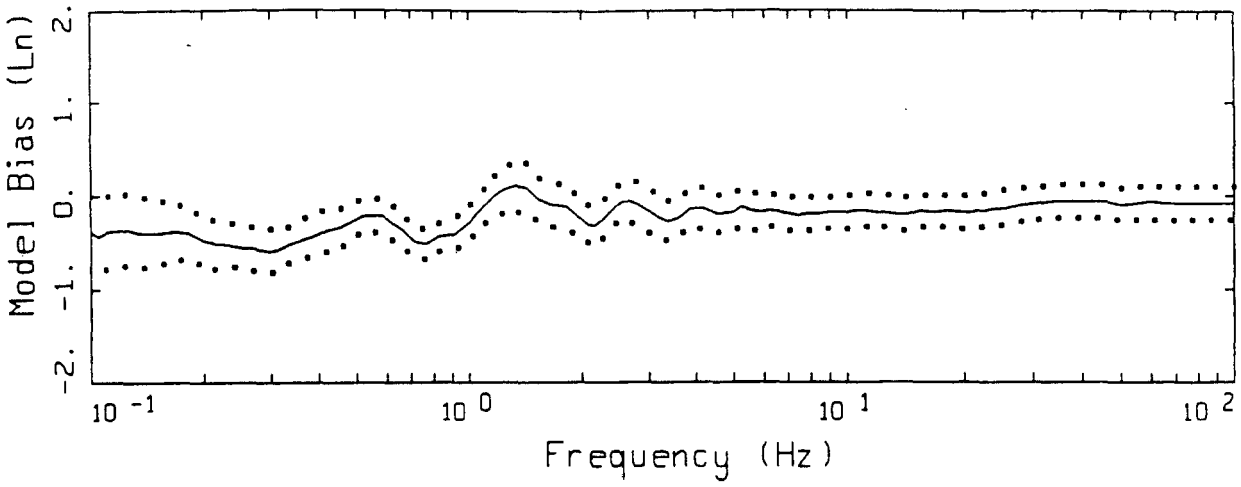

LEGEND
MODELING BIAS
90% CONFIDENCE INTERVAL OF MODELING BIAS
90% CONFIDENCE INTERVAL OF MODELING BIAS

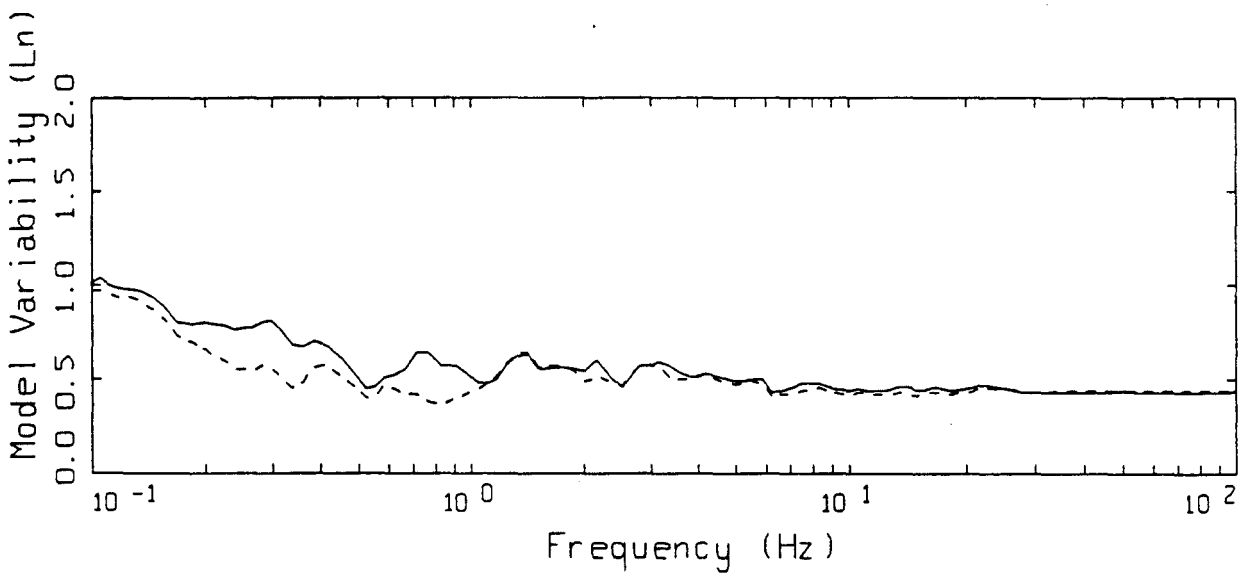

LEGEND
MEAN=0.0
BIAS CORRECTED

LANDERS POINT-SOURCE
NONLINEAR, ALL MOJAVE 18 SITES

Figure 5.78

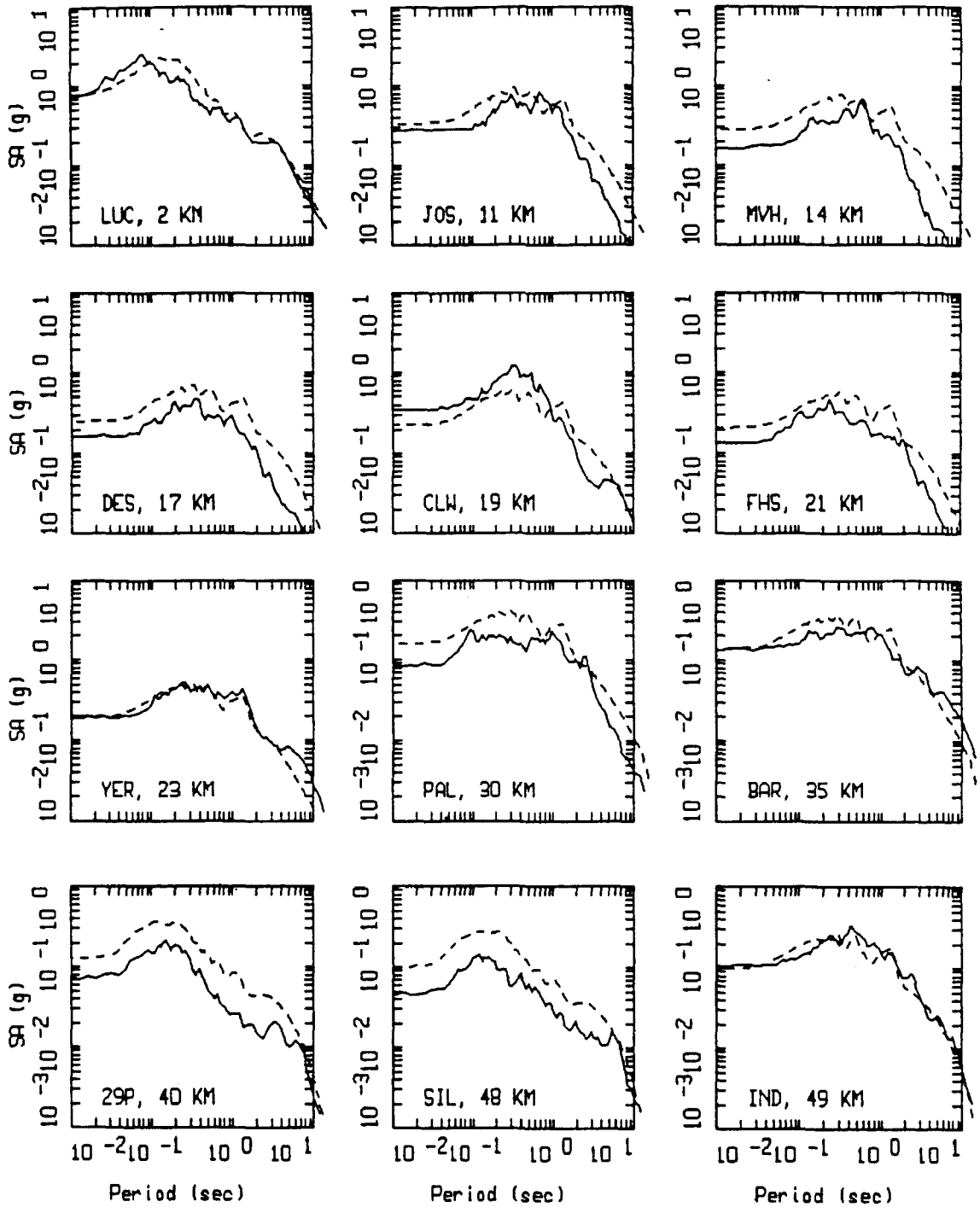

LANDERS, POINT SOURCE MODELING, PAGE 1 OF 5.
NONLINEAR.

LEGEND
——— DATA
----- MODEL

Figure Set 5.79

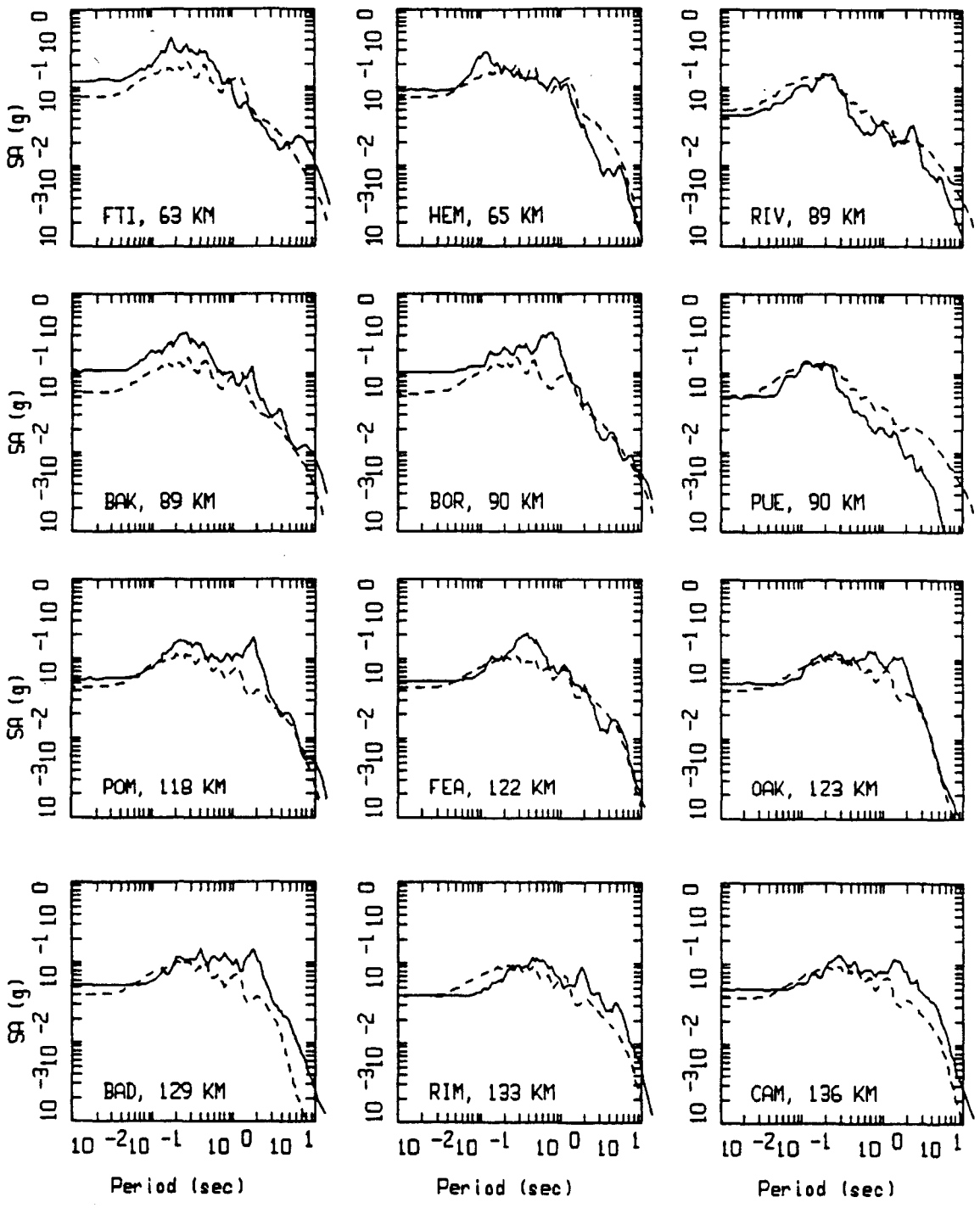

LANDERS, POINT SOURCE MODELING, PAGE 2 OF 5.
NONLINEAR.

LEGEND

——— DATA

- - - - - MODEL

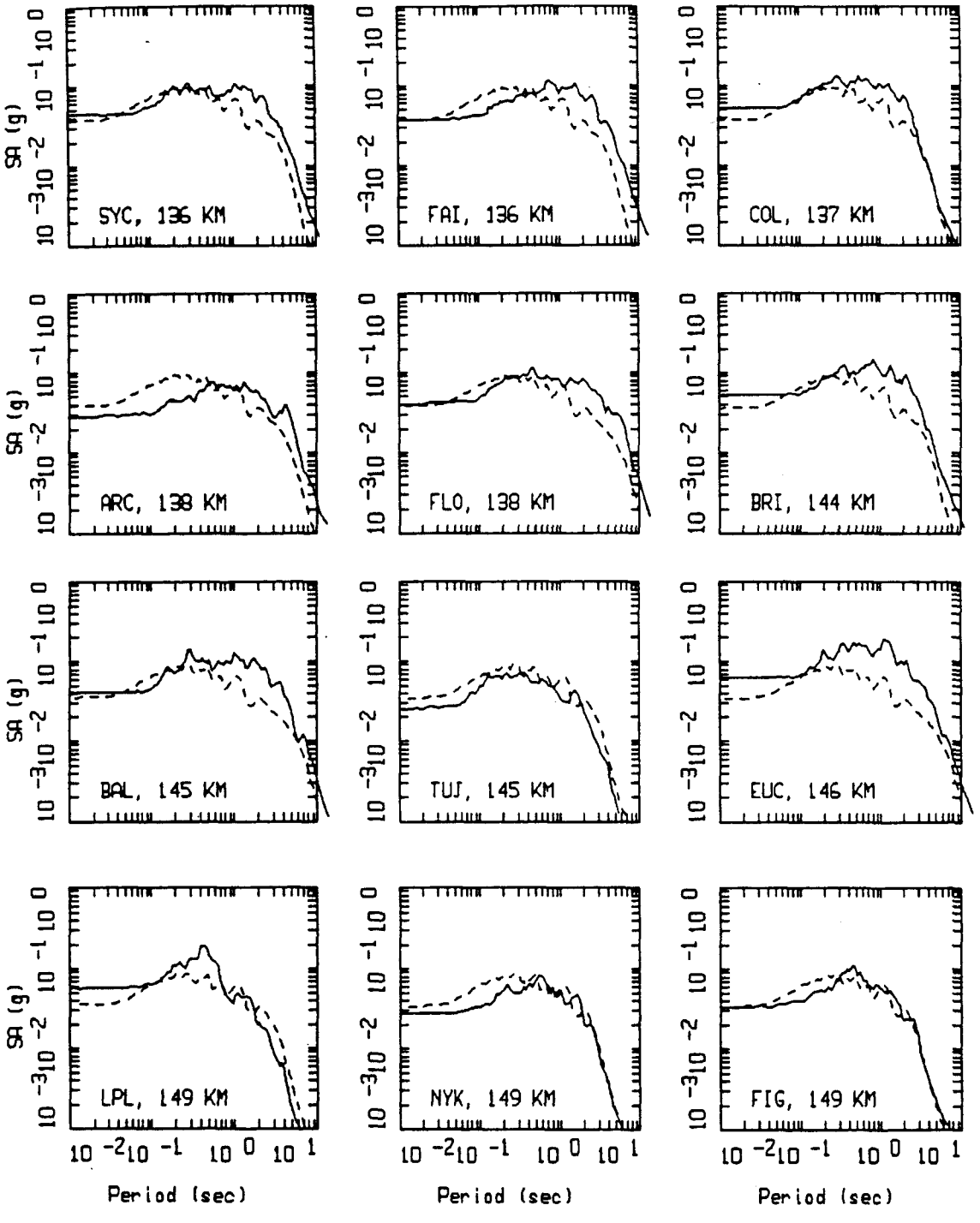

LANDERS, POINT SOURCE MODELING, PAGE 3 OF 5.
NONLINEAR.

LEGEND
——— DATA
- - - - - MODEL

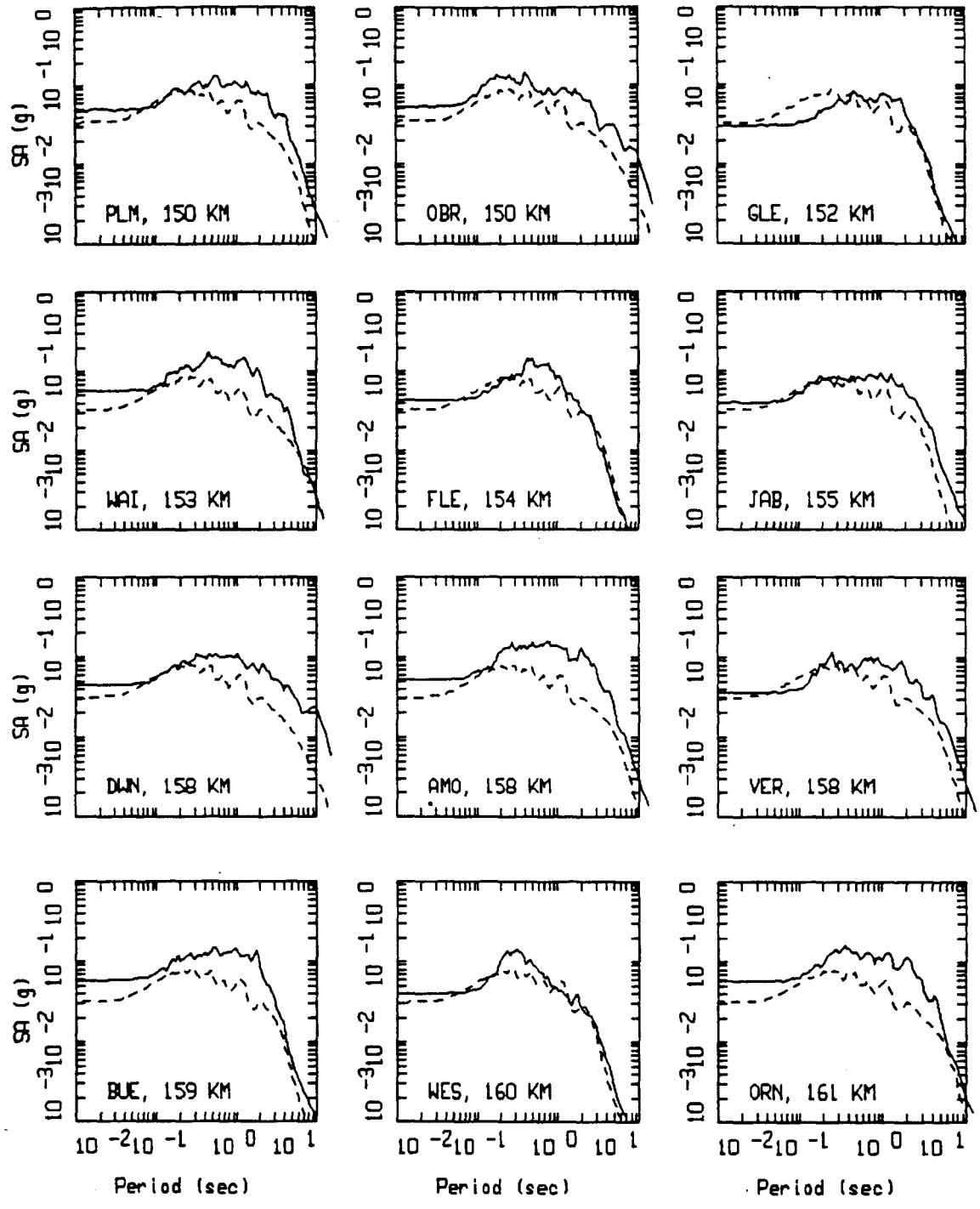

LANDERS, POINT SOURCE MODELING, PAGE 4 OF 5.
NONLINEAR.

LEGEND
——— DATA
- - - - - MODEL

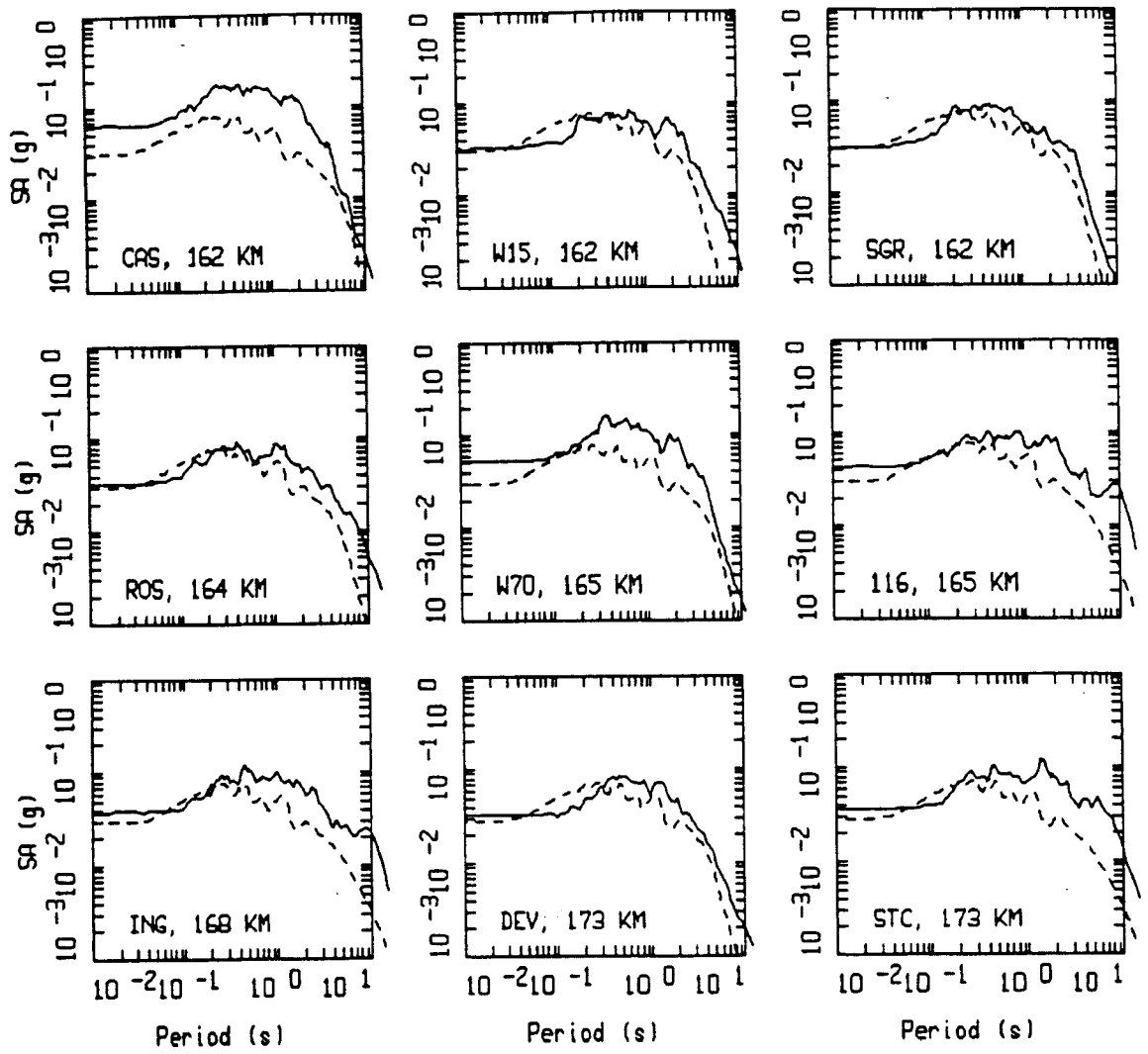

LANDERS, POINT SOURCE MODELING, PAGE 5 OF 5.

NONLINEAR.

LEGEND

——— DATA

----- MODEL

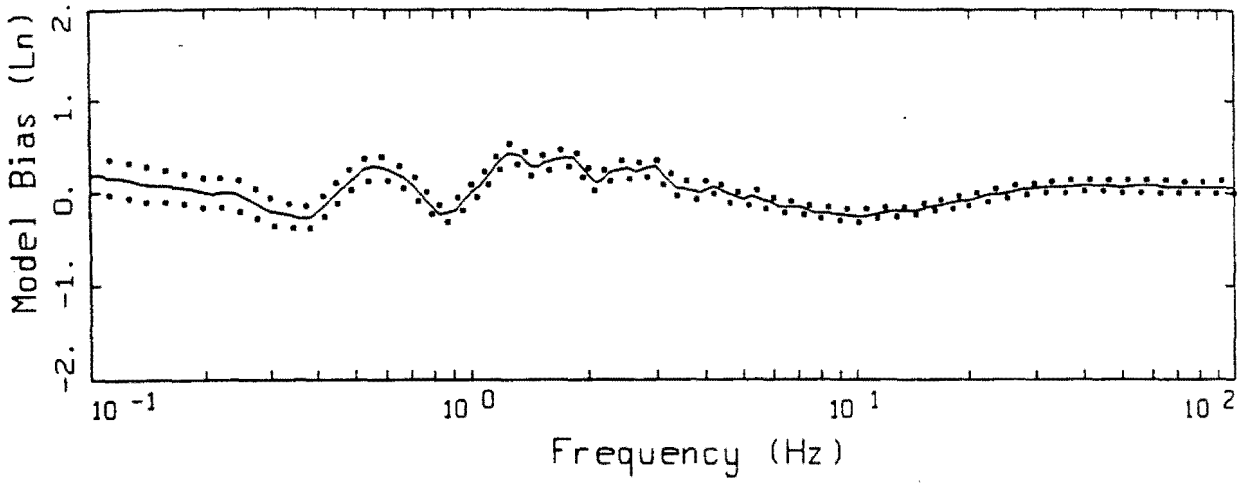

LEGEND
MODELING BIAS
90% CONFIDENCE INTERVAL OF MODELING BIAS
90% CONFIDENCE INTERVAL OF MODELING BIAS

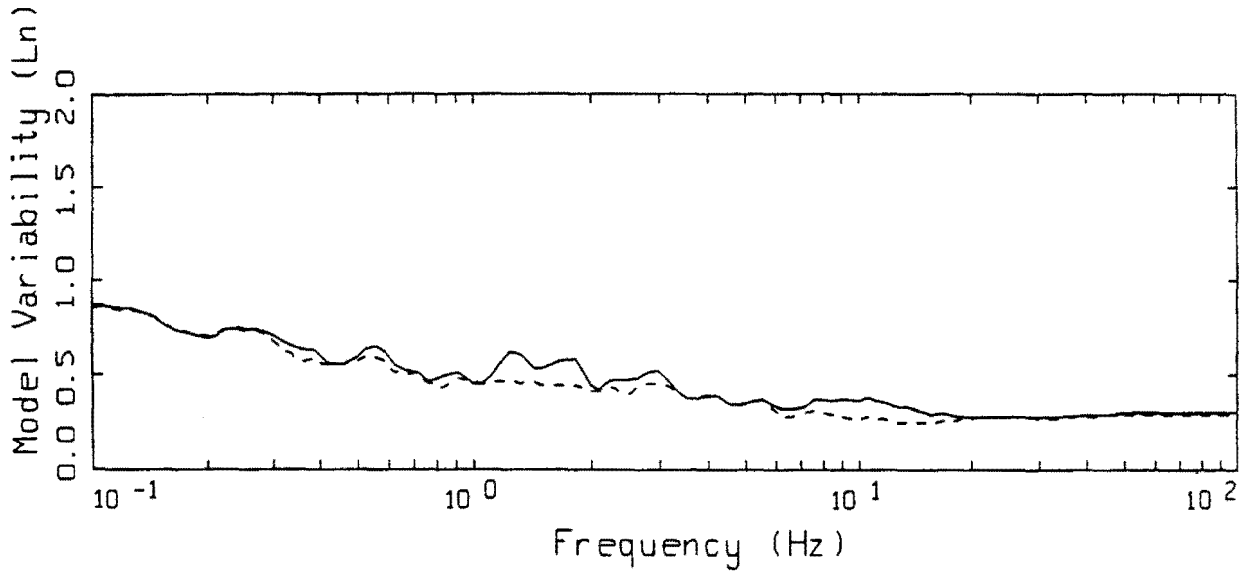

LEGEND
MEAN=0.0
BIAS CORRECTED

LANDERS FINITE-SOURCE
NONLINEAR, ALL 57 SITES

Figure 5.80

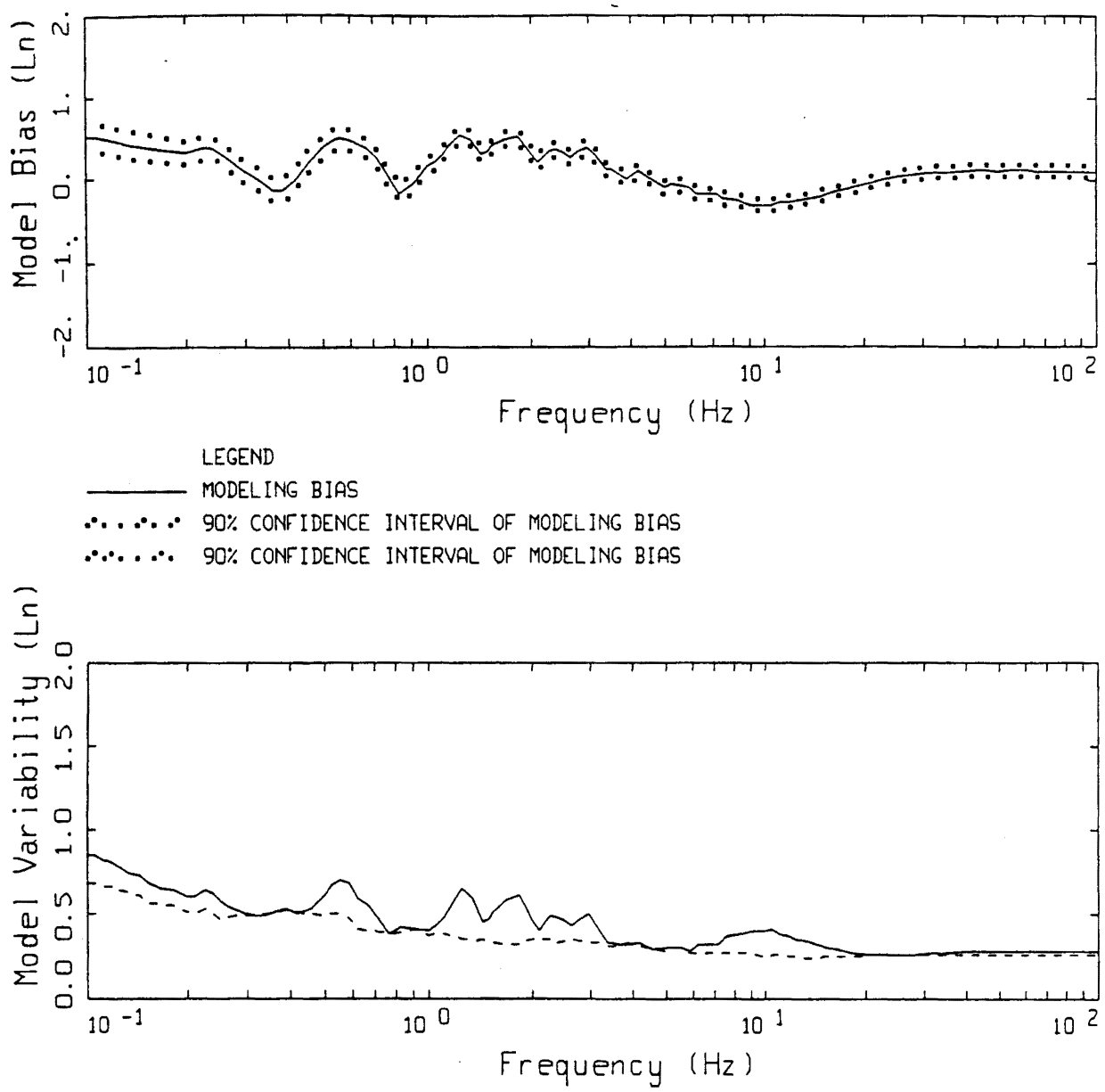
Model Bias (Ln)
2.
1.
0.
-1.
-2.
10 -1
10 0
10 1
10 2
Frequency (Hz)
LEGEND
MODELING BIAS
90% CONFIDENCE INTERVAL OF MODELING BIAS
90% CONFIDENCE INTERVAL OF MODELING BIAS
Model Variability (Ln)
0.0 0.5 1.0 1.5 2.0
10 -1
10 0
10 1
10 2
Frequency (Hz)
LEGEND
MEAN=0.0
BIAS CORRECTED
LANDERS FINITE-SOURCE
NONLINEAR, ALL LA 39 SITES

Figure 5.81

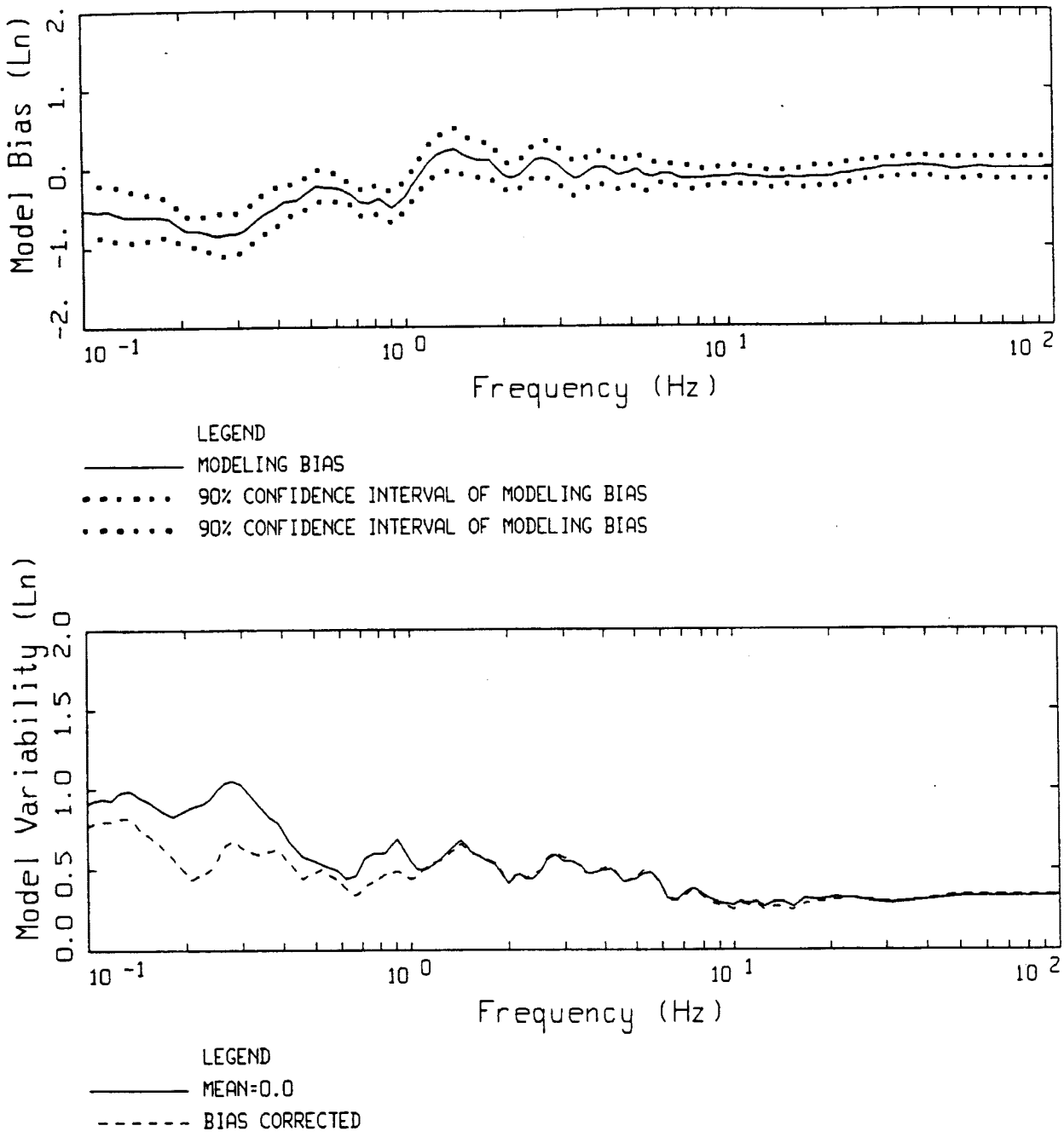

LANDERS FINITE-SOURCE
NONLINEAR, ALL MOJAVE 18 SITES

Figure 5.82

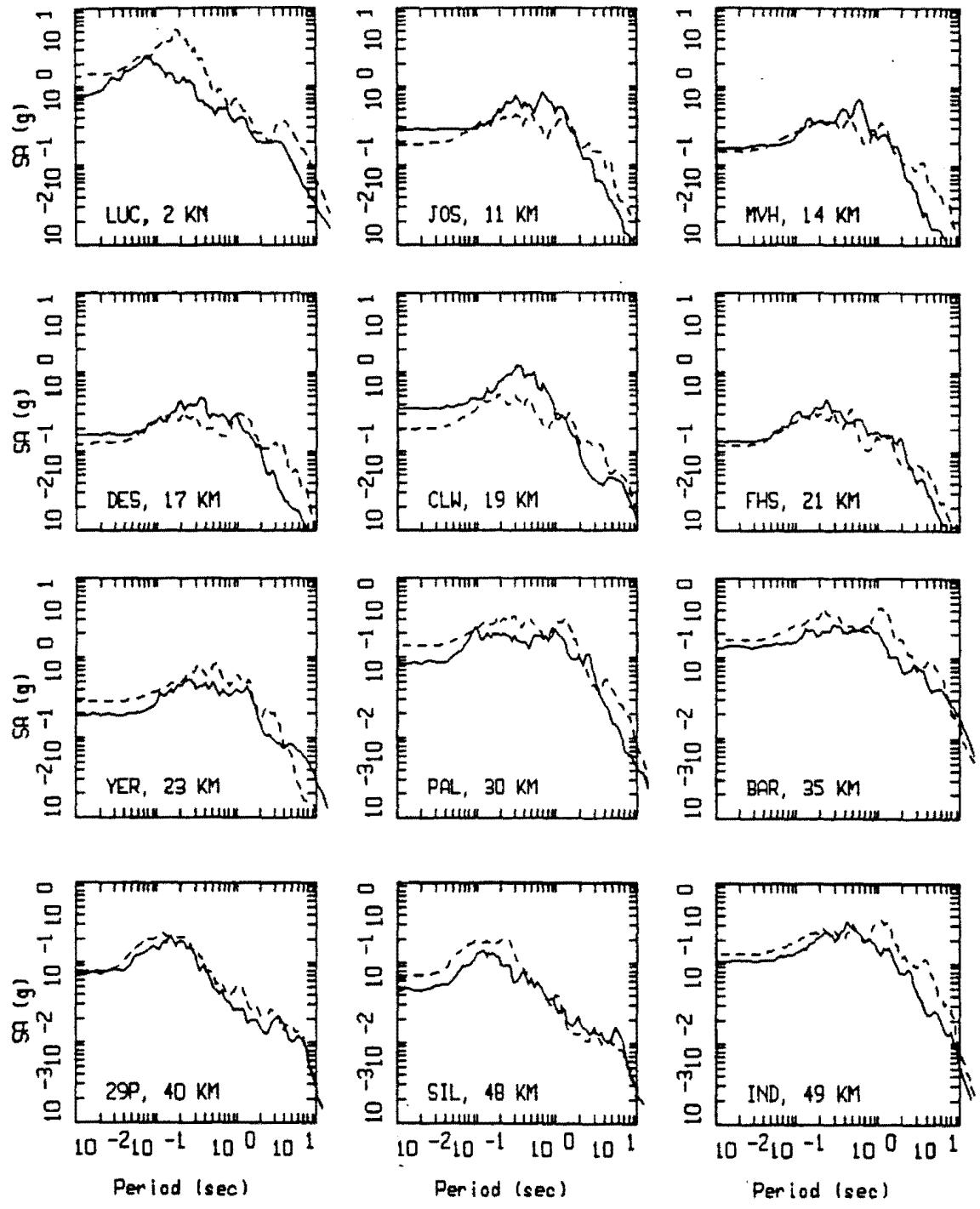

LANDERS, FINITE SOURCE MODELING, PAGE 1 OF 5.
NONLINEAR.

LEGEND
——— DATA
- - - - - MODEL

Figure Set 5.83

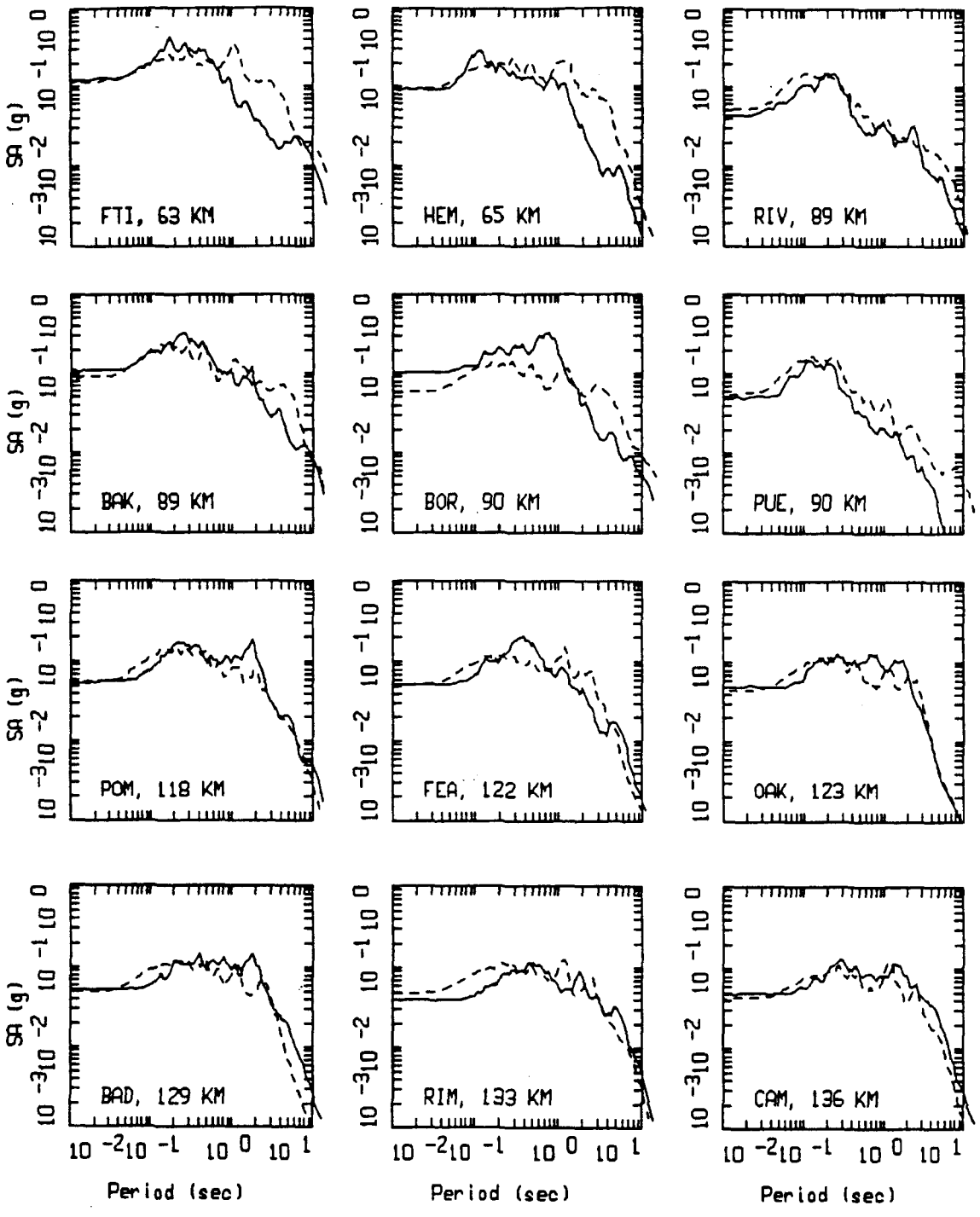

LANDERS, FINITE SOURCE MODELING, PAGE 2 OF 5.
NONLINEAR.

LEGEND

——— DATA

----- MODEL

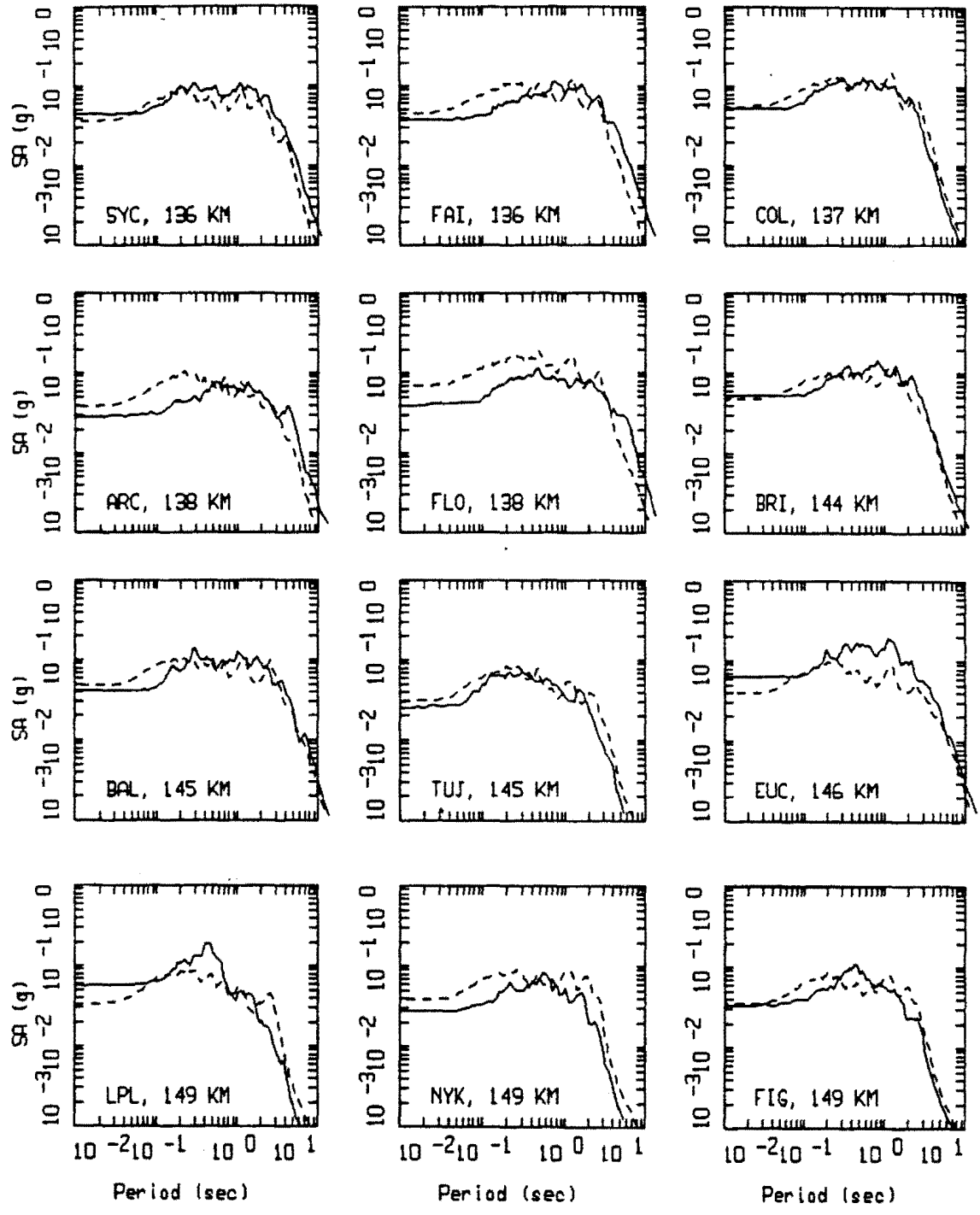

LANDERS, FINITE SOURCE MODELING, PAGE 3 OF 5.
NONLINEAR.

LEGEND
——— DATA
- - - - - MODEL

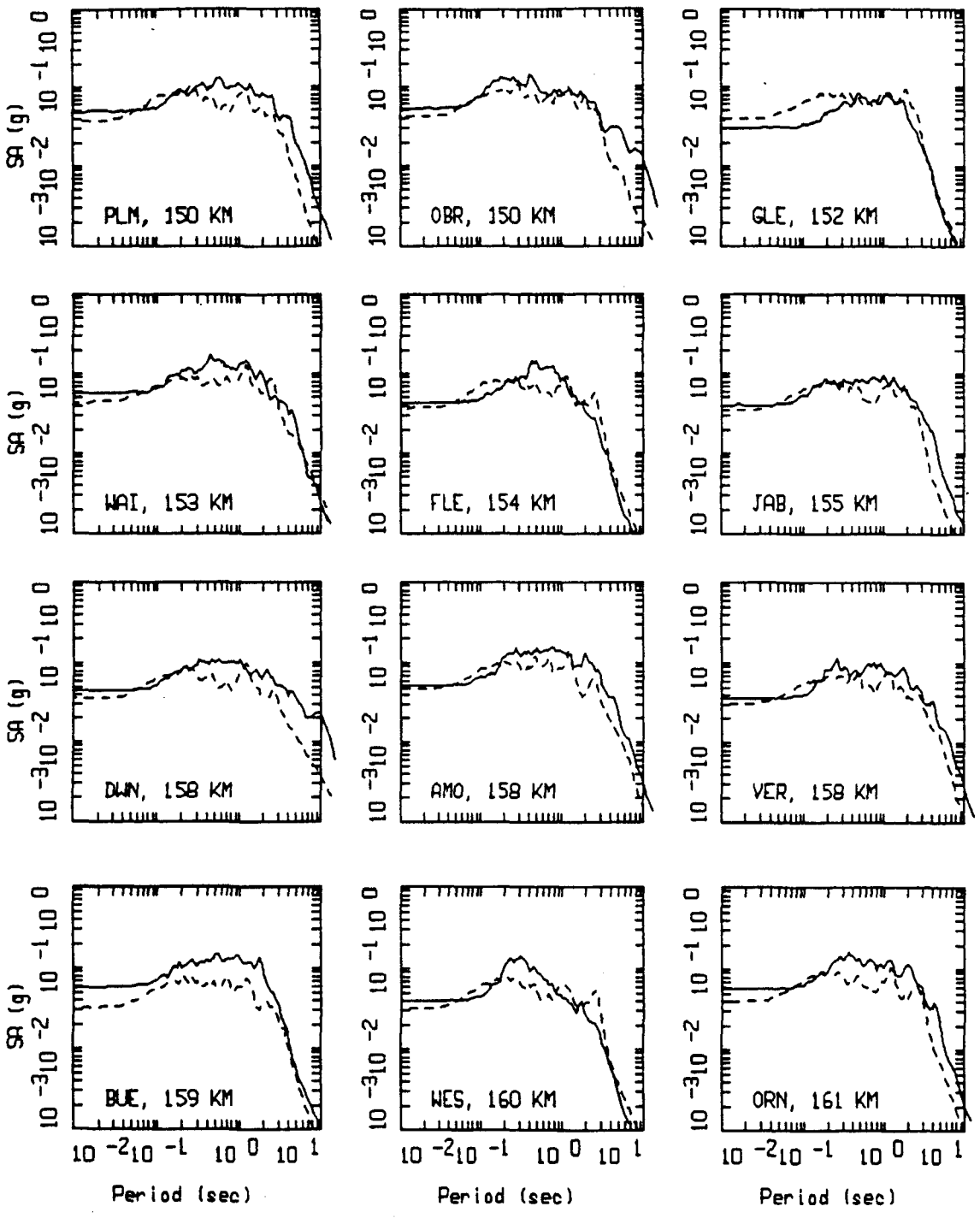

CANDERS, FINITE SOURCE MODELING, PAGE 4 OF 5.
NONLINEAR.

LEGEND
——— DATA
----- MODEL

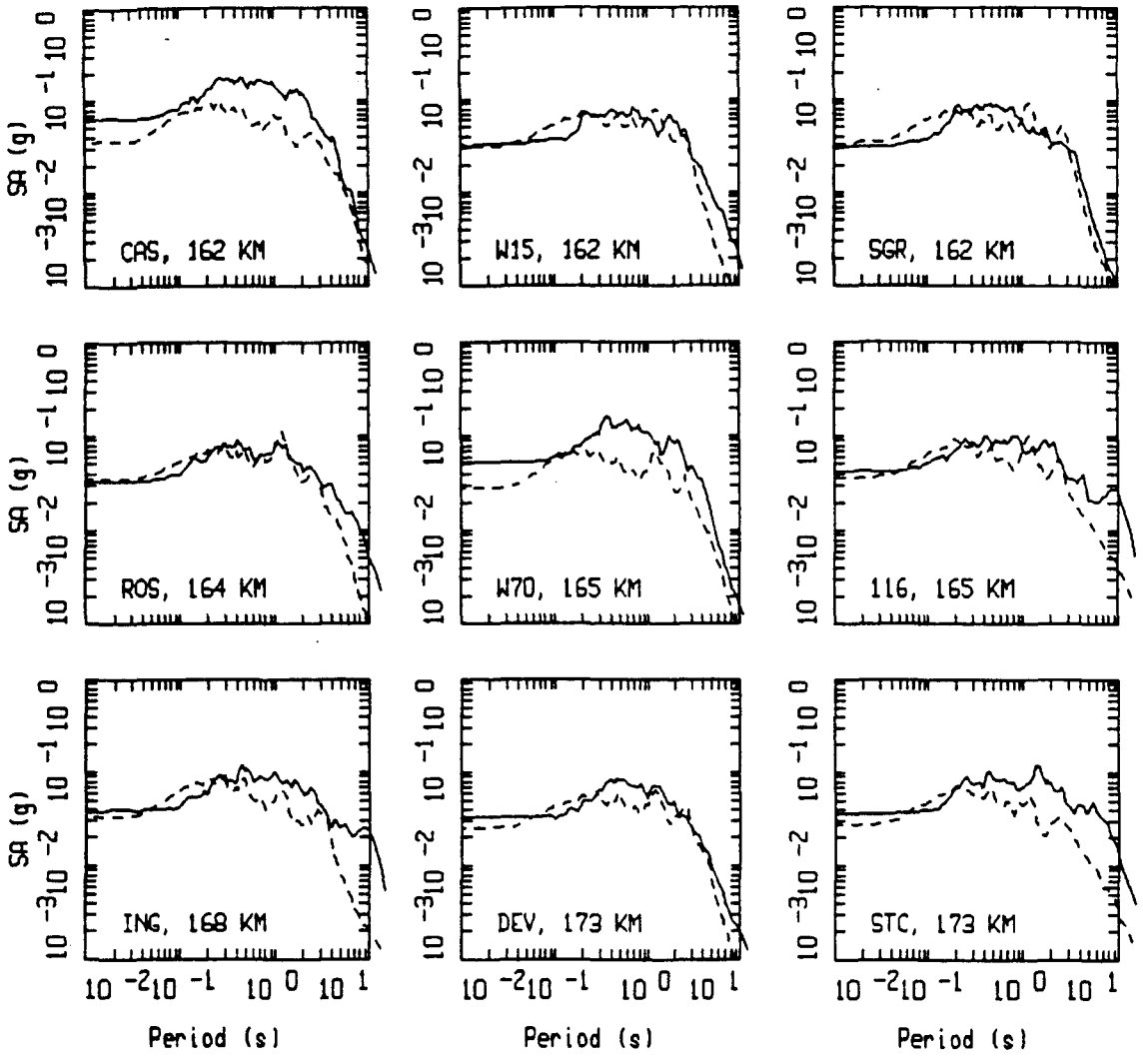

LANDERS, FINITE SOURCE MODELING, PAGE 5 OF 5.

NONLINEAR.

LEGEND

——— DATA

----- MODEL

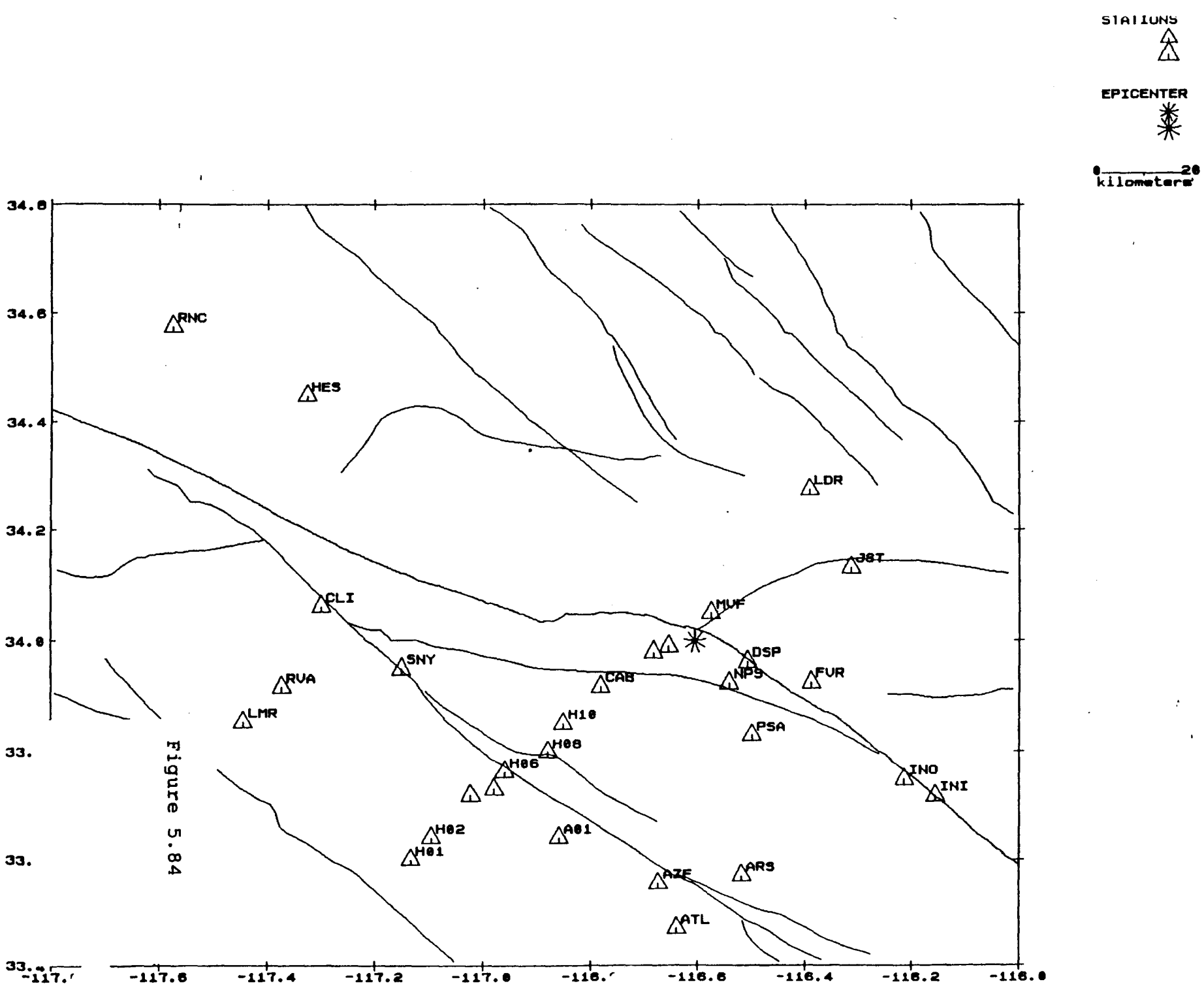

Figure 5.84

EQ3D-v4.00 FILE: SITES.HP2 EPICENT.HP2
. MFAC:1.0 XFAC:1.0 Nm=30 Nx=0

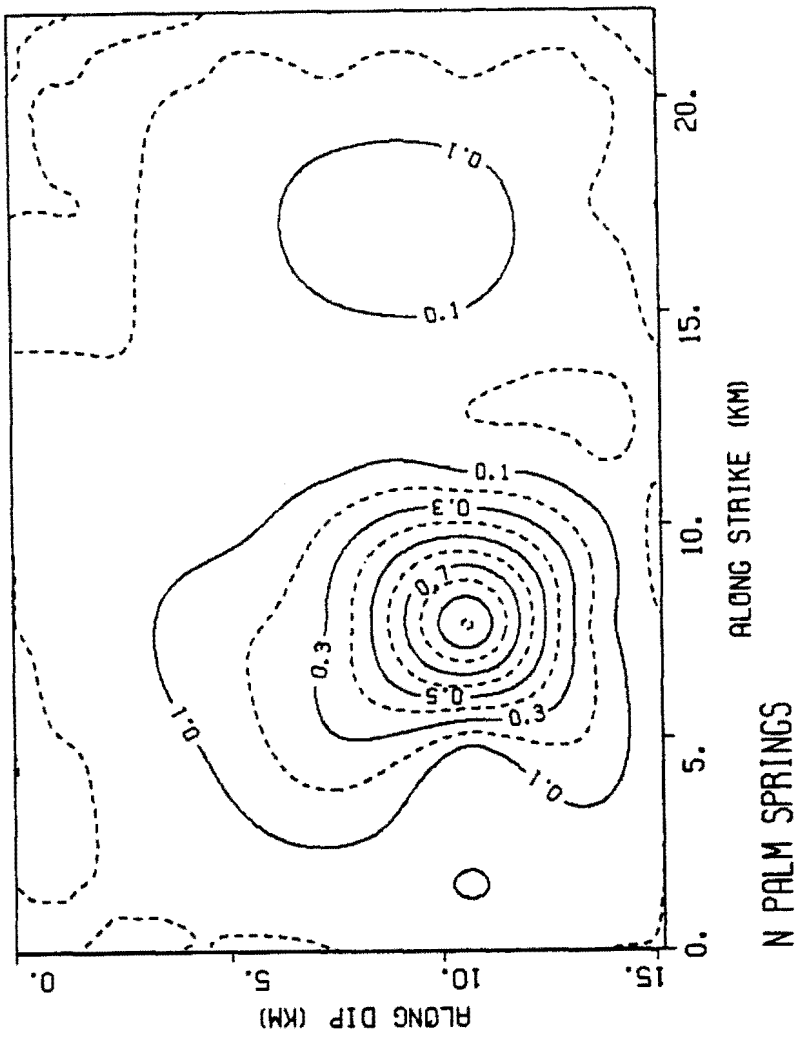
N PALM SPRINGS
ALONG STRIKE (KM)
ALONG DIP (KM)
0.
5.
10.
15.
20.
0.1
0.3
0.5
0.7
1.0

Figure 5.85

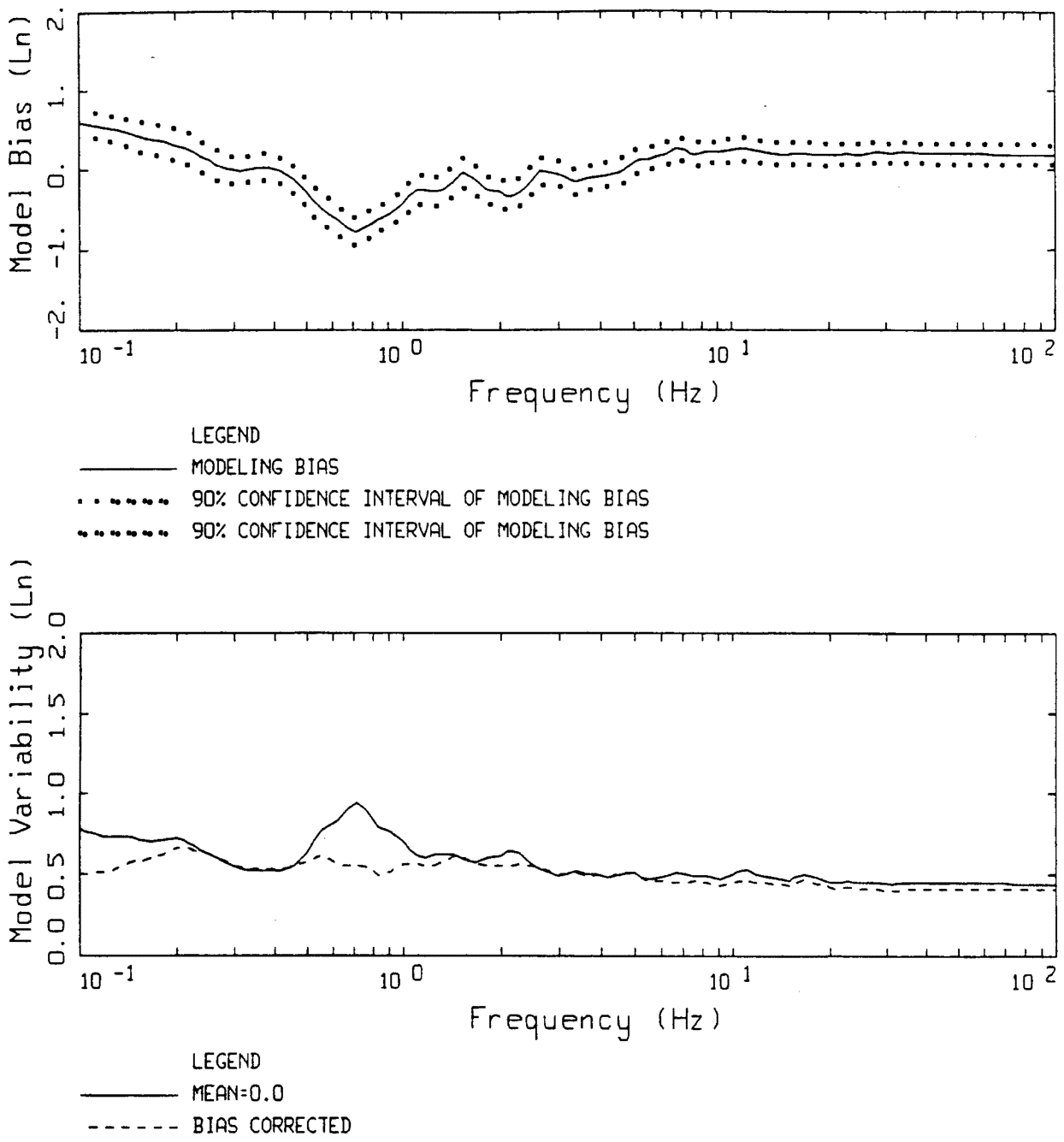

N PALM SPRINGS POINT-SOURCE
NONLINEAR, ALL 29 SITES

Figure 5.86

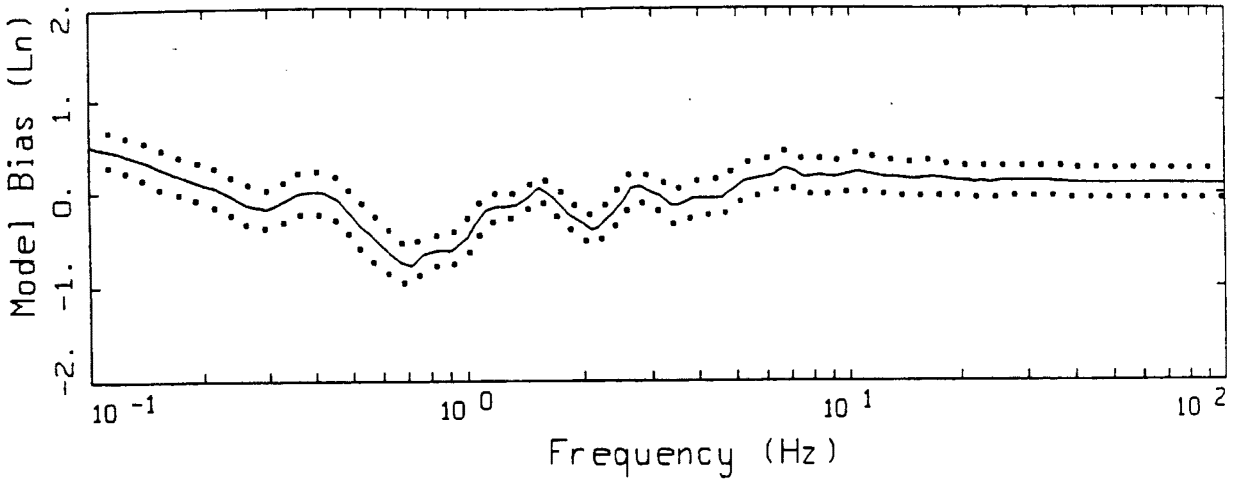

LEGEND
MODELING BIAS
90% CONFIDENCE INTERVAL OF MODELING BIAS
90% CONFIDENCE INTERVAL OF MODELING BIAS

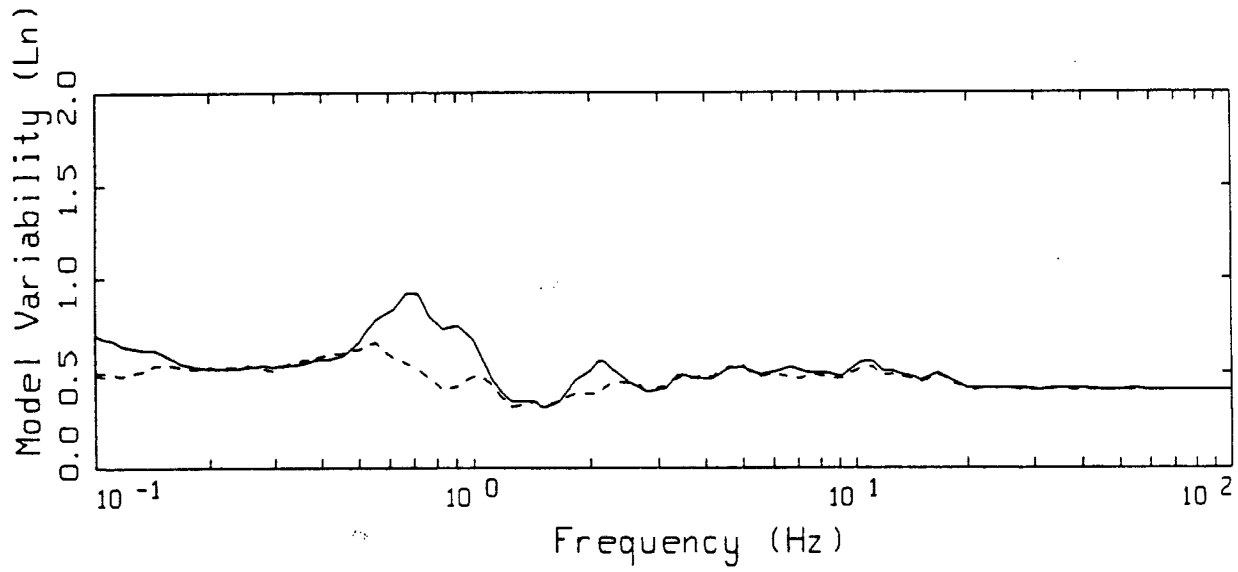

LEGEND
MEAN=0.0
BIAS CORRECTED

N PALM SPRINGS POINT-SOURCE
NONLINEAR, 20 SOIL SITES

Figure 5.87

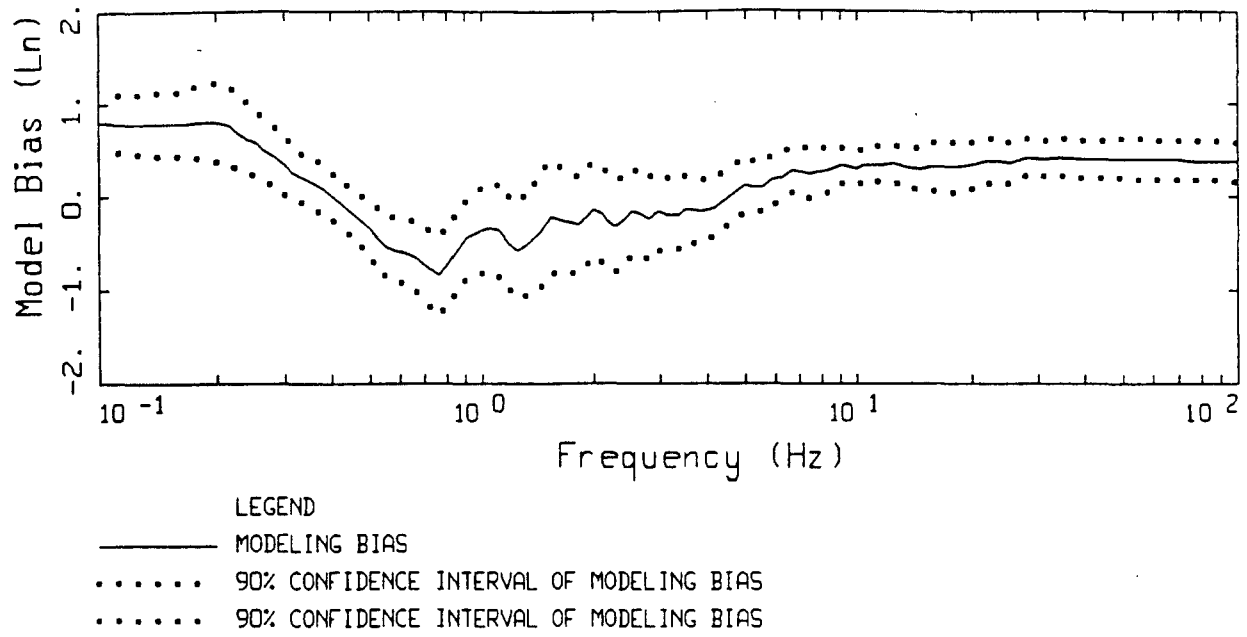

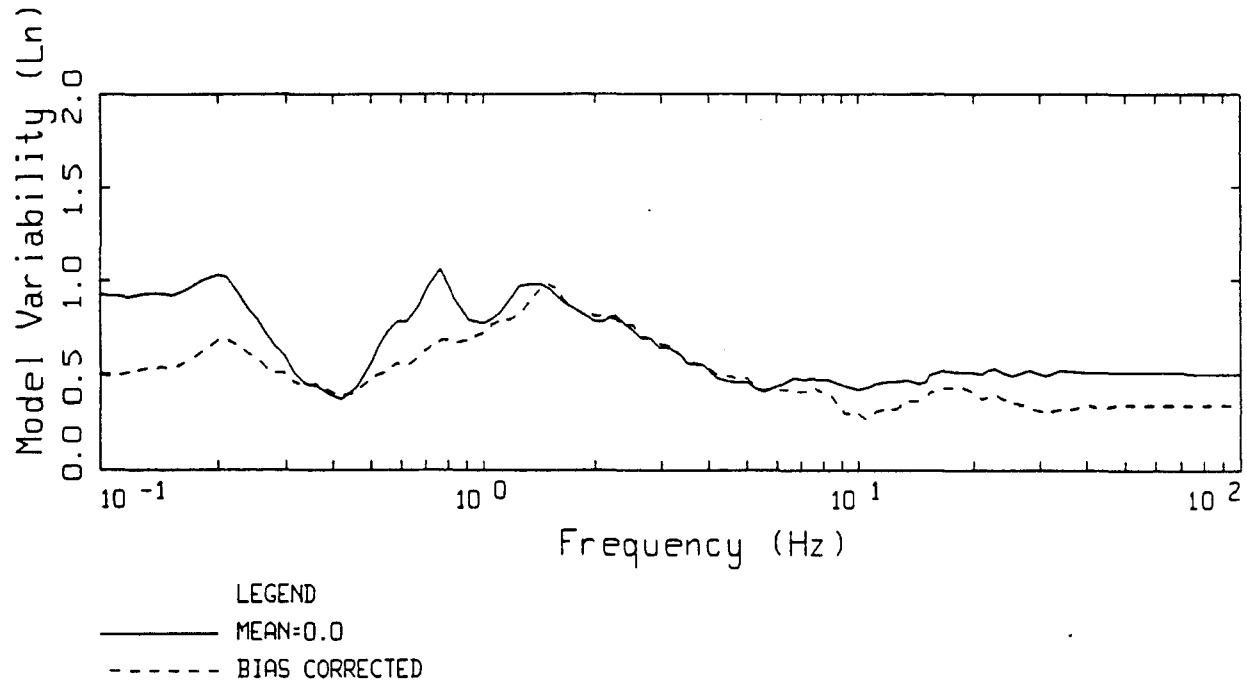

N PALM SPRINGS POINT-SOURCE
NONLINEAR, 9 ROCK SITES

Figure 5.88

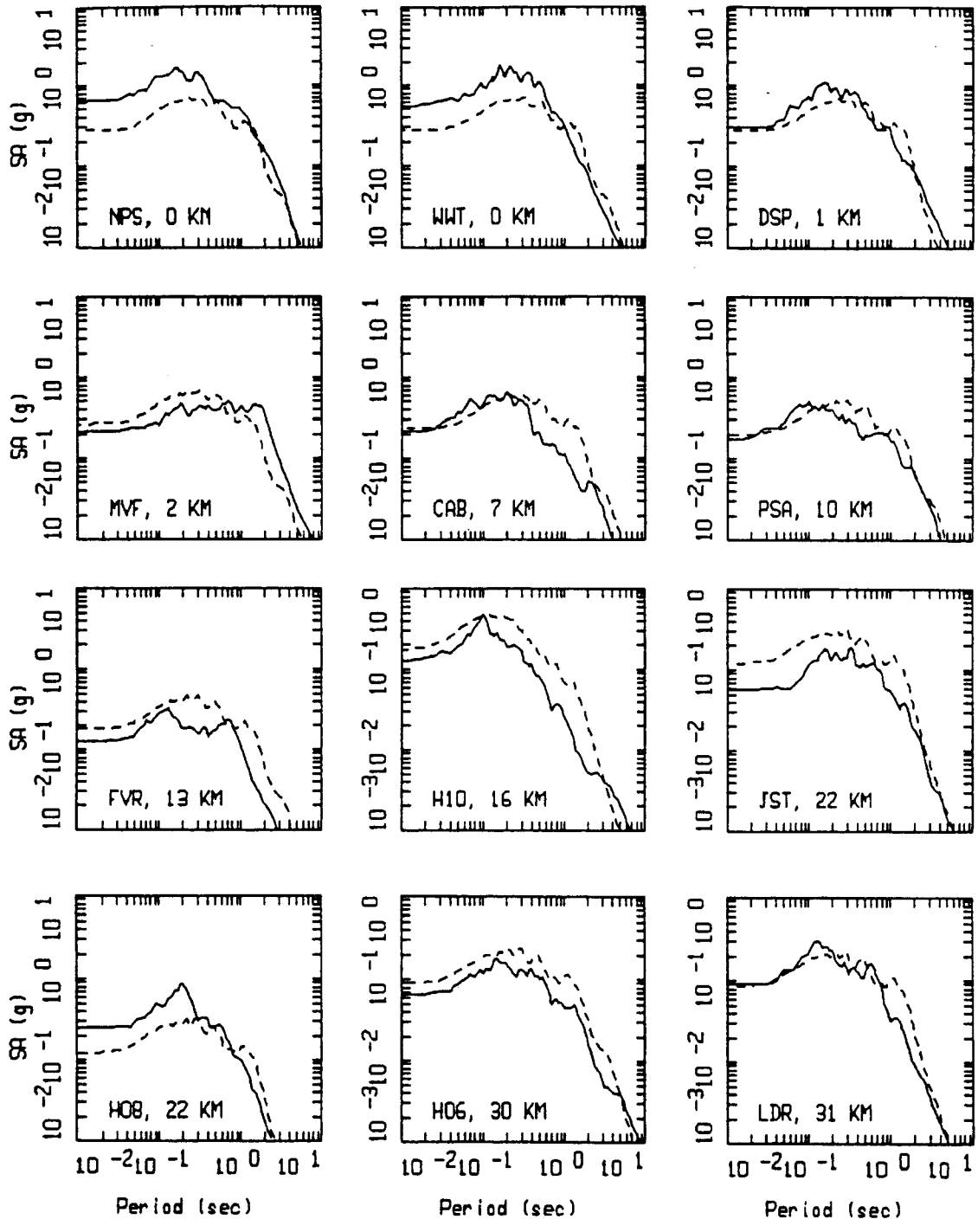

N PALM SPRINGS, POINT SOURCE MODELING, PAGE 1 OF 3.
NONLINEAR.

LEGEND
——— DATA
- - - - - MODEL

Figure Set 5.89

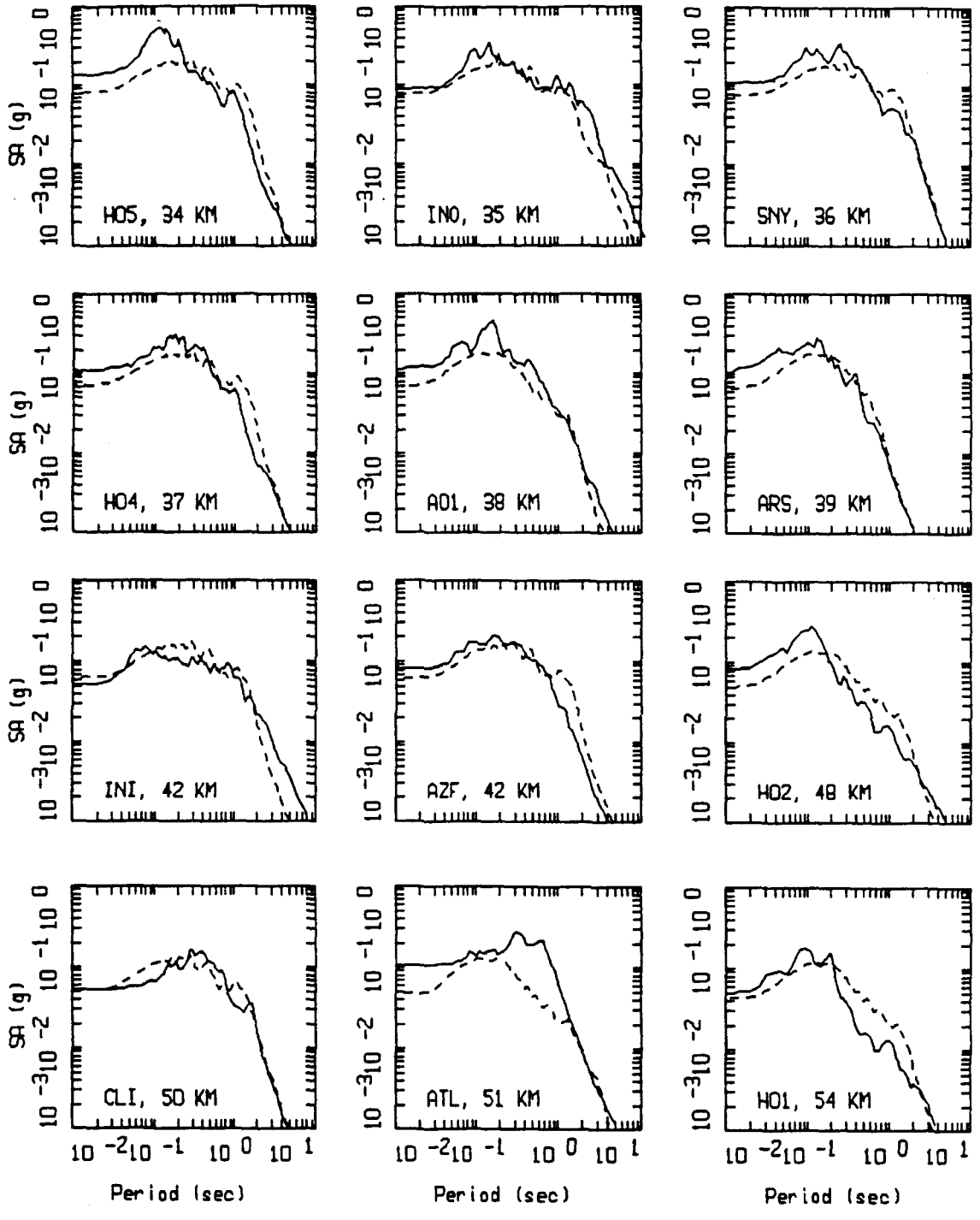

N PALM SPRINGS, POINT SOURCE MODELING, PAGE 2 OF 3.
NONLINEAR.

LEGEND
——— DATA
- - - - - MODEL

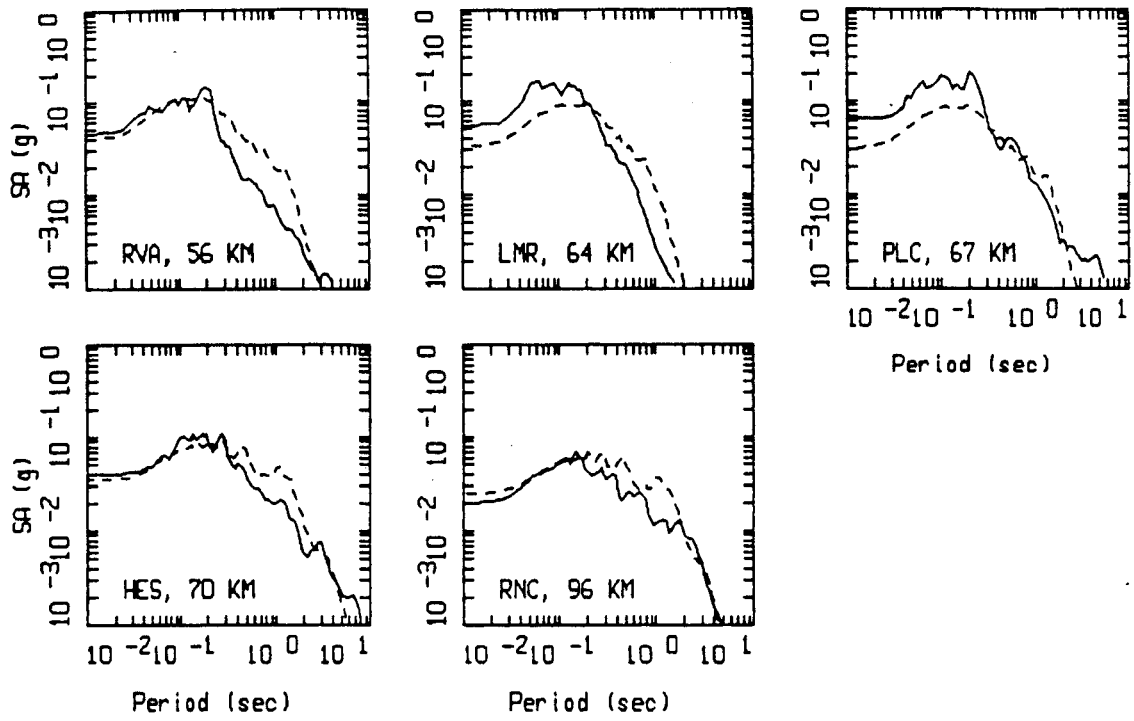

N PALM SPRINGS, POINT SOURCE MODELING, PAGE 3 OF 3.
NONLINEAR.

LEGEND
——— DATA
----- MODEL

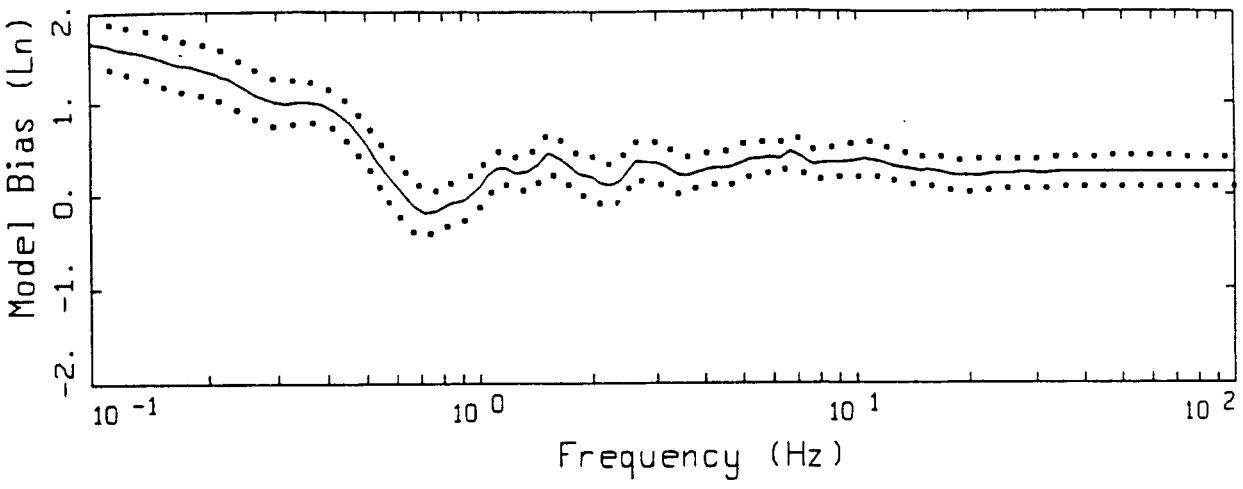

LEGEND
MODELING BIAS
90% CONFIDENCE INTERVAL OF MODELING BIAS
90% CONFIDENCE INTERVAL OF MODELING BIAS

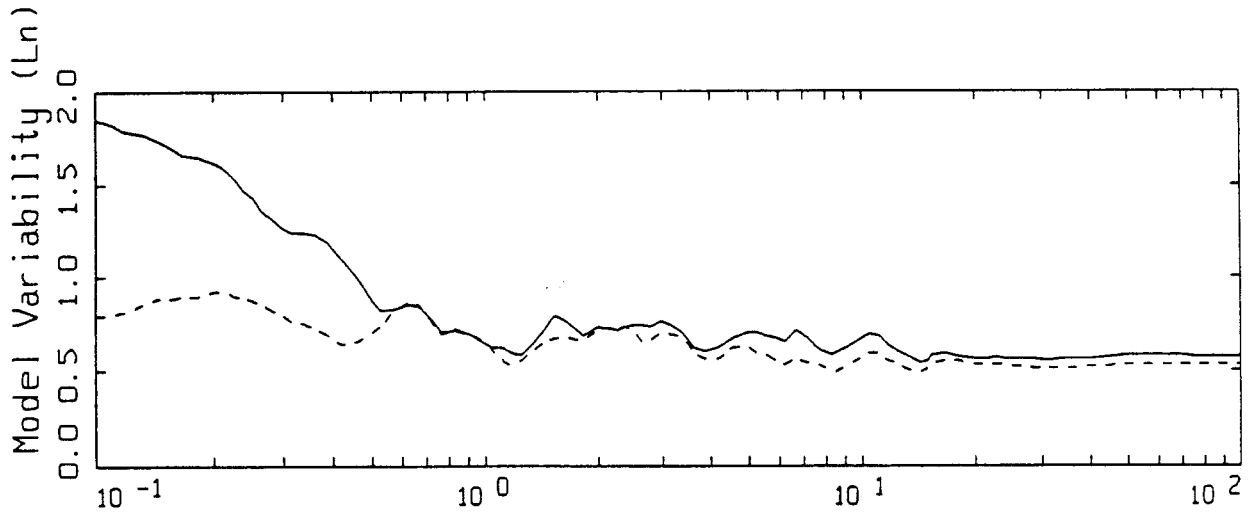

LEGEND
MEAN=0.0
BIAS CORRECTED

N PALM SPRINGS FINITE-SOURCE
NONLINEAR, ALL 29 SITES

Figure 5.90

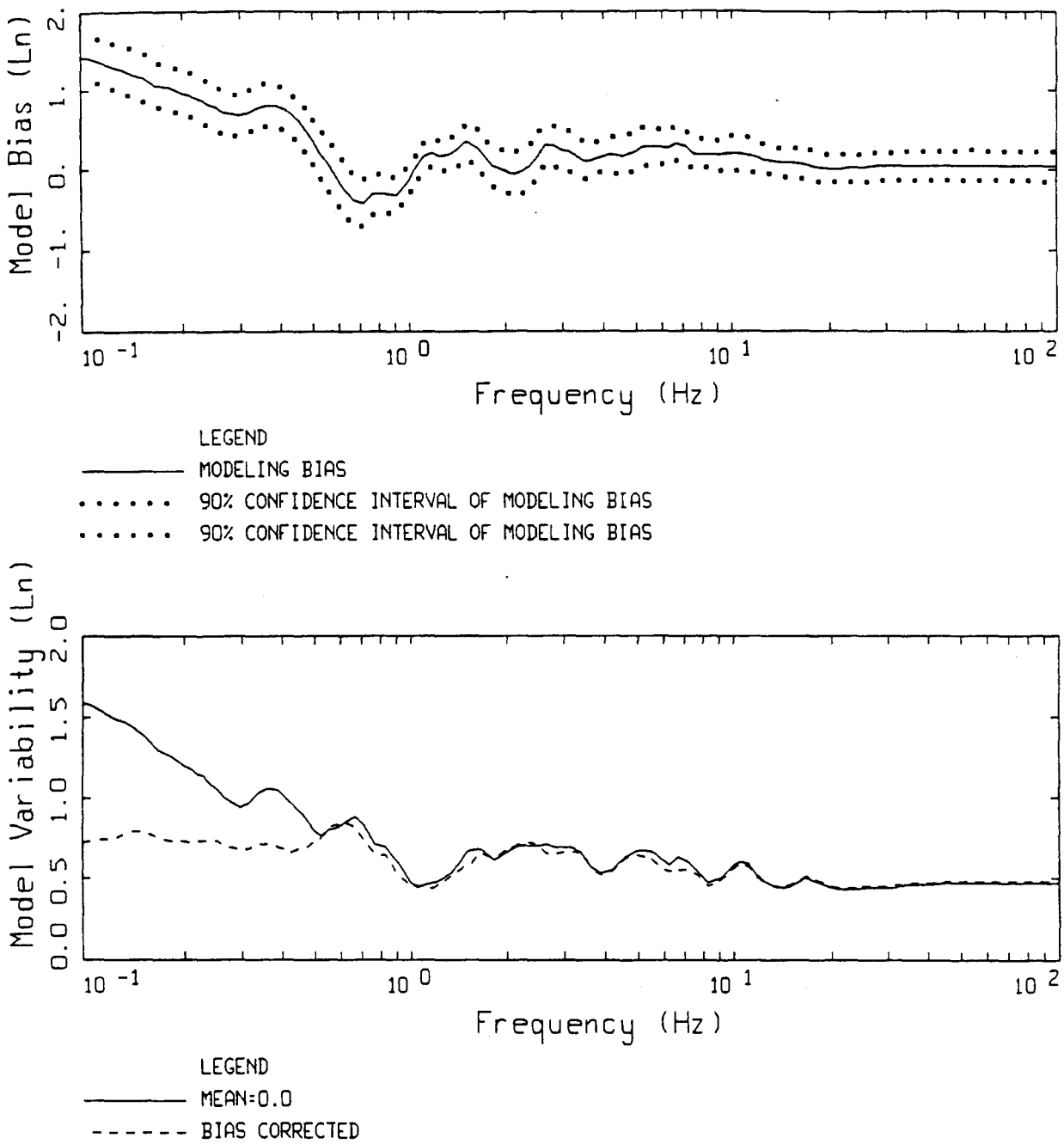
Model Bias (Ln)
2.
1.
0.
-1.
-2.
10 -1
10 0
10 1
10 2
Frequency (Hz)
LEGEND
MODELING BIAS
90% CONFIDENCE INTERVAL OF MODELING BIAS
90% CONFIDENCE INTERVAL OF MODELING BIAS
Model Variability (Ln)
0.0 0.5 1.0 1.5 2.0
10 -1
10 0
10 1
10 2
Frequency (Hz)
LEGEND
MEAN=0.0
BIAS CORRECTED
N PALM SPRINGS FINITE-SOURCE
NONLINEAR, 20 SOIL SITES

Figure 5.91

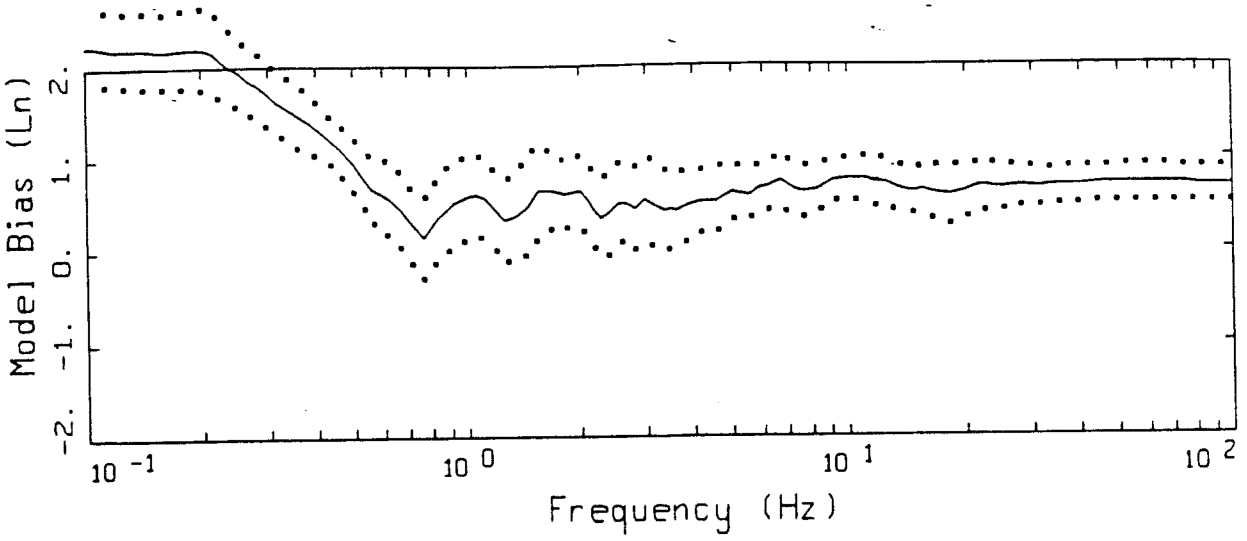

LEGEND
MODELING BIAS
90% CONFIDENCE INTERVAL OF MODELING BIAS
90% CONFIDENCE INTERVAL OF MODELING BIAS

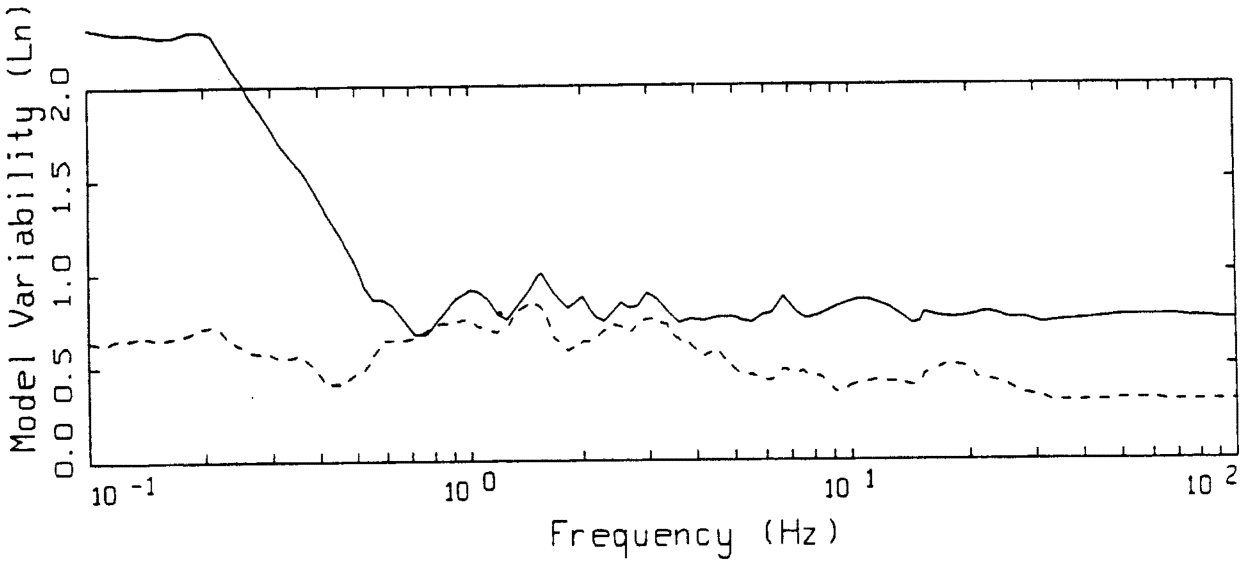

LEGEND
MEAN=0.0
BIAS CORRECTED

N PALM SPRINGS FINITE-SOURCE
NONLINEAR, 9 ROCK SITES

Figure 5.92

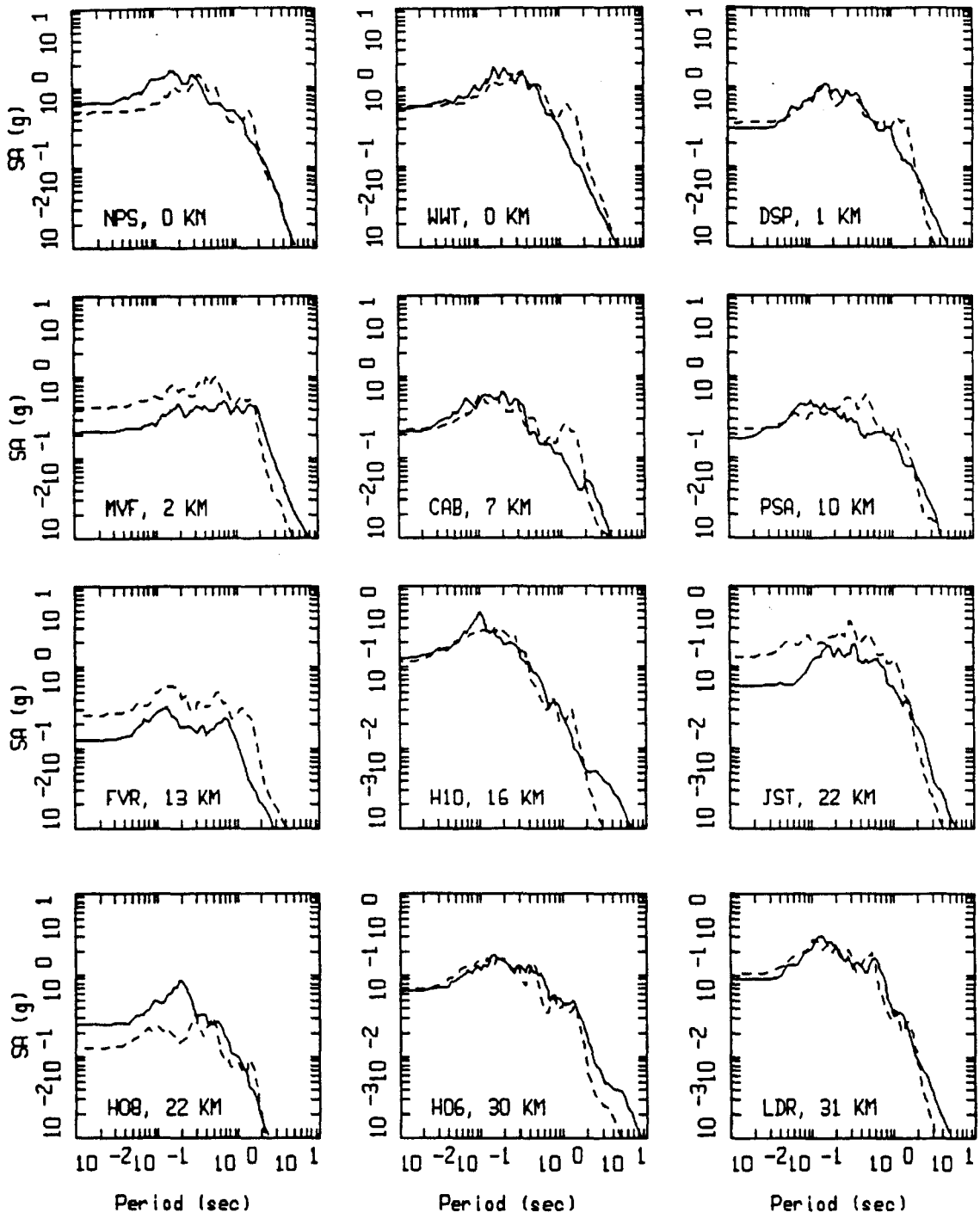

Ñ PALM SPRINGS, FINITE SOURCE MODELING, PAGE 1 OF 3.
NONLINEAR.

Figure Set 5.93

LEGEND

——— DATA

----- MODEL

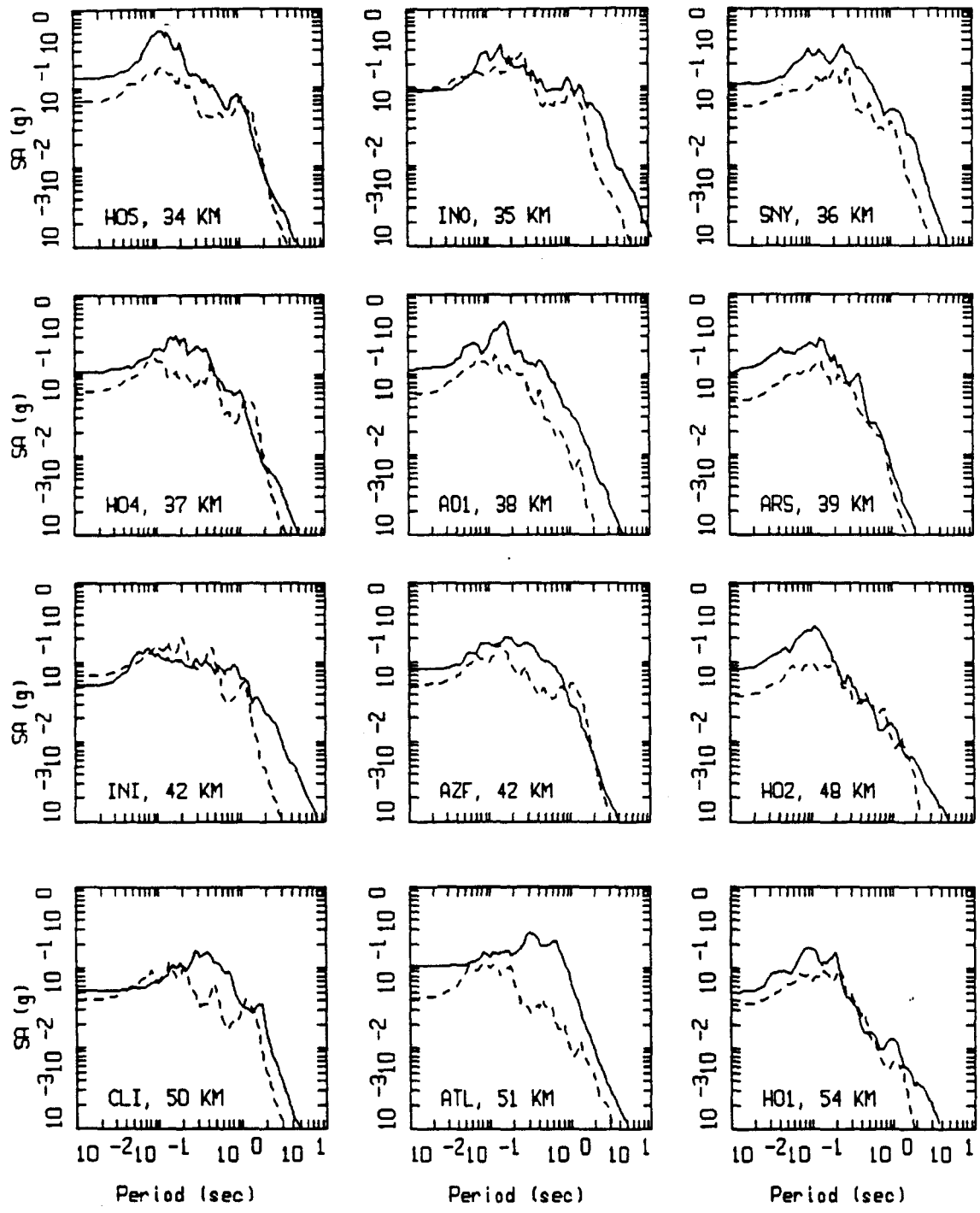

N PALM SPRINGS, FINITE SOURCE MODELING, PAGE 2 OF 3.
NONLINEAR.

LEGEND

——— DATA

- - - - - MODEL

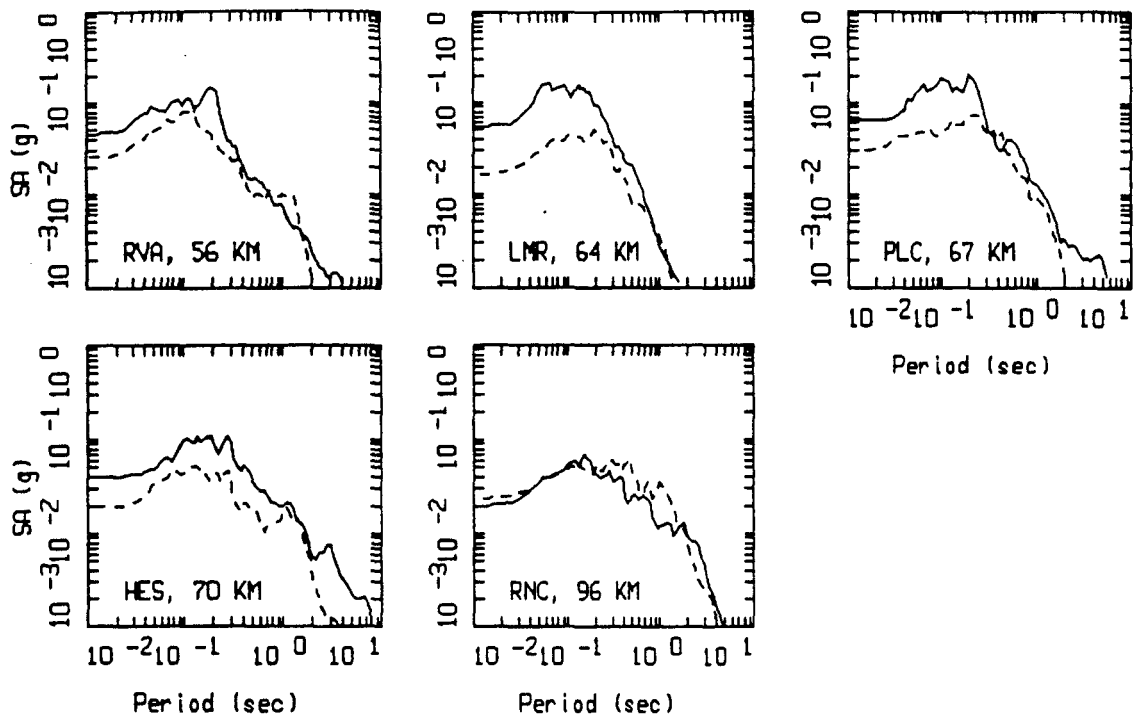

N PALM SPRINGS, FINITE SOURCE MODELING, PAGE 3 OF 3.
NONLINEAR.

LEGEND
——— DATA
- - - - - MODEL

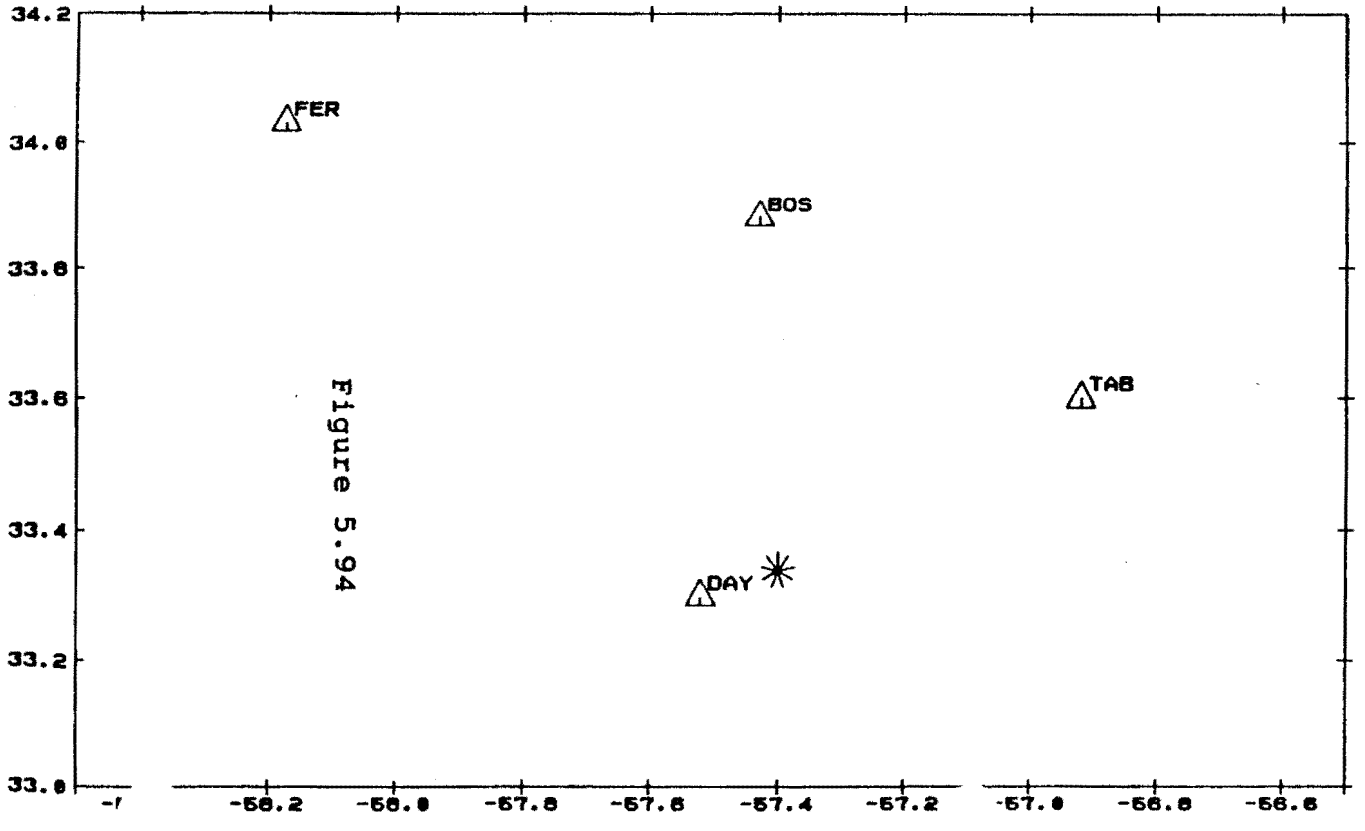

Figure 5.94

STATIONS

EPICENTER

0 20
kilometers

EQ3D-v4.00 FILE: SITES.HP2 EPICENT.HP2
. SCA:1300000 MFAC:1.0 XFAC:1.0 Nm=5 Nx=0

TABAS
ALONG STRIKE (KM)
0.
10.
20.
30.
40.
50.
60.
70.
80.
90.
ALONG DIP (KM)
45.
35.
25.
15.
5.
0.1
0.3
1.0

Figure 5.95

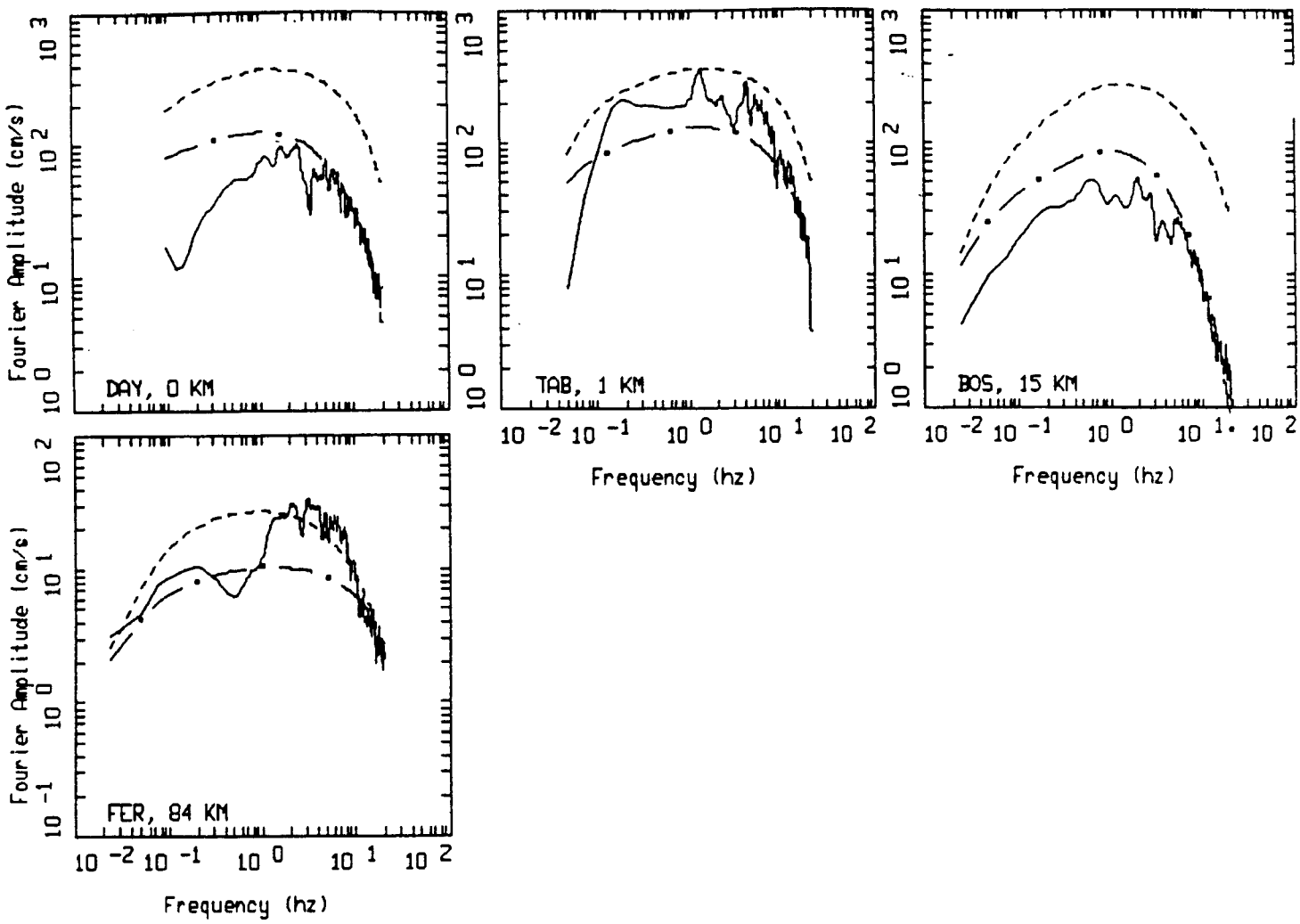

TABAS EARTHQUAKE, M=7.4, PAGE 1 OF 1.

LEGEND

——— DATA

- - - - - INITIAL MODEL

— • — FINAL MODEL

Figure 5.96

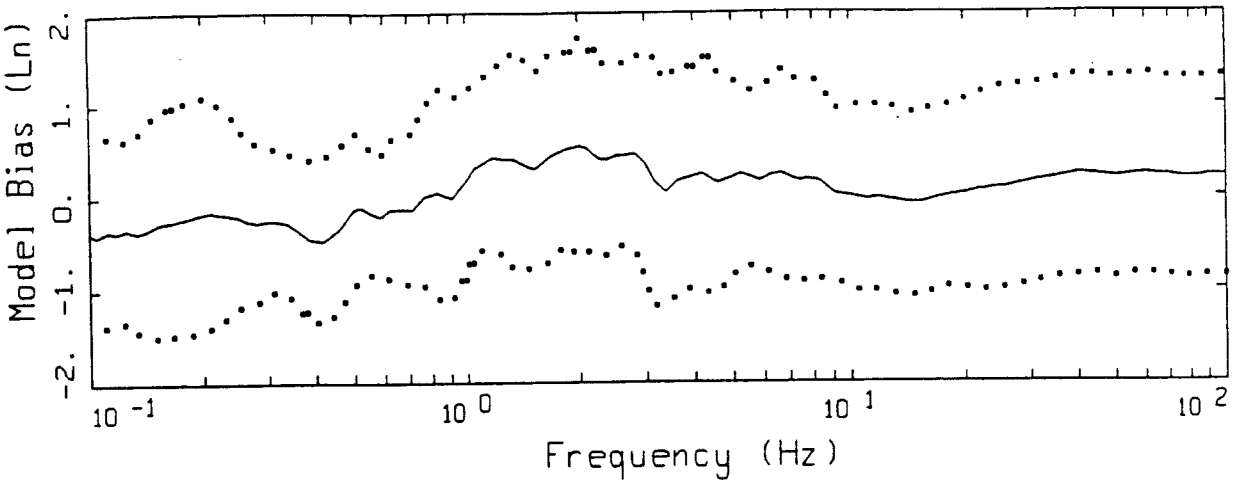

LEGEND
MODELING BIAS
90% CONFIDENCE INTERVAL OF MODELING BIAS
90% CONFIDENCE INTERVAL OF MODELING BIAS

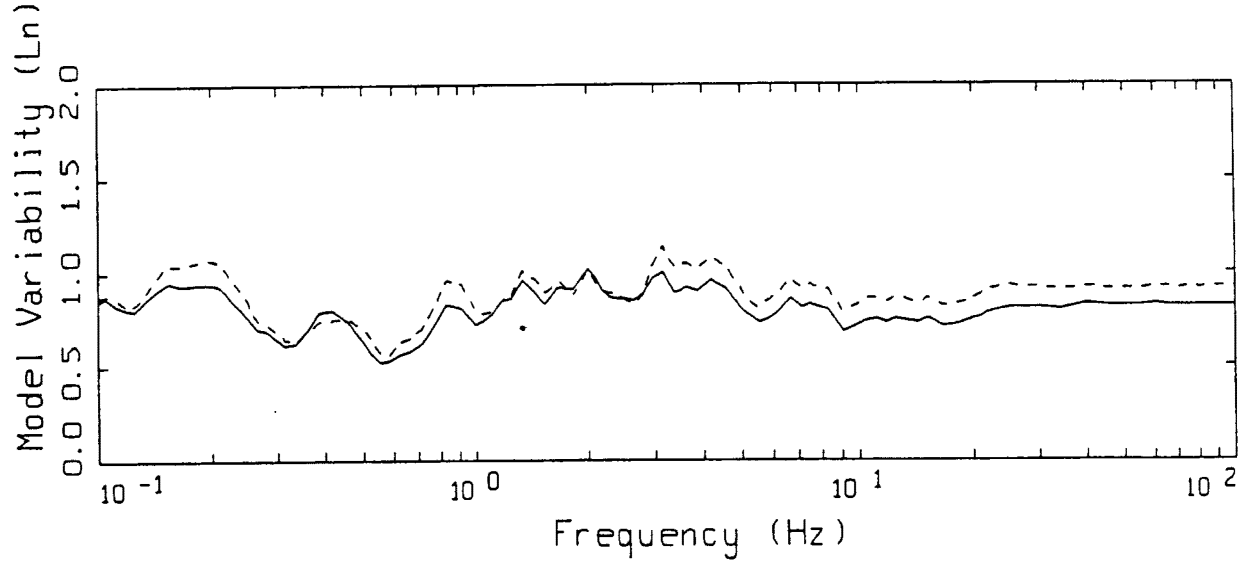

LEGEND
MEAN=0.0
BIAS CORRECTED

TABAS POINT-SOURCE
NONLINEAR, ALL 4 SITES

Figure 5.97

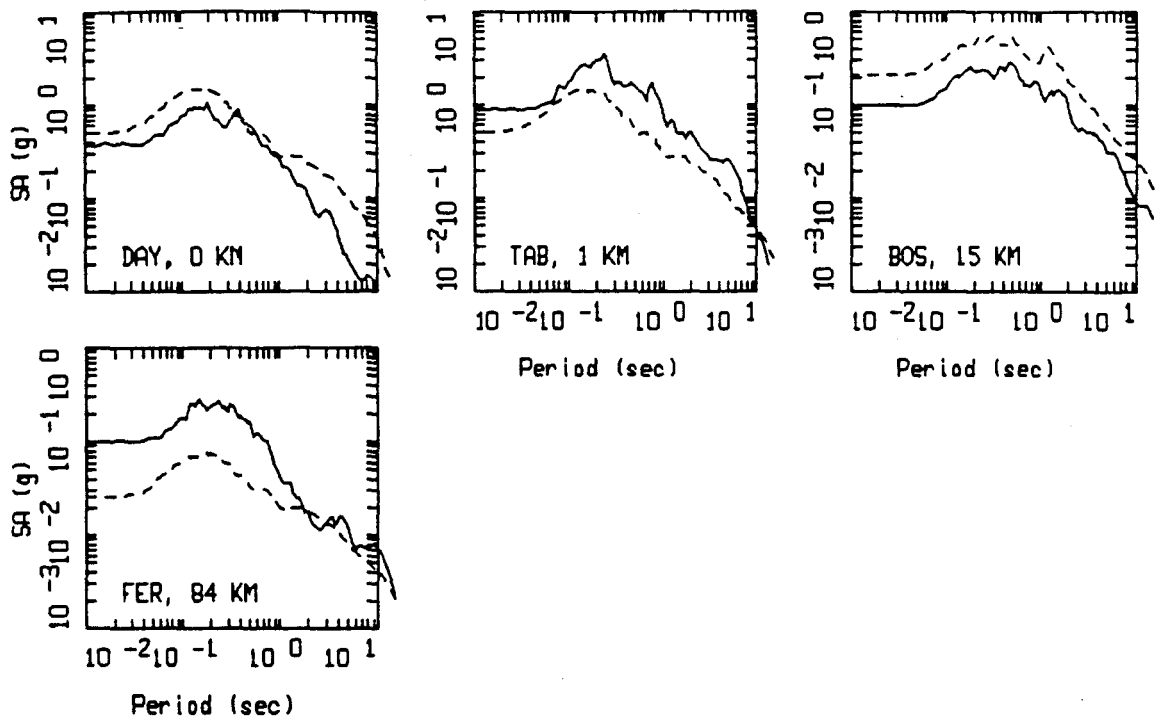

TABAS, POINT SOURCE MODELING, PAGE 1 OF 1.
NONLINEAR.

LEGEND
——— DATA
----- MODEL

Figure 5.98

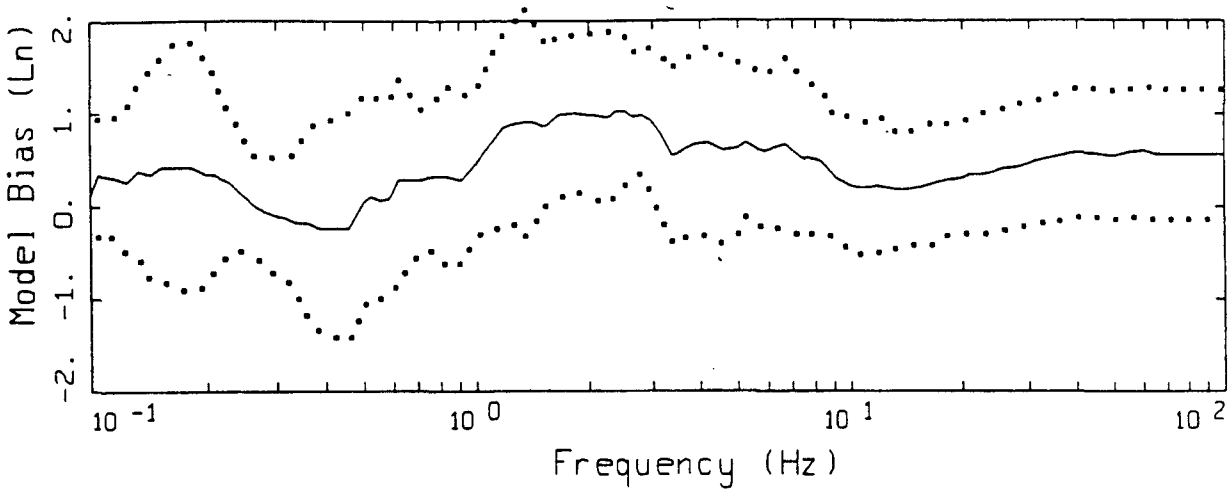

LEGEND
MODELING BIAS
90% CONFIDENCE INTERVAL OF MODELING BIAS
90% CONFIDENCE INTERVAL OF MODELING BIAS

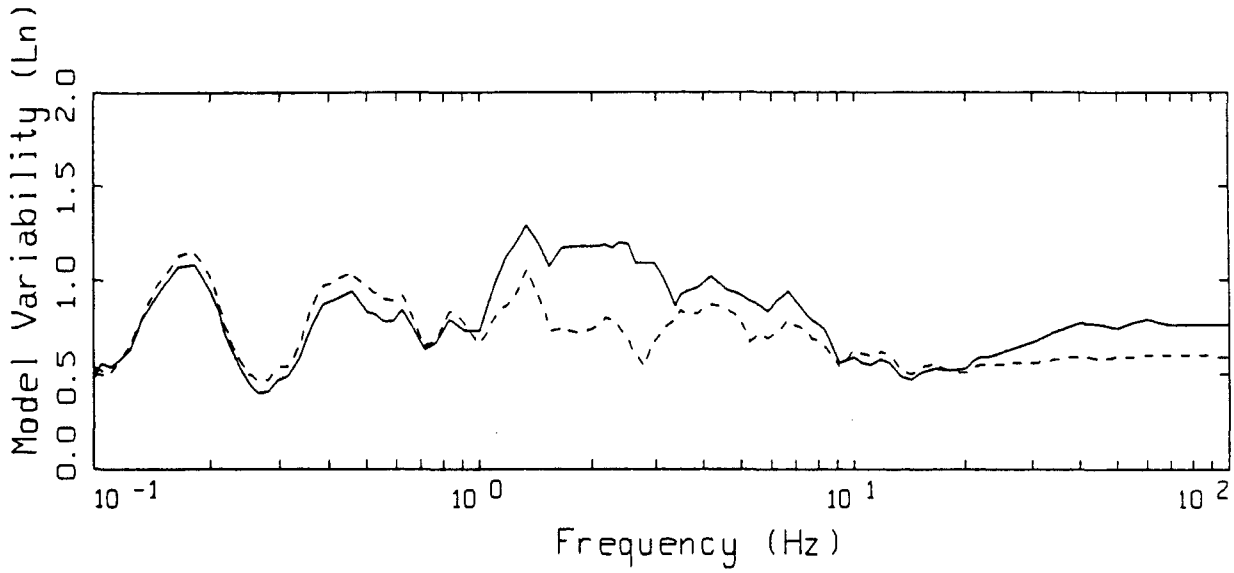

LEGEND
MEAN=0.0
BIAS CORRECTED

TABAS FINITE-SOURCE
NONLINEAR, ALL 4 SITES

Figure 5.99

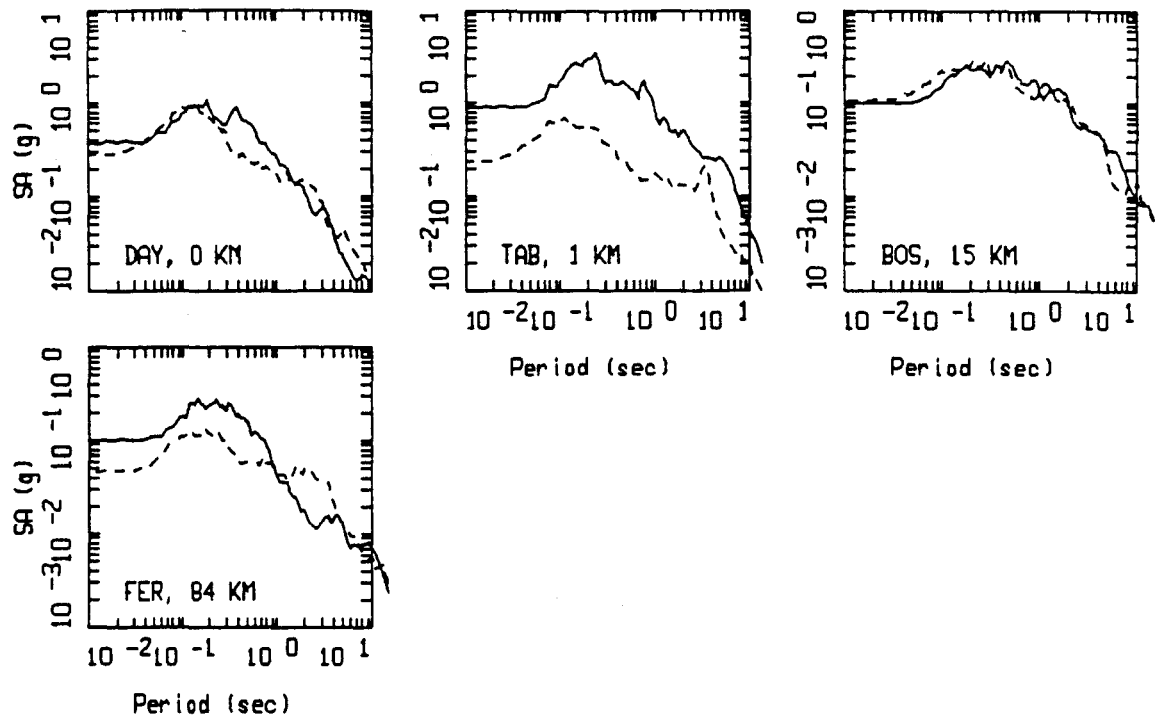

TABAS, FINITE SOURCE MODELING, PAGE 1 OF 1.
NONLINEAR.

LEGEND
——— DATA
----- MODEL

Figure 5.100

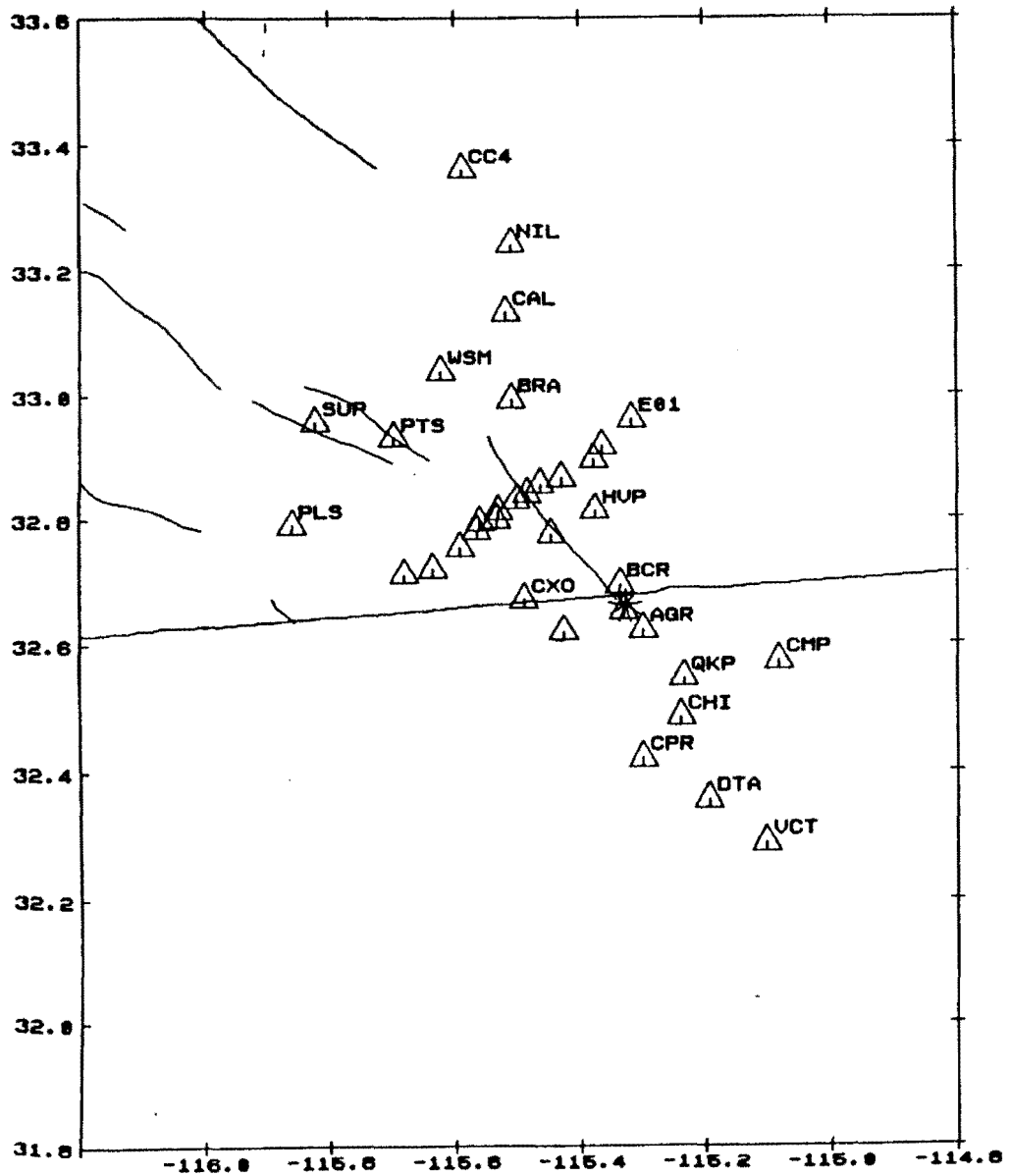
STAT
EPICENTER
0 20
kilometers
33.6
33.4
33.2
33.0
32.8
32.6
32.4
32.2
32.0
31.8
-116.0
-115.8
-115.6
-115.4
-115.2
-115.0
-114.8
CC4
NIL
CAL
WSM
BRA
E01
SUR
PTS
HVP
PLS
BCR
CXO
AGR
CMP
QKP
CHI
CPR
DTA
VCT
EQ3D-V4.00 FILE: SITESMS.HP2 EPIMS.HP2
. 3CA:130000 MFAC:1.0 XFAC:1.0 Nm=38 Nx=0

Figure 5.101

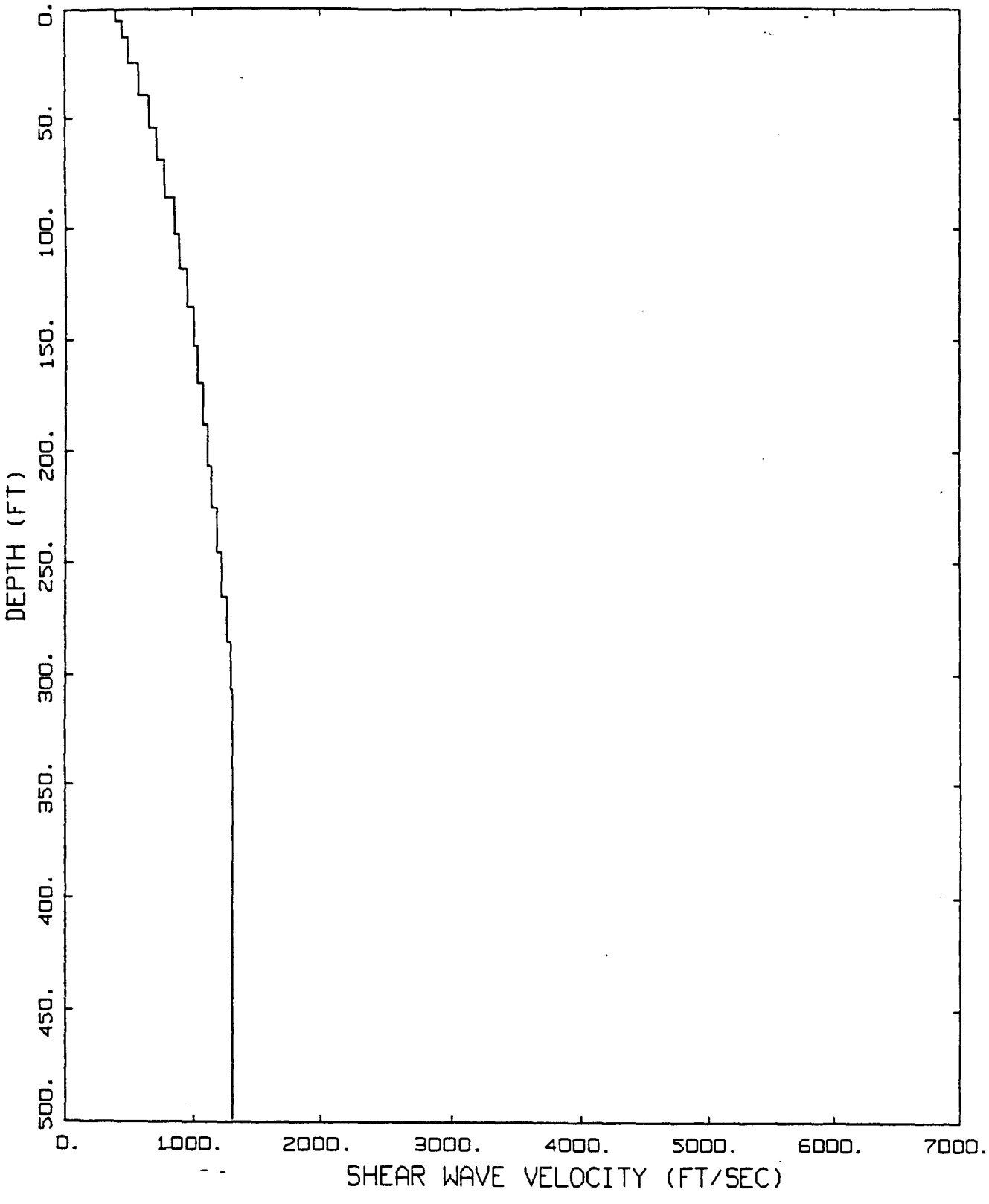

GENERIC IMPERIAL VALLEY SOIL

Figure 5.102

LEGEND

PROFILE

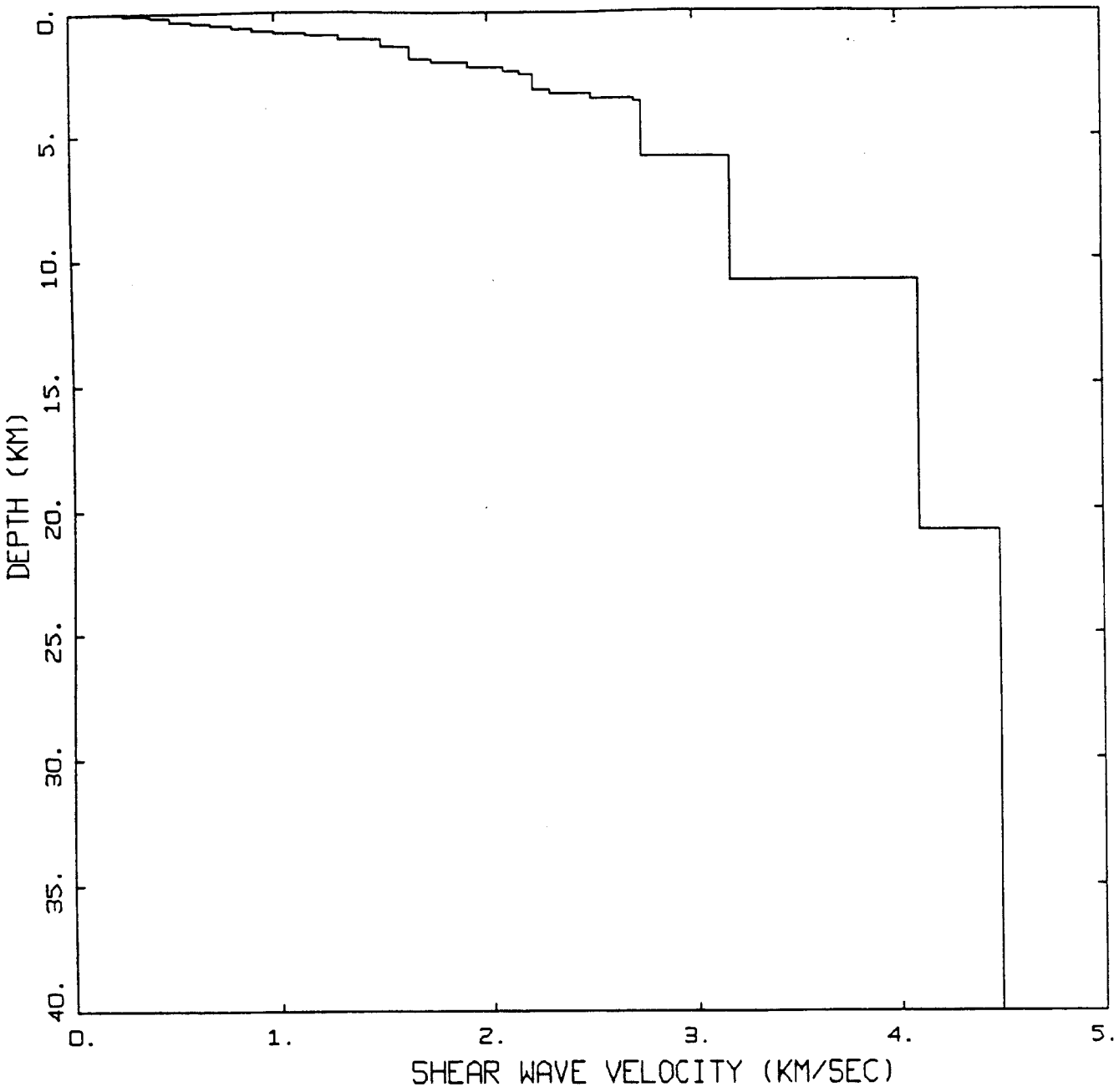

GENERIC IMPERIAL VALLEY CRUST

LEGEND

CRUSTAL MODEL

Figure 5.103

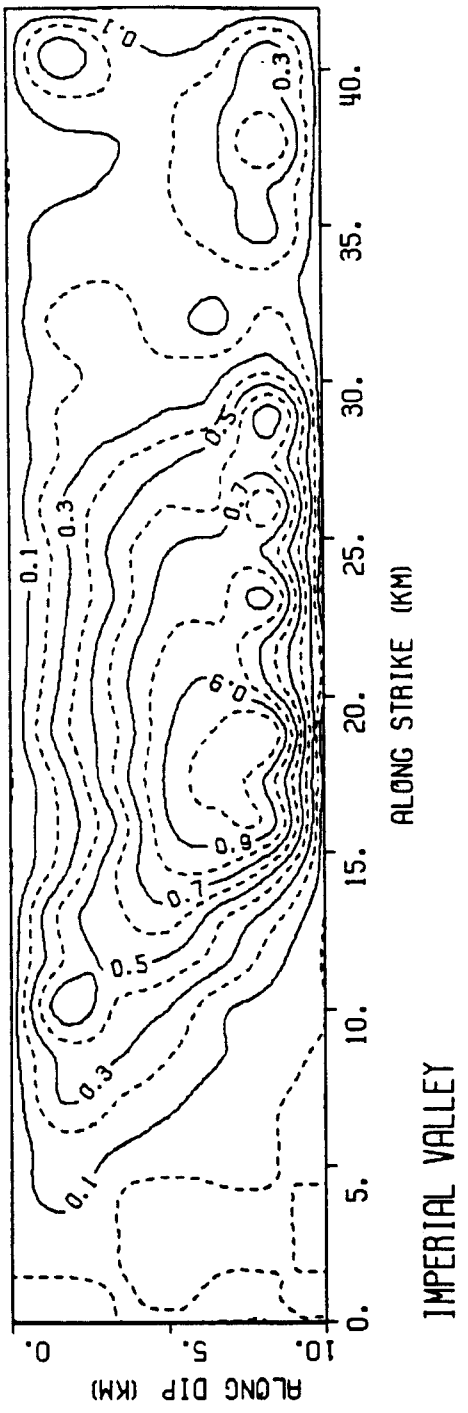
IMPERIAL VALLEY
ALONG STRIKE (KM)
ALONG DIP (KM)
0.
5.
10.
15.
20.
25.
30.
35.
40.
0.1
0.3
0.5
0.7
0.9
1.0

Figure 5.104

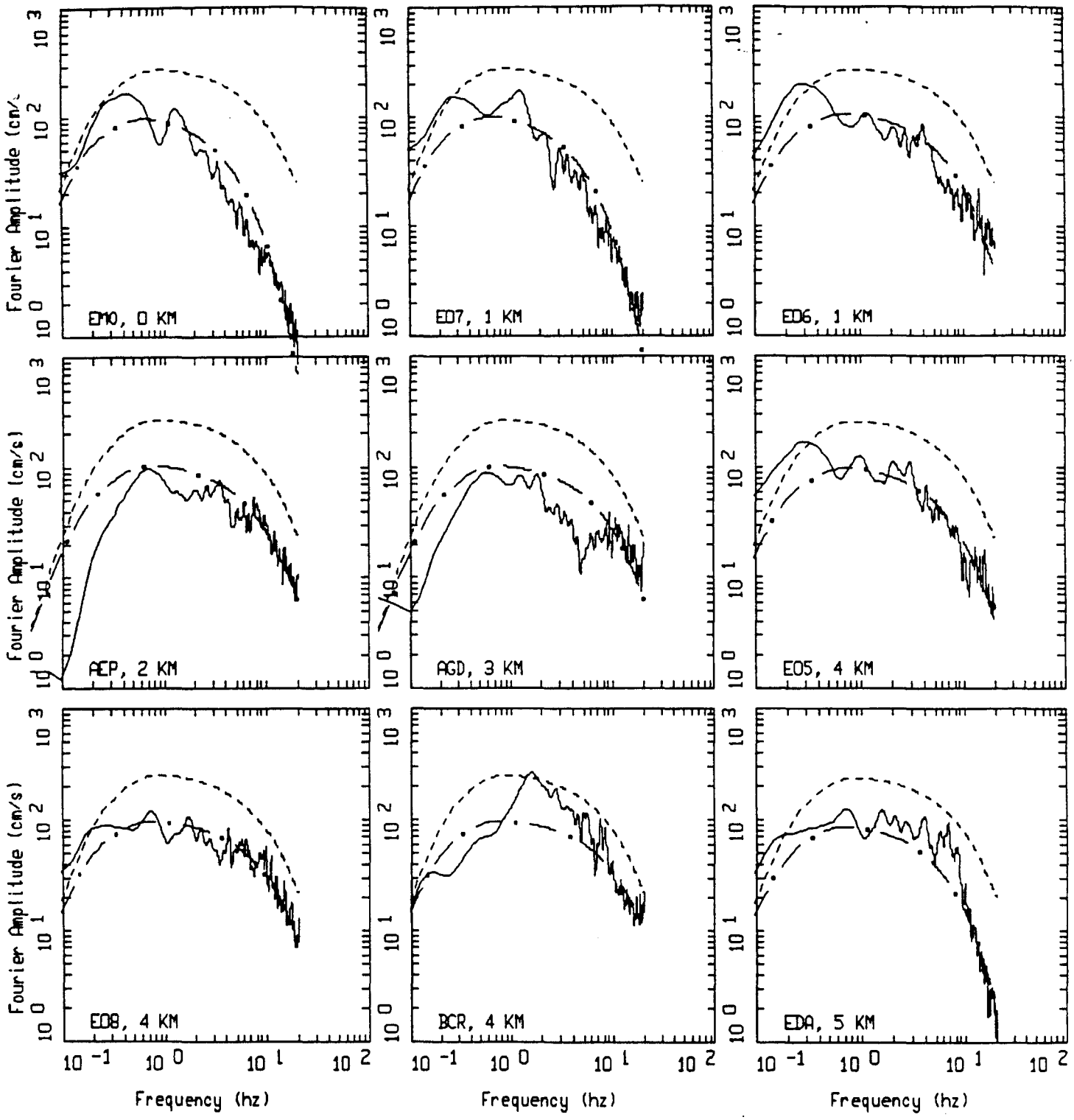

IMPERIAL VALLEY MAINSHOCK, M=6.4, PAGE 1 OF 4.
35 SITES.

Figure Set 5.105

LEGEND

——— DATA

- - - - - INITIAL MODEL

— • — FINAL MODEL

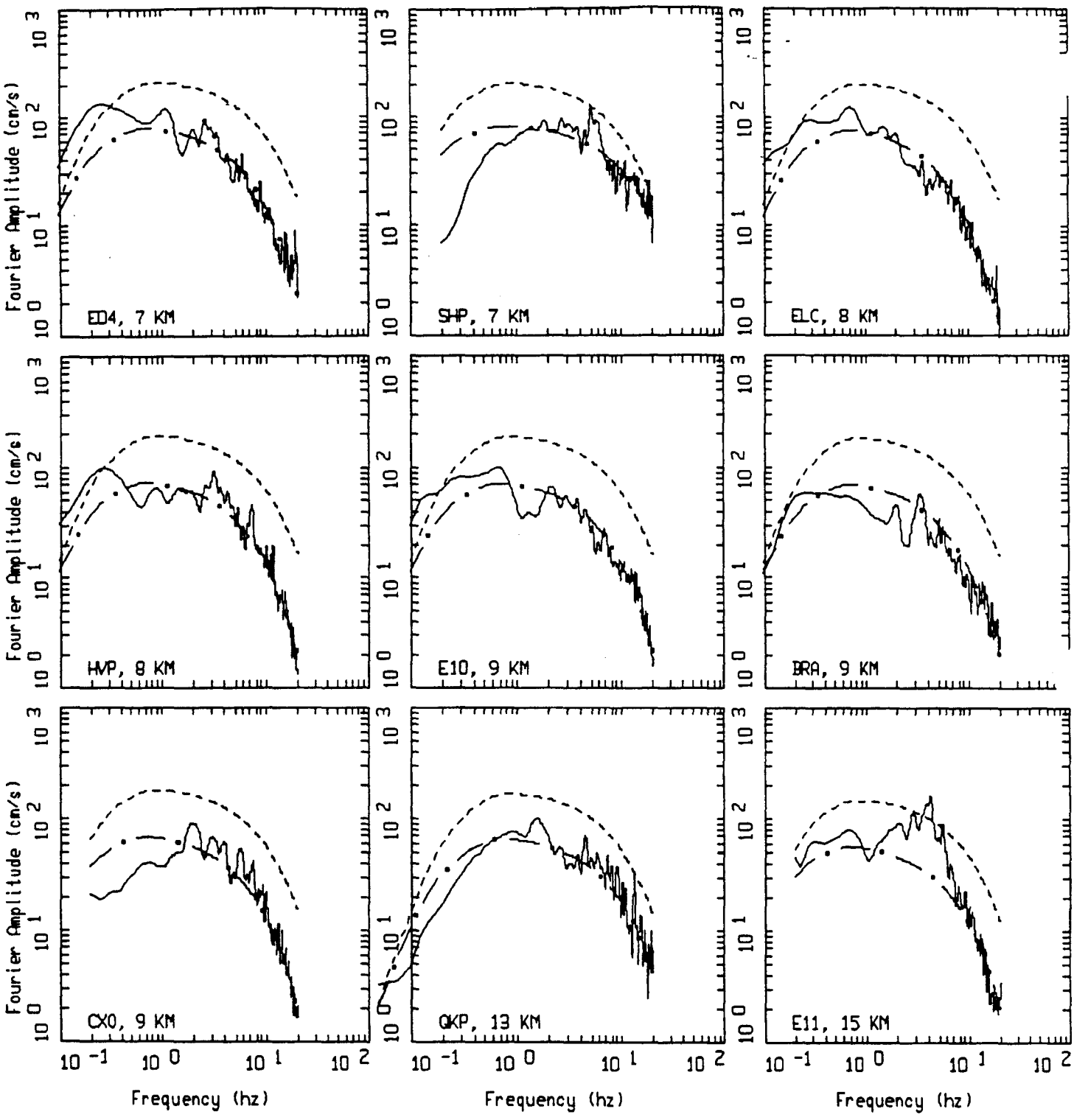

IMPERIAL VALLEY MAINSHOCK, M=6.4, PAGE 2 OF 4.
35 SITES.

LEGEND

——— DATA

- - - - - INITIAL MODEL

—•— FINAL MODEL

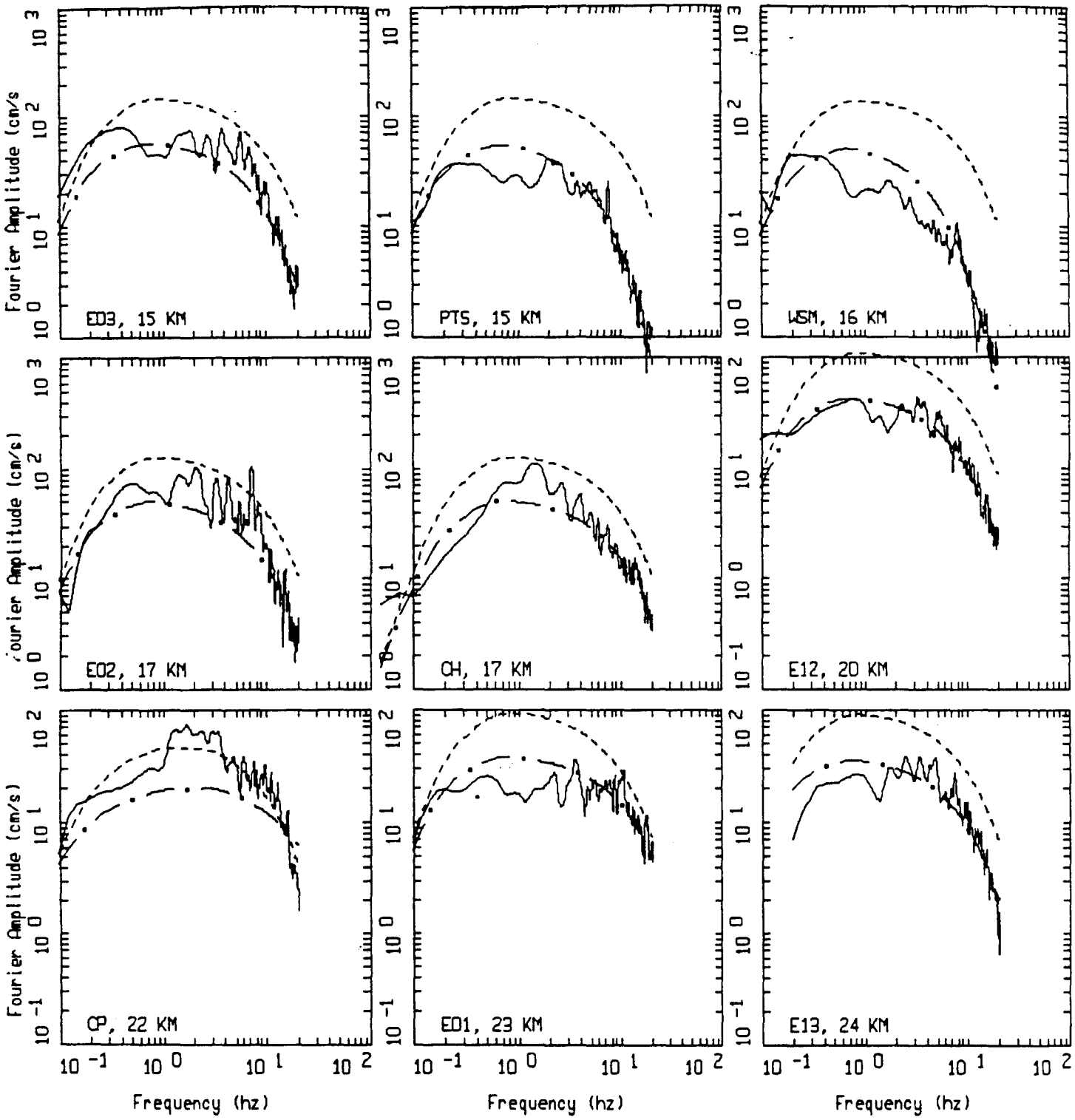

IMPERIAL VALLEY MAINSHOCK, M=6.4, PAGE 3 OF 4.
35 SITES.

LEGEND

——— DATA

- - - - - INITIAL MODEL

— • — FINAL MODEL

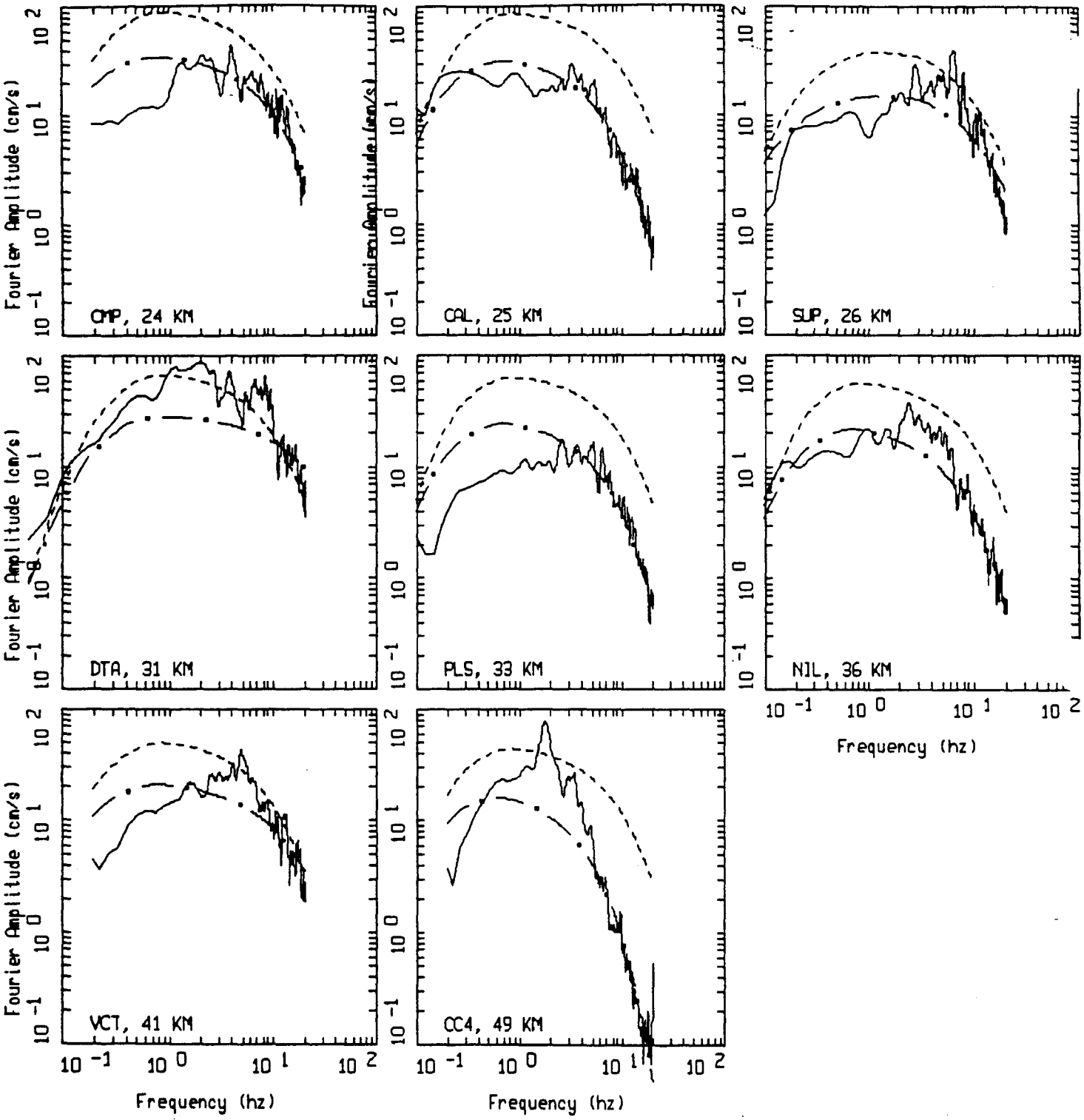

IMPERIAL VALLEY MAINSHOCK, M=6.4, PAGE 4 OF 4.
35 SITES.

LEGEND

——— DATA

- - - - - INITIAL MODEL

—•— FINAL MODEL

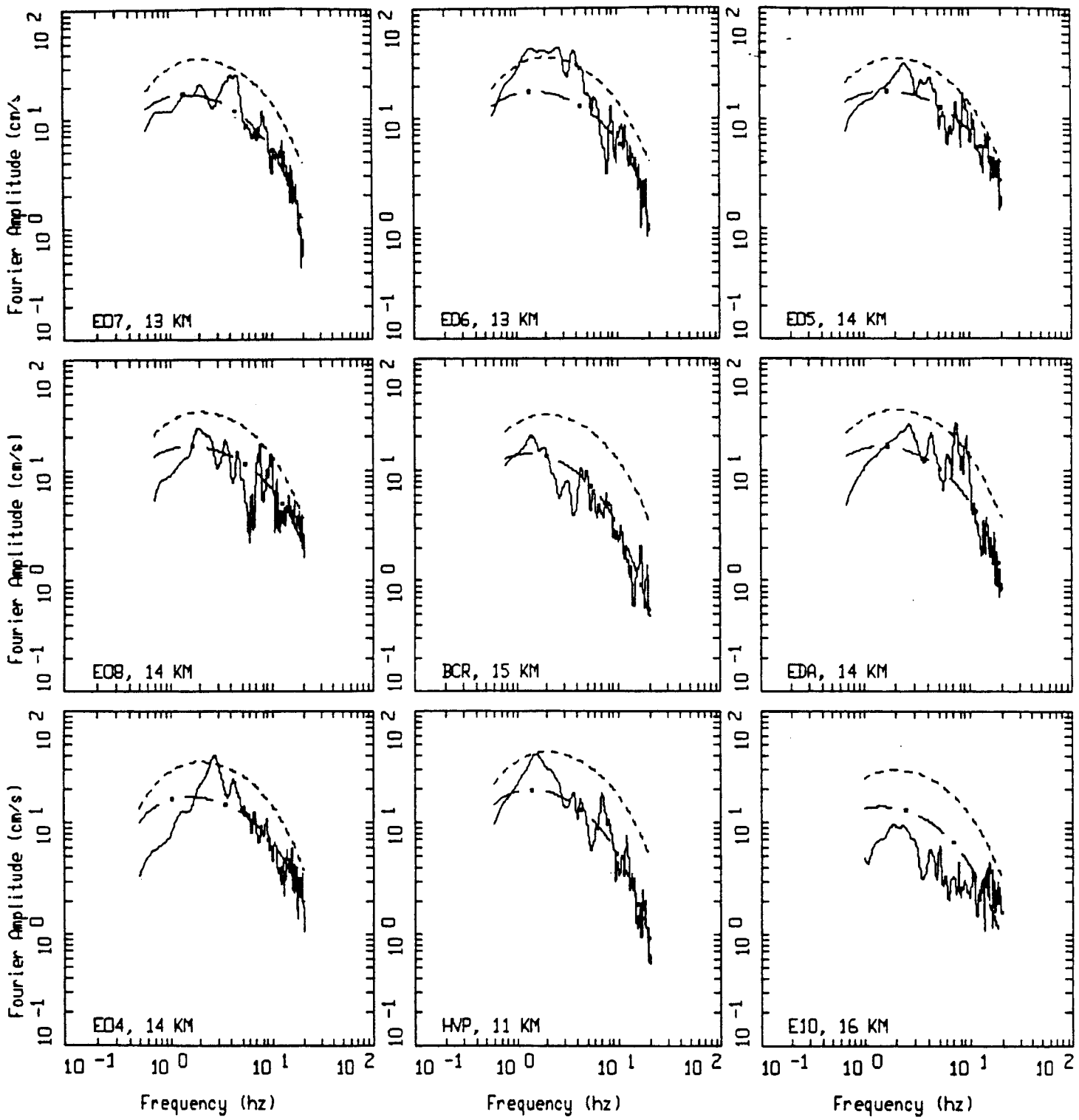

IMPERIAL VALLEY AFTERSHOCK, M=5.3, PAGE 1 OF 2.

Figure Set 5.106

LEGEND

——— DATA

- - - - - INITIAL MODEL

—— • —— FINAL MODEL

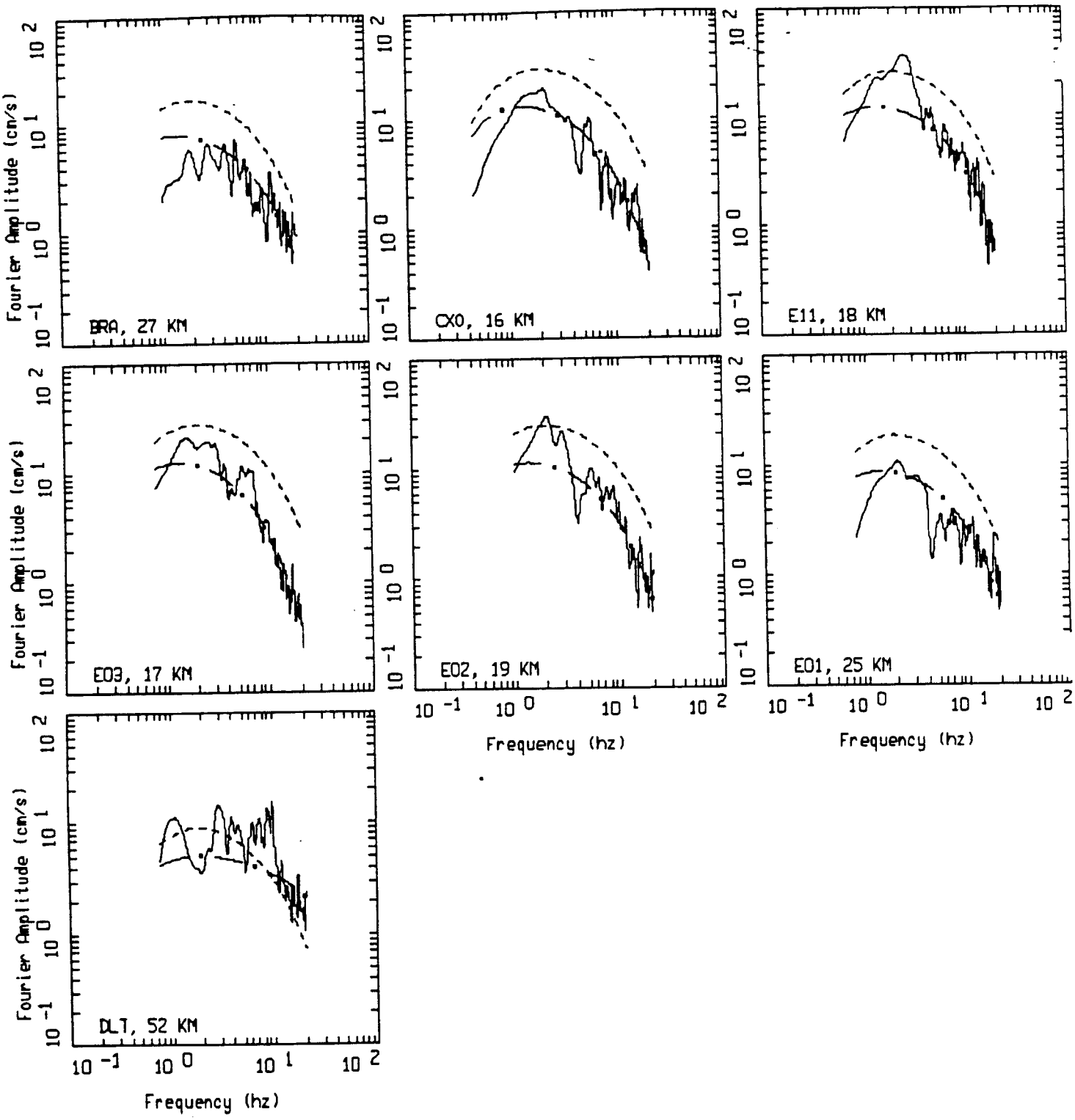

IMPERIAL VALLEY AFTERSHOCK, M=5.3, PAGE 2 OF 2.

LEGEND

——— DATA

- - - - - INITIAL MODEL

— • — FINAL MODEL

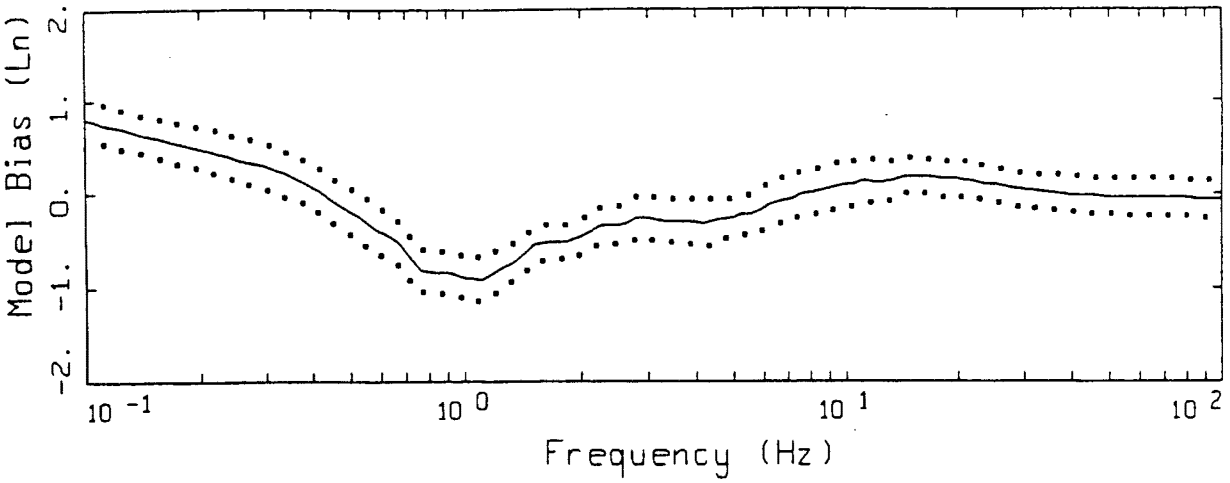

LEGEND
MODELING BIAS
90% CONFIDENCE INTERVAL OF MODELING BIAS
90% CONFIDENCE INTERVAL OF MODELING BIAS

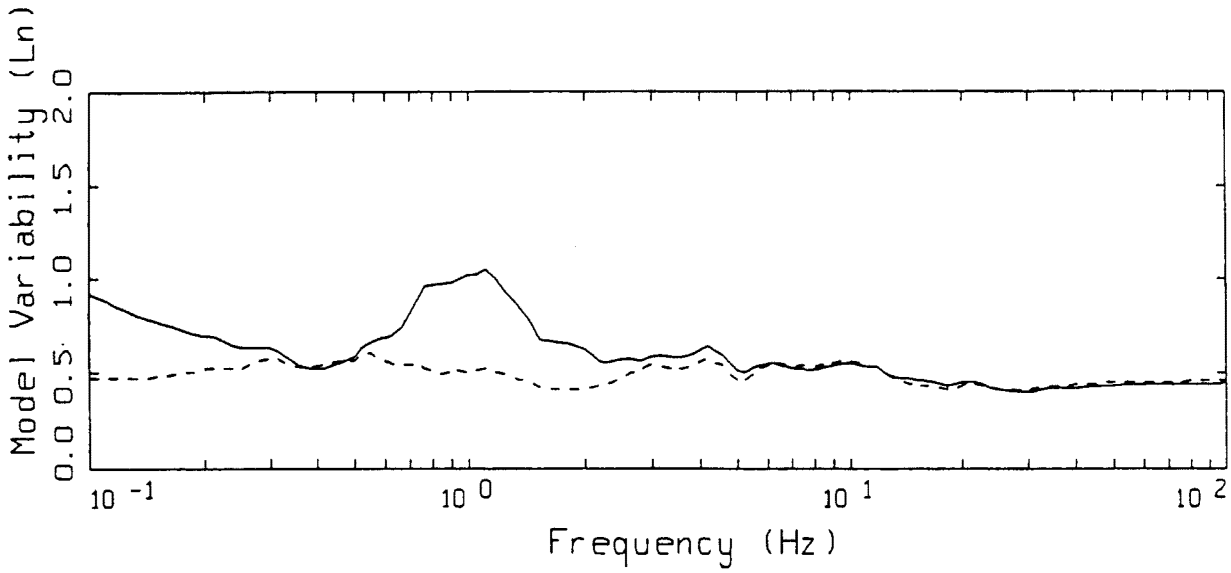

LEGEND
MEAN=0.0
BIAS CORRECTED

IMPERIAL VALLEY AS POINT-SOURCE
NONLINEAR, ALL 16 SITES

Figure 5.107

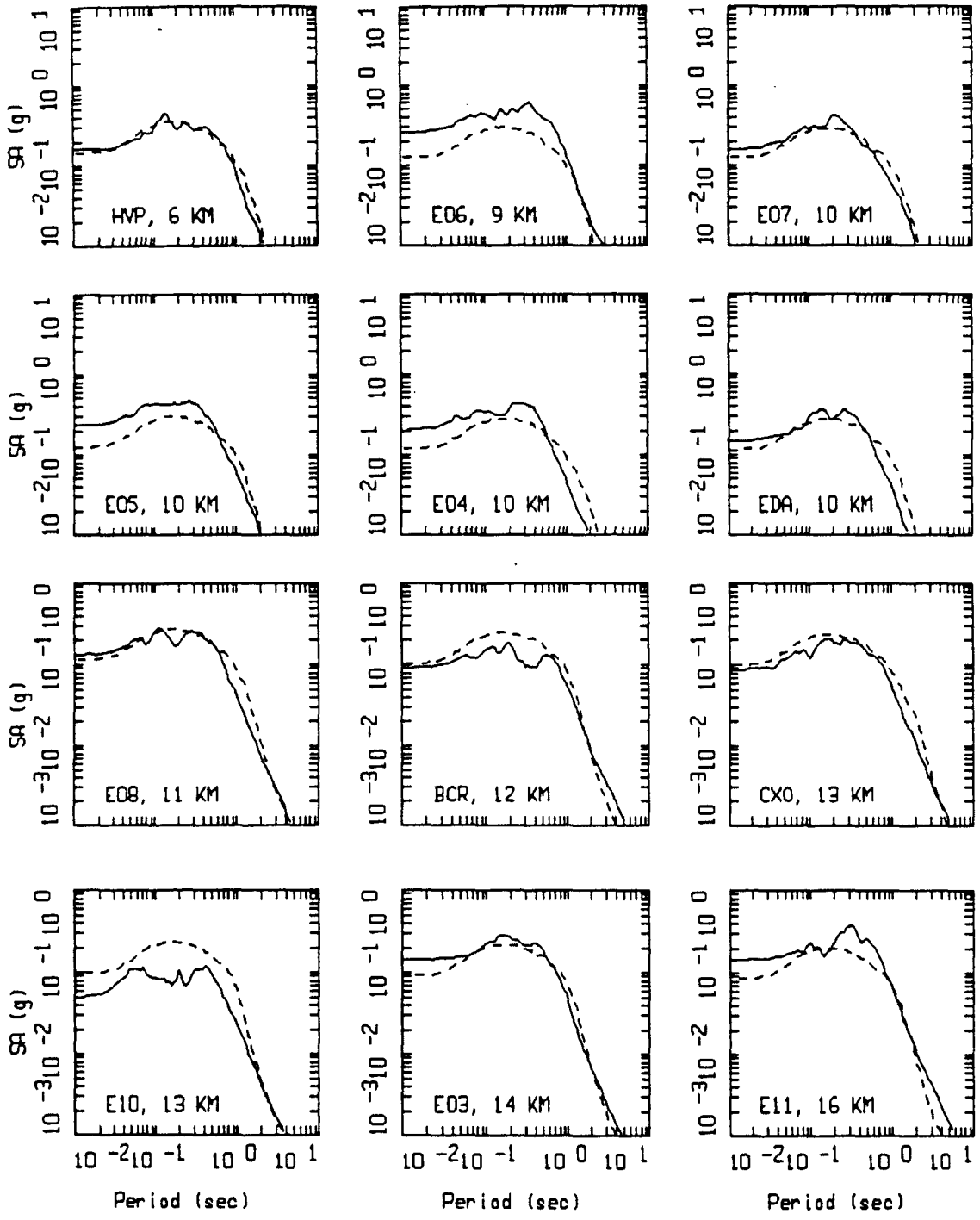

IMPERIAL VALLEY AS, POINT SOURCE MODELING, PAGE 1 OF 2.
NONLINEAR.

Figure Set 5.108

LEGEND

——— DATA

----- MODEL

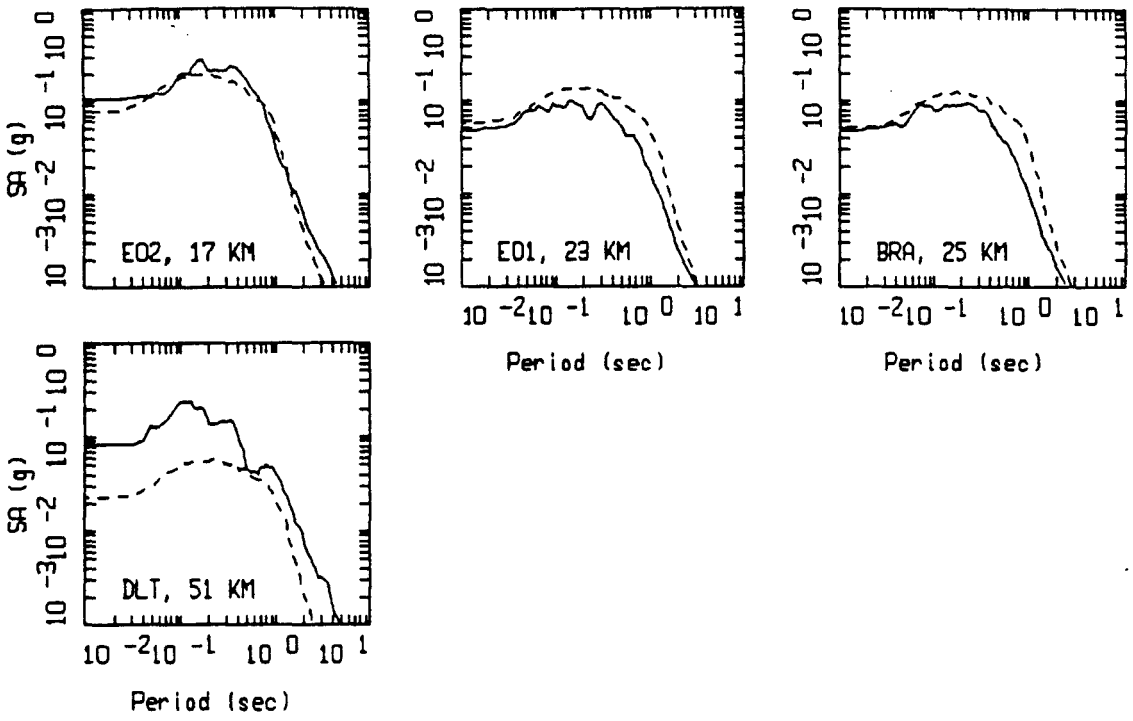

IMPERIAL VALLEY AS, POINT SOURCE MODELING, PAGE 2 OF 2.
NONLINEAR.

LEGEND

——— DATA

- - - - - MODEL

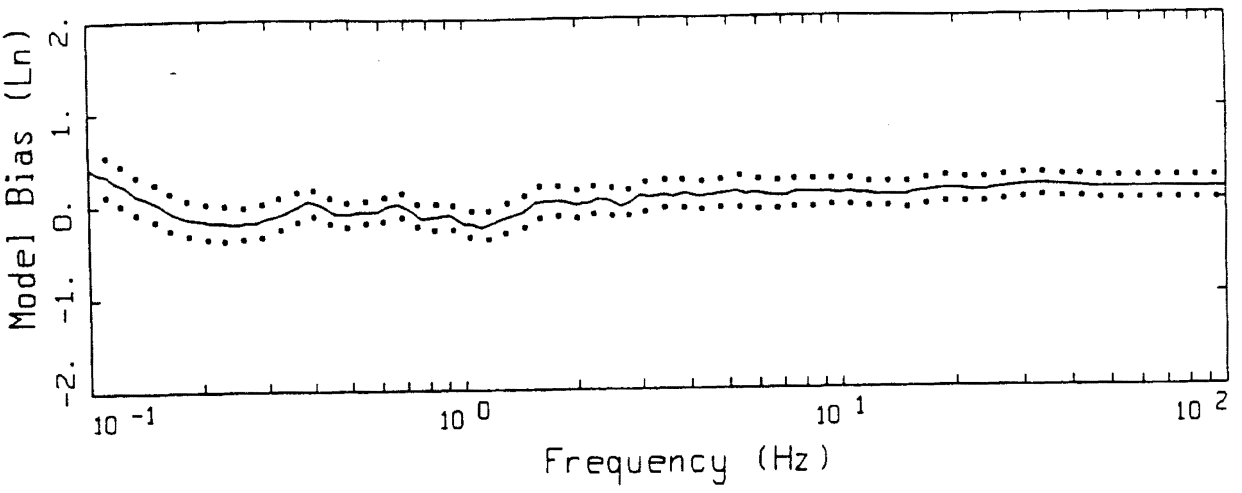

LEGEND
——— MODELING BIAS
..... 90% CONFIDENCE INTERVAL OF MODELING BIAS
..... 90% CONFIDENCE INTERVAL OF MODELING BIAS

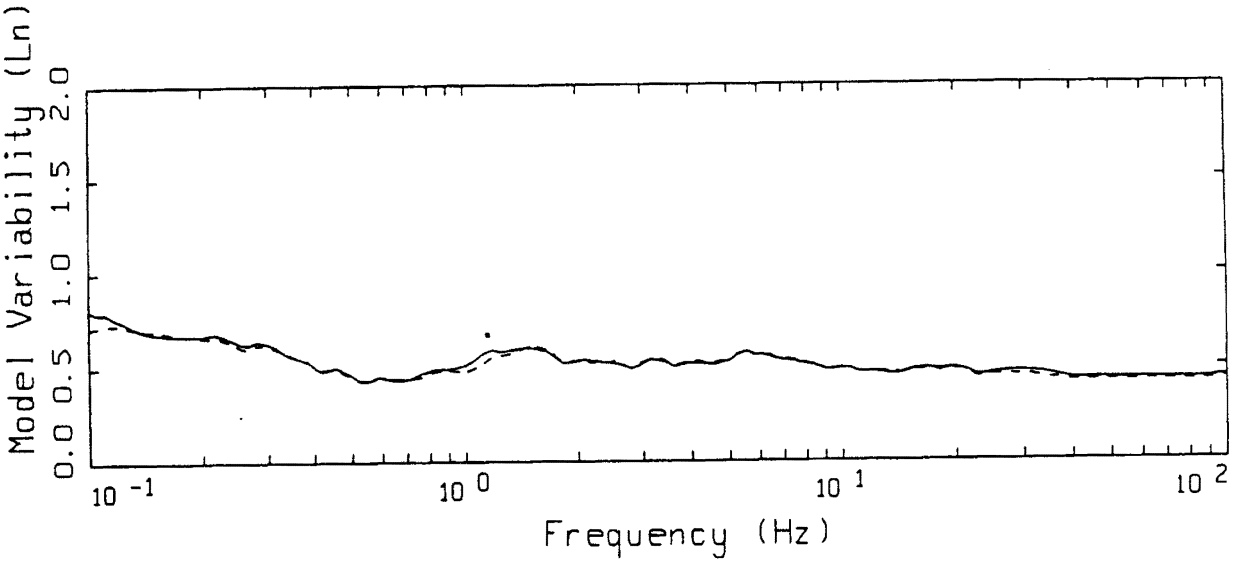

LEGEND
——— MEAN=0.0
------ BIAS CORRECTED

IMPERIAL VALLEY POINT-SOURCE
NONLINEAR, ALL 35 SITES

Figure 5.109

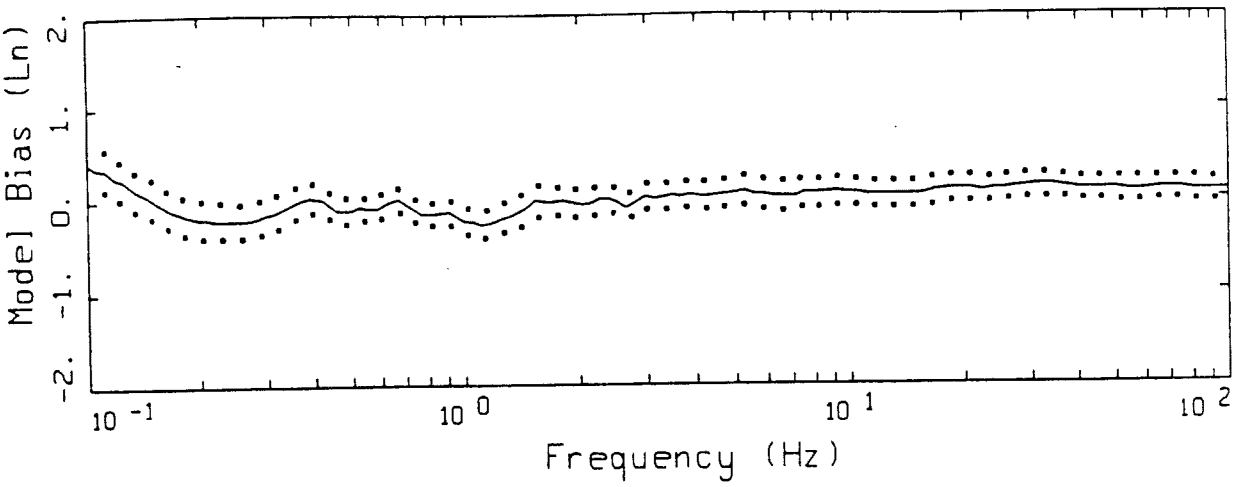

LEGEND
——— MODELING BIAS
. . .. . . 90% CONFIDENCE INTERVAL OF MODELING BIAS
. . .. 90% CONFIDENCE INTERVAL OF MODELING BIAS

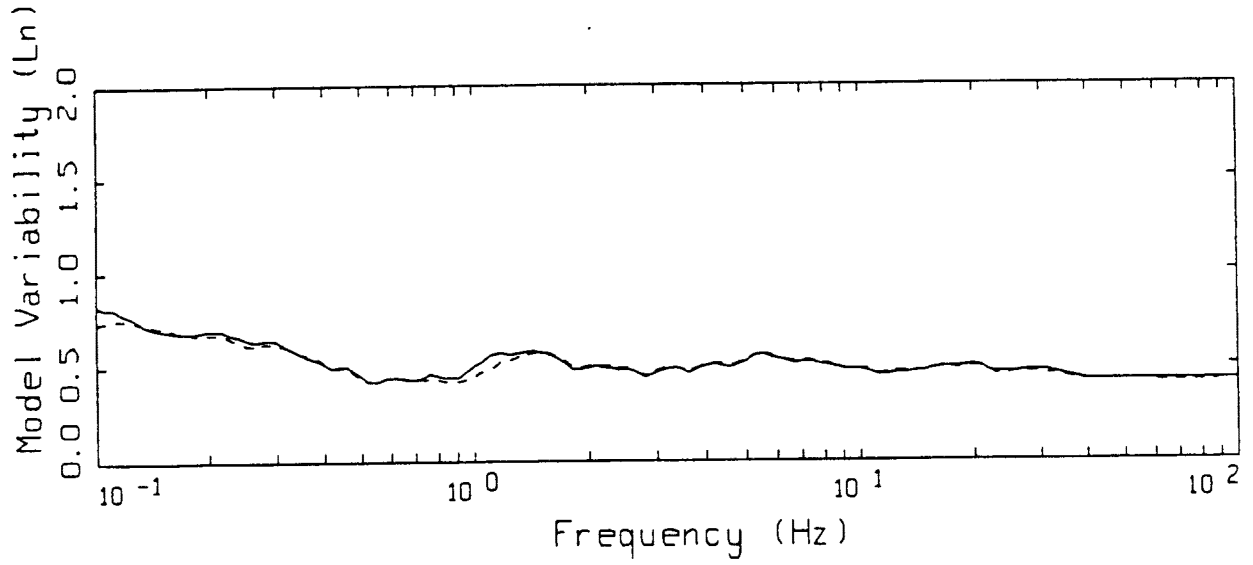

LEGEND
——— MEAN=0.0
------ BIAS CORRECTED

IMPERIAL VALLEY POINT-SOURCE
NONLINEAR, 33 SOIL SITES

Figure 5.110

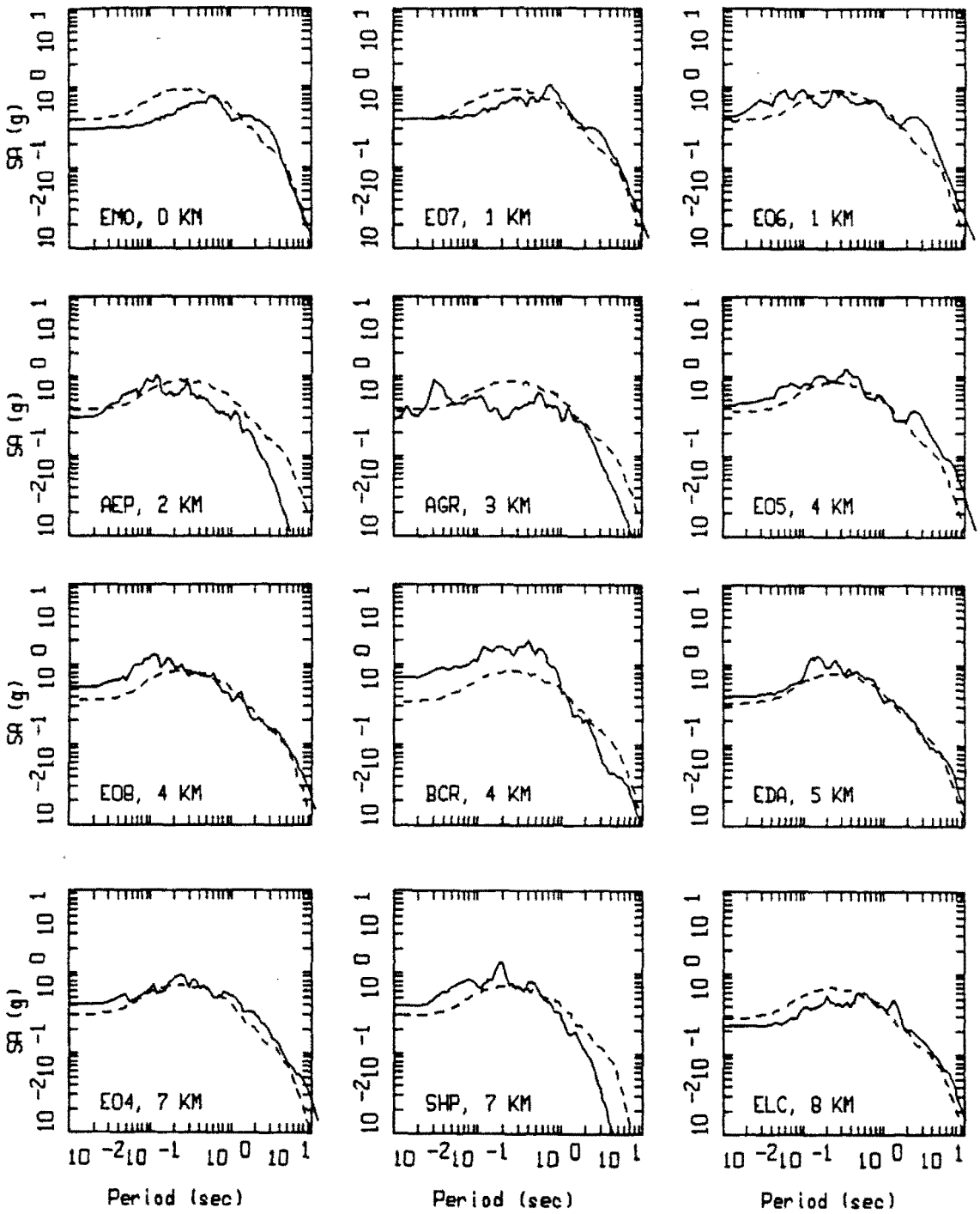

IMPERIAL VALLEY, POINT SOURCE MODELING, PAGE 1 OF 3.
NONLINEAR.

LEGEND
——— DATA
----- MODEL

Figure Set 5.111

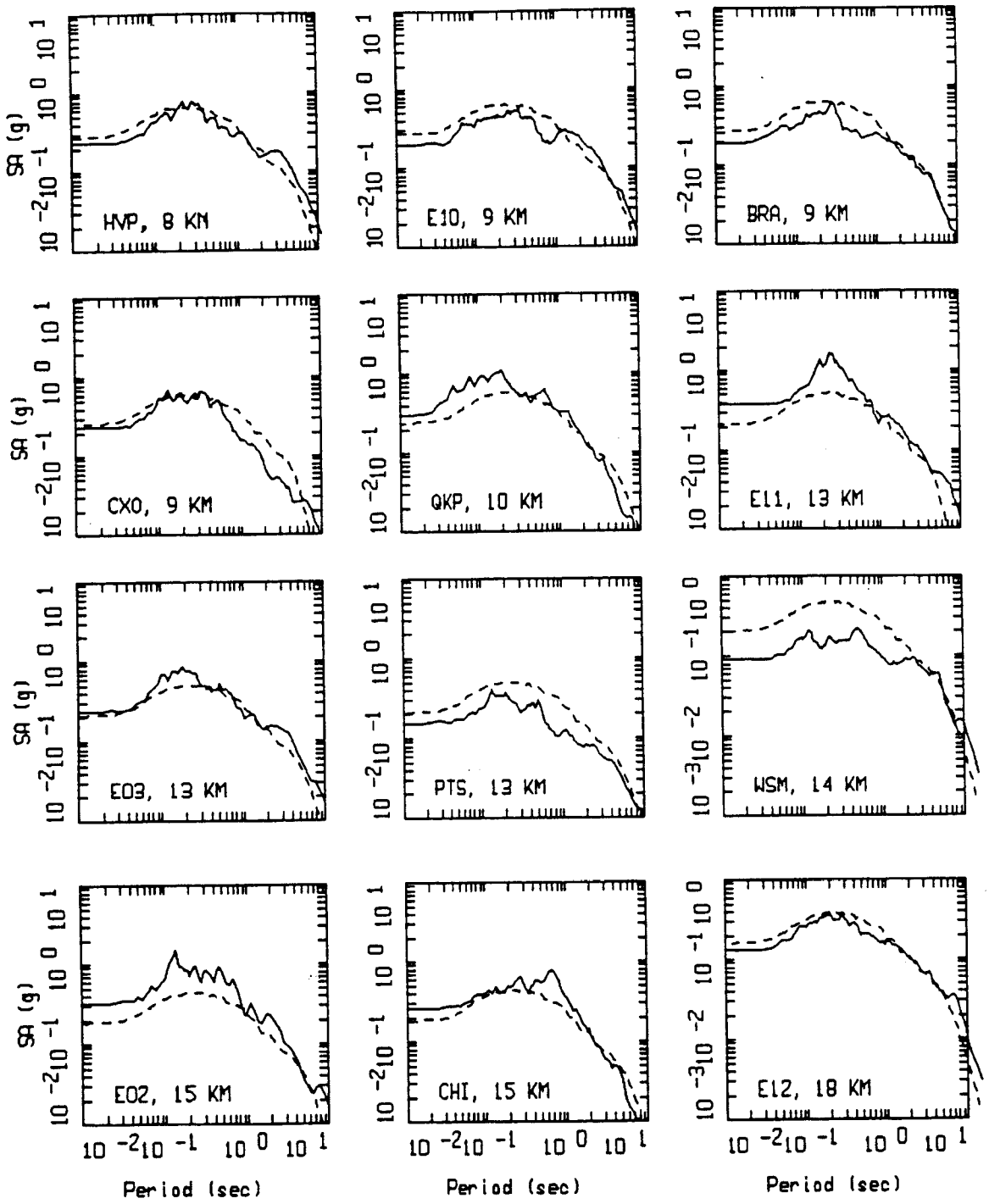

IMPERIAL VALLEY, POINT SOURCE MODELING, PAGE 2 OF 3.
NONLINEAR.

LEGEND

——— DATA

----- MODEL

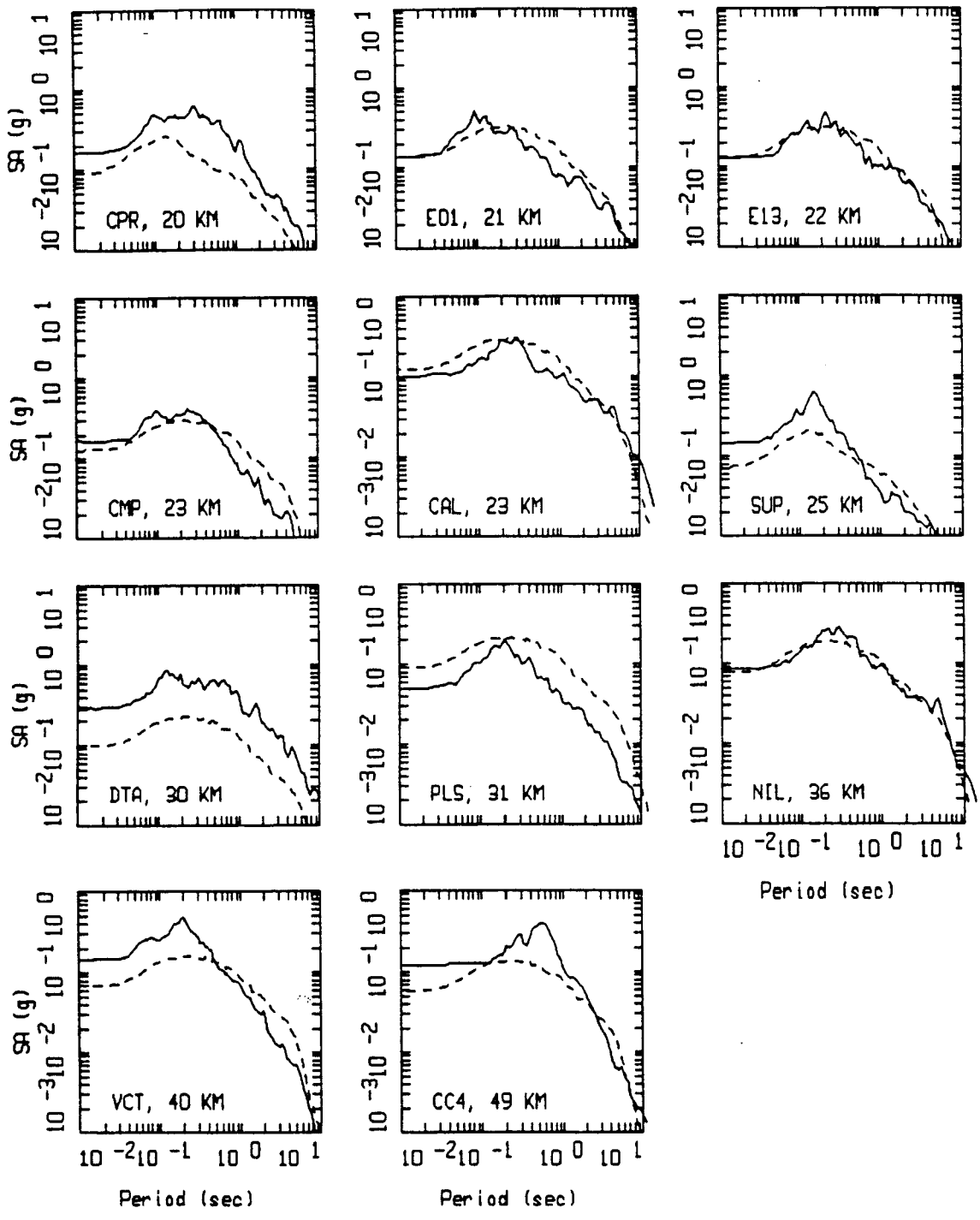

IMPERIAL VALLEY, POINT SOURCE MODELING, PAGE 3 OF 3.
NONLINEAR.

LEGEND

——— DATA

----- MODEL

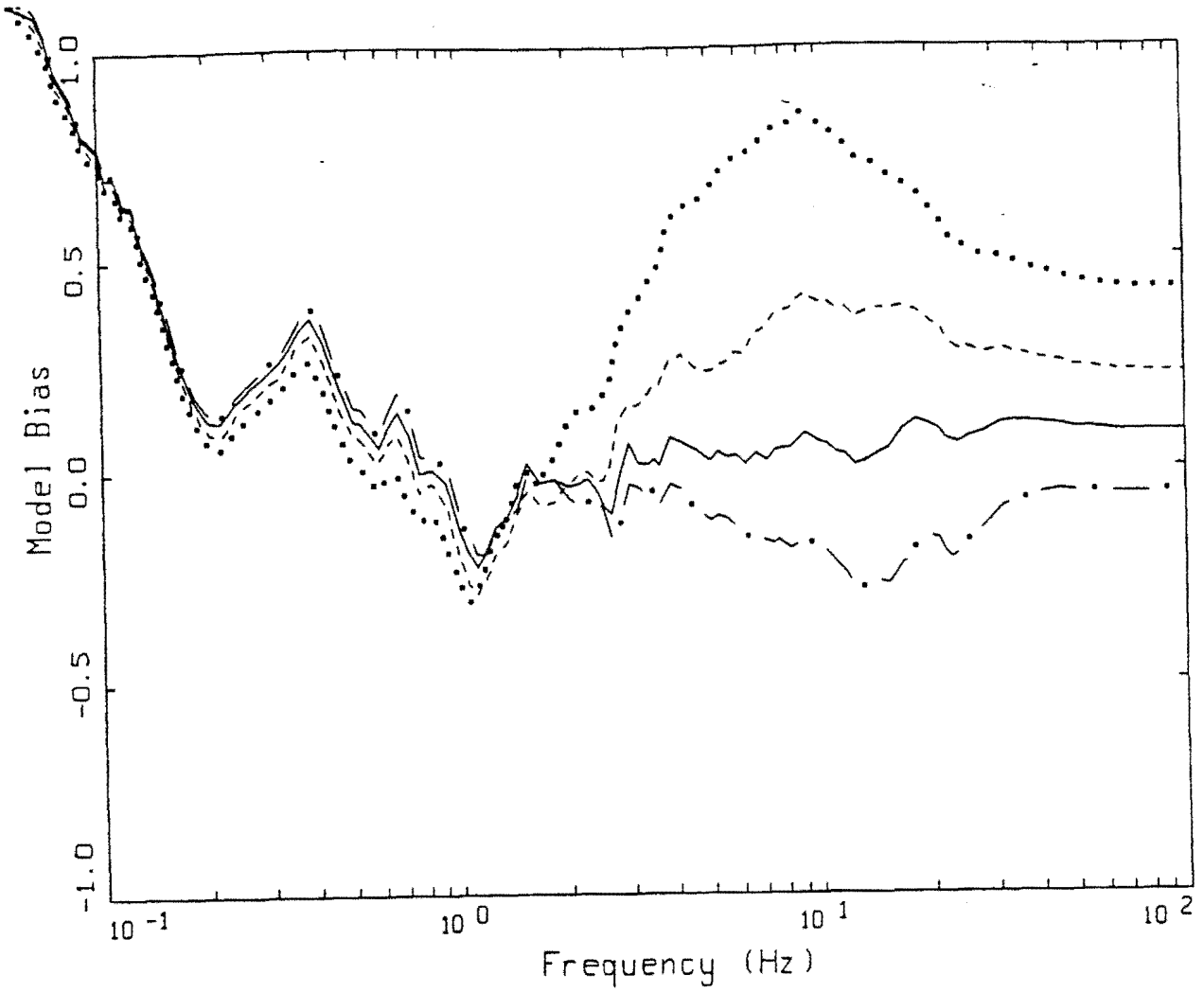

IMPERIAL VALLEY POINT SOURCE, MODELING BIAS
NONLINEAR, ALL 15 EC SITES TO 15 KM

LEGEND

——— MODELING BIAS (IMPERIAL VALLEY CURVES)

. . . . MODELING BIAS (EPRI CURVES)

- - - - - MODELING BIAS (GENERIC DEEP SOIL CURVES)

— . — MODELING BIAS (LINEAR ANALYSIS, KAPPA = 0.03 SEC)

Figure 5.112

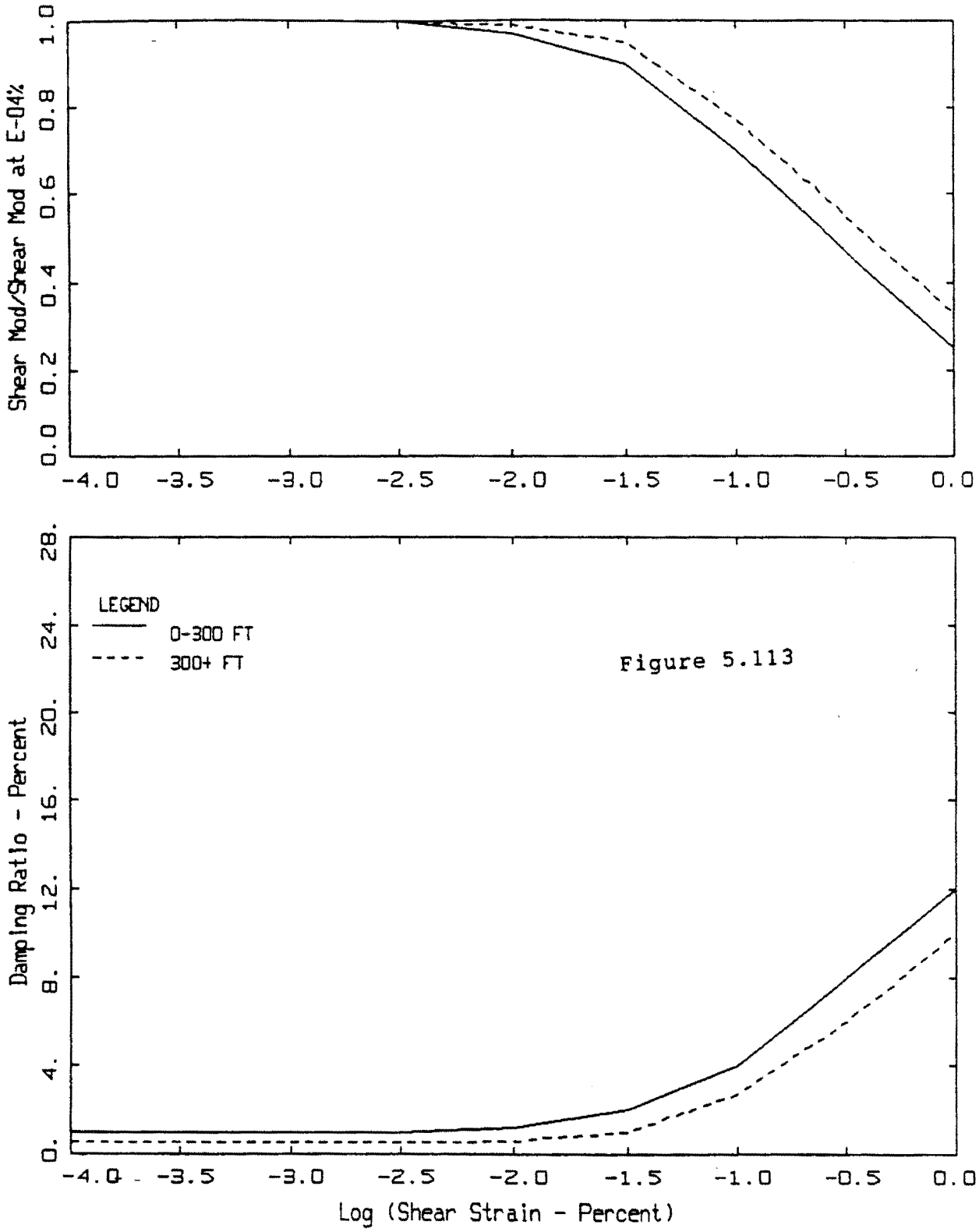

Figure 5.113

MODULUS REDUCTION AND DAMPING CURVES FOR EL CENTRO

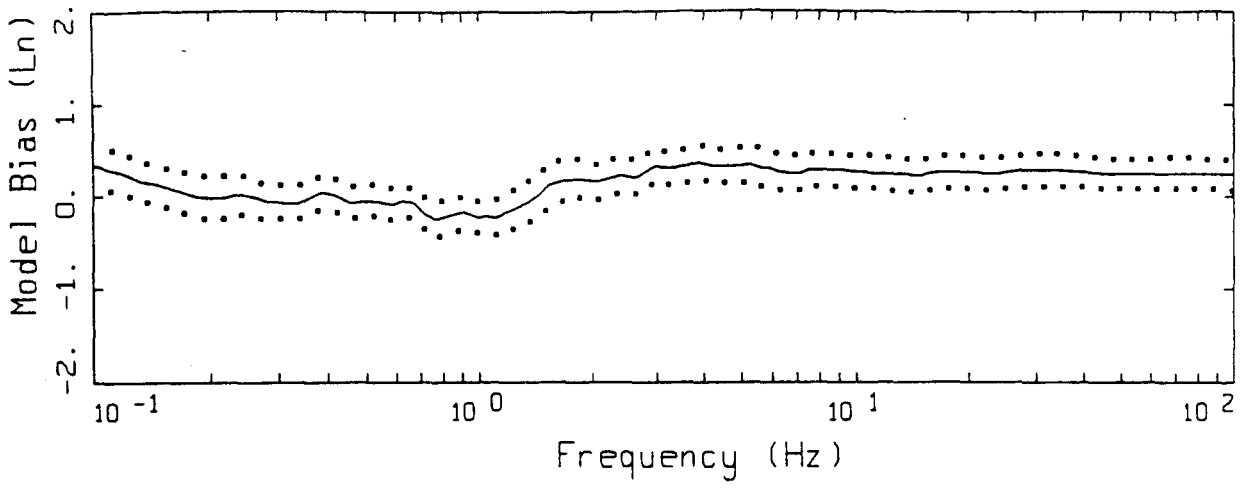

LEGEND
MODELING BIAS
90% CONFIDENCE INTERVAL OF MODELING BIAS
90% CONFIDENCE INTERVAL OF MODELING BIAS

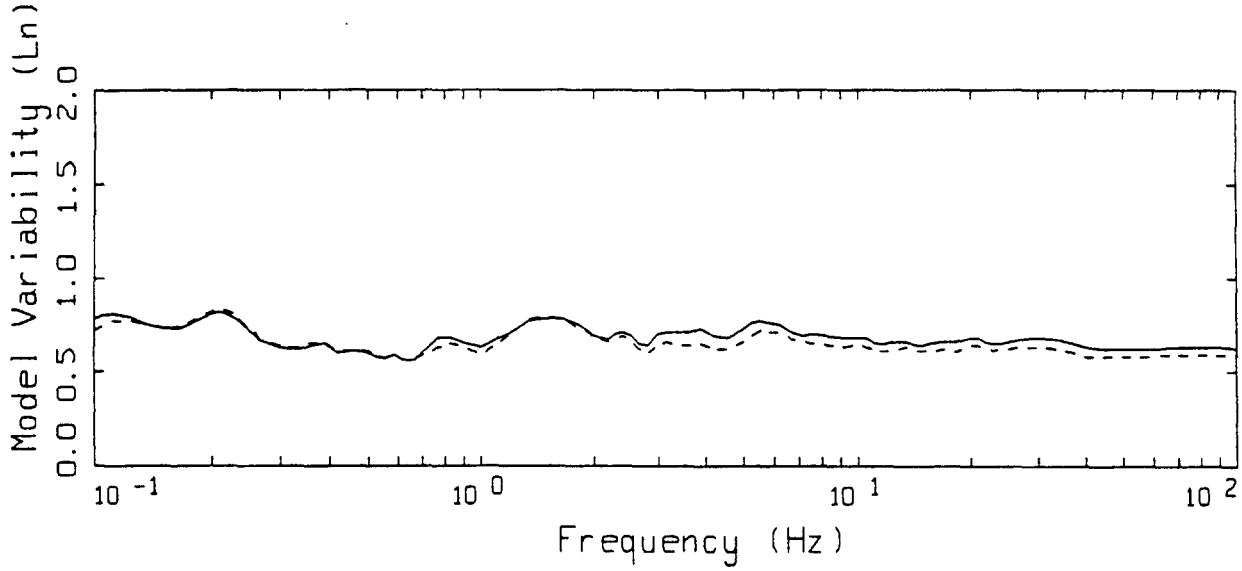

LEGEND
MEAN=0.0
BIAS CORRECTED

IMPERIAL VALLEY FINITE-SOURCE
NONLINEAR, ALL 35 SITES

Figure 5.114

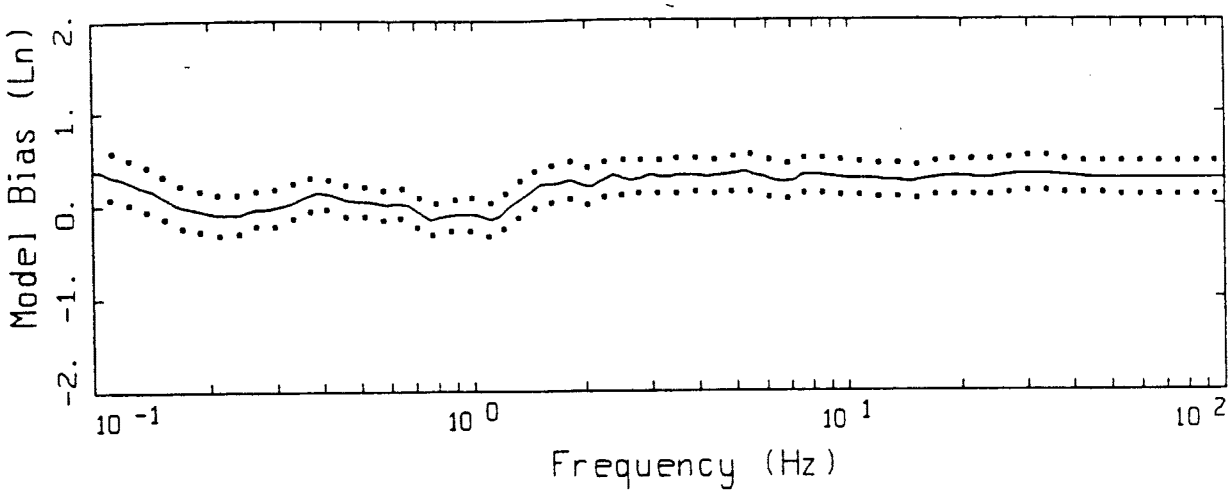

LEGEND
MODELING BIAS
90% CONFIDENCE INTERVAL OF MODELING BIAS
90% CONFIDENCE INTERVAL OF MODELING BIAS

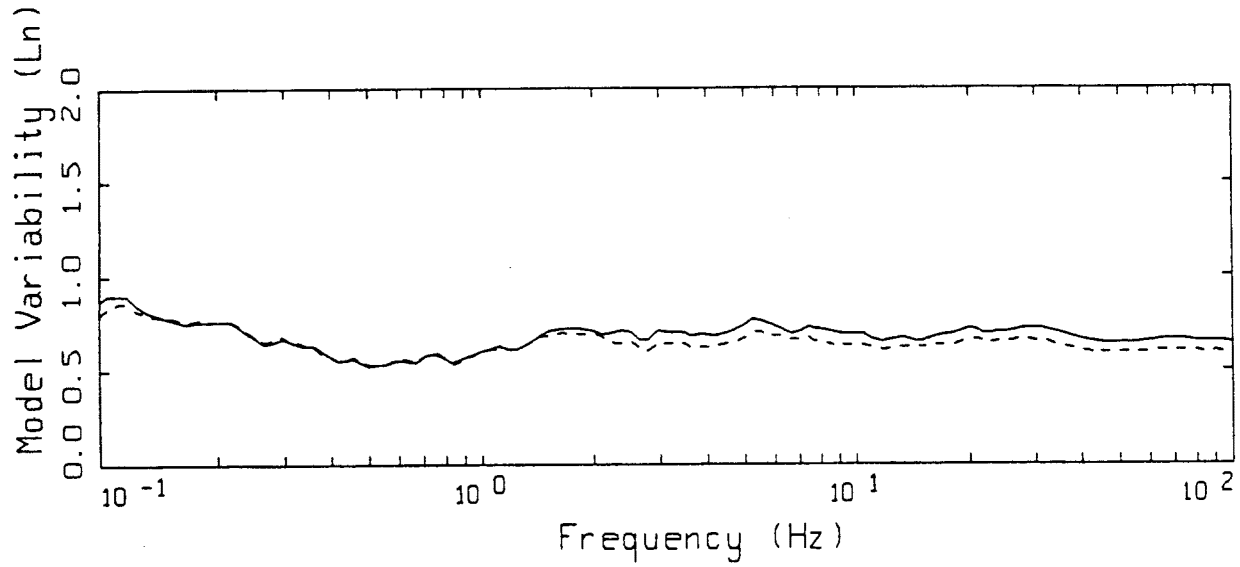

LEGEND
MEAN=0.0
BIAS CORRECTED

IMPERIAL VALLEY FINITE-SOURCE
NONLINEAR, 33 SOIL SITES

Figure 5.115

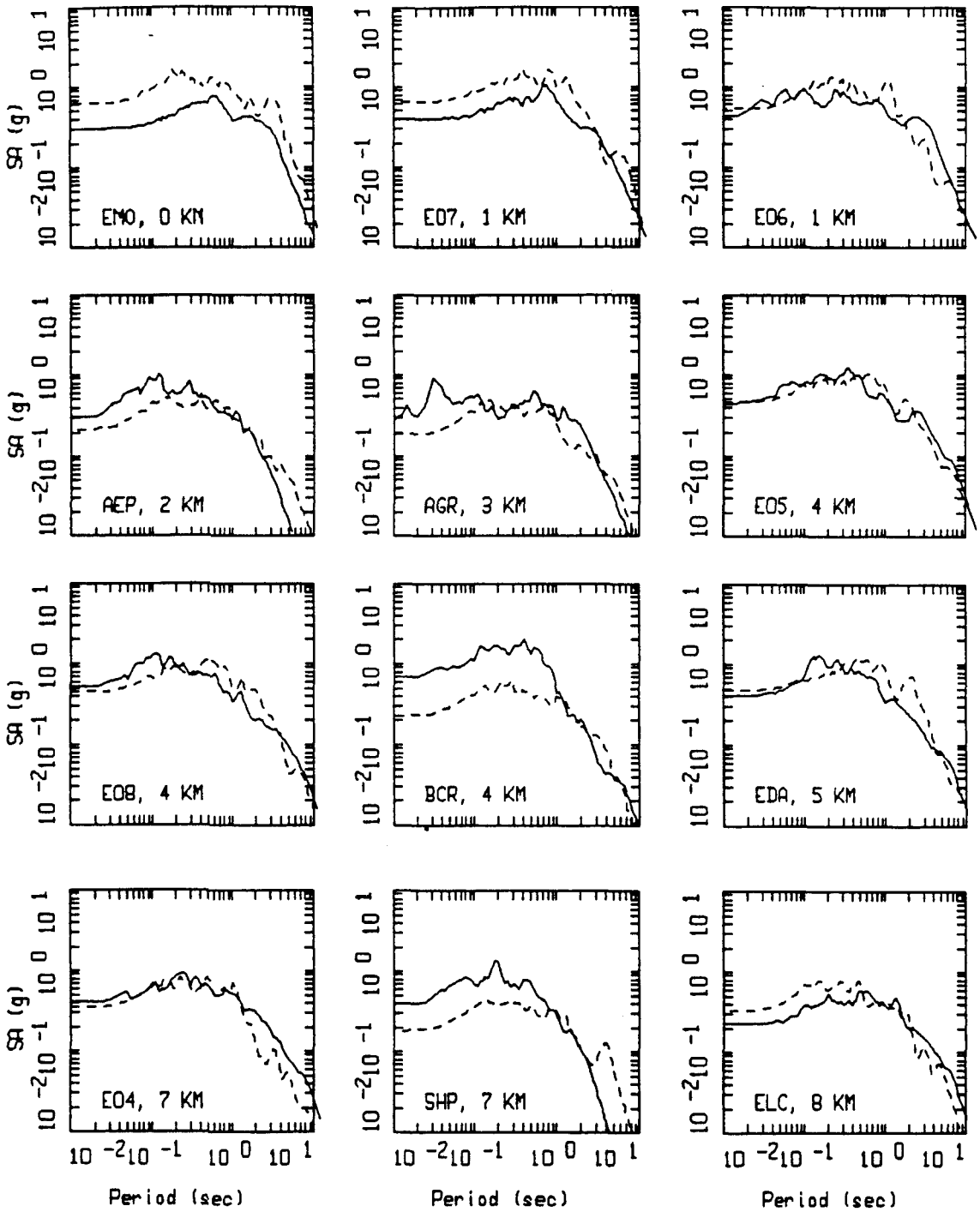

IMPERIAL VALLEY, FINITE SOURCE MODELING, PAGE 1 OF 3.
NONLINEAR.

LEGEND
DATA
MODEL

Figure Set 5.116

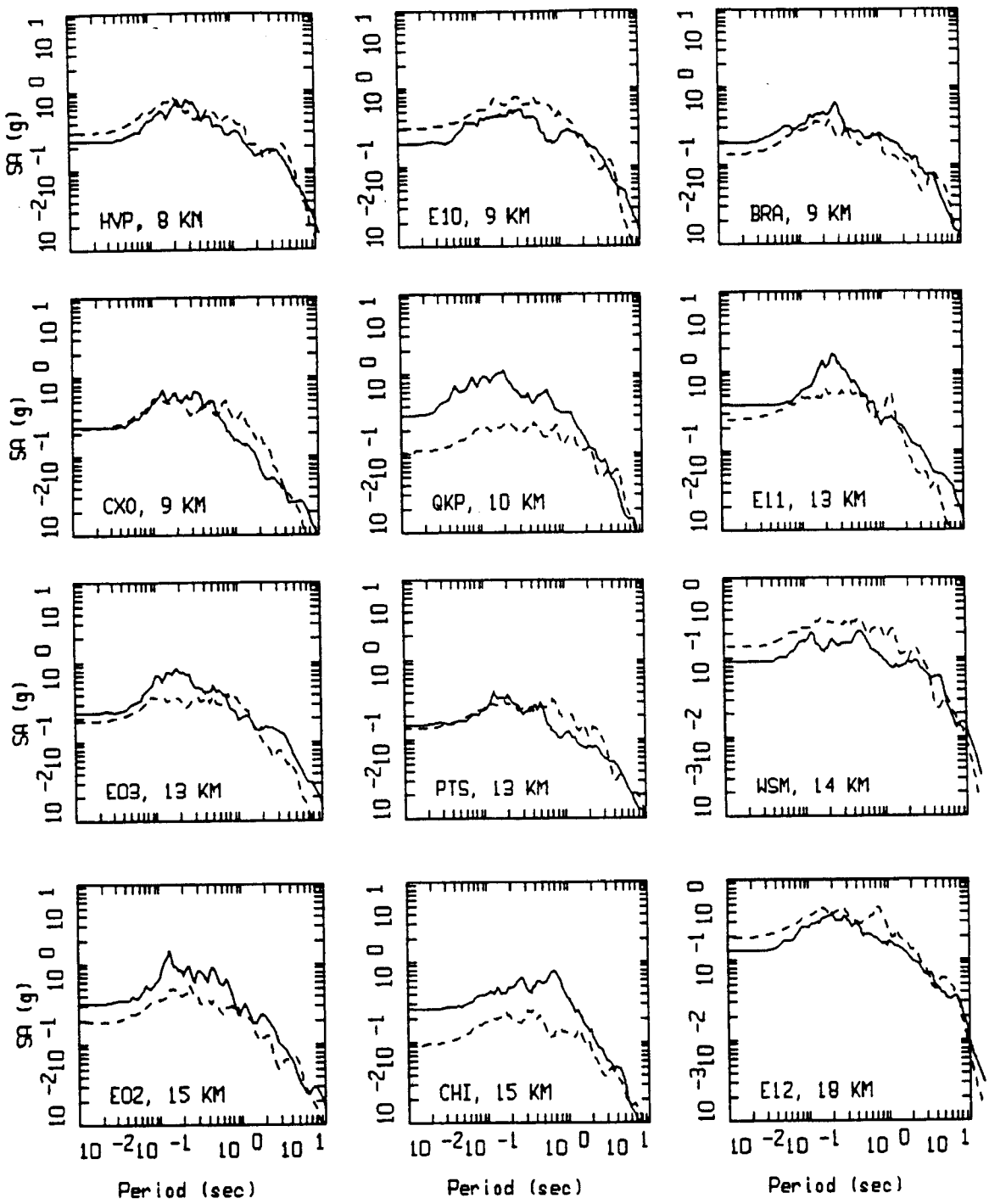

IMPERIAL VALLEY, FINITE SOURCE MODELING, PAGE 2 OF 3.
NONLINEAR.

LEGEND

——— DATA

----- MODEL

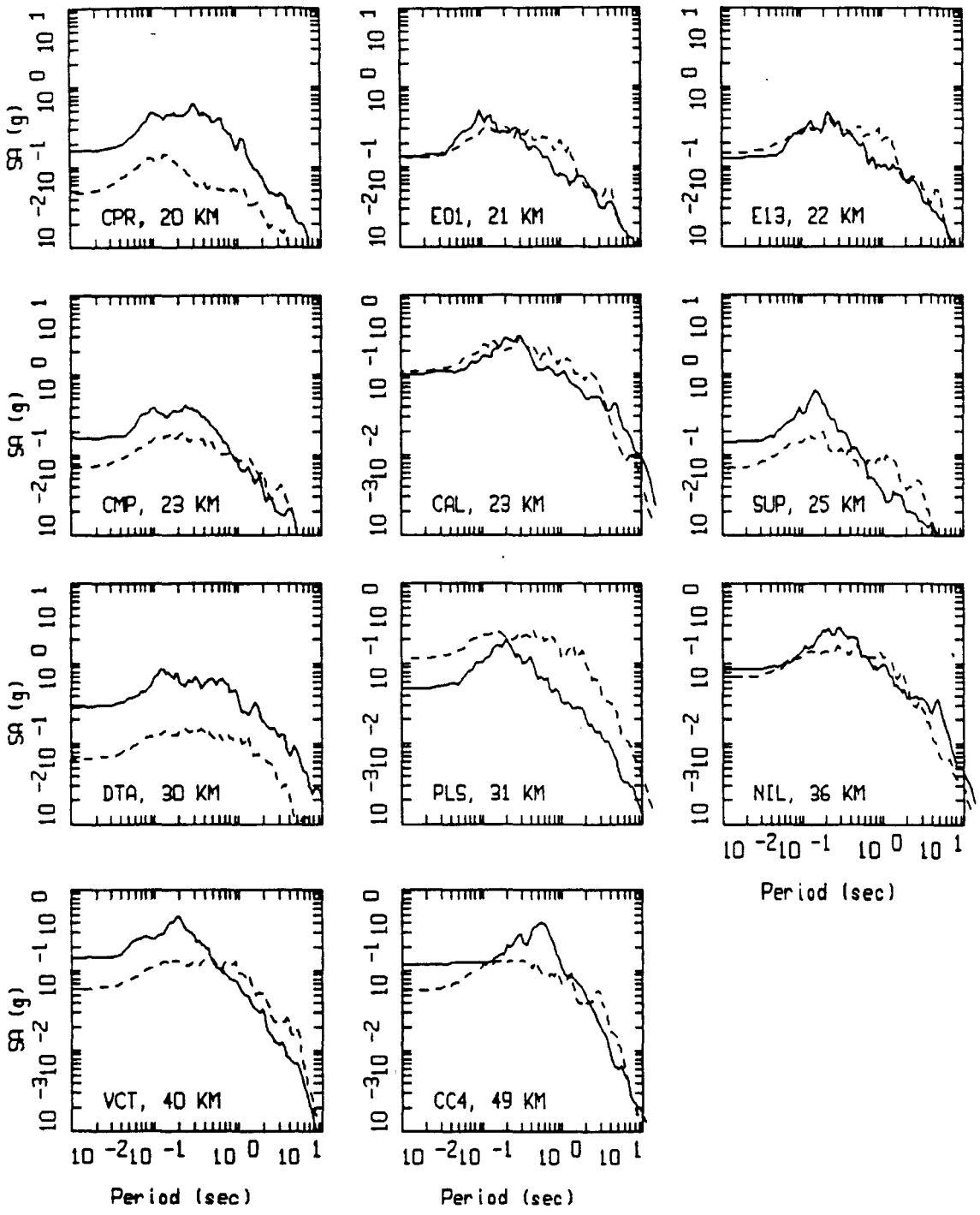

IMPERIAL VALLEY, FINITE SOURCE MODELING, PAGE 3 OF 3.
NONLINEAR.

LEGEND

——— DATA

- - - - - MODEL

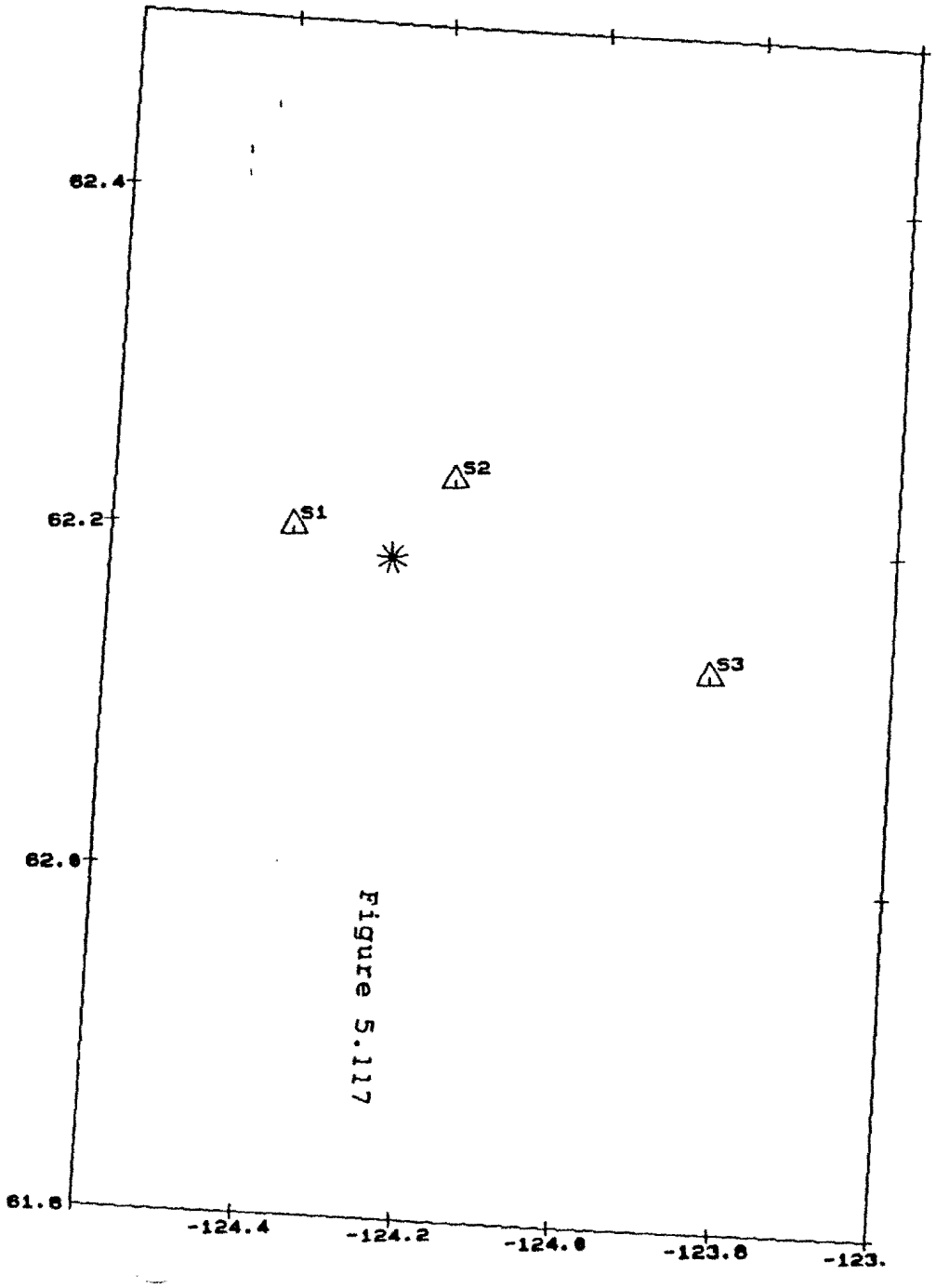
EPICENTER
0 10
kilometers
62.4
62.2
62.0
61.8
-124.4
-124.2
-124.0
-123.8
-123.
S1
S2
S3
EQ3D-V4.00 FILE: SITES.MP2 EPICENT.MP2
. SCA:500000 MFAC:1.0 XFAC:1.0 Nm=4 Nx=0

Figure 5.117

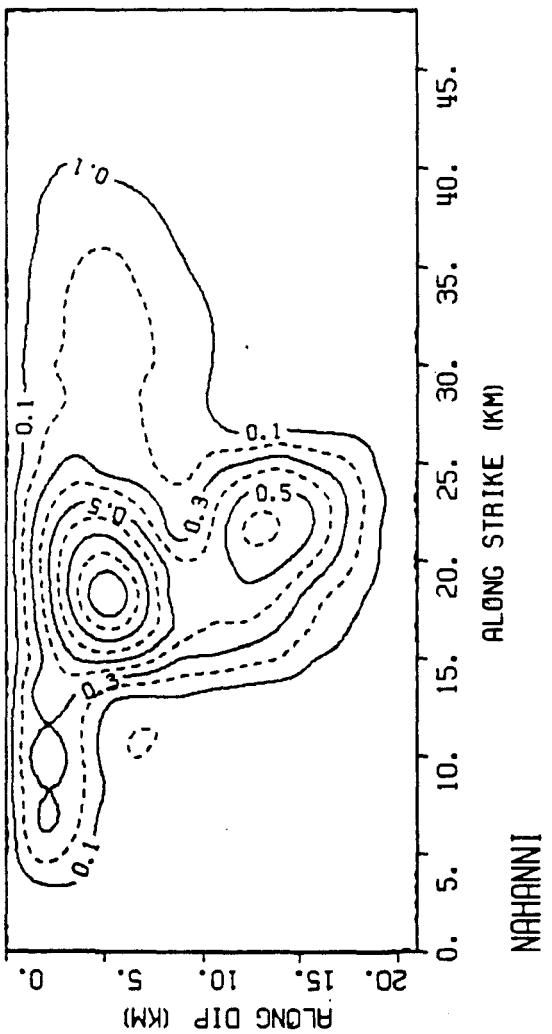
NAHANNI
ALONG STRIKE (KM)
ALONG DIP (KM)
0.
5.
10.
15.
20.
25.
30.
35.
40.
45.
1.0
0.5
0.3
0.1

Figure 5.118

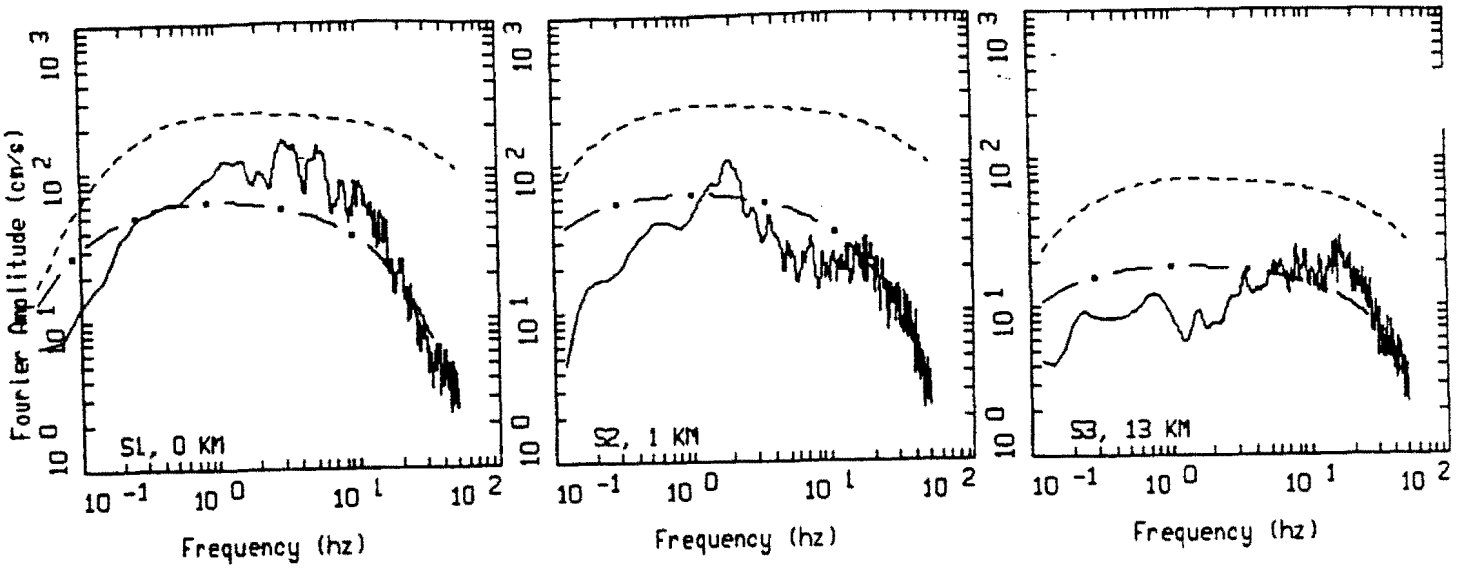

NAHANNI EARTHQUAKE 12/23/85, M=6.8.

LEGEND

——— DATA

- - - - - INITIAL MODEL

— • — FINAL MODEL

Figure 5.119

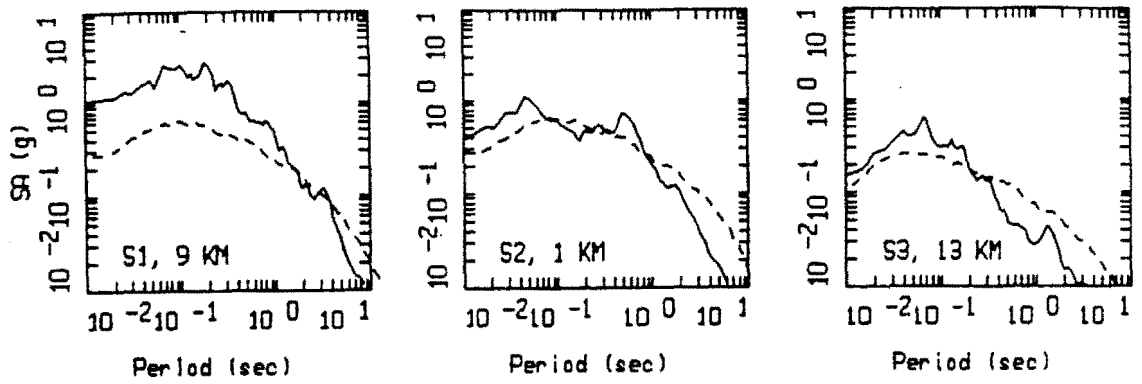

NAHANNI, POINT SOURCE MODELING, PAGE 1 OF 1.

LINEAR.

LEGEND

——— DATA

- - - - - MODEL

Figure 5.120

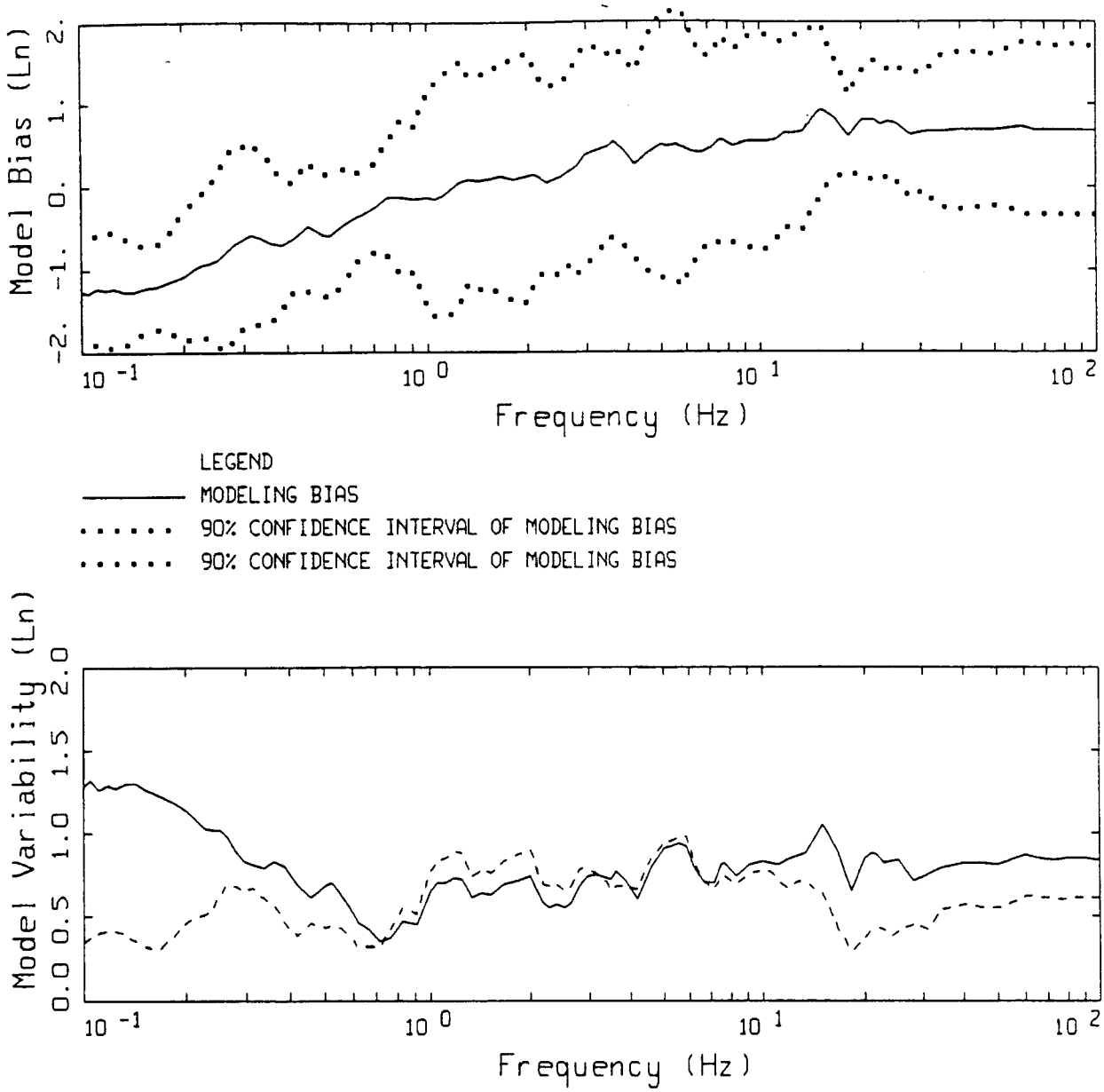
Model Bias (Ln)
2.
1.
0.
-1.
-2.
10 -1
10 0
10 1
10 2
Frequency (Hz)
LEGEND
MODELING BIAS
90% CONFIDENCE INTERVAL OF MODELING BIAS
90% CONFIDENCE INTERVAL OF MODELING BIAS
Model Variability (Ln)
0.0 0.5 1.0 1.5 2.0
10 -1
10 0
10 1
10 2
Frequency (Hz)
LEGEND
MEAN=0.0
BIAS CORRECTED
NAHANNI POINT-SOURCE
LINEAR, ALL 3 SITES

Figure 5.121

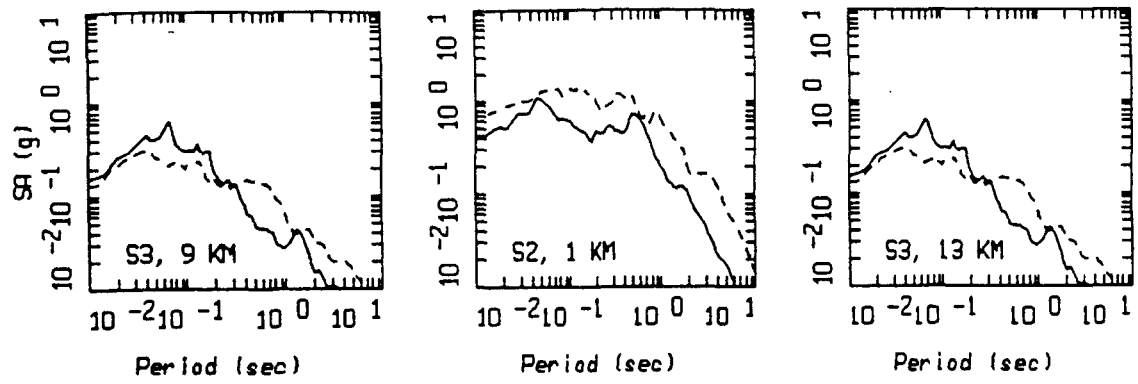

NAHANNI, FINITE SOURCE MODELING, PAGE 1 OF 1.

LINEAR.

LEGEND

——— DATA

- - - - - MODEL

Figure 5.122

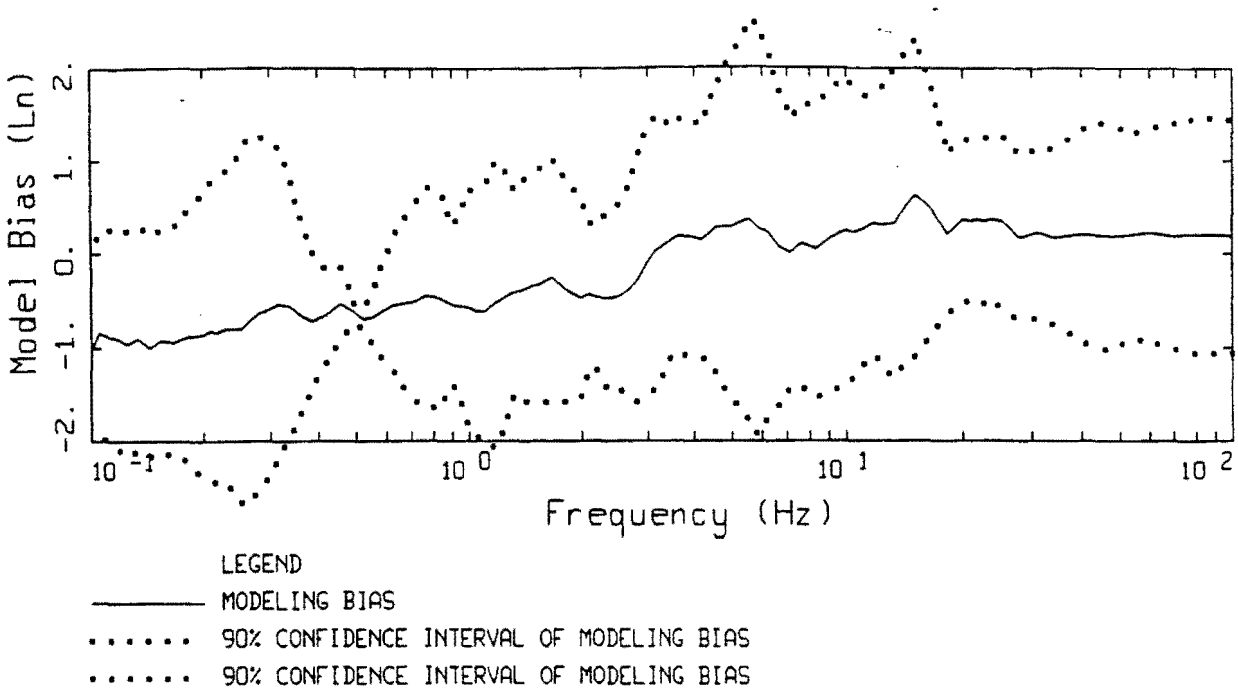

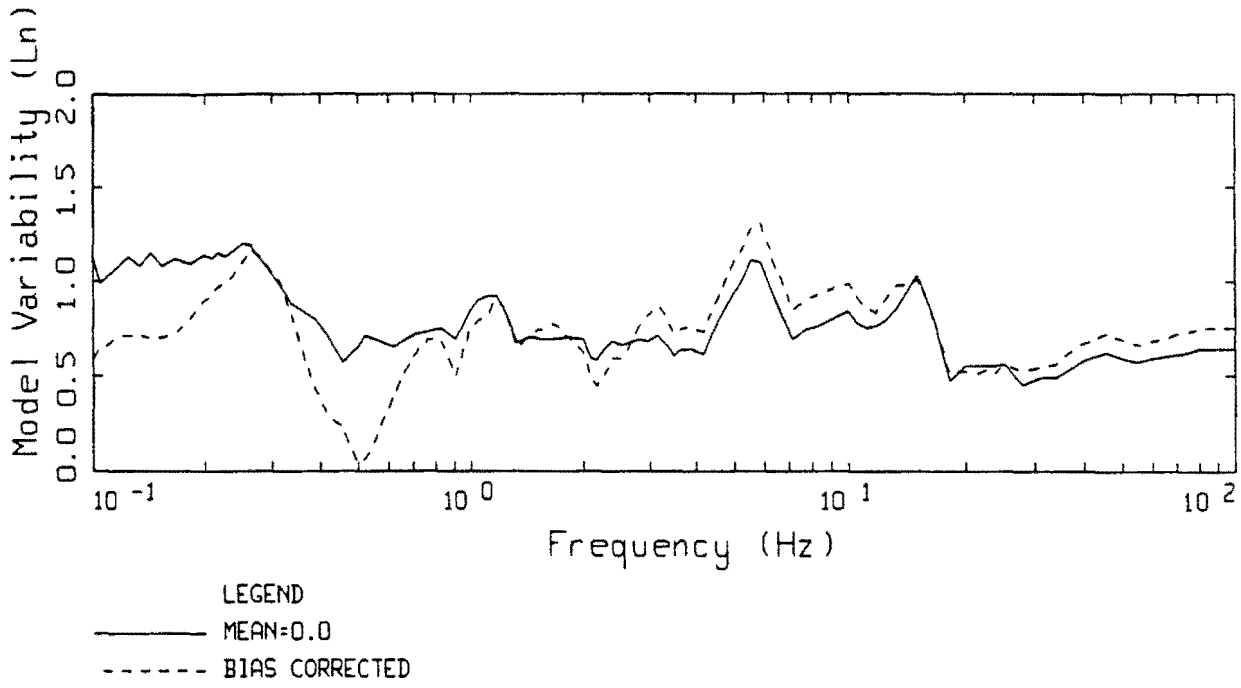

NAHANNI FINITE-SOURCE
LINEAR, ALL 3 SITES

Figure 5.123

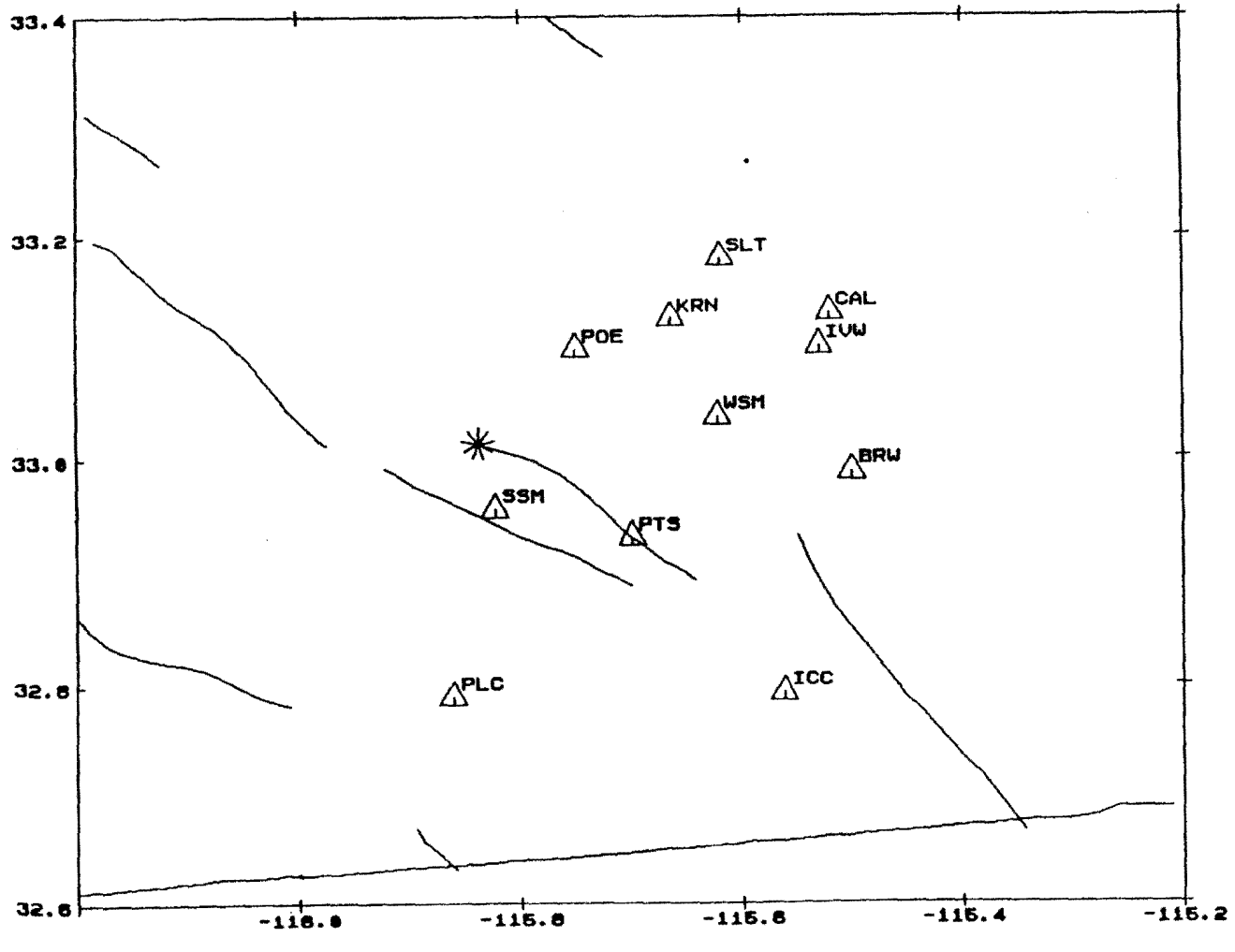

Figure 5.124

EQ3D-V4.00 FILE: SITES.HP2 EPICENT.HP2
. SCA:700000 MFAC:1.0 XFAC:1.0 Nm=12 Nx=0

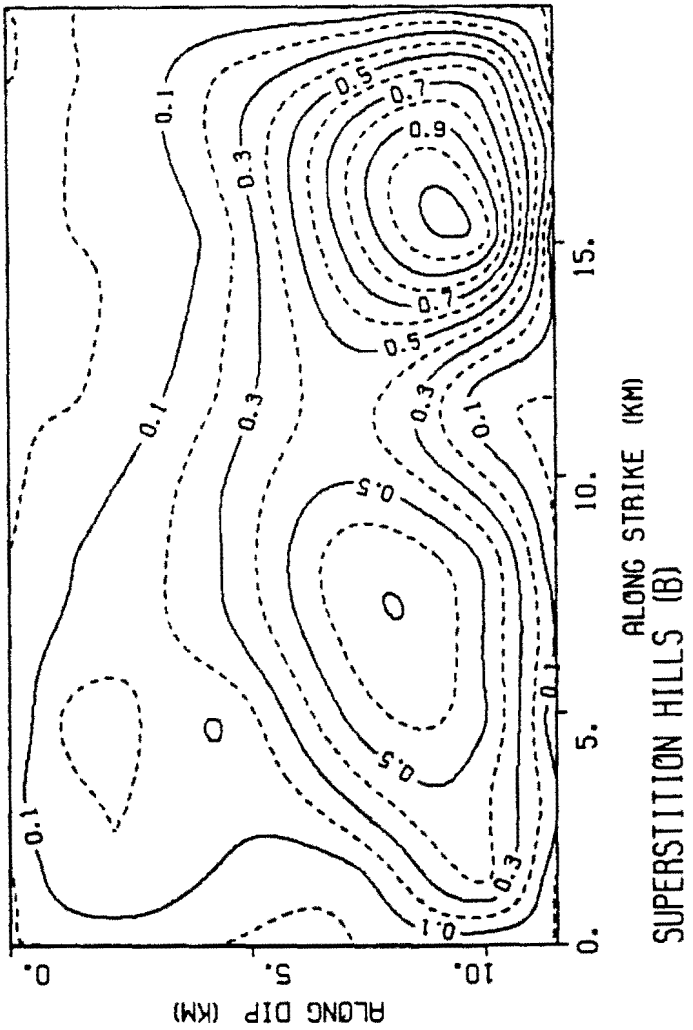
SUPERSTITION HILLS (B)
ALONG STRIKE (KM)
ALONG DIP (KM)
0.
5.
10.
15.
0.1
0.3
0.5
0.7
0.9

Figure 5.125

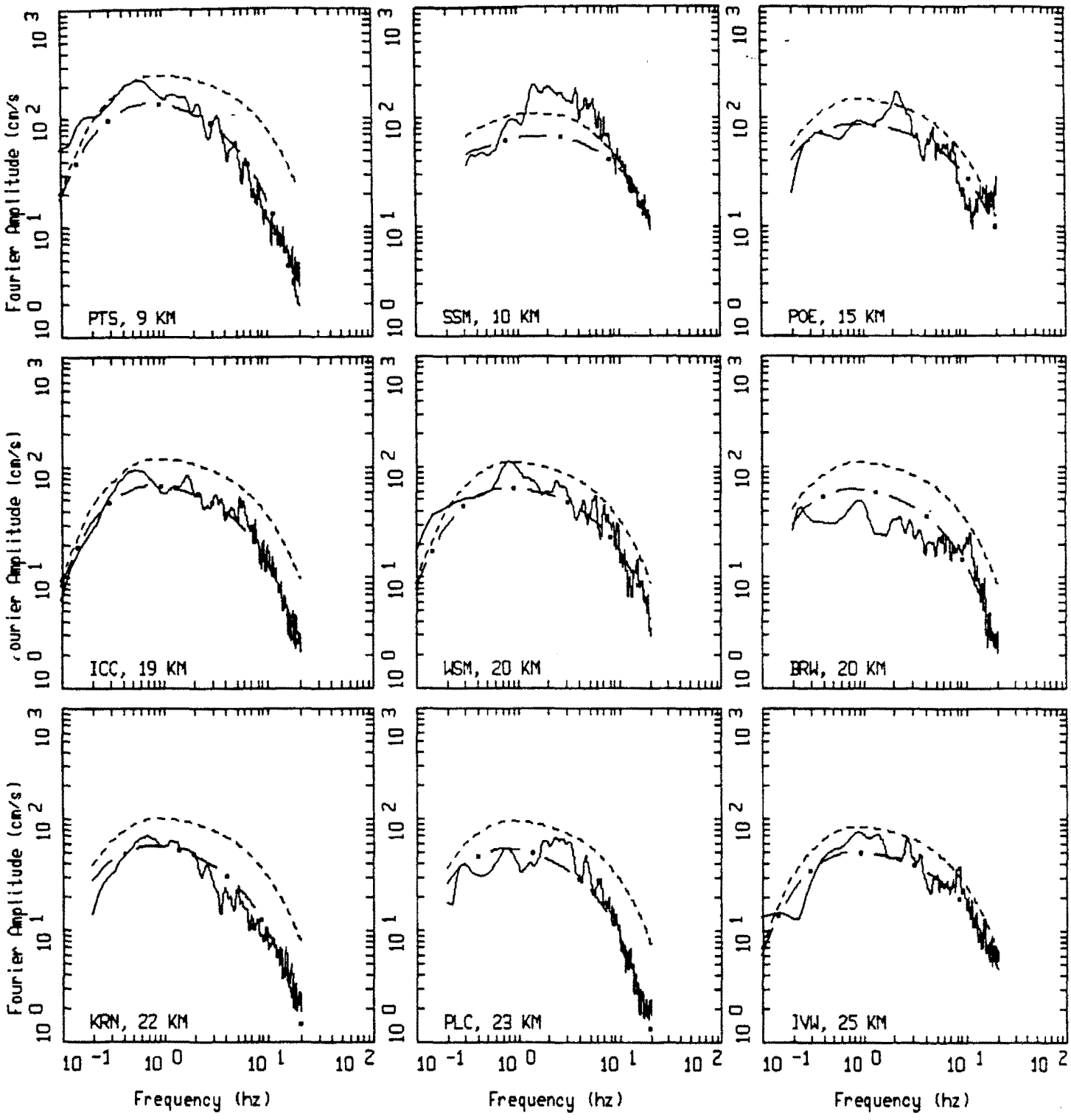

SUPERSTITION_HILLS(B) EARTHQUAKE, M=6.4, PAGE 1 OF 2.

Figure Set 5.126

LEGEND

——— DATA

- - - - - INITIAL MODEL

— • — FINAL MODEL

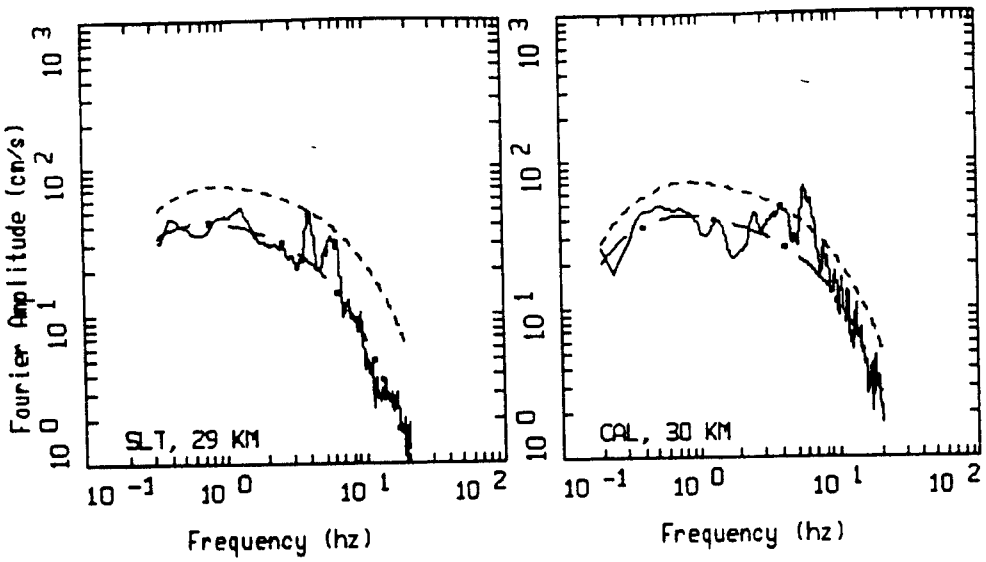

SUPERSTITION HILLS(B) EARTHQUAKE, M=6.4, PAGE 2 OF 2.

LEGEND

——— DATA

- - - - - INITIAL MODEL

—— • —— FINAL MODEL

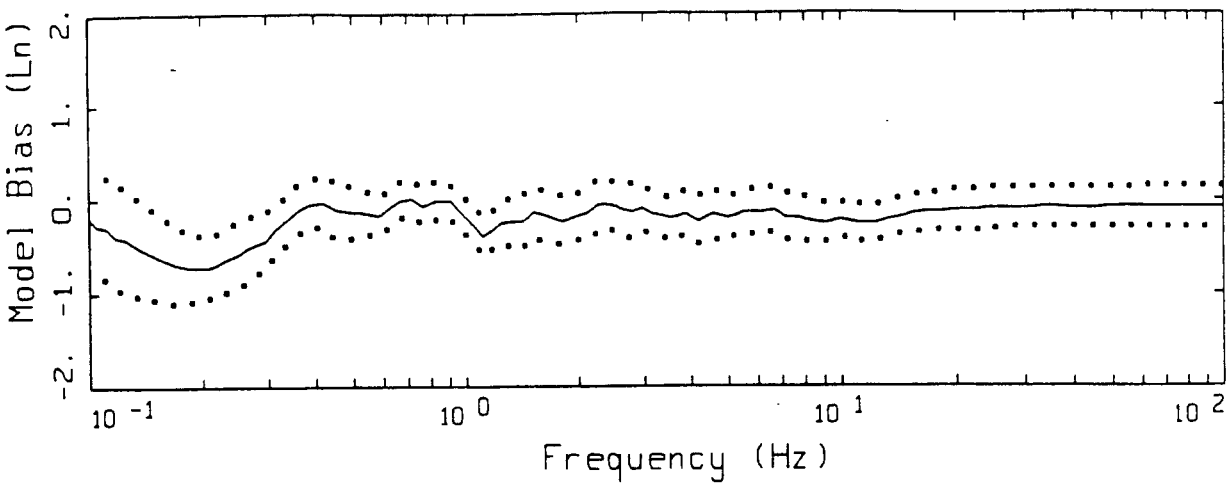

LEGEND
——— MODELING BIAS
. . . . . 90% CONFIDENCE INTERVAL OF MODELING BIAS
. . . . . 90% CONFIDENCE INTERVAL OF MODELING BIAS

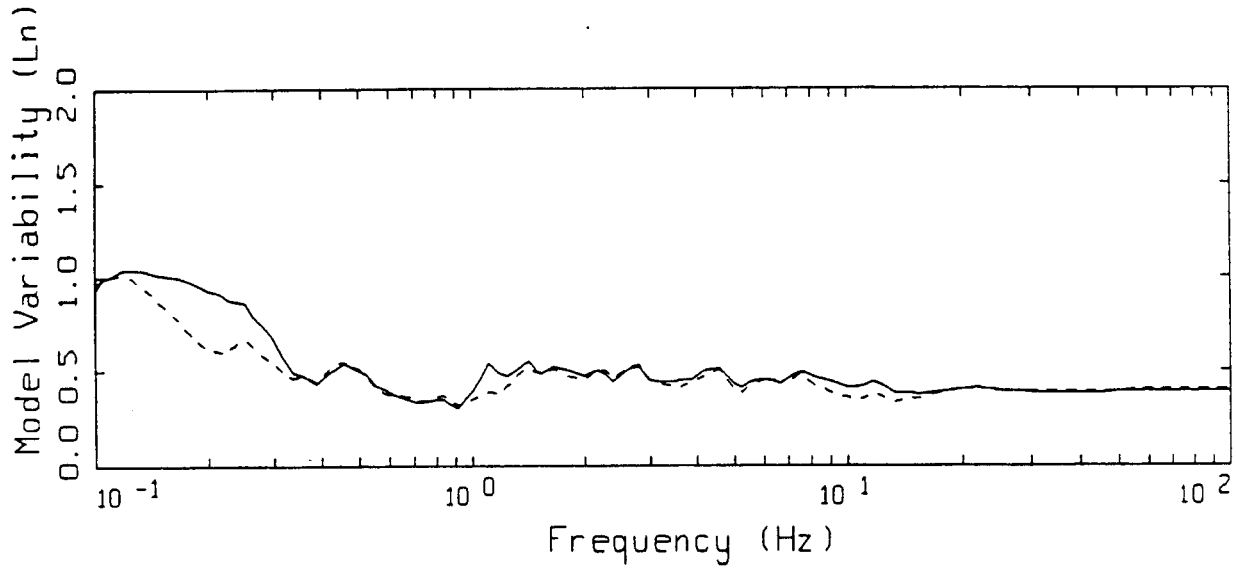

LEGEND
——— MEAN=0.0
- - - - - - BIAS CORRECTED

SUPERSTITION HILLS(B) POINT-SOURCE
NONLINEAR, ALL 11 SITES

Figure 5.127

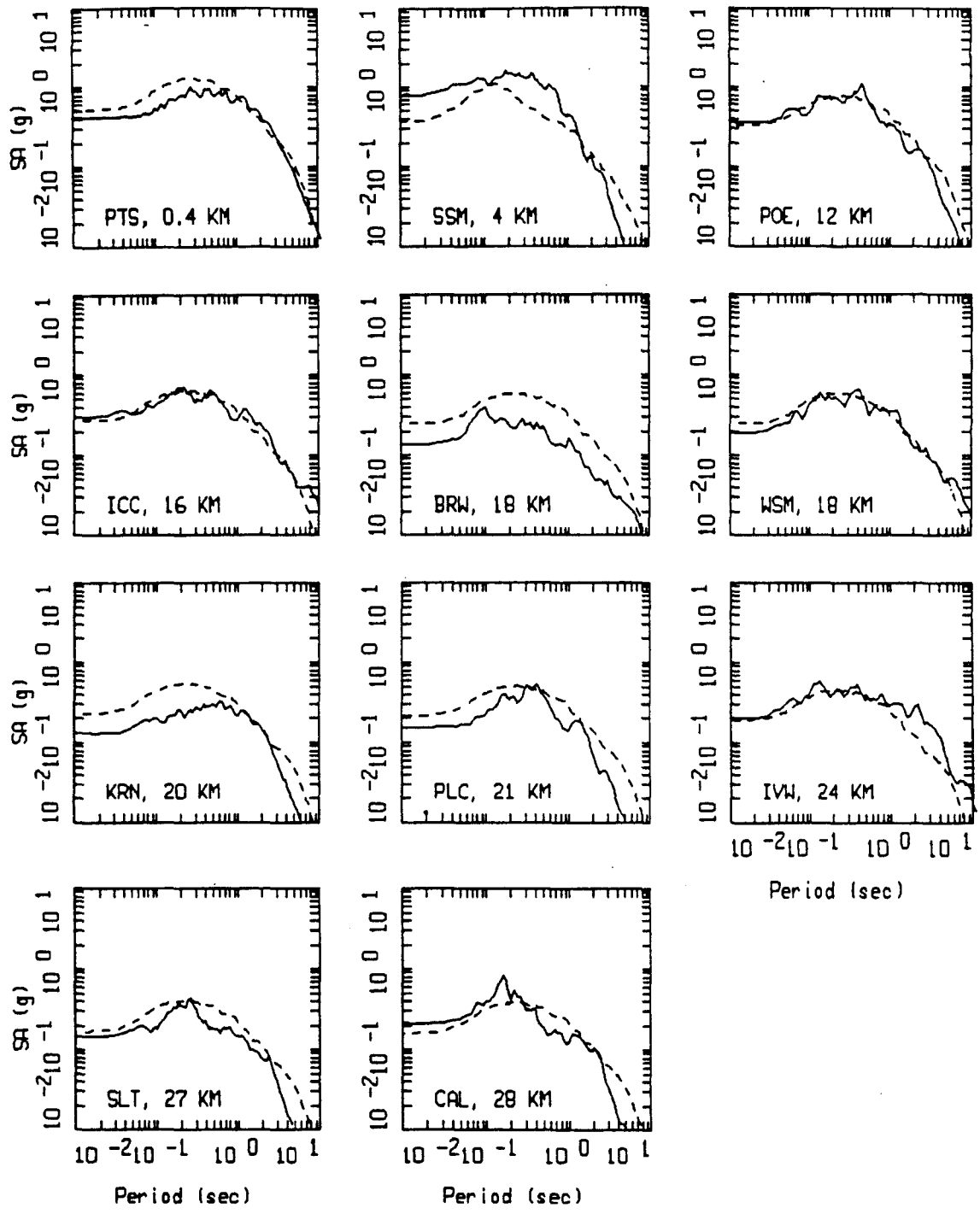

SUPERSTITION HILLS(B), POINT SOURCE MODELING, PAGE 1 OF 1.
NONLINEAR.

Figure 5.128

LEGEND

——— AVG OF TWO HORIZONTAL SPECTRA

- - - - - MODEL

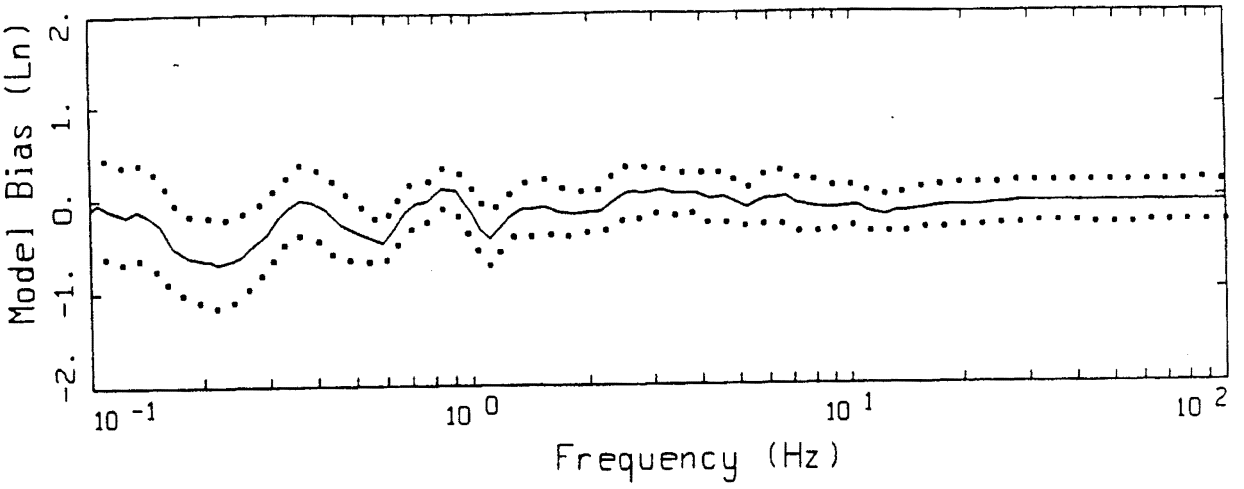

LEGEND
MODELING BIAS
90% CONFIDENCE INTERVAL OF MODELING BIAS
90% CONFIDENCE INTERVAL OF MODELING BIAS

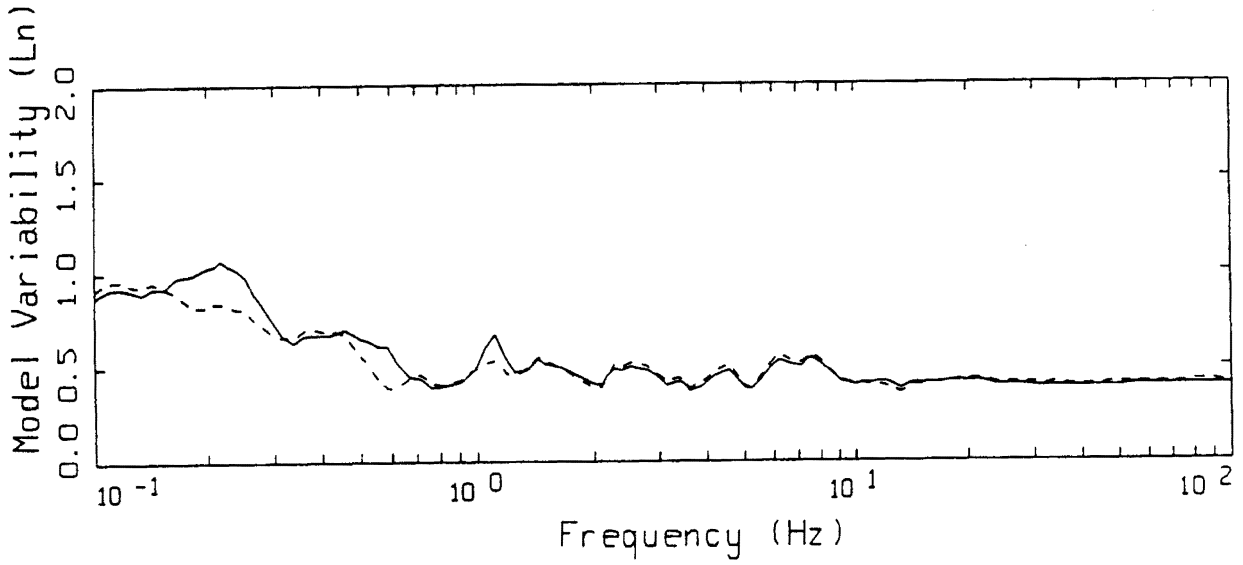

LEGEND
MEAN=0.0
BIAS CORRECTED

SUPERSTITION HILLS(B) FINITE-SOURCE
NONLINEAR, ALL 11 SITES

Figure 5.129

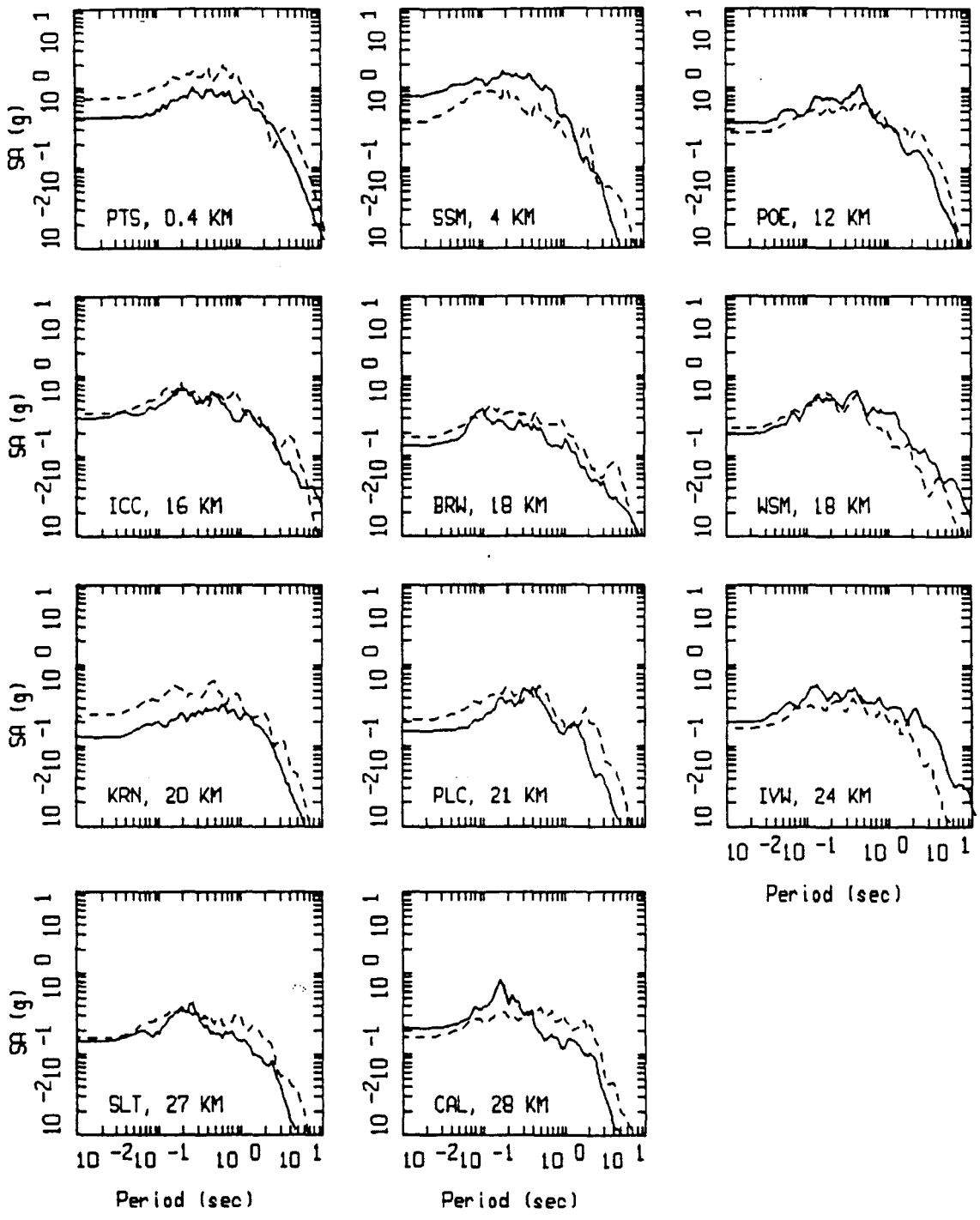

SUPERSTITION HILLS(B), FINITE SOURCE MODELING, PAGE 1 OF 1.
NONLINEAR.

Figure 5.130

LEGEND

——— AVG OF TWO HORIZONTAL SPECTRA

----- MODEL

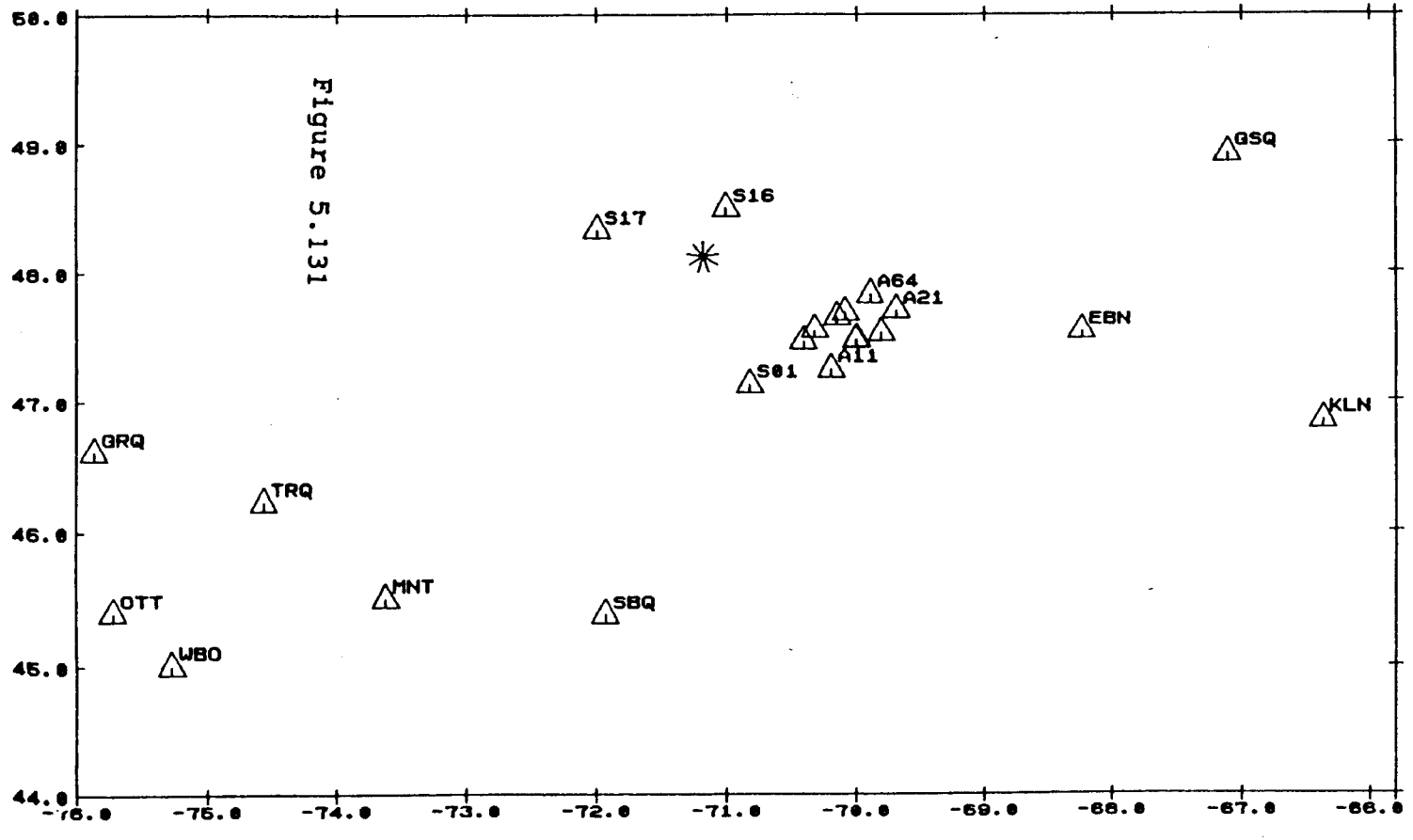

Figure 5.131

STAT

EPICENTER

0 100
kilometers

EQ3D-V4.00 FILE: SITES.HP2 EPICENT.HP2
. SCA:0.000000 MFAC:1.0 XFAC:1.0 Nm=23 Nx=0

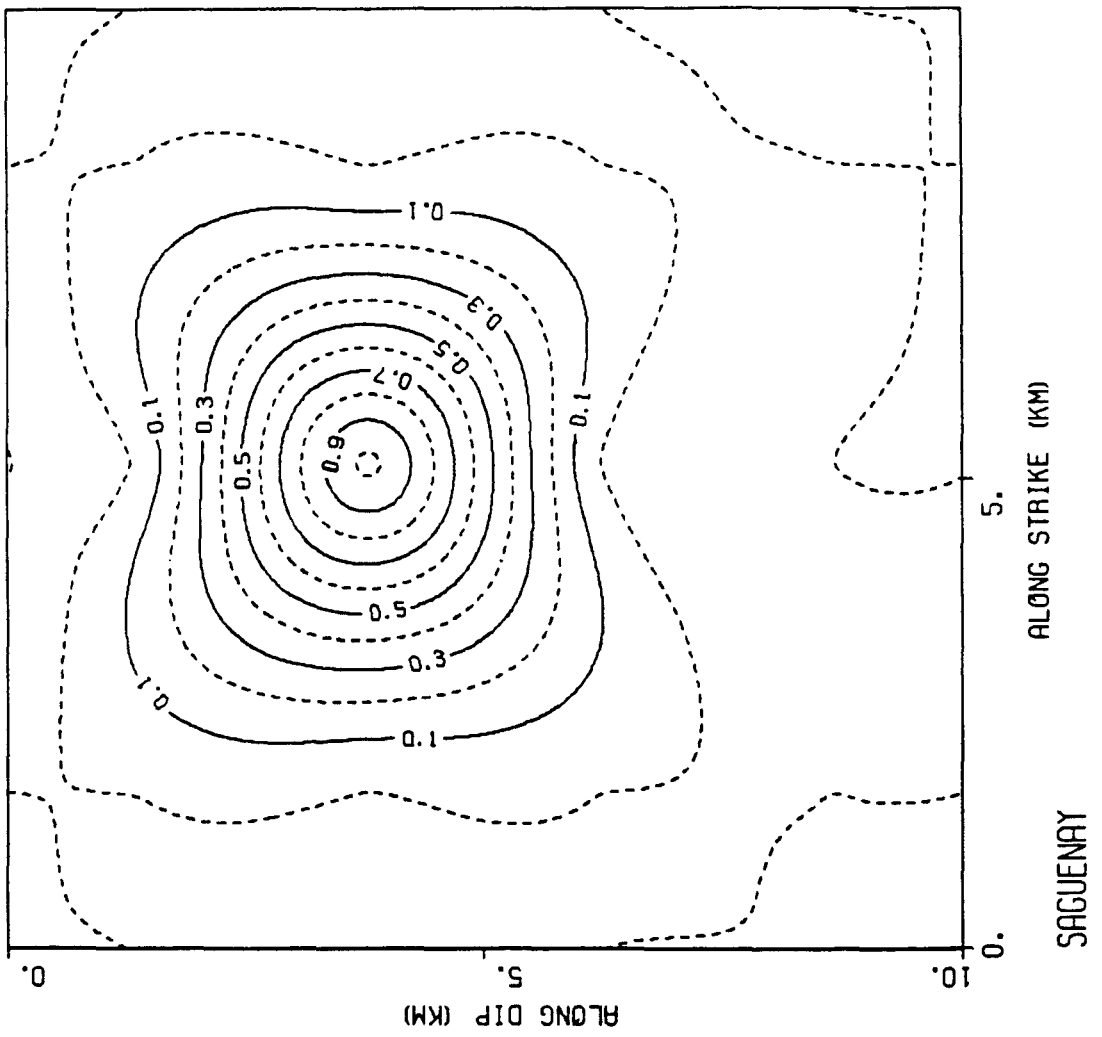
0.1
0.3
0.5
0.7
0.9
0.5
0.3
0.1
1.0
0.1
1.0
0.
5.
10.
ALONG DIP (KM)
0.
5.
ALONG STRIKE (KM)
SAGUENAY

Figure 5.132

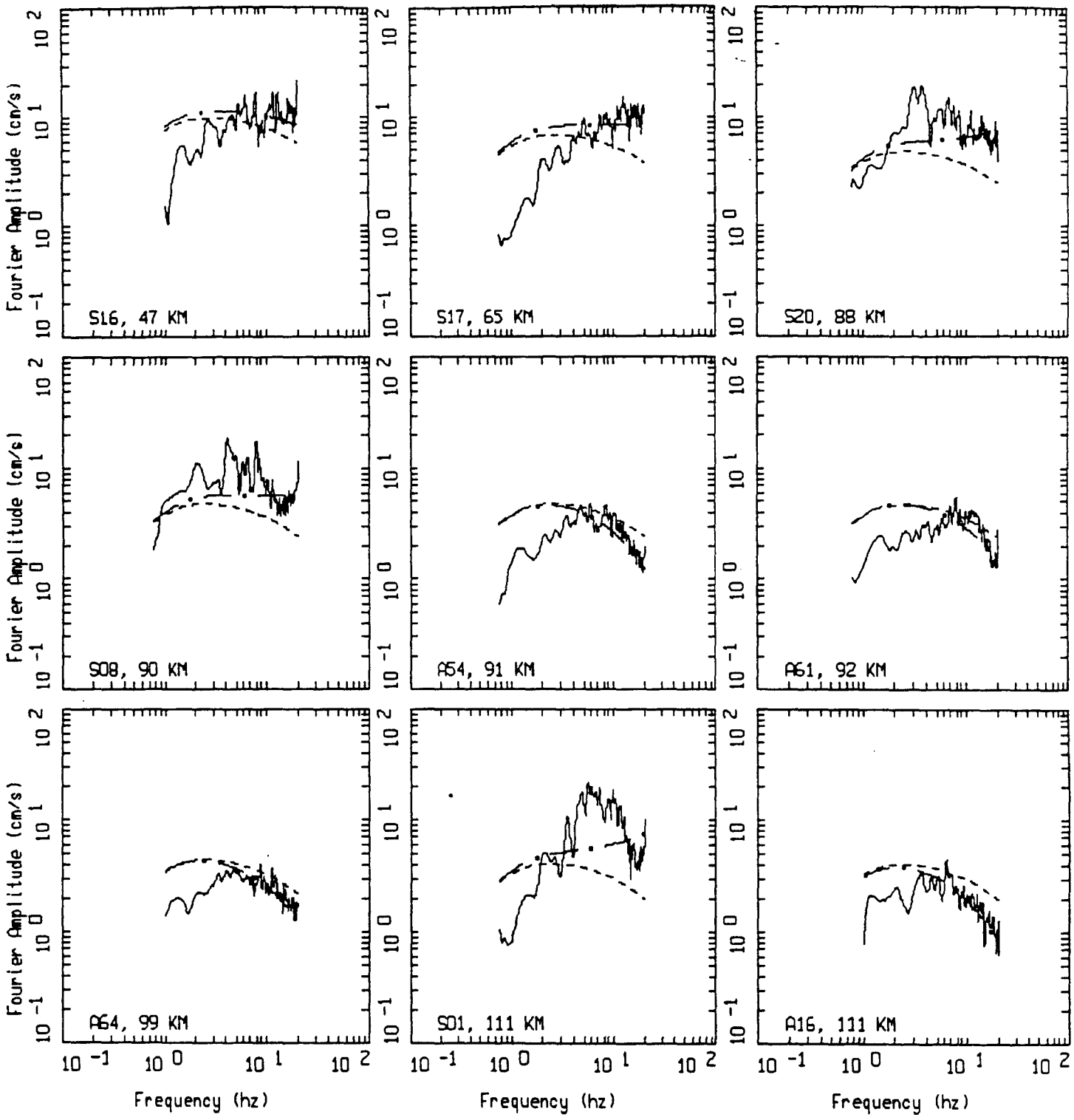

SAGUENAY EARTHQUAKE, M=5.8, PAGE 1 OF 3.

LEGEND

——— DATA

- - - - - INITIAL MODEL

— • — FINAL MODEL

Figure Set 5.133

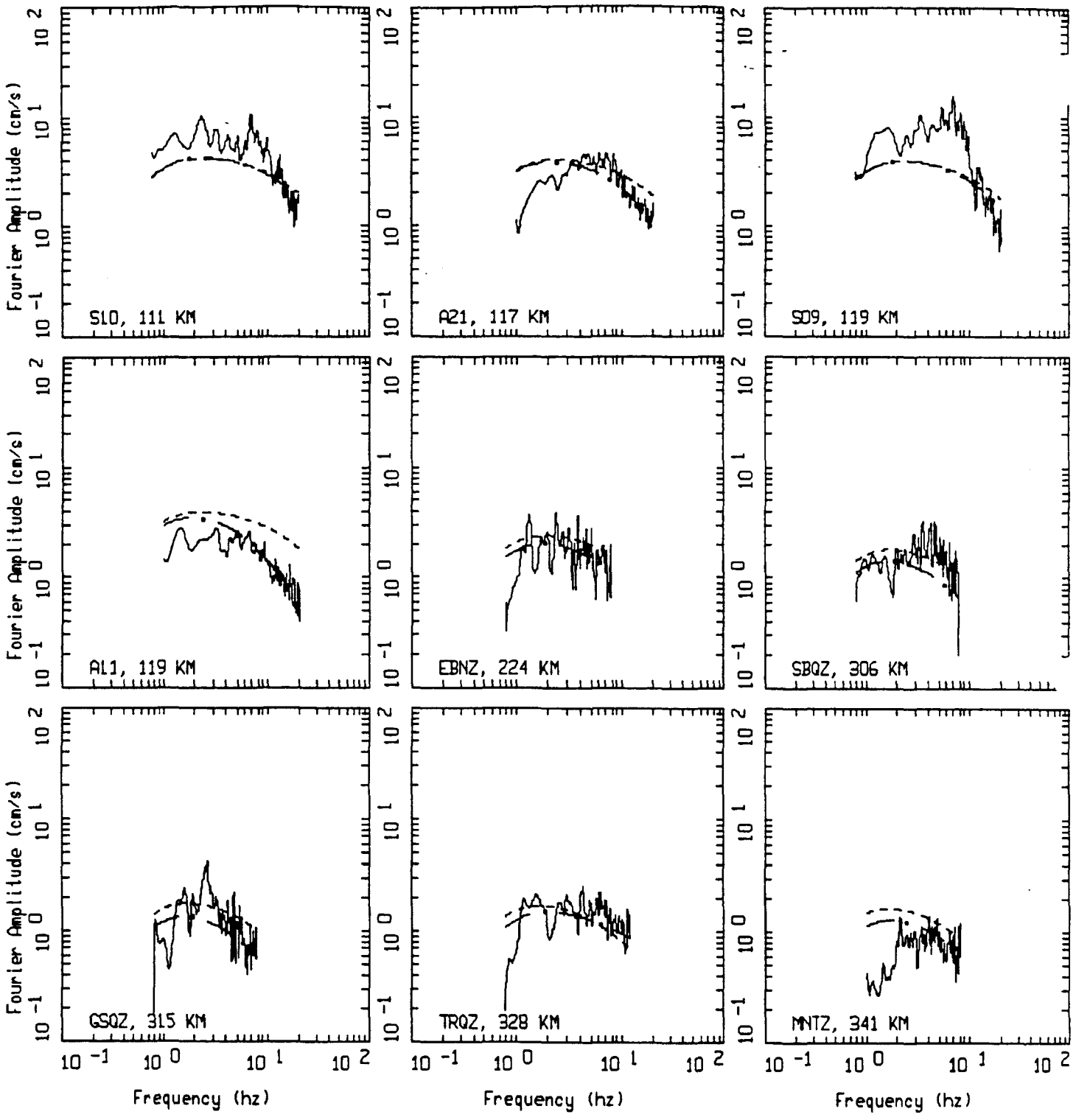

SAGUENAY EARTHQUAKE, M=5.8, PAGE 2 OF 3.

LEGEND

DATA

INITIAL MODEL

FINAL MODEL

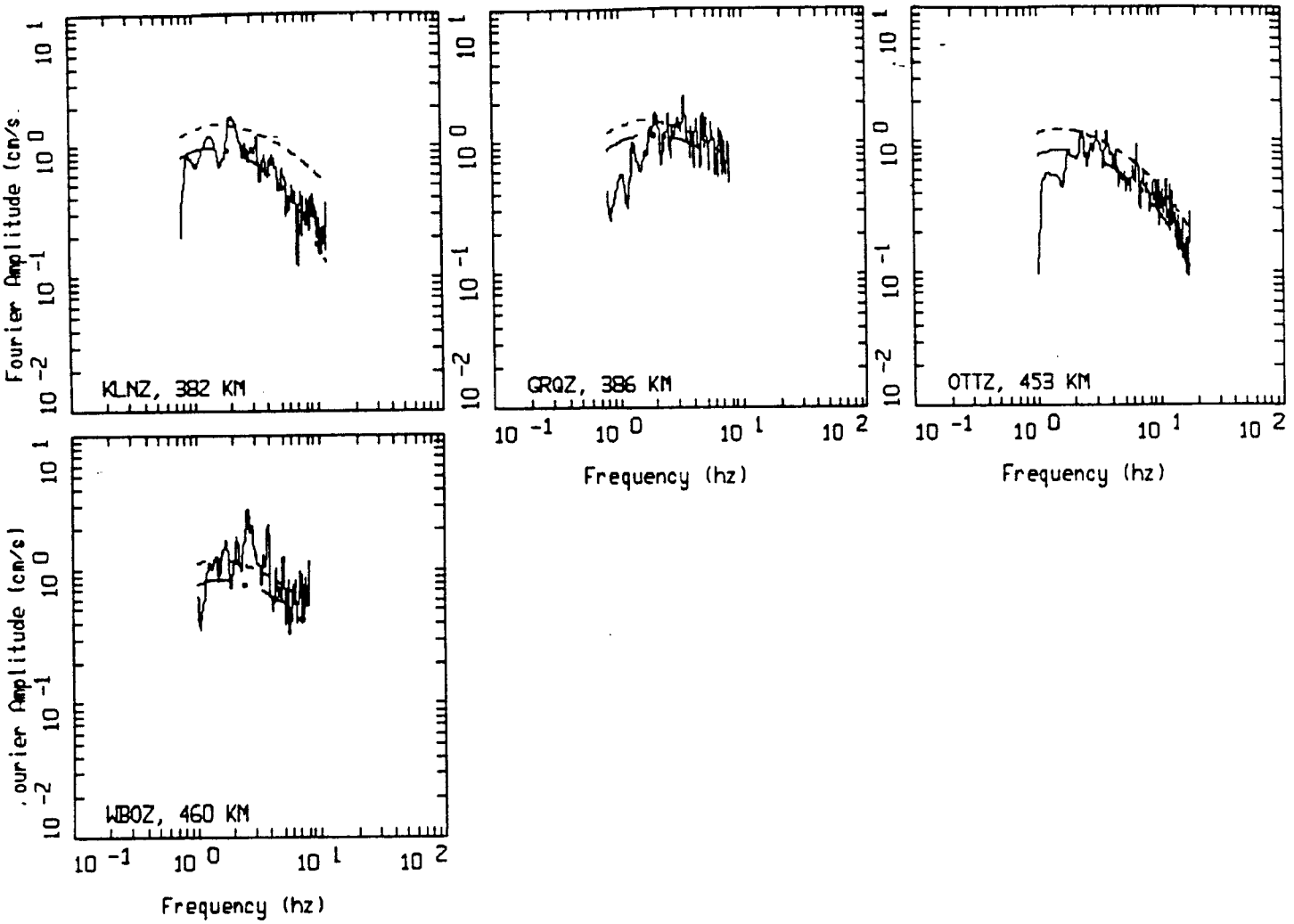

SAGUENAY EARTHQUAKE, M=5.8, PAGE 3 OF 3.

LEGEND

——— DATA

- - - - - INITIAL MODEL

— • — FINAL MODEL

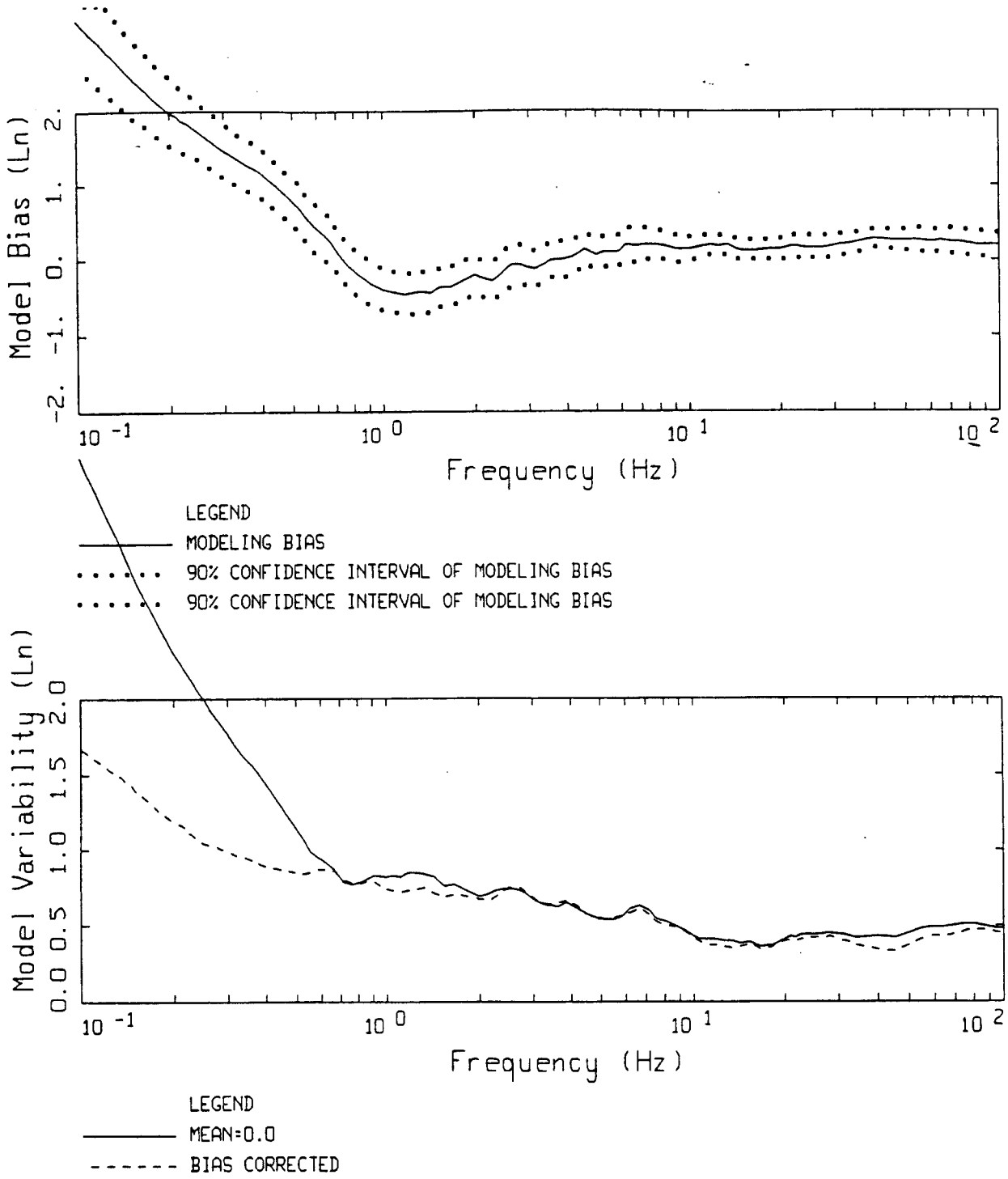
Model Bias (Ln)
2.
1.
0.
-1.
-2.
10 -1
10 0
10 1
10 2
Frequency (Hz)
LEGEND
MODELING BIAS
90% CONFIDENCE INTERVAL OF MODELING BIAS
90% CONFIDENCE INTERVAL OF MODELING BIAS
Model Variability (Ln)
0.0 0.5 1.0 1.5 2.0
10 -1
10 0
10 1
10 2
Frequency (Hz)
LEGEND
MEAN=0.0
BIAS CORRECTED
SAGUENAY POINT-SOURCE
LINEAR, ALL 22 SITES

Figure 5.134

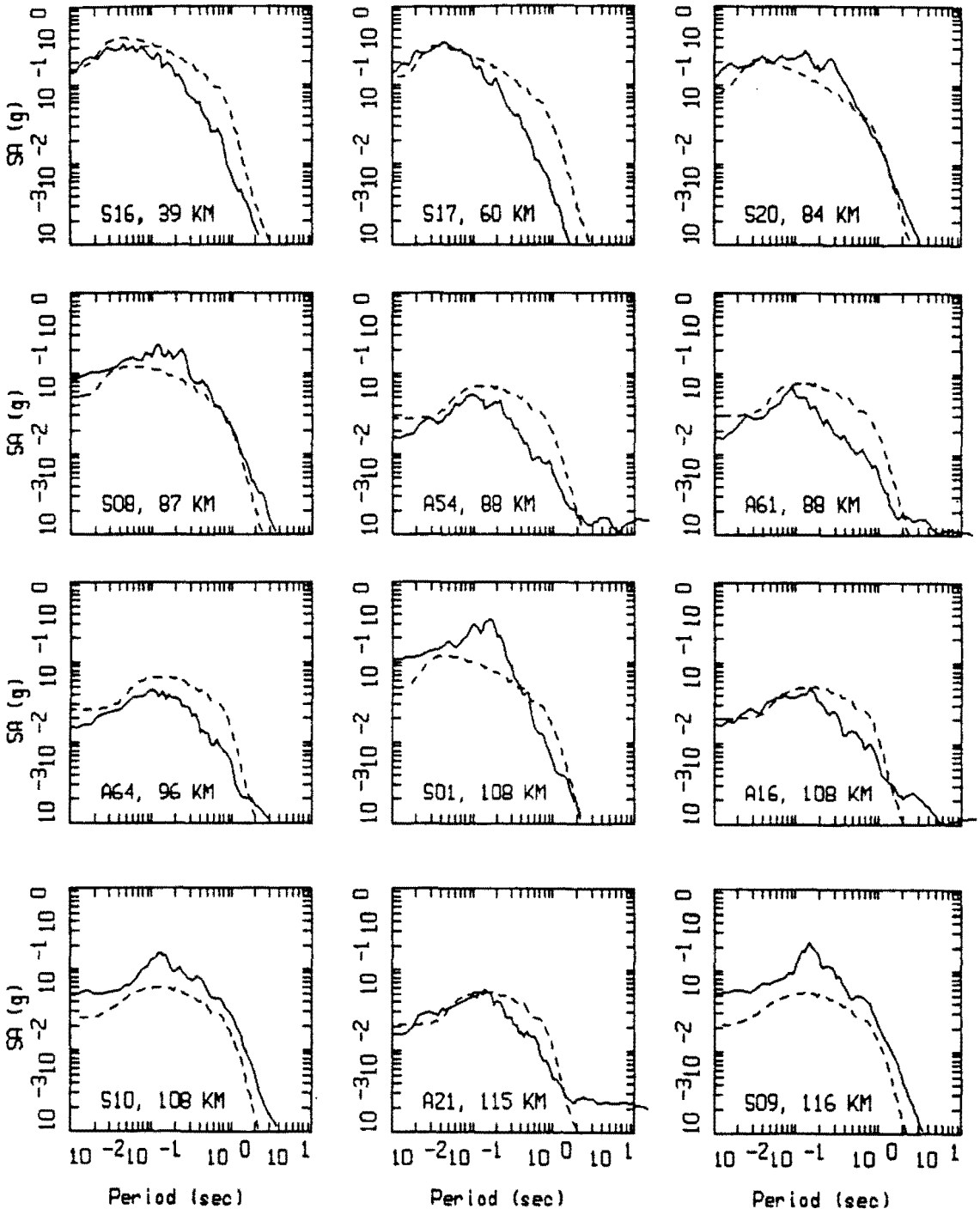

SAGUENAY, POINT SOURCE MODELING, PAGE 1 OF 2.
LINEAR.

Figure Set 5.135

LEGEND
——— DATA
----- MODEL

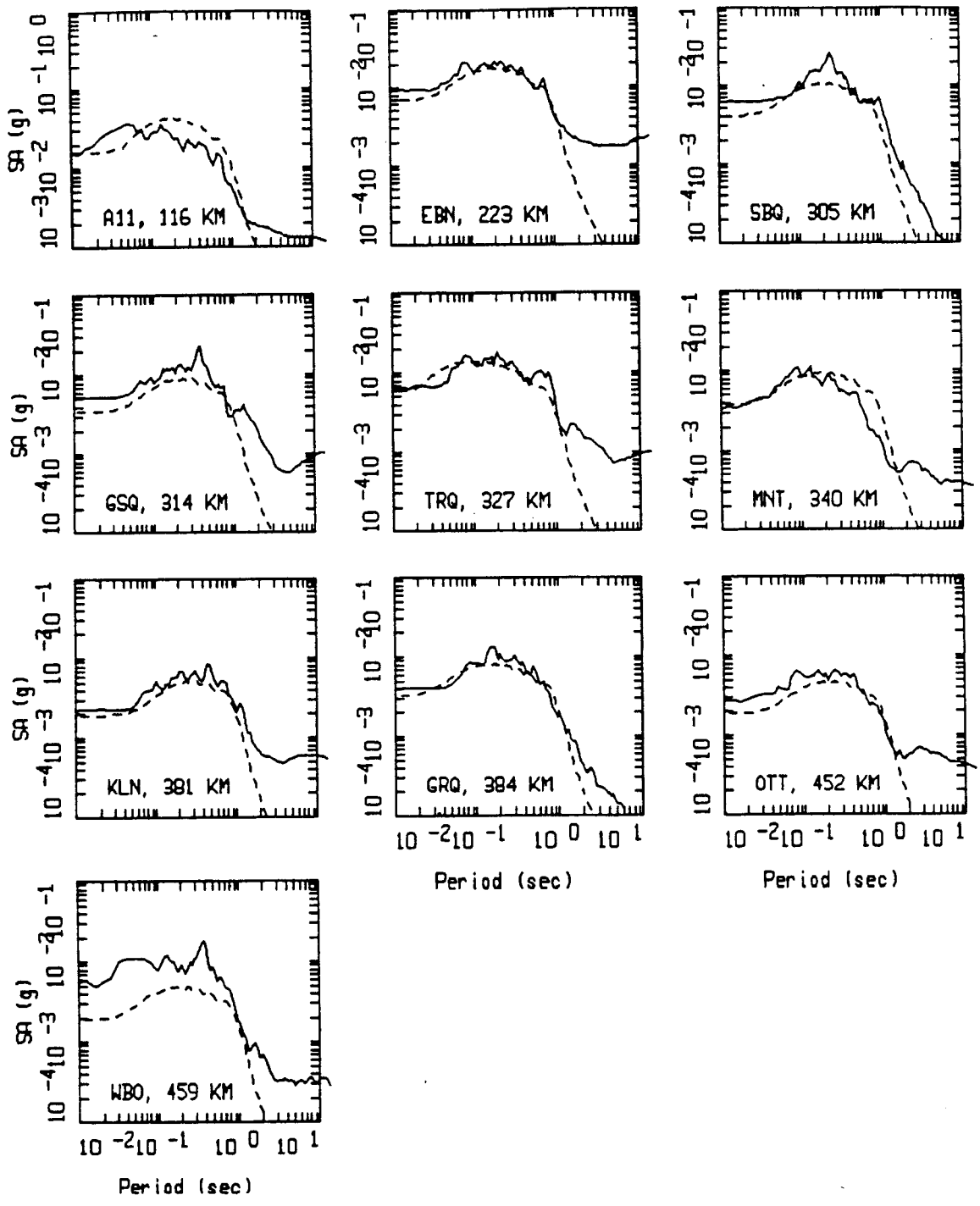

SAGUENAY, POINT SOURCE MODELING, PAGE 2 OF 2.
LINEAR.

LEGEND

——— DATA

----- MODEL

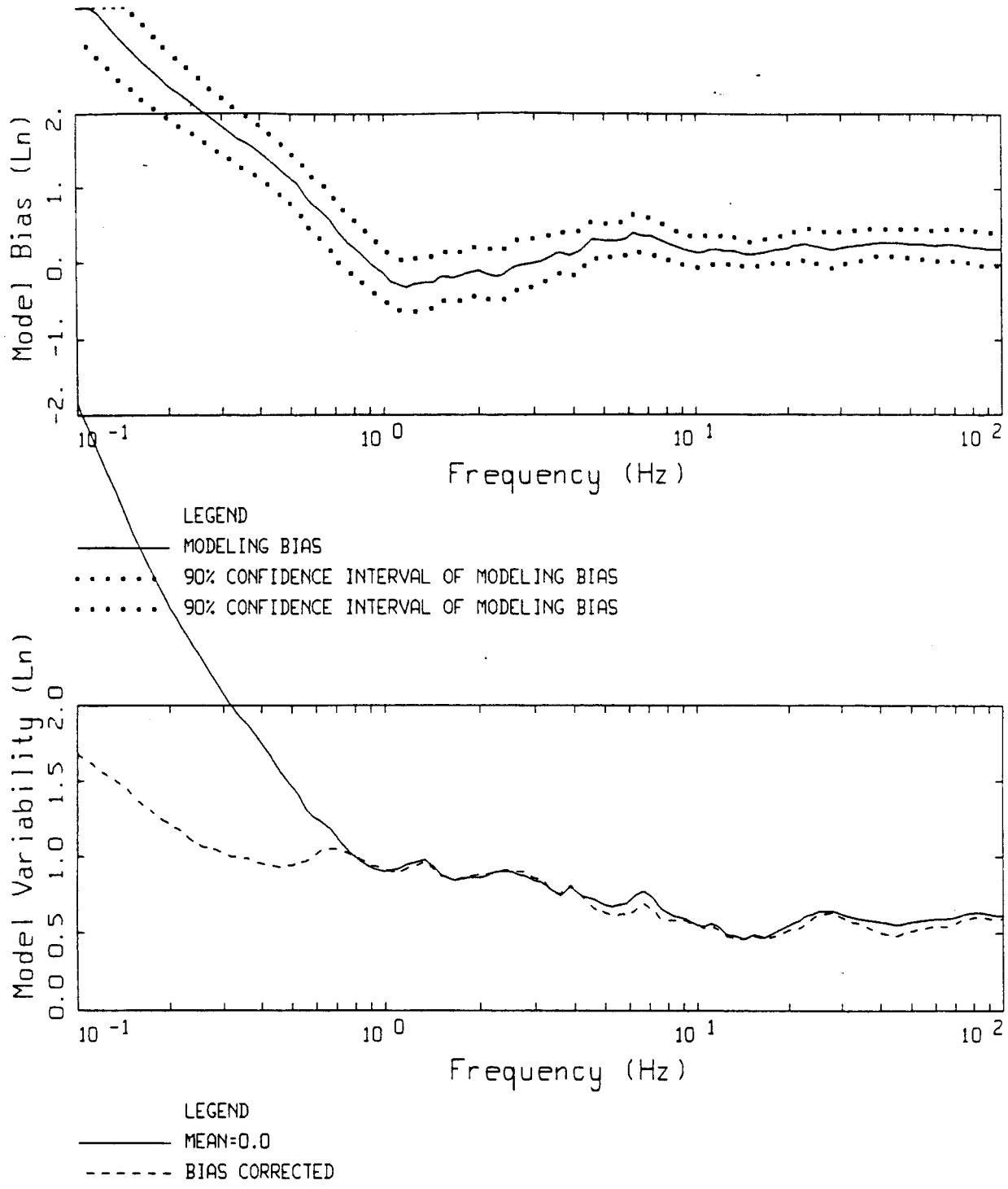

SAGUENAY FINITE-SOURCE
LINEAR, ALL 22 SITES

Figure 5.136

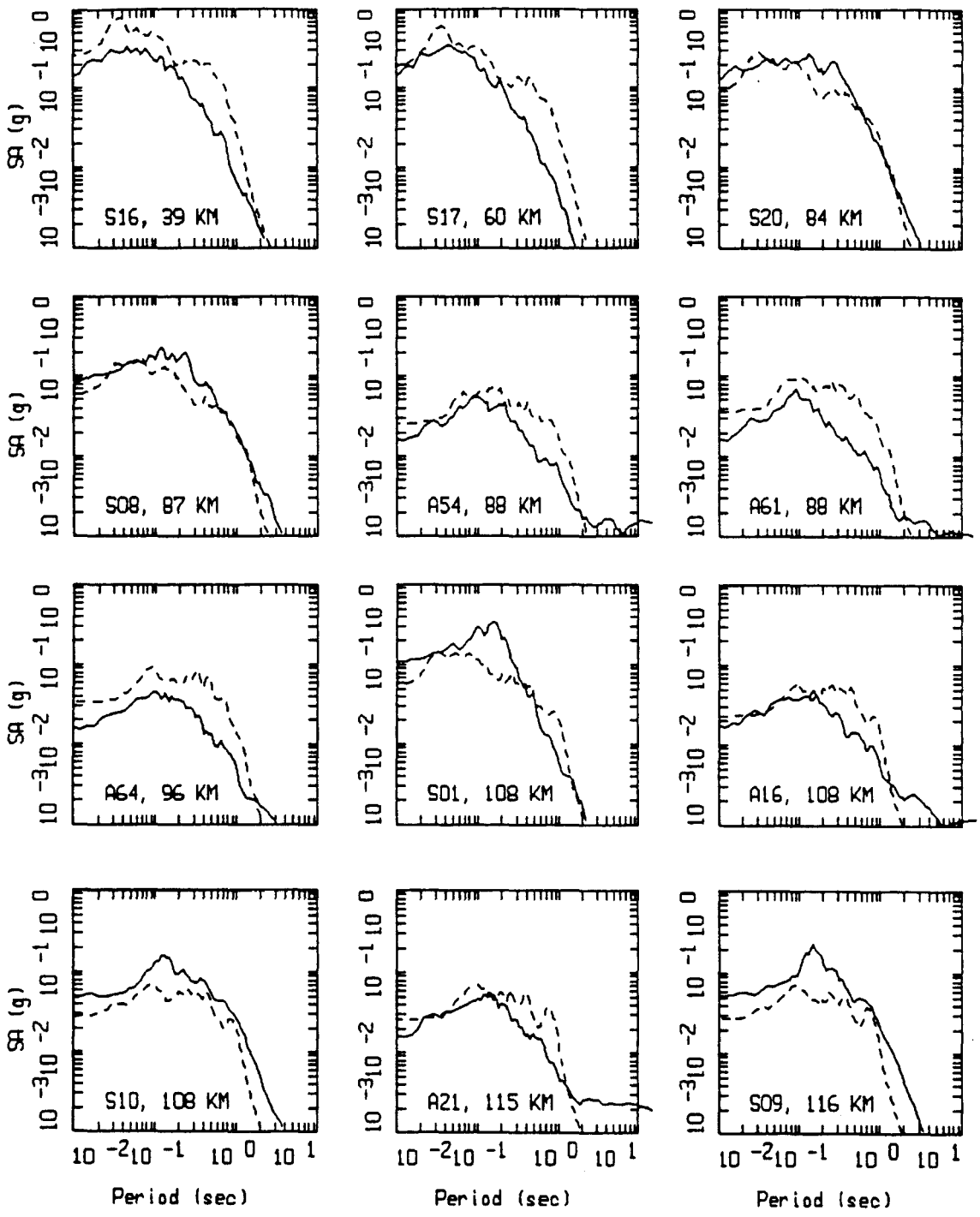

SAGUENAY, FINITE SOURCE MODELING, PAGE 1 OF 2.
LINEAR.

Figure Set 5.137

LEGEND
——— DATA
----- MODEL

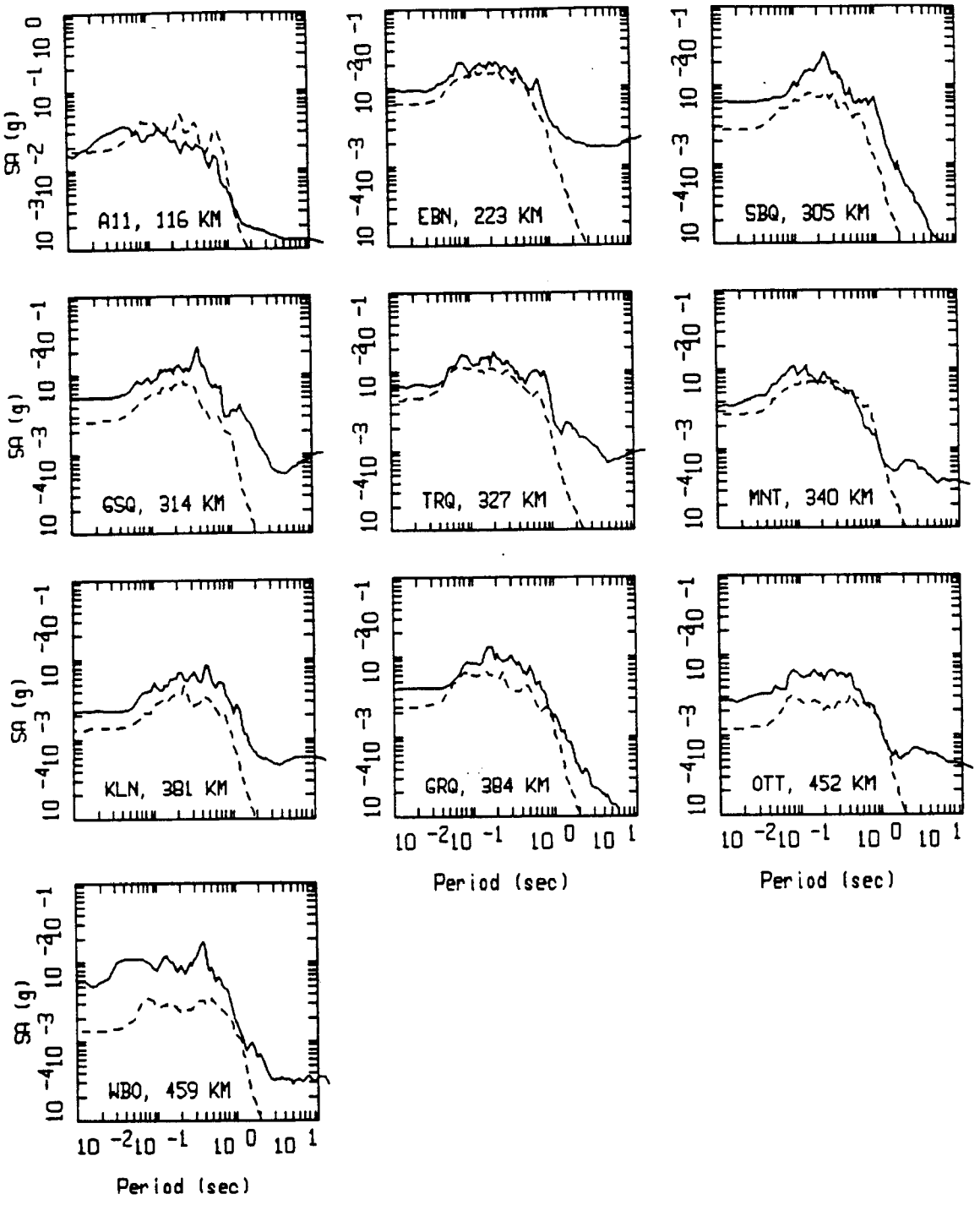

SAGUENAY, FINITE SOURCE MODELING, PAGE 2 OF 2.
LINEAR.

LEGEND

——— DATA

----- MODEL

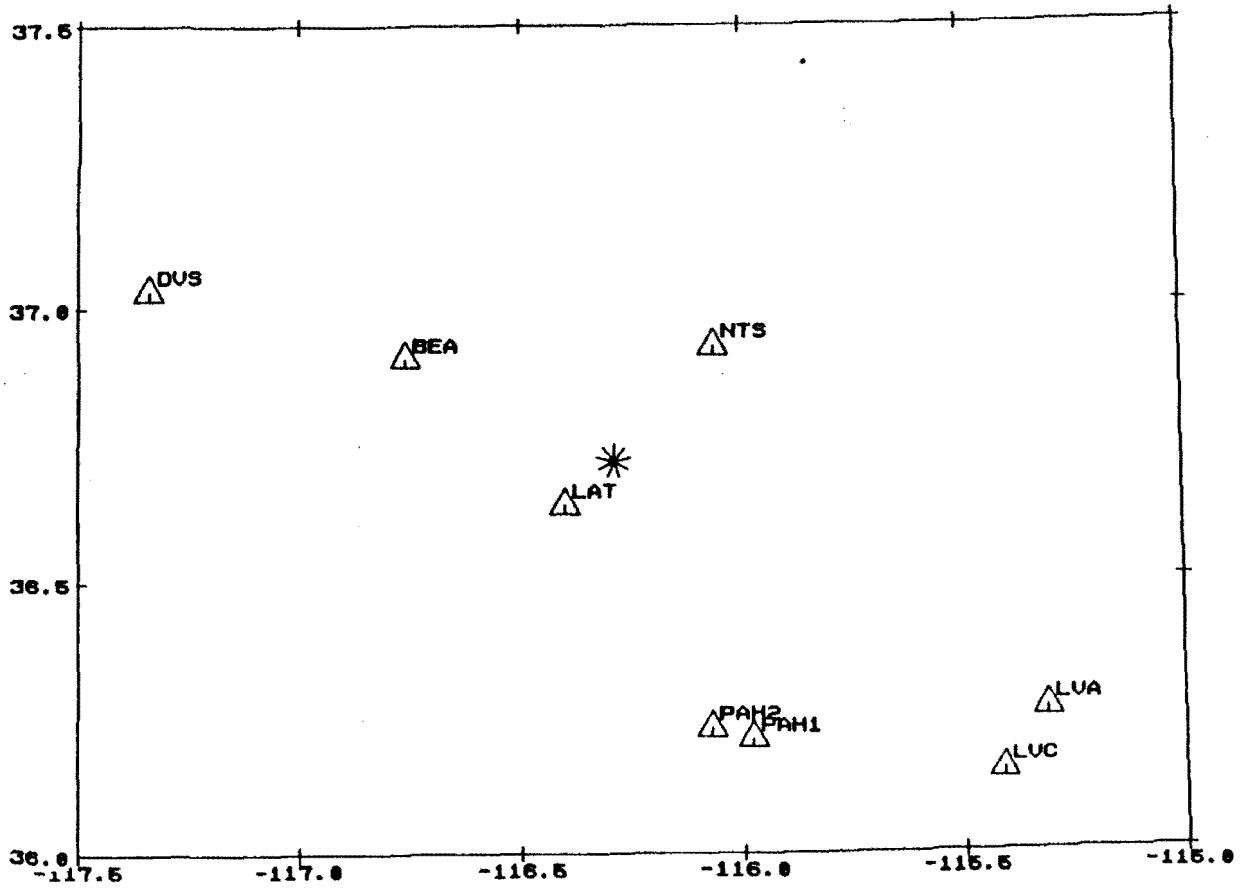

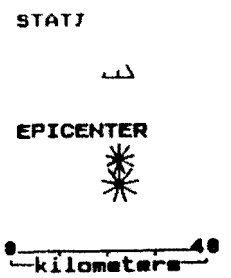

EQ3D-v4.00 FILE: SITES.HP2 EPICENT.HP2
. SCA:1500000 MFAC:1.0 XFAC:1.0 Nm=0 Nx=0

Figure 5.138

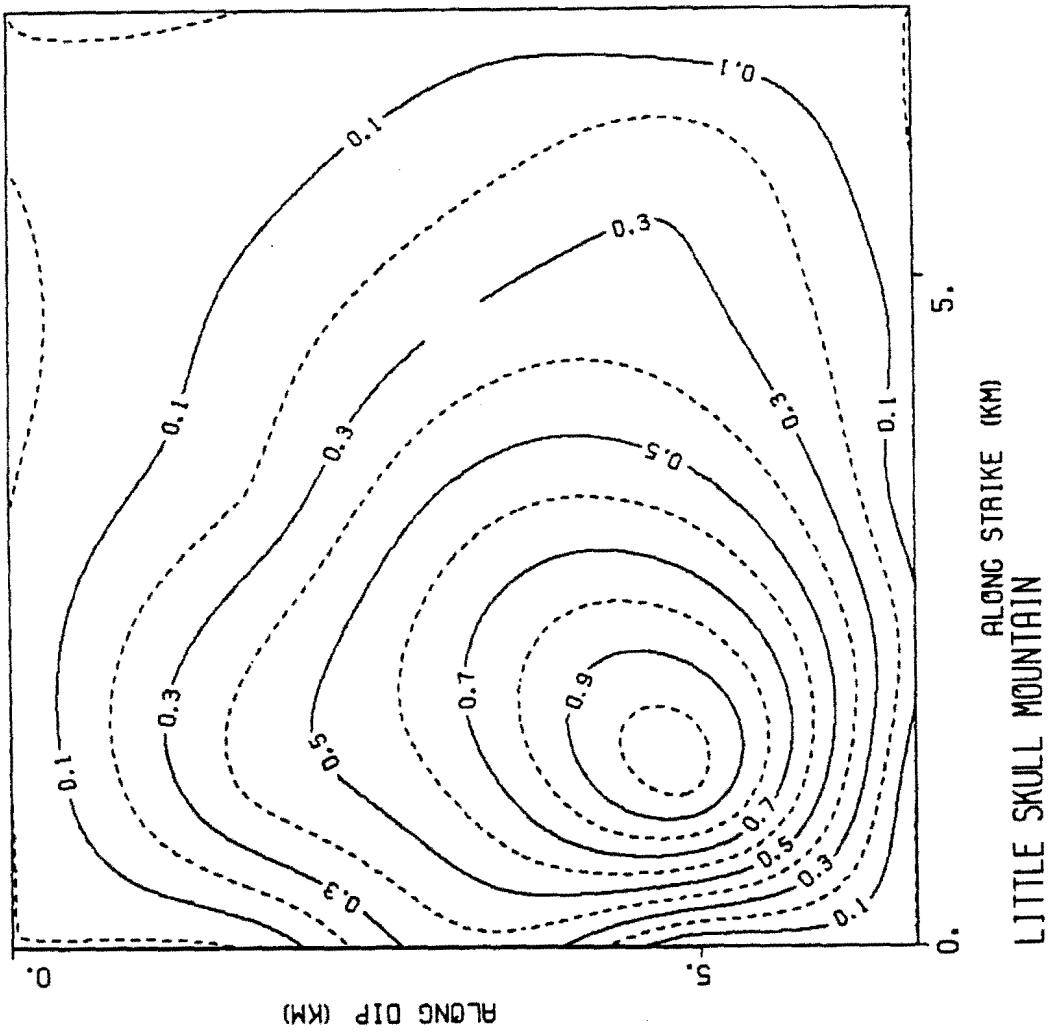
LITTLE SKULL MOUNTAIN
ALONG STRIKE (KM)
ALONG DIP (KM)
0.
5.
0.1
0.3
0.5
0.7
0.9

Figure 5.139

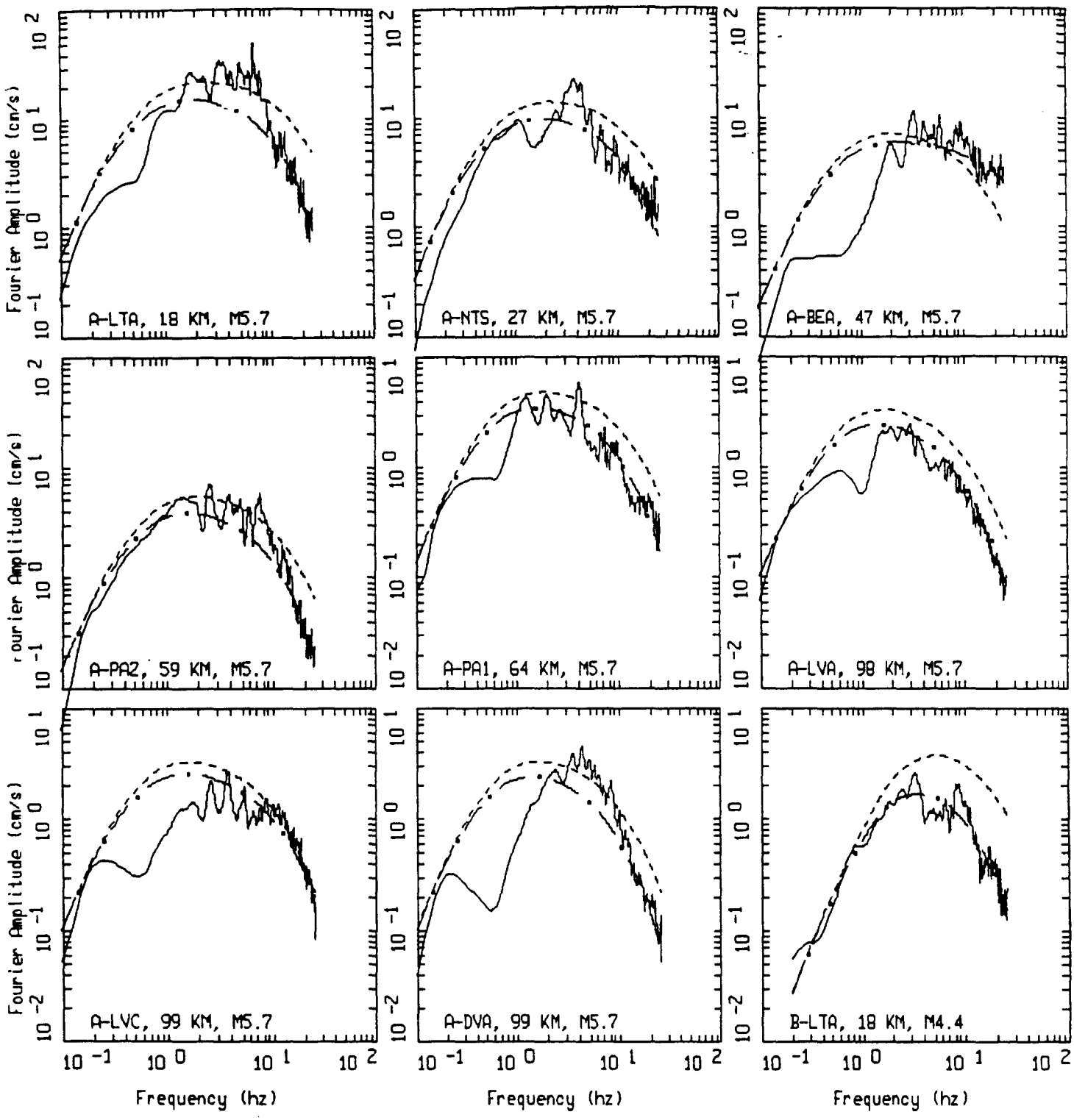

LITTLE SKULL MTN EARTHQUAKES, PAGE 1 OF 2.

Figure Set 5.140

LEGEND

——— DATA

- - - - - INITIAL MODEL

— • — FINAL MODEL

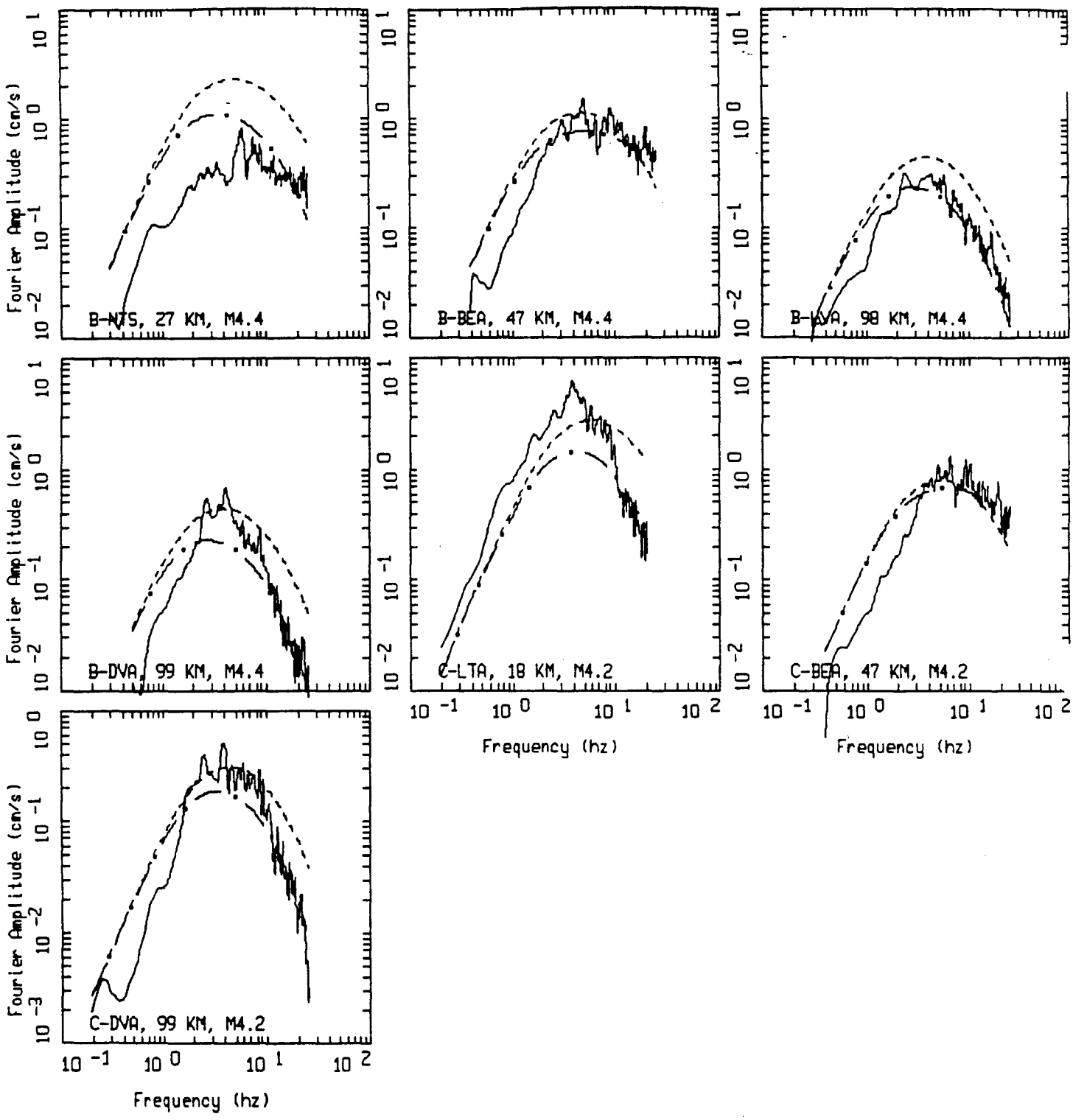

LITTLE SKULL MTN EARTHQUAKES, PAGE 2 OF 2.

LEGEND

——— DATA

- - - - - INITIAL MODEL

— • — FINAL MODEL

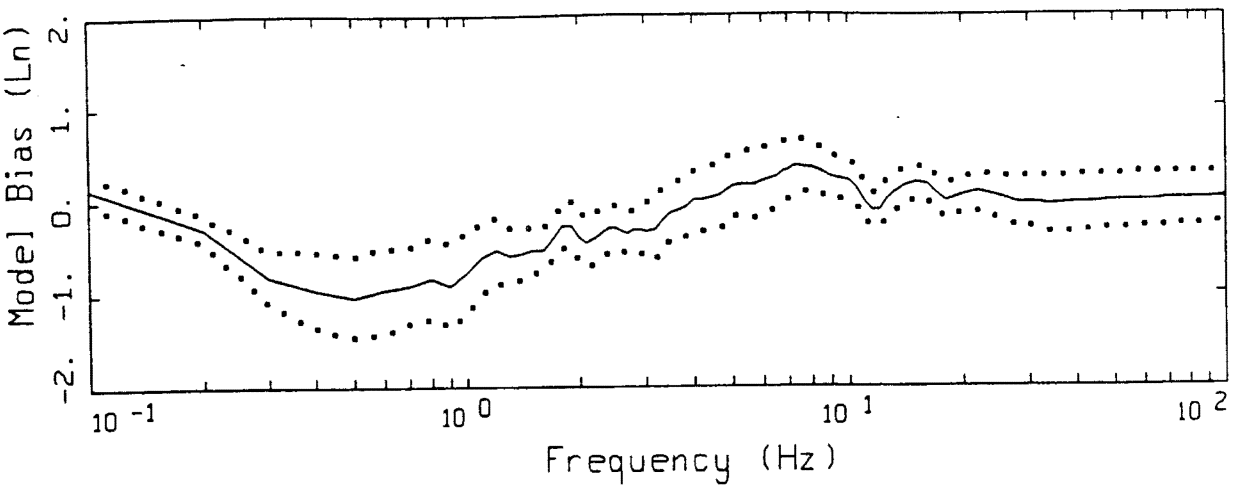

LEGEND
MODELING BIAS
90% CONFIDENCE INTERVAL OF MODELING BIAS
90% CONFIDENCE INTERVAL OF MODELING BIAS

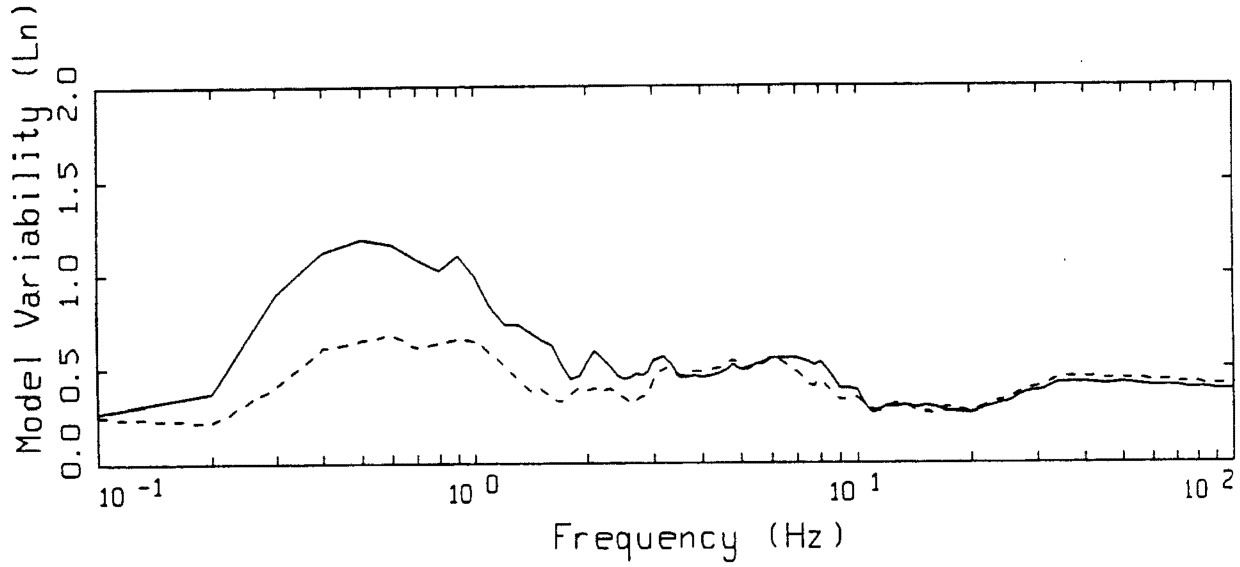

LEGEND
MEAN=0.0
BIAS CORRECTED

LITTLE SKULL MTN POINT-SOURCE
NONLINEAR, ALL 8 SITES

Figure 5.141

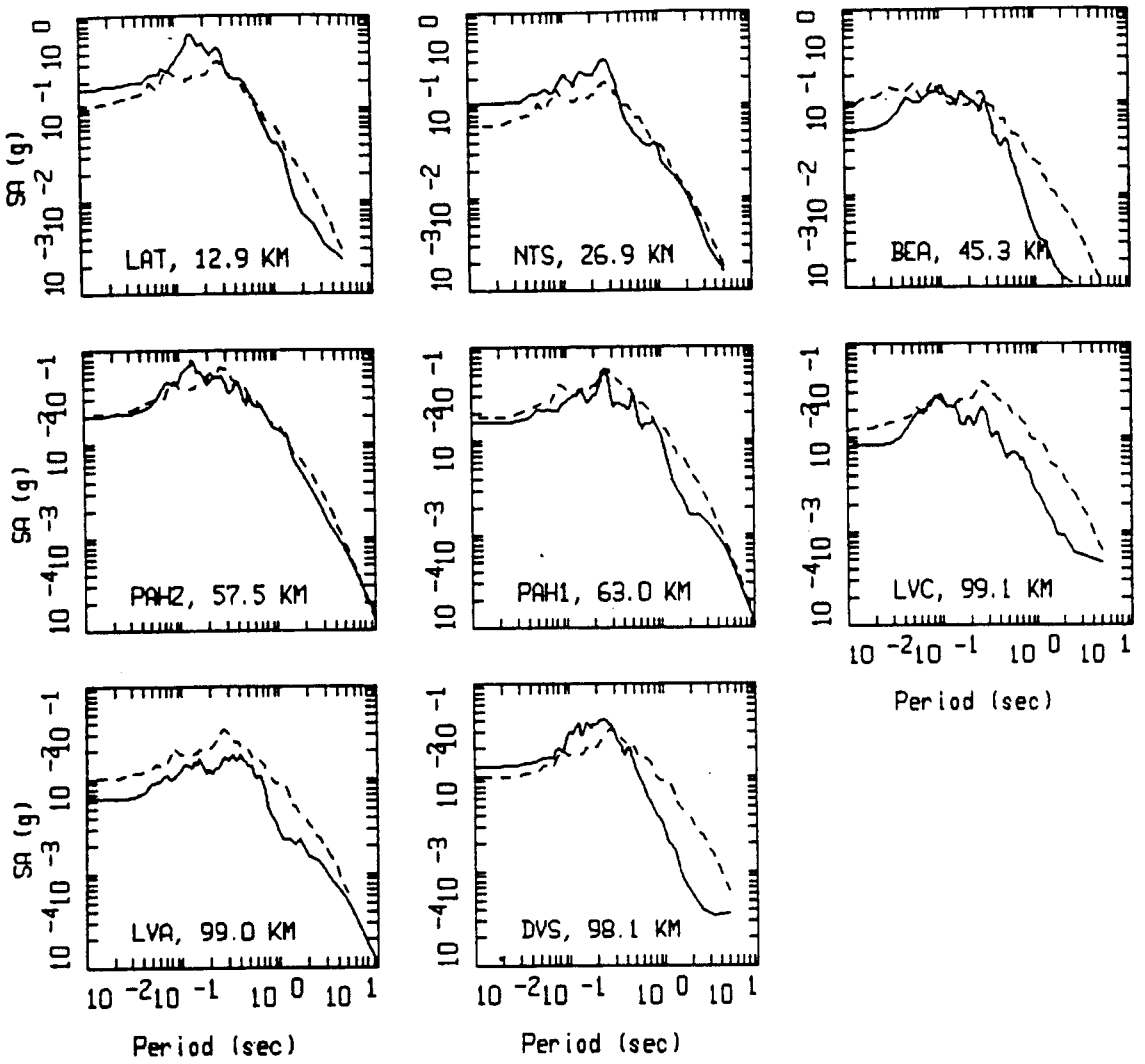

LITTLE SKULL MTN, POINT SOURCE MODELING, PAGE 1 OF 1.
NONLINEAR.

LEGEND
——— DATA
----- MODEL

Figure 5.142

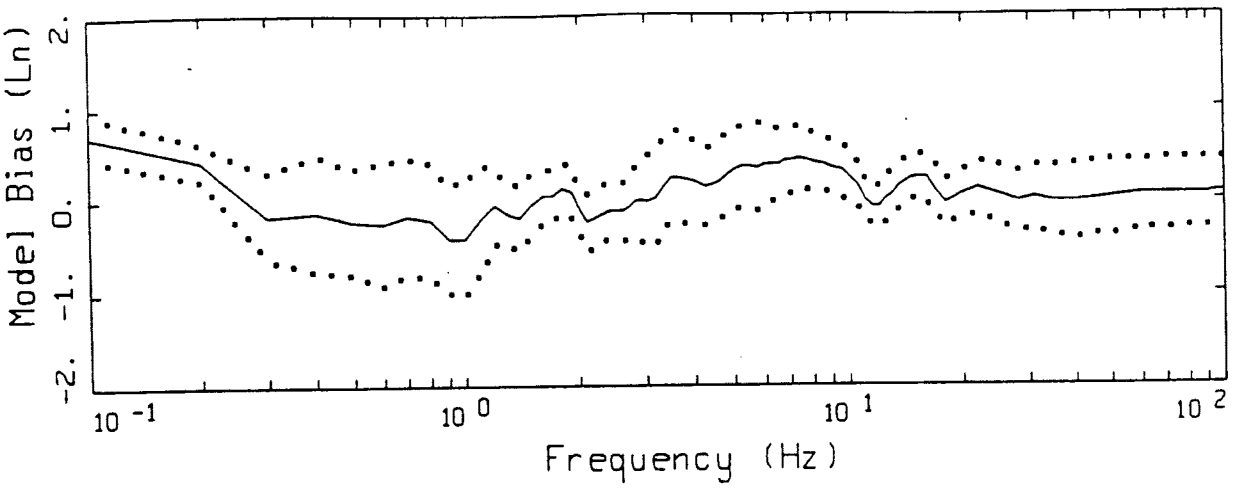

LEGEND
MODELING BIAS
90% CONFIDENCE INTERVAL OF MODELING BIAS
90% CONFIDENCE INTERVAL OF MODELING BIAS

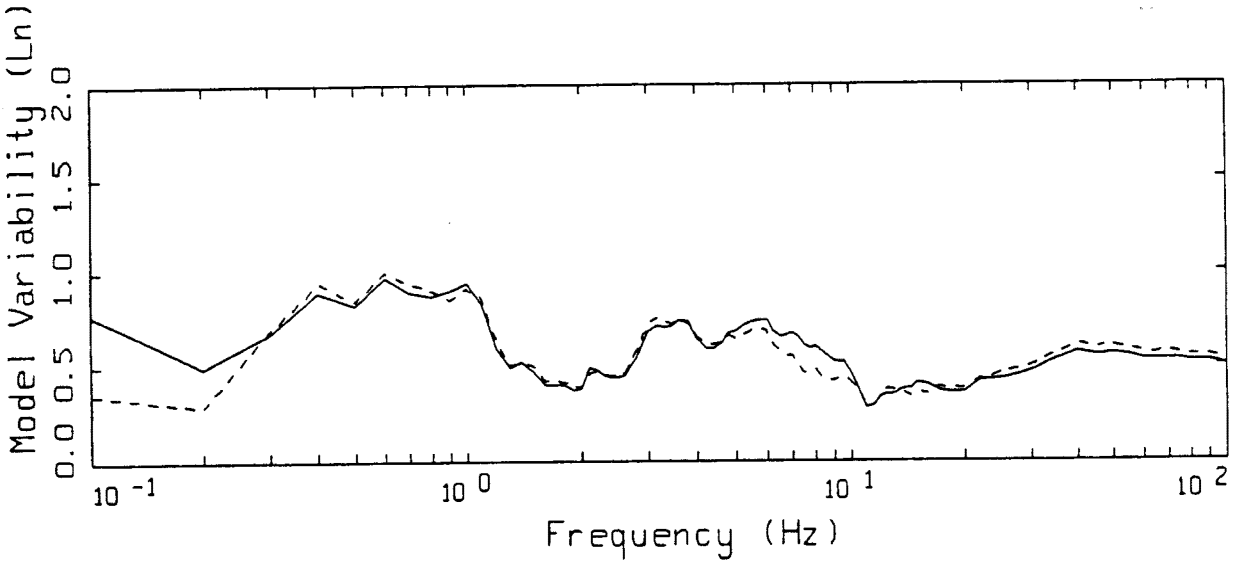

LEGEND
MEAN=0.0
BIAS CORRECTED

LITTLE SKULL MTN FINITE-SOURCE
NONLINEAR, ALL 8 SITES

Figure 5.143

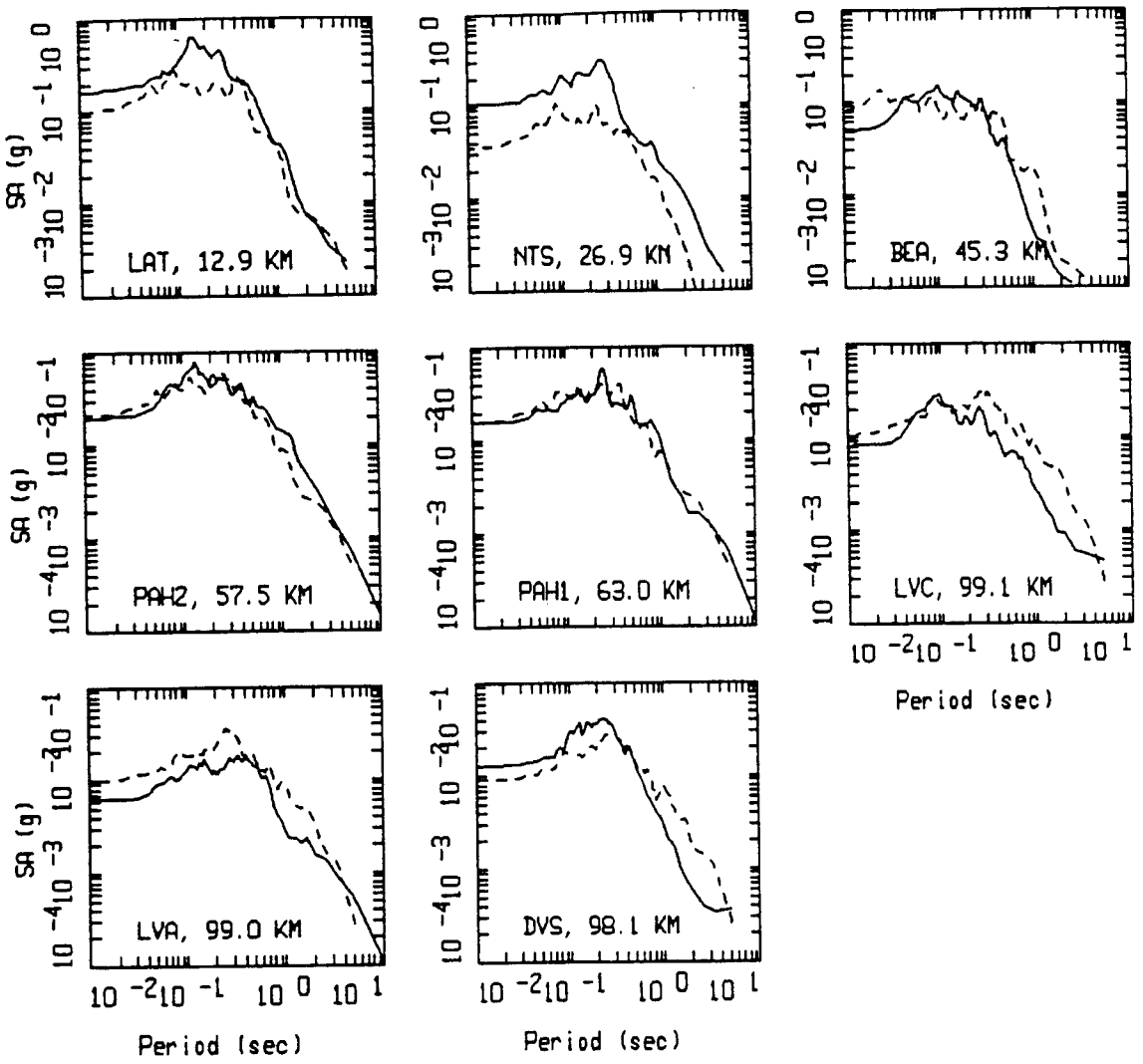

LITTLE SKULL MTN, FINITE SOURCE MODELING, PAGE 1 OF 1.
NONLINEAR.

LEGEND
——— DATA
- - - - - MODEL

Figure 5.144

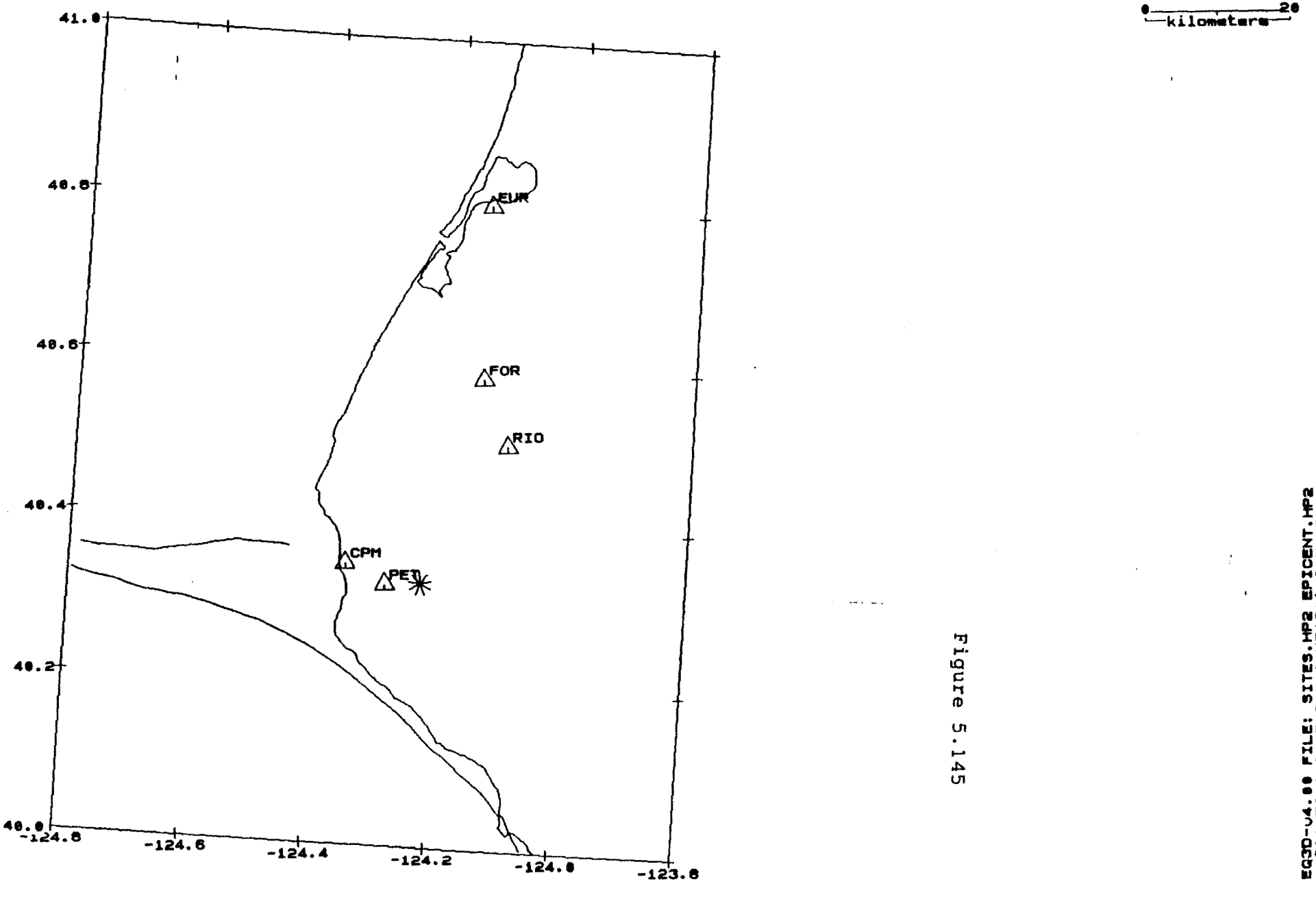
STAT
EPICENTER
0
20
kilometers
41.0
40.8
40.6
40.4
40.2
40.0
-124.8
-124.6
-124.4
-124.2
-124.0
-123.8
EUR
FOR
RIO
CPM
PET
EQ3D-V4.00 FILE: SITES.HP2 EPICENT.HP2
. SCA:700000 MFAC:1.0 XFAC:1.0 Nm=0 Nx=0

Figure 5.145

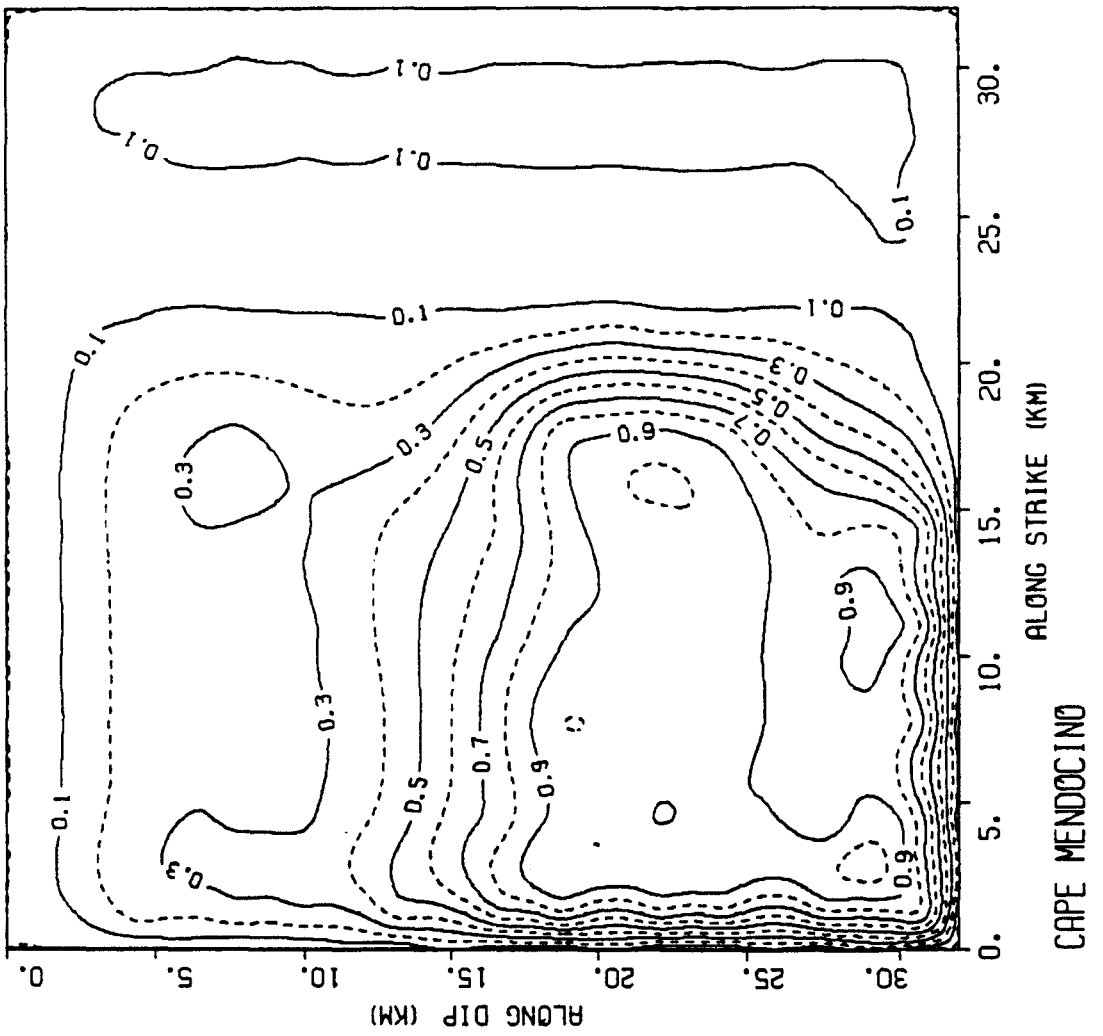
CAPE MENDOCINO
ALONG STRIKE (KM)
ALONG DIP (KM)
0.
5.
10.
15.
20.
25.
30.
0.1
0.3
0.5
0.7
0.9

Figure 5.146

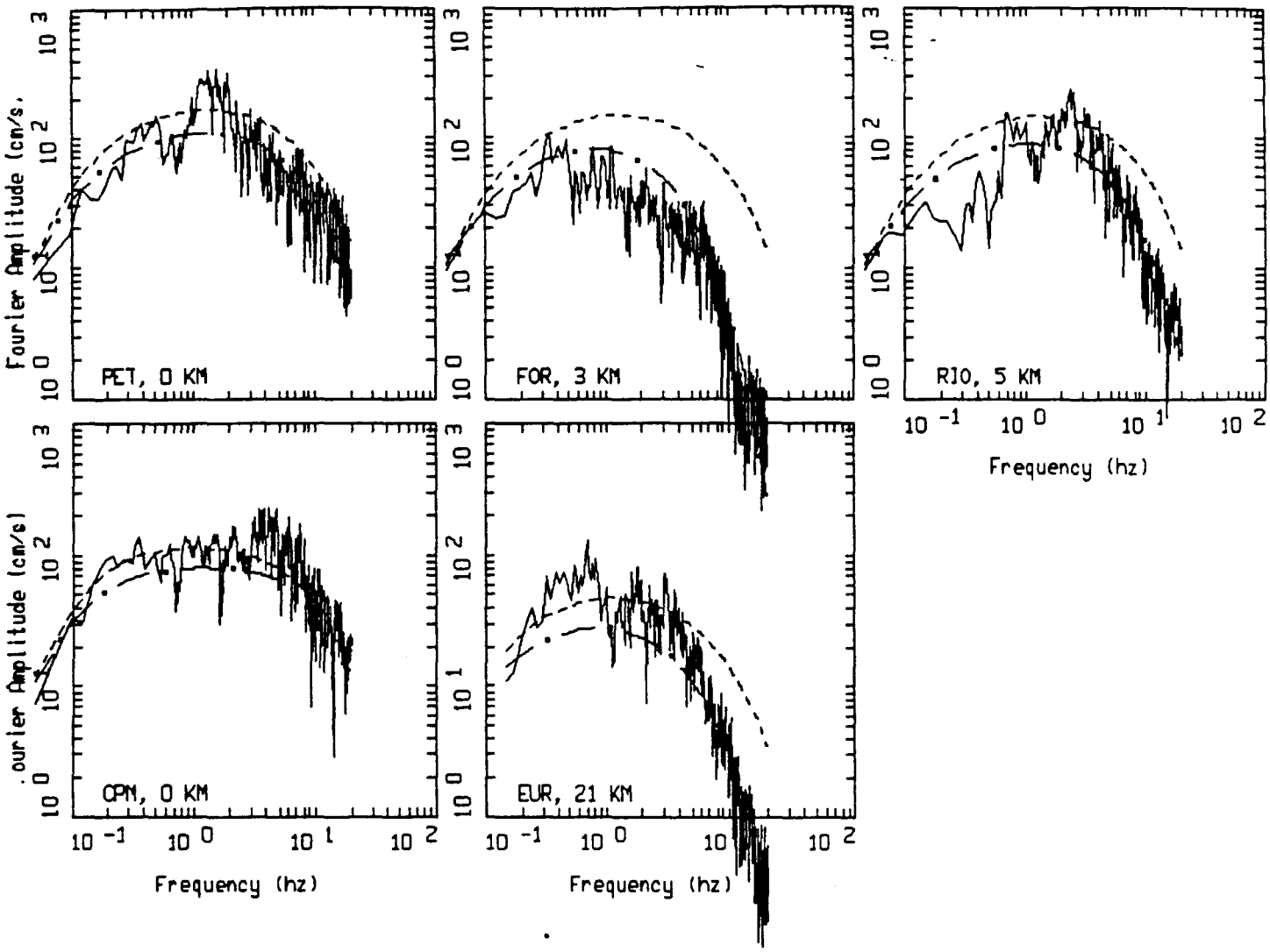

CAPE MENDOCINO EARTHQUAKE 4/25/92, M=6.8.

LEGEND

——— DATA

- - - - - INITIAL MODEL

— • — FINAL MODEL

Figure 5.147

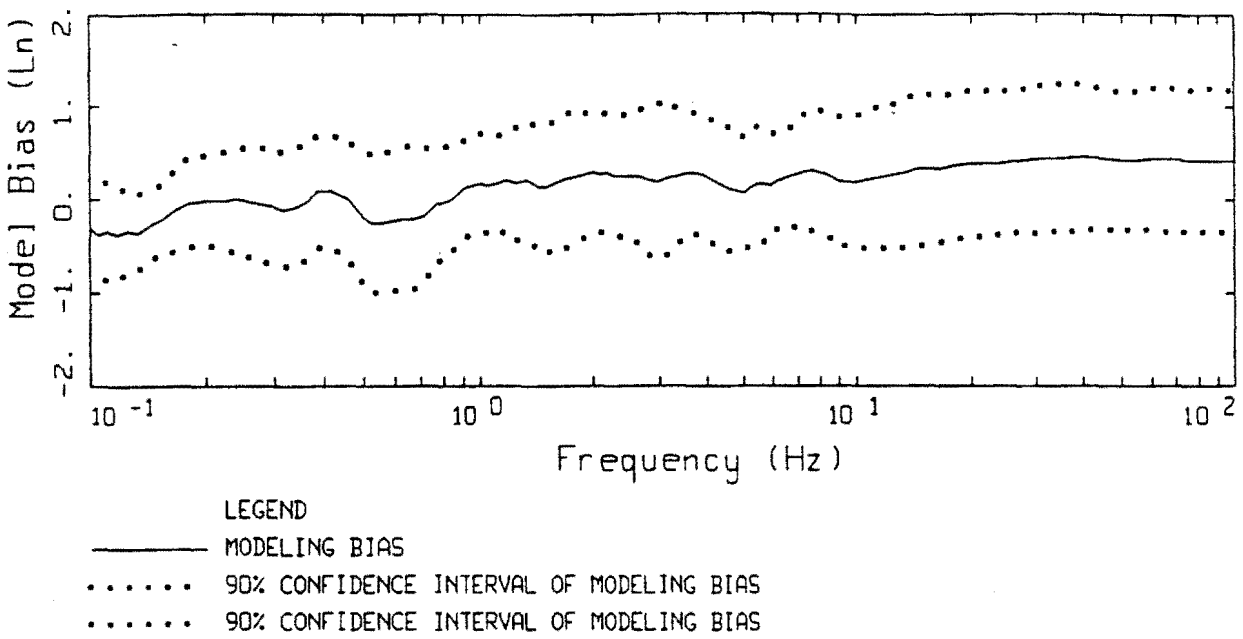

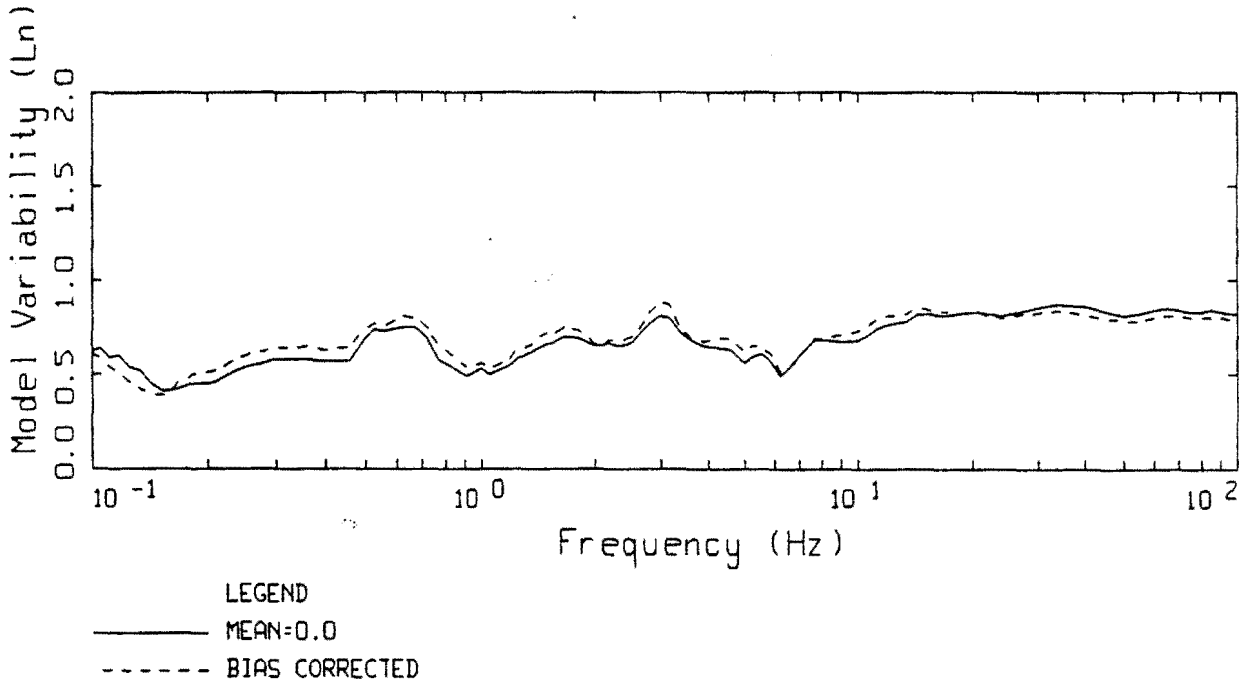

CAPE MENDOCINO POINT-SOURCE
NONLINEAR, ALL 5 SITES

Figure 5.148

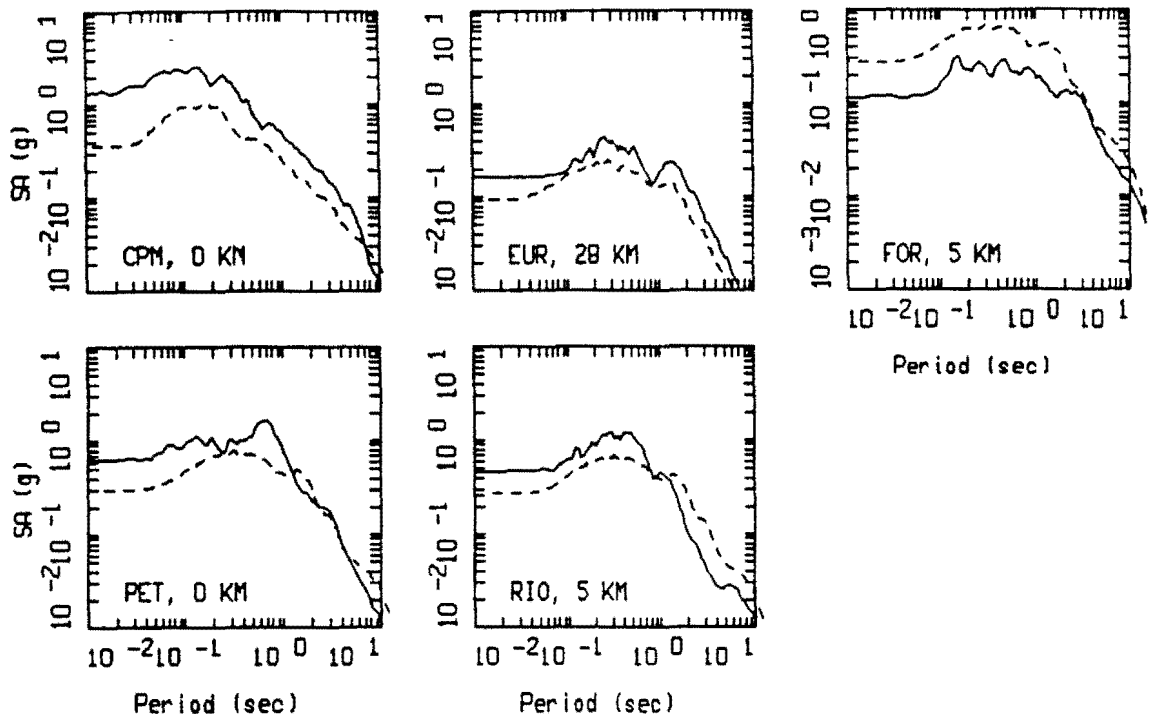

CAPE MENDOCINO, POINT SOURCE MODELING, PAGE 1 OF 1.
NONLINEAR.

LEGEND
——— DATA
----- MODEL

Figure 5.149

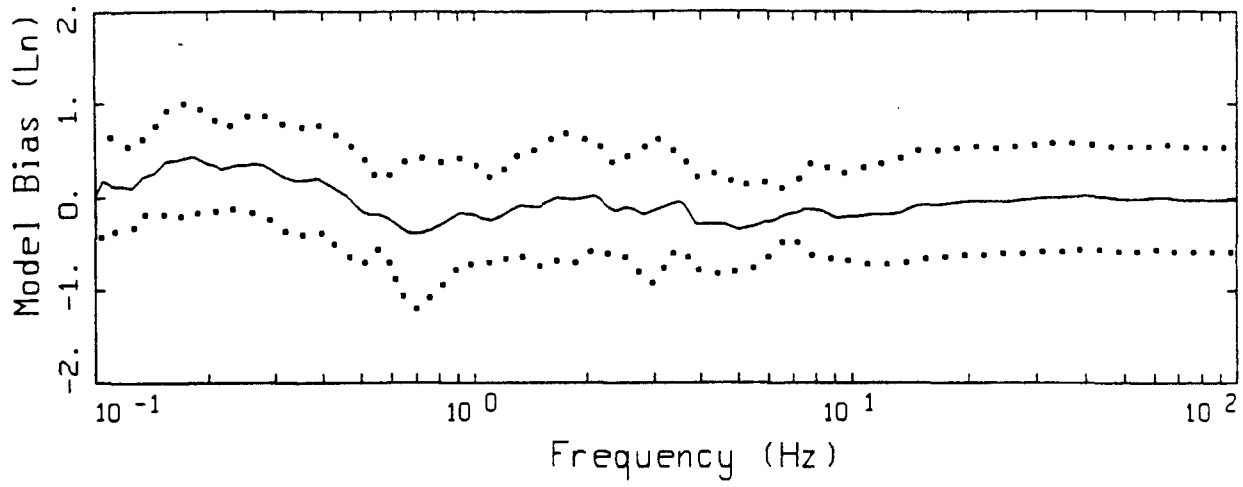

LEGEND
MODELING BIAS
90% CONFIDENCE INTERVAL OF MODELING BIAS
90% CONFIDENCE INTERVAL OF MODELING BIAS

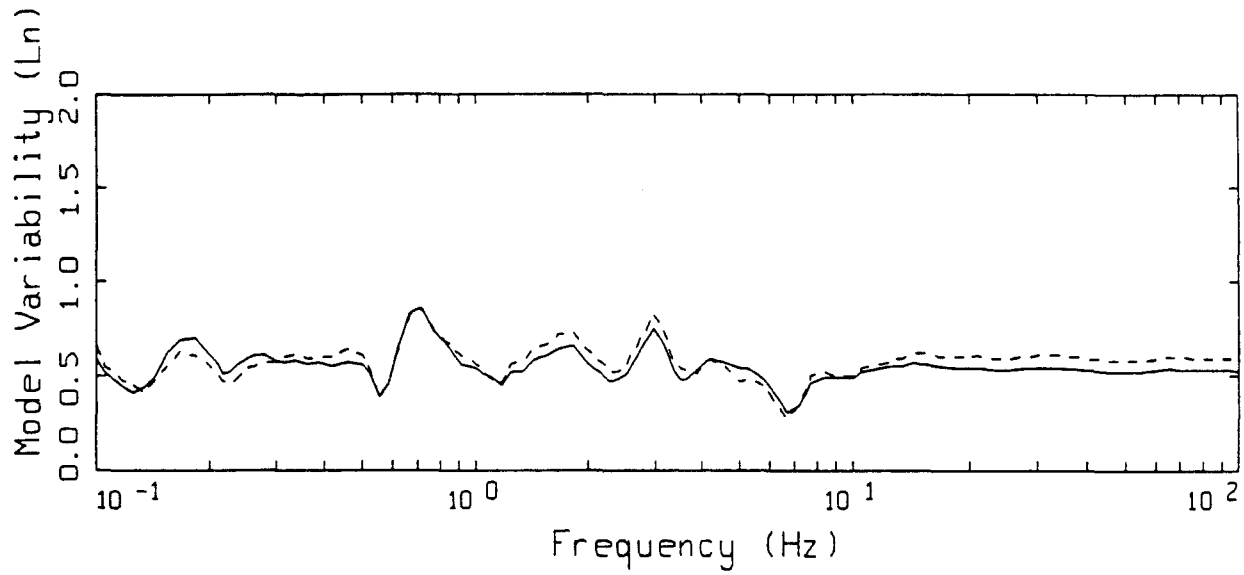

LEGEND
MEAN=0.0
BIAS CORRECTED

CAPE MENDOCINO FINITE-SOURCE
NONLINEAR, ALL 5 SITES

Figure 5.150

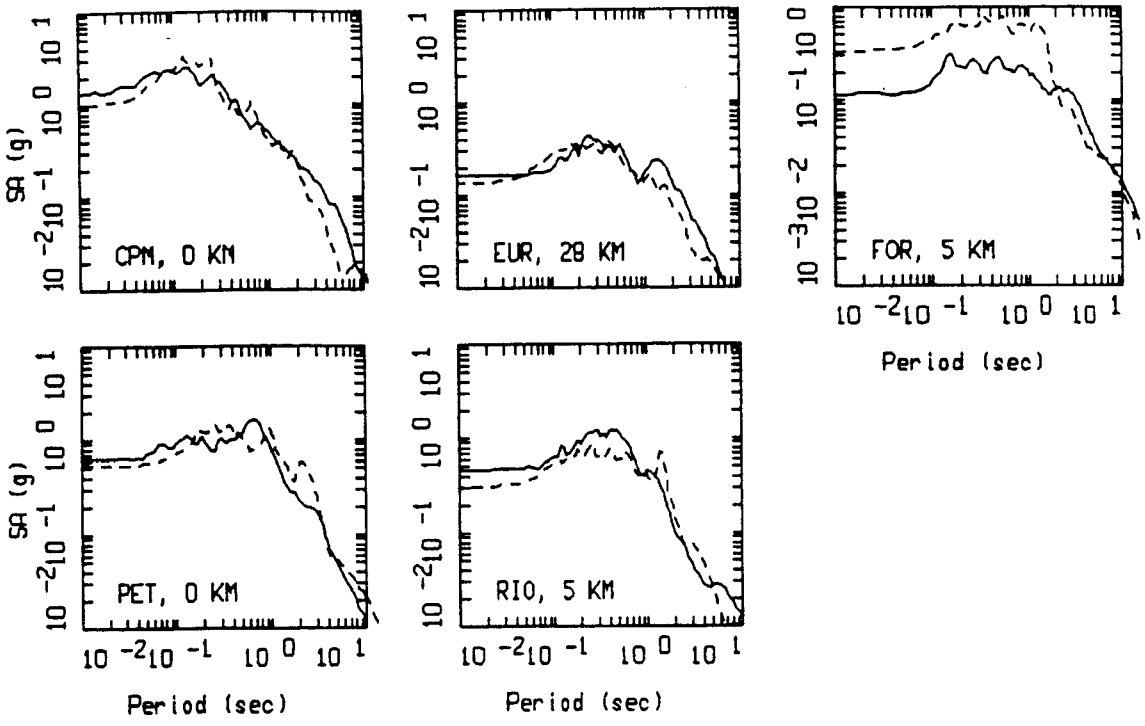

CAPE MENDOCINO, FINITE SOURCE MODELING, PAGE 1 OF 1.
NONLINEAR.

LEGEND
——— DATA
----- MODEL

Figure 5.151

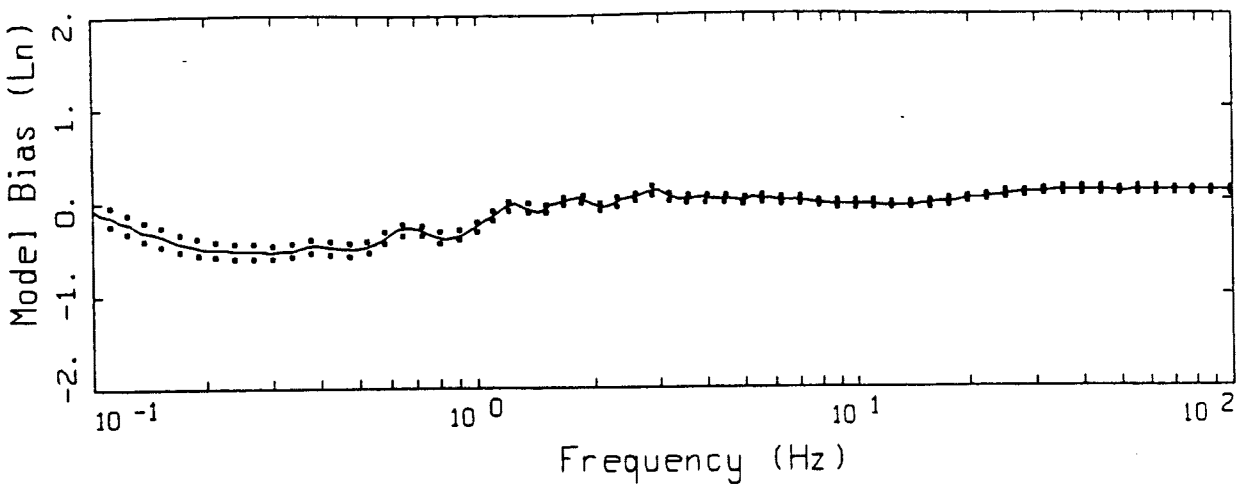

LEGEND
MODELING BIAS
90% CONFIDENCE INTERVAL OF MODELING BIAS
90% CONFIDENCE INTERVAL OF MODELING BIAS

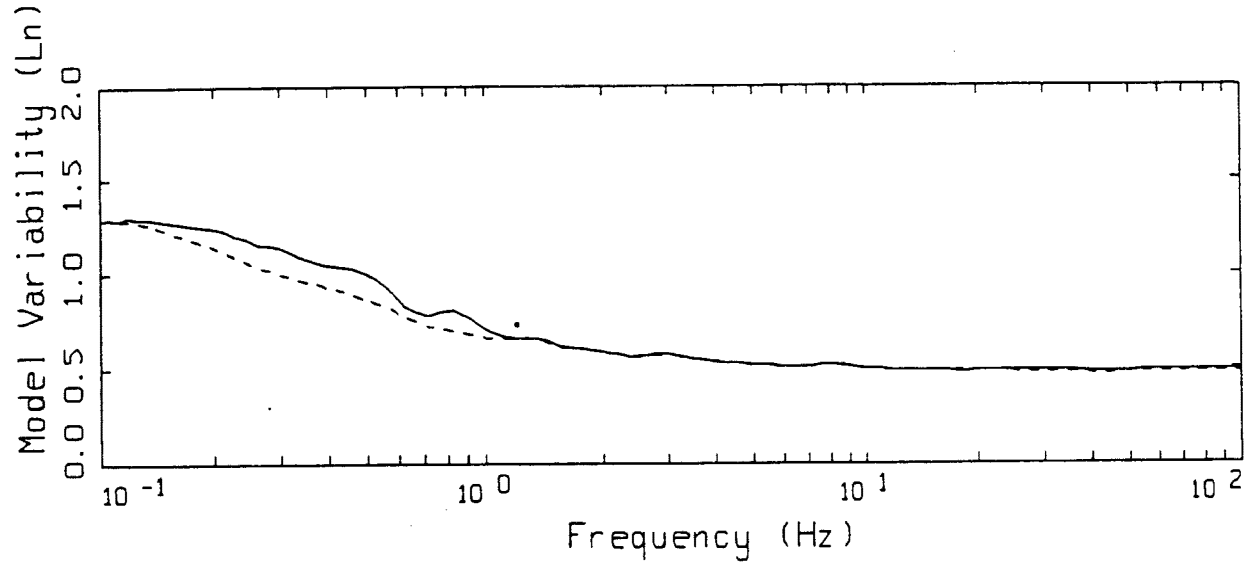

LEGEND
MEAN=0.0
BIAS CORRECTED

16 EARTHQUAKES POINT-SOURCE
NONLINEAR, ALL 503 SITES

Figure 5.152

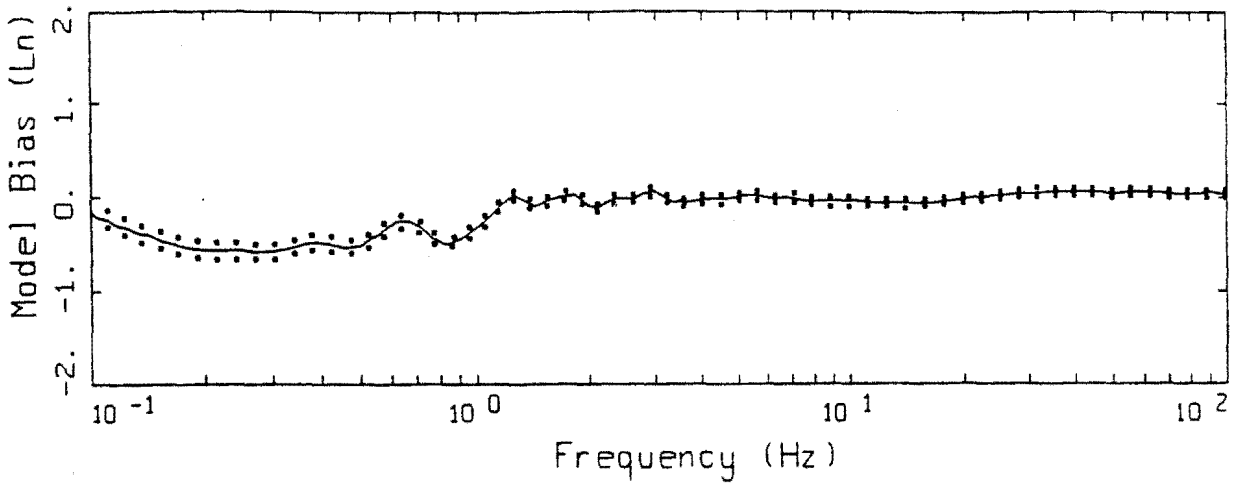

LEGEND
——— MODELING BIAS
..... 90% CONFIDENCE INTERVAL OF MODELING BIAS
..... 90% CONFIDENCE INTERVAL OF MODELING BIAS

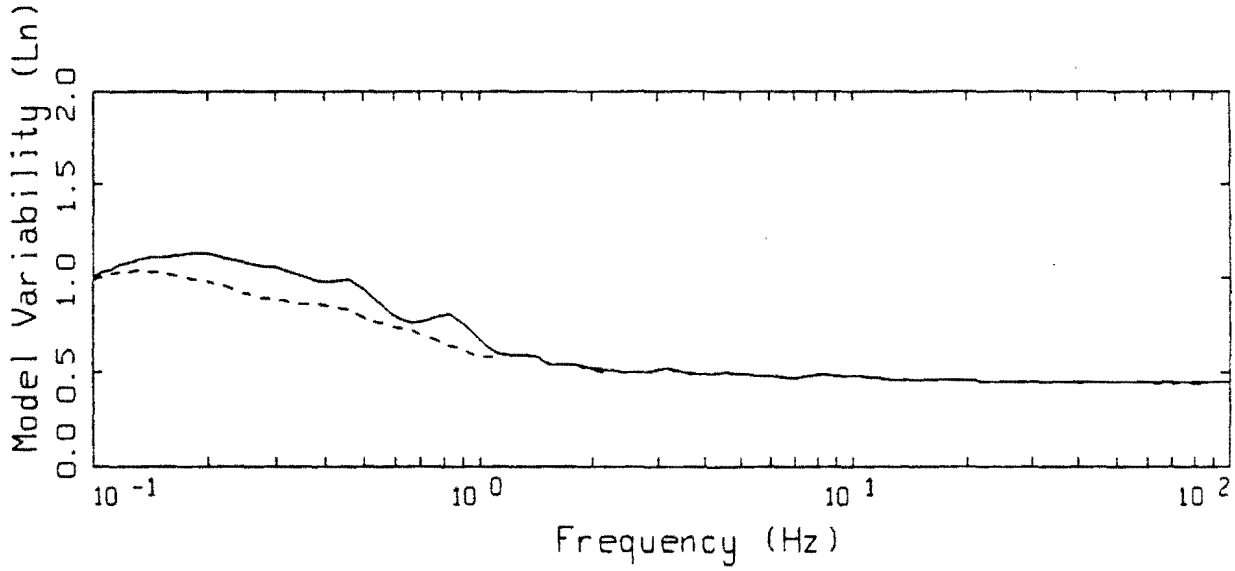

LEGEND
——— MEAN=0.0
------ BIAS CORRECTED

16 EARTHQUAKES POINT-SOURCE
NONLINEAR, ALL 344 SOIL SITES

Figure 5.153

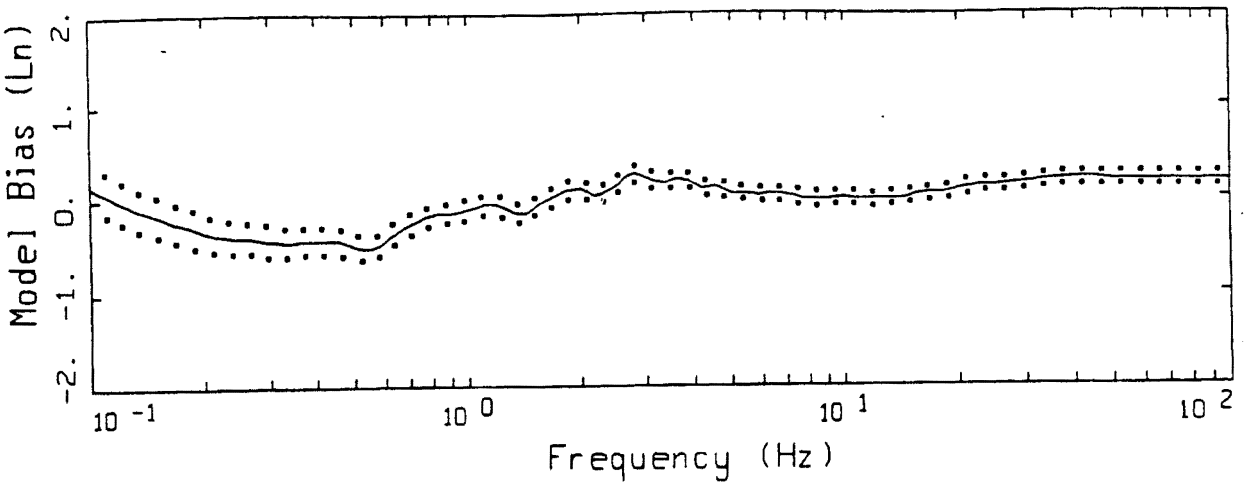

LEGEND
MODELING BIAS
90% CONFIDENCE INTERVAL OF MODELING BIAS
90% CONFIDENCE INTERVAL OF MODELING BIAS

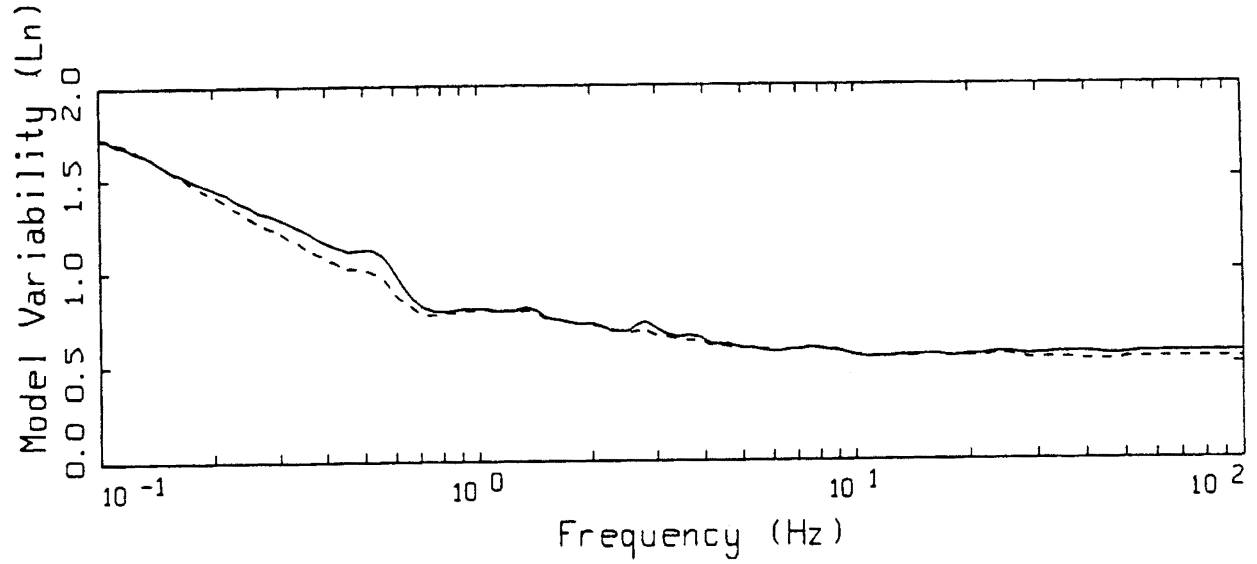

LEGEND
MEAN=0.0
BIAS CORRECTED

16 EARTHQUAKES POINT-SOURCE
NONLINEAR, ALL 159 ROCK SITES

Figure 5.154

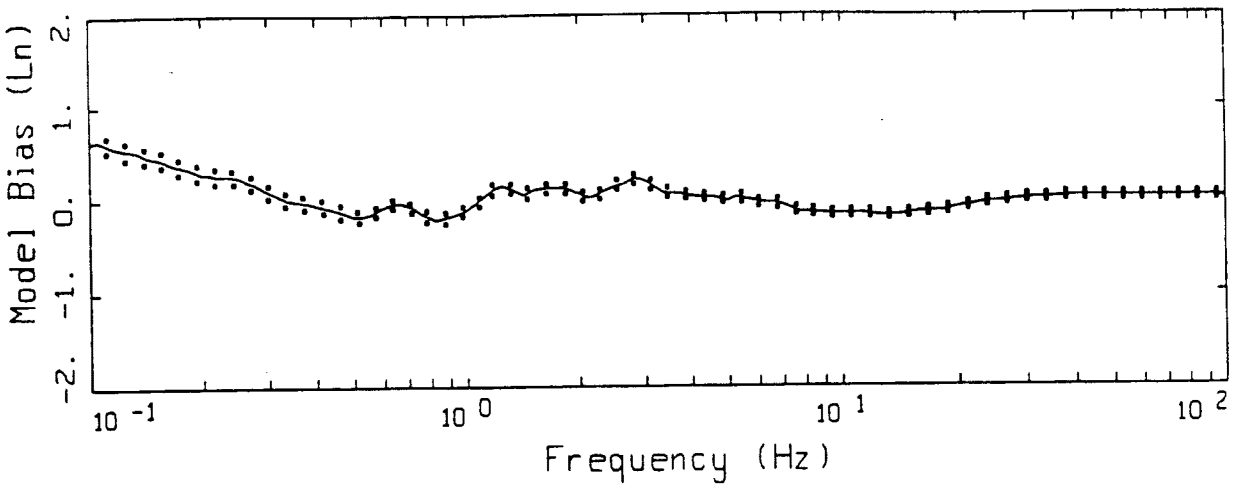

LEGEND
MODELING BIAS
90% CONFIDENCE INTERVAL OF MODELING BIAS
90% CONFIDENCE INTERVAL OF MODELING BIAS

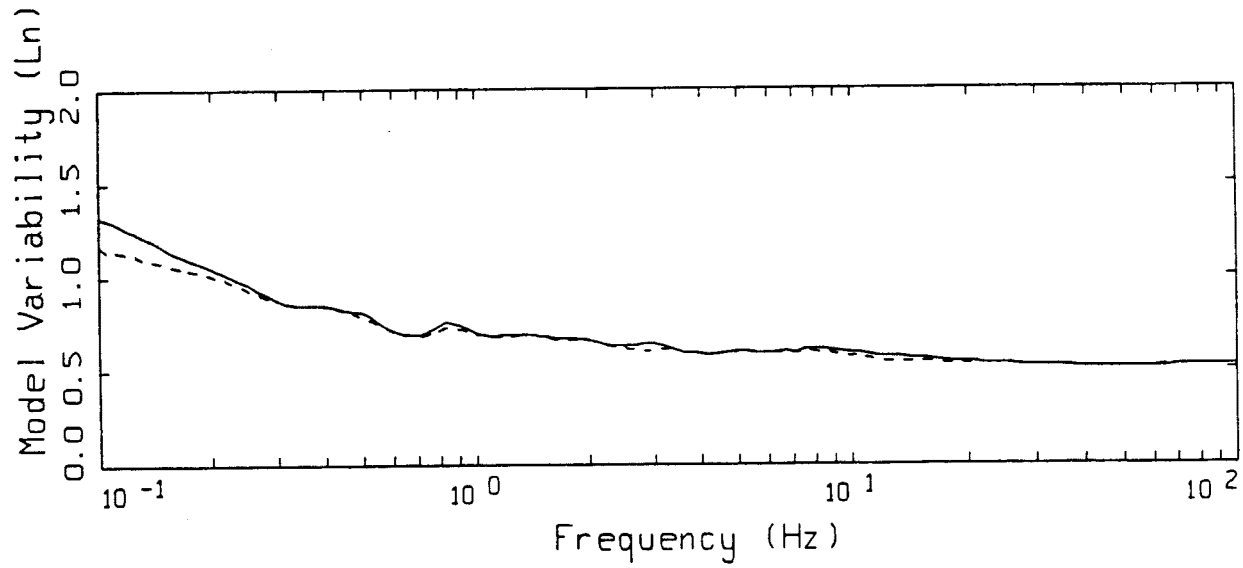

LEGEND
MEAN=0.0
BIAS CORRECTED

15 EARTHQUAKES FINITE-SOURCE
NONLINEAR, ALL 487 SITES

Figure 5.155

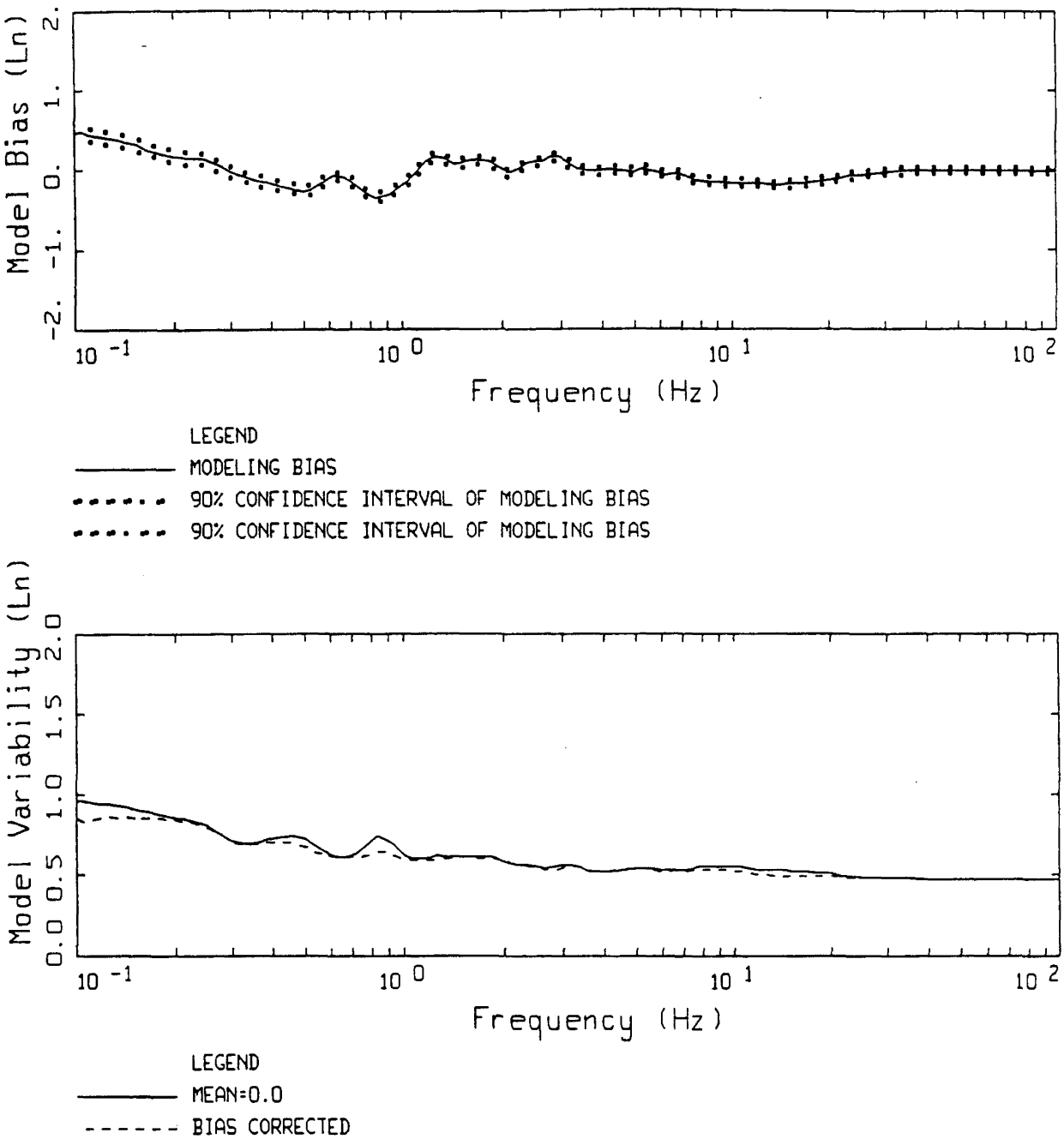
Model Bias (Ln)
2.
1.
0.
-1.
-2.
10 -1
10 0
10 1
10 2
Frequency (Hz)
LEGEND
MODELING BIAS
90% CONFIDENCE INTERVAL OF MODELING BIAS
90% CONFIDENCE INTERVAL OF MODELING BIAS
Model Variability (Ln)
0.0
0.5
1.0
1.5
2.0
10 -1
10 0
10 1
10 2
Frequency (Hz)
LEGEND
MEAN=0.0
BIAS CORRECTED
15 EARTHQUAKES FINITE-SOURCE
NONLINEAR, ALL 328 SOIL SITES

Figure 5.156

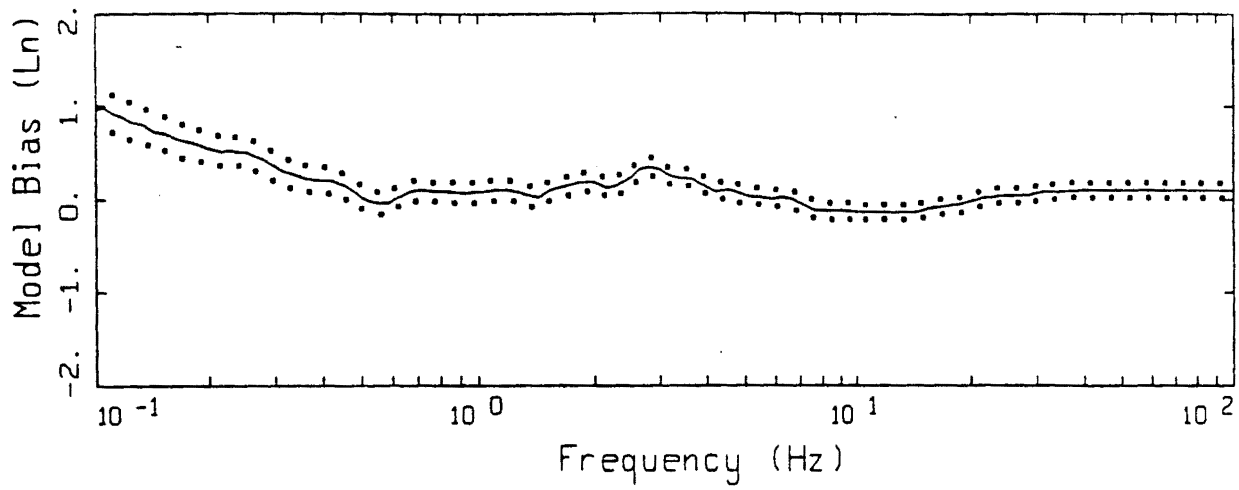

LEGEND
MODELING BIAS
90% CONFIDENCE INTERVAL OF MODELING BIAS
90% CONFIDENCE INTERVAL OF MODELING BIAS

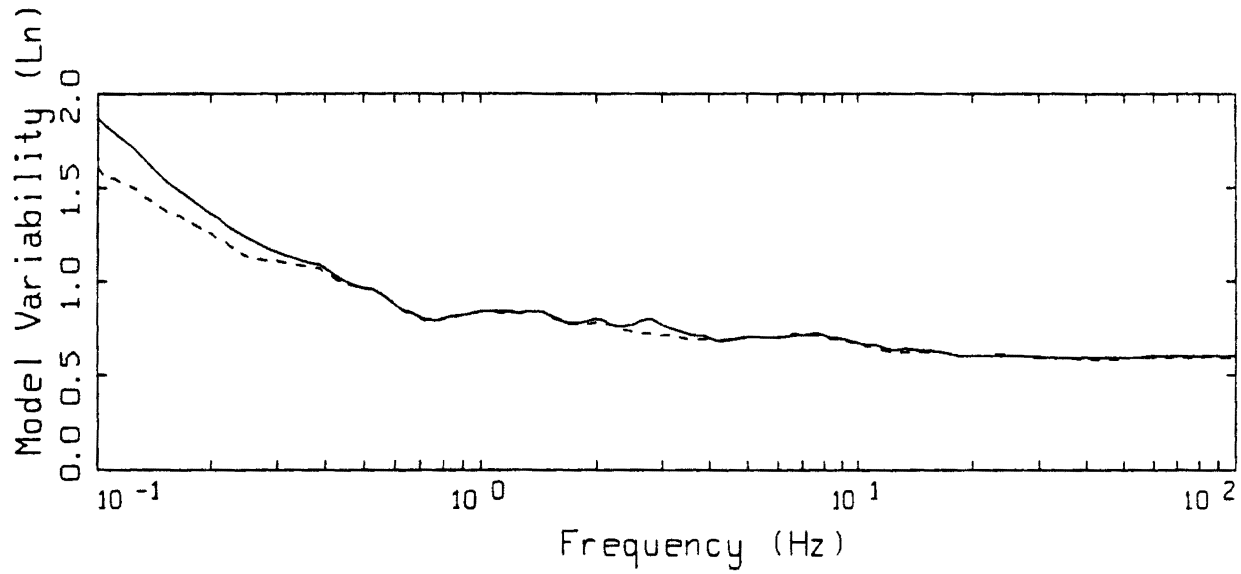

LEGEND
MEAN=0.0
BIAS CORRECTED

15 EARTHQUAKES FINITE-SOURCE
NONLINEAR, ALL 159 ROCK SITES

Figure 5.157

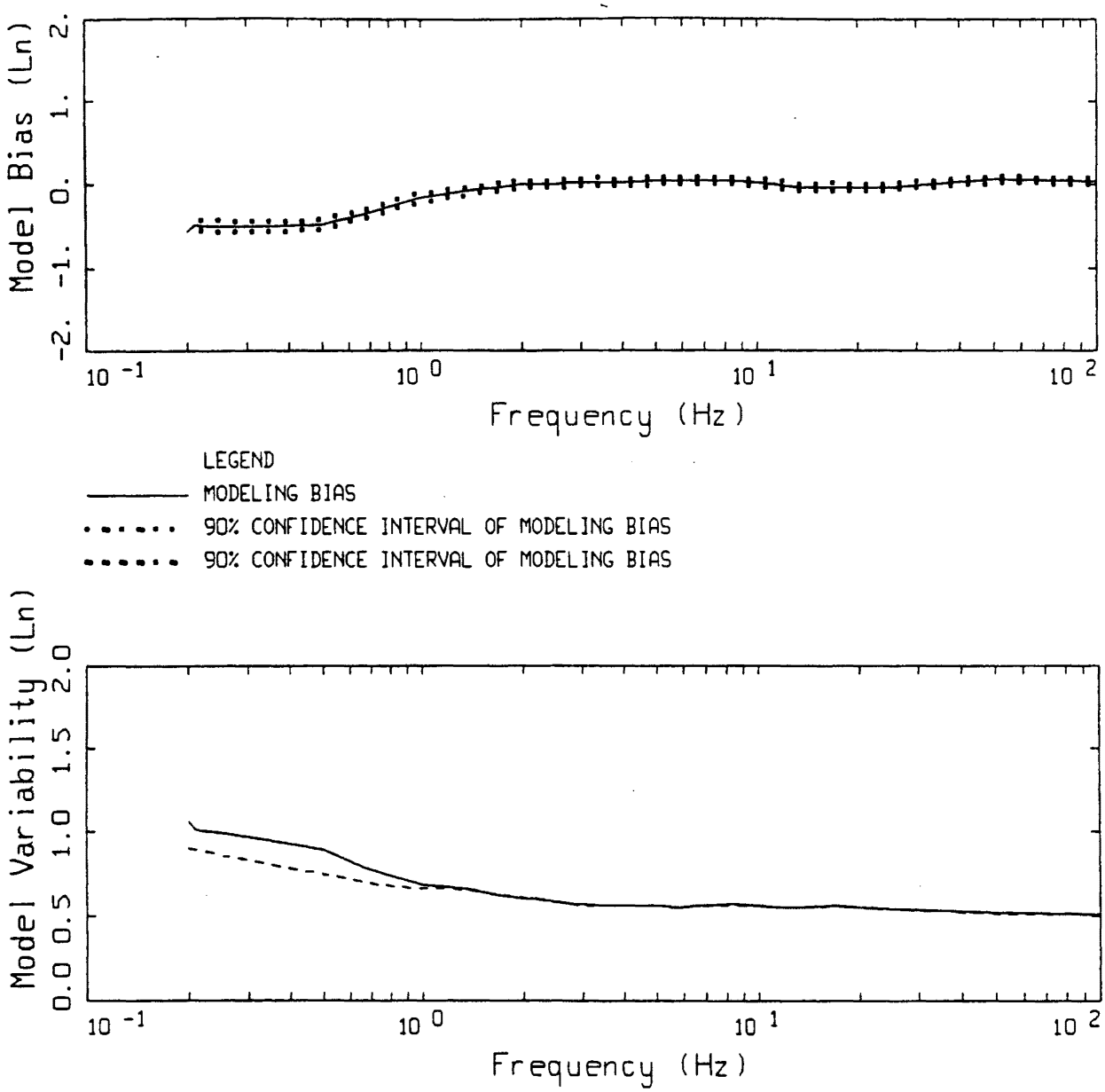
Model Bias (Ln)
2.
1.
0.
-1.
-2.
10 -1
10 0
10 1
10 2
Frequency (Hz)
LEGEND
MODELING BIAS
90% CONFIDENCE INTERVAL OF MODELING BIAS
90% CONFIDENCE INTERVAL OF MODELING BIAS
Model Variability (Ln)
0.0
0.5
1.0
1.5
2.0
10 -1
10 0
10 1
10 2
Frequency (Hz)
LEGEND
MEAN=0.0
BIAS CORRECTED
15 EARTHQUAKES, EMPIRICAL RELATION
ALL 481 SITES

Figure 5.158

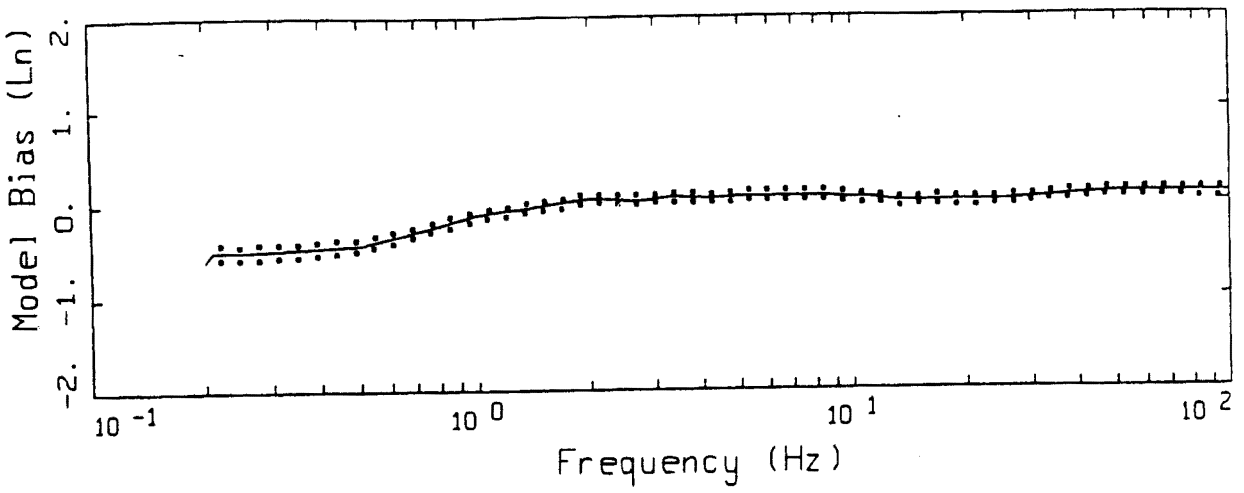

LEGEND
MODELING BIAS
90% CONFIDENCE INTERVAL OF MODELING BIAS
90% CONFIDENCE INTERVAL OF MODELING BIAS

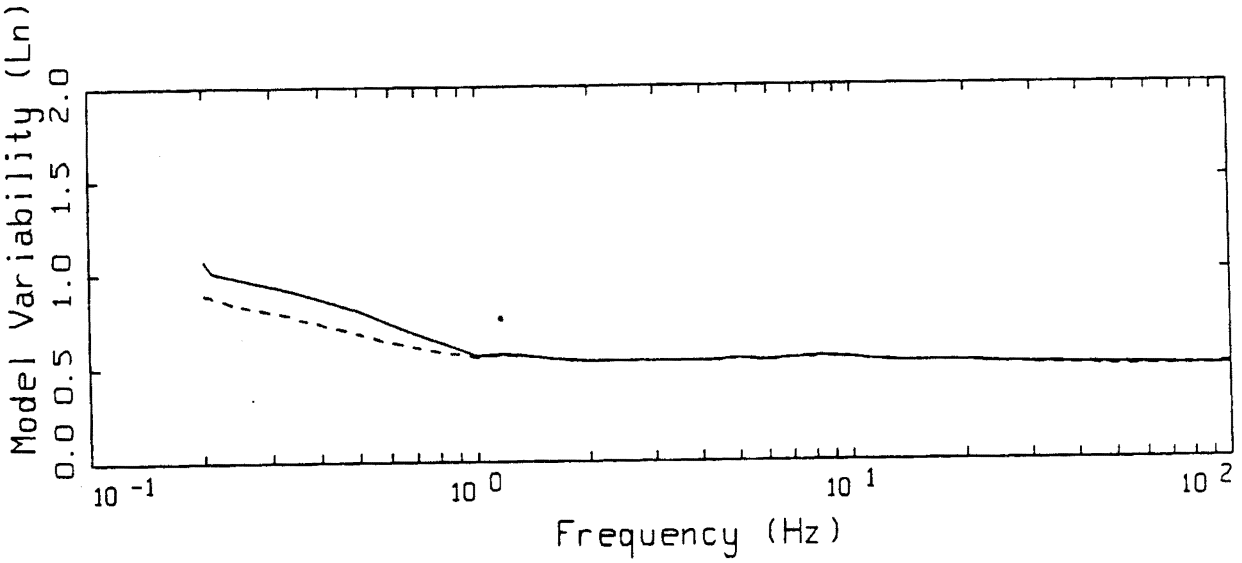

LEGEND
MEAN=0.0
BIAS CORRECTED

15 EARTHQUAKES, EMPIRICAL RELATION
344 SOIL SITES

Figure 5.159

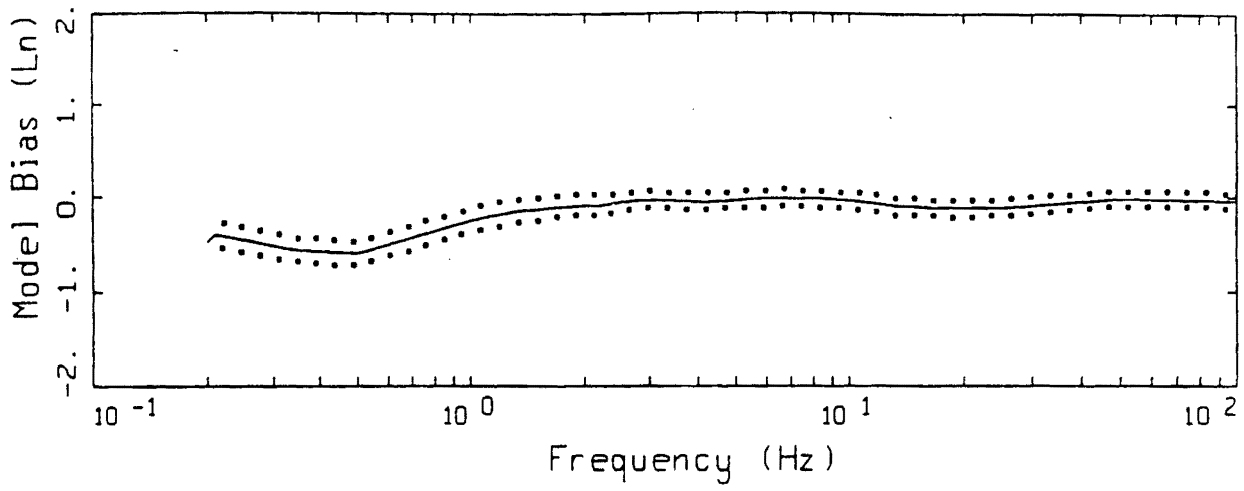

LEGEND
MODELING BIAS
90% CONFIDENCE INTERVAL OF MODELING BIAS
90% CONFIDENCE INTERVAL OF MODELING BIAS

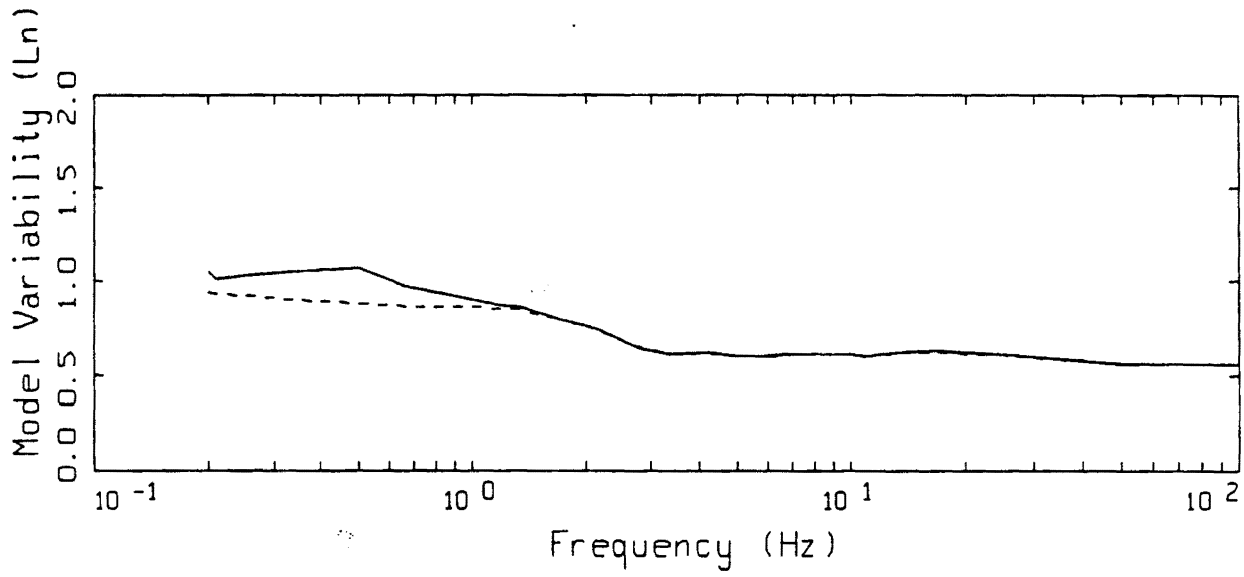

LEGEND
MEAN=0.0
BIAS CORRECTED

15 EARTHQUAKES, EMPIRICAL RELATION
137 ROCK SITES

Figure 5.160

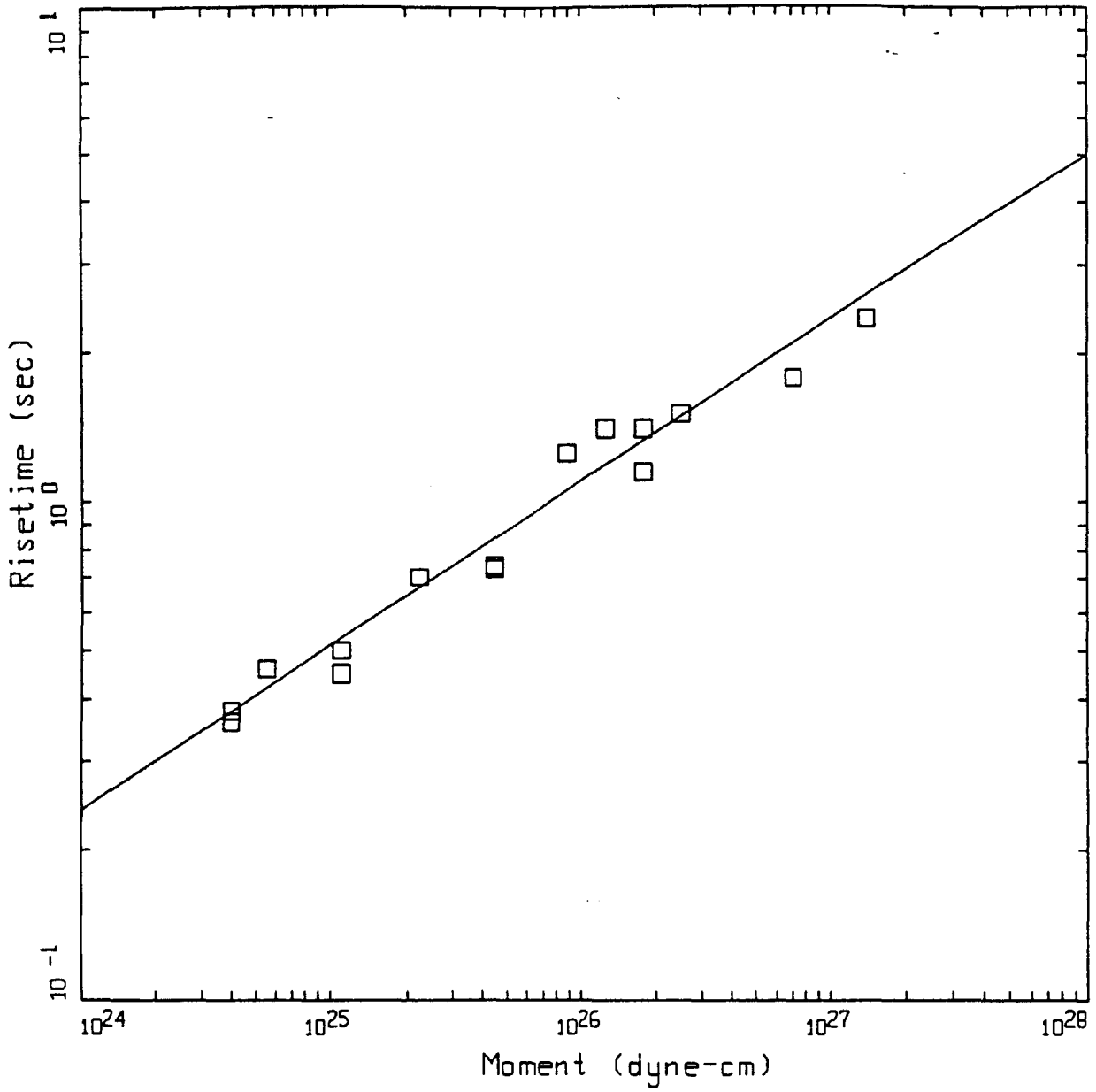

RISETIME VS MOMENT

LEGEND

MODELING RESULTS

LOG(T) = 0.33 * LOG(MO) - 8.54

Figure 5.161

Chapter 6 Figure Captions

Figure Set 6.1. Comparison of **M** 6.5 attenuation of peak ground acceleration for soft rock conditions. Solid line: empirical attenuation (Appendix A) for a vertical strike-slip fault. Open circles: finite-source model simulations using direct, multiply, and post-critically reflected rays (Chapter 2) for the Loma Prieta crustal model (Table 5.7). X's: finite-source simulations using 1/R geometrical attenuation. Dashed line: Point-source simulations using 1/R ($1/\sqrt{R}$, $R > 50$ km) geometrical attenuation, a depth of 8 km, and a stress drop of 59 bars (Table 6.1). Q(f) model is 176 $f^{0.6}$ (North Coast, Table 4.1) and kappa is 0.038 sec (Table 6.1).

Figure Set 6.2. Comparison of **M** 5.5 and **M** 7.5 attenuation of peak ground acceleration for soft rock conditions. Solid line: empirical attenuation (Appendix A) for a vertical strike-slip fault. Open circles: average finite-source model simulations using direct, multiply, and post-critically reflected rays (Chapter 2) for three crustal models (Loma Prieta, Northridge, and Landers). Dashed line: Point-source simulations using 1/R ($1/\sqrt{R}$, $R > 50$ km) geometrical attenuation, a depth of 6 km for **M** 5.5 and 8 km for **M** 7.5, and a stress drop of 59 bars (Table 6.1). Q(f) model is appropriate for each earthquake province (Table 4.1) and kappa is 0.038 sec (Table 6.1).

Figure Set 6.3a. Spectral match to the response spectra of the empirical attenuation relation (Appendix A) for a vertical strike-slip mechanism. Magnitudes are M 5.5, 6.5, and 7.5 at fault distances 1, 5, 10, 20, 50, 100, and 20 km and the site condition is soft rock. Model simulations use RVT to compute the response spectra and the derived Fourier amplitude spectra are used in the empirical inversions for stress drop, kappa, and Q(f) models.

Figure Set 6.3b. Spectral match to the response spectra of the empirical attenuation relation (Appendix A) for a vertical strike-slip mechanism. Magnitudes are M 5.5, 6.5, and 7.5 at fault distances 1, 5, 10, 20, 50, 100, and 20 km and the site condition is deep soil. Model simulations use RVT to compute the response spectra and the derived Fourier amplitude spectra are used in the empirical inversions for stress drop, kappa, and Q(f) models.

Figure 6.4. Mean and $\pm$ 1 σ transfer functions (Fourier amplitude spectra) from 8 km to the surface computed from 30 randomly generated soft rock profiles using the correlation model of Appendix C.

Figure 6.5. Mean and $\pm$ 1 σ transfer functions (Fourier amplitude spectra) from 8 km to the surface computed from 30 randomly generated deep soil profiles using the correlation model of Appendix C.

Figure 6.6. Smooth generic transfer functions for soft rock and deep soil based upon figures 6.4 and 6.5 respectively.

Figure 6.7. Comparison of mean and median transfer functions computed for the deep soil profile. Transfer functions have been smoothed with a 2 Hz triangular smoothing window.

Figure Set 6.8. Comparison of Fourier amplitude spectra from the empirical inversions. Solid lines: spectra from the fits to the empirical attenuation response spectra (Figure Set 6.3a) for a vertical strike-slip mechanism. Dashed lines: initial model calculations. Dash-dotted lines: final model calculations. Rock site conditions.

Figure Set 6.9. Comparison of Fourier amplitude spectra from the empirical inversions. Solid lines: spectra from the fits to the empirical attenuation response spectra (Figure Set 6.3b) for a vertical strike-slip mechanism. Dashed lines: initial model calculations. Dash-dotted lines: final model calculations. Deep soil site conditions.

Figure Set 6.10. Comparison of point-source model simulations to the response spectra computed from the empirical attenuation relation (Appendix A) for a vertical strike-slip mechanism. Magnitudes are M 5.5, 6.5, and 7.5 at fault distances 1, 5, 10, 20, 50, 100, and 20 km and the site condition is soft rock. Model simulations use RVT to compute the response spectra with the inversion parameters (Table 6.1).

Figure Set 6.11. Comparison of point-source model simulations to the response spectra computed from the empirical attenuation relation (Appendix A) for a vertical strike-slip mechanism. Magnitudes are M 5.5, 6.5, and 7.5 at fault distances 1, 5, 10, 20, 50, 100, and 20 km and the site condition is deep soil. Model simulations use RVT to compute the response spectra with the inversion parameters (Table 6.1).

Figure 6.12. Generic G/G_{max} and hysteretic damping curves for cohesionless soils (EPRI, 1993).

Figure 6.13. Generic G/G_{max} and hysteretic damping curves for Peninsular Range deep cohesionless soils.

Figure 6.14. Generic G/G_{max} and hysteretic damping curves for soft rock.

Figure Set 6.15. Comparison of point-source model simulations to the response spectra computed from the empirical attenuation relation (Appendix A) for a vertical strike-slip mechanism. Magnitude is M 6.5, point-source depth is 8 km, and the stress drop is 59 bars (Table 6.1). Fault distances are 200, 100, 50, 20, 10, 5, and 1 km. Site condition over soft rock.

Figure Set 6.16. Comparison of point-source model simulations to the response spectra computed from the empirical attenuation relation (Appendix A) for a vertical strike-slip mechanism. Magnitude is M 6.5, point-source depth is 8 km, and the stress drop is 59 bars (Table 6.1). Fault distances are 200, 100, 50, 20, 10, 5, and 1 km. Site condition over deep soil.

Figure Set 6.17. Model bias and variability estimates for the empirical attenuation relation (Appendix A) computed over 7 soil sites for the point-source model. Magnitude is M 6.5 and distances are 0, 7, 15, 30, 60, 100, and 200 km.

Figure Set 6.18. Model bias and variability estimates for the empirical attenuation relation (Appendix A) computed over 7 rock sites for the point-source model. Magnitude is M 6.5 and distances are 0, 7, 15, 30, 60, 100, and 200 km.

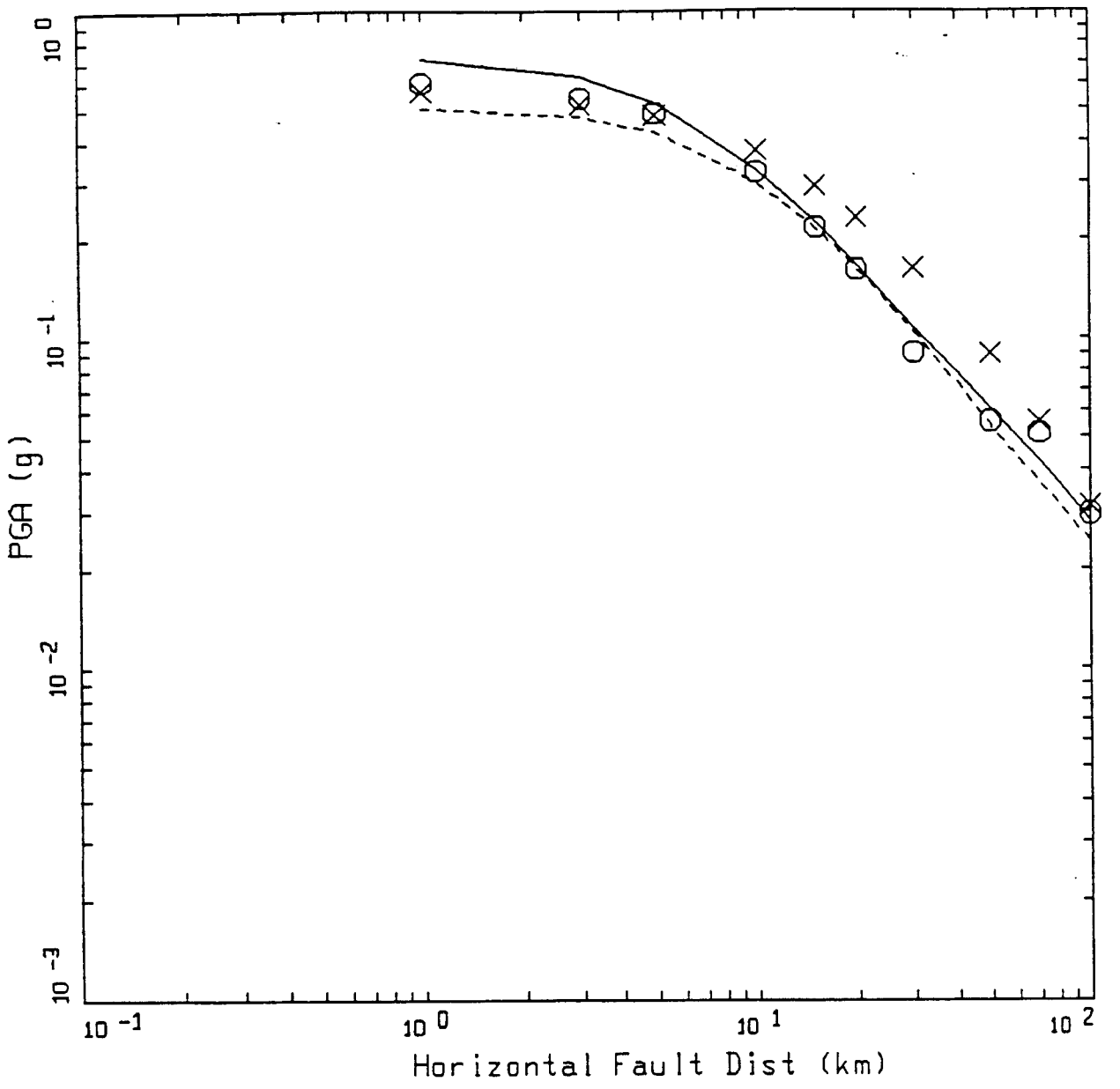

M=6.5
AVERAGE PGA ATTENUATION

LEGEND
EMPIRICAL
FINITE SOURCE: AVG OVER 11 SLIP MODELS, 11 SITES, LOMA PRIETA CRUST
FINITE SOURCE: AVG OVER 11 SLIP MODELS, 11 SITES, LOMA PRIETA CRUST (1/R)
POINT SOURCE

Figure 6.1

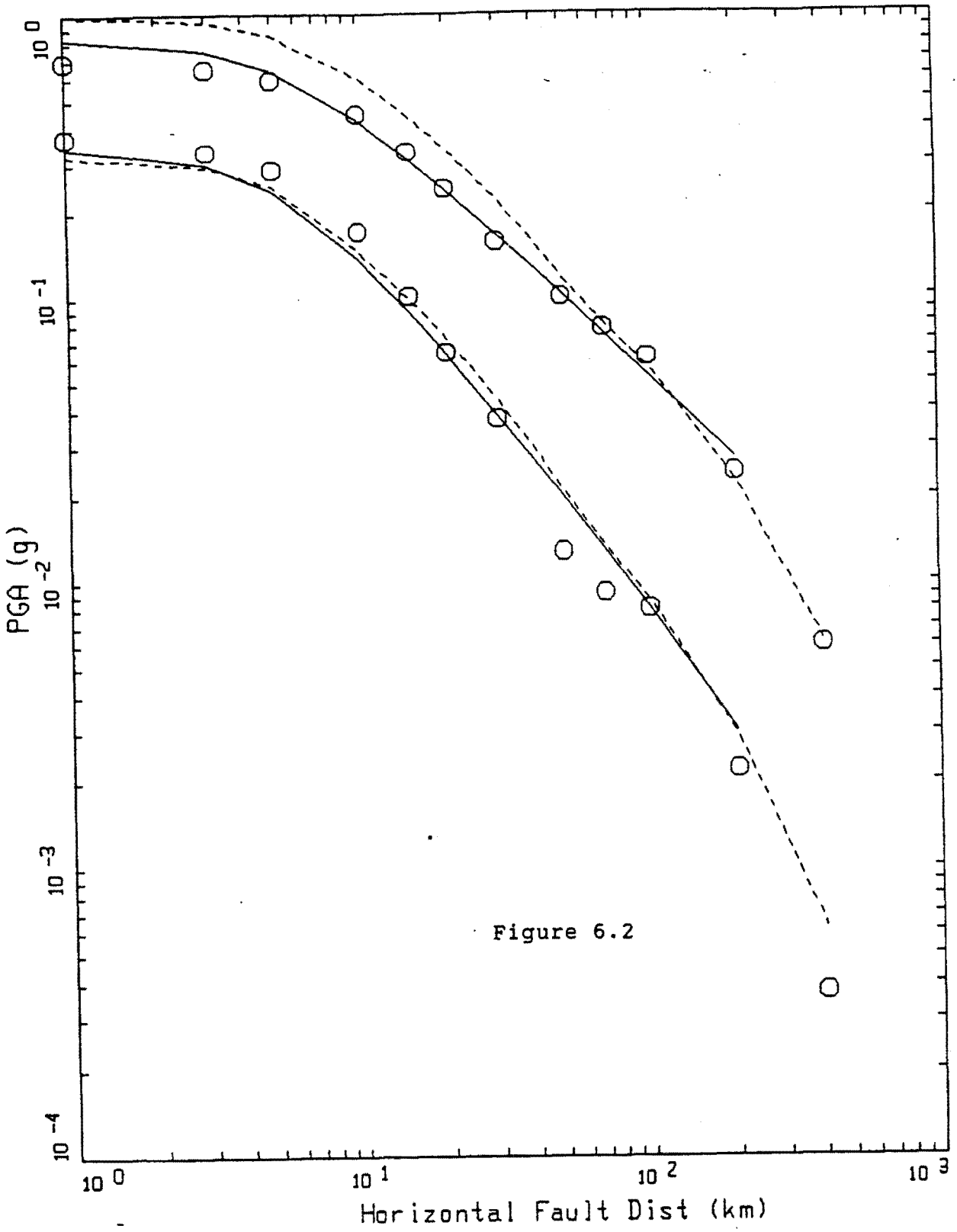

Figure 6.2

M=5.5 AND M=7.5
AVERAGE PGA ATTENUATION

LEGEND

EMPIRICAL

FINITE SOURCE: AVG OVER 11 SLIP MODELS, 11 SITES, 3 CRUSTAL MODELS

POINT SOURCE

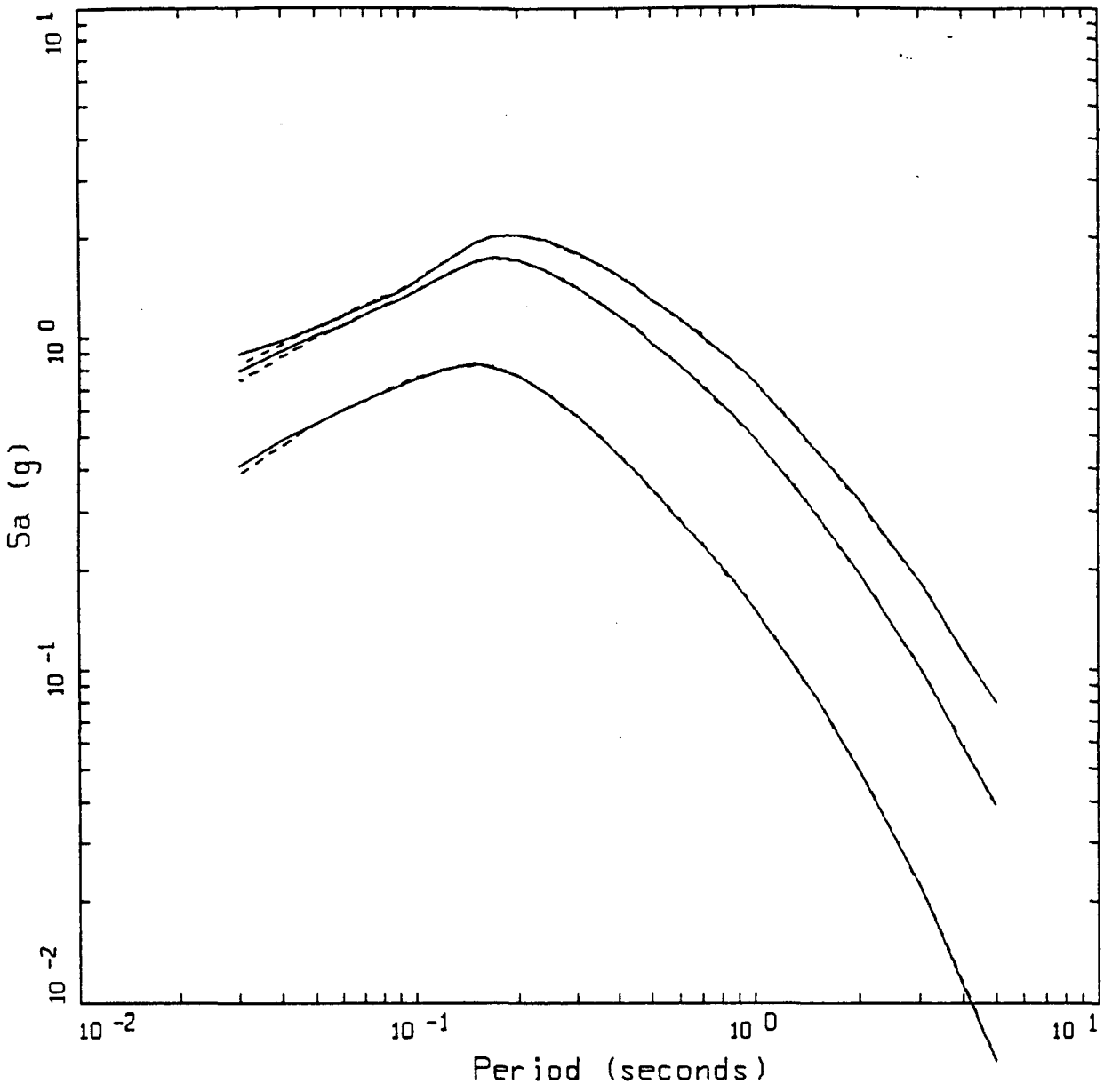

SPECTRAL MATCH TO EMPIRICAL
ROCK, STRIKE SLIP, R=001 KM

LEGEND

——— EMPIRICAL, M = 5.5
----- 5 %, RVT RESPONSE SPECTRUM, M = 5.5
——— EMPIRICAL, M = 6.5
----- 5 %, RVT RESPONSE SPECTRUM, M = 6.5
——— EMPIRICAL, M = 7.5
----- 5 %, RVT RESPONSE SPECTRUM, M = 7.5

Figure Set 6.3a

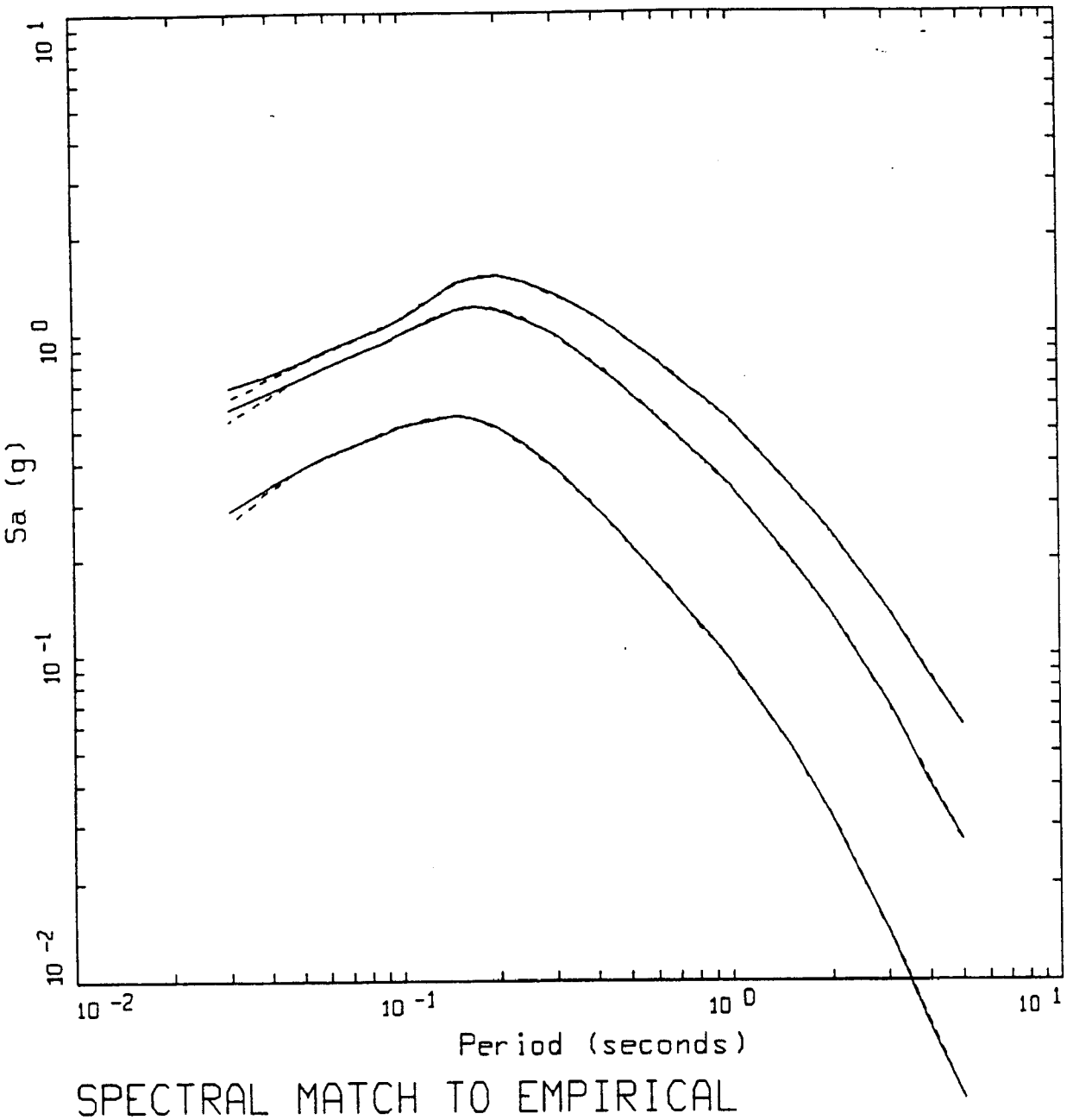

SPECTRAL MATCH TO EMPIRICAL ROCK, STRIKE SLIP, R=005 KM

LEGEND

——— EMPIRICAL, M = 5.5

----- 5 %, RVT RESPONSE SPECTRUM, M = 5.5

——— EMPIRICAL, M = 6.5

----- 5 %, RVT RESPONSE SPECTRUM, M = 6.5

——— EMPIRICAL, M = 7.5

----- 5 %, RVT RESPONSE SPECTRUM, M = 7.5

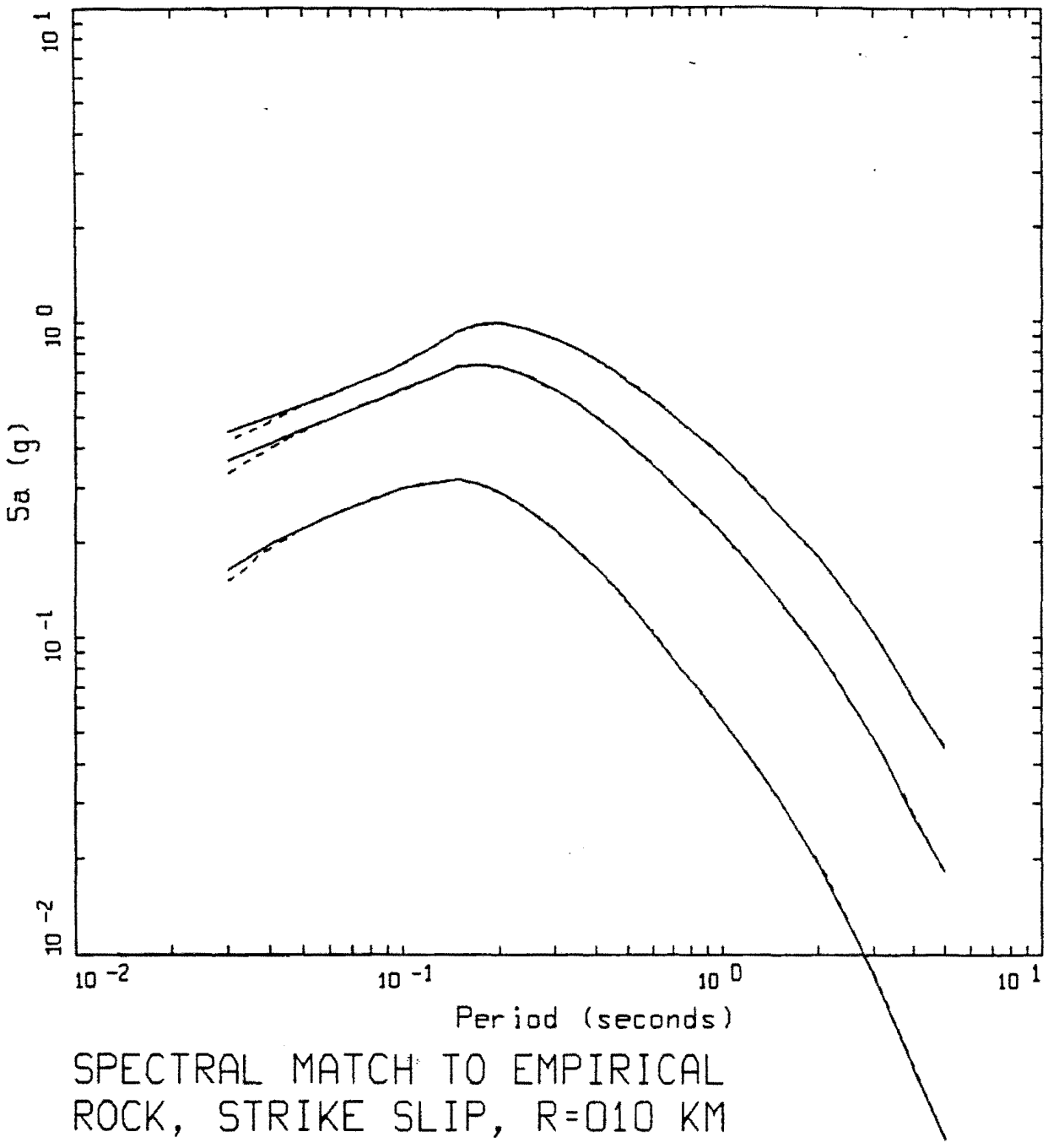

SPECTRAL MATCH TO EMPIRICAL
ROCK, STRIKE SLIP, R=010 KM

LEGEND

——— EMPIRICAL, M = 5.5

----- 5 %, RVT RESPONSE SPECTRUM, M = 5.5

——— EMPIRICAL, M = 6.5

----- 5 %, RVT RESPONSE SPECTRUM, M = 6.5

——— EMPIRICAL, M = 7.5

----- 5 %, RVT RESPONSE SPECTRUM, M = 7.5

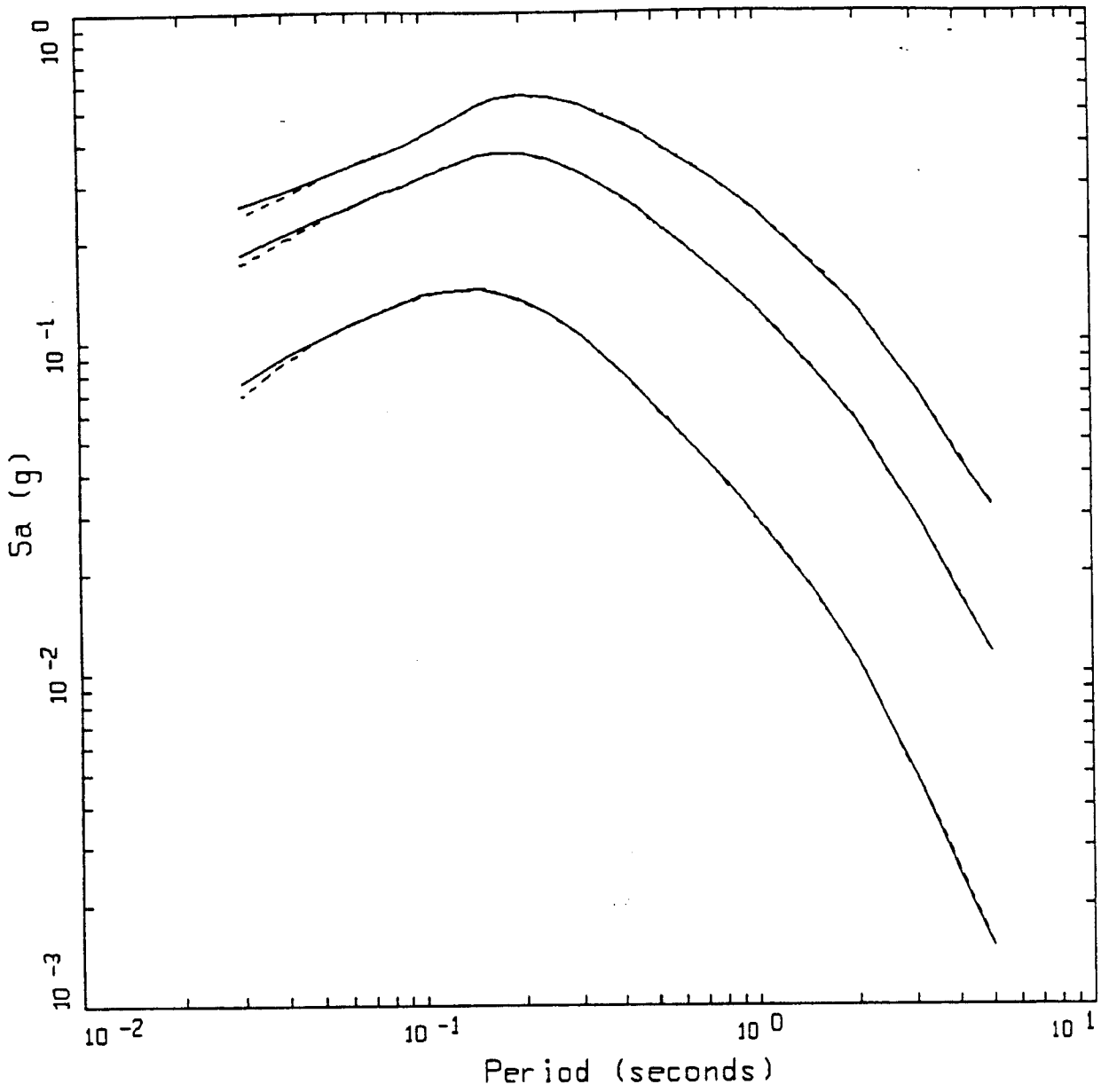

SPECTRAL MATCH TO EMPIRICAL ROCK, STRIKE SLIP, R=020 KM

LEGEND

——— EMPIRICAL, M = 5.5

----- 5 %, RVT RESPONSE SPECTRUM, M = 5.5

——— EMPIRICAL, M = 6.5

----- 5 %, RVT RESPONSE SPECTRUM, M = 6.5

——— EMPIRICAL, M = 7.5

----- 5 %, RVT RESPONSE SPECTRUM, M = 7.5

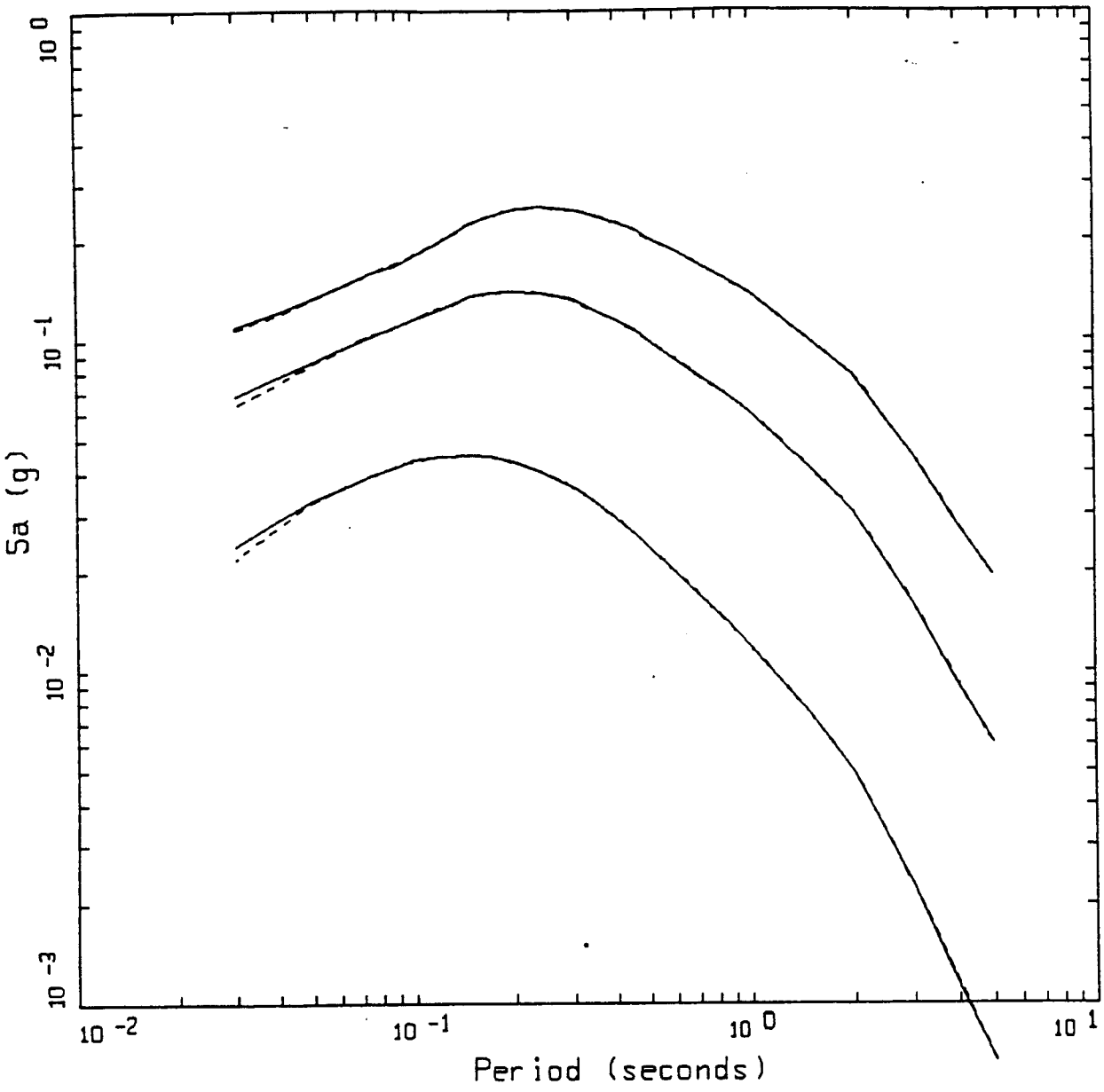

SPECTRAL MATCH TO EMPIRICAL ROCK, STRIKE SLIP, R=050 KM

LEGEND

——— EMPIRICAL, M = 5.5

----- 5 %, RVT RESPONSE SPECTRUM, M = 5.5

——— EMPIRICAL, M = 6.5

----- 5 %, RVT RESPONSE SPECTRUM, M = 6.5

——— EMPIRICAL, M = 7.5

----- 5 %, RVT RESPONSE SPECTRUM, M = 7.5

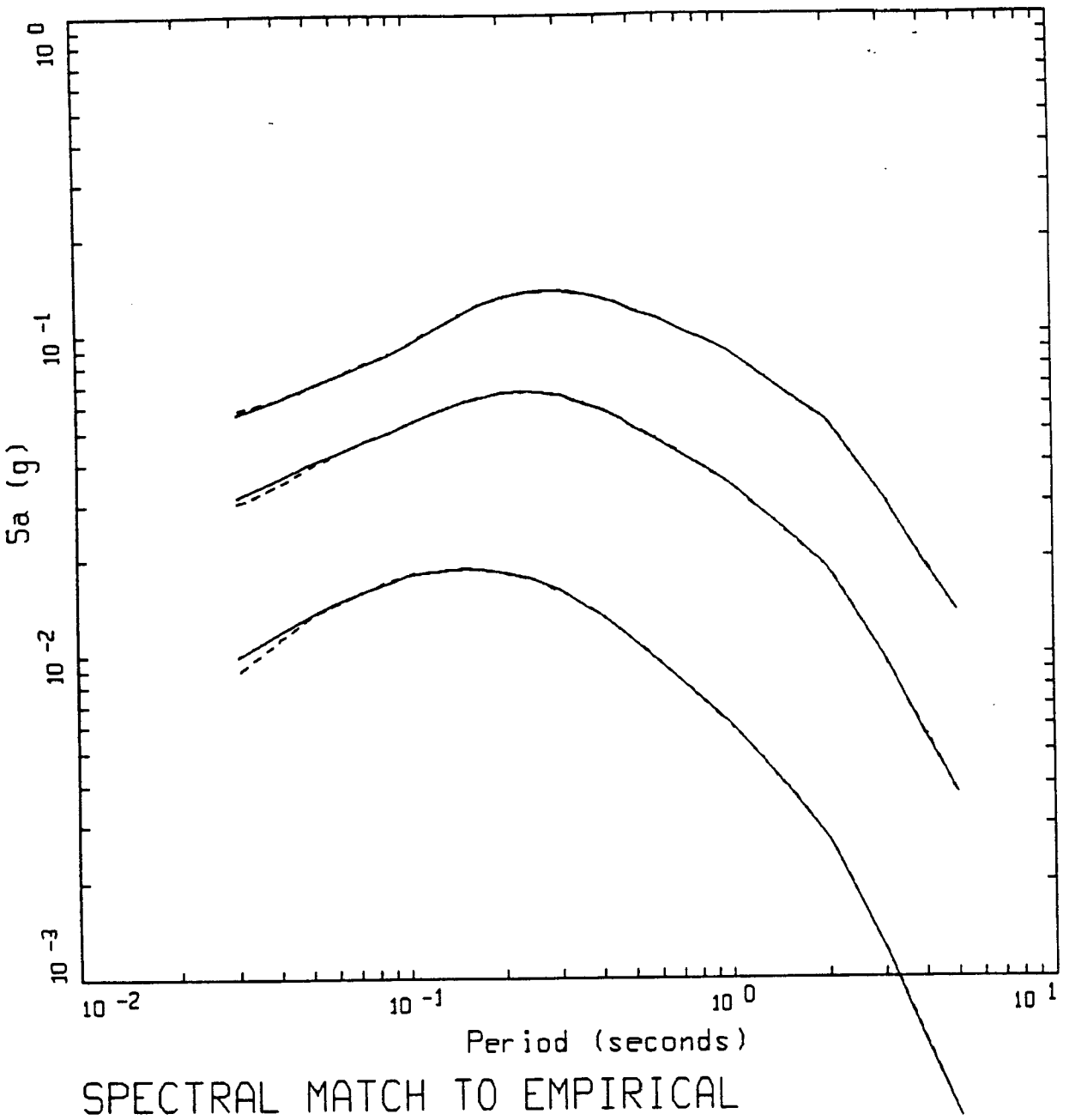

SPECTRAL MATCH TO EMPIRICAL
ROCK, STRIKE SLIP, R=100 KM

LEGEND

——— EMPIRICAL, M = 5.5

----- 5 %, RVT RESPONSE SPECTRUM, M = 5.5

——— EMPIRICAL, M = 6.5

----- 5 %, RVT RESPONSE SPECTRUM, M = 6.5

——— EMPIRICAL, M = 7.5

----- 5 %, RVT RESPONSE SPECTRUM, M = 7.5

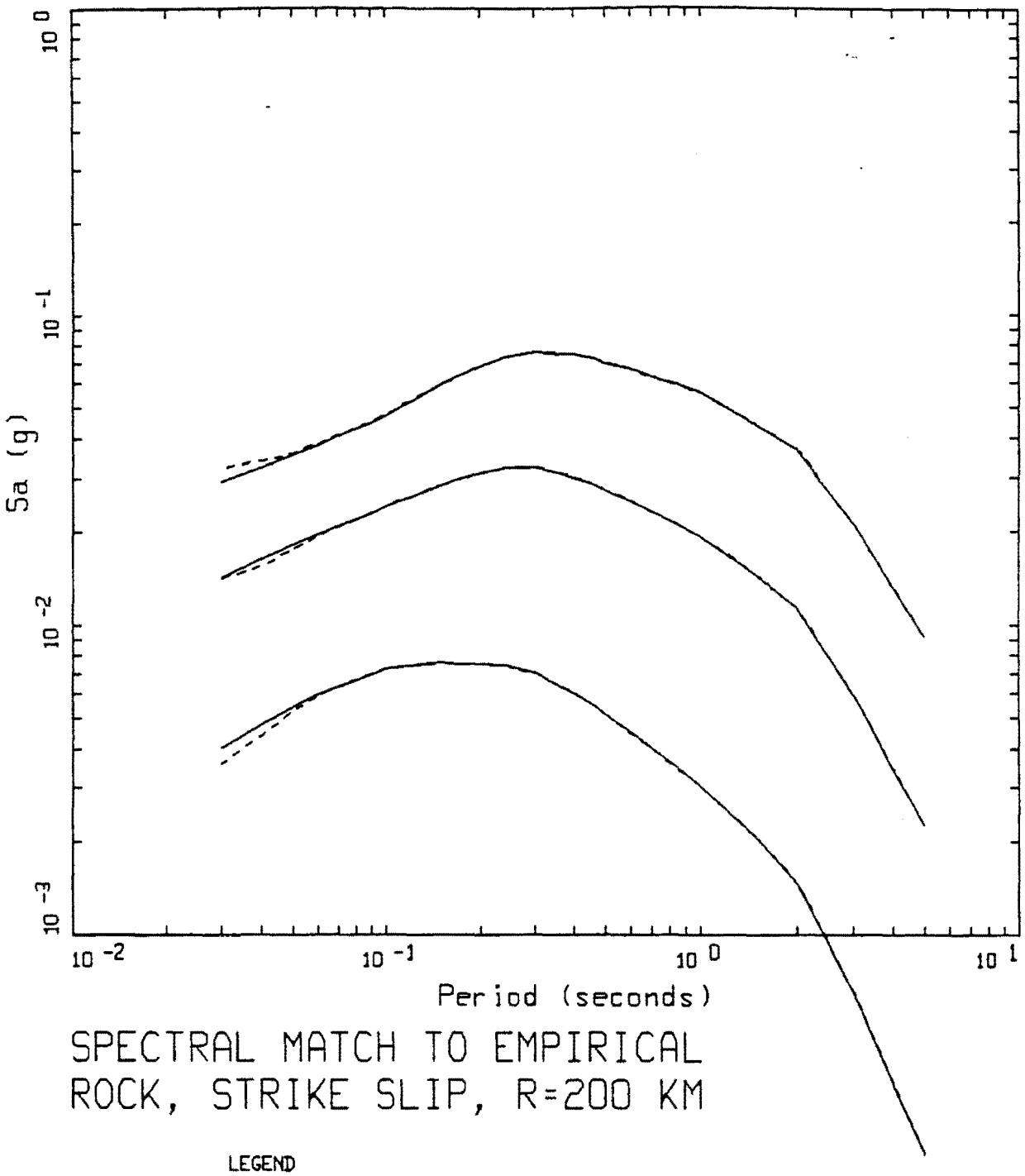

SPECTRAL MATCH TO EMPIRICAL
ROCK, STRIKE SLIP, R=200 KM

LEGEND

——— EMPIRICAL, M = 5.5

----- 5 %, RVT RESPONSE SPECTRUM, M = 5.5

——— EMPIRICAL, M = 6.5

----- 5 %, RVT RESPONSE SPECTRUM, M = 6.5

——— EMPIRICAL, M = 7.5

----- 5 %, RVT RESPONSE SPECTRUM, M = 7.5

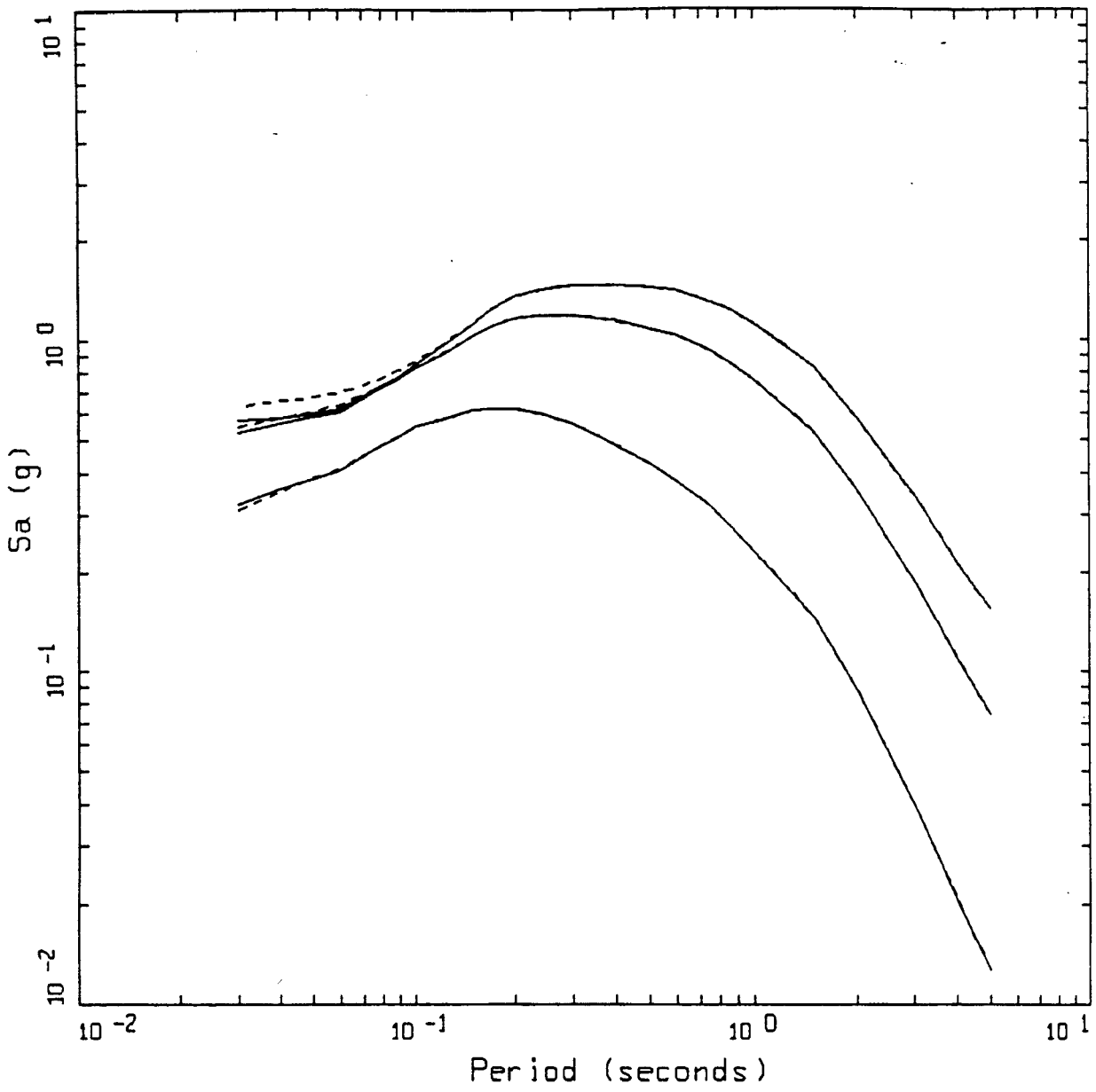

SPECTRAL MATCH TO EMPIRICAL
SOIL, STRIKE SLIP, R=001 KM

LEGEND

——— EMPIRICAL, M = 5.5
----- 5 %, RVT RESPONSE SPECTRUM, M = 5.5
——— EMPIRICAL, M = 6.5
----- 5 %, RVT RESPONSE SPECTRUM, M = 6.5
——— EMPIRICAL, M = 7.5
----- 5 %, RVT RESPONSE SPECTRUM, M = 7.5

Figure Set 6.3b

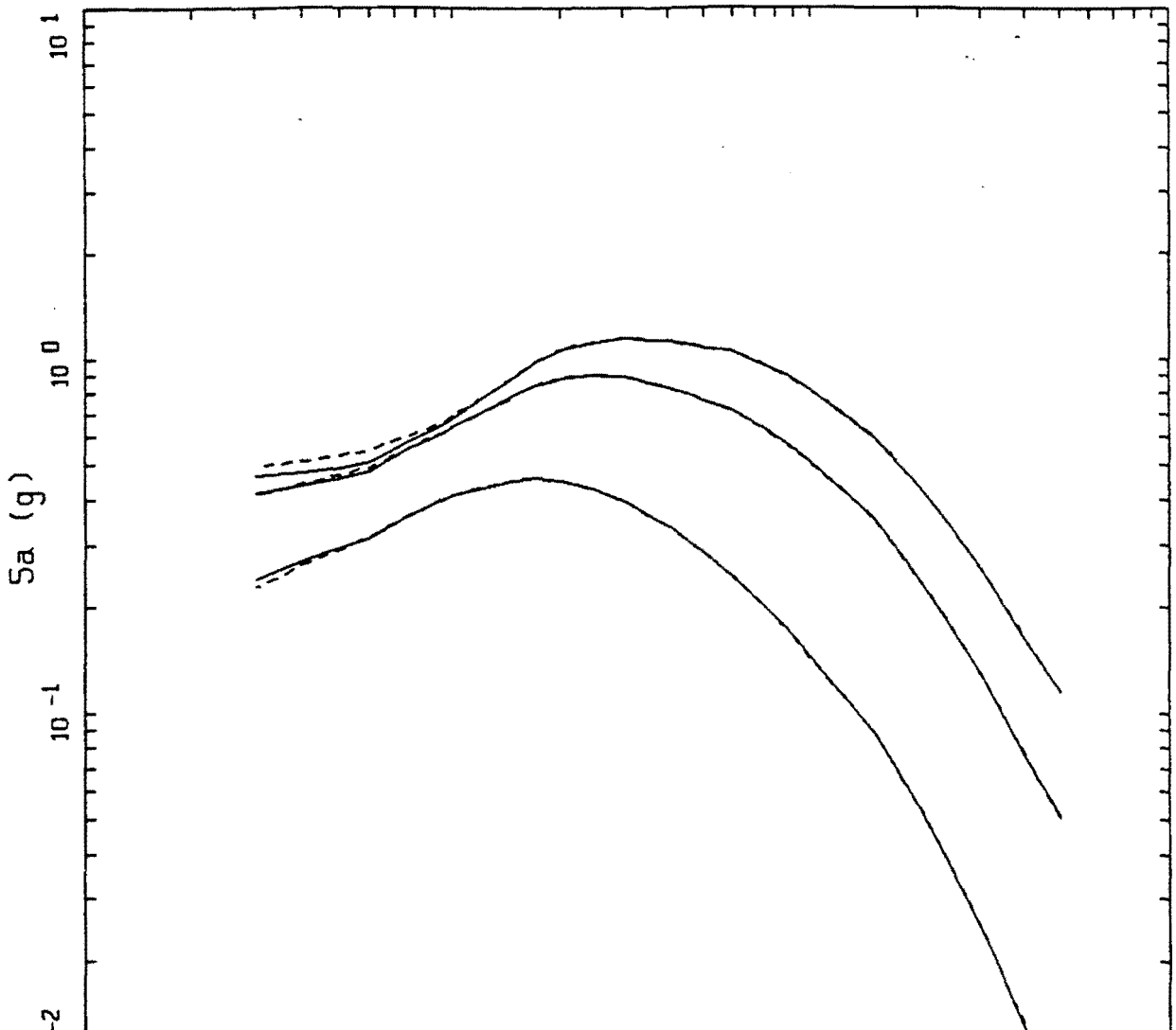

SPECTRAL MATCH TO EMPIRICAL SOIL, STRIKE SLIP, R=005 KM

LEGEND

——— EMPIRICAL, M = 5.5

----- 5 %, RVT RESPONSE SPECTRUM, M = 5.5

——— EMPIRICAL, M = 6.5

----- 5 %, RVT RESPONSE SPECTRUM, M = 6.5

——— EMPIRICAL, M = 7.5

----- 5 %, RVT RESPONSE SPECTRUM, M = 7.5

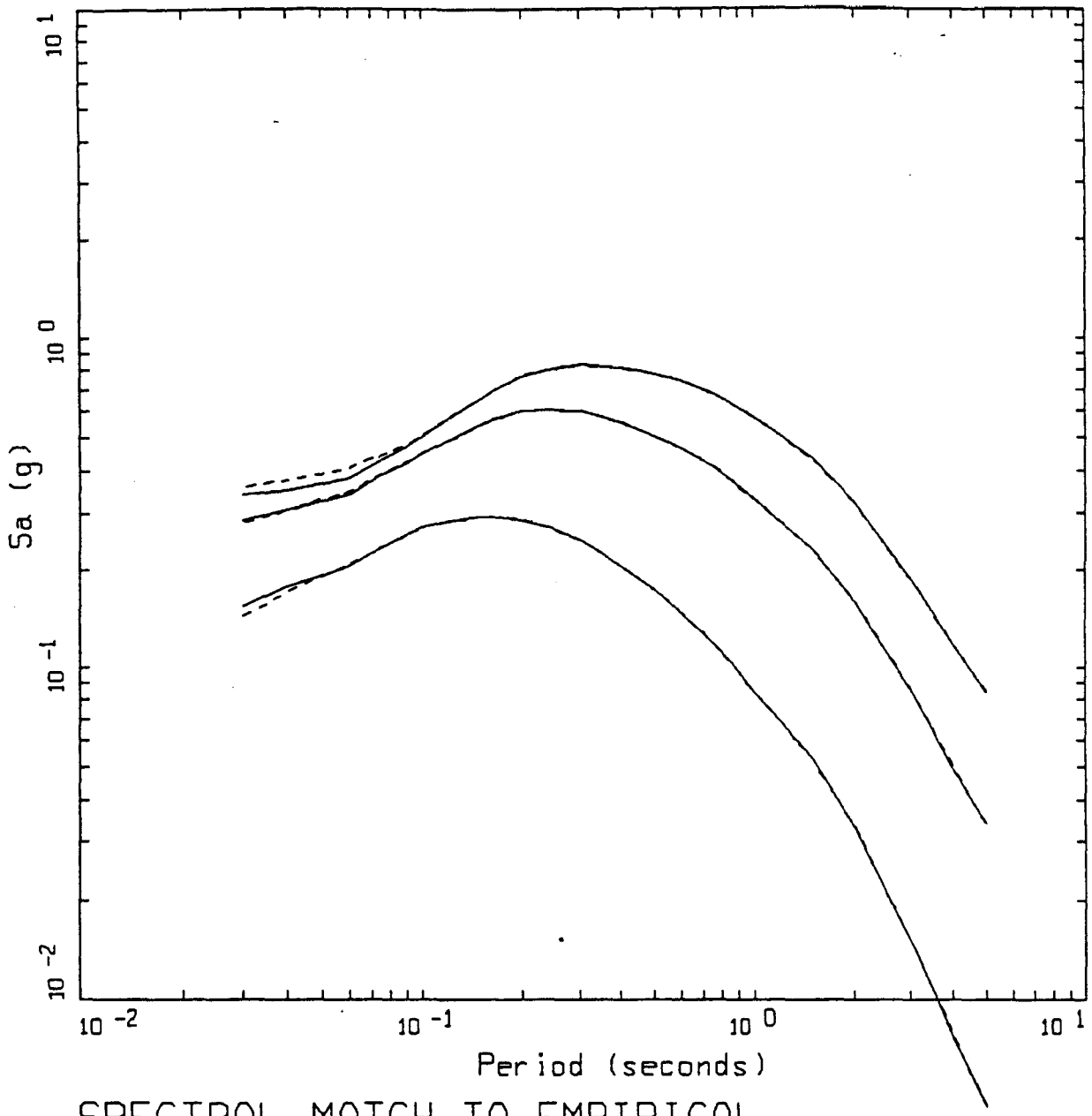

SPECTRAL MATCH TO EMPIRICAL
SOIL, STRIKE SLIP, R=010 KM

LEGEND

——— EMPIRICAL, M = 5.5

----- 5 %, RVT RESPONSE SPECTRUM, M = 5.5

——— EMPIRICAL, M = 6.5

----- 5 %, RVT RESPONSE SPECTRUM, M = 6.5

——— EMPIRICAL, M = 7.5

----- 5 %, RVT RESPONSE SPECTRUM, M = 7.5

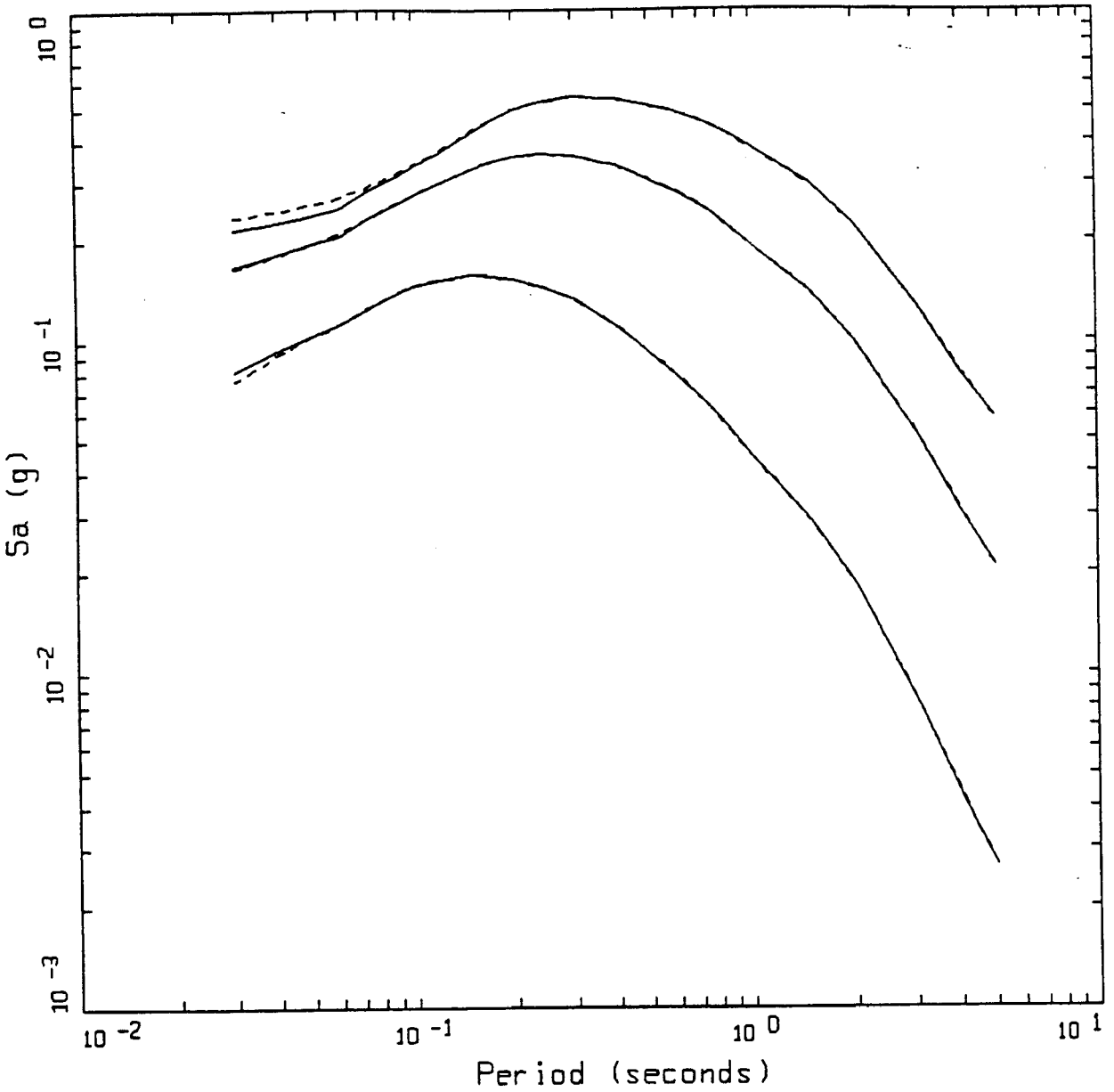

SPECTRAL MATCH TO EMPIRICAL
SOIL, STRIKE SLIP, R=020 KM

LEGEND

——— EMPIRICAL, M = 5.5
----- 5 %, RVT RESPONSE SPECTRUM, M = 5.5
——— EMPIRICAL, M = 6.5
----- 5 %, RVT RESPONSE SPECTRUM, M = 6.5
——— EMPIRICAL, M = 7.5
----- 5 %, RVT RESPONSE SPECTRUM, M = 7.5

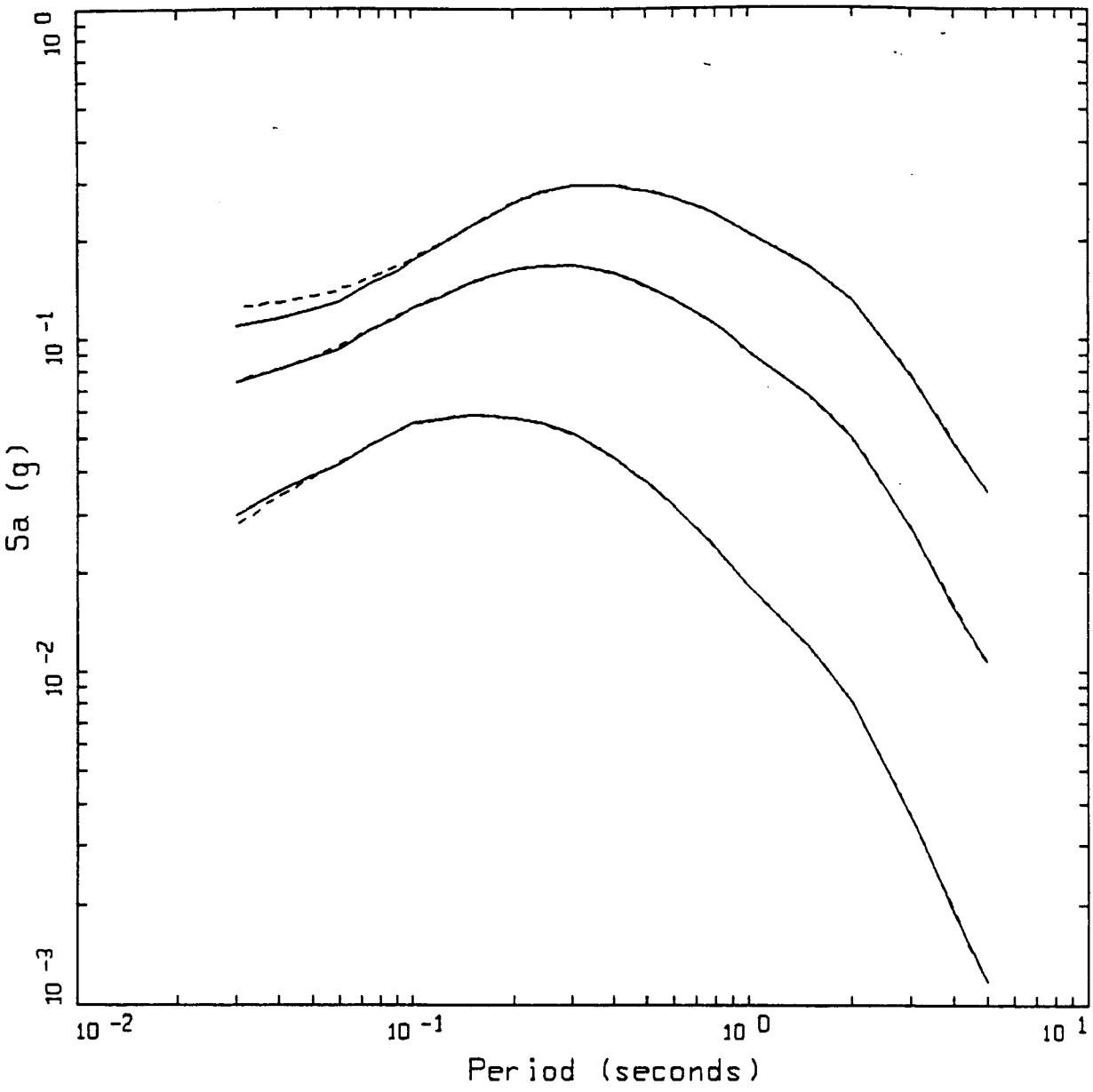

SPECTRAL MATCH TO EMPIRICAL SOIL, STRIKE SLIP, R=050 KM

LEGEND

——— EMPIRICAL, M = 5.5

----- 5 %, RVT RESPONSE SPECTRUM, M = 5.5

——— EMPIRICAL, M = 6.5

----- 5 %, RVT RESPONSE SPECTRUM, M = 6.5

——— EMPIRICAL, M = 7.5

----- 5 %, RVT RESPONSE SPECTRUM, M = 7.5

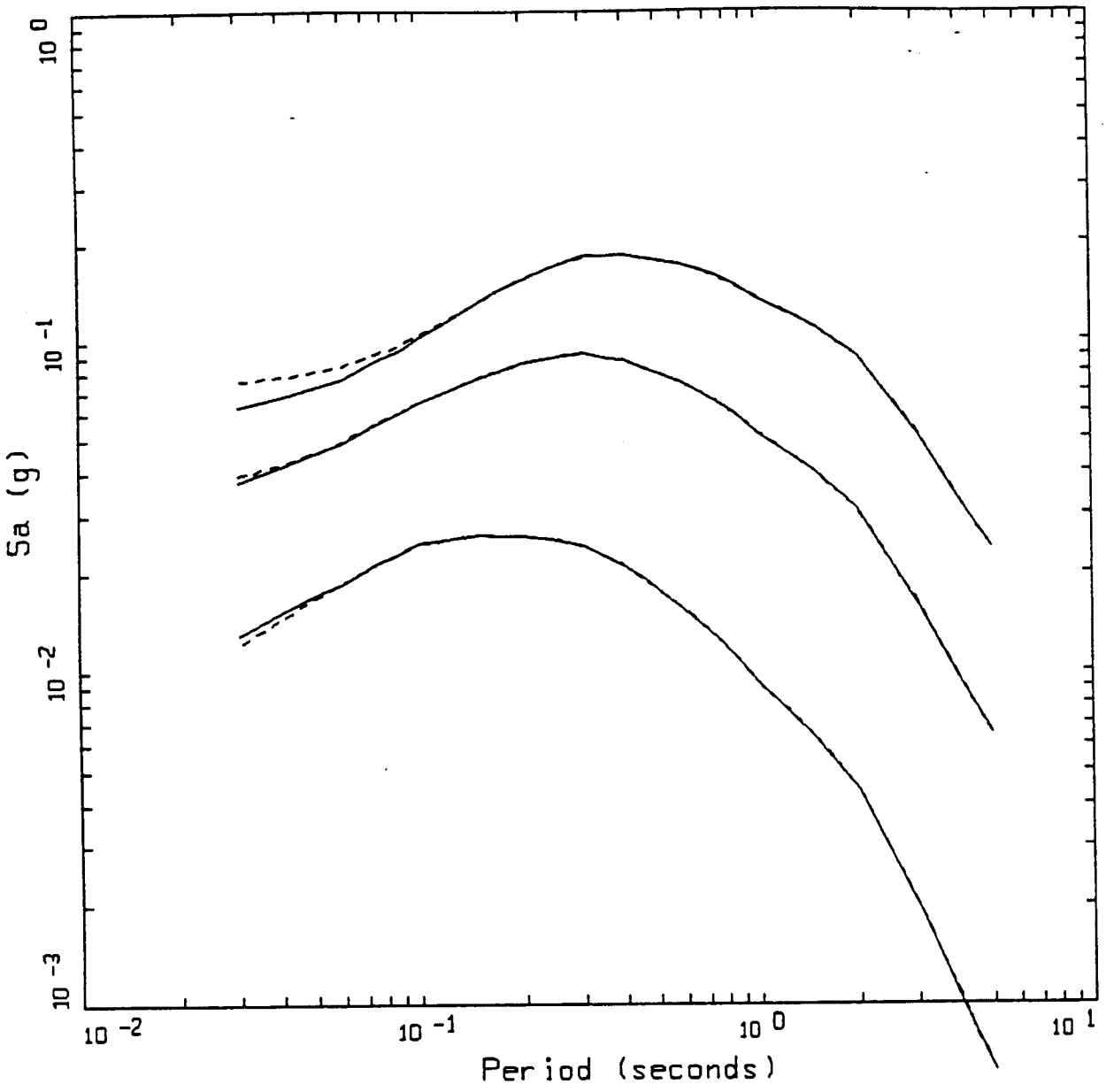

SPECTRAL MATCH TO EMPIRICAL SOIL, STRIKE SLIP, R=100 KM

LEGEND

——— EMPIRICAL, M = 5.5

----- 5 %, RVT RESPONSE SPECTRUM, M = 5.5

——— EMPIRICAL, M = 6.5

----- 5 %, RVT RESPONSE SPECTRUM, M = 6.5

——— EMPIRICAL, M = 7.5

----- 5 %, RVT RESPONSE SPECTRUM, M = 7.5

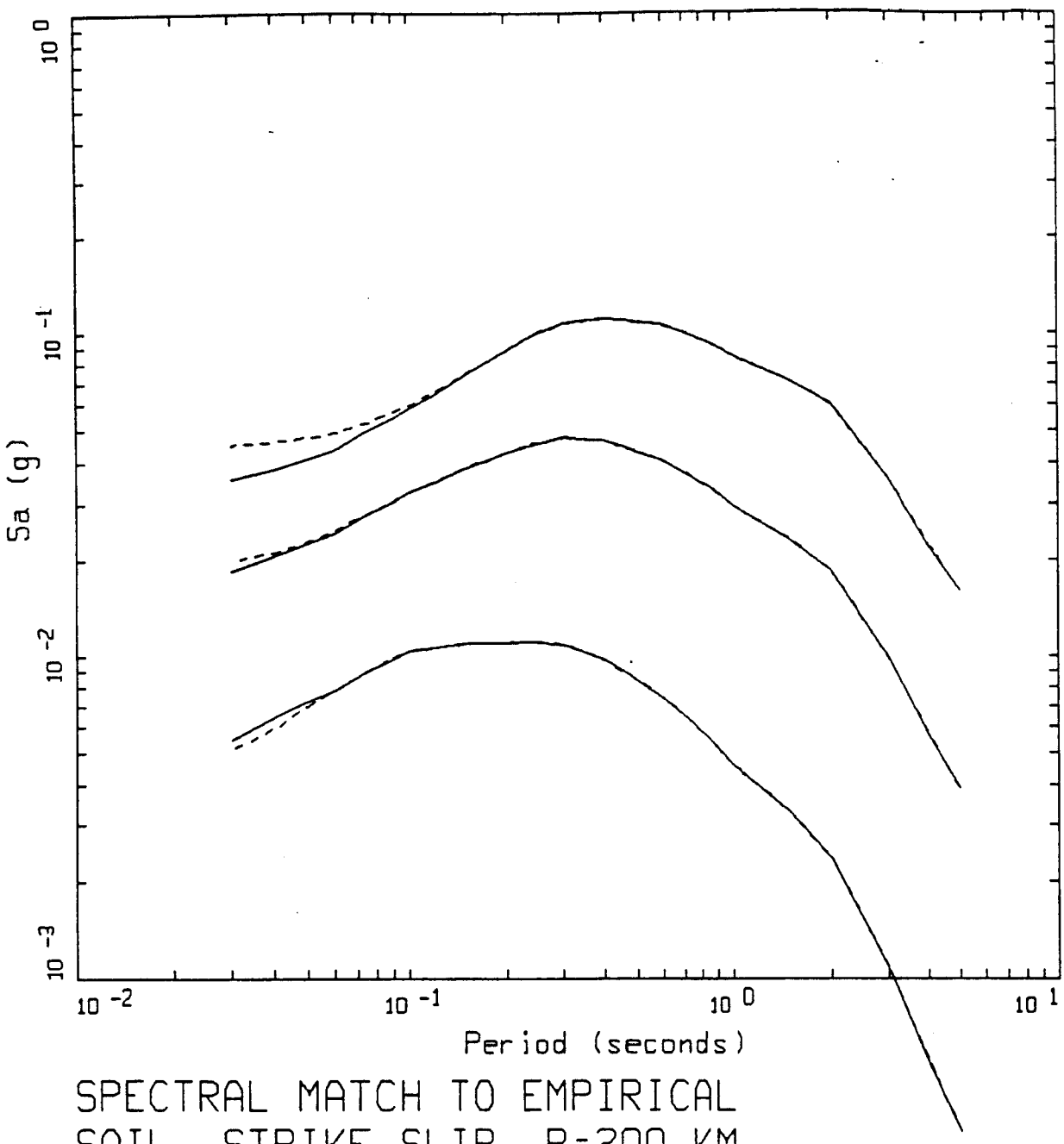

SPECTRAL MATCH TO EMPIRICAL SOIL, STRIKE SLIP, R=200 KM

LEGEND

——— EMPIRICAL, M = 5.5

----- 5 %, RVT RESPONSE SPECTRUM, M = 5.5

——— EMPIRICAL, M = 6.5

----- 5 %, RVT RESPONSE SPECTRUM, M = 6.5

——— EMPIRICAL, M = 7.5

----- 5 %, RVT RESPONSE SPECTRUM, M = 7.5

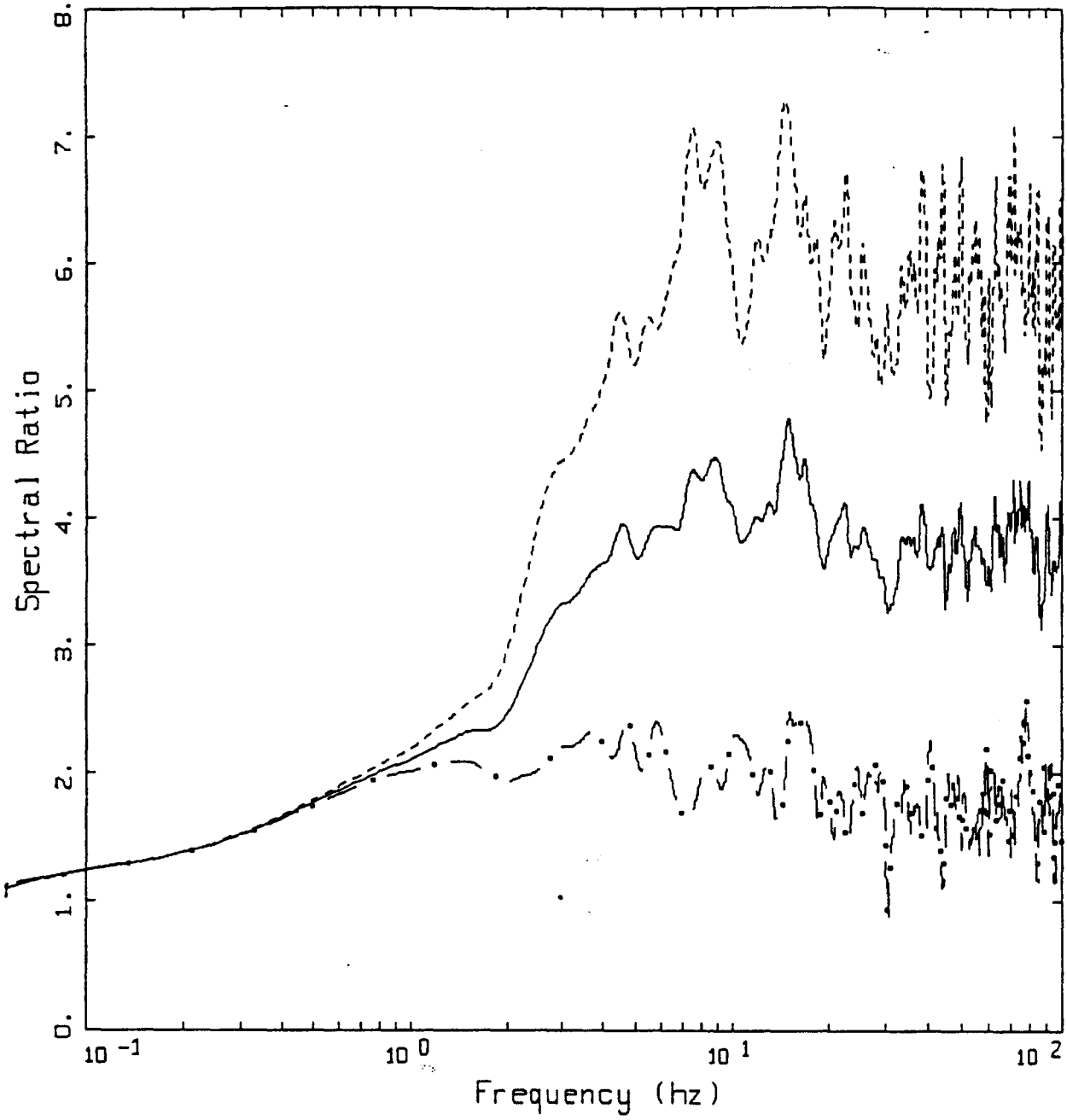

GENERIC TRANSFER FUNCTION
ROCK

LEGEND

----- 68TH PERCENTILE, 1 Hz SMOOTHING

——— 50TH PERCENTILE, 1 Hz SMOOTHING

— • — 32TH PERCENTILE, 1 Hz SMOOTHING

Figure 6.4

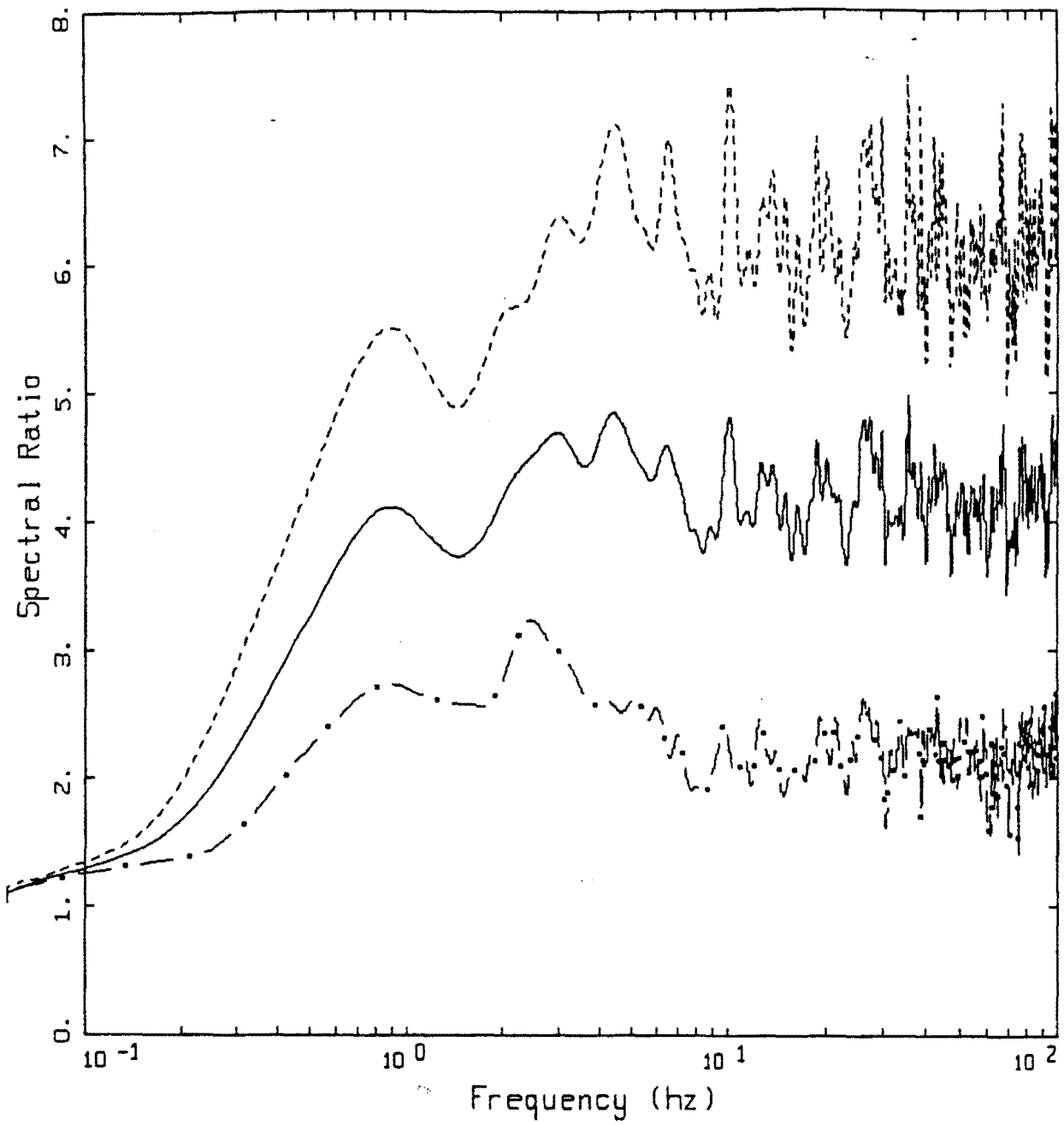

GENERIC TRANSFER FUNCTION
SOIL

LEGEND

----- 68TH PERCENTILE, 1 Hz SMOOTHING

——— 50TH PERCENTILE, 1 Hz SMOOTHING

— • — 32TH PERCENTILE, 1 Hz SMOOTHING

Figure 6.5

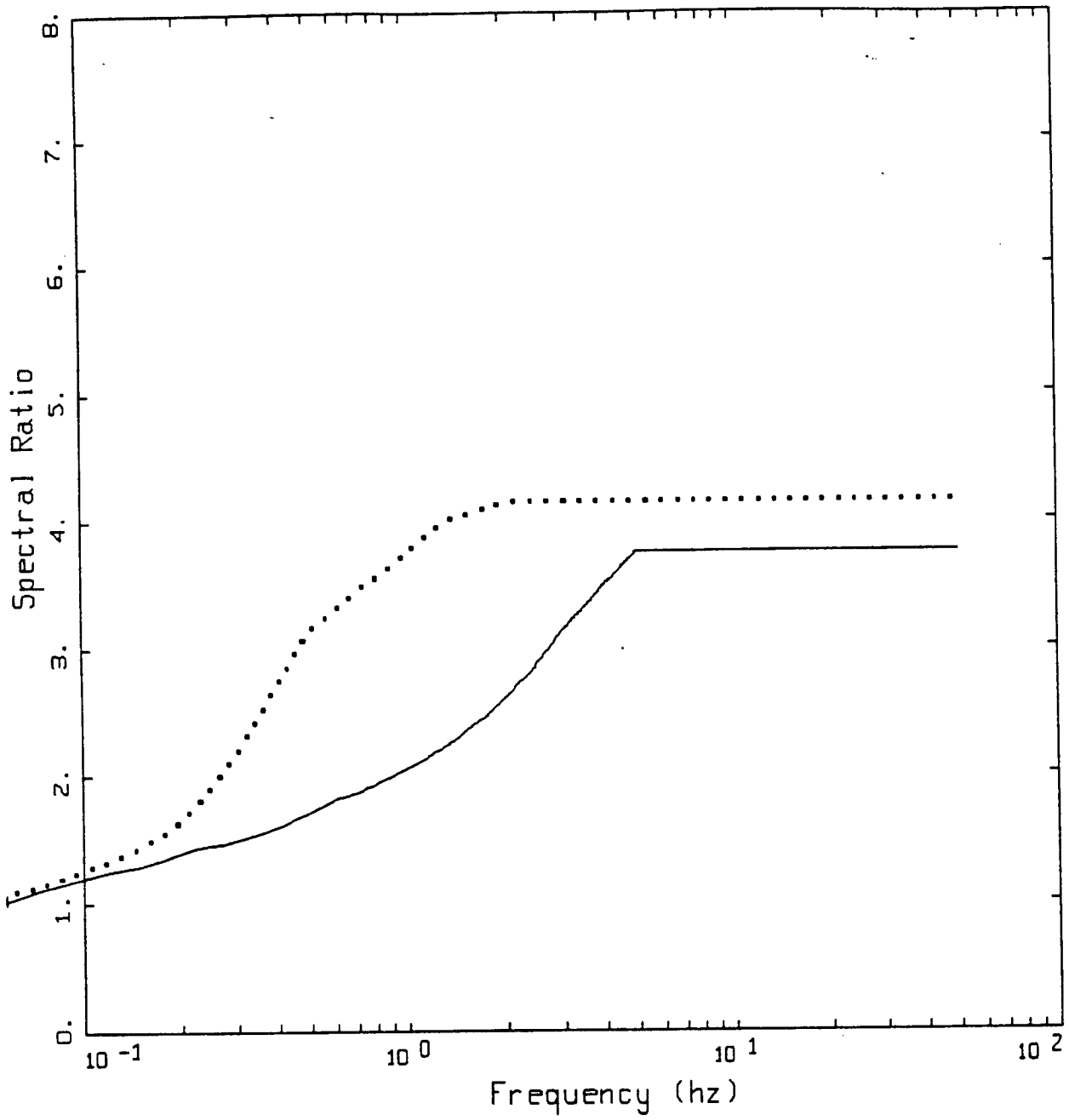

GENERIC TRANSER FUNCTION
ROCK, SOIL SMOOTHED

LEGEND
ROCK
SOIL

Figure 6.6

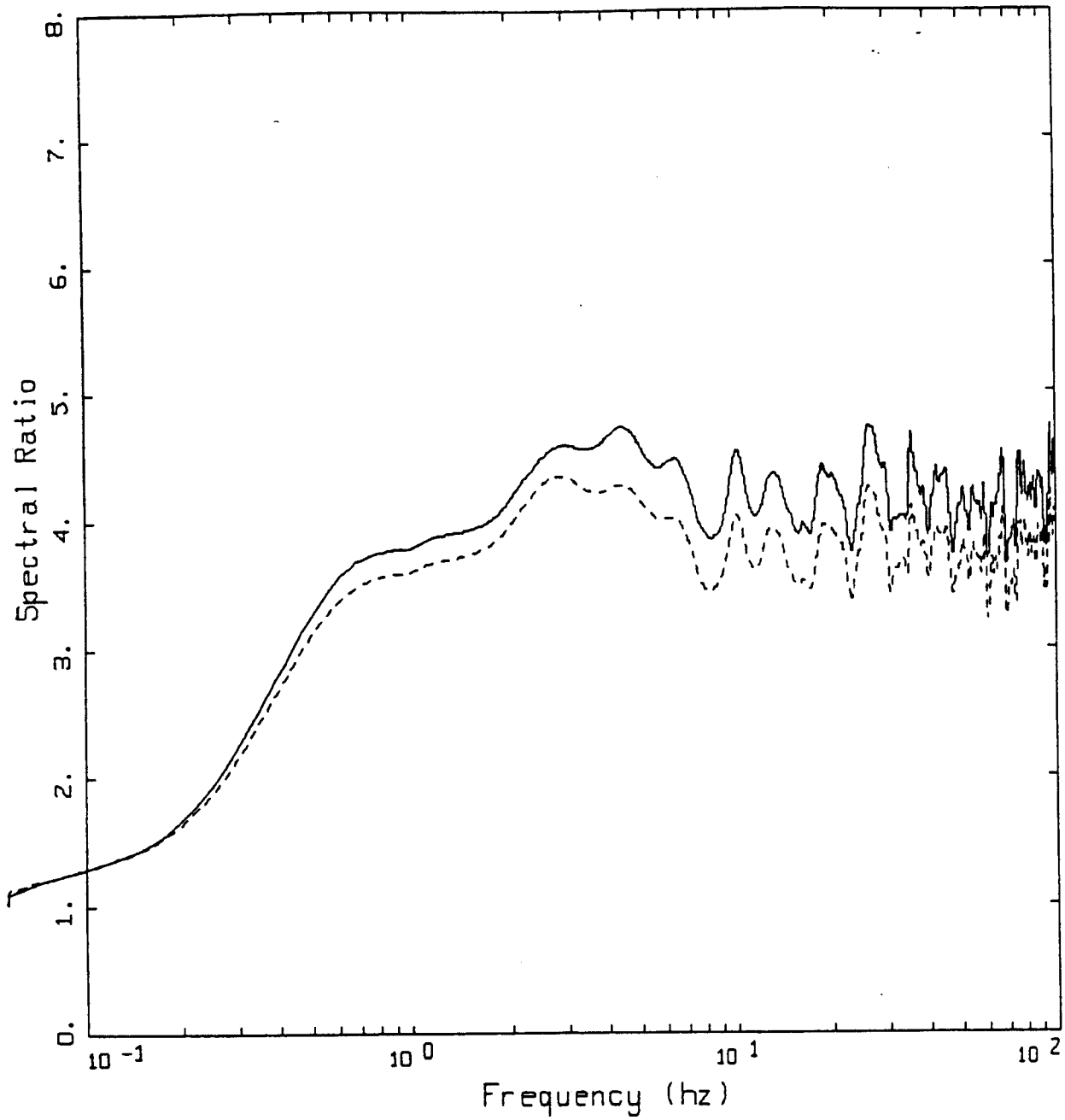

GENERIC TRANSFER FUNCTIONS
SOIL

LEGEND

——— MEAN, 2 Hz SMOOTHING

----- MEDIAN, 2 Hz SMOOTHING

Figure 6.7

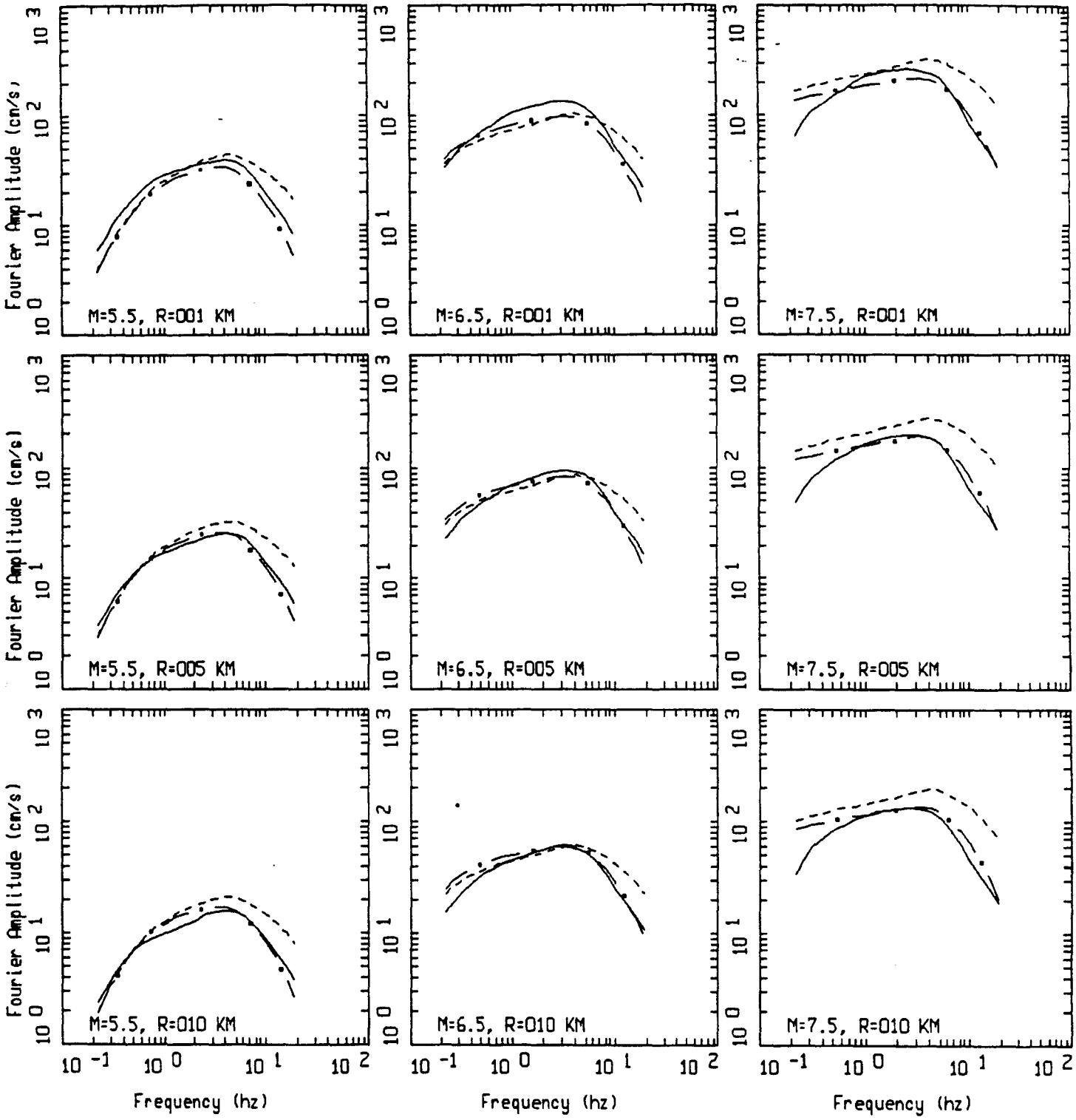

EMPIRICAL M=5.5, 6.5, 7.5, PAGE 1 OF 3.
ROCK

LEGEND
DATA
INITIAL MODEL
FINAL MODEL

Figure Set 6.8

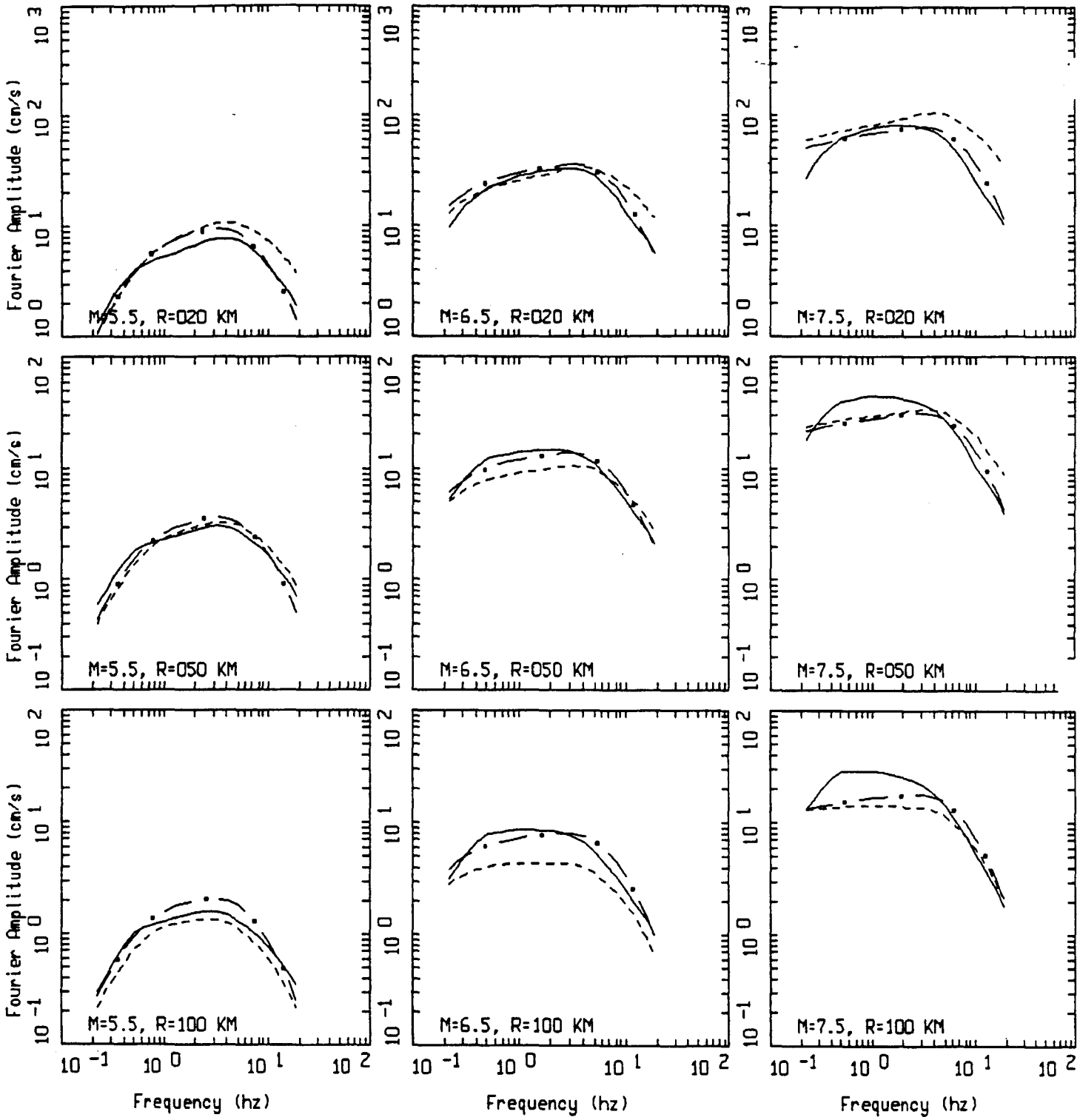

EMPIRICAL M=5.5, 6.5, 7.5, PAGE 2 OF 3.
ROCK

LEGEND

——— DATA

- - - - - INITIAL MODEL

— • — FINAL MODEL

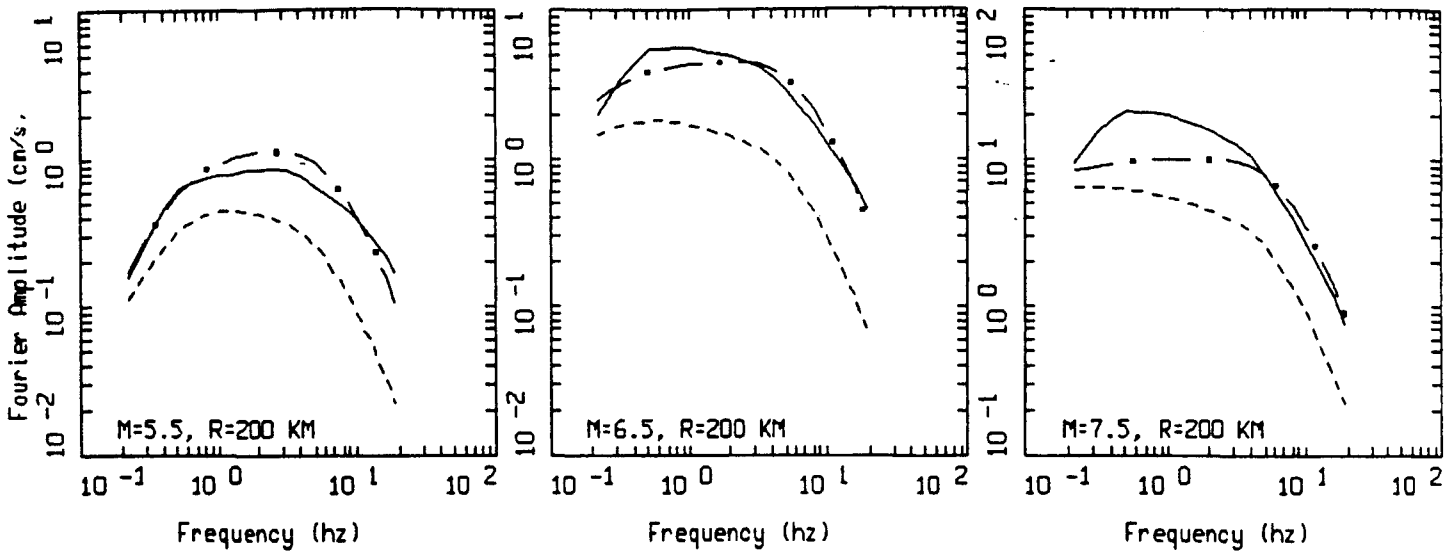

EMPIRICAL M=5.5, 6.5, 7.5, PAGE 3 OF 3.
ROCK

LEGEND

——— DATA

- - - - - INITIAL MODEL

—•— FINAL MODEL

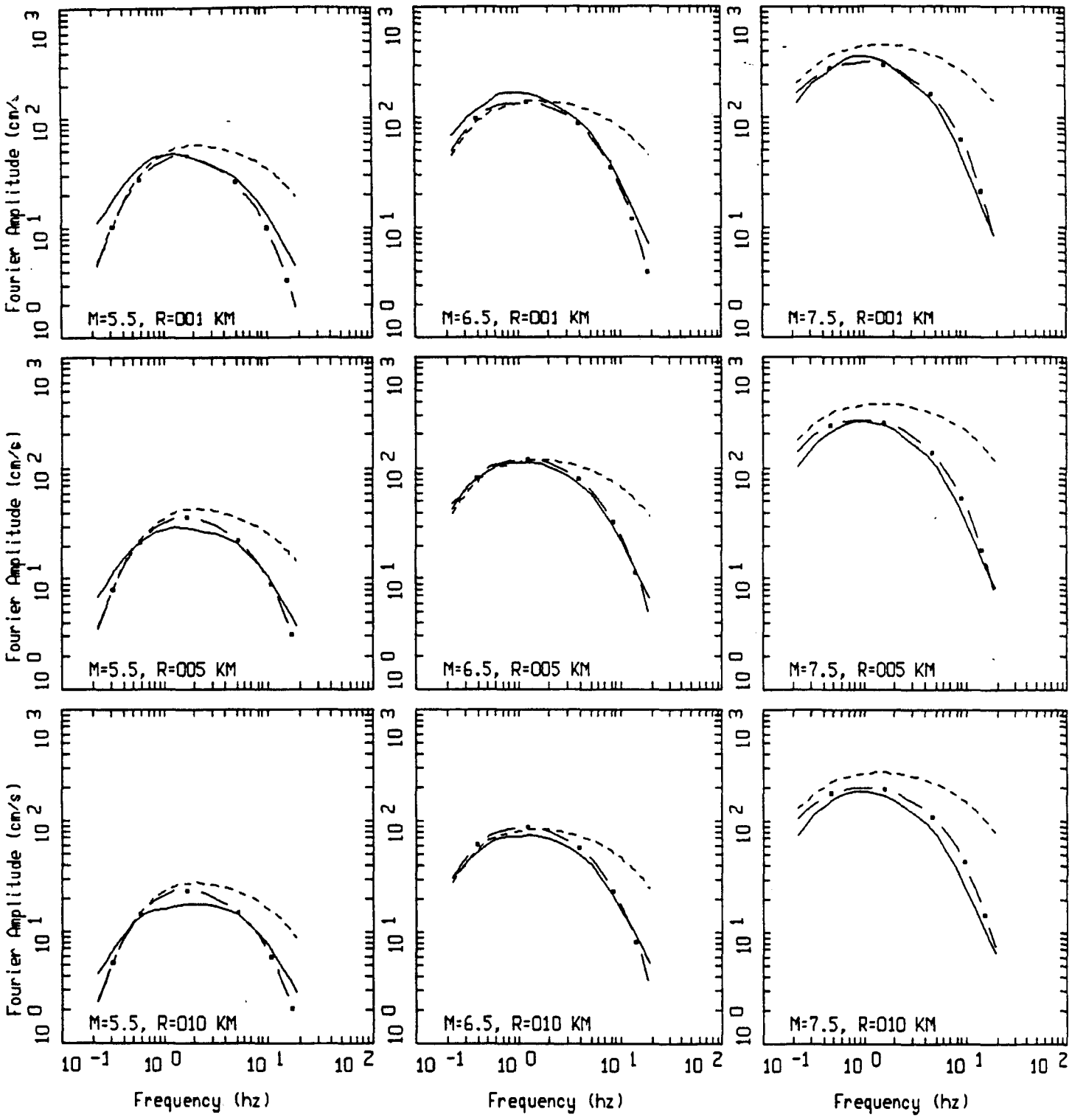

EMPIRICAL M=5.5, 6.5, 7.5, PAGE 1 OF 3.
SOIL

LEGEND
——— DATA
- - - - - INITIAL MODEL
— • — FINAL MODEL

Figure Set 6.9

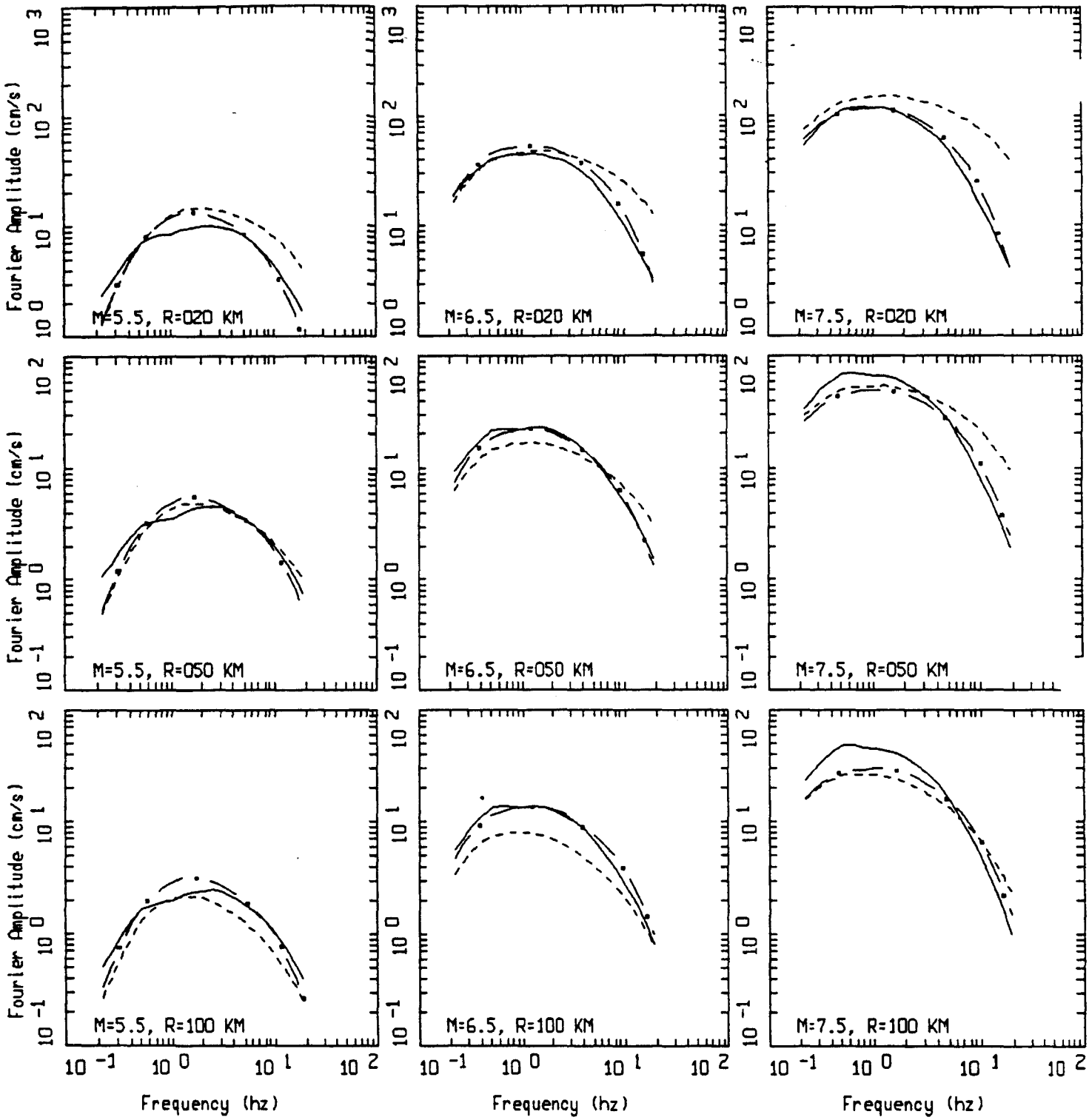

EMPIRICAL M=5.5, 6.5, 7.5, PAGE 2 OF 3.
SOIL

LEGEND

——— DATA

- - - - - INITIAL MODEL

—— • —— FINAL MODEL

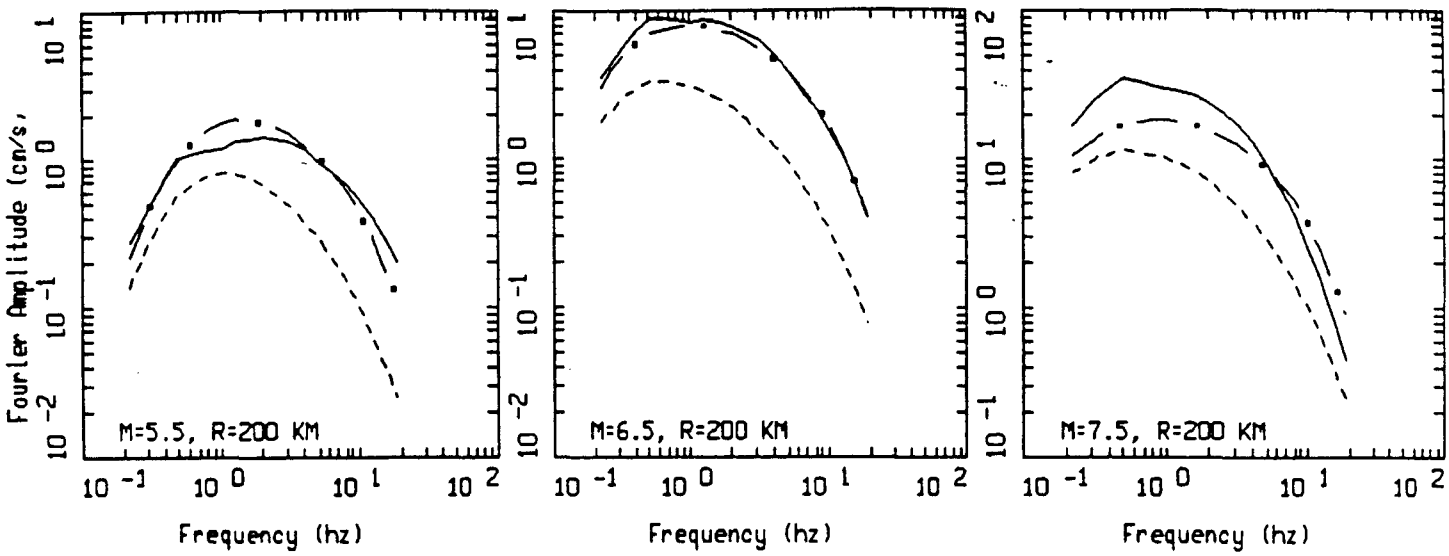

EMPIRICAL M=5.5, 6.5, 7.5, PAGE 3 OF 3.
SOIL

LEGEND

——— DATA

- - - - - INITIAL MODEL

—•— FINAL MODEL

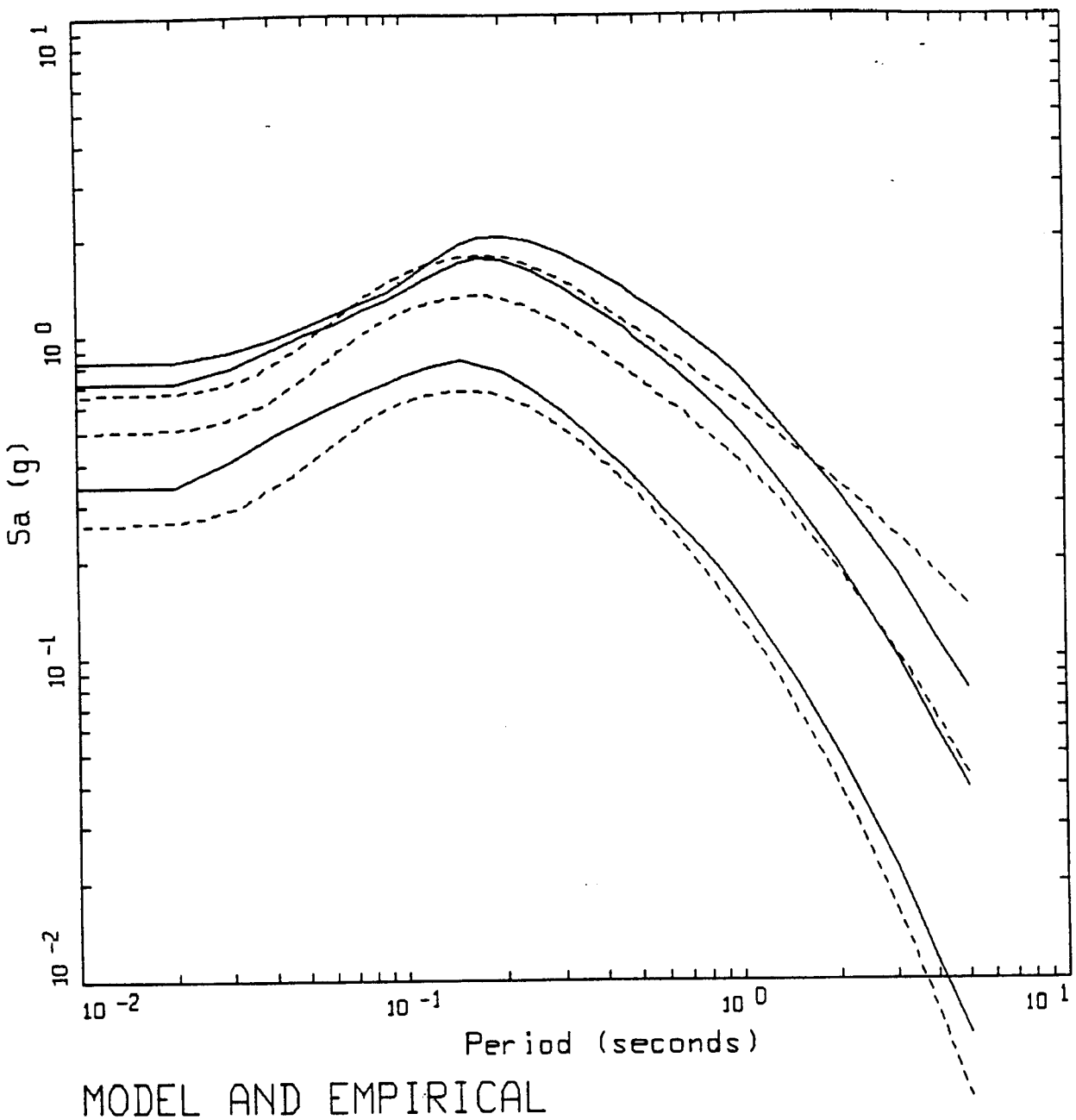

MODEL AND EMPIRICAL
ROCK, STRIKE SLIP, R=001 KM

LEGEND

——— EMPIRICAL, M = 5.5
----- 5 %, MODEL, M = 5.5
——— EMPIRICAL, M = 6.5
----- 5 %, MODEL, M = 6.5
——— EMPIRICAL, M = 7.5
----- 5 %, MODEL, M = 7.5

Figure Set 6.10

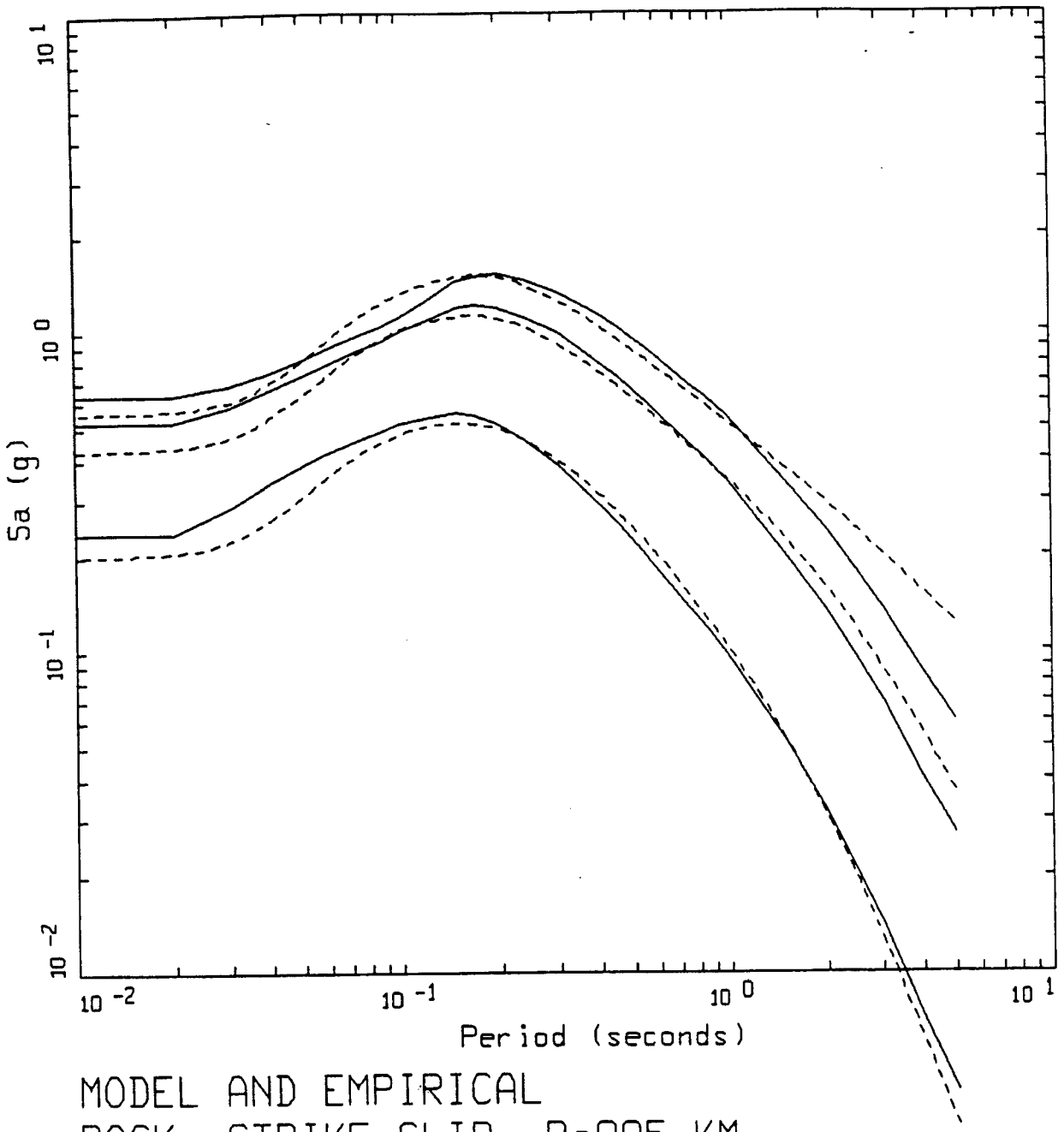

MODEL AND EMPIRICAL
ROCK, STRIKE SLIP, R=005 KM

LEGEND

——— EMPIRICAL, M = 5.5
----- 5 %, MODEL, M = 5.5
——— EMPIRICAL, M = 6.5
----- 5 %, MODEL, M = 6.5
——— EMPIRICAL, M = 7.5
----- 5 %, MODEL, M = 7.5

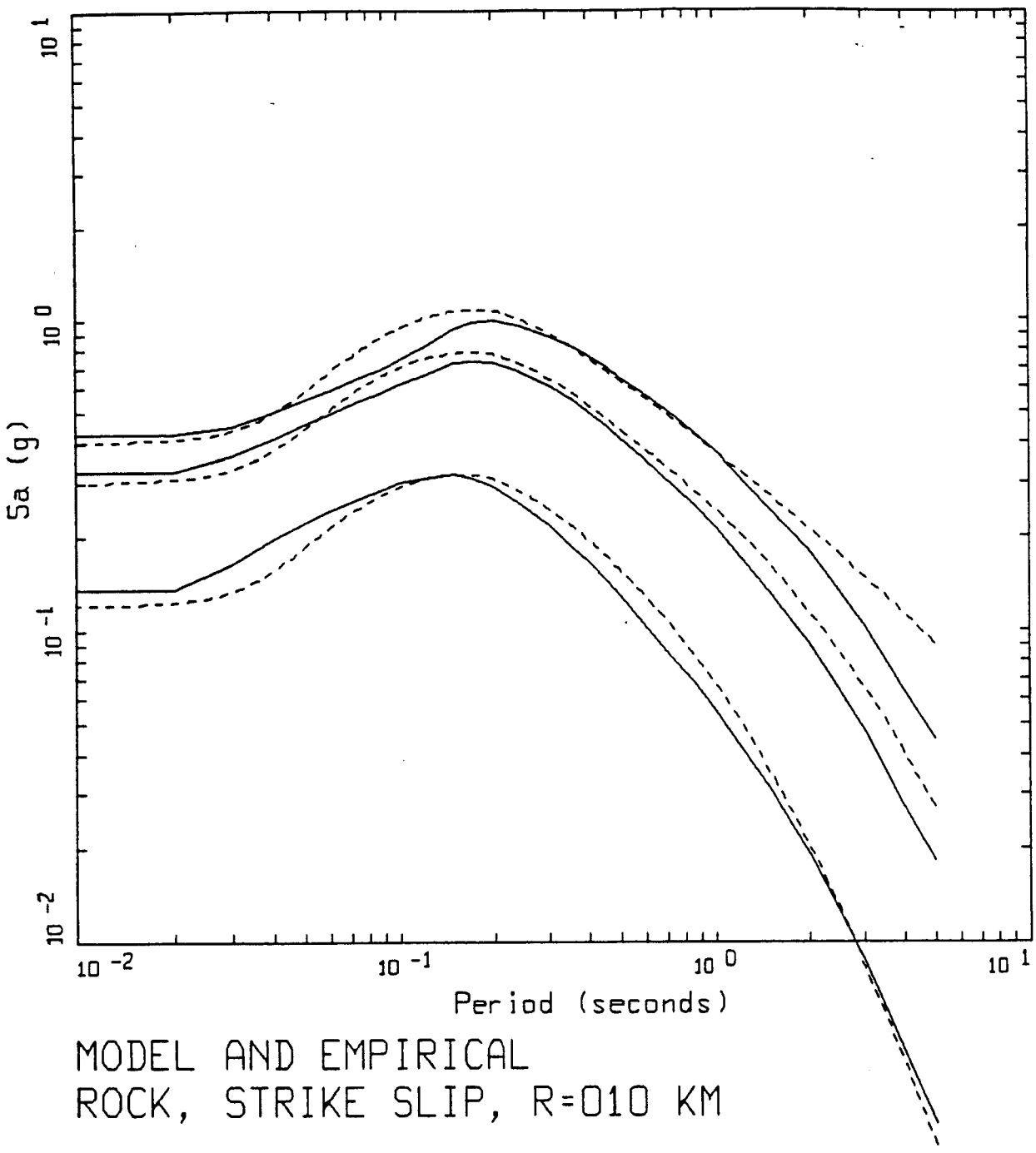

MODEL AND EMPIRICAL
ROCK, STRIKE SLIP, R=010 KM

LEGEND

EMPIRICAL, M = 5.5
5 %, MODEL, M = 5.5
EMPIRICAL, M = 6.5
5 %, MODEL, M = 6.5
EMPIRICAL, M = 7.5
5 %, MODEL, M = 7.5

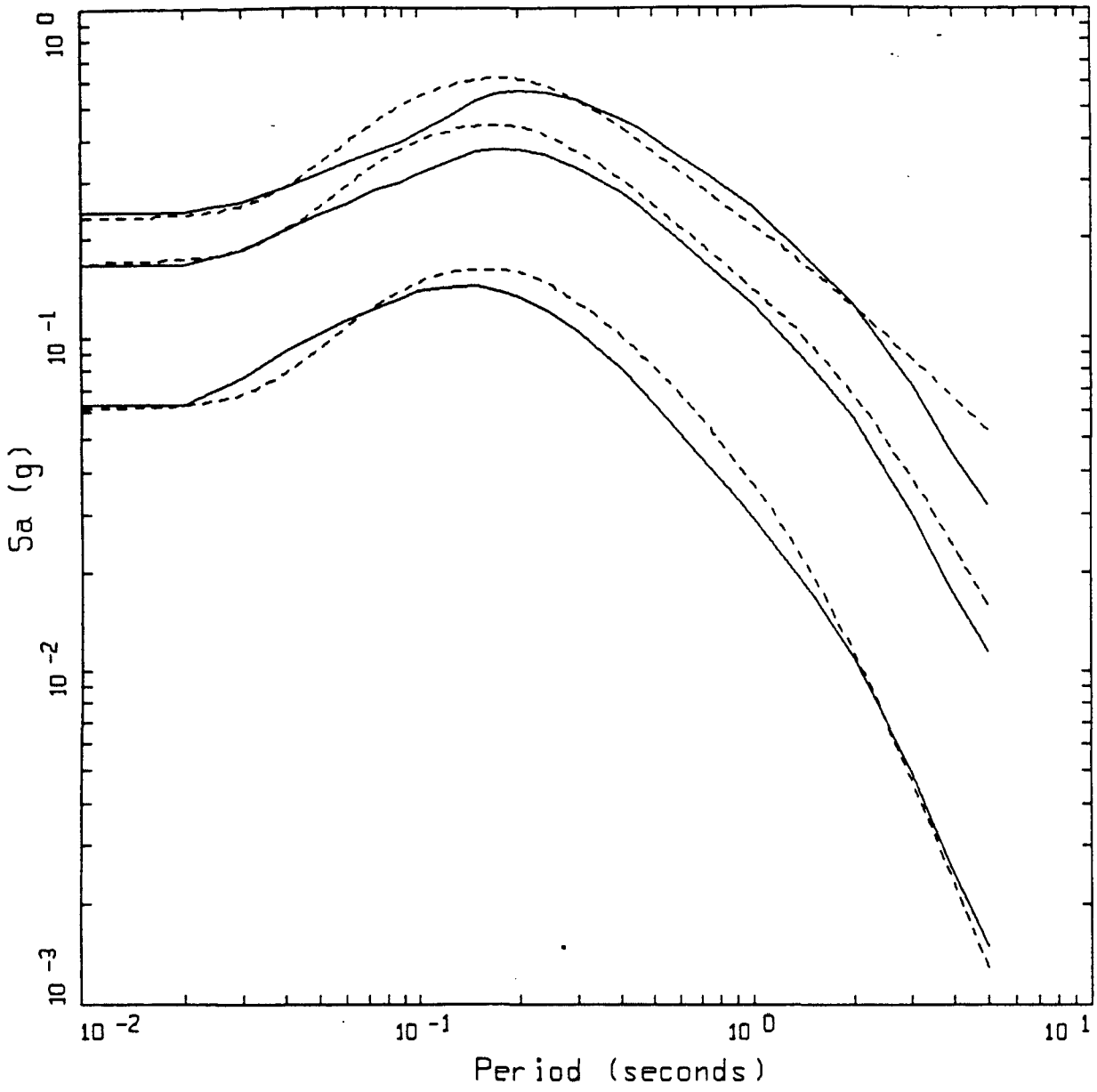

MODEL AND EMPIRICAL
ROCK, STRIKE SLIP, R=020 KM

LEGEND

EMPIRICAL, M = 5.5

5 %, MODEL, M = 5.5

EMPIRICAL, M = 6.5

5 %, MODEL, M = 6.5

EMPIRICAL, M = 7.5

5 %, MODEL, M = 7.5

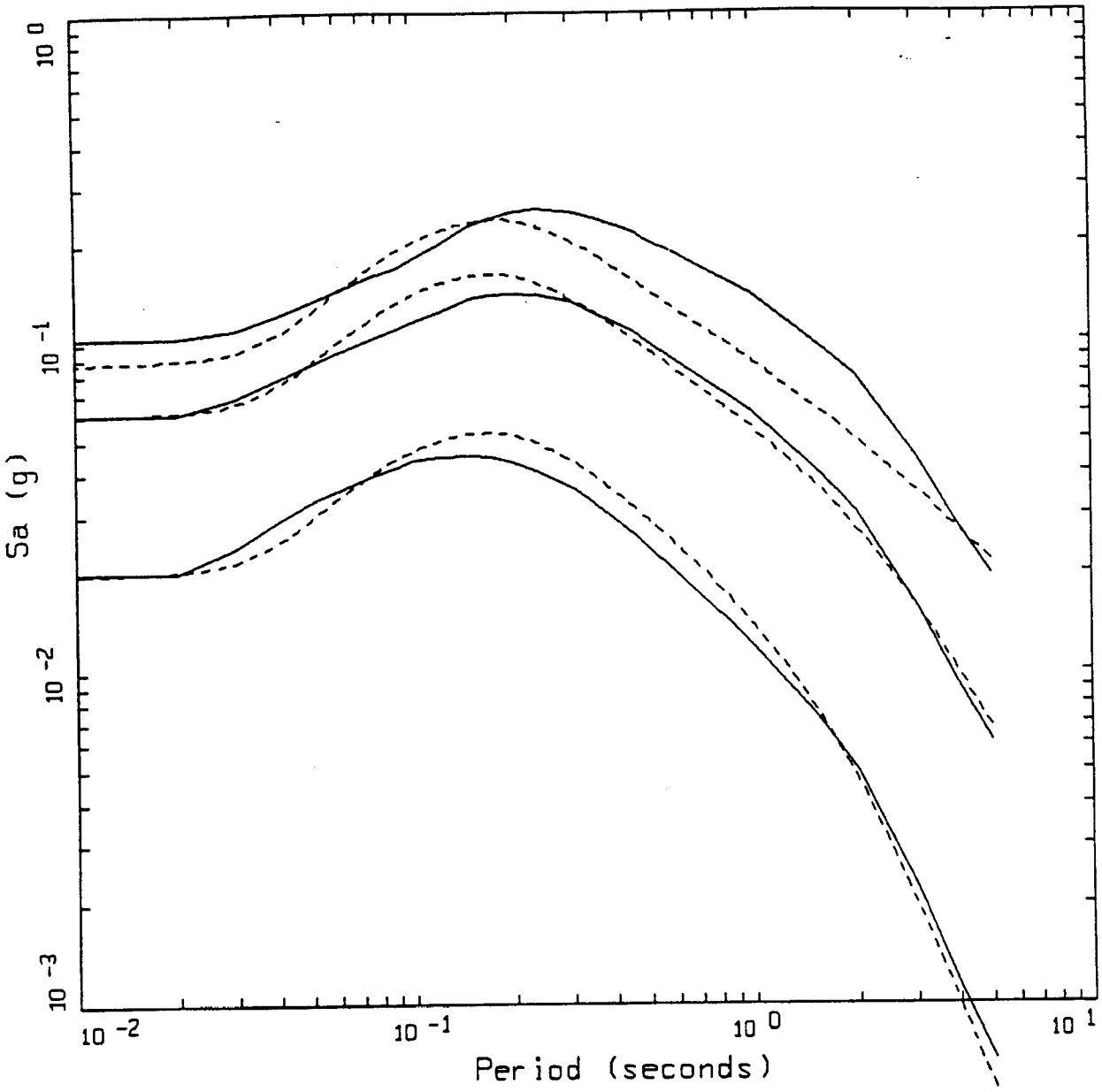

MODEL AND EMPIRICAL
ROCK, STRIKE SLIP, R=050 KM

LEGEND

——— EMPIRICAL, M = 5.5

----- 5 %, MODEL, M = 5.5

——— EMPIRICAL, M = 6.5

----- 5 %, MODEL, M = 6.5

——— EMPIRICAL, M = 7.5

----- 5 %, MODEL, M = 7.5

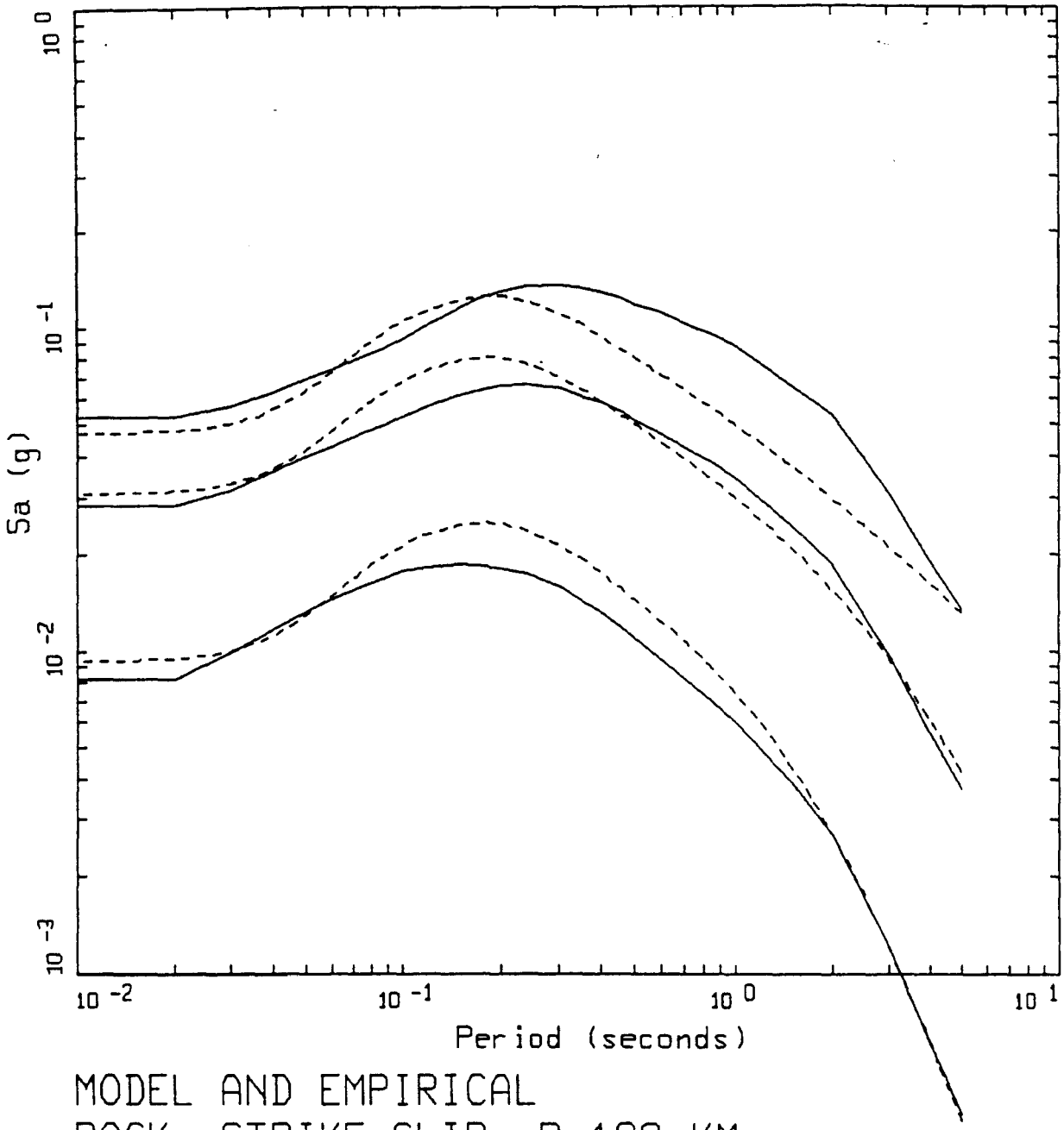

MODEL AND EMPIRICAL
ROCK, STRIKE SLIP, R=100 KM

LEGEND

——— EMPIRICAL, M = 5.5
----- 5 %, MODEL, M = 5.5
——— EMPIRICAL, M = 6.5
----- 5 %, MODEL, M = 6.5
——— EMPIRICAL, M = 7.5
----- 5 %, MODEL, M = 7.5

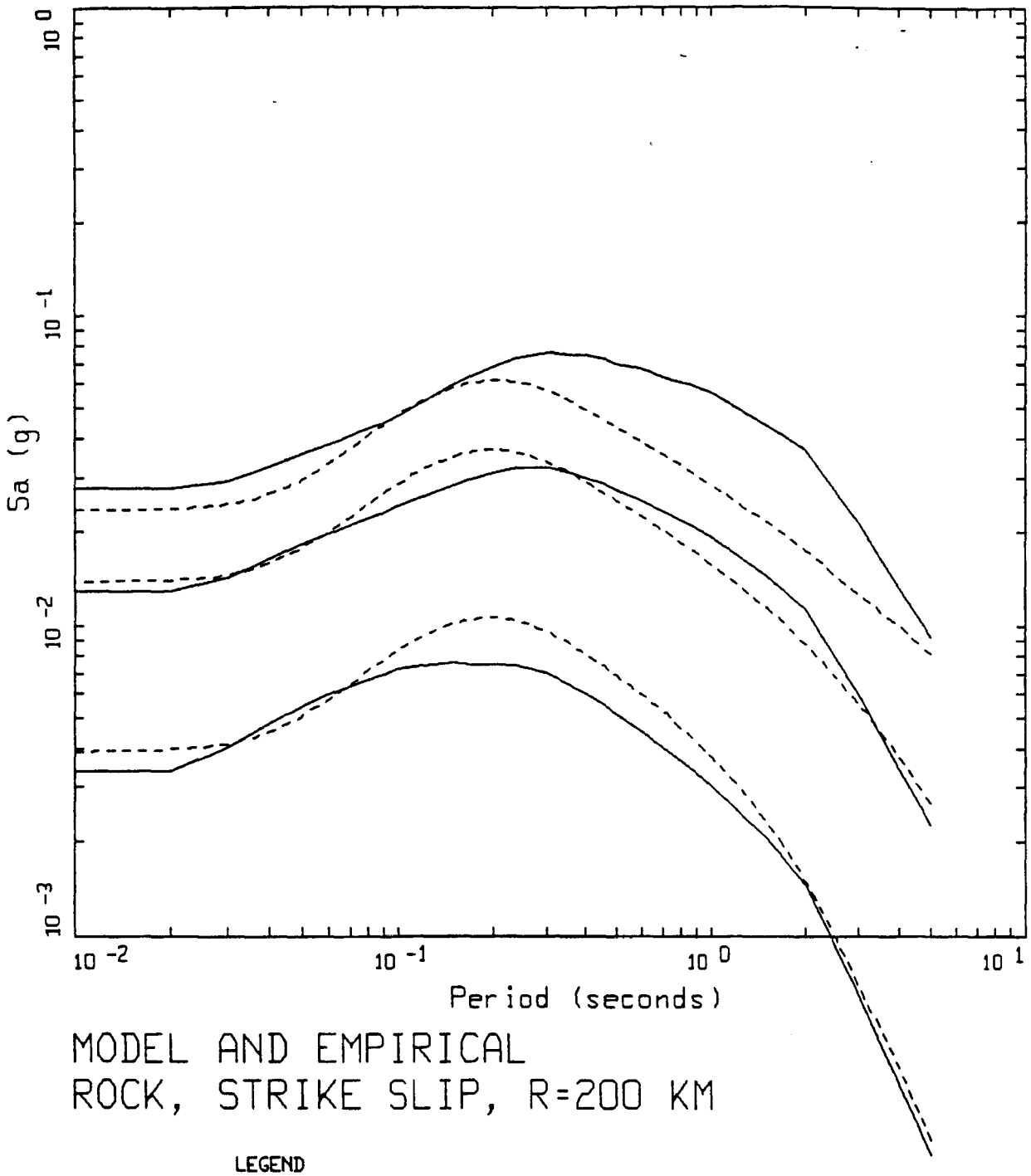

MODEL AND EMPIRICAL
ROCK, STRIKE SLIP, R=200 KM

LEGEND

——— EMPIRICAL, M = 5.5

----- 5 %, MODEL, M = 5.5

——— EMPIRICAL, M = 6.5

----- 5 %, MODEL, M = 6.5

——— EMPIRICAL, M = 7.5

----- 5 %, MODEL, M = 7.5

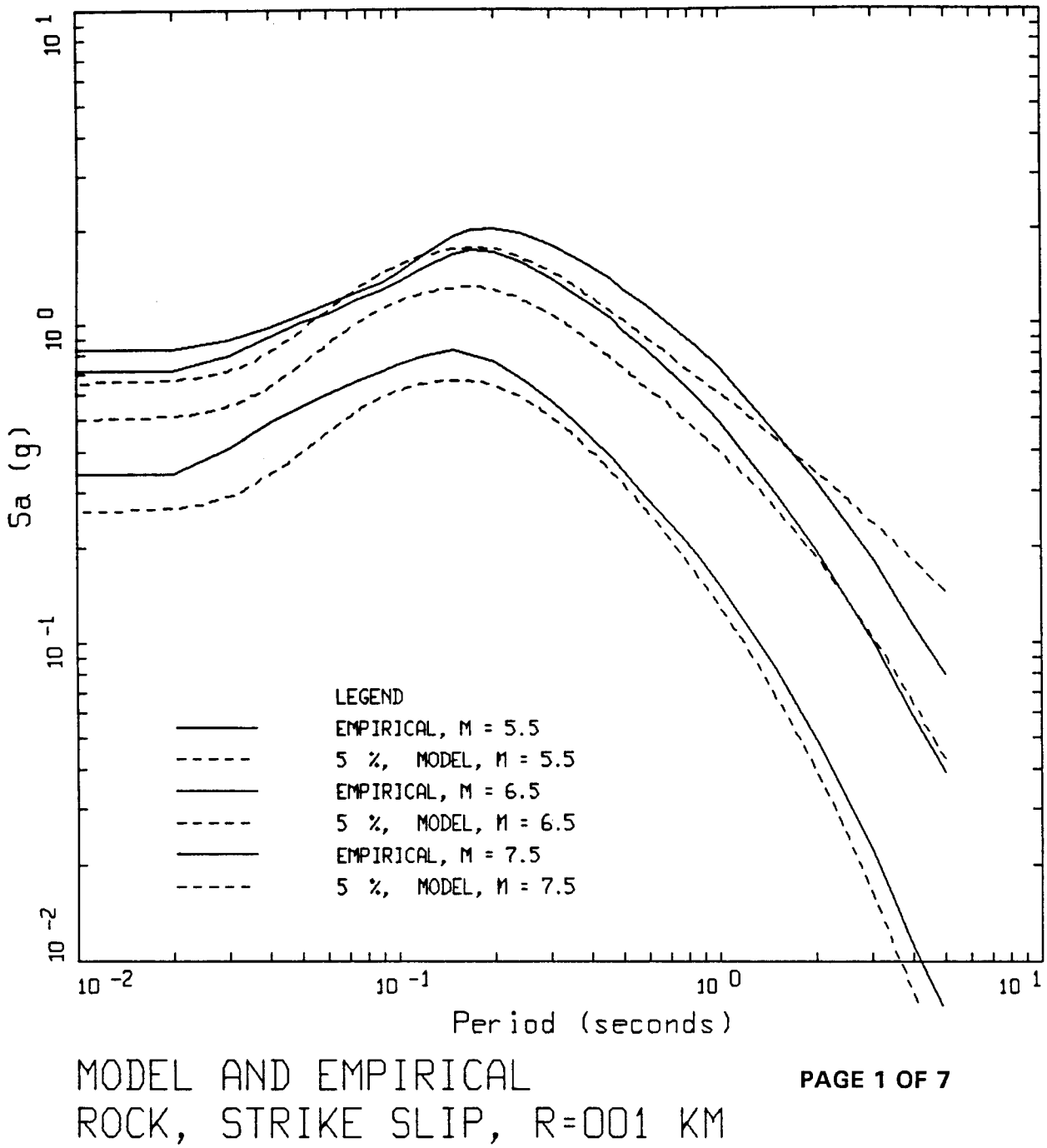

Figure Set 6.10. Comparison of point-source model simulations to the response spectra computed from the empirical attenuation relation (Appendix A) for a vertical strike-slip mechanism. Magnitudes are M 5.5, 6.5, and 7.5 at fault distances 1, 5, 10, 20, 50, 100, and 20 km and the site condition is soft rock. Model simulations use RVT to compute the response spectra with the inversion parameters (Table 6.1).

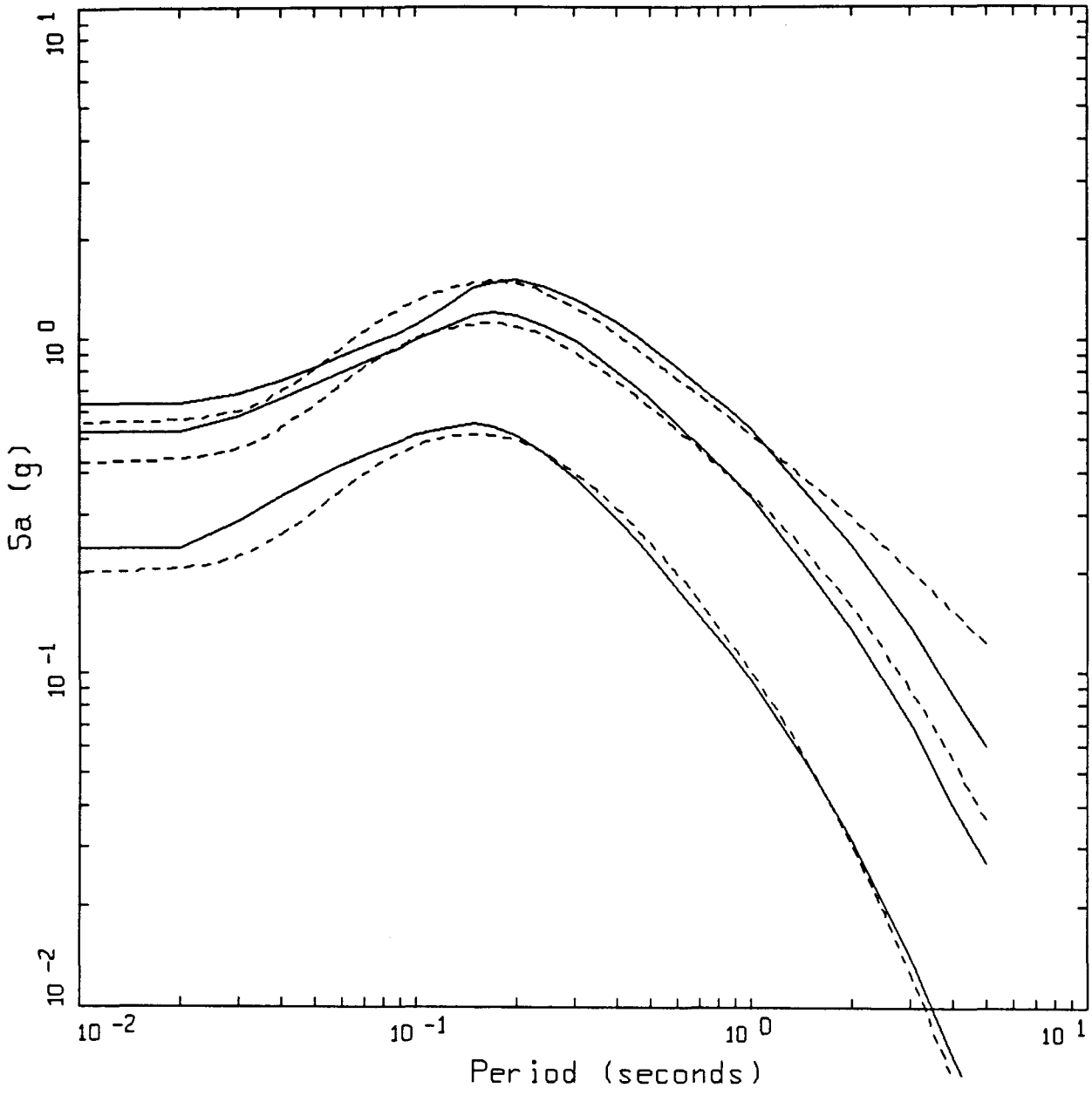

MODEL AND EMPIRICAL
ROCK, STRIKE SLIP, R=005 KM

LEGEND

——— EMPIRICAL, M = 5.5

----- 5 %, MODEL, M = 5.5

——— EMPIRICAL, M = 6.5

----- 5 %, MODEL, M = 6.5

——— EMPIRICAL, M = 7.5

----- 5 %, MODEL, M = 7.5

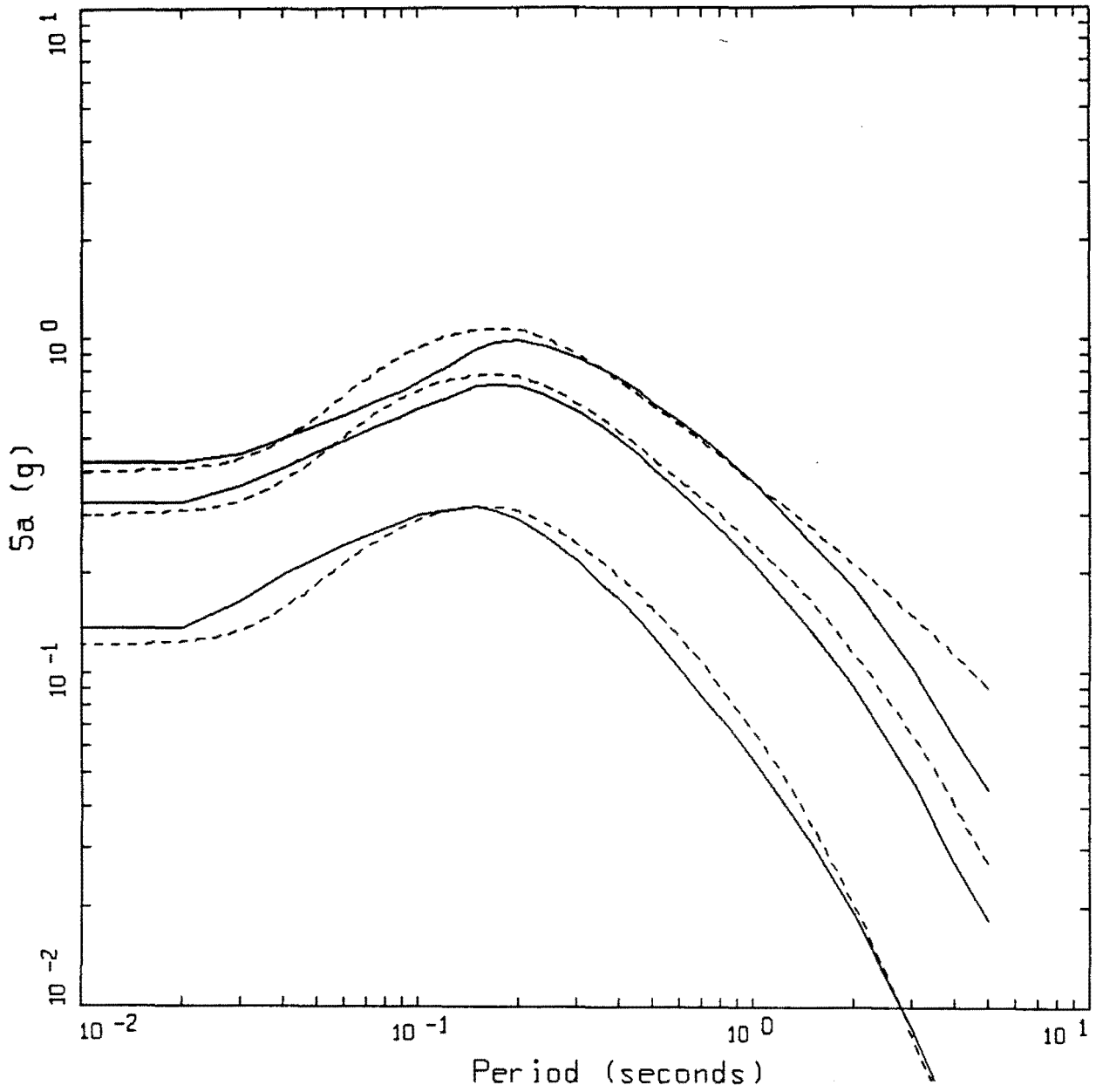

MODEL AND EMPIRICAL
ROCK, STRIKE SLIP, R=010 KM

LEGEND

———	EMPIRICAL, M = 5.5
- - - - -	5 %, MODEL, M = 5.5
———	EMPIRICAL, M = 6.5
- - - - -	5 %, MODEL, M = 6.5
———	EMPIRICAL, M = 7.5
- - - - -	5 %, MODEL, M = 7.5

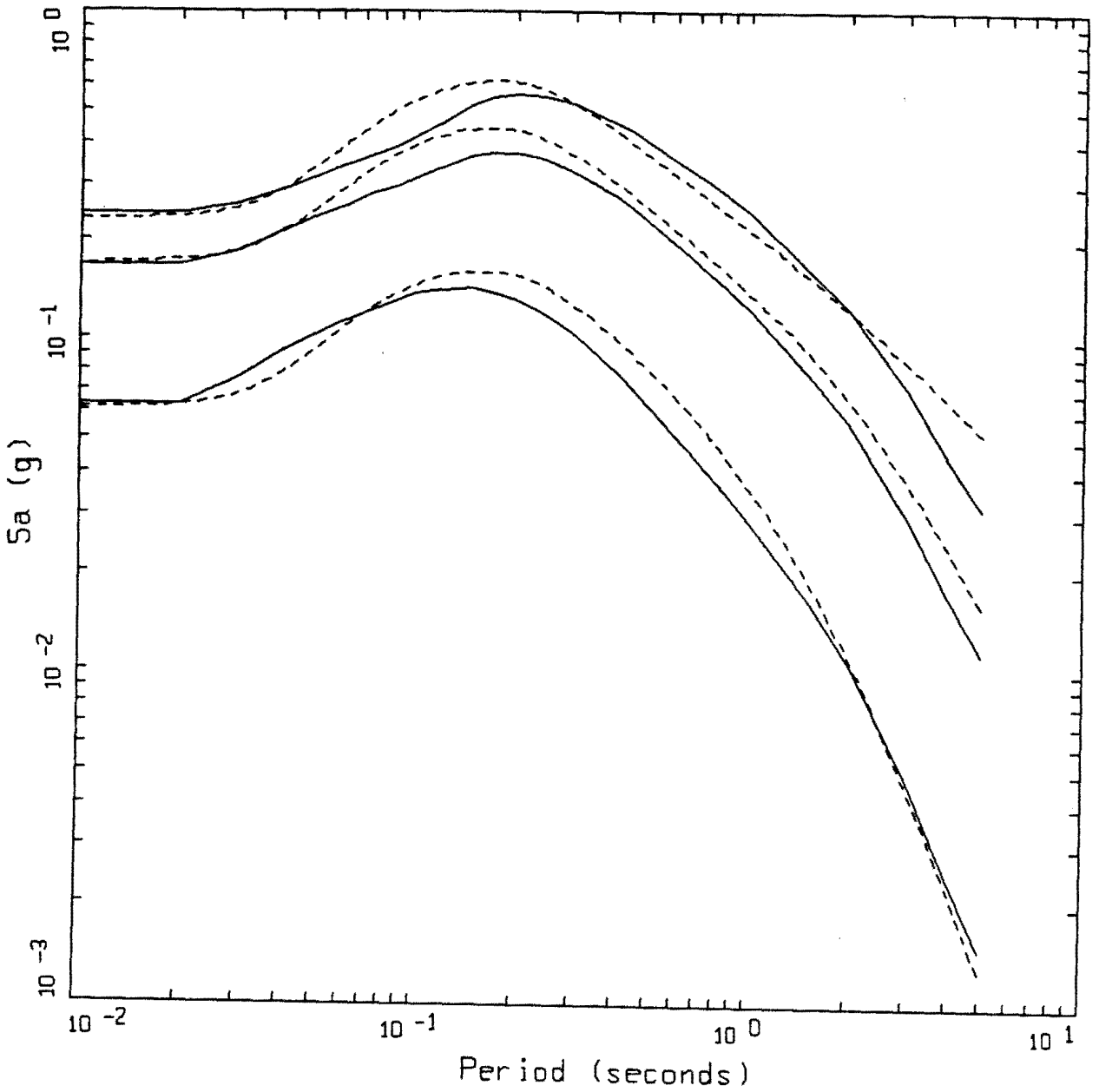

MODEL AND EMPIRICAL
ROCK, STRIKE SLIP, R=020 KM

LEGEND

——— EMPIRICAL, M = 5.5
- - - - - 5 %, MODEL, M = 5.5
——— EMPIRICAL, M = 6.5
- - - - - 5 %, MODEL, M = 6.5
——— EMPIRICAL, M = 7.5
- - - - - 5 %, MODEL, M = 7.5

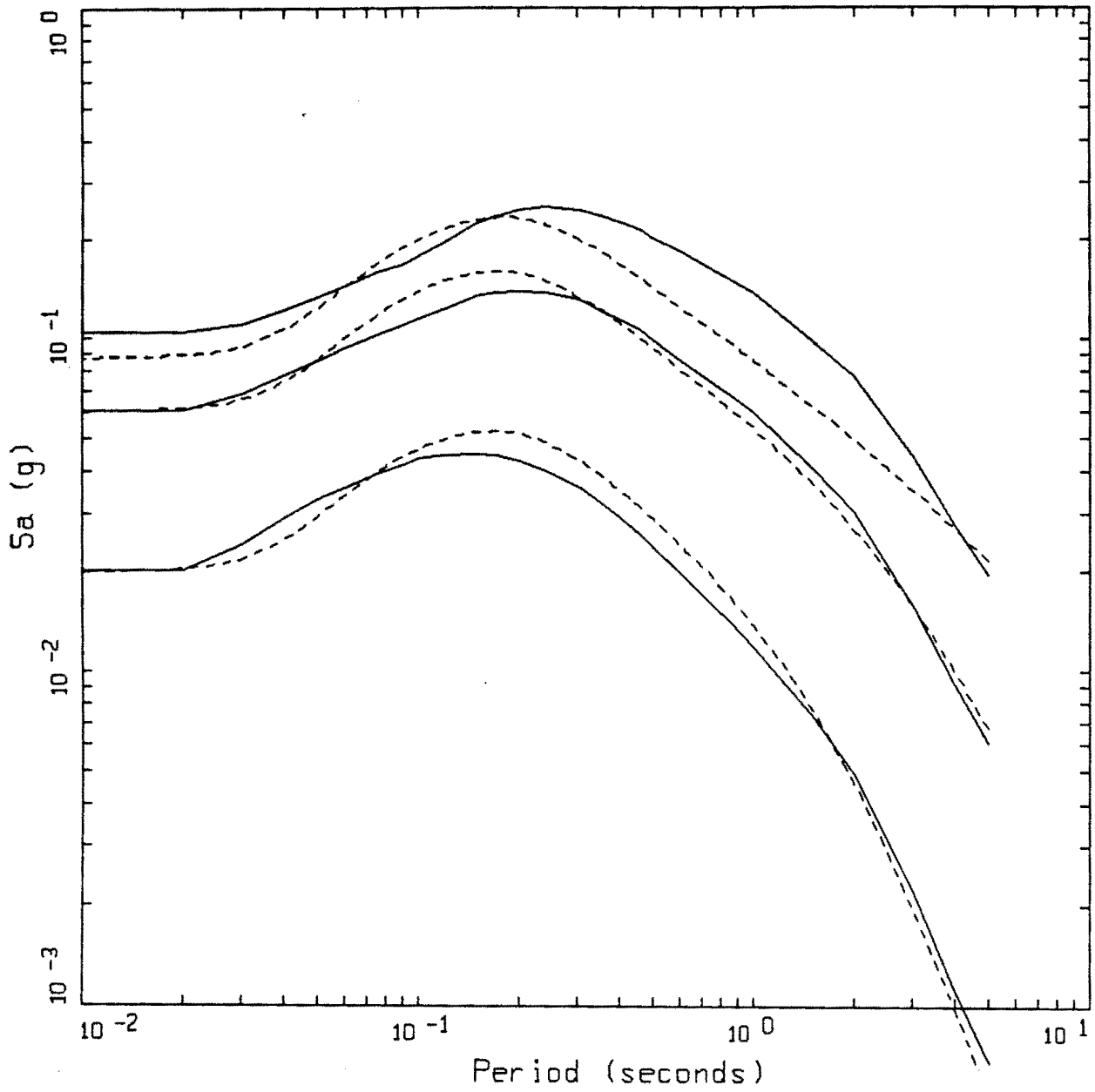

MODEL AND EMPIRICAL
ROCK, STRIKE SLIP, R=050 KM

LEGEND

——— EMPIRICAL, M = 5.5

----- 5 %, MODEL, M = 5.5

——— EMPIRICAL, M = 6.5

----- 5 %, MODEL, M = 6.5

——— EMPIRICAL, M = 7.5

----- 5 %, MODEL, M = 7.5

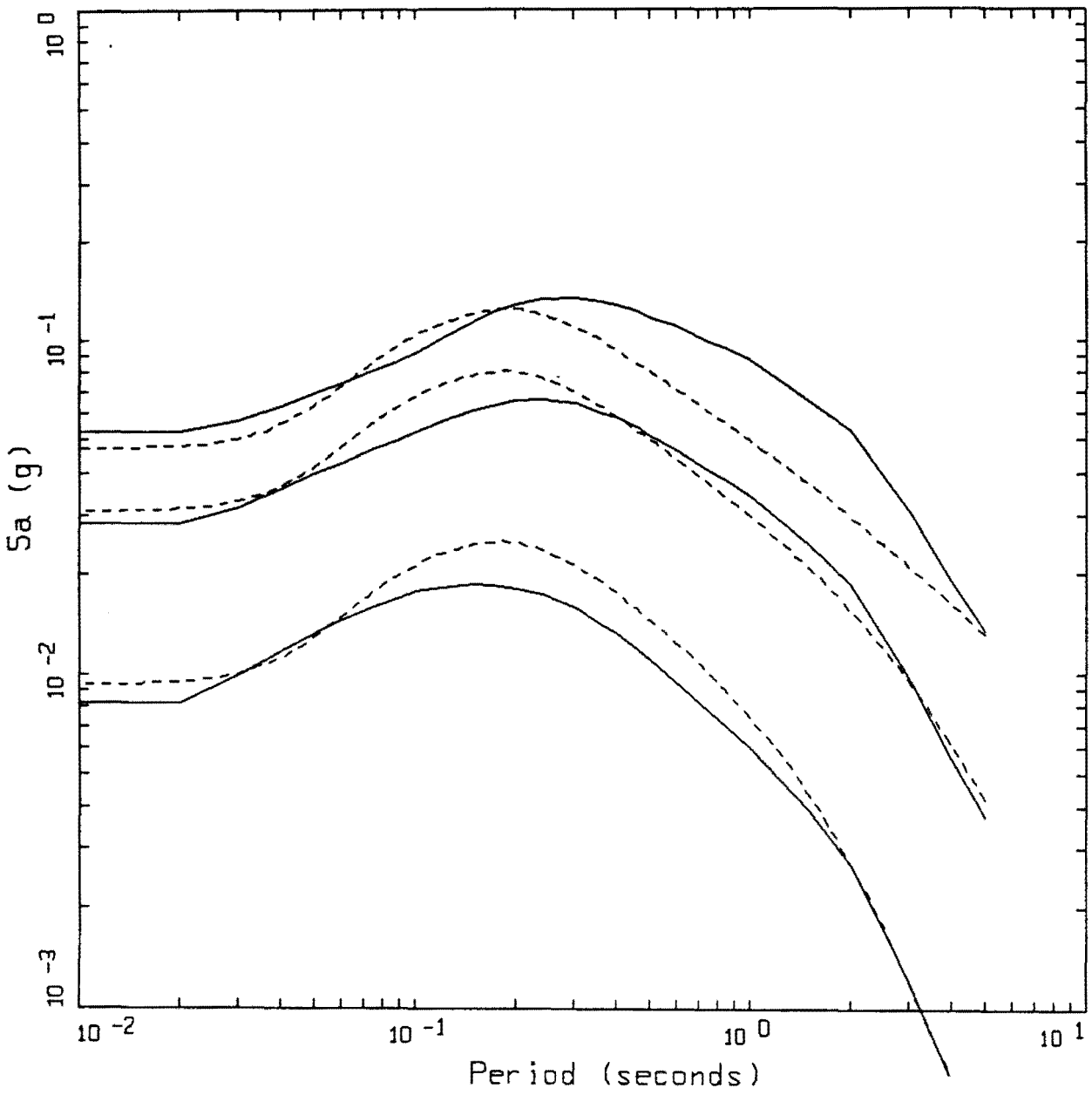

MODEL AND EMPIRICAL ROCK, STRIKE SLIP, R=100 KM

LEGEND

——— EMPIRICAL, M = 5.5

- - - - - 5 %, MODEL, M = 5.5

——— EMPIRICAL, M = 6.5

- - - - - 5 %, MODEL, M = 6.5

——— EMPIRICAL, M = 7.5

- - - - - 5 %, MODEL, M = 7.5

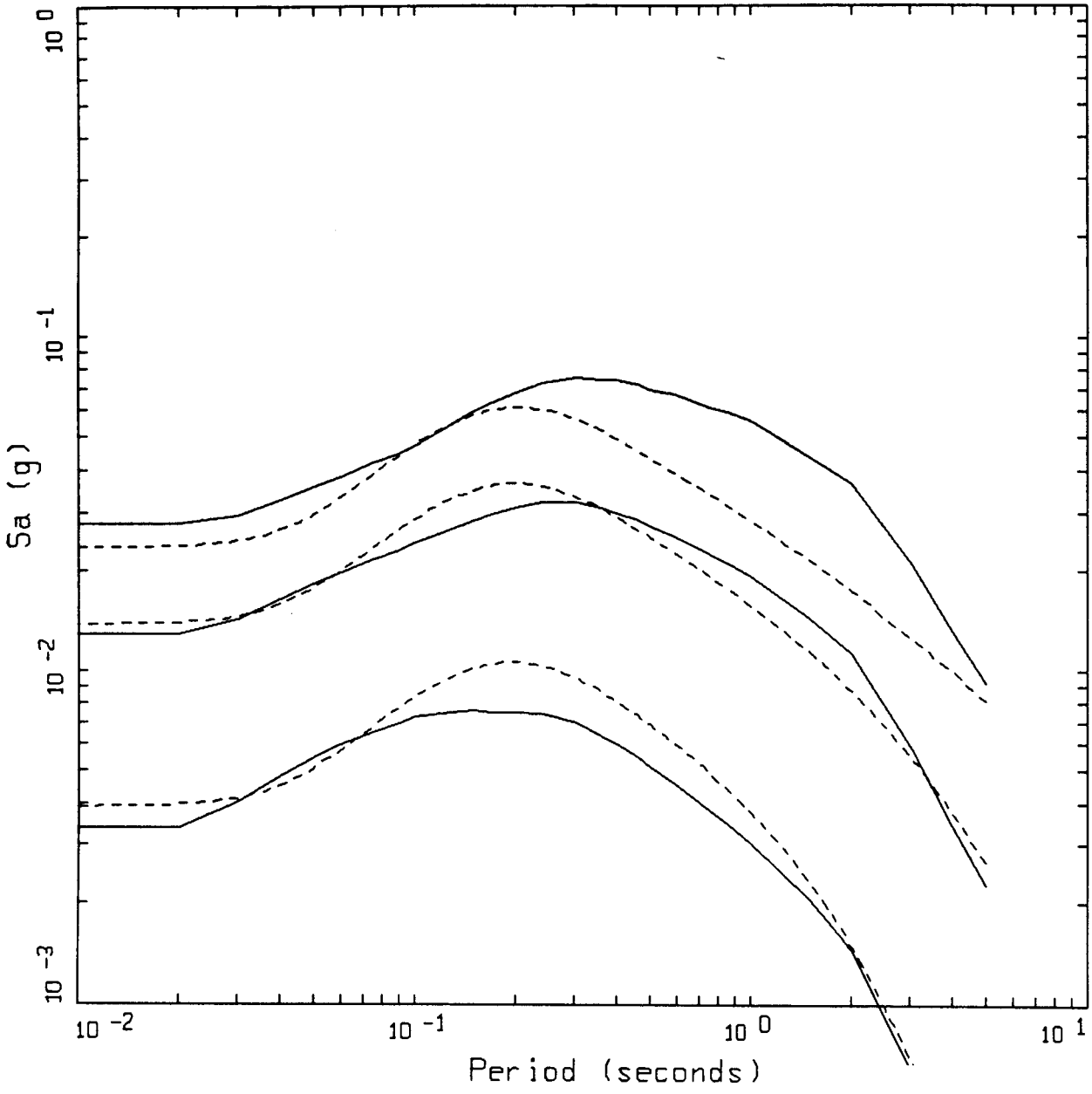

MODEL AND EMPIRICAL ROCK, STRIKE SLIP, R=200 KM

LEGEND

———	EMPIRICAL, M = 5.5
- - - - -	5 %, MODEL, M = 5.5
———	EMPIRICAL, M = 6.5
- - - - -	5 %, MODEL, M = 6.5
———	EMPIRICAL, M = 7.5
- - - - -	5 %, MODEL, M = 7.5

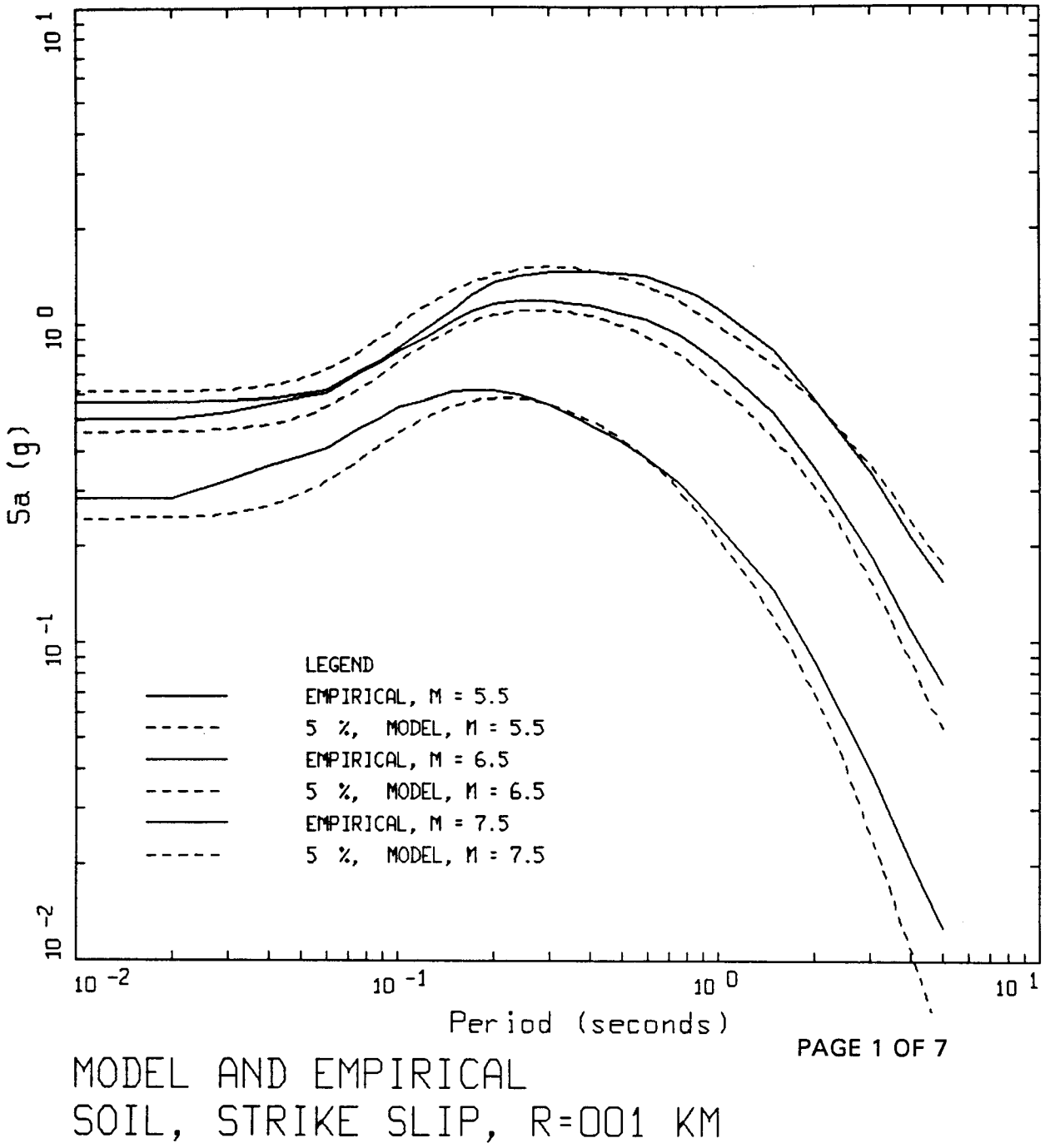

Figure Set 6.11. Comparison of point-source model simulations to the response spectra computed from the empirical attenuation relation (Appendix A) for a vertical strike-slip mechanism. Magnitudes are **M** 5.5, 6.5, and 7.5 at fault distances 1, 5, 10, 20, 50, 100, and 20 km and the site condition is deep soil. Model simulations use RVT to compute the response spectra with the inversion parameters (Table 6.1).

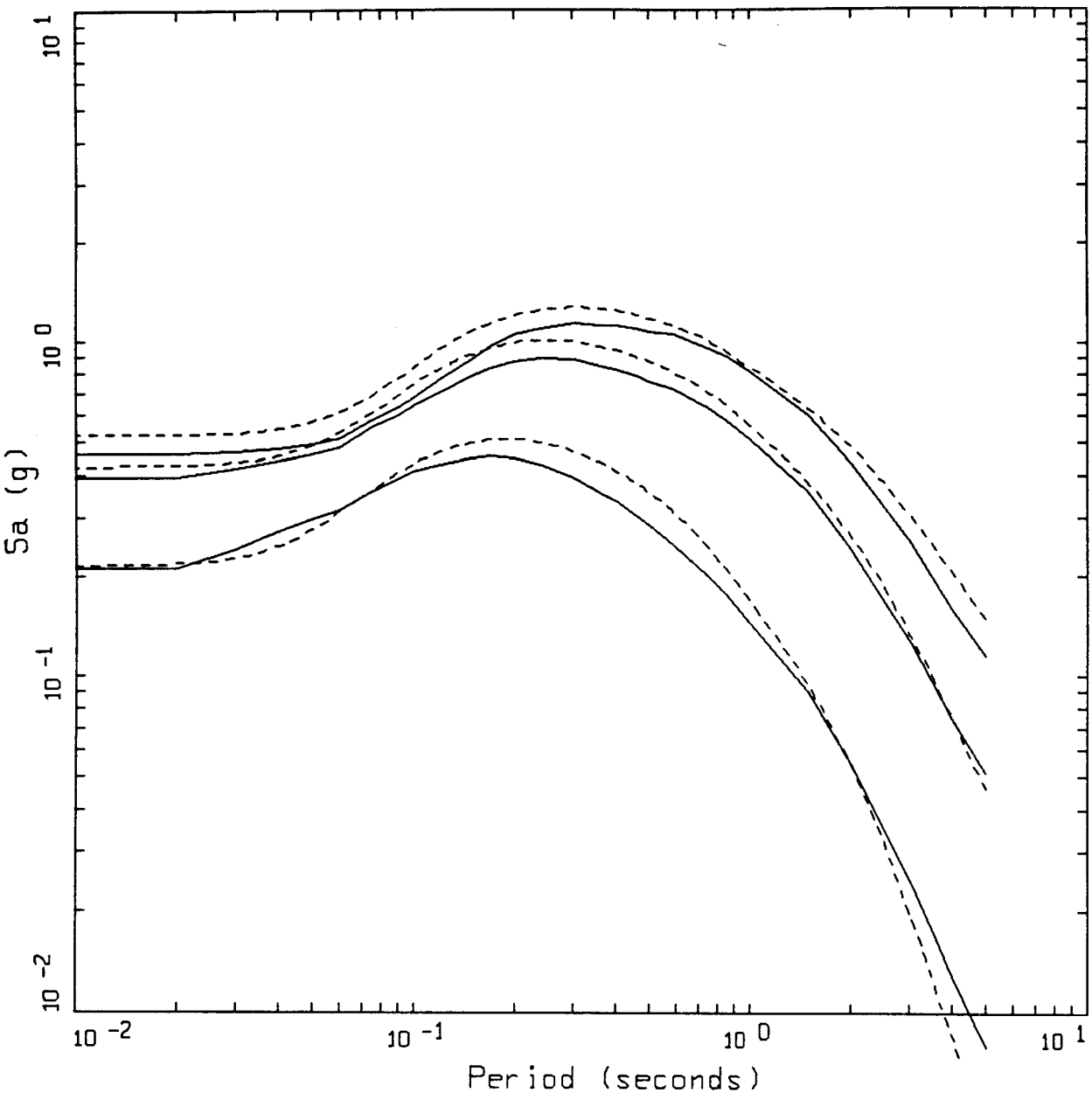

MODEL AND EMPIRICAL SOIL, STRIKE SLIP, R=005 KM

LEGEND

———	EMPIRICAL, M = 5.5
- - - - -	5 %, MODEL, M = 5.5
———	EMPIRICAL, M = 6.5
- - - - -	5 %, MODEL, M = 6.5
———	EMPIRICAL, M = 7.5
- - - - -	5 %, MODEL, M = 7.5

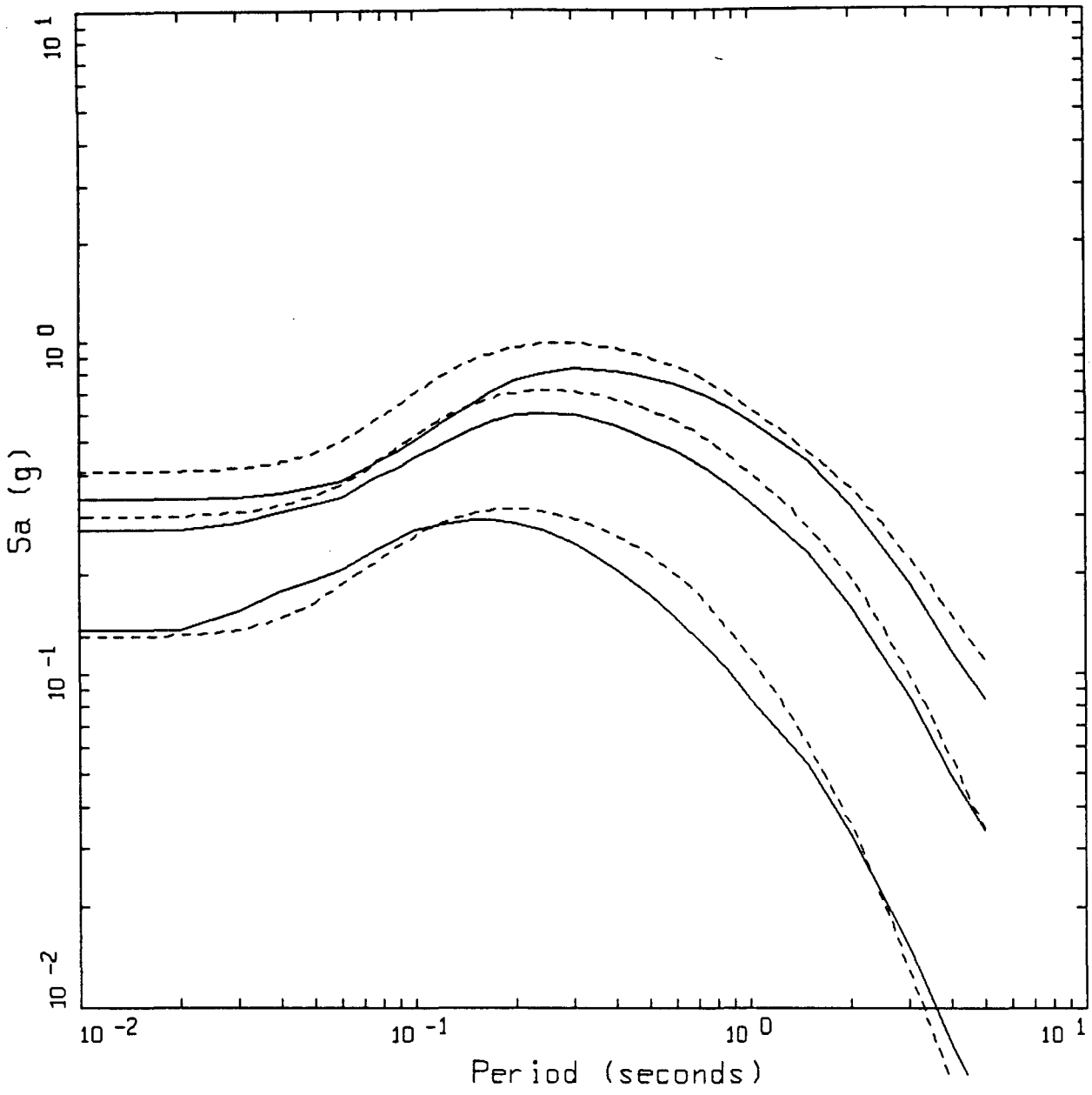

MODEL AND EMPIRICAL SOIL, STRIKE SLIP, R=010 KM

LEGEND

——— EMPIRICAL, M = 5.5

- - - - - 5 %, MODEL, M = 5.5

——— EMPIRICAL, M = 6.5

- - - - - 5 %, MODEL, M = 6.5

——— EMPIRICAL, M = 7.5

- - - - - 5 %, MODEL, M = 7.5

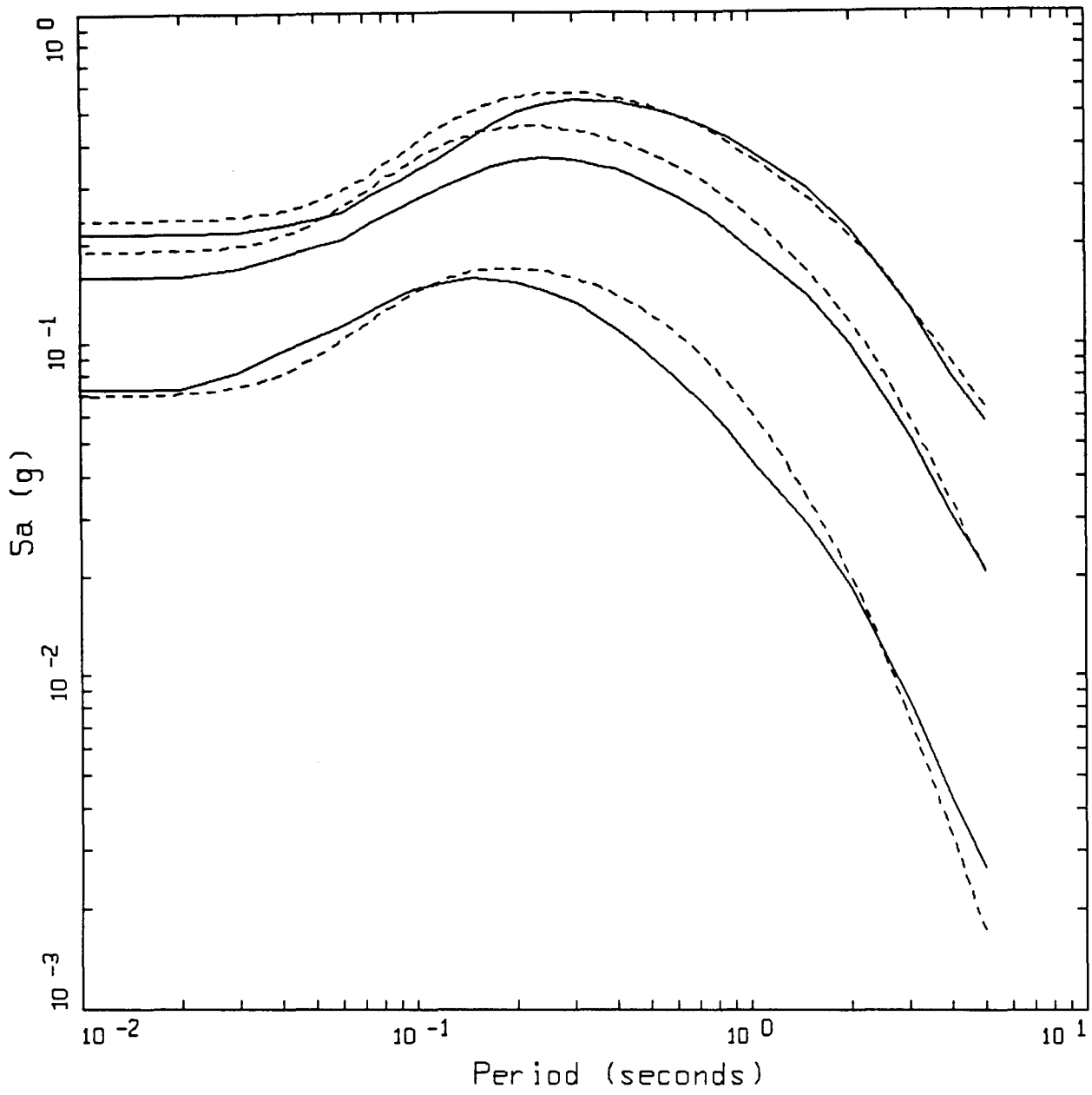

MODEL AND EMPIRICAL
SOIL, STRIKE SLIP, R=020 KM

LEGEND

———	EMPIRICAL, M = 5.5
- - - - -	5 %, MODEL, M = 5.5
———	EMPIRICAL, M = 6.5
- - - - -	5 %, MODEL, M = 6.5
———	EMPIRICAL, M = 7.5
- - - - -	5 %, MODEL, M = 7.5

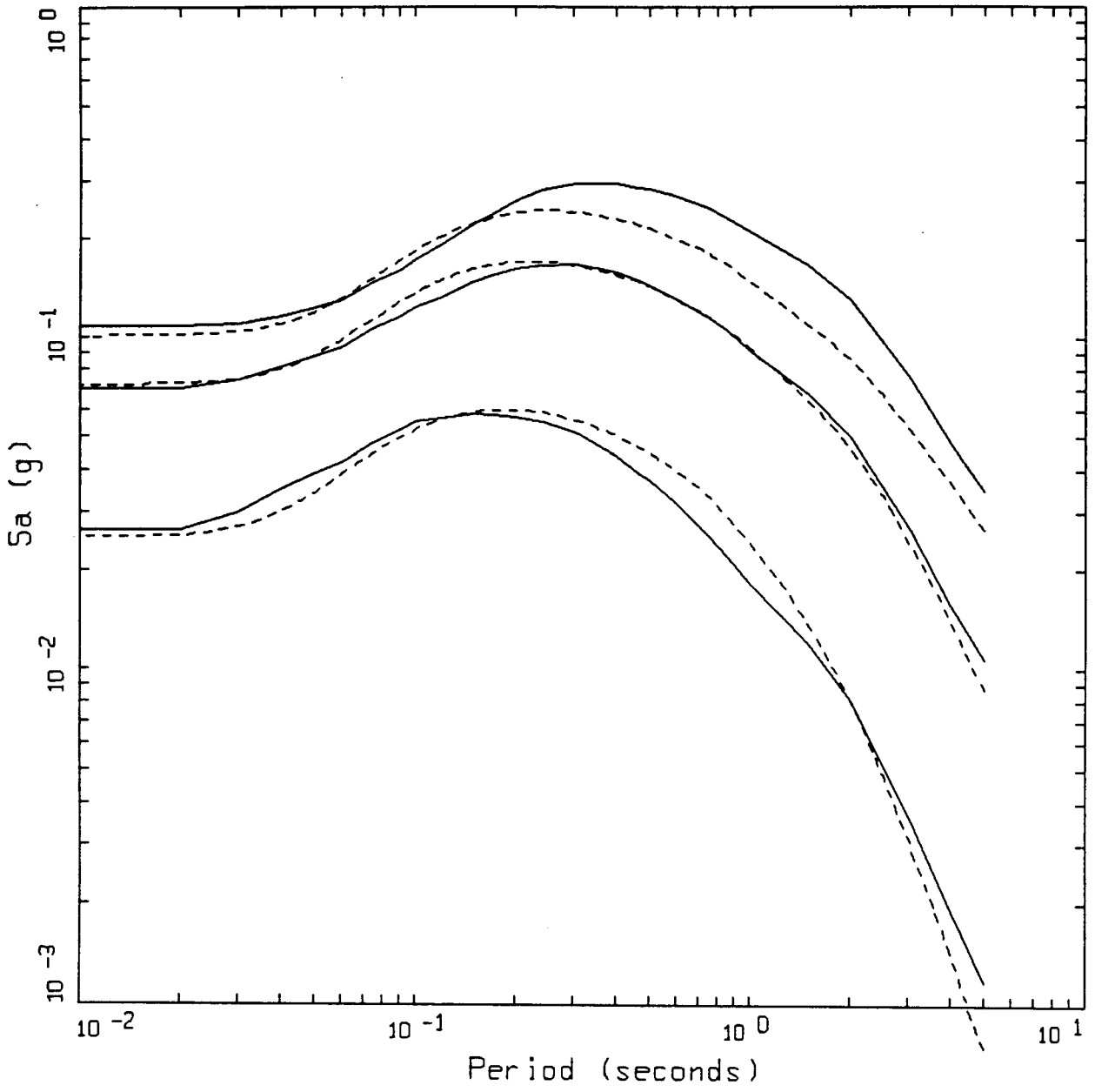

MODEL AND EMPIRICAL SOIL, STRIKE SLIP, R=050 KM

LEGEND

———	EMPIRICAL, M = 5.5
- - - - -	5 %, MODEL, M = 5.5
———	EMPIRICAL, M = 6.5
- - - - -	5 %, MODEL, M = 6.5
———	EMPIRICAL, M = 7.5
- - - - -	5 %, MODEL, M = 7.5

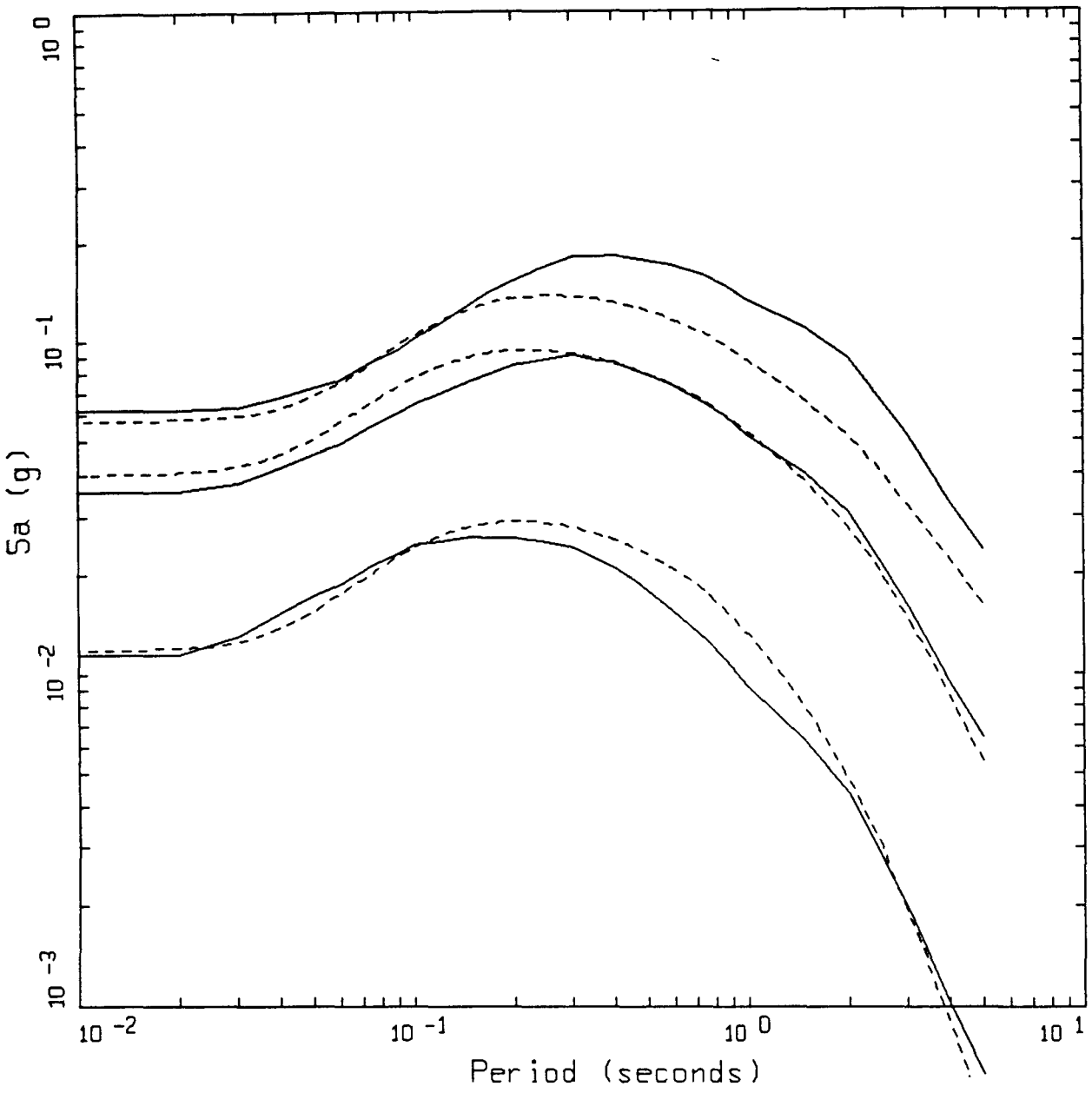

MODEL AND EMPIRICAL SOIL, STRIKE SLIP, R=100 KM

LEGEND

——— EMPIRICAL, M = 5.5

- - - - - 5 %, MODEL, M = 5.5

——— EMPIRICAL, M = 6.5

- - - - - 5 %, MODEL, M = 6.5

——— EMPIRICAL, M = 7.5

- - - - - 5 %, MODEL, M = 7.5

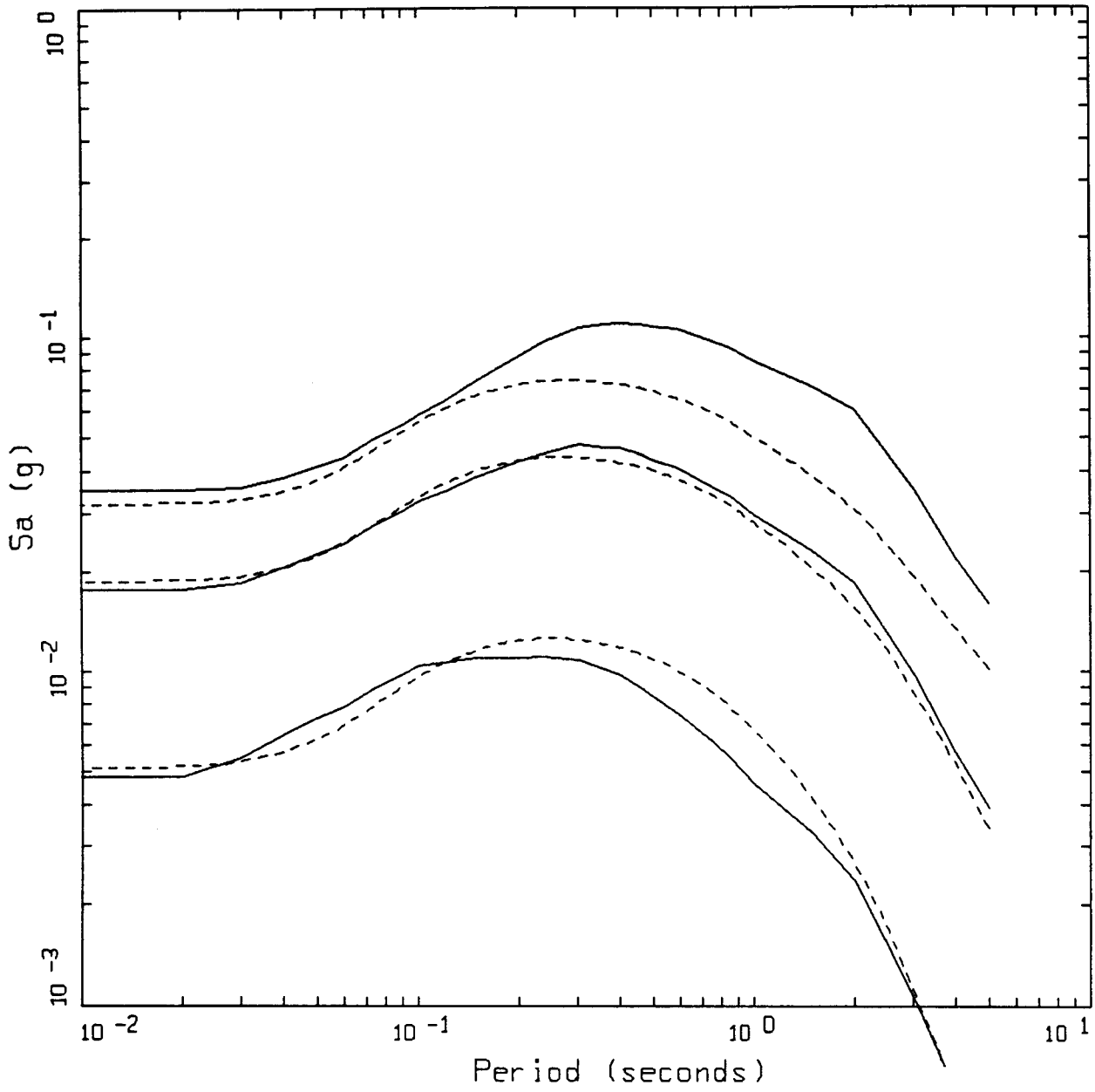

MODEL AND EMPIRICAL SOIL, STRIKE SLIP, R=200 KM

LEGEND

———	EMPIRICAL, M = 5.5
- - - - -	5 %, MODEL, M = 5.5
———	EMPIRICAL, M = 6.5
- - - - -	5 %, MODEL, M = 6.5
———	EMPIRICAL, M = 7.5
- - - - -	5 %, MODEL, M = 7.5

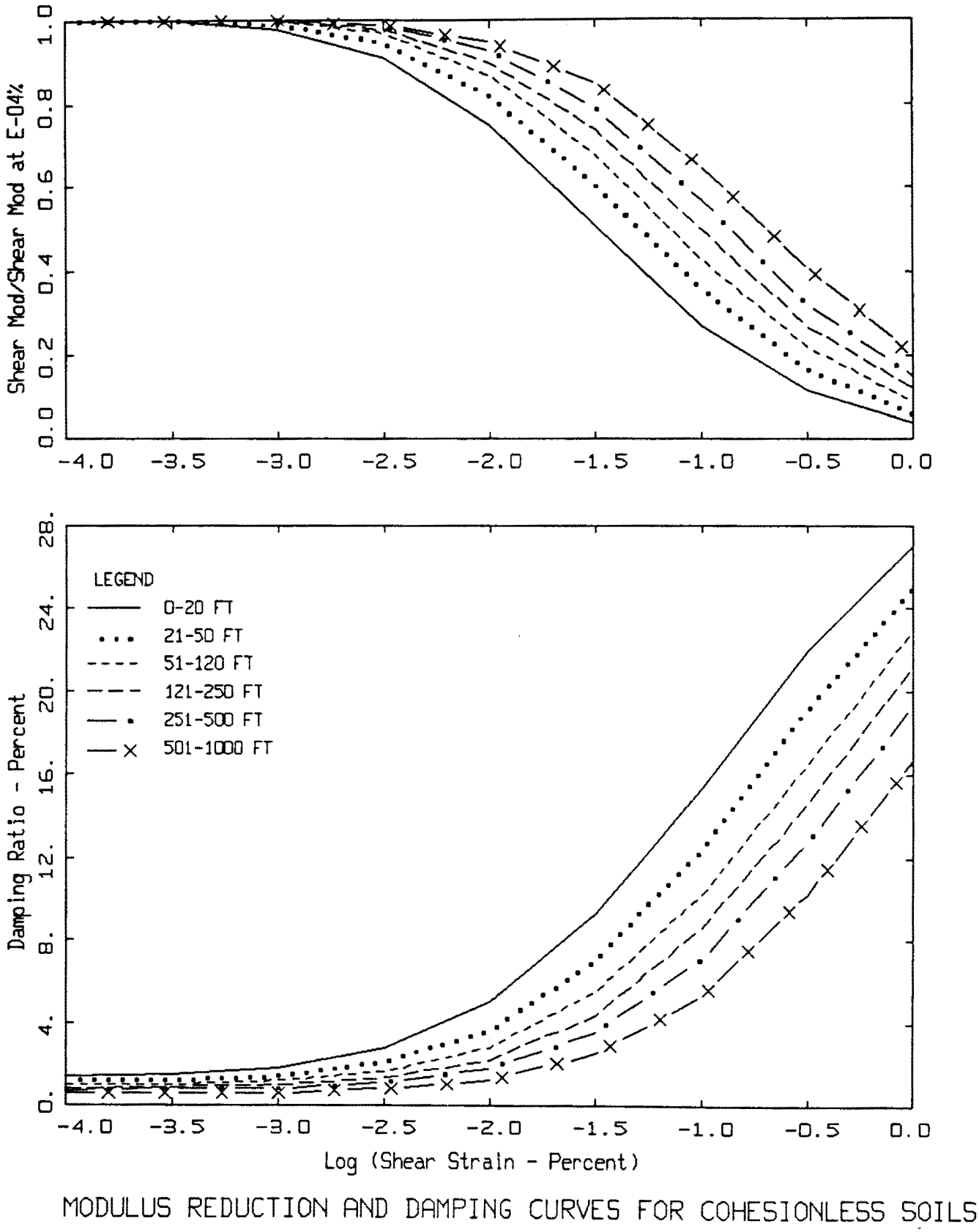

Figure 6.12. Generic G/G_{max} and hysteretic damping curves for cohesionless soils (EPRI, 1993).

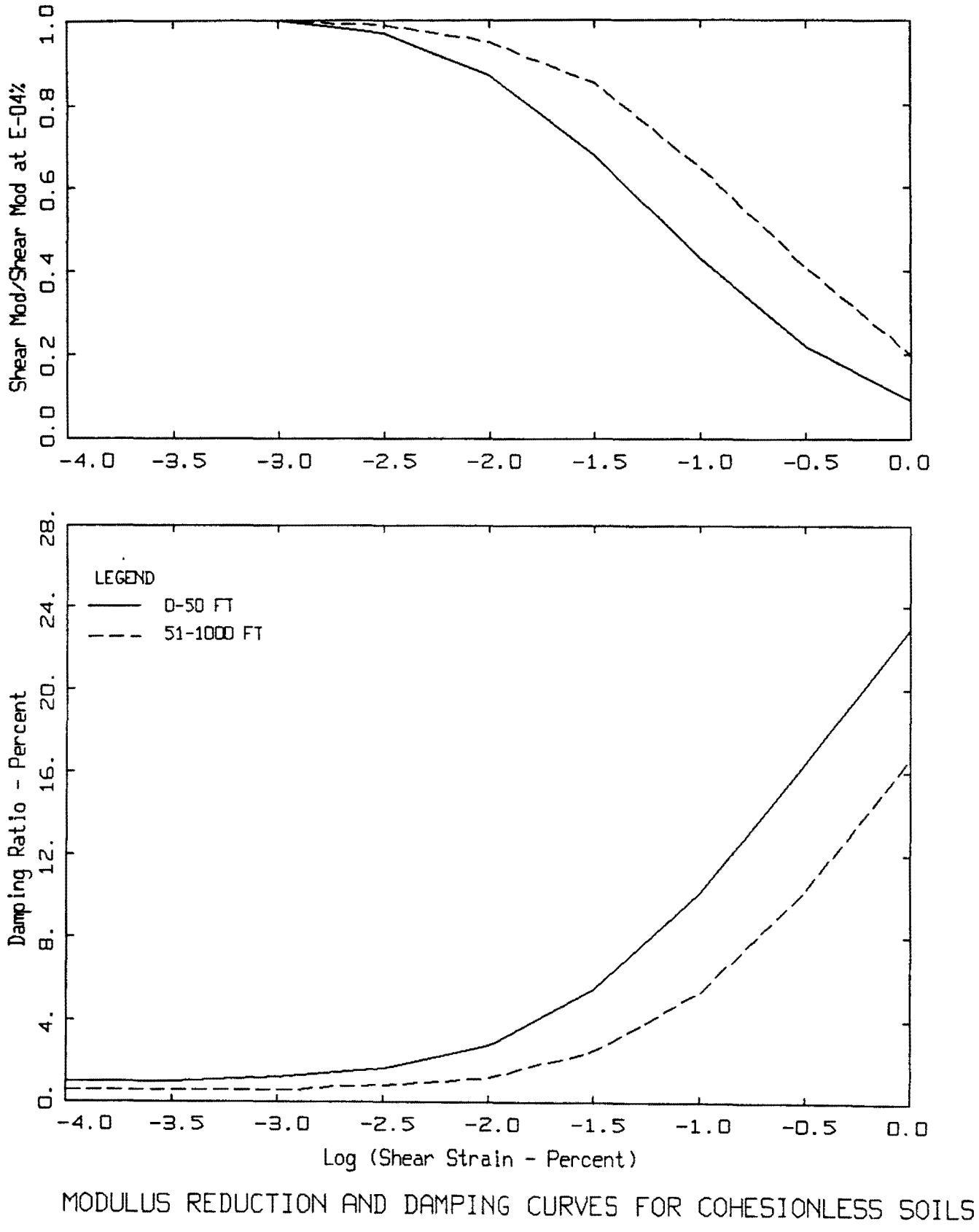

Figure 6.13. Generic G/G_{max} and hysteretic damping curves for Peninsular Range deep cohesionless soils.

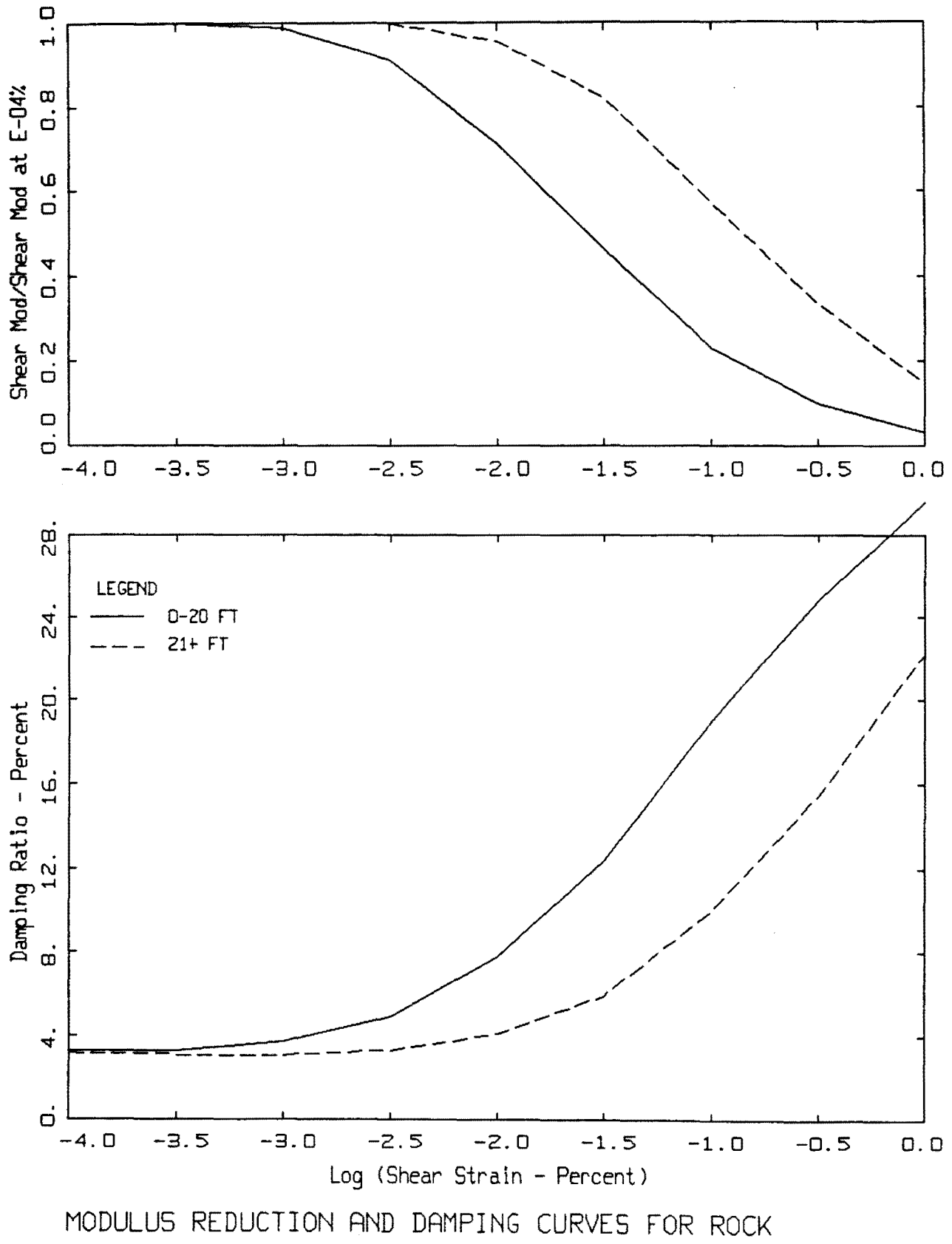

Figure 6.14. Generic G/G_{max} and hysteretic damping curves for soft rock.

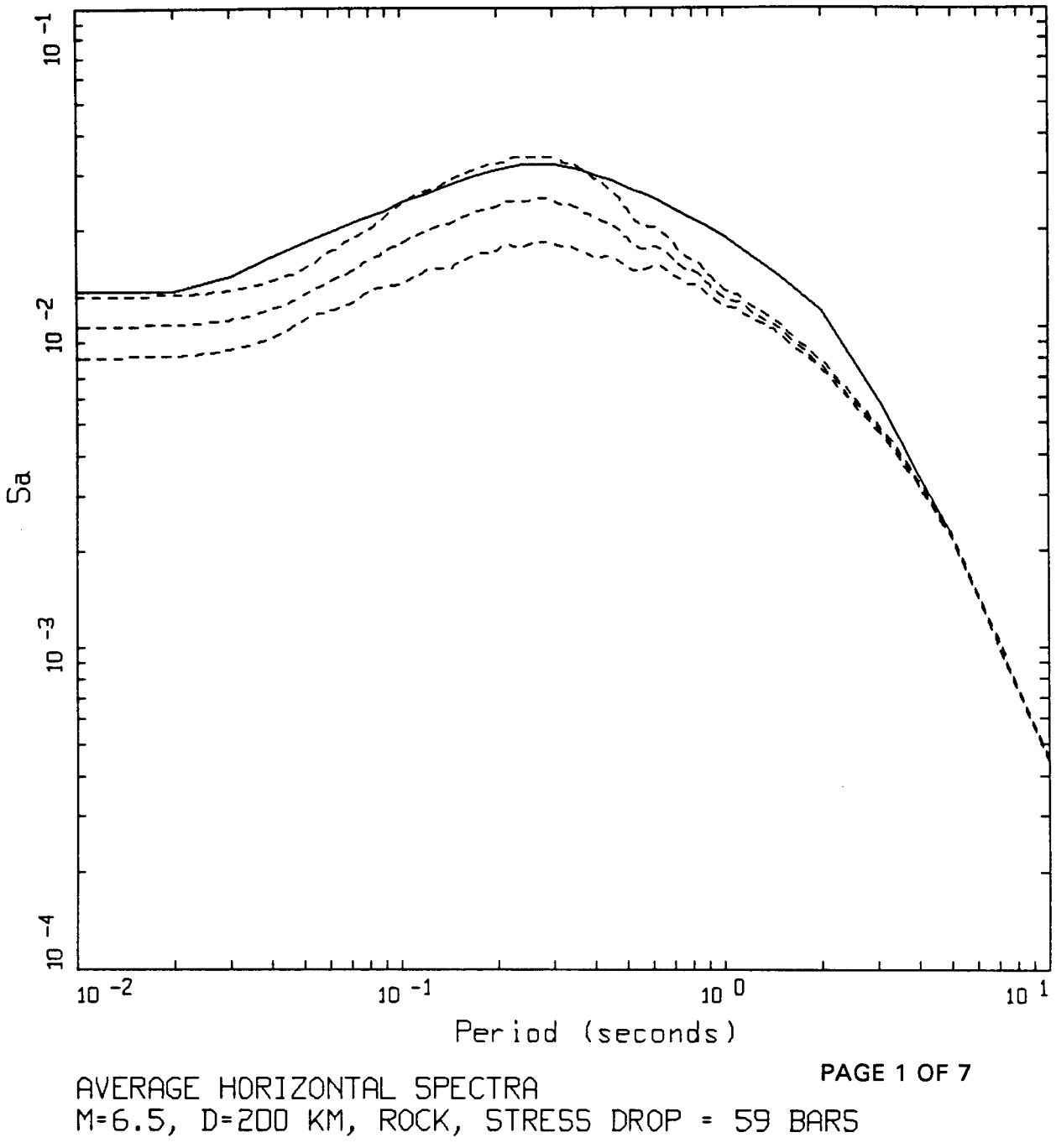

Figure Set 6.15. Comparison of point-source model simulations to the response spectra computed from the empirical attenuation relation (Appendix A) for a vertical strike-slip mechanism. Magnitude is M 6.5, point-source depth is 8 km, and the stress drop is 59 bars (Table 6.1). Fault distances are 200, 100, 50, 20, 10, 5, and 1 km. Site condition over soft rock.

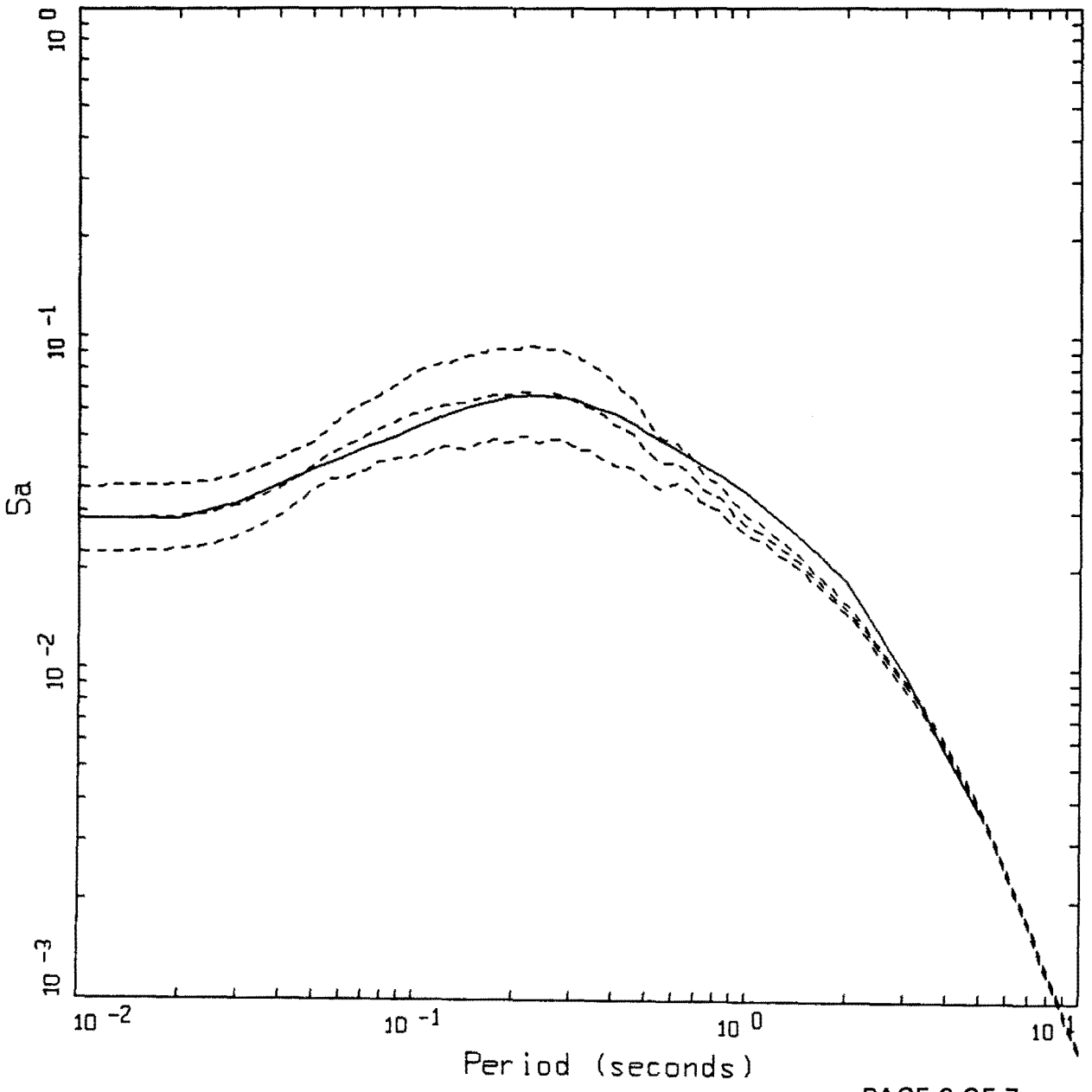

AVERAGE HORIZONTAL SPECTRA
M=6.5, D=100 KM, ROCK, STRESS DROP = 59 BARS

LEGEND

———— EMPIRICAL

- - - - - 84TH PERCENTILE

- - - - - 50TH PERCENTILE

- - - - - 16TH PERCENTILE

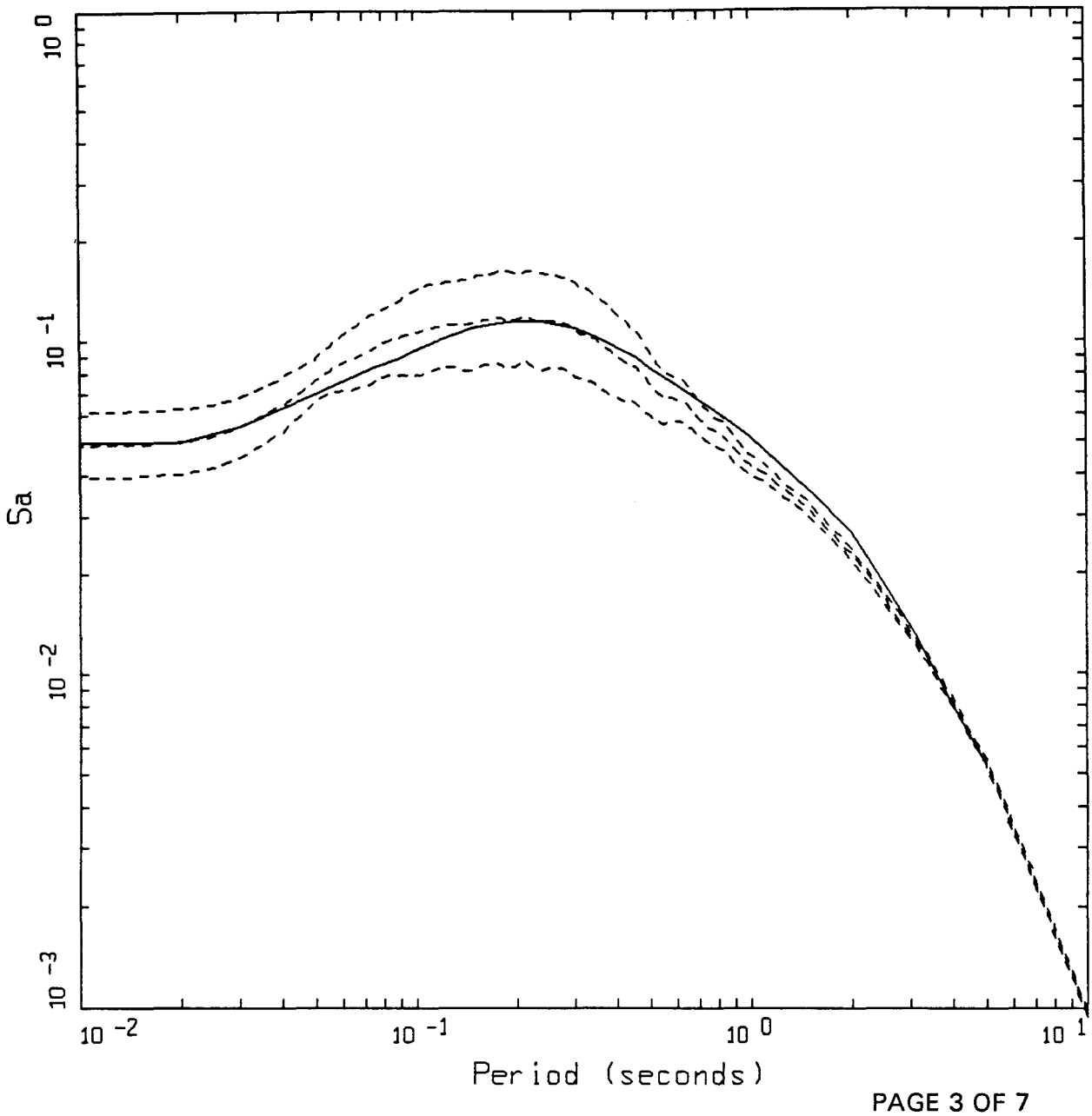

AVERAGE HORIZONTAL SPECTRA
M=6.5, D=60 KM, ROCK, STRESS DROP = 59 BARS

LEGEND

——— EMPIRICAL

- - - - - 84TH PERCENTILE

- - - - - 50TH PERCENTILE

- - - - - 16TH PERCENTILE

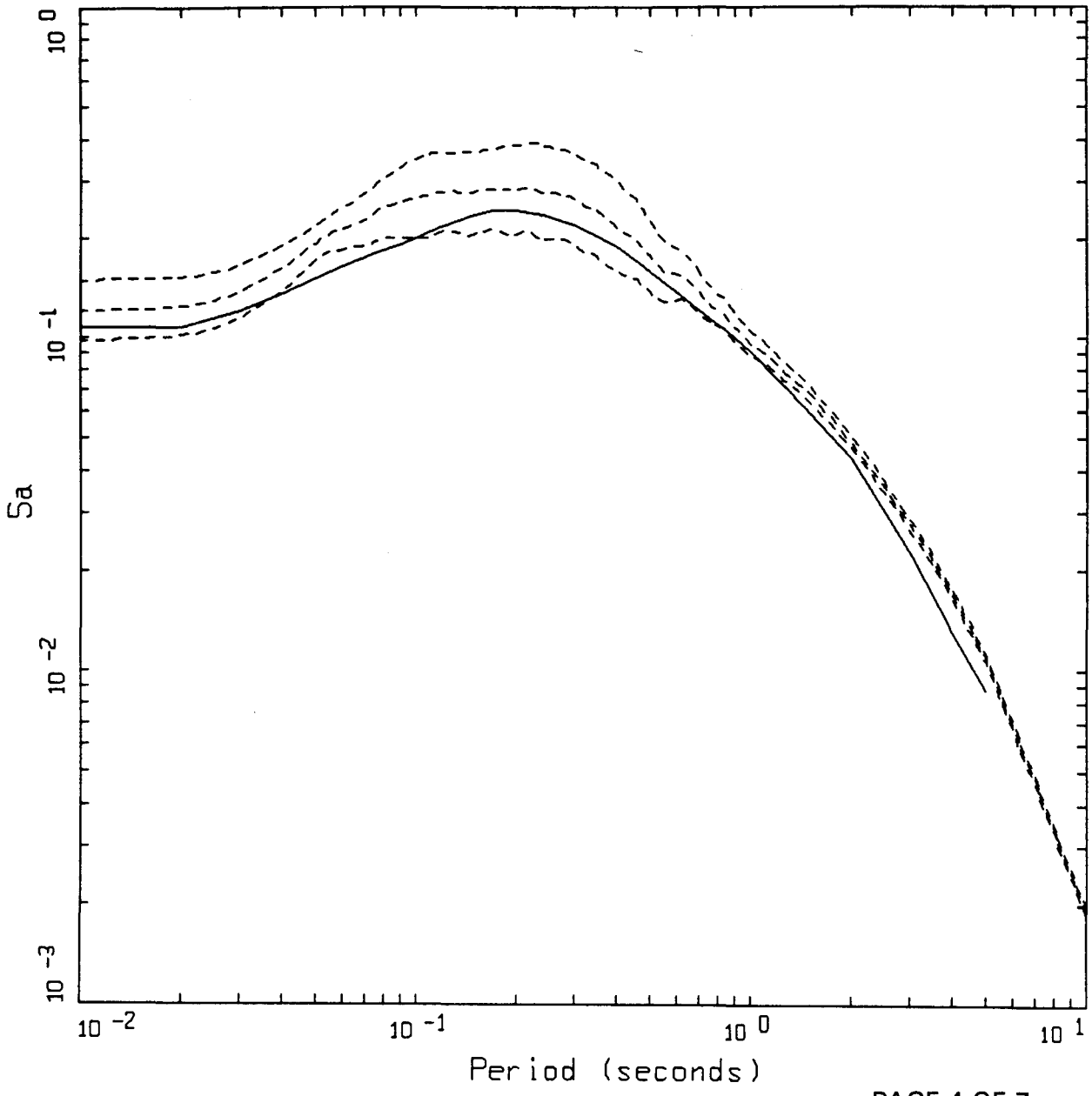

AVERAGE HORIZONTAL SPECTRA
M=6.5, D=30 KM, ROCK, STRESS DROP = 59 BARS

LEGEND

———— EMPIRICAL

- - - - - 84TH PERCENTILE

- - - - - 50TH PERCENTILE

- - - - - 16TH PERCENTILE

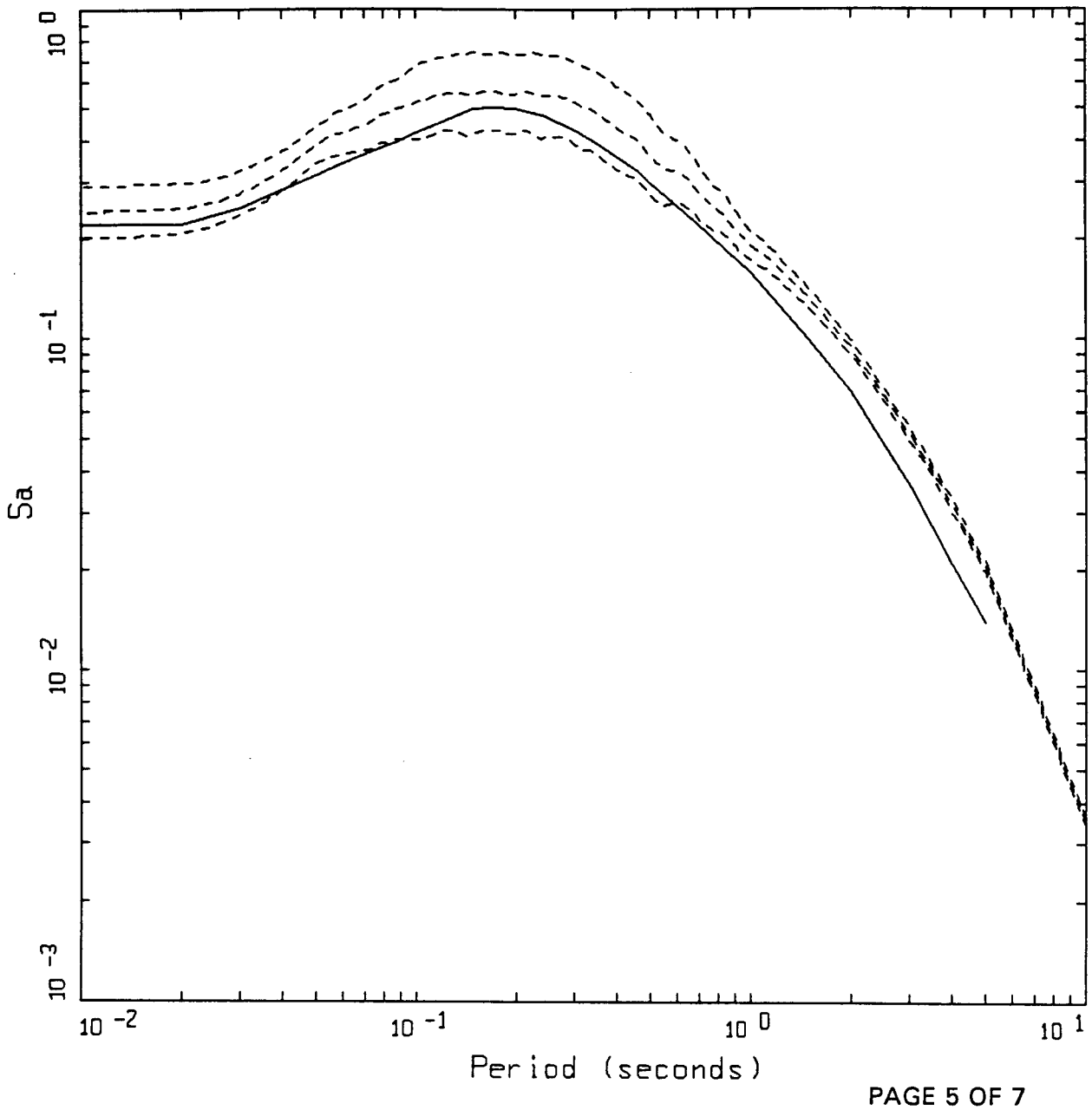

AVERAGE HORIZONTAL SPECTRA
M=6.5, D=15 KM, ROCK, STRESS DROP = 59 BARS

LEGEND

———— EMPIRICAL
- - - - - 84TH PERCENTILE
- - - - - 50TH PERCENTILE
- - - - - 16TH PERCENTILE

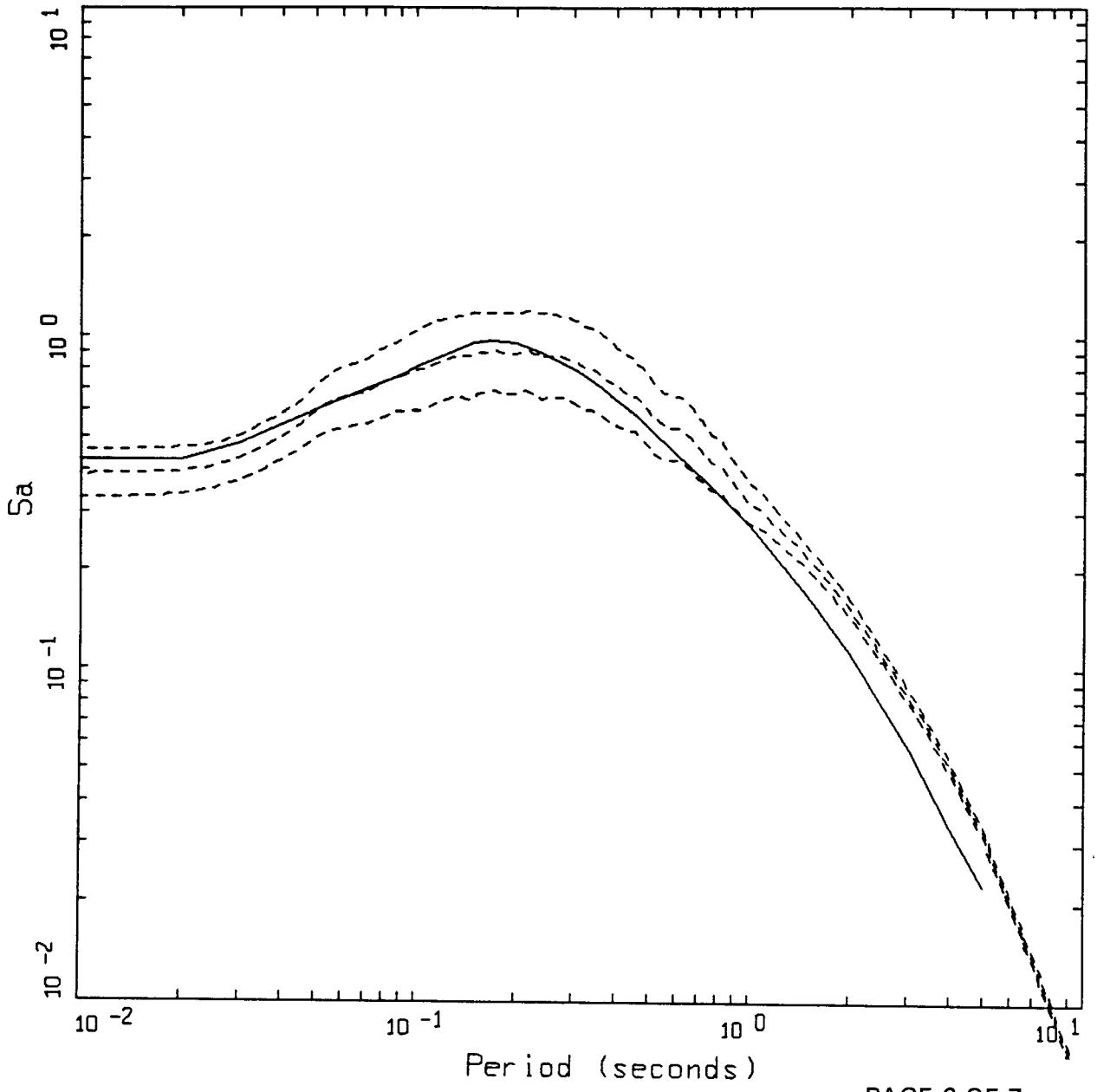

AVERAGE HORIZONTAL SPECTRA
M=6.5, D=07 KM, ROCK, STRESS DROP = 59 BARS

LEGEND

———— EMPIRICAL

- - - - - 84TH PERCENTILE

- - - - - 50TH PERCENTILE

- - - - - 16TH PERCENTILE

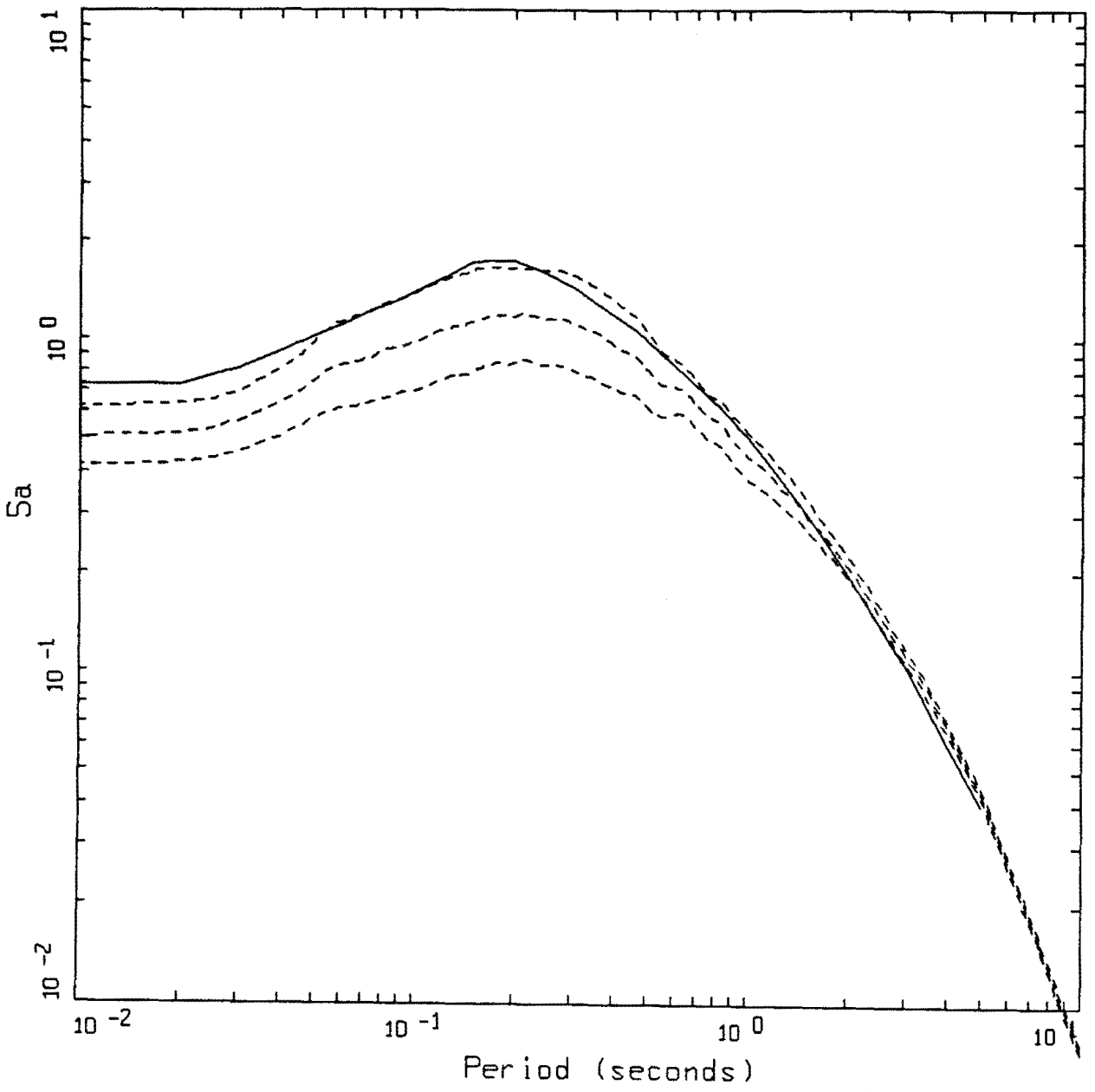

AVERAGE HORIZONTAL SPECTRA
M=6.5, D=00 KM, ROCK, STRESS DROP = 59 BARS

LEGEND

EMPIRICAL

84TH PERCENTILE

50TH PERCENTILE

16TH PERCENTILE

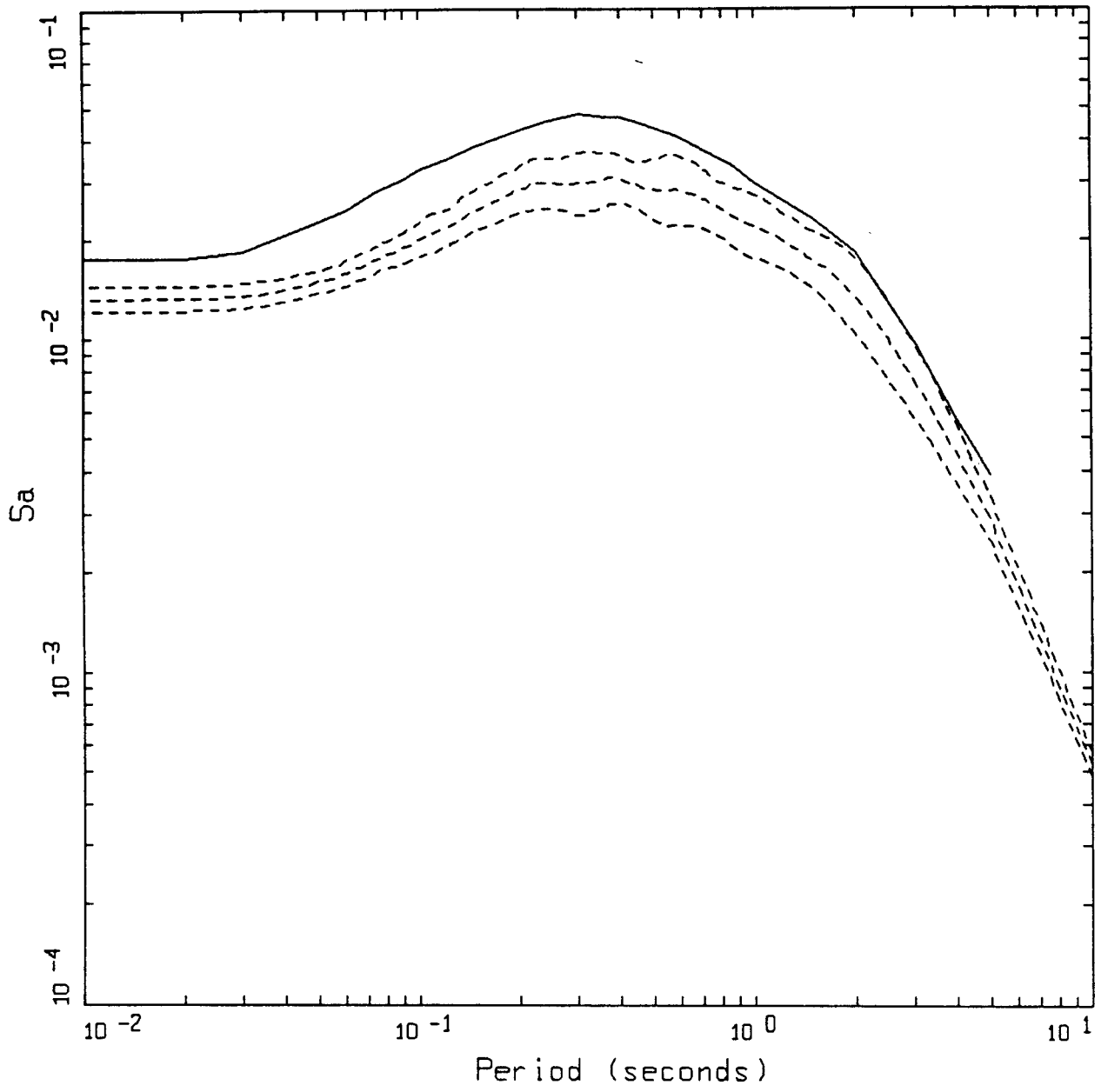

Figure Set 6.16. Comparison of point-source model simulations to the response spectra computed from the empirical attenuation relation (Appendix A) for a vertical strike-slip mechanism. Magnitude is M 6.5, point-source depth is 8 km, and the stress drop is 59 bars (Table 6.1). Fault distances are 200, 100, 50, 20, 10, 5, and 1 km. Site condition over deep soil.

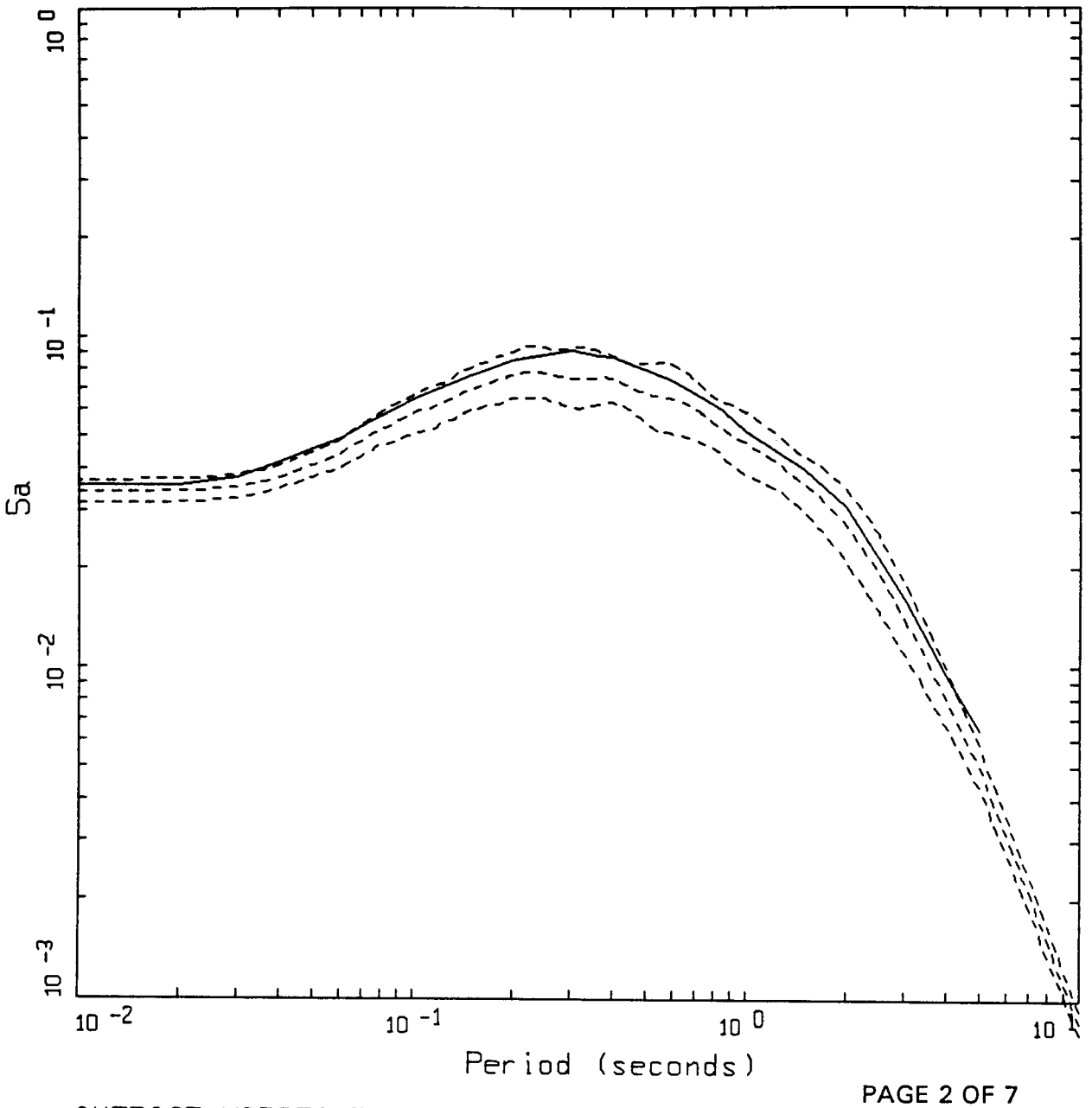

AVERAGE HORIZONTAL SPECTRA
M=6.5, D=100 KM, SOIL, STRESS DROP = 59 BARS

LEGEND

——— EMPIRICAL

- - - - - 84TH PERCENTILE

- - - - - 50TH PERCENTILE

- - - - - 16TH PERCENTILE

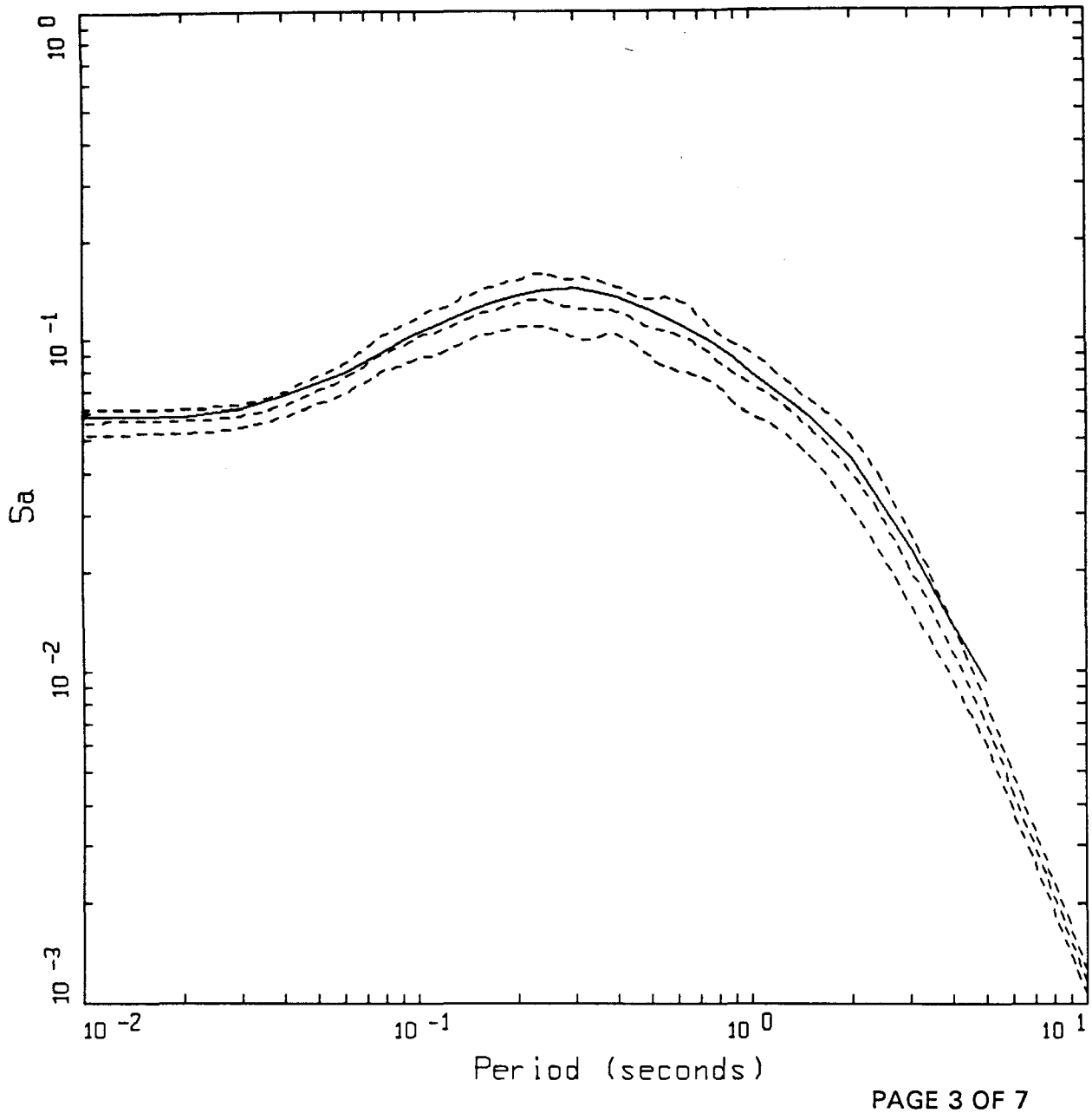

AVERAGE HORIZONTAL SPECTRA
M=6.5, D=60 KM, SOIL, STRESS DROP = 59 BARS

LEGEND

———— EMPIRICAL

- - - - - 84TH PERCENTILE

- - - - - 50TH PERCENTILE

- - - - - 16TH PERCENTILE

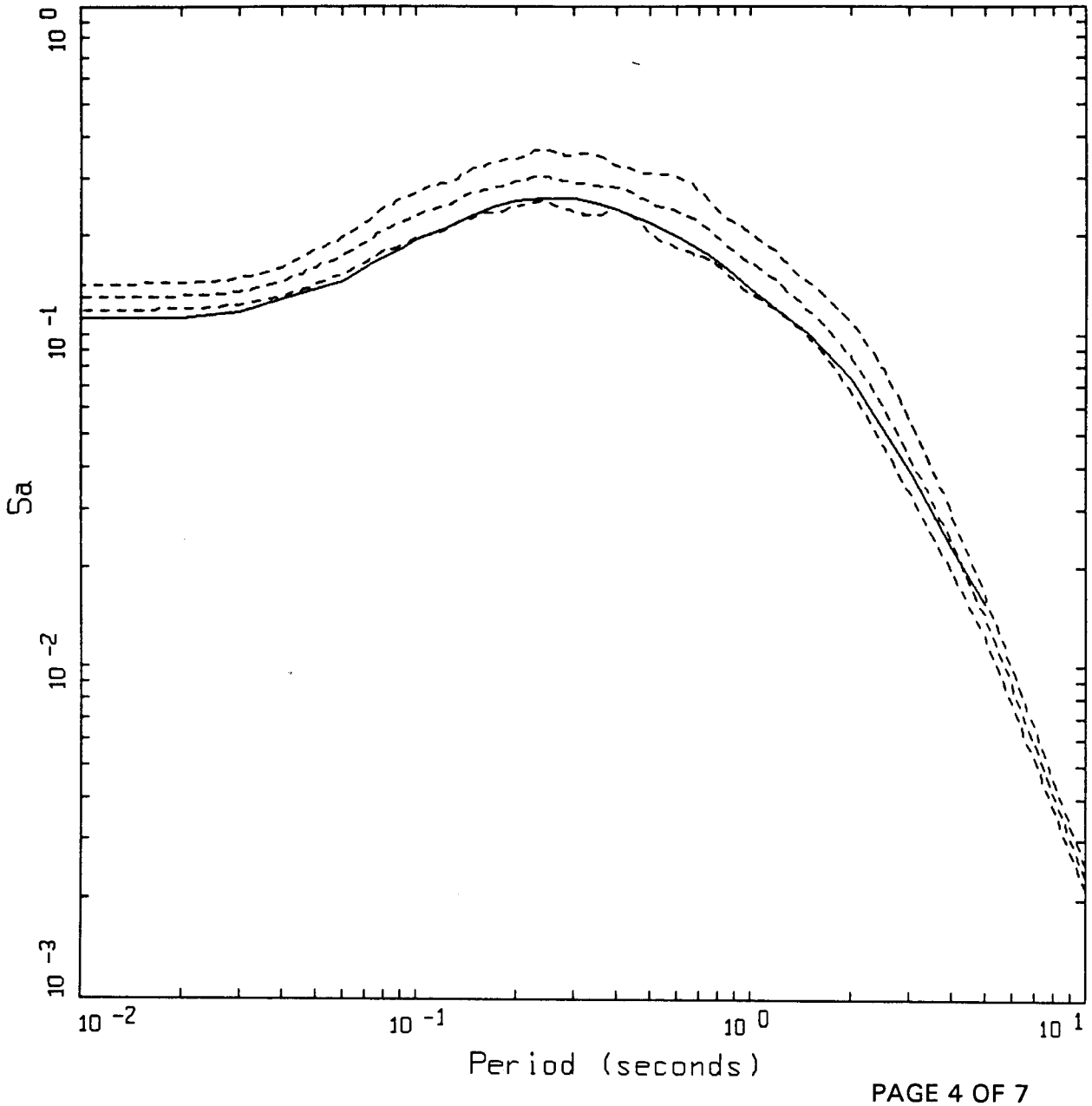

AVERAGE HORIZONTAL SPECTRA
M=6.5, D=30 KM, SOIL, STRESS DROP = 59 BARS

LEGEND

———— EMPIRICAL

- - - - - 84TH PERCENTILE

- - - - - 50TH PERCENTILE

- - - - - 16TH PERCENTILE

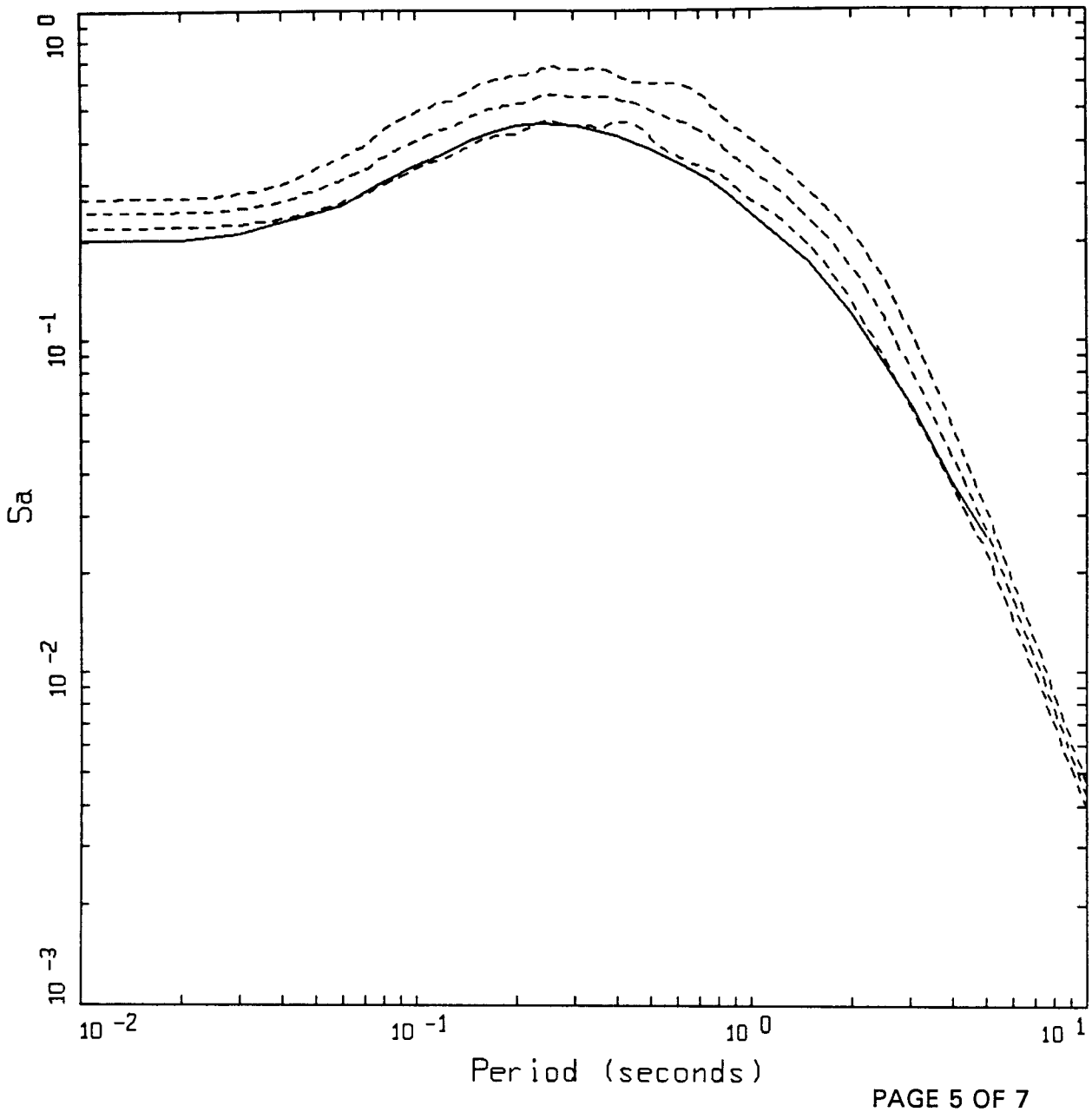

AVERAGE HORIZONTAL SPECTRA
M=6.5, D=15 KM, SOIL, STRESS DROP = 59 BARS

LEGEND
EMPIRICAL
84TH PERCENTILE
50TH PERCENTILE
16TH PERCENTILE

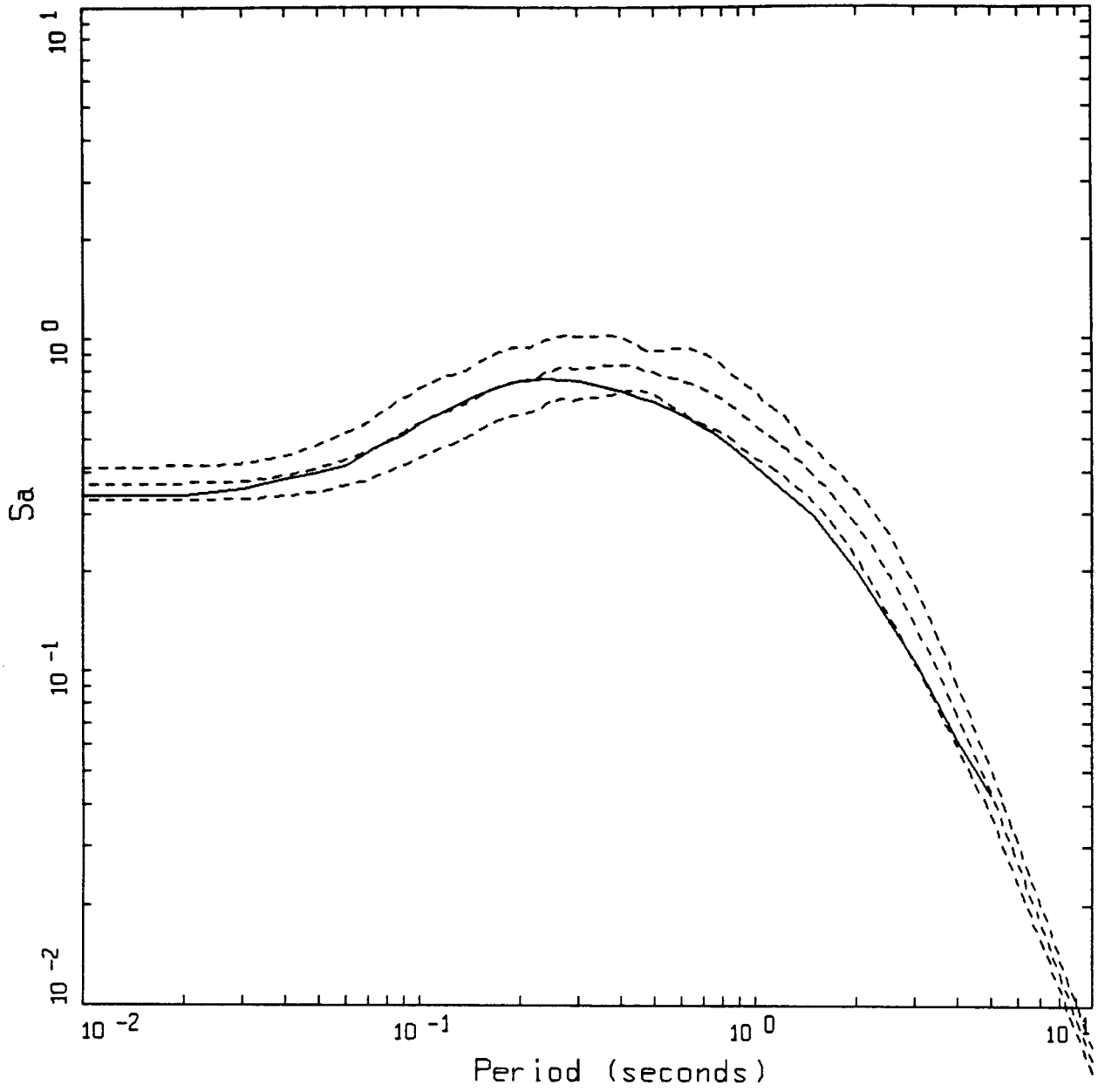

AVERAGE HORIZONTAL SPECTRA
M=6.5, D=07 KM, SOIL, STRESS DROP = 59 BARS

LEGEND
EMPIRICAL
84TH PERCENTILE
50TH PERCENTILE
16TH PERCENTILE

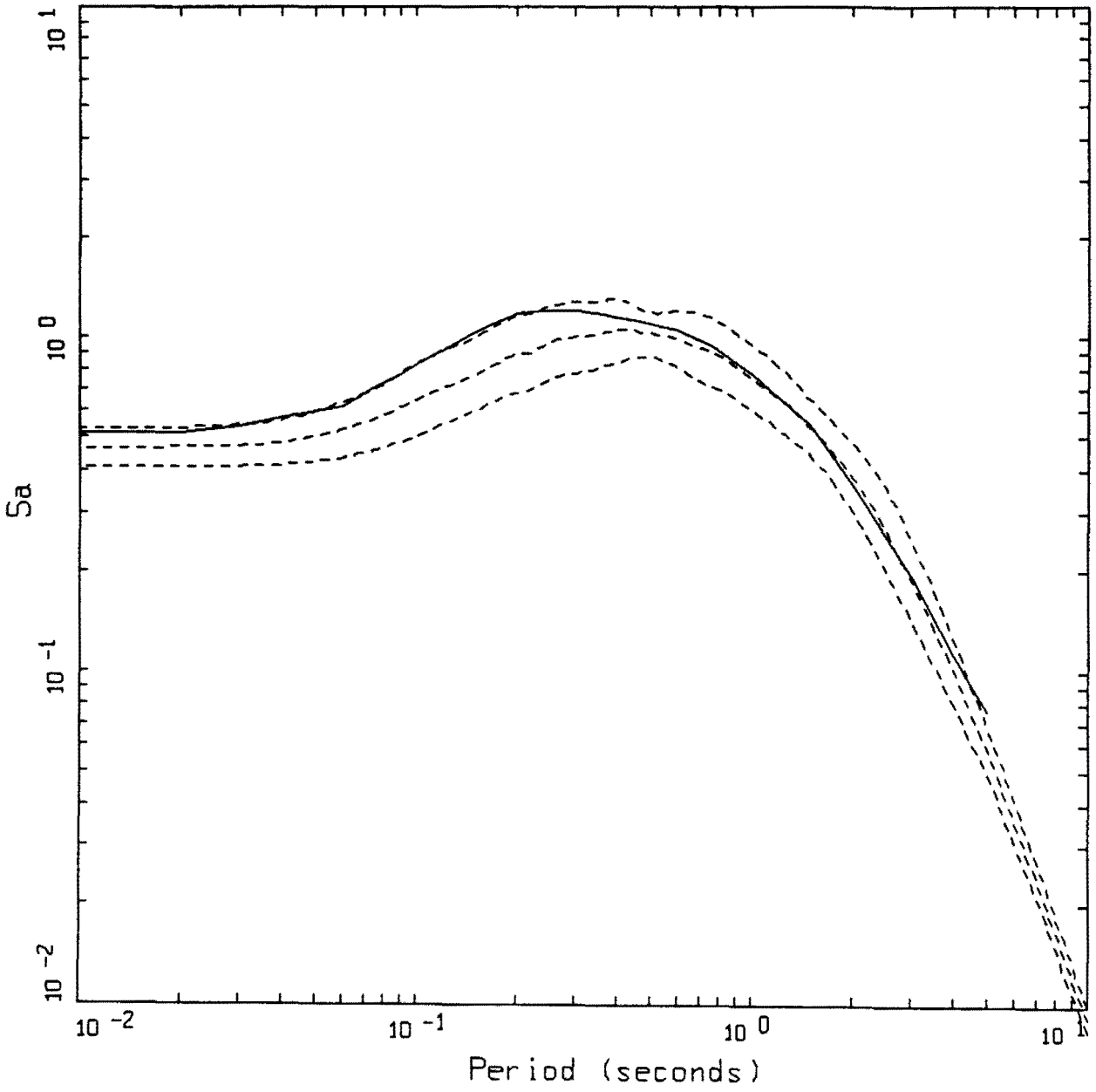

AVERAGE HORIZONTAL SPECTRA
M=6.5, D=0 KM, SOIL, STRESS DROP = 59 BARS

LEGEND

——— EMPIRICAL

- - - - - 84TH PERCENTILE

- - - - - 50TH PERCENTILE

- - - - - 16TH PERCENTILE

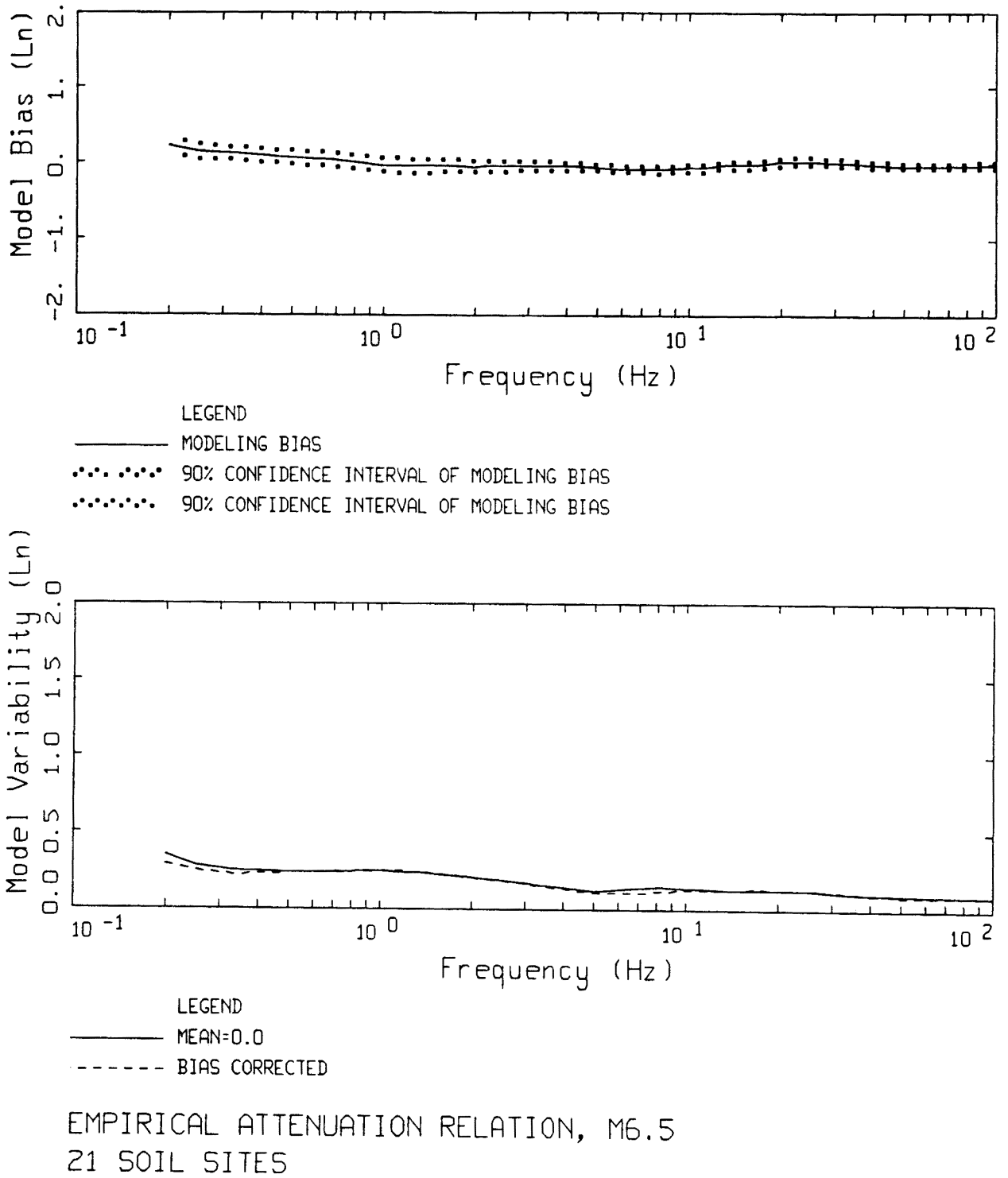

Figure 6.17. Model bias and variability estimates for the empirical attenuation relation (Appendix A) computed over 7 soil sites for the point-source model. Magnitude is M 6.5 and distances are 0, 7, 15, 30, 60, 100, and 200 km.

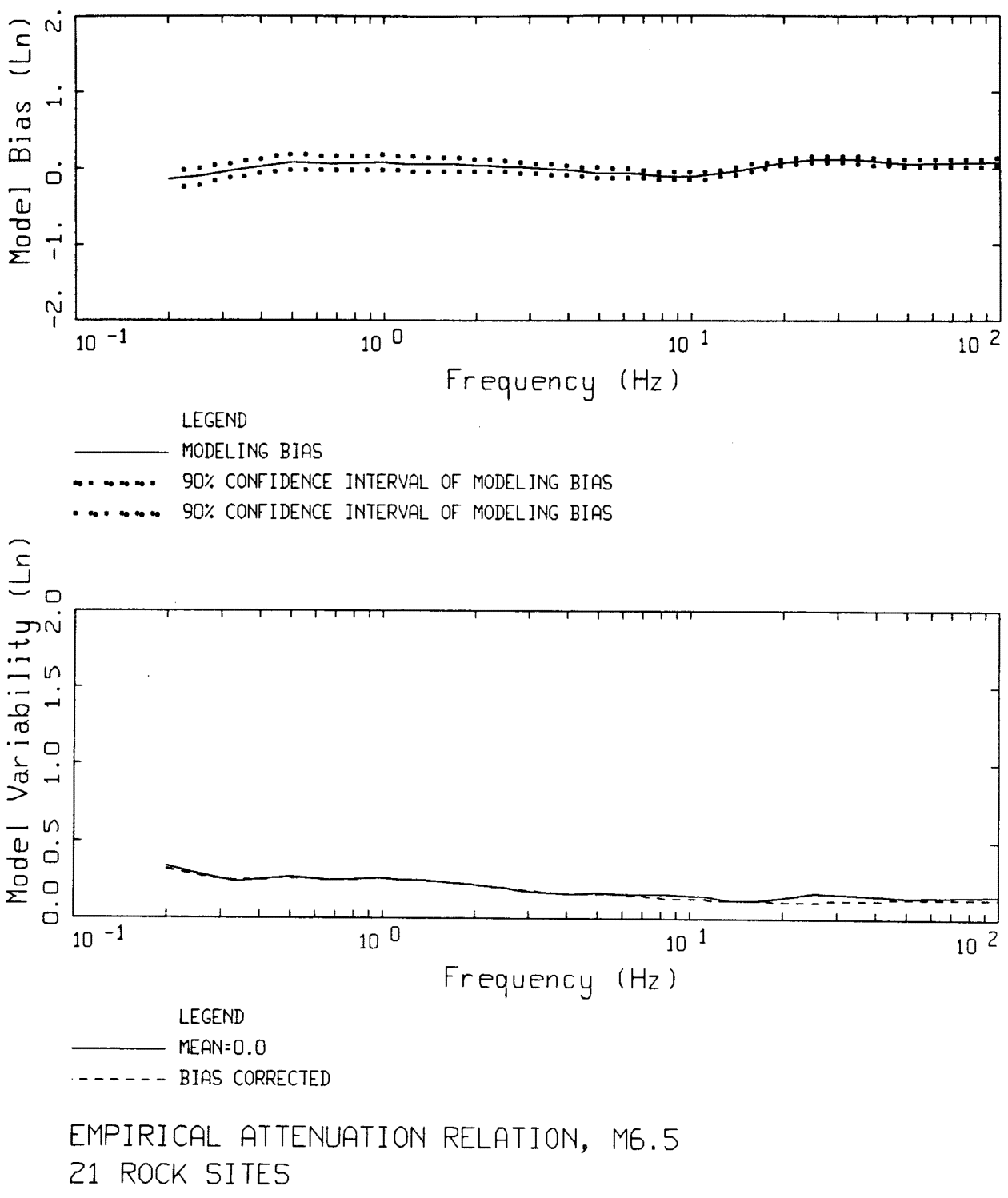

Figure 6.18. Model bias and variability estimates for the empirical attenuation relation (Appendix A) computed over 7 rock sites for the point-source model. Magnitude is M 6.5 and distances are 0, 7, 15, 30, 60, 100, and 200 km.

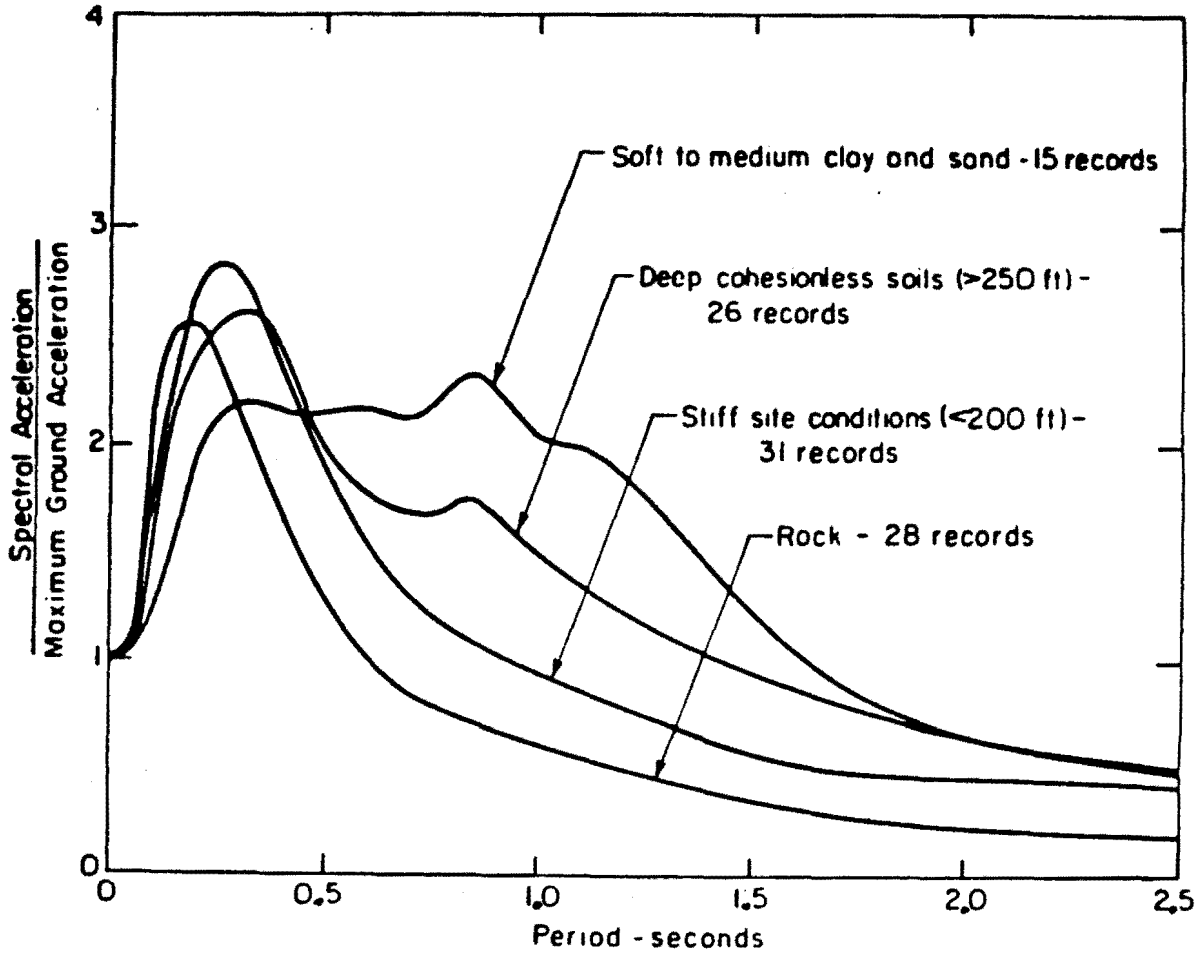

Figure 7.1. Average 5% damping response spectral shapes (Sa/a) computed from motions recorded on different soil conditions (after Seed, et al., 1976).

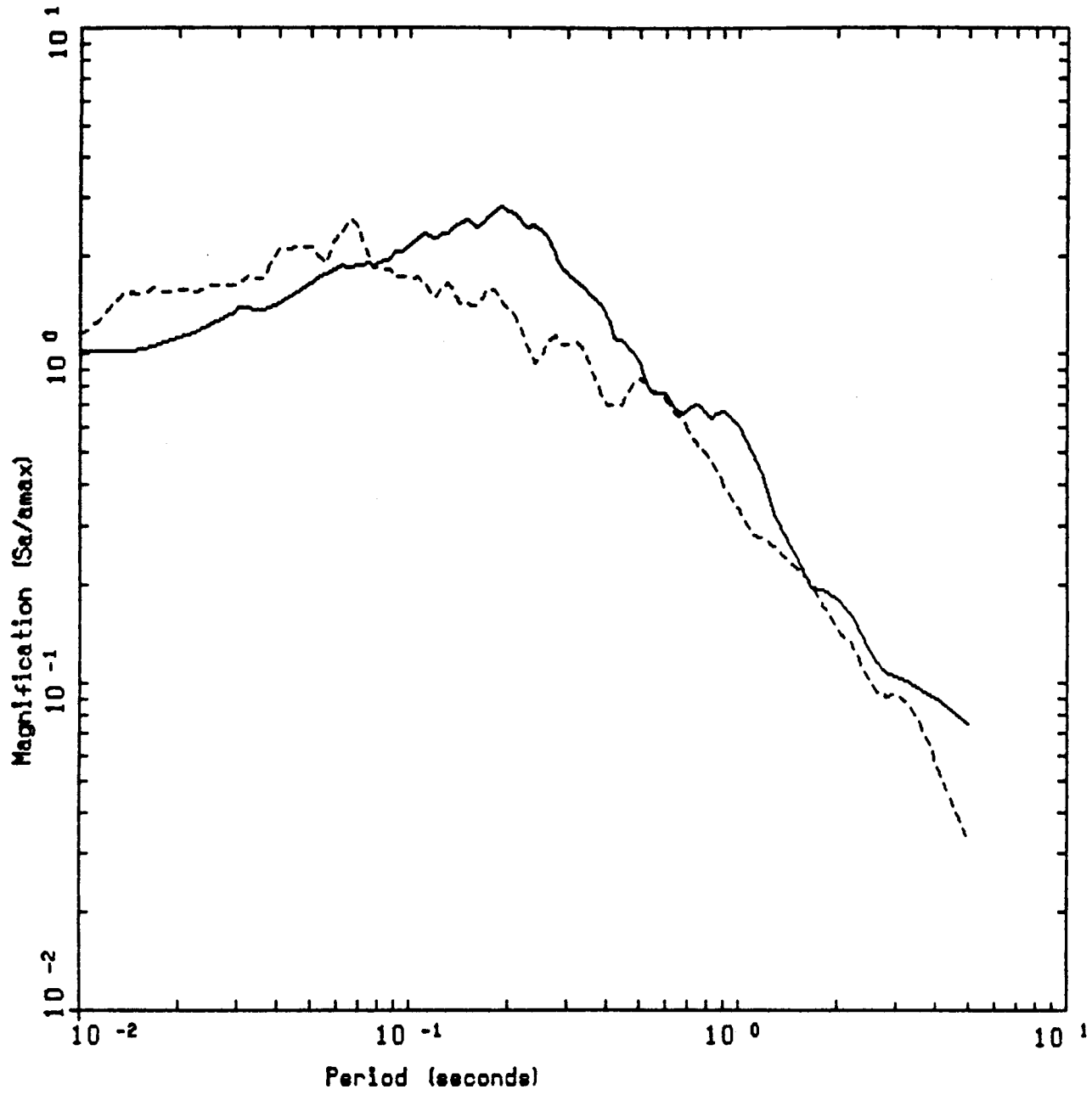

LEGEND

——— 5 %, WNA ROCK: AVERAGE OF 12 HORIZONTAL COMPONENTS

----- 5 %, ENA ROCK: AVERAGE OF 6 HORIZONTAL COMPONENTS

Figure 7.2. Comparison of average 5% response spectral shapes (Sa/a_{max} computed from strong motion data recorded at rock sites in ENA (dashed line) and WNA (solid line). ENA average shape is from recordings of the m_b = 6.4 Nahanni earthquake. The WNA average shape is from recordings of the San Fernando M_L = 6.4 and Imperial Valley M_L = 6.6 earthquakes.

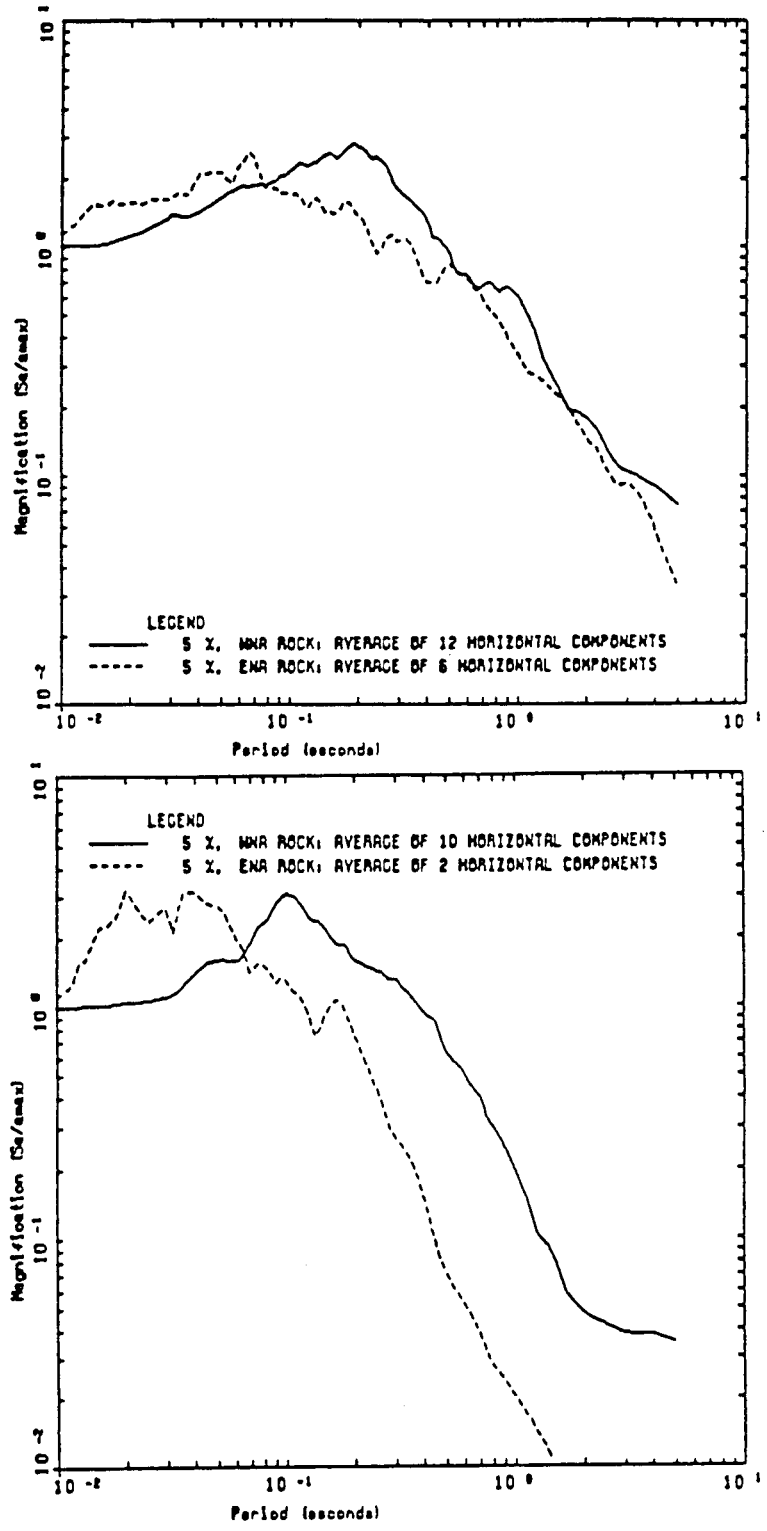

Figure 7.3. Average 5% damping response spectral shapes (Sa/a) computed from motions recorded on rock sites at close distances to **M** = 6.4 earthquakes (top figure) and **M** = 4.0 earthquakes (bottom figure). In each figure the solid line corresponds to motions recorded in WNA, dashed line to motions recorded in ENA.

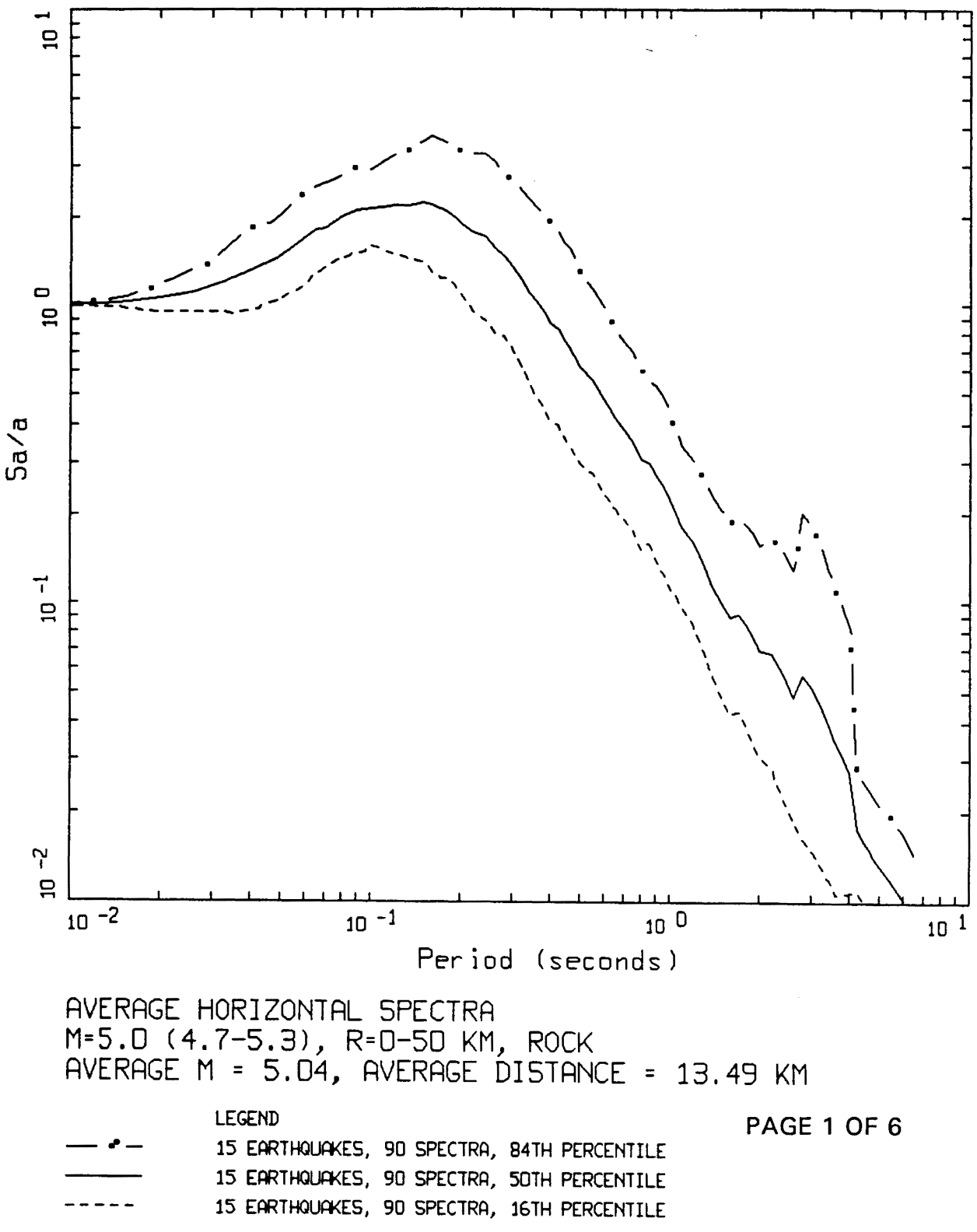

Figure Set 7.4. Statistical 5% damping response spectral shapes computed for the magnitude bins listed in Table 7.1. Distances are within 50 km and the data are from the Strong Motion Database listed in Appendix B. Soft rock site conditions.

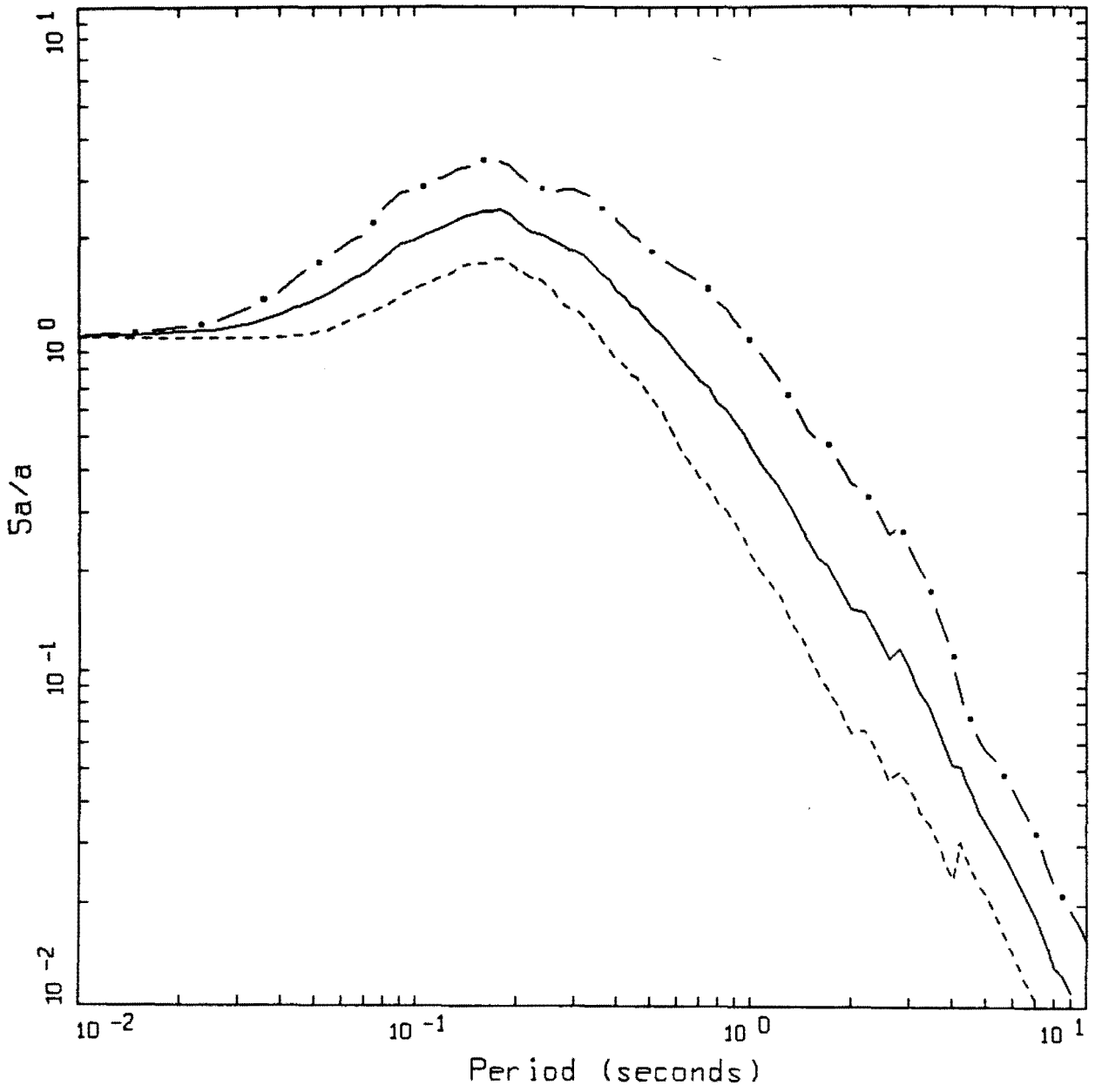

AVERAGE HORIZONTAL SPECTRA
M=5.5 (5.2-5.8), R=0-50 KM, ROCK
AVERAGE M = 5.49, AVERAGE DISTANCE = 16.89 KM

LEGEND

— • — 18 EARTHQUAKES, 108 SPECTRA, 84TH PERCENTILE

——— 18 EARTHQUAKES, 108 SPECTRA, 50TH PERCENTILE

- - - - - 18 EARTHQUAKES, 108 SPECTRA, 16TH PERCENTILE

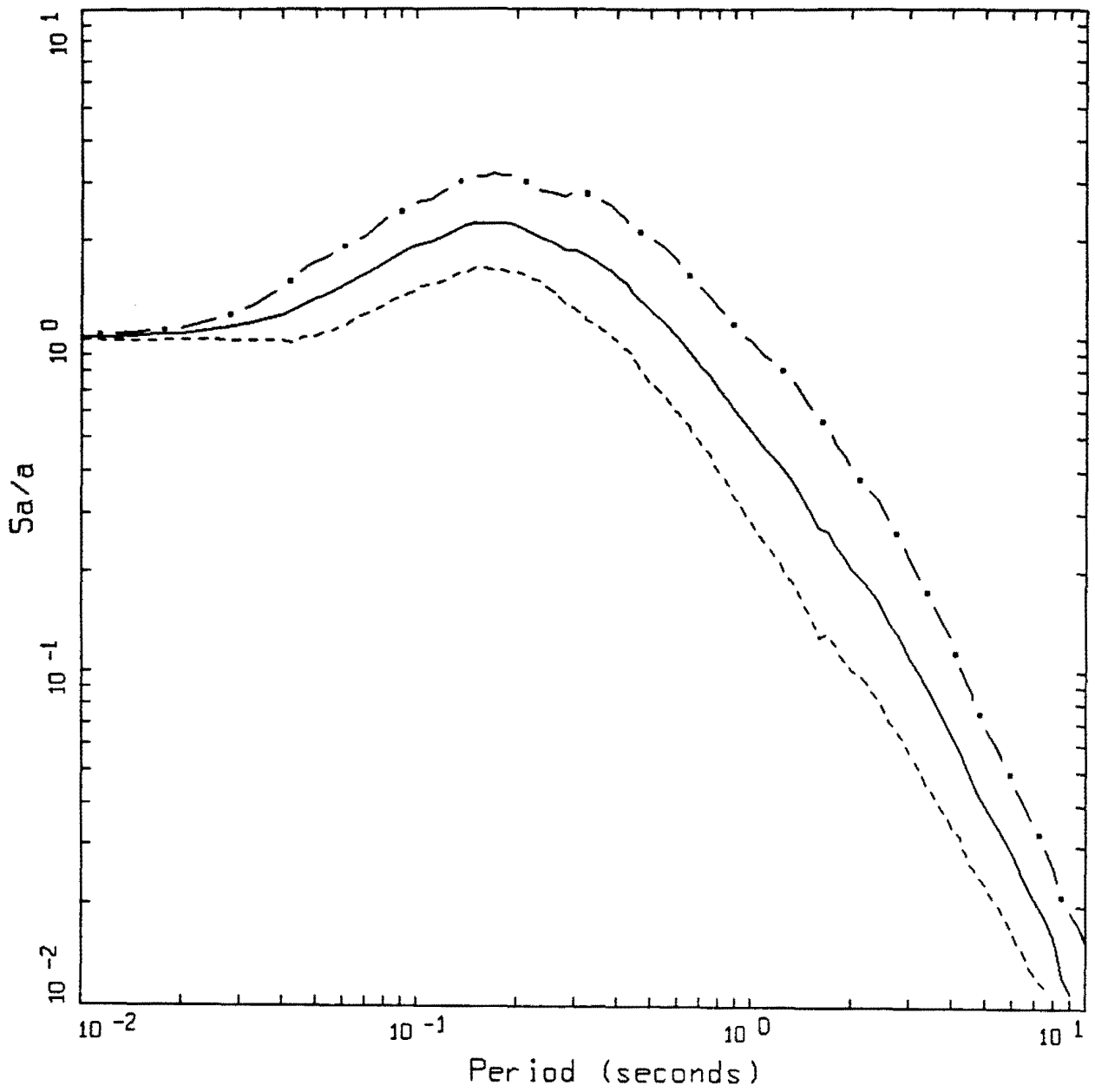

AVERAGE HORIZONTAL SPECTRA
M=6.0 (5.7-6.3), R=0-50 KM, ROCK
AVERAGE M = 5.98, AVERAGE DISTANCE = 22.10 KM

LEGEND

— • — 21 EARTHQUAKES, 146 SPECTRA, 84TH PERCENTILE
——— 21 EARTHQUAKES, 146 SPECTRA, 50TH PERCENTILE
- - - - - 21 EARTHQUAKES, 146 SPECTRA, 16TH PERCENTILE

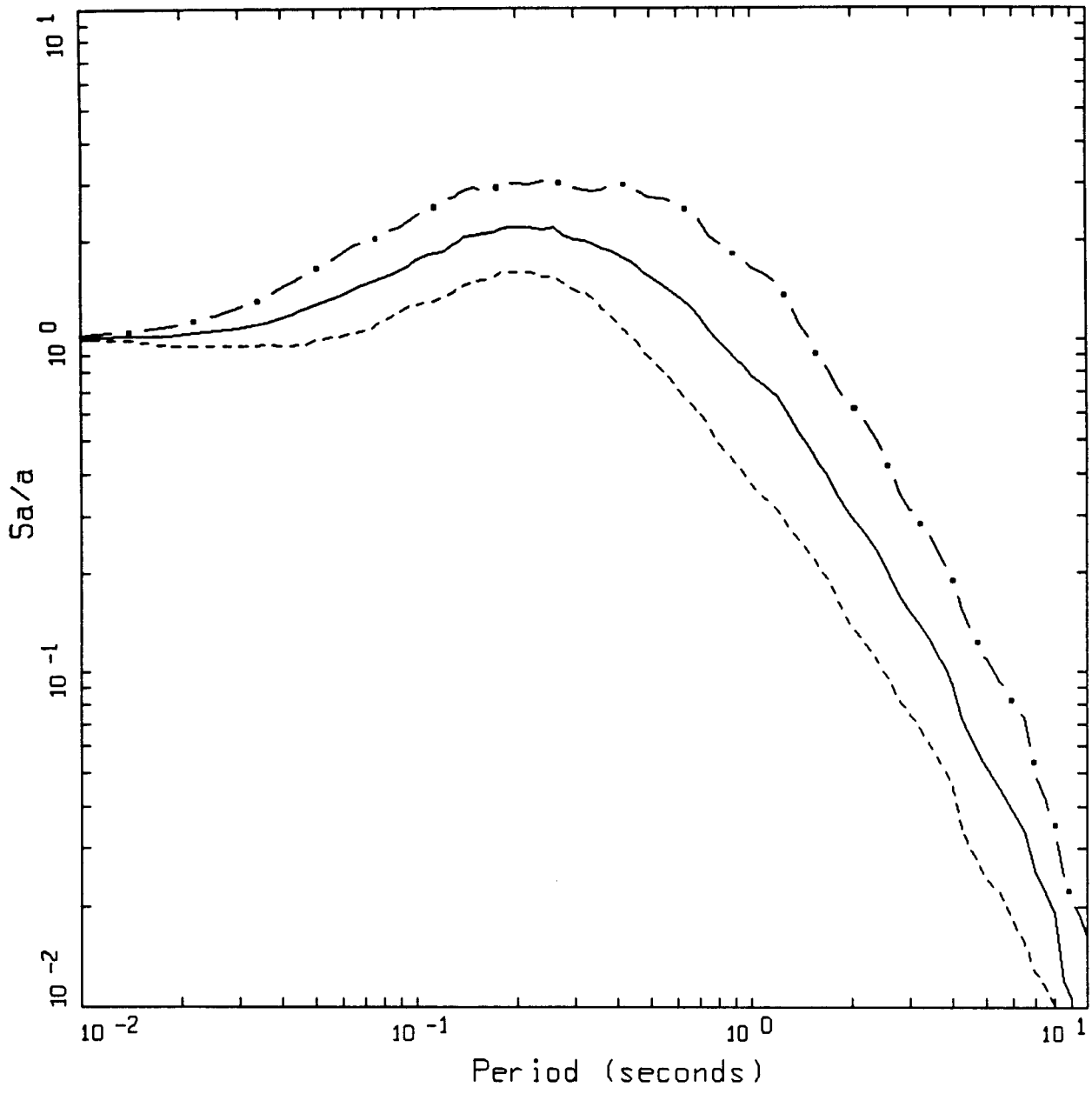

AVERAGE HORIZONTAL SPECTRA
M=6.5 (6.2-6.8), R=0-50 KM, ROCK
AVERAGE M = 6.51, AVERAGE DISTANCE = 27.07 KM

LEGEND

— • — 12 EARTHQUAKES, 148 SPECTRA, 84TH PERCENTILE
——— 12 EARTHQUAKES, 148 SPECTRA, 50TH PERCENTILE
- - - - - 12 EARTHQUAKES, 148 SPECTRA, 16TH PERCENTILE

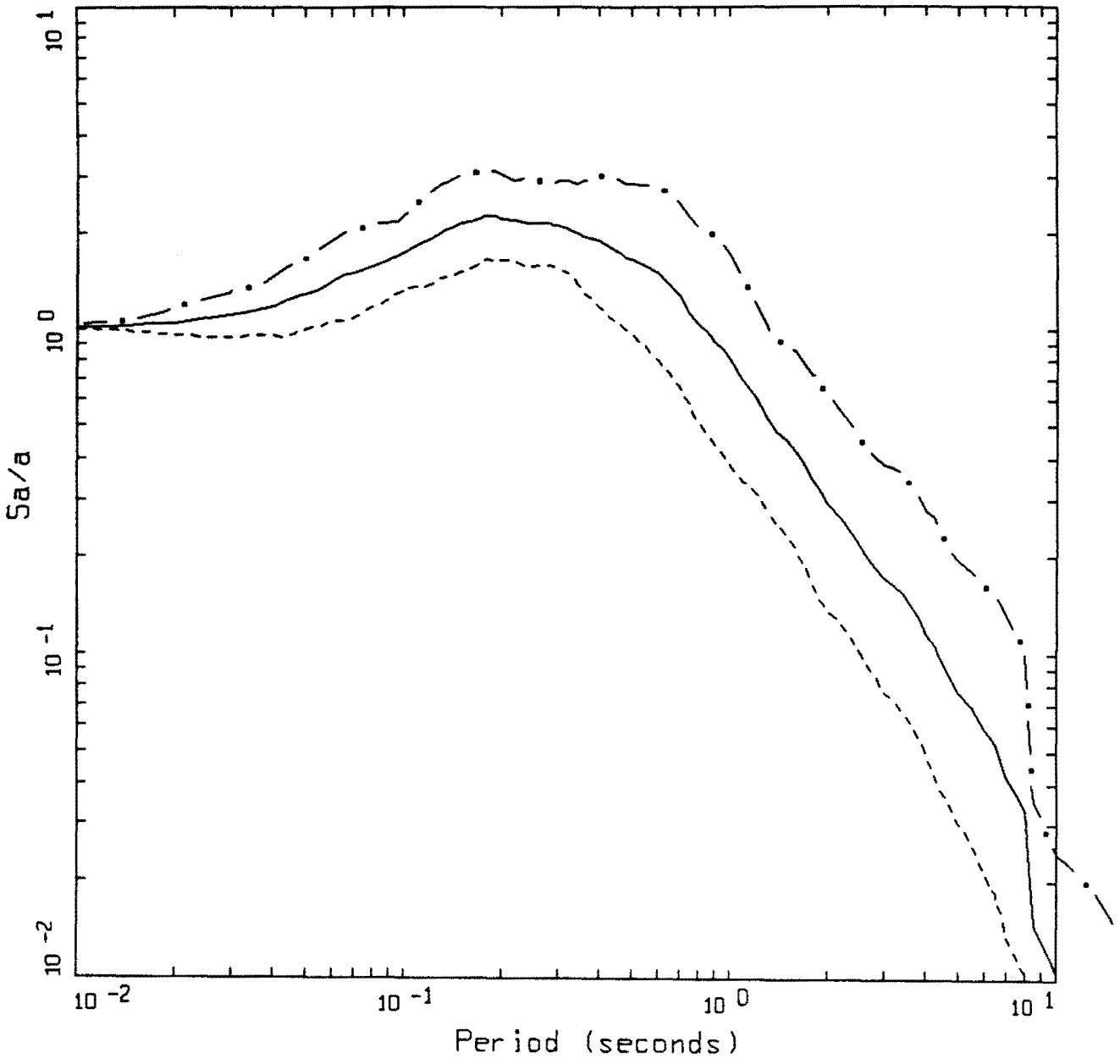

AVERAGE HORIZONTAL SPECTRA
M=7.0 (6.7-7.3), R=0-50 KM, ROCK
AVERAGE M = 6.83, AVERAGE DISTANCE = 26.40 KM

LEGEND

— • — 7 EARTHQUAKES, 104 SPECTRA, 84TH PERCENTILE
——— 7 EARTHQUAKES, 104 SPECTRA, 50TH PERCENTILE
- - - - - 7 EARTHQUAKES, 104 SPECTRA, 16TH PERCENTILE

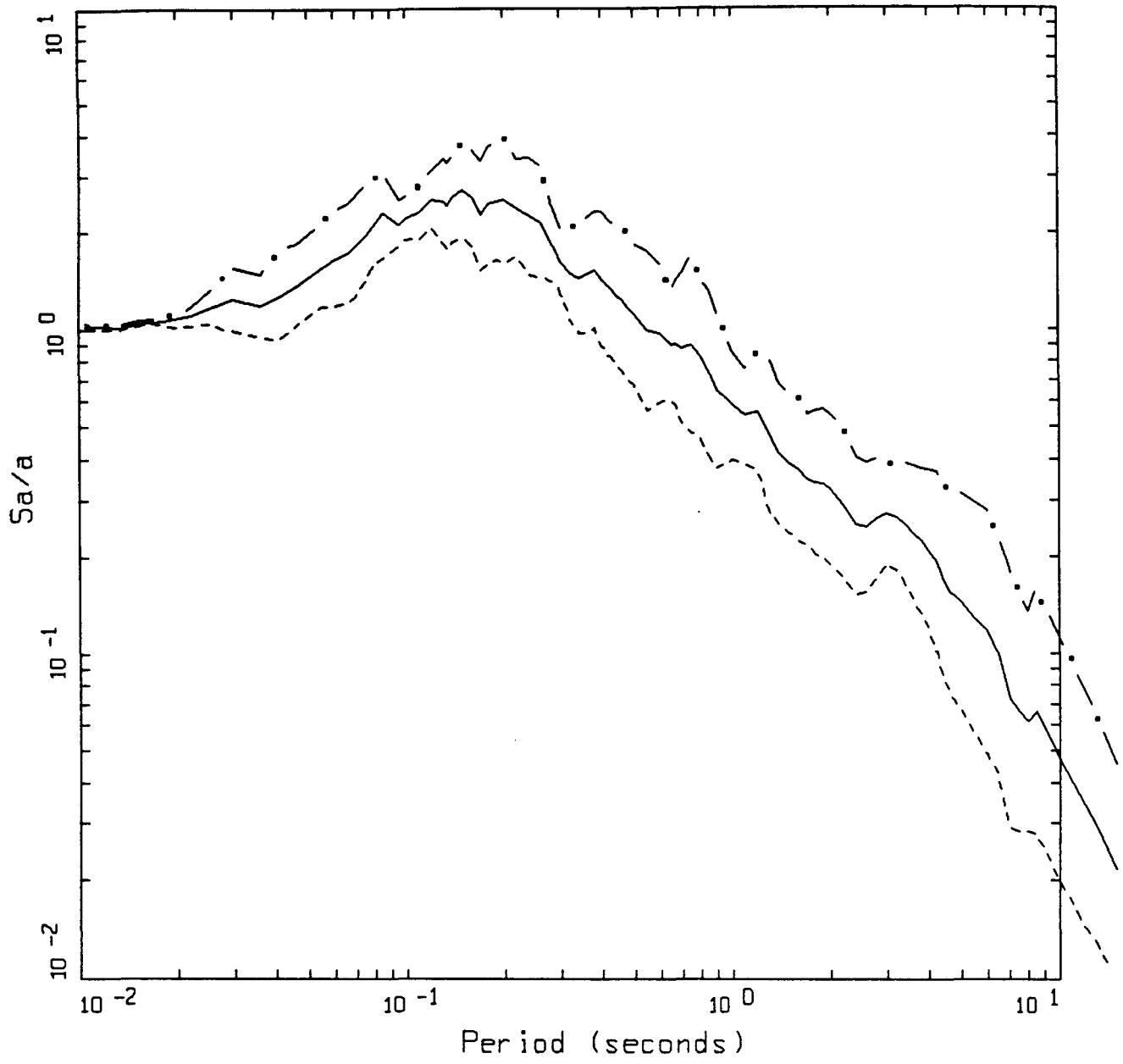

AVERAGE HORIZONTAL SPECTRA
M=7.5 (7.2-9.0), R=0-50 KM, ROCK
AVERAGE M = 7.35, AVERAGE DISTANCE = 15.83 KM

LEGEND

— • — 2 EARTHQUAKES, 8 SPECTRA, 84TH PERCENTILE
——— 2 EARTHQUAKES, 8 SPECTRA, 50TH PERCENTILE
- - - - - 2 EARTHQUAKES, 8 SPECTRA, 16TH PERCENTILE

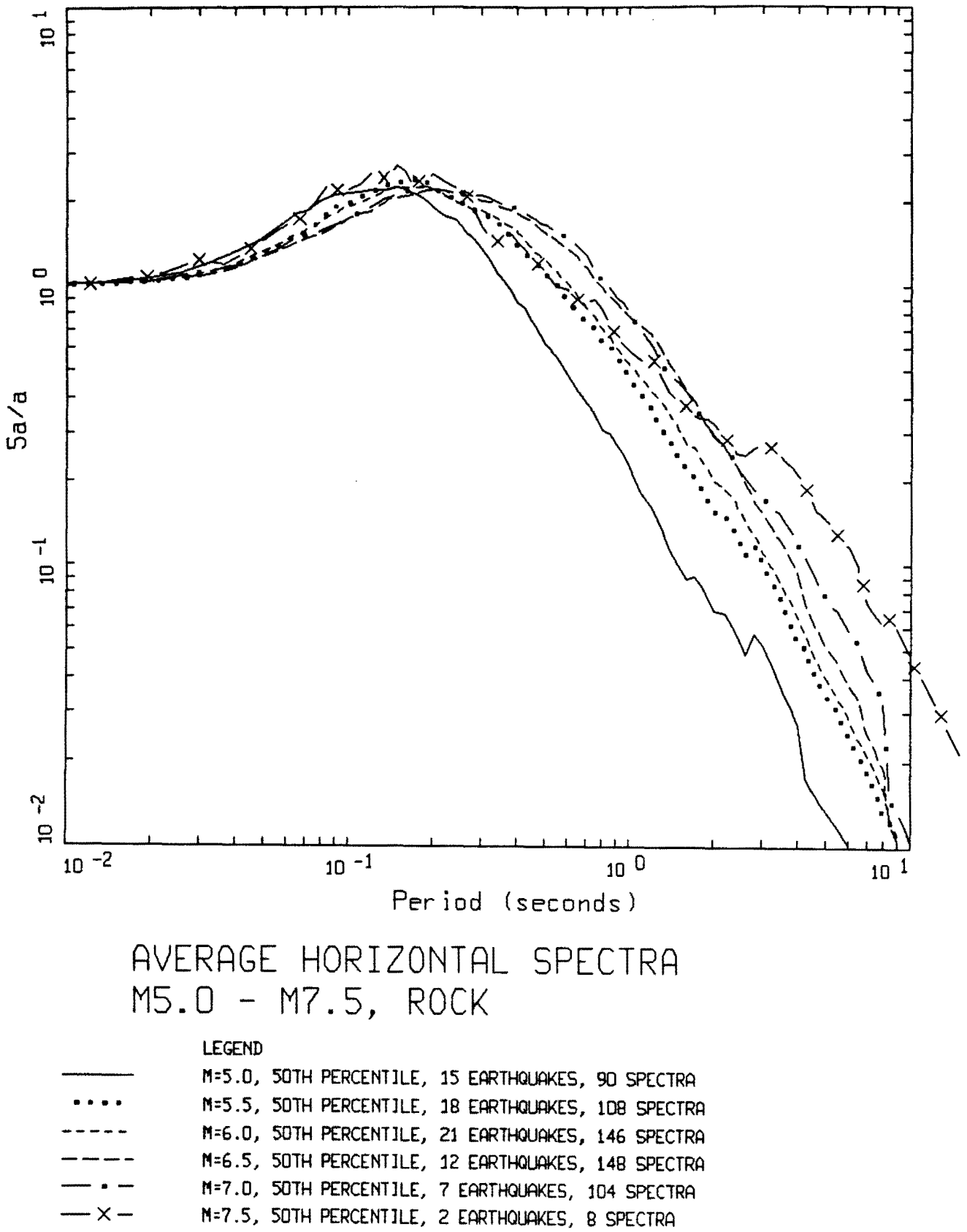

Figure 7.5. Summary plot of median statistical response spectral shapes. Soft rock site conditions.

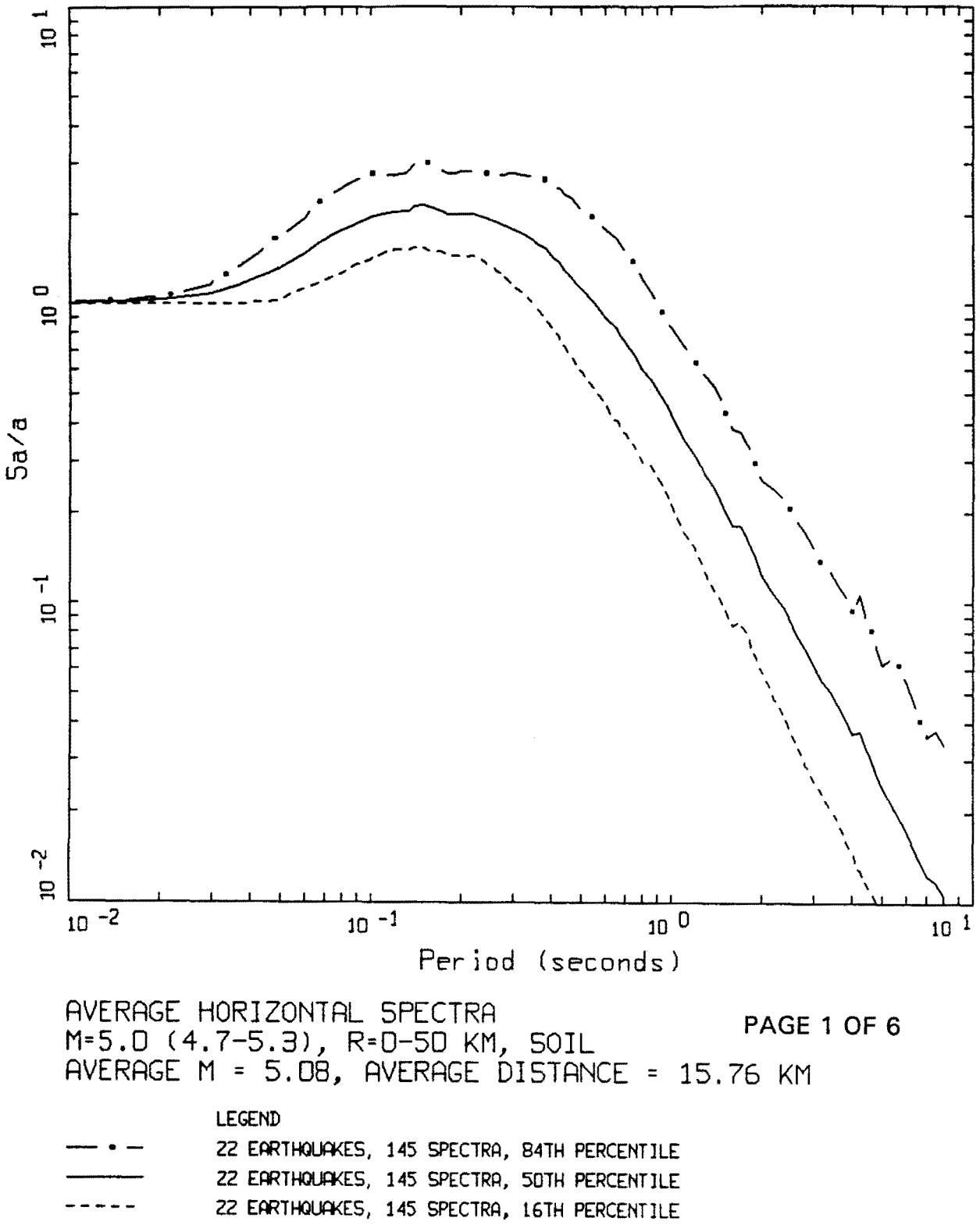

Figure Set 7.6. Statistical 5% damping response spectral shapes computed for the magnitude bins listed in Table 7.1. Distances are within 50 km and the data are from the Strong Motion Database listed in Appendix B. Deep soil site conditions.

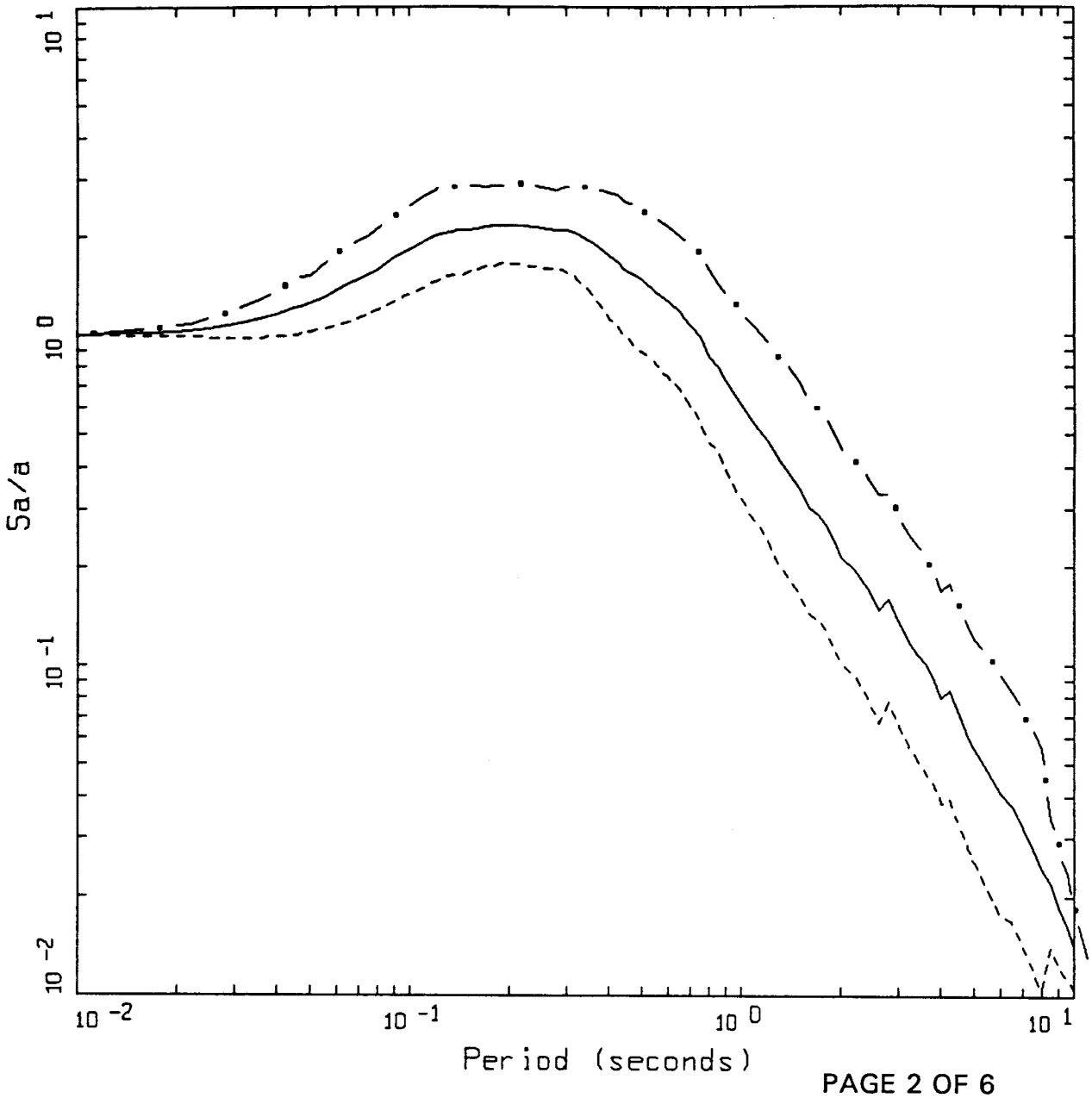

AVERAGE HORIZONTAL SPECTRA
M=5.5 (5.2-5.8), R=0-50 KM, SOIL
AVERAGE M = 5.45, AVERAGE DISTANCE = 18.29 KM

LEGEND

— • — 35 EARTHQUAKES, 159 SPECTRA, 84TH PERCENTILE

——— 35 EARTHQUAKES, 159 SPECTRA, 50TH PERCENTILE

- - - - - 35 EARTHQUAKES, 159 SPECTRA, 16TH PERCENTILE

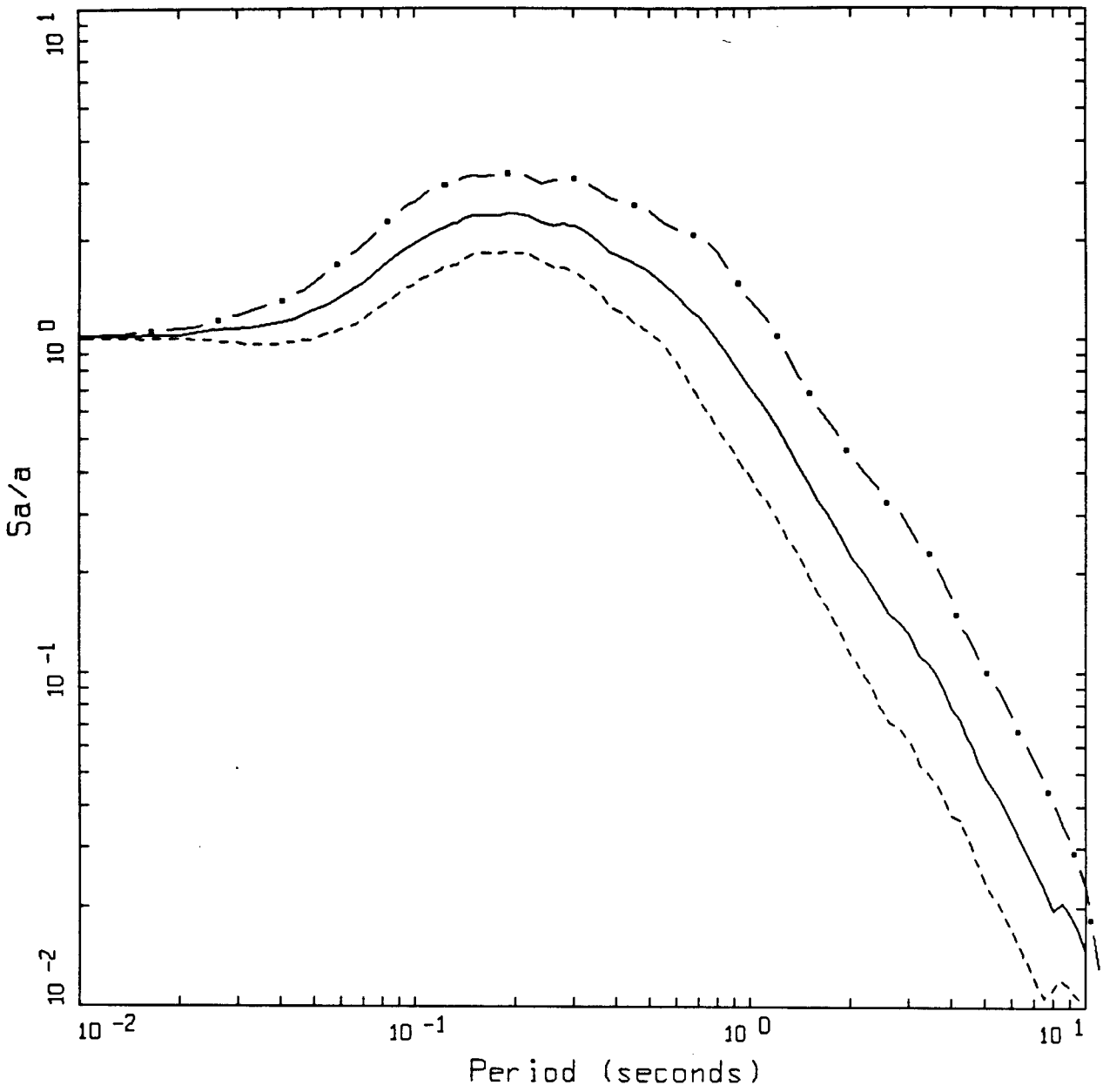

AVERAGE HORIZONTAL SPECTRA

M=6.0 (5.7-6.3), R=0-50 KM, SOIL
AVERAGE M = 6.02, AVERAGE DISTANCE = 23.20 KM

LEGEND

— • — 25 EARTHQUAKES, 337 SPECTRA, 84TH PERCENTILE
——— 25 EARTHQUAKES, 337 SPECTRA, 50TH PERCENTILE
- - - - - 25 EARTHQUAKES, 337 SPECTRA, 16TH PERCENTILE

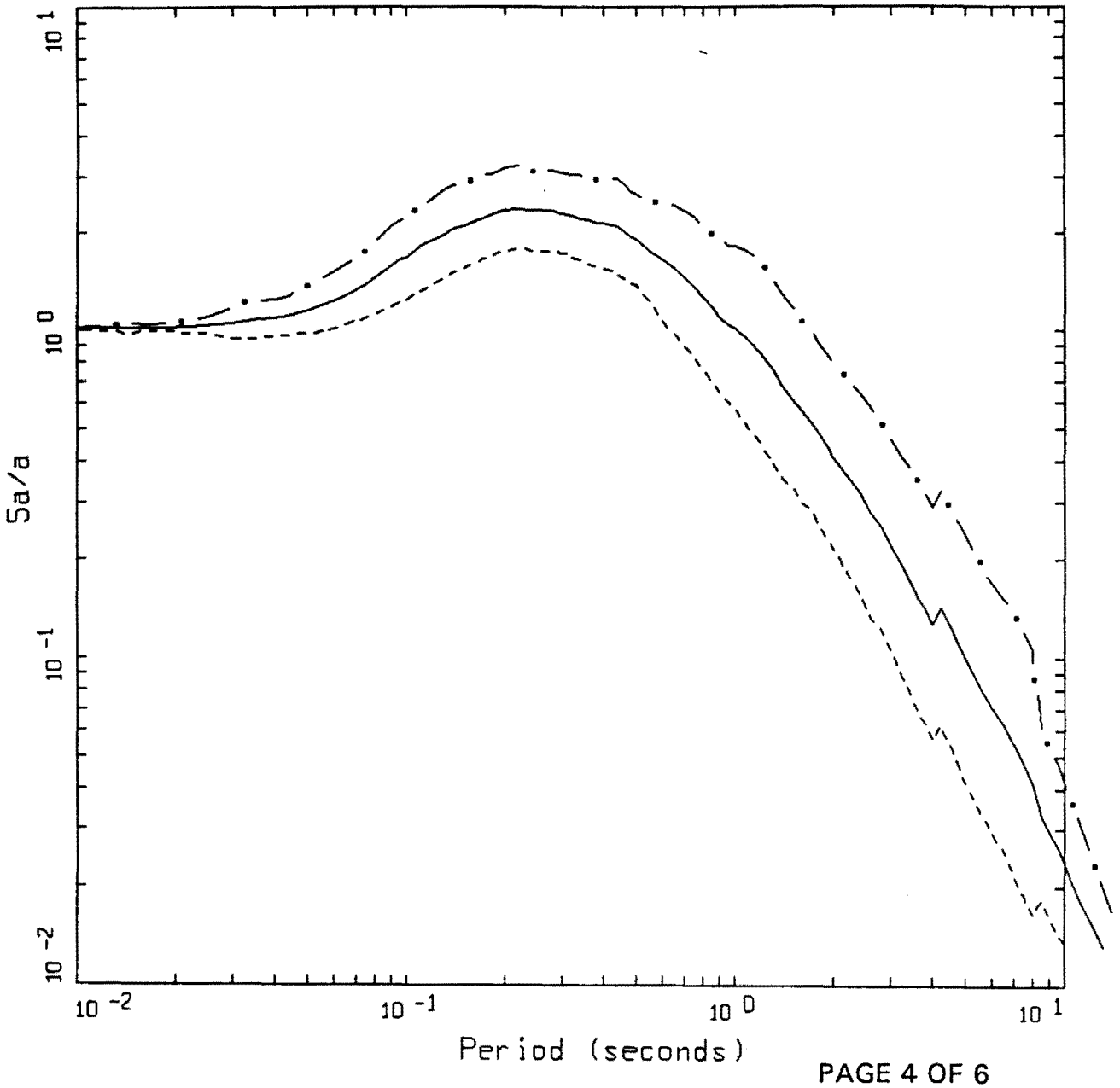

AVERAGE HORIZONTAL SPECTRA
M=6.5 (6.2-6.8), R=0-50 KM, SOIL
AVERAGE M = 6.50, AVERAGE DISTANCE = 27.27 KM

LEGEND

— • — 17 EARTHQUAKES, 342 SPECTRA, 84TH PERCENTILE

——— 17 EARTHQUAKES, 342 SPECTRA, 50TH PERCENTILE

- - - - - 17 EARTHQUAKES, 342 SPECTRA, 16TH PERCENTILE

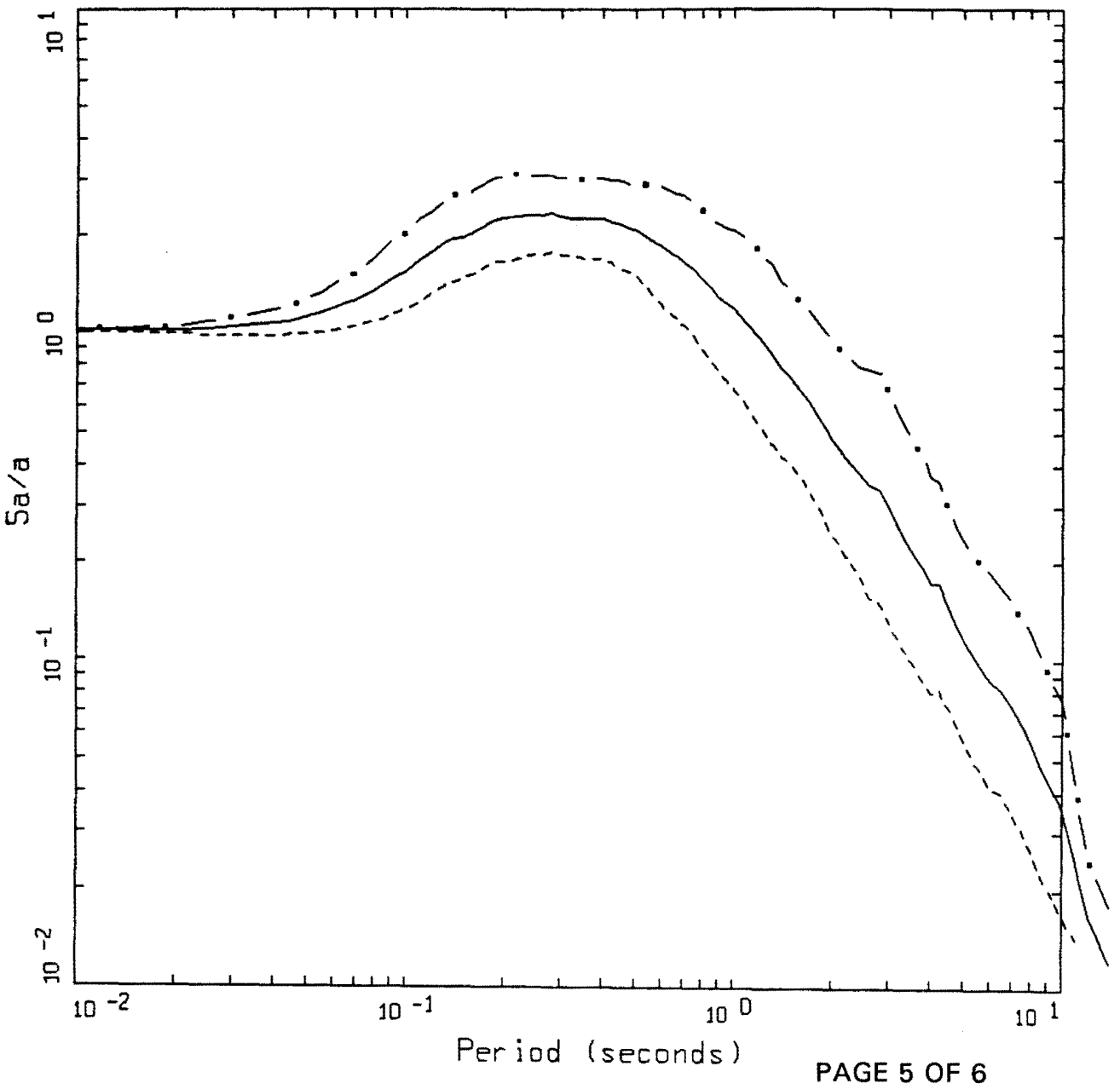

AVERAGE HORIZONTAL SPECTRA
M=7.0 (6.7-7.3), R=0-50 KM, SOIL
AVERAGE M = 6.88, AVERAGE DISTANCE = 28.29 KM

LEGEND

— • — 8 EARTHQUAKES, 219 SPECTRA, 84TH PERCENTILE

——— 8 EARTHQUAKES, 219 SPECTRA, 50TH PERCENTILE

- - - - - 8 EARTHQUAKES, 219 SPECTRA, 16TH PERCENTILE

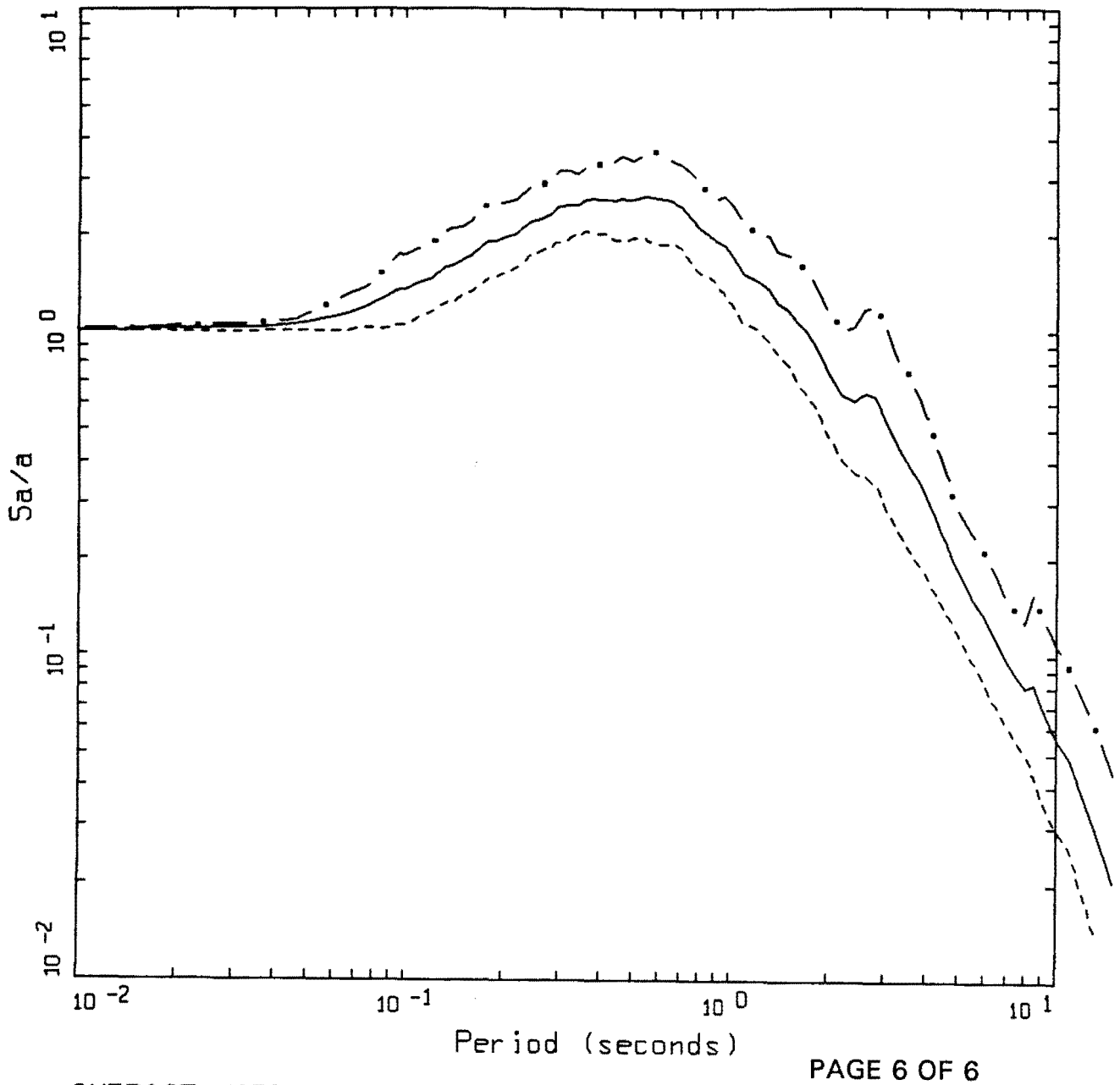

AVERAGE HORIZONTAL SPECTRA
M=7.5 (7.2-9.0), R=0-50 KM, SOIL
AVERAGE M = 7.31, AVERAGE DISTANCE = 34.00 KM

LEGEND

— • — 4 EARTHQUAKES, 50 SPECTRA, 84TH PERCENTILE

——— 4 EARTHQUAKES, 50 SPECTRA, 50TH PERCENTILE

- - - - - 4 EARTHQUAKES, 50 SPECTRA, 16TH PERCENTILE

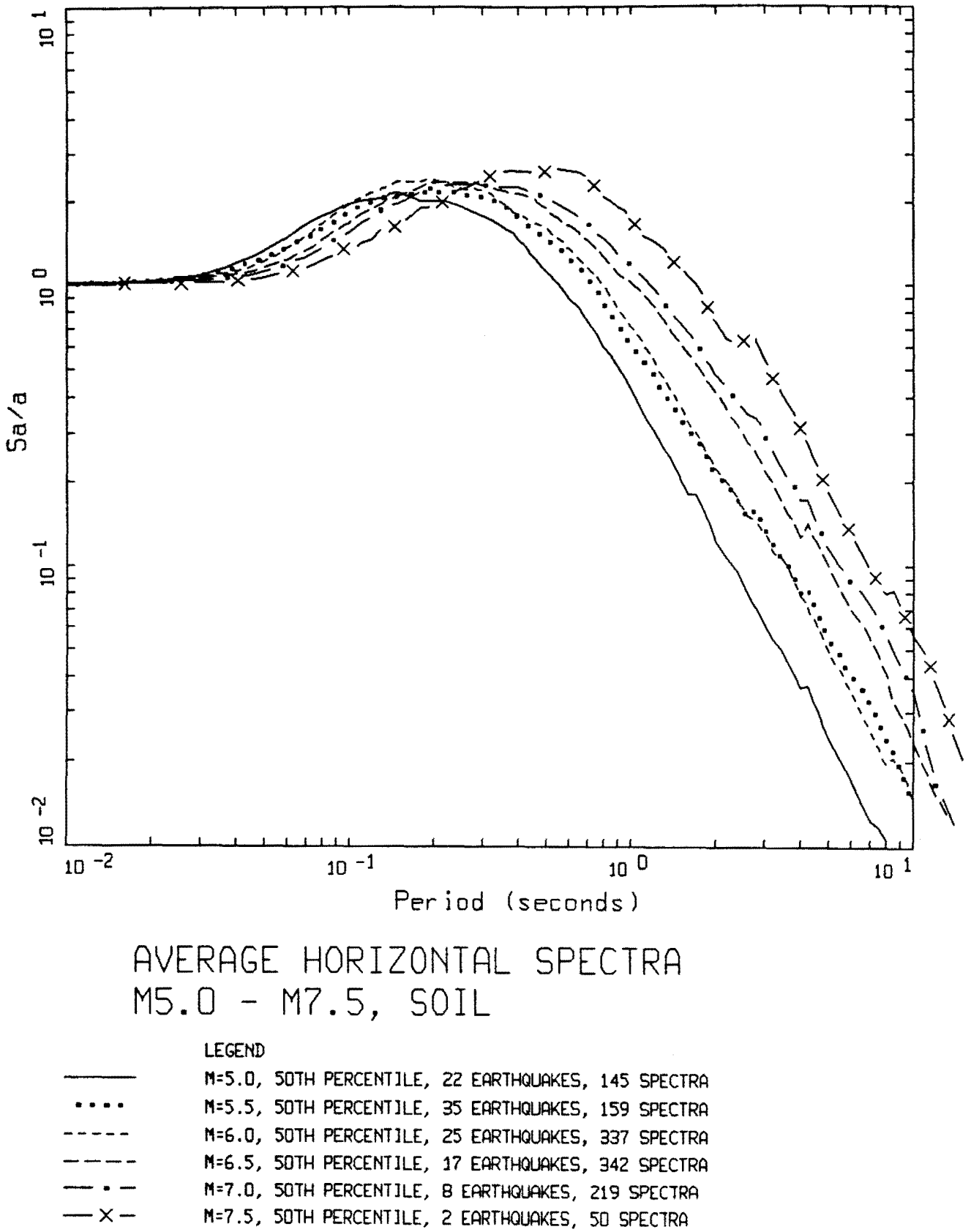

Figure 7.7. Summary plot of median statistical response spectral shapes. Deep soil site conditions.

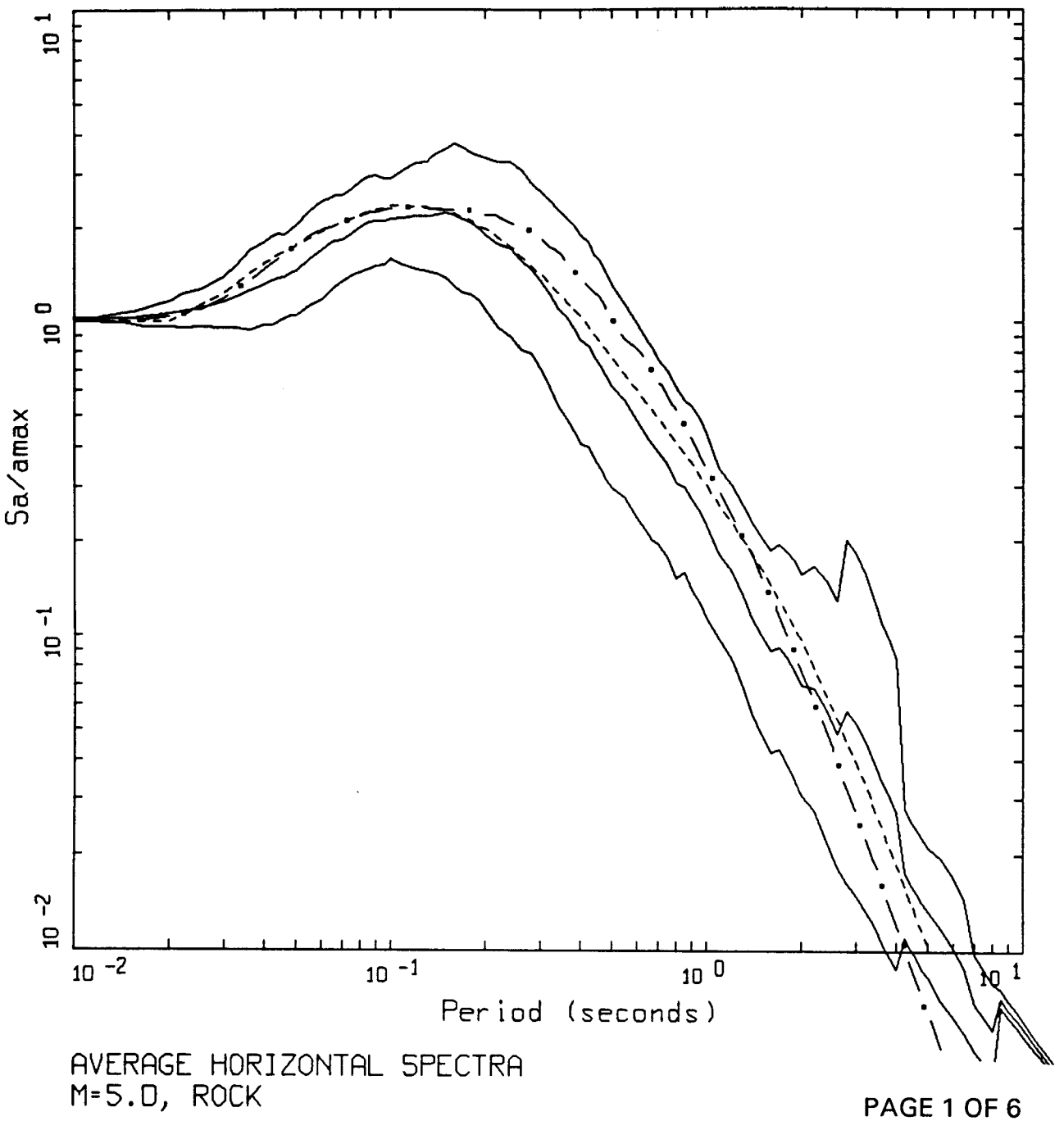

Figure Set 7.8. Comparison of statistical response spectral shapes with median point-source model predictions and the empirical attenuation relation (Appendix A) for a vertical strike-slip fault. Magnitudes and distances are listed in Table 7.1. The point-source stress drop is 59 bars (Table 6.1). Soft rock site conditions.

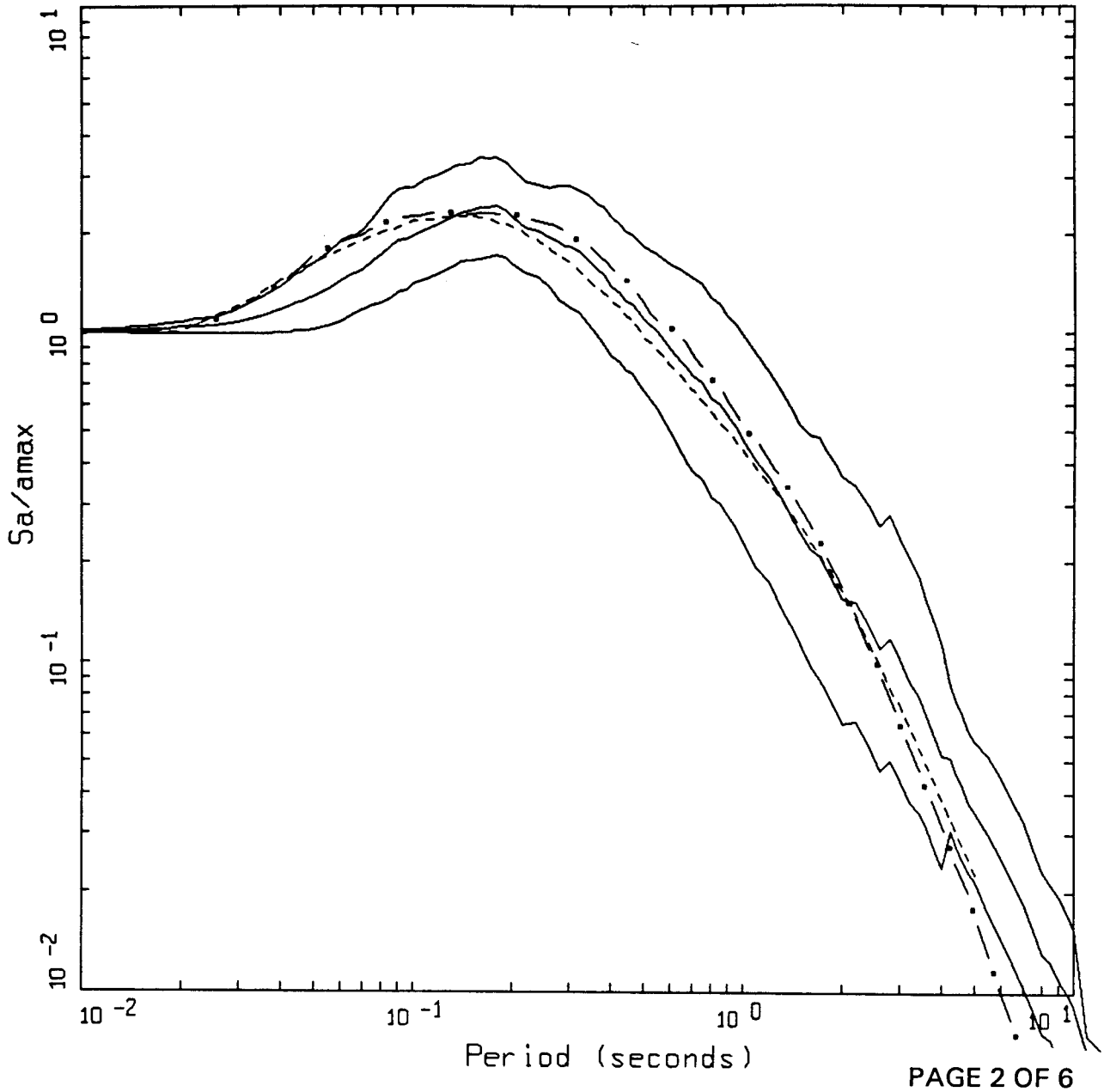

AVERAGE HORIZONTAL SPECTRA
M=5.5, ROCK

LEGEND

- 84TH PERCENTILE, DATA
- 50TH PERCENTILE, DATA
- 16TH PERCENTILE, DATA
- 50TH PERCENTILE, MODEL
- EMPIRICAL

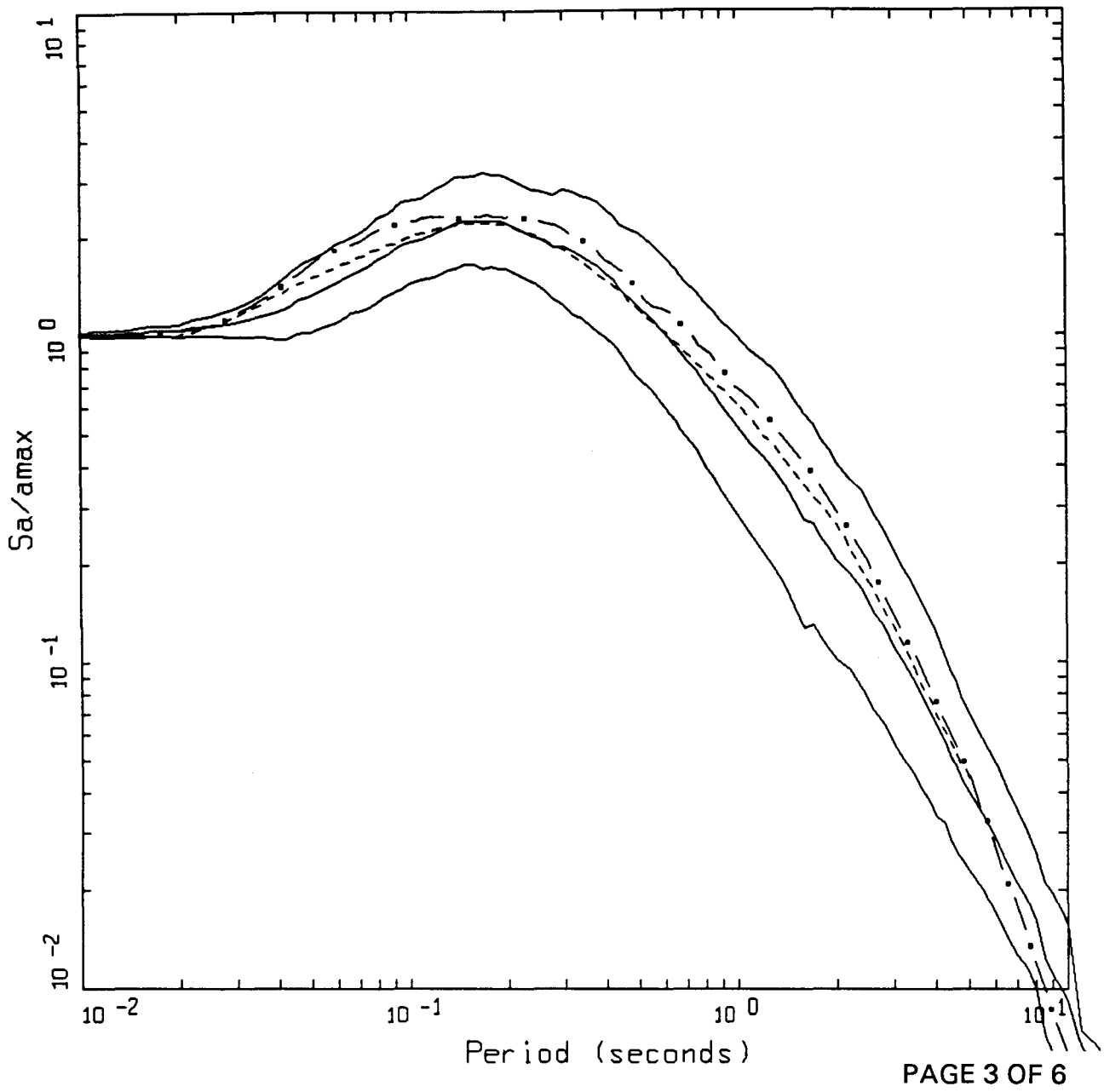

AVERAGE HORIZONTAL SPECTRA
M=6.0, ROCK

LEGEND

———— 84TH PERCENTILE, DATA
———— 50TH PERCENTILE, DATA
———— 16TH PERCENTILE, DATA
— • — 50TH PERCENTILE, MODEL
- - - - - EMPIRICAL

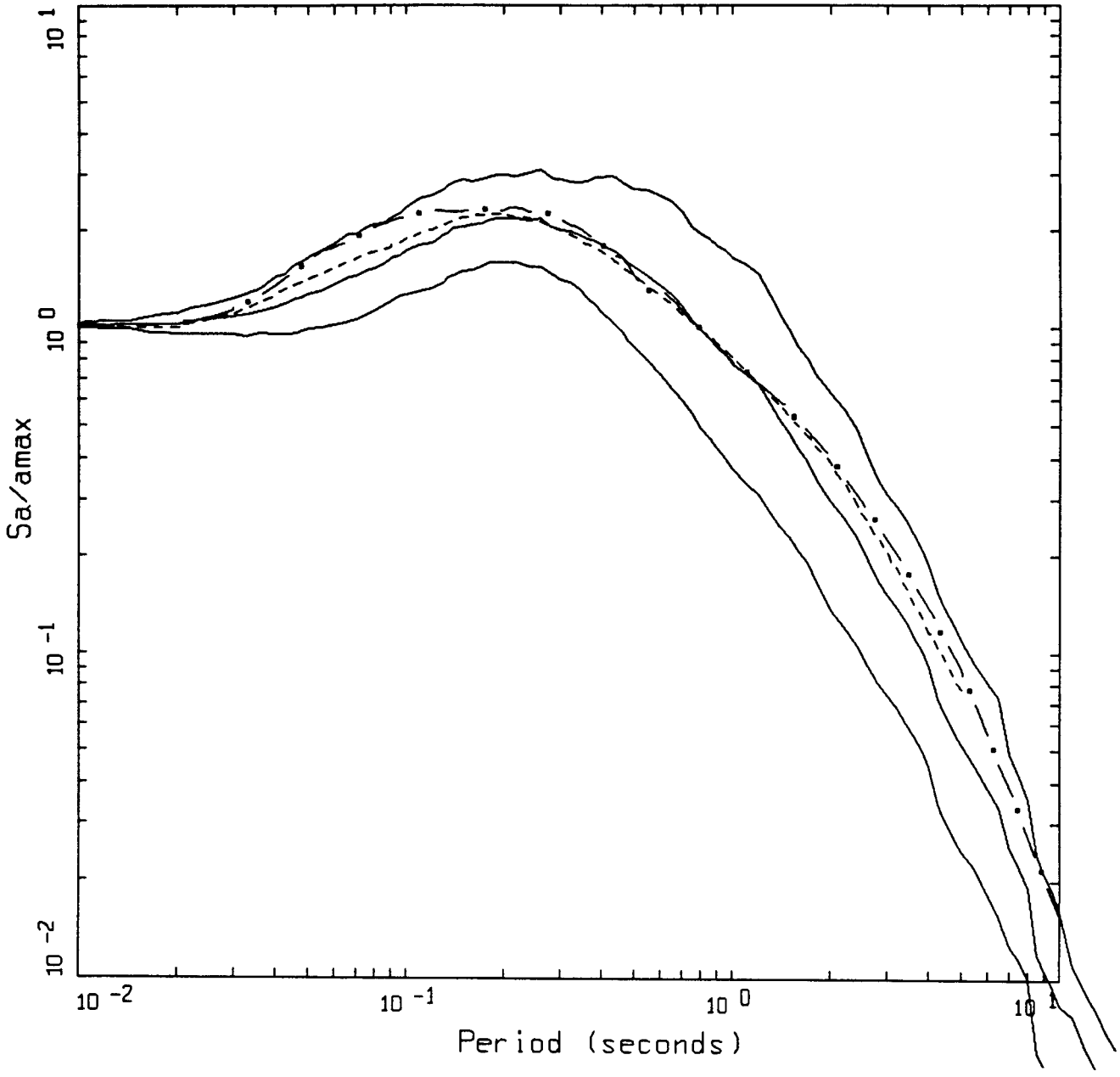

AVERAGE HORIZONTAL SPECTRA
M=6.5, ROCK

LEGEND

- 84TH PERCENTILE, DATA
- 50TH PERCENTILE, DATA
- 16TH PERCENTILE, DATA
- 50TH PERCENTILE, MODEL
- EMPIRICAL

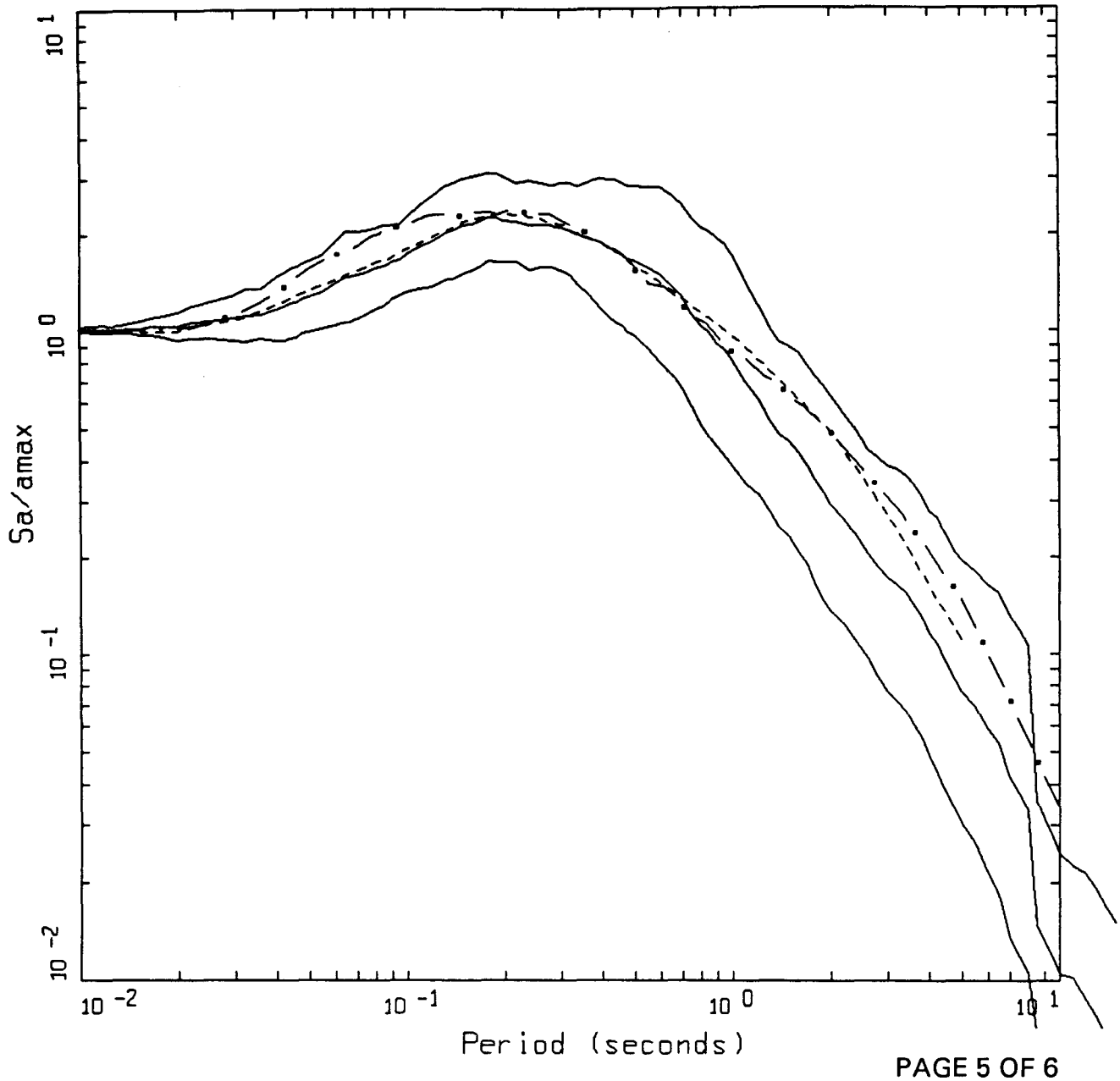

AVERAGE HORIZONTAL SPECTRA
M=7.0, ROCK

LEGEND

84TH PERCENTILE, DATA

50TH PERCENTILE, DATA

16TH PERCENTILE, DATA

50TH PERCENTILE, MODEL

EMPIRICAL

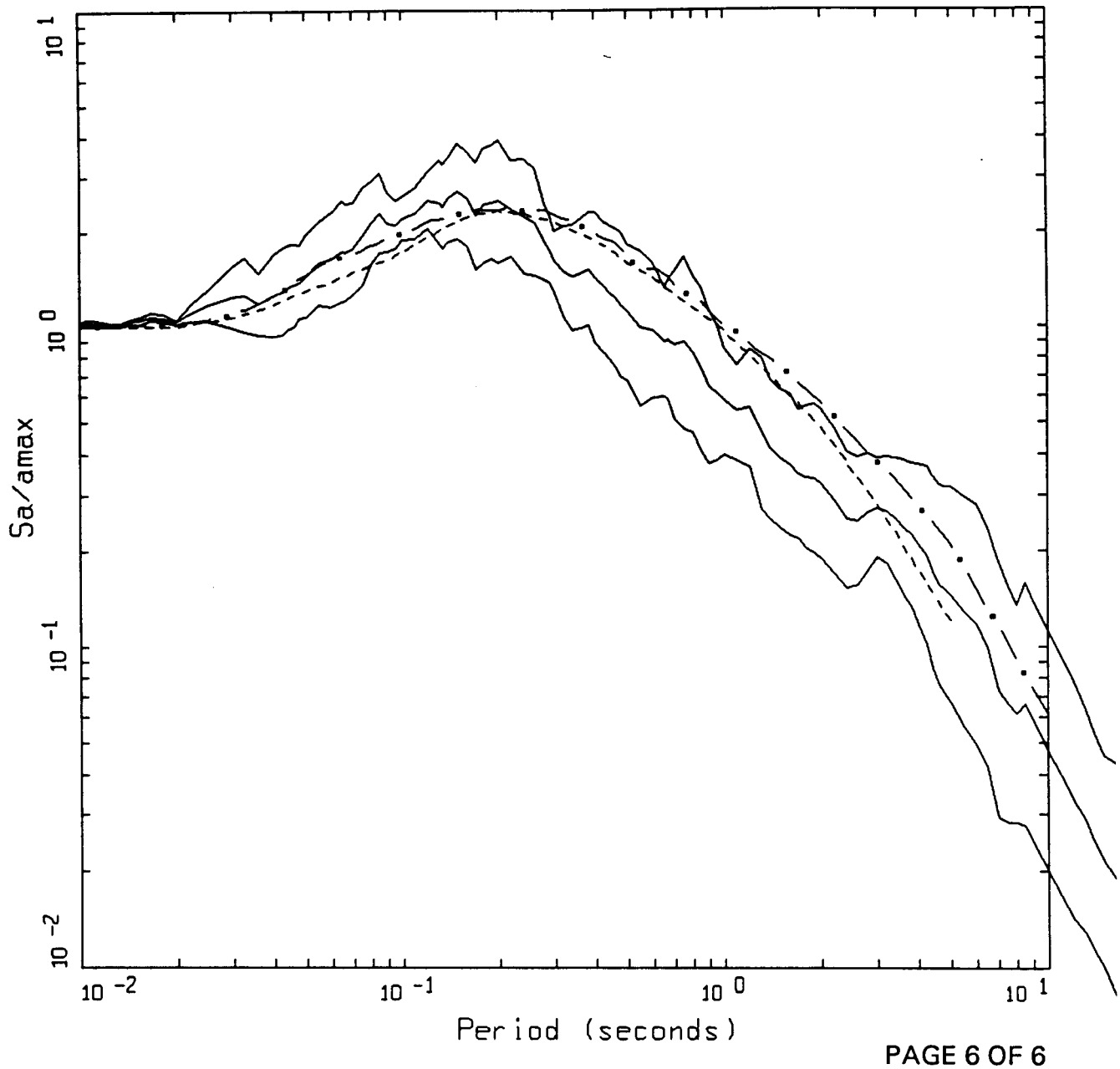

AVERAGE HORIZONTAL SPECTRA
M=7.5, ROCK

LEGEND

———— 84TH PERCENTILE, DATA
———— 50TH PERCENTILE, DATA
———— 16TH PERCENTILE, DATA
— • — 50TH PERCENTILE, MODEL
- - - - - EMPIRICAL

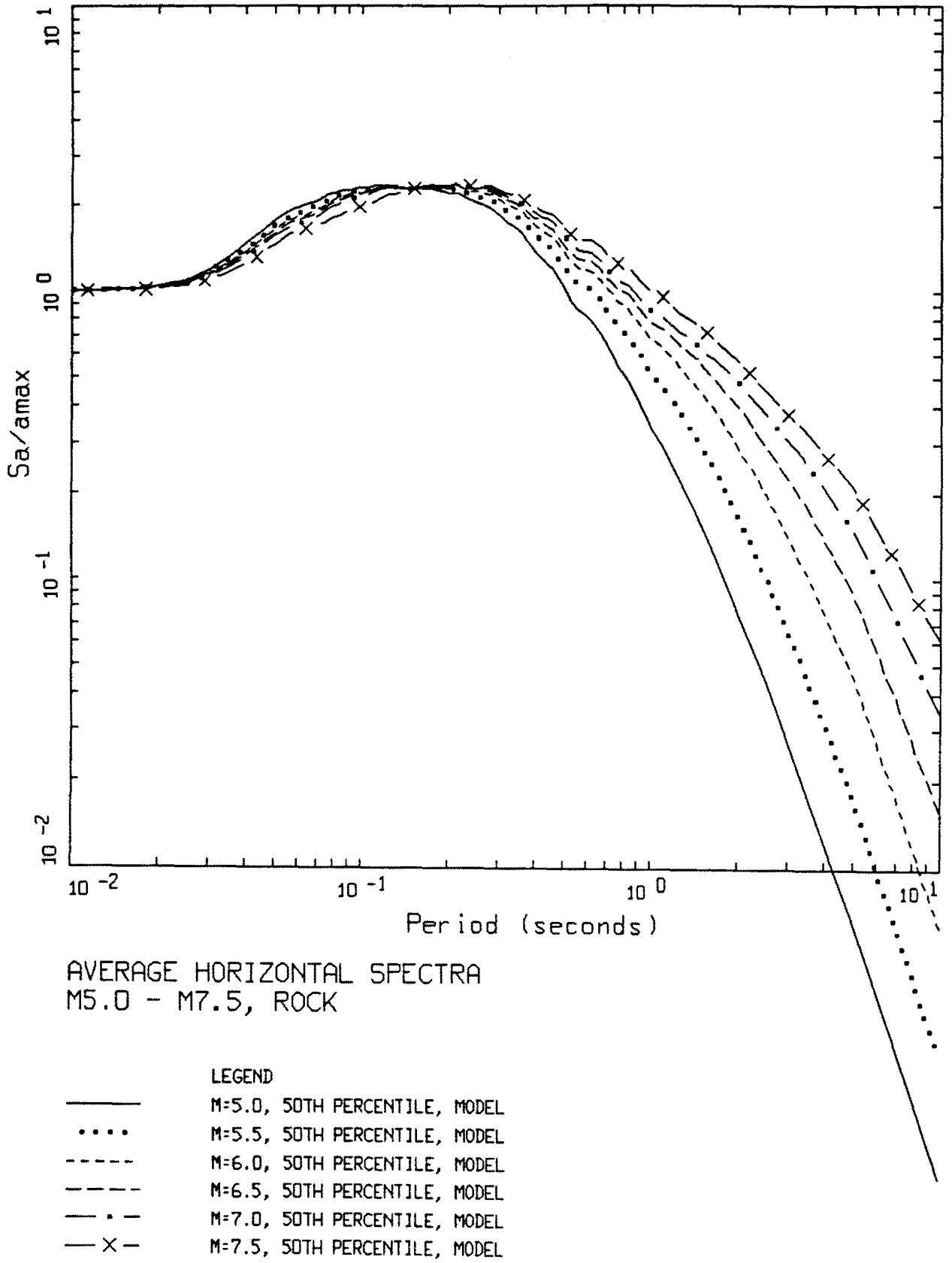

Figure 7.9. Summary plot of the magnitude dependency of median point-source shapes. Soft rock site conditions.

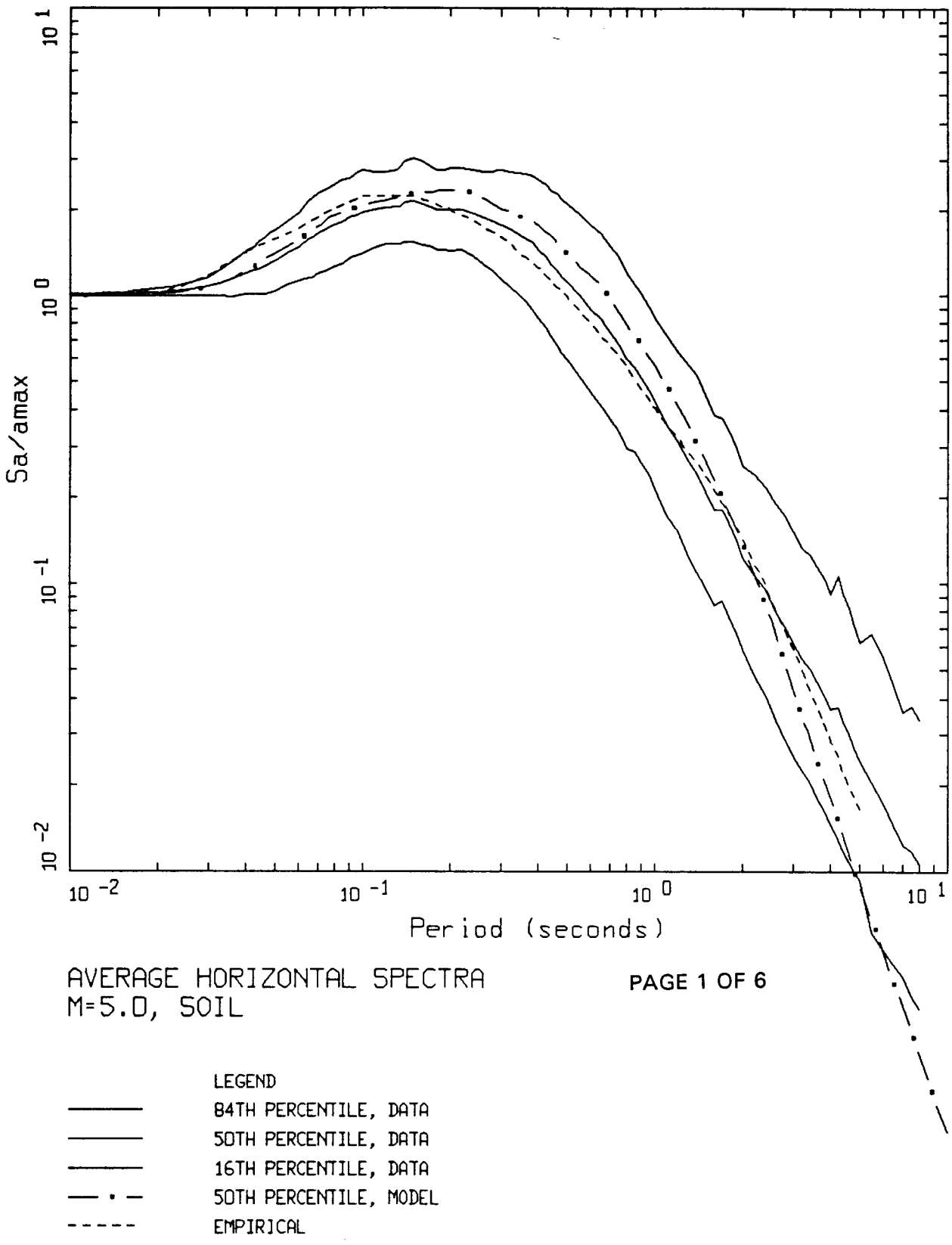

Figure Set 7.10. Comparison of statistical response spectral shapes with median point-source model predictions and the empirical attenuation relation (Appendix A) for a vertical strike-slip fault. Magnitudes and distances are listed in Table 7.1. The point-source stress drop is 59 bars (Table 6.1). Deep soil site conditions.

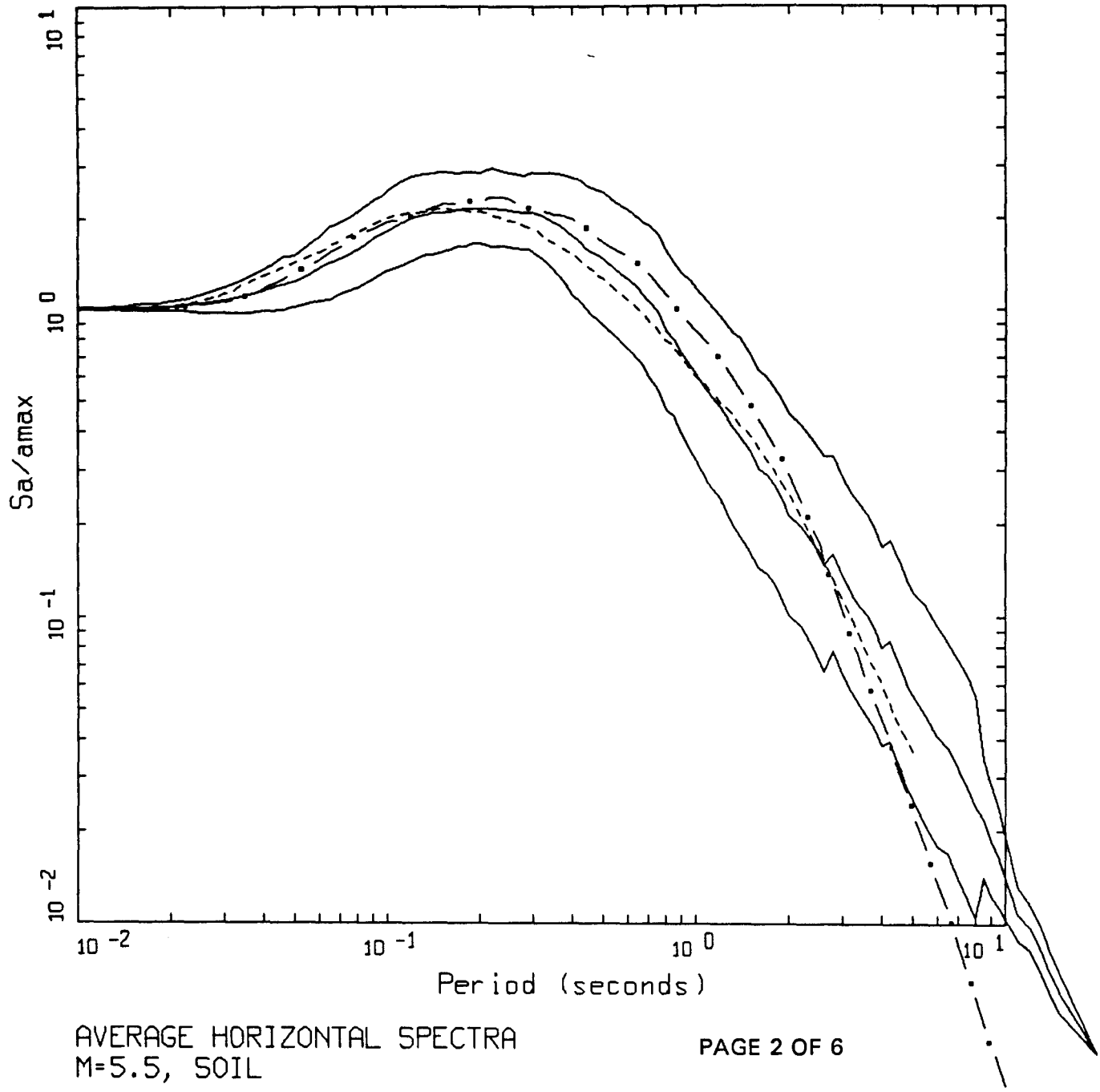

AVERAGE HORIZONTAL SPECTRA
M=5.5, SOIL

LEGEND

———— 84TH PERCENTILE, DATA
———— 84TH PERCENTILE, DATA
———— 84TH PERCENTILE, DATA
— • — 50TH PERCENTILE, MODEL
- - - - - EMPIRICAL

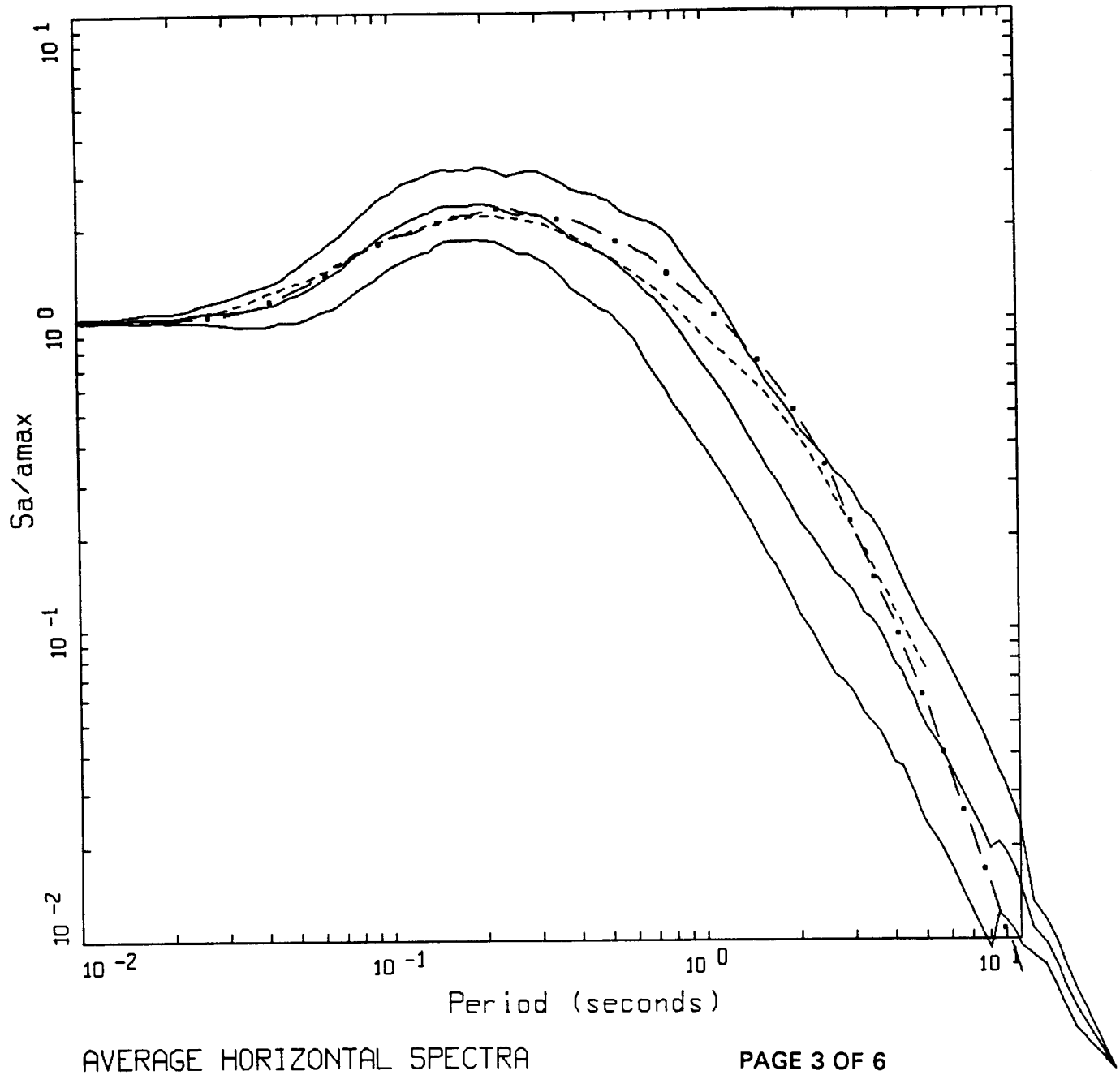

AVERAGE HORIZONTAL SPECTRA
M=6.0, SOIL

LEGEND

- 84TH PERCENTILE, DATA
- 50TH PERCENTILE, DATA
- 16TH PERCENTILE, DATA
- 50TH PERCENTILE, MODEL
- EMPIRICAL

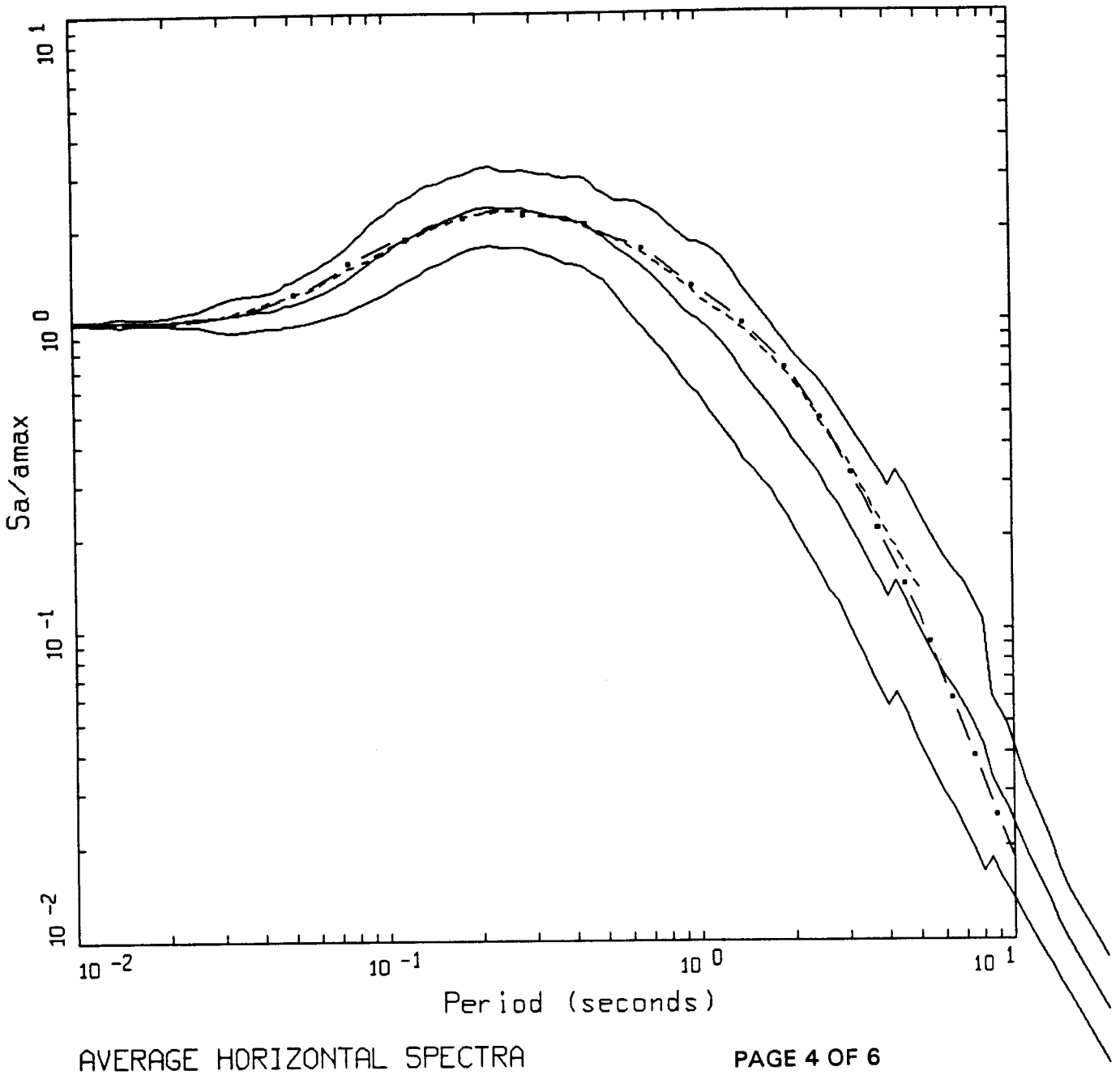

AVERAGE HORIZONTAL SPECTRA
M=6.5, SOIL

LEGEND

———— 84TH PERCENTILE, DATA
———— 50TH PERCENTILE, DATA
———— 16TH PERCENTILE, DATA
— • — 50TH PERCENTILE, MODEL
- - - - - EMPIRICAL

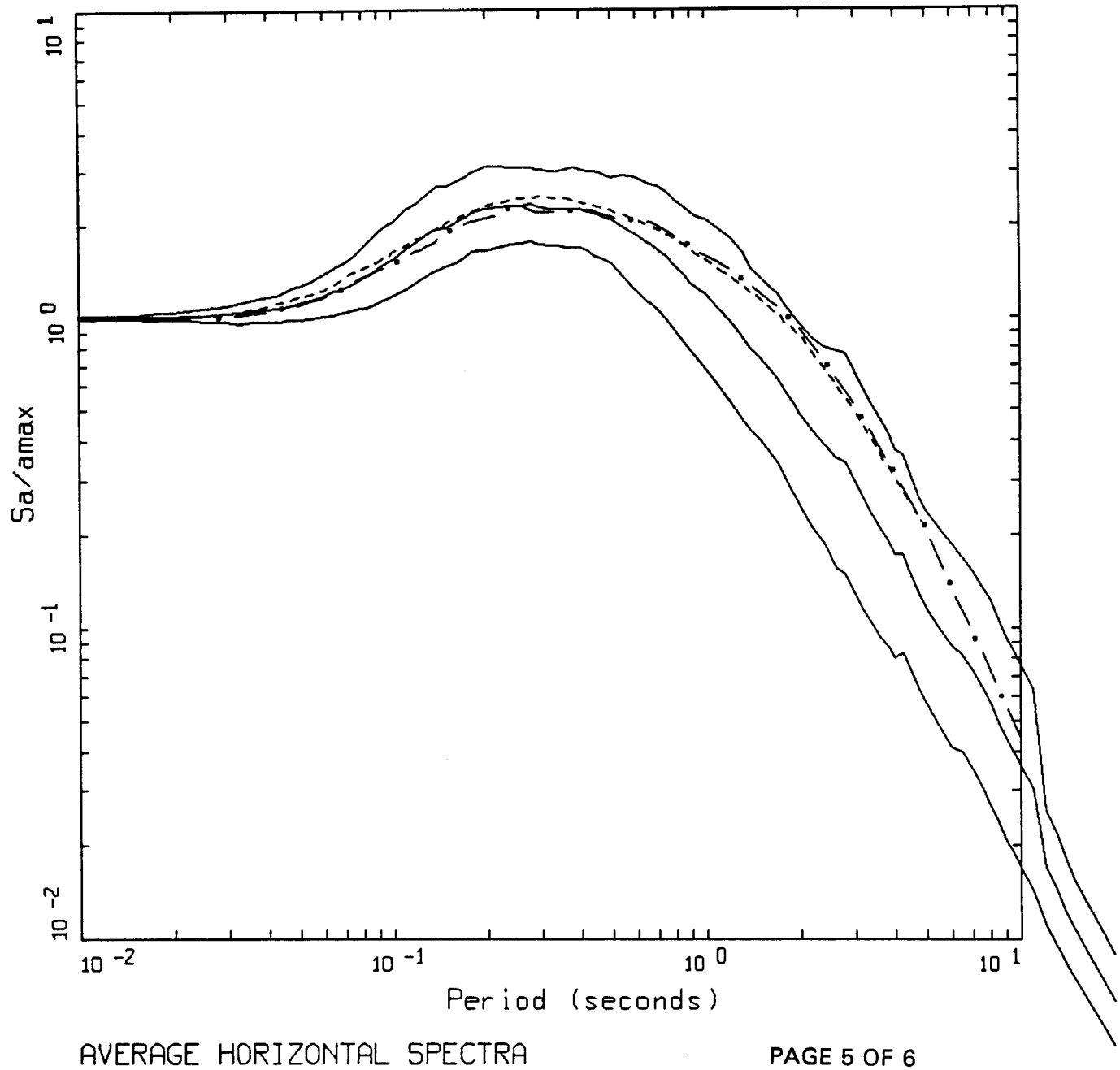

AVERAGE HORIZONTAL SPECTRA
M=7.0, SOIL

LEGEND

84TH PERCENTILE, DATA

50TH PERCENTILE, DATA

16TH PERCENTILE, DATA

50TH PERCENTILE, MODEL

EMPIRICAL

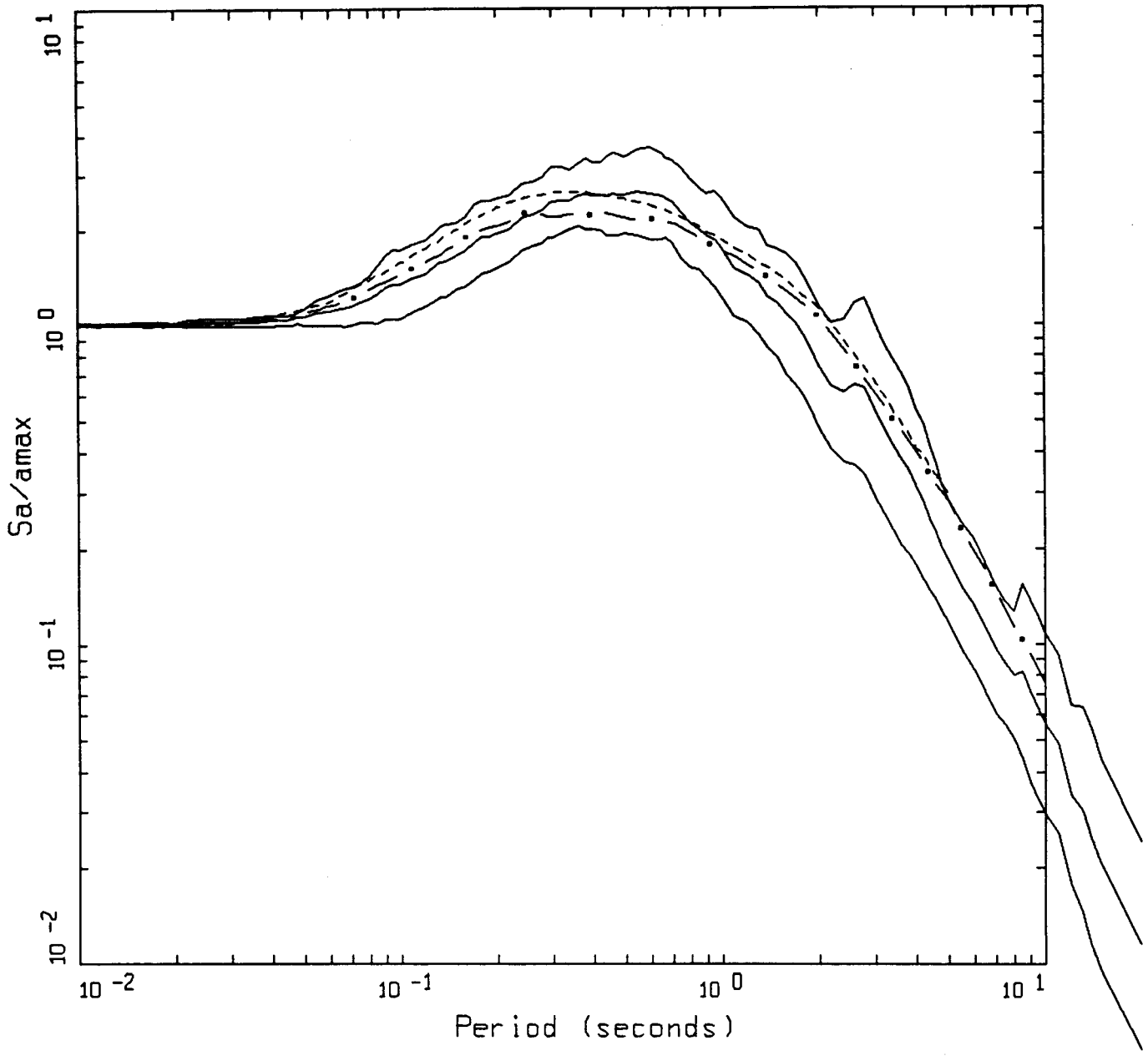

AVERAGE HORIZONTAL SPECTRA
M=7.5, SOIL

LEGEND

———— 84TH PERCENTILE, DATA
———— 50TH PERCENTILE, DATA
———— 16TH PERCENTILE, DATA
— • — 50TH PERCENTILE, MODEL
- - - - - EMPIRICAL

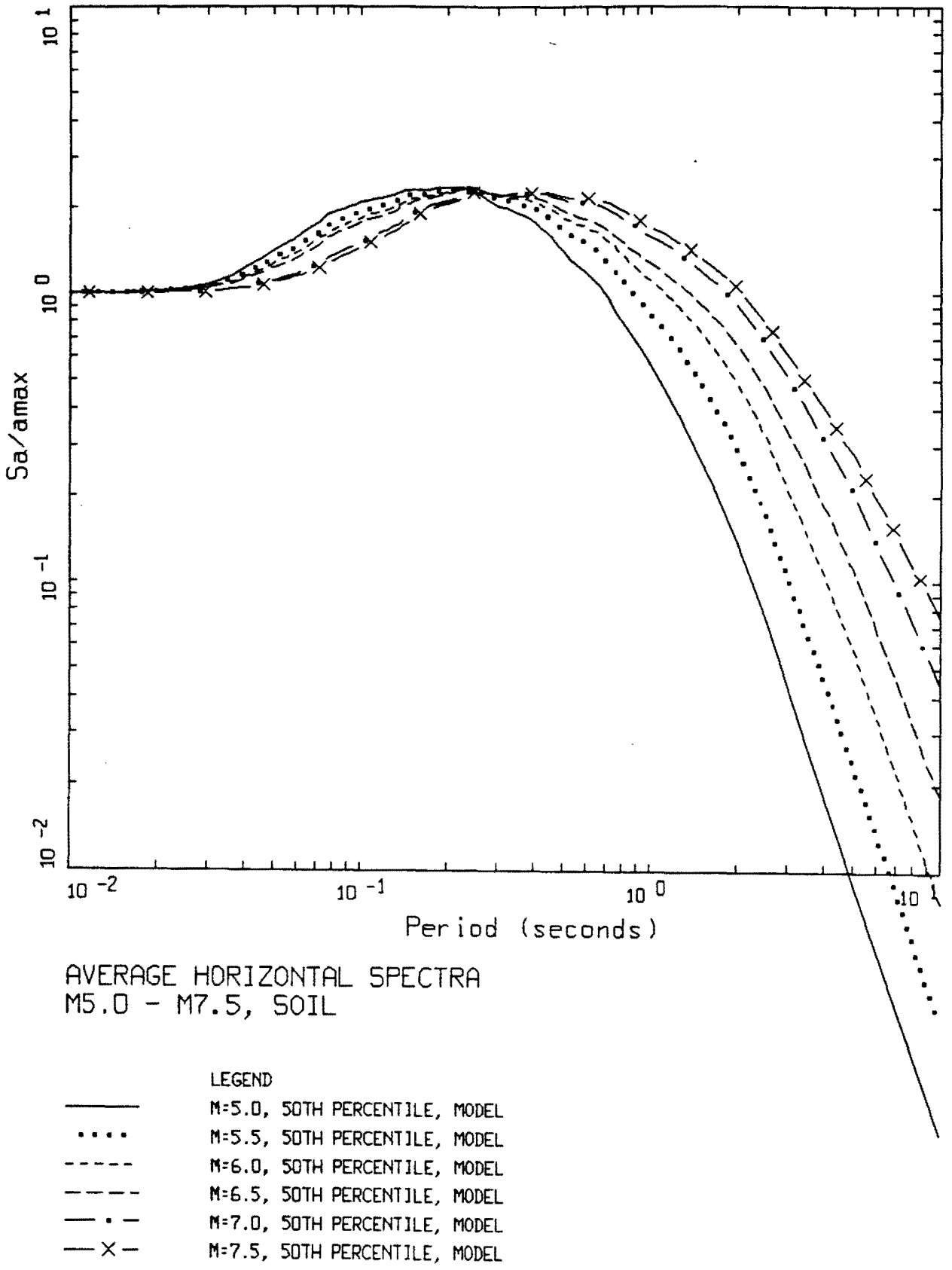

Figure 7.11. Summary plot of the magnitude dependency of median point-source shapes. Deep soil site conditions.

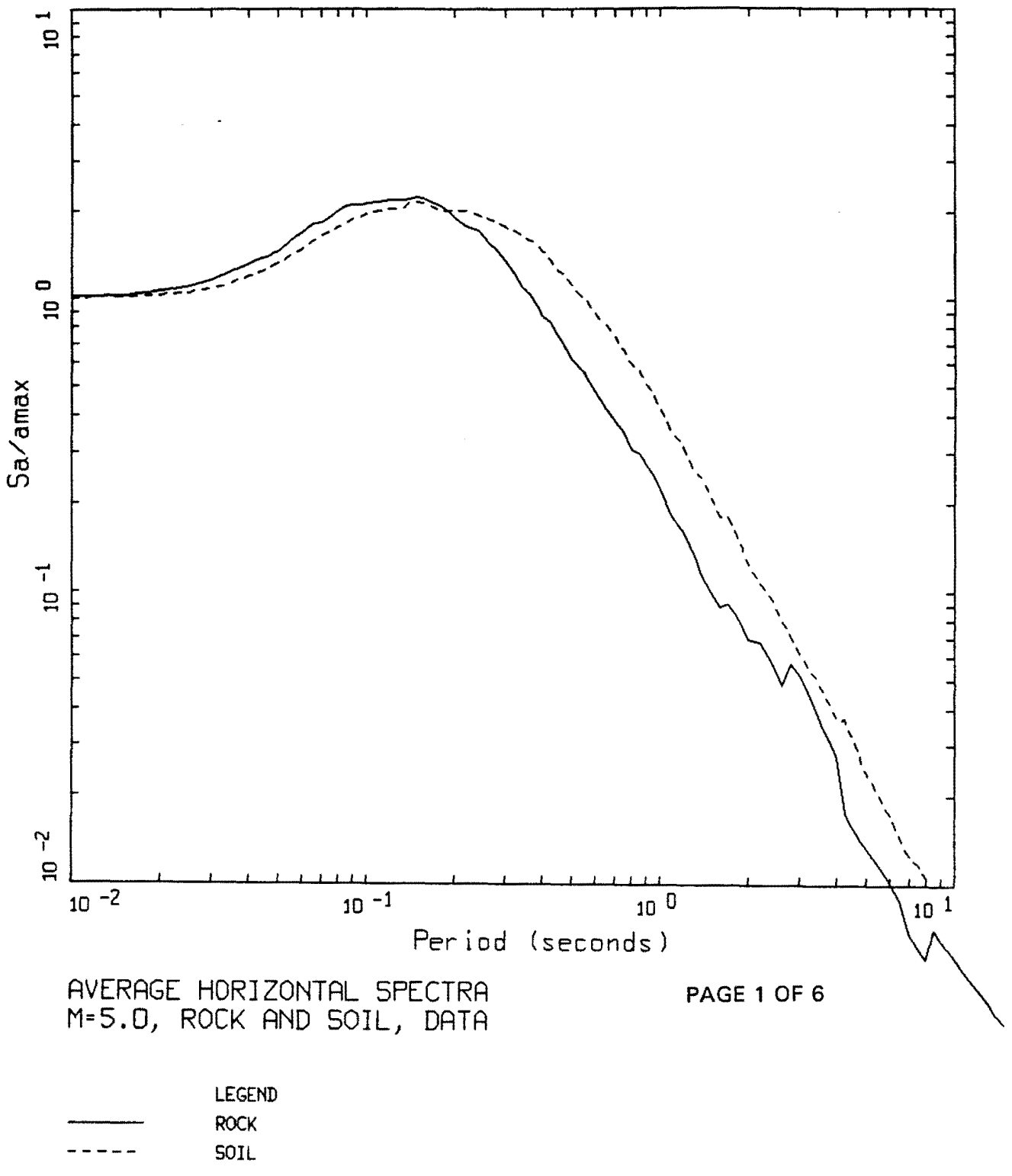

Figure Set 7.12. Comparison of soft rock and deep soil 5% damped statistical response spectral shaped for the magnitude bins listed in Table 7.1.

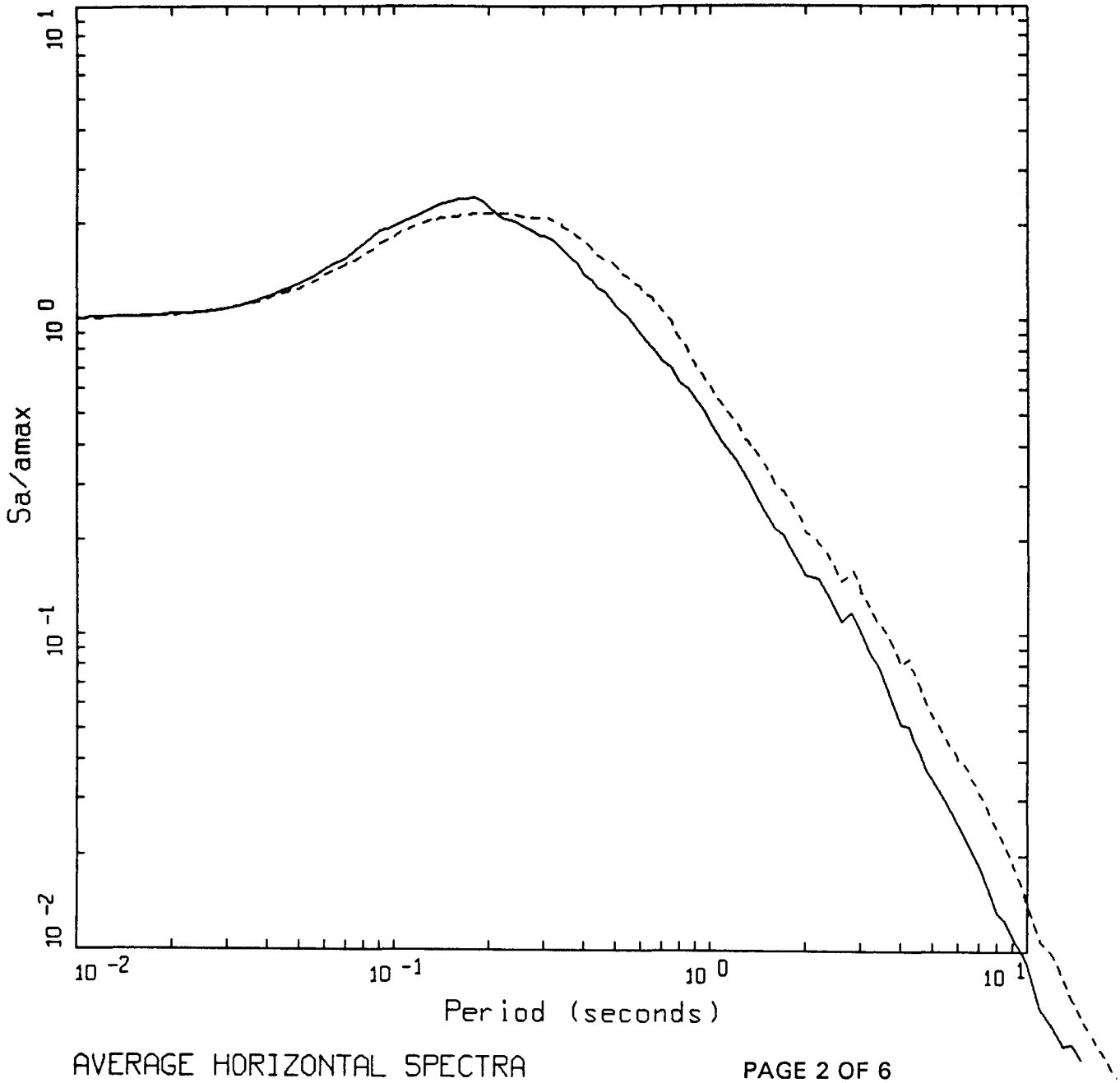

AVERAGE HORIZONTAL SPECTRA
M=5.5, ROCK AND SOIL, DATA

LEGEND
ROCK
SOIL

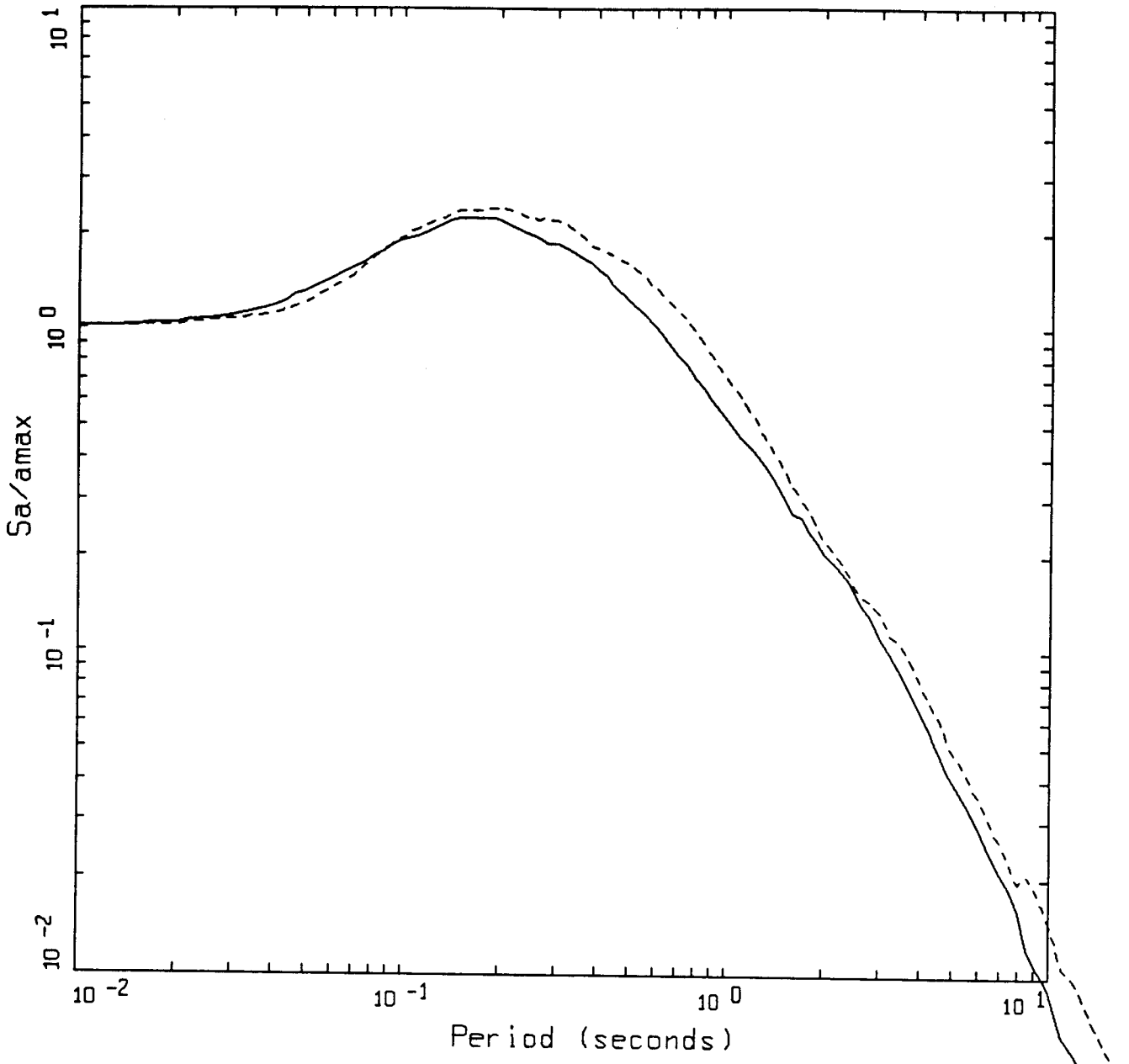

AVERAGE HORIZONTAL SPECTRA
M=6.0, ROCK AND SOIL, DATA

LEGEND

——— ROCK

- - - - - SOIL

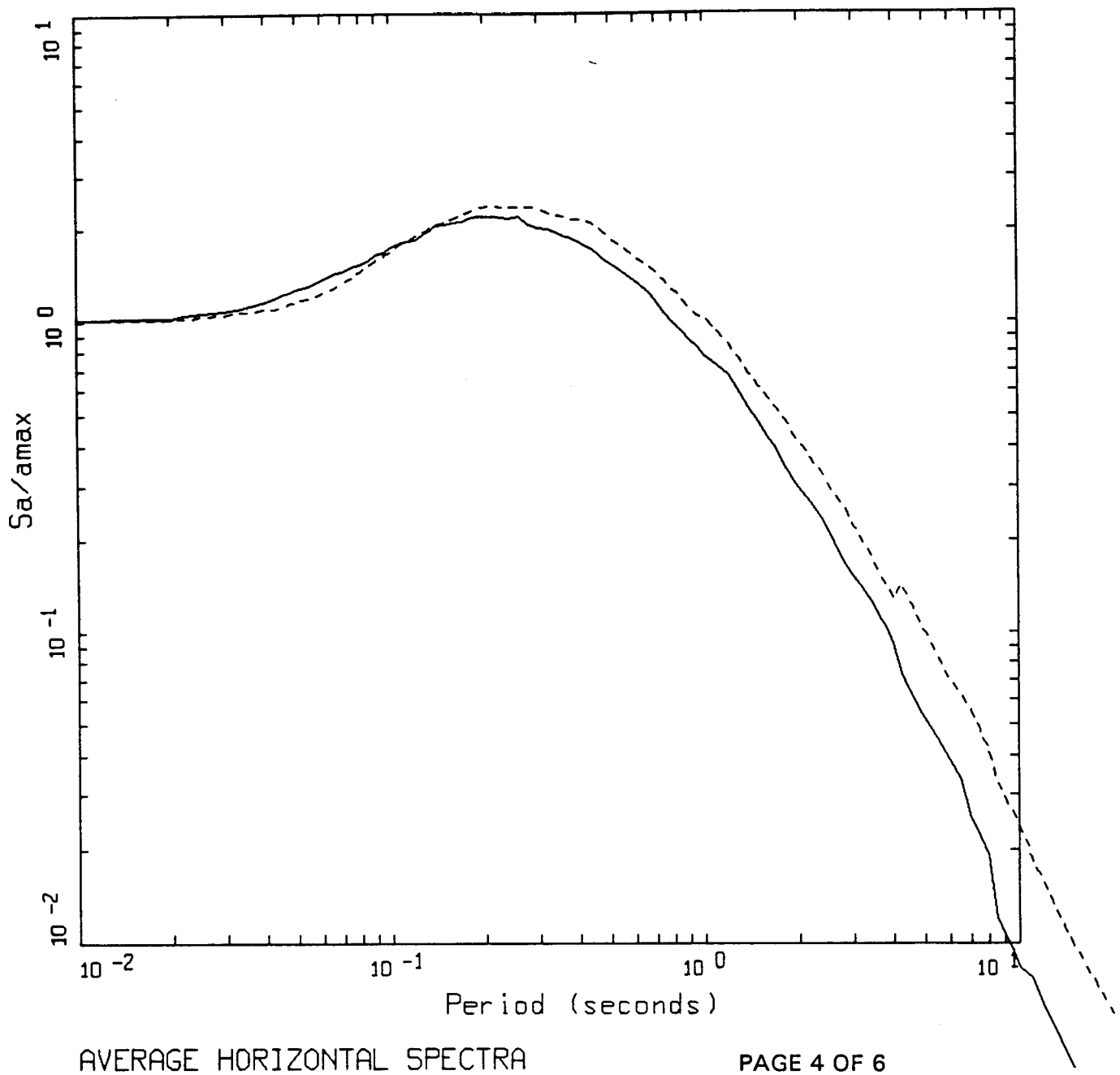

AVERAGE HORIZONTAL SPECTRA
M=6.5, ROCK AND SOIL, DATA

LEGEND

——— ROCK

- - - - - SOIL

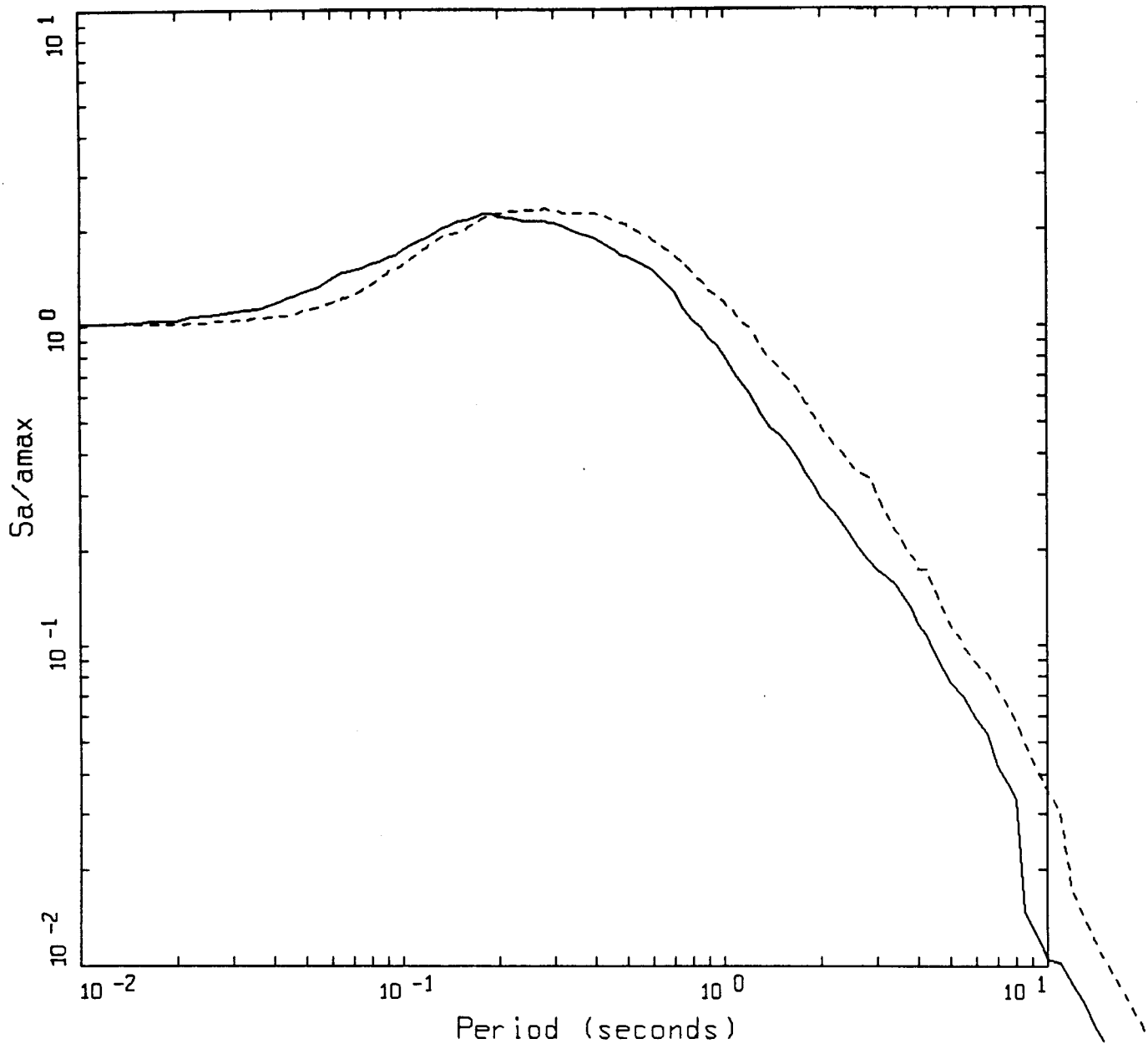

AVERAGE HORIZONTAL SPECTRA
M=7.0, ROCK AND SOIL, DATA

LEGEND

——— ROCK

- - - - - SOIL

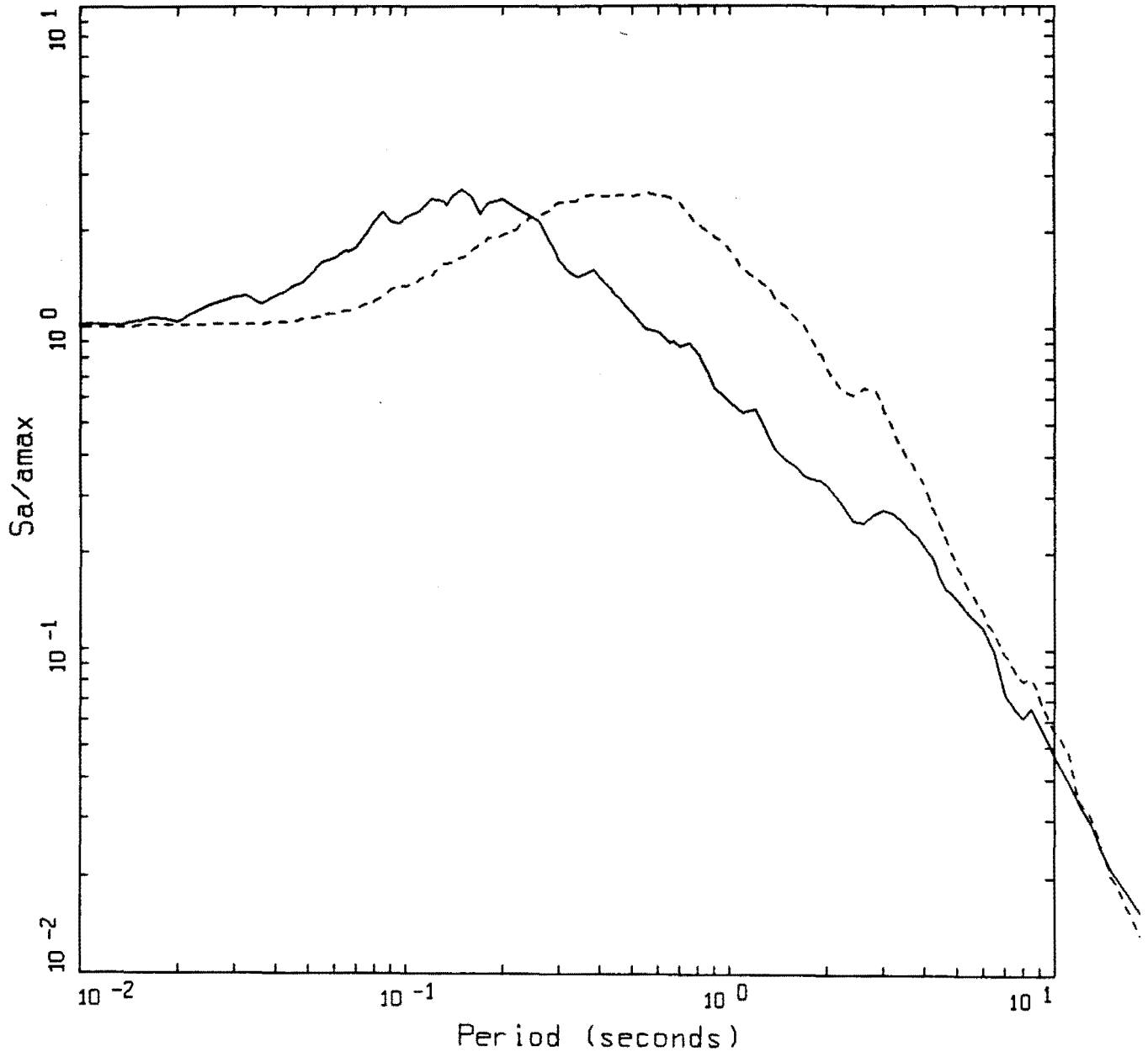

AVERAGE HORIZONTAL SPECTRA
M=7.5, ROCK AND SOIL, DATA

LEGEND

——— ROCK

- - - - - SOIL

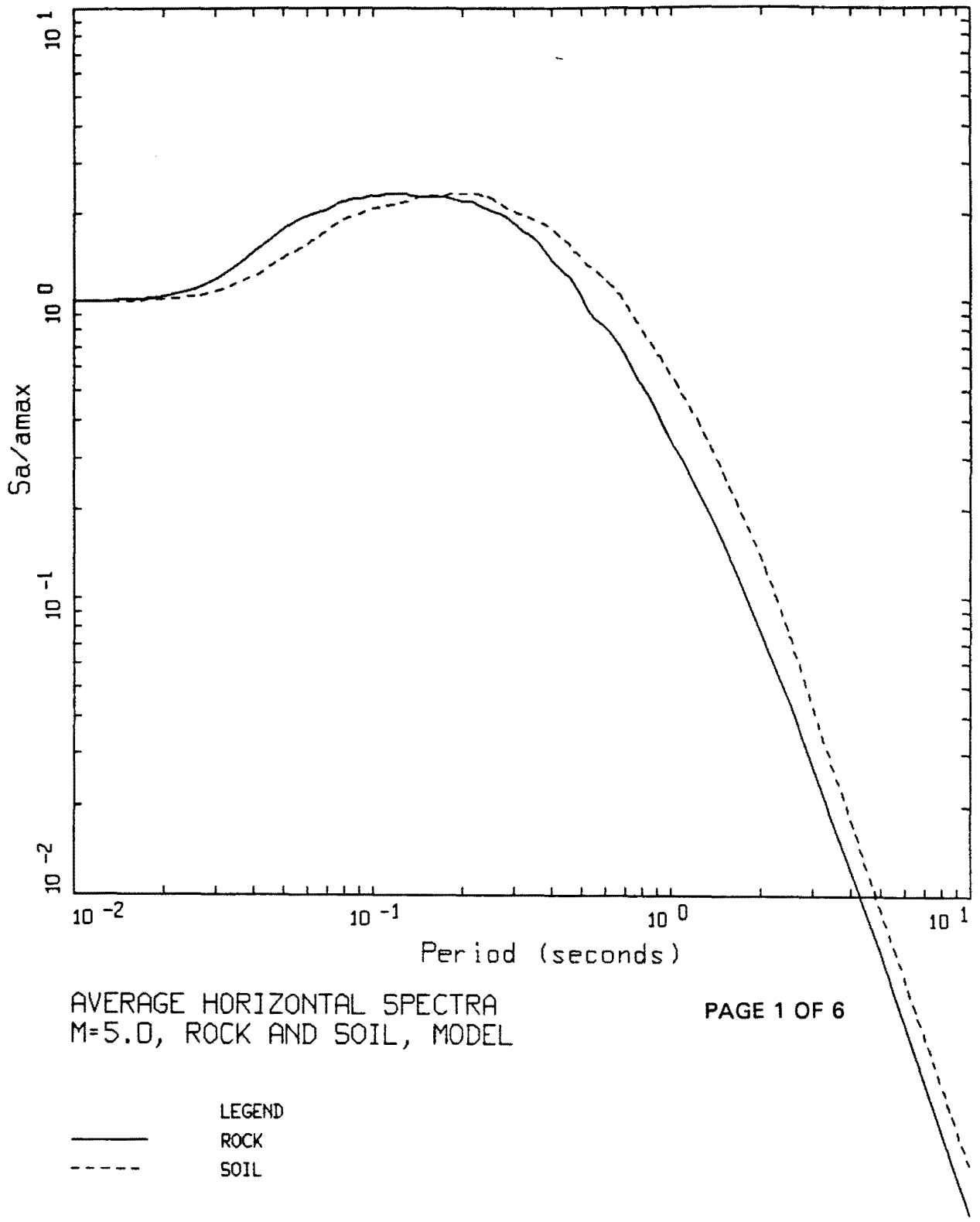

Figure Set 7.13. Comparison of soft rock and deep soil 5% damped point-source model response spectral shapes for the magnitude bins listed in Table 7.1.

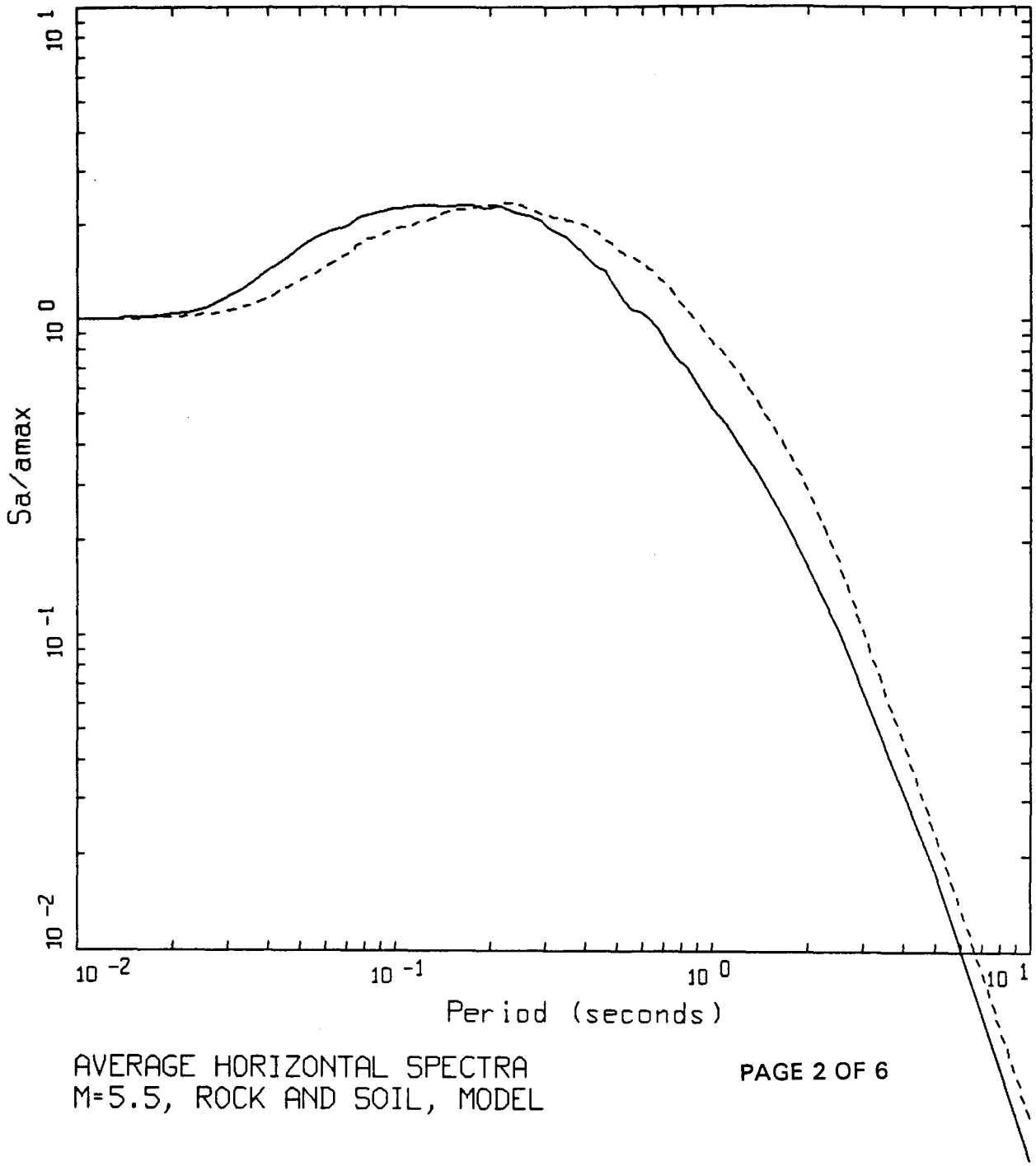

AVERAGE HORIZONTAL SPECTRA
M=5.5, ROCK AND SOIL, MODEL

LEGEND

——— ROCK

- - - - - SOIL

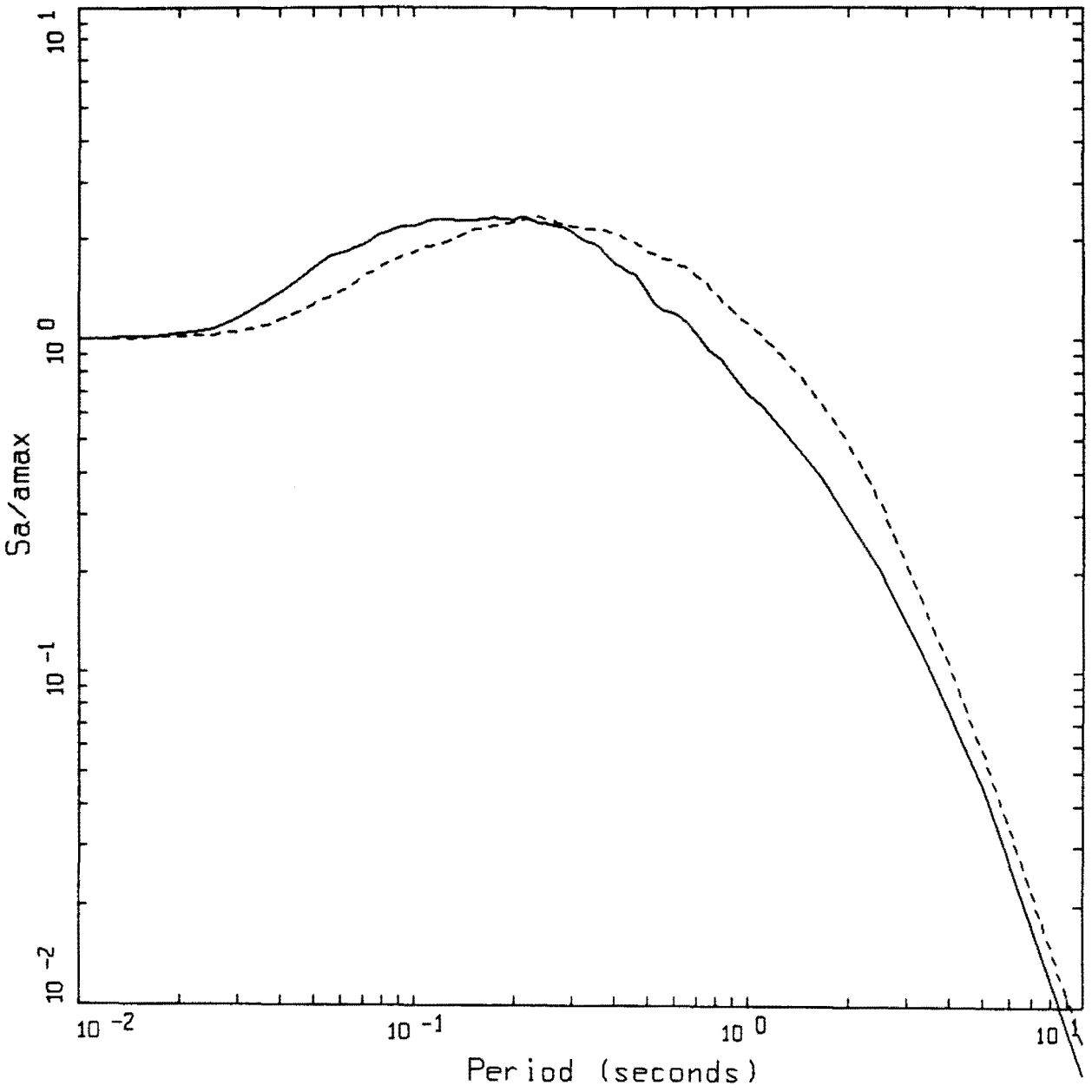

AVERAGE HORIZONTAL SPECTRA
M=6.0, ROCK AND SOIL, MODEL

LEGEND

——— ROCK

- - - - - SOIL

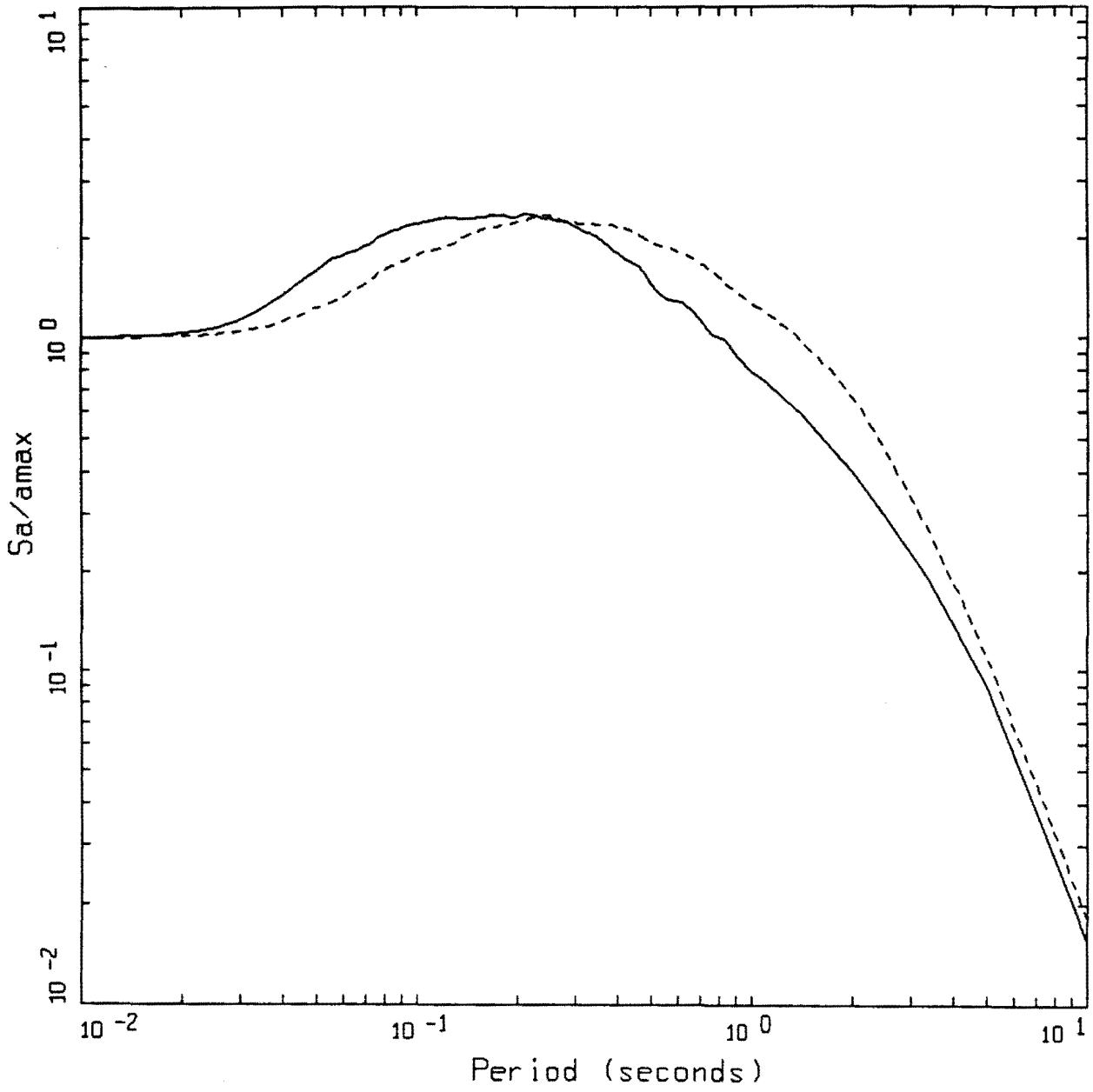

AVERAGE HORIZONTAL SPECTRA
M=6.5, ROCK AND SOIL, MODEL

LEGEND

——— ROCK

- - - - - SOIL

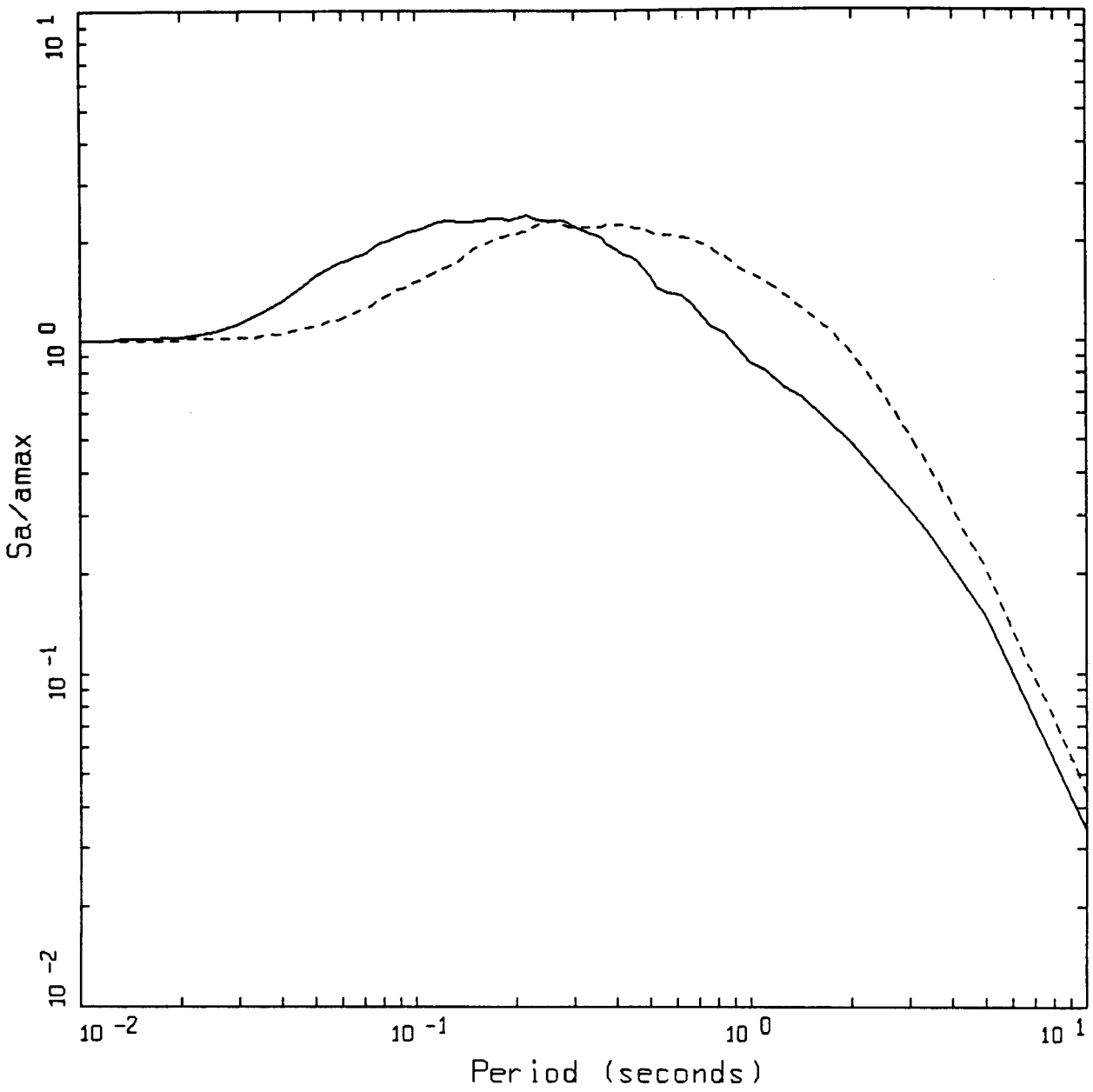

AVERAGE HORIZONTAL SPECTRA
M=7.0, ROCK AND SOIL, MODEL

LEGEND

——— ROCK

- - - - - SOIL

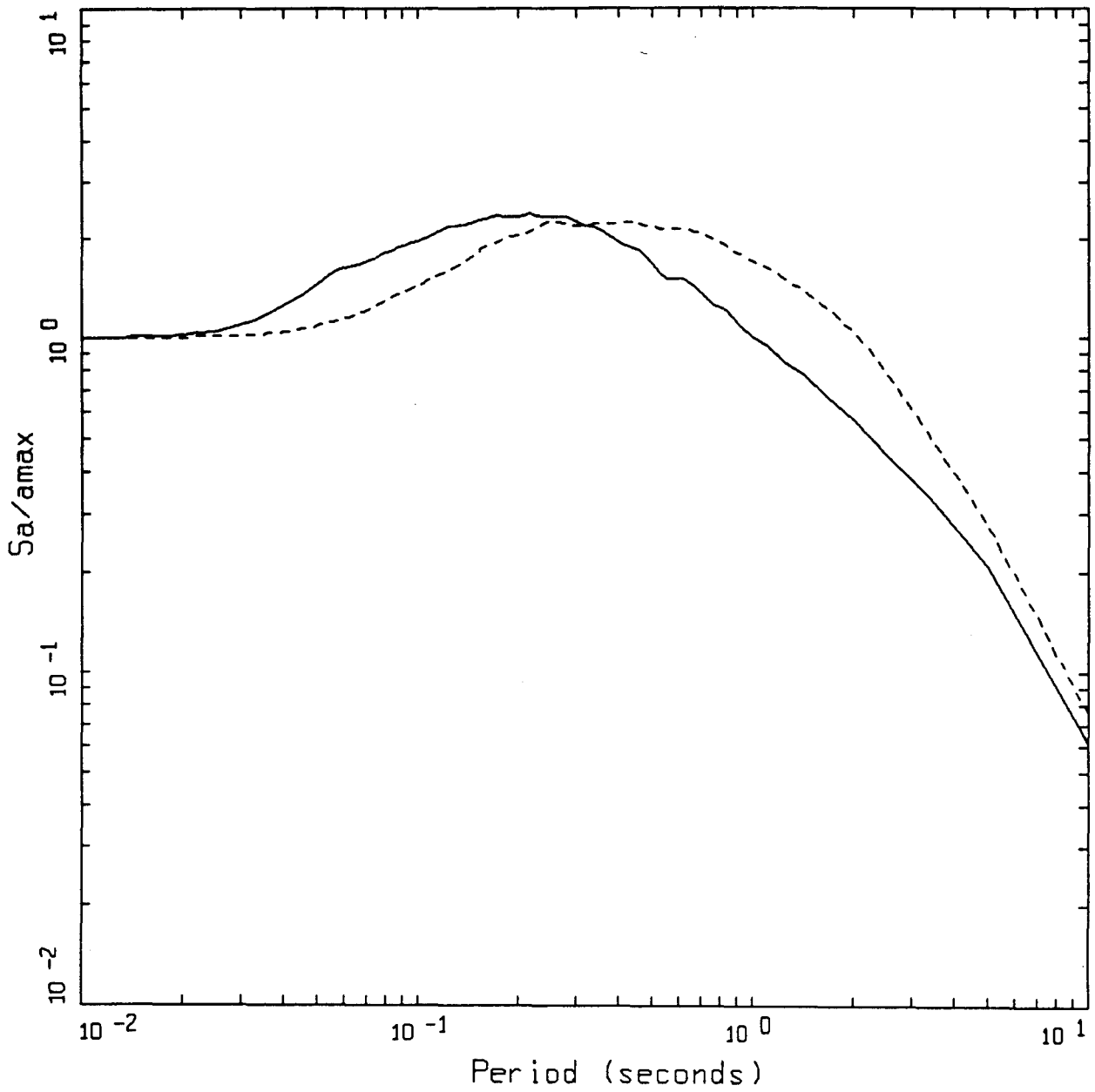

AVERAGE HORIZONTAL SPECTRA
M=7.5, ROCK AND SOIL, MODEL

LEGEND

——— ROCK

- - - - - SOIL

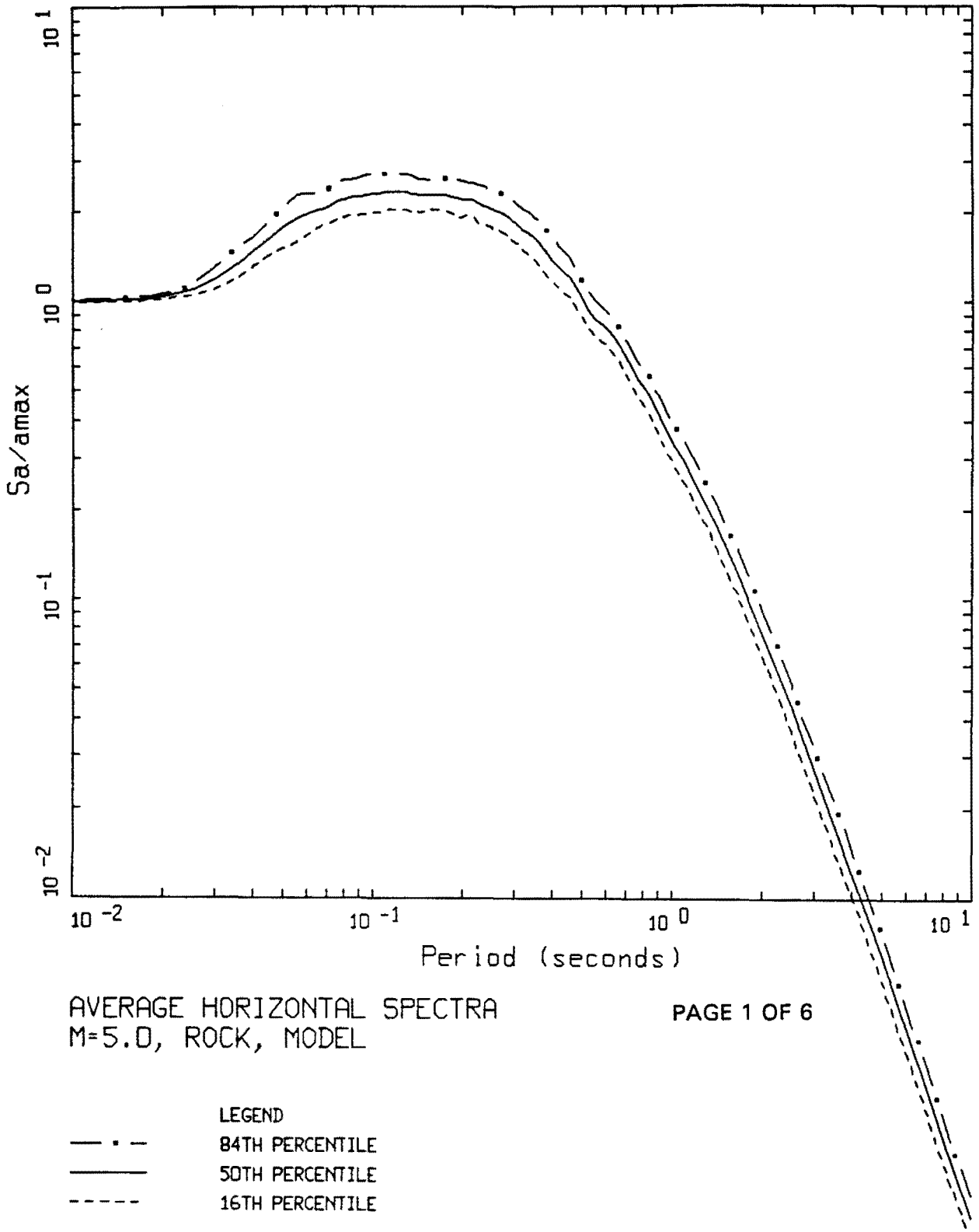

Figure Set 7.14. Median and $\pm$ 1 σ response spectral shapes computed with the point-source model computed from 30 randomly generated soft rock profiles using the correlation model of Appendix C.

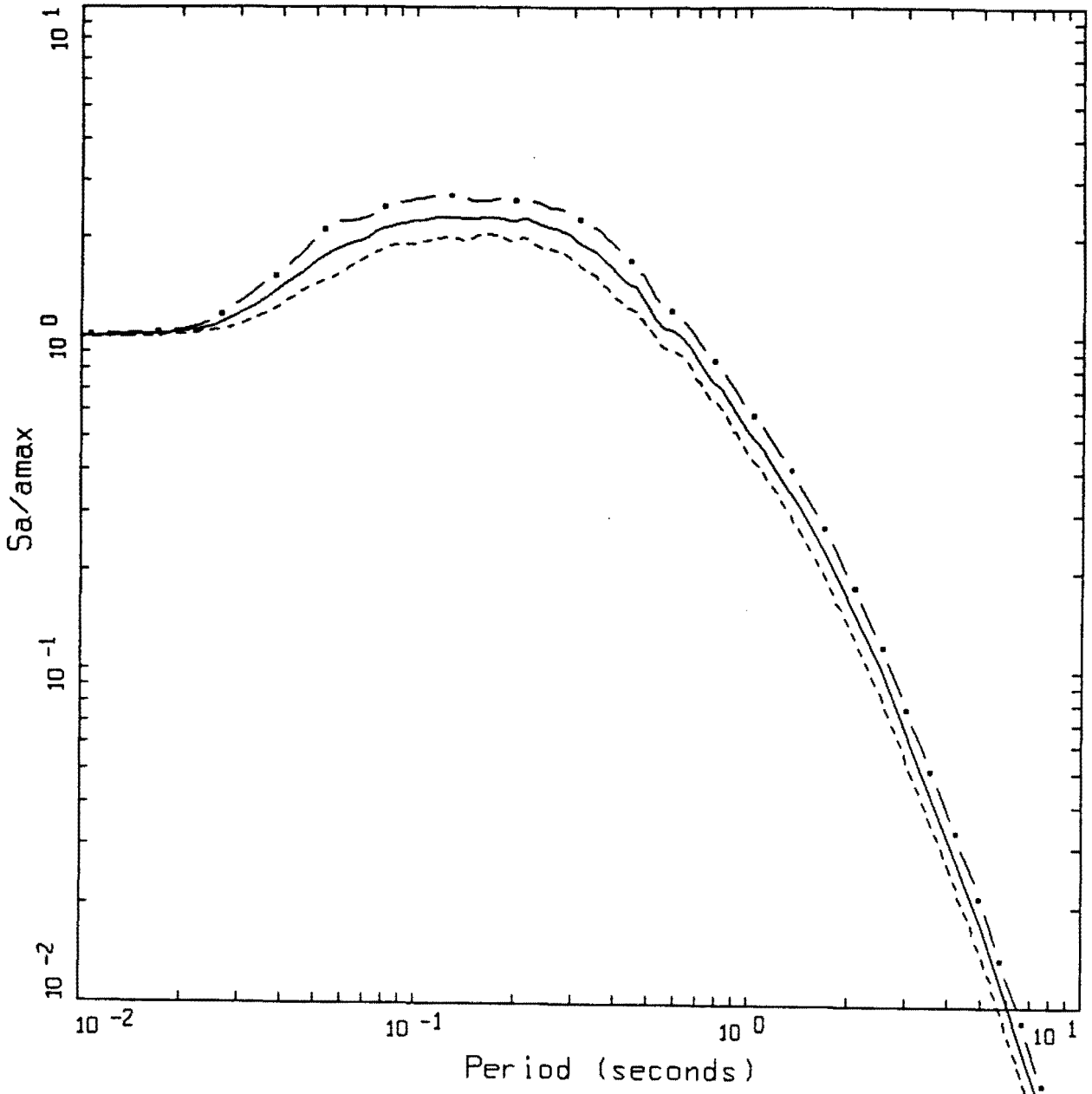

AVERAGE HORIZONTAL SPECTRA
M=5.5, ROCK, MODEL

LEGEND

— • — 84TH PERCENTILE

——— 50TH PERCENTILE

- - - - - 16TH PERCENTILE

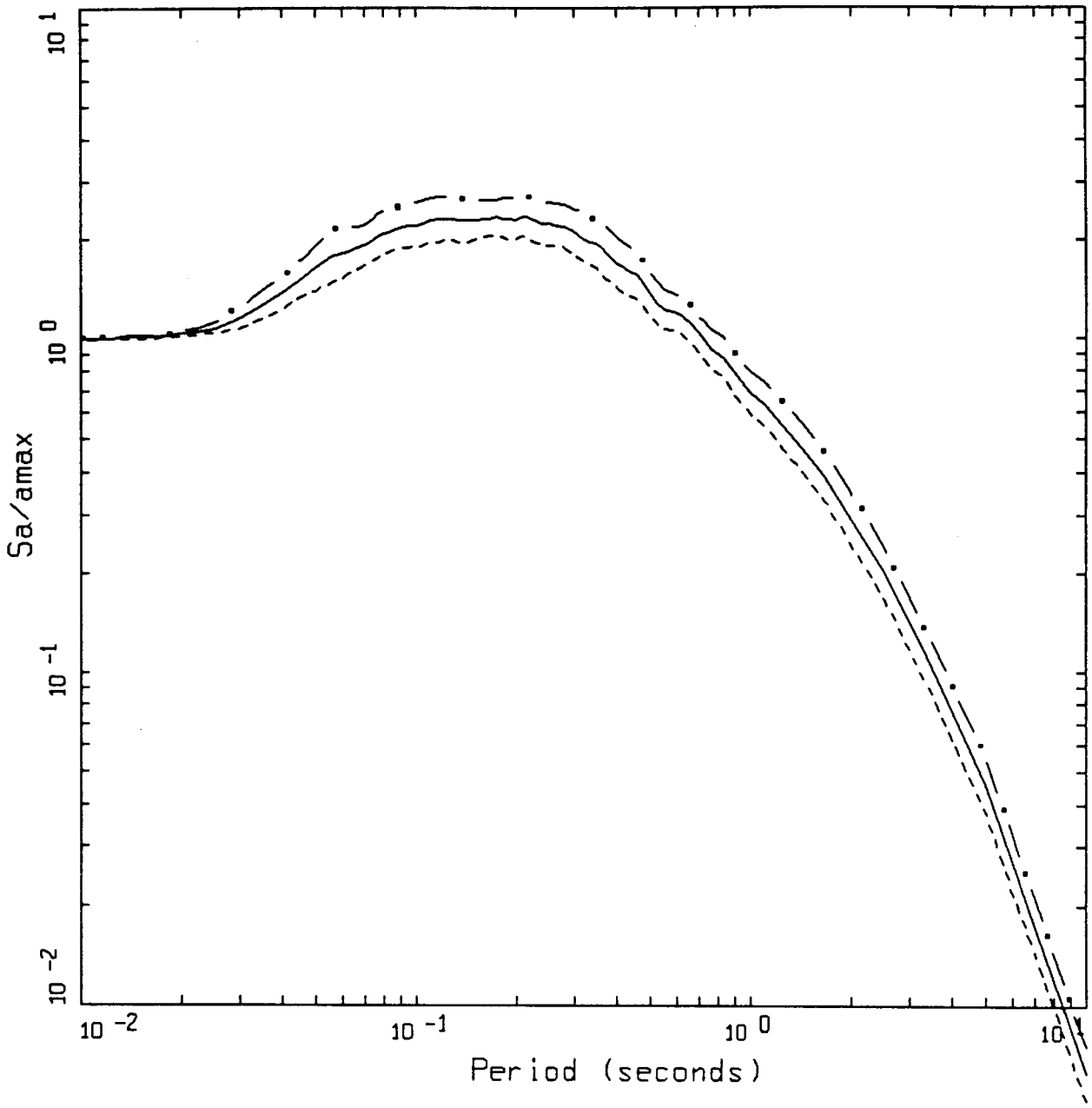

AVERAGE HORIZONTAL SPECTRA
M=6.0, ROCK, MODEL

LEGEND

— • — 84TH PERCENTILE

——— 50TH PERCENTILE

- - - - - 16TH PERCENTILE

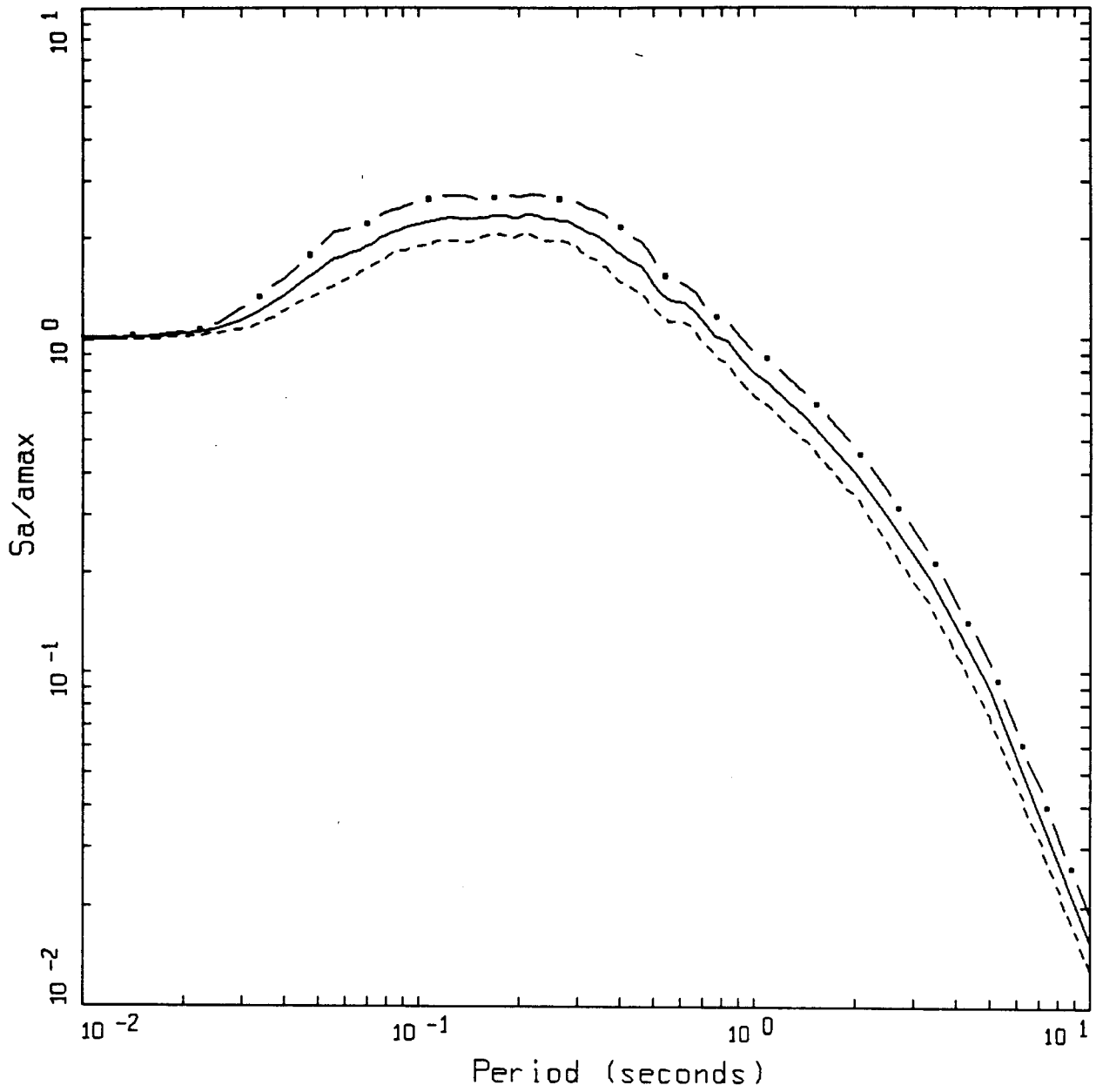

AVERAGE HORIZONTAL SPECTRA
M=6.5, ROCK, MODEL

LEGEND

— • — 84TH PERCENTILE

——— 50TH PERCENTILE

- - - - - 16TH PERCENTILE

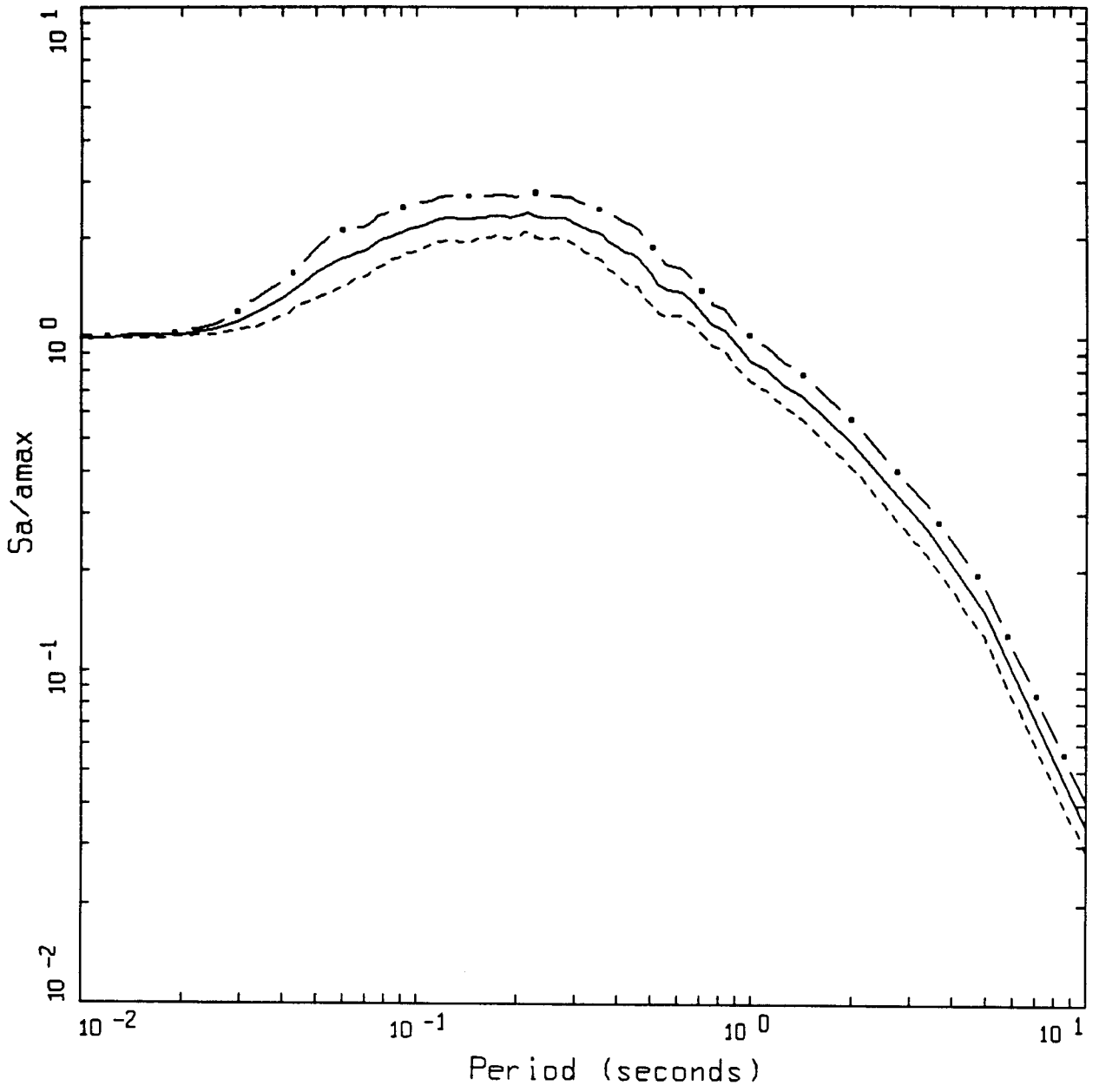

AVERAGE HORIZONTAL SPECTRA
M=7.0, ROCK, MODEL

LEGEND

— • — 84TH PERCENTILE

——— 50TH PERCENTILE

- - - - - 16TH PERCENTILE

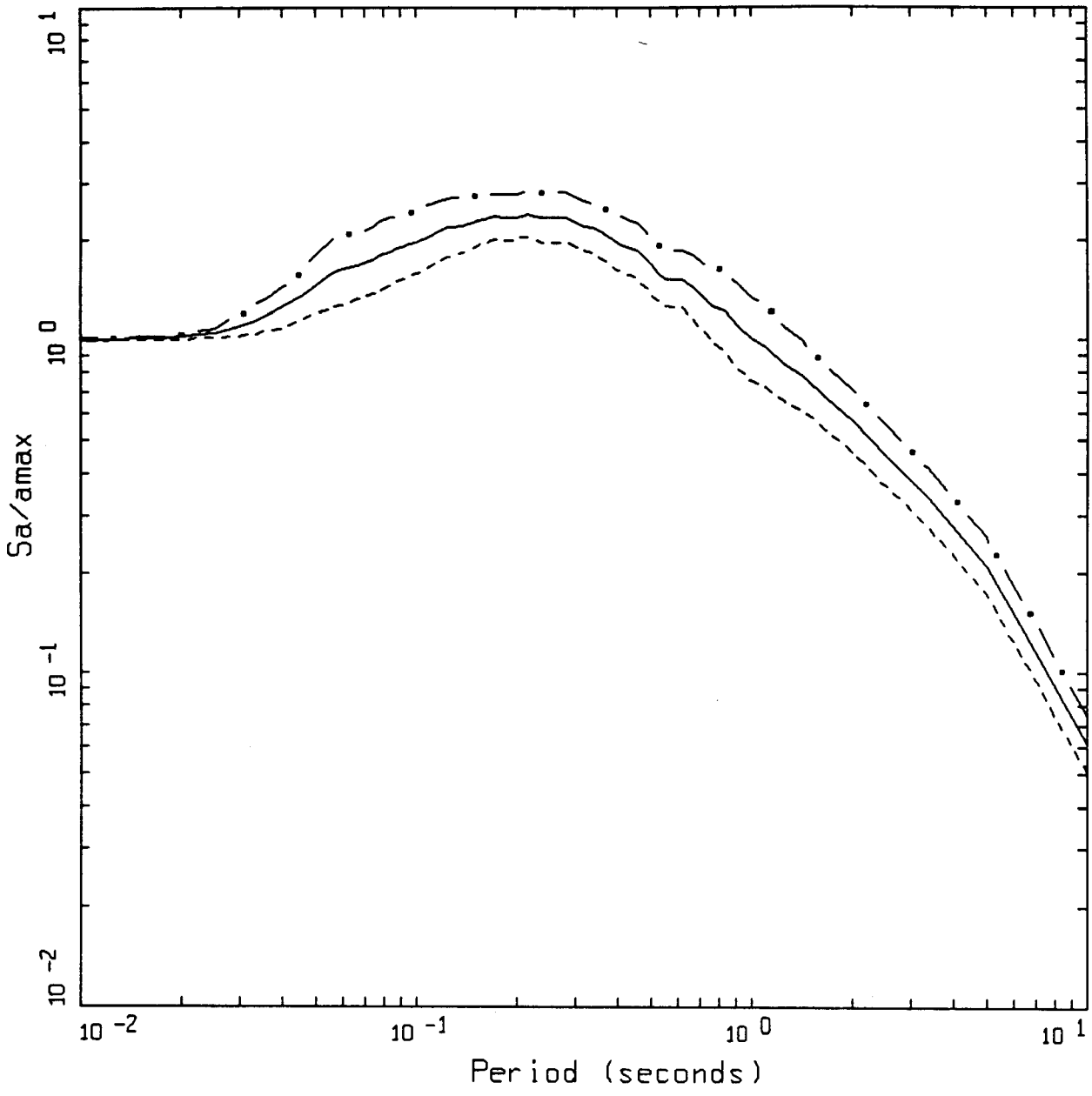

AVERAGE HORIZONTAL SPECTRA
M=7.5, ROCK, MODEL

LEGEND

— • — 84TH PERCENTILE

——— 50TH PERCENTILE

- - - - - 16TH PERCENTILE

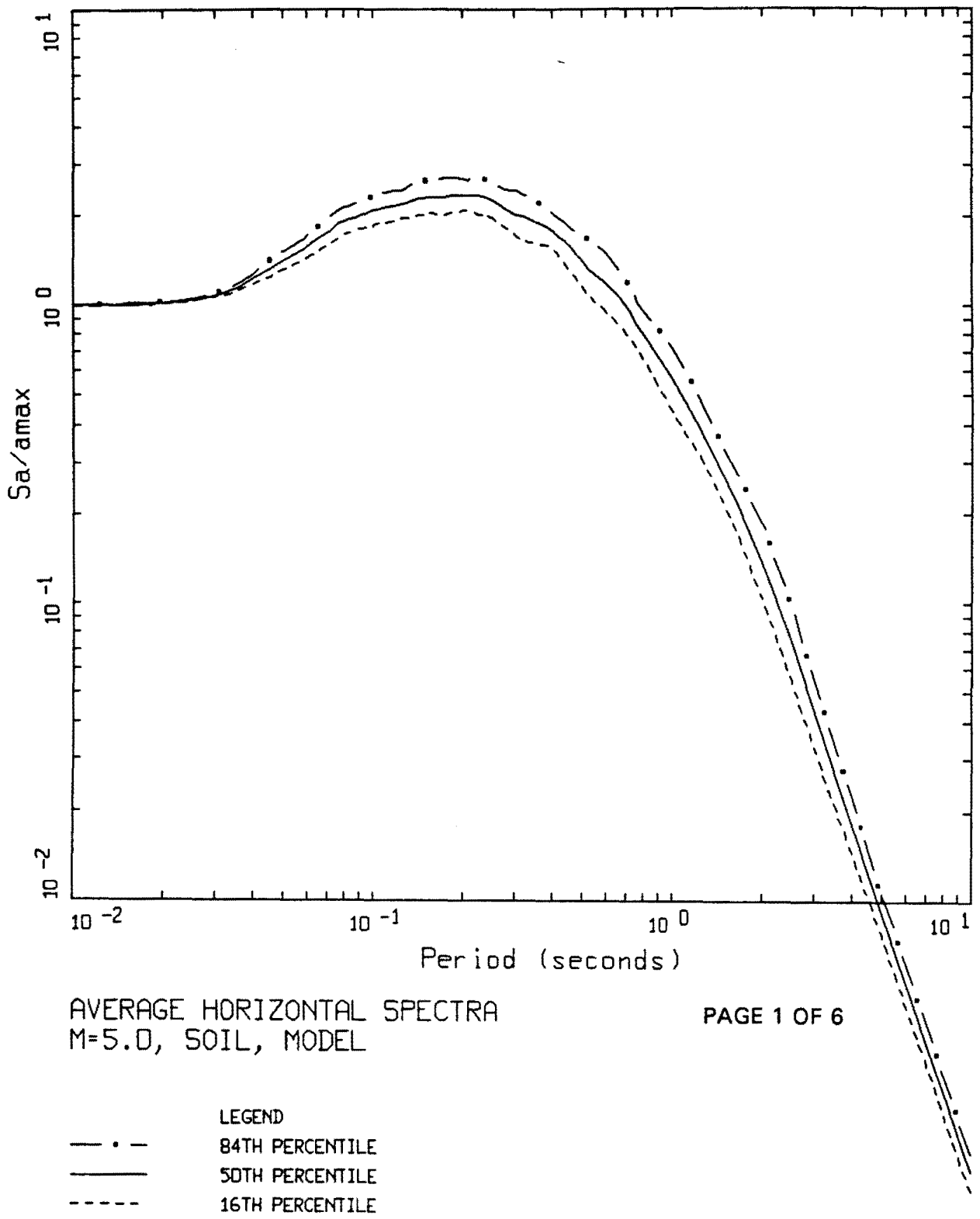

Figure Set 7.15. Median and $\pm$ 1 σ response spectral shapes computed with the point-source model computed from 30 randomly generated deep soil profiles using the correlation model of Appendix C.

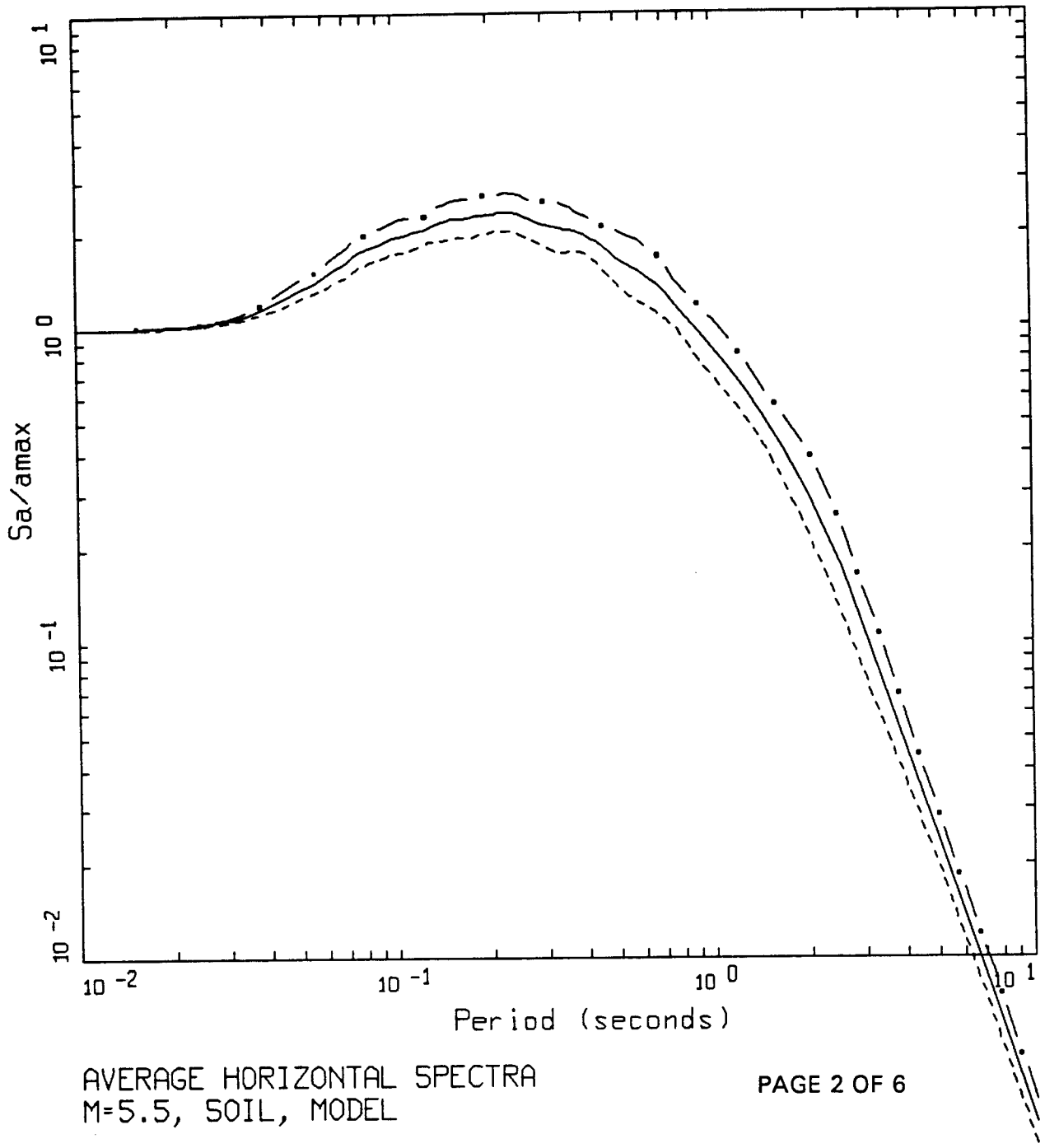

AVERAGE HORIZONTAL SPECTRA
M=5.5, SOIL, MODEL

LEGEND

— • — 84TH PERCENTILE

——— 50TH PERCENTILE

- - - - - 16TH PERCENTILE

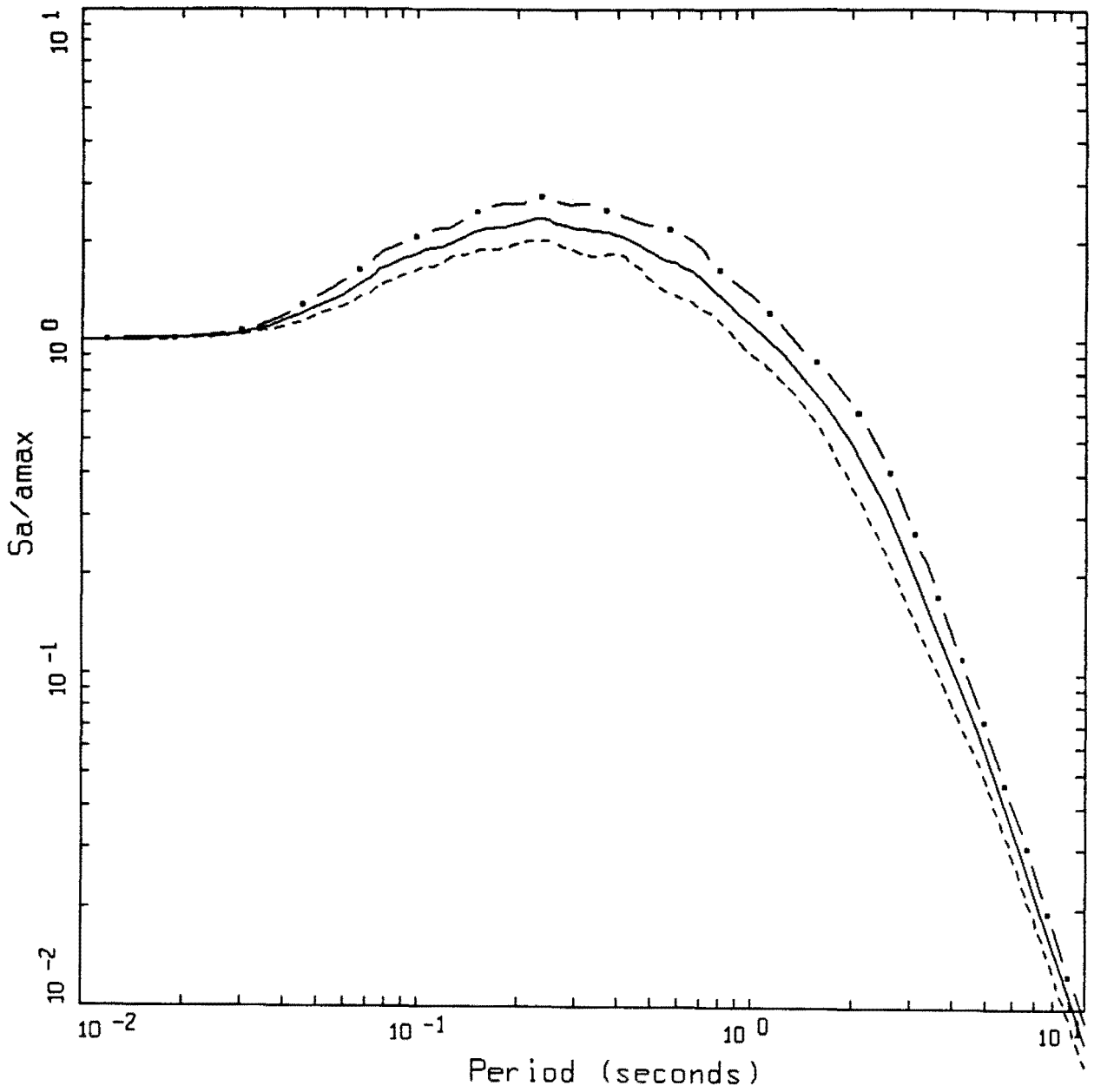

AVERAGE HORIZONTAL SPECTRA
M=6.0, SOIL, MODEL

LEGEND

— • — 84TH PERCENTILE

——— 50TH PERCENTILE

- - - - - 16TH PERCENTILE

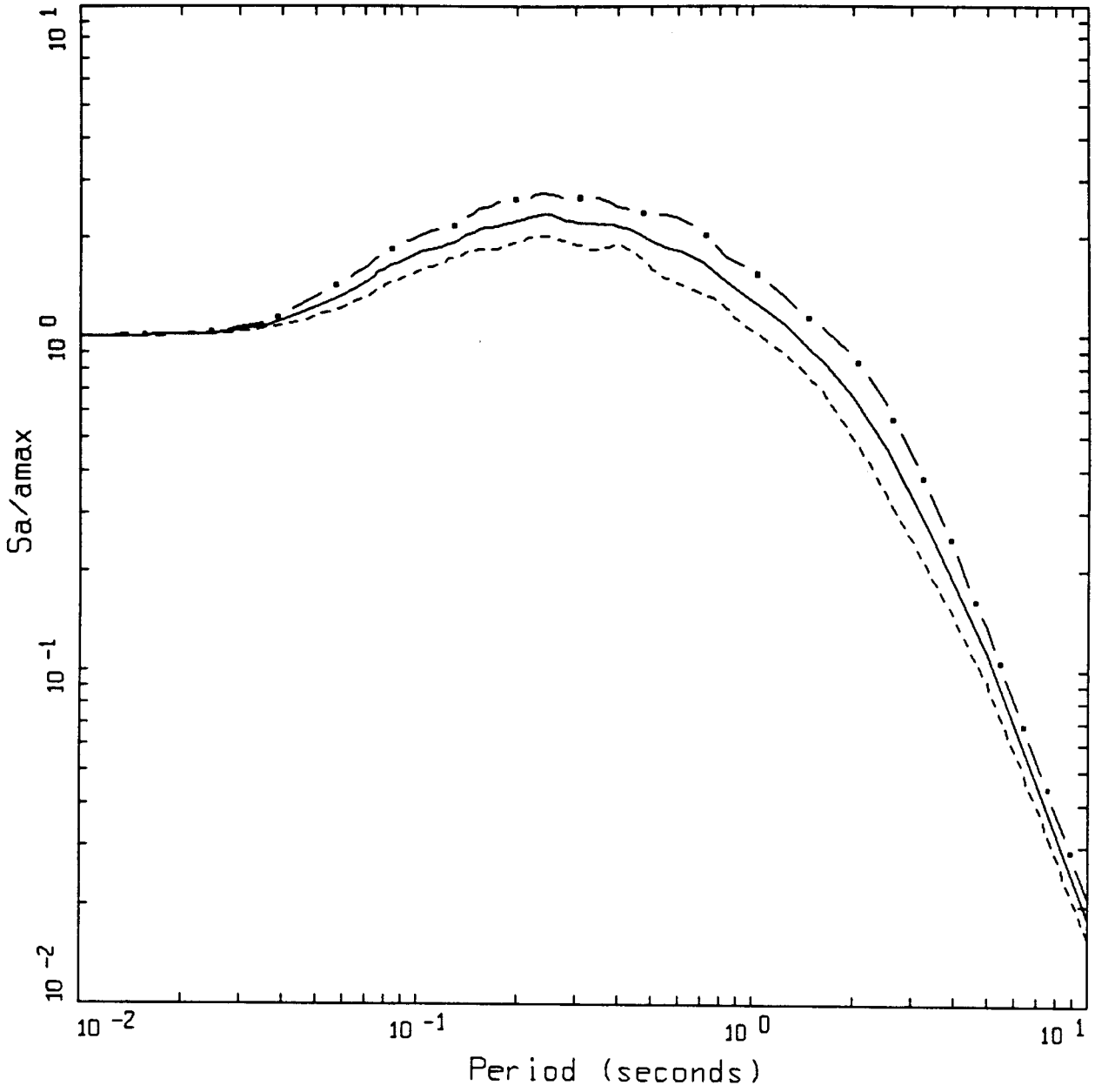

AVERAGE HORIZONTAL SPECTRA
M=6.5, SOIL, MODEL

LEGEND

— • — 84TH PERCENTILE

——— 50TH PERCENTILE

- - - - - 16TH PERCENTILE

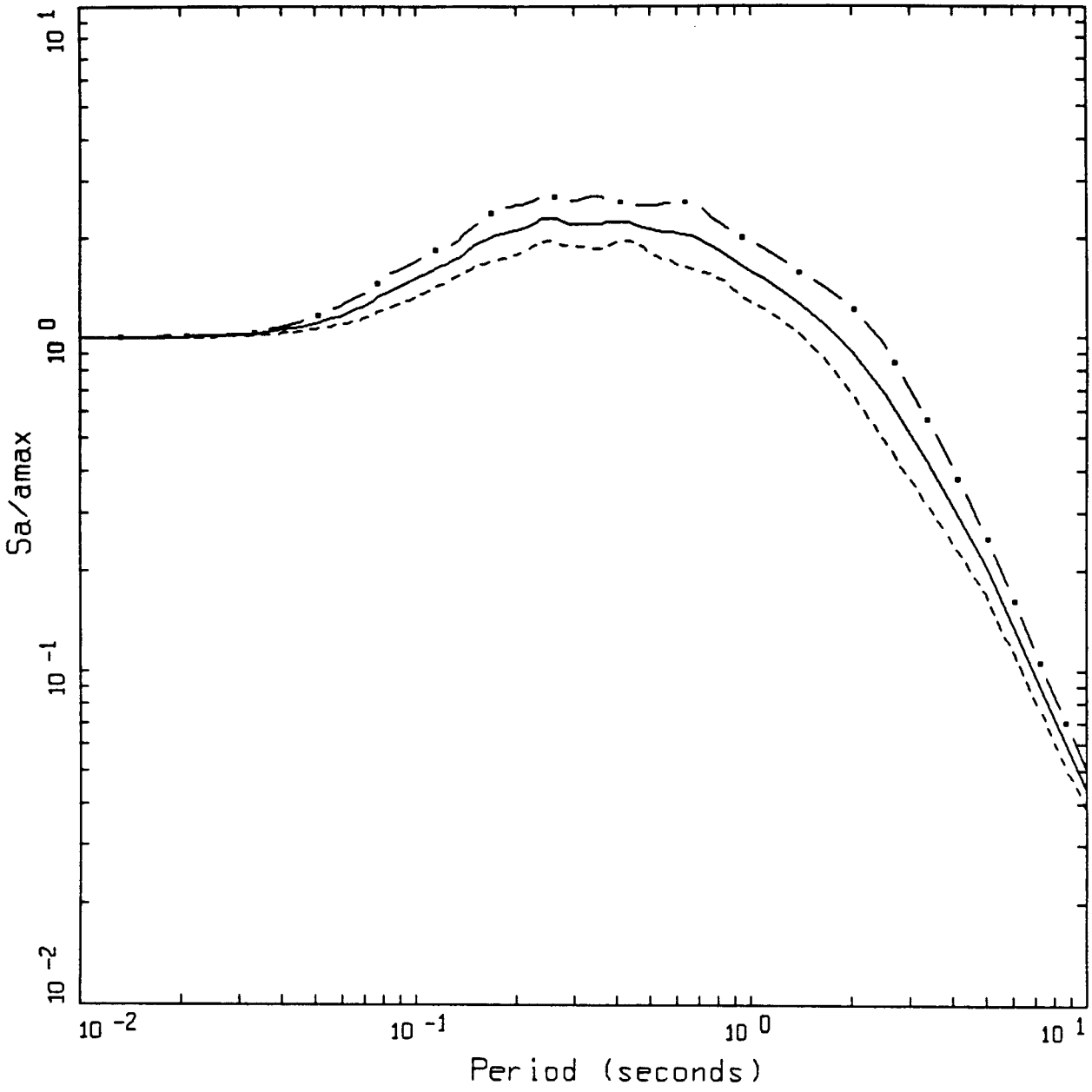

AVERAGE HORIZONTAL SPECTRA
M=7.0, SOIL, MODEL

LEGEND

— • — 84TH PERCENTILE

——— 50TH PERCENTILE

- - - - - 16TH PERCENTILE

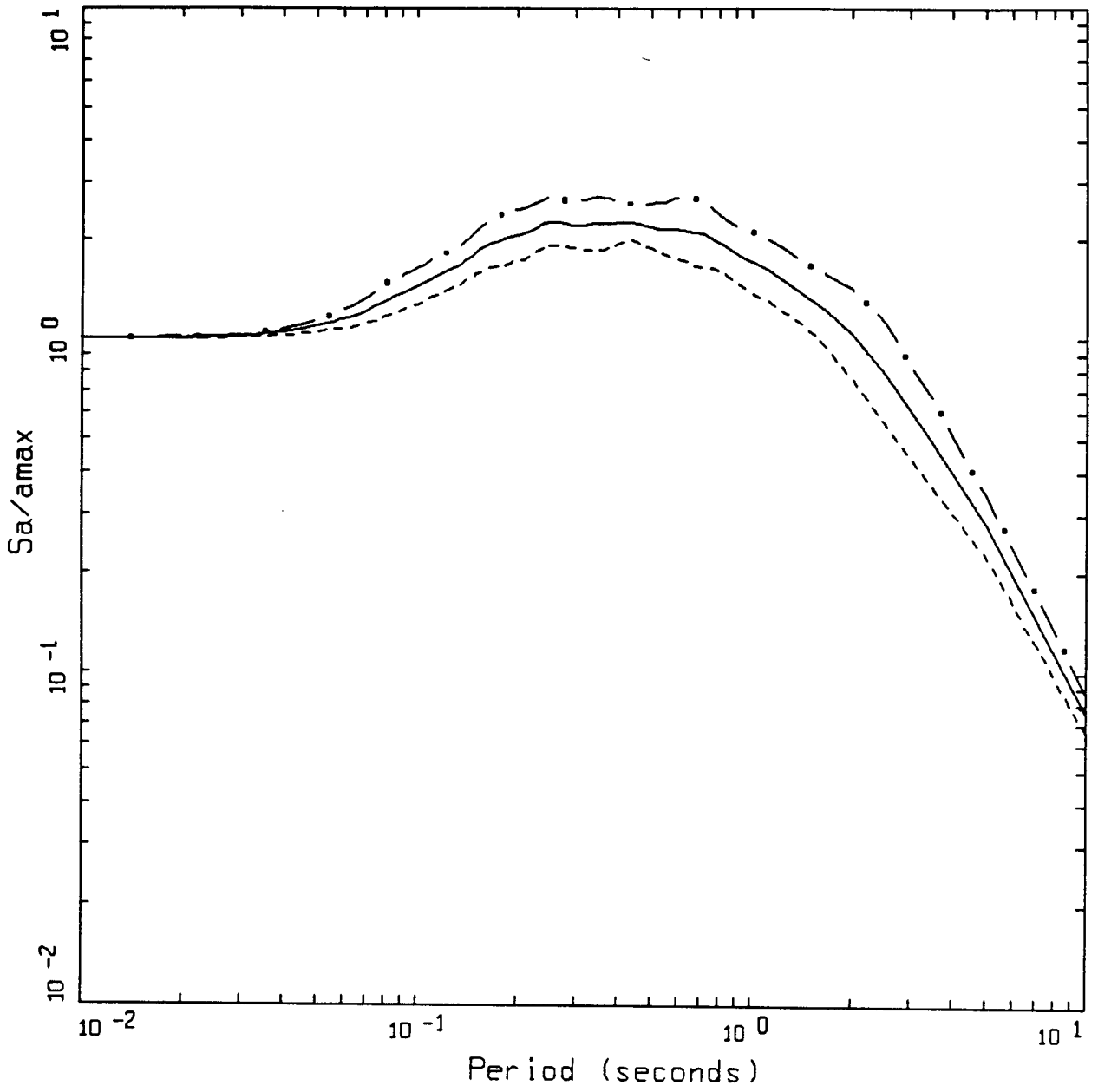

AVERAGE HORIZONTAL SPECTRA
M=7.5, SOIL, MODEL

LEGEND

— • — 84TH PERCENTILE

——— 50TH PERCENTILE

- - - - - 16TH PERCENTILE

APPENDIX A

Empirical Ground Motion Models

Empirical Ground Motion Models

by

Norman Abrahamson

Walter Silva

Draft Report

Prepared for

Brookhaven National Laboratory

May 6, 1996

Table of Contents

Section 1
Introduction

The objectiive of this study is to develop empirical models for the attenuation of response spectral values and duration for both the average horizontal and the vertical components that can be used to support the calibration/validation of the point-source and finite-fault stochastic models for numerical simulation of ground motions. These empirical models models can be used to constrain the source, path and site parameters used in the numerical simulation for the range of magnitudes, distances, and site conditions covered by the empirical data base.

Ground motion attenuation relations can be regionalized into three categories: shallow crustal earthquakes in active tectonic regions (e.g. Western North America), shallow crustal events in stable continental regions (e.g. Central and Eastern North America), and subduction zones (e.g. Pacific Northwest and Alaska). In this study, we are only considering shallow crustal events in active tectonic regions.

Section 2
Strong Motion Data Set

The data set used in this study is based on world-wide data which consists of strong ground motions from shallow crustal events near active plate margins (section 1), excluding subduction events. Events up through the 1994 Northridge earthquake are considered. In all there are 853 recordings from 98 earthquakes in the full data set.

All available recordings from events with magnitude greater than 4.5 were considered including aftershocks. Recordings with unknown or poor estimates of the magnitude, mechanism, distance, or site condition were excluded from the data set. This reduced the data set used in this analysis to 655 recordings from 58 earthquakes. The 58 events used in the analysis are listed in Table 2-1.

Record Processing

All of the records were reprocessed using a common reprocessing procedure. The correction procedure involves 5 steps:

1) interpolation of uncorrected unevenly sampled records to 400 samples/sec;
2) frequency domain low-pass filtering using a causal 5-pole Butterworth filter with the corner frequency selected for each record based on visual examination of the Fourier amplitude spectrum;
3) removing the instrument response;
4) decimating to 100 or 20 samples/sec depending on the low-pass filter corner frequency; and

5) applying a time domain baseline correction procedure and a final high-pass filter.

The baseline correction procedure uses a polynomial in degree 0-10 depending upon the initial integrated displacements. The characteristics of the high-pass filter is that of an overdamped oscillator (Grazer,1979). It is flat about its corner frequency and falls off proportional to frequency on either side. The filter is applied in the time domain twice, forward and reverse, resulting in a zero phase shift processed record. As with the polynomial baseline correction, the high-pass filter parameters are selected based on visual examination of the filtered integrated displacements for a suite of parameter values. The response spectral values are only used in the regression if the frequency is greater than 1.25 time the high-pass corner frequency and less than 1/1.25 times the low-pass corner frequency. This insures that the filter will not have a significant effect on the spectral values used in the regression. This requirement produces a data set that varies as a function of period. The number of recordings in the final data set is shown in Figure 2-1 as a function of period.

Site Classification

The site classification is based on the Geomatrix site class that is given in Table 2-2. In this study, we have combined Geomatrix site class C and D into a single deep soil site category. The Geomatrix A and B classes (rock and shallow soil) were also combined into a single "rock" site category.

Distance Definition

There are several different distance definitions that have been used for developing attenuation relations. In this study, we have used the closest

distance to the rupture plane. This is the same distance as used by Idriss (1991) and Sadigh et al. (1993). The distribution of the data in terms of magnitude and distance space is shown in Figures 2-2a-d and 2-3a-d for the horizontal and vertical components, respectively.

Table 2-1
Earthquakes Used in the Regression Analysis

Event #	Earthquake	Date & Time	Mag
6	Imperial Valley	1940 0519 0437	7.0
12	Kern County	1952 0721 1153	7.4
20	San Francisco	1957 0322 1944	5.3
25	Parkfield	1966 0628 0426	6.1
28	Borrego Mtn	1968 0409 0230	6.8
29	Lytle Creek	1970 0912 1430	5.4
30	San Fernando	1971 0209 1400	6.6
31	Point Mugu	1973 0221 1445	5.8
32	Hollister	1974 1128 2301	5.2
34	Oroville	1975 0801 2020	6.0
35	Oroville	1975 0802 2022	5.0
36	Oroville	1975 0802 2059	4.4
37	Oroville	1975 0808 0700	4.7
38	Friuli, Italy	1976 0506 2000	6.5
39	Gazli, USSR	1976 0517	6.8
41	Friuli, Italy	1976 0915 0315	6.1
42	Santa Barbara	1978 0813	6.0
43	Tabas, Iran	1978 0916	7.4
44	Coyote Lake	1979 0806 1705	5.7
45	Imperial Valley	1979 1015 2316	6.5
46	Imperial Valley	1979 1015 2319	5.2
47	Imperial Valley	1979 1016 0658	5.5
48	Livermore	1980 0124 1900	5.8
49	Livermore	1980 0127 0233	5.4
50	Anza	1980 0225 1047	4.9
57	Mammoth Lakes AS	1980 0527 1901	4.9
58	Mammoth Lakes AS	1980 0531 1516	4.9
59	Victoria, Mexico	1980 0609 0328	6.4
60	Mammoth Lakes AS	1980 0611 0441	5.0
62	Taiwan (SMART #5)	1981 0129	5.7
63	Westmorland	1981 0426 1209	5.8
66	Coalinga	1983 0502 2342	6.4
67	Coalinga	1983 0509 0249	5.0
68	Coalinga	1983 0611 0309	5.3
69	Coalinga	1983 0709 0740	5.2
70	Coalinga	1983 0722 0239	5.8
71	Coalinga	1983 0722 0343	4.9
72	Coalinga	1983 0725 2231	5.2
74	Coalinga	1983 0909 0916	5.3
76	Morgan Hill	1984 0424 2115	6.2
77	Bishop (Rnd Val)	1984 1123 1912	5.8
79	Nahanni, Canada	1985 1223	6.8

Table 2-1
Earthquakes Used in the Regression Analysis (Cont)

Event #	Earthquake	Date & Time	Mag
80	Hollister	1986 0126 1920	5.4
82	Taiwan (SMART #40)	1986 0520	6.4
83	N. Palm Springs	1986 0708 0920	6.0
84	Chalfant Valley	1986 0720 1429	5.9
85	Chalfant Valley	1986 0721 1442	6.2
86	Chalfant Valley	1986 0721 1451	5.6
87	Chalfant Valley	1986 0731 0722	5.8
89	Whittier Narrows	1987 1001 1442	6.0
90	Whittier Narrows	1987 1004 1059	5.3
91	Superstitn Hills(A)	1987 1124 0514	6.3
92	Superstitn Hills(B)	1987 1124 1316	6.7
93	Spitak, Armenia	1988 1207	6.8
94	Loma Prieta	1989 1018 0005	6.9
96	Cape Mendocino	1992 0425 1806	7.1
97	Landers	1992 0628 1158	7.3
98	Northridge	1994 0117 1231	6.7

Table 2-2
Site Classification (Geomatrix)

A	Rock (Vs > 600 m/s) or very thin soil (< 5m) over rock.
B	Shallow Soil Soil 5-20 m thick over rock
C	Deep Soil in Narrow Canyon Soil > 20 m thick Canyon < 2 km wide
D	Deep Soil in Broad Canyon Soil > 20 m thick Canyon >2 km wide
E	Soft Soil (Vs < 150 m/s)

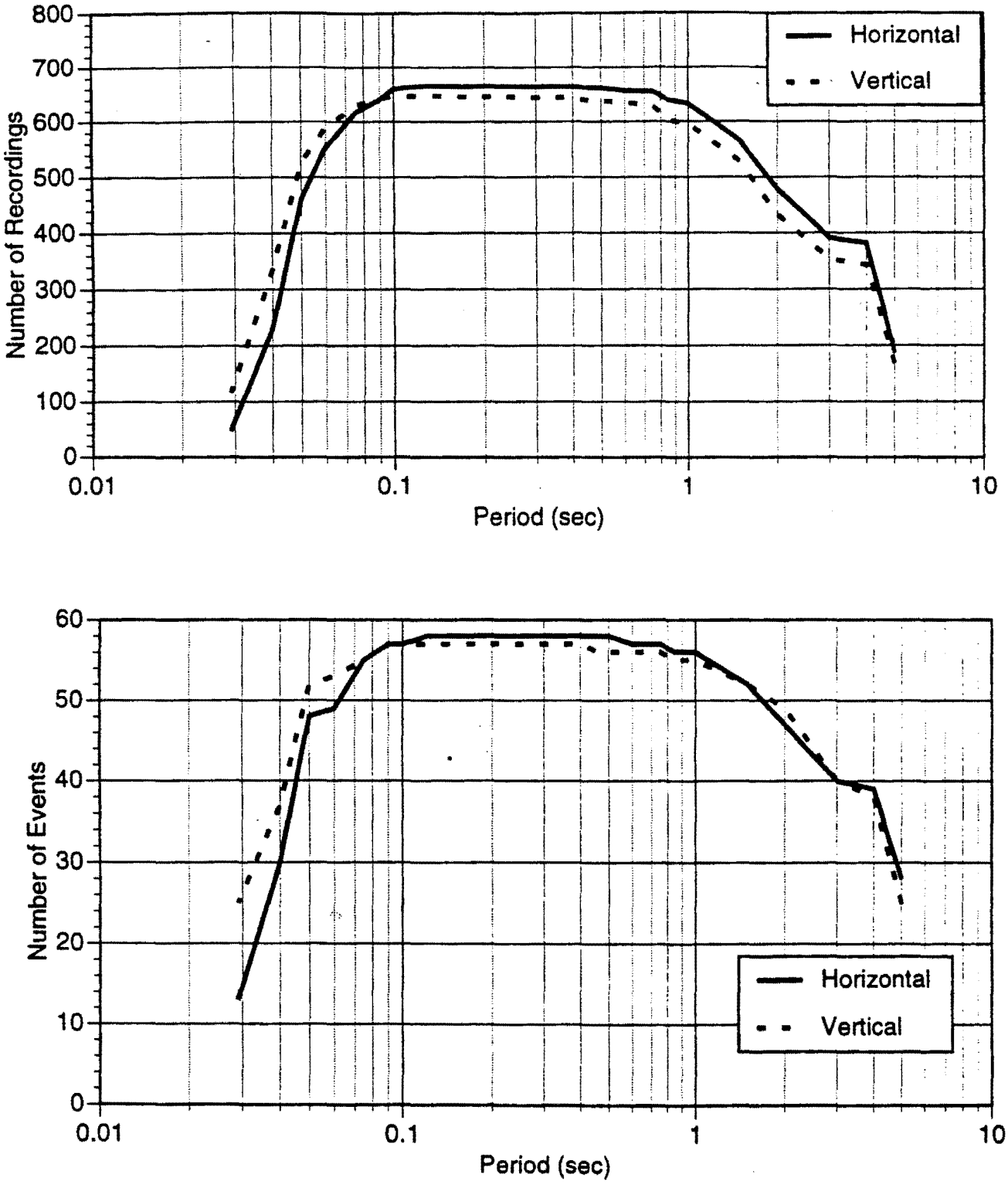

Figure 2-1. Period dependence of the number of events (lower) and number of recordings (upper) used in this study.

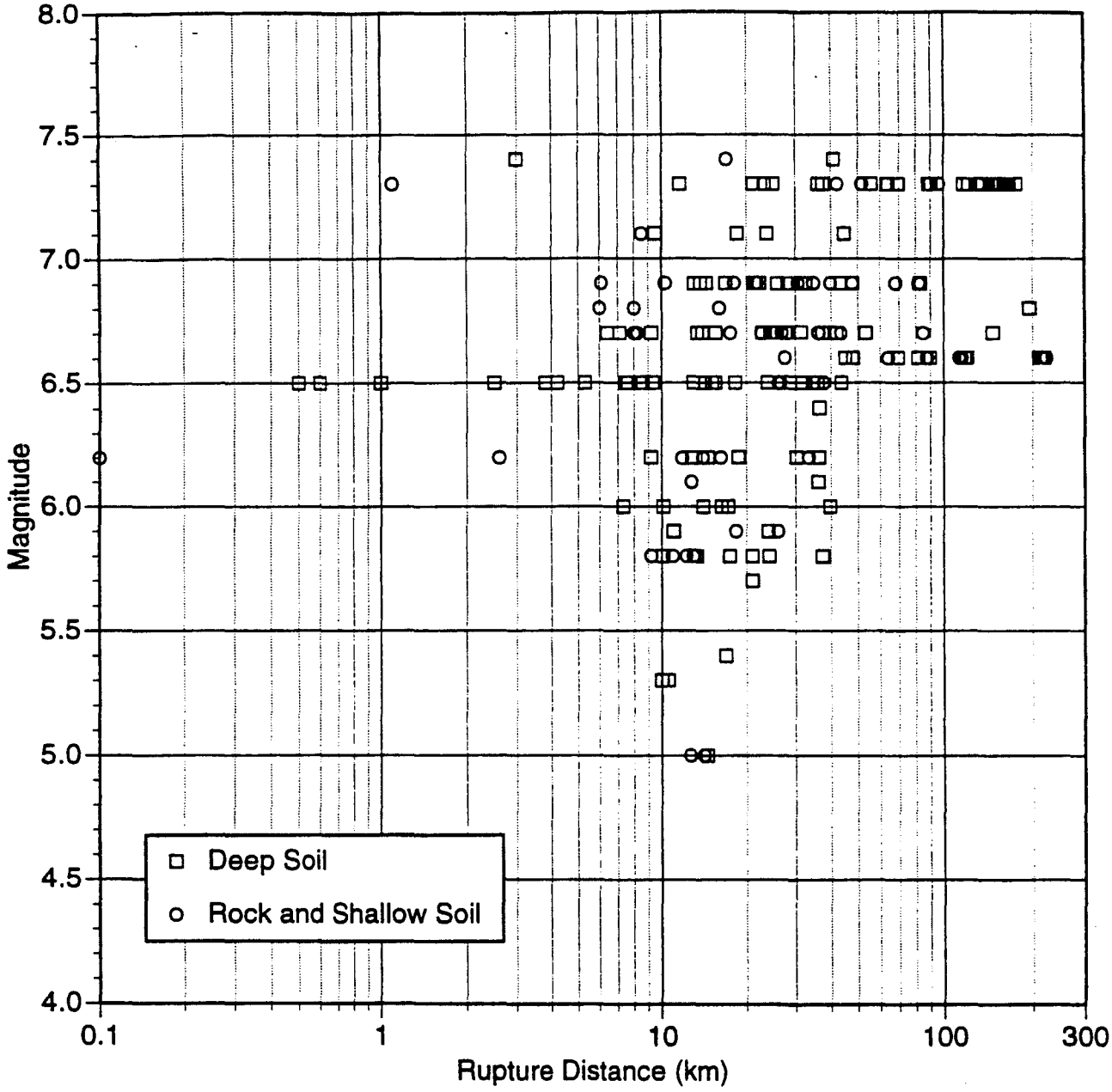

Figure 2-2a. Distribution of data for T=5.0 seconds period for the horizontal component.

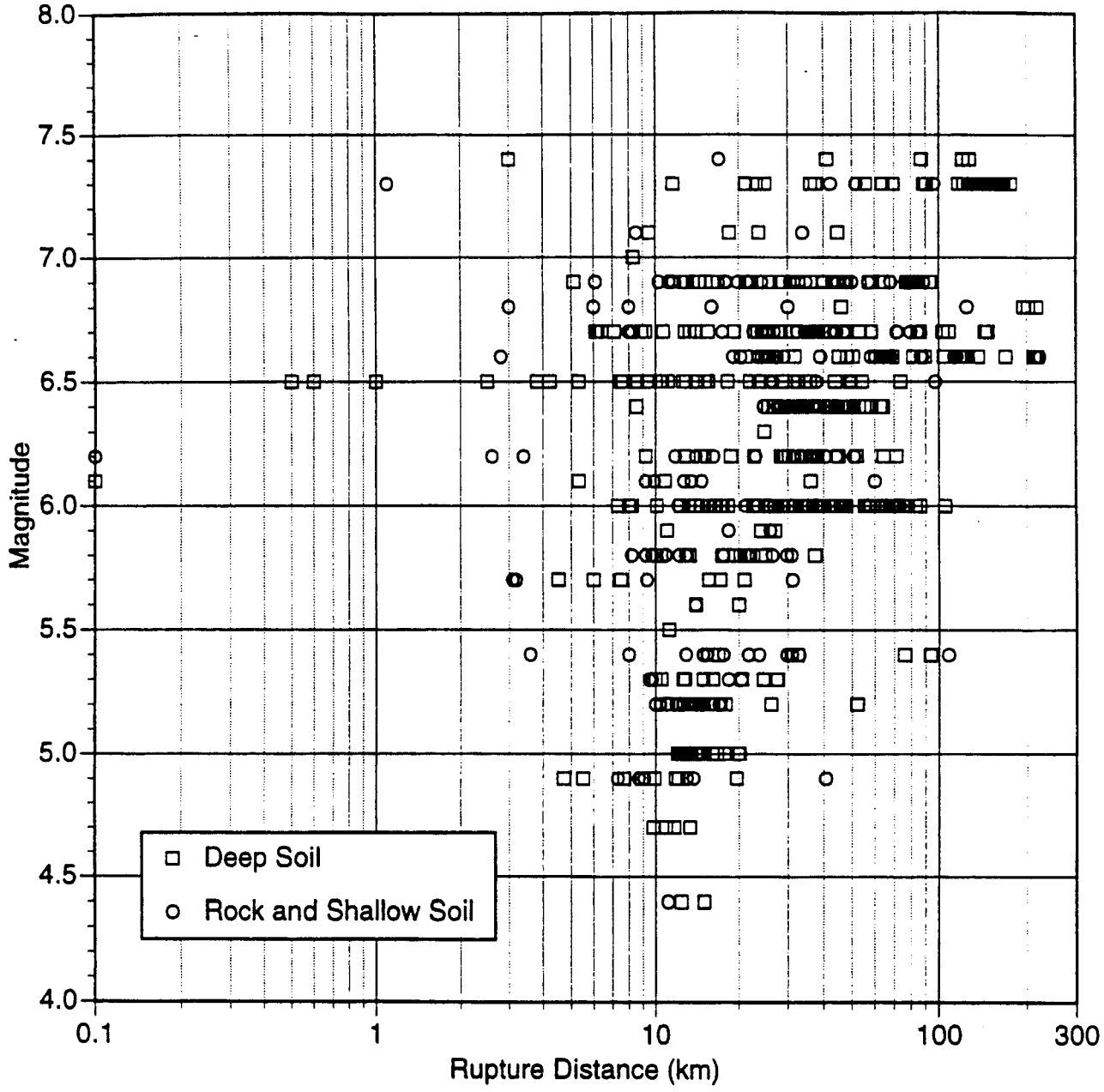

Figure 2-2b. Distribution of data for T=1.0 seconds period for the horizontal component.

T=0.2 sec

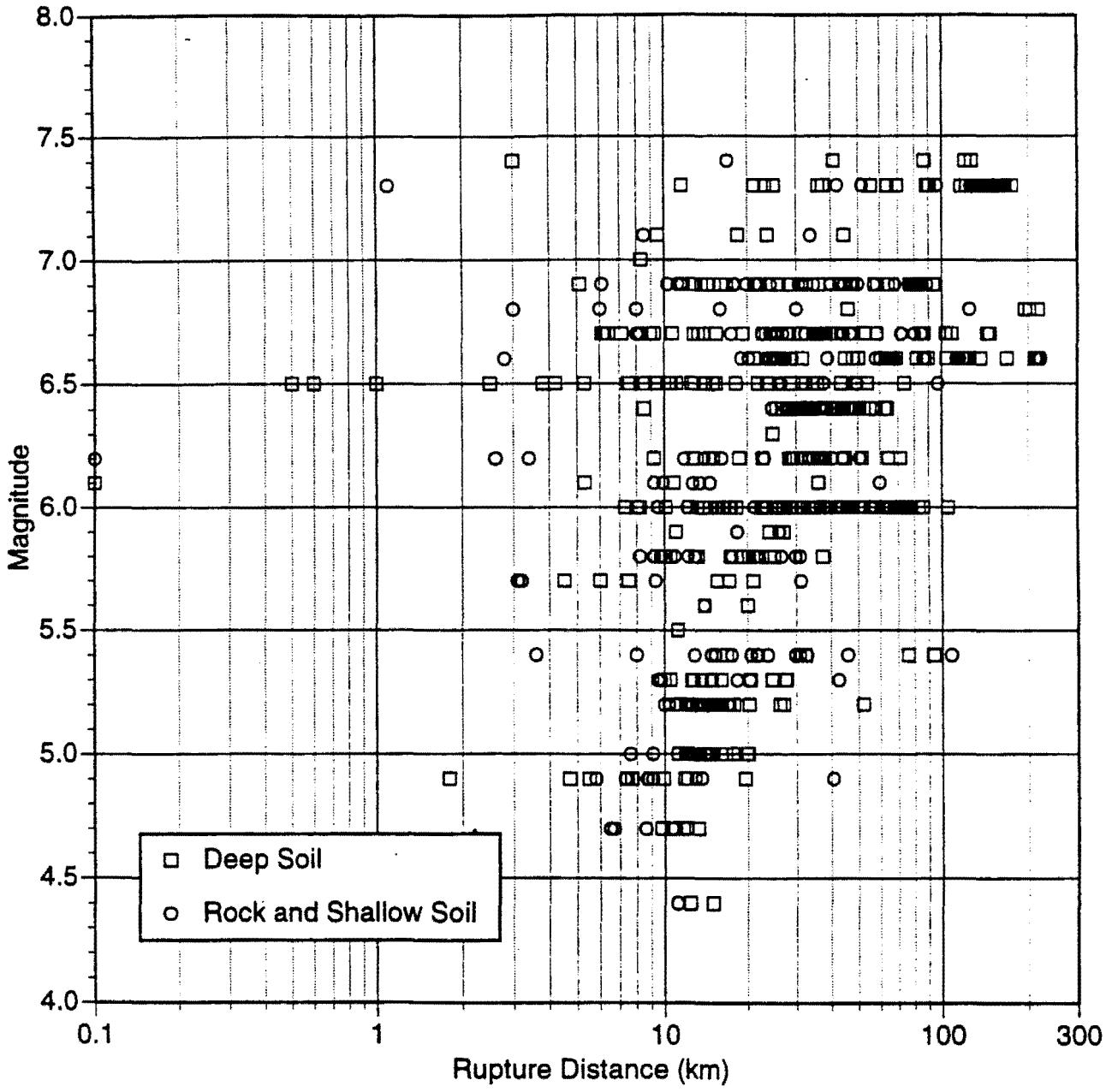

Figure 2-2c. Distribution of data for T=0.2 seconds period for the horizontal component.

T=0.075 sec

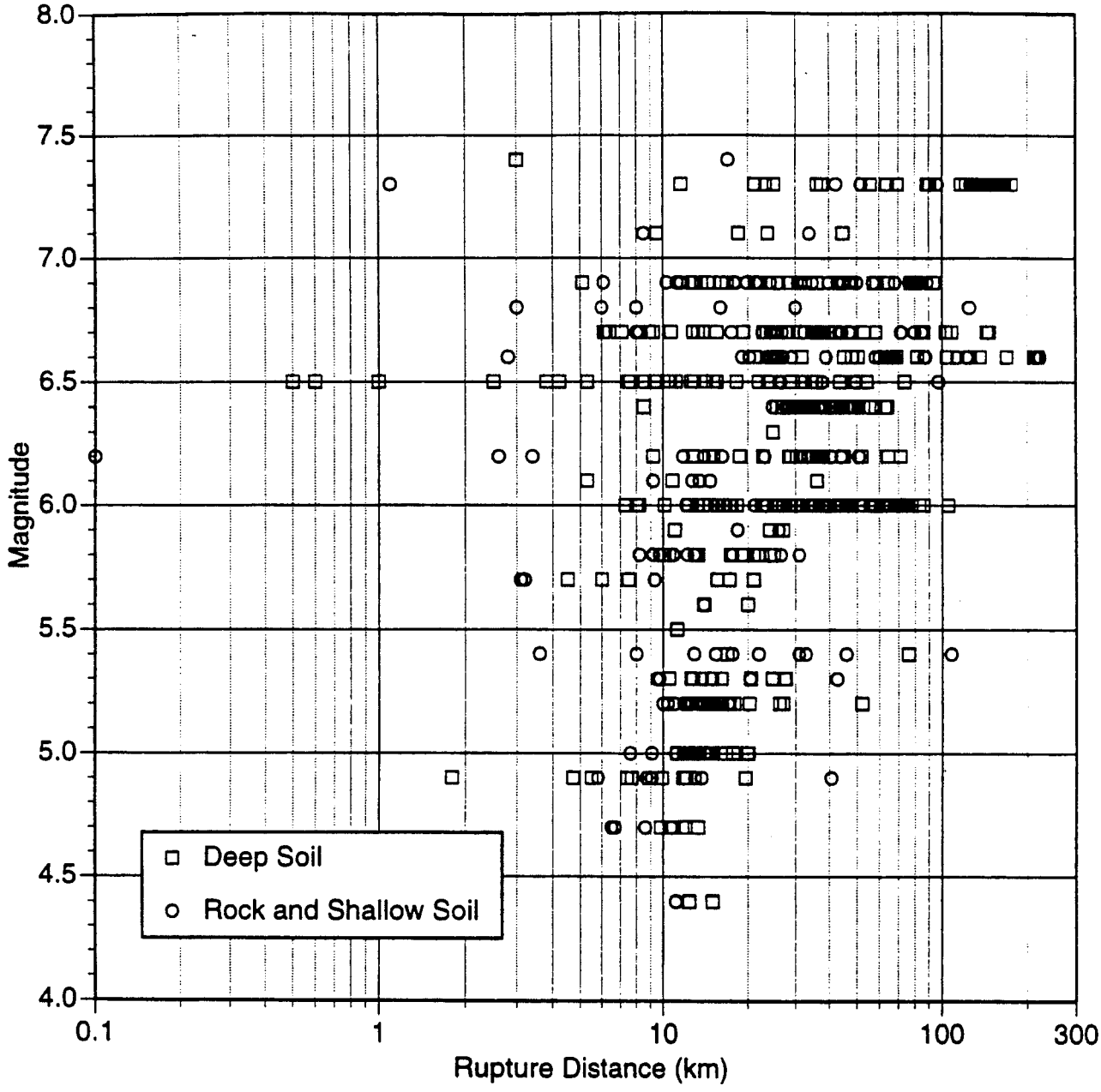

Figure 2-2d. Distribution of data for T=0.075 seconds period for the horizontal component.

T=5.0 sec

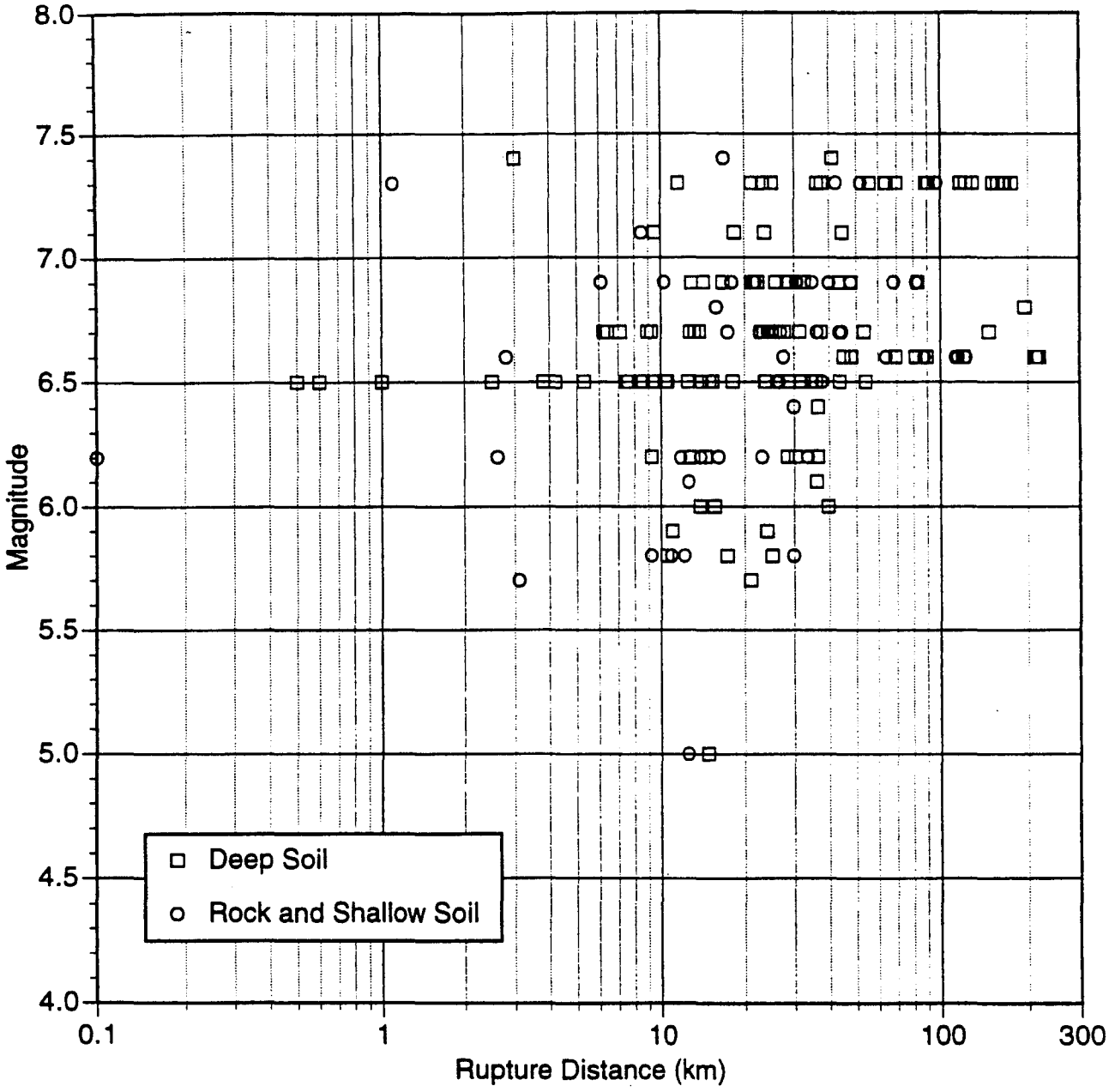

Figure 2-3a. Distribution of data for T=5.0 seconds period for the vertical component.

T=1.0 sec

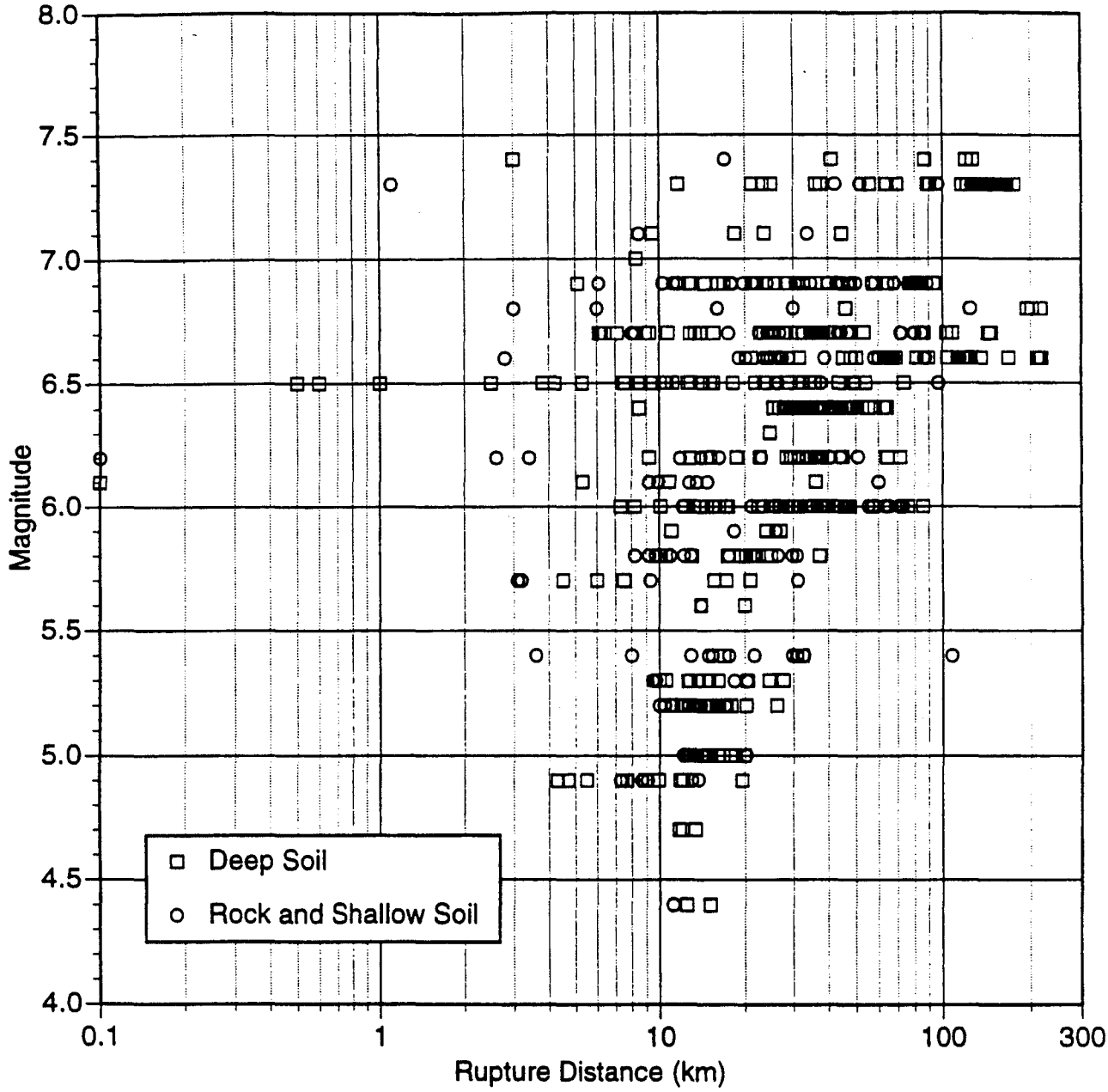

Figure 2-3b. Distribution of data for T=1.0 seconds period for the vertical component.

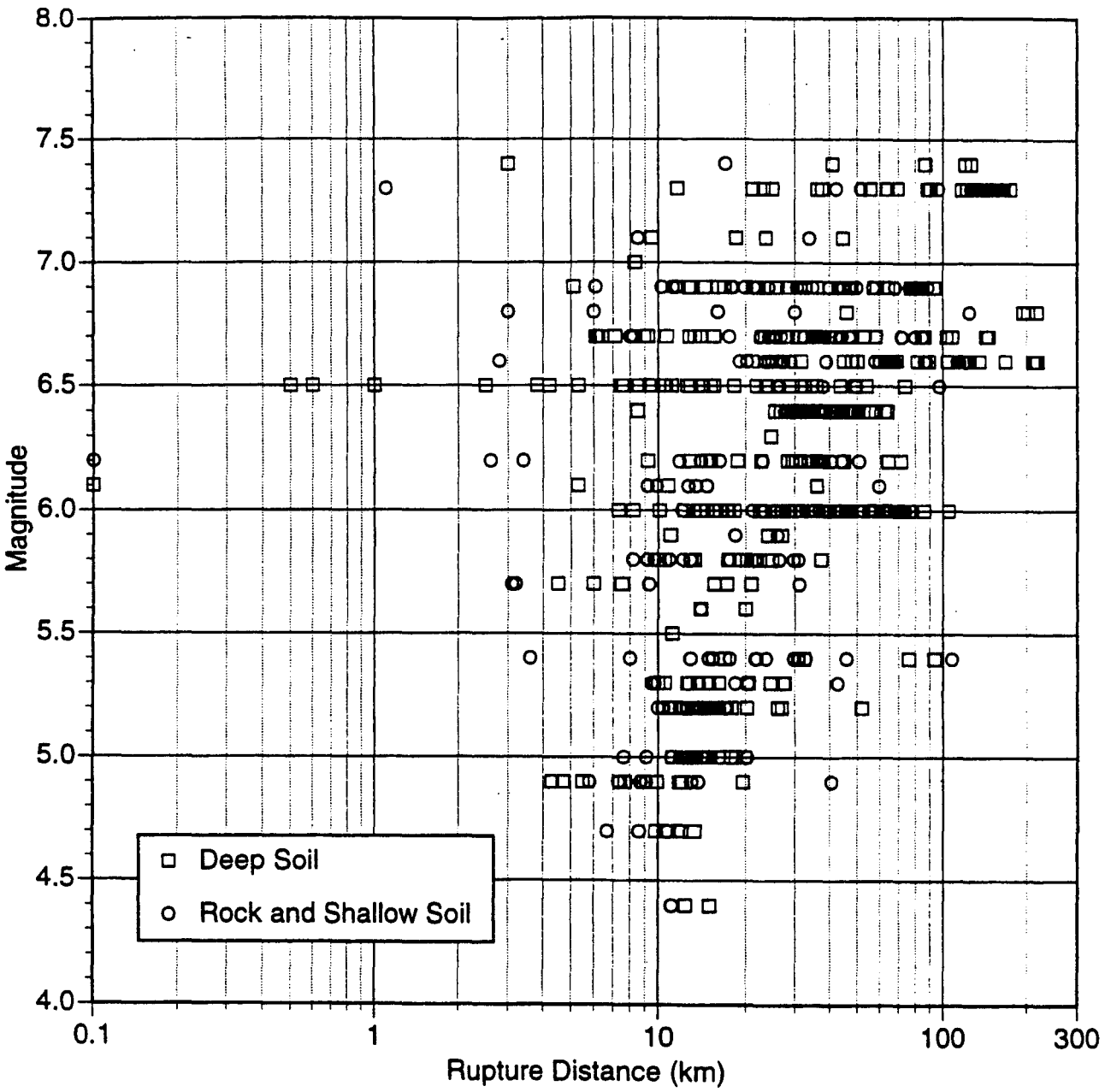

Figure 2-3c. Distribution of data for T=0.2 seconds period for the vertical component.

T=0.075 sec

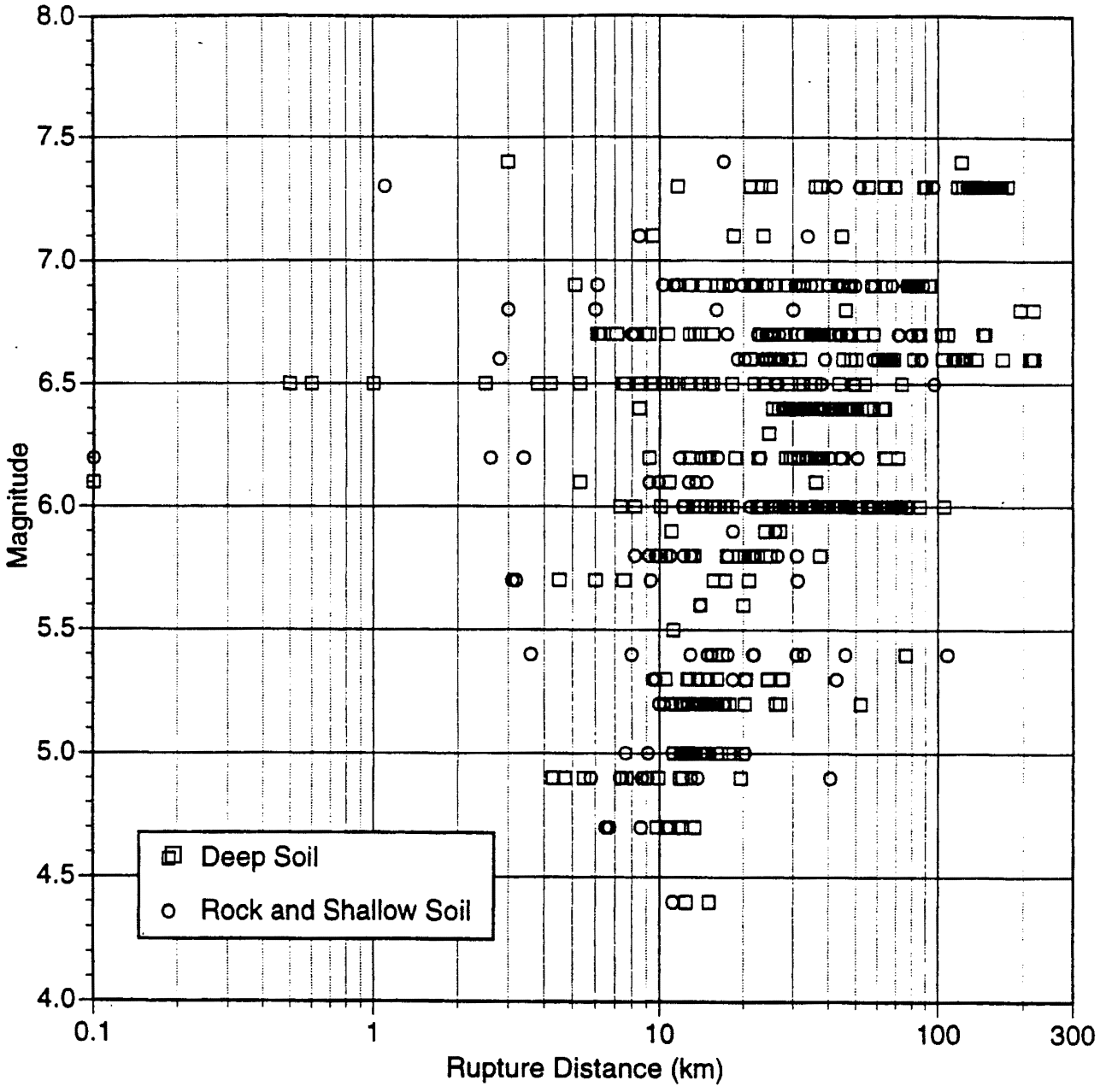

Figure 2-3d. Distribution of data for T=0.075 seconds period for the vertical component.

Section 3
Attenuation Relations

The strong motion data base described in Section 2 is used to develop attenuation relations for response spectral values for both the average horizontal and vertical components.

Regression Method

The regression analysis uses the random effects model. The random effects model is a maximum likelihood method that accounts for correlations in the data recorded by a single earthquake. For example, if an earthquake has a higher than average stress-drop, then the ground motions at all sites from this event are expected to be higher than average. We use the procedure described by Abrahamson and Youngs (1992) to apply the random effect model.

The Joyner and Boore (1981) two-step method also considers the correlation in the data from a single earthquake by explicitly estimating an event term for each event in the first step. Like the two-step method, the random effect model produces two standard errors: an inter-event term (τ) and intra-event term (σ). There two standard errors are then combined to give the total standard error. The random effects model differs from the two-step method described by Joyner and Boore (1981) in that it considers that for events with only a few recordings, part of the mean event term may be due to random variations of the data (intra-event variations) and poor sampling of the event. As described by Abrahamson and Youngs (1992), for poorly sampled events, the random effects method estimates how much of the event term is likely to be due to random sampling of the intra-event distribution and how much is likely to be due to systematic differences between the event and

the average. If all of the events have a large number of recordings, then the two-step method and the random effects method become equivalent.

Regression Model

In developing the functional form of the regression equation, we combined features of the regression equations that have been used in different previous studies. The general functional form that we consider is given by:

$$\ln Sa(g) = f_1(m,r) + F\, f_3(m) + HW\, f_4(m,r) + S\, f_5(\widehat{pga}_{rock}) \qquad (3\text{-}1)$$

where m is moment magnitude, r is the closest distance to the rupture plane in km, F is the fault type (1 for reverse, 0.5 for reverse/oblique, and 0 otherwise), HW is the dummy variable for hanging wall sites (1 for sites over the hanging wall, 0 otherwise), and S is a dummy variable for the site class (0 for rock or shallow soil, 1 for deep soil). For the horizontal component, the geometric mean of the two horizontals is used.

The function $f_1(m,r)$ is the basic functional form of the attenuation for strike-slip events recorded at rock sites. For $f_1(m,r)$, we have used the following form:

$$f_1(m,r) = \begin{cases} a_1 + a_2(m-m_1) + a_{12}(8.5-m)^n + [a_3+a_{13}(m-m_1)]\ln(R) & \text{for } m \le m_1 \\ a_1 + a_4(m-m_1) + a_{12}(8.5-m)^n + [a_3+a_{13}(m-m_1)]\ln(R) & \text{for } m > m_1 \end{cases} \qquad (3\text{-}2)$$

where

$$R = \sqrt{r^2 + c_4^2}. \qquad (3\text{-}3)$$

This form is a composite of several previous studies. The slope of the log distance term is magnitude dependent as was used by Idriss (1991). The Idriss model differs from our model in that it uses exponential models for the magnitude dependence of the slope whereas we have used a linear dependence. The saturation of high frequency ground motion at short distances is accommodated by the magnitude dependent slope.

For long periods, the a linear magnitude dependence is not adequate. Most recent studies have found that higher order terms are needed. Boore et al include a quadratic term; Campbell (1993) includes a hyperbolic arctangent term, Idriss (1991) includes an exponential magnitude term, and Sadigh et al (1993) includes a higher order polynomial term. A notable exception is the recent Crouse model (no ref) which uses only a linear term. However, this model has very little data below magnitude 6 which may not provide a wide enough magnitude range to resolve the higher order terms. These difference models give fairly similar functional forms when fit to the same data. We have adopted the functional form used by Sadigh et al. (1993).

For the distance term inside the log, we have used the $\sqrt{r^2+c_4^2}$ model similar to that used by Boore et al. In the Boore et al. model, the c_4 term can be interpreted as a fictitious depth. In our model, however, we are using the rupture distance for r (which can include depth for dipping faults and for fault that do not reach the surface), so the interpretation of c_4 as a depth term is not clear. Nevertheless, we have adopted the $\sqrt{r^2+c_4^2}$ model because it yields a marginally better fit to the data.

Style-of-Faulting Factor

The distinction between ground motions from strike-slip and reverse faults was introduced by Campbell (1982) and has become common in recent attenuation relations (e.g. Idriss, 1991; Sadigh et al. 1993; Boore et al., 1995, Campbell, 1994). The difference in ground motion between reverse and strike-slip events is called the style-of-faulting factor. Most attenuation relations have considered a constant style-of-faulting factor that applies to all magnitudes and distances. Sadigh et al. (1993) and Campbell (1994) included a magnitude and distance dependence of the style-of-faulting

In this study, we have used a functional form that allows for a magnitude and period of the style-of-faulting factor:

$$f_3(m) = \begin{cases} a_5 & \text{for } m \le 5.8 \\ a_5 + \dfrac{(a_6-a_5)}{m_1-5.8}(m-5.8) & \text{for } 5.8 < m < m_1 \\ a_6 & \text{for } m \ge m_1 \end{cases} \qquad (3\text{-}4)$$

Hanging Wall Effect

We also followed the approach used by Somerville and Abrahamson (1995) to model the differences in the motion on the hanging wall and foot wall of dipping faults. In this previous study, a comparison was made between the ground motions for sites on the hanging wall with those on the foot wall and with those off the ends of the fault rupture. A significant systematic increase in ground motions was found for sites over the hanging wall, but the decrease in ground motion for sites on the foot wall was not as systematic. As a result, the ground motion fro dipping faults was separated into two categories: sites on the hanging wall side of the rupture and

within the edge of the rupture, and sites on the foot wall side or off the end of the rupture. The hanging wall effect is considered to be primarily a geometric effect that results from this distance definition used in this study. The magnitude and distance dependence of the functional form, $f_4(m,r)$, for the hanging wall effect is taken from Somerville and Abrahamson (1995) and is modeled as separable in magnitude and distance so that

$$f_4(m,r) = f_{HW}(m)\, f_{HW}(r) \tag{3-5}$$

where

$$f_{hw}(m) = \begin{cases} 0 & \text{for } m \le 5.5 \\ m-5.5 & \text{for } 5.5 < m < 6.5 \\ 1 & \text{for } m \ge 6.5 \end{cases} \tag{3-6}$$

and

$$f_{hw}(r) = \begin{cases} 0 & r<4 \\ a_9(r-4)/4 & 4 < r < 8 \\ a_9 & 8 < r < 18 \\ a_9(1-(r-18)/7) & 18 < r < 25 \\ 0 & 25 < r \end{cases} \tag{3-7}$$

Site Response

A key aspect is the use of a functional form that accommodates non-linear soil response. We followed the approach used by Youngs (1993) in which the soil amplification is a function of the expected peak acceleration on rock. This approach allows a single regression for both soil and rock while preserving the differences between soil and rock attenuation.

The non-linear soil response is modeled by

$$f_5(\widehat{PGA}_{rock}) = a_{10} + a_{11} \ln(\widehat{PGA}_{rock} + c_5) \quad (3\text{-}8)$$

where $\widehat{PGA}_{rock}$ is the expected peak acceleration on rock in g (as predicted by the attenuation relation with S=0). A similar functional form was proposed by Youngs (1993); the only difference here is the addition of the c_5 term.

Standard Error

Several recent attenuation studies have found that the standard error is dependent on the magnitude of the earthquake (Sadigh, 1993; Idriss, 1991; Campbell, 1993) or is dependent on the level of shaking (Campbell and Borzognia, 1994). This issue is discussed at length in Youngs et al (1995).

In this study, both the inter-event (τ) and intra-event (σ) standard errors are allowed to be magnitude dependent and are modeled as follows:

$$\sigma(m) = \begin{cases} b_1 & \text{for } m \le 5.0 \\ b_1 - b_2(m-5) & \text{for } 5.0 < m < 7.0 \\ b_1 - 2b_2 & \text{for } m \ge 7.0 \end{cases} \quad (3\text{-}9)$$

and

$$\tau(m) = \begin{cases} b_3 & \text{for } m \le 5.0 \\ b_3 - b_4(m-5) & \text{for } 5.0 < m < 7.0 \\ b_3 - 2b_4 & \text{for } m \ge 7.0 \end{cases} \quad (3\text{-}10)$$

The magnitude dependence of the standard error is estimated using the random effects model which avoids underestimating the standard error for large magnitude

events due to the fewer number of events (as compared to small and moderate magnitude events).

The total standard error is then computed by adding the variance of the two error terms. The total standard error was then smoothed and fit to the form

$$\sigma_{total}(m) = \begin{cases} b_5 & \text{for } m \leq 5.0 \\ b_5 - b_6(m-5) & \text{for } 5.0 < m < 7.0 \\ b_5 - 2b_6 & \text{for } m \geq 7.0 \end{cases} \qquad (3\text{-}11)$$

Sa vs Sa/pga

In many previous studies for response spectral attenuation, the regression has been separated into two steps: a regression for the peak acceleration and a regression for the normalized spectral shape. This approach the advantage that the spectral shape is only weakly dependent on distance for distances less than 50 km. Therefore, the distance attenuation rate for spectral values should be close to the distance attenuation rate for peak acceleration. By fitting the normalized spectral, the magnitude dependence of the spectral shape can easily be seen. One assumption that is usually made with this approach is that the magnitude saturation term (term inside the log) for spectral acceleration is the same as for peak acceleration. This assumption greatly simplifies the functional form of the normalized spectral shape. This assumption is the biggest potential drawback of using the normalized spectra approach. The Boore et al. model shows that the c_4 term is period dependent. If a period dependent c_4 term is used, then you have lost most of the advantage of using normalized spectral shapes.

We have dealt with this issue by fitting the Sa values directly (not normalized shapes) but restricting some of the coefficients to be independent of period. Reducing the number of coefficients that are period dependent helps to keep the spectral smoothly varying functions of distance, magnitude, and period without introducing bumps into the spectrum.

Regression Results - Horizontal Component

The regression is computed using multiple steps. The multiple steps are used to constrain the resulting model to be a smooth function of period for all magnitudes, distances, mechanisms and site conditions. In each step, we smoothed the coefficients that were reasonably uncorrelated with each other. For highly correlated coefficients, one coefficient was smoothed and then the other coefficients were re-estimated.

In the first step, the peak acceleration is fit to Eq. (3-1) with a_{12} set to zero. The values of a_{13}, a_2, and a_4 are then fixed for the subsequent spectral values regression. In the second step, the spectral acceleration values are fit to Eq. (3-1). In the third step, the c_4 term was held fixed, and all of the other model parameters were estimated. Following this step, smoothed models were fit to the period dependence of the a_3, a_5, a_6, a_9, a_{11}, and a_{12} coefficients. In the fourth step, the all coefficients except a_{10} and a_1 were fixed. The resulting values of a_{10} were then fit to a smooth model. In the fifth step, all coefficients except a_1 were held fixed and new a_1 values were estimated. The final smoothing on a1 considered that the model should produce smooth spectra for spectral velocity and displacement as well as for spectral acceleration. The final smoothed coefficients are listed in Table 3-1.

The magnitude dependence of the standard errors for the final fit was then evaluated. The raw estimates of the inter-event and intra-event standard errors were combined to estimate the total standard error. A smoothed model was then fit to these total standard errors to produce the final model for the standard error (Table 3-2).

The residuals of the model as shown in Figures 3-1a,c and 3-2a,c for periods of 1.0, 0.3, and 0.1 seconds. Since we are using the random effects model, there are two parts to the residual: an intra-event term and an inter-event term. These residuals are shown separately in Figures 3-1 and 3-2.

Regression Results - Vertical Component

The model for the vertical component was developed using the same functional form and multiple step procedure as for the horizontal component. The final smoothed model coefficients are listed in Table 3-3. The smoothed standard errors are listed in Table 3-4. The residuals for periods of 1.0, 0.3, and 0.1 sec are shown in Figures 3-3a,c and 3-4a,c.

Model Predictions

Examples of the median ground motions for strike-slip events are shown in Figures 3-5 and 3-6 for the horizontal component and in Figures 3-7 and 3-8 for the vertical component.

Table 3-1. Coefficients for the Average Horizontal Component

period	c4	a1	a2	a3	a4	a5	a6	a9	a10	a11	a12	a13	m1	c5	n
5.00	3.50	-1.460	0.512	-0.7250	-0.144	0.400	-0.200	0.000	0.664	0.040	-0.2150	0.17	6.4	0.03	2
4.00	3.50	-1.130	0.512	-0.7250	-0.144	0.400	-0.200	0.039	0.640	0.040	-0.1956	0.17	6.4	0.03	2
3.00	3.50	-0.690	0.512	-0.7250	-0.144	0.400	-0.156	0.089	0.630	0.040	-0.1726	0.17	6.4	0.03	2
2.00	3.50	-0.150	0.512	-0.7250	-0.144	0.400	-0.094	0.160	0.610	0.040	-0.1400	0.17	6.4	0.03	2
1.50	3.55	0.260	0.512	-0.7721	-0.144	0.438	-0.049	0.210	0.600	0.040	-0.1200	0.17	6.4	0.03	2
1.00	3.70	0.828	0.512	-0.8383	-0.144	0.490	0.013	0.281	0.423	0.000	-0.1020	0.17	6.4	0.03	2
0.85	3.81	1.020	0.512	-0.8648	-0.144	0.512	0.038	0.309	0.370	-0.028	-0.0927	0.17	6.4	0.03	2
0.75	3.90	1.160	0.512	-0.8852	-0.144	0.528	0.057	0.331	0.320	-0.050	-0.0862	0.17	6.4	0.03	2
0.60	4.12	1.428	0.512	-0.9218	-0.144	0.557	0.091	0.370	0.194	-0.089	-0.0740	0.17	6.4	0.03	2
0.50	4.30	1.615	0.512	-0.9515	-0.144	0.581	0.119	0.370	0.085	-0.121	-0.0635	0.17	6.4	0.03	2
0.46	4.38	1.717	0.512	-0.9652	-0.144	0.592	0.132	0.370	0.020	-0.136	-0.0594	0.17	6.4	0.03	2
0.40	4.52	1.860	0.512	-0.9880	-0.144	0.610	0.154	0.370	-0.065	-0.160	-0.0518	0.17	6.4	0.03	2
0.36	4.62	1.955	0.512	-1.0052	-0.144	0.610	0.170	0.370	-0.123	-0.173	-0.0460	0.17	6.4	0.03	2
0.30	4.80	2.114	0.512	-1.0350	-0.144	0.610	0.198	0.370	-0.219	-0.195	-0.0360	0.17	6.4	0.03	2
0.24	4.97	2.293	0.512	-1.0790	-0.144	0.610	0.232	0.370	-0.350	-0.223	-0.0238	0.17	6.4	0.03	2
0.20	5.10	2.406	0.512	-1.1150	-0.144	0.610	0.260	0.370	-0.445	-0.245	-0.0138	0.17	6.4	0.03	2
0.17	5.19	2.430	0.512	-1.1350	-0.144	0.610	0.260	0.370	-0.522	-0.265	-0.0040	0.17	6.4	0.03	2
0.15	5.27	2.407	0.512	-1.1450	-0.144	0.610	0.260	0.370	-0.577	-0.280	0.0050	0.17	6.4	0.03	2
0.12	5.39	2.272	0.512	-1.1450	-0.144	0.610	0.260	0.370	-0.591	-0.280	0.0180	0.17	6.4	0.03	2
0.10	5.50	2.160	0.512	-1.1450	-0.144	0.610	0.260	0.370	-0.598	-0.280	0.0280	0.17	6.4	0.03	2
0.09	5.54	2.100	0.512	-1.1450	-0.144	0.610	0.260	0.370	-0.609	-0.280	0.0300	0.17	6.4	0.03	2
0.075	5.58	2.037	0.512	-1.1450	-0.144	0.610	0.260	0.370	-0.628	-0.280	0.0300	0.17	6.4	0.03	2
0.06	5.60	1.940	0.512	-1.1450	-0.144	0.610	0.260	0.370	-0.665	-0.280	0.0300	0.17	6.4	0.03	2
0.05	5.60	1.870	0.512	-1.1450	-0.144	0.610	0.260	0.370	-0.620	-0.267	0.0280	0.17	6.4	0.03	2
0.04	5.60	1.780	0.512	-1.1450	-0.144	0.610	0.260	0.370	-0.555	-0.251	0.0245	0.17	6.4	0.03	2
0.03	5.60	1.690	0.512	-1.1450	-0.144	0.610	0.260	0.370	-0.470	-0.230	0.0143	0.17	6.4	0.03	2
0.02	5.60	1.640	0.512	-1.1450	-0.144	0.610	0.260	0.370	-0.417	-0.230	0.0000	0.17	6.4	0.03	2
0.01	5.60	1.640	0.512	-1.1450	-0.144	0.610	0.260	0.370	-0.417	-0.230	0.0000	0.17	6.4	0.03	2

Table 3-2. Coefficients for Standard Errors for the Average Horizontal Component

period	b5	b6
5.00	0.89	0.087
4.00	0.88	0.092
3.00	0.87	0.097
2.00	0.85	0.105
1.50	0.84	0.110
1.00	0.83	0.118
0.85	0.82	0.121
0.75	0.81	0.123
0.60	0.81	0.127
0.50	0.80	0.130
0.46	0.80	0.132
0.40	0.79	0.135
0.36	0.79	0.135
0.30	0.78	0.135
0.24	0.77	0.135
0.20	0.77	0.135
0.17	0.76	0.135
0.15	0.75	0.135
0.12	0.75	0.135
0.10	0.74	0.135
0.09	0.74	0.135
0.075	0.73	0.135
0.06	0.72	0.135
0.05	0.71	0.135
0.04	0.71	0.135
0.03	0.70	0.135
0.02	0.70	0.135
0.01	0.70	0.135

Table 3-3. Coefficients for the Vertical Component

period	c4	a1	a2	a3	a4	a5	a6	a9	a10	a11	a12	a13	m1	c5	n
5.00	2.50	-2.053	0.909	-0.7200	0.275	0.260	-0.100	0.240	0.040	-0.220	-0.0670	0.06	6.4	0.3	3
4.00	2.50	-1.857	0.909	-0.7200	0.275	0.260	-0.100	0.240	0.040	-0.220	-0.0565	0.06	6.4	0.3	3
3.00	2.50	-1.581	0.909	-0.7200	0.275	0.260	-0.100	0.240	0.040	-0.220	-0.0431	0.06	6.4	0.3	3
2.00	2.50	-1.224	0.909	-0.7200	0.275	0.260	-0.008	0.240	0.040	-0.220	-0.0240	0.06	6.4	0.3	3
1.50	2.50	-0.966	0.909	-0.7285	0.275	0.260	0.058	0.240	0.025	-0.220	-0.0180	0.06	6.4	0.3	3
1.00	2.50	-0.602	0.909	-0.7404	0.275	0.260	0.150	0.240	0.004	-0.220	-0.0115	0.06	6.4	0.3	3
0.85	2.50	-0.469	0.909	-0.7451	0.275	0.309	0.150	0.273	-0.004	-0.220	-0.0097	0.06	6.4	0.3	3
0.75	2.50	-0.344	0.909	-0.7488	0.275	0.348	0.150	0.299	-0.010	-0.220	-0.0083	0.06	6.4	0.3	3
0.60	2.85	-0.087	0.909	-0.7896	0.275	0.416	0.150	0.345	-0.022	-0.220	-0.0068	0.06	6.4	0.3	3
0.50	3.26	0.145	0.909	-0.8291	0.275	0.471	0.150	0.383	-0.031	-0.220	-0.0060	0.06	6.4	0.3	3
0.46	3.45	0.271	0.909	-0.8472	0.275	0.497	0.150	0.400	-0.036	-0.220	-0.0056	0.06	6.4	0.3	3
0.40	3.77	0.478	0.909	-0.8776	0.275	0.539	0.150	0.428	-0.043	-0.220	-0.0050	0.06	6.4	0.3	3
0.36	4.01	0.617	0.909	-0.9004	0.275	0.571	0.150	0.450	-0.048	-0.220	-0.0047	0.06	6.4	0.3	3
0.30	4.42	0.878	0.909	-0.9400	0.275	0.580	0.150	0.488	-0.057	-0.220	-0.0042	0.06	6.4	0.3	3
0.24	4.93	1.312	0.909	-1.0274	0.275	0.580	0.109	0.533	-0.069	-0.220	-0.0035	0.06	6.4	0.3	3
0.20	5.35	1.648	0.909	-1.0987	0.275	0.580	0.076	0.571	-0.078	-0.220	-0.0030	0.06	6.4	0.3	3
0.17	5.72	1.960	0.909	-1.1623	0.275	0.580	0.047	0.604	-0.087	-0.220	-0.0025	0.06	6.4	0.3	3
0.15	6.00	2.170	0.909	-1.2113	0.275	0.580	0.024	0.630	-0.093	-0.220	-0.0022	0.06	6.4	0.3	3
0.12	6.00	2.480	0.909	-1.2986	0.275	0.580	-0.017	0.630	-0.104	-0.220	-0.0015	0.06	6.4	0.3	3
0.10	6.00	2.700	0.909	-1.3700	0.275	0.580	-0.050	0.630	-0.114	-0.220	-0.0010	0.06	6.4	0.3	3
0.09	6.00	2.730	0.909	-1.3700	0.275	0.567	-0.050	0.630	-0.119	-0.220	-0.0009	0.06	6.4	0.3	3
0.075	6.00	2.750	0.909	-1.3700	0.275	0.545	-0.050	0.630	-0.129	-0.220	-0.0007	0.06	6.4	0.3	3
0.06	6.00	2.710	0.909	-1.3700	0.275	0.518	-0.050	0.630	-0.140	-0.220	-0.0004	0.06	6.4	0.3	3
0.05	6.00	2.620	0.909	-1.3700	0.275	0.496	-0.050	0.630	-0.140	-0.220	-0.0002	0.06	6.4	0.3	3
0.04	6.00	2.420	0.909	-1.3700	0.275	0.469	-0.050	0.630	-0.140	-0.220	0.0000	0.06	6.4	0.3	3
0.03	6.00	2.100	0.909	-1.3168	0.275	0.432	-0.050	0.630	-0.140	-0.220	0.0000	0.06	6.4	0.3	3
0.02	6.00	1.642	0.909	-1.2520	0.275	0.390	-0.050	0.630	-0.140	-0.220	0.0000	0.06	6.4	0.3	3
0.01	6.00	1.642	0.909	-1.2520	0.275	0.390	-0.050	0.630	-0.140	-0.220	0.0000	0.06	6.4	0.3	3

Table 3-4. Coefficients for Standard Errors for the Vertical Component

period	b5	b6
5.00	0.78	0.050
4.00	0.75	0.050
3.00	0.72	0.050
2.00	0.69	0.050
1.50	0.69	0.050
1.00	0.69	0.050
0.85	0.69	0.050
0.75	0.69	0.050
0.60	0.69	0.050
0.50	0.69	0.050
0.46	0.69	0.050
0.40	0.69	0.050
0.36	0.69	0.050
0.30	0.69	0.050
0.24	0.69	0.050
0.20	0.69	0.050
0.17	0.70	0.056
0.15	0.72	0.063
0.12	0.74	0.075
0.10	0.76	0.085
0.09	0.76	0.085
0.075	0.76	0.085
0.06	0.76	0.085
0.05	0.76	0.085
0.04	0.76	0.085
0.03	0.76	0.085
0.02	0.76	0.085
0.01	0.76	0.085

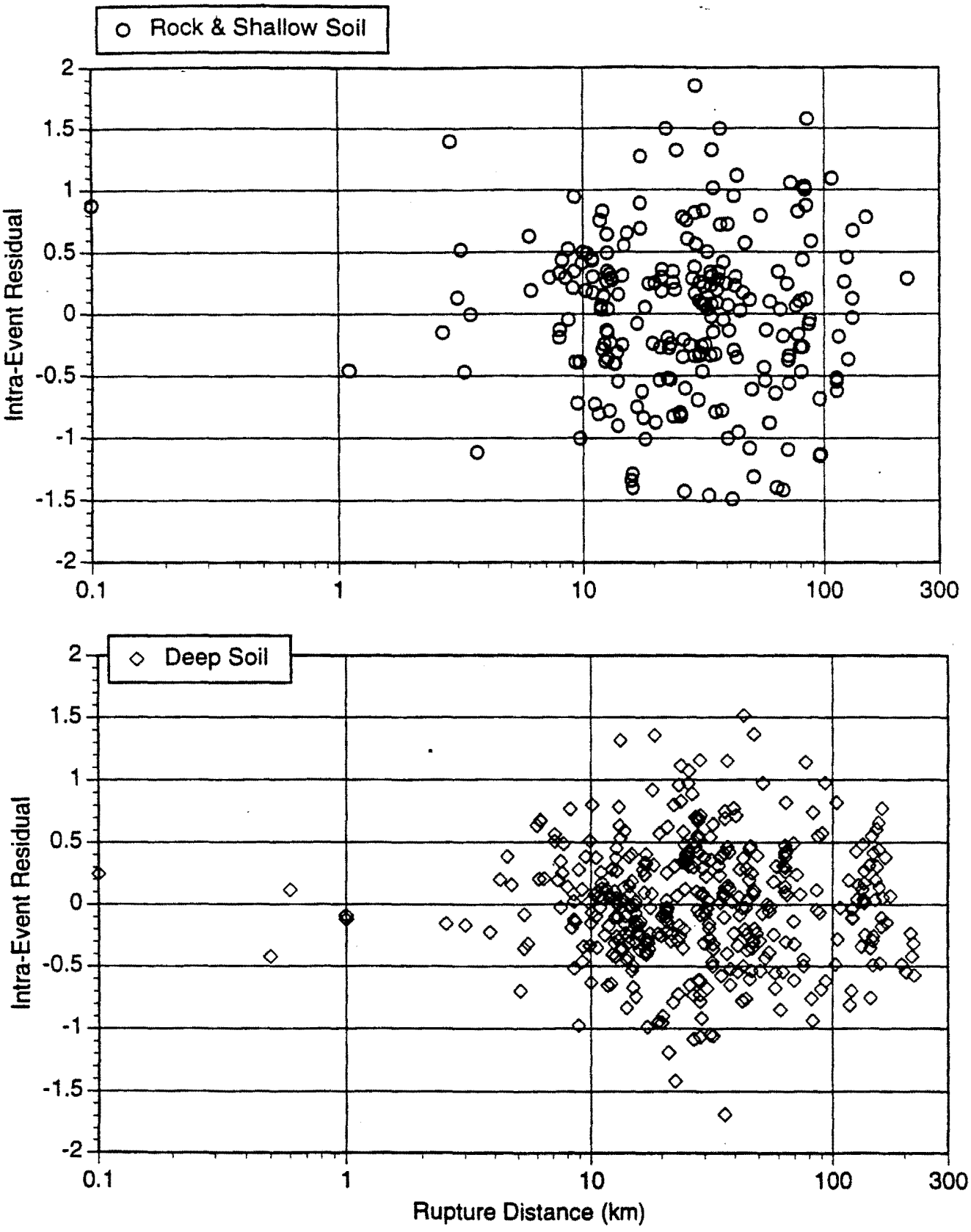

Figure 3-1a. Intra-event residual for T=1.0 sec, Horizontal component.

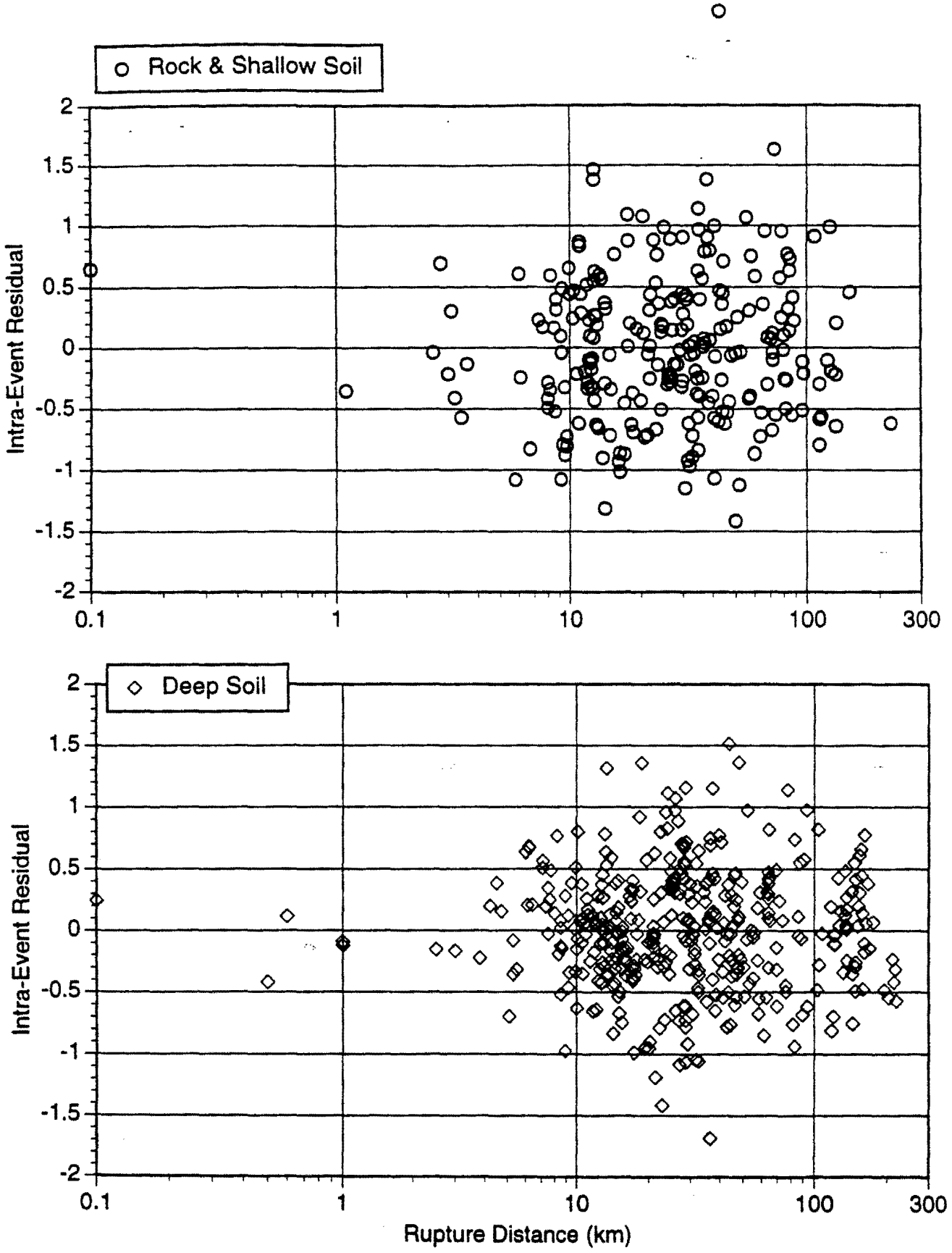

Figure 3-1b. Intra-event residual for T=0.3 sec, Horizontal component.

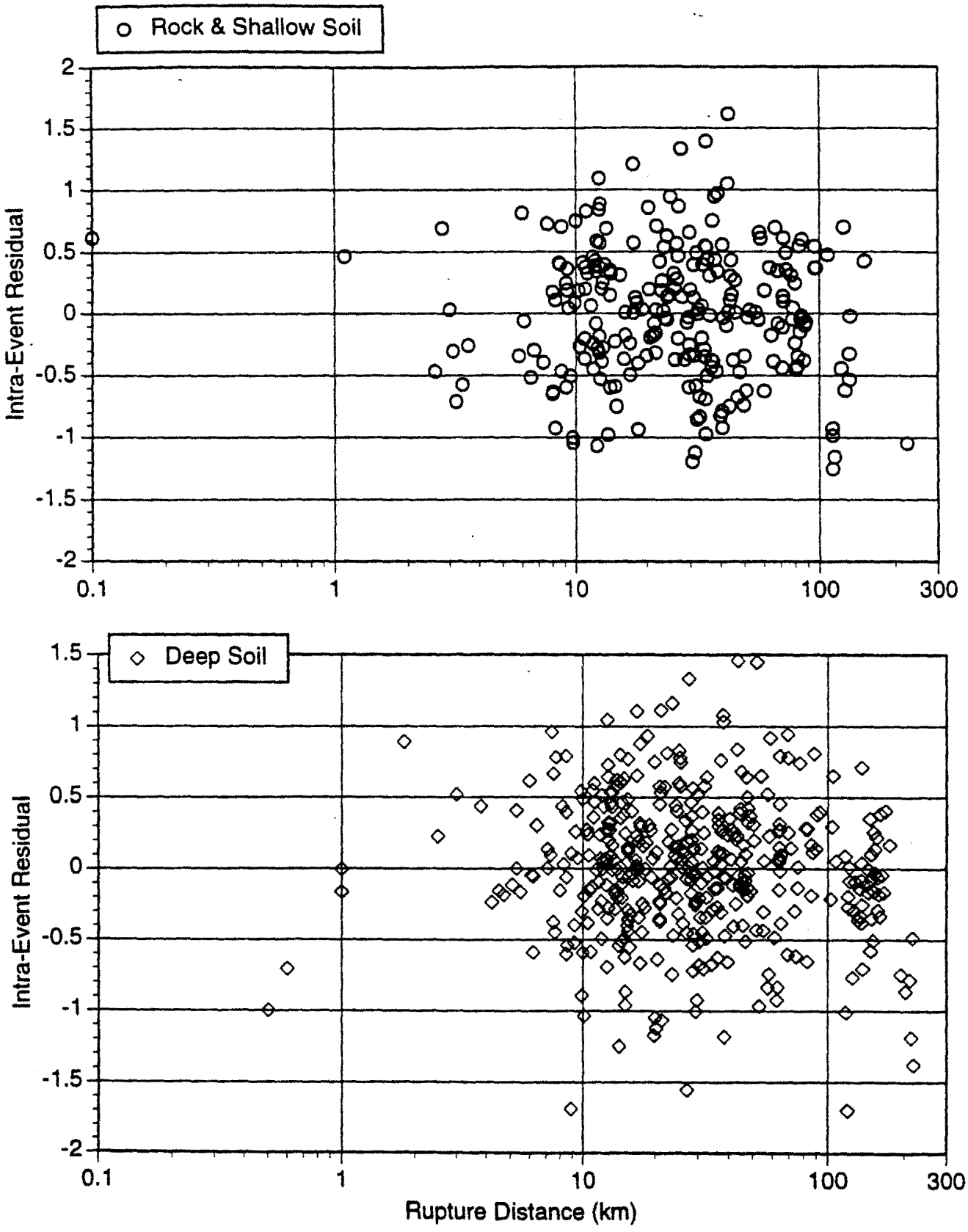

Figure 3-1c. Intra-event residual for T=0.1 sec, Horizontal component.

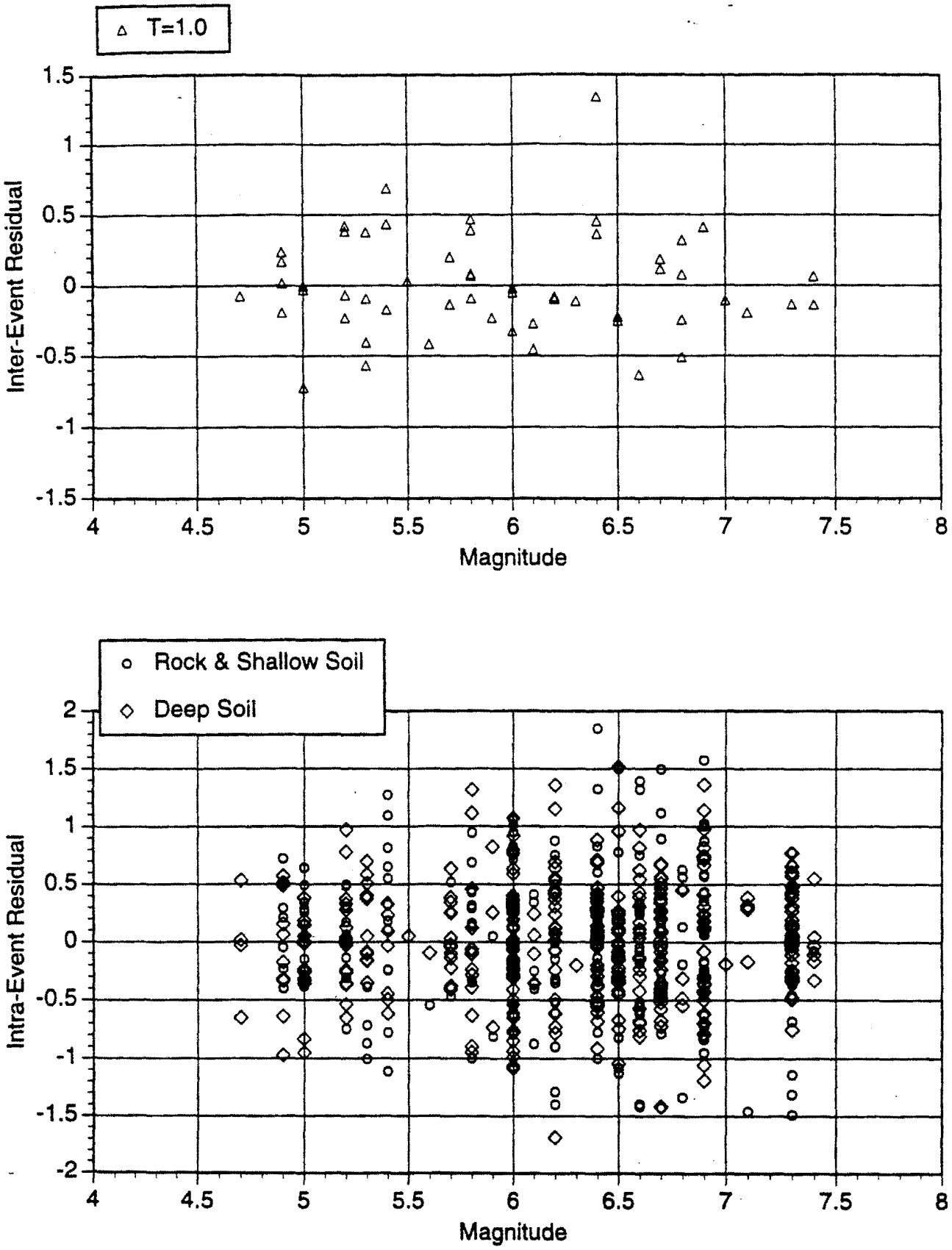

Figure 3-2a. Magnitude dependence of residuals. T=1.0 sec, horizontal component.

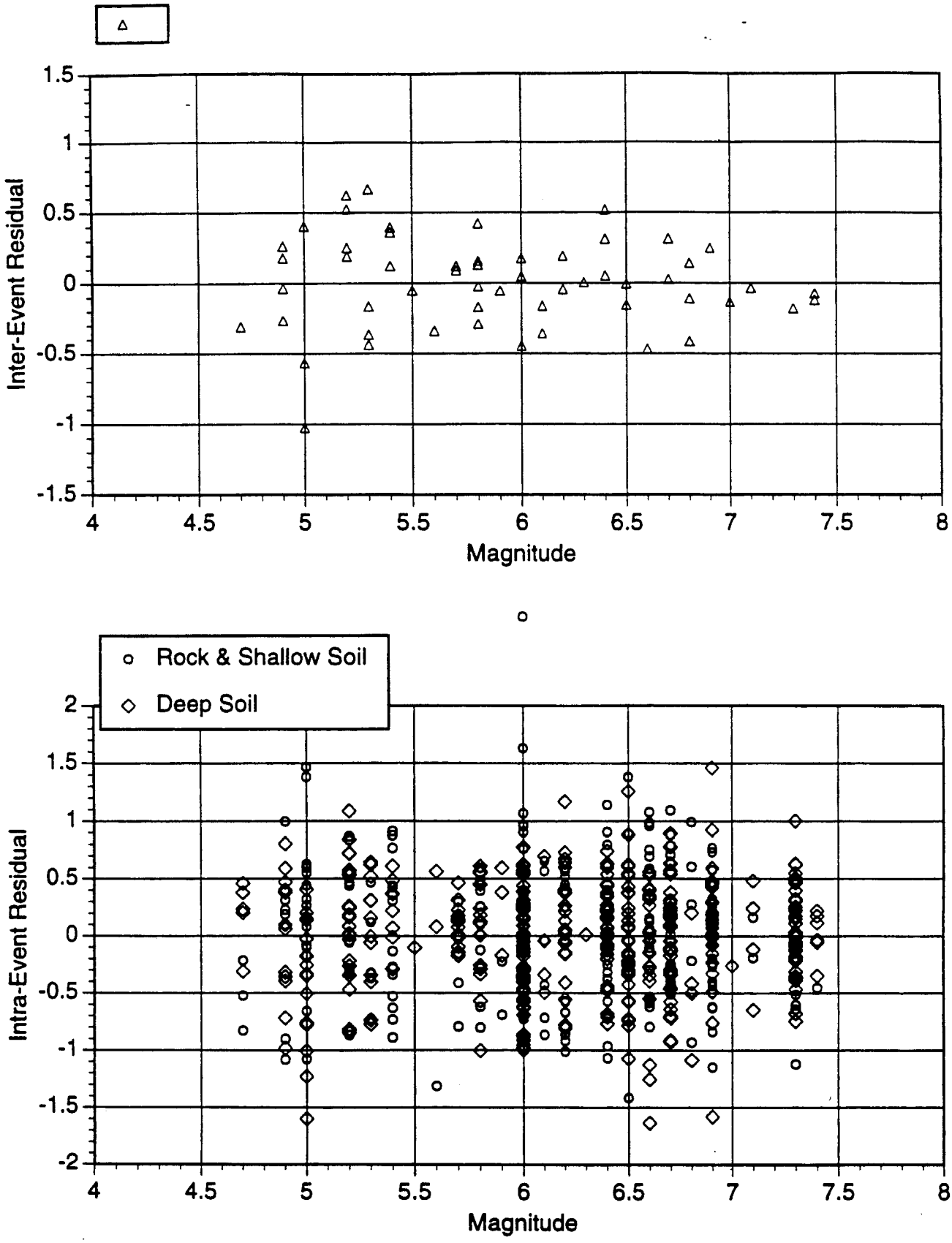

Figure 3-2b. Magnitude dependence of residuals. T=0.3 sec, horizontal component.

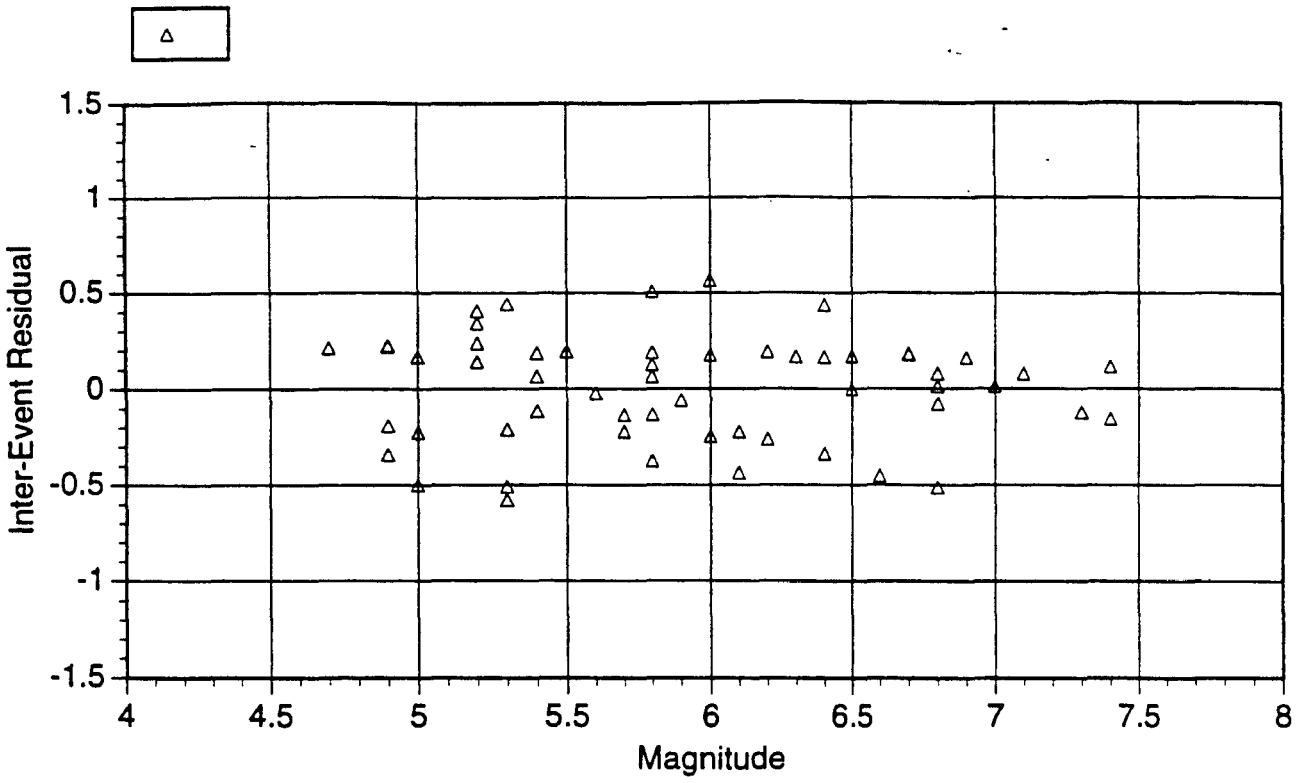

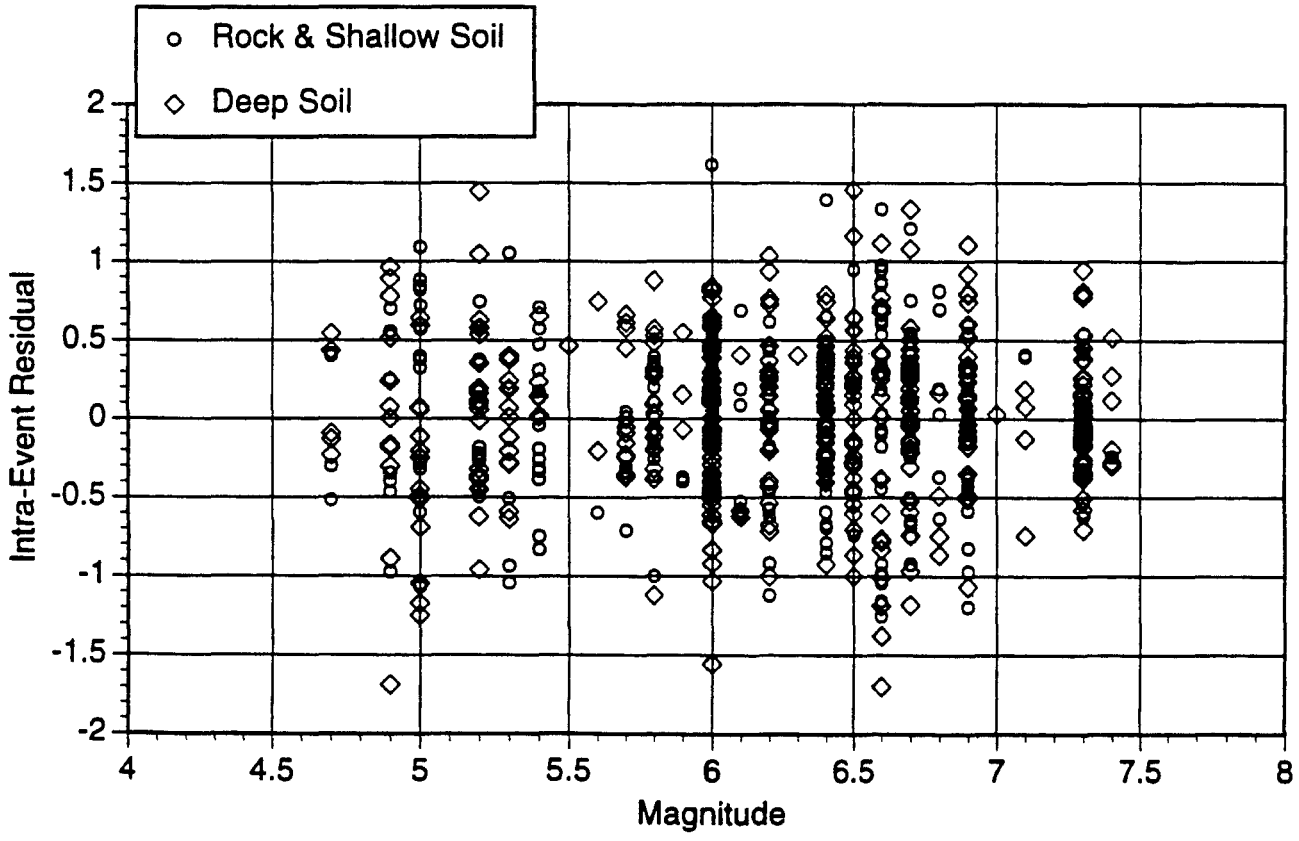

Figure 3-2c. Magnitude dependence of residuals. T=0.1 sec, horizontal component.

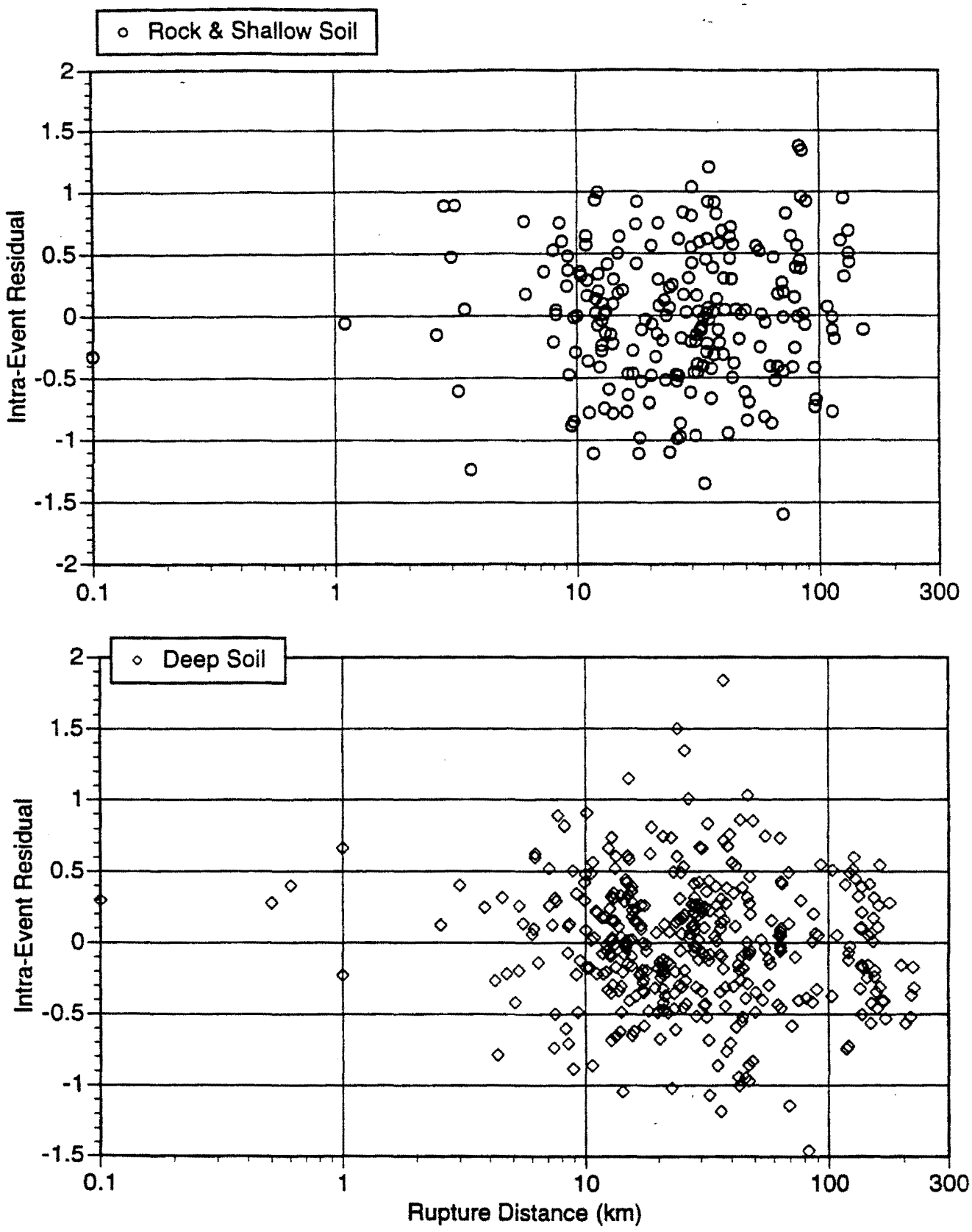

Figure 3-3a. Intra-event residual for T=1.0 sec, Vertical component.

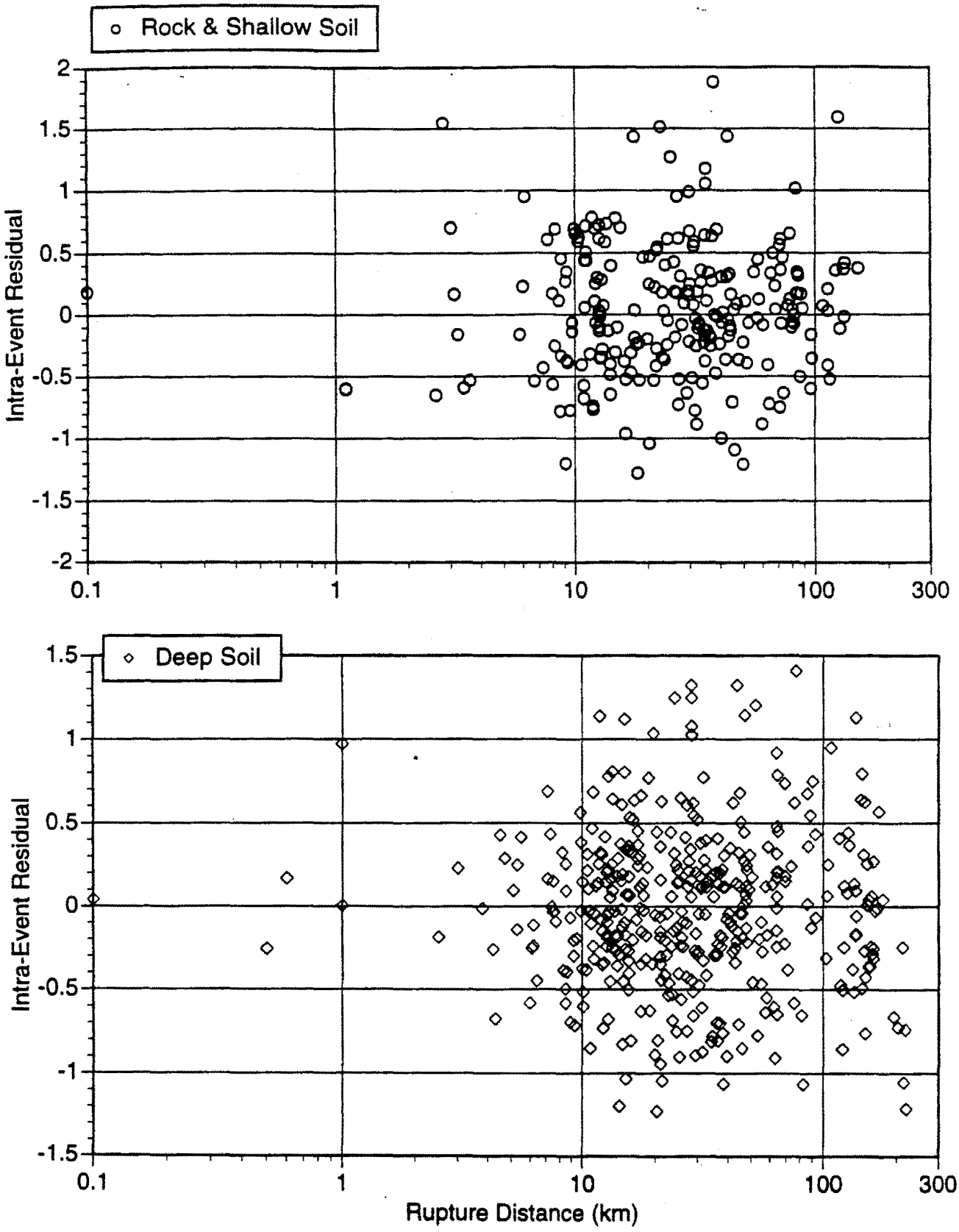

Figure 3-3b. Intra-event residual for T=0.3 sec, Vertical component.

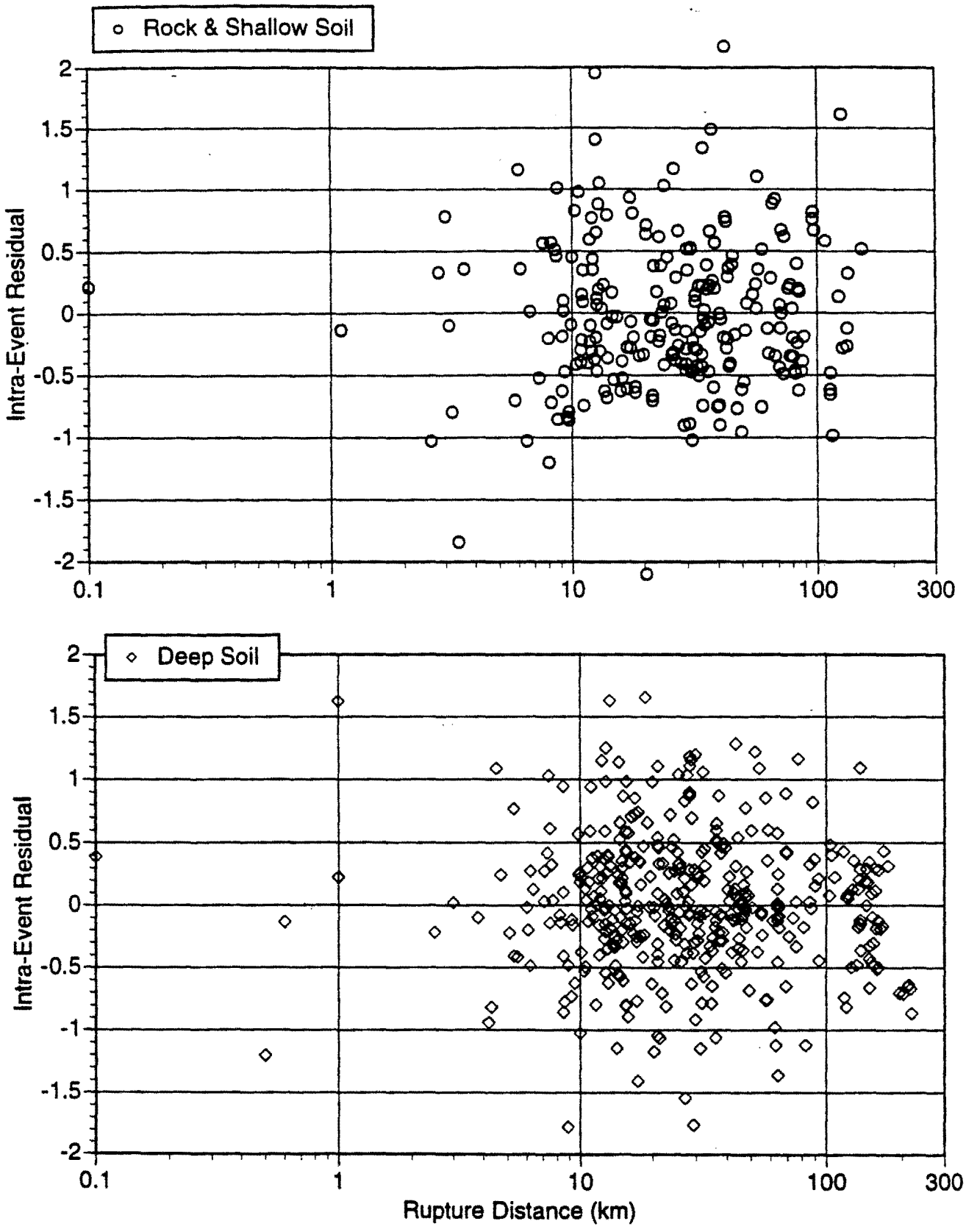

Figure 3-3c. Intra-event residual for T=0.1 sec, Vertical component.

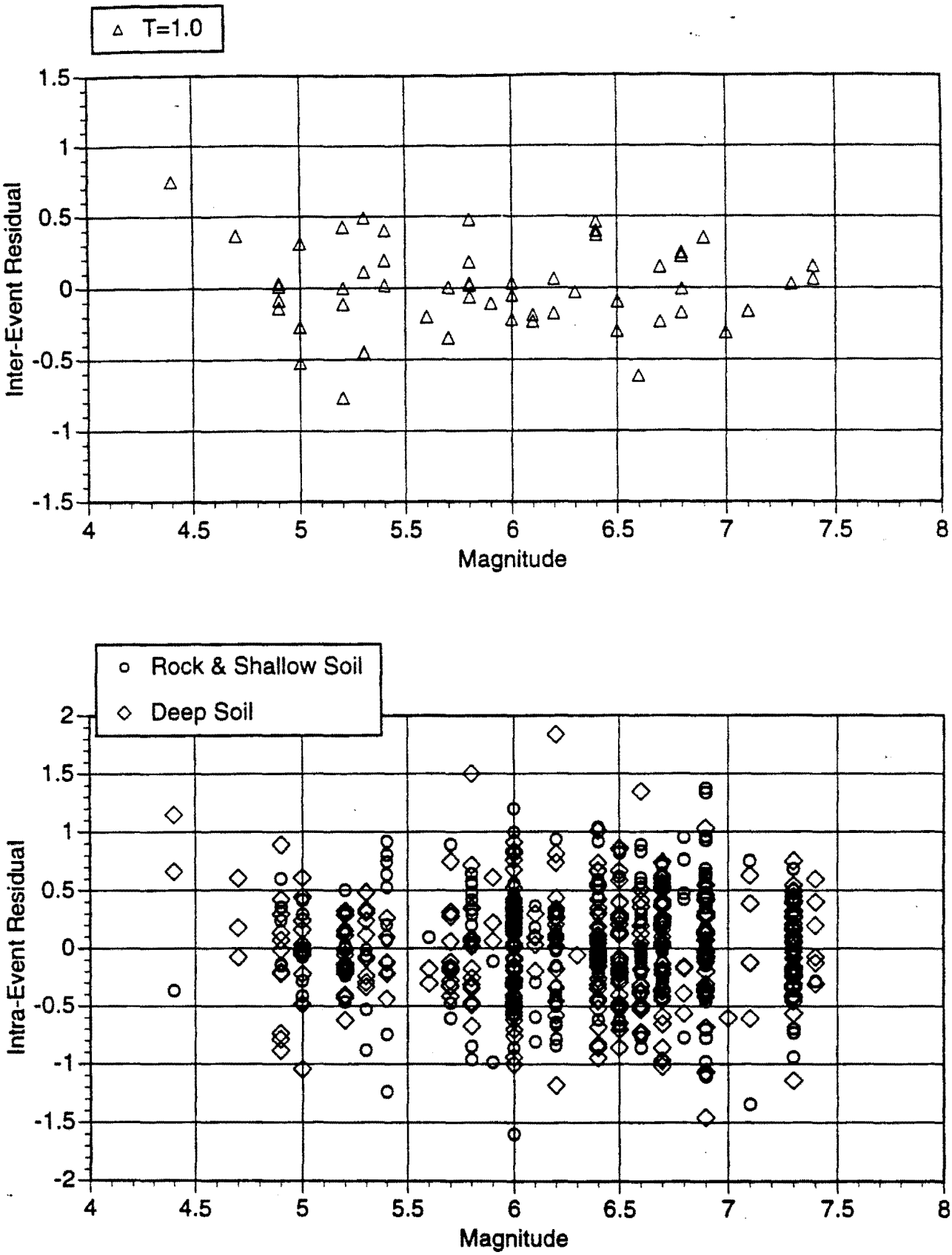

Figure 3-4a. Magnitude dependence of residuals. T=1.0 sec, vertical component.

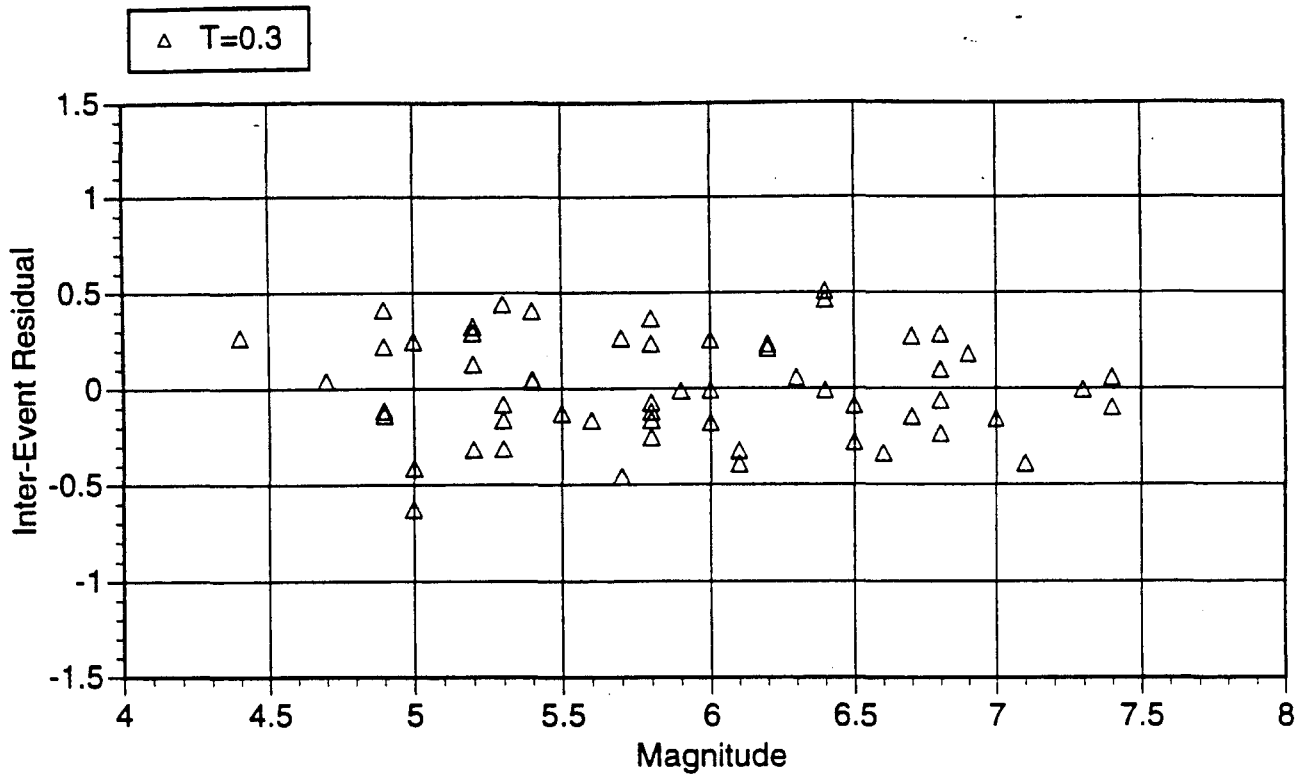

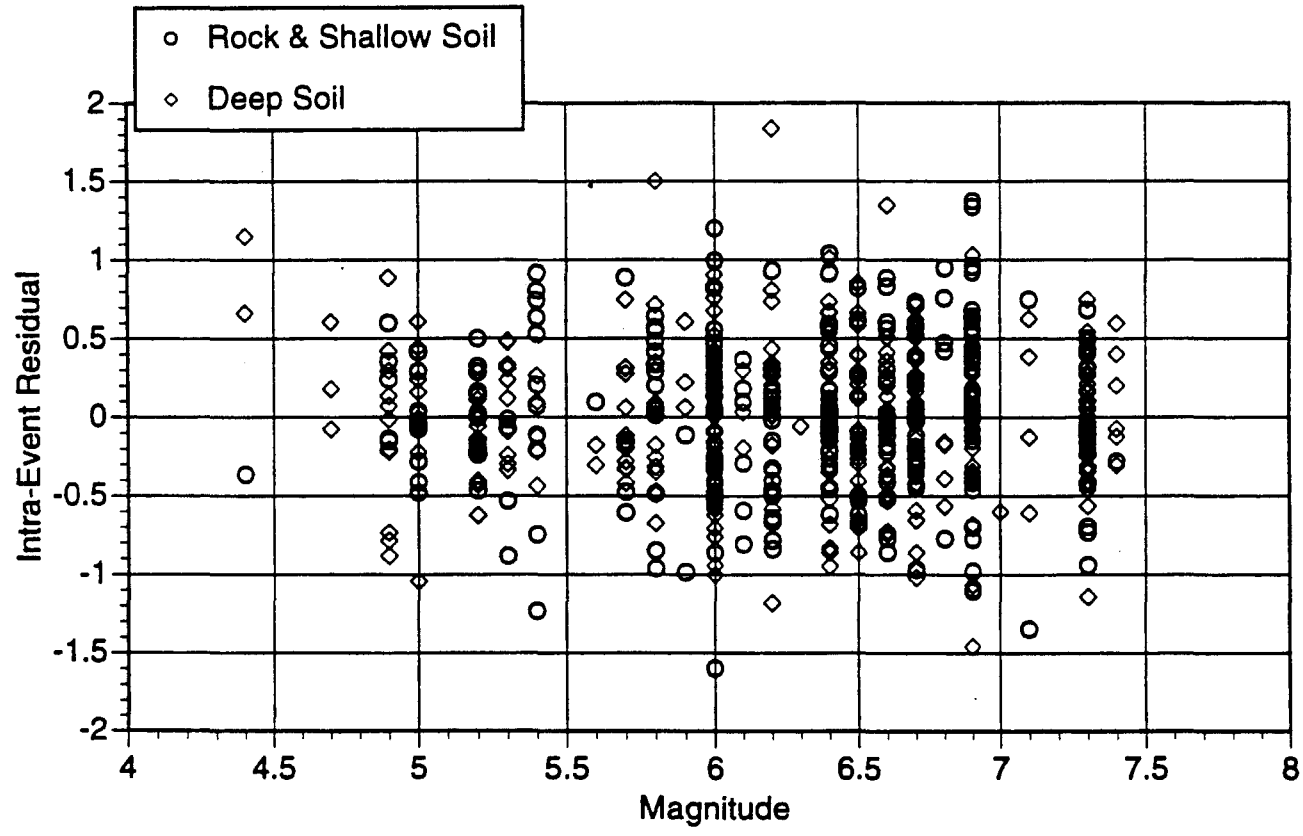

Figure 3-4b. Magnitude dependence of residuals. T=0.3 sec, vertical component.

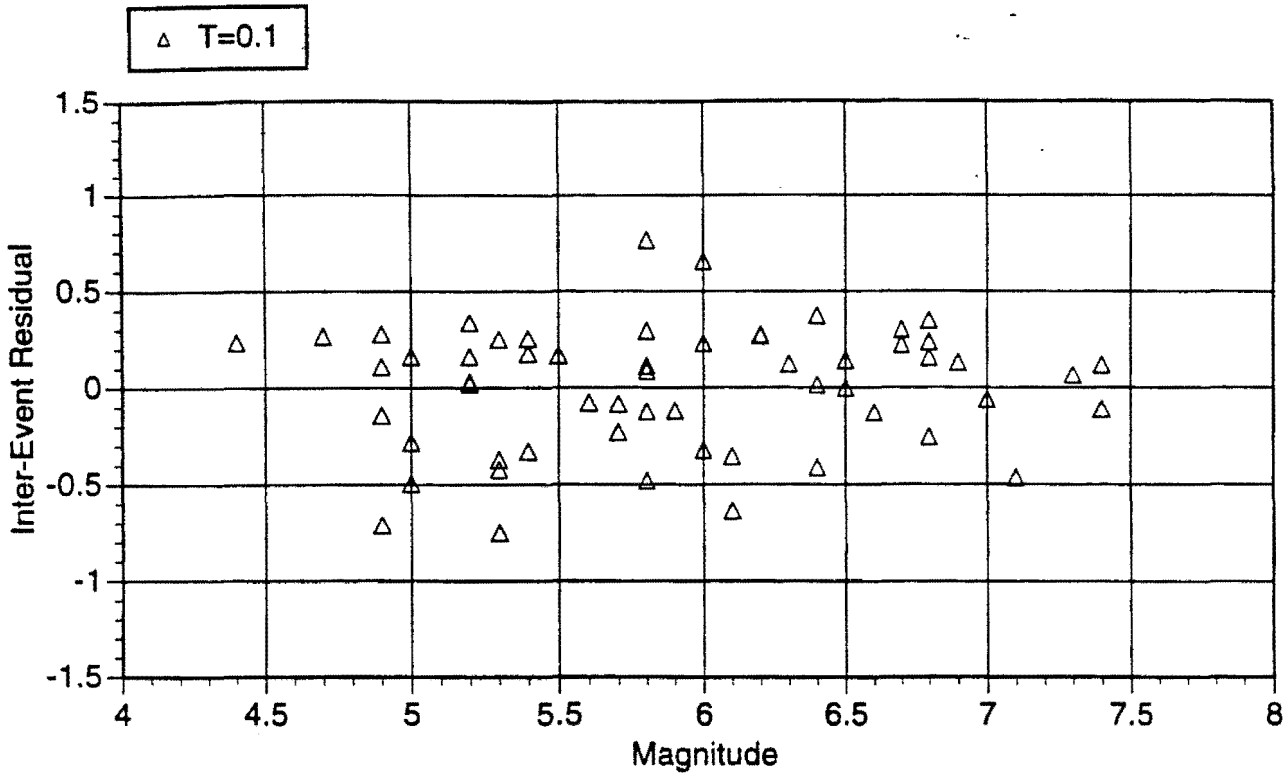

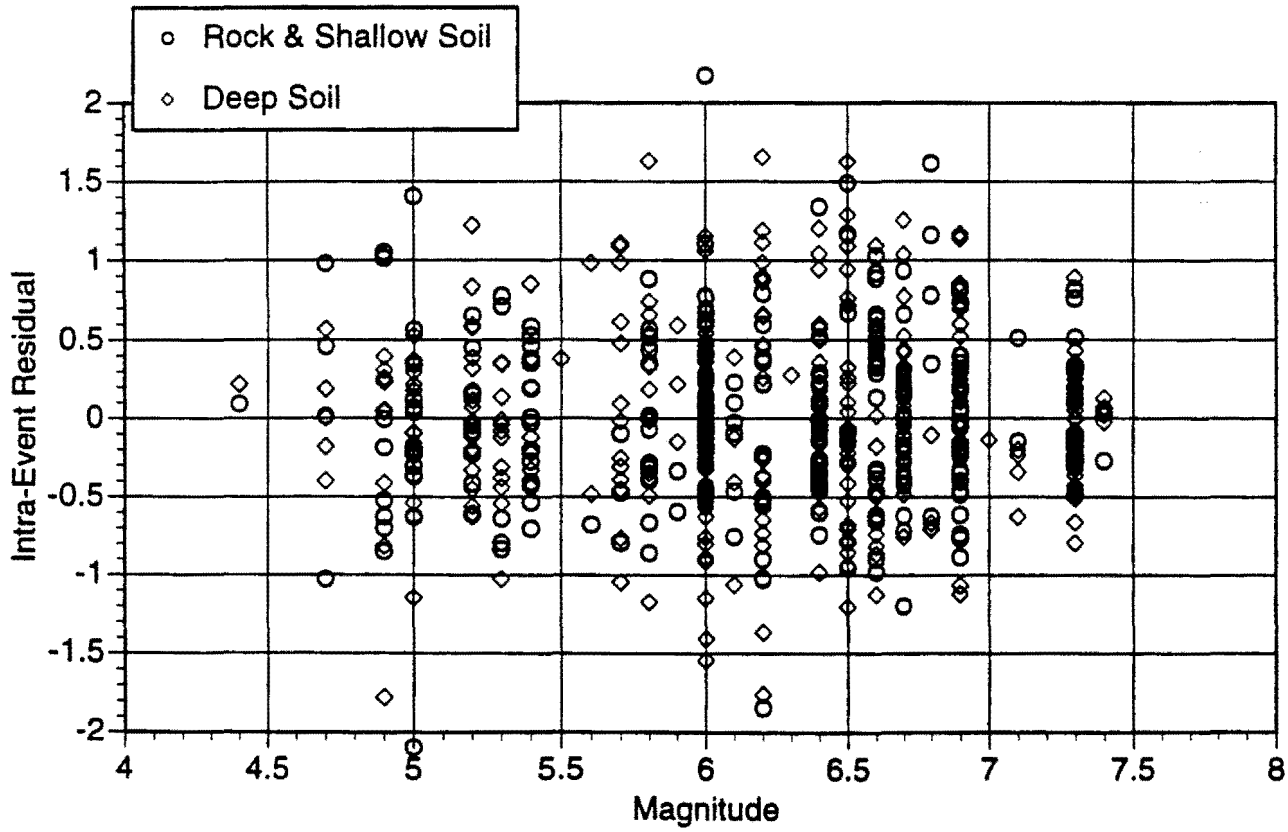

Figure 3-4c. Magnitude dependence of residuals. T=0.1 sec, vertical component.

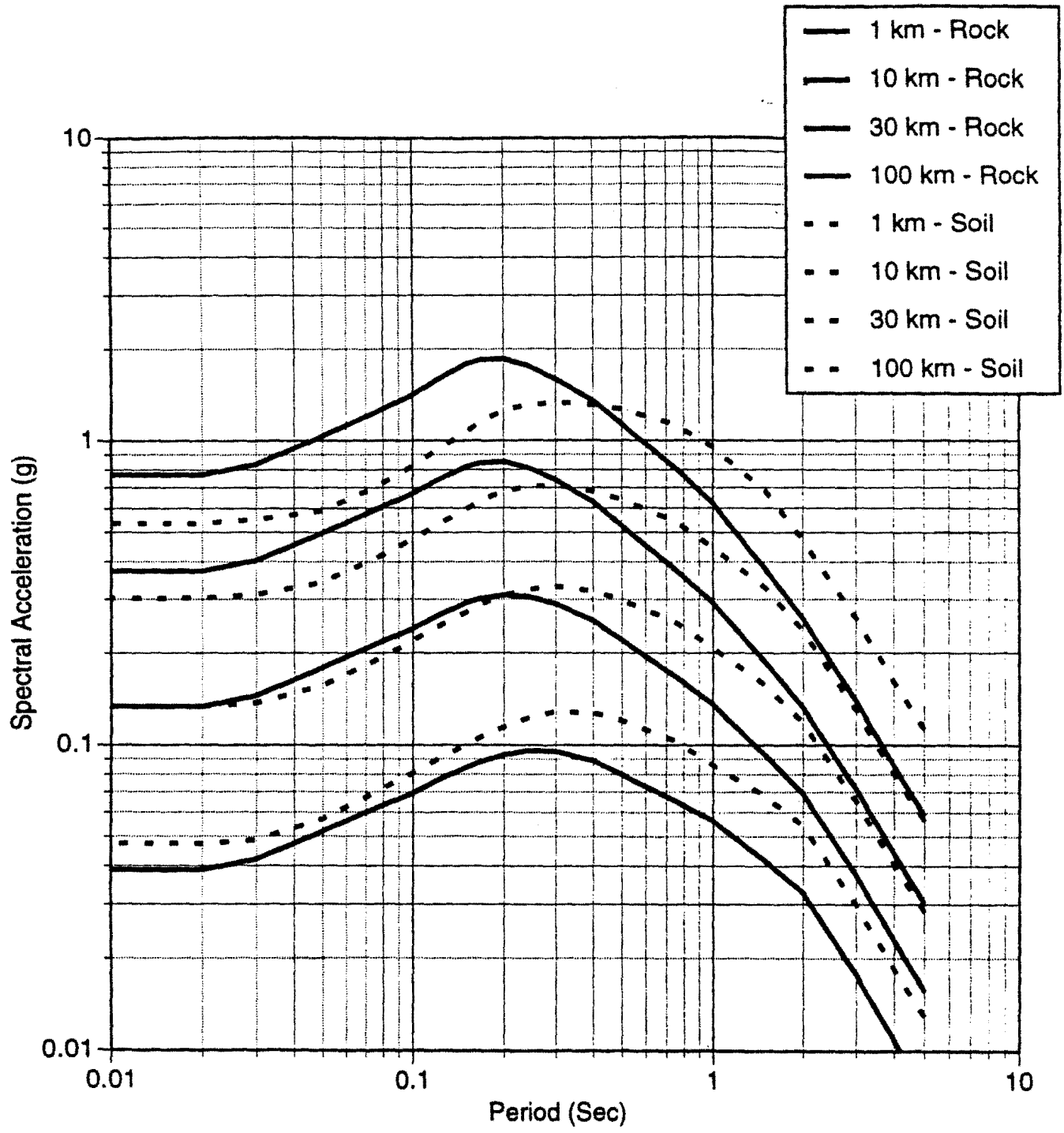

Figure 3-5. Median model predictions for a magnitude 7 strike-slip event: horizontal component.

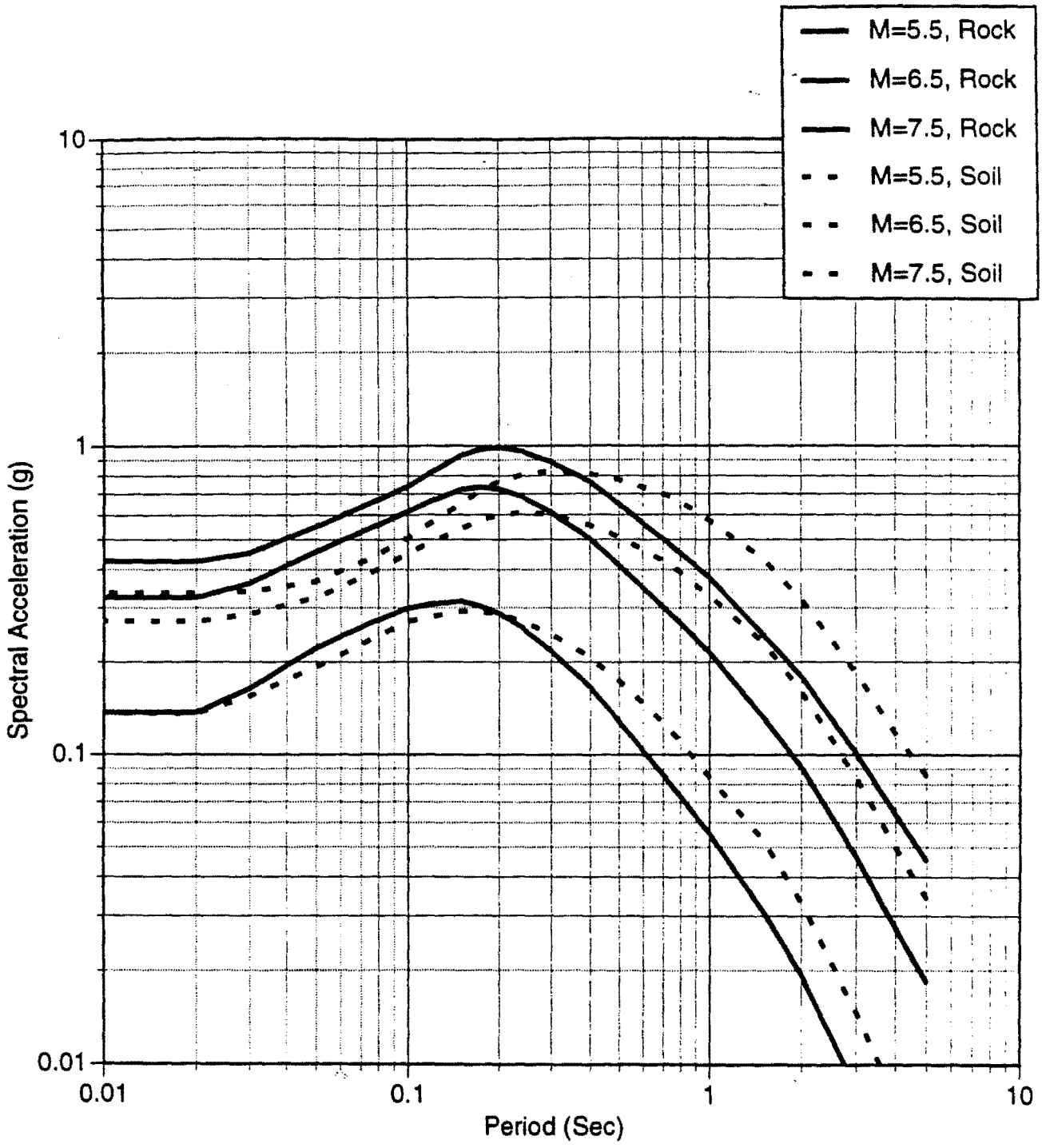

Figure 3-6. Median model predictions for a strike-slip event at 10 km: horizontal component.

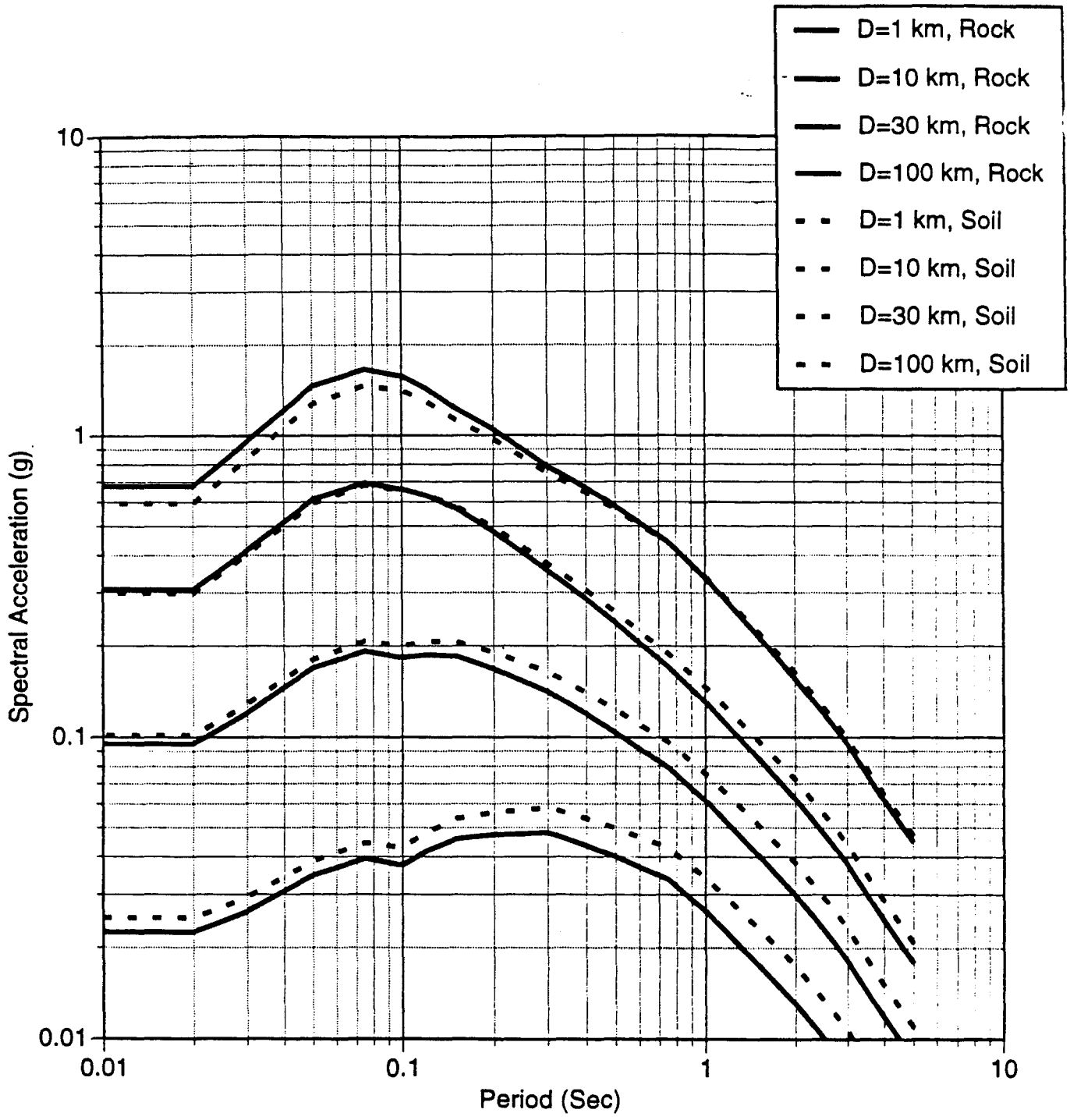

Figure 3-7. Median model predictions for a magnitude 7 strike-slip event: vertical component.

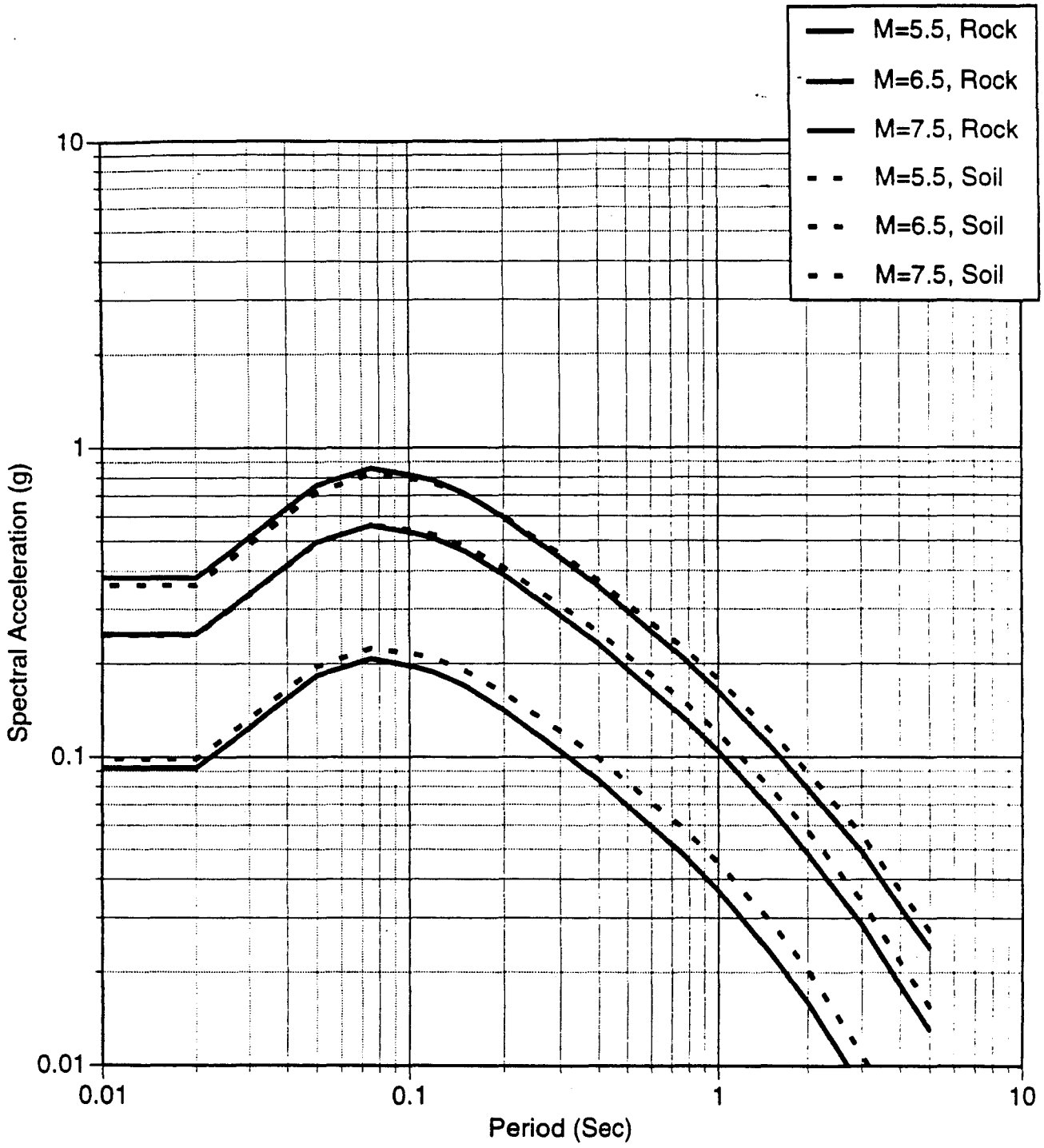

Figure 3-8. Median model predictions for a strike-slip event at 10 km: vertical component.

Section 4

Spectral Scaling for Other Damping Values

The attenuation relations developed in Section 3 are for 5% damping. Ground motion estimates for other damping values are developed in terms of the ratio to the 5% damped spectra for both the average horizontal and vertical components.

Regression Procedure and Results

The regression procedure for developing the model for the spectral ratios at various damping values followed a multi-step process. Preliminary analysis showed that the damping ratio does not have a significant dependence on site condition or distance. In the first step, the spectral ratios at each period were modeled by a constant, $C_1(T,\beta)$, for each of the eight spectral damping values (β=0.5, 1.0, 2.0, 3.0, 7.0, 10.0, 15.0, and 20.0%). The raw regression results are plotted in Figures 4-1a,b for horizontal and vertical. These figures show that the period dependence of C_1 is similar for each damping value and that C_1 is approximately constant between periods of 0.2 to 0.7 seconds. To take advantage of these characteristics, the C_1 values were normalized by the average value C_1 between a period range of 0.2-0.7 seconds for each damping value. These normalizing factors, C_{1ave}, are listed in Table 4-1 for the eight damping values for both the horizontal and vertical models. The normalized C_1 values are denoted C'_1 and are given by

$$C'_1(T,\beta) = \frac{C_1(T,\beta)}{C_{1ave}(\beta)} \qquad (4\text{-}1)$$

The magnitude dependence of C'_1 was evaluated by computing C'_1 values for subsets of the data in 0.5 unit magnitude bins. The average results for all 8 damping values are plotted in Figures 4-2 and 4-3 for the horizontal and vertical components, respectively. These figures indicate that the magnitude dependence of C'_1 is greater for long periods (T>0.7 sec) than for intermediate and short periods. The C'_1 results for each of the eight damping values are plotted in Figures 4-4a-h and 4-5a-h for the horizontal and vertical components at periods longer than 0.7 seconds. The long period variation in C'_1 was modeled by fitting the estimates of C'_1 for the individual magnitude bins to a function of the form

$$C_1'(M,T_j) = f_1(M)\, f_2(T_j) + f_3(T_j) \tag{4-2}$$

Based on the magnitude dependence shown in Figures 4-4 and 4-5, $f_1(M)$ was modeled using the following form,

$$f_1(M) = (M-6) + b_3\,(8.5-M)^2 \tag{4-3a}$$

The period dependence functions $f_2(T_j)$ and $f_3(T_j)$ were modeled as constant values for each period for this step in the regression procedure

$$f_2(T_j) = \sum_{i=1}^{8} \gamma_i\, \delta_{ij} \tag{4-3b}$$

$$f_3(T_j) = \sum_{i=1}^{8} a_i\, \delta_{ij} \tag{4-3c}$$

where δ_{ij} is the dirac delta function which equals 1 for i=j and 0 otherwise. The ratio of the quadratic to linear magnitude scaling, b_3, was assumed to be the same for all periods. However, the absolute level of scaling was allowed to be period dependent. In this step, the coefficient b_3 was estimated to be -0.774. In subsequent steps, b_3 was held fixed at this value.

The values of the coefficients γ_j and a_j are plotted in Figures 4-6 and 4-7 for periods greater 0.7 seconds. Based on the trend in Figure 4-6, a linear model on ln(T) was selected to model the period dependence of γ_j. The function was constrained such that the function equals 0.0 at a period of 0.75 seconds:

$$f_2(T_j) = d_1 (0.288 + \ln(T_j)) \qquad (4\text{-}4)$$

A second regression on the C'_1 data was then performed to estimate the value of d_1 where $f_3(T_j)$ was the same as given in equation (4-3c). Because the data for the vertical component produced similar values for the b_3 and d_1 terms (see Figures 4-6 and 4-7), the values of b_3 and d_1 for the horizontal component were also applied to the vertical component.

Figure 4-8 shows the a_j values that were estimated in the third step while holding all other coefficients fixed for both the horizontal and vertical. A quadratic function in period was selected to model these a_j values:

$$f_3(T) = e_1 \ln(T + 0.25) + e_2 (\ln(T + 0.25))^2 + 1.0 \qquad (4\text{-}5)$$

This model was constrained such that $f_3(T)$ equals 1.0 at a period of 0.75 seconds to insure a continuous function. The estimates of e_1 and e_2 are listed in Table 4-2 for both the horizontal and vertical components.

The final model for the spectral ratio damping model for periods greater than 0.7 seconds is obtained by combining equations (4-2a), (4-4), and (4-5) and multiplying by the C_{lave} value for each damping level

$$C_1(M,T) = C_{lave}\left[(M-6)+b_3(8.5-M)^2\right]\left[d_1(0.288+\ln(T))\right]+ C_{lave}\left[e_1\ln(T+0.25)+e_2(\ln(T+0.25))^2+1.0\right] \qquad (4\text{-}6)$$

The coefficients are listed in Tables 4-1 and 4-2 for both the horizontal and vertical component of motion, respectively.

For periods between 0.7 - 0.3 seconds, the normalized C'_1 model equals unity for both the horizontal and vertical component. For shorter periods, the C'_1 values were smoothed with respect to period.

The final model can be written as

$$\ln\left(\frac{Sa(\beta,T)}{Sa(5\%,T)}\right) = \begin{cases} C_1(\beta,T) & \text{for } T < 0.70 \text{ sec} \\ C_1(\beta,T) + g_2(\beta,T)(M-6) + g_3(\beta,T)(8.5-M)^2 & \text{for } T > 0.70 \text{ sec} \end{cases} \qquad (4\text{-}7)$$

The coefficients for this model are listed in Tables 4-4, 4-5 and 4-6.

Model Predictions

The resulting damping ratio model is shown for magnitudes 5, 6, 7, and 8 in Figures 4-9 to 4-12 for the horizontal component and in Figures 4-13 to 4-16 for the vertical component.

Table 4-1

C_{1ave} values for separate damping levels.

Damping %	Horizontal C_{1ave}	Vertical C_{1ave}
0.5	0.4808	0.5548
1.0	0.3759	0.4333
2.0	0.2379	0.2727
3.0	0.1409	0.1605
7.0	-0.1056	-0.1169
10.0	-0.2292	-0.2512
15.0	-0.3854	-0.4177
20.0	-0.5069	-0.5453

Table 4-2

Regression coefficients for the horizontal and vertical spectral damping ratio model

Coefficient	Horizontal Value	Vertical Value
b_3	-0.774	-0.774
d_1	0.0235	0.0235
e_1	-0.0084	-0.0106
e_2	-0.0789	-0.0862

Table 4-3

C'_1 values for T < 0.70 seconds

Period (sec)	Horizontal C'_1	Vertical C'_1
0.60	1.000	1.000
0.50	1.000	1.000
0.46	1.000	1.000
0.40	1.000	1.000
0.36	1.000	1.000
0.30	1.000	1.000
0.24	1.000	1.018
0.20	1.000	1.041
0.17	1.000	1.067
0.15	0.960	1.075
0.12	0.900	1.060
0.10	0.808	1.033
0.09	0.755	0.986
0.075	0.664	0.912
0.06	0.552	0.832
0.05	0.460	0.760
0.04	0.348	0.676
0.03	0.194	0.452
0.02	0.000	0.000

Table 4-4a
Horizontal C_1 values for separate damping levels.

Period (sec)	C1 (0.5%)	C1 (1.0%)	C1 (2.0%)	C1 (3.0%)	C1 (7.0%)	C1 (10.0%)	C1 (15.0%)	C1 (20.0%)
5.000	0.3698	0.2891	0.1830	0.1084	-0.0812	-0.1763	-0.2964	-0.3899
4.000	0.3955	0.3092	0.1957	0.1159	-0.0869	-0.1886	-0.3171	-0.4170
3.000	0.4233	0.3310	0.2095	0.1241	-0.0930	-0.2018	-0.3393	-0.4463
2.000	0.4526	0.3538	0.2239	0.1326	-0.0994	-0.2157	-0.3628	-0.4771
1.500	0.4667	0.3648	0.2309	0.1368	-0.1025	-0.2225	-0.3741	-0.4920
1.000	0.4780	0.3737	0.2365	0.1401	-0.1050	-0.2279	-0.3832	-0.5040
0.850	0.4801	0.3753	0.2375	0.1407	-0.1054	-0.2289	-0.3848	-0.5061
0.750	0.4808	0.3759	0.2379	0.1409	-0.1056	-0.2292	-0.3854	-0.5069
0.600	0.4808	0.3759	0.2379	0.1409	-0.1056	-0.2292	-0.3854	-0.5069
0.500	0.4808	0.3759	0.2379	0.1409	-0.1056	-0.2292	-0.3854	-0.5069
0.460	0.4808	0.3759	0.2379	0.1409	-0.1056	-0.2292	-0.3854	-0.5069
0.400	0.4808	0.3759	0.2379	0.1409	-0.1056	-0.2292	-0.3854	-0.5069
0.360	0.4808	0.3759	0.2379	0.1409	-0.1056	-0.2292	-0.3854	-0.5069
0.300	0.4808	0.3759	0.2379	0.1409	-0.1056	-0.2292	-0.3854	-0.5069
0.240	0.4808	0.3759	0.2379	0.1409	-0.1056	-0.2292	-0.3854	-0.5069
0.200	0.4808	0.3759	0.2379	0.1409	-0.1056	-0.2292	-0.3854	-0.5069
0.170	0.4808	0.3759	0.2379	0.1409	-0.1056	-0.2292	-0.3854	-0.5069
0.150	0.4616	0.3609	0.2284	0.1353	-0.1014	-0.2200	-0.3700	-0.4866
0.120	0.4327	0.3383	0.2141	0.1268	-0.0950	-0.2063	-0.3469	-0.4562
0.100	0.3885	0.3037	0.1922	0.1138	-0.0853	-0.1852	-0.3114	-0.4096
0.090	0.3630	0.2838	0.1796	0.1064	-0.0797	-0.1730	-0.2910	-0.3827
0.075	0.3193	0.2496	0.1580	0.0936	-0.0701	-0.1522	-0.2559	-0.3366
0.060	0.2654	0.2075	0.1313	0.0778	-0.0583	-0.1265	-0.2127	-0.2798
0.050	0.2212	0.1729	0.1094	0.0648	-0.0486	-0.1054	-0.1773	-0.2332
0.040	0.1673	0.1308	0.0828	0.0490	-0.0367	-0.0798	-0.1341	-0.1764
0.030	0.0933	0.0729	0.0462	0.0273	-0.0205	-0.0445	-0.0748	-0.0983
0.020	0.0000	0.0000	0.0000	0.0000	0.0000	0.0000	0.0000	0.0000

Table 4-4b
Vertical C_1 values for separate damping levels.

Period (sec)	C1 (0.5%)	C1 (1.0%)	C1 (2.0%)	C1 (3.0%)	C1 (7.0%)	C1 (10.0%)	C1 (15.0%)	C1 (20.0%)
5.000	0.4135	0.3230	0.2033	0.1196	-0.0871	-0.1872	-0.3114	-0.4065
4.000	0.4462	0.3485	0.2193	0.1291	-0.0940	-0.2020	-0.3359	-0.4385
3.000	0.4814	0.3760	0.2366	0.1393	-0.1014	-0.2180	-0.3625	-0.4732
2.000	0.5186	0.4050	0.2549	0.1500	-0.1093	-0.2348	-0.3904	-0.5097
1.500	0.5365	0.4190	0.2637	0.1552	-0.1131	-0.2429	-0.4039	-0.5273
1.000	0.5511	0.4304	0.2709	0.1594	-0.1161	-0.2495	-0.4149	-0.5417
0.850	0.5538	0.4325	0.2722	0.1602	-0.1167	-0.2507	-0.4169	-0.5443
0.750	0.5548	0.4333	0.2727	0.1605	-0.1169	-0.2512	-0.4177	-0.5453
0.600	0.5548	0.4333	0.2727	0.1605	-0.1169	-0.2512	-0.4177	-0.5453
0.500	0.5548	0.4333	0.2727	0.1605	-0.1169	-0.2512	-0.4177	-0.5453
0.460	0.5548	0.4333	0.2727	0.1605	-0.1169	-0.2512	-0.4177	-0.5453
0.400	0.5548	0.4333	0.2727	0.1605	-0.1169	-0.2512	-0.4177	-0.5453
0.360	0.5548	0.4333	0.2727	0.1605	-0.1169	-0.2512	-0.4177	-0.5453
0.300	0.5548	0.4333	0.2727	0.1605	-0.1169	-0.2512	-0.4177	-0.5453
0.240	0.5647	0.4411	0.2776	0.1634	-0.1190	-0.2557	-0.4252	-0.5551
0.200	0.5776	0.4511	0.2839	0.1671	-0.1217	-0.2615	-0.4348	-0.5677
0.170	0.5920	0.4623	0.2910	0.1713	-0.1247	-0.2680	-0.4457	-0.5818
0.150	0.5965	0.4658	0.2932	0.1726	-0.1257	-0.2701	-0.4491	-0.5862
0.120	0.5880	0.4593	0.2890	0.1701	-0.1239	-0.2662	-0.4427	-0.5780
0.100	0.5732	0.4477	0.2818	0.1658	-0.1208	-0.2595	-0.4316	-0.5634
0.090	0.5471	0.4273	0.2689	0.1583	-0.1153	-0.2477	-0.4119	-0.5378
0.075	0.5062	0.3954	0.2488	0.1464	-0.1067	-0.2292	-0.3811	-0.4976
0.060	0.4615	0.3604	0.2268	0.1335	-0.0972	-0.2090	-0.3475	-0.4536
0.050	0.4216	0.3293	0.2072	0.1220	-0.0888	-0.1909	-0.3174	-0.4144
0.040	0.3751	0.2930	0.1844	0.1085	-0.0790	-0.1698	-0.2824	-0.3687
0.030	0.2507	0.1958	0.1232	0.0725	-0.0528	-0.1135	-0.1887	-0.2464
0.020	0.0000	0.0000	0.0000	0.0000	0.0000	0.0000	0.0000	0.0000

Table 4-5a
Horizontal g_2 values for separate damping levels.

Period (sec)	g2 (0.5%)	g2 (1.0%)	g2 (2.0%)	g2 (3.0%)	g2 (7.0%)	g2 (10.0%)	g2 (15.0%)	g2 (20.0%)
5.000	0.0214	0.0168	0.0106	0.0063	-0.0047	-0.0102	-0.0172	-0.0226
4.000	0.0189	0.0148	0.0094	0.0055	-0.0042	-0.0090	-0.0152	-0.0199
3.000	0.0157	0.0122	0.0078	0.0046	-0.0034	-0.0075	-0.0126	-0.0165
2.000	0.0111	0.0087	0.0055	0.0032	-0.0024	-0.0053	-0.0089	-0.0117
1.500	0.0078	0.0061	0.0039	0.0023	-0.0017	-0.0037	-0.0063	-0.0083
1.000	0.0033	0.0025	0.0016	0.0010	-0.0007	-0.0016	-0.0026	-0.0034
0.850	0.0014	0.0011	0.0007	0.0004	-0.0003	-0.0007	-0.0011	-0.0015
0.750	0.0000	0.0000	0.0000	0.0000	0.0000	0.0000	0.0000	0.0000
0.600	0.0000	0.0000	0.0000	0.0000	0.0000	0.0000	0.0000	0.0000
0.500	0.0000	0.0000	0.0000	0.0000	0.0000	0.0000	0.0000	0.0000
0.460	0.0000	0.0000	0.0000	0.0000	0.0000	0.0000	0.0000	0.0000
0.400	0.0000	0.0000	0.0000	0.0000	0.0000	0.0000	0.0000	0.0000
0.360	0.0000	0.0000	0.0000	0.0000	0.0000	0.0000	0.0000	0.0000
0.300	0.0000	0.0000	0.0000	0.0000	0.0000	0.0000	0.0000	0.0000
0.240	0.0000	0.0000	0.0000	0.0000	0.0000	0.0000	0.0000	0.0000
0.200	0.0000	0.0000	0.0000	0.0000	0.0000	0.0000	0.0000	0.0000
0.170	0.0000	0.0000	0.0000	0.0000	0.0000	0.0000	0.0000	0.0000
0.150	0.0000	0.0000	0.0000	0.0000	0.0000	0.0000	0.0000	0.0000
0.120	0.0000	0.0000	0.0000	0.0000	0.0000	0.0000	0.0000	0.0000
0.100	0.0000	0.0000	0.0000	0.0000	0.0000	0.0000	0.0000	0.0000
0.090	0.0000	0.0000	0.0000	0.0000	0.0000	0.0000	0.0000	0.0000
0.075	0.0000	0.0000	0.0000	0.0000	0.0000	0.0000	0.0000	0.0000
0.060	0.0000	0.0000	0.0000	0.0000	0.0000	0.0000	0.0000	0.0000
0.050	0.0000	0.0000	0.0000	0.0000	0.0000	0.0000	0.0000	0.0000
0.040	0.0000	0.0000	0.0000	0.0000	0.0000	0.0000	0.0000	0.0000
0.030	0.0000	0.0000	0.0000	0.0000	0.0000	0.0000	0.0000	0.0000
0.020	0.0000	0.0000	0.0000	0.0000	0.0000	0.0000	0.0000	0.0000

Table 4-5b

Vertical g_2 values for separate damping levels.

Period (sec)	g2 (0.5%)	g2 (1.0%)	g2 (2.0%)	g2 (3.0%)	g2 (7.0%)	g2 (10.0%)	g2 (15.0%)	g2 (20.0%)
5.000	0.0247	0.0193	0.0122	0.0072	-0.0052	-0.0112	-0.0186	-0.0243
4.000	0.0218	0.0170	0.0107	0.0063	-0.0046	-0.0099	-0.0164	-0.0215
3.000	0.0181	0.0141	0.0089	0.0052	-0.0038	-0.0082	-0.0136	-0.0178
2.000	0.0128	0.0100	0.0063	0.0037	-0.0027	-0.0058	-0.0096	-0.0126
1.500	0.0090	0.0071	0.0044	0.0026	-0.0019	-0.0041	-0.0068	-0.0089
1.000	0.0038	0.0029	0.0018	0.0011	-0.0008	-0.0017	-0.0028	-0.0037
0.850	0.0016	0.0013	0.0008	0.0005	-0.0003	-0.0007	-0.0012	-0.0016
0.750	0.0000	0.0000	0.0000	0.0000	0.0000	0.0000	0.0000	0.0000
0.600	0.0000	0.0000	0.0000	0.0000	0.0000	0.0000	0.0000	0.0000
0.500	0.0000	0.0000	0.0000	0.0000	0.0000	0.0000	0.0000	0.0000
0.460	0.0000	0.0000	0.0000	0.0000	0.0000	0.0000	0.0000	0.0000
0.400	0.0000	0.0000	0.0000	0.0000	0.0000	0.0000	0.0000	0.0000
0.360	0.0000	0.0000	0.0000	0.0000	0.0000	0.0000	0.0000	0.0000
0.300	0.0000	0.0000	0.0000	0.0000	0.0000	0.0000	0.0000	0.0000
0.240	0.0000	0.0000	0.0000	0.0000	0.0000	0.0000	0.0000	0.0000
0.200	0.0000	0.0000	0.0000	0.0000	0.0000	0.0000	0.0000	0.0000
0.170	0.0000	0.0000	0.0000	0.0000	0.0000	0.0000	0.0000	0.0000
0.150	0.0000	0.0000	0.0000	0.0000	0.0000	0.0000	0.0000	0.0000
0.120	0.0000	0.0000	0.0000	0.0000	0.0000	0.0000	0.0000	0.0000
0.100	0.0000	0.0000	0.0000	0.0000	0.0000	0.0000	0.0000	0.0000
0.090	0.0000	0.0000	0.0000	0.0000	0.0000	0.0000	0.0000	0.0000
0.075	0.0000	0.0000	0.0000	0.0000	0.0000	0.0000	0.0000	0.0000
0.060	0.0000	0.0000	0.0000	0.0000	0.0000	0.0000	0.0000	0.0000
0.050	0.0000	0.0000	0.0000	0.0000	0.0000	0.0000	0.0000	0.0000
0.040	0.0000	0.0000	0.0000	0.0000	0.0000	0.0000	0.0000	0.0000
0.030	0.0000	0.0000	0.0000	0.0000	0.0000	0.0000	0.0000	0.0000
0.020	0.0000	0.0000	0.0000	0.0000	0.0000	0.0000	0.0000	0.0000

Table 4-6a
Horizontal g_3 values for separate damping levels.

Period (sec)	g3 (0.5%)	g3 (1.0%)	g3 (2.0%)	g3 (3.0%)	g3 (7.0%)	g3 (10.0%)	g3 (15.0%)	g3 (20.0%)
5.000	-0.0166	-0.0130	-0.0082	-0.0049	0.0036	0.0079	0.0133	0.0175
4.000	-0.0146	-0.0114	-0.0072	-0.0043	0.0032	0.0070	0.0117	0.0154
3.000	-0.0121	-0.0095	-0.0060	-0.0036	0.0027	0.0058	0.0097	0.0128
2.000	-0.0086	-0.0067	-0.0042	-0.0025	0.0019	0.0041	0.0069	0.0090
1.500	-0.0061	-0.0047	-0.0030	-0.0018	0.0013	0.0029	0.0049	0.0064
1.000	-0.0025	-0.0020	-0.0012	-0.0007	0.0006	0.0012	0.0020	0.0027
0.850	-0.0011	-0.0009	-0.0005	-0.0003	0.0002	0.0005	0.0009	0.0012
0.750	0.0000	0.0000	0.0000	0.0000	0.0000	0.0000	0.0000	0.0000
0.600	0.0000	0.0000	0.0000	0.0000	0.0000	0.0000	0.0000	0.0000
0.500	0.0000	0.0000	0.0000	0.0000	0.0000	0.0000	0.0000	0.0000
0.460	0.0000	0.0000	0.0000	0.0000	0.0000	0.0000	0.0000	0.0000
0.400	0.0000	0.0000	0.0000	0.0000	0.0000	0.0000	0.0000	0.0000
0.360	0.0000	0.0000	0.0000	0.0000	0.0000	0.0000	0.0000	0.0000
0.300	0.0000	0.0000	0.0000	0.0000	0.0000	0.0000	0.0000	0.0000
0.240	0.0000	0.0000	0.0000	0.0000	0.0000	0.0000	0.0000	0.0000
0.200	0.0000	0.0000	0.0000	0.0000	0.0000	0.0000	0.0000	0.0000
0.170	0.0000	0.0000	0.0000	0.0000	0.0000	0.0000	0.0000	0.0000
0.150	0.0000	0.0000	0.0000	0.0000	0.0000	0.0000	0.0000	0.0000
0.120	0.0000	0.0000	0.0000	0.0000	0.0000	0.0000	0.0000	0.0000
0.100	0.0000	0.0000	0.0000	0.0000	0.0000	0.0000	0.0000	0.0000
0.090	0.0000	0.0000	0.0000	0.0000	0.0000	0.0000	0.0000	0.0000
0.075	0.0000	0.0000	0.0000	0.0000	0.0000	0.0000	0.0000	0.0000
0.060	0.0000	0.0000	0.0000	0.0000	0.0000	0.0000	0.0000	0.0000
0.050	0.0000	0.0000	0.0000	0.0000	0.0000	0.0000	0.0000	0.0000
0.040	0.0000	0.0000	0.0000	0.0000	0.0000	0.0000	0.0000	0.0000
0.030	0.0000	0.0000	0.0000	0.0000	0.0000	0.0000	0.0000	0.0000
0.020	0.0000	0.0000	0.0000	0.0000	0.0000	0.0000	0.0000	0.0000

Table 4-6b
Vertical g_3 values for separate damping levels.

Period (sec)	g3 (0.5%)	g3 (1.0%)	g3 (2.0%)	g3 (3.0%)	g3 (7.0%)	g3 (10.0%)	g3 (15.0%)	g3 (20.0%)
5.000	-0.0191	-0.0150	-0.0094	-0.0055	0.0040	0.0087	0.0144	0.0188
4.000	-0.0169	-0.0132	-0.0083	-0.0049	0.0036	0.0076	0.0127	0.0166
3.000	-0.0140	-0.0109	-0.0069	-0.0040	0.0029	0.0063	0.0105	0.0138
2.000	-0.0099	-0.0077	-0.0049	-0.0029	0.0021	0.0045	0.0075	0.0097
1.500	-0.0070	-0.0055	-0.0034	-0.0020	0.0015	0.0032	0.0053	0.0069
1.000	-0.0029	-0.0023	-0.0014	-0.0008	0.0006	0.0013	0.0022	0.0029
0.850	-0.0013	-0.0010	-0.0006	-0.0004	0.0003	0.0006	0.0010	0.0012
0.750	0.0000	0.0000	0.0000	0.0000	0.0000	0.0000	0.0000	0.0000
0.600	0.0000	0.0000	0.0000	0.0000	0.0000	0.0000	0.0000	0.0000
0.500	0.0000	0.0000	0.0000	0.0000	0.0000	0.0000	0.0000	0.0000
0.460	0.0000	0.0000	0.0000	0.0000	0.0000	0.0000	0.0000	0.0000
0.400	0.0000	0.0000	0.0000	0.0000	0.0000	0.0000	0.0000	0.0000
0.360	0.0000	0.0000	0.0000	0.0000	0.0000	0.0000	0.0000	0.0000
0.300	0.0000	0.0000	0.0000	0.0000	0.0000	0.0000	0.0000	0.0000
0.240	0.0000	0.0000	0.0000	0.0000	0.0000	0.0000	0.0000	0.0000
0.200	0.0000	0.0000	0.0000	0.0000	0.0000	0.0000	0.0000	0.0000
0.170	0.0000	0.0000	0.0000	0.0000	0.0000	0.0000	0.0000	0.0000
0.150	0.0000	0.0000	0.0000	0.0000	0.0000	0.0000	0.0000	0.0000
0.120	0.0000	0.0000	0.0000	0.0000	0.0000	0.0000	0.0000	0.0000
0.100	0.0000	0.0000	0.0000	0.0000	0.0000	0.0000	0.0000	0.0000
0.090	0.0000	0.0000	0.0000	0.0000	0.0000	0.0000	0.0000	0.0000
0.075	0.0000	0.0000	0.0000	0.0000	0.0000	0.0000	0.0000	0.0000
0.060	0.0000	0.0000	0.0000	0.0000	0.0000	0.0000	0.0000	0.0000
0.050	0.0000	0.0000	0.0000	0.0000	0.0000	0.0000	0.0000	0.0000
0.040	0.0000	0.0000	0.0000	0.0000	0.0000	0.0000	0.0000	0.0000
0.030	0.0000	0.0000	0.0000	0.0000	0.0000	0.0000	0.0000	0.0000
0.020	0.0000	0.0000	0.0000	0.0000	0.0000	0.0000	0.0000	0.0000

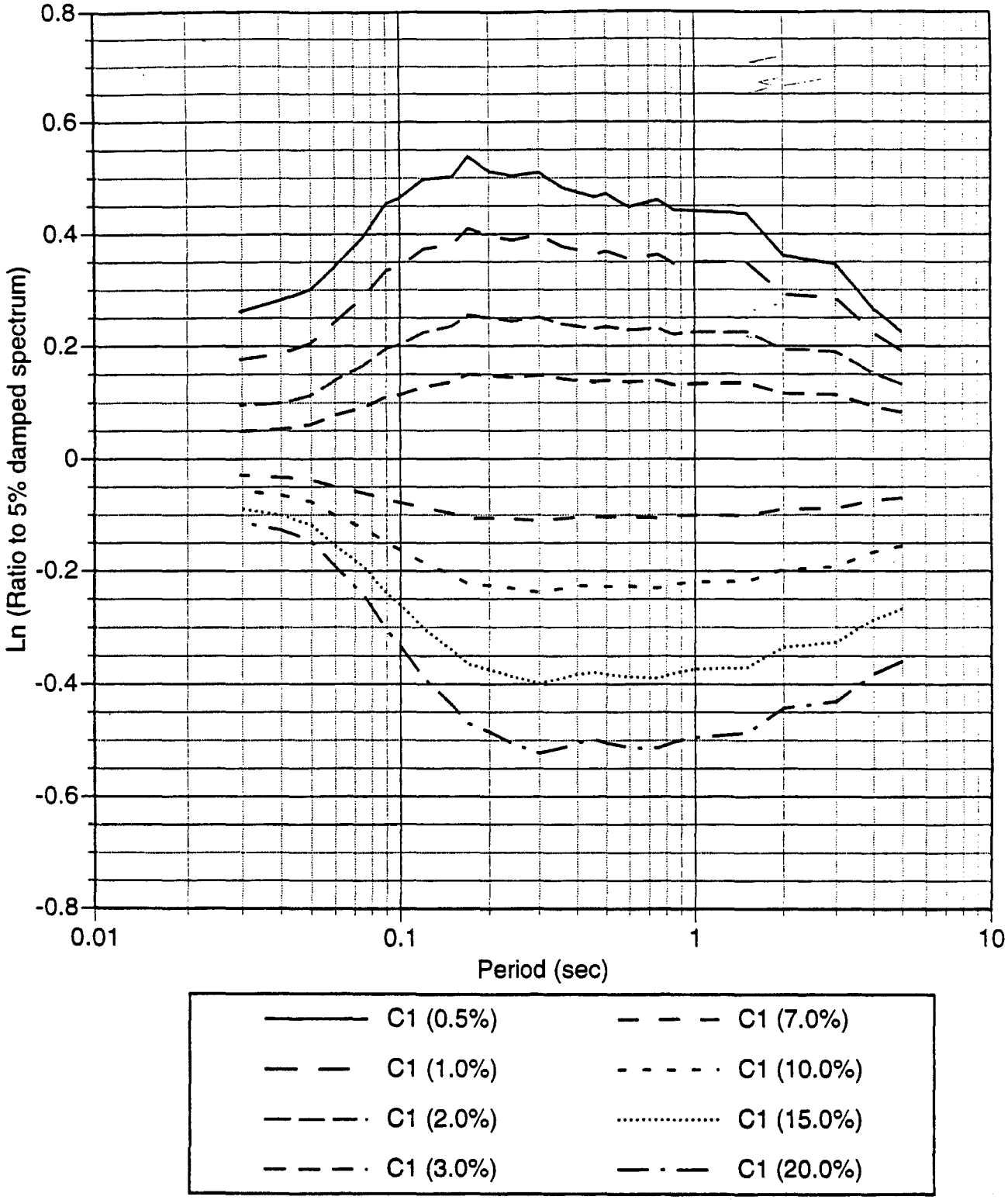

Figure 1a. Horizontal C1 values for all magnitudes.

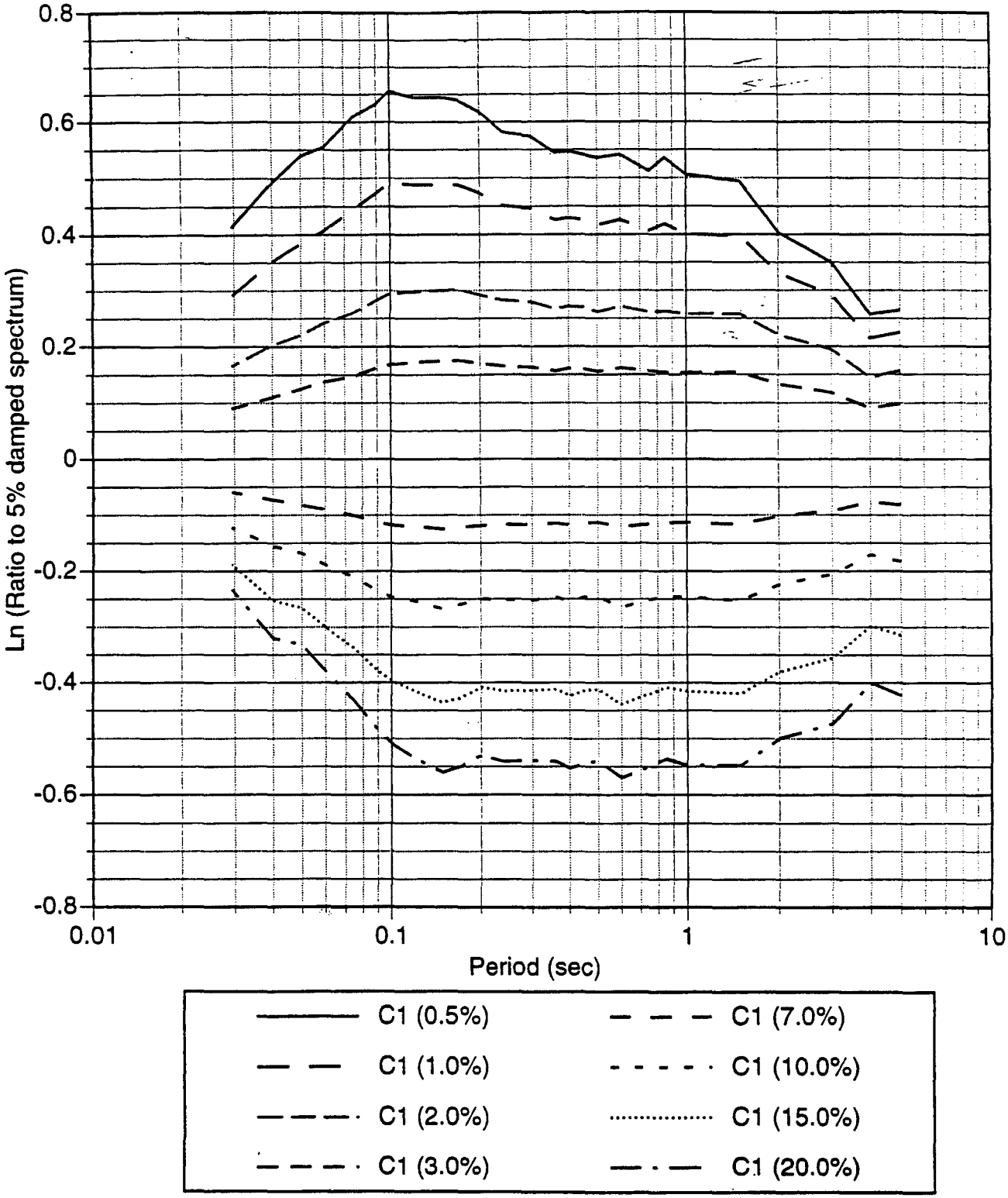

Figure 1b. Vertical C1 values for all magnitudes.

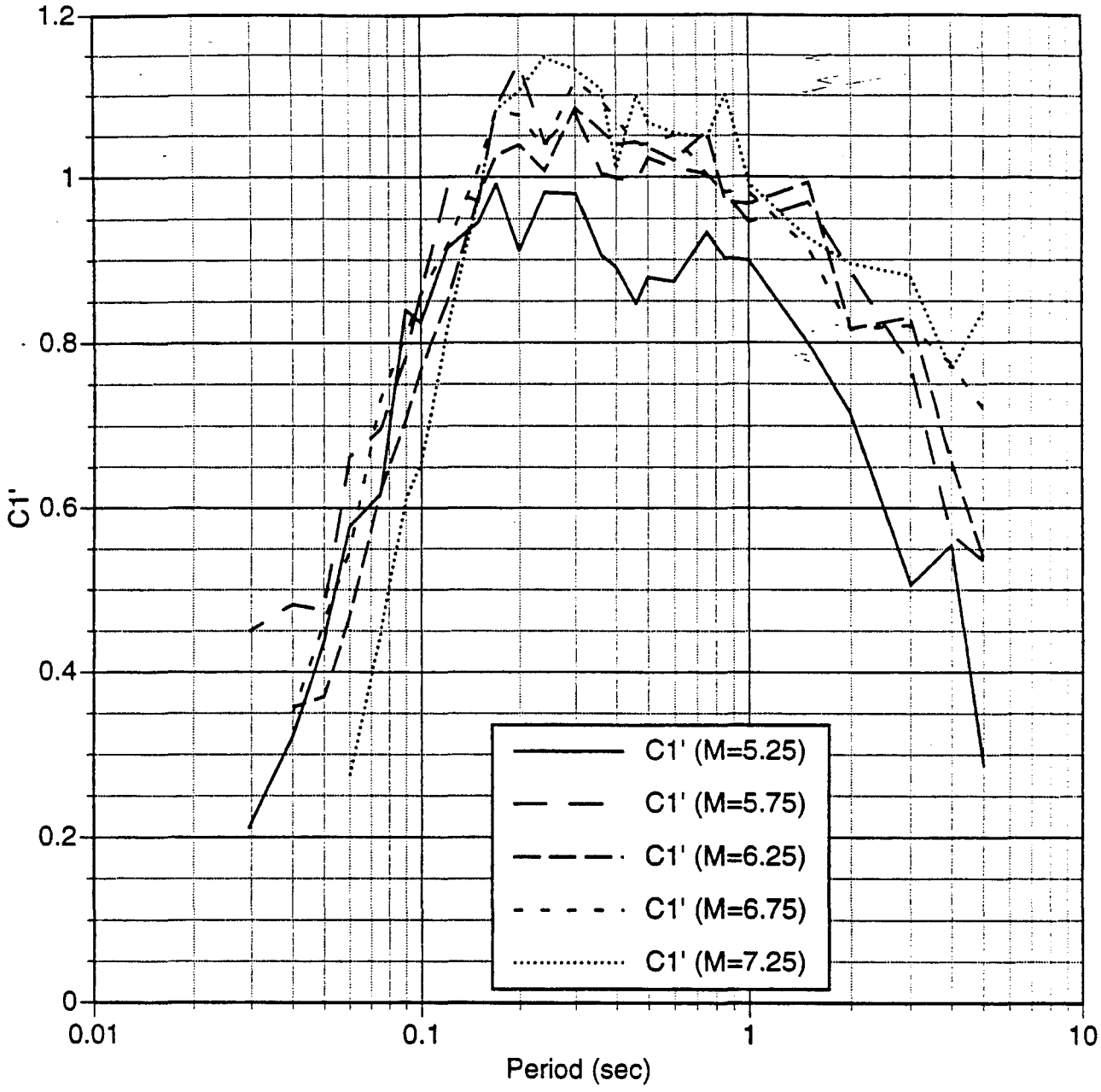

Figure 2. Magnitude dependence of C1' (horizontal) averaged over all eight damping levels.

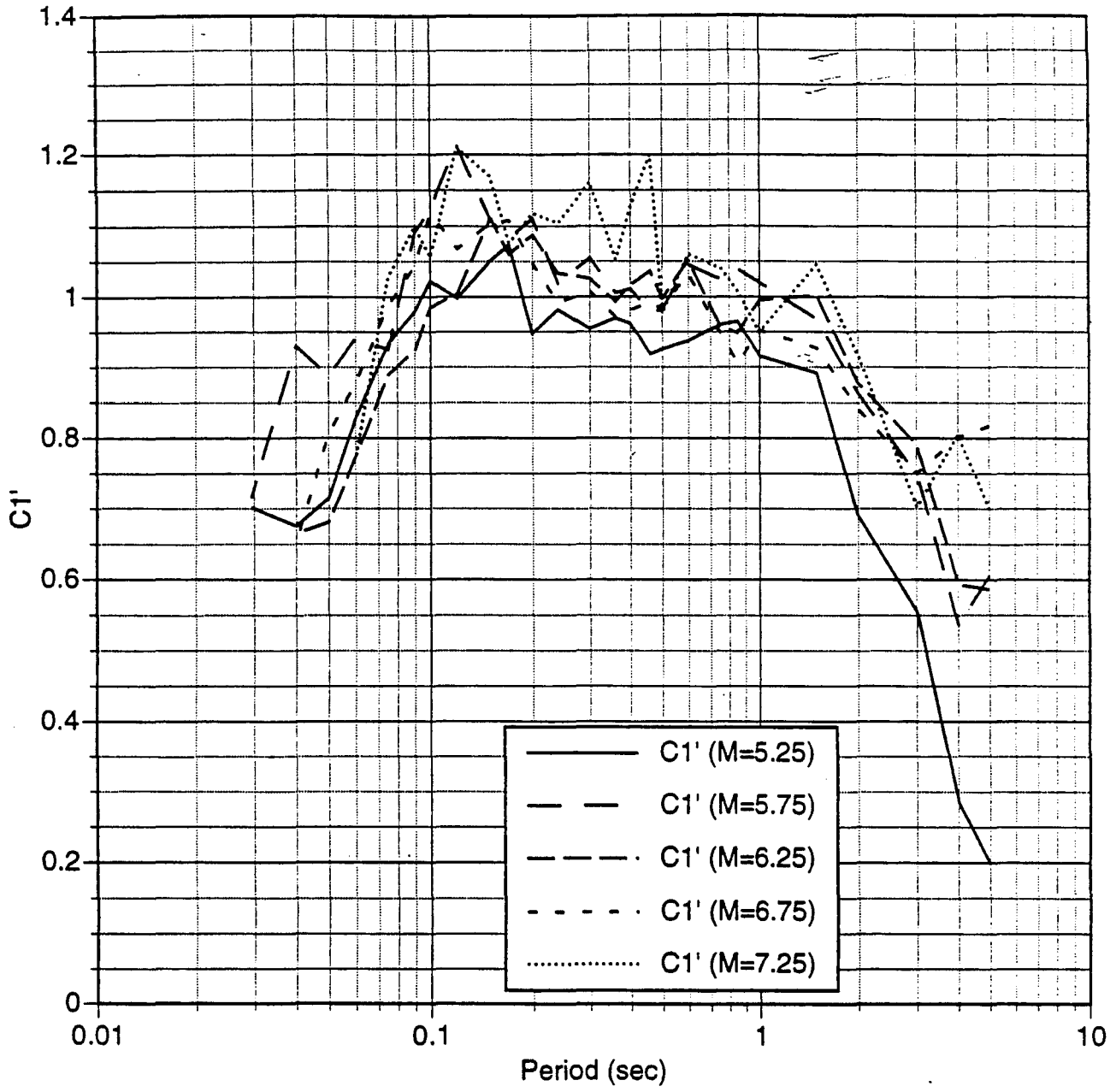

Figure 3. Magnitude dependence of C1' (~~horizontal~~ vertical) averaged over all eight damping levels.

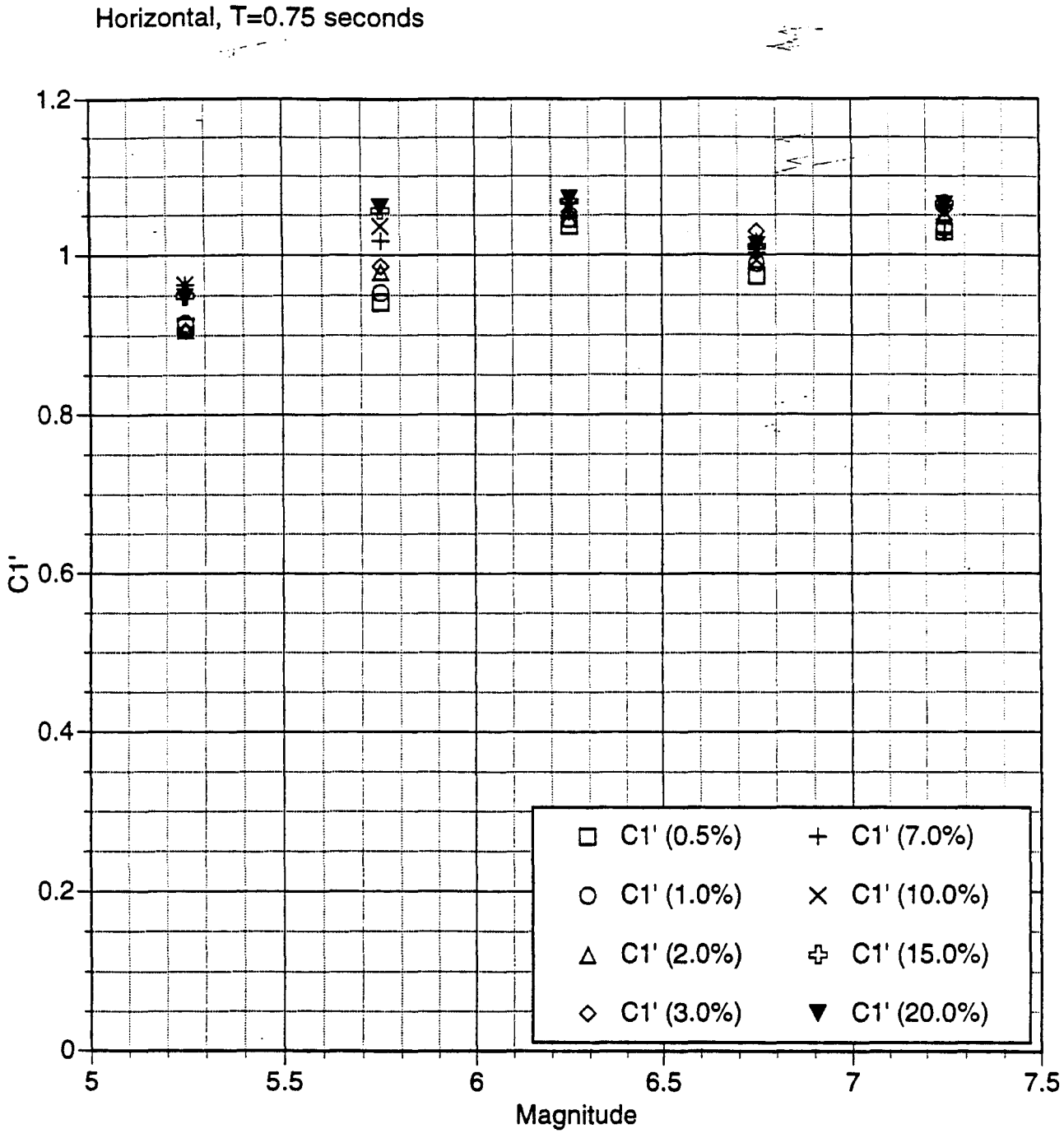

Figure 4a. Magnitude dependence of C1' for 0.5 unit magnitude bins.

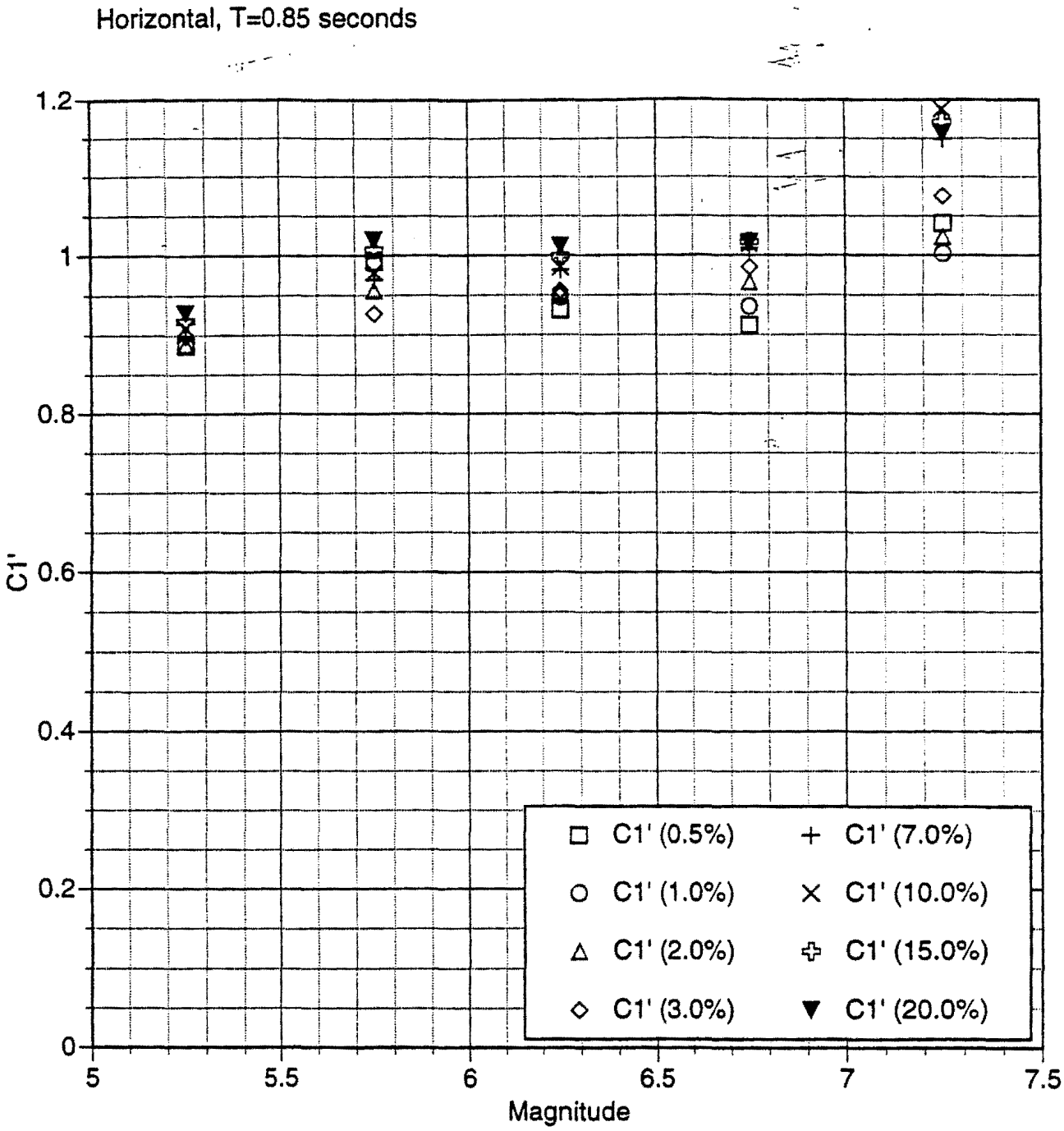

Figure 4b. Magnitude dependence of C1' for 0.5 unit magnitude bins.

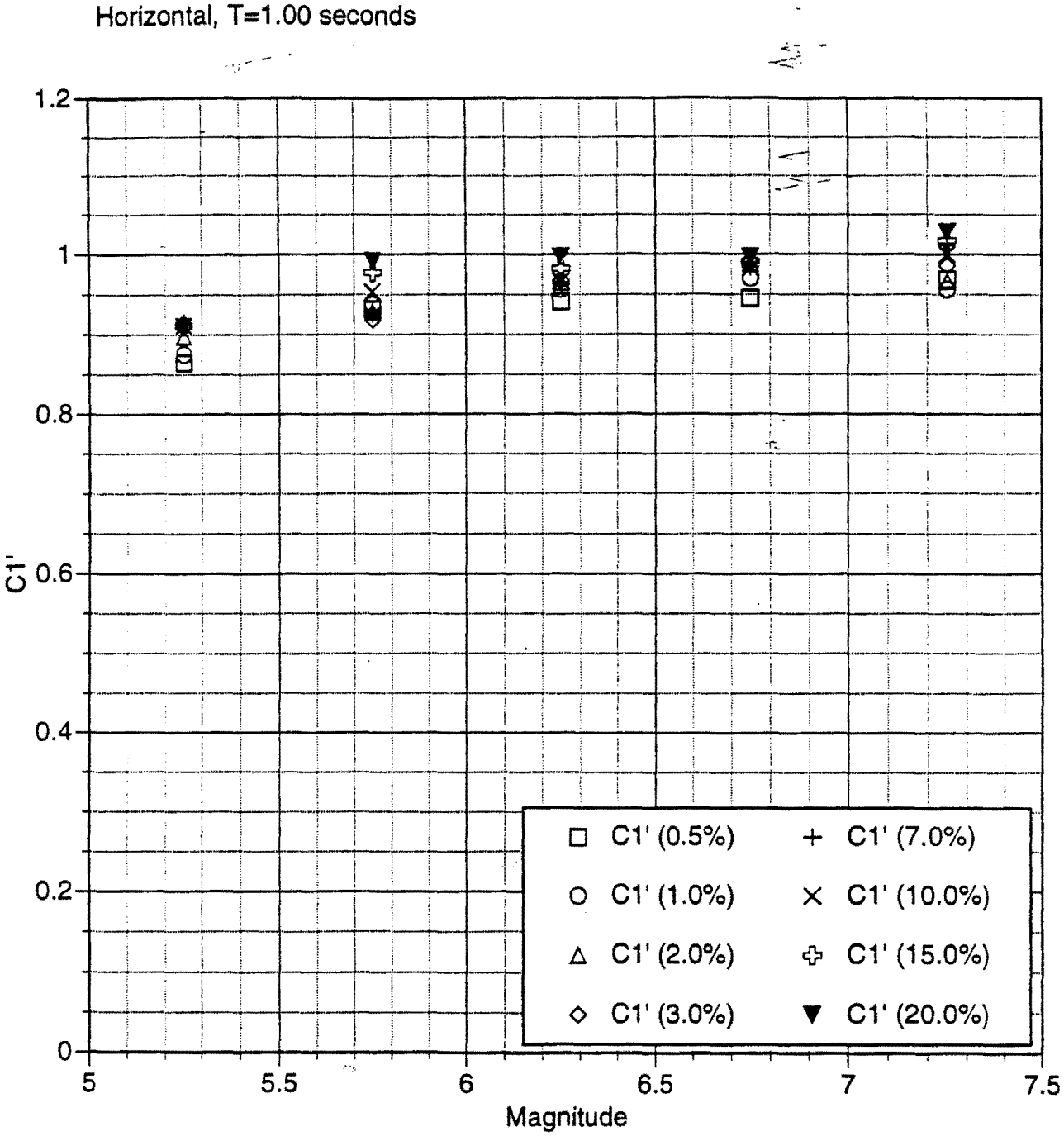

Figure 4c. Magnitude dependence of C1' for 0.5 unit magnitude bins.

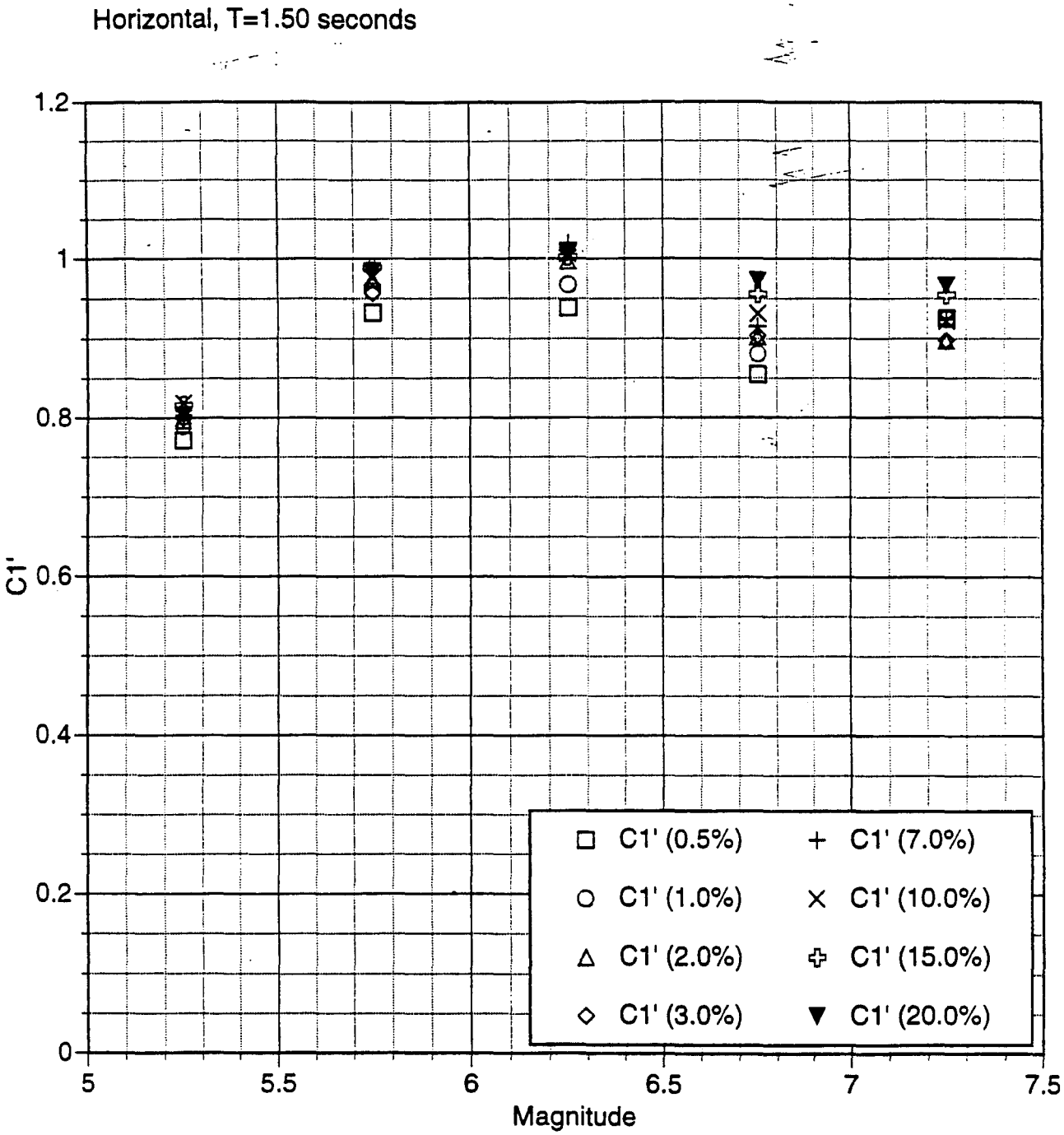

Figure 4d. Magnitude dependence of C1' for 0.5 unit magnitude bins.

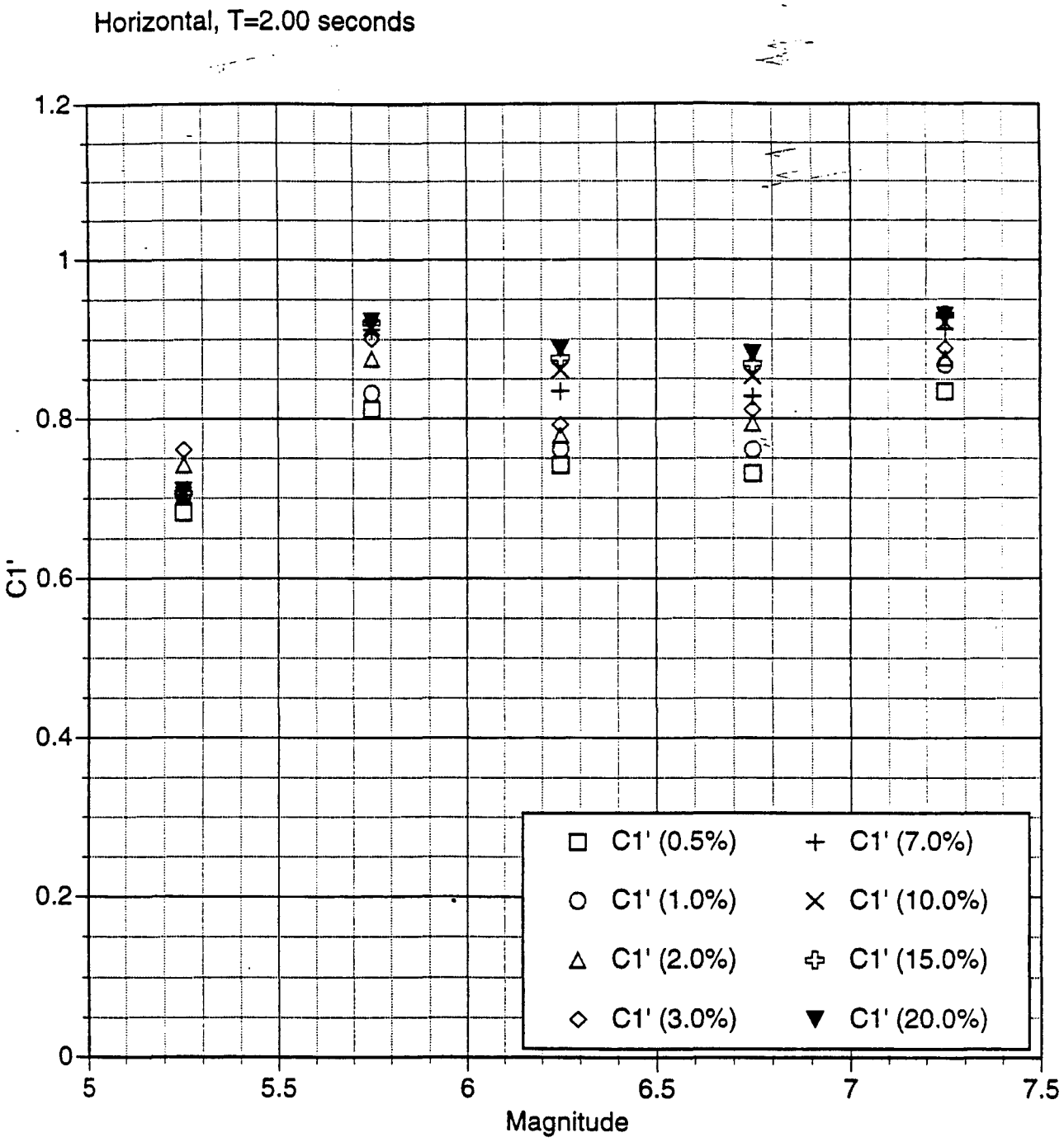

Figure 4e. Magnitude dependence of C1' for 0.5 unit magnitude bins.

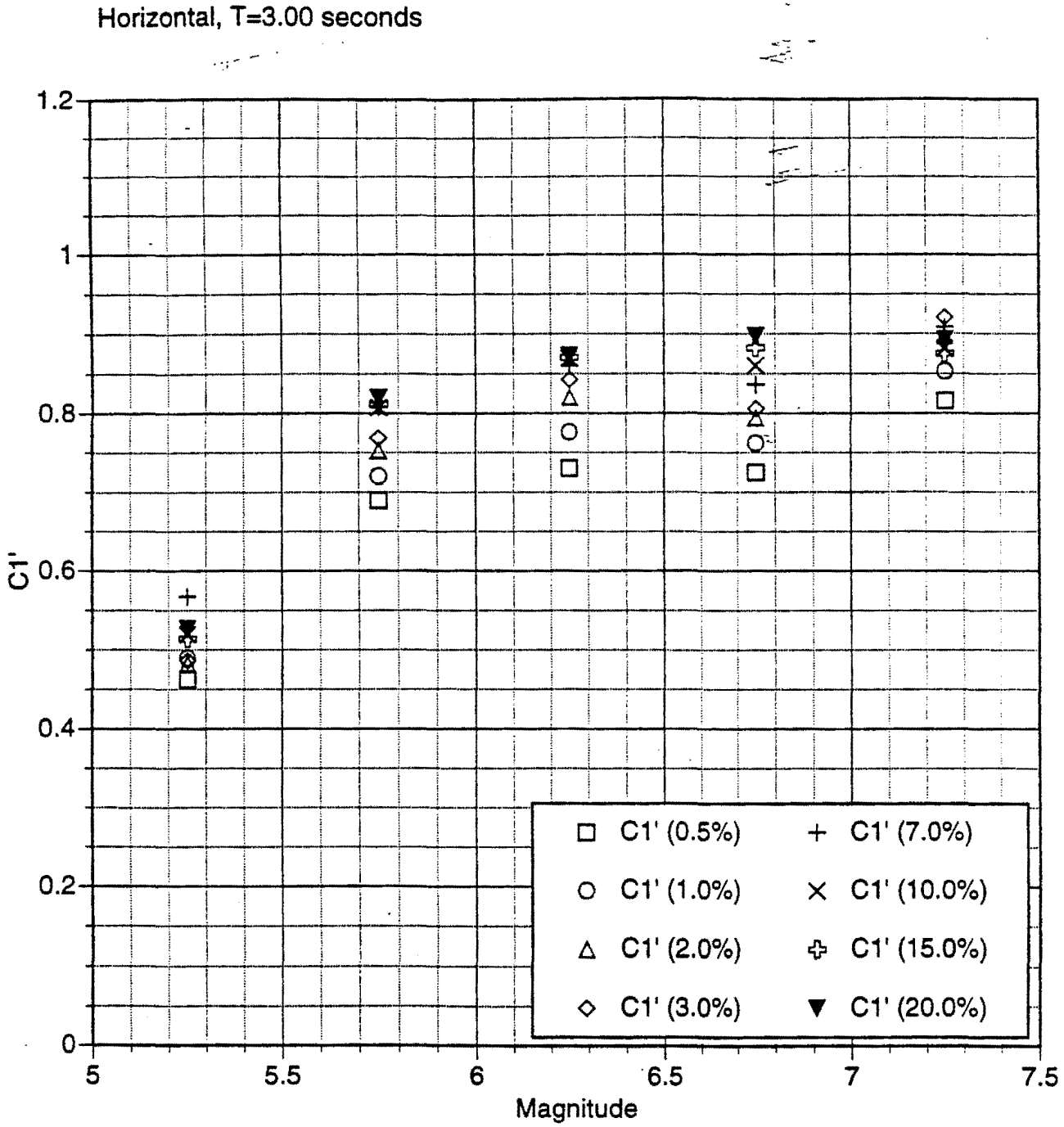

Figure 4f. Magnitude dependence of C1' for 0.5 unit magnitude bins.

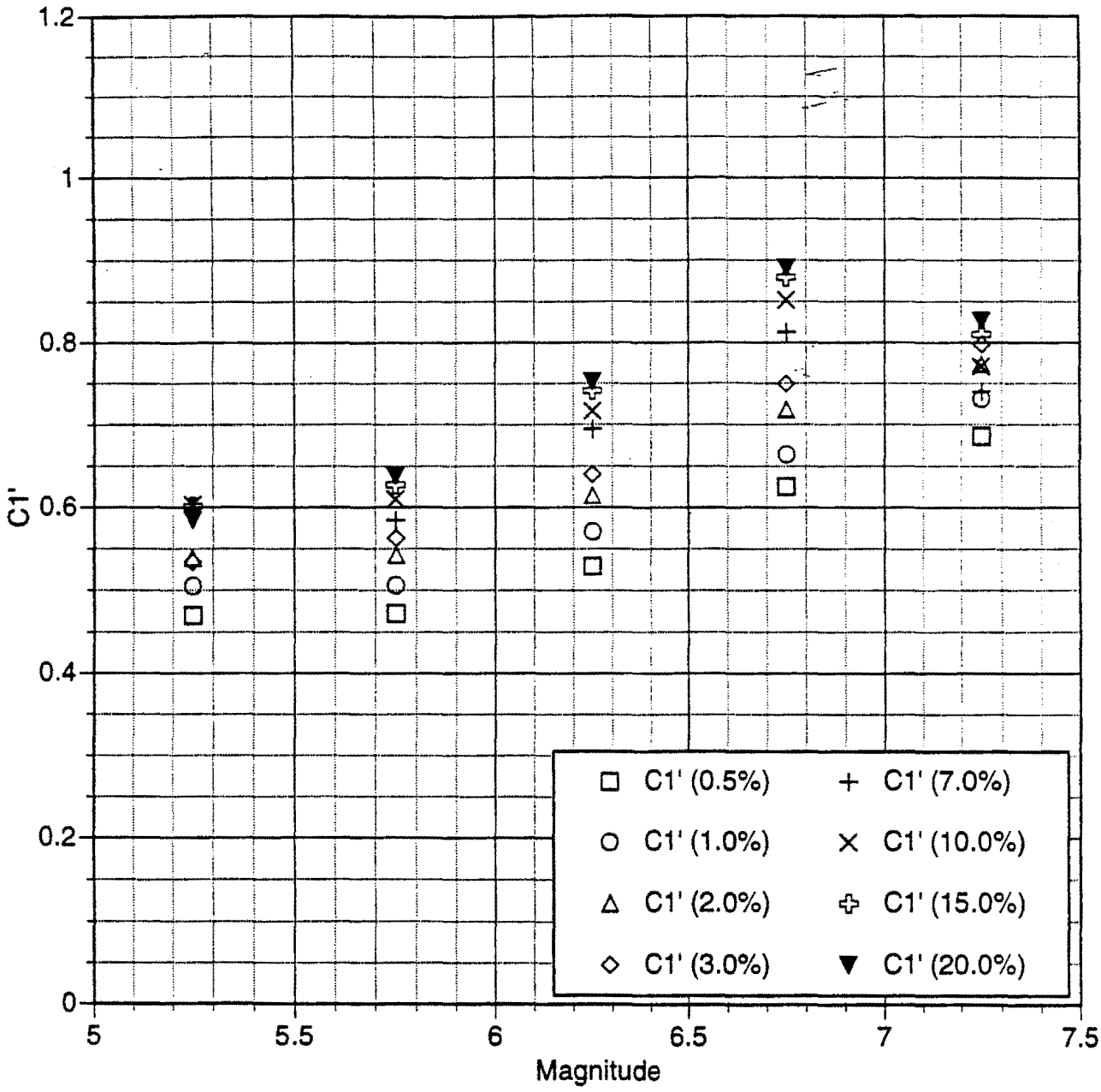

Figure 4g. Magnitude dependence of C1' for 0.5 unit magnitude bins.

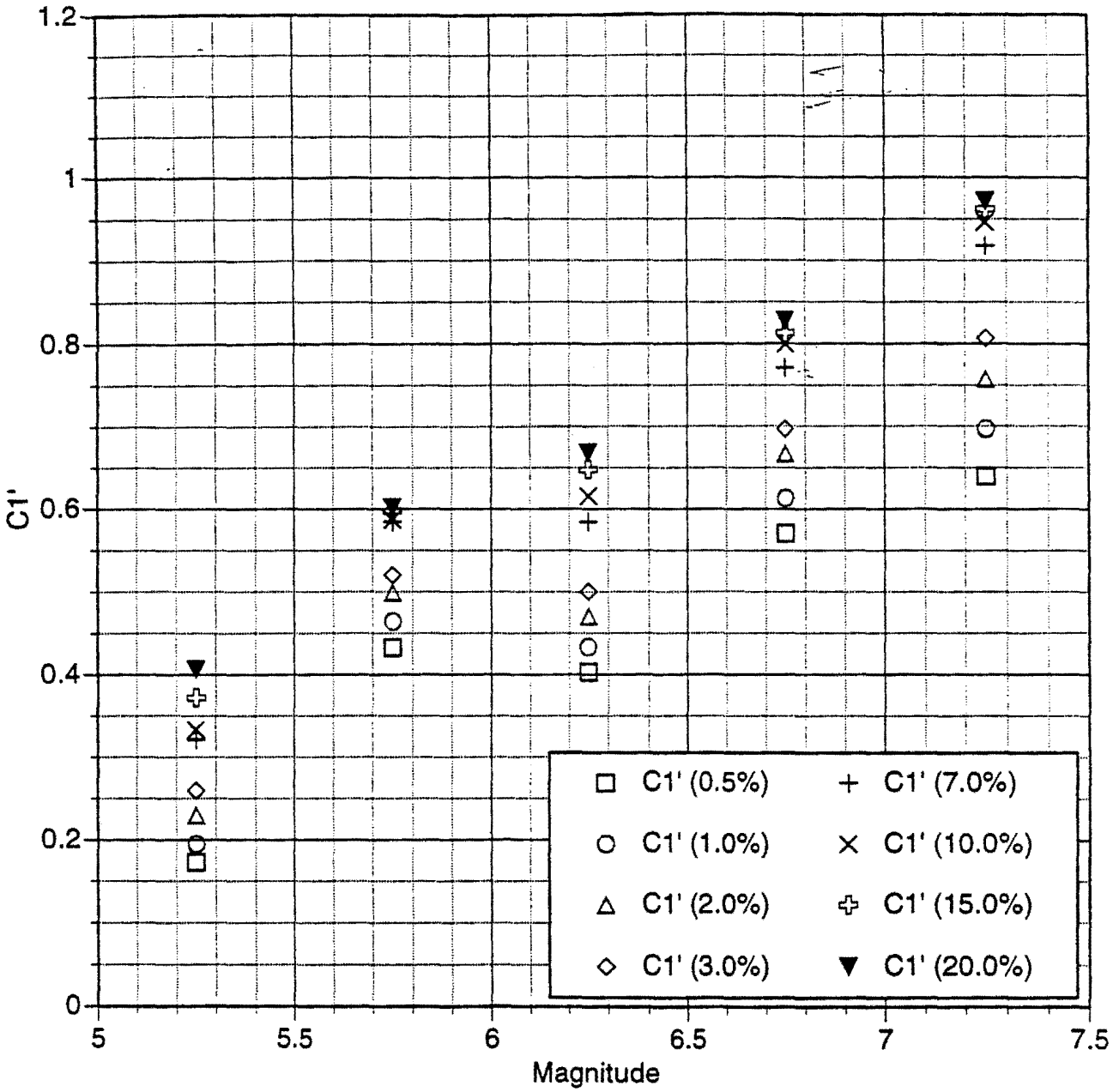

Figure 4h. Magnitude dependence of C1' for 0.5 unit magnitude bins.

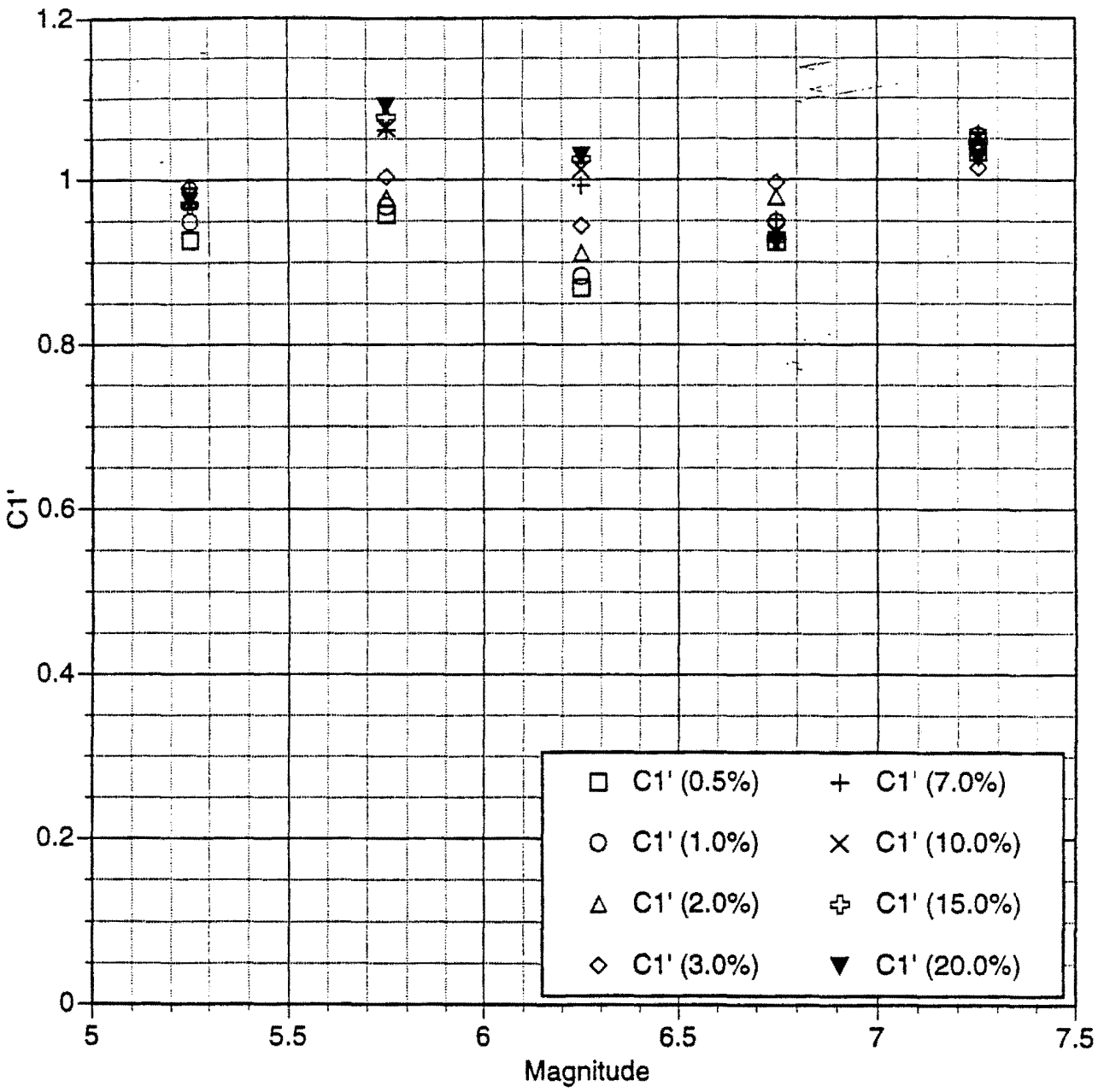

Figure 5a. Magnitude dependence of C1' for 0.5 unit magnitude bins.

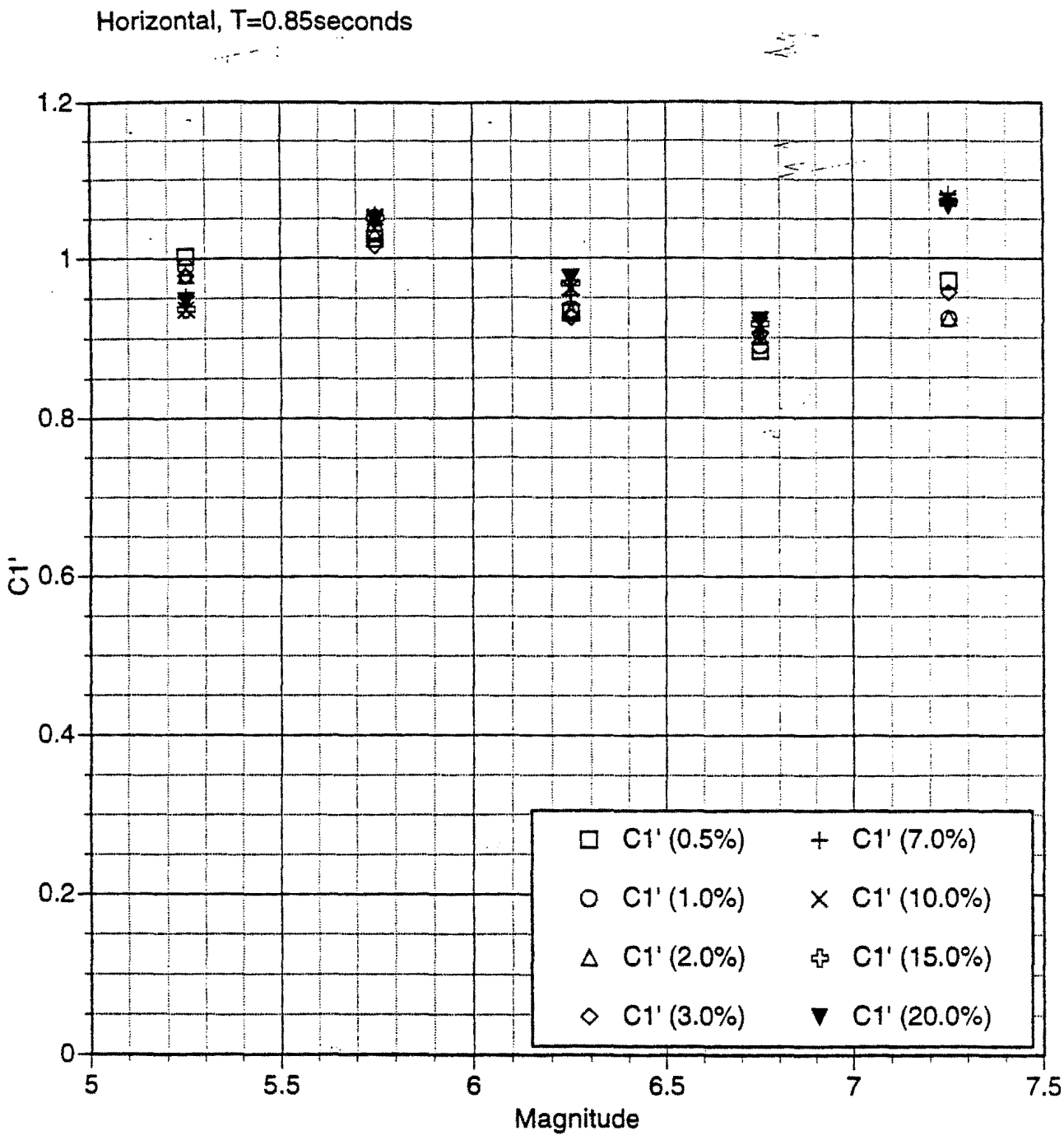

Figure 5b. Magnitude dependence of C1' for 0.5 unit magnitude bins.

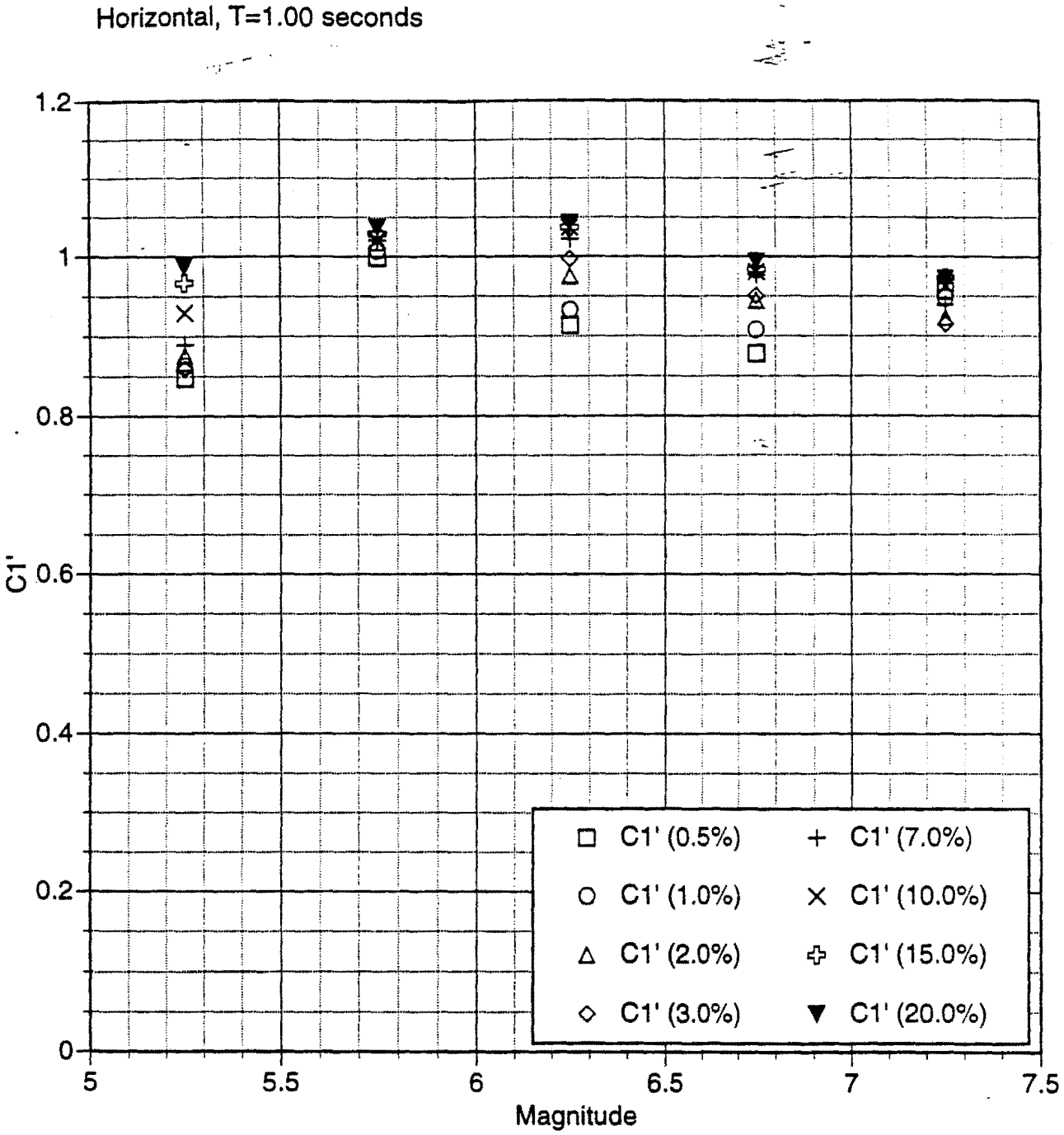

Figure 5c. Magnitude dependence of C1' for 0.5 unit magnitude bins.

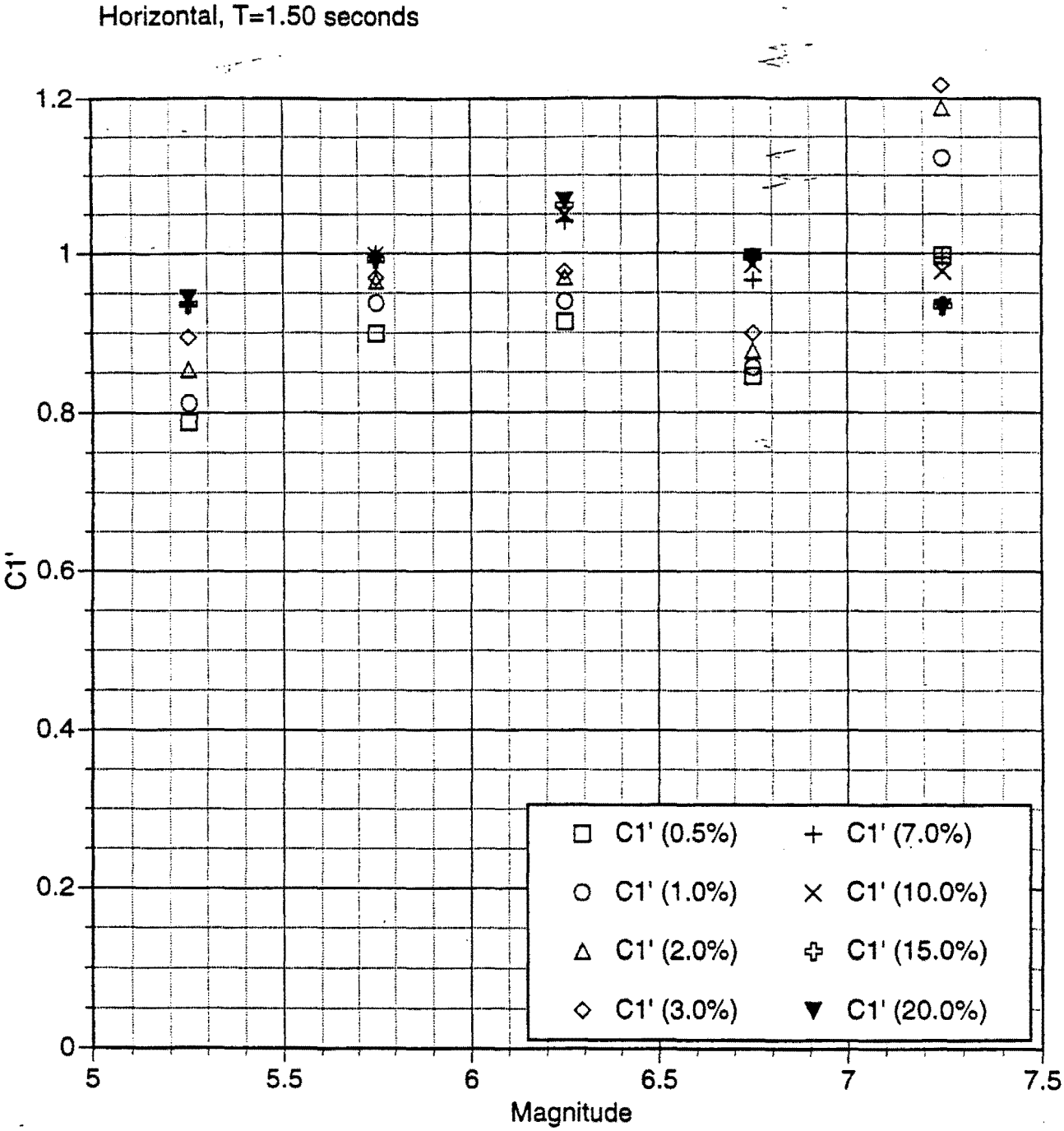

Figure 5d. Magnitude dependence of C1' for 0.5 unit magnitude bins.

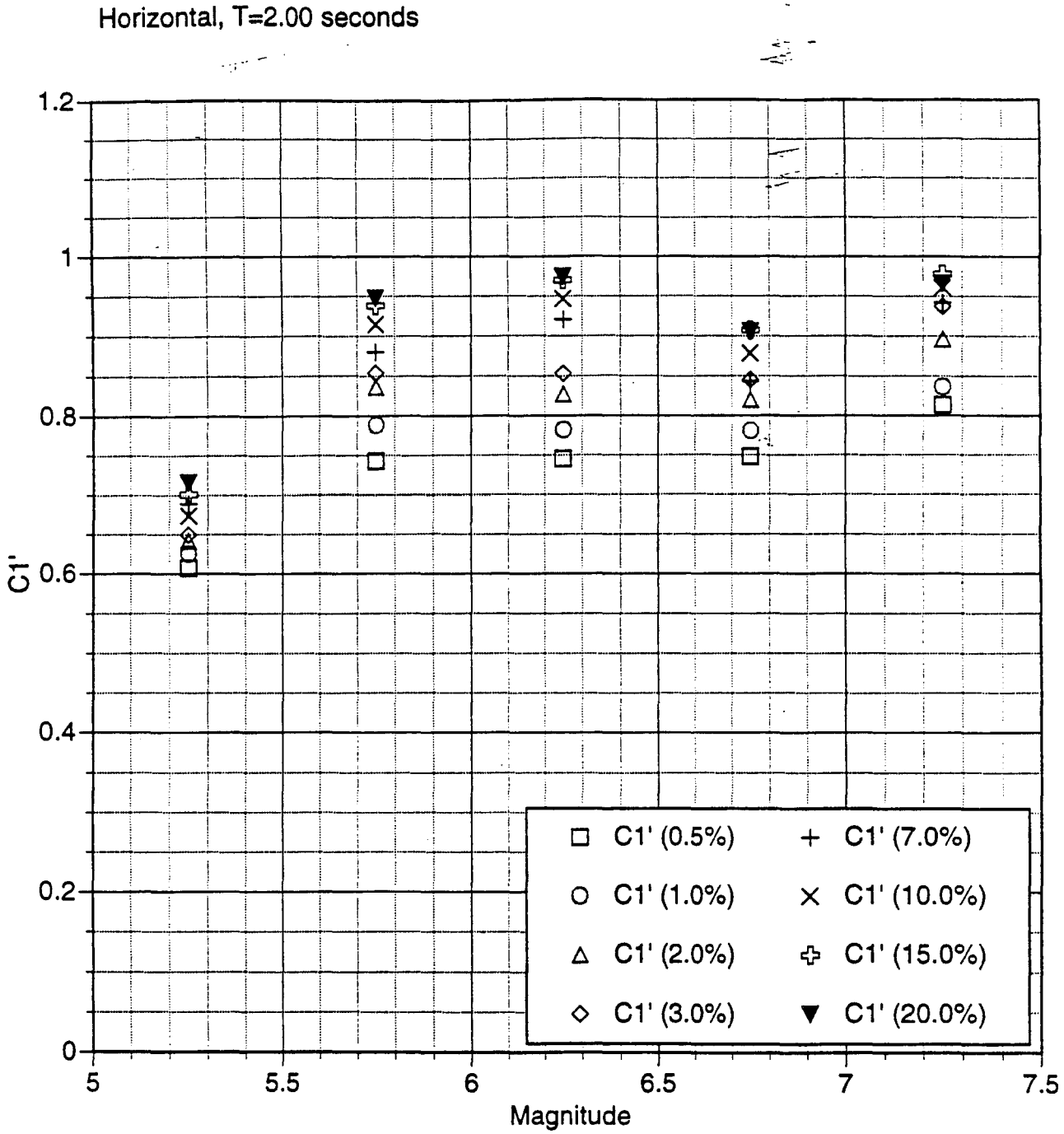

Figure 5e. Magnitude dependence of C1' for 0.5 unit magnitude bins.

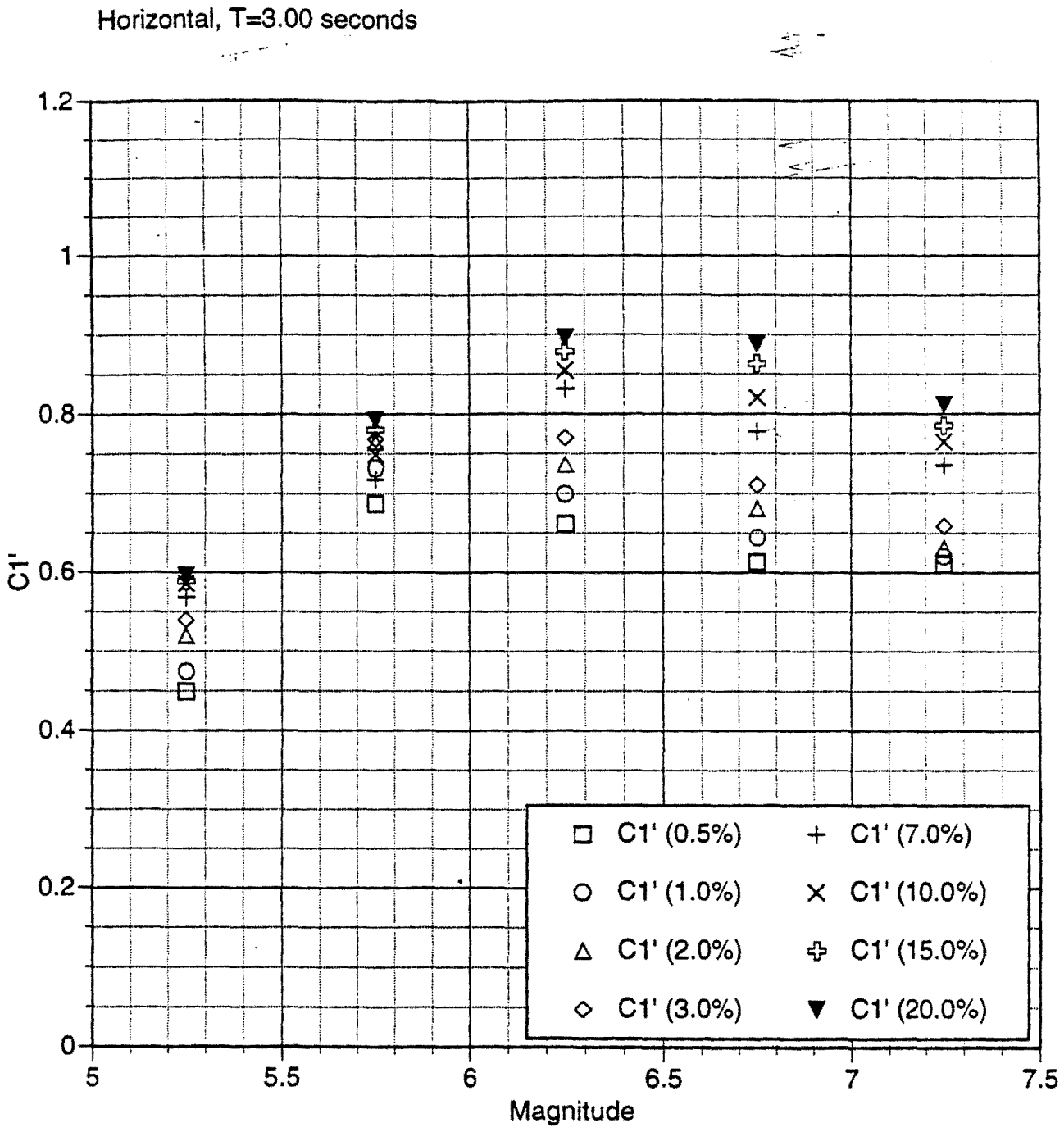

Figure 5f. Magnitude dependence of C1' for 0.5 unit magnitude bins.

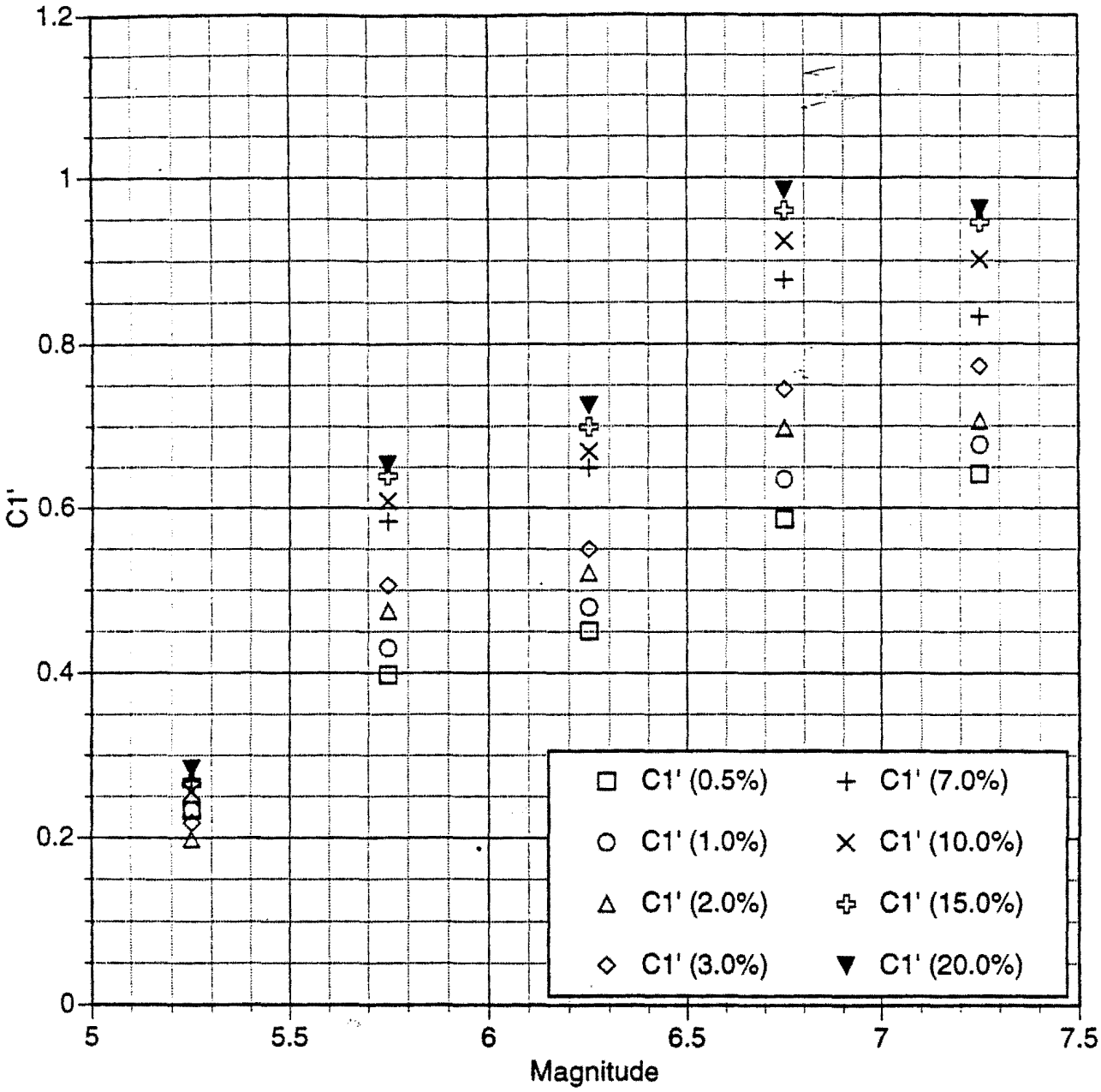

Figure 5g. Magnitude dependence of C1' for 0.5 unit magnitude bins.

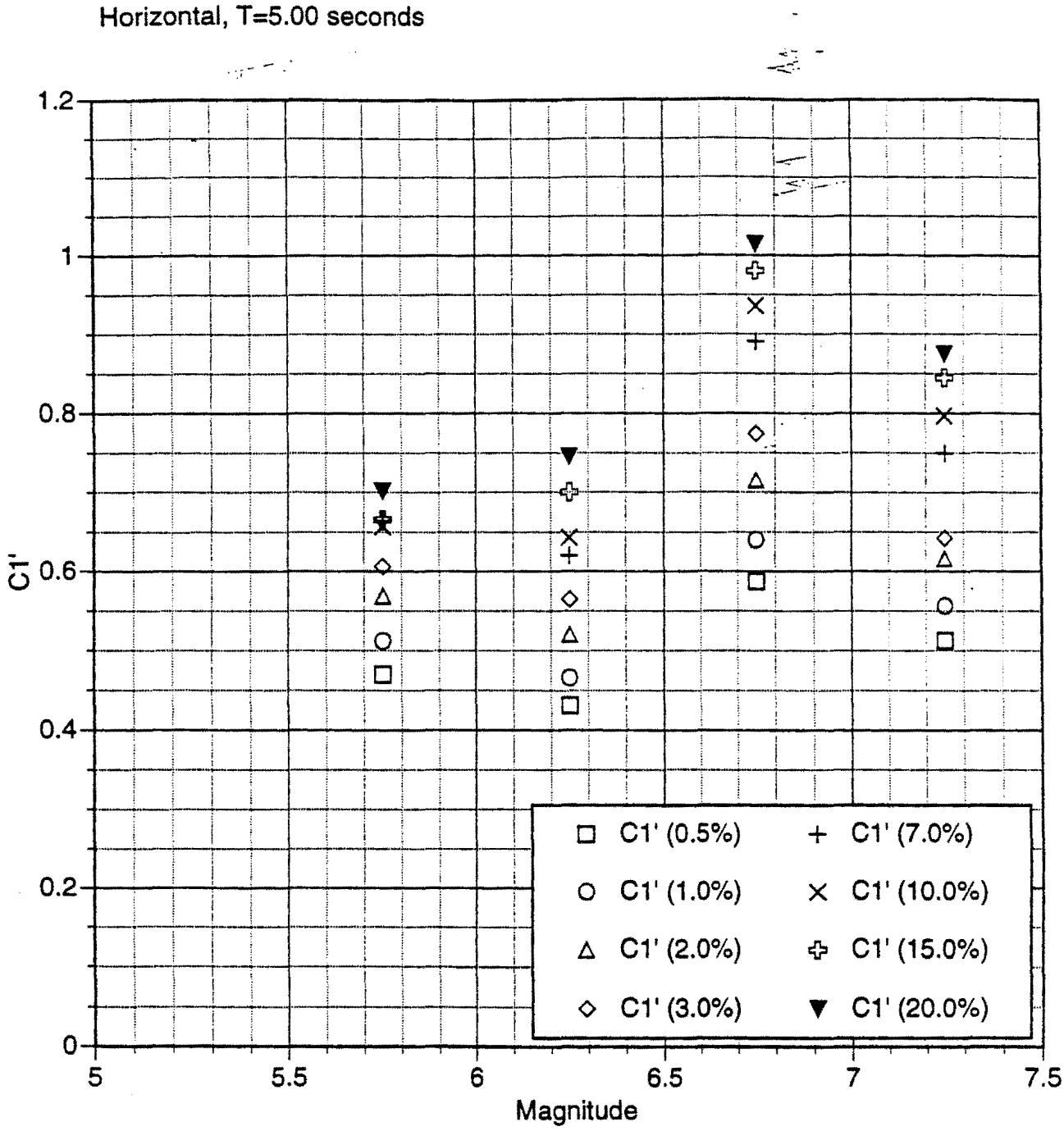

Figure 5h. Magnitude dependence of C1' for 0.5 unit magnitude bins.

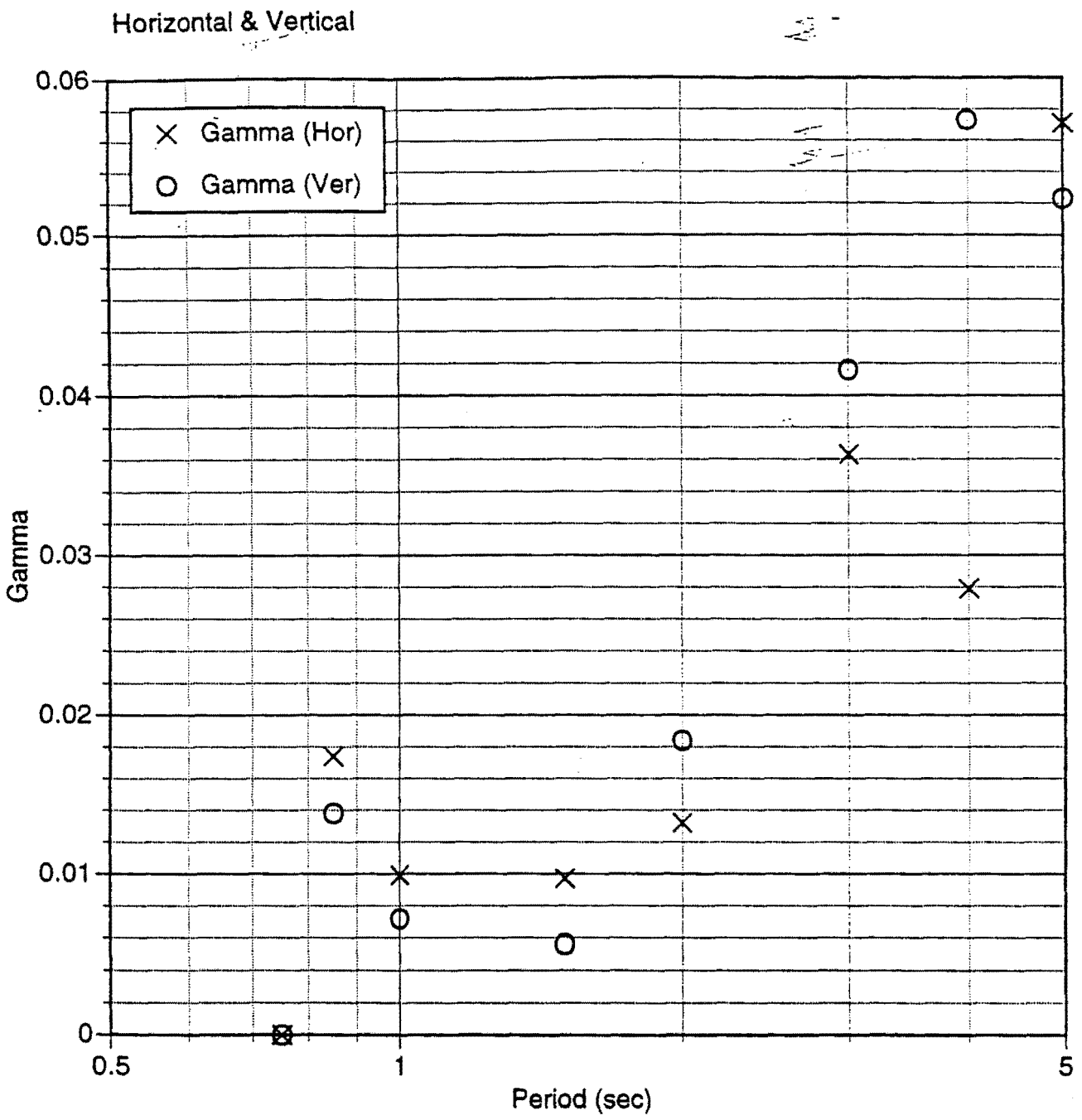

Figure 6. Gamma regression values for both the horzontal and vertical component of motion.

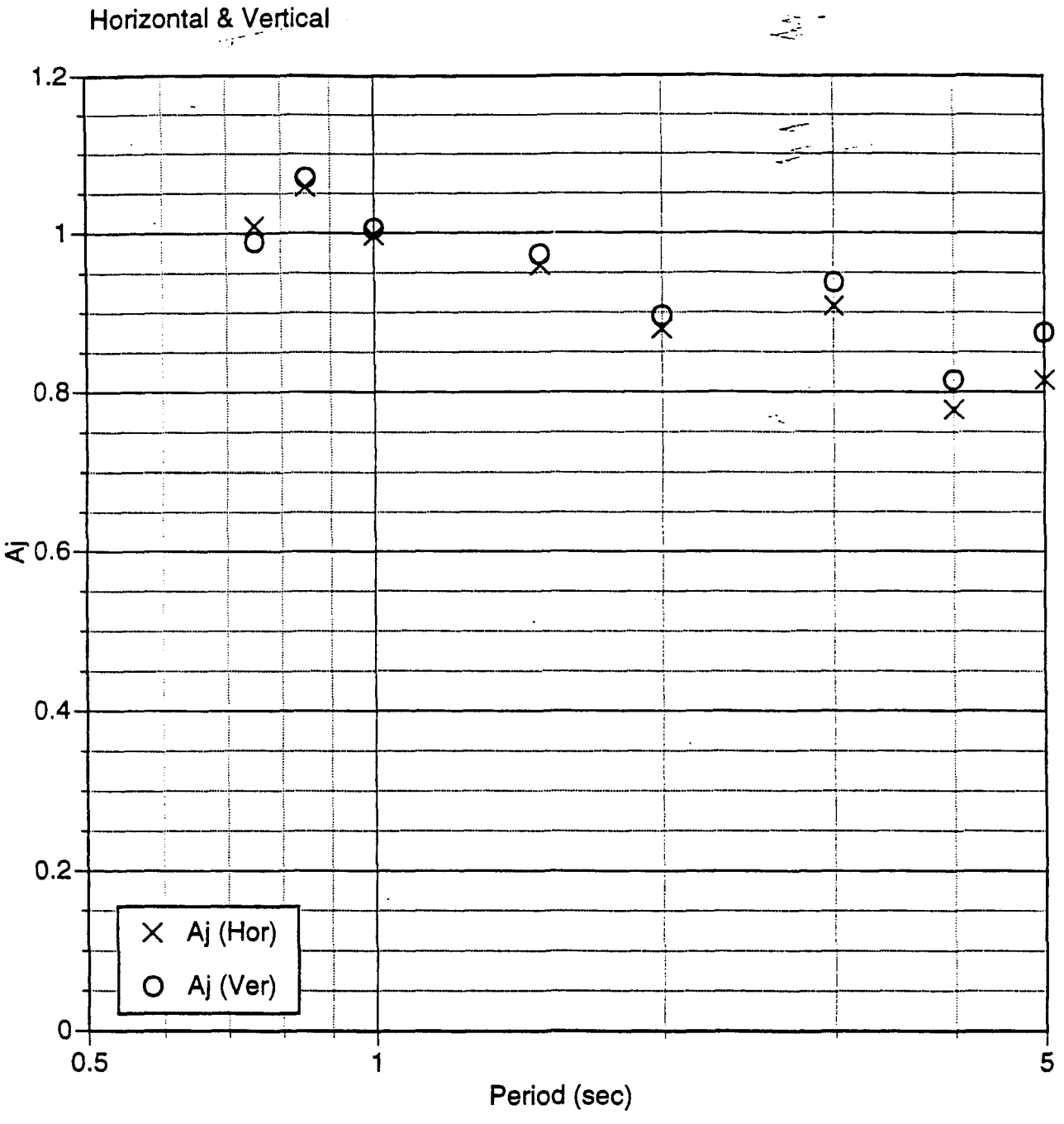

Figure 7. A_j regression values for both the horzontal and vertical component of motion.

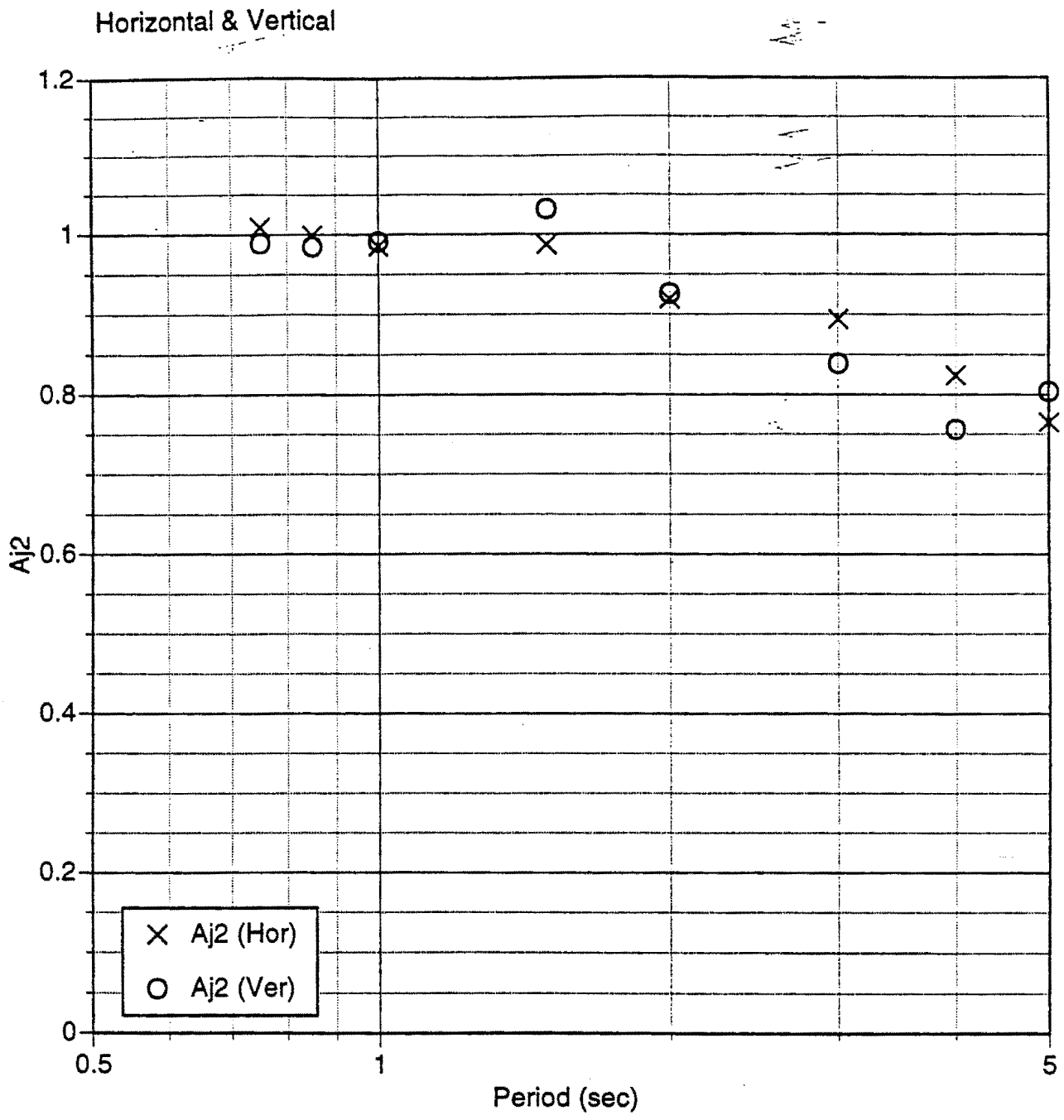

Figure 8. A_j2 regression values for both the horzontal and vertical component of motion.

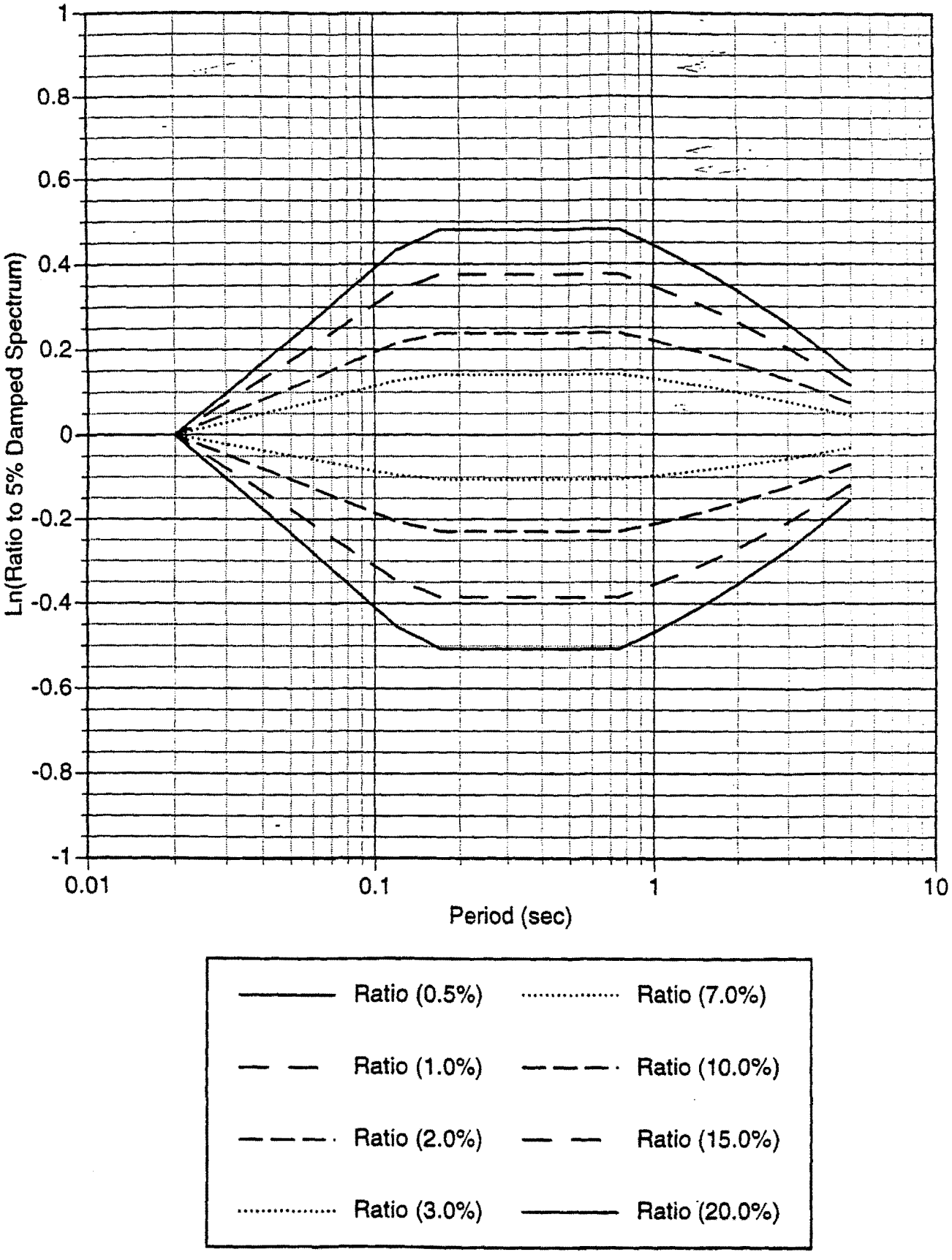

FIgure 9. Horizontal spectral ratio model for magnitude 5.

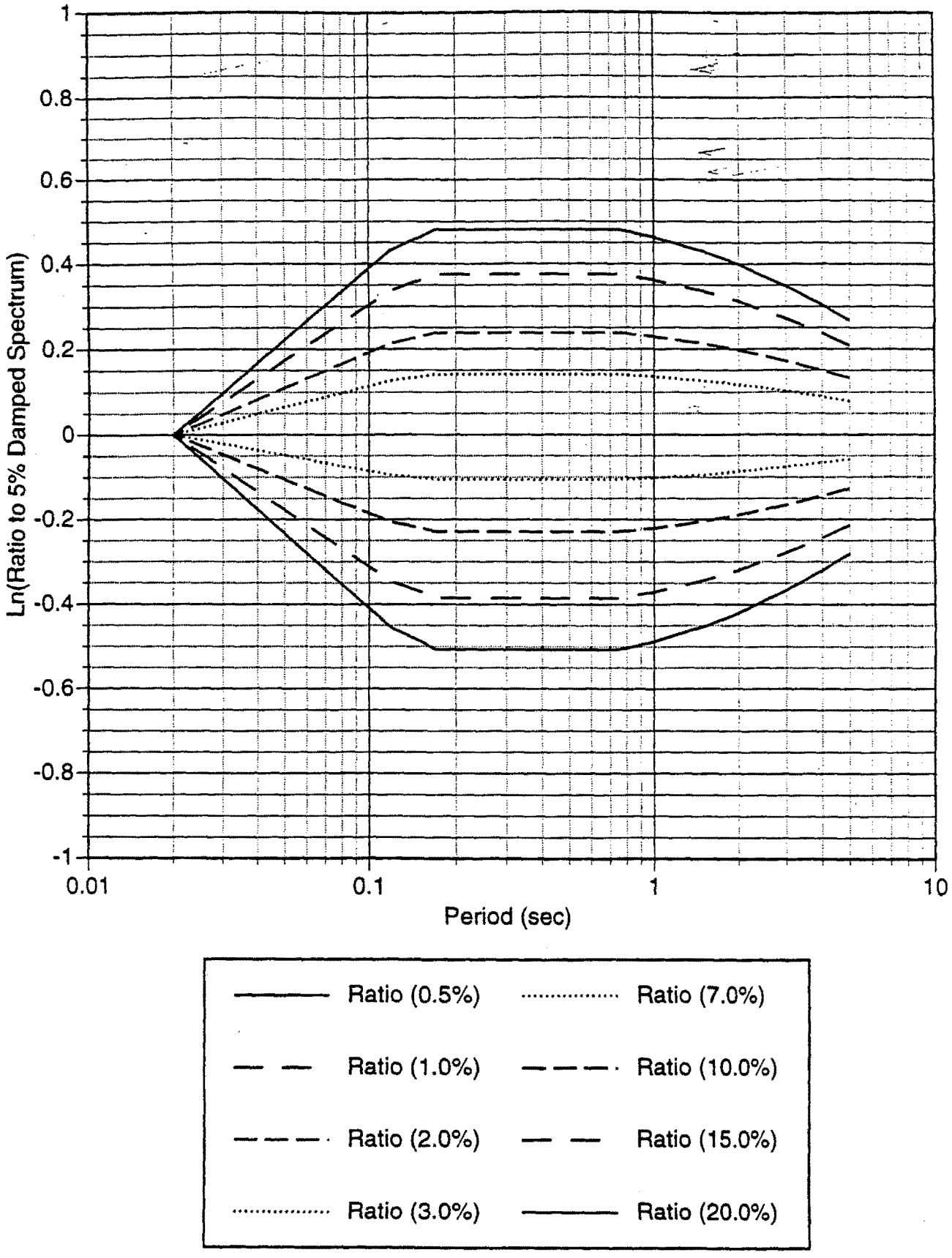

Figure 10. Horizontal spectral ratio model for magnitude 6.

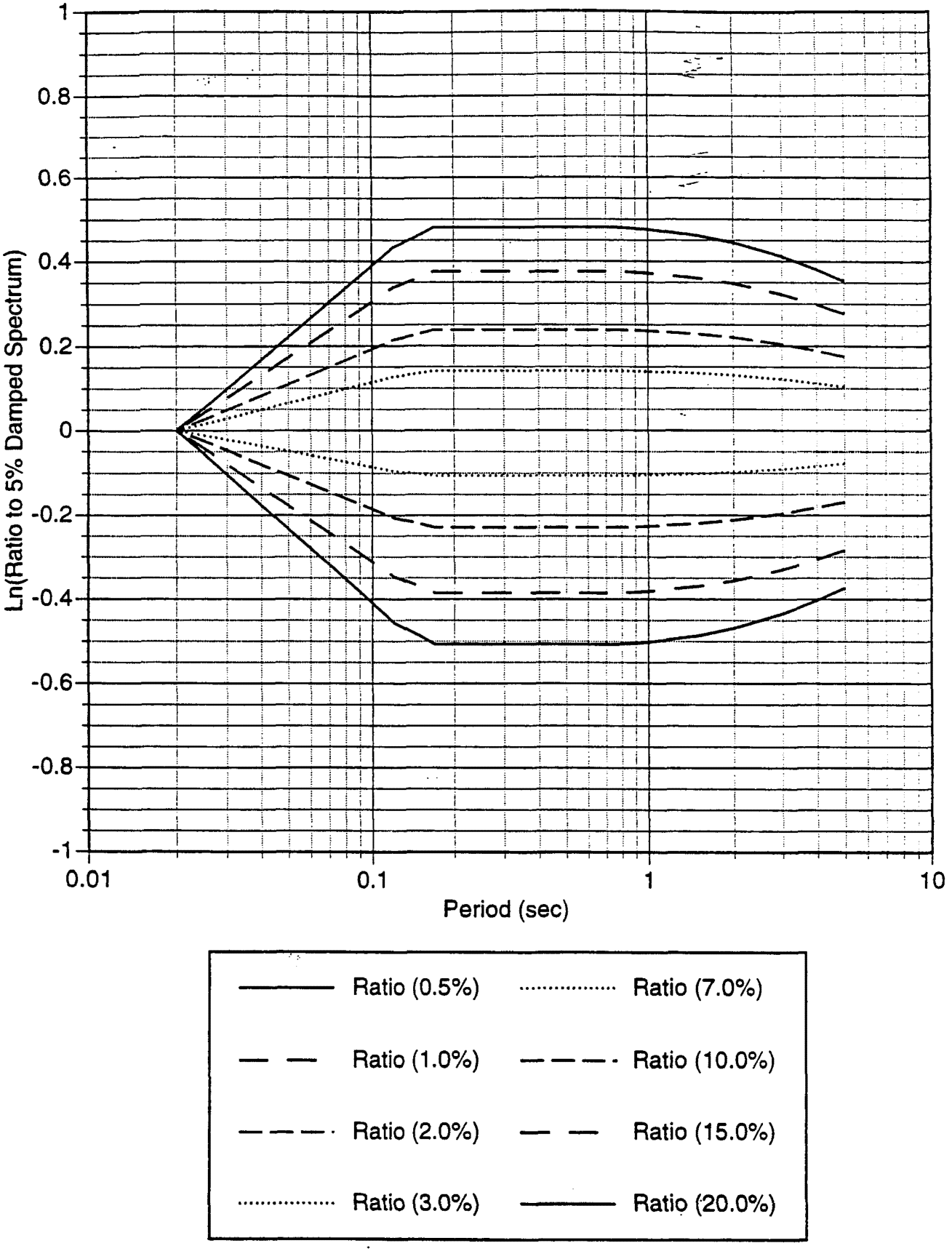

FIgure 11. Horizontal spectral ratio model for magnitude 7.

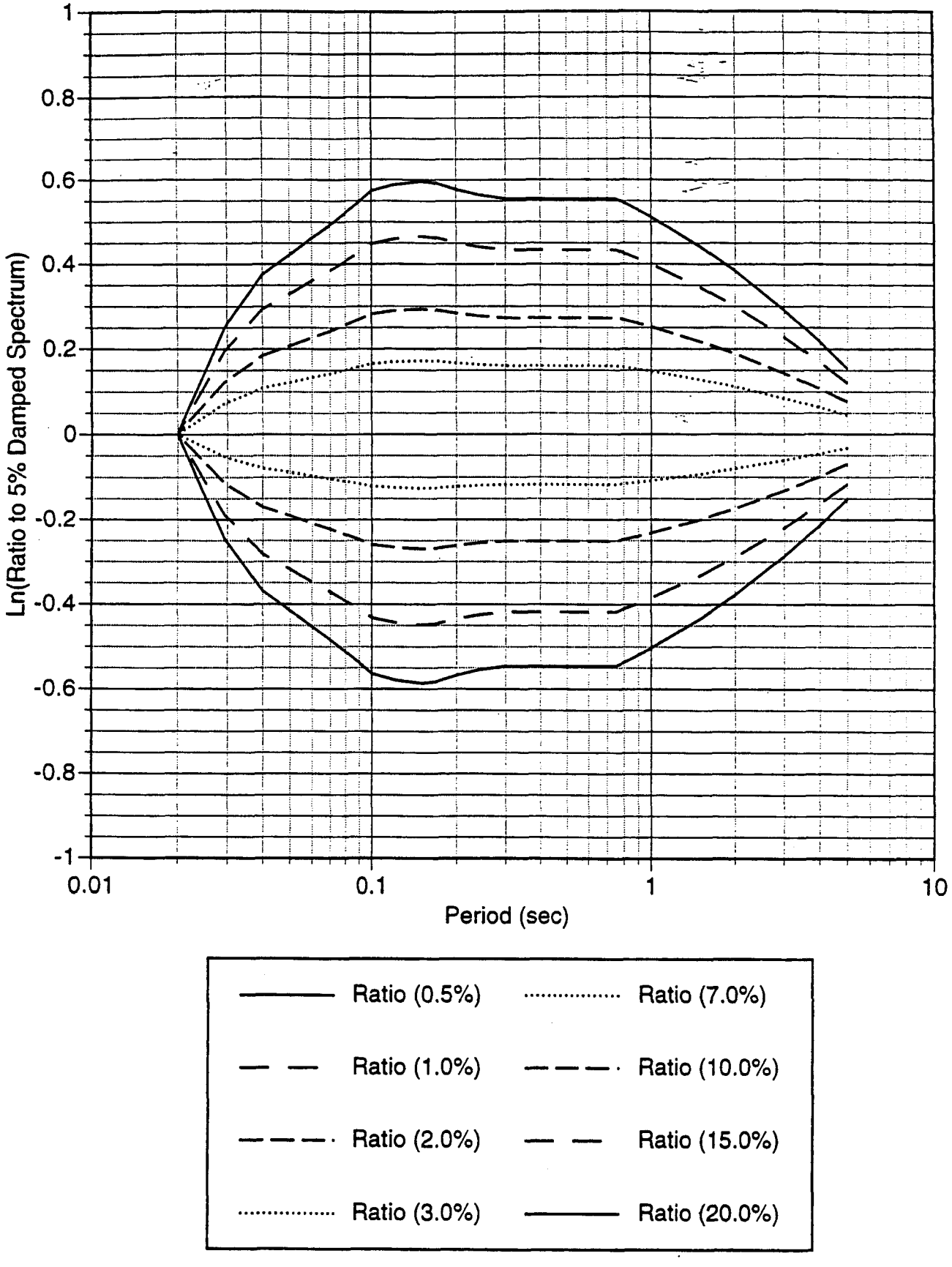

Figure 13. Vertical spectral ratio model for magnitude 5.

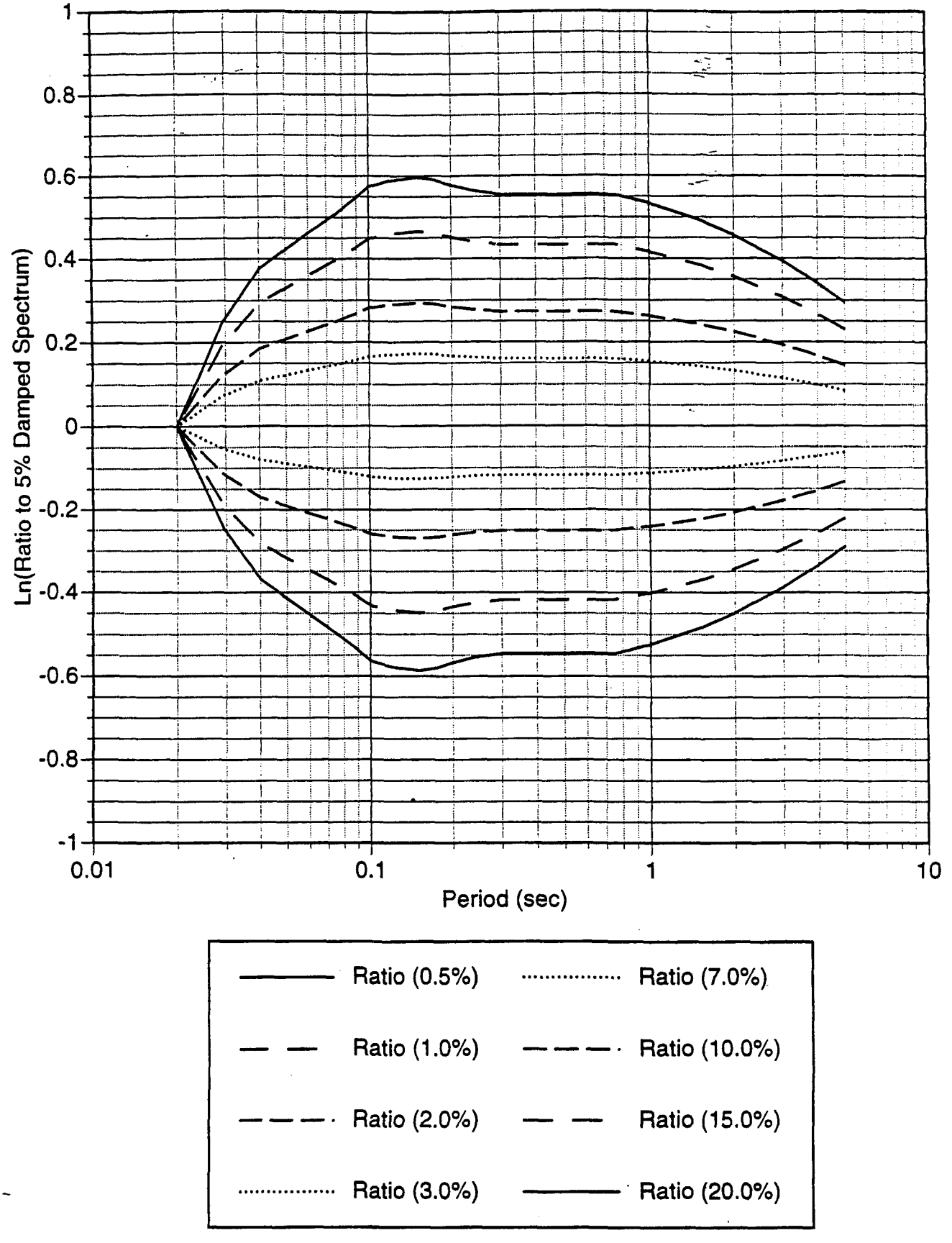

FIgure 14. Vertical spectral ratio model for magnitude 6.

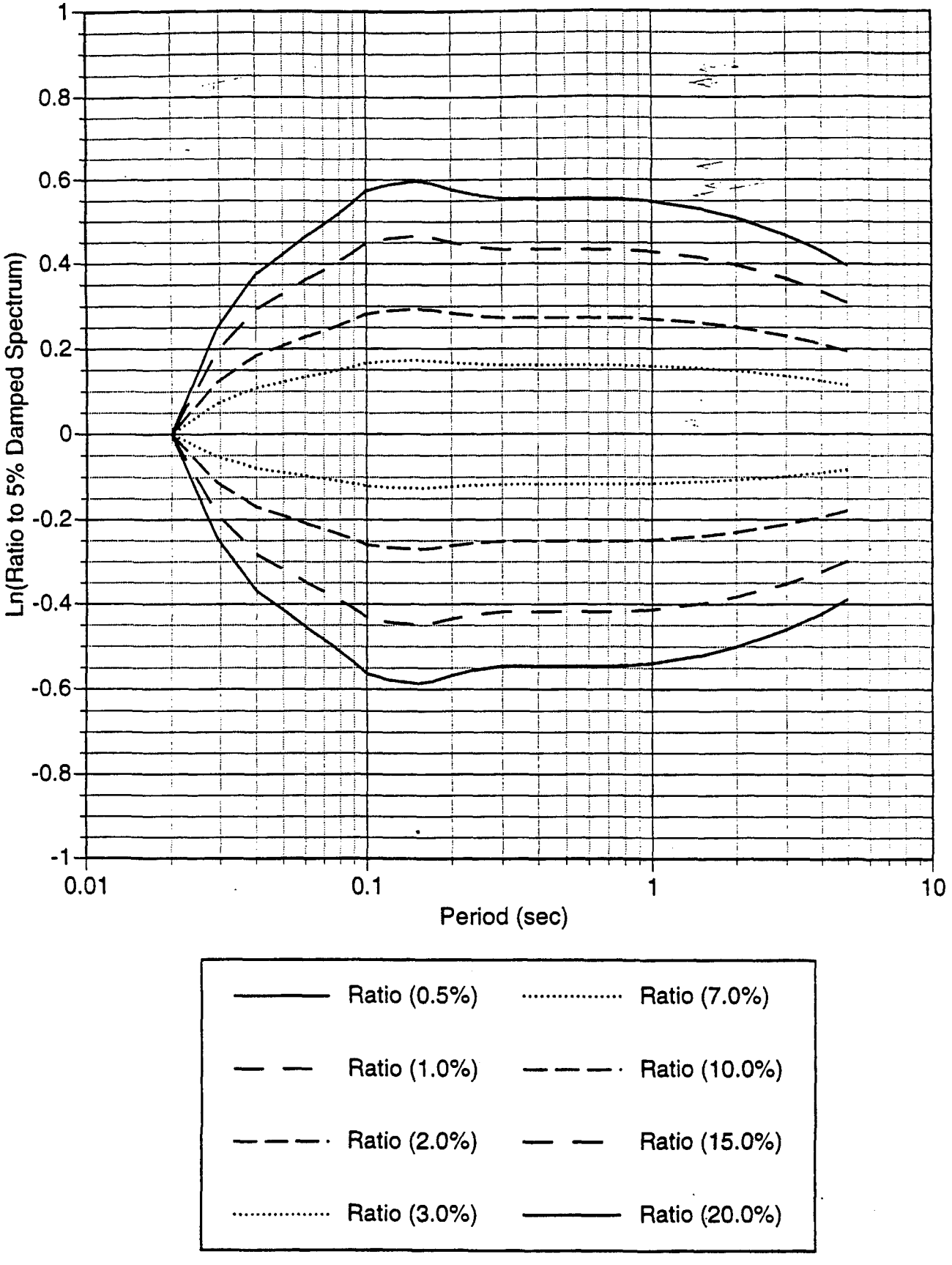

FIgure 15. Vertical spectral ratio model for magnitude 7.

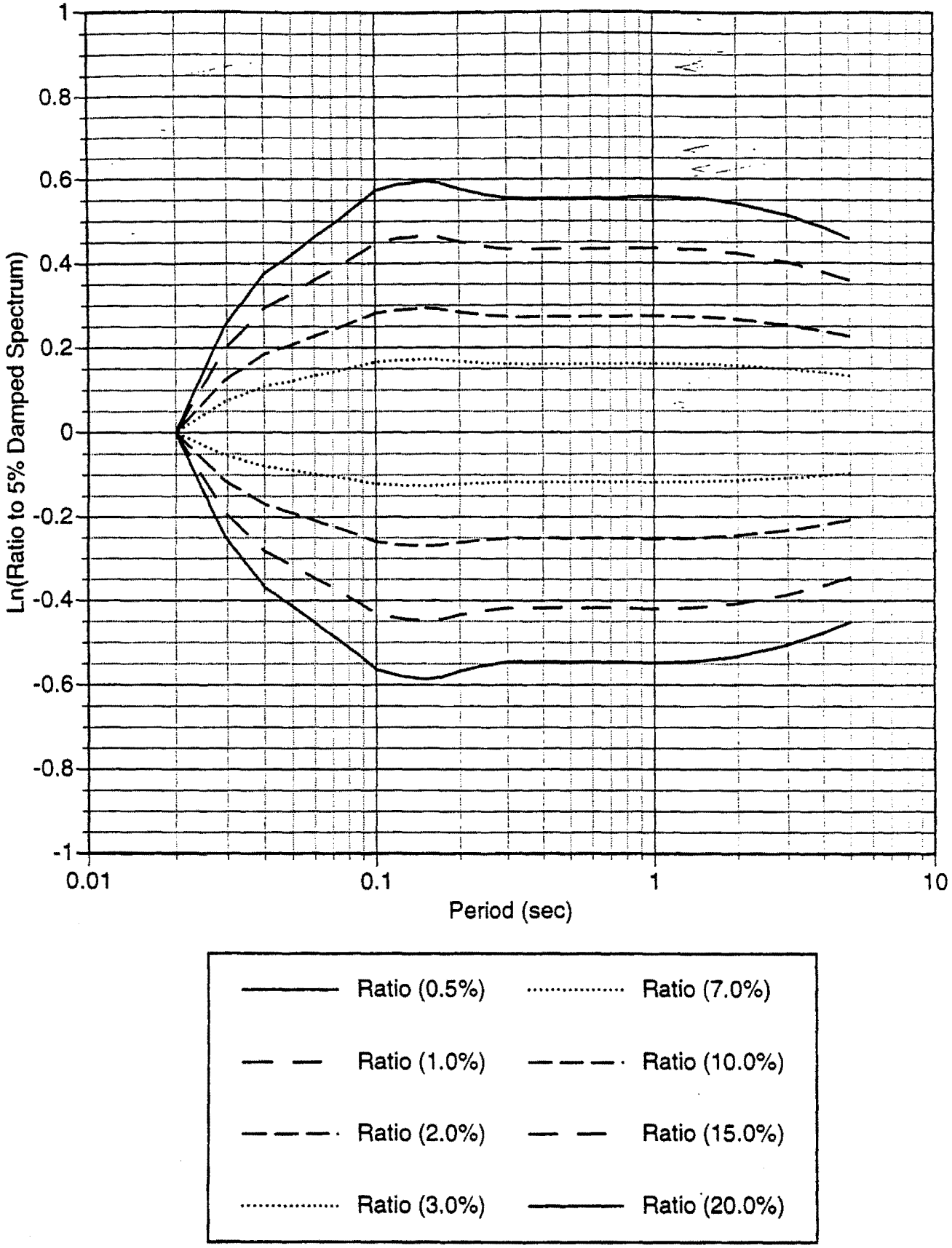

FIgure 16. Vertical spectral ratio model for magnitude 8.

Section 5

Empirical Model for Duration of Strong Ground Motion

Introduction

Although the duration is an important characteristic of strong ground motion, there has been much less effort for developing empirical models of the duration than there has been for developing empirical models of response spectra attenuation relations. Part of the difficulty has been that there are several different definitions of duration that have been used in previous studies. As a result, while qualitatively duration is well understood, quantitatively, there is a wide range of duration estimates for the same set of recordings.

In this study, we have used the definition of duration based on the normalized arias intensity of acceleration because this is the duration that is most appropriate for the RVT models. The normalized arias intensity is defined as

$$I(t) = \frac{\int_0^t a^2(\tau)\, d\tau}{\int_0^\infty a^2(\tau)\, d\tau} \qquad (5\text{-}1)$$

where $a(\tau)$ is the acceleration time history and the normalized intensity, I(t), ranges from 0 to 1. The duration is defined as the time interval between which I(t) reaches two values. That is, given I(t), we then develop the inverse relation for t(I). The duration, $D_{I1\text{-}I2}$, is given by

$$D_{I1\text{-}I2} = t(I_2) - t(I_1) \qquad (5\text{-}2)$$

For example, if I_1=0.05 and I_2=0.75, then D_{I1-I2} is the duration of the 5-75% normalized arias intensity.

Approach

A two-step approach is used to develop the empirical model for the duration. In the first step, a model is developed describing the magnitude, distance, and site dependence of the duration for the 5-75% normalized arias intensity ($D_{0.05-0.75}$). In the second step, a model is developed describing the the ratio of the duration at other normalized arias intensity levels (e.g. 5-95%) relative to the 5-75% duration. Together, these two models provide a description of the magnitude, distance, and site dependence of the duration for a range of normalized arias intensities.

$D_{0.05-0.75}$ Model

In the first step, the model is developed for $D_{0.05-0.75}$. Previous studies have found that at short distances on rock sites, $D_{0.05-0.75}$ is similar to the source duration which is approximated by $1/f_c$, where f_c is the corner frequency of the earthquake (ref). That is, for short distances at rock sites:

$$D_{0.05-0.75} = \frac{1}{f_c(M_o, \Delta\sigma)} \tag{5-3}$$

where

$$f_c(M_o, \Delta\sigma) = 4.9 \times 10^6 \beta \left(\frac{\Delta\sigma}{M_o}\right)^{1/3} \tag{5-4}$$

and β is the shear wave velocity at the source (in km/s), $\Delta\sigma$ is the stress drop (in bars), and M_o is the moment (in dyne-cm).

At larger distances, the duration increases due to complexities in the wave propagation (scattering and 3-D effects). At soil sites, the duration is typically larger than at rock sites. The distance dependence and site dependence are considered to be additive to the source duration. This leads to a model of the form:

$$D_{0.05-0.75} = \frac{1}{f_c(M_o, \Delta\sigma)} + f_1(r) + f_2(S,r) \qquad (5\text{-}5)$$

where $f_1(r)$ is the distance dependence on rock and $f_2(S,r)$ is the site dependence which allows for coupling of the site and distance dependence.

The magnitude dependence of the duration is determined by the magnitude dependence of the corner frequency, f_c, which is in turn determined by the magnitude dependence of the moment and stress-drop. The moment is related to magnitude by

$$\log_{10} M_o = 1.5M + 16.05 \qquad (5\text{-}6)$$

The magnitude dependence of the stress drop is estimated as part of the regression analysis.

Previous studies have found that the distance dependence of duration on rock, $f_1(r)$, is approximately proportional to distance (ref). The distance dependence of $D_{0.05\text{-}0.75}$ is shown in Figures 5-1a and 5-1b for the horizontal component and in Figures 5-2a and 5-2b for the vertical component. These data also indicate that the duration increases linearly with distance at large distances. At short distances the duration is

approximately independent of distance. This leads to a piecewise continuous form for $f_1(r)$:

$$f_1(r) = \begin{cases} 0 & \text{for } r \le r_c \\ c_2(r-r_c) & \text{for } r > r_c \end{cases} \quad (5\text{-}7)$$

where r_c is a cutoff distance determined by the regression analysis.

For the site dependence, $f_2(S,r)$, a constant is used for short distances. A distance dependence of the site effect is also considered, leading to the following model:

$$f_2(r) = \begin{cases} c_1 S & \text{for } r \le r_c \\ \{c_1 + c_3(r-r_c)\}S & \text{for } r > r_c \end{cases} \quad (5\text{-}8)$$

where S is the site term coefficient and is equal to zero for rock sites and 1 for soil sites. In the preliminary evaluations, the regression analyses were preformed with and without the c_3 term. We found that the addition of the c_3 term did not significantly improve the fit so this term is not used further. We also found that the distributions of residuals were skewed (Figure 5-3a-b). The hypothesis that the duration residuals are normally distributed can be rejected with greater than 95% confidence. The skewed distribution of residuals is consistent with a lognormal distribution.

Assuming a lognormal distribution, the resulting model is

$$\text{Ln}\,(D_{0.05-0.75}) = \text{Ln}\left[\frac{\left(\frac{\Delta\sigma(M)}{10^{1.5M+16.05}}\right)^{-1/3}}{4.9\text{x}10^6\,\beta} + Sc_1 + c_2(r-r_c)\right] \quad \text{for } r \ge r_c \quad (5\text{-}9a)$$

and

$$\text{Ln}\,(D_{0.05-0.75}) = \text{Ln}\left[\frac{\left(\frac{\Delta\sigma(M)}{10^{1.5M+16.05}}\right)^{-1/3}}{4.9\text{x}10^{6}\,\beta} + Sc_1\right] \quad \text{for } r < r_c \qquad (5\text{-}9b)$$

In the regression analysis, β is fixed at 3.2 km/s.

In the initial regression, the stress drop term (Eq 5-9a, 5-9b) was treated as a constant for all magnitudes. The r_c term is not well resolved and ranges from 5 to 15 km. Since rc is not well resolved by the data set, it's value was set to be 10 km. The remaining coefficents estimated from the initial regression are listed in Table 5-1. The distributions of the residuals shown in Figures 5-4a and 5-4b indicate that a lognormal distribution is appropriate; the hypothesis that the duration residuals are lognormally distributed cannot be rejected with 40% confidence.

It is important to note that the "duration" stress drop given in Table 5-1 is a ground motion parameter with units of bars that leads to the appropriate duration under the assumption that the 5-75% normalized arias intensity is given by $1/f_c$. It is not necessarily the same as the static stress drop or RMS stress drop.

The magnitude dependence of $\Delta\sigma$ was evaluated by estimating the $\Delta\sigma$ value for discrete 1/2 magnitude unit ranges while holding all of the other coefficients fixed to their values from Table 5-1. The estimated stress drop for the individual magnitude bins are shown in Figures 5-5a and 5-5b for the horizontal and vertical components respectively. The standard errors of the mean estimates are also shown. An exponential form, of the magnitude dependence of $\Delta\sigma$ was selected because it is consistent with the trend in the estimates shown in Figures 5-5a and 5-

5b and because it is consistent with the exponential magnitude dependence of the moment. (For short distances on rock, the magnitude dependence of the log duration reduces to a linear function in magnitude if an exponential mangitude dependence of $\Delta\sigma$ is used.) The magnitude dependence of $\Delta\sigma$ is modeled by

$$\Delta\sigma(M) = \exp\{b_1+b_2(M-6)\} \qquad (5\text{-}10)$$

Using this form for $\Delta\sigma(M)$ in Eq (5-9), the regression analysis was repeated holding the remaining coefficients fixed to their values from the initial regression (from Table 5-1). The estimates of the coefficients are listed in Table 5-2. The solid curves in Figures 5-5a and 5-5b show the resulting model for duration stress drop. The magnitude dependence of $\Delta\sigma$ found here (increasing duration stress drop with increasing magnitude) indicates that the magnitude dependence of the duration is weaker than implied by constant stress drop scaling.

The residuals are computed for separate magnitude bins to evaluate the fit. The magnitudes were divided into 1/2 magnitude bins. The residuals for the horizontal and vertical duration ($D_{0.05\text{-}0.75}$) are shown as a fuction of distance in Figures 5-6a-g and Figures 5-7a-g, respectively.

The resulting magnitude and distance dependdence of the model for the 5-75% duration is shown in Figures 5-8a-db.

Duration for Other Ranges

The second part of the duration regression evaluates the shape of the normalized arias intensity so that the duration at the other ranges can be estimated. For each recording, the duration values were normalized by the $D_{0.05\text{-}0.75}$ value for the

individual recording. The mean normalized durations for the average horizontal component are shown in Figures 5-9 to 5-12 for separate magnitude and distance ranges. Similar curves for the vertical component are shown in Figures 5-13 to 5-16. The normalized duration does not show a significant systematic dependence on either magnitude or distance so a magnitude and distance independent functional form is used. Several alternative forms were evaluated and the following power relations was found to provide a good fit to the mean:

$$\ln\left(\frac{D_{0.05-I}}{D_{0.05-0.75}}\right) = a_1 + a_2 \ln\left(\frac{I-0.05}{1-I}\right) + a_3\left(\ln\left(\frac{I-0.05}{1-I}\right)\right)^2 \qquad (5\text{-}11)$$

The coefficients were estimated using ordinary least-squares and are listed in Table 5-3. The mean predicted relation is compated to the mean of the data in Figures 5-17a,b for the horizontal and vertical components, respectively.

Duration Model

Combing the two model, the resulting duration model is given by

$$\text{Ln}\,(D_{0.05-I}) = \text{Ln}\left[\frac{\left(\frac{\Delta\sigma(M)}{10^{1.5M+16.05}}\right)^{-1/3}}{4.9\text{x}10^6\,\beta} + Sc_1 + c_2(r - r_c)\right] + \ln\left(\frac{D_{0.05-I}}{D_{0.05-0.75}}\right) \qquad (5\text{-}12a)$$

for $r \geq r_c$ and by

$$\text{Ln}\,(D_{0.05-I}) = \text{Ln}\left[\frac{\left(\frac{\Delta\sigma(M)}{10^{1.5M+16.05}}\right)^{-1/3}}{4.9\text{x}10^6\,\beta} + Sc_1\right] + \ln\left(\frac{D_{0.05-I}}{D_{0.05-0.75}}\right) \qquad (5\text{-}12b)$$

for $r < r_c$. The mean residuals from this model are shown in Figures 18a-b.

The standard error is computed from this combined model to estimate the total standard error directly (not a combination of the standard error of the two parts of the model). The standard errors are plotted in Figures 5-19 and are listed in Table 5-4.

Model Predictions

The resulting model for the horizontal duration for distances of 1, 30, and 100 km are shown in Figures 5-20a-c (rock) and Figures 5-21a-c (soil). Similar plots of the model predictions for the vertical component are shown in Figures 5-22a-c and 5-23a-c.

Table 5-1

Inital Regression Estimates of Coefficients

for $D_{0.05-0.75}$ using $\Delta\sigma$ Independent of Magnitude

Coefficient	Horizontal	Vertical
c_1	0.805 ± 0.130	1.076 ± 0.155
c_2	0.063 ± 0.006	0.107 ± 0.008
$\Delta\sigma$	230 ± 34	152 ± 23
r_c	10*	10*
β	3.2*	3.2*

*fixed values

Table 5-2

Regression Estimates of Coefficients

for $D_{0.05-0.75}$ using Magnitude Dependent $\Delta\sigma$

Coefficient	Horizontal	Vertical
c_1	0.805*	1.076*
c_2	0.063*	0.107*
b_1	5.204 ± 0.105	4.61 ±
b_2	0.851 ± 0.146	1.536 ±
r_c	10*	10*
β	3.2*	3.2*
SE	0.55	0.46

*fixed values

Table 5-3

Regression Estimates for the Normalized Duration

Coefficient	Horizontal	Vertical
a_1	-0.532 ± 0.005	-0.466 ± 0.009
a_2	0.552 ± 0.002	0.540 ± 0.005
a_3	-0.0262 ± 0.0013	-0.0537 ± 0.0026

Table 5-4

Standard Error for Duration (Eq. 5-12a,b)

I	Horizontal	Vertical
0.10	0.843	0.915
0.15	0.759	0.841
0.20	0.713	0.788
0.25	0.691	0.742
0.30	0.674	0.703
0.35	0.660	0.666
0.40	0.646	0.630
0.45	0.636	0.609
0.50	0.628	0.583
0.55	0.616	0.555
0.60	0.605	0.535
0.65	0.594	0.519
0.70	0.582	0.500
0.75	0.565	0.478
0.80	0.545	0.462
0.85	0.528	0.454
0.90	0.510	0.443
0.95	0.493	0.449

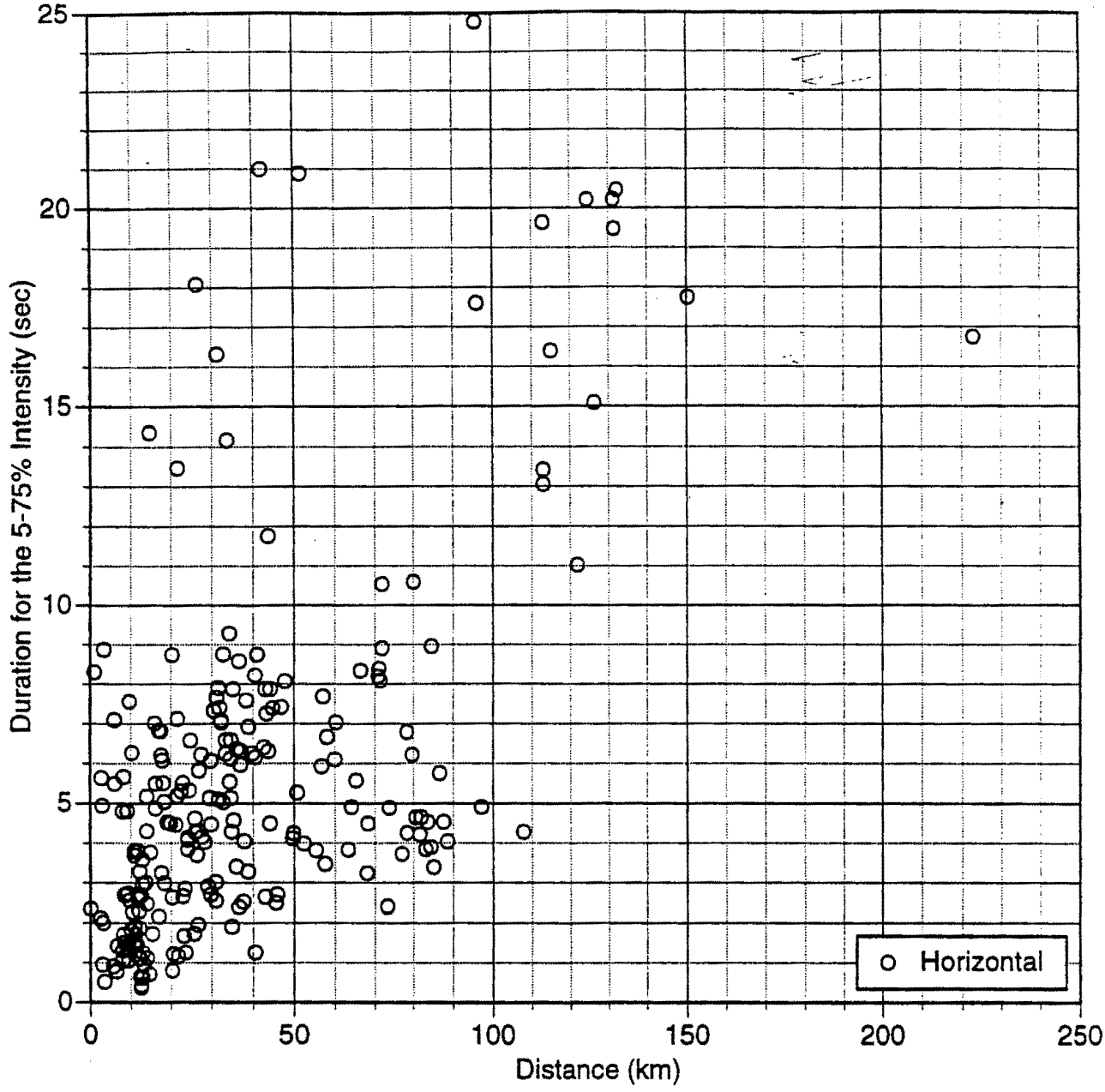

Figure 1a. Distance dependence of the horizontal duration for the 5-75% intensity for rock site conditions.

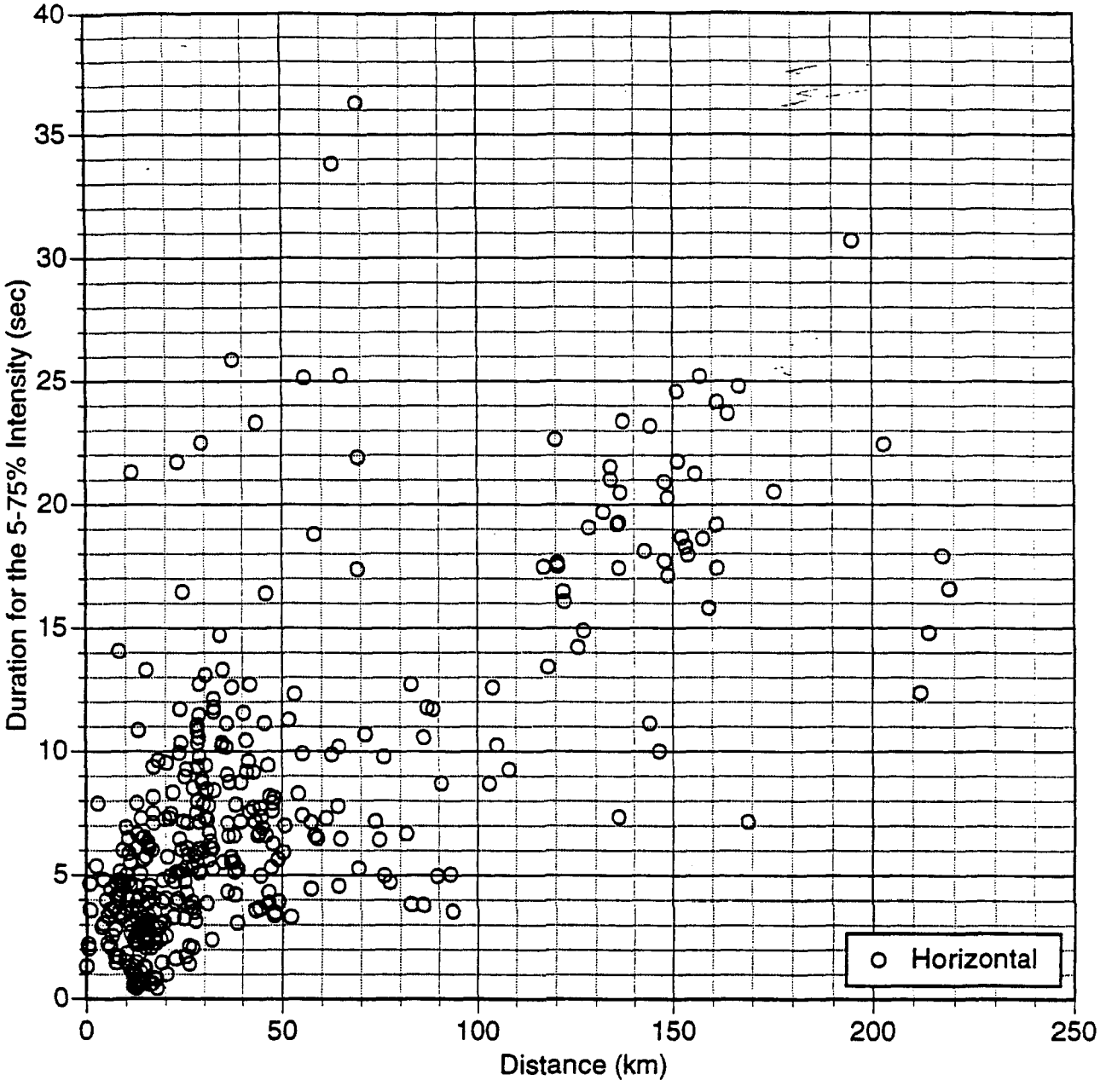

Figure 1b. Distance dependence of the horizontal duration for the 5-75% intensity for soil site conditions.

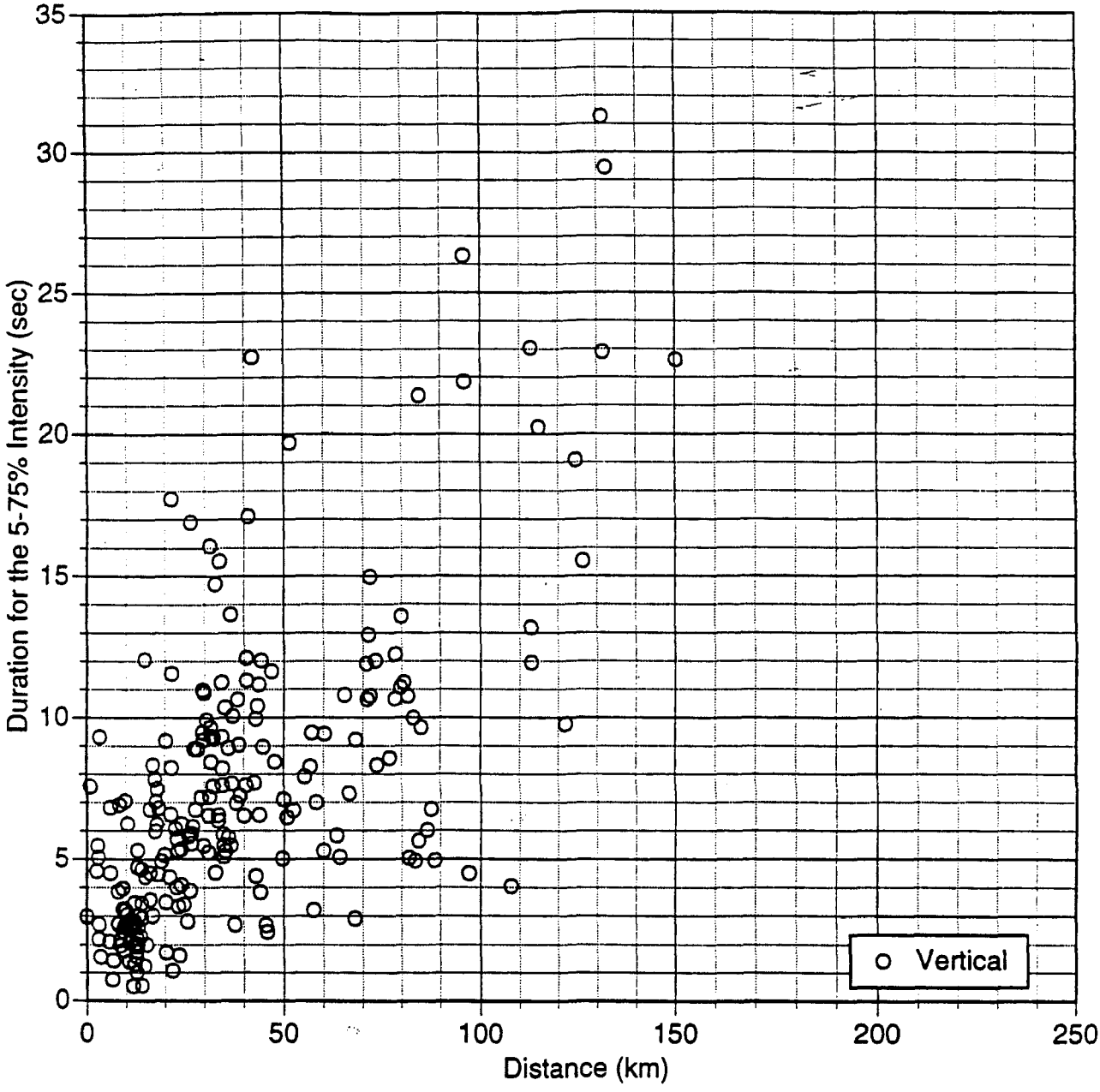

Figure 2a. Distance dependence of the vertical duration for the 5-75% intensity for rock site conditions.

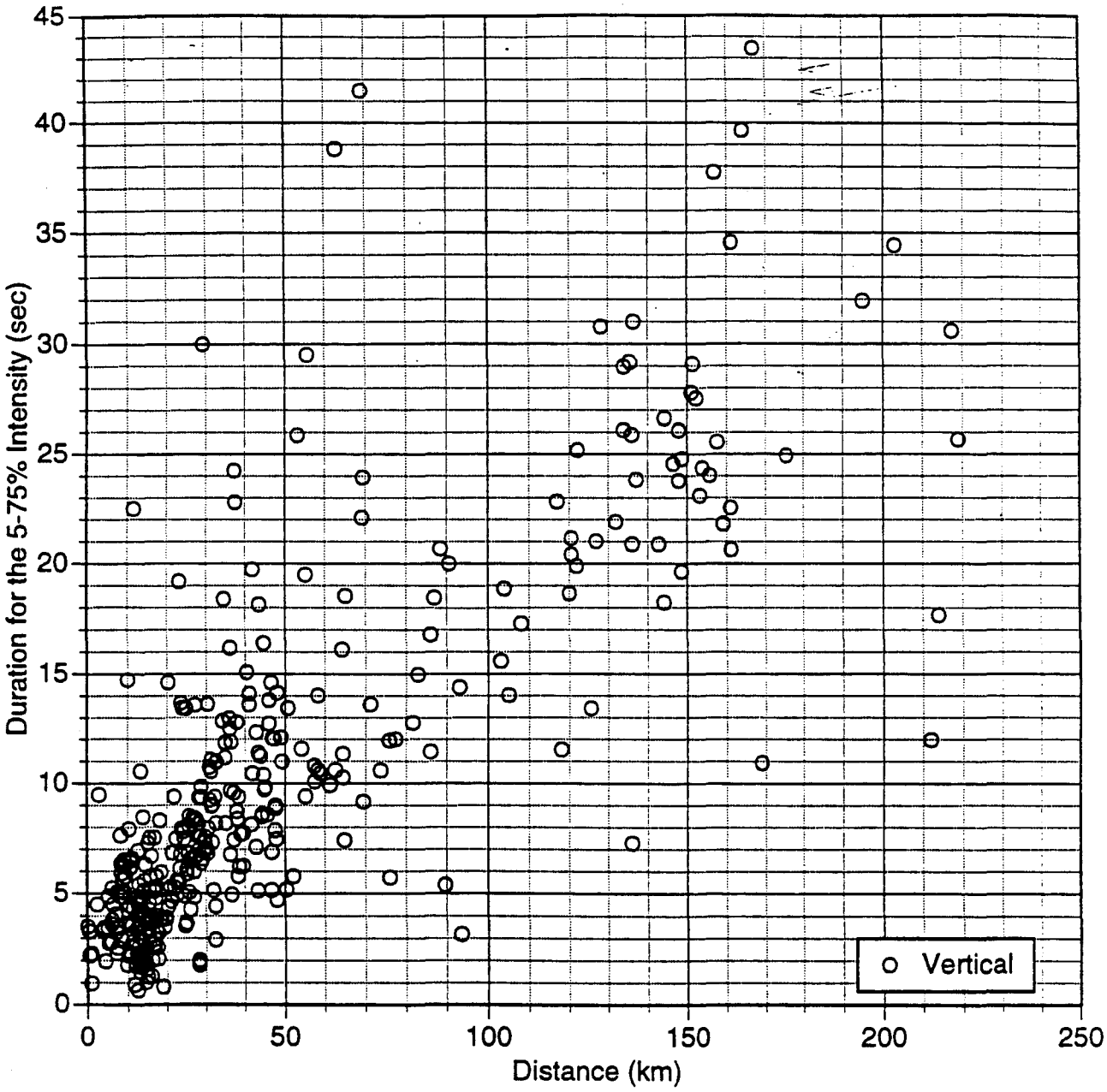

Figure 2b. Distance dependence of the vertical duration for the 5-75% intensity for soil site conditions.

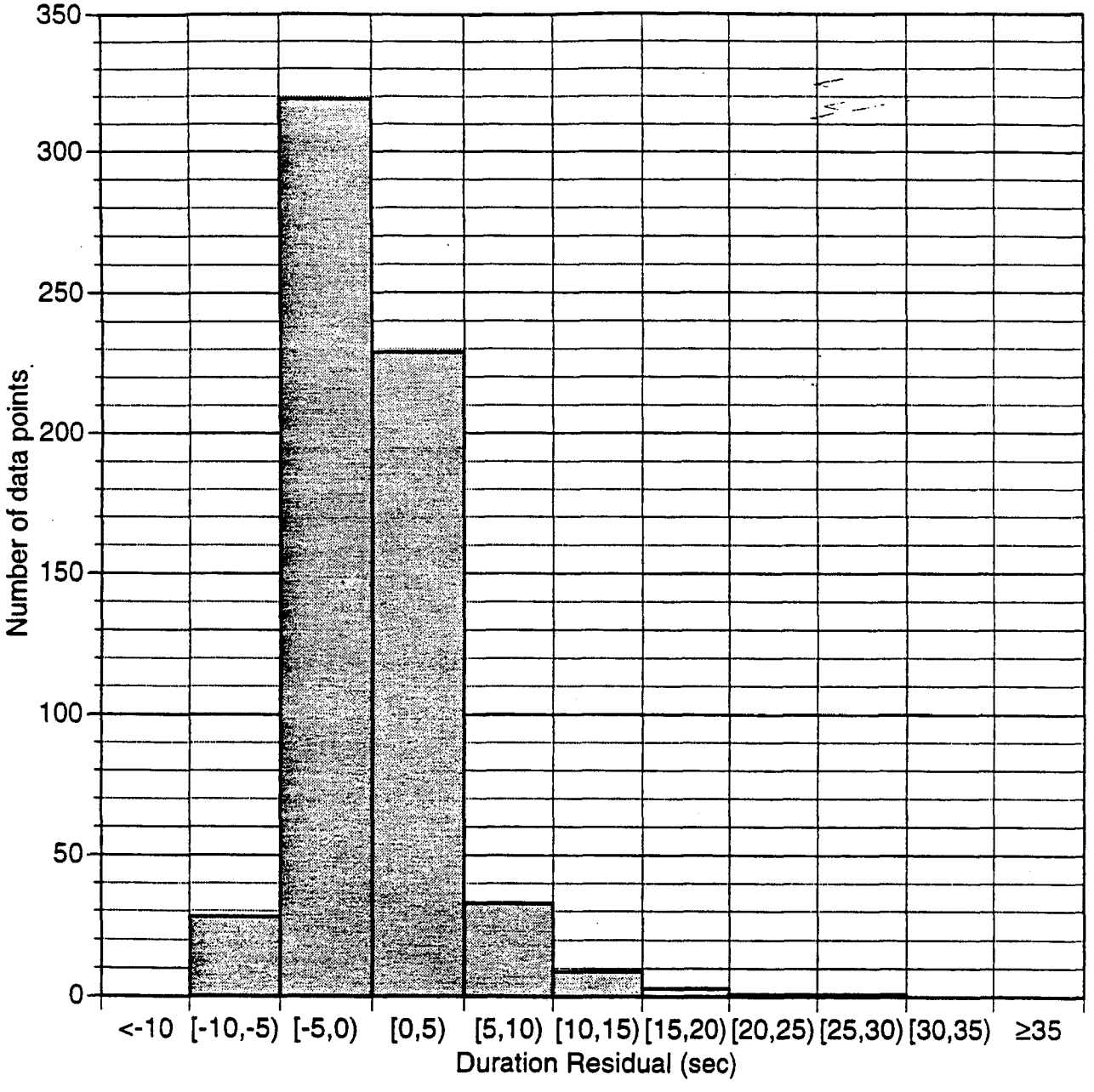

Figure 3a. Distribution of the horizontal 5-75% intensity model (Eq 9).

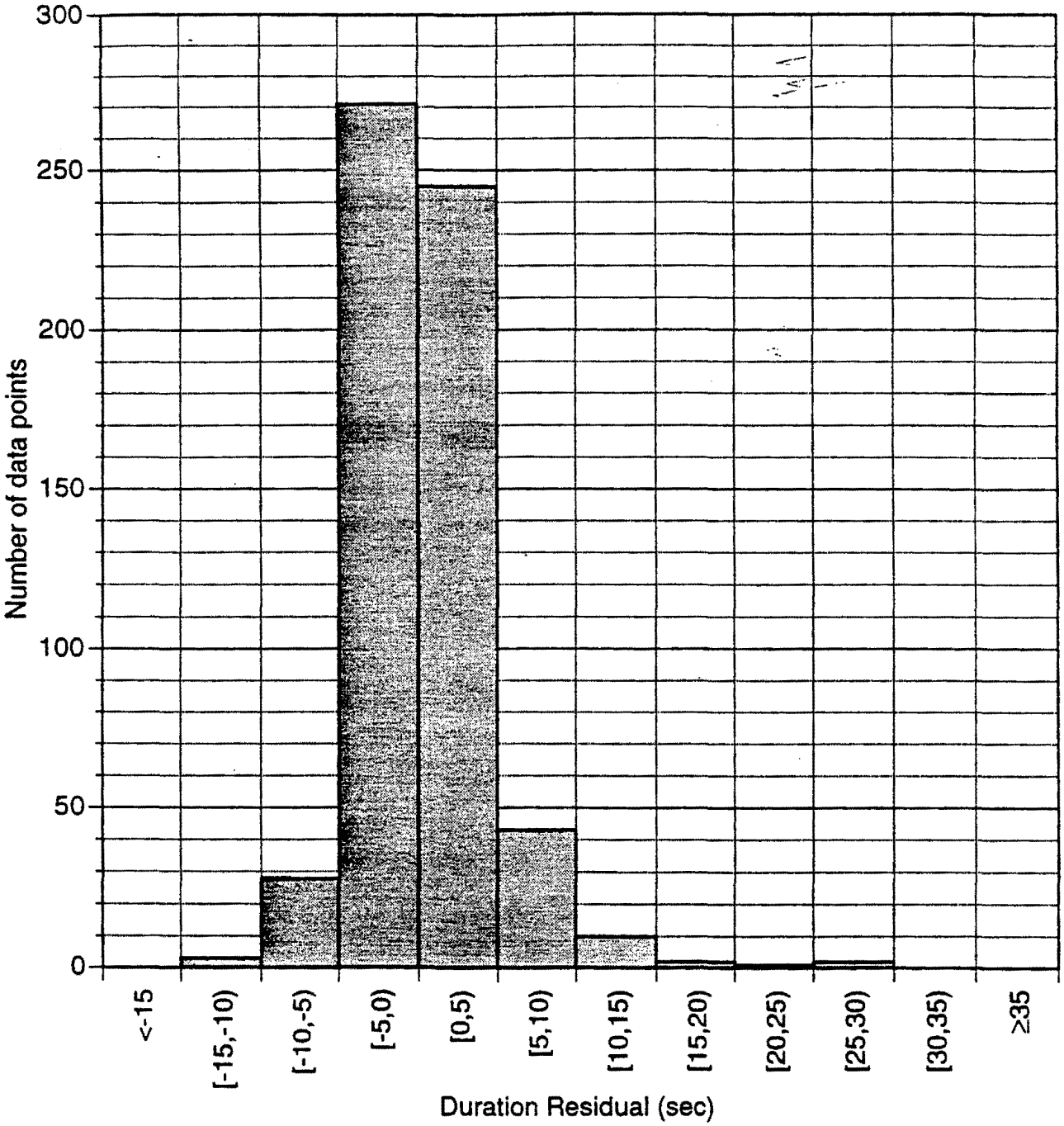

Figure 3b. Distribution of the vertical 5-75% intensity model (Eq 9).

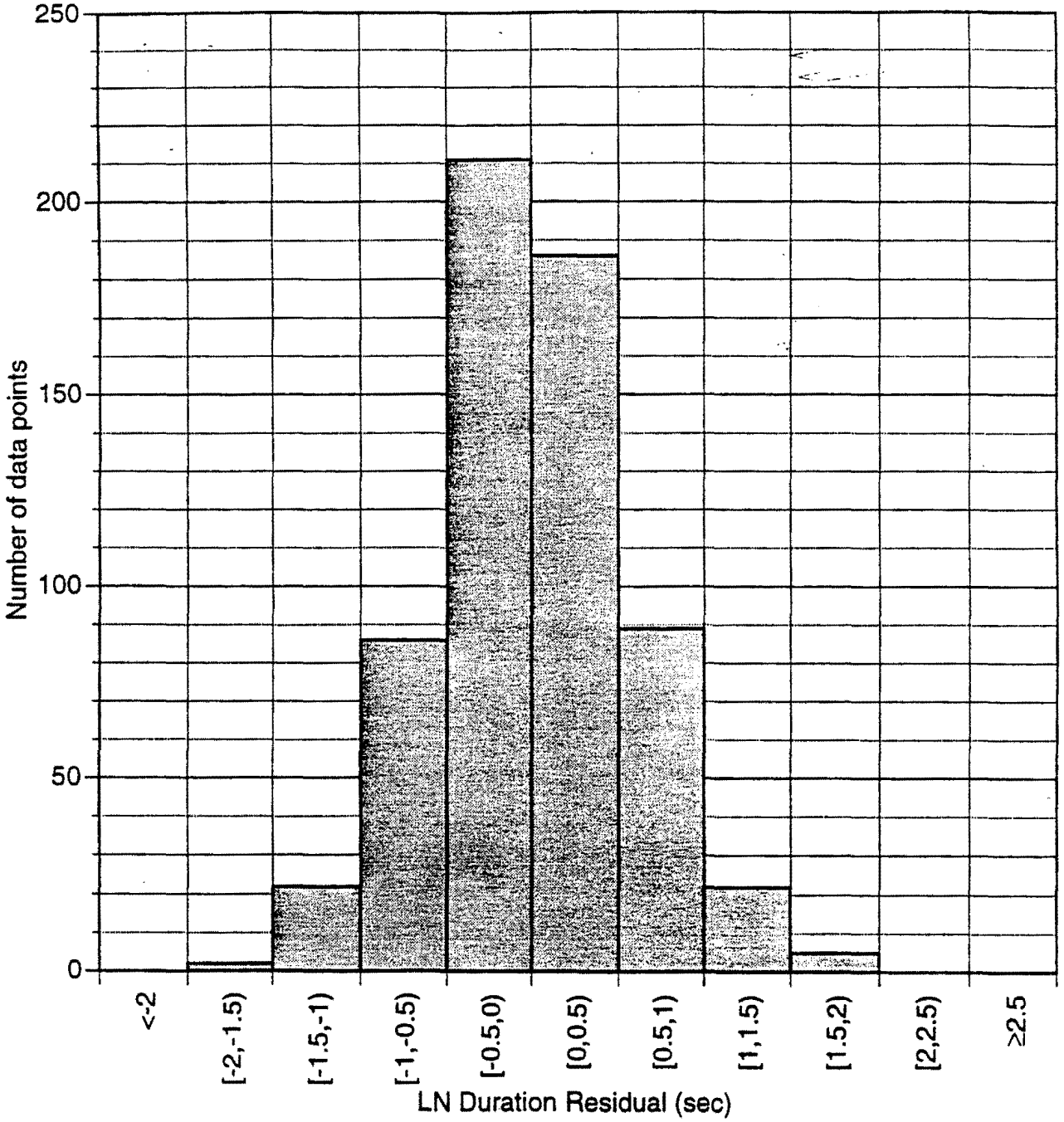

Figure 4a. Distribution of the horizontal 5-75% intensity model (Eq 9).

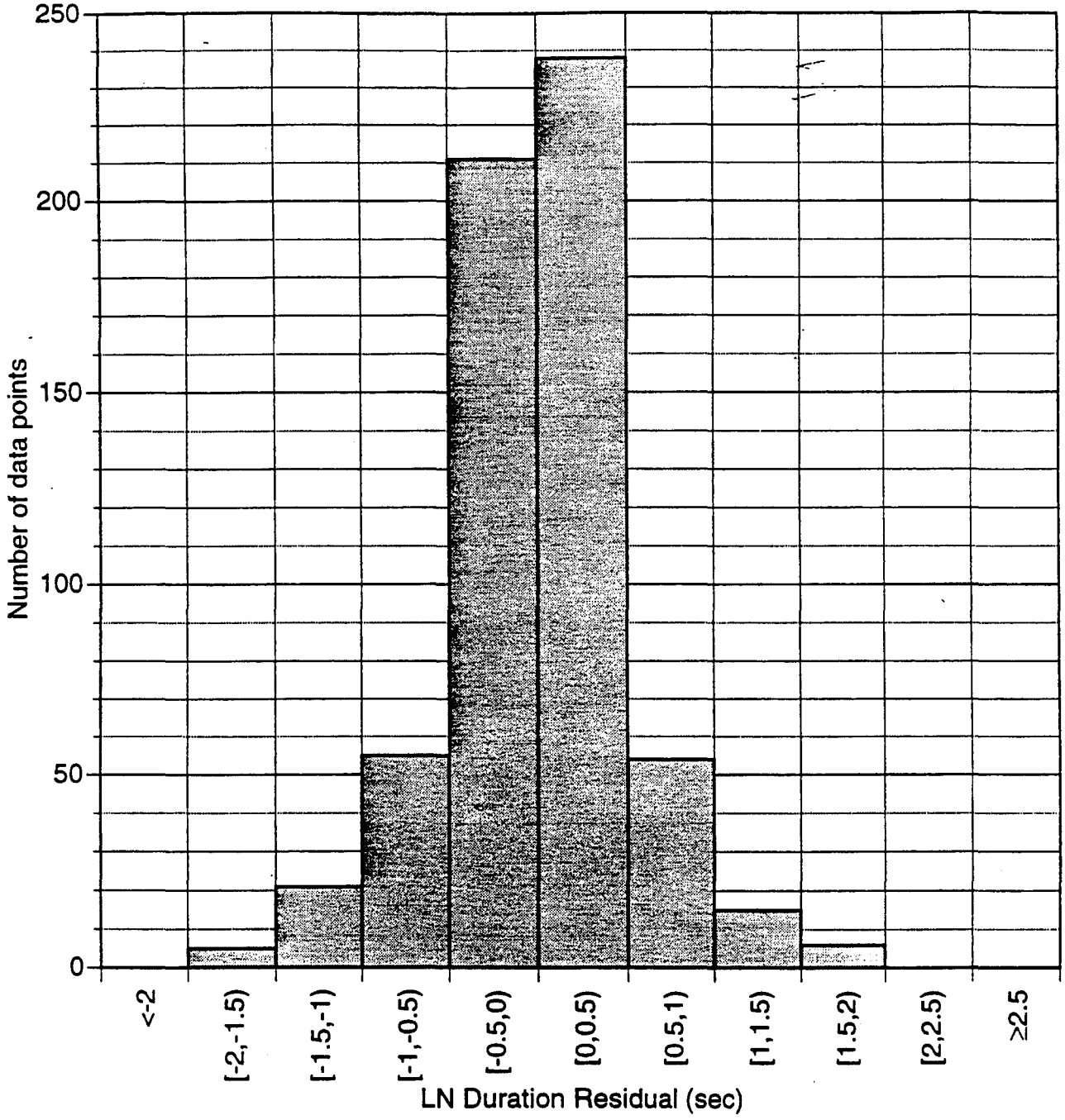

Figure 4b. Distribution of the vertical 5-75% intensity model (Eq 9).

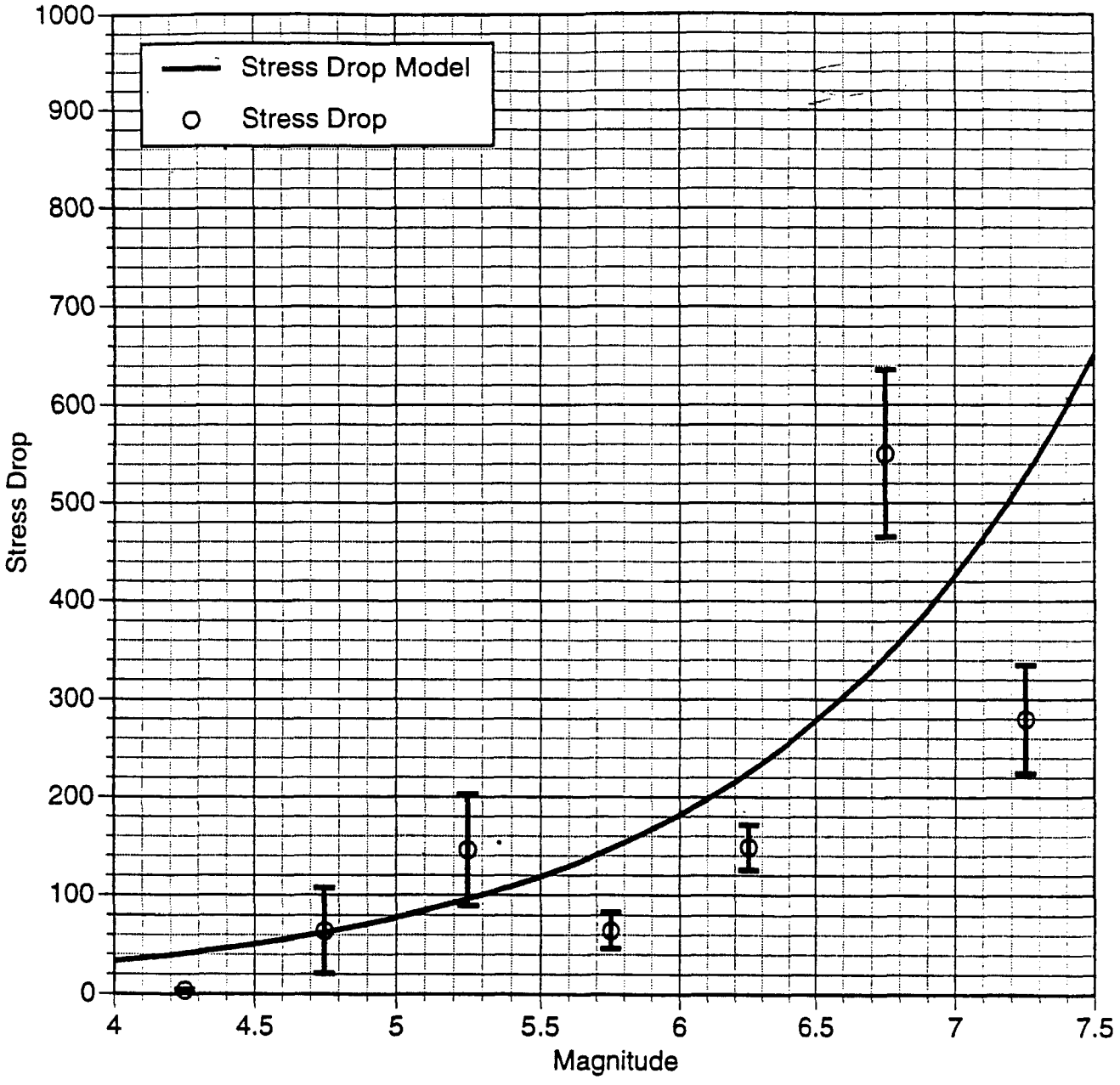

Figure 5a. Stress drop estimates and model for the horizontal component.

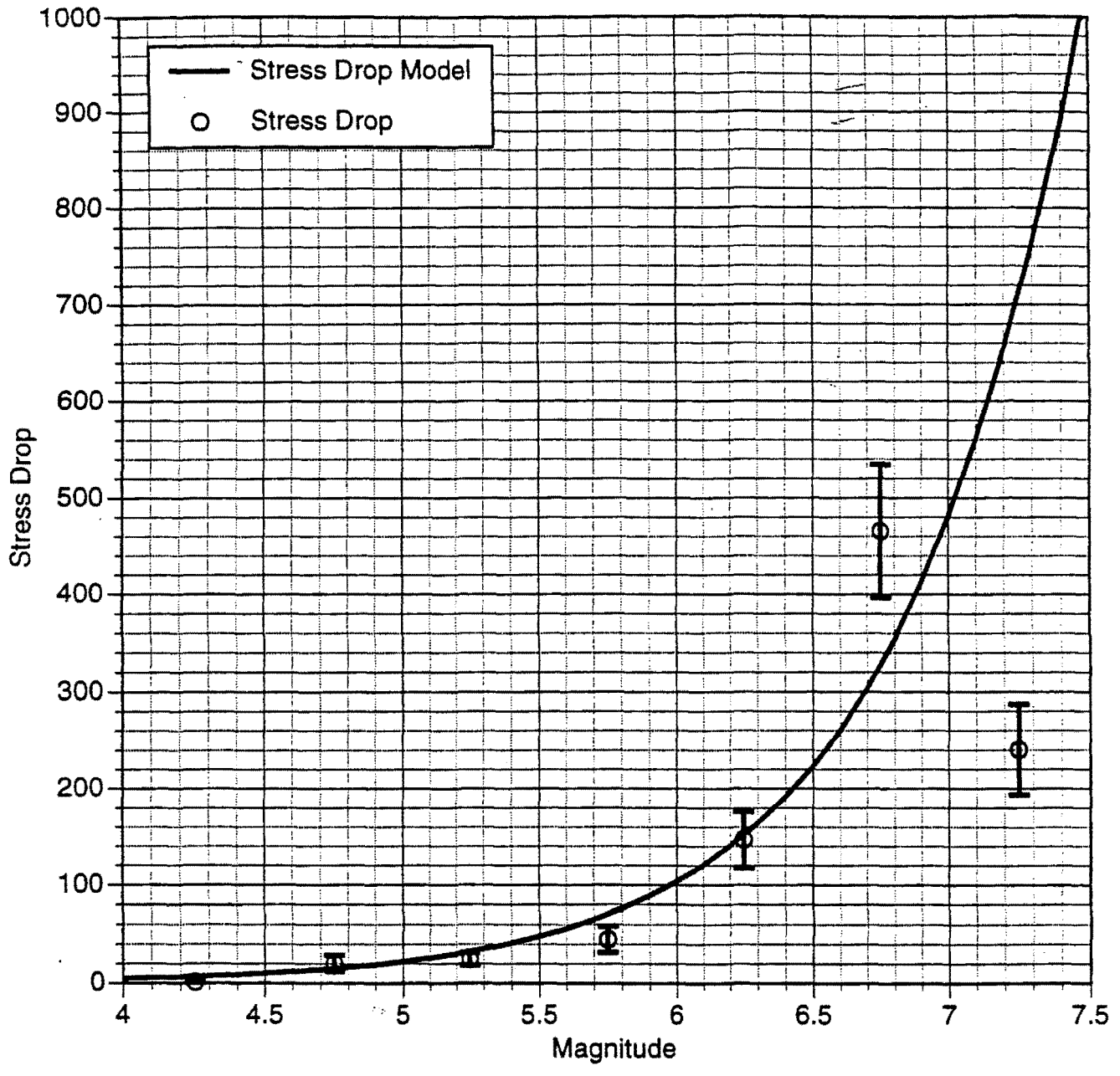

Figure 5b. Stress drop estimates and model for the vertical component.

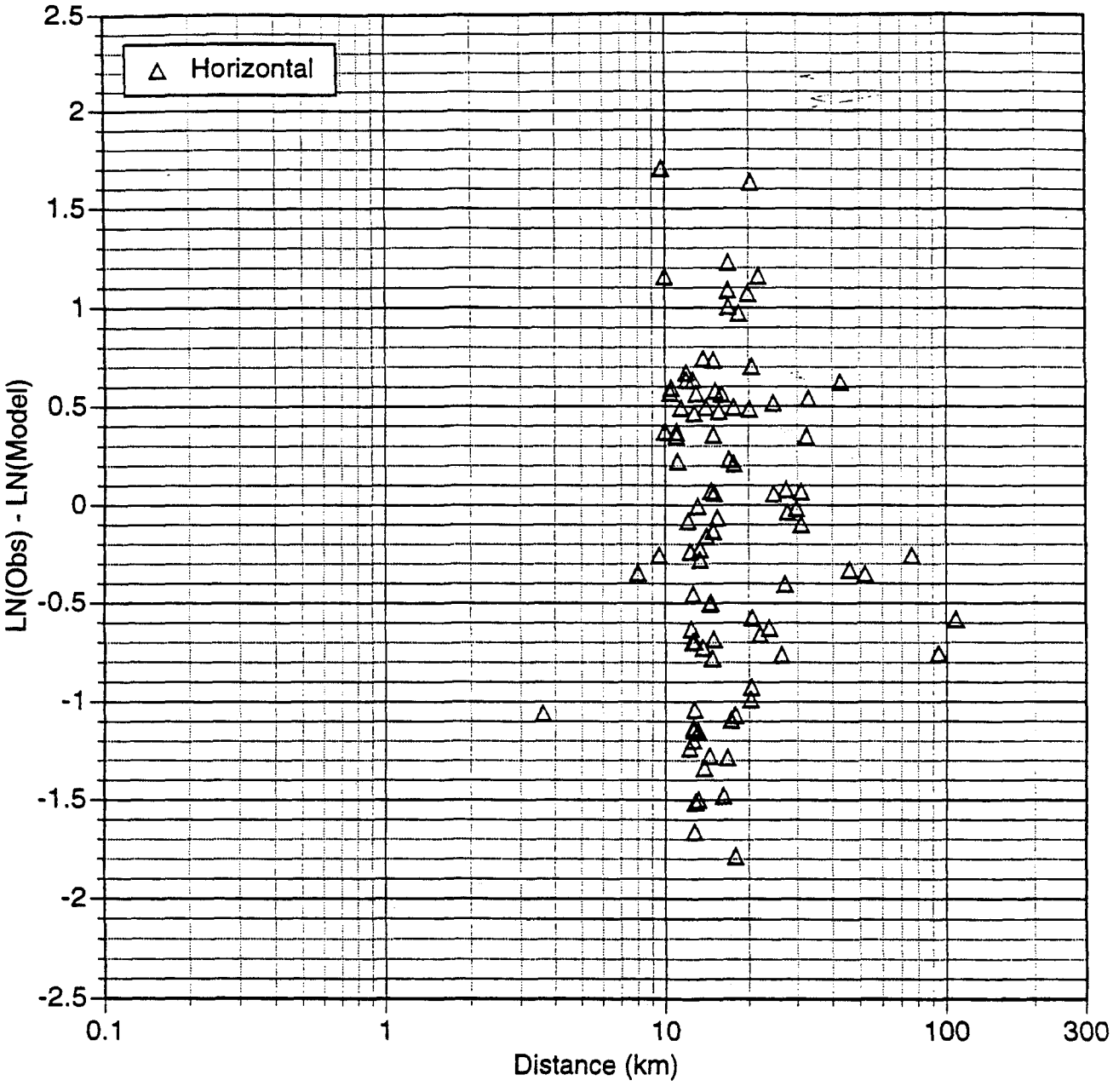

Figure 6a. Horizontal residuals for magnitudes between 5.0 < M < 5.5.

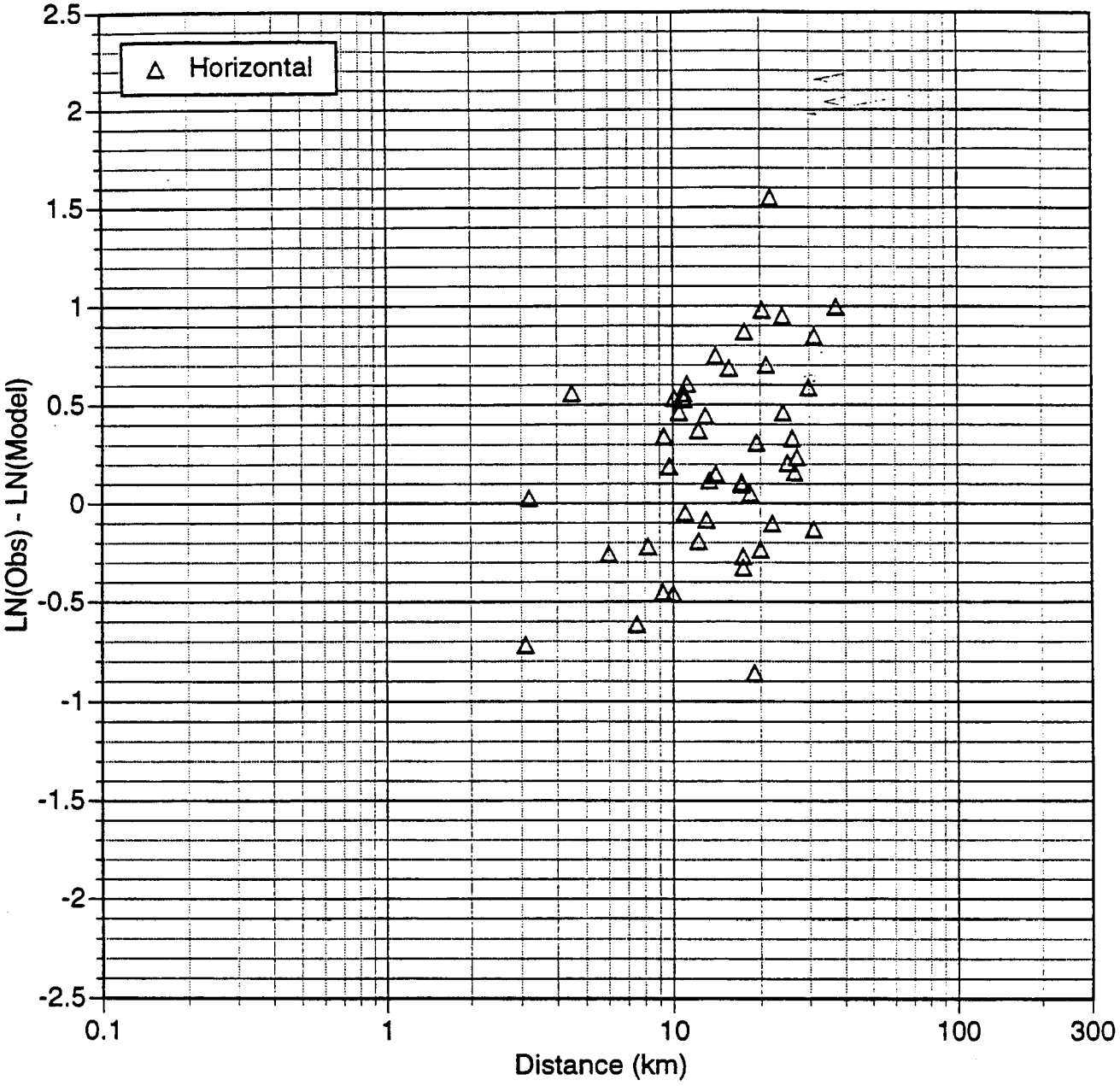

Figure 6b. Horizontal residuals for magnitudes between 5.5 < M < 6.0.

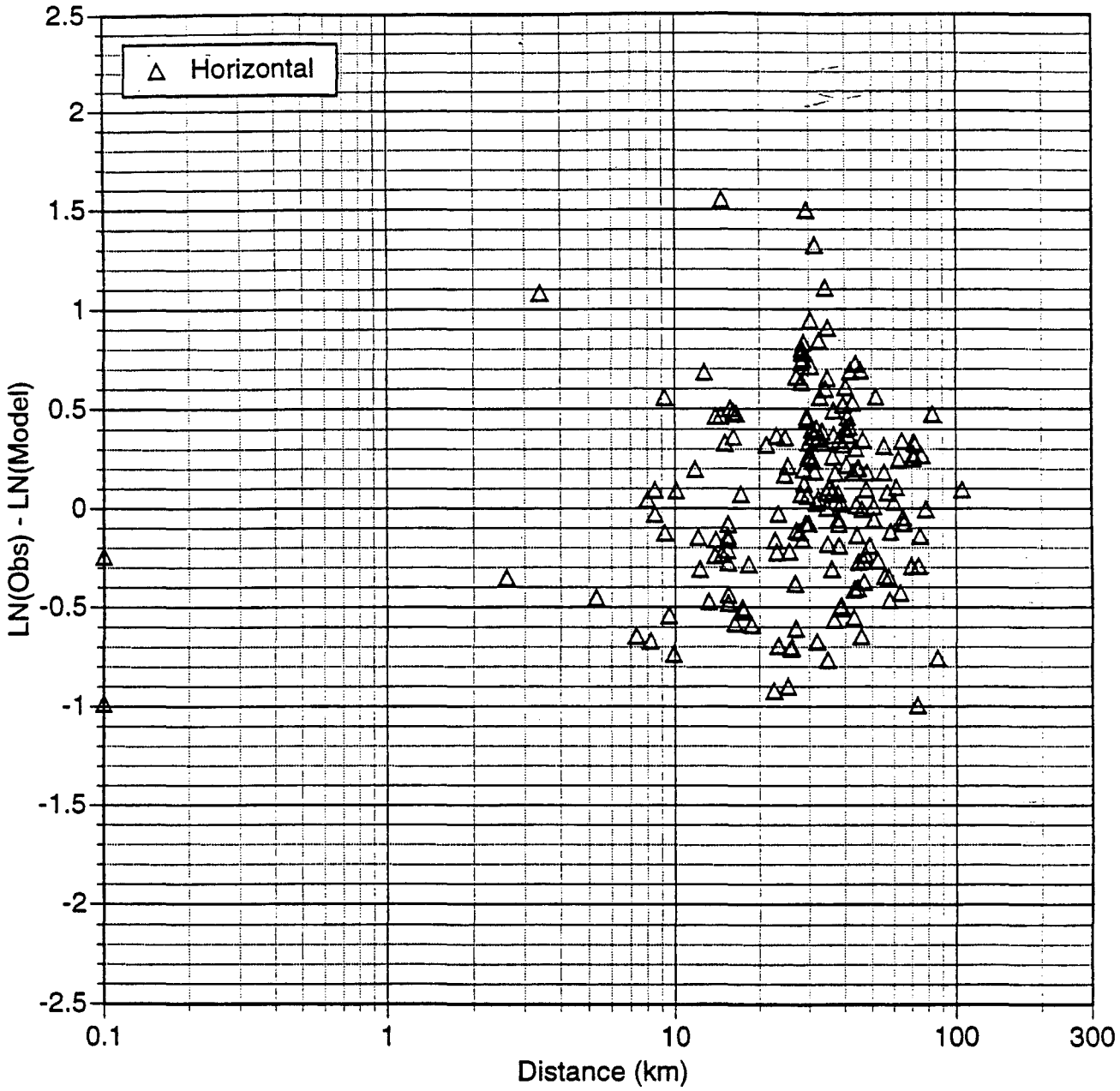

Figure 6c. Horizontal residuals for magnitudes between 6.0 < M < 6.5.

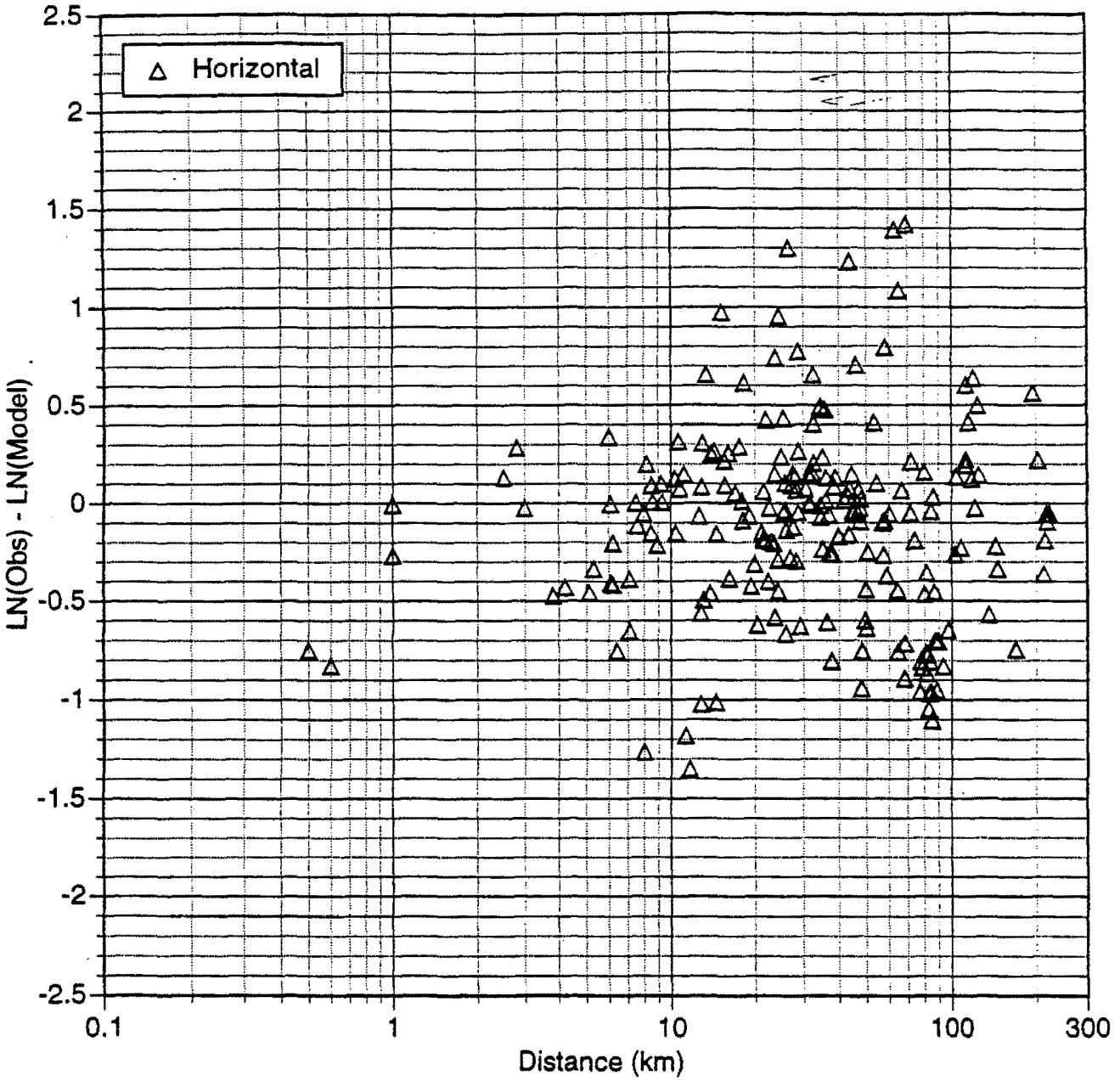

Figure 6d. Horizontal residuals for magnitudes between 6.5 < M < 7.0.

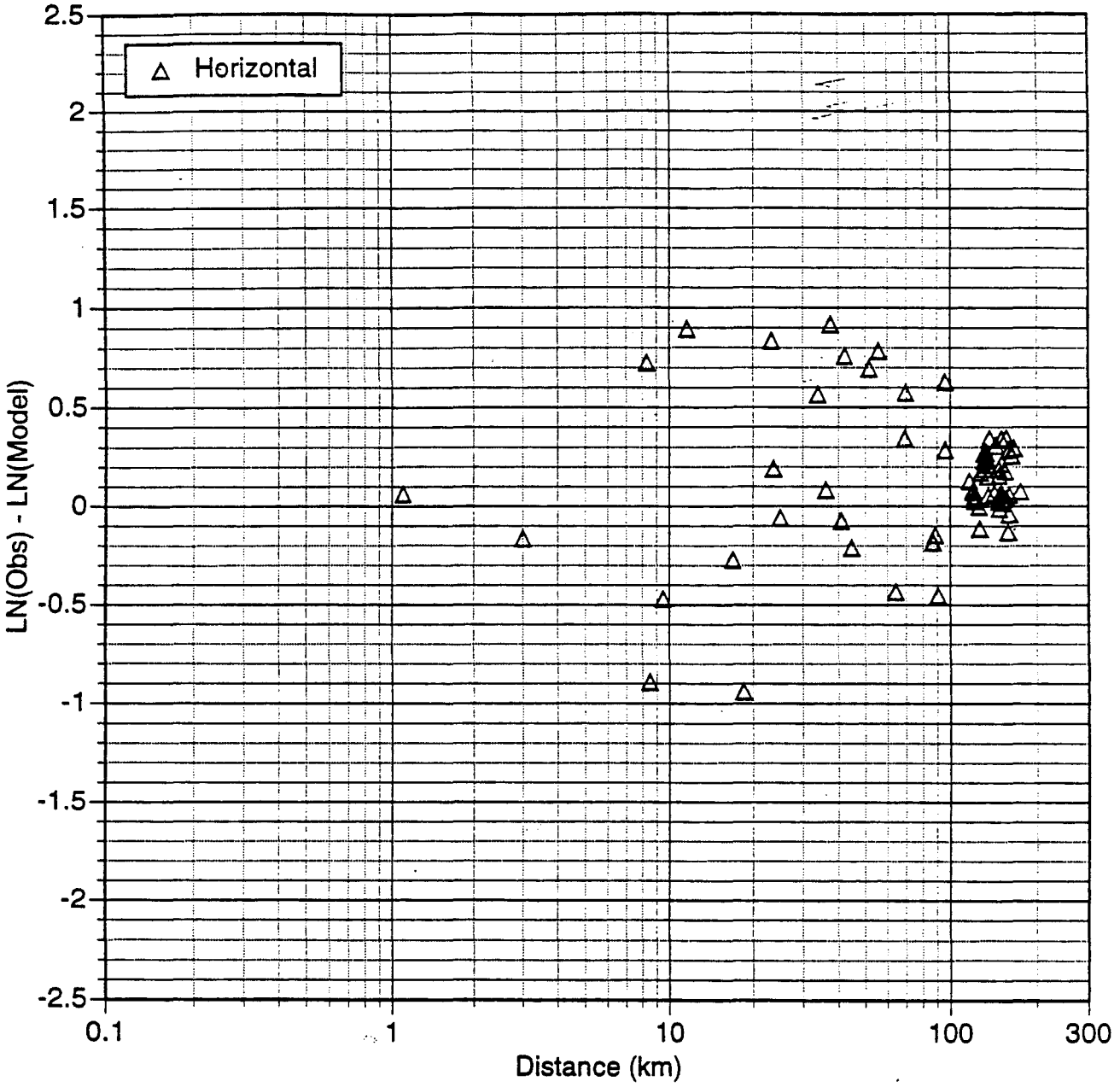

Figure 6e. Horizontal residuals for magnitudes between 7.0 < M < 7.5.

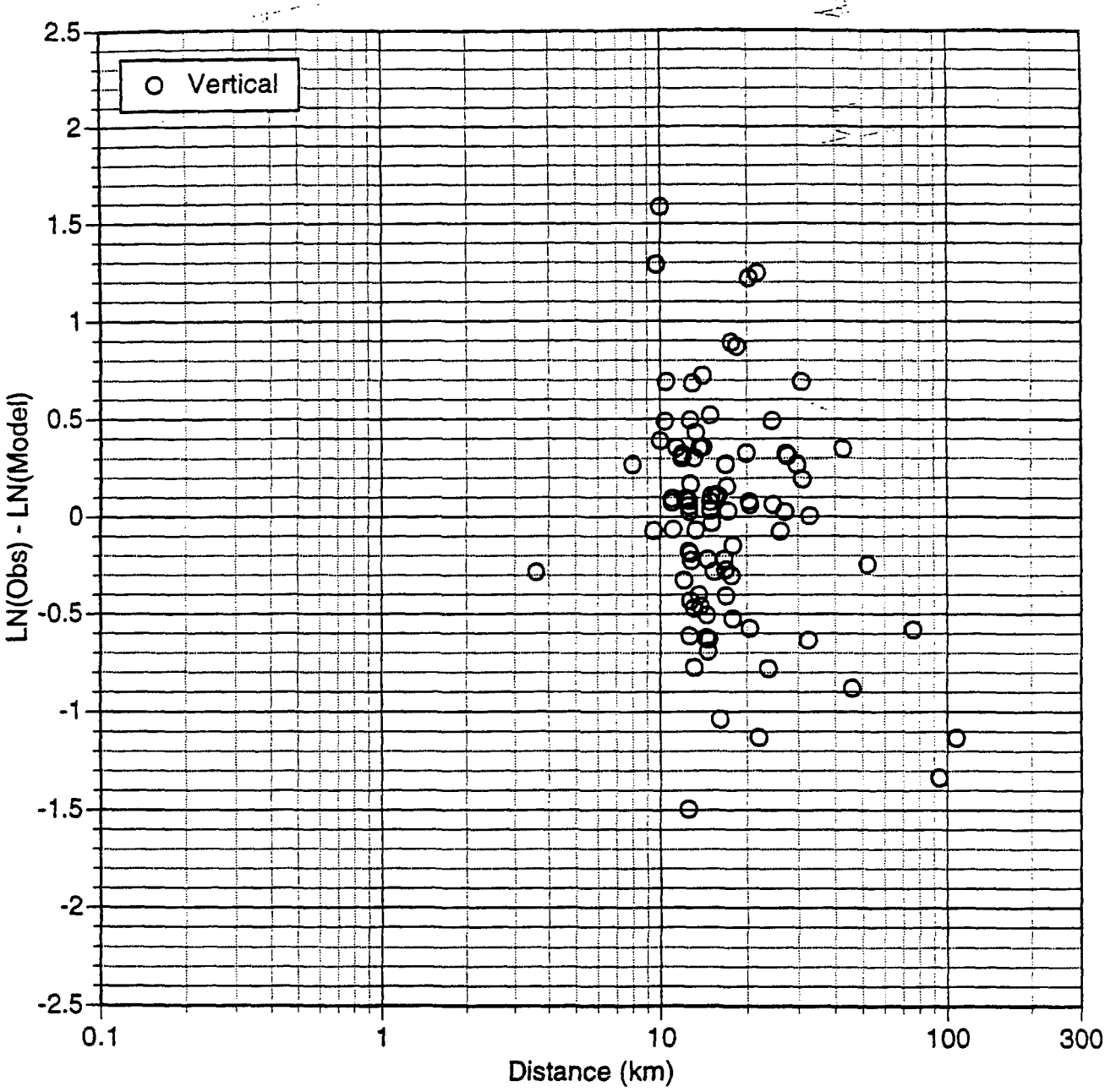

Figure 7a. Vertical residuals for magnitudes between 5.0 < M < 5.5.

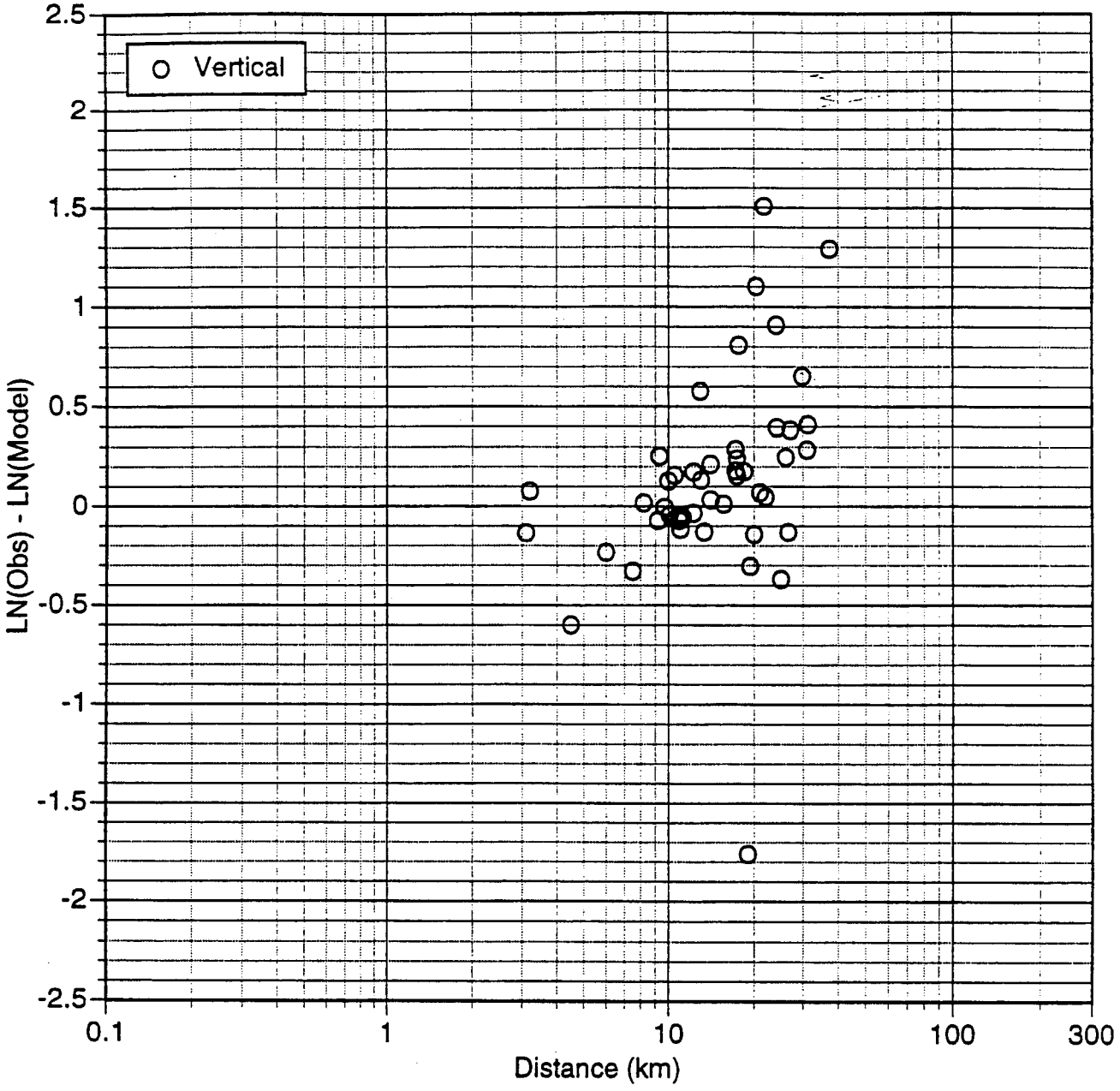

Figure 7b. Vertical residuals for magnitudes between 5.5 < M < 6.0.

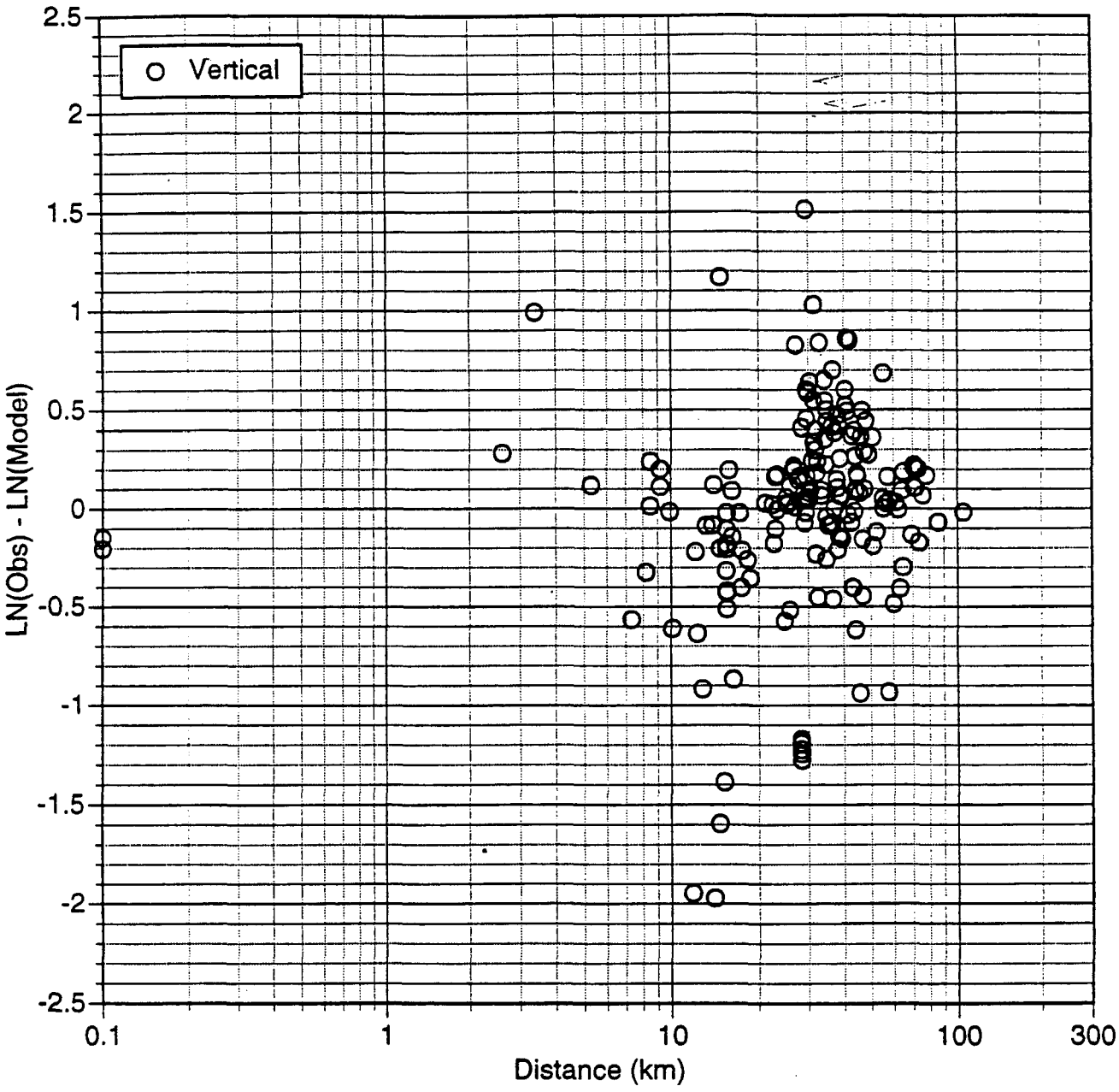

Figure 7c. Vertical residuals for magnitudes between 6.0 < M < 6.5.

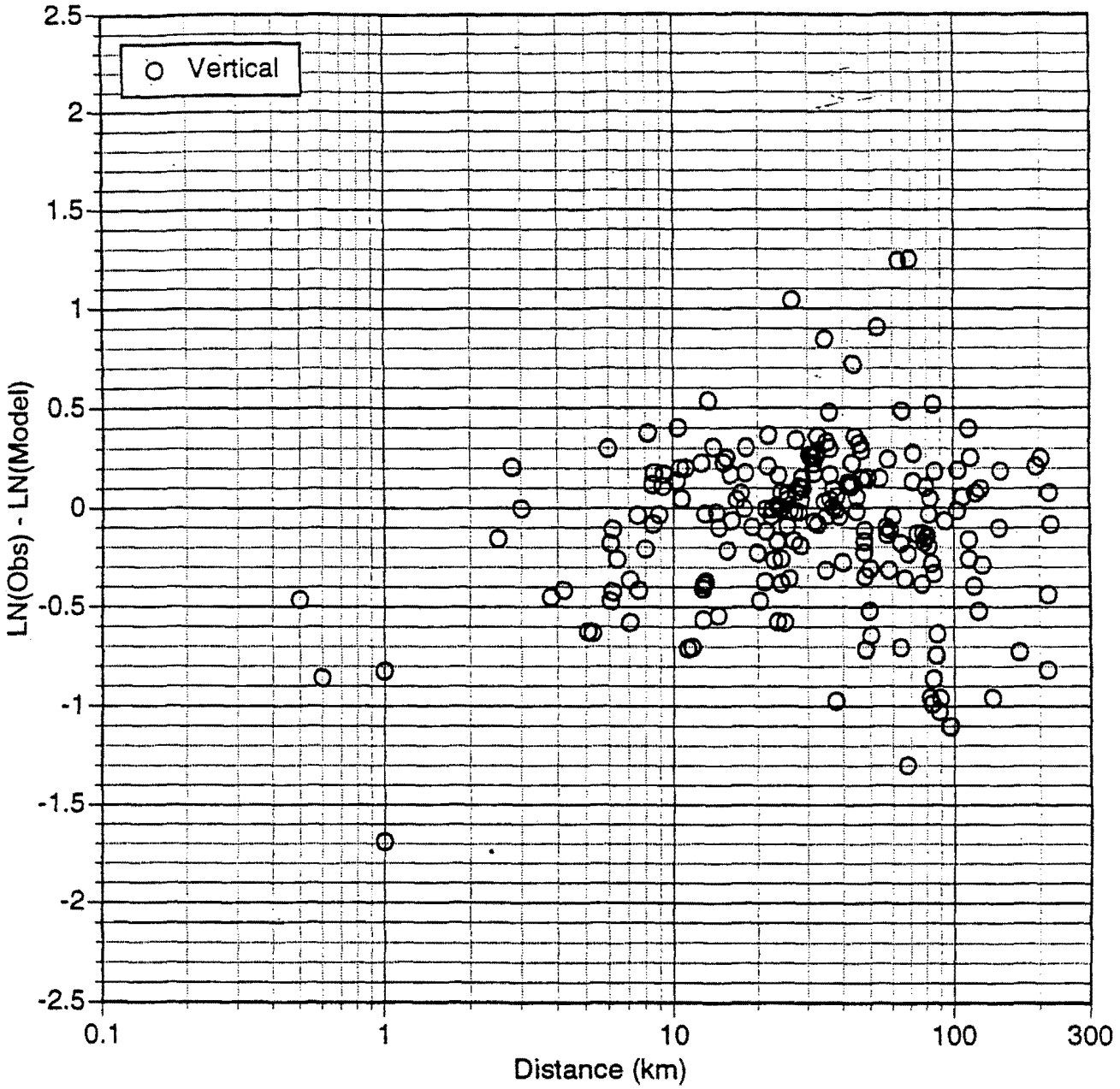

Figure 7d. Vertical residuals for magnitudes between 6.5 < M < 7.0.

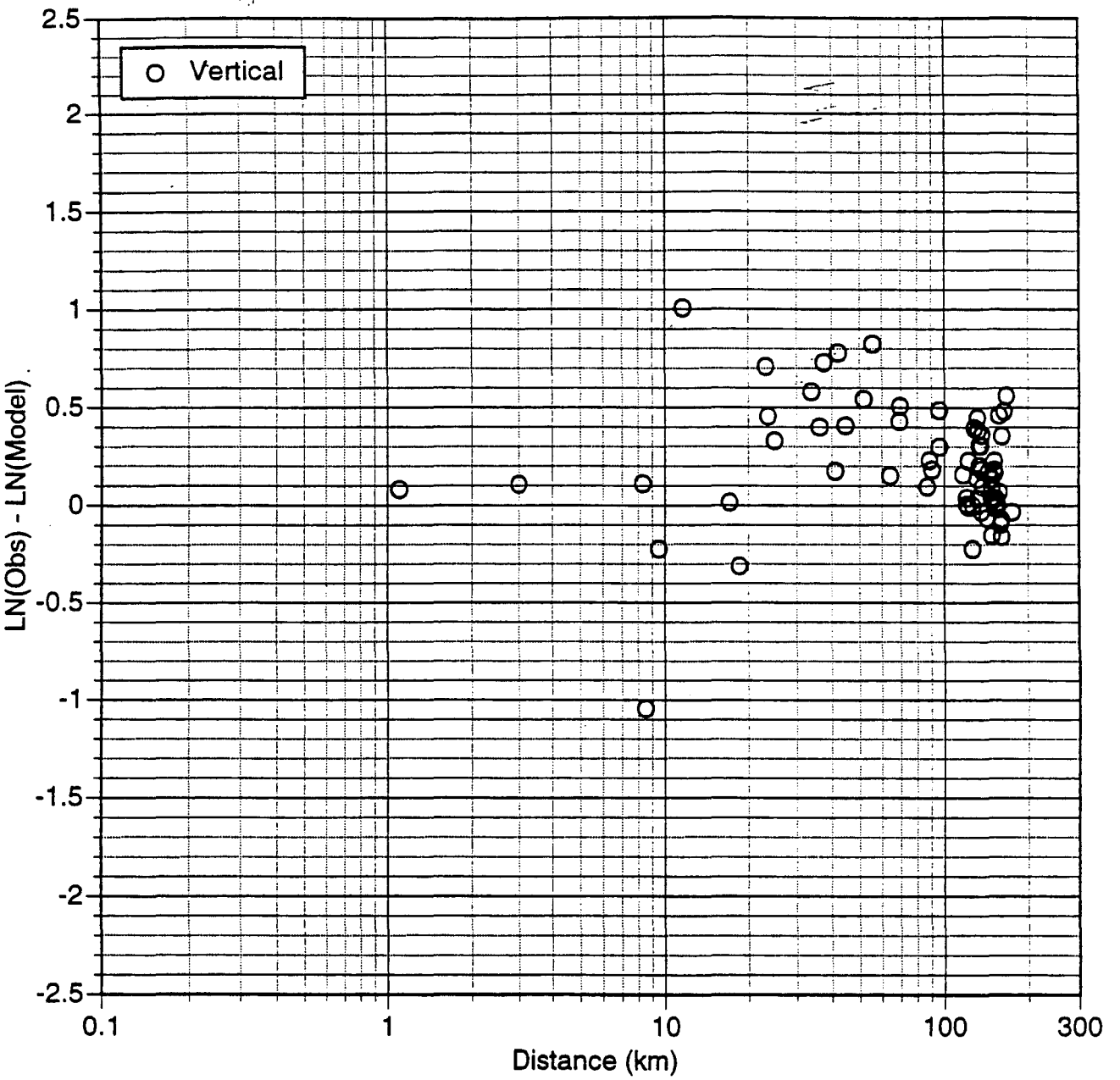

Figure 7e. Vertical residuals for magnitudes between 7.0 < M < 7.5.

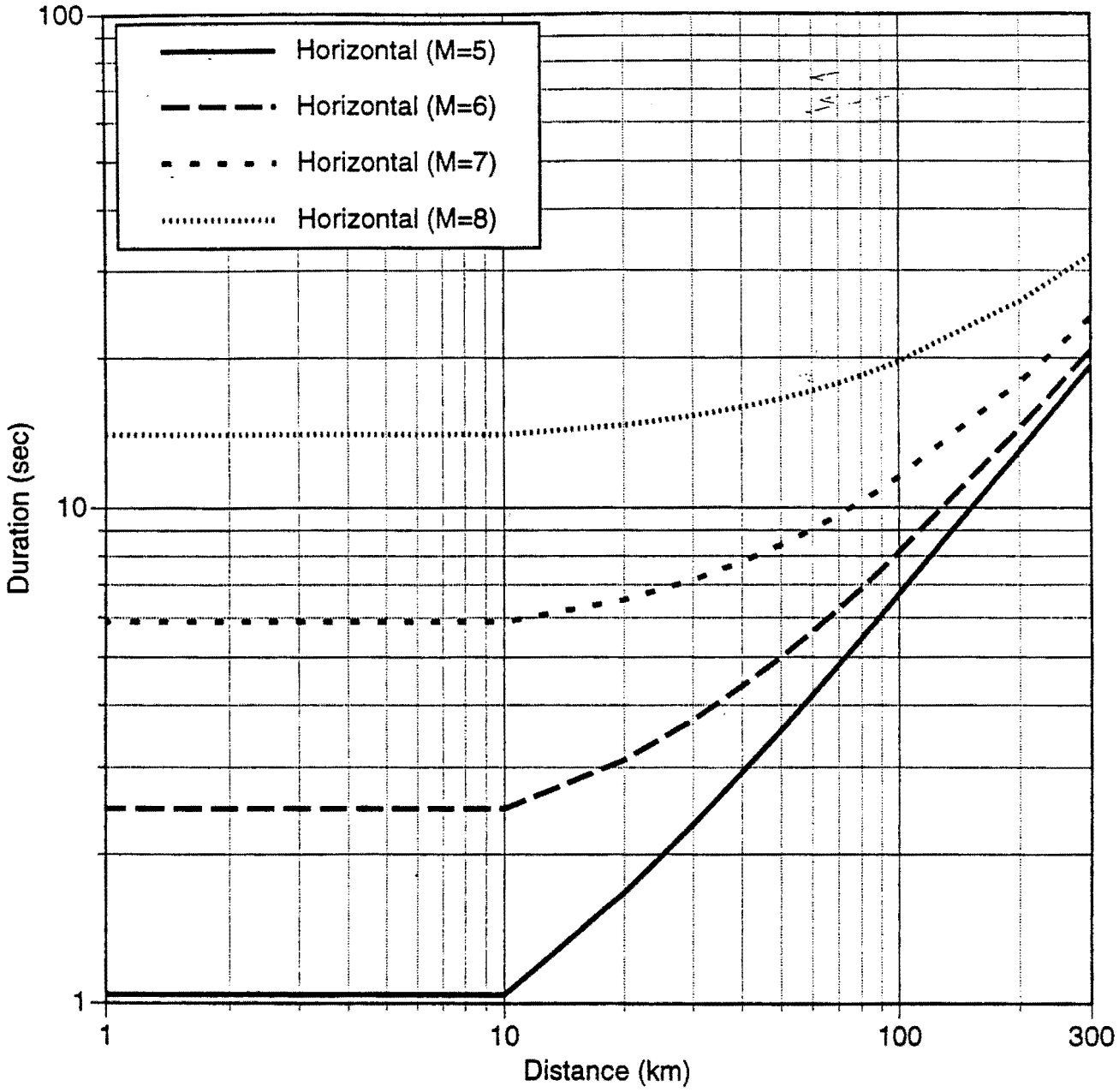

Figure 8a. Horizontal 5-75% intensity duration model for rock site conditions.

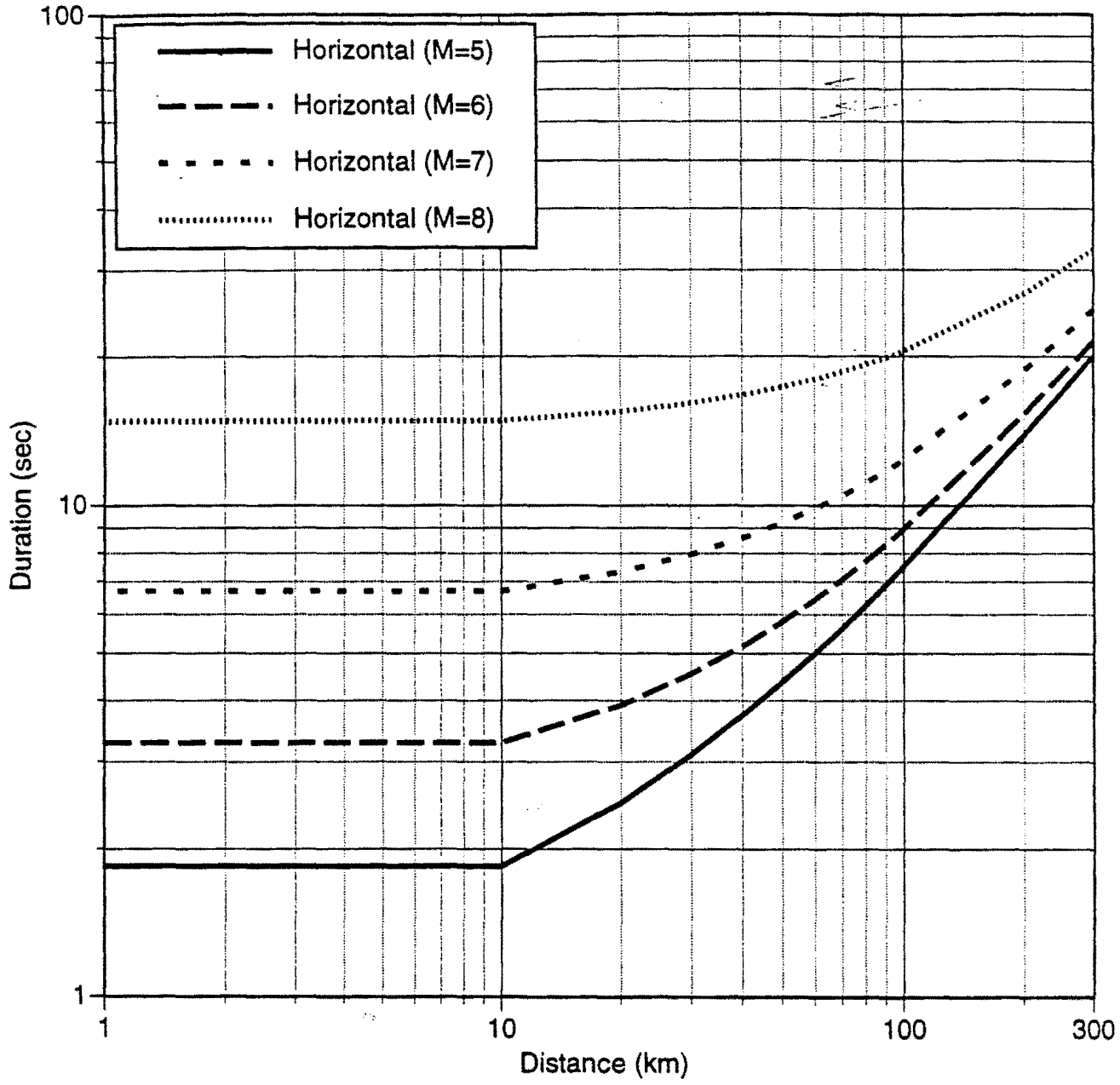

Figure 8b. Horizontal 5-75% intensity duration model for soil site conditions.

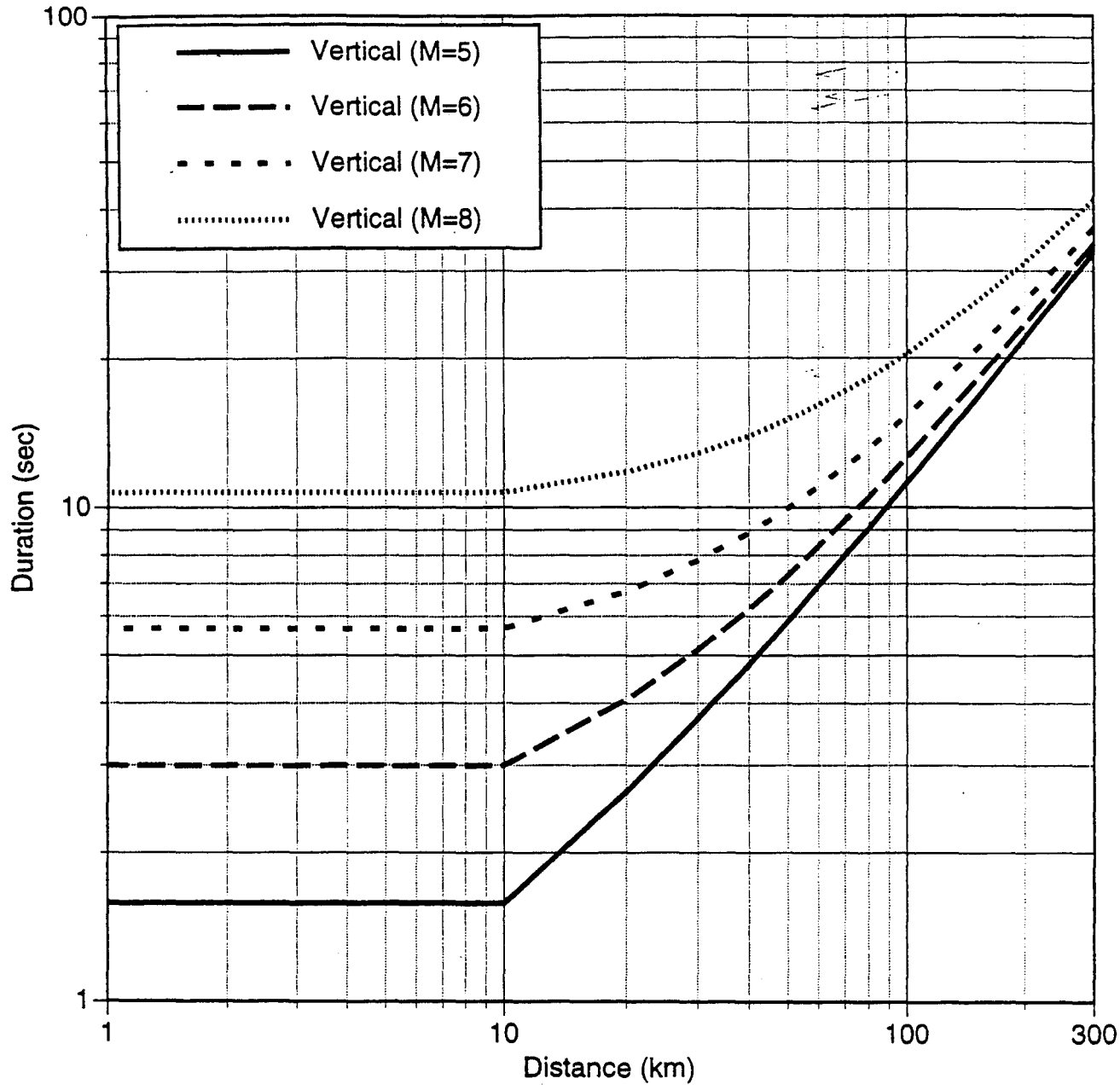

Figure 8c. Vertical 5-75% intensity duration model for rock site conditions.

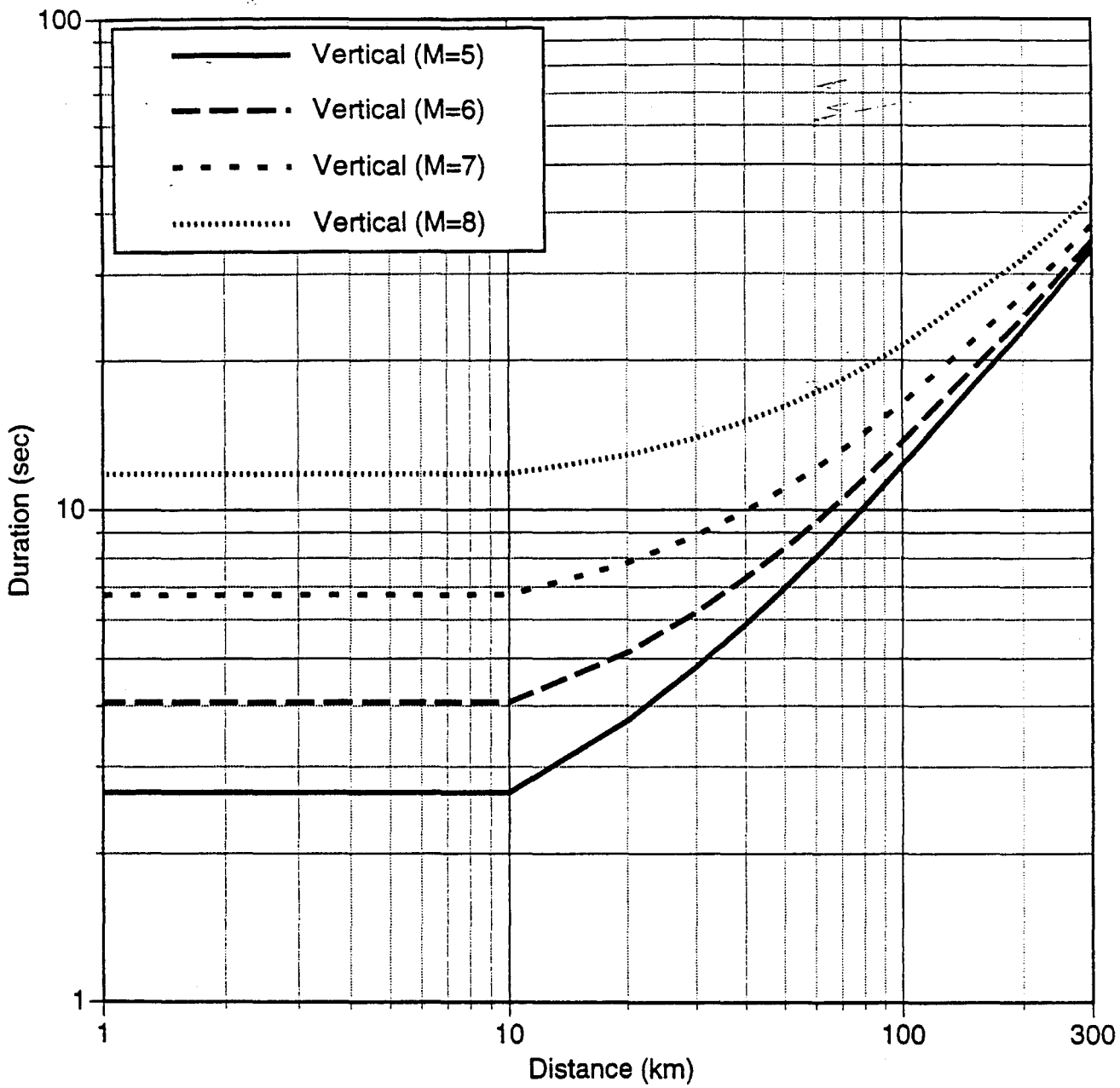

Figure 8d. Vertical 5-75% intensity duration model for soil site conditions.

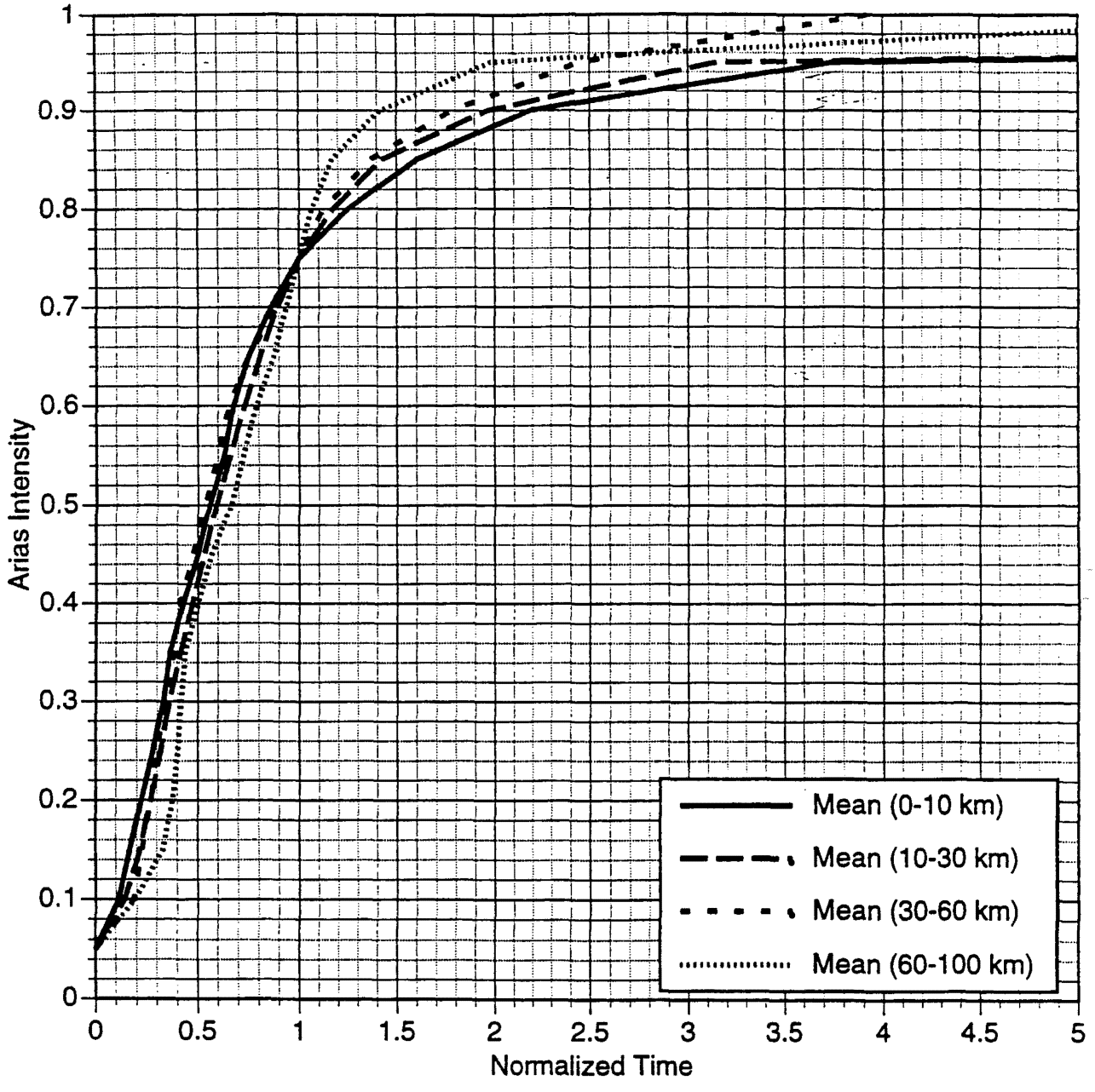

Figure 9a. Mean normalized durations averaged over distance bins for the horizontal component for rock site conditions and $5.0 < M < 5.5$.

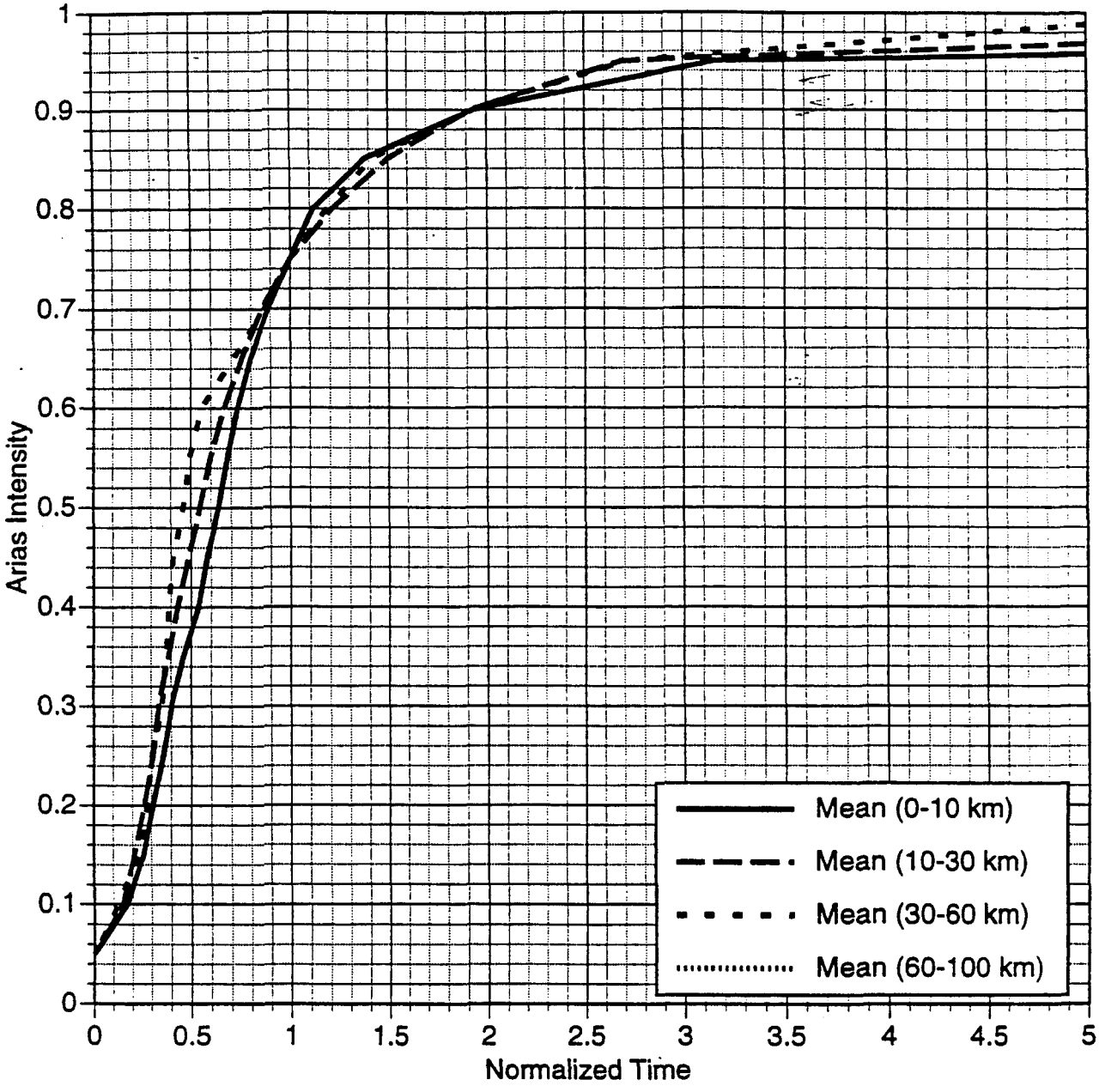

Figure 9b. Mean normalized durations averaged over distance bins for the horizontal component for rock site conditions and $5.5 < M < 6.0$.

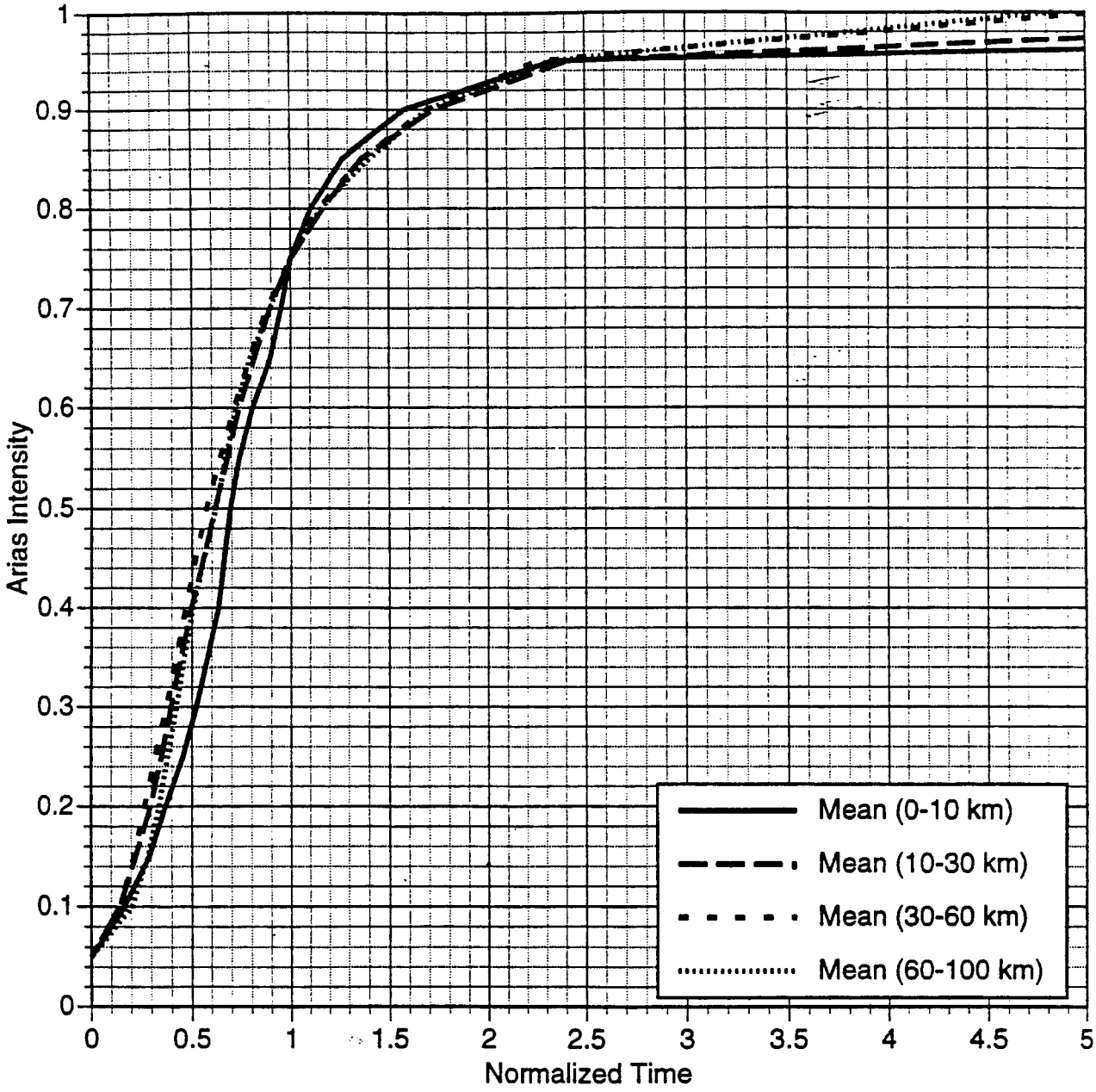

Figure 9c. Mean normalized durations averaged over distance bins for the horizontal component for rock site conditions and $6.0 < M < 6.5$.

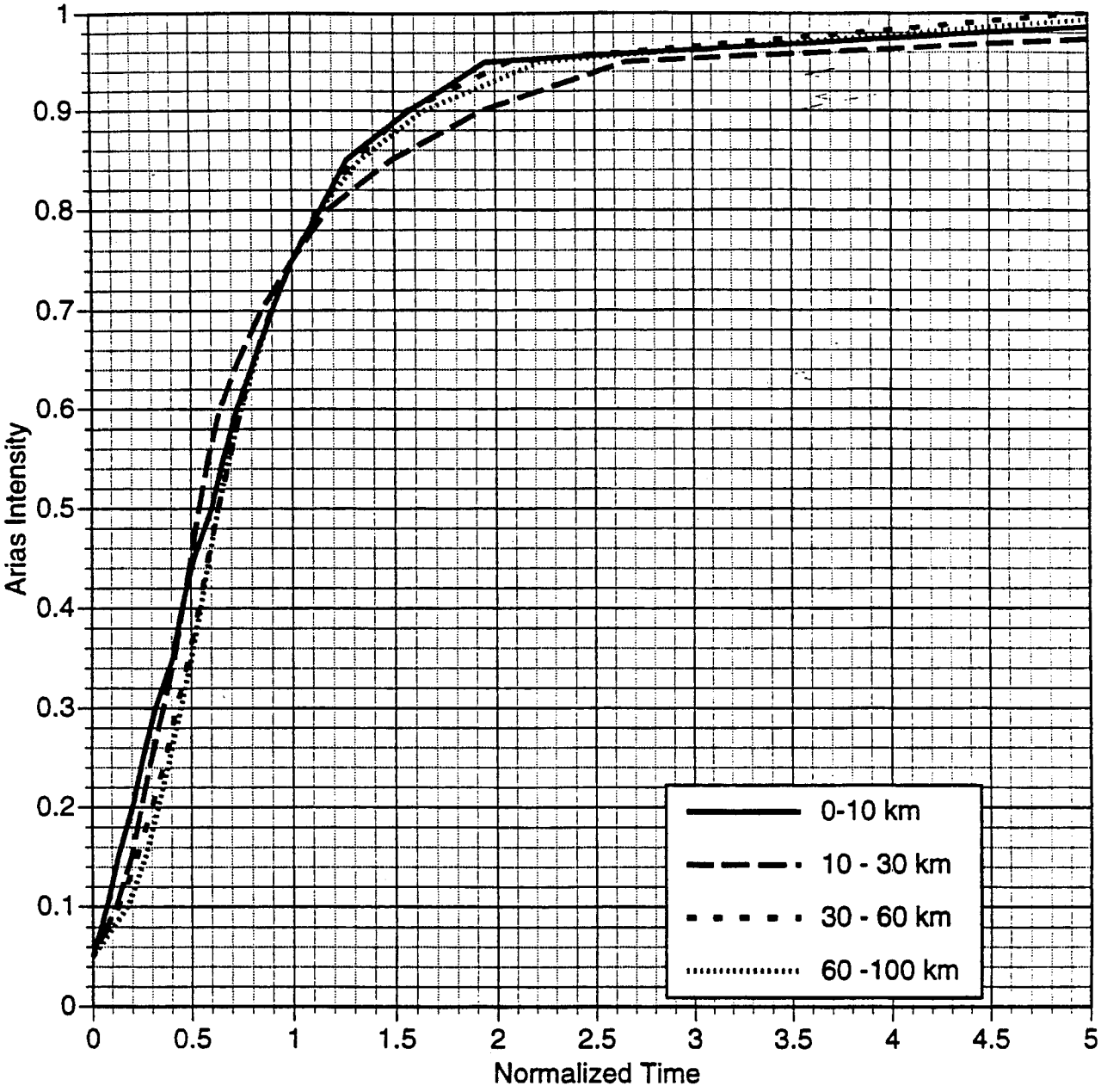

Figure 9d. Mean normalized durations averaged over distance bins for the horizontal component for rock site conditions and $6.5 < M < 7.0$.

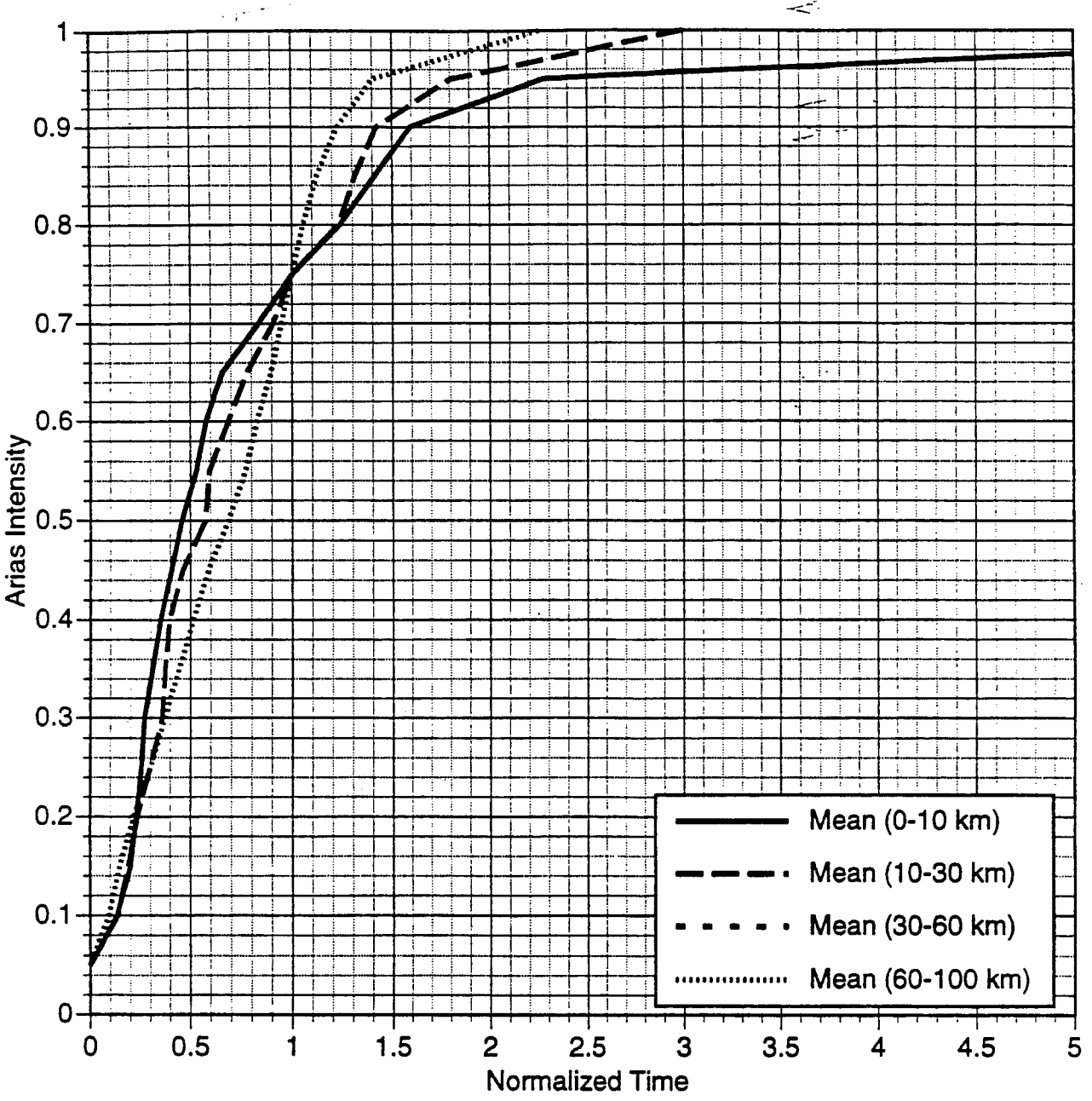

Figure 9e. Mean normalized durations averaged over distance bins for the horizontal component for rock site conditions and $7.0 < M < 7.5$.

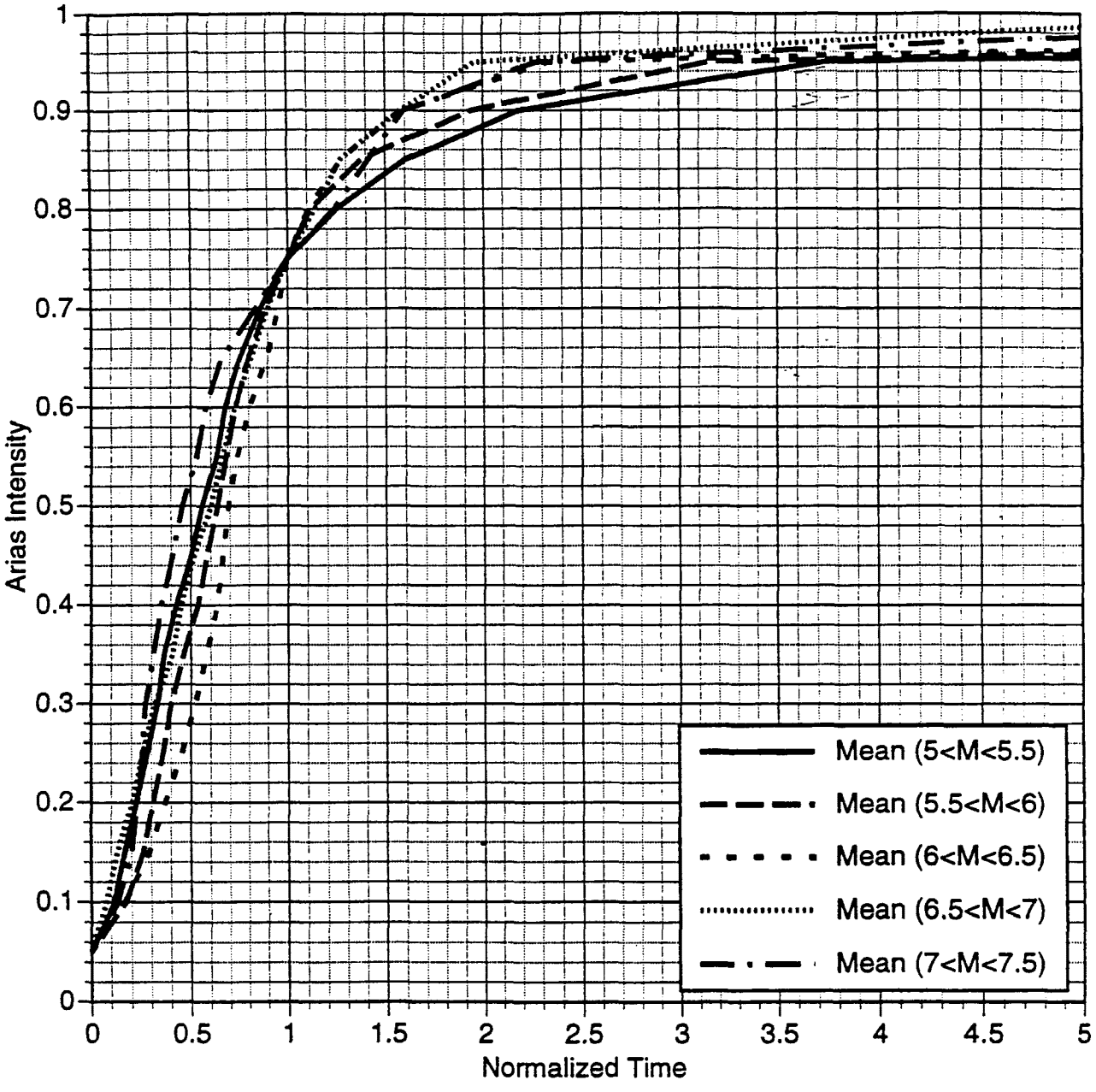

Figure 10a. Mean normalized durations averaged over magnitude bins for the horizontal component for rock site conditions and distance = 0-10 km.

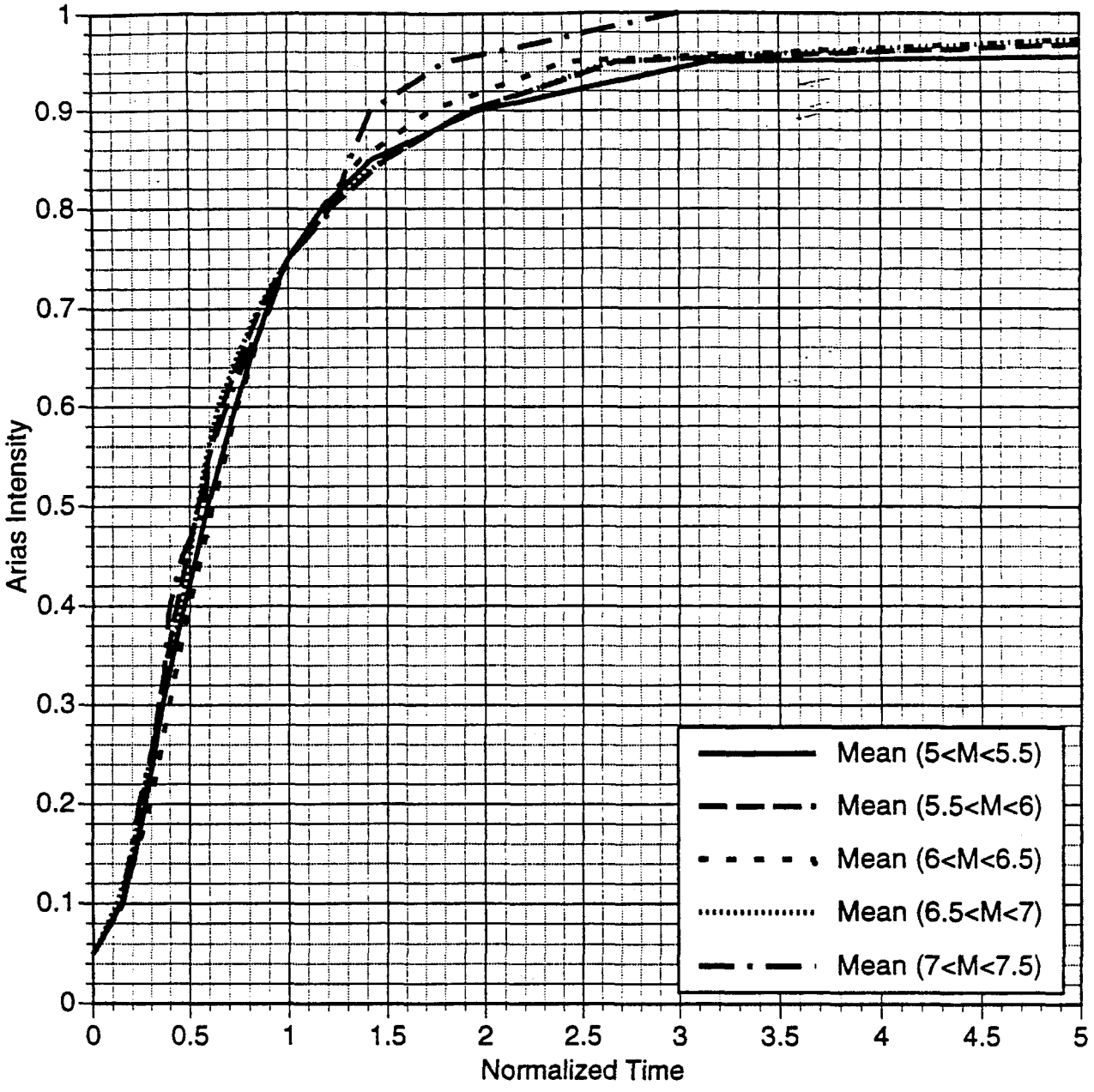

Figure 10b. Mean normalized durations averaged over magnitude bins for the horizontal component for rock site conditions and distance = 10-30 km.

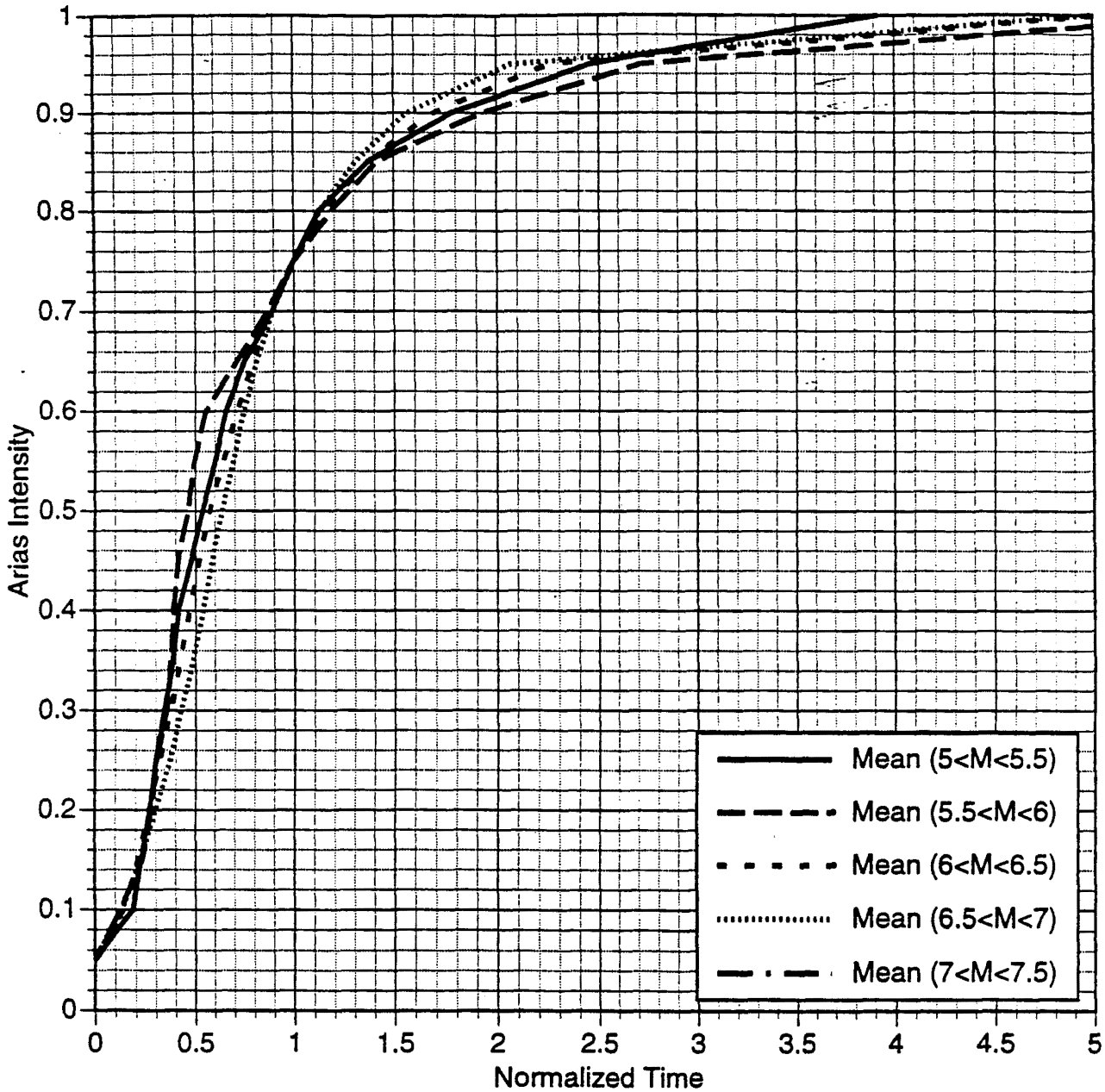

Figure 10c. Mean normalized durations averaged over magnitude bins for the horizontal component for rock site conditions and distance = 30-60 km.

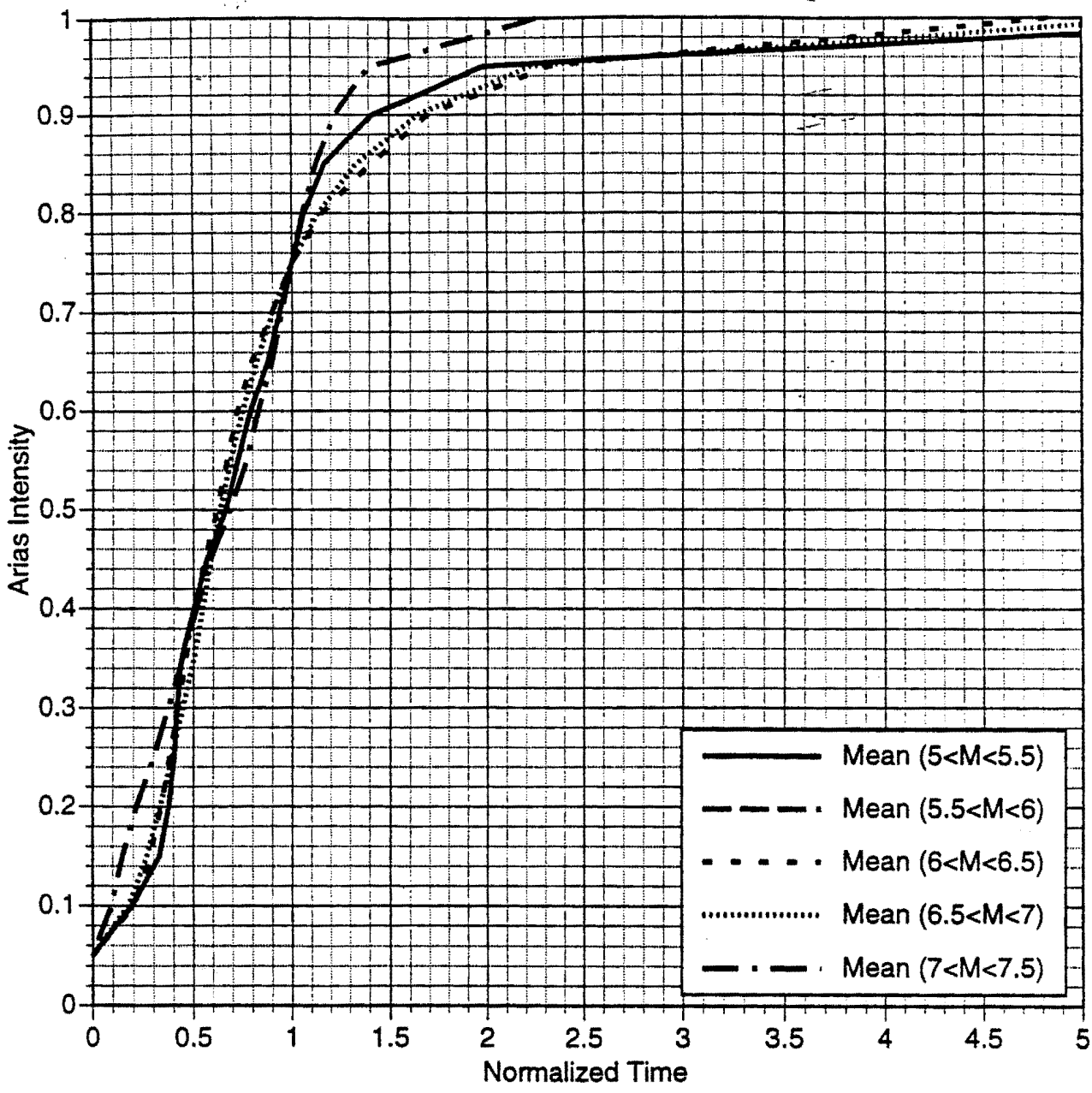

Figure 10d. Mean normalized durations averaged over magnitude bins for the horizontal component for rock site conditions and distance = 60-100 km.

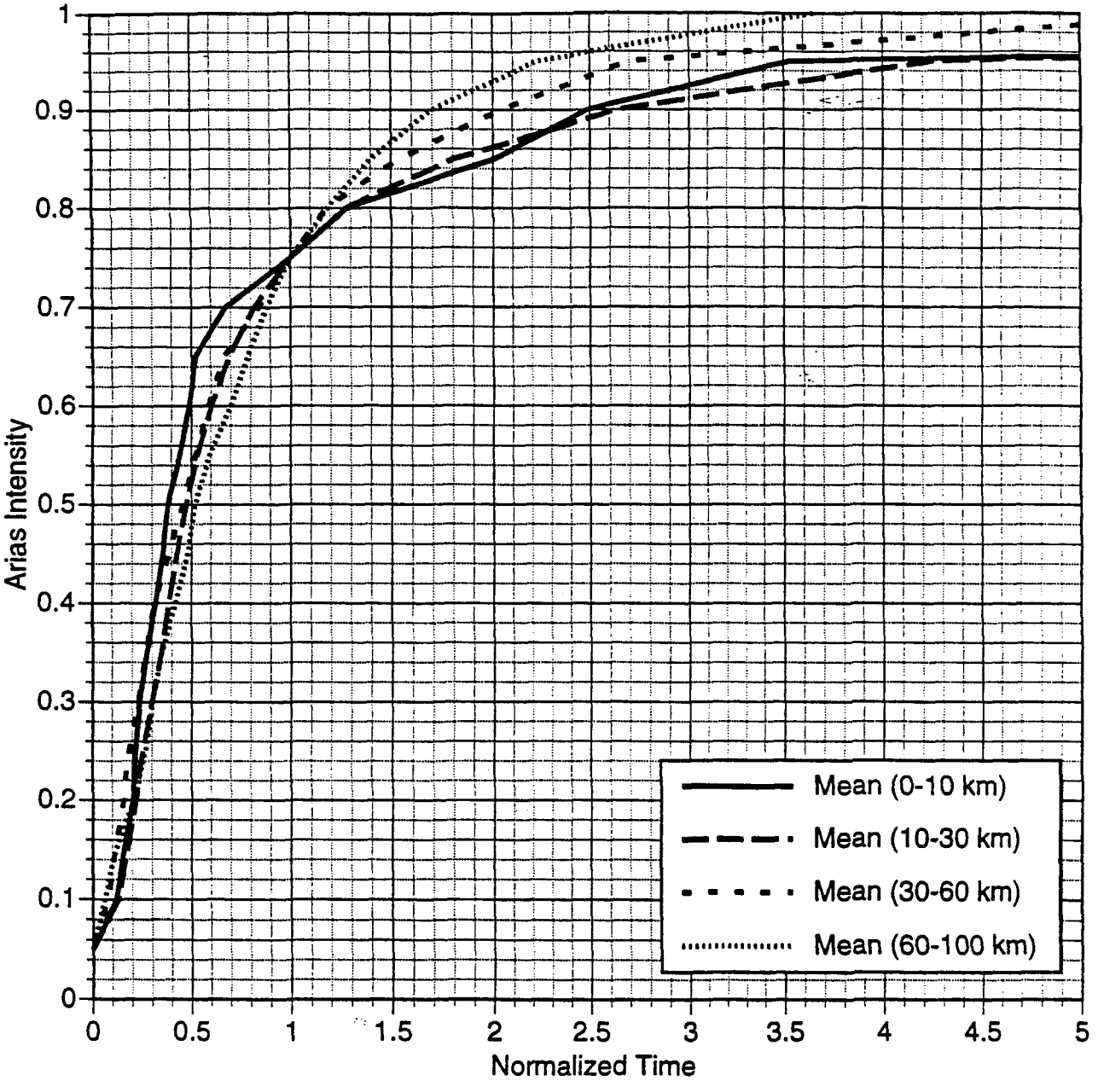

Figure 11a. Mean normalized durations averaged over distance bins for the horizontal component for soil site conditions and $5.0 < M < 5.5$.

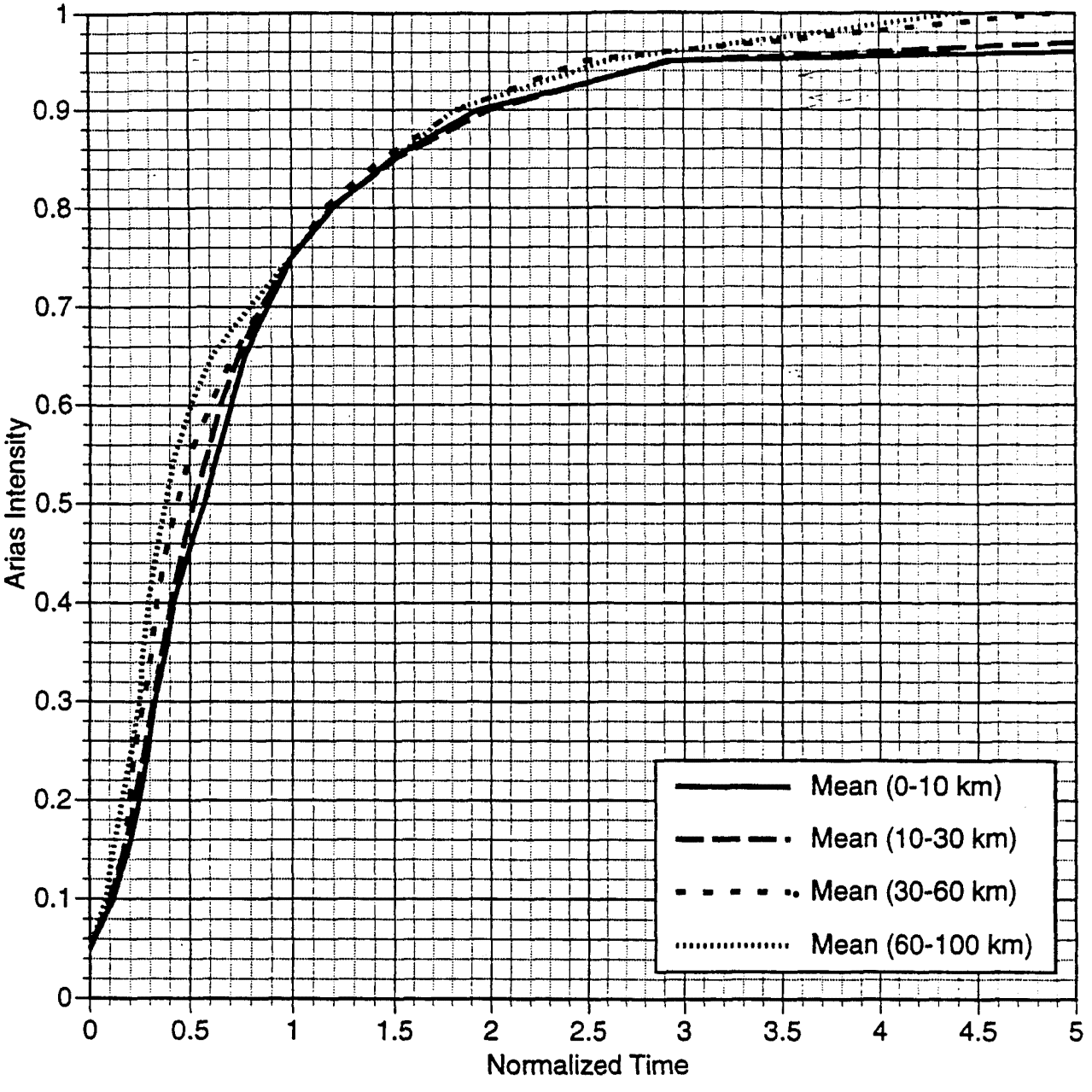

Figure 11b. Mean normalized durations averaged over distance bins for the horizontal component for soil site conditions and $5.5 < M < 6.0$.

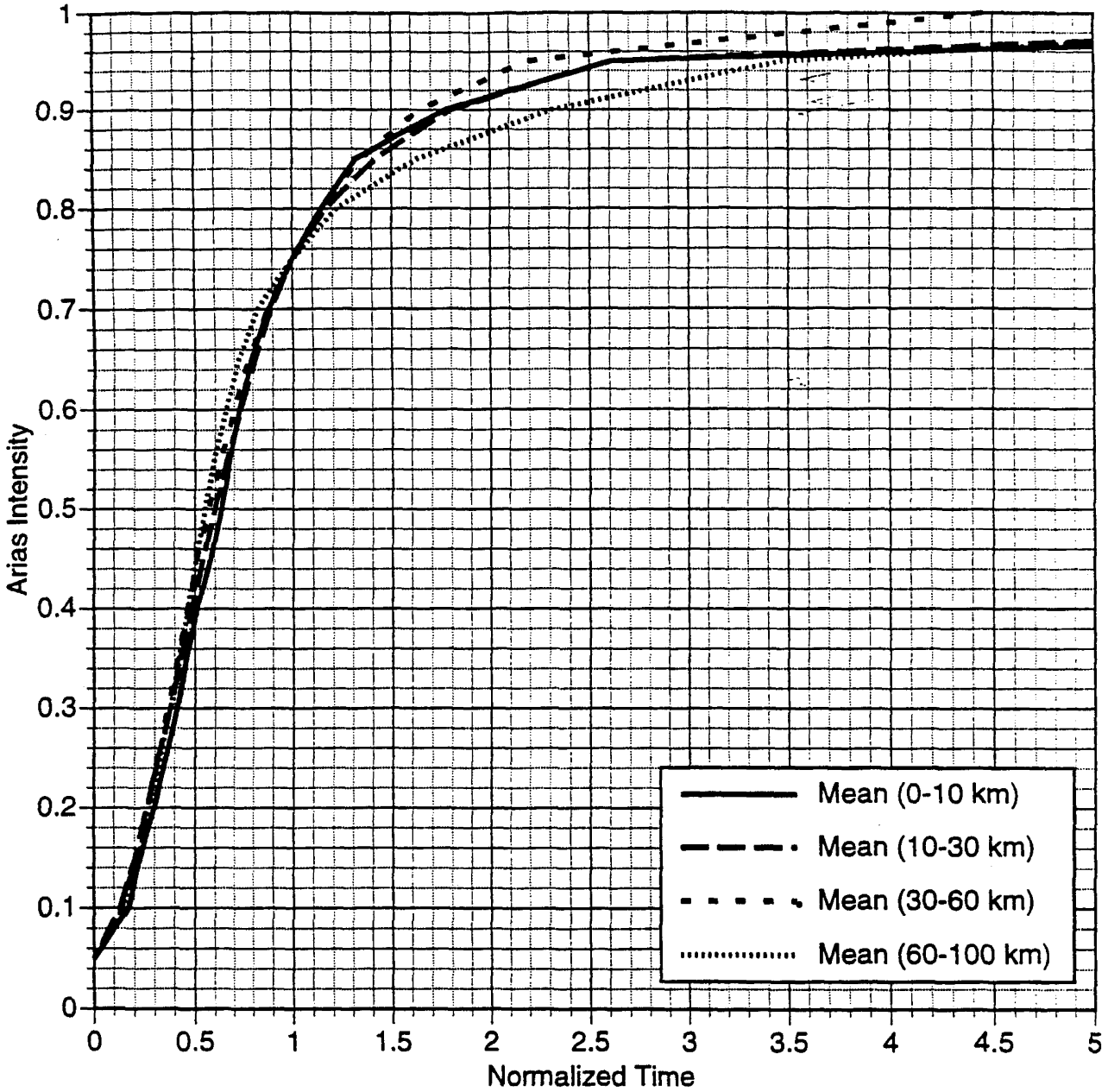

Figure 11c. Mean normalized durations averaged over distance bins for the horizontal component for soil site conditions and $6.0 < M < 6.5$.

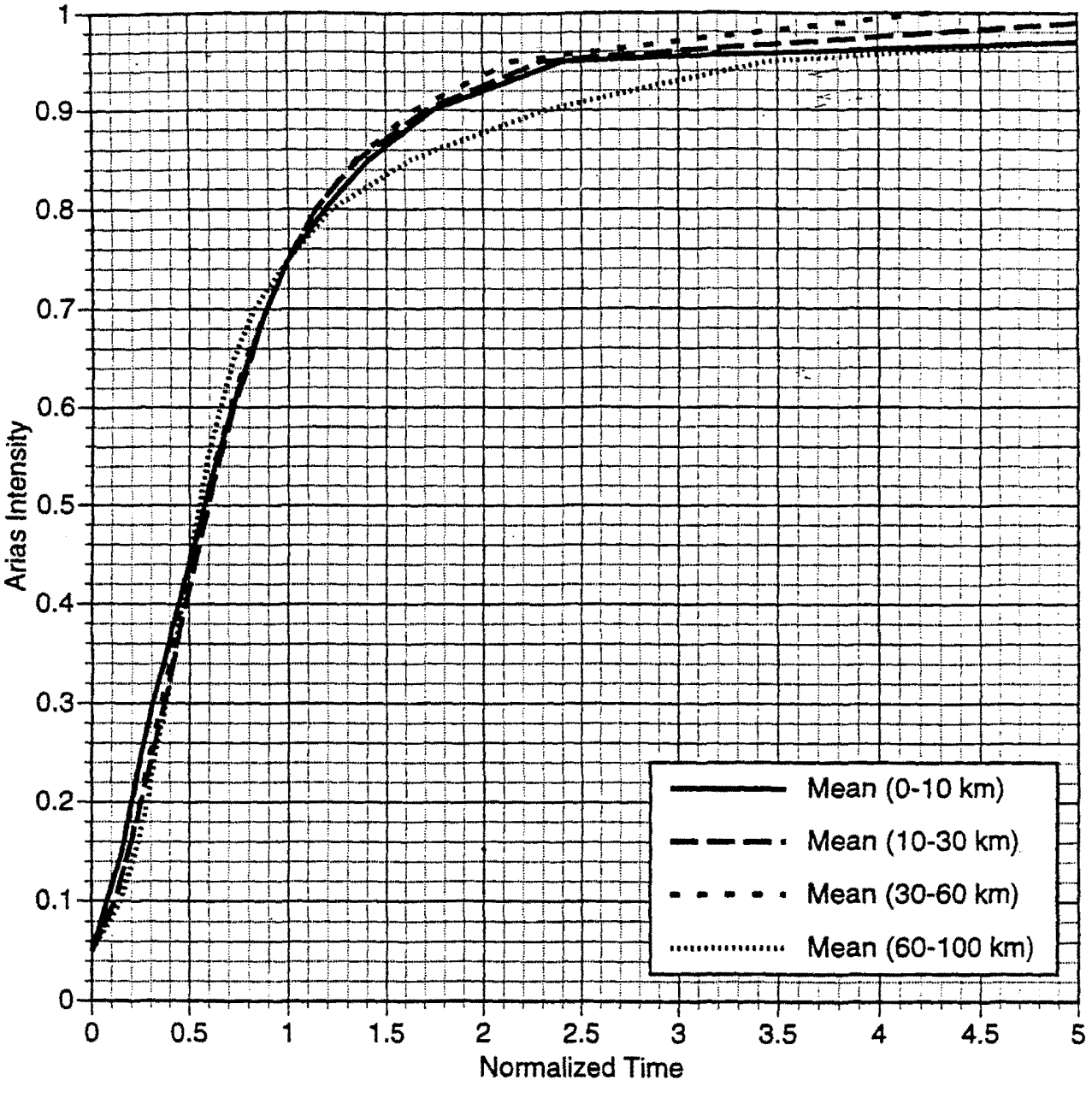

Figure 11d. Mean normalized durations averaged over distance bins for the horizontal component for soil site conditions and $6.5 < M < 7.0$.

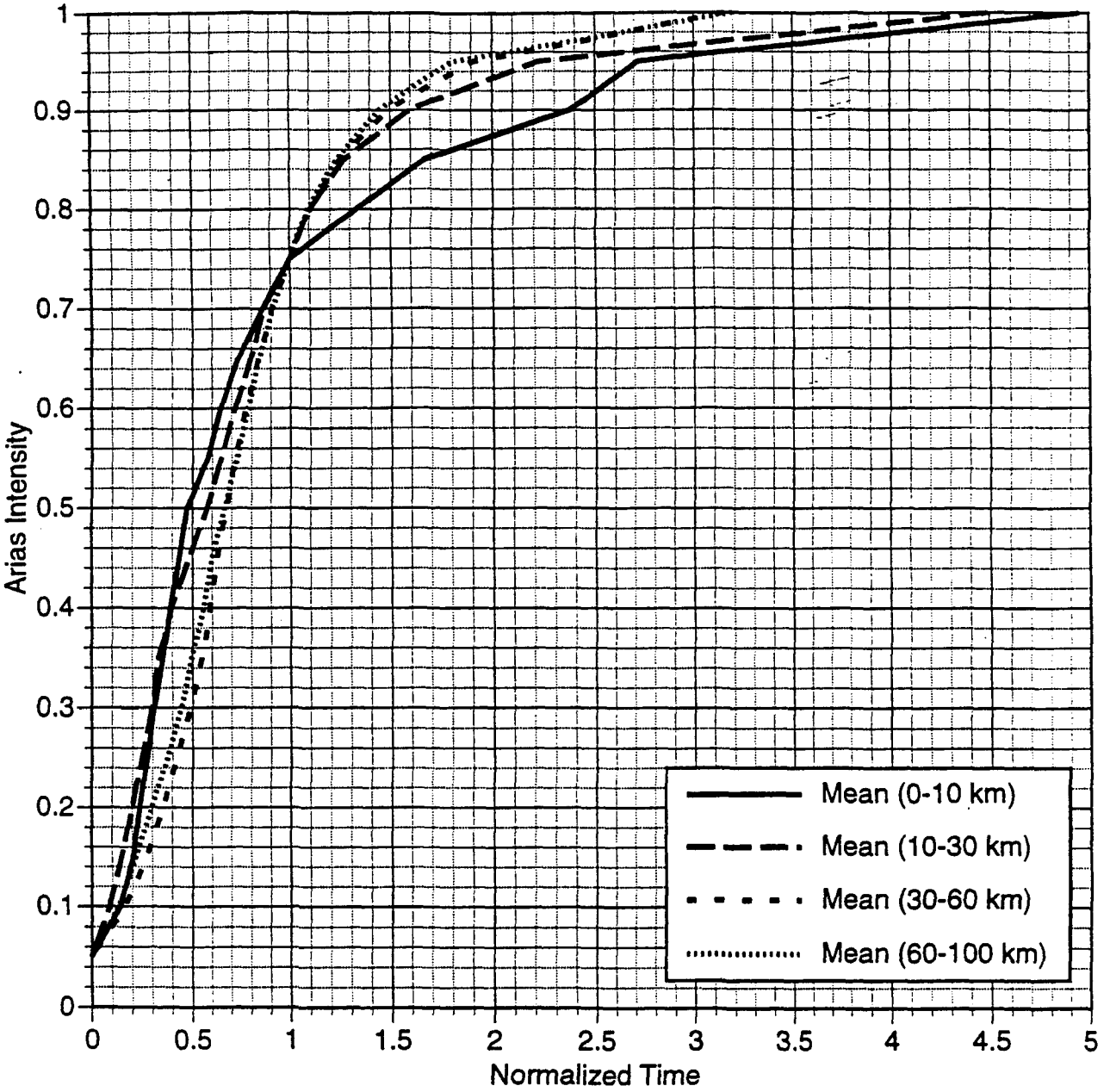

Figure 11e. Mean normalized durations averaged over distance bins for the horizontal component for soil site conditions and $7.0 < M < 7.5$.

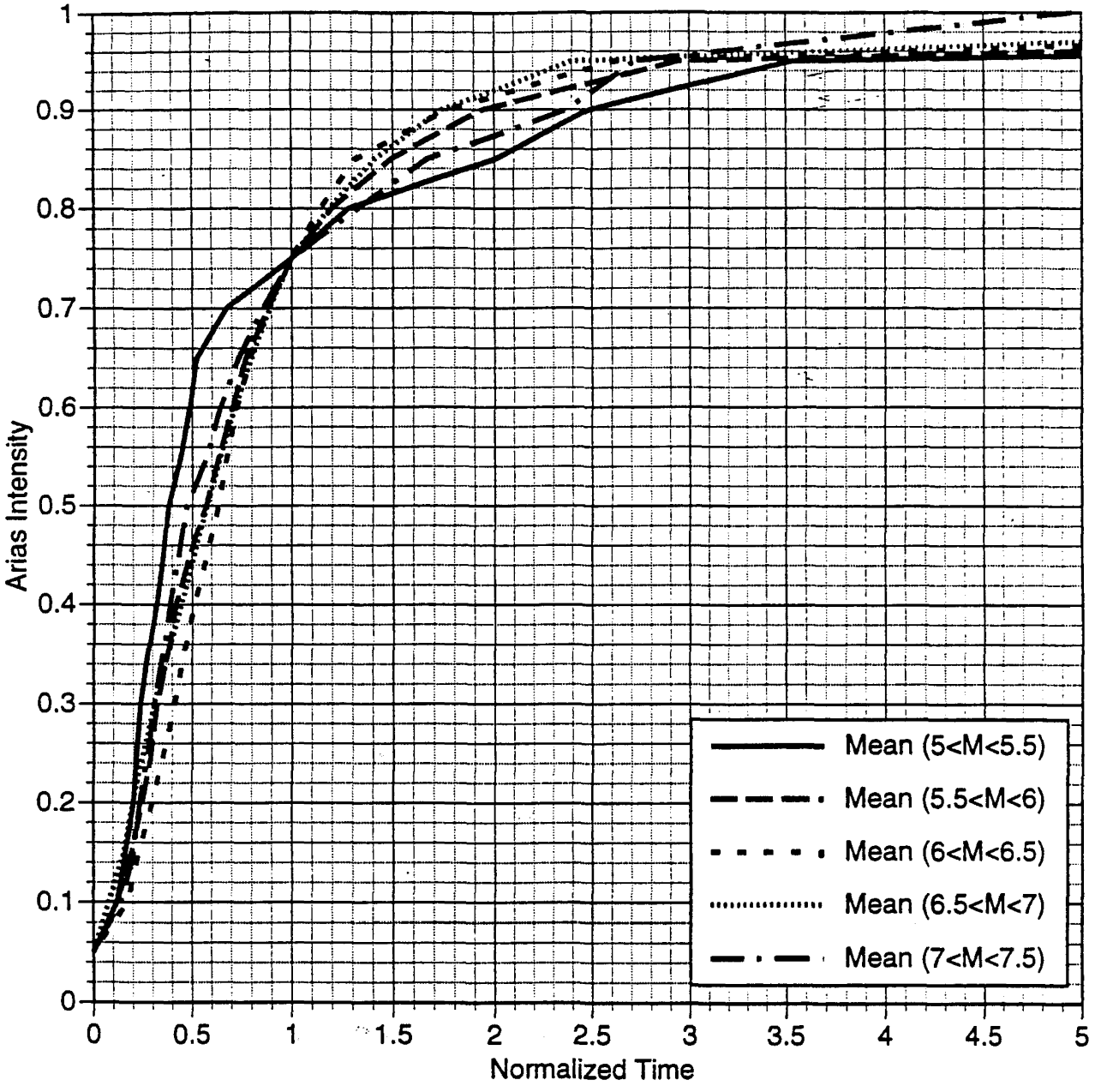

Figure 12a. Mean normalized durations averaged over magnitude bins for the horizontal component for soil site conditions and distance = 0-10 km.

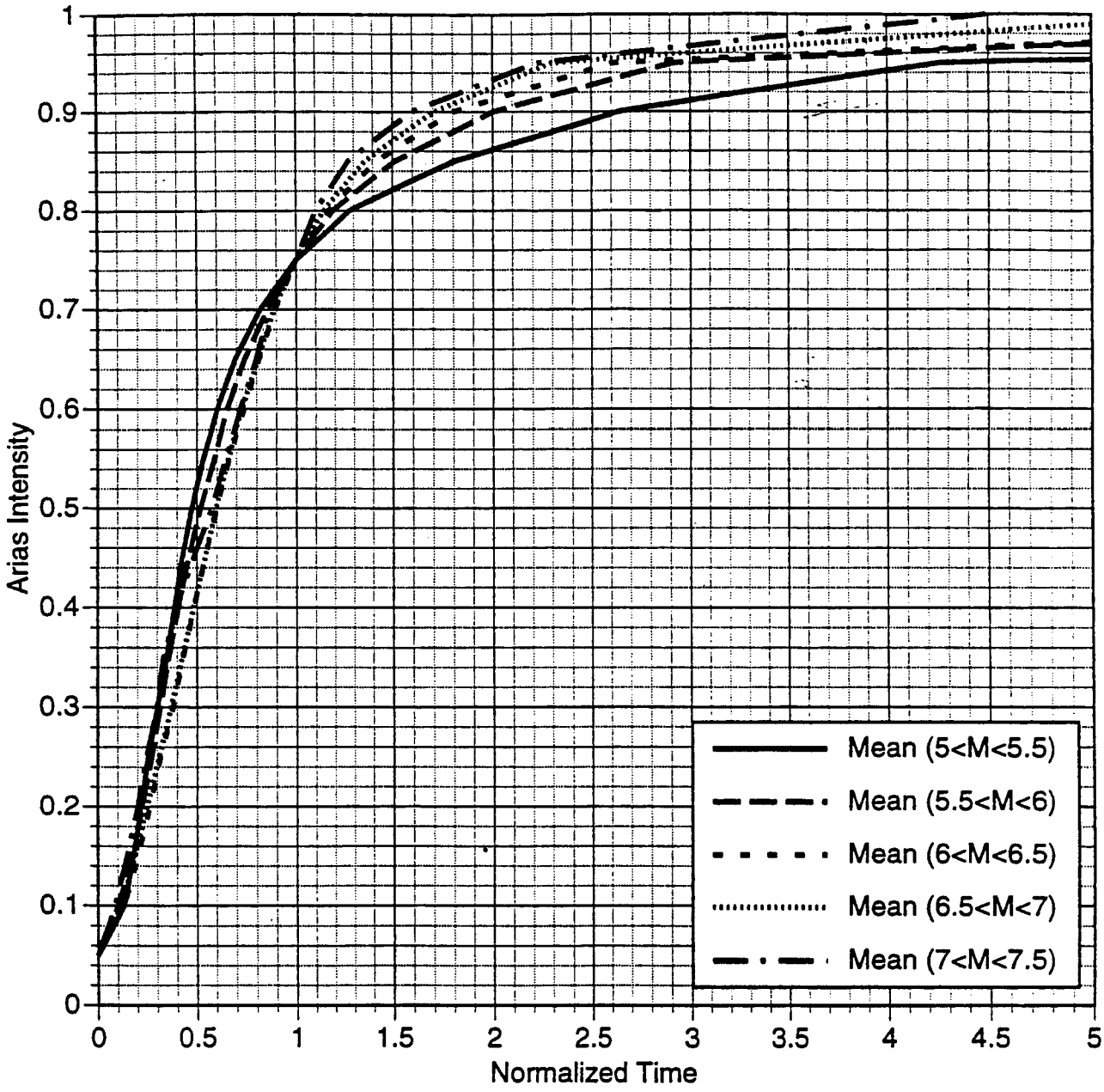

Figure 12b. Mean normalized durations averaged over magnitude bins for the horizontal component for soil site conditions and distance = 10-30 km.

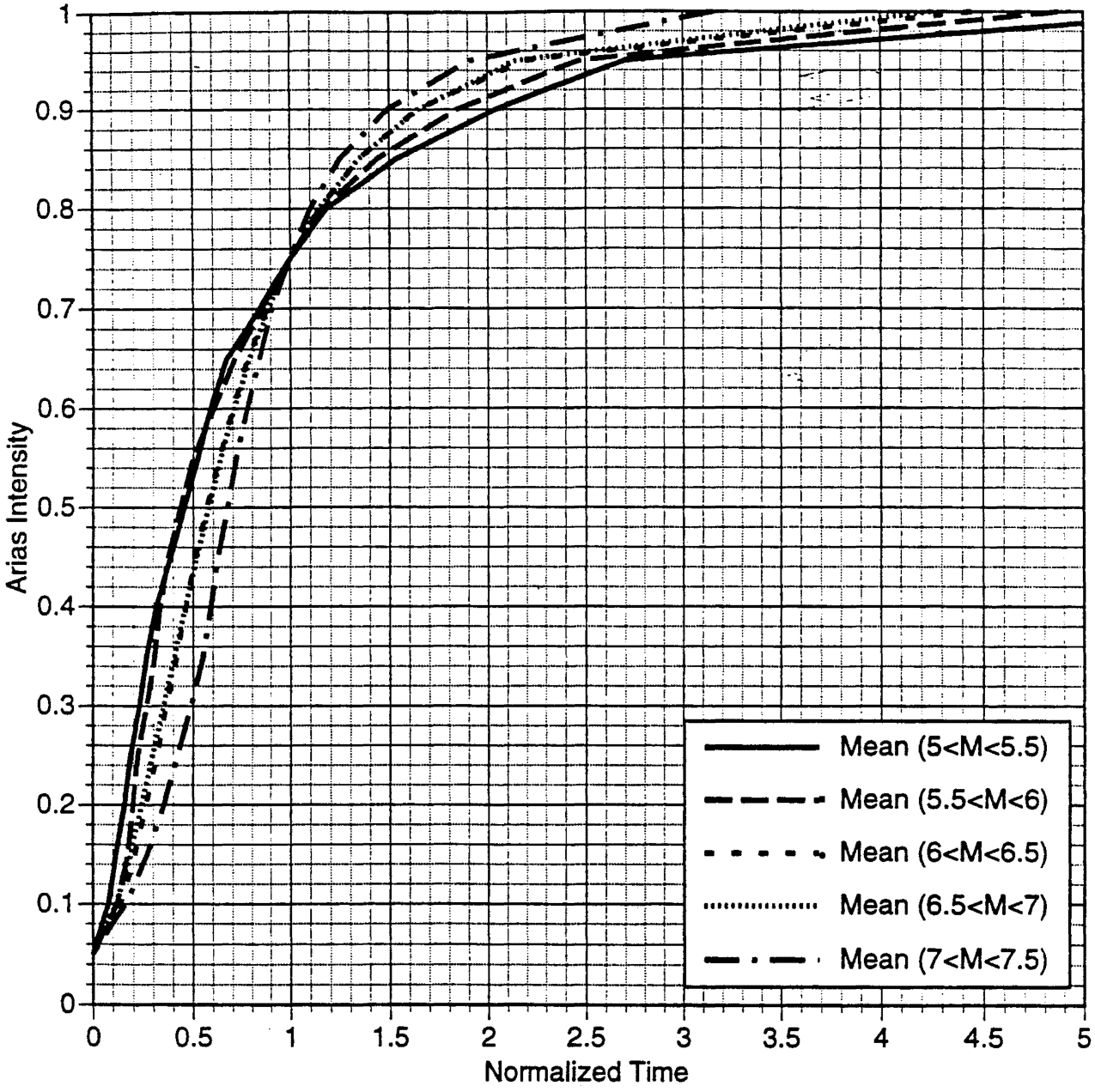

Figure 12c. Mean normalized durations averaged over magnitude bins for the horizontal component for soil site conditions and distance = 30-60 km.

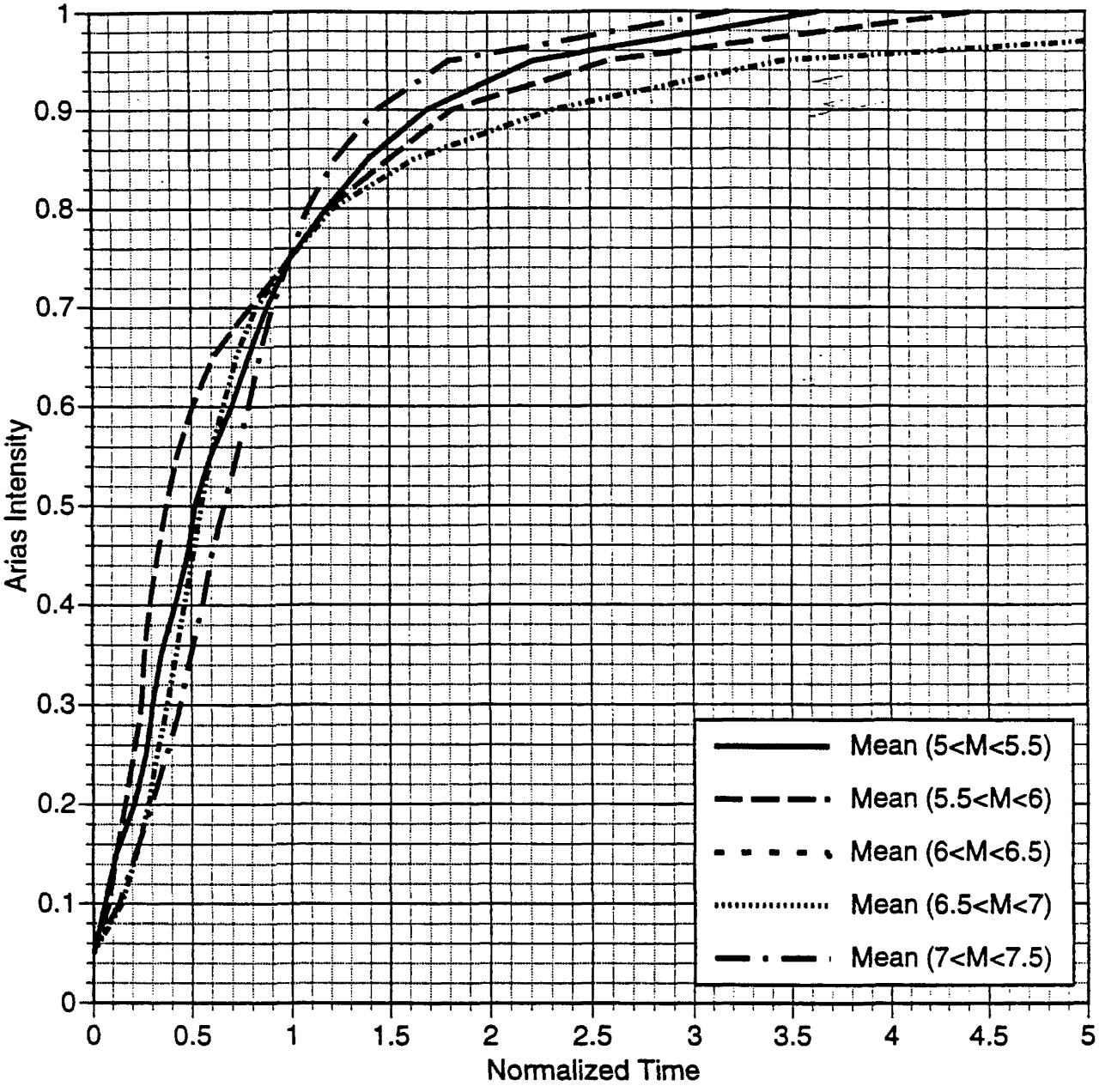

Figure 12d. Mean normalized durations averaged over magnitude bins for the horizontal component for soil site conditions and distance = 60-100 km.

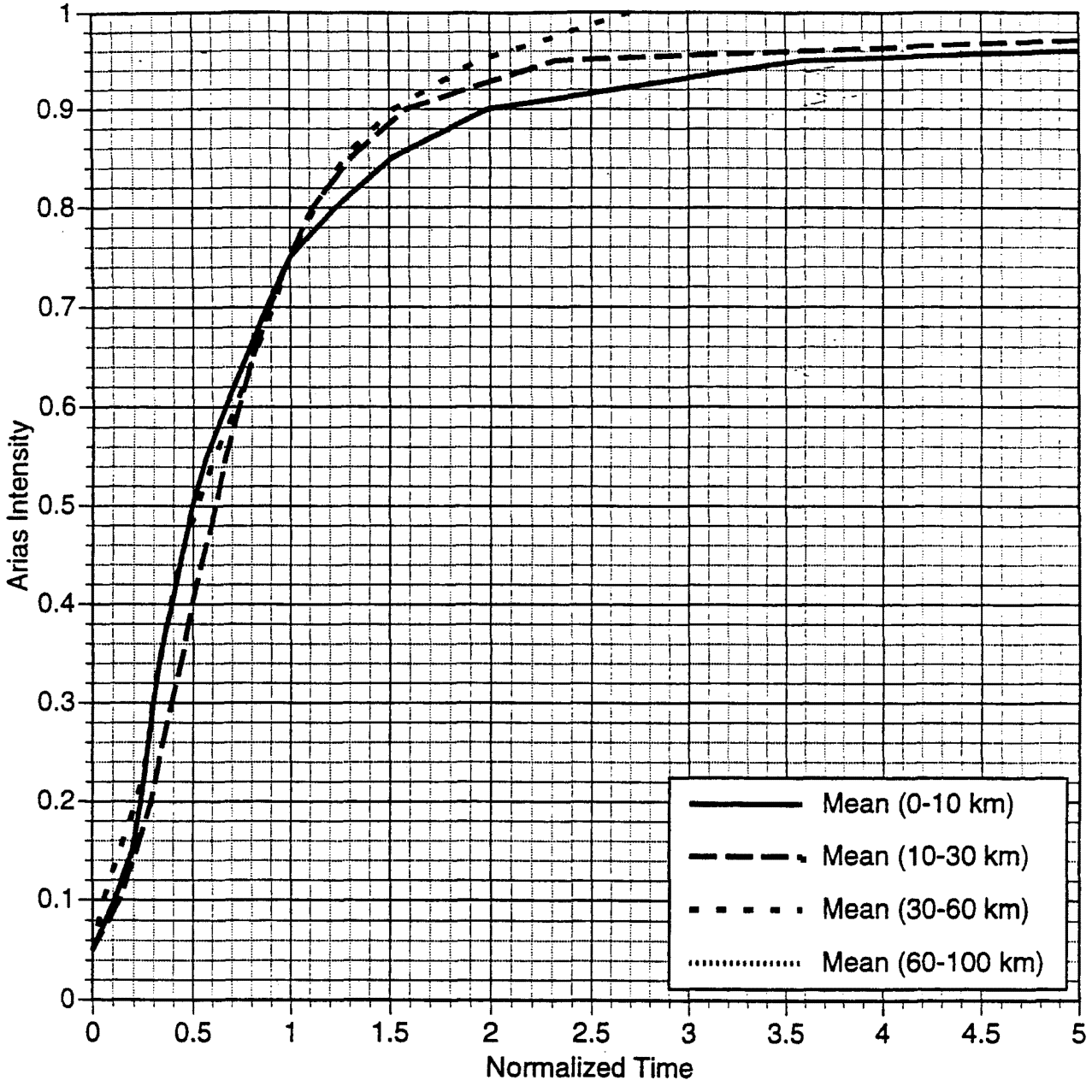

Figure 13a. Mean normalized durations averaged over distance bins for the vertical component for rock site conditions and $5.0 < M < 5.5$.

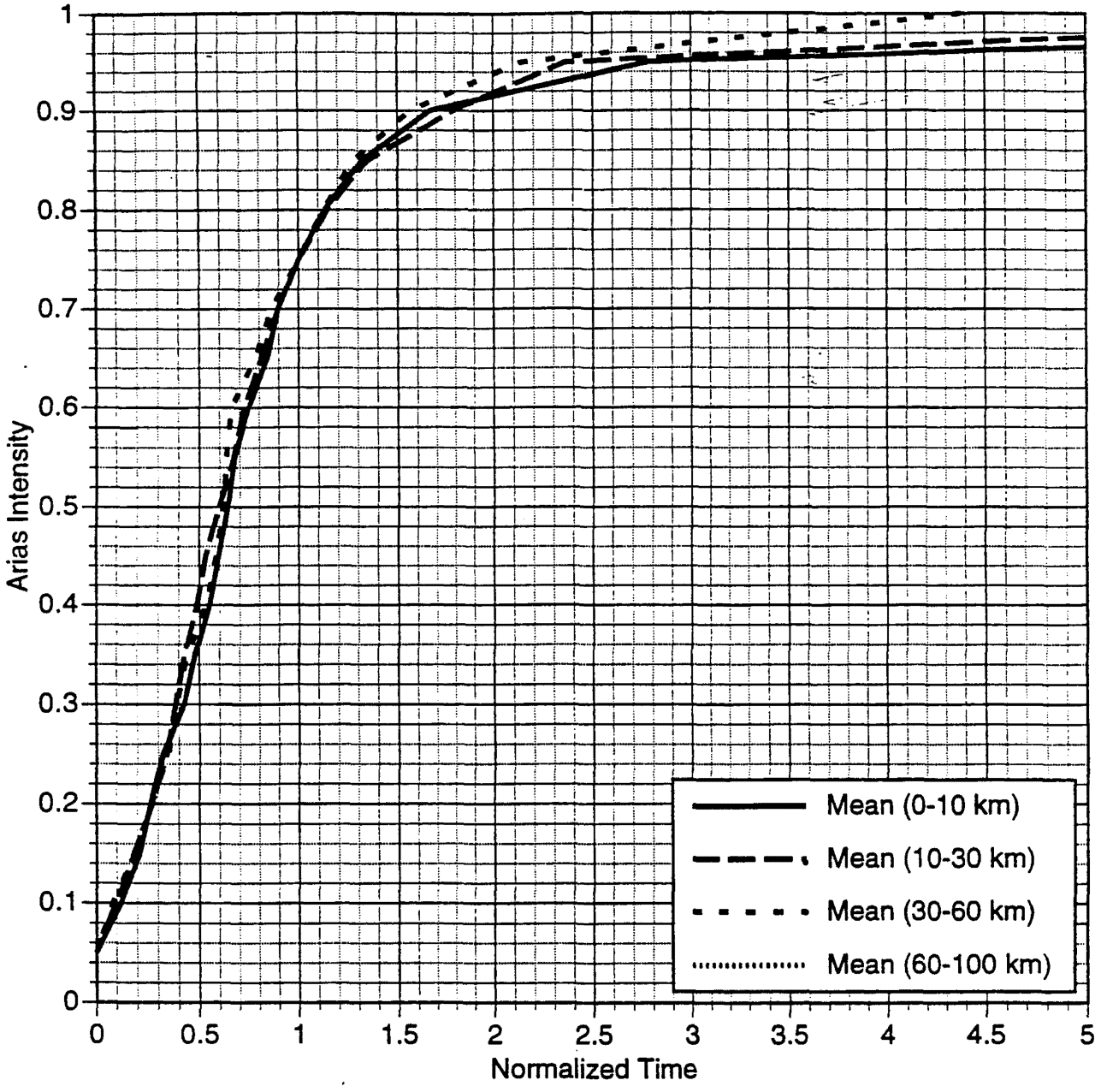

Figure 13b. Mean normalized durations averaged over distance bins for the vertical component for rock site conditions and $5.5 < M < 6.0$.

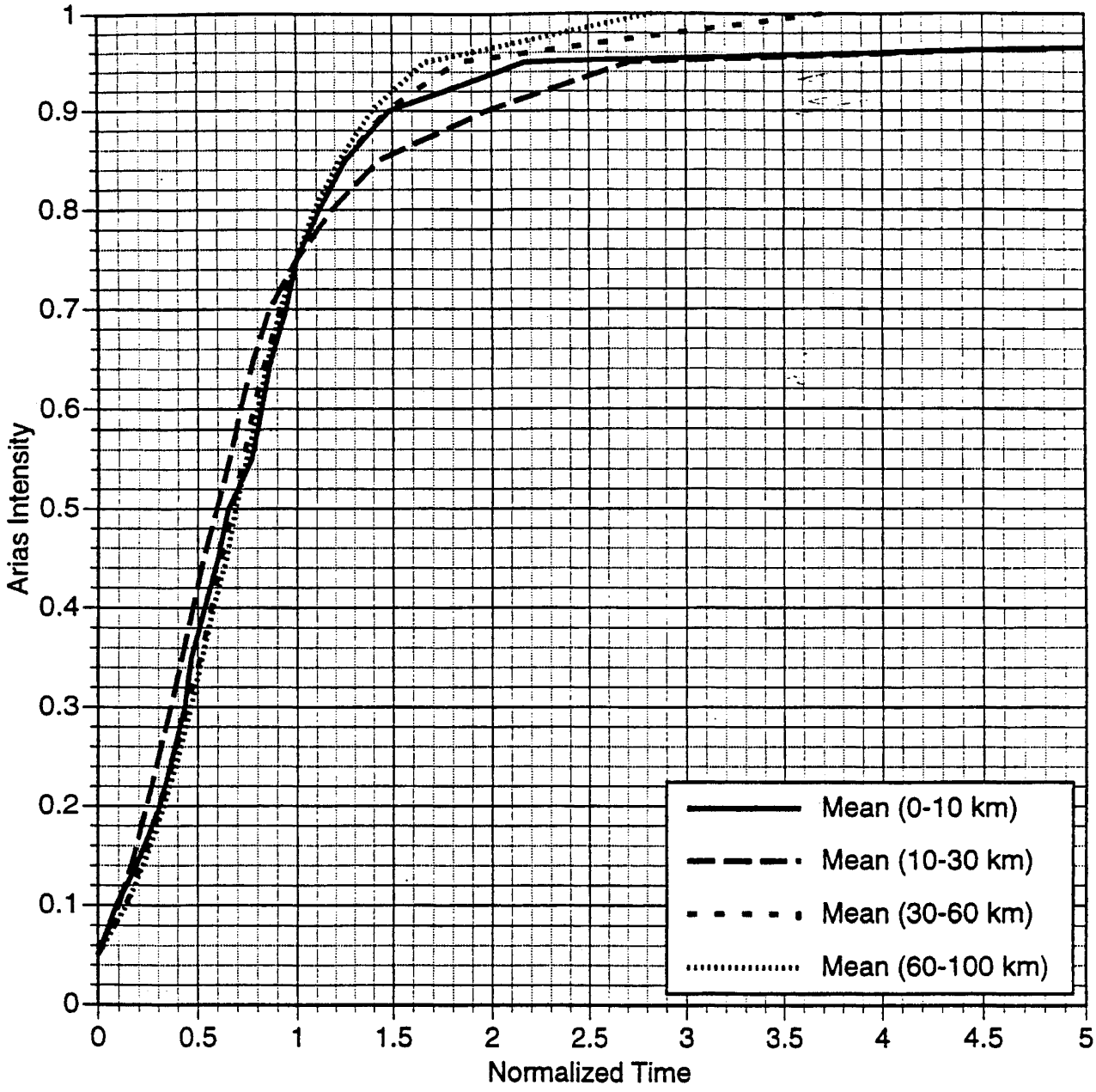

Figure 13c. Mean normalized durations averaged over distance bins for the vertical component for rock site conditions and $6.0 < M < 6.5$.

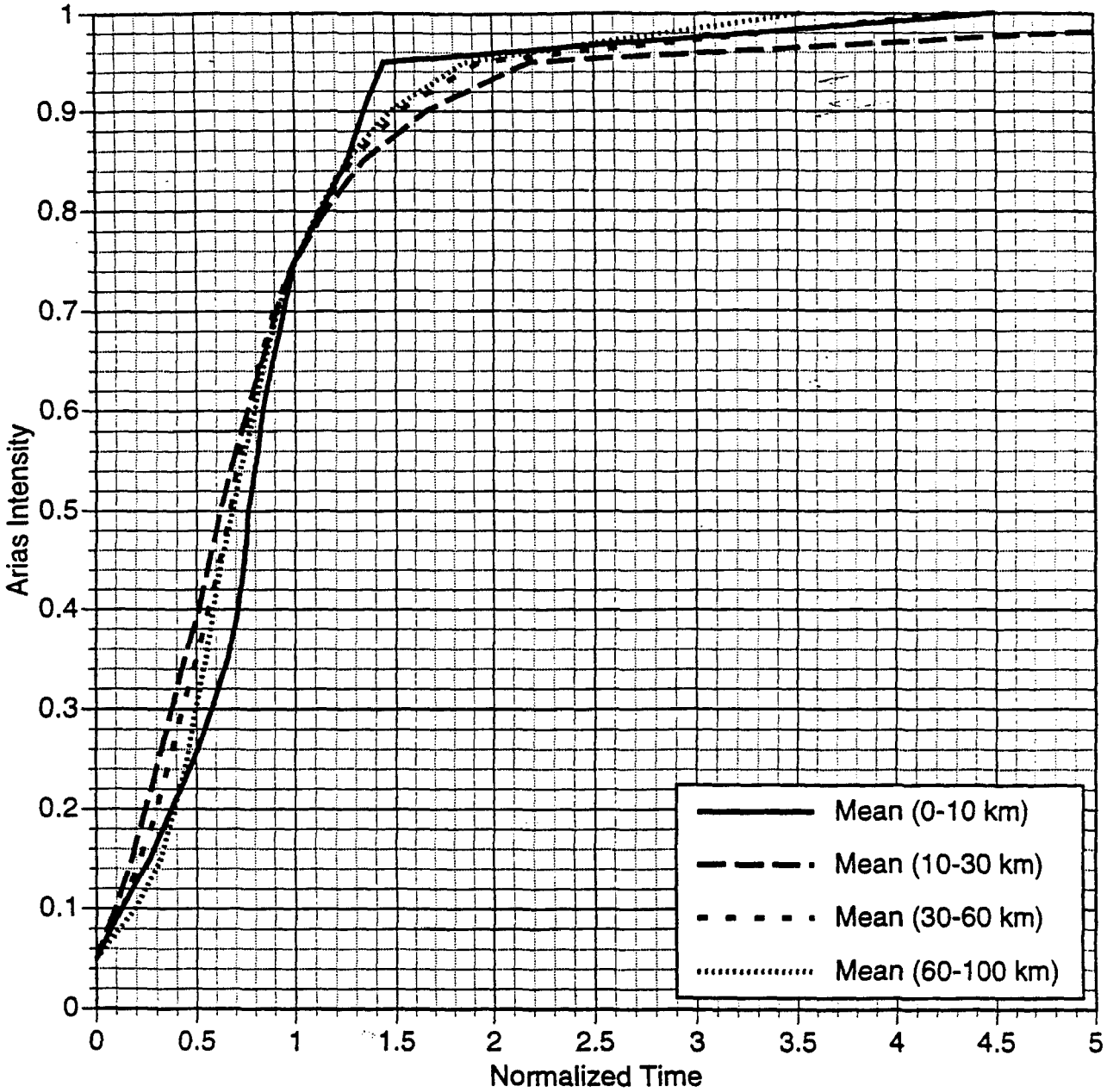

Figure 13d. Mean normalized durations averaged over distance bins for the vertical component for rock site conditions and $6.5 < M < 7.0$.

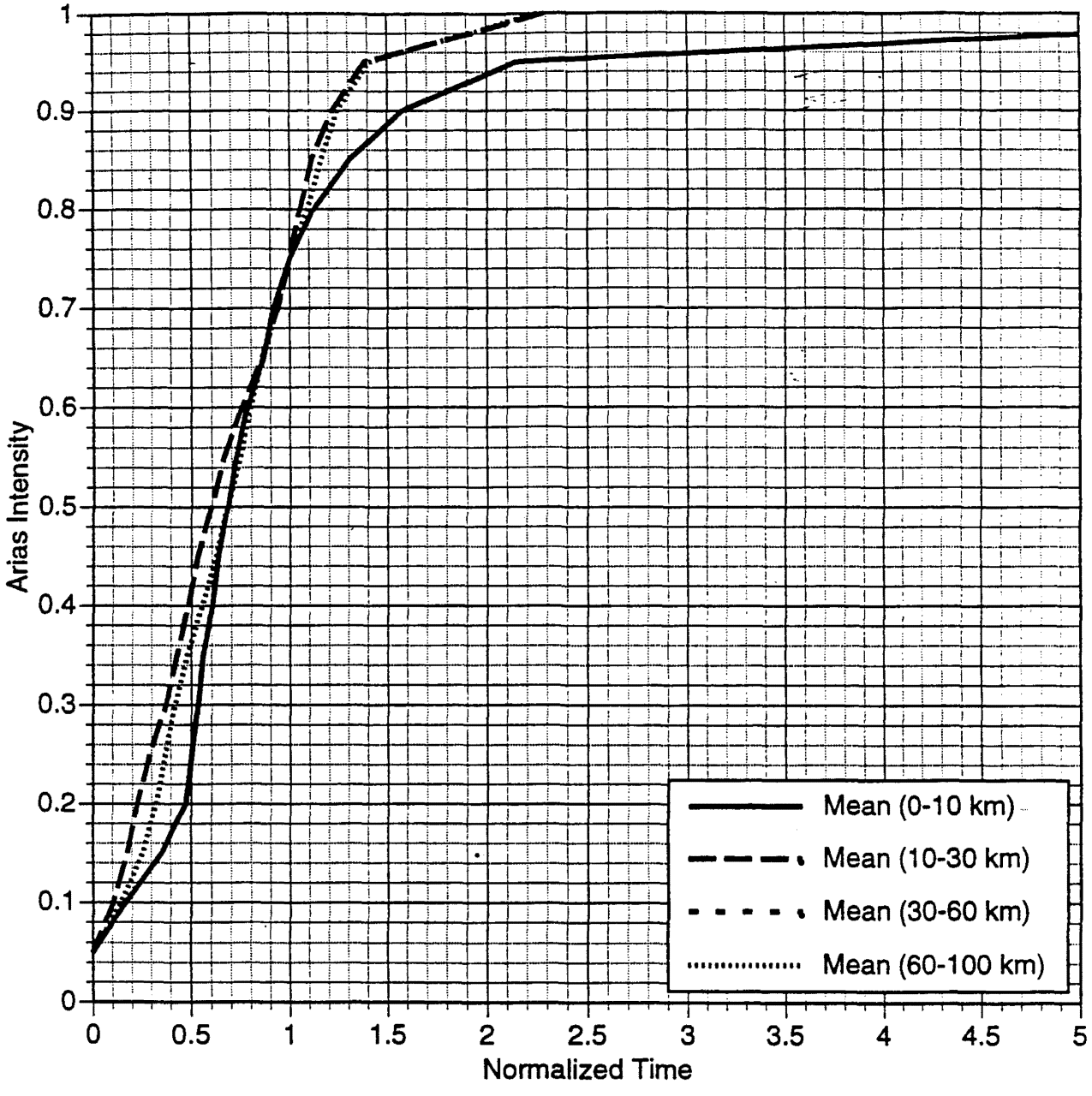

Figure 13e. Mean normalized durations averaged over distance bins for the vertical component for rock site conditions and $7.0 < M < 7.5$.

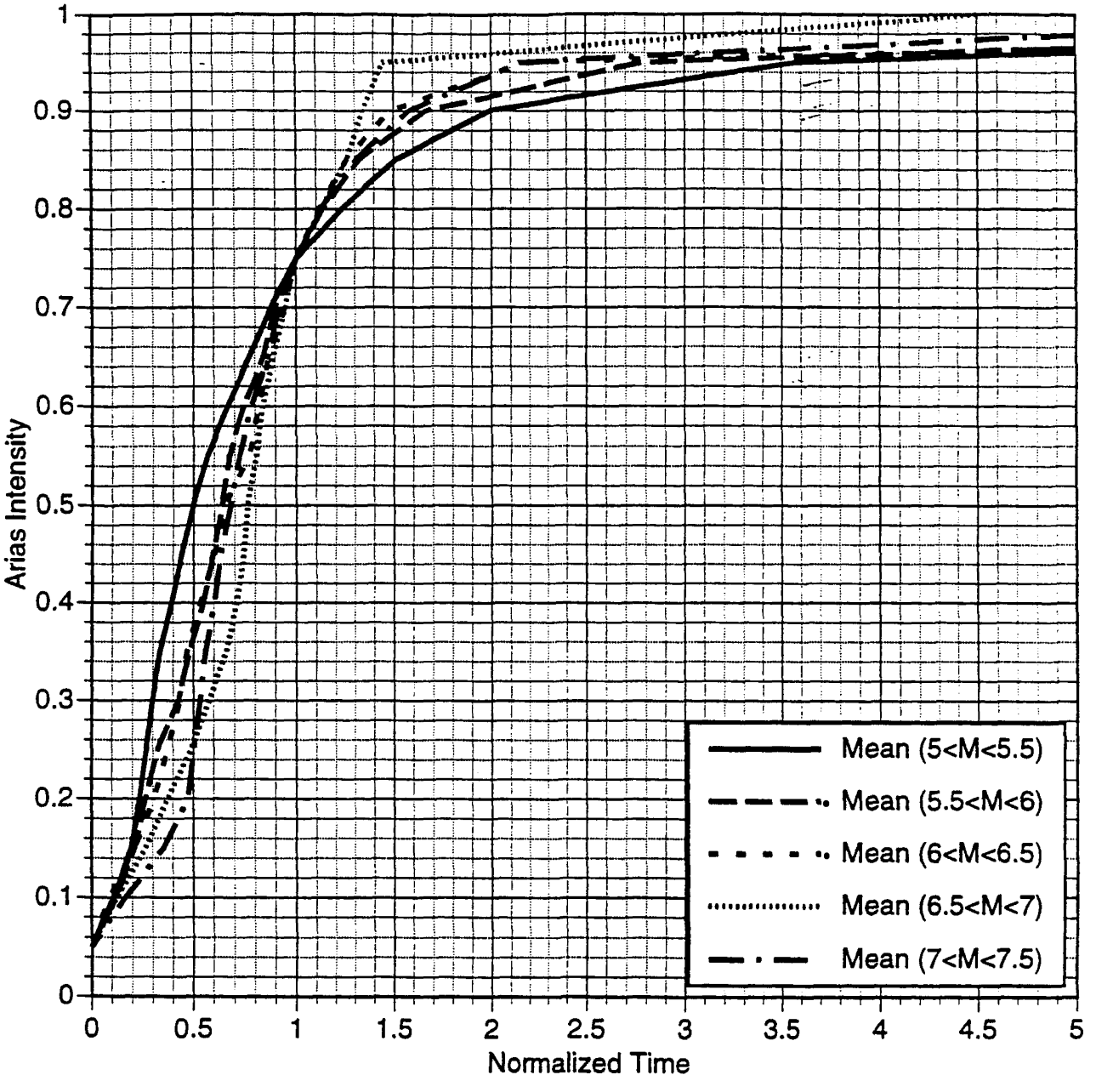

Figure 14a. Mean normalized durations averaged over magnitude bins for the vertical component for rock site conditions and distance = 0-10 km.

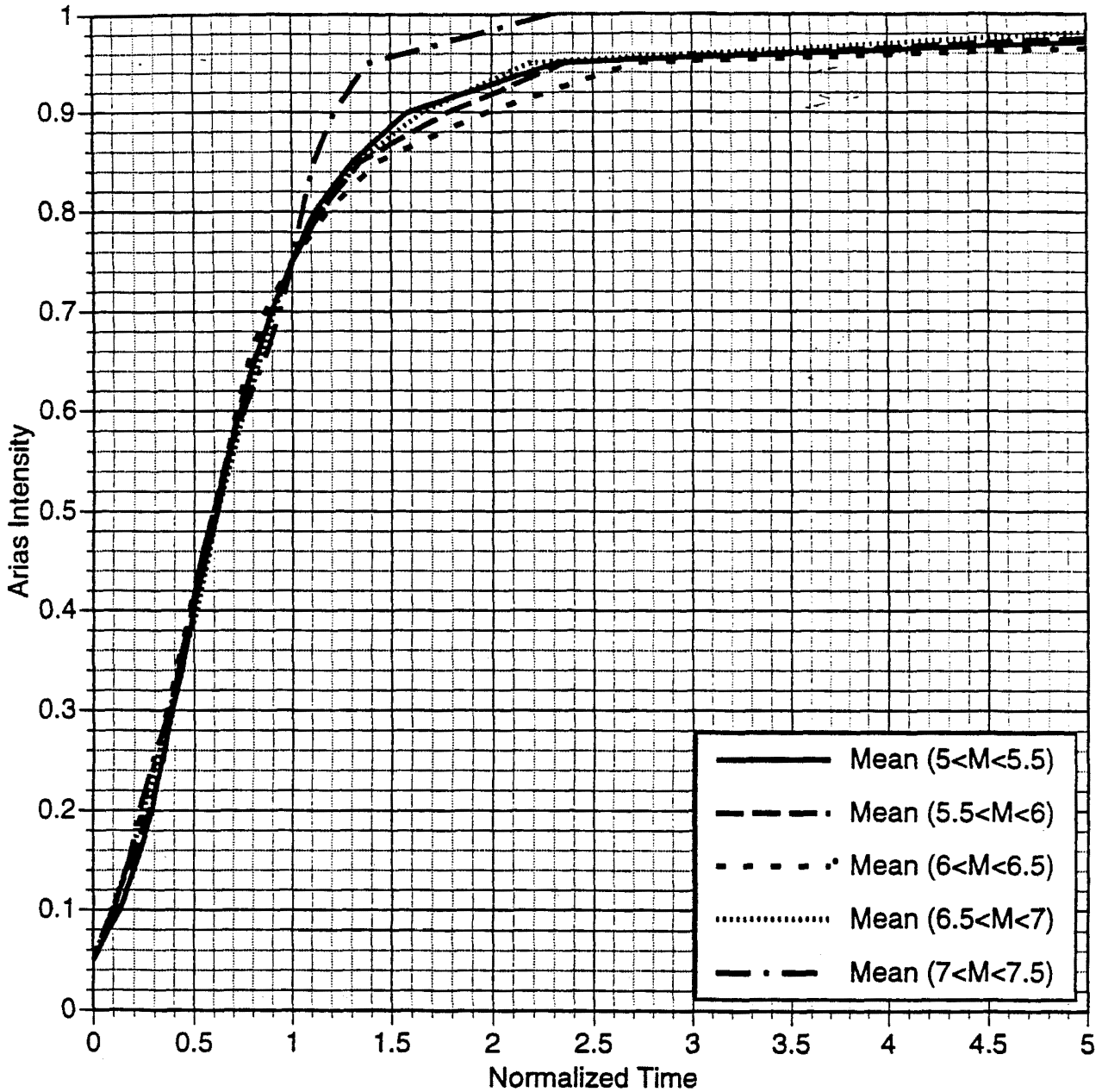

Figure 14b. Mean normalized durations averaged over magnitude bins for the vertical component for rock site conditions and distance = 10-30 km.

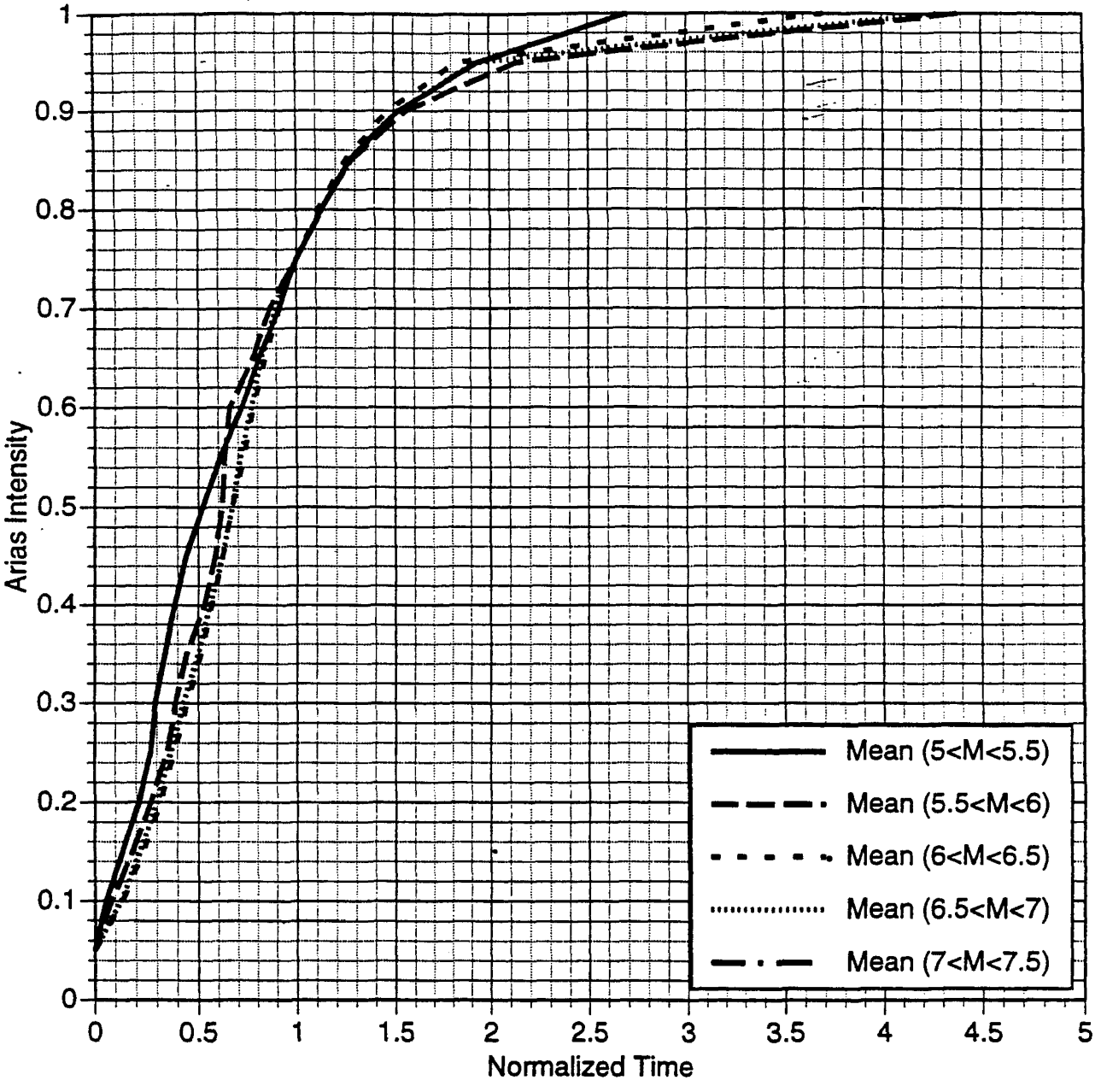

Figure 14c. Mean normalized durations averaged over magnitude bins for the vertical component for rock site conditions and distance = 30-60 km.

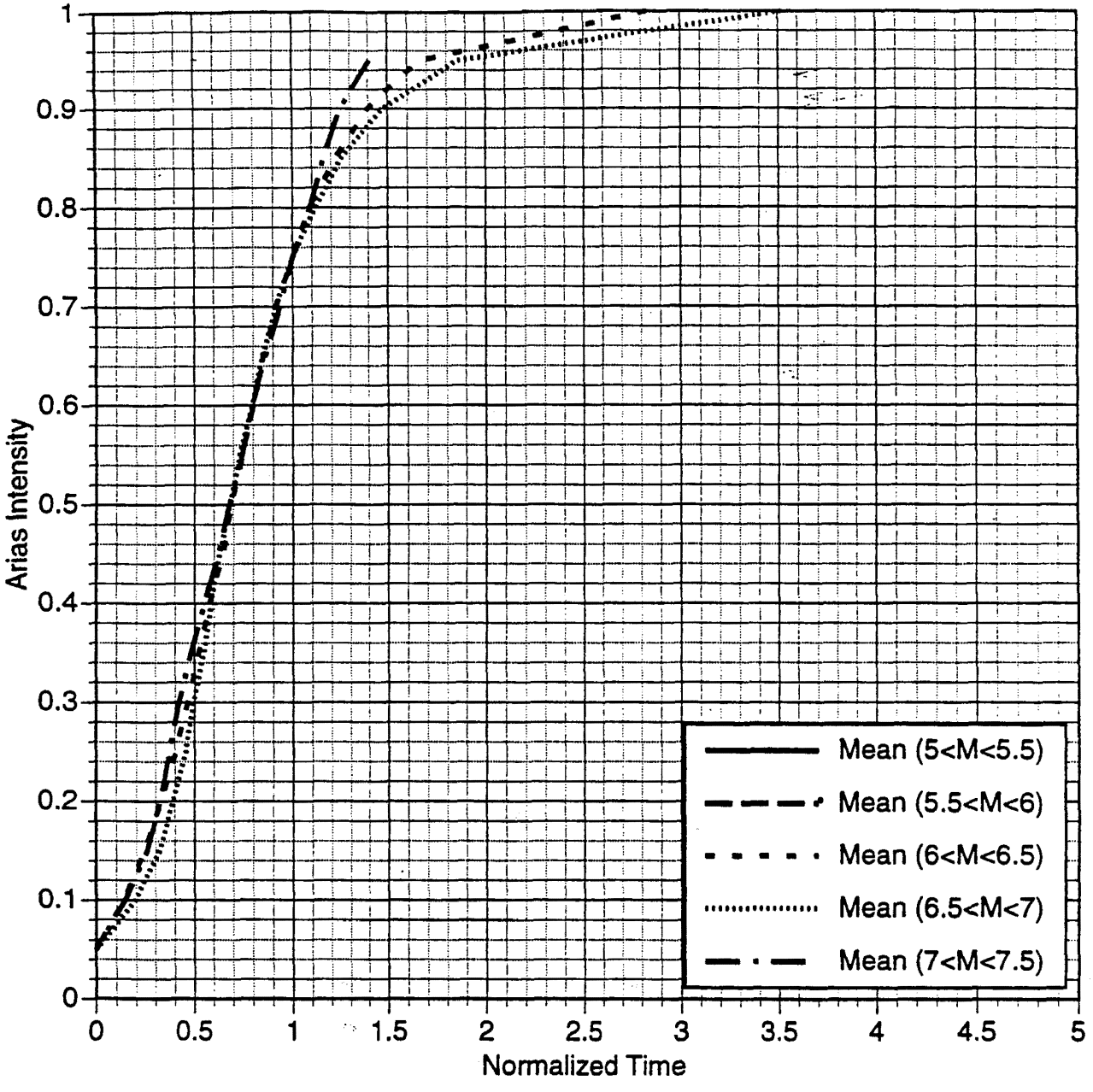

Figure 14d. Mean normalized durations averaged over magnitude bins for the vertical component for rock site conditions and distance = 60-100 km.

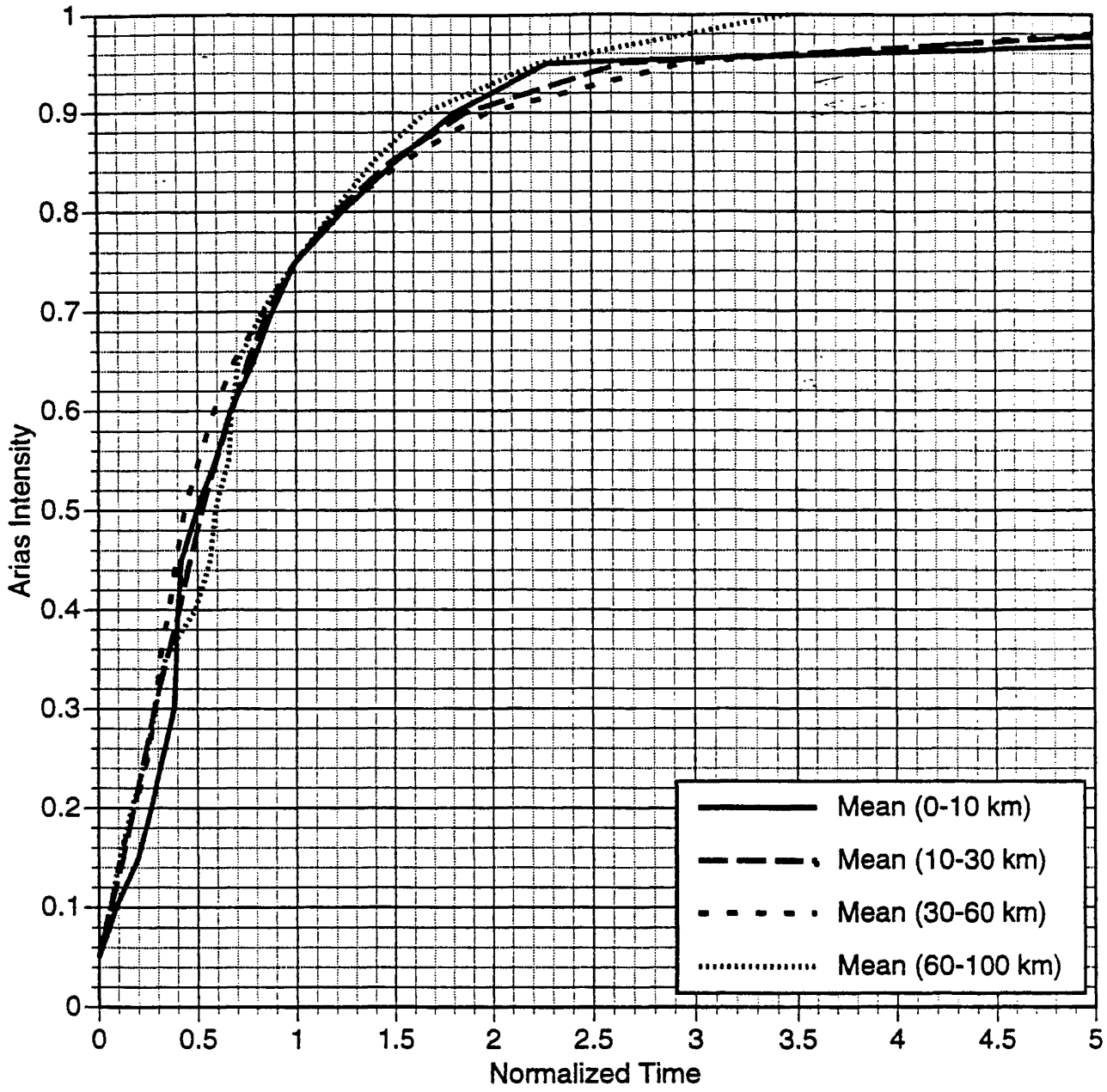

Figure 15a. Mean normalized durations averaged over distance bins for the vertical component for soil site conditions and $5.0 < M < 5.5$.

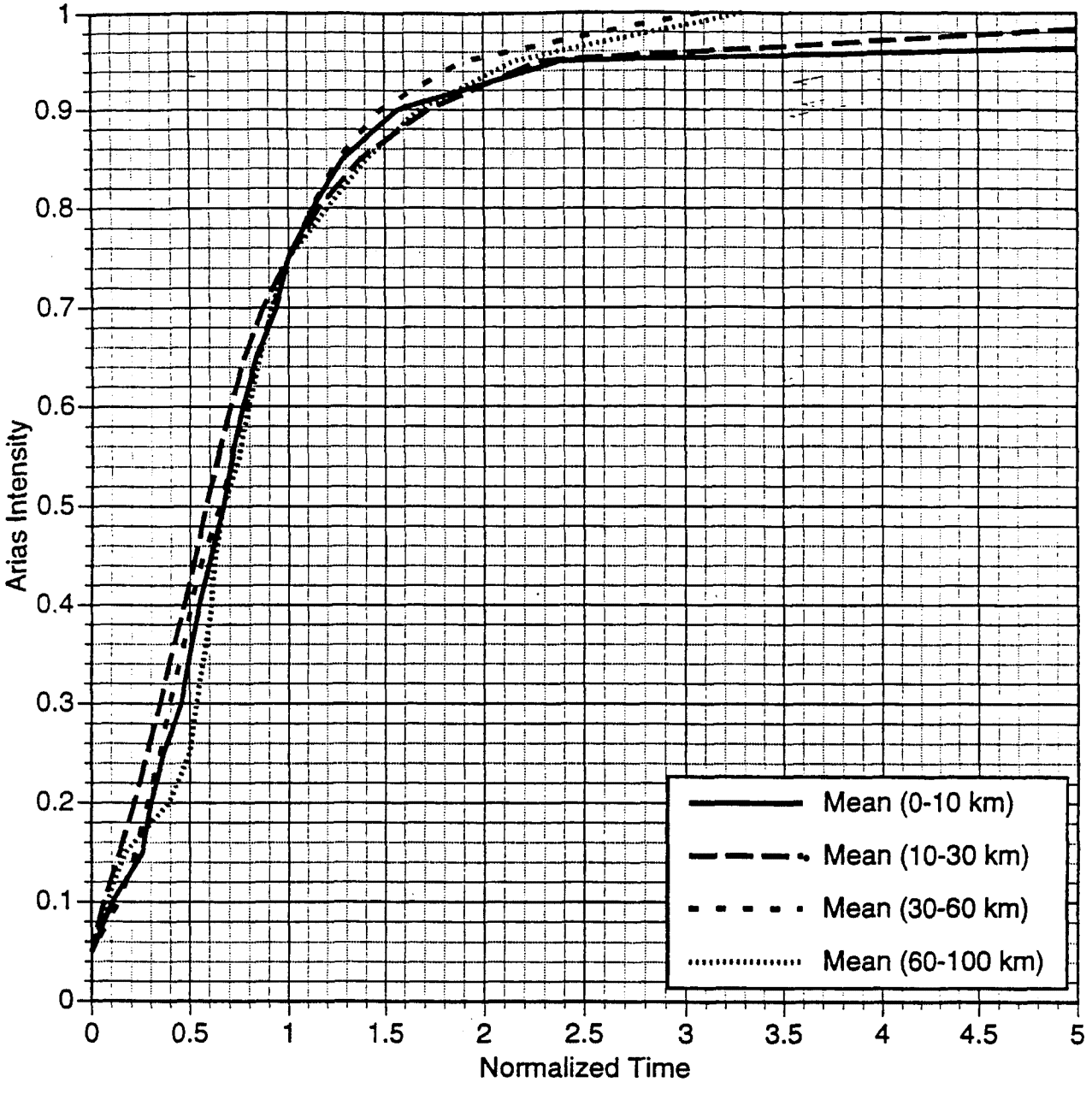

Figure 15b. Mean normalized durations averaged over distance bins for the vertical component for soil site conditions and $5.5 < M < 6.0$.

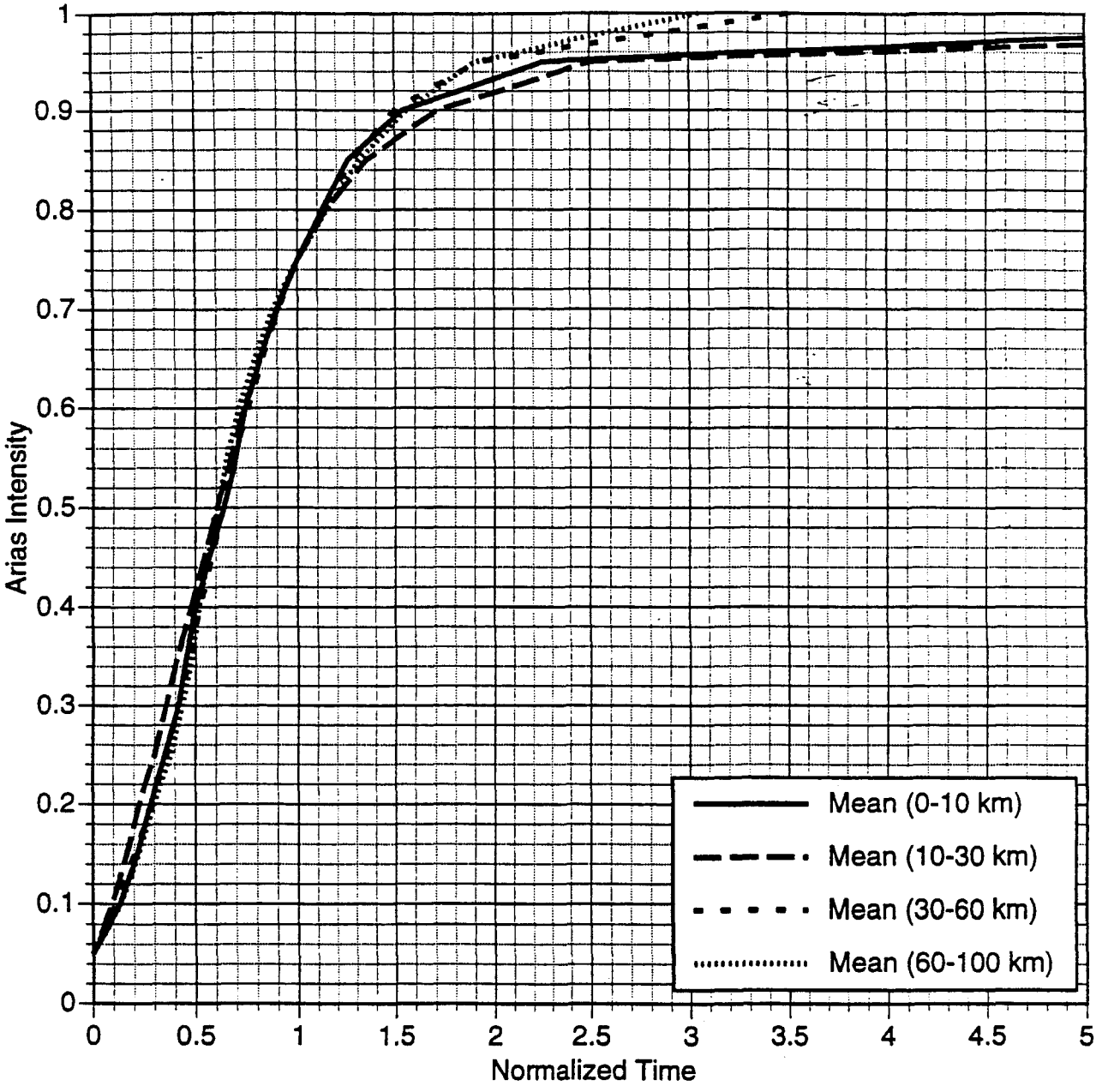

Figure 15c. Mean normalized durations averaged over distance bins for the vertical component for soil site conditions and $6.0 < M < 6.5$.

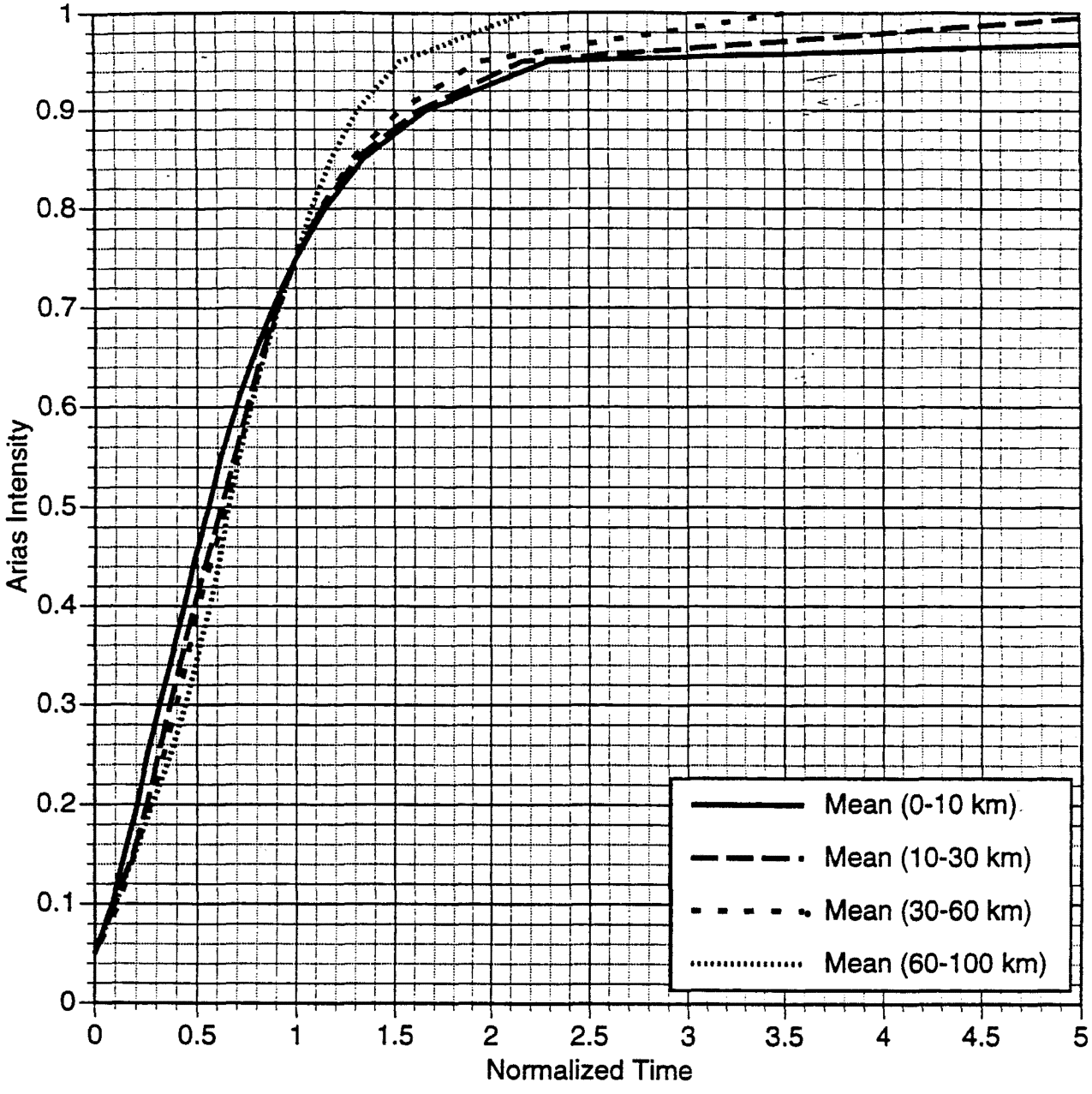

Figure 15d. Mean normalized durations averaged over distance bins for the vertical component for soil site conditions and $6.5 < M < 7.0$.

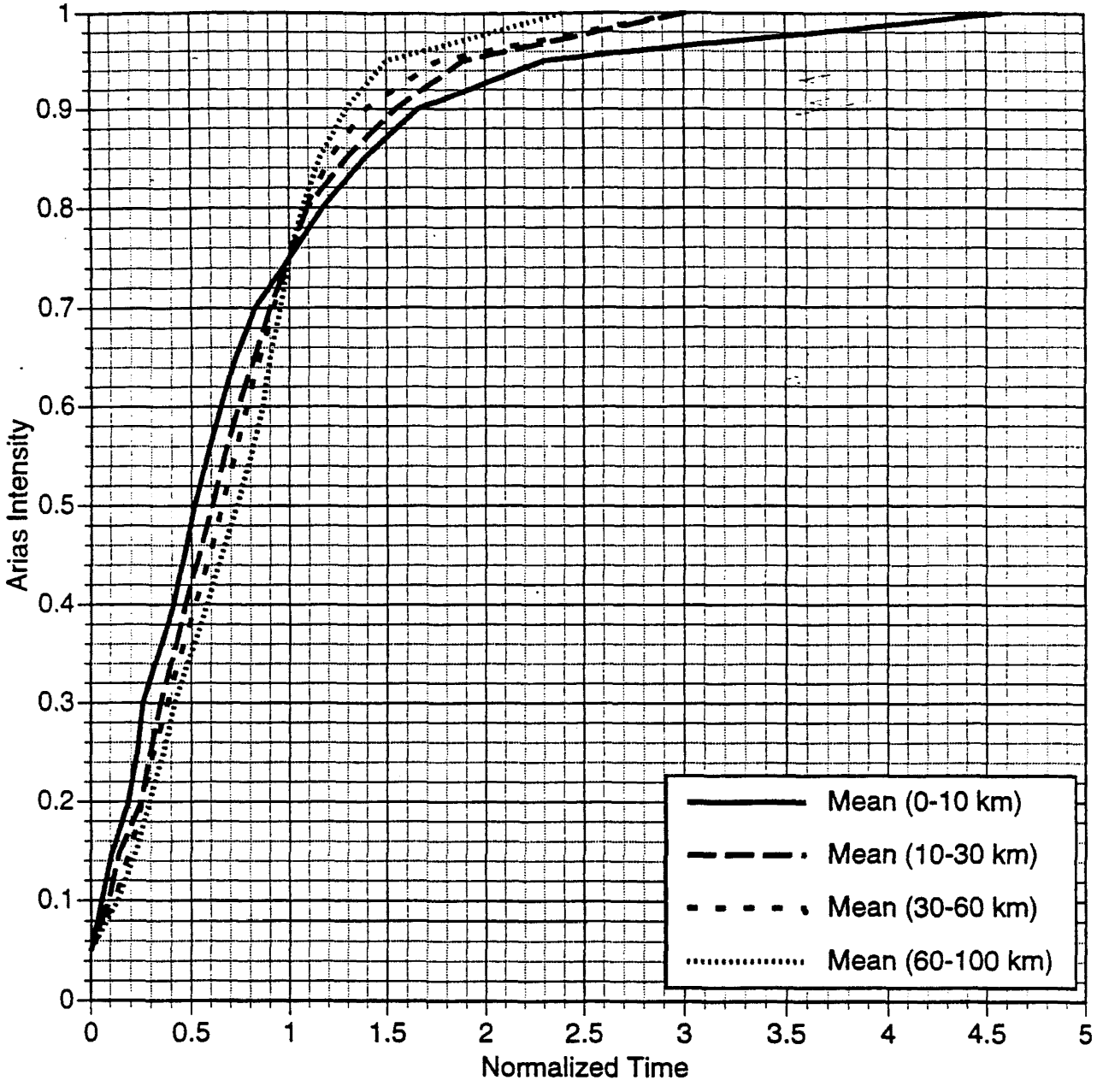

Figure 15e. Mean normalized durations averaged over distance bins for the vertical component for soil site conditions and $7.0 < M < 7.5$.

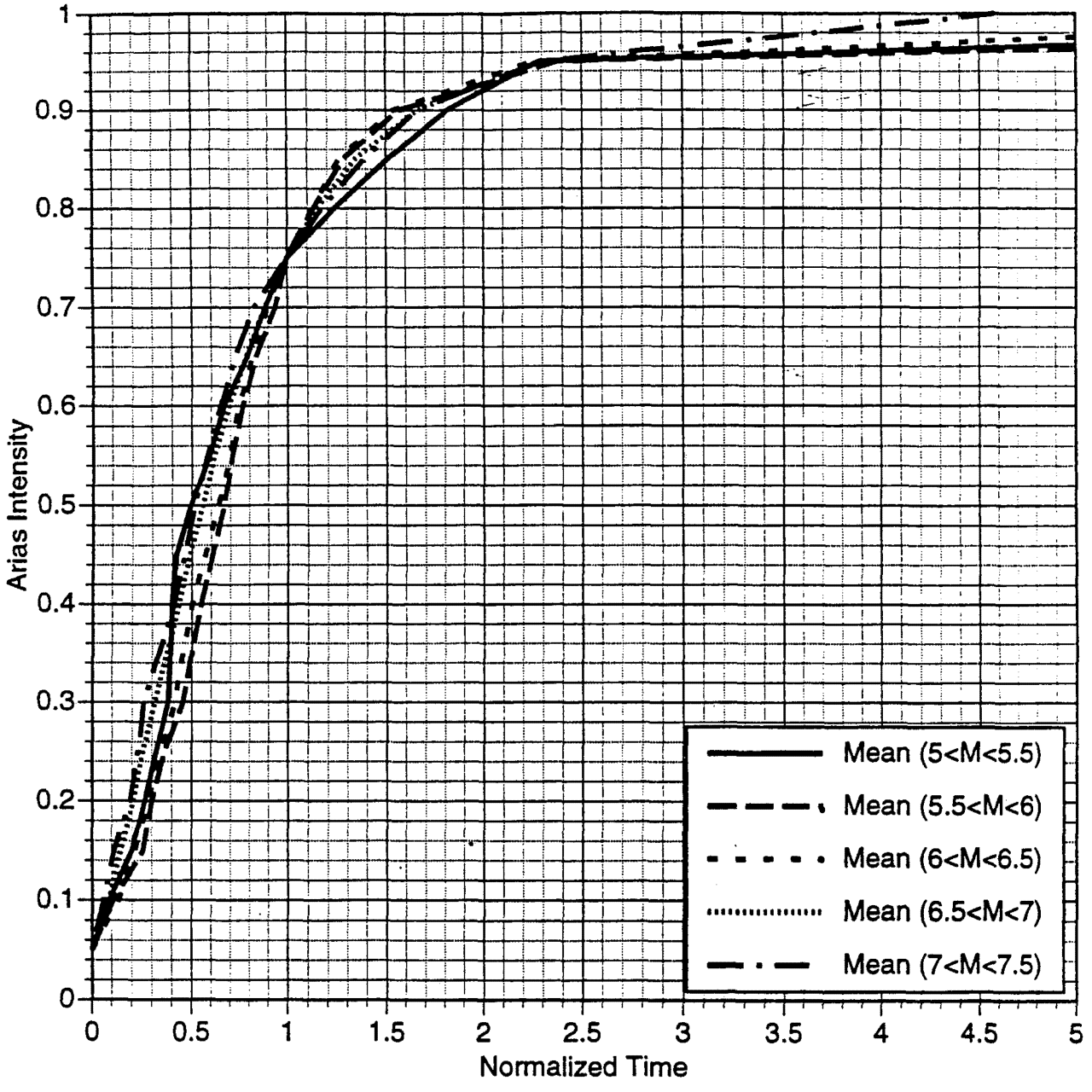

Figure 16a. Mean normalized durations averaged over magnitude bins for the vertical component for soil site conditions and distance = 0-10 km.

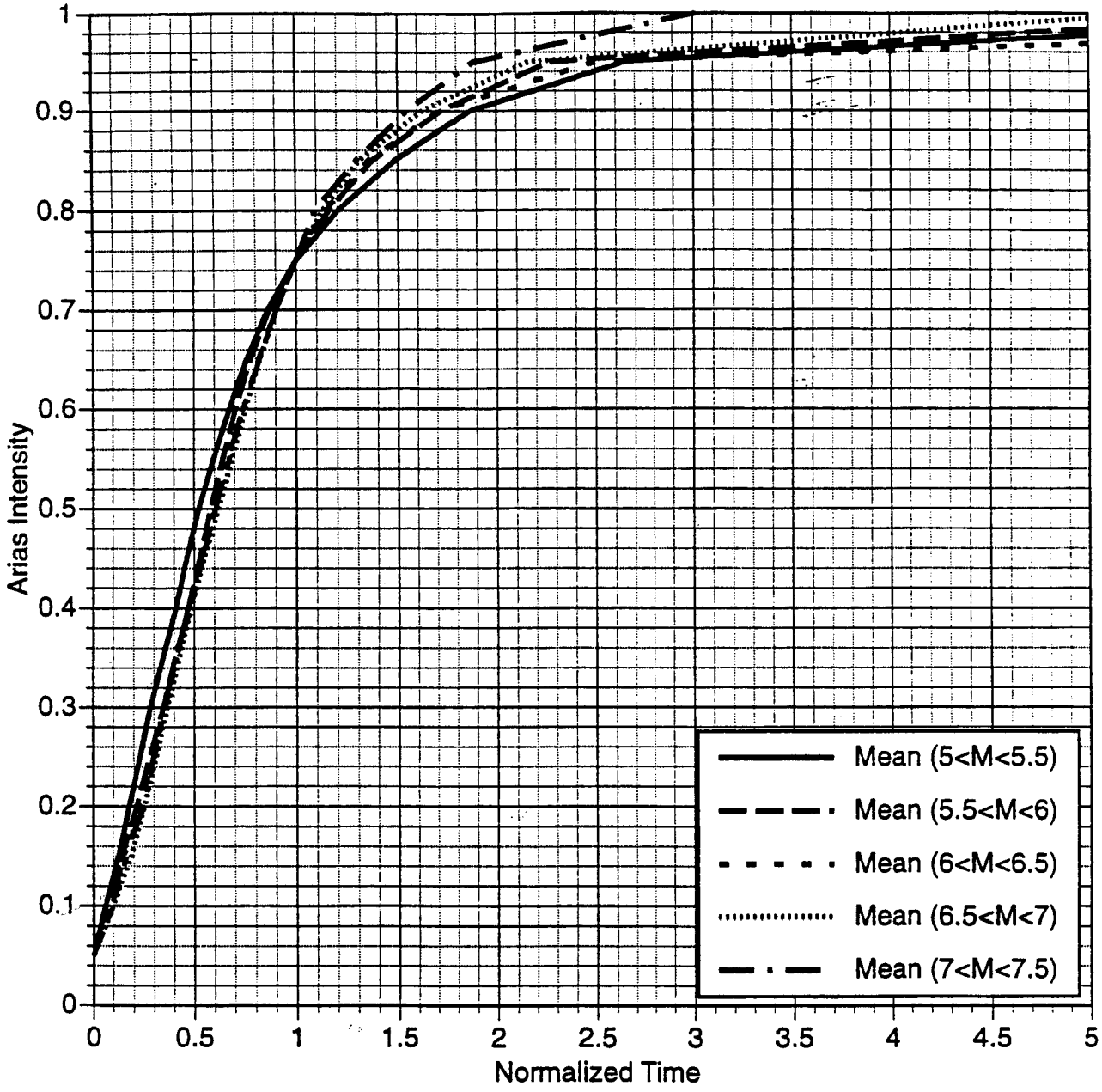

Figure 16b. Mean normalized durations averaged over magnitude bins for the vertical component for soil site conditions and distance = 10-30 km.

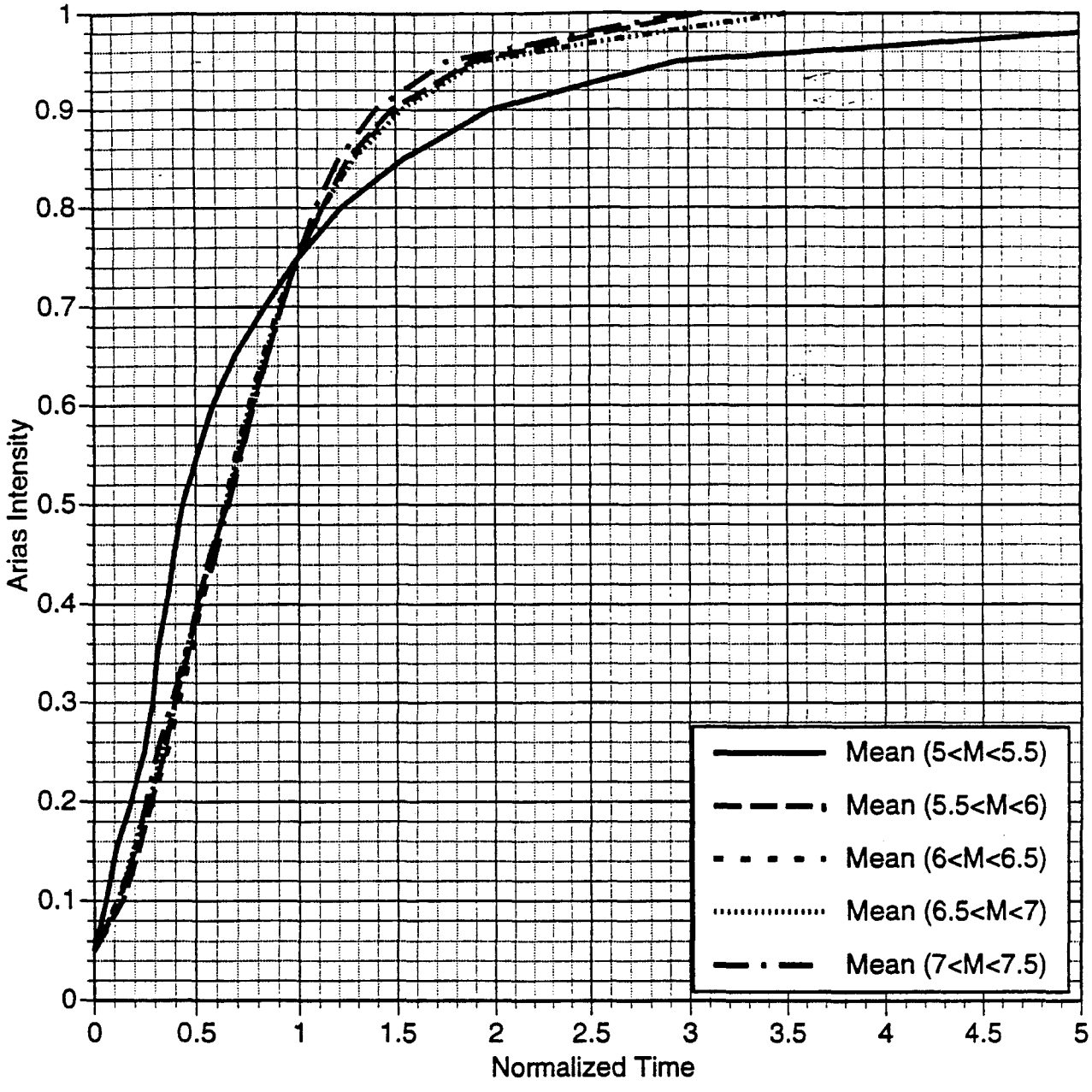

Figure 16c. Mean normalized durations averaged over magnitude bins for the vertical component for soil site conditions and distance = 30-60 km.

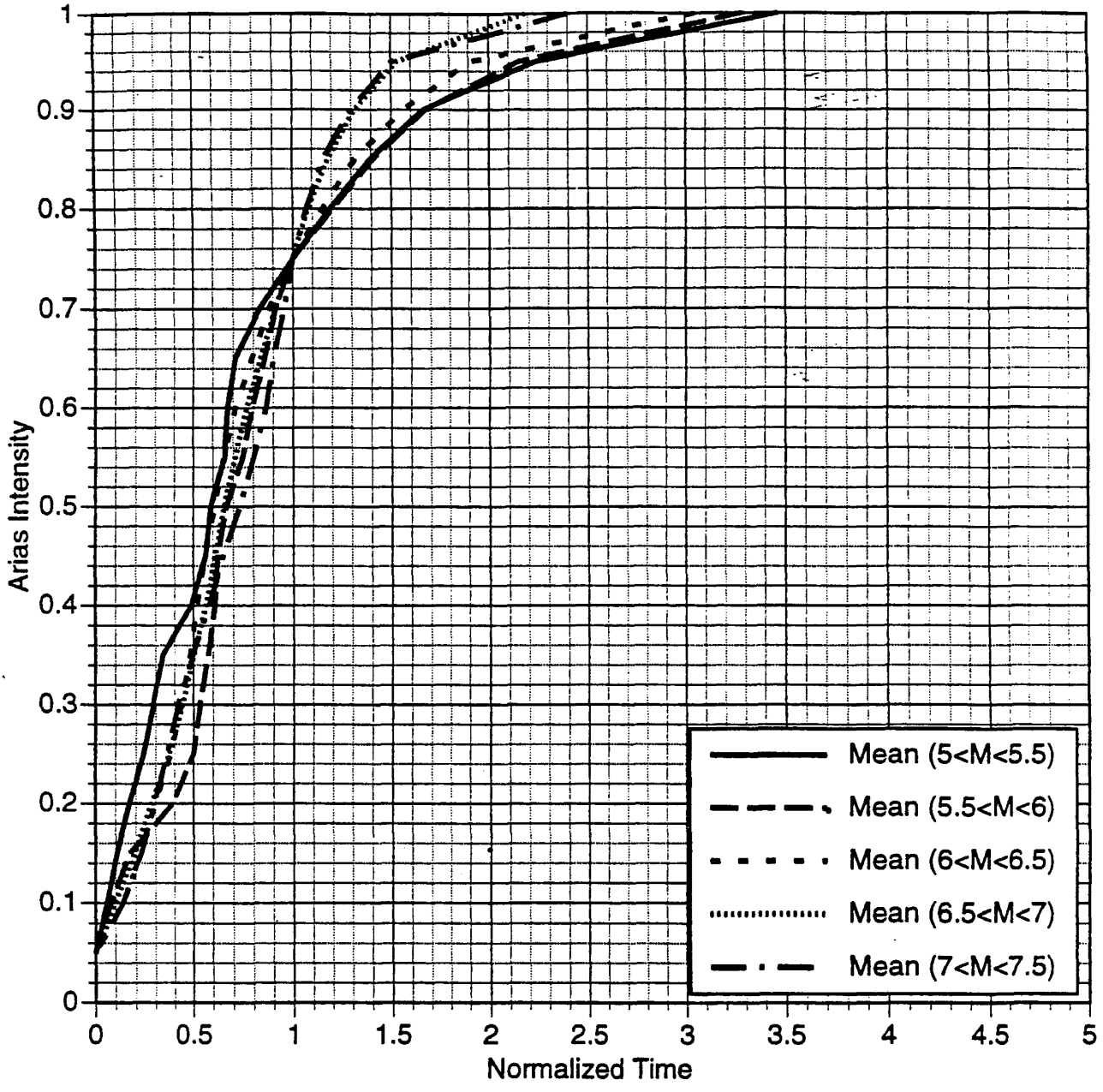

Figure 16d. Mean normalized durations averaged over magnitude bins for the vertical component for soil site conditions and distance = 60-100 km.

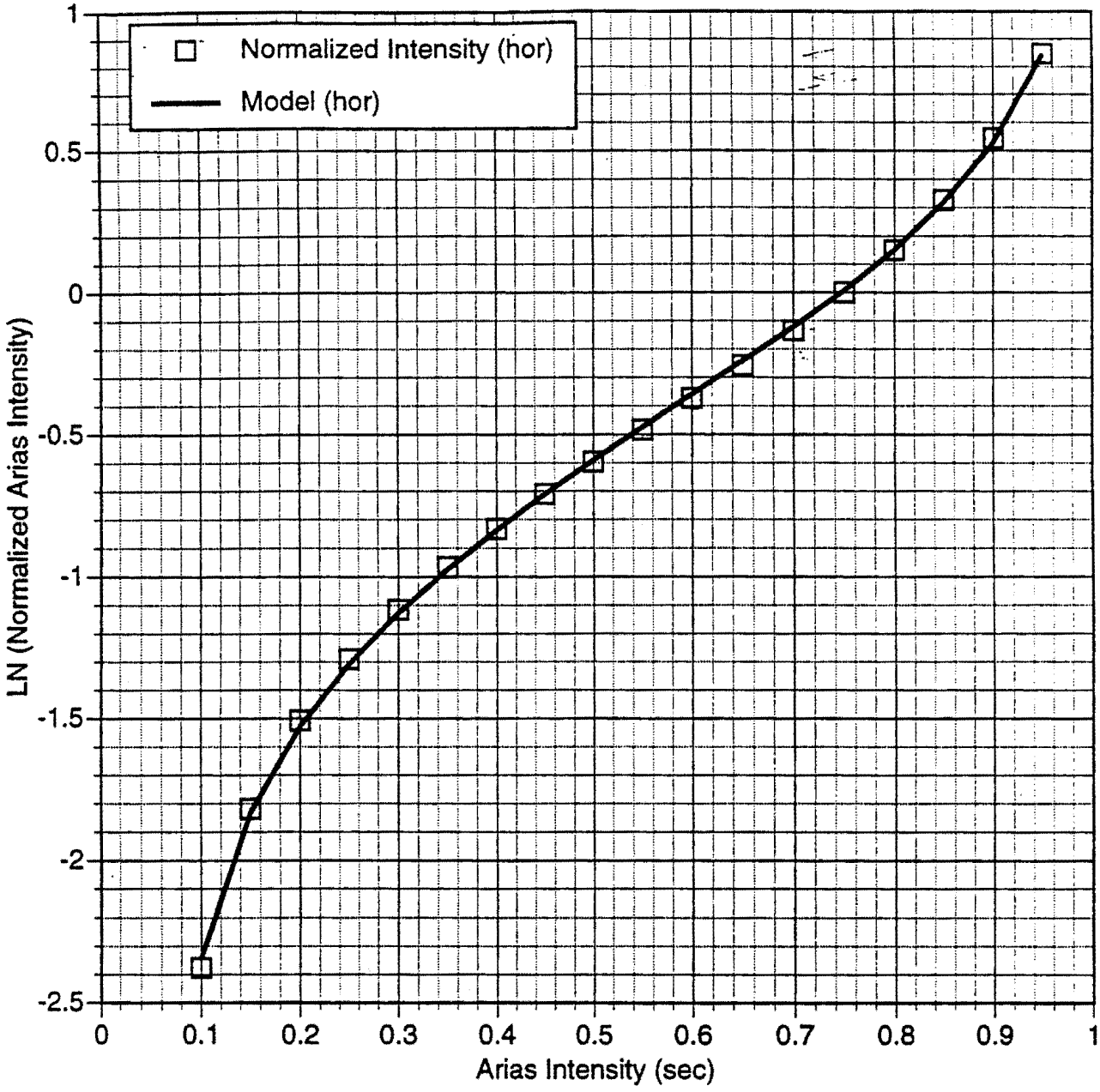

Figure 17a. Mean predicted model (Eq. 11) compared to the mean of the data for the horizontal component.

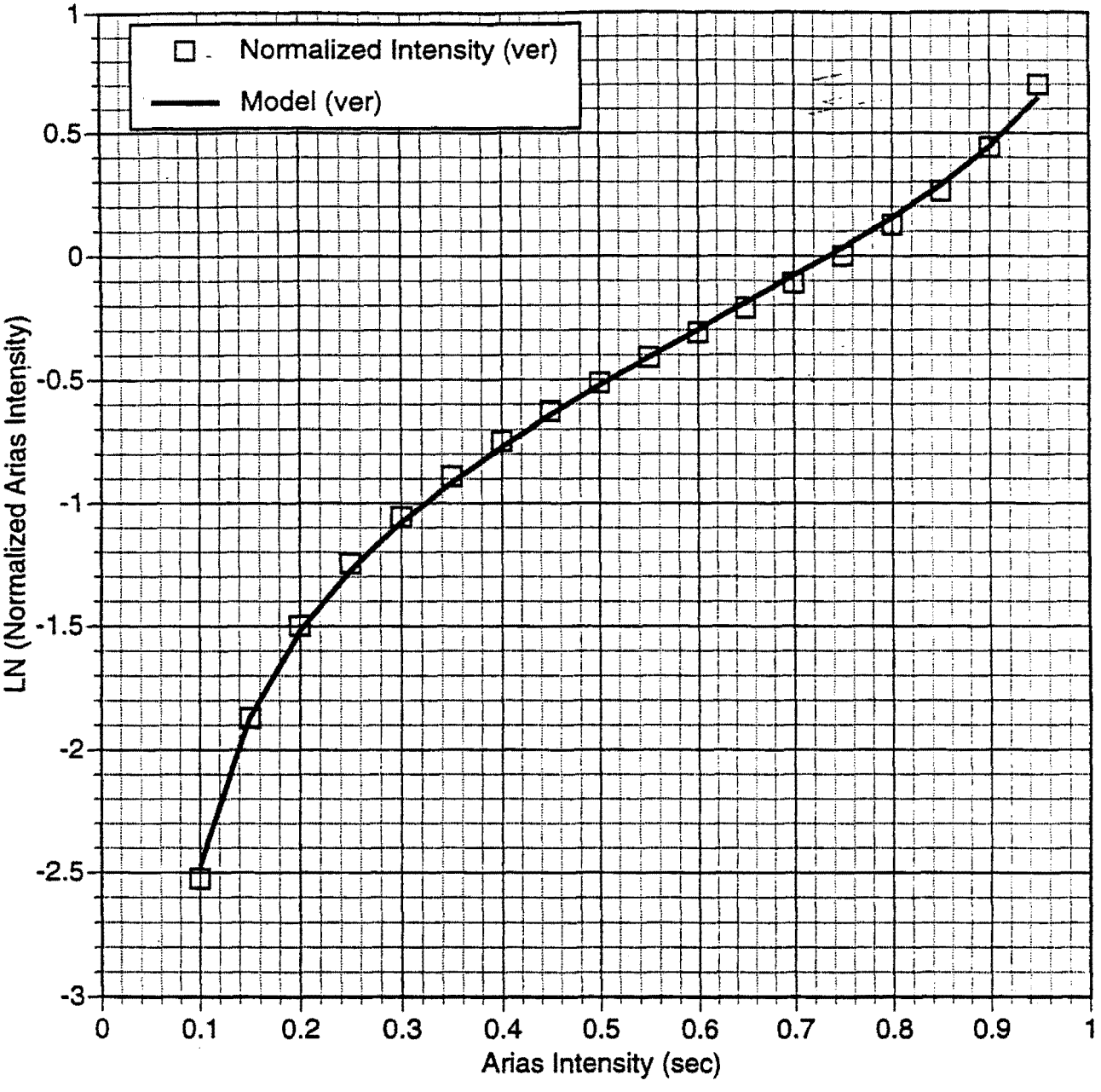

Figure 17b. Mean predicted model (Eq. 11) compared to the mean of the data for the vertical component.

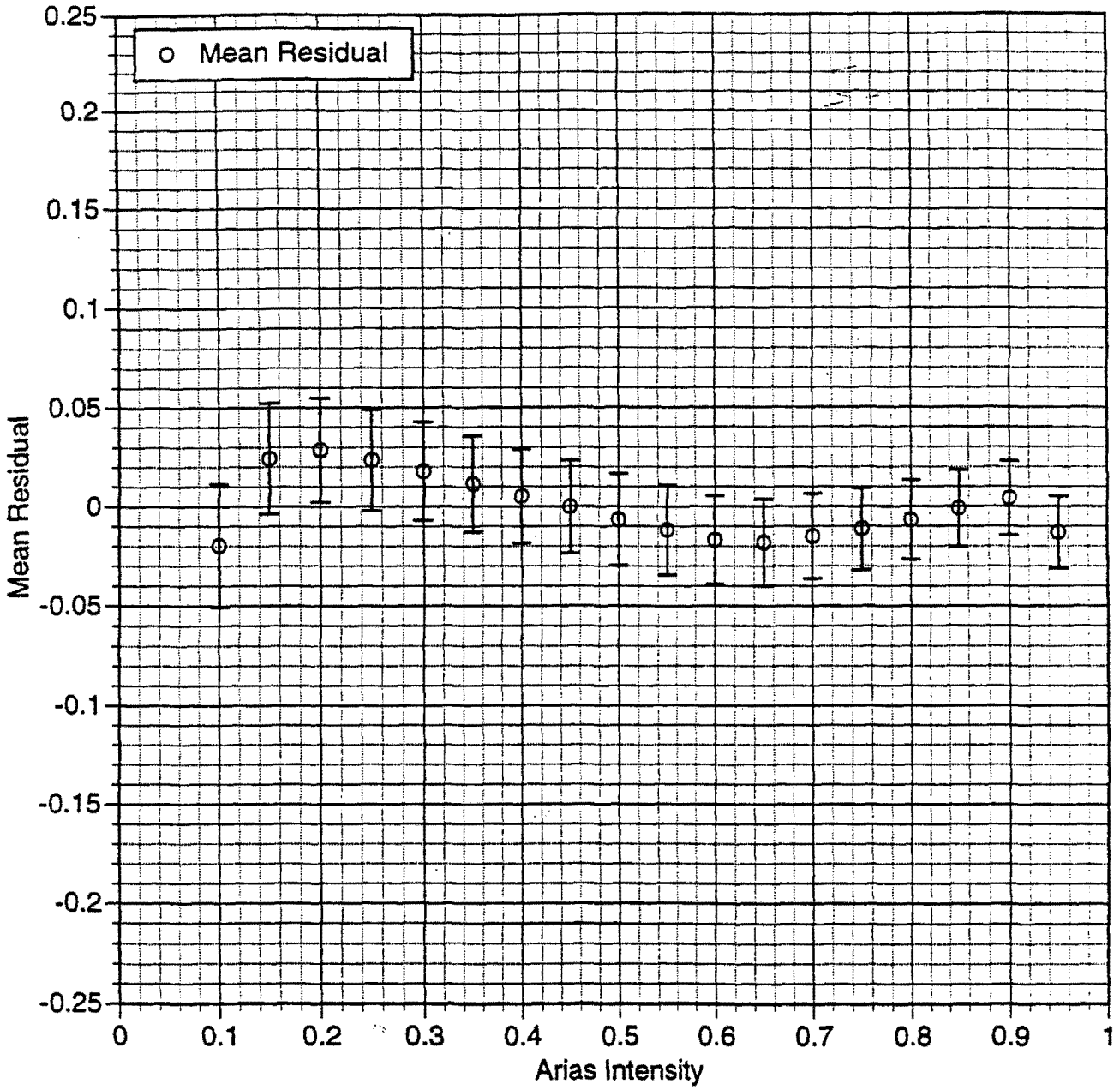

Figure 18a. Mean residuals and standard errors of the mean for the horizontal duration model (Eq 12).

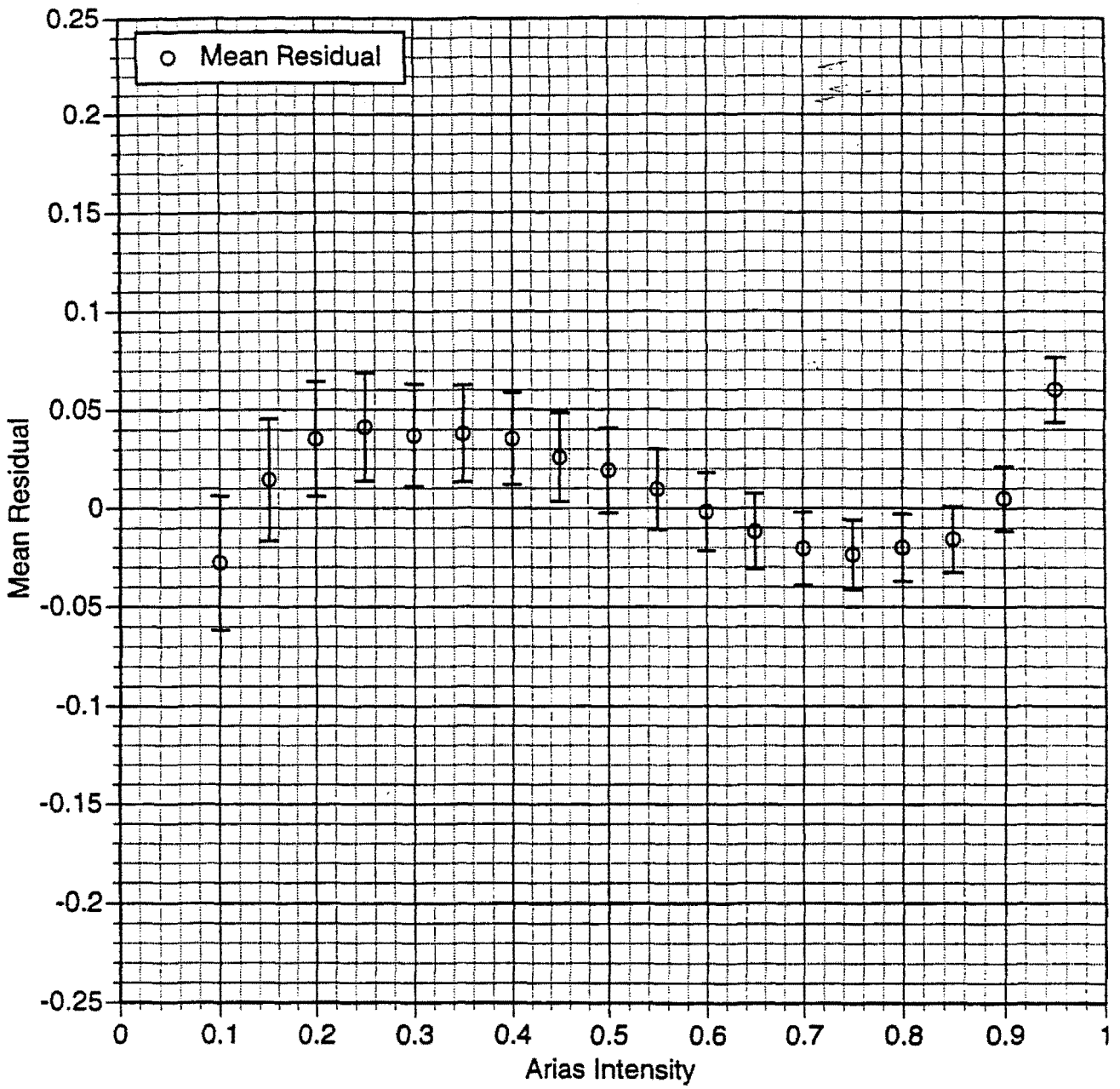

Figure 18b. Mean residuals and standard errors of the mean for the vertical duration model (Eq 12).

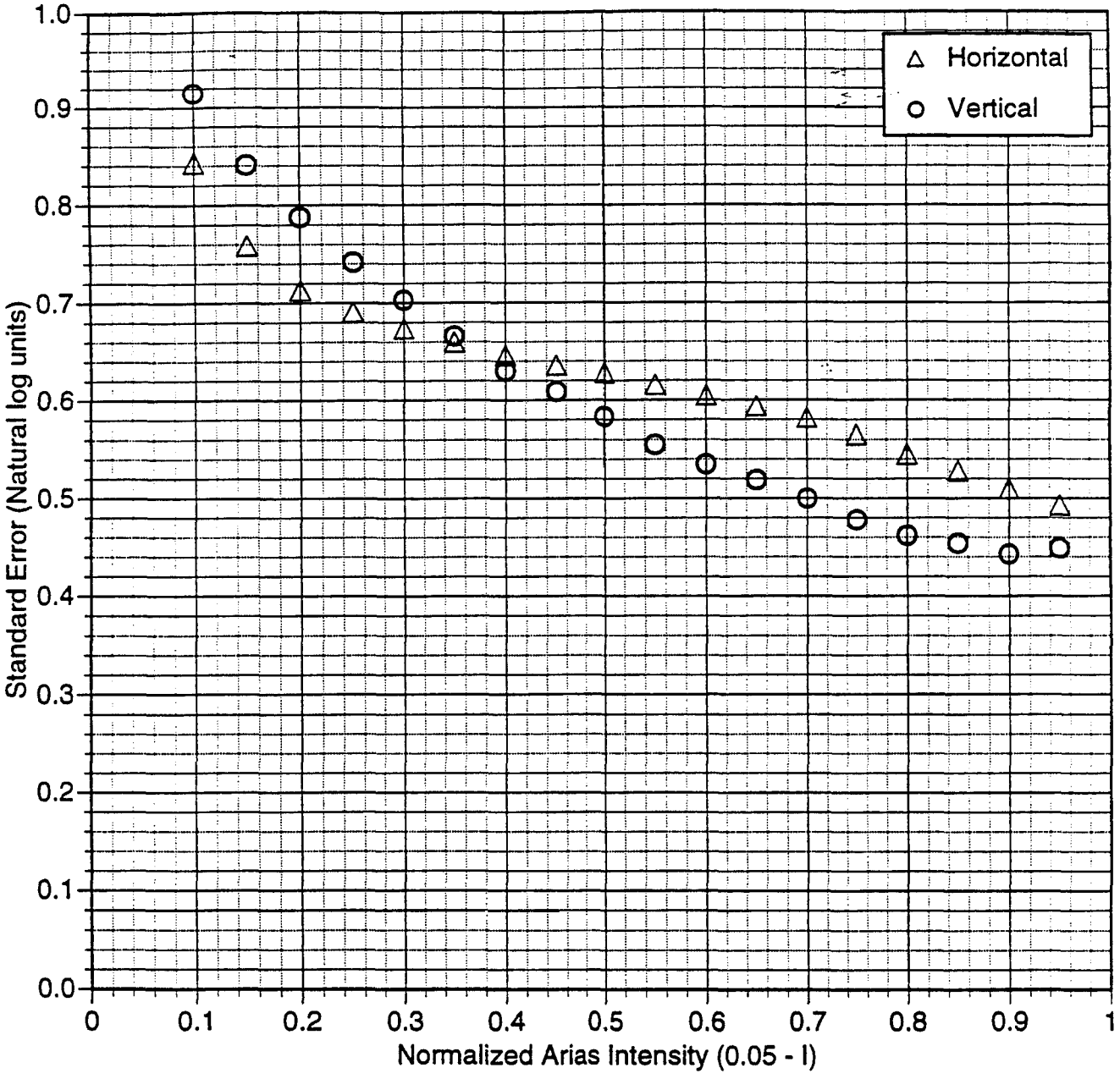

Figure 19. Standard errors for the horizontal and vertical duration models.

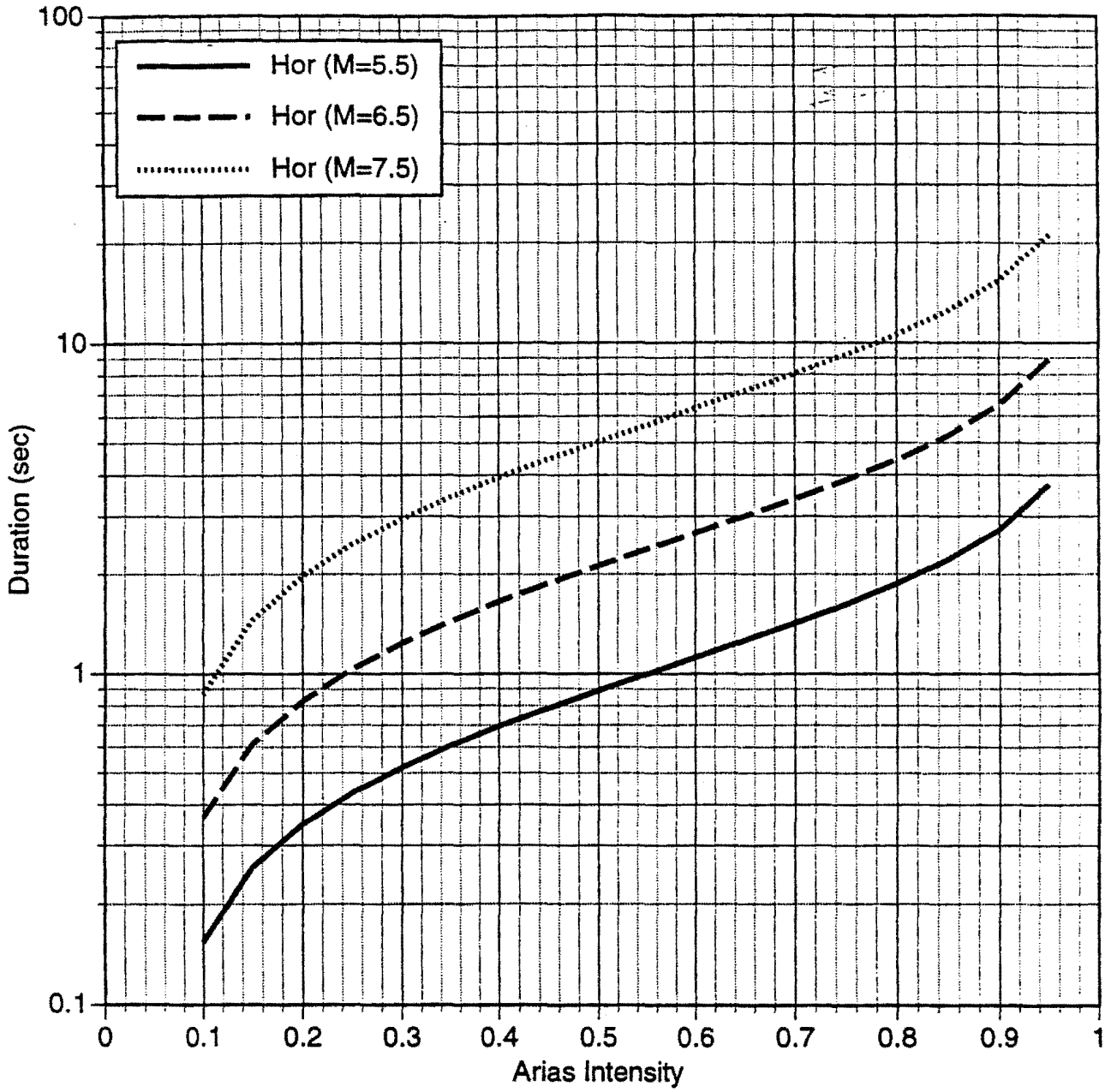

Figure 20a. Duration model for horizontal component for rock site conditions and distance of 1 km.

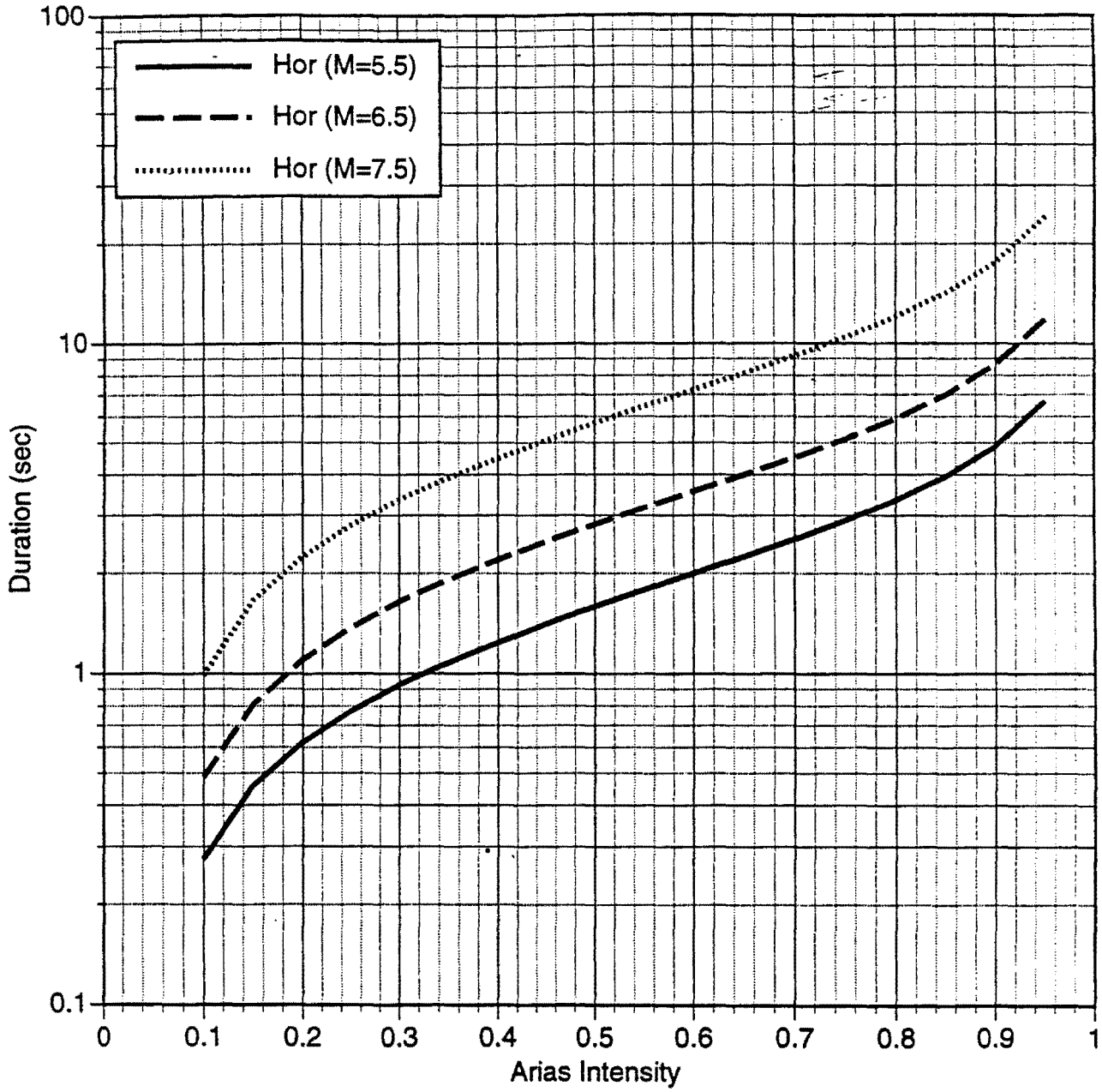

Figure 20b. Duration model for horizontal component for rock site conditions and distance of 30 km.

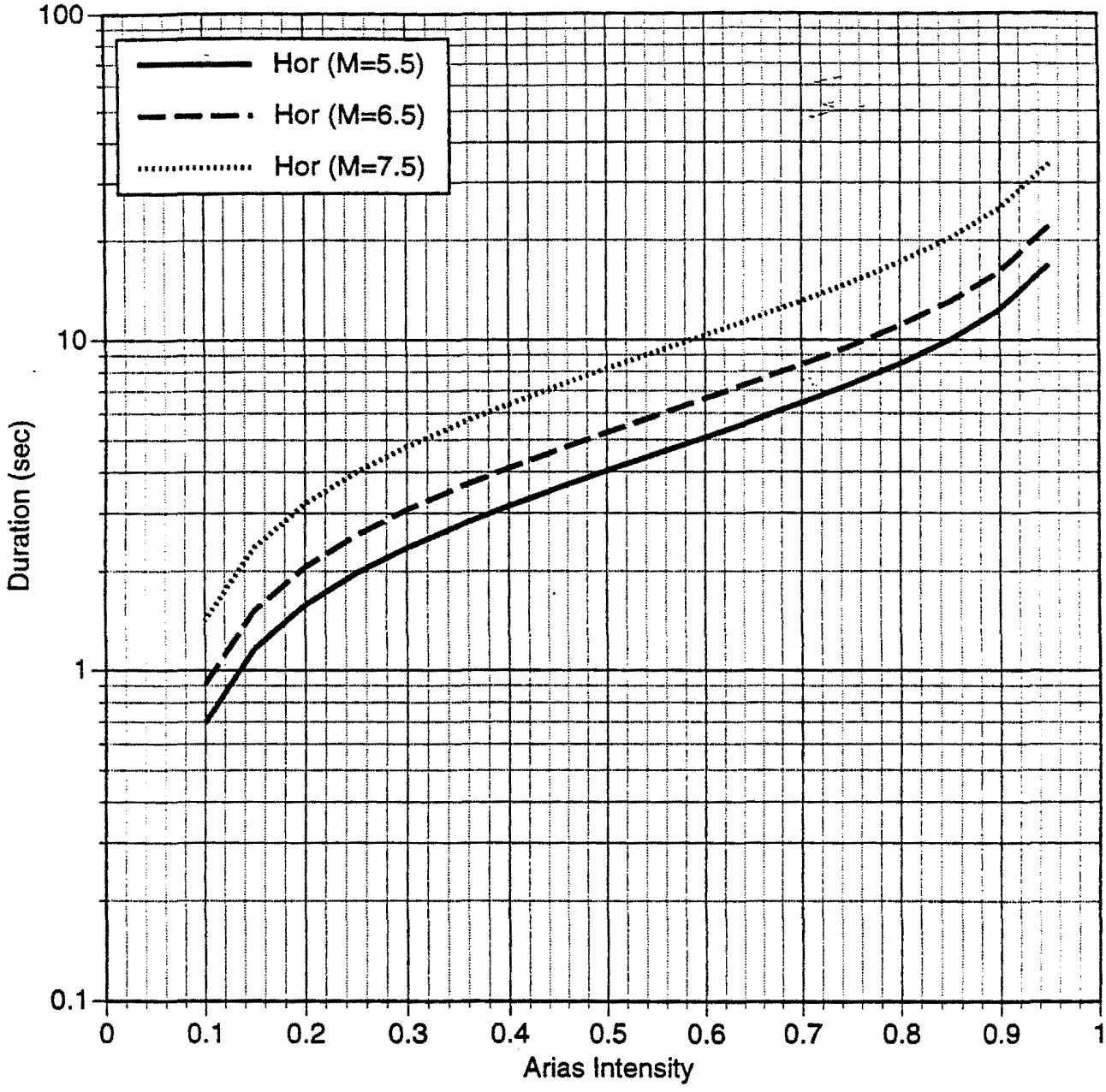

Figure 20c. Duration model for horizontal component for rock site conditions and distance of 100 km.

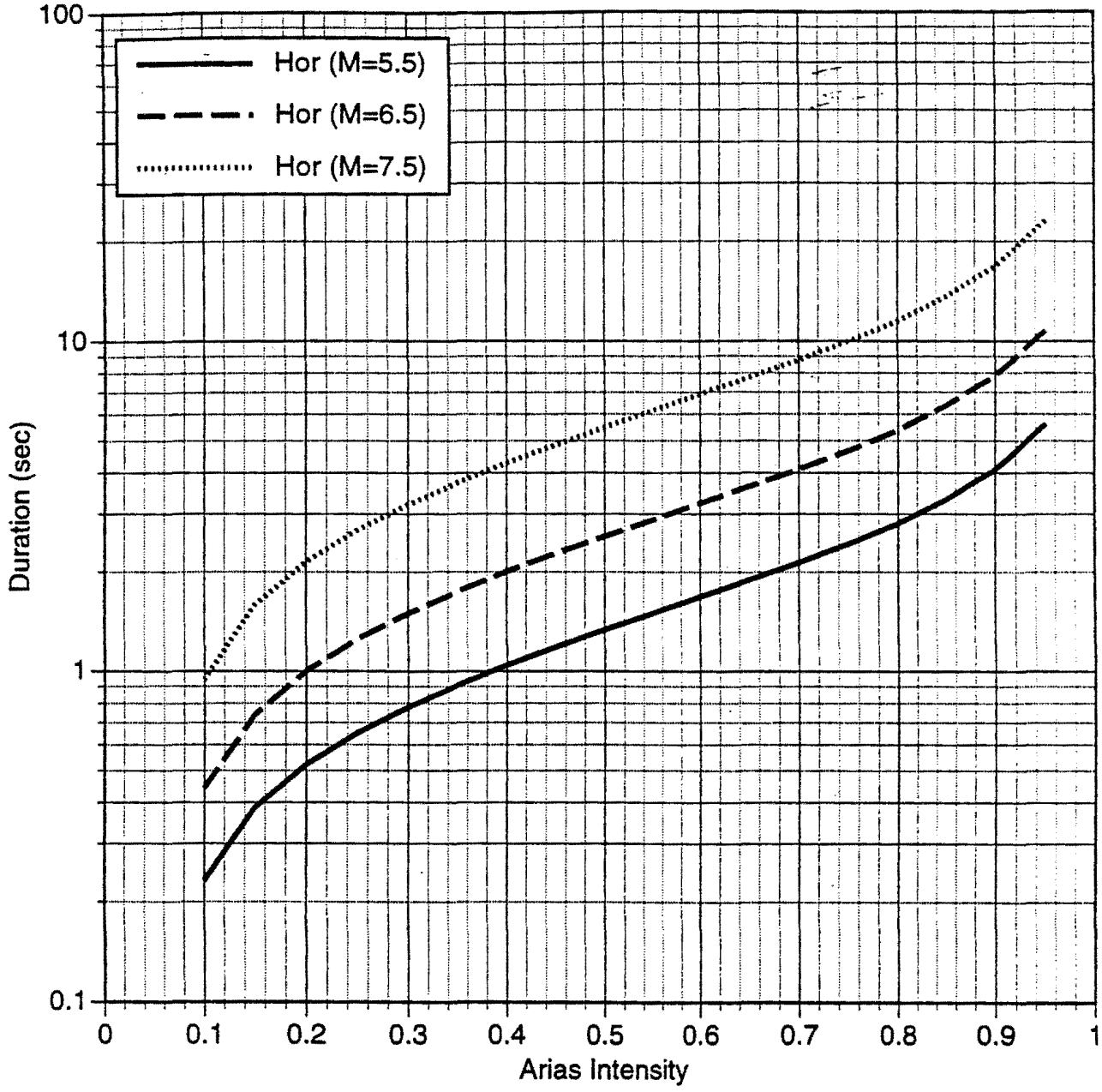

Figure 21a. Duration model for horizontal component for soil site conditions and distance of 1 km.

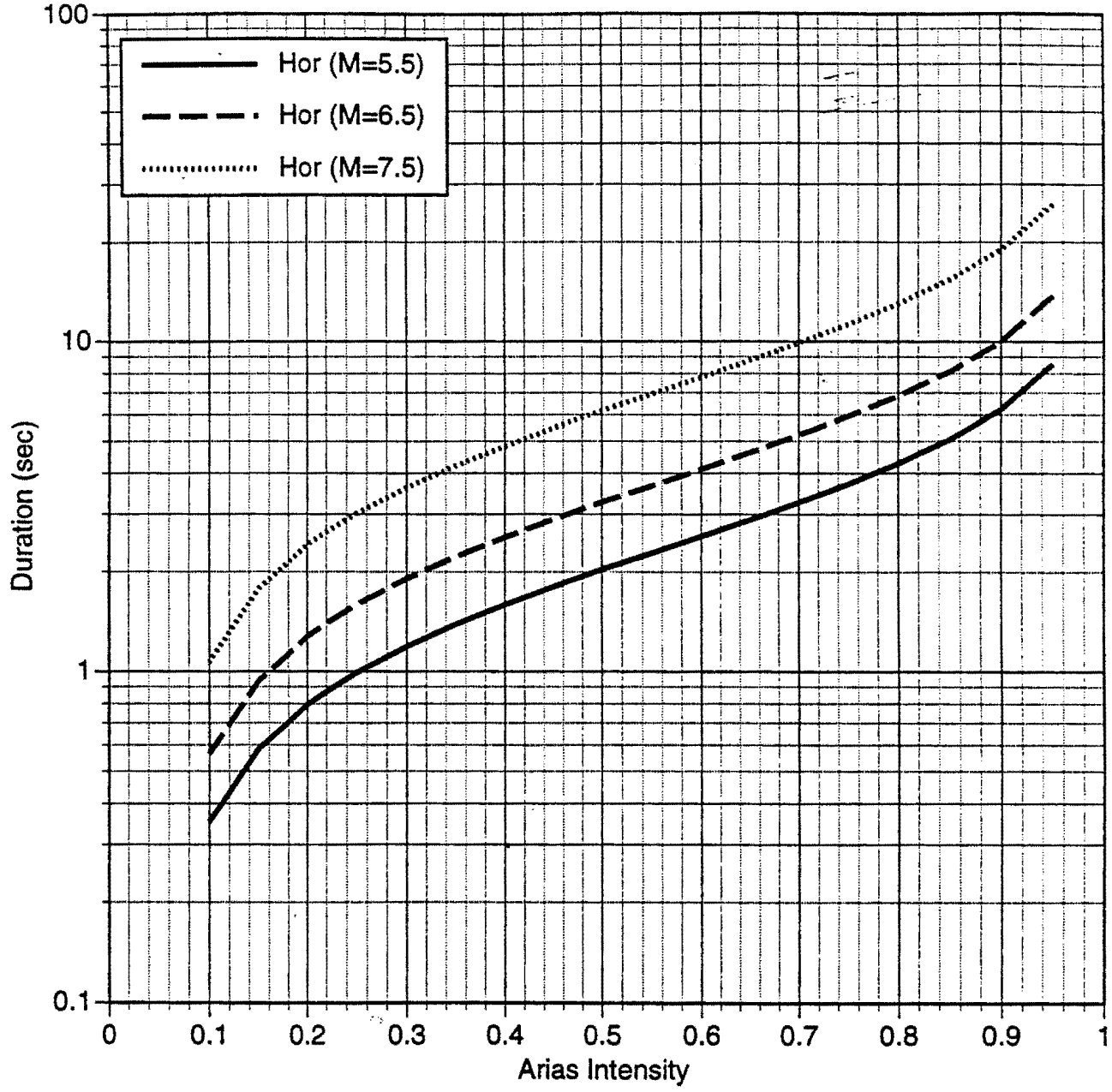

Figure 21b. Duration model for horizontal component for soil site conditions and distance of 30 km.

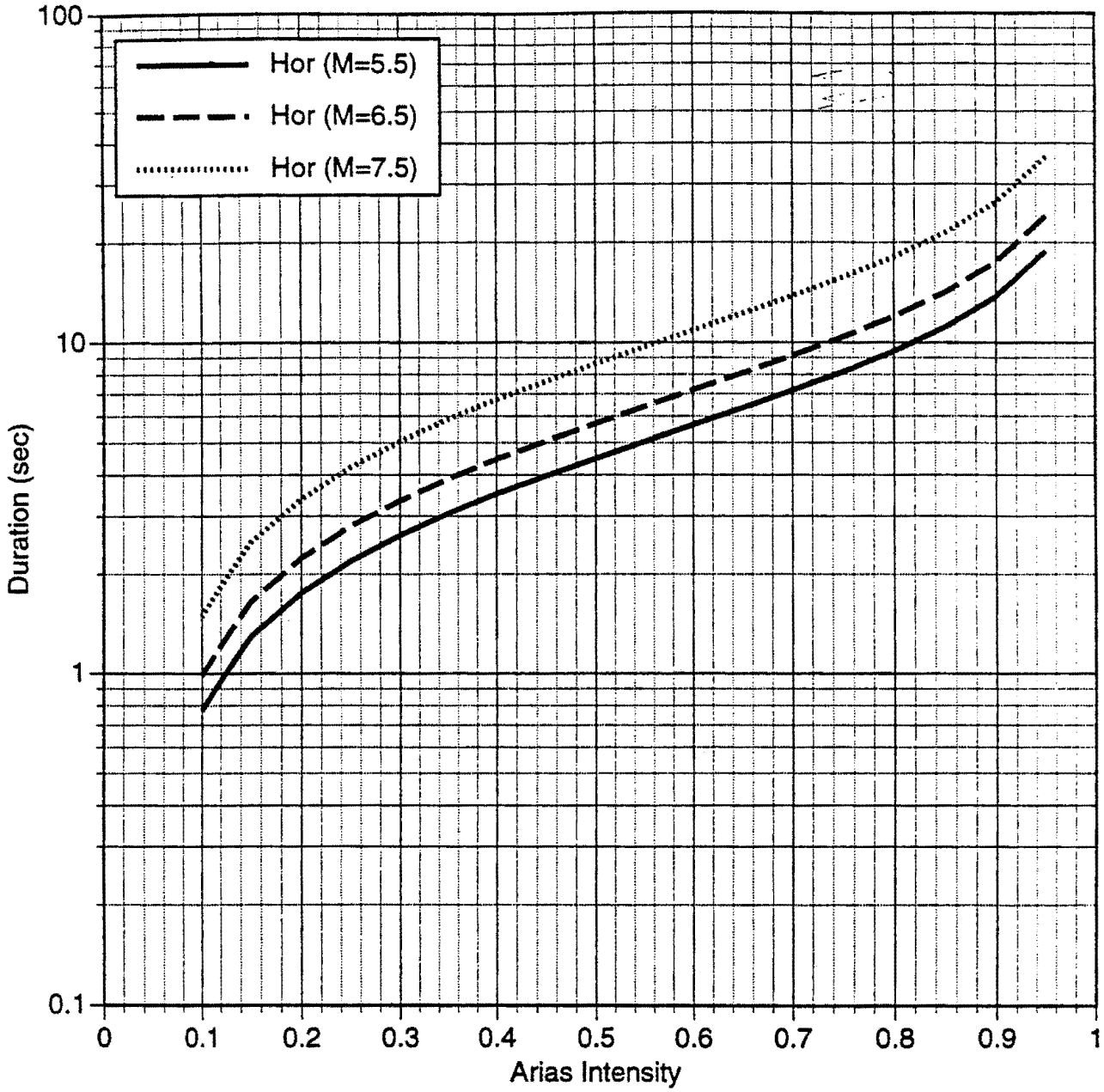

Figure 21c. Duration model for horizontal component for soil site conditions and distance of 100 km.

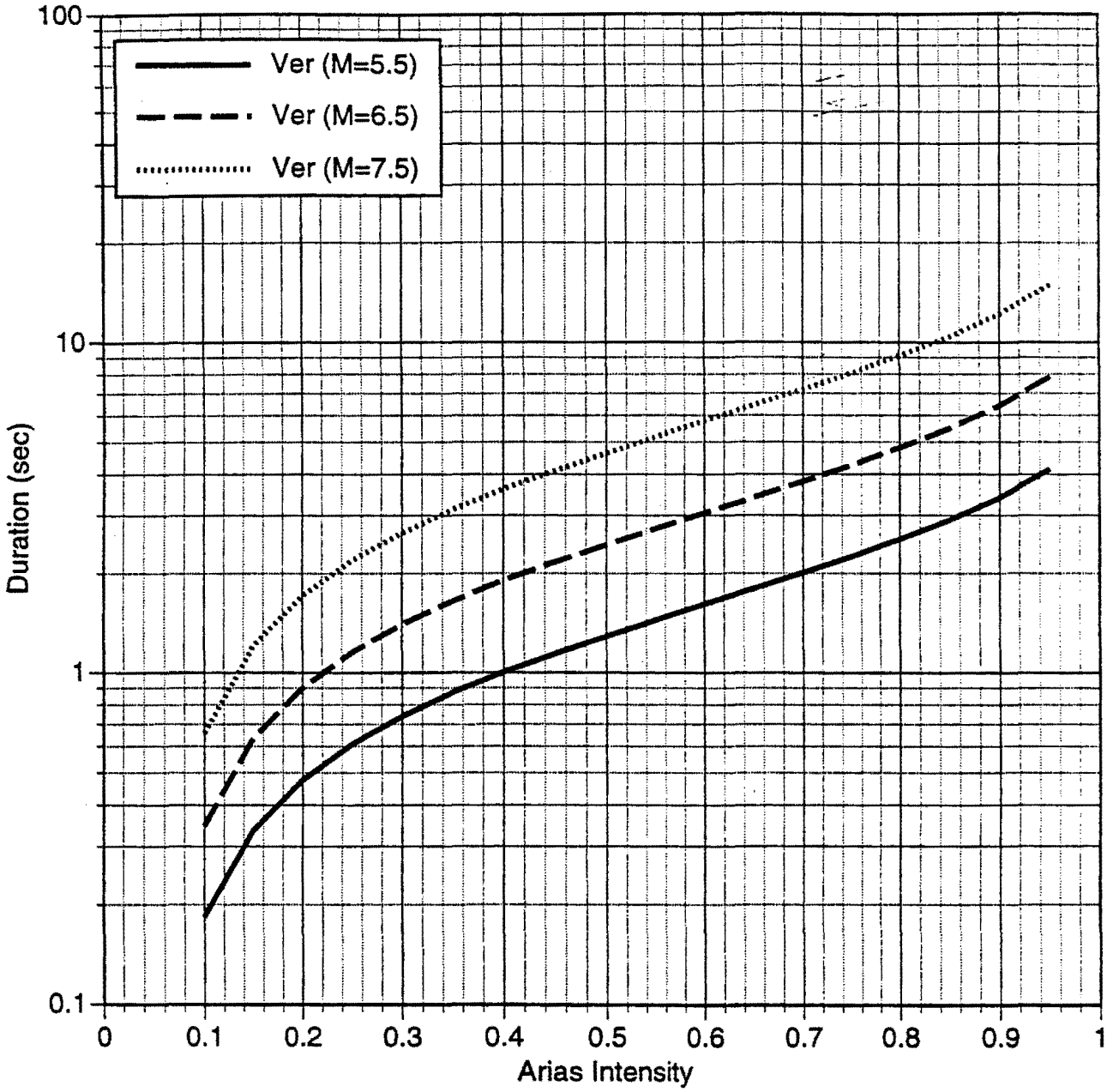

Figure 22a. Duration model for vertical component for rock site conditions and distance of 1 km.

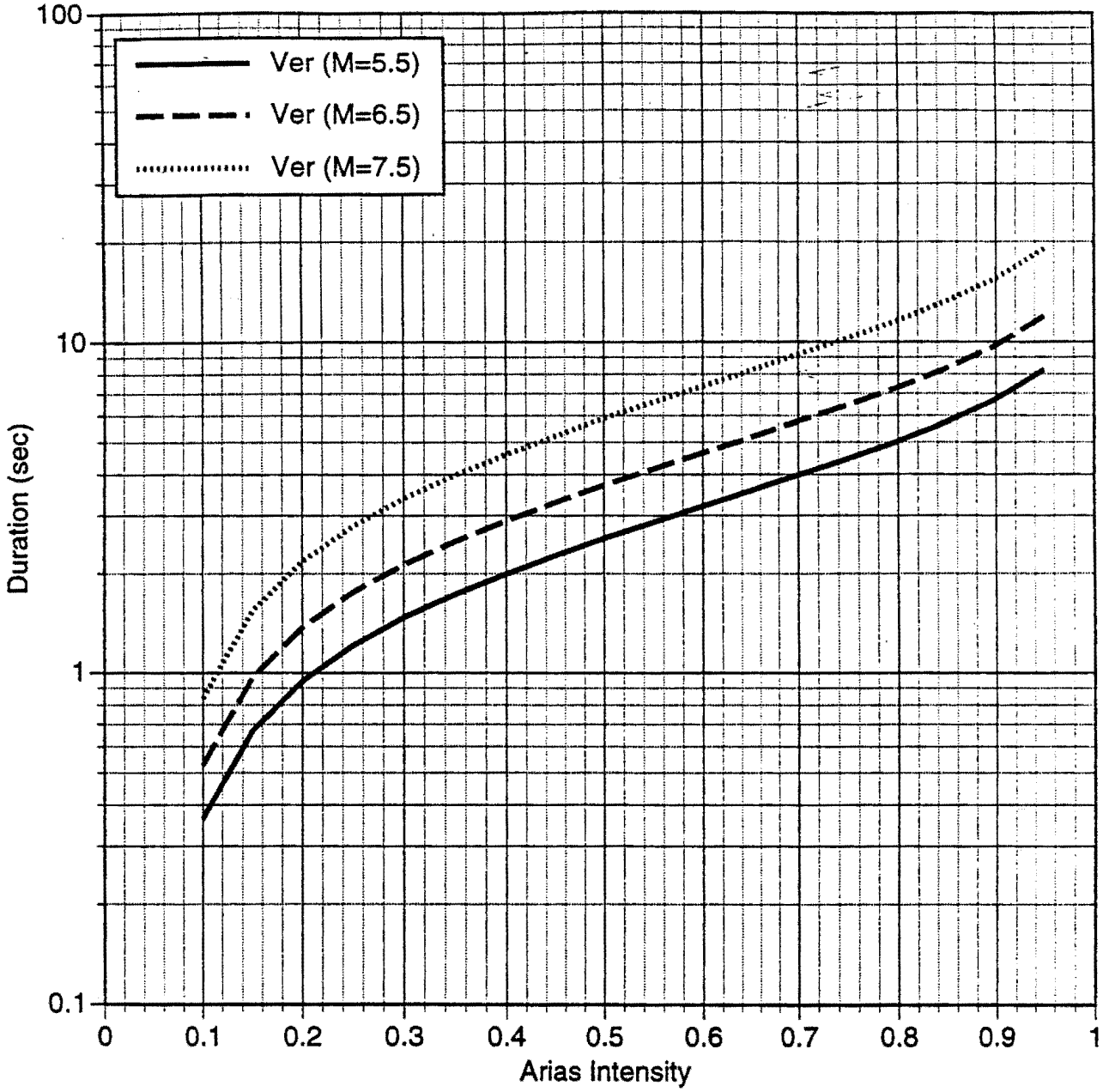

Figure 22b. Duration model for vertical component for rock site conditions and distance of 30 km.

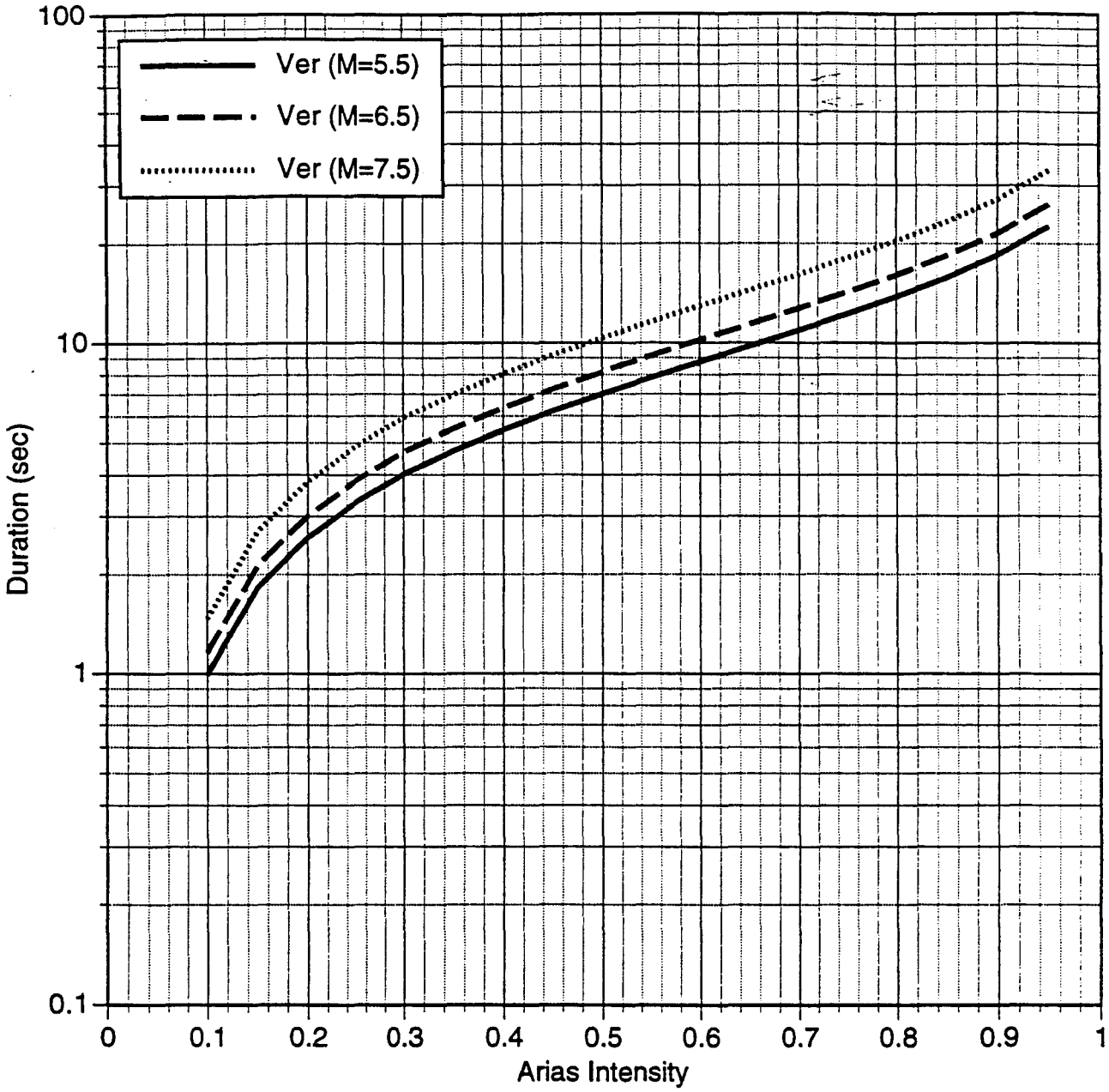

Figure 22c. Duration model for vertical component for rock site conditions and distance of 100 km.

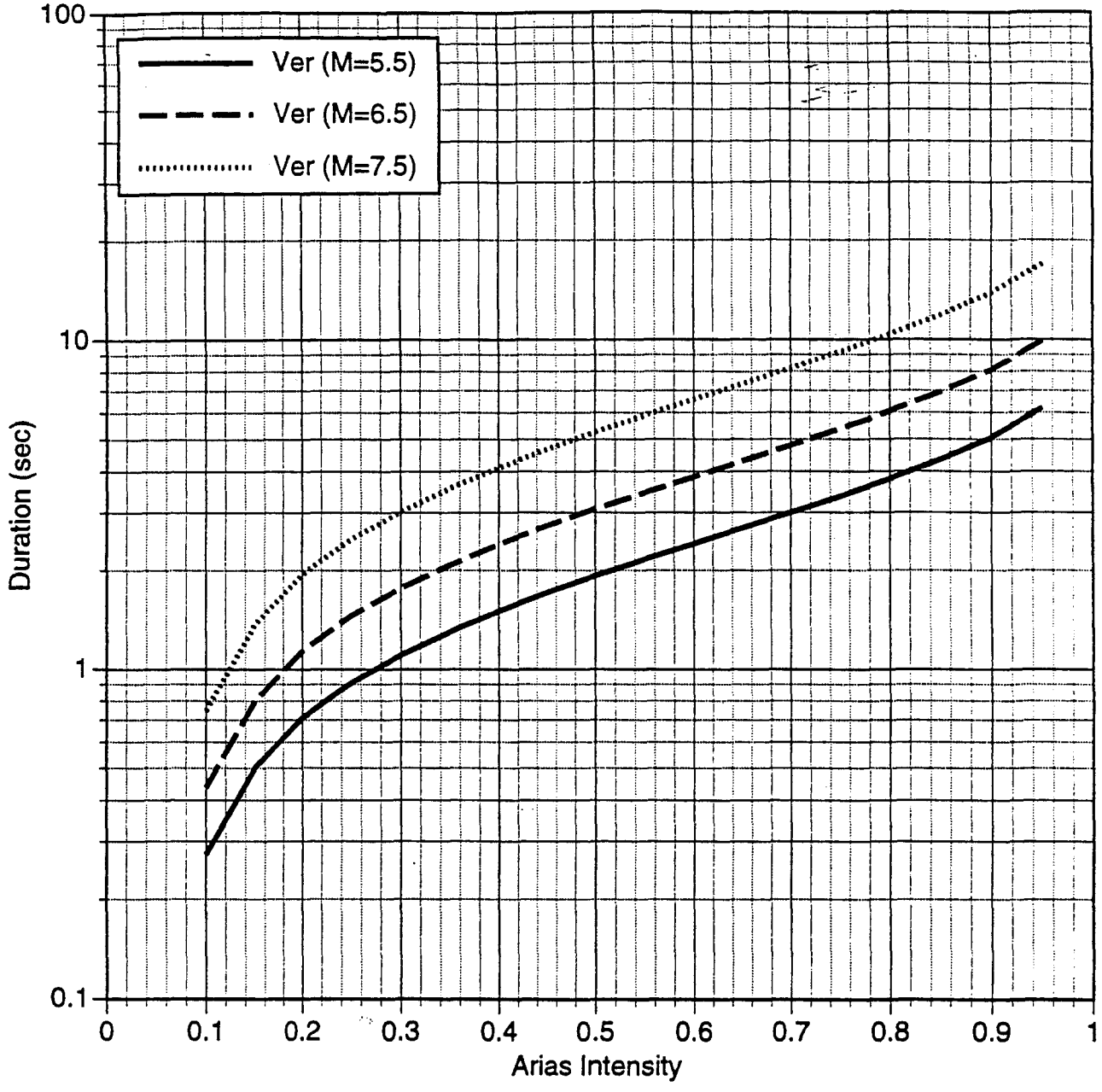

Figure 23a. Duration model for vertical component for soil site conditions and distance of 1 km.

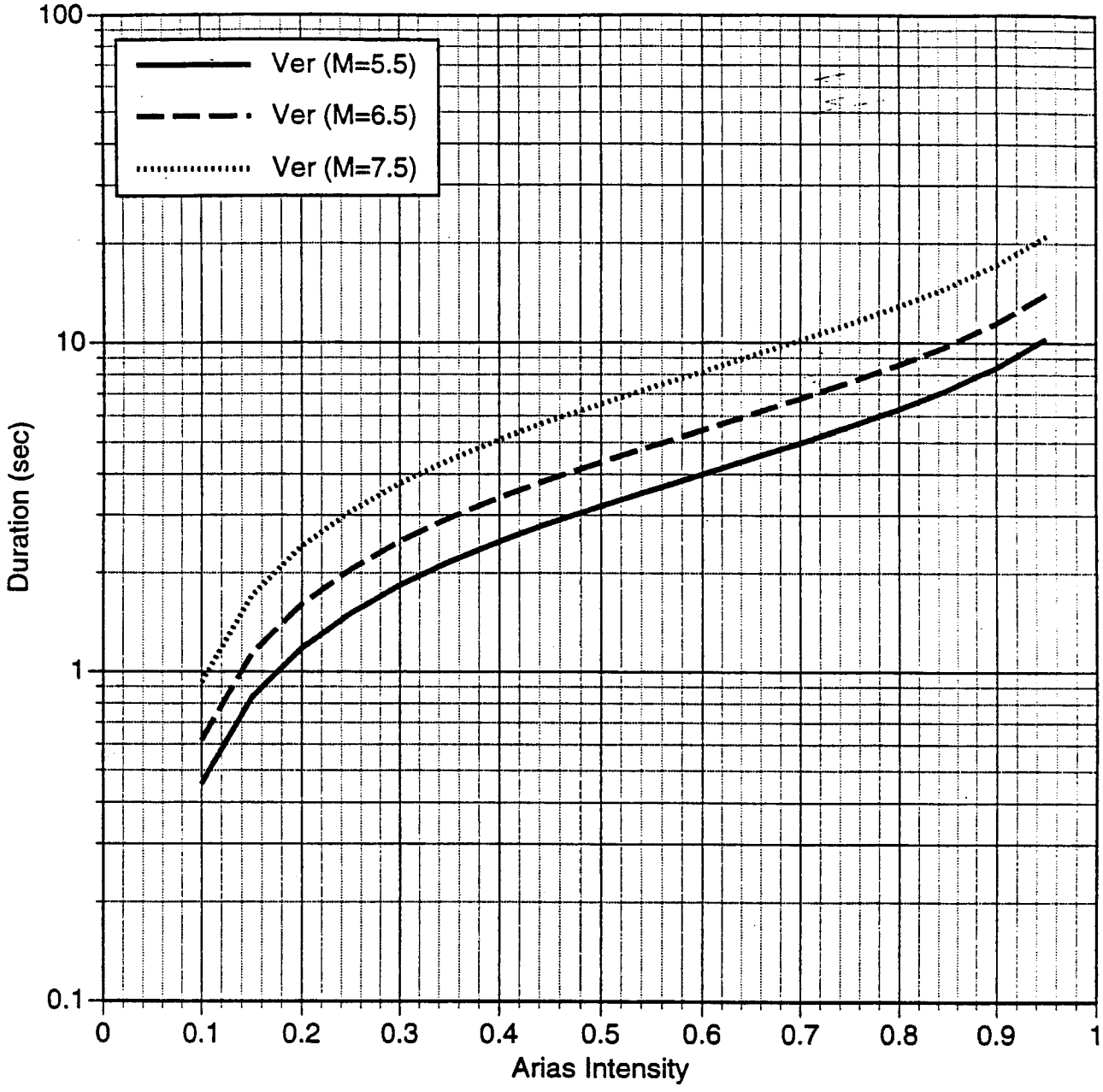

Figure 23b. Duration model for vertical component for soil site conditions and distance of 30 km.

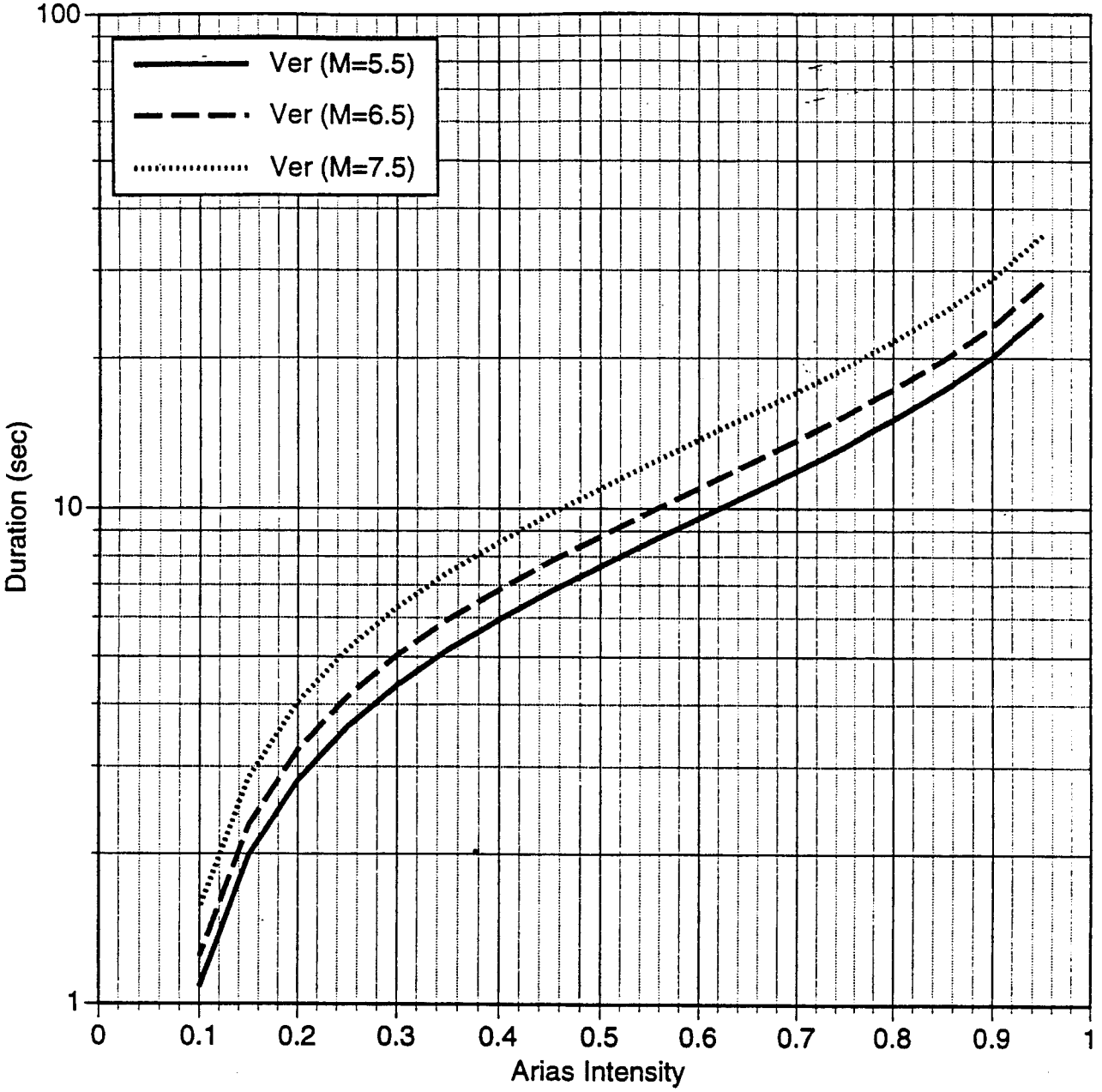

Figure 23c. Duration model for vertical component for soil site conditions and distance of 100 km.

References

Abrahamson, N. A. and R. R. Youngs (1992). A stable algorithm for regression analyses using the random effects model, Bull. Seism. Soc. Am., 505-510.

Boore, D. M., W. B. Joyner, and T. Fumal (1993). Estimation of response spectra and peak accelerations from Western North American earthquakes: an interim report, U.S. Geological Survey, OFR 93-509.

Boore, D. M., W. B. Joyner, and T. Fumal (1994). Update of Boore Joyner Fumal (1993) attenuation to account for style-of-faulting effects. (written communication to SCEC, April 1994).

Campbell, K. W. (1993). Empirical prediction of near-source ground motion from large earthquakes, Proc. International Workshop on Earthquake Hazard and Large Dams in the Himalaya, January 15-16, 1993, New Delhi, India.

Campbell, K. W. and Y. Bozorgnia (1994). Near-source attenuation of peak horizontal acceleration from worldwide accelerograms recorded from 1957 to 1993, Proc. Fifth National Conf. Earthquake Eng., III, 283-192.

Youngs, R. R. (1993). Soil amplification and vertical to horizontal ratios for analysis of strong motion data from active tectonic regions, Appendix 2C in Guidelines for Determing Design Basis Ground Motions, Vol 2: appendices for ground motion estimation, TR-102293.

Grazier, V. M. (1979) Determination of the true ground displacement by using strong motion records, Phys. Solid Earth, Izv. Acad. Sc. USSR, English ed published by AGU, 15:(12) 875-885.

Idriss, I. M. (1991). Selection of Earthquake ground motions at rock sites, Report prepared for the Structures Div., Building and Fire Research Lab., NIST.

Sadigh, K, C-Y Chang, N. A. Abrahamson, S. J. Chiou, and M. Power, (1993). Specification of long period motions: updated attenuation relations for rock site conditions and adjustment factors for near-fault effects, Proc. ATC 17-1., 59-70.

Somerville, P. G. and N. A. Abrahamson (1995). Prediction of ground motions for thrust earthquakes, Report to CSMIP.

APPENDIX B

Strong-Motion Catalog

PACIFIC ENGINEERING AND ANALYSIS STRONG-MOTION CATALOG 02/24/95

Earthquake No.	Location, Dist	Date & Time YEAR MODY HRMN	Magnitude (2) M ML MS OTH	Station (3) No. Description Codes Dir\Filename	Filter Corners HP LP	PGA (g)	PGV (cm/s)	PGD (cm)	Closest Site Mech, Dip (1) H/F	(km)(4)	(5)
					(hz) (hz)						
0001	Helena, Montana	1935 1031 1838	6.2 5.5 6.0	2022 Carroll College							
	8.0*			EZA HELENA\A-HMCDWN	0.20 15.0	0.102	7.3	2.29			
				00	99						
				HELENA\A-HMC180	0.20 15.0	0.150	5.8	1.00			
				HELENA\A-HMC270	0.20 15.0	0.173	16.5	2.37			
0002	Helena, Montana	1935 1031 1918		2229 Helena Fed Bldg							
	36.7*			EAA HELENA\B-FEB-UP	0.50 20.0	0.012	0.3	0.57			
				01	99						
				HELENA\B-FEB000	1.00 20.0	0.047	0.7	0.23			
				HELENA\B-FEB090	0.50 20.0	0.041	0.7	0.45			
0003	Humbolt Bay	1937 0207 0442	5.8 5.8	USGS 1023 Ferndale City Hall							
	73.7*			BQD HUMBOLT\FRN-UP	0.60 10.0	0.019	1.2	0.12			
				99	99						
				HUMBOLT\FRN225	0.50 10.0	0.044	2.6	0.30			
				HUMBOLT\FRN315	0.30 10.0	0.038	3.2	0.45			
0004	Imperial Valley	1938 0606 0242	5.0	USGS 117 El Centro Array #9							
	36.7*			EQD IMPVALL\B-ELC-UP	1.50 20.0	0.012	0.3	0.01			
				99	99				C		
				IMPVALL\B-ELC000	1.00 12.0	0.012	0.5	0.04			
				IMPVALL\B-ELC090	0.60 12.0	0.019	0.8	0.06			
0005	Northwest Calif	1938 0912 0610	5.5 5.5 5.5	USGS 1023 Ferndale City Hall							
	55.0*			BQD NWCALIF\A-FRNDWN	0.30 15.0	0.030	1.4	0.14			
				99	99						
				NWCALIF\A-FRN045	0.50 11.0	0.134	7.2	0.58			
				NWCALIF\A-FRN135	0.20 11.0	0.097	5.4	0.78			
0006	Imperial Valley	1940 0519 0437	7.0 7.2	USGS 117 El Centro Array #9							

8.3 EQD IMPVALL\I-ELCVRT 0.20 15.0 0.205 10.7 9.16
00 00 C
IMPVALL\I-ELC180 0.20 15.0 0.313 29.8 13.32

IMPVALL\I-ELC270 0.20 15.0 0.215 30.2 23.91

0007 Northwest Calif 1941 0209 0945 6.6 USGS 1023 Ferndale City Hall
97.2* BQD NWCALIF\C-FRN-UP 0.10 12.0 0.018 1.5 0.26
99 99
NWCALIF\C-FRN045 0.50 13.0 0.062 3.6 0.89

NWCALIF\C-FRN135 0.50 10.0 0.039 3.2 0.54

0008 Northern Calif 1941 1003 1614 6.4 USGS 1023 Ferndale City Hall
49.6* BQD NCALIF\F-FRN-UP 0.50 13.0 0.038 2.6 0.26
99 99
NCALIF\F-FRN225 0.20 13.0 0.114 5.9 1.77

NCALIF\F-FRN315 0.50 13.0 0.122 6.3 1.15

0009 Borrego 1942 1021 1622 6.5 USGS 117 El Centro Array #9
49.0* EQD BORREGO\B-ELC-UP 0.20 20.0 0.033 1.1 0.30
99 99 C
BORREGO\B-ELC000 0.10 15.0 0.068 3.9 1.37

BORREGO\B-ELC090 0.10 15.0 0.044 4.0 1.41

0010 Imperial Valley 1951 0124 0717 5.6 USGS 117 El Centro Array #9
28.5* EQD IMPVALL\C-ELC-UP 0.40 20.0 0.013 0.6 0.14
99 99 C
IMPVALL\C-ELC000 0.40 13.0 0.029 2.4 0.39

IMPVALL\C-ELC090 0.15 12.0 0.030 2.9 0.92

0011 Northwest Calif 1951 1008 0411 5.8 USGS 1023 Ferndale City Hall
56.0* BQD NWCALIF\B-FRN-UP 0.40 20.0 0.031 2.1 0.22
99 99
NWCALIF\B-FRN224 0.50 12.0 0.105 4.6 0.47

NWCALIF\B-FRN314 0.50 12.0 0.110 6.1 0.82

0012 Kern County 1952 0721 1153 7.4 7.7 USGS 135 LA - Hollywood Stor FF
120.5 IPD KERN\HOLVRT 0.50 17.4 0.022 2.5 0.68
03 99 C
KERN\HOL090 0.50 13.9 0.044 6.0 2.44

KERN\HOL180

0.50 14.7 0.057 5.3 1.68

USGS 135 LA - Hollywood Stor Lot 120.5 IPD
KERN\PEL-UP 0.20 20.0 0.021 2.8 2.55

99 C KERN\PEL090

0.20 15.0 0.042 7.5 4.79

KERN\PEL180

0.20 13.0 0.058 6.2 1.86

CDMG 80053 Pasadena - CIT Athenaeum 127.0
CQD KERN\PASVRT 0.50 12.5 0.027 2.9 0.86

99 B KERN\PAS180

0.50 12.5 0.045 5.6 1.25

KERN\PAS270

0.20 12.1 0.053 9.2 2.53

USGS 283 Santa Barbara Courthouse 87.0
CQD KERN\SBAVRT 0.50 12.3 0.041 4.4 1.27

99 B KERN\SBA042

0.50 14.3 0.087 12.1 2.81

KERN\SBA132

0.50 13.2 0.127 15.5 4.06

USGS 1095 Taft Lincoln School 41.0 FQD
KERN\TAFVRT 0.05 13.2 0.109 6.6 4.56

02 B KERN\TAF021

0.05 13.9 0.156 15.3 9.25

KERN\TAF111

0.05 13.2 0.178 17.5 8.99

0013 Northern Calif 1952 0922 1141 5.2 5.2 5.5 USGS 1023 Ferndale City Hall
39.3* BQD NCALIF\A-FRNVRT 0.40 10.0 0.028 1.9 0.30

99 99
NCALIF\A-FRN044 0.30 12.0 0.062 5.6 1.17

NCALIF\A-FRN134 0.30 10.0 0.074 5.5 0.98

0014 Southern Calif 1952 1122 0746 6.0 USGS 1083 San Luis Obispo
70.0* CBB SCALIF\SLO-UP 0.20 13.0 0.028 2.4 0.74

99 99
SCALIF\SLO234 0.20 13.0 0.036 2.8 0.93

SCALIF\SLO324

0.50 13.0 0.054 3.3 0.55

0015 Imperial Valley 1953 0614 0417 5.5 USGS 117 El Centro Array #9
28.5* EQD IMPVALL\G-ELC-UP 0.50 20.0 0.024 0.6 0.06

99 99 C
IMPVALL\G-ELC000 0.60 15.0 0.006 0.4 0.06

IMPVALL\G-ELC090 0.25 12.0 0.049 5.4 1.00

0016 Central Calif 1954 0425 2033 5.3 USGS 1028 Hollister City Hall
28.0* CHD CTRCALIF\A-HCH-UP 0.30 11.0 0.020 1.6 0.26
99 99 C
CTRCALIF\A-HCH181 0.40 10.0 0.049 4.7 0.63

CTRCALIF\A-HCH271 0.50 10.0 0.051 3.9 0.42

0017 Northern Calif 1954 1221 1956 6.5 USGS 1023 Ferndale City Hall
31.5* BQD NCALIF\H-FRN-UP 0.50 13.0 0.039 6.9 2.03
99 99
NCALIF\H-FRN044 0.20 20.0 0.159 33.9 13.34

NCALIF\H-FRN314 0.50 13.0 0.189 25.3 5.86

0018 Imperial Valley 1955 1217 0607 5.4 USGS 117 El Centro Array #9
28.4* EQD IMPVALL\E-ELC-UP 0.60 15.0 0.028 0.9 0.07
99 99 C
IMPVALL\E-ELC000 0.23 12.0 0.056 4.0 0.79

IMPVALL\E-ELC090 0.20 15.0 0.042 3.7 0.70

0019 El Alamo 1956 1217 1433 6.8 USGS 117 El Centro Array #9
130.0 EQD ELALAMO\ELC-UP 0.50 20.0 0.014 1.7 0.77
99 99 C
ELALAMO\ELC180 0.10 15.0 0.033 4.1 2.89

ELALAMO\ELC270 0.10 15.0 0.052 6.6 4.93

0020 San Francisco 1957 0322 1944 5.3 5.3 USGS 1117 Golden Gate Park
9.5* IBA SANFRAN\GGP-UP 0.30 25.0 0.047 1.1 0.18
02 02 A
SANFRAN\GGP010 0.80 20.0 0.095 3.9 0.19

SANFRAN\GGP100 0.30 20.0 0.112 4.6 0.43

0021 Central Calif 1960 0120 0326 5.0 USGS 1028 Hollister City Hall
14.9* CHD CTRCALIF\B-HCH-UP 0.40 12.0 0.027 1.7 0.25
99 99 C
CTRCALIF\B-HCH181 0.40 11.0 0.041 2.2 0.38

CTRCALIF\B-HCH271 0.50 11.0 0.063 3.6 0.60

0022 Northern Calif 1960 0606 0117 5.7 5.7 5.7 USGS 1023 Ferndale City Hall
58.9* BQD NCALIF\B-FRN-UP 0.30 15.0 0.016 0.9 0.17
99 99
NCALIF\B-FRN224 0.30 15.0 0.072 3.8 0.59

NCALIF\B-FRN314 0.40 15.0 0.065 3.0 0.35

0023 Hollister 1961 0409 0723 5.6 USGS 1028 Hollister City Hall
19.6* CHD HOLLISTR\B-HCH-UP 0.11 11.0 0.051 4.7 1.77
99 99 C
HOLLISTR\B-HCH181 0.25 11.0 0.074 6.3 1.31

HOLLISTR\B-HCH271 0.11 11.0 0.196 12.4 4.29

0024 Hollister 1961 0409 0725 5.5 USGS 1028 Hollister City Hall
12.6* CHD HOLLISTR\C-HCH-UP 0.30 13.0 0.049 3.0 0.53
99 99 C
HOLLISTR\C-HCH181 0.40 12.0 0.072 4.9 0.71

HOLLISTR\C-HCH271 0.30 11.0 0.075 9.7 1.75

0025 Parkfield 1966 0628 0426 6.1 6.1 CDMG 1013 Cholame #2
0.1 IHD PARKF\C02DWN 0.20 20.0 0.255 13.7 3.79
00 00 C
PARKF\C02065 0.20 10.0 0.476 75.1 22.49
CDMG 1014 Cholame #5 5.3 IHC
PARKF\C05DWN 0.20 21.0 0.138 6.9 2.66
00 C PARKF\C05085
0.20 17.4 0.442 24.7 5.15
PARKF\C05355
0.20 20.0 0.367 21.8 3.83
CDMG 1015 Cholame #8 9.2 ABB
PARKF\C08DWN 0.20 24.0 0.116 4.3 1.48
00 C PARKF\C08050
0.20 20.0 0.246 10.2 3.60
PARKF\C08320
0.20 20.0 0.273 11.3 3.20
CDMG 1016 Cholame #12 14.7 IBB
PARKF\C12DWN 0.20 20.0 0.053 4.6 2.10
00 B PARKF\C12050
0.20 20.0 0.059 5.8 2.56
PARKF\C12320
0.20 20.0 0.063 6.8 3.55
USGS 1083 San Luis Obispo 60.0 CBB
PARKF\SLOVRT 0.20 15.0 0.007 0.8 0.28

00 PARKF\SLO234
0.20 15.0 0.012 1.0 0.30
PARKF\SLO324
0.20 12.0 0.014 1.0 0.46
CDMG 1438 Temblor pre-1969 9.9 IJA
PARKF\TMBDWN 0.20 16.9 0.136 4.4 1.10
00 B
PARKF\TMB205 0.20 14.7 0.357 21.5 3.87
PARKF\TMB295
0.20 15.1 0.272 15.0 3.40

0026 Northern Calif 1967 1210 1206 5.6 5.6 5.8 USGS 1023 Ferndale City Hall
30.8* BQD NCALIF\C-FRN-UP 0.40 12.0 0.032 3.3 0.46
99 99
NCALIF\C-FRN224 0.30 20.0 0.283 9.2 1.23

NCALIF\C-FRN314 0.20 13.0 0.113 11.1 1.58

0027 Northern Calif 1967 1218 1725 5.2 USGS 1028 Hollister City Hall
45.0* CHD NCALIF\E-HCH-UP 0.50 15.0 0.011 0.5 0.09
99 99 C
NCALIF\E-HCH181 0.30 15.0 0.013 2.0 0.37

NCALIF\E-HCH271 0.30 15.0 0.013 1.0 0.27

0028 Borrego Mtn 1968 0409 0230 6.8 6.7 6.5 USGS 117 El Centro Array #9
46.0 EQD BORREGO\A-EC9VRT 0.20 16.4 0.030 3.3 1.99
00 00 C
BORREGO\A-EC9180 0.20 12.5 0.130 26.3 12.18

BORREGO\A-EC9270 0.20 12.8 0.057 13.2 10.03
USGS 135 LA - Hollywood Stor PE Lot 217.4
IPD BORREGO\A-PEL-UP 0.20 30.0 0.005 1.1 1.10
00 C
BORREGO\A-PEL090 0.20 13.0 0.012 2.9 1.30

BORREGO\A-PEL180 0.10 13.0 0.011 2.3 2.33
USGS 130 LB - Terminal Island 195.0 CCD
BORREGO\A-TLI-UP 0.10 20.0 0.005 1.6 1.76
00 C
BORREGO\A-TLI249 0.10 15.0 0.010 2.8 2.53

BORREGO\A-TLI339 0.10 15.0 0.009 3.0 5.46
CDMG 475 Pasadena - Athenaeum 203.0
CQD BORREGO\A-PAS-UP 0.50 13.0 0.004 0.5 0.38

00 E

BORREGO\A-PAS180 0.50 13.0 0.007 1.4 0.82

BORREGO\A-PAS270 0.50 13.0 0.009 1.8 0.64

SCE 280 San Onofre - So Cal Edison 124.7 ABB

BORREGO\A-SONVRT 0.20 15.0 0.062 1.9 0.50

00

BORREGO\A-SON033 0.10 20.0 0.041 3.7 1.72

BORREGO\A-SON303 0.20 20.0 0.045 3.7 1.30

0029 Lytle Creek 1970 0912 1430 5.4 5.4 CDMG 24278 Castaic - Old Ridge Route 107.8* A-B LYTLECR\ORRDWN 0.70 20.0 0.010 0.4 0.03

03 99 B

LYTLECR\ORR021 0.50 20.0 0.021 0.9 0.07

LYTLECR\ORR291 0.50 20.0 0.026 1.5 0.15

CDWR 111 Cedar Springs, Allen Ranch 20.6*

AAA LYTLECR\CSM095 0.60 15.0 0.071 1.8 0.11

99 A

LYTLECR\CSM185 1.10 20.0 0.050 1.2 0.06

CDWR 112 Cedar Springs Pumphouse 23.7*

AAB LYTLECR\CSDDWN 1.00 15.0 0.037 1.3 0.08

99

LYTLECR\CSD126 0.50 20.0 0.069 2.6 0.14

LYTLECR\CSD216 0.40 15.0 0.077 3.7 0.39

USGS 113 Colton, So Cal Edison 32.4* ACD

LYTLECR\CLN-UP 0.60 15.0 0.035 1.3 0.11

99 C

LYTLECR\CLN090 0.40 12.0 0.033 1.6 0.17

LYTLECR\CLN180 0.50 11.0 0.038 1.3 0.14

CDWR 620 Devil's Canyon 21.9* CAA

LYTLECR\DCFDWN 1.10 30.0 0.084 1.8 0.10

99

LYTLECR\DCF090 1.00 20.0 0.146 3.3 0.18

LYTLECR\DCF180 1.00 30.0 0.151 5.6 0.23

CDMG 125 Lake Hughes #1 93.5* APC

LYTLECR\L01DWN 1.10 15.0 0.006 0.3 0.02

99

LYTLECR\L01021 0.80 10.0 0.009 0.7 0.08

LYTLECR\L01291 0.35 20.0 0.008 0.6 0.10

CDMG 24303 LA - Hollywood Stor FF 76.0*
IPD LYTLECR\PEL-UP 0.90 20.0 0.007 0.3 0.02
99 C
LYTLECR\PEL090 0.30 20.0 0.017 1.0 0.14

LYTLECR\PEL180 0.40 20.0 0.018 0.7 0.06
CDMG 278 Puddingstone Dam (Abutment) 32.8*
IVB LYTLECR\PUDDWN 0.35 20.0 0.014 0.7 0.12
99
LYTLECR\PUD055 0.50 20.0 0.018 0.9 0.09

LYTLECR\PUD326 0.50 20.0 0.019 0.9 0.12
LAFC 104 Santa Anita Dam 45.9* IGA
LYTLECR\SADDWN 1.20 25.0 0.013 0.3 0.01
99
LYTLECR\SAD003 1.00 25.0 0.042 1.6 0.10

LYTLECR\SAD273 0.40 25.0 0.018 0.5 0.04
USGS 290 Wrightwood - 6074 Park Dr 15.4*
BAB LYTLECR\WTWDWN 0.60 40.0 0.078 2.3 0.25
99 B
LYTLECR\WTW115 0.60 20.0 0.162 10.1 1.02

LYTLECR\WTW205 0.70 30.0 0.200 10.5 0.62

0030 San Fernando 1971 0209 1400 6.6 6.6 2 2516 Via Tejon PV
65.1 CBC SFERN\PVEDWN 0.20 20.0 0.020 2.0 1.26
02 99
SFERN\PVE065 0.20 20.0 0.026 3.8 2.19
SFERN\PVE155
0.20 20.0 0.041 4.2 3.11
CIT 103 Anza Post Office 169.0 AAC
SFERN\AZPDWN 0.50 35.0 0.015 0.7 0.20
99 SFERN\AZP045
0.50 35.0 0.027 1.4 0.25
SFERN\AZP315
0.50 35.0 0.037 2.2 0.30
USGS 1004 Bakersfield - Harvey Aud 120.0
CCD SFERN\BFA-UP 0.10 15.0 0.007 0.7 0.69
99 SFERN\BFA180
0.10 13.0 0.007 1.4 1.08
SFERN\BFA270
0.10 20.0 0.007 1.2 1.23
USGS 105 Borrego Springs Fire Sta 212.0 AAC
SFERN\BSFDWN 0.10 30.0 0.005 1.2 1.13

99 SFERN\BSF135
0.10 23.0 0.009 1.2 1.22
SFERN\BSF225
0.10 30.0 0.009 1.2 0.90
USGS 1 Buena Vista - Taft 118.0 AQD
SFERN\BVPDWN 0.20 20.0 0.007 0.6 0.41
99 SFERN\BVP090
0.10 13.0 0.012 1.5 1.51
SFERN\BVP180
0.10 15.0 0.012 1.3 0.68
ACOE 108 Carbon Canyon Dam 66.4
AMA SFERN\CNDDWN 0.50 35.0 0.043 1.6 0.93
99 SFERN\CND130
0.50 35.0 0.070 2.7 1.27
SFERN\CND220
0.50 35.0 0.071 3.9 0.85
CDMG 24278 Castaic - Old Ridge Route 24.9
A-B SFERN\CRRDWN 0.50 35.0 0.171 6.5 1.28
99 B
SFERN\CRR021 0.50 35.0 0.324 15.6 2.31
SFERN\CRR291
0.50 35.0 0.268 25.9 4.67
CDWR 111 Cedar Springs, Allen Ranch 86.6
AAA SFERN\CSMDWN 0.20 35.0 0.009 0.9 0.53
99 A
SFERN\CSM095 0.20 35.0 0.020 1.7 0.49
SFERN\CSM185
0.20 35.0 0.015 1.4 0.57
CDWR 112 Cedar Springs - Pump 87.6 AAB
SFERN\CSPDWN 0.10 20.0 0.012 0.8 0.30
99 SFERN\CSP126
0.10 20.0 0.027 2.0 0.31
SFERN\CSP216
0.10 20.0 0.025 2.9 0.40
USGS 1013 Cholame-Shandon Array #2 @ 219.0
IHD SFERN\C02DWN 0.10 50.0 0.004 1.3 1.18
99 C SFERN\C02051
0.10 20.0 0.004 1.2 1.31
SFERN\C02321
0.10 30.0 0.005 1.1 0.92
USGS 1015 Cholame-Shandon Array #8 223.0
ABB SFERN\C08051 0.10 23.0 0.005 1.0 0.75
99 C SFERN\C08321
0.10 23.0 0.006 1.6 0.97
USGS 113 Colton - So Cal Edison @ 89.6

ACD SFERN\CLNVRT 0.10 15.0 0.023 1.1 0.16
99 C
SFERN\CLN090 0.10 13.0 0.032 1.8 0.29
SFERN\CLN180
0.10 13.0 0.039 2.2 0.32
CDMG 121 Fairmont Dam 29.1 AGA
SFERN\FTR-UP 0.50 35.0 0.039 3.5 0.71
99 SFERN\FTR056
0.50 35.0 0.071 4.7 0.72
SFERN\FTR326
0.50 35.0 0.109 6.5 1.10
USGS 998 Fort Tejon 64.1 AAB
SFERN\FTJVRT 0.10 23.0 0.016 0.7 0.21
99 SFERN\FTJ000
0.10 20.0 0.026 1.1 0.36
SFERN\FTJ090
0.10 20.0 0.022 1.4 0.27
CDWR 994 Gormon - Oso Pump Plant 48.1
EBC SFERN\OPPVRT 0.10 23.0 0.039 3.6 0.72
99 C
SFERN\OPP000 0.10 23.0 0.084 7.9 1.27
SFERN\OPP270
0.10 30.0 0.105 6.8 1.76
CDMG 12331 Hemet Fire Station 136.0
AQD SFERN\H05DWN 0.50 35.0 0.026 1.5 0.32
99 C SFERN\H05135
0.50 35.0 0.033 2.2 0.38
SFERN\H05225
0.50 35.0 0.047 2.6 0.33
ACOE 1035 Isabella Dam (Aux Abut) 113.0
AGA SFERN\ISDDWN 0.10 20.0 0.006 1.3 1.33
99 SFERN\ISD014
0.10 13.0 0.006 1.4 1.94
SFERN\ISD284
0.10 13.0 0.009 1.6 2.03
USGS 135 LA - Hollywood Stor Lot 21.2 IPD
SFERN\PEL-UP 0.50 35.0 0.136 4.3 1.52
99 C SFERN\PEL090
0.20 35.0 0.210 18.9 12.40
SFERN\PEL180
0.20 35.0 0.174 14.9 6.25
CDMG 125 Lake Hughes #1 25.8 APC
SFERN\L01DWN 0.20 35.0 0.098 11.4 2.76
99 SFERN\L01021
0.50 35.0 0.145 17.3 2.88

SFERN\L01111

0.50 35.0 0.110 14.0 1.93

USGS 126 Lake Hughes #4 24.2 IGA

SFERN\L04DWN 0.50 35.0 0.164 6.4 0.93

99 C SFERN\L04111

0.50 35.0 0.192 5.6 0.92

SFERN\L04201

0.50 35.0 0.153 8.4 1.85

USGS 127 Lake Hughes #9 23.5 AGA

SFERN\L09DWN 0.50 35.0 0.088 2.3 0.87

99 SFERN\L09021

0.50 35.0 0.157 4.5 1.28

SFERN\L09291

0.50 35.0 0.134 3.9 1.12

CDMG 128 Lake Hughes #12 20.3 AEB

SFERN\L12DWN 0.50 35.0 0.167 3.7 0.65

99 B SFERN\L12021

0.50 35.0 0.366 17.0 1.65

SFERN\L12291

0.50 35.0 0.283 12.7 2.97

USGS 130 LB - Terminal Island 69.2 CCD

SFERN\TLI-UP 0.10 50.0 0.017 3.9 3.03

99 C SFERN\TLI249

0.10 20.0 0.029 9.6 8.25

SFERN\TLI339

0.10 20.0 0.029 6.8 6.17

CDWR 1041 Maricopa Array #1 115.0 IBB

SFERN\MA1DWN 0.10 20.0 0.005 1.1 1.40

99 SFERN\MA1130

0.10 13.0 0.007 1.7 1.53

SFERN\MA1220

0.10 20.0 0.011 2.4 2.33

CDWR 1042 Maricopa Array #2 113.0 IBB

SFERN\MA2DWN 0.20 20.0 0.007 0.7 0.64

99 SFERN\MA2130

0.10 20.0 0.011 6.8 9.12

SFERN\MA2220

0.10 15.0 0.009 1.6 1.77

CDWR 1043 Maricopa Array #3 113.0 IBB

SFERN\MA3DWN 0.10 15.0 0.007 2.9 2.15

99 SFERN\MA3130

0.10 20.0 0.008 2.2 1.85

SFERN\MA3220

0.10 20.0 0.010 2.0 2.16

CDMG 24279 Pacoima Dam 2.8 AMB

SFERN\PCDDWN 0.10 35.0 0.699 56.5 18.25

02 SFERN\PCD164

0.10 35.0 1.226 112.5 35.50

SFERN\PCD254

0.50 35.0 1.160 54.3 11.73

USGS 262 Palmdale Fire Station 25.4 AQD

SFERN\PDL120 0.50 35.0 0.121 12.3 2.65

99 B

SFERN\PDL210 0.50 35.0 0.151 8.1 1.85

CDMG 80053 Pasadena - CIT Athenaeum 31.7

CQD SFERN\PASDWN 0.50 35.0 0.095 4.5 0.70

99 B

SFERN\PAS000 0.50 35.0 0.088 6.4 1.36

SFERN\PAS090

0.20 35.0 0.110 13.3 7.78

USGS 266 Pasadena - Old Seismo Lab 19.1

CGA SFERN\PSLDWN 0.50 35.0 0.090 4.4 1.40

99 SFERN\PSL180

0.50 35.0 0.089 5.3 0.86

SFERN\PSL270

0.50 35.0 0.202 10.9 2.39

CDWR 269 Pearblossom Pump 38.9 AGB

SFERN\PPPDWN 0.20 35.0 0.050 2.1 0.95

99 B SFERN\PPP000

0.20 35.0 0.102 4.7 1.53

SFERN\PPP270

0.20 35.0 0.136 5.6 1.61

CDMG 272 Port Huenume 63.0 BBD

SFERN\PHN-UP 0.50 35.0 0.011 3.0 1.78

99 SFERN\PHN180

0.50 35.0 0.027 6.1 3.50

SFERN\PHN270

0.50 35.0 0.025 3.9 2.65

CDMG 278 Puddingstone Dam (Abut) 50.4

IVD SFERN\PUDDWN 0.50 35.0 0.036 1.6 0.51

99 SFERN\PUD055

0.50 35.0 0.074 4.0 0.76

SFERN\PUD325

0.50 35.0 0.065 3.1 0.43

USGS 314 San Diego Gas & Electric 214.0

ABD SFERN\SDCDWN 0.10 33.0 0.003 1.0 0.90

99 SFERN\SDC000

0.10 30.0 0.006 1.5 1.16

SFERN\SDC090

0.10 30.0 0.004 1.2 1.00

USGS 465 San Juan Capistrano 104.0 ABC

SFERN\SJCDWN 0.50 35.0 0.021 2.0 0.67
99 SFERN\SJC033

0.50 35.0 0.046 3.3 1.05 SFERN\SJC303

0.50 35.0 0.035 3.7 0.79

SCE 280 San Onofre - So Cal Edison 122.0 ABB

SFERN\SONDWN 0.10 23.0 0.011 0.8 0.77
99 SFERN\SON033

0.10 20.0 0.013 1.7 0.74 SFERN\SON303

0.20 20.0 0.016 1.8 0.63

LAFC 104 Santa Anita Dam 27.0 IGA

SFERN\SADDWN 0.20 35.0 0.062 3.9 1.80
99 SFERN\SAD003

0.20 35.0 0.151 4.7 2.30 SFERN\SAD273

0.20 35.0 0.212 6.1 2.89

CDMG 285 Santa Felita Dam (Outlet) 27.5

ABA SFERN\FSDVRT 0.10 20.0 0.065 4.1 2.36
99 SFERN\FSD172

0.10 20.0 0.148 9.4 7.02 SFERN\FSD262

0.10 13.0 0.152 6.5 3.46

CDWR 1027 Tehachapi Pump 68.0 AAA

SFERN\TEHDWN 0.20 35.0 0.045 1.7 0.28
99 SFERN\TEH090

0.20 35.0 0.053 2.0 0.37 SFERN\TEH180

0.20 35.0 0.025 1.0 0.13

USGS 282 UCSB - Fluid Mech Lab 125.6

CPD SFERN\SBF-UP 0.20 30.0 0.011 1.3 0.73
99 SFERN\SBF042

0.20 30.0 0.017 2.7 1.41 SFERN\SBF132

0.20 30.0 0.017 3.0 1.29

ACOE 287 Upland - San Antonio Dam 58.1

AAA SFERN\SODDWN 0.50 35.0 0.032 1.3 0.54
99 B

SFERN\SOD015 0.50 35.0 0.058 2.9 0.55 SFERN\SOD285

0.50 35.0 0.079 3.5 0.50

CDWR 1102 Wheeler Ridge - Ground 81.6

IBD SFERN\WRPVRT 0.10 30.0 0.014 1.4 1.46
99 C

SFERN\WRP090 0.10 23.0 0.027 2.0 1.47
SFERN\WRP180
0.10 23.0 0.031 1.7 1.23
ACOE 289 Whittier Narrows Dam 45.1 IHD
SFERN\WNDDWN 0.10 30.0 0.032 3.7 2.61
99
SFERN\WND143 0.10 20.0 0.100 9.3 5.79
SFERN\WND233
0.10 20.0 0.107 9.7 5.04
USGS 290 Wrightwood - 6074 Park Dr 60.3
BAB SFERN\WTWDWN 0.20 40.0 0.028 1.6 0.78
99 B
SFERN\WTW025 0.20 30.0 0.061 2.6 0.47
SFERN\WTW295
0.20 30.0 0.044 3.3 0.68

0031 Point Mugu 1973 0221 1445 5.8 5.9 5.2 CDMG 25281 Port Hueneme
25.0* BBD PTMUGU\PHN-UP 0.15 30.0 0.047 2.2 0.39
02 99 C
PTMUGU\PHN180 0.20 25.0 0.112 14.8 2.59

PTMUGU\PHN270 0.20 30.0 0.083 4.6 0.80

0032 Hollister 1974 1128 2301 5.2 5.2 4.5 CDMG 47379 Gilroy Array #1
12.3* IFA HOLLISTR\A-G01157 1.50 25.0 0.105 2.7 0.13
00 00 A
HOLLISTR\A-G01247 1.10 25.0 0.132 4.0 0.17
USGS 1028 Hollister City Hall 11.1* CHD
HOLLISTR\A-HCH-UP 0.30 20.0 0.071 3.5 0.36
00 C
HOLLISTR\A-HCH181 0.40 15.0 0.089 6.2 0.56

HOLLISTR\A-HCH271 0.40 11.0 0.177 10.3 1.25
CDMG 1377 San Juan Bautista, 24 Polk St 11.4*
AQD HOLLISTR\A-SJBDWN 1.00 20.0 0.046 1.5 0.10
00 B
HOLLISTR\A-SJB033 0.80 20.0 0.049 2.2 0.17

HOLLISTR\A-SJB123 0.40 15.0 0.130 7.3 0.64

0033 Northern Calif 1975 0607 0846 5.2 5.2 5.7 CDMG 1249 Cape Mendocino,
Petrolia 28.9* IFA NCALIF\D-CPMDWN 2.00 30.0 0.026 0.8 0.04
99 99
NCALIF\D-CPM030 1.50 25.0 0.115 3.1 0.10

NCALIF\D-CPM120 2.00 20.0 0.179 4.9 0.16
USGS 1023 Ferndale City Hall 22.8* BQD
NCALIF\D-FRN-UP 0.20 15.0 0.239 8.9 1.77
99
NCALIF\D-FRN224 0.40 15.0 0.173 11.8 1.58

NCALIF\D-FRN314 0.40 15.0 0.038 2.7 0.28
CDMG 1398 Petrolia, General Store 29.9* IMD
NCALIF\D-PGSDWN 1.00 35.0 0.041 1.8 0.10
99
NCALIF\D-PGS075 0.45 25.0 0.156 8.6 0.92

NCALIF\D-PGS345 0.40 30.0 0.131 7.8 0.55
CDMG 1277 Shelter Cove, Sta A 59.2* IBA
NCALIF\D-SCA200 1.00 20.0 0.032 1.5 0.11
99
NCALIF\D-SCA290 1.00 20.0 0.031 1.2 0.07
CDMG 1278 Shelter Cove, Sta B 60.2* IBB
NCALIF\D-SCP070 1.30 30.0 0.081 2.3 0.10
99
NCALIF\D-SCP160 1.50 25.0 0.093 2.8 0.11

0034 Oroville 1975 0801 2020 6.0 5.7 CDWR 1051 Oroville Seismograph
Station 9.5* AJA OROVILLE\A-ORV037 1.00 10.0 0.092 3.7 0.17
01 99
OROVILLE\A-ORV307 1.00 10.0 0.072 2.8 0.22

0035 Oroville 1975 0802 2022 5.0 5.1 CIT 1545 Oroville Airport
14.6* ACD OROVILLE\B-OAPDWN 0.30 25.0 0.015 1.1 0.32
01 99
OROVILLE\B-OAP180 0.20 15.0 0.036 2.5 0.82

OROVILLE\B-OAP270 0.40 25.0 0.015 1.4 0.33
CDMG 1546 Up & Down Cafe (OR1) 12.7*
ADD OROVILLE\B-OR1DWN 0.60 30.0 0.021 1.1 0.18
99
OROVILLE\B-OR1000 0.70 25.0 0.034 1.1 0.15

OROVILLE\B-OR1270 0.20 20.0 0.030 2.9 0.72

0036 Oroville 1975 0802 2059 4.4 5.2 CIT 1544 Medical Center
11.1* ABB OROVILLE\C-OMCDWN 0.80 30.0 0.030 1.1 0.83
04 99
OROVILLE\C-OMC246 0.40 40.0 0.079 3.0 0.32

OROVILLE\C-OMC336 0.35 30.0 0.043 2.2 0.22
CIT 1545 Oroville Airport 15.0* ACD
OROVILLE\C-OAPDWN 0.30 40.0 0.025 1.2 0.24
99
OROVILLE\C-OAP180 0.30 30.0 0.020 2.2 0.62

OROVILLE\C-OAP270 0.50 40.0 0.024 1.1 0.91
CDMG 1546 Up & Down Cafe (OR1) 12.4*
ADD OROVILLE\C-OR1DWN 0.70 40.0 0.065 1.1 0.14
99
OROVILLE\C-OR1000 0.35 30.0 0.069 1.7 0.36

OROVILLE\C-OR1090 0.40 30.0 0.050 2.5 0.43

0037 Oroville 1975 0808 0700 4.7 4.9 CIT 1542 Broadbeck Residence
9.8* ACC OROVILLE\D-EBHDWN 1.30 40.0 0.073 1.7 0.06
01 99
OROVILLE\D-EBH000 0.70 30.0 0.168 3.1 0.17

OROVILLE\D-EBH090 0.70 40.0 0.117 3.4 0.22
CDMG 1550 Duffy Residence (OR5) 10.9*
ACD OROVILLE\D-OR5DWN 1.00 40.0 0.051 0.7 0.05
99
OROVILLE\D-OR5090 0.50 40.0 0.085 2.0 0.20

OROVILLE\D-OR5180 0.80 40.0 0.061 2.2 0.12
CIT 1543 DWR Garage 6.5* AAA
OROVILLE\D-DWRDWN 5.00 40.0 0.106 0.7 0.01
99
OROVILLE\D-DWR090 1.50 50.0 0.141 1.1 0.04

OROVILLE\D-DWR180 3.00 40.0 0.209 1.8 0.02
CDMG 1493 Johnson Ranch 10.7* AAB
OROVILLE\D-DJRDWN 2.00 50.0 0.089 1.1 0.02
99
OROVILLE\D-DJR000 1.00 45.0 0.191 3.9 0.10

OROVILLE\D-DJR090 1.00 40.0 0.095 1.6 0.05
CDMG 1496 Nelson Ranch (OR7) 6.7*
ABB OROVILLE\D-OR7DWN 1.50 50.0 0.110 1.3 0.02
99
OROVILLE\D-OR7180 1.00 40.0 0.088 1.3 0.05

OROVILLE\D-OR7270 1.20 50.0 0.114 1.9 0.05
CIT 1545 Oroville Airport 11.7* ACD

```
OROVILLE\D-OAPDWN 0.80  50.0   0.072    1.1    0.07
                                    99
OROVILLE\D-OAP180 0.70  40.0   0.047    1.1    0.06

OROVILLE\D-OAP270 0.35  30.0   0.065    2.4    0.27
                                CDMG 1549 Pacific Heights Rd (OR4)        12.0*
ACD  OROVILLE\D-OR4DWN 0.80  40.0   0.042    1.0    0.09
                                    99
OROVILLE\D-OR4235 0.60  40.0   0.065    2.6    0.27

OROVILLE\D-OR4325 1.00  40.0   0.069    2.1    0.11
                                CDMG 1551 Summit Ave (OR6)            8.6*
AAA  OROVILLE\D-OR6DWN 1.50  40.0   0.059    0.8    0.02
                                    99
OROVILLE\D-OR6035 1.50  35.0   0.101    2.3    0.08

OROVILLE\D-OR6125 1.30  35.0   0.081    1.2    0.04
                                CDMG 1546 Up & Down Cafe (OR1)           13.3*
ADD  OROVILLE\D-OR1DWN 0.70  40.0   0.048    1.2    0.13
                                    99
OROVILLE\D-OR1000 0.50  40.0   0.152    3.9    0.20

OROVILLE\D-OR1090 0.40  40.0   0.101    3.5    0.40

0038 Friuli, Italy    1976 0506 2000  6.5 6.2 6.5          8002 Barcis                  49.7*
ABB  FRIULI\A-BCS-UP   0.20  37.0   0.014    1.0    0.18
  99                                  99
FRIULI\A-BCS000   0.20  30.0   0.029    1.3    0.53

FRIULI\A-BCS270   0.20  30.0   0.030    1.2    0.27
                                    8004 Codroipo              34.6*   ADD
FRIULI\A-CDO-UP   0.10  30.0   0.035    5.9    3.33
                                    99
FRIULI\A-CDO000   0.10  25.0   0.062   10.7    3.03

FRIULI\A-CDO270   0.10  25.0   0.090    8.5    3.09
                                    8005 Conegliano            73.7*   ADD
FRIULI\A-CLV-UP   0.50  25.0   0.025    2.4    0.70
                                    99
FRIULI\A-CLV000   0.50  20.0   0.049    3.5    0.76

FRIULI\A-CLV270   0.50  20.0   0.069    4.2    1.03
                                    8007 Feltre                97.1*   ABA
FRIULI\A-FLT-UP   0.20  30.0   0.019    0.8    0.24
                                    99
```

FRIULI\A-FLT000 0.20 30.0 0.033 1.5 0.26

FRIULI\A-FLT270 0.20 30.0 0.038 1.3 0.28

8012 Tolmezzo 37.7* ABB

FRIULI\A-TMZ-UP 0.10 45.0 0.268 10.7 2.50

99

FRIULI\A-TMZ000 0.10 30.0 0.351 22.0 4.10

FRIULI\A-TMZ270 0.10 30.0 0.315 30.8 5.10

0039 Gazli, USSR 1976 0517 6.8 7.3 9201 Karakyr 3.0*

AAA GAZLI\GAZVRT 0.50 38.0 1.264 54.2 30.15

02 01

GAZLI\GAZ000 0.50 38.0 0.608 65.4 25.29

GAZLI\GAZ090

0.50 38.0 0.718 71.6 23.71

0040 Fruili, Italy 1976 0911 1631 5.5 8023 Buia 13.6*

ABC FRIULI\BUI-UP 0.40 20.0 0.029 3.1 0.68

99 99

FRIULI\BUI-NS 0.20 12.0 0.041 6.2 1.18

FRIULI\BUI-WE

0.13 20.0 0.041 3.9 1.02

8014 Forgaria Cornino 18.2* ABB

FRIULI\FOC-UP 0.60 20.0 0.046 3.1 0.22

99 B

FRIULI\FOC-NS 0.20 15.0 0.112 7.6 0.94

FRIULI\FOC-WE

0.30 20.0 0.093 8.4 0.68

8022 San Rocco 17.9* ABA

FRIULI\SAR-UP 0.40 15.0 0.013 1.8 0.34

99 FRIULI\SAR-NS

0.20 15.0 0.029 2.3 0.48

FRIULI\SAR-WE

0.40 20.0 0.072 4.3 0.90

0041 Friuli, Italy 1976 0915 0315 6.1 8023 Buia 10.8*

ABC FRIULI\B-BUI-UP 0.50 48.0 0.074 6.5 1.58

99 99

FRIULI\B-BUI000 0.50 30.0 0.110 10.2 2.22

FRIULI\B-BUI270 0.50 33.0 0.091 10.6 1.61

8004 Codroipo 36.1* ADD

FRIULI\B-COD-UP 0.10 32.0 0.013 4.0 1.74

99

FRIULI\B-COD000 0.10 28.0 0.030 2.7 1.21

FRIULI\B-COD270 0.10 25.0 0.019 3.7 1.90

8014 Forgaria Cornino 13.5* ABB

FRIULI\B-COR-UP 0.50 48.0 0.095 5.6 1.35

99

FRIULI\B-COR000 0.50 40.0 0.260 9.3 1.07

FRIULI\B-COR270 0.20 42.0 0.212 9.7 1.83

8022 San Rocco 12.7* ABA

FRIULI\B-SRO-UP 0.10 38.0 0.058 6.3 2.12

99

FRIULI\B-SRO000 0.10 32.0 0.060 4.8 1.14

FRIULI\B-SRO270 0.10 33.0 0.134 7.6 1.99

0042 Santa Barbara 1978 0813 6.0 5.1 6.0 USGS 106 Cachuma Dam Toe
36.6* AAA SBARB\CAD-UP 0.20 29.0 0.024 1.6 0.40
03 99
SBARB\CAD250 0.10 36.0 0.072 6.3 1.26

SBARB\CAD340

0.20 30.0 0.034 2.6 0.55

USGS 283 Santa Barbara Courthouse 14.0*

CQD SBARB\SBA-UP 0.10 30.0 0.077 3.5 0.83

01 B

SBARB\SBA132 0.10 26.0 0.102 7.4 1.80

SBARB\SBA222

0.10 30.0 0.203 16.3 2.99

0043 Tabas, Iran 1978 0916 7.4 7.7 7.4 69 Bajestan
TABAS\BAJ-V1 0.05 0.029 5.7 6.16
02 99
TABAS\BAJ-L1 0.02 15.0 0.094 7.6 10.77

TABAS\BAJ-T1

0.02 15.0 0.067 5.7 10.03

70 Boshrooy

TABAS\BOS-V1 0.06 0.085 11.6 8.36

99 TABAS\BOS-L1

0.04 20.0 0.107 13.7 10.50

TABAS\BOS-T1

0.04 20.0 0.089 18.0 18.27

9102 Dayhook 17.0* ABA

TABAS\DAYVRT 0.10 0.183 12.0 4.97

01

TABAS\DAY-LN 0.10 0.328 20.6 12.56

TABAS\DAY-TR
0.10 0.406 26.5 8.75
71 Fairdows
TABAS\FER-V1 0.04 0.053 7.6 6.78
99 TABAS\FER-L1
0.02 20.0 0.087 5.7 4.61
TABAS\FER-T1
0.04 20.0 0.108 8.6 9.69
72 Kashmar
TABAS\KSH-V1 0.05 20.0 0.026 7.4 6.78
99 TABAS\KSH-L1
0.03 20.0 0.034 10.7 10.60
TABAS\KSH-T1
0.02 20.0 0.037 11.4 7.10
73 Sedeh
TABAS\SED-V1 0.02 20.0 0.013 6.1 11.61
99 TABAS\SED-L1
0.02 20.0 0.026 5.6 6.42
TABAS\SED-T1
0.02 20.0 0.027 4.1 4.91
9101 Tabas 3.0* ABB
TABAS\TABVRT 0.05 0.688 45.6 17.04
02
TABAS\TAB-LN 0.05 0.836 97.8 36.92
TABAS\TAB-TR
0.05 0.852 121.4 94.58

0044 Coyote Lake 1979 0806 1705 5.7 5.7 5.6 CDMG 57217 Coyote Lake Dam (SW Abut) 3.2 IFA COYOTELK\CYC-UP 0.30 30.0 0.121 6.4 0.67
00 00
COYOTELK\CYC160 0.30 40.0 0.157 10.8 1.31
COYOTELK\CYC250 0.20 40.0 0.279 20.3 2.33
CDMG 47379 Gilroy Array #1 9.3 IFA
COYOTELK\G01-UP 0.30 40.0 0.072 2.5 0.41
00 A
COYOTELK\G01230 0.30 40.0 0.103 3.4 0.48
COYOTELK\G01320 0.25 40.0 0.132 8.3 1.52
CDMG 47380 Gilroy Array #2 7.5 IQD
COYOTELK\G02-UP 0.20 50.0 0.166 7.0 1.18
00 C
COYOTELK\G02050 0.20 40.0 0.211 10.9 2.29
COYOTELK\G02140 0.20 40.0 0.339 24.9 5.81

CDMG 47381 Gilroy Array #3 6.0 IHD

COYOTELK\G03-UP 0.30 40.0 0.160 5.2 1.26
00 C

COYOTELK\G03050 0.20 40.0 0.272 18.7 3.42

COYOTELK\G03140 0.15 40.0 0.228 28.8 4.87

CDMG 57382 Gilroy Array #4 4.5 AHD

COYOTELK\G04-UP 0.30 40.0 0.387 11.7 2.47
00 C

COYOTELK\G04270 0.20 25.0 0.248 23.1 2.60

COYOTELK\G04360 0.12 25.0 0.271 26.3 4.78

CDMG 57383 Gilroy Array #6 3.1 IKA

COYOTELK\G06-UP 0.10 30.0 0.146 12.8 3.92
00 B

COYOTELK\G06230 0.08 25.0 0.434 49.2 7.77

COYOTELK\G06320 0.20 40.0 0.316 24.5 3.85

CDMG 57191 Halls Valley 31.2 IFB

COYOTELK\HVR-UP 0.50 20.0 0.027 1.3 0.13
00 C

COYOTELK\HVR150 0.30 15.0 0.039 2.2 0.27

COYOTELK\HVR240 0.30 15.0 0.050 4.8 0.48

CDMG 1377 San Juan Bautista 15.6 AQD

COYOTELK\SJB-UP 0.20 20.0 0.111 4.7 0.95
00 B

COYOTELK\SJB213 0.20 20.0 0.108 7.6 0.95

COYOTELK\SJB303 0.20 20.0 0.107 7.5 1.02

CDMG 1492 SJB Overpass, Bent 3 g.l. 17.2

DQD COYOTELK\SJ3-UP 0.30 50.0 0.060 2.3 0.21
00

COYOTELK\SJ3067 0.60 60.0 0.097 5.9 0.55

COYOTELK\SJ3337 0.23 60.0 0.124 7.6 1.07

CDMG 1492 SJB Overpass, Bent 5 g.l. 17.2

DQD COYOTELK\SJ5-UP 0.30 50.0 0.036 2.2 0.23
00

COYOTELK\SJ5067 0.30 50.0 0.073 5.6 0.77

COYOTELK\SJ5337 0.25 60.0 0.114 7.4 1.08

0045 Imperial Valley 1979 1015 2316 6.5 6.6 6.9 UNAM/UCSD 6616 Aeropuerto Mexicali 8.5 I-D IMPVALL\H-AEP-UP 0.05 0.142 5.6 2.31

00 00 C
IMPVALL\H-AEP045 0.05 0.327 42.8 10.10

IMPVALL\H-AEP315 0.05 0.260 24.9 3.81
UNAM/UCSD 6618 Agrarias 12.9 IQD
IMPVALL\H-AGDWN 0.20 0.835 11.1 5.17
00
IMPVALL\H-AG003 0.05 0.370 35.6 10.02

IMPVALL\H-AG273 0.05 0.221 42.4 11.70
USGS 5054 Bonds Corner 2.5 AQD
IMPVALL\H-BCR-UP 0.10 40.0 0.425 12.2 4.02
00 C
IMPVALL\H-BCR140 0.10 40.0 0.588 45.2 16.78

IMPVALL\H-BCR230 0.10 40.0 0.775 45.9 14.89
USGS 5060 Brawley Airport 8.5 AQD
IMPVALL\H-BRA-UP 0.10 40.0 0.146 8.4 3.49
00 C
IMPVALL\H-BRA225 0.10 40.0 0.160 35.9 22.44

IMPVALL\H-BRA315 0.10 40.0 0.220 38.9 13.46
USGS 5053 Calexico Fire Station 10.6 AQD
IMPVALL\H-CXO-UP 0.10 40.0 0.187 6.7 2.49
00 C
IMPVALL\H-CXO225 0.10 40.0 0.275 21.2 9.02

IMPVALL\H-CXO315 0.20 40.0 0.202 16.0 9.20
USGS 5061 Calipatria Fire Sta 23.8 BQD
IMPVALL\H-CAL-UP 0.10 40.0 0.055 3.9 2.76
00 C
IMPVALL\H-CAL225 0.10 40.0 0.128 15.4 10.91

IMPVALL\H-CAL315 0.10 40.0 0.078 13.3 6.22
UNAM/UCSD 6604 Cerro Prieto 26.5
AVA IMPVALL\H-CPDWN 0.10 0.212 6.8 3.29
00 B
IMPVALL\H-CP147 0.10 0.169 11.6 4.25

IMPVALL\H-CP237 0.10 0.157 18.6 7.95
UNAM/UCSD 6621 Chihuahua 28.7 IQD
IMPVALL\H-CHDWN 0.05 0.218 5.1 1.28
00 C
IMPVALL\H-CH012 0.05 0.270 24.9 9.08

IMPVALL\H-CH282 0.05 0.254 30.1 12.89
USGS 5066 Coachella Canal #4 49.3 AQD
IMPVALL\H-CC4-UP 0.20 40.0 0.038 3.6 0.66
00 C
IMPVALL\H-CC4045 0.20 40.0 0.115 12.5 2.33

IMPVALL\H-CC4135 0.20 40.0 0.128 15.6 2.95
UNAM/UCSD 6622 Compuertas 32.6
IQD IMPVALL\H-CMPDWN 0.20 0.075 2.9 0.98
00 C
IMPVALL\H-CMP015 0.20 0.186 13.9 2.92

IMPVALL\H-CMP285 0.20 0.147 9.5 2.49
UNAM/UCSD 6617 Cucapah 23.6 IQD
IMPVALL\H-QKP-UP 0.05 0.140 3.1 1.37
00 C
IMPVALL\H-QKP085 0.05 0.309 36.3 10.44
UNAM/UCSD 6605 Delta 43.6 IQD
IMPVALL\H-DTADWN 0.05 0.145 14.8 8.62
00 C
IMPVALL\H-DTA262 0.05 0.238 26.0 12.06

IMPVALL\H-DTA352 0.05 0.351 33.0 19.02
CDMG 5154 EC County Center FF 7.6 IDD
IMPVALL\H-ELC-UP 0.10 50.0 0.246 18.1 9.70
00 C
IMPVALL\H-ELC002 0.10 40.0 0.213 37.5 15.98

IMPVALL\H-ELC092 0.10 35.0 0.235 68.8 39.35
CDMG 5155 EC Meloland Overpass FF 0.5
IDD IMPVALL\H-EMO-UP 0.10 50.0 0.248 28.9 8.36
00 C
IMPVALL\H-EMO000 0.10 40.0 0.314 71.7 25.53

IMPVALL\H-EMO270 0.10 50.0 0.296 90.5 31.71
USGS 5056 El Centro Array #1 15.5 AQD
IMPVALL\H-E01-UP 0.10 40.0 0.056 3.8 2.14
00 C
IMPVALL\H-E01140 0.10 40.0 0.139 16.0 9.96

IMPVALL\H-E01230 0.10 40.0 0.134 10.7 6.97
USGS 5115 El Centro Array #2 10.4 IQD
IMPVALL\H-E02-UP 0.10 40.0 0.110 7.6 5.14
00 C
IMPVALL\H-E02140 0.10 40.0 0.315 31.5 14.34

USGS 5057 El Centro Array #3 9.3 AQD

IMPVALL\H-E03-UP 0.10 40.0 0.127 8.7 4.70
00 D

IMPVALL\H-E03140 0.10 40.0 0.266 46.8 18.92

IMPVALL\H-E03230 0.10 40.0 0.221 39.9 23.31

USGS 955 El Centro Array #4 4.2 IQD

IMPVALL\H-E04-UP 0.10 40.0 0.248 16.0 10.66
00 C

IMPVALL\H-E04140 0.10 40.0 0.485 37.4 20.23

IMPVALL\H-E04230 0.10 40.0 0.360 76.6 59.02

USGS 952 El Centro Array #5 1.0 IQD

IMPVALL\H-E05-UP 0.10 40.0 0.537 38.5 19.69
00 C

IMPVALL\H-E05140 0.10 40.0 0.519 46.9 35.35

IMPVALL\H-E05230 0.10 40.0 0.379 90.5 63.03

USGS 5158 El Centro Array #6 1.0 IQD

IMPVALL\H-E06-UP 0.20 40.0 1.655 57.5 26.41
00 C

IMPVALL\H-E06140 0.10 40.0 0.410 64.9 27.69

IMPVALL\H-E06230 0.10 40.0 0.439 109.8 65.89

USGS 5028 El Centro Array #7 0.6 AQD

IMPVALL\H-E07-UP 0.10 40.0 0.544 26.4 9.32
00 C

IMPVALL\H-E07140 0.10 40.0 0.338 47.6 24.68

IMPVALL\H-E07230 0.10 40.0 0.463 109.3 44.74

USGS 5159 El Centro Array #8 3.8 AQD

IMPVALL\H-E08-UP 0.10 40.0 0.439 22.3 11.87
00 C

IMPVALL\H-E08140 0.10 40.0 0.602 54.3 32.32

IMPVALL\H-E08230 0.10 40.0 0.454 49.1 35.59

USGS 412 El Centro Array #10 8.6 AQD

IMPVALL\H-E10-UP 0.10 40.0 0.105 8.8 6.90
00 C

IMPVALL\H-E10050 0.10 40.0 0.171 47.5 31.10

IMPVALL\H-E10320 0.10 40.0 0.224 41.0 19.38

USGS 5058 El Centro Array #11 12.6 AQD

IMPVALL\H-E11-UP 0.10 40.0 0.140 11.1 6.82
00 C

IMPVALL\H-E11140 0.20 40.0 0.364 34.5 16.07

IMPVALL\H-E11230 0.10 40.0 0.380 42.1 18.70
USGS 931 El Centro Array #12 18.2 IQD
IMPVALL\H-E12-UP 0.10 40.0 0.066 6.7 5.31
00 C
IMPVALL\H-E12140 0.10 40.0 0.143 17.6 11.30

IMPVALL\H-E12230 0.10 40.0 0.116 21.8 12.06
USGS 5059 El Centro Array #13 21.9 AQD
IMPVALL\H-E13-UP 0.20 40.0 0.046 3.2 1.67
00 C
IMPVALL\H-E13140 0.20 40.0 0.117 14.7 7.33

IMPVALL\H-E13230 0.20 40.0 0.139 13.0 5.84
USGS 5165 El Centro Differential Array 5.3 IQD
IMPVALL\H-EDA-UP 0.10 40.0 0.707 20.7 11.55
00 C
IMPVALL\H-EDA270 0.10 40.0 0.352 71.2 45.80

IMPVALL\H-EDA360 0.10 40.0 0.480 40.8 14.04
USGS 5055 Holtville Post Office 7.5 AQD
IMPVALL\H-HVP-UP 0.10 40.0 0.230 9.9 5.69
00 C
IMPVALL\H-HVP225 0.10 40.0 0.253 48.8 31.54

IMPVALL\H-HVP315 0.10 40.0 0.221 49.8 31.96
CDMG 724 Niland Fire Station 35.9 AQD
IMPVALL\H-NIL-UP 0.10 40.0 0.034 3.8 2.04
00 C
IMPVALL\H-NIL090 0.10 30.0 0.109 11.9 6.88

IMPVALL\H-NIL360 0.10 40.0 0.069 8.3 5.26
USGS 5051 Parachute Test Site 14.2 AQD
IMPVALL\H-PTS-UP 0.10 40.0 0.159 6.8 4.76
00 B
IMPVALL\H-PTS225 0.10 40.0 0.111 17.8 12.35

IMPVALL\H-PTS315 0.10 40.0 0.204 16.1 9.94
USGS 5052 Plaster City 31.7 AQD
IMPVALL\H-PLS-UP 0.10 40.0 0.026 2.4 0.98
00 C
IMPVALL\H-PLS045 0.10 40.0 0.042 3.2 1.34

IMPVALL\H-PLS135 0.10 40.0 0.057 5.4 1.94

UNAM/UCSD 6619 SAHOP Casa Flores 11.1
I-C IMPVALL\H-SHP-UP 0.20 0.379 9.2 1.53
00 C
IMPVALL\H-SHP000 0.20 0.287 19.6 2.71

IMPVALL\H-SHP270 0.20 0.506 30.9 5.64
USGS 286 Superstition Mtn Camera 26.0
AGA IMPVALL\H-SUP-UP 0.10 40.0 0.077 2.3 1.14
00 B
IMPVALL\H-SUP045 0.10 40.0 0.109 5.2 2.21

IMPVALL\H-SUP135 0.10 40.0 0.195 8.8 2.78
UNAM/UCSD 6610 Victoria 54.1 IQD
IMPVALL\H-VCT-UP 0.05 0.059 1.6 0.68
00 C
IMPVALL\H-VCT075 0.05 0.122 6.4 2.09

IMPVALL\H-VCT345 0.20 0.167 8.3 1.05
CDMG 5169 Westmorland Fire Sta 15.1
ADD IMPVALL\H-WSM-UP 0.10 40.0 0.082 6.8 2.58
00 C
IMPVALL\H-WSM090 0.10 40.0 0.074 21.2 16.59

IMPVALL\H-WSM180 0.10 40.0 0.110 21.9 10.00

0046 Imperial Valley 1979 1015 2319 5.2 5.2 USGS 5054 Bonds Corner
15.6* AQD IMPVALL\A-BCR-UP 3.00 35.0 0.052 0.9 0.02
00 00 C
IMPVALL\A-BCR140 0.80 30.0 0.084 3.6 0.34

IMPVALL\A-BCR230 0.30 30.0 0.100 8.2 1.42
USGS 5060 Brawley Airport 27.0* AQD
IMPVALL\A-BRA-UP 1.00 40.0 0.026 0.6 0.02
00 C
IMPVALL\A-BRA225 0.80 30.0 0.034 2.0 0.16

IMPVALL\A-BRA315 1.00 30.0 0.067 2.4 0.12
USGS 5053 Calexico Fire Station 15.0* AQD
IMPVALL\A-CXO-UP 0.90 40.0 0.035 0.9 0.05
00 C
IMPVALL\A-CXO225 0.45 30.0 0.116 8.0 0.87

IMPVALL\A-CXO315 0.40 35.0 0.068 5.2 0.51
6605 Delta 52.1* IQD
IMPVALL\A-DLTDWN 1.00 25.0 0.023 0.7 0.04

				00		C		
IMPVALL\A-DLT262	0.80	25.0	0.059	2.6	0.21			
IMPVALL\A-DLT352	0.40	30.0	0.112	5.5	0.84			
				USGS 5056 El Centro Array #1			26.1*	AQD
IMPVALL\A-E01-UP	0.80	40.0	0.027	0.4	0.03			
				00		C		
IMPVALL\A-E01140	0.80	30.0	0.080	3.8	0.39			
IMPVALL\A-E01230	0.70	30.0	0.029	1.1	0.12			
				USGS 5115 El Centro Array #2			20.3*	IQD
IMPVALL\A-E02-UP	0.70	40.0	0.032	0.9	0.06			
				00		C		
IMPVALL\A-E02140	0.60	25.0	0.150	9.5	0.95			
IMPVALL\A-E02230	1.00	40.0	0.072	3.3	0.23			
				USGS 5057 El Centro Array #3			17.9*	AQD
IMPVALL\A-E03-UP	0.60	40.0	0.031	0.6	0.07			
				00		D		
IMPVALL\A-E03140	0.50	33.0	0.179	9.5	0.97			
IMPVALL\A-E03230	0.80	40.0	0.112	4.2	0.30			
				USGS 955 El Centro Array #4			14.4*	IQD
IMPVALL\A-E04-UP	0.60	40.0	0.097	1.2	0.13			
				00		C		
IMPVALL\A-E04140	0.50	40.0	0.262	8.8	0.64			
IMPVALL\A-E04230	0.45	35.0	0.157	9.6	0.65			
				USGS 952 El Centro Array #5			13.8*	IQD
IMPVALL\A-E05-UP	0.50	50.0	0.079	0.8	0.07			
				00		C		
IMPVALL\A-E05140	0.70	35.0	0.238	10.7	0.75			
IMPVALL\A-E05230	0.60	35.0	0.239	13.3	1.06			
				CDMG 942 El Centro Array #6			13.1*	IQD
IMPVALL\A-E06-UP	0.40	50.0	0.080	1.7	0.10			
				00		C		
IMPVALL\A-E06140	0.60	30.0	0.189	12.1	1.15			
IMPVALL\A-E06230	0.35	30.0	0.366	20.8	2.83			
				USGS 5028 El Centro Array #7			13.1*	AQD
IMPVALL\A-E07-UP	0.70	50.0	0.060	0.8	0.06			
				00		C		
IMPVALL\A-E07140	0.60	40.0	0.132	5.0	0.52			

IMPVALL\A-E07230 0.40 40.0 0.192 12.2 1.00
CDMG 958 El Centro Array #8 13.6* AQD
IMPVALL\A-E08-UP 0.60 50.0 0.067 1.1 0.08
00 C
IMPVALL\A-E08140 0.70 45.0 0.120 5.6 0.35

IMPVALL\A-E08230 0.60 45.0 0.145 9.1 0.87
USGS 412 El Centro Array #10 15.1* AQD
IMPVALL\A-E10-UP 0.60 35.0 0.021 0.4 0.06
00 C
IMPVALL\A-E10050 1.00 30.0 0.066 3.2 0.25

IMPVALL\A-E10320 0.50 30.0 0.037 2.9 0.44
USGS 5058 El Centro Array #11 17.2* AQD
IMPVALL\A-E11-UP 0.60 40.0 0.055 1.3 0.08
00 C
IMPVALL\A-E11140 0.70 35.0 0.124 7.3 0.74

IMPVALL\A-E11230 0.45 30.0 0.173 11.1 1.02
USGS 5165 El Centro Diff Array 13.3* IQD
IMPVALL\A-EDA-UP 0.60 40.0 0.097 1.6 0.08
00 C
IMPVALL\A-EDA270 0.60 30.0 0.169 10.1 0.82

IMPVALL\A-EDA360 0.70 30.0 0.135 6.7 0.41
USGS 5055 Holtville Post Office 12.2* AQD
IMPVALL\A-HVP-UP 0.80 40.0 0.044 1.0 0.08
00 C
IMPVALL\A-HVP225 0.60 30.0 0.127 7.3 0.56

IMPVALL\A-HVP315 0.50 30.0 0.211 15.4 2.14

0047 Imperial Valley 1979 1016 0658 5.5 CDMG 5169 Westmorland Fire Sta
11.2* ADD IMPVALL\F-WSM-UP 1.00 50.0 0.115 2.0 0.15
00 00 C
IMPVALL\F-WSM180 0.25 40.0 0.171 11.0 2.83

IMPVALL\F-WSM360 0.70 40.0 0.089 4.7 0.62

0048 Livermore 1980 0124 1900 5.8 5.8 5.8 CDMG 67070 Antioch - 510 G St
20.3 ACD LIVERMOR\A-ANT-UP 0.20 20.0 0.012 1.5 0.47
00 00 B
LIVERMOR\A-ANT270 0.20 13.0 0.051 5.1 0.80

LIVERMOR\A-ANT360 0.20 13.0 0.023 2.6 0.72

CDWR 1265 Del Valle Dam (Toe) 12.9 ABB
LIVERMOR\A-DVD-UP 0.30 30.0 0.083 4.2 1.00
00
LIVERMOR\A-DVD156 0.10 25.0 0.125 9.3 3.15

LIVERMOR\A-DVD246 0.15 20.0 0.229 20.5 3.71
CDMG 57064 Fremont - Mission San Jose 29.8
AMB LIVERMOR\A-FRE-UP 0.13 13.0 0.027 2.3 0.55
LIVERMOR\A-DVD246 0.15 20.0 0.229 20.5 3.71
00 B
LIVERMOR\A-FRE075 0.30 13.0 0.044 4.4 0.85

LIVERMOR\A-FRE345 0.30 20.0 0.055 3.9 0.93
CDMG 58219 Hayward - CSUH Stadium 31.0
BKA LIVERMOR\A-HAY-UP 0.23 25.0 0.020 1.1 0.20
00
LIVERMOR\A-HAY146 0.20 25.0 0.072 4.1 0.75

LIVERMOR\A-HAY236 0.20 25.0 0.057 2.7 0.40
CDMG 57134 San Ramon Fire Station 21.7
ABB LIVERMOR\A-SRM-UP 0.30 20.0 0.016 2.0 0.40
00 C
LIVERMOR\A-SRM070 0.15 15.0 0.058 3.3 1.00

LIVERMOR\A-SRM340 0.20 15.0 0.040 4.0 1.24
CDMG 57187 San Ramon - Eastman Kodak 17.6
ABB LIVERMOR\A-KOD-UP 0.40 30.0 0.042 2.8 0.45
00 C
LIVERMOR\A-KOD180 0.08 20.0 0.154 18.9 6.13

LIVERMOR\A-KOD270 0.20 20.0 0.076 6.1 1.69
CDMG 57063 Tracy - Sewage Treatm Plant 37.3
BQC LIVERMOR\A-TRA-UP 0.20 20.0 0.021 3.1 0.98
00 C
LIVERMOR\A-TRA093 0.15 20.0 0.050 7.5 2.35

LIVERMOR\A-TRA183 0.08 15.0 0.073 7.6 1.81

0049 Livermore 1980 0127 0233 5.4 5.4 5.5 CDMG 67067 Antioch - 510 G St
30.9 ACD LIVERMOR\B-ANT-UP 0.30 15.0 0.015 0.8 0.11
00 00 B
LIVERMOR\B-ANT270 0.20 15.0 0.112 5.8 0.62

LIVERMOR\B-ANT360 0.30 12.0 0.050 2.7 0.32
CDWR 1265 Del Valle Dam (Toe) 12.9 ABB

LIVERMOR\B-DVD-UP 0.30 30.0 0.028 0.8 0.13
00
LIVERMOR\B-DVD156 0.40 25.0 0.043 1.8 0.14

LIVERMOR\B-DVD246 0.30 20.0 0.041 2.8 0.33
CDMG 57064 Fremont - Mission San Jose 29.8
AMB LIVERMOR\B-FRE-UP 0.20 15.0 0.017 1.5 0.23
00 B
LIVERMOR\B-FRE075 0.30 15.0 0.035 4.7 0.79

LIVERMOR\B-FRE345 0.25 12.0 0.038 3.3 0.52
CDMG 58219 Hayward - CSUH Stadium 31.0
BKA LIVERMOR\B-HAY-UP 0.60 25.0 0.014 0.9 0.09
00
LIVERMOR\B-HAY146 0.30 20.0 0.053 4.5 0.58

LIVERMOR\B-HAY236 0.15 20.0 0.028 1.4 0.30
CDMG 57T01 Livermore - Fagundas Ranch 3.6
ABB LIVERMOR\B-LFA-UP 0.30 30.0 0.098 2.5 0.17
00 C
LIVERMOR\B-LFA270 0.30 25.0 0.258 9.6 0.55

LIVERMOR\B-LFA360 0.30 20.0 0.233 11.4 1.18
CDMG 57T02 Livermore - Morgan Terr Park 8.0
ABA LIVERMOR\B-LMO-UP 0.40 30.0 0.078 4.1 0.39
00 B
LIVERMOR\B-LMO265 0.25 30.0 0.198 11.7 1.02

LIVERMOR\B-LMO355 0.40 30.0 0.252 9.8 1.30
CDMG 57187 San Ramon - Eastman Kodak 17.6
ABB LIVERMOR\B-KOD-UP 0.30 30.0 0.037 4.0 0.50
00 C
LIVERMOR\B-KOD180 0.20 25.0 0.301 19.1 2.82

LIVERMOR\B-KOD270 0.25 25.0 0.097 5.6 0.62
CDMG 57134 San Ramon Fire Station 21.7
ABB LIVERMOR\B-SRM-UP 0.40 20.0 0.022 1.5 0.21
00 C
LIVERMOR\B-SRM070 0.40 15.0 0.049 3.4 0.43

LIVERMOR\B-SRM340 0.30 15.0 0.059 4.2 0.46

0050 Anza 1980 0225 1047 4.9 4.7 USGS 5160 Anza Fire Station
12.1* AHC ANZA\AZF-UP 0.50 30.0 0.037 1.4 0.91
00 00 A

ANZA\AZF225 0.25 25.0 0.065 3.3 0.36

ANZA\AZF315

0.60 25.0 0.066 2.6 0.16

USGS 5044 Anza - Pinyon Flat 13.0* IGA

ANZA\PFT-UP 0.40 30.0 0.046 1.1 0.08

00 A ANZA\PFT045

0.40 30.0 0.110 2.5 0.11

ANZA\PFT135

0.20 25.0 0.131 5.1 0.49

USGS 5045 Anza - Terwilliger Valley 5.8* I-A

ANZA\TVY-UP 2.00 30.0 0.068 1.7 0.06

00 A ANZA\TVY045

1.10 30.0 0.131 3.9 0.17

ANZA\TVY135

1.30 30.0 0.081 1.7 0.06

USGS 5049 Borrego Air Ranch 40.6* AAA

ANZA\BAR-UP 0.90 40.0 0.014 0.6 0.06

00 B ANZA\BAR225

0.60 25.0 0.047 2.6 0.28

ANZA\BAR315

0.70 25.0 0.036 1.2 0.10

USGS 5047 Rancho De Anza 19.6* IHC

ANZA\RDA-UP 0.60 40.0 0.052 1.6 0.12

00 B ANZA\RDA045

0.60 40.0 0.097 6.7 0.55

ANZA\RDA135

0.50 35.0 0.092 6.0 0.45

0051 Mammoth Lakes 1980 0525 1634 6.3 6.1 6.1 CDMG 54099 Convict Creek 9.0* AQD MAMMOTH\I-CVK-UP 0.20 41.0 0.388 20.5 5.93

03 00

MAMMOTH\I-CVK090 0.10 60.0 0.416 23.3 4.66

MAMMOTH\I-CVK180 0.10 50.0 0.442 23.1 5.42

CDMG 54214 Long Valley dam (Upr L Abut) 15.5*

IVA MAMMOTH\I-LVD-UP 0.10 40.0 0.123 8.4 1.72

00

MAMMOTH\I-LVD000 0.10 57.0 0.430 23.6 7.52

MAMMOTH\I-LVD090 0.10 50.0 0.271 13.9 3.06

CDMG 54301 Mammoth Lakes H. S. 14.0*

BVD MAMMOTH\I-MLS-UP 0.10 60.0 0.253 11.2 2.55

00

MAMMOTH\I-MLS270 0.50 44.0 0.321 15.7 1.57

MAMMOTH\I-MLS360 0.50 51.0 0.239 14.4 1.65

0052 Mammoth Lakes 1980 0525 1649 5.7 6.0 CDMG 54099 Convict Creek
16.3* AQD MAMMOTH\J-CVK-UP 0.50 47.0 0.129 9.0 1.05
00 00
MAMMOTH\J-CVK090 0.50 35.0 0.160 11.3 1.95

MAMMOTH\J-CVK180 0.50 35.0 0.178 12.2 2.26
CDMG 54214 Long Valley Dam (Upr L Abut) 24.3*
IVA MAMMOTH\J-LVD-UP 0.50 27.0 0.038 1.5 0.29
00
MAMMOTH\J-LVD000 0.50 40.0 0.194 5.1 0.65

MAMMOTH\J-LVD090 0.50 30.0 0.065 4.4 0.59
CDMG 54301 Mammoth Lakes H. S. 14.2*
BVD MAMMOTH\J-MLS-UP 0.10 60.0 0.264 9.0 1.56
00
MAMMOTH\J-MLS000 0.50 50.0 0.441 22.5 2.28

MAMMOTH\J-MLS270 0.10 52.0 0.390 23.9 2.72

0053 Mammoth Lakes 1980 0525 1944 6.0 6.1 CDMG 54099 Convict Creek
17.4* AQD MAMMOTH\A-CVK-UP 0.20 40.0 0.195 8.5 1.59
00 (6.7) 00
MAMMOTH\A-CVK090 0.08 30.0 0.219 18.5 4.87

MAMMOTH\A-CVK180 0.08 35.0 0.208 16.1 2.29
CDMG 54214 Long Valley Dam (Downst) 19.7*
IVA MAMMOTH\A-LVD-UP 0.30 40.0 0.078 4.4 0.42
00
MAMMOTH\A-LVD000 0.15 40.0 0.107 5.9 1.21

MAMMOTH\A-LVD090 0.20 35.0 0.070 5.5 1.33
CDMG 54214 Long Valley Dam (L Abut) 19.7*
IVA MAMMOTH\A-LVL-UP 0.40 50.0 0.068 4.0 0.45
00
MAMMOTH\A-LVL000 0.35 50.0 0.104 6.6 1.06

MAMMOTH\A-LVL090 0.20 50.0 0.077 5.4 1.69
CDMG 54214 Long Valley Dam (Upr L Abut) 19.7*
IVA MAMMOTH\A-LUL-UP 0.35 35.0 0.119 4.3 0.53
00
MAMMOTH\A-LUL000 0.20 40.0 0.484 14.2 1.77

MAMMOTH\A-LUL090 0.10 40.0 0.188 10.8 3.28

0054 Mammoth Lakes 1980 0525 2035 5.7 5.7 CDMG 54099 Convict Creek
3.0* AQD MAMMOTH\B-CVK-UP 0.20 45.0 0.345 6.2 0.52
00 (5.5) 00
MAMMOTH\B-CVK090 0.20 35.0 0.380 13.3 1.16

MAMMOTH\B-CVK180 0.20 35.0 0.432 21.0 2.31
CDMG 54214 Long Valley Dam (Downst) 14.4*
IVA MAMMOTH\B-LVD-UP 1.00 40.0 0.058 2.1 0.12
00
MAMMOTH\B-LVD000 0.50 30.0 0.089 5.0 0.59

MAMMOTH\B-LVD090 0.30 30.0 0.046 2.3 0.35
CDMG 54214 Long Valley Dam (L Abut) 14.4*
IVA MAMMOTH\B-LVL-UP 0.30 40.0 0.141 5.0 0.36
00
MAMMOTH\B-LVL000 0.50 40.0 0.231 18.3 1.56

MAMMOTH\B-LVL090 0.30 40.0 0.185 8.0 0.93
CDMG 54214 Long Valley Dam (Upr L Abut) 14.4*
IVA MAMMOTH\B-LUL-UP 0.30 35.0 0.146 5.0 0.36
00
MAMMOTH\B-LUL000 0.50 40.0 0.245 18.5 1.56

MAMMOTH\B-LUL090 0.40 40.0 0.195 8.0 0.82

0055 Mammoth Lakes 1980 0526 1858 6.1 5.8 CDMG 54099 Convict Creek
10.5* AQD MAMMOTH\K-CVK-UP 0.50 40.0 0.050 3.8 0.46
00 00
MAMMOTH\K-CVK090 0.50 30.0 0.133 7.8 0.82

MAMMOTH\K-CVK180 0.20 31.0 0.099 3.8 0.41
CDMG 54214 Long Valley Dam (Upr L Abut) 17.5*
IVA MAMMOTH\K-LVD-UP 0.50 30.0 0.027 1.2 0.22
00
MAMMOTH\K-LVD000 0.50 31.0 0.110 6.0 0.63

MAMMOTH\K-LVD090 0.50 23.0 0.071 6.3 0.65

0056 Mammoth Lakes 1980 0527 1451 6.0 6.2 6.0 CDMG 54100 Benton
48.6* AQD MAMMOTH\L-BEN-UP 0.50 40.0 0.064 3.1 0.52
03 00
MAMMOTH\L-BEN270 0.50 38.0 0.109 7.0 0.98

MAMMOTH\L-BEN360 0.50 33.0 0.175 11.2 1.18
CDMG 54424 Bishop 43.7* CAA

MAMMOTH\L-BPL-UP 0.20 50.0 0.084 3.0 0.77
00
MAMMOTH\L-BPL070 0.20 40.0 0.091 5.5 1.48

MAMMOTH\L-BPL160 0.20 40.0 0.114 5.3 1.41
CDMG 54099 Convict Creek 18.6* AQD
MAMMOTH\L-CVK-UP 0.10 50.0 0.188 9.6 1.62
00
MAMMOTH\L-CVK090 0.10 40.0 0.266 19.1 1.74

MAMMOTH\L-CVK180 0.10 40.0 0.316 16.2 3.19
CDMG 54214 Long Valley Dam (Upr L Abut) 20.0*
IVA MAMMOTH\L-LVD-UP 0.50 43.0 0.314 11.7 1.08
00
MAMMOTH\L-LVD000 0.50 40.0 0.921 28.9 3.17

MAMMOTH\L-LVD090 0.20 51.0 0.408 33.9 6.41

0057 Mammoth Lakes 1980 0527 1901 4.9 5.0 USGS 43 Fish & Game (FIS)
5.5* IQD MAMMOTH\C-FIS-UP 0.20 50.0 0.038 1.7 0.21
00 00
MAMMOTH\C-FIS000 0.20 50.0 0.103 4.2 0.37

MAMMOTH\C-FIS090 0.11 40.0 0.098 5.2 0.73
USC 3 Green Church 4.7* IQD
MAMMOTH\C-XGRVRT 0.80 30.0 0.079 2.2 0.19
00
MAMMOTH\C-XGR056 0.25 25.0 0.167 10.7 1.05

MAMMOTH\C-XGR146 0.30 30.0 0.170 12.1 1.06
USC 35 Long Valley Fire Sta 4.3* ACC
MAMMOTH\C-XLVVRT 0.70 20.0 0.018 1.0 0.10
00
MAMMOTH\C-XLV000 0.70 25.0 0.022 1.7 0.24

MAMMOTH\C-XLV270 0.50 20.0 0.031 1.6 0.15
USC 36 Mammoth Elem School 8.7* AAB
MAMMOTH\C-XMMVRT 0.60 20.0 0.015 1.3 0.19
00
MAMMOTH\C-XMM000 0.80 20.0 0.050 2.8 0.26

MAMMOTH\C-XMM270 0.60 15.0 0.078 5.0 0.30
USC 34 USC Cash Baugh Ranch 9.9* AQD
MAMMOTH\C-XCBVRT 0.45 20.0 0.025 1.9 0.22
00

MAMMOTH\C-XCB180 0.50 25.0 0.031 3.3 0.46

MAMMOTH\C-XCB270 0.40 20.0 0.038 2.9 0.36
USC 37 USC McGee Creek 1.8* AAD
MAMMOTH\C-XMG000 0.70 30.0 0.325 8.6 0.53
00
MAMMOTH\C-XMG270 0.90 25.0 0.131 5.0 0.33

0058 Mammoth Lakes 1980 0531 1516 4.9 5.1 USGS 41 Cashbaugh (CBR)
11.8* IQD MAMMOTH\D-CBR-UP 0.40 80.0 0.093 4.1 0.22
00 00
MAMMOTH\D-CBR000 0.10 60.0 0.106 2.6 0.28

MAMMOTH\D-CBR090 0.20 60.0 0.134 6.7 0.40
USGS 42 Convict Lakes (CON) 8.7* IQB
MAMMOTH\D-CONDWN 1.00 70.0 0.114 2.0 0.12
00
MAMMOTH\D-CON180 0.80 60.0 0.196 4.0 0.29

MAMMOTH\D-CON270 0.70 70.0 0.206 6.5 0.44
USGS 43 Fish & Game (FIS) 7.7* IQD
MAMMOTH\D-FIS-UP 0.60 60.0 0.081 3.3 0.27
00
MAMMOTH\D-FIS000 0.50 60.0 0.281 9.5 0.52

MAMMOTH\D-FIS090 0.30 50.0 0.145 10.2 1.19
USGS 44 Hot Creek (HCF) 9.9* IQD
MAMMOTH\D-HFC-UP 0.35 100.0 0.049 1.8 0.20
00
USC 35 Long Valley Fire Sta 8.9* AAC
MAMMOTH\D-XLVVRT 0.80 20.0 0.019 0.7 0.06
00
MAMMOTH\D-XLV000 0.60 20.0 0.026 1.2 0.17

MAMMOTH\D-XLV270 0.50 20.0 0.031 1.5 0.12
USC 36 Mammoth Elem School 7.3* AAB
MAMMOTH\D-XMMVRT 0.45 30.0 0.045 1.5 0.29
00
MAMMOTH\D-XMM000 0.30 15.0 0.099 6.1 0.57

MAMMOTH\D-XMM270 0.40 20.0 0.091 6.1 0.51
USC 40 USC Convict Lakes 9.1* AAB
MAMMOTH\D-XCVVRT 0.30 40.0 0.050 1.5 0.16
00
MAMMOTH\D-XCV075 0.50 30.0 0.164 6.0 0.48

MAMMOTH\D-XCV165 0.80 30.0 0.141 2.9 0.20
USC 37 USC McGee Creek 7.4* AAD
MAMMOTH\D-XMGVRT 0.50 30.0 0.179 3.6 0.12
00
MAMMOTH\D-XMG000 1.00 20.0 0.053 13.4 0.44

MAMMOTH\D-XMG270 0.60 30.0 0.184 5.5 0.28

0059 Victoria, Mexico 1980 0609 0328 6.1 6.4 UNAM/UCSD 6604 Cerro Prieto
34.8* AVA VICT\CPE-UP 0.20 62.5 0.304 12.1 4.9
00 00 B VICT\CPE045
0.20 62.5 0.621 31.6 13.2
VICT\CPE315
0.20 62.5 0.587 19.9 9.4
UNAM/UCSD 6621 Chihuahua 36.6*
IQD VICT\CHIDWN 0.20 23.0 0.098 5.5 2.6
00 C VICT\CHI102
0.20 22.0 0.150 24.8 9.2
VICT\CHI192
0.20 27.0 0.092 15.6 9.9
UNAM/UCSD 6617 Cucapah 41.9* IQD
VICT\CUP-UP 0.20 49.0 0.067 10.9 5.1
00 C VICT\CUP085
0.20 44.0 0.092 13.1 5.6
UNAM/UCSD 6619 SAHOP Casa Flores 58.3*
I-C VICT\SHP-UP 0.50 62.5 0.047 2.4 0.5
00 C VICT\SHP010
0.20 28.0 0.101 7.8 2.6
VICT\SHP280
0.20 27.0 0.068 9.0 2.1
UNAM/UCSD 6624 Victoria Hospital Sotano 62.6*
--D VICT\HPB-UP 0.50 62.5 0.024 1.9 0.6
00 VICT\HPB000
0.20 26.0 0.045 5.2 2.5
VICT\HPB270
0.20 62.5 0.032 5.3 1.7

0060 Mammoth Lakes 1980 0611 0441 5.0 USGS 42 Convict Lakes (CON)
7.6* IQB MAMMOTH\H-CONDWN 1.50 80.0 0.091 1.1 0.03
00 00
MAMMOTH\H-CON180 0.80 80.0 0.191 2.4 0.08

MAMMOTH\H-CON270 1.50 70.0 0.183 2.2 0.05
USGS 43 Fish & Game (FIS) 11.2* IQD

MAMMOTH\H-FIS-UP 0.90 50.0 0.029 0.5 0.04
00
MAMMOTH\H-FIS000 0.90 60.0 0.061 1.6 0.07

MAMMOTH\H-FIS090 0.60 50.0 0.055 1.1 0.06
USC 3 Green Church 12.0* IQD
MAMMOTH\H-XGRVRT 1.00 30.0 0.024 0.5 0.03
00
MAMMOTH\H-XGR056 0.60 25.0 0.023 1.5 0.16

MAMMOTH\H-XGR146 0.40 30.0 0.033 1.4 0.14
USGS 44 Hot Creek (HCF) 12.8* IQD
MAMMOTH\H-HCF-UP 0.60 80.0 0.022 0.5 0.05
00
MAMMOTH\H-HCF000 0.60 60.0 0.065 1.3 0.05

MAMMOTH\H-HCF090 0.50 50.0 0.099 1.5 0.10
USC 35 Long Valley Fire Sta 14.2* AAC
MAMMOTH\H-XLVVRT 0.60 20.0 0.004 0.3 0.04
00
MAMMOTH\H-XLV000 0.60 20.0 0.015 0.4 0.06

MAMMOTH\H-XLV270 0.60 20.0 0.006 0.3 0.03
USC 36 Mammoth Elem School 12.3*
AAB MAMMOTH\H-XMM000 0.50 13.0 0.012 0.6 0.06
00
MAMMOTH\H-XMM270 0.80 15.0 0.018 0.8 0.05
USGS 45 McGee Creek (MGE) 11.9* IQC
MAMMOTH\H-MGE-UP 2.00 60.0 0.036 0.7 0.03
00
MAMMOTH\H-MGE000 1.00 70.0 0.066 1.4 0.08

MAMMOTH\H-MGE090 1.00 60.0 0.056 1.2 0.07
USC 40 USC Convict Lakes 9.1* AAB
MAMMOTH\H-XCVVRT 1.00 40.0 0.038 0.4 0.02
00
MAMMOTH\H-XCV075 2.00 30.0 0.030 0.6 0.02

MAMMOTH\H-XCV165 2.00 30.0 0.046 0.6 0.02
USC 52 USC McGee Creek 11.1* AAA
MAMMOTH\H-XMGVRT 1.30 40.0 0.090 0.8 0.03
00
MAMMOTH\H-XMG117 0.70 35.0 0.078 1.6 0.10

MAMMOTH\H-XMG207 1.00 25.0 0.211 3.0 0.09

0061 Trinidad 1980 1108 1027 CDMG 1498 Rio Dell Overpass, E Ground
71.9* APC TRINIDAD\B-RDE-UP 0.10 35.0 0.050 4.1 4.06
99 99 B
TRINIDAD\B-RDE000 0.10 45.0 0.163 9.0 9.02

TRINIDAD\B-RDE270 0.10 40.0 0.134 9.9 9.89
CDMG 1498 Rio Dell Overpass, FF 71.9* IPC
TRINIDAD\B-RDL-UP 0.10 30.0 0.028 2.7 2.72
99 B
TRINIDAD\B-RDL000 0.10 30.0 0.061 7.0 7.03

TRINIDAD\B-RDL270 0.10 30.0 0.147 8.5 8.48
CDMG 1498 Rio Dell Overpass, W Ground 71.9*
APC TRINIDAD\B-RDW-UP 0.10 40.0 0.041 3.7 3.66
99 B
TRINIDAD\B-RDW000 0.10 40.0 0.150 9.1 9.09

TRINIDAD\B-RDW270 0.10 40.0 0.156 11.2 11.20

0062 Taiwan SMART1(5) 1981 0129 6.3 5.7 25 SMART1 C00
21.0 IZD SMART1\05C00DN 0.20 25.0 0.043 1.7 0.40
02 99
SMART1\05C00EW 0.50 25.0 0.096 6.0 0.91

SMART1\05C00NS 0.20 25.0 0.114 13.4 1.93
26 SMART1 I06 21.0 IZD
SMART1\05I06DN 0.50 25.0 0.032 1.3 0.28
99
SMART1\05I06EW 0.50 25.0 0.090 4.2 0.81

SMART1\05I06NS 0.50 25.0 0.077 9.8 1.50
27 SMART1 I12 21.0 IZD
SMART1\05I12DN 0.20 25.0 0.060 2.0 0.46
99
SMART1\05I12EW 0.10 25.0 0.140 5.1 1.20

SMART1\05I12NS 0.10 25.0 0.113 12.5 2.14
28 SMART1 M01 21.0 IZD
SMART1\05M01DN 0.10 25.0 0.095 2.4 0.35
99
SMART1\05M01EW 0.10 25.0 0.082 4.8 1.00

SMART1\05M01NS 0.10 25.0 0.178 15.9 2.19
29 SMART1 M07 21.0 IZD
SMART1\05M07DN 0.20 25.0 0.050 1.5 0.34

99
SMART1\05M07EW 0.10 25.0 0.111 5.6 0.86

SMART1\05M07NS 0.10 25.0 0.109 10.9 1.74
30 SMART1 O01 21.0 IZD
SMART1\05O01DN 0.20 25.0 0.032 1.3 0.35
99
SMART1\05O01EW 0.20 25.0 0.089 6.4 0.91

SMART1\05O01NS 0.20 25.0 0.115 13.7 2.23
31 SMART1 O07 21.0 IZD
SMART1\05O07DN 0.20 25.0 0.028 1.9 0.42
99
SMART1\05O07EW 0.10 25.0 0.086 6.9 0.92

SMART1\05O07NS 0.20 25.0 0.080 11.7 2.18

0063 Westmorland 1981 0426 1209 5.8 5.6 USGS 5060 Brawley Airport
22.0* AQD WESTMORL\BRA-UP 0.60 40.0 0.101 2.2 0.23
00 00 C
WESTMORL\BRA225 0.15 40.0 0.169 12.7 3.09

WESTMORL\BRA315 0.70 33.0 0.171 5.8 0.48
CDMG 724 Niland Fire Station 19.4* AQD
WESTMORL\NIL-UP 0.25 40.0 0.126 2.9 0.47
00 C
WESTMORL\NIL000 0.30 33.0 0.105 5.6 0.69

WESTMORL\NIL090 0.30 33.0 0.176 6.6 0.80
USGS 5051 Parachute Test Site 24.1* AQD
WESTMORL\PTS-UP 0.35 35.0 0.157 11.2 1.78
00 B
WESTMORL\PTS225 0.10 30.0 0.242 39.2 26.88

WESTMORL\PTS315 0.10 33.0 0.155 26.6 12.97
USGS 5062 Salton Sea Wildlife Ref. 10.1* AQD
WESTMORL\WLF-UP 0.25 50.0 0.214 4.8 1.08
00 D
WESTMORL\WLF225 0.07 33.0 0.199 16.4 4.45

WESTMORL\WLF315 0.08 33.0 0.176 12.3 2.33
USGS 286 Superstition Mtn Camera 26.5*
AGA WESTMORL\SUP-UP 0.70 35.0 0.045 1.3 0.09
00 B

WESTMORL\SUP045 0.70 30.0 0.071 3.6 0.24

WESTMORL\SUP135 0.70 30.0 0.116 5.0 0.49
CDMG 5169 Westmorland Fire Sta 13.3*
ADD WESTMORL\WSM-UP 0.90 40.0 0.838 10.4 0.46
00 C
WESTMORL\WSM090 0.08 40.0 0.368 48.7 10.61

WESTMORL\WSM180 0.05 40.0 0.496 34.4 10.89

0064 Mammoth Lakes 1983 0107 0138 5.2 CDMG 54099 Convict Creek
9.5* AQD MAMMOTH\F-CVK-UP 0.20 40.0 0.097 7.9 1.65
99 99
MAMMOTH\F-CVK090 0.15 30.0 0.165 14.4 2.05

MAMMOTH\F-CVK180 0.15 30.0 0.153 18.7 2.88

0065 Mammoth Lakes 1983 0107 0324 5.4 CDMG 54099 Convict Creek
10.8* AQD MAMMOTH\G-CVK-UP 0.30 40.0 0.073 5.7 0.75
99 99
MAMMOTH\G-CVK090 0.40 30.0 0.150 8.4 0.97

MAMMOTH\G-CVK180 0.20 30.0 0.101 7.1 1.50

0066 Coalinga 1983 0502 2342 6.4 6.7 6.5 CDMG 46314 Cantua Creek School
25.5 AHD COALINGA\H-CAK-UP 0.20 26.0 0.094 5.1 1.86
03 99
COALINGA\H-CAK270 0.20 23.0 0.227 23.6 5.83

COALINGA\H-CAK360 0.20 23.0 0.281 25.8 3.71
CDMG 36452 Parkfield - Cholame 1E 41.6
IHD COALINGA\H-C01-UP 0.50 30.0 0.059 6.6 1.82
99
COALINGA\H-C01000 0.20 20.0 0.090 10.8 2.66

COALINGA\H-C01090 0.20 20.0 0.089 15.2 2.64
CDMG 36230 Parkfield - Cholame 2E 40.5 IJB
COALINGA\H-TM2-UP 0.50 26.0 0.017 2.3 0.52
99
COALINGA\H-TM2000 0.50 23.0 0.026 2.9 0.62

COALINGA\H-TM2090 0.20 22.0 0.037 5.4 1.40
CDMG 36228 Parkfield - Cholame 2WA 42.8
IHD COALINGA\H-C02-UP 0.20 23.0 0.044 5.1 1.39
99

COALINGA\H-C02000 0.20 22.0 0.109 11.3 2.60

COALINGA\H-C02090 0.20 26.0 0.114 9.6 1.79

CDMG 36450 Parkfield - Cholame 3E 38.4

IMA COALINGA\H-TM3-UP 0.20 26.0 0.024 3.0 0.60
99

COALINGA\H-TM3000 0.20 23.0 0.044 4.4 1.61

COALINGA\H-TM3090 0.20 22.0 0.056 6.5 1.75

CDMG 36410 Parkfield - Cholame 3W 43.9

IHC COALINGA\H-C03-UP 0.20 27.0 0.034 4.5 1.46
99

COALINGA\H-C03000 0.20 21.0 0.098 7.6 1.86

COALINGA\H-C03090 0.20 24.0 0.084 8.3 1.41

CDMG 36412 Parkfield - Cholame 4AW 46.0

IHC COALINGA\H-C4A-UP 0.50 33.0 0.022 2.0 0.50
99

COALINGA\H-C4A000 0.20 21.0 0.047 5.0 0.90

COALINGA\H-C4A090 0.20 20.0 0.078 8.0 1.32

CDMG 36411 Parkfield - Cholame 4W 44.7

IHC COALINGA\H-C04-UP 0.20 30.0 0.041 3.5 0.87
99

COALINGA\H-C04000 0.20 21.0 0.136 11.3 1.79

COALINGA\H-C04090 0.20 23.0 0.136 9.1 1.42

CDMG 36227 Parkfield - Cholame 5W 47.3

IHC COALINGA\H-C05-UP 0.50 30.0 0.034 2.3 1.14
99 C

COALINGA\H-C05270 0.20 22.0 0.147 10.8 1.07

COALINGA\H-C05360 0.20 22.0 0.131 10.0 1.28

CDMG 36451 Parkfield - Cholame 6W 49.0

IHC COALINGA\H-C06-UP 0.20 30.0 0.037 3.2 0.62
99

COALINGA\H-C06000 0.50 21.0 0.126 11.0 1.34

COALINGA\H-C06090 0.20 28.0 0.102 9.9 1.26

CDMG 36226 Parkfield - Cholame 8W 50.7

IQD COALINGA\H-C08-UP 0.20 27.0 0.024 3.3 0.90
99 C

COALINGA\H-C08000 0.20 23.0 0.098 8.6 1.53

COALINGA\H-C08270 0.50 21.0 0.100 8.0 1.25

CDMG 36229 Parkfield - Cholame 12W 55.2

IQD COALINGA\H-C12-UP 0.20 30.0 0.023 3.0 1.08

99

COALINGA\H-C12270 0.20 23.0 0.040 4.2 1.01

COALINGA\H-C12360 0.20 21.0 0.053 5.5 1.57

CDMG 36407 Parkfield - Fault Zone 1 40.4 IHD

COALINGA\H-COW-UP 0.20 31.0 0.040 8.6 2.45

99

COALINGA\H-COW000 0.20 20.0 0.194 23.3 7.82

COALINGA\H-COW090 0.20 21.0 0.111 17.8 4.79

CDMG 36413 Parkfield - Fault Zone 2 37.9 IHD

COALINGA\H-Z02-UP 0.50 33.0 0.039 3.8 0.94

99

COALINGA\H-Z02000 0.20 22.0 0.116 22.7 6.05

COALINGA\H-Z02090 0.20 25.0 0.133 19.7 4.40

CDMG 36408 Parkfield - Fault Zone 3 36.4 IHD

COALINGA\H-COH-UP 0.10 31.0 0.049 6.0 2.32

99

COALINGA\H-COH000 0.10 27.0 0.140 13.7 4.76

COALINGA\H-COH090 0.10 22.0 0.164 24.5 4.94

CDMG 36414 Parkfield - Fault Zone 4 34.3 IPB

COALINGA\H-Z04-UP 0.20 30.0 0.046 6.2 2.29

99

COALINGA\H-Z04000 0.20 22.0 0.067 12.6 3.36

COALINGA\H-Z04090 0.20 28.0 0.120 20.4 4.43

CDMG 36454 Parkfield - Fault Zone 6 32.8 IPB

COALINGA\H-Z06-UP 0.20 31.0 0.026 5.0 1.74

99

COALINGA\H-Z06000 0.20 24.0 0.055 9.1 3.85

COALINGA\H-Z06090 0.20 24.0 0.056 11.6 3.19

CDMG 36431 Parkfield - Fault Zone 7 31.0 IQC

COALINGA\H-Z07-UP 0.20 31.0 0.054 7.8 1.88

99

COALINGA\H-Z07000 0.20 30.0 0.122 21.1 7.34

COALINGA\H-Z07090 0.20 30.0 0.119 14.9 3.36

CDMG 36449 Parkfield - Fault Zone 8 29.6 IMB

COALINGA\H-Z08-UP 0.20 29.0 0.054 4.9 1.66

99

COALINGA\H-Z08000 0.20 21.0 0.131 17.3 4.21

COALINGA\H-Z08090 0.20 27.0 0.116 14.2 1.71

CDMG 36443 Parkfield - Fault Zone 9 31.9 IPB

COALINGA\H-Z09-UP 0.20 30.0 0.026 3.8 1.61

99

COALINGA\H-Z09000 0.20 23.0 0.057 9.4 2.91

COALINGA\H-Z09090 0.20 28.0 0.050 8.9 2.46

CDMG 36444 Parkfield - Fault Zone 10 30.4

IQD COALINGA\H-Z10-UP 0.20 26.0 0.043 5.8 2.57

99

COALINGA\H-Z10000 0.20 24.0 0.073 15.3 7.05

COALINGA\H-Z10090 0.20 21.0 0.131 16.1 3.15

CDMG 36453 Parkfield - Fault Zone 11 28.4

IMB COALINGA\H-Z11-UP 0.20 28.0 0.042 4.8 1.80

99

COALINGA\H-Z11000 0.20 21.0 0.097 11.9 2.35

COALINGA\H-Z11090 0.20 28.0 0.087 6.6 1.83

CDMG 36138 Parkfield - Fault Zone 12 29.5 IHC

COALINGA\H-PRK-UP 0.20 27.0 0.070 7.9 2.10

99

COALINGA\H-PRK090 0.20 20.0 0.110 12.1 3.26

COALINGA\H-PRK180 0.20 20.0 0.112 14.6 5.69

CDMG 36456 Parkfield - Fault Zone 14 29.9 IHC

COALINGA\H-Z14-UP 0.10 30.0 0.097 11.4 4.13

99

COALINGA\H-Z14000 0.20 23.0 0.282 40.9 8.10

COALINGA\H-Z14090 0.10 23.0 0.274 28.3 5.10

CDMG 36445 Parkfield - Fault Zone 15 29.9 IQB

COALINGA\H-Z15-UP 0.20 24.0 0.084 10.4 2.08

99

COALINGA\H-Z15000 0.20 20.0 0.168 21.2 4.91

COALINGA\H-Z15090 0.20 22.0 0.117 14.1 2.94

CDMG 36457 Parkfield - Fault Zone 16 28.1 IQC

COALINGA\H-Z16-UP 0.20 30.0 0.061 6.5 1.92

99

COALINGA\H-Z16000 0.20 26.0 0.195 17.7 3.48

COALINGA\H-Z16090 0.20 27.0 0.122 12.0 1.83

```
                                        CDMG 36415 Parkfield - Gold Hill 1W      46.5
IHD  COALINGA\H-PG1-UP  0.20  30.0  0.035   4.7   1.53
                                          99
COALINGA\H-PG1000  0.20  24.0  0.119  16.7   4.54

COALINGA\H-PG1090  0.20  22.0  0.065  10.1   2.57
                                        CDMG 36421 Parkfield - Gold Hill 2E      32.3   IQD
 COALINGA\H-GH2-UP  0.20  32.0  0.035   3.3   0.90
                                          99
COALINGA\H-GH2000  0.20  30.0  0.072   6.5   1.73

COALINGA\H-GH2090  0.20  30.0  0.076   7.6   1.40
                                        CDMG 36416 Parkfield - Gold Hill 2W      36.6   IPB
 COALINGA\H-PG2-UP  0.20  32.0  0.036   4.4   1.58
                                          99
COALINGA\H-PG2000  0.20  21.0  0.083  11.4   3.72

COALINGA\H-PG2090  0.20  20.0  0.074  11.7   2.64
                                        CDMG 36439 Parkfield - Gold Hill 3E      29.2   IQD
 COALINGA\H-GH3-UP  0.20  30.0  0.054   8.4   1.50
                                          99
COALINGA\H-GH3000  0.20  26.0  0.094  11.0   2.87

COALINGA\H-GH3090  0.20  27.0  0.072   6.4   1.56
                                        CDMG 36420 Parkfield - Gold Hill 3W      38.8   IPB
 COALINGA\H-PG3-UP  0.20  36.0  0.067   7.5   1.77
                                          99
COALINGA\H-PG3000  0.20  30.0  0.137  11.0   2.76

COALINGA\H-PG3090  0.20  30.0  0.122   9.0   1.74
                                        CDMG 36433 Parkfield - Gold Hill 4W      41.0   IPB
 COALINGA\H-PG4-UP  0.20  30.0  0.029   4.9   1.53
                                          99
COALINGA\H-PG4000  0.20  31.0  0.056   8.1   2.28

COALINGA\H-PG4090  0.20  30.0  0.097   6.3   1.86
                                        CDMG 36434 Parkfield - Gold Hill 5W      43.7   IPB
 COALINGA\H-PG5-UP  0.20  30.0  0.034   3.9   1.53
                                          99
COALINGA\H-PG5000  0.20  26.0  0.073   8.5   2.62

COALINGA\H-PG5090  0.20  30.0  0.054   5.9   1.55
                                        CDMG 36432 Parkfield - Gold Hill 6W      48.0   IPC
 COALINGA\H-PG6-UP  0.20  30.0  0.037   3.2   0.80
                                          99
```

COALINGA\H-PG6000 0.20 30.0 0.059 8.2 1.55

COALINGA\H-PG6090 0.20 30.0 0.069 7.4 1.21

CDMG 36422 Parkfield - Stone Corral 2E 34.4

IMA COALINGA\H-SC2-UP 0.20 35.0 0.033 4.0 1.65
99

COALINGA\H-SC2000 0.20 25.0 0.061 8.1 2.65

COALINGA\H-SC2090 0.20 30.0 0.095 7.1 1.75

CDMG 36437 Parkfield - Stone Corral 3E 31.8

IMA COALINGA\H-SC3-UP 0.20 30.0 0.033 3.6 1.06
99

COALINGA\H-SC3000 0.20 23.0 0.151 8.7 2.92

COALINGA\H-SC3090 0.20 30.0 0.106 8.1 1.39

CDMG 36438 Parkfield - Stone Corral 4E 29.6

IMA COALINGA\H-SC4-UP 0.20 26.0 0.030 3.0 0.89
99

COALINGA\H-SC4000 0.20 21.0 0.063 8.2 2.33

COALINGA\H-SC4090 0.20 22.0 0.072 6.7 1.39

CDMG 36455 Parkfield - Vineyard Cany 1E 26.7

IQC COALINGA\H-PV1-UP 0.20 26.0 0.082 10.4 3.03
99

COALINGA\H-PV1000 0.20 24.0 0.167 20.9 5.03

COALINGA\H-PV1090 0.20 23.0 0.230 27.6 6.21

CDMG 36448 Parkfield - Vineyard Cany 1W 29.5

IQC COALINGA\H-VC1-UP 0.50 28.0 0.068 6.1 1.49
99

COALINGA\H-VC1000 0.50 26.0 0.081 8.2 2.12

COALINGA\H-VC1090 0.50 23.0 0.087 11.1 2.41

CDMG 36177 Parkfield - Vineyard Cany 2E 24.6

IFA COALINGA\H-PGD065 0.20 30.0 0.161 16.2 3.30
99

CDMG 36447 Parkfield - Vineyard Cany 2W 30.7

IHC COALINGA\H-VC2-UP 0.20 40.0 0.057 5.2 1.54
99

COALINGA\H-VC2000 0.20 30.0 0.073 7.4 1.47

COALINGA\H-VC2090 0.20 30.0 0.083 6.9 1.22

CDMG 36176 Parkfield - Vineyard Cany 3W 32.3

IPA COALINGA\H-VYC-UP 0.20 31.0 0.056 6.2 1.75
99

COALINGA\H-VYC020 0.20 30.0 0.098 11.8 2.95

COALINGA\H-VYC110 0.20 30.0 0.137 13.5 2.57

CDMG 36446 Parkfield - Vineyard Cany 4W 34.6

IMB COALINGA\H-VC4-UP 0.20 30.0 0.024 2.8 0.64

99

COALINGA\H-VC4000 0.20 30.0 0.064 6.5 1.37

COALINGA\H-VC4090 0.20 27.0 0.046 4.2 0.95

CDMG 36440 Parkfield - Vineyard Cany 5W 37.1

IHB COALINGA\H-VC5-UP 0.20 30.0 0.048 4.9 1.09

99

COALINGA\H-VC5090 0.20 21.0 0.062 6.9 1.47

CDMG 36441 Parkfield - Vineyard Cany 6W 41.0

IPC COALINGA\H-VC6-UP 0.20 30.0 0.038 4.8 1.62

COALINGA\H-VC6000 0.20 25.0 0.054 9.5 2.76

COALINGA\H-VC6090 0.20 27.0 0.076 5.4 1.82

USGS 1162 Pleasant Valley P.P. - bldg 8.5 AHD

COALINGA\H-PPB-UP 0.20 30.0 0.206 12.3 2.53

01

COALINGA\H-PPB045 0.20 20.0 0.380 32.4 6.43

COALINGA\H-PPB135 0.20 22.0 0.285 19.1 2.59

USGS 1162 Pleasant Valley P.P. - yard 8.5 AHD

COALINGA\H-PPS-UP 0.20 31.0 0.353 16.1 2.35

01

COALINGA\H-PPS045 0.20 40.0 0.592 60.2 8.77

COALINGA\H-PPS135 0.20 31.0 0.551 36.4 3.96

CDMG 46175 Slack Canyon 27.7 IGA

COALINGA\H-SCN-UP 0.20 21.0 0.053 6.8 2.42

01

COALINGA\H-SCN045 0.20 21.0 0.166 16.1 4.19

COALINGA\H-SCN315 0.20 21.0 0.153 13.3 2.72

0067 Coalinga 1983 0509 0249 5.0 5.3 4.7 USGS 4 ALP (temp)

19.9* IQD COALINGA\A-ALP-UP 0.30 35.0 0.018 1.0 0.09

02 99

COALINGA\A-ALP085 0.20 30.0 0.040 2.9 0.39

COALINGA\A-ALP355 0.20 30.0 0.021 1.5 0.16

USGS 1607 Anticline Ridge Free-field 12.6* IPA

COALINGA\A-ATC-UP 2.00 30.0 0.250 4.3 0.11
99
COALINGA\A-ATC270 0.40 30.0 0.576 16.5 0.96

COALINGA\A-ATC360 0.50 40.0 0.673 20.4 1.18
USGS 1607 Anticline Ridge Pad 12.6* APA
COALINGA\A-ATP-UP 0.60 45.0 0.380 8.1 0.22
99
COALINGA\A-ATP270 0.50 40.0 0.452 16.8 0.85

COALINGA\A-ATP360 0.60 35.0 0.412 23.2 1.27
CDMG 46T05 Anticline Ridge - Palmer Ave 12.6*
APB COALINGA\A-CPL-UP 1.00 30.0 0.049 1.7 0.10
99
COALINGA\A-CPL000 0.35 25.0 0.292 12.1 0.78

COALINGA\A-CPL090 0.40 25.0 0.216 9.2 0.64
USGS 1606 Burnett Construction 17.7* AHD
COALINGA\A-BNT-UP 0.40 30.0 0.077 2.0 0.15
99
COALINGA\A-BNT270 0.50 30.0 0.095 3.5 0.37

COALINGA\A-BNT360 0.40 25.0 0.095 4.5 0.35
CDMG 46T04 CHP (temp) 16.7* AHD
COALINGA\A-CHP-UP 0.80 30.0 0.047 1.7 0.12
99
COALINGA\A-CHP000 0.40 25.0 0.145 5.2 0.47

COALINGA\A-CHP090 0.50 20.0 0.114 6.0 0.33
CDMG 46T07 Harris Ranch - Hdqtrs (temp) 17.8*
AHD COALINGA\A-XCH-UP 0.70 20.0 0.071 1.8 0.10
99
COALINGA\A-XCH000 0.70 20.0 0.080 2.9 0.13

COALINGA\A-XCH090 0.40 15.0 0.154 6.4 0.67
USGS 5 LLN (temp) 13.1* IPA
COALINGA\A-LLN-UP 0.40 50.0 0.059 2.2 0.18
99
COALINGA\A-LLN000 0.30 50.0 0.130 7.8 0.49

COALINGA\A-LLN090 0.30 40.0 0.076 3.8 0.38
USGS 6 MIT (temp) 12.5* IQD
COALINGA\A-MIT-UP 0.40 50.0 0.158 3.8 0.30
99
COALINGA\A-MIT010 0.15 50.0 0.130 4.6 0.48

USGS 1604 Oil City 13.3* APB

COALINGA\A-OLC-UP 0.70 40.0 0.098 3.0 0.13
99

COALINGA\A-OLC270 0.50 30.0 0.250 9.3 0.71

COALINGA\A-OLC360 0.70 30.0 0.284 9.3 0.39

USGS 1608 Oil Fields Fire Station 12.1* APA

COALINGA\A-OLF-UP 0.70 30.0 0.147 2.9 0.11
99

COALINGA\A-OLF270 0.70 30.0 0.247 7.9 0.34

COALINGA\A-OLF360 0.60 30.0 0.178 5.0 0.26

CDMG 46T06 Oil fields - Skunk Hollow 12.7*

APA COALINGA\A-COL-UP 1.00 35.0 0.082 1.7 0.07
99

COALINGA\A-COL000 0.50 35.0 0.313 9.3 0.41

COALINGA\A-COL090 0.50 25.0 0.343 10.8 0.56

USGS 1609 Palmer Ave 12.7* APB

COALINGA\A-PLM-UP 1.00 30.0 0.095 2.1 0.13
99

COALINGA\A-PLM270 0.50 15.0 0.202 7.5 0.34

COALINGA\A-PLM360 0.30 20.0 0.289 13.6 0.75

USBR 1162 Pleasant Valley P.P. - yard 14.6*

AHD COALINGA\A-PVP-UP 0.40 30.0 0.102 2.6 0.16
99

COALINGA\A-PVP045 0.20 30.0 0.078 9.5 1.04

COALINGA\A-PVP135 0.50 25.0 0.220 9.3 0.50

USGS 7 SGT (temp) 14.1* IZA

COALINGA\A-SGT-UP 0.30 50.0 0.071 2.7 0.15
99

COALINGA\A-SGT080 0.10 60.0 0.139 5.8 0.70

COALINGA\A-SGT350 0.10 60.0 0.244 7.4 0.68

USGS 1605 Skunk Hollow 12.4* APA

COALINGA\A-SKH-UP 0.70 35.0 0.077 1.9 0.12
99

COALINGA\A-SKH270 0.30 25.0 0.171 6.1 0.49

COALINGA\A-SKH360 0.30 25.0 0.104 4.6 0.37

USGS 8 SUB (temp) 14.5* IQD

COALINGA\A-SUB-UP 0.40 50.0 0.079 2.0 0.15
99

COALINGA\A-SUB000 0.15 35.0 0.116 5.9 0.85

COALINGA\A-SUB090 0.10 40.0 0.216 12.2 1.42
CDMG 1703 Sulphur Baths (temp) 20.3*
APA COALINGA\A-CSU-UP 0.50 20.0 0.005 0.3 0.06
99
COALINGA\A-CSU000 0.60 15.0 0.008 0.5 0.04

COALINGA\A-CSU090 0.80 20.0 0.004 0.3 0.03
USGS 9 TRA (temp) 14.9* IQD
COALINGA\A-TRA-UP 0.10 50.0 0.079 4.9 0.36
99
COALINGA\A-TRA000 0.20 35.0 0.131 9.4 0.97

COALINGA\A-TRA090 0.20 30.0 0.088 6.9 0.70
USGS 10 VEW (temp) 12.6* IPA
COALINGA\A-VEW-UP 0.08 60.0 0.065 1.5 0.19
99
COALINGA\A-VEW005 0.05 60.0 0.146 8.7 1.09

COALINGA\A-VEW095 0.05 60.0 0.121 7.8 0.75
USGS 11 YUB (temp) 20.1* IQD
COALINGA\A-YUB080 0.60 40.0 0.034 1.3 0.10
99
COALINGA\A-YUB350 0.40 40.0 0.022 0.9 0.07

0068 Coalinga 1983 0611 0309 5.3 5.2 5.4 USGS 1606 Burnett Construction
10.5* AHD COALINGA\B-BNT-UP 0.20 30.0 0.083 4.1 0.80
02 99
COALINGA\B-BNT270 0.15 25.0 0.165 8.0 2.43

COALINGA\B-BNT360 0.15 20.0 0.191 10.0 1.91
CDMG 46T04 CHP (temp) 10.0* AHD
COALINGA\B-CHP-UP 0.20 15.0 0.028 3.8 0.76
99
COALINGA\B-CHP000 0.10 15.0 0.055 5.8 1.96

COALINGA\B-CHP090 0.10 15.0 0.061 4.7 1.95
CDMG 1703 Sulphur Baths (temp) 9.7* APA
COALINGA\B-CSU-UP 0.20 20.0 0.034 3.5 1.47
99
COALINGA\B-CSU000 0.20 20.0 0.044 5.1 2.29

COALINGA\B-CSU090 0.20 20.0 0.037 4.5 1.64

0069 Coalinga 1983 0709 0740 5.2 5.4 4.9 USGS 1607 Anticline Ridge Free-Field
11.0* IPA COALINGA\C-ATC-UP 0.30 40.0 0.115 3.7 0.43
02 (5.3) 99
COALINGA\C-ATC270 0.30 30.0 0.330 16.1 1.20

COALINGA\C-ATC360 0.45 40.0 0.275 8.9 0.46
USGS 1607 Anticline Ridge Pad 11.0* APA
COALINGA\C-ATP-UP 0.30 30.0 0.137 4.7 0.34
99
COALINGA\C-ATP270 0.40 30.0 0.378 16.1 1.03

COALINGA\C-ATP360 0.40 25.0 0.261 9.2 0.53
USGS 1606 Burnett Construction 15.9* AHD
COALINGA\C-BNT-UP 0.40 30.0 0.074 3.2 0.26
99
COALINGA\C-BNT270 0.50 30.0 0.119 6.6 0.50

COALINGA\C-BNT360 0.40 30.0 0.149 7.7 0.52
CDMG 46T04 CHP (temp) 14.9* AHD
COALINGA\C-CHP-UP 0.45 30.0 0.079 2.4 0.22
99
COALINGA\C-CHP000 0.30 25.0 0.204 8.0 0.62

COALINGA\C-CHP090 0.30 25.0 0.171 5.4 0.38
USGS 1604 Oil City 10.0* APB
COALINGA\C-OLC-UP 0.40 30.0 0.210 4.6 0.29
99
COALINGA\C-OLC270 0.20 30.0 0.387 13.8 1.59

COALINGA\C-OLC360 0.20 30.0 0.370 12.4 0.89
USGS 1608 Oil Fields Fire Station 11.9* IPA
COALINGA\C-OLF-UP 0.25 30.0 0.062 2.0 0.22
99
COALINGA\C-OLF270 0.60 30.0 0.088 3.0 0.26

COALINGA\C-OLF360 0.12 30.0 0.096 4.1 0.71
USGS 1608 Oil Fields Fire Stn - Pad 11.9* APA
COALINGA\C-OLP-UP 0.40 30.0 0.073 1.9 0.20
99
COALINGA\C-OLP270 0.10 25.0 0.094 3.4 0.53

COALINGA\C-OLP360 0.40 25.0 0.109 4.0 0.32
USGS 1609 Palmer Ave 14.0* APB
COALINGA\C-PLM-UP 0.60 25.0 0.073 2.1 0.10
99

COALINGA\C-PLM270 0.60 20.0 0.109 3.2 0.24

COALINGA\C-PLM360 0.50 20.0 0.211 7.0 0.43
USGS 1605 Skunk Hollow 12.6* APA
COALINGA\C-SKH-UP 0.50 30.0 0.161 3.1 0.19
99
COALINGA\C-SKH270 0.40 30.0 0.187 6.4 0.32

COALINGA\C-SKH360 0.30 20.0 0.141 6.2 0.37
CDMG 1703 Sulphur Baths (temp) 17.0*
APA COALINGA\C-CSU-UP 0.50 30.0 0.041 1.0 0.09
99
COALINGA\C-CSU000 0.35 30.0 0.055 2.2 0.21

COALINGA\C-CSU090 0.40 25.0 0.074 1.5 0.15
USGS 1651 Transmitter Hill 10.4* APA
COALINGA\C-TSM-UP 0.30 30.0 0.114 3.3 0.35
99
COALINGA\C-TSM270 0.20 25.0 0.205 12.0 1.34

COALINGA\C-TSM360 0.30 30.0 0.194 9.9 0.87

0070 Coalinga 1983 0722 0239 5.8 6.0 5.7 USGS 1606 Burnett Construction
10.5 AHD COALINGA\D-BNT-UP 0.10 30.0 0.210 10.2 1.09
02 (5.9) 99
COALINGA\D-BNT270 0.30 30.0 0.269 14.2 2.32

COALINGA\D-BNT360 0.50 25.0 0.323 16.2 1.43
CDMG 46T04 CHP (temp) 10.0 AHD
COALINGA\D-CHP-UP 0.30 30.0 0.204 7.1 1.10
99
COALINGA\D-CHP000 0.40 30.0 0.324 14.4 1.39

COALINGA\D-CHP090 0.30 30.0 0.605 20.7 2.32
USGS 1604 Oil City 8.2 APB
COALINGA\D-OLC-UP 0.60 30.0 0.568 12.5 1.20
99
COALINGA\D-OLC270 0.15 30.0 0.866 42.2 6.14

COALINGA\D-OLC360 0.80 30.0 0.447 24.8 2.23
USGS 1608 Oil Fields Fire Station 10.9 IPA
COALINGA\D-OLF-UP 0.10 30.0 0.135 7.7 2.82
99
COALINGA\D-OLF270 0.20 30.0 0.219 14.0 2.85

COALINGA\D-OLF360 0.10 30.0 0.187 14.8 3.82
USGS 1608 Oil Fields Fire Station Pad 10.9 APA
COALINGA\D-OLP-UP 0.10 30.0 0.152 8.5 3.19
99
COALINGA\D-OLP270 0.05 30.0 0.217 18.1 2.90

COALINGA\D-OLP360 0.08 25.0 0.210 14.8 4.38
USGS 1609 Palmer Ave 12.2 APB
COALINGA\D-PLM-UP 0.20 25.0 0.201 6.9 1.35
99
COALINGA\D-PLM270 0.06 20.0 0.272 12.8 3.31

COALINGA\D-PLM360 0.09 20.0 0.290 21.5 3.31
USBR 1162 Pleasant Valley P.P. - FF 17.4 AHD
COALINGA\D-PVP-UP 0.07 30.0 0.128 5.9 2.50
99
COALINGA\D-PVP270 0.03 30.0 0.228 21.6 6.24

COALINGA\D-PVP360 0.10 30.0 0.408 18.9 5.64
USBR 1162 Pleasant Valley P.P. - yard 17.4 AHD
COALINGA\D-PVY-UP 0.40 30.0 0.316 12.9 0.92
99
COALINGA\D-PVY045 0.08 30.0 0.602 34.8 8.06

COALINGA\D-PVY135 0.10 30.0 0.327 12.1 2.33
USGS 1605 Skunk Hollow 12.2 APA
COALINGA\D-SKH-UP 0.10 40.0 0.230 10.0 2.89
99
COALINGA\D-SKH270 0.07 30.0 0.375 16.4 6.23

COALINGA\D-SKH360 0.10 30.0 0.233 18.9 2.65
CDMG 1703 Sulphur Baths (temp) 9.7 APA
COALINGA\D-CSU-UP 0.30 30.0 0.082 4.1 0.69
99
COALINGA\D-CSU000 0.30 25.0 0.141 5.5 0.79

COALINGA\D-CSU090 0.30 25.0 0.127 6.3 0.66
USGS 1651 Transmitter Hill 9.2 APA
COALINGA\D-TSM-UP 0.10 40.0 0.394 11.0 3.60
99
COALINGA\D-TSM270 0.10 30.0 0.840 44.1 6.80

COALINGA\D-TSM360 0.08 40.0 1.083 39.7 5.41

0071 Coalinga 1983 0722 0343 4.9 5.0 CDMG 46T04 CHP (temp)

12.1* AHD COALINGA\E-CHP-UP 0.70 30.0 0.118 3.1 0.17
02 99
COALINGA\E-CHP000 0.50 25.0 0.148 5.7 0.43

COALINGA\E-CHP090 0.30 25.0 0.202 8.2 0.74
CDMG 1703 Sulphur Baths (temp) 13.7*
APA COALINGA\E-CSU-UP 0.20 20.0 0.029 1.1 0.17
99
COALINGA\E-CSU000 0.50 20.0 0.039 1.6 0.21

COALINGA\E-CSU090 0.20 20.0 0.030 1.0 0.16

0072 Coalinga 1983 0725 2231 5.2 5.3 5.1 CDMG 46T04 CHP (temp)
12.7* AHD COALINGA\F-CHP-UP 0.30 40.0 0.332 8.4 0.61
02 (5.1) 99
COALINGA\F-CHP000 0.30 40.0 0.431 18.7 1.21

COALINGA\F-CHP090 0.10 40.0 0.733 37.6 5.24
CDMG 1703 Sulphur Baths (temp) 14.7*
APA COALINGA\F-CSU-UP 0.40 30.0 0.139 6.5 0.32
99
COALINGA\F-CSU000 0.30 30.0 0.152 8.5 1.27

COALINGA\F-CSU090 0.30 25.0 0.230 10.9 0.76

0073 Trinidad offshore 1983 0824 1336 5.5 5.7 CDMG 1498 Rio Dell Overpass, E Ground 67.6* APC TRINIDAD\RDE-UP 0.30 30.0 0.030 1.6 0.43
99 99 B
TRINIDAD\RDE000 0.15 30.0 0.194 8.5 0.82

TRINIDAD\RDE270 0.30 30.0 0.145 6.4 4.93
CDMG 1498 Rio Dell Overpass, W Ground 67.6*
APC TRINIDAD\RDW-UP 0.50 40.0 0.033 1.8 1.62
99 B
TRINIDAD\RDW000 0.40 40.0 0.166 6.5 0.56

TRINIDAD\RDW270 0.20 35.0 0.128 4.6 0.84

0074 Coalinga 1983 0909 0916 5.3 5.3 5.4 CDMG 46T04 CHP (temp)
13.7* AHD COALINGA\G-CHP-UP 0.80 30.0 0.030 0.8 0.07
00 99
COALINGA\G-CHP000 0.90 20.0 0.023 1.0 0.09

COALINGA\G-CHP090 0.90 20.0 0.033 1.3 0.07
CDMG 1703 Sulphur Baths (temp) 18.4*

APA COALINGA\G-CSU-UP 0.80 20.0 0.016 0.6 0.04
99
COALINGA\G-CSU000 0.80 15.0 0.014 0.6 0.06

COALINGA\G-CSU090 0.80 15.0 0.016 0.6 0.06

0075 Taiwan SMART1(25) 1983 0921 6.8 6.5 25 SMART1 C00
83.0 IZD SMART1\25C00EW 0.20 25.0 0.028 4.2 0.91
03 99
SMART1\25C00NS 0.20 25.0 0.028 3.5 1.16
32 SMART1 E01 83.0 IZD
SMART1\25E01DN 0.50 25.0 0.013 1.8 0.31
99
SMART1\25E01EW 0.20 25.0 0.028 --- 0.96

SMART1\25E01NS 0.20 25.0 0.028 4.1 0.71
33 SMART1 E02 83.0 IZD
SMART1\25E02DN 0.10 25.0 0.005 0.5 0.20
99
SMART1\25E02EW 0.10 25.0 0.020 1.4 0.30

SMART1\25E02NS 0.10 25.0 0.022 2.2 0.41
62 SMART1 I01 83.0 IZD
SMART1\25I01DN 0.10 25.0 0.008 1.5 0.40
99
SMART1\25I01EW 0.10 25.0 0.023 3.9 0.87

SMART1\25I01NS 0.10 25.0 0.037 4.6 0.85
61 SMART1 I07 83.0 IZD
SMART1\25I07DN 0.10 25.0 0.009 1.4 0.43
99
SMART1\25I07EW 0.10 25.0 0.035 3.8 0.79

SMART1\25I07NS 0.10 25.0 0.032 4.0 0.97
28 SMART1 M01 83.0 IZD
SMART1\25M01DN 0.10 25.0 0.005 0.8 ----
99
SMART1\25M01EW 0.10 25.0 0.020 2.7 0.67

SMART1\25M01NS 0.10 25.0 0.039 5.0 0.82
60 SMART1 M06 83.0 IZD
SMART1\25M06DN 0.10 25.0 0.010 1.7 0.40
99
SMART1\25M06EW 0.10 25.0 0.021 2.8 ----

SMART1\25M06NS 0.10 25.0 0.031 4.3 1.10
30 SMART1 O01 83.0 IZD
SMART1\25O01DN 0.10 25.0 0.007 0.9 ----
99
SMART1\25O01EW 0.50 25.0 0.028 3.2 0.52
SMART1\25O01NS 0.10 25.0 0.027 2.8 0.69
31 SMART1 O07 83.0 IZD
SMART1\25O07DN 0.10 25.0 0.015 1.6 ----
99
SMART1\25O07EW 0.10 25.0 0.025 4.2 1.42
SMART1\25O07NS 0.10 25.0 0.026 3.3 1.10
0076 Morgan Hill 1984 0424 2115 6.2 6.2 6.1 CDMG 57066 Agnews State Hospital
29.4 AQD MORGAN\AGW-UP 0.20 18.0 0.016 3.2 1.56
00 C
00
MORGAN\AGW240 0.20 14.0 0.032 5.0 2.33
MORGAN\AGW330 0.20 13.0 0.032 5.5 2.05
USGS 1652 Anderson Dam (Downstream) 2.6
AFA MORGAN\AND-UP 0.10 45.0 0.204 9.8 1.81
00 B
MORGAN\AND250 0.10 30.0 0.423 25.3 4.58
MORGAN\AND340 0.10 38.0 0.289 27.6 6.33
CDMG 58375 APEEL 1 - Redwood City 54.1
IQE MORGAN\A01-UP 0.50 28.0 0.016 0.8 0.16
00 D
MORGAN\A01040 0.20 21.0 0.046 3.4 0.66
MORGAN\A01310 0.20 23.0 0.068 3.9 0.63
USGS/CDMG 1180 APEEL 1E - Hayward 51.8
IHD MORGAN\A1E000 0.20 22.0 0.041 2.6 0.75
00 B
MORGAN\A1E090 0.20 19.0 0.027 3.1 0.61
CDMG 47125 Capitola 38.1 AQD
MORGAN\CAP-UP 0.20 35.0 0.045 2.1 0.39
00 C
MORGAN\CAP042 0.20 30.0 0.099 4.9 0.61
MORGAN\CAP132 0.20 28.0 0.142 8.1 1.62
CDMG 57007 Corralitos 22.7 APD
MORGAN\CLS-UP 0.20 27.0 0.040 4.0 0.54
00 B

MORGAN\CLS220 0.20 24.0 0.081 6.4 1.17

MORGAN\CLS310 0.20 26.0 0.109 10.8 2.13

CDMG 57217 Coyote Lake Dam (SW Abut) 0.1

IFA MORGAN\CYC-UP 0.10 50.0 0.388 15.6 2.65

00

MORGAN\CYC195 0.10 39.0 0.711 51.6 12.00

MORGAN\CYC285 0.10 45.0 1.298 80.8 9.63

CDMG 57067 Fremont - Mission San Jose 31.4

AMB MORGAN\FMS-UP 0.50 21.0 0.018 1.3 0.40

00 B

MORGAN\FMS075 0.50 21.0 0.025 2.4 0.76

MORGAN\FMS345 0.20 18.0 0.021 3.2 1.03

CDMG 47379 Gilroy Array #1 16.2 IFA

MORGAN\G01-UP 0.10 33.0 0.092 3.3 1.07

00 A

MORGAN\G01230 0.10 29.0 0.069 2.9 1.26

MORGAN\G01320 0.10 40.0 0.098 2.9 1.02

CDMG 47380 Gilroy Array #2 15.1 IQD

MORGAN\G02-UP 0.20 37.0 0.578 10.8 0.92

00 C

MORGAN\G02000 0.20 31.0 0.162 5.1 1.42

MORGAN\G02090 0.10 37.0 0.212 12.6 2.10

CDMG 47381 Gilroy Array #3 14.6 IHD

MORGAN\G03-UP 0.10 42.0 0.395 9.9 1.22

00 C

MORGAN\G03000 0.10 37.0 0.194 11.2 2.41

MORGAN\G03090 0.10 32.0 0.200 12.7 3.45

CDMG 57382 Gilroy Array #4 12.8 AHD

MORGAN\G04-UP 0.10 39.0 0.408 11.8 1.70

00 C

MORGAN\G04270 0.10 25.0 0.224 19.3 4.33

MORGAN\G04360 0.10 27.0 0.348 17.4 3.11

CDMG 57383 Gilroy Array #6 11.8 IKA

MORGAN\G06-UP 0.10 30.0 0.405 14.1 1.86

00 B

MORGAN\G06000 0.10 35.0 0.222 11.4 2.45

MORGAN\G06090 0.10 27.0 0.292 36.7 6.12

			CDMG 57425 Gilroy Array #7				14.0	AHB
MORGAN\GMR-UP	0.10	40.0	0.428	5.4	0.93			
			00			C		
MORGAN\GMR000	0.10	31.0	0.190	7.4	2.06			
MORGAN\GMR090	0.10	30.0	0.113	6.0	1.79			
			CDMG 47006 Gilroy Gavilan Coll.				16.2	AFB
MORGAN\GIL-UP	0.50	42.0	0.081	2.3	0.41			
			00			B		
MORGAN\GIL067	0.10	30.0	0.114	3.6	0.87			
MORGAN\GIL337	0.10	30.0	0.095	2.9	0.93			
			CDMG 57191 Halls Valley				3.4	IFB
MORGAN\HVR-UP	0.20	28.0	0.110	12.2	1.25			
			00			C		
MORGAN\HVR150	0.20	26.0	0.156	12.5	1.84			
MORGAN\HVR240	0.20	30.0	0.312	39.4	7.66			
			USGS 1028 Hollister City Hall				32.5	CHD
MORGAN\HCA-UP	0.20	25.0	0.118	3.9	1.07			
			00			C		
MORGAN\HCA001	0.20	19.0	0.071	7.4	1.60			
MORGAN\HCA271	0.20	24.0	0.071	9.0	3.81			
			USGS 1656 Hollister Diff. Array				28.3	IQD
MORGAN\HDA-UP	0.20	24.0	0.222	7.0	0.81			
			00					
MORGAN\HDA165	0.20	29.0	0.089	8.7	1.72			
MORGAN\HDA255	0.20	23.0	0.088	11.9	1.89			
			USGS 1656 Hollister Diff Array #1				28.3	IQD
MORGAN\HD1-UP	0.10	35.0	0.213	6.2	0.90			
			00					
MORGAN\HD1165	0.20	33.0	0.095	9.7	1.53			
MORGAN\HD1255	0.20	30.0	0.088	11.6	1.76			
			USGS 1656 Hollister Diff Array #3				28.3	IQD
MORGAN\HD3-UP	0.10	35.0	0.243	8.9	0.98			
			00					
MORGAN\HD3165	0.10	30.0	0.078	7.2	1.47			
MORGAN\HD3255	0.20	30.0	0.081	10.0	1.90			
			USGS 1656 Hollister Diff Array #4				28.3	IQD
MORGAN\HD4-UP	0.10	35.0	0.282	9.8	1.03			
			00					

MORGAN\HD4165 0.10 30.0 0.098 10.3 1.68

MORGAN\HD4255 0.20 30.0 0.092 10.2 1.90

USGS 1656 Hollister Diff Array #5 28.3 IQD

MORGAN\HD5-UP 0.20 35.0 0.250 8.0 1.10

00

MORGAN\HD5165 0.20 30.0 0.098 10.3 2.00

MORGAN\HD5255 0.20 30.0 0.101 11.6 1.88

CDMG 56012 Los Banos 64.4 AHD

MORGAN\LBN-UP 0.50 20.0 0.011 1.0 0.50

00 C

MORGAN\LBN090 0.50 18.0 0.051 5.8 1.75

MORGAN\LBN180 0.50 18.0 0.057 8.3 1.89

CDMG 1377 San Juan Bautista 30.3 AQD

MORGAN\SJB-UP 0.10 21.0 0.052 2.7 1.35

00 B

MORGAN\SJB213 0.10 21.0 0.044 4.3 1.73

MORGAN\SJB303 0.10 21.0 0.036 4.4 1.52

USGS 1655 San Justo Dam (L Abut) 34.9 FPD

MORGAN\SJL-UP 0.50 32.0 0.033 2.2 0.52

00

MORGAN\SJL270 0.20 29.0 0.081 6.5 2.59

MORGAN\SJL360 0.20 30.0 0.070 5.1 1.86

USGS 1655 San Justo Dam (R Abut) 34.9

FPD MORGAN\SJR-UP 0.20 25.0 0.044 2.8 1.04

00

MORGAN\SJR270 0.20 24.0 0.078 7.0 3.07

MORGAN\SJR360 0.20 23.0 0.060 5.8 2.16

CDMG 58235 Saratoga - WVC E Wall 28.7

AQD MORGAN\WVE000 0.50 30.0 0.098 4.6 0.61

00

CDMG 58235 Saratoga - WVC NE Corner 28.7

AQD MORGAN\WNE270 0.20 30.0 0.041 3.5 0.99

00

CDMG 58235 Saratoga - WVC SE Corner 28.7

AQD MORGAN\WSE270 0.50 30.0 0.045 3.1 0.88

00

CDMG 58223 SF Intern. Airport 71.2 AHD

MORGAN\SFO-UP 0.50 32.0 0.018 0.8 0.28

00 C

MORGAN\SFO050 0.50 26.0 0.048 3.2 0.40

MORGAN\SFO320 0.50 24.0 0.048 2.7 0.47
CDMG 58135 UCSC Lick Observatory 44.1
AKB MORGAN\LOB-UP 0.50 22.0 0.031 1.2 0.32
00 E
MORGAN\LOB050 0.50 21.0 0.039 2.0 0.29

MORGAN\LOB320 0.50 22.0 0.076 3.6 0.62

0077 Bishop (Rnd Val) 1984 1123 1912 5.8 5.5 5.7 USGS 1661 McGee Creek - Surface
19.0* IQC ROUNDVAL\MCG-UP 2.00 15.0 0.106 2.2 0.05
00 00
ROUNDVAL\MCG270 1.50 40.0 0.088 1.8 0.07

ROUNDVAL\MCG360 1.00 40.0 0.128 2.2 0.07

0078 Taiwan SMART1(33) 1985 0612 6.5 5.8 25 SMART1 C00
45.0 IZD SMART1\33C00DN 0.20 25.0 0.021 0.9 0.16
99 99
SMART1\33C00EW 0.20 25.0 0.083 3.9 ----

SMART1\33C00NS 0.20 25.0 0.051 3.1 ----
62 SMART1 I01 45.0 IZD
SMART1\33I01DN 0.50 25.0 0.025 0.9 0.15
99
SMART1\33I01EW 0.50 25.0 0.142 5.6 0.37

SMART1\33I01NS 0.50 25.0 0.070 3.5 0.28
61 SMART1 I07 45.0 IZD
SMART1\33I07DN 0.20 25.0 0.014 0.6 0.25
99
SMART1\33I07EW 0.20 25.0 0.055 2.8 0.41

SMART1\33I07NS 0.20 25.0 0.040 2.2 0.29
28 SMART1 M01 45.0 IZD
SMART1\33M01DN 0.20 25.0 0.015 0.6 ----
99
SMART1\33M01EW 0.20 25.0 0.031 2.0 ----

SMART1\33M01NS 0.20 25.0 0.052 2.3 ----
29 SMART1 M07 45.0 IZD
SMART1\33M07DN 0.20 25.0 0.021 0.7 0.20
99
SMART1\33M07EW 0.20 25.0 0.095 4.8 0.58

SMART1\33M07NS 0.20 25.0 0.050 3.1 0.81
30 SMART1 O01 45.0 IZD
SMART1\33O01DN 0.50 25.0 0.014 0.4 ----
99
SMART1\33O01EW 0.50 25.0 0.063 2.0 0.25

SMART1\33O01NS 0.50 25.0 0.052 2.1 0.31
31 SMART1 O07 45.0 IZD
SMART1\33O07DN 0.20 25.0 0.014 0.9 ----
99
SMART1\33O07EW 0.20 25.0 0.057 2.9 1.00

SMART1\33O07NS 0.20 25.0 0.048 2.8 0.85

0079 Nahanni, Canada 1985 1223 6.8 6.9 6097 Site 1 6.0
IZA NAHANNI\S1-UP 0.20 62.5 2.086 40.5 12.12
03 01
NAHANNI\S1010 0.05 62.5 0.978 46.0 9.67
NAHANNI\S1280
0.05 62.5 1.096 46.1 14.58
6098 Site 2 8.0 IZA
NAHANNI\S2240 0.10 62.5 0.489 29.3 7.61
01
NAHANNI\S2330 0.05 62.5 0.323 33.1 6.54
6099 Site 3 16.0 IZA
NAHANNI\S3-UP 0.05 62.5 0.140 6.8 3.02
02
NAHANNI\S3270 0.10 62.5 0.148 6.1 3.13
NAHANNI\S3360
0.05 62.5 0.139 3.3 1.06

0080 Hollister 1986 0126 1920 5.4 5.5 USGS 1656 Hollister Diff Array #1
16.9* IQD HOLLISTR\D-HD1-UP 0.20 45.0 0.172 5.2 0.56
00 00
HOLLISTR\D-HD1255 0.10 45.0 0.101 9.3 1.95

HOLLISTR\D-HD1345 0.10 40.0 0.114 8.3 2.29
USGS 1656 Hollister Diff Array #3 16.9* IQD
HOLLISTR\D-HD3-UP 0.30 40.0 0.124 5.0 0.51
00
HOLLISTR\D-HD3255 0.20 35.0 0.106 7.9 1.60

HOLLISTR\D-HD3345 0.40 40.0 0.104 9.2 1.41
USGS 1656 Hollister Diff Array #4 16.9* IQD

HOLLISTR\D-HD4-UP 0.30 40.0 0.073 4.1 0.50
00
HOLLISTR\D-HD4255 0.10 35.0 0.102 9.0 1.91
CDMG 47189 SAGO South - Surface 14.9*
IGA HOLLISTR\D-SG3-UP 0.30 20.0 0.053 3.4 0.53
00 B
HOLLISTR\D-SG3205 0.25 20.0 0.044 5.3 1.27

HOLLISTR\D-SG3295 0.15 15.0 0.090 9.3 1.70

0081 Mt. Lewis 1986 0331 1155 5.6 5.8 5.5 CDMG 57191 Halls Valley
15.5* IFB MTLEWIS\HVR-UP 0.40 20.0 0.072 3.9 0.56
99 99 C
MTLEWIS\HVR000 0.30 20.0 0.140 8.5 1.65

MTLEWIS\HVR090 0.10 20.0 0.159 18.4 4.40

0082 Taiwan SMART1(40) 1986 0520 6.4 6.5 6.4 25 SMART1 C00
64.0 IZD SMART1\40C00DN 0.20 25.0 0.038 4.1 1.21
03 99
SMART1\40C00EW 0.20 25.0 0.172 33.0 6.94

SMART1\40C00NS 0.20 25.0 0.232 19.4 5.07
32 SMART1 E01 64.0 IZD
SMART1\40E01DN 0.20 25.0 0.046 4.9 1.15
99
SMART1\40E01EW 0.20 25.0 0.203 36.5 7.60

SMART1\40E01NS 0.20 25.0 0.183 15.1 3.06
62 SMART1 I01 64.0 IZD
SMART1\40I01DN 0.20 25.0 0.036 4.1 0.86
99
SMART1\40I01EW 0.20 25.0 0.183 32.4 6.90

SMART1\40I01NS 0.20 25.0 0.175 18.1 4.24
61 SMART1 I07 64.0 IZD
SMART1\40I07DN 0.20 25.0 0.041 3.7 ----
99
SMART1\40I07EW 0.20 25.0 0.167 30.6 7.06

SMART1\40I07NS 0.20 25.0 0.150 17.7 4.10
28 SMART1 M01 64.0 IZD
SMART1\40M01DN 0.20 25.0 0.035 3.9 1.05
99
SMART1\40M01EW 0.20 25.0 0.156 26.3 5.75

SMART1\40M01NS 0.20 25.0 0.173 22.8 4.02
29 SMART1 M07 64.0 IZD
SMART1\40M07DN 0.20 25.0 0.039 4.2 0.81
99
SMART1\40M07EW 0.20 25.0 0.182 37.9 8.54

SMART1\40M07NS 0.20 25.0 0.254 23.7 6.01
30 SMART1 O01 64.0 IZD
SMART1\40O01DN 0.20 25.0 0.034 3.3 0.99
99
SMART1\40O01EW 0.20 25.0 0.106 20.7 4.89

SMART1\40O01NS 0.20 25.0 0.160 21.9 3.73
31 SMART1 O07 64.0 IZD
SMART1\40O07DN 0.20 25.0 0.074 4.3 0.83
99
SMART1\40O07EW 0.20 25.0 0.159 28.3 6.83

SMART1\40O07NS 0.20 25.0 0.163 16.1 3.50

0083 N. Palm Springs 1986 0708 0920 6.0 5.9 6.0 USGS 5224 Anza - Red Mountain
45.6 AGA PALMSPR\A01-UP 0.50 50.0 0.072 2.2 0.21
03 (6.0) 99 A
PALMSPR\A01270 0.30 35.0 0.104 5.2 0.62

PALMSPR\A01360 0.60 40.0 0.129 3.4 0.46
USGS 5231 Anza - Tule Canyon 55.4 AGA
PALMSPR\ATL-UP 0.40 30.0 0.049 2.6 0.30
99 B
PALMSPR\ATL270 0.30 30.0 0.110 6.5 0.71

PALMSPR\ATL360 0.35 35.0 0.095 7.5 0.71
USGS 5160 Anza Fire Station 46.7 AHC
PALMSPR\AZF-UP 0.50 50.0 0.056 2.3 0.23
99 A
PALMSPR\AZF225 0.50 40.0 0.099 5.8 0.29

PALMSPR\AZF315 0.60 30.0 0.067 4.0 0.50
USGS 5073 Cabazon 16.3 AHD
PALMSPR\CAB-UP 0.20 45.0 0.363 7.4 0.84
02
PALMSPR\CAB180 0.15 40.0 0.217 7.6 1.96

PALMSPR\CAB270 0.15 40.0 0.212 16.3 2.24

CDOT 754 Colton Interchange - Vault 57.4

BHD PALMSPR\CLI-UP 0.40 30.0 0.017 1.6 0.40
99

PALMSPR\CLI082 0.40 30.0 0.042 3.5 0.59

PALMSPR\CLI352 0.40 30.0 0.065 4.1 0.43

USGS 5157 Cranston Forest Station 35.3 AQB

PALMSPR\CFR-UP 0.70 45.0 0.118 4.0 0.55
99 B

PALMSPR\CFR225 0.60 45.0 0.153 7.4 0.91

PALMSPR\CFR315 0.60 45.0 0.169 11.7 1.14

CDMG 12149 Desert Hot Springs 8.0 AQD

PALMSPR\DSP000 0.50 46.0 0.331 29.5 5.69
01 B

PALMSPR\DSP090 0.50 40.0 0.271 15.7 3.61

USGS 5069 Fun Valley 15.8 AHC

PALMSPR\FVR-UP 0.13 50.0 0.071 3.7 0.67
99 B

PALMSPR\FVR045 0.21 35.0 0.129 6.4 1.06

PALMSPR\FVR135 0.25 40.0 0.119 10.6 1.38

CDMG 12331 Hemet Fire Station 43.3 AQD

PALMSPR\H05-UP 0.50 47.0 0.094 3.1 0.25
99 C

PALMSPR\H05270 0.50 35.0 0.144 4.9 0.73

PALMSPR\H05360 0.50 31.0 0.132 4.9 0.38

CDMG 23321 Hesperia 75.9 AQD

PALMSPR\HES-UP 0.20 39.0 0.033 1.2 0.42
99 B

PALMSPR\HES002 0.20 25.0 0.041 2.3 0.70

PALMSPR\HES092 0.20 30.0 0.037 1.7 0.91

USGS 5043 Hurkey Creek Park 34.9 AQB

PALMSPR\HCP-UP 0.40 50.0 0.097 3.6 0.55
99 B

PALMSPR\HCP045 0.60 50.0 0.240 7.4 0.45

PALMSPR\HCP135 0.50 50.0 0.187 9.1 0.89

CDMG 726 Indio - Coachella Canal 45.7 IQD

PALMSPR\INI-UP 0.50 40.0 0.054 1.8 0.62
99 C

PALMSPR\INI000 0.50 30.0 0.053 5.3 1.18

PALMSPR\INI090 0.50 33.0 0.050 3.2 1.23
USGS 5067 Indio 39.6 AHD
PALMSPR\INO-UP 0.10 40.0 0.087 3.1 1.40
99
PALMSPR\INO225 0.10 35.0 0.064 6.6 2.21
PALMSPR\INO315 0.10 35.0 0.117 12.3 3.62
CDMG 22170 Joshua Tree 29.8 AGC
PALMSPR\JST-UP 0.50 36.0 0.040 3.6 0.60
99 B
PALMSPR\JST000 0.50 30.0 0.052 3.7 0.75
PALMSPR\JST090 0.50 24.0 0.065 3.9 0.48
CDMG 707 Lake Mathews Dike Toe 73.7
AJA PALMSPR\LMR-UP 2.00 40.0 0.039 0.5 0.02
99
PALMSPR\LMR162 1.00 50.0 0.061 1.5 0.08
PALMSPR\LMR252 1.00 35.0 0.046 0.8 0.03
CDMG 22T13 Landers Fire Station 38.2 AQD
PALMSPR\LDR-UP 0.50 40.0 0.055 2.4 0.42
99
PALMSPR\LDR000 0.50 30.0 0.081 4.3 0.42
PALMSPR\LDR090 0.50 30.0 0.098 4.6 0.53
USGS 5071 Morongo Valley 10.1 AHC
PALMSPR\MVF-UP 0.30 50.0 0.395 10.6 1.61
01 B
PALMSPR\MVF045 0.08 50.0 0.218 31.4 8.51
PALMSPR\MVF135 0.08 50.0 0.205 40.9 14.96
CDMG 13198 Murrieta Hot Springs 63.3 IGA
PALMSPR\H01-UP 0.50 28.0 0.032 0.8 0.31
99 A
PALMSPR\H01000 0.50 40.0 0.053 1.8 0.30
PALMSPR\H01090 0.50 40.0 0.049 1.3 0.32
USGS 5070 North Palm Springs 8.2 AHD
PALMSPR\NPS-UP 0.40 40.0 0.435 12.1 1.16
01 B
PALMSPR\NPS210 0.15 20.0 0.594 73.3 11.46
PALMSPR\NPS300 0.23 30.0 0.694 33.8 3.88
CDMG 12025 Palm Springs Airport 16.6 IQD
PALMSPR\PSA000 0.20 50.0 0.158 12.4 2.30

99 C

PALMSPR\PSA090 0.20 60.0 0.187 12.2 2.07

CDMG 12168 Puerta La Cruz 71.9 AQB

PALMSPR\PLC-UP 0.20 44.0 0.035 1.6 0.34

99 B

PALMSPR\PLC258 0.20 38.0 0.075 2.4 0.27

PALMSPR\PLC348 0.20 32.0 0.055 1.8 0.32

CDMG 5253 Rancho Cucamonga ff 82.8

IHD PALMSPR\RNC000 0.20 40.0 0.021 1.3 0.33

99

PALMSPR\RNC090 0.30 40.0 0.019 1.1 0.27

CDMG 13123 Riverside Airport 71.1 AQB

PALMSPR\RVA-UP 0.50 48.0 0.023 0.6 0.14

99 B

PALMSPR\RVA180 0.50 40.0 0.051 1.2 0.14

PALMSPR\RVA270 0.50 42.0 0.040 1.0 0.15

CDMG 12204 San Jacinto - Soboba 32.0

AGC PALMSPR\H08-UP 0.50 50.0 0.203 6.4 0.76

99 B

PALMSPR\H08000 0.50 48.0 0.250 9.6 1.14

PALMSPR\H08090 0.50 49.0 0.239 9.2 1.21

CDMG 12202 San Jacinto Vall. Cem 39.6

AQD PALMSPR\H06-UP 0.50 40.0 0.053 1.8 0.30

99 C

PALMSPR\H06270 0.20 38.0 0.069 3.1 0.99

PALMSPR\H06360 0.20 31.0 0.063 4.4 1.22

USGS 5230 Santa Rosa Mountain 43.8 AGA

PALMSPR\ARS-UP 1.00 50.0 0.051 1.5 0.10

99

PALMSPR\ARS270 1.50 60.0 0.102 2.2 0.10

PALMSPR\ARS360 1.50 60.0 0.103 2.2 0.10

CDMG 12206 Silent Valley - Poppet F 25.8 IGA

PALMSPR\H10-UP 0.50 50.0 0.095 3.0 0.47

02 A

PALMSPR\H10000 0.50 47.0 0.139 3.9 0.55

PALMSPR\H10090 0.50 49.0 0.113 4.0 0.80

USGS 5038 Sunnymead 44.4 BHD

PALMSPR\SNY-UP 0.50 40.0 0.056 2.6 0.33

99

PALMSPR\SNY225 0.30 40.0 0.093 3.9 0.58

PALMSPR\SNY315 0.40 40.0 0.012 5.1 0.56

CDMG 13172 Temecula Fire Station 73.2

AQB PALMSPR\TEM-UP 0.50 27.0 0.028 1.2 0.24

99 C

PALMSPR\TEM000 0.50 25.0 0.121 6.9 0.53

PALMSPR\TEM090 0.50 25.0 0.098 4.6 0.68

USGS 5072 Whitewater Trout Farm 7.3 AHC

PALMSPR\WWT-UP 0.50 40.0 0.471 13.4 1.02

01 A

PALMSPR\WWT180 0.10 40.0 0.492 34.7 6.38

PALMSPR\WWT270 0.15 45.0 0.612 31.5 4.58

CDMG 13199 Winchester Bergman Ran 57.6

AGA PALMSPR\H02-UP 0.50 48.0 0.072 1.6 0.25

99 A

PALMSPR\H02000 0.50 42.0 0.070 1.9 0.19

PALMSPR\H02090 0.50 50.0 0.093 1.8 0.29

CDMG 13201 Winchester Page Bros R 46.8

IQD PALMSPR\H04-UP 0.50 59.0 0.070 2.0 0.34

99

PALMSPR\H04000 0.50 50.0 0.106 3.8 0.69

PALMSPR\H04090 0.50 37.0 0.110 4.3 0.64

0084 Chalfant Valley 1986 0720 1429 5.9 CDMG 54100 Benton

27.0* AQD CHALFANT\B-BEN-UP 0.60 30.0 0.030 1.3 0.14

00 00

CHALFANT\B-BEN270 0.30 30.0 0.061 3.0 0.57

CHALFANT\B-BEN360 0.20 30.0 0.052 2.4 0.47

CDMG 54171 Bishop - LADWP South St 24.0*

AQD CHALFANT\B-LAD-UP 0.10 40.0 0.049 3.3 0.96

00

CHALFANT\B-LAD180 0.11 20.0 0.129 8.5 2.38

CHALFANT\B-LAD270 0.10 20.0 0.094 8.6 3.05

CDMG 54424 Bishop - Paradise Lodge 18.4*

AVA CHALFANT\B-PAR-UP 0.20 40.0 0.067 2.9 0.96

00

CHALFANT\B-PAR070 0.11 30.0 0.046 1.7 0.24

CHALFANT\B-PAR160 0.13 30.0 0.095 6.3 1.69
CDMG 54T03 Lake Crowley - Shehorn Res. 26.0*
AAB CHALFANT\B-SHE-UP 0.70 30.0 0.029 0.9 0.06
00
CHALFANT\B-SHE009 0.16 30.0 0.051 2.2 0.54

CHALFANT\B-SHE099 0.16 25.0 0.031 1.8 0.53
CDMG 54428 Zack Brothers Ranch 11.0*
AAD CHALFANT\B-ZAK-UP 0.11 45.0 0.205 5.4 2.06
00
CHALFANT\B-ZAK270 0.11 40.0 0.285 17.3 4.00

CHALFANT\B-ZAK360 0.10 30.0 0.207 22.3 5.41

0085 Chalfant Valley 1986 0721 1442 6.2 6.3 6.0 CDMG 54100 Benton
37.2 AQD CHALFANT\A-BEN-UP 0.50 30.0 0.127 6.8 1.53
00 00
CHALFANT\A-BEN270 0.10 40.0 0.209 13.6 2.88

CHALFANT\A-BEN360 0.20 33.0 0.177 15.7 3.12
CDMG 54171 Bishop - LADWP South St 9.2
AQD CHALFANT\A-LAD-UP 0.10 40.0 0.140 6.7 2.25
00
CHALFANT\A-LAD180 0.10 40.0 0.248 19.2 7.04

CHALFANT\A-LAD270 0.10 30.0 0.175 19.4 6.72
CDMG 54424 Bishop - Paradise Lodge 23.0
AVA CHALFANT\A-PAR-UP 0.10 50.0 0.127 5.9 1.41
00
CHALFANT\A-PAR070 0.20 30.0 0.165 4.9 2.17

CHALFANT\A-PAR160 0.10 40.0 0.161 12.4 3.26
CDMG 54099 Convict Creek 44.9 AQD
CHALFANT\A-CVC-UP 0.20 40.0 0.036 3.1 1.09
00
CHALFANT\A-CVC000 0.10 30.0 0.060 4.0 1.57

CHALFANT\A-CVC090 0.20 30.0 0.071 3.9 1.07
CDMG 54T03 Lake Crowley - Shehorn Res. 36.0
AAB CHALFANT\A-SHE-UP 0.50 40.0 0.085 3.2 0.49
00
CHALFANT\A-SHE009 0.50 30.0 0.163 7.0 0.77

CHALFANT\A-SHE099 0.50 30.0 0.091 5.5 1.61
CDMG 54214 Long Valley Dam (Downstr) 33.4

IVA CHALFANT\A-LVD-UP 0.10 50.0 0.047 3.4 1.01
00
CHALFANT\A-LVD000 0.10 40.0 0.095 4.8 1.30

CHALFANT\A-LVD090 0.10 40.0 0.056 6.4 2.58
CDMG 54214 Long Valley Dam (L Abut) 33.4
IVA CHALFANT\A-LVL-UP 0.10 43.0 0.075 3.3 1.45
00
CHALFANT\A-LVL000 0.10 50.0 0.082 7.0 1.34

CHALFANT\A-LVL090 0.10 50.0 0.074 7.9 3.06
CDMG 54T04 Mammoth Lakes Sheriff Subst. 50.8
AVB CHALFANT\A-MAM-UP 0.50 23.0 0.026 1.6 0.39
00
CHALFANT\A-MAM020 0.50 20.0 0.042 2.2 0.42

CHALFANT\A-MAM290 0.50 20.0 0.048 2.8 0.54
USGS 661 McGee Creek Surface 36.3 IQC
CHALFANT\A-MCG-UP 0.10 50.0 0.069 1.4 0.52
00
CHALFANT\A-MCG270 0.10 50.0 0.078 2.3 0.65

CHALFANT\A-MCG360 0.10 35.0 0.083 2.4 0.88
CDMG 54101 Tinemaha Res. Free Field 40.6
AVA CHALFANT\A-TIN-UP 0.50 30.0 0.023 1.7 0.54
00
CHALFANT\A-TIN000 0.50 30.0 0.037 3.6 1.12

CHALFANT\A-TIN090 0.50 30.0 0.037 6.3 1.21
CDMG 54428 Zack Brothers Ranch 18.7
AAD CHALFANT\A-ZAK-UP 0.20 50.0 0.321 12.5 2.80
00
CHALFANT\A-ZAK270 0.10 33.0 0.447 36.9 7.01

CHALFANT\A-ZAK360 0.10 33.0 0.400 44.5 8.56

0086 Chalfant Valley 1986 0721 1451 5.6 CDMG 54171 Bishop - LADWP South St 14.0* AQD CHALFANT\C-LAD-UP 0.40 40.0 0.057 2.2 0.23
00 00
CHALFANT\C-LAD270 0.23 25.0 0.106 4.9 0.53

CHALFANT\C-LAD360 0.30 20.0 0.070 6.5 0.56
CDMG 54424 Bishop - Paradise Lodge 14.0*
AVA CHALFANT\C-PAR-UP 0.20 40.0 0.053 1.1 0.19
00

CHALFANT\C-PAR070 0.20 30.0 0.037 1.9 0.34

CHALFANT\C-PAR160 0.20 30.0 0.061 2.1 0.28
CDMG 54428 Zack Brothers Ranch 20.0*
AAD CHALFANT\C-ZAK-UP 0.20 40.0 0.079 2.1 0.15
00
CHALFANT\C-ZAK270 0.13 35.0 0.143 7.4 0.67

CHALFANT\C-ZAK360 0.30 30.0 0.108 5.1 0.58

0087 Chalfant Valley 1986 0731 0722 5.8 CDMG 54171 Bishop - LADWP South St 13.0* AQD CHALFANT\D-LAD-UP 0.20 40.0 0.067 2.8 0.60
00 00
CHALFANT\D-LAD070 0.10 20.0 0.120 10.4 2.71

CHALFANT\D-LAD160 0.15 25.0 0.176 12.2 1.72
CDMG 54428 Zack Brothers Ranch 21.0*
AAD CHALFANT\D-ZAK-UP 0.22 40.0 0.046 1.6 0.37
00
CHALFANT\D-ZAK270 0.13 30.0 0.064 4.1 0.91

CHALFANT\D-ZAK360 0.11 30.0 0.060 4.3 0.84

0088 Taiwan SMART1(45) 1986 1114 7.3 7.0 7.8 25 SMART1 C00
39.0 IZD SMART1\45C00DN 0.10 25.0 0.080 7.0 3.19
02 99
SMART1\45C00EW 0.10 25.0 0.122 29.4 9.74

SMART1\45C00NS 0.10 25.0 0.153 28.3 10.73
32 SMART1 E01 39.0 IZD
SMART1\45E01DN 0.10 25.0 0.075 6.9 3.47
99
SMART1\45E01EW 0.10 25.0 0.159 2.5 8.26

SMART1\45E01NS 0.10 25.0 0.189 23.2 9.46
33 SMART1 E02 39.0 IZD
SMART1\45E02DN 0.10 25.0 0.052 5.5 3.03
99
SMART1\45E02EW 0.10 25.0 0.136 13.7 5.84

SMART1\45E02NS 0.10 25.0 0.143 12.5 6.07
62 SMART1 I01 39.0 IZD
SMART1\45I01DN 0.10 25.0 0.075 7.1 4.22
99
SMART1\45I01EW 0.10 25.0 0.132 30.5 9.05

SMART1\45I01NS 0.10 25.0 0.141 29.8 10.34
61 SMART1 I07 39.0 IZD
SMART1\45I07DN 0.10 25.0 0.089 6.9 3.22
99
SMART1\45I07EW 0.10 25.0 0.118 23.3 10.69

SMART1\45I07NS 0.10 25.0 0.122 27.0 9.64
28 SMART1 M01 39.0 IZD
SMART1\45M01DN 0.10 25.0 0.078 6.1 2.26
99
SMART1\45M01EW 0.10 25.0 0.119 27.0 8.91

SMART1\45M01NS 0.10 25.0 0.141 21.8 9.93
29 SMART1 M07 39.0 IZD
SMART1\45M07DN 0.20 25.0 0.106 8.6 3.19
99
SMART1\45M07EW 0.10 25.0 0.156 26.8 9.09

SMART1\45M07NS 0.20 25.0 0.160 22.5 7.62
30 SMART1 O01 39.0 IZD
SMART1\45O01DN 0.10 25.0 0.063 6.3 3.31
99
SMART1\45O01EW 0.10 25.0 0.126 21.8 9.66

SMART1\45O01NS 0.10 25.0 0.174 21.2 7.90
63 SMART1 O02 39.0 IZD
SMART1\45O02DN 0.10 25.0 0.062 7.0 4.66
99
SMART1\45O02EW 0.10 25.0 0.160 20.4 9.90

SMART1\45O02NS 0.10 25.0 0.242 26.2 11.56
64 SMART1 O04 39.0 IZD
SMART1\45O04DN 0.10 25.0 0.081 7.2 2.95
99
SMART1\45O04EW 0.10 25.0 0.126 31.9 9.11

SMART1\45O04NS 0.10 25.0 0.163 25.3 9.84
65 SMART1 O06 39.0 IZD
SMART1\45O06DN 0.10 25.0 0.079 7.0 2.44
99
SMART1\45O06EW 0.10 25.0 0.171 24.5 8.91

SMART1\45O06NS 0.10 25.0 0.190 22.8 8.65
31 SMART1 O07 39.0 IZD

SMART1\45O07DN 0.10 25.0 0.106 8.7 2.36
99
SMART1\45O07EW 0.10 25.0 0.154 19.4 8.17

SMART1\45O07NS 0.10 25.0 0.164 23.2 11.13
66 SMART1 O08 39.0 IZD
SMART1\45O08DN 0.10 25.0 0.105 9.2 4.18
99
SMART1\45O08EW 0.10 25.0 0.142 24.5 9.33

SMART1\45O08NS 0.10 25.0 0.163 30.1 13.21
67 SMART1 O10 39.0 IZD
SMART1\45O10DN 0.10 25.0 0.062 6.2 3.82
99
SMART1\45O10EW 0.10 25.0 0.148 24.2 9.97

SMART1\45O10NS 0.10 25.0 0.116 26.8 10.08
68 SMART1 O12 39.0 IZD
SMART1\45O12DN 0.20 25.0 0.065 6.1 1.99
99
SMART1\45O12EW 0.10 25.0 0.139 24.5 8.82

SMART1\45O12NS 0.10 25.0 0.159 23.3 10.61

0089 Whittier Narrows 1987 1001 1442 6.0 5.9 5.7 CDMG 24461 Alahambra, Fremont Sch 13.2 AMD WHITTIER\A-ALH-UP 0.40 50.0 0.190 5.5 0.84
02 99
WHITTIER\A-ALH180 0.50 35.0 0.333 22.0 2.42

WHITTIER\A-ALH270 0.30 40.0 0.414 16.3 2.32
CDMG 24402 Altadena - Eaton Canyon 17.5
AQD WHITTIER\A-ALT-UP 0.40 40.0 0.163 3.3 0.44
01
WHITTIER\A-ALT000 0.40 35.0 0.299 11.4 1.20

WHITTIER\A-ALT090 0.40 35.0 0.151 5.7 0.50
USC 90088 Anaheim - W Ball Rd #
WHITTIER\A-BAL-UP 0.60 25.0 0.062 1.8 0.10
99 C
WHITTIER\A-BAL000 0.25 25.0 0.060 6.6 1.33

WHITTIER\A-BAL090 0.50 25.0 0.055 3.4 0.63
USC 90093 Arcadia - Campus Dr #
WHITTIER\A-CAM-UP 0.28 25.0 0.229 6.2 0.56
99 C

WHITTIER\A-CAM009 0.15 25.0 0.300 21.0 3.12

WHITTIER\A-CAM279 0.38 25.0 0.163 6.8 0.73

CDMG 24087 Arleta - Nordhoff Fire Sta 38.9

AQD WHITTIER\A-ARL-UP 0.35 40.0 0.089 3.3 0.58

99

WHITTIER\A-ARL180 0.40 30.0 0.093 5.4 0.55

WHITTIER\A-ARL270 0.50 30.0 0.091 4.7 0.85

USC 90069 Baldwin Park - N Holly #

WHITTIER\A-NHO-UP 0.30 25.0 0.080 2.2 0.75

99 B

WHITTIER\A-NHO180 0.13 25.0 0.127 8.6 2.50

WHITTIER\A-NHO270 0.50 25.0 0.061 4.3 0.54

USC 90094 Bell Gardens - Jaboneria #

WHITTIER\A-JAB-UP 0.40 25.0 0.095 2.7 0.40

99 C

WHITTIER\A-JAB207 0.25 25.0 0.219 18.9 2.54

WHITTIER\A-JAB297 0.10 25.0 0.212 21.8 4.83

USC 90014 Beverly Hills - 12520 Mulhol #

WHITTIER\A-MU2-UP 0.40 25.0 0.068 2.4 0.32

99 B

WHITTIER\A-MU2032 0.35 25.0 0.089 5.1 0.53

WHITTIER\A-MU2122 0.33 22.5 0.138 6.4 0.58

USC 90013 Beverly Hills - 14145 Mulhol #

WHITTIER\A-MUL-UP 0.38 25.0 0.043 2.0 0.25

99 C

WHITTIER\A-MUL009 0.33 25.0 0.104 6.5 0.58

WHITTIER\A-MUL279 0.35 25.0 0.126 10.3 1.05

USC 90061 Big Tujunga, Angeles Nat F #

WHITTIER\A-TUJ-UP 0.75 25.0 0.085 2.3 0.19

99 B

WHITTIER\A-TUJ262 0.40 25.0 0.126 4.6 0.61

WHITTIER\A-TUJ352 0.90 25.0 0.178 6.7 0.37

USGS 951 Brea Dam (Downstream) 23.3

IPD WHITTIER\A-BRD-UP 0.50 40.0 0.094 3.1 0.22

99

WHITTIER\A-BRD040 0.60 35.0 0.163 6.2 0.36

WHITTIER\A-BRD130 0.60 40.0 0.313 14.5 0.77

```
                                        USGS  951 Brea Dam (L Abut)                23.3     IPB
WHITTIER\A-BRL-UP  0.70  40.0  0.097   2.7   0.20
                                          99
WHITTIER\A-BRL040  0.50  40.0  0.118   6.2   0.60

WHITTIER\A-BRL130  0.50  30.0  0.149  10.2   0.82
                                        USC  90087 Brea - S Flower Av #
WHITTIER\A-FLO-UP  0.20  25.0  0.103   9.1   1.31
                                          99                              C
WHITTIER\A-FLO020  0.16  25.0  0.115   7.1   1.21
                                        USC  90012 Burbank - N Buena Vista #
WHITTIER\A-BUE-UP  0.35  25.0  0.105   3.2   0.53
                                          99                              C
WHITTIER\A-BUE250  0.25  25.0  0.233  16.0   1.33

WHITTIER\A-BUE340  0.30  25.0  0.190  11.6   1.16
                                        USC  90052 Calabasas - N Las Virg #
WHITTIER\A-VIR-UP  0.40  25.0  0.023   1.6   0.15
                                          99                              B
WHITTIER\A-VIR200  0.33  25.0  0.042   2.3   0.35

WHITTIER\A-VIR290  0.45  25.0  0.025   1.2   0.13
                                        USC  90053 Canoga Park - Topanga Can #
WHITTIER\A-TOP-UP  0.35  25.0  0.055   1.9   0.30
                                          99                              C
WHITTIER\A-TOP106  0.25  25.0  0.139   7.9   0.76

WHITTIER\A-TOP196  0.28  25.0  0.116   8.1   1.13
                                        USC  90057 Canyon Country - W Lost Cany #
WHITTIER\A-LOS-UP  0.40  25.0  0.073   1.9   0.26
                                          99                              C
WHITTIER\A-LOS000  0.38  25.0  0.109   7.5   0.49

WHITTIER\A-LOS270  0.23  22.5  0.103   7.0   0.85
                                        USGS  108 Carbon Canyon Dam (L Abut)      26.8
AMA  WHITTIER\A-CBN-UP  0.80  45.0  0.058   2.4   0.13
                                          99
WHITTIER\A-CBN040  0.80  40.0  0.200   6.5   0.51

WHITTIER\A-CBN130  0.50  40.0  0.221   8.7   0.64
                                        USC  90040 Carson - Catskill Ave #
WHITTIER\A-CAT-UP  0.50  25.0  0.037   1.3   0.15
                                          99                              C
WHITTIER\A-CAT090  0.18  25.0  0.042   3.8   0.75
```

WHITTIER\A-CAT180 0.55 25.0 0.059 2.4 0.32

USC 90081 Carson - Water St #

WHITTIER\A-WAT-UP 0.50 25.0 0.046 2.0 0.23

99 C

WHITTIER\A-WAT180 0.20 25.0 0.104 9.0 1.91

WHITTIER\A-WAT270 0.30 25.0 0.133 11.3 1.54

CDMG 24277 Castaic - Hasley Canyon 70.9

A-B WHITTIER\A-CSH-UP 0.50 20.0 0.021 1.5 0.16

99

WHITTIER\A-CSH000 0.70 15.0 0.031 1.9 0.19

WHITTIER\A-CSH090 0.50 15.0 0.035 2.6 0.31

CDMG 24278 Castaic - Old Ridge Route 78.3

A-B WHITTIER\A-CSR-UP 1.00 23.0 0.026 1.1 0.08

99 B

WHITTIER\A-CSR000 0.80 15.0 0.071 4.4 0.40

WHITTIER\A-CSR090 0.80 20.0 0.065 4.5 0.38

USC 90078 Compton - Castlegate St #

WHITTIER\A-CAS-UP 0.50 25.0 0.167 3.3 0.19

99

WHITTIER\A-CAS000 0.09 25.0 0.332 27.1 5.04

WHITTIER\A-CAS270 0.28 25.0 0.333 14.1 1.48

USC 90068 Covina - S Grand Ave #

WHITTIER\A-GRA-UP 0.33 25.0 0.064 3.1 0.46

99 C

WHITTIER\A-GRA015 0.45 25.0 0.076 5.4 0.90

WHITTIER\A-GRA105 0.40 25.0 0.068 4.1 0.62

USC 90070 Covina - W Badillo #

WHITTIER\A-BAD-UP 0.50 25.0 0.082 2.9 0.22

99 C

WHITTIER\A-BAD000 0.28 25.0 0.134 7.7 1.33

WHITTIER\A-BAD270 0.38 25.0 0.081 4.0 0.63

USC 90079 Downey - Birchdale #

WHITTIER\A-BIR-UP 0.60 25.0 0.230 4.1 0.31

99

WHITTIER\A-BIR090 0.28 25.0 0.243 13.7 1.92

WHITTIER\A-BIR180 0.15 25.0 0.299 37.8 4.95

CDMG 14368 Downey - Co Maint Bldg 18.3

AQD WHITTIER\A-DWN-UP 1.00 40.0 0.177 3.3 0.23

99

WHITTIER\A-DWN180 0.20 30.0 0.221 28.8 3.95

WHITTIER\A-DWN270 0.25 30.0 0.141 13.4 1.60

USC 90066 El Monte - Fairview Av # .

WHITTIER\A-FAI-UP 0.30 25.0 0.136 4.8 0.45

99 C

WHITTIER\A-FAI000 0.33 25.0 0.120 6.7 0.93

WHITTIER\A-FAI270 0.13 25.0 0.228 15.0 4.06

CDMG 13122 Featherly Park - Maint 38.6

AMC WHITTIER\A-FEA-UP 1.30 40.0 0.050 1.4 0.07

99

WHITTIER\A-FEA000 0.80 25.0 0.071 3.6 0.26

WHITTIER\A-FEA090 0.90 25.0 0.087 5.1 0.33

USC 90002 Fountain Valley - Euclid # .

WHITTIER\A-EUC-UP 0.38 25.0 0.049 1.1 0.16

99 C

WHITTIER\A-EUC022 0.30 25.0 0.071 4.1 0.76

WHITTIER\A-EUC292 0.30 25.0 0.062 6.0 1.75

USGS 709 Garvey Res. - Control Bldg 12.1 APB

WHITTIER\A-GRV-UP 0.70 40.0 0.362 9.9 0.75

01

WHITTIER\A-GRV060 0.15 40.0 0.384 15.8 2.49

WHITTIER\A-GRV330 0.20 40.0 0.457 19.0 4.31

USC 90063 Glendale - Las Palmas # .

WHITTIER\A-PAL-UP 0.63 27.0 0.143 5.7 0.39

99 C

WHITTIER\A-PAL177 0.28 25.0 0.296 17.1 1.82

WHITTIER\A-PAL267 0.45 25.0 0.166 8.4 0.81

USC 90065 Glendora - N Oakbank # .

WHITTIER\A-OAK-UP 0.38 25.0 0.071 3.3 0.48

99 B

WHITTIER\A-OAK080 0.35 25.0 0.092 3.4 0.50

WHITTIER\A-OAK170 0.23 25.0 0.110 5.0 0.81

USC 90073 Hacienda Heights - Colima # .

WHITTIER\A-COM-UP 0.50 25.0 0.096 2.2 0.25

99 C

WHITTIER\A-COM140 0.23 25.0 0.195 8.6 0.84

WHITTIER\A-COM230 0.45 25.0 0.201 6.3 0.62

CDMG 12331 Hemet Fire Station 105.0

AQD WHITTIER\A-HEM-UP 1.00 30.0 0.027 0.9 0.07

99 C

WHITTIER\A-HEM270 0.70 25.0 0.038 1.4 0.13

WHITTIER\A-HEM360 0.80 25.0 0.032 1.6 0.10

CDMG 13197 Huntington Beach - Lake St 42.8

AQD WHITTIER\A-HNT-UP 0.22 30.0 0.027 1.3 0.26

99

WHITTIER\A-HNT270 0.25 25.0 0.045 1.7 0.49

WHITTIER\A-HNT360 0.17 25.0 0.044 3.4 1.27

CDMG 14196 Inglewood - Union Oil 25.2

IQD WHITTIER\A-ING-UP 0.50 30.0 0.069 2.4 0.24

99

WHITTIER\A-ING000 0.60 40.0 0.299 8.9 0.78

WHITTIER\A-ING090 0.25 40.0 0.247 18.1 1.92

CDMG 14403 LA - 116th St School 22.5

AQD WHITTIER\A-116-UP 0.20 30.0 0.105 3.0 0.49

99

WHITTIER\A-116270 0.20 30.0 0.294 17.6 1.97

WHITTIER\A-116360 0.20 30.0 0.396 21.0 1.75

CDMG 24157 LA - Baldwin Hills 27.0 IPD

WHITTIER\A-BLD-UP 0.40 35.0 0.114 4.0 0.37

99

WHITTIER\A-BLD000 0.30 35.0 0.142 8.7 1.40

WHITTIER\A-BLD090 0.40 30.0 0.159 8.0 0.72

USC 90054 LA - Centinela St #

WHITTIER\A-CEN-UP 0.33 25.0 0.032 1.2 0.27

99 C

WHITTIER\A-CEN155 0.30 25.0 0.059 3.0 0.55

WHITTIER\A-CEN245 0.25 25.0 0.044 2.6 0.34

CDMG 24389 LA - Century City CC North 31.4

IQD WHITTIER\A-CTN-UP 0.50 23.0 0.039 1.6 0.20

99

WHITTIER\A-CTN000 0.60 30.0 0.078 3.1 0.34

WHITTIER\A-CTN090 0.35 30.0 0.111 6.2 0.70

CDMG 24390 LA - Century City CC South 31.3

IQD WHITTIER\A-CTS-UP 0.40 30.0 0.021 1.7 0.25

99

WHITTIER\A-CTS000 0.20 25.0 0.051 3.5 0.61

WHITTIER\A-CTS090 0.30 25.0 0.063 5.4 0.83

USC 90015 LA - Chalon Rd #

WHITTIER\A-CHA-UP 1.00 25.0 0.019 0.7 0.07

99 B

WHITTIER\A-CHA030 0.38 25.0 0.036 2.3 0.21

WHITTIER\A-CHA120 0.75 25.0 0.020 1.1 0.12

USC 90033 LA - Cypress Ave #

WHITTIER\A-CYP-UP 0.40 25.0 0.084 2.9 0.29

99 B

WHITTIER\A-CYP053 0.33 25.0 0.156 8.0 0.88

WHITTIER\A-CYP143 0.28 25.0 0.137 9.1 1.35

USC 90025 LA - E Vernon Ave #

WHITTIER\A-VER-UP 0.40 25.0 0.086 2.7 0.39

99 C

WHITTIER\A-VER083 0.18 25.0 0.146 12.8 1.43

WHITTIER\A-VER173 0.16 25.0 0.175 8.8 1.37

USC 90034 LA - Fletcher Dr #

WHITTIER\A-FLT-UP 0.30 25.0 0.103 7.6 1.03

99 C

WHITTIER\A-FLT144 0.28 25.0 0.171 19.4 2.17

WHITTIER\A-FLT234 0.30 25.0 0.213 12.6 1.45

CDMG 24303 LA - Hollywood Stor FF 25.2

IPD WHITTIER\A-HOL-UP 0.45 50.0 0.070 2.8 0.42

99 C

WHITTIER\A-HOL000 0.40 25.0 0.221 9.0 1.43

WHITTIER\A-HOL090 0.40 25.0 0.124 6.9 1.12

USC 90016 LA - N Faring Rd #

WHITTIER\A-FAR-UP 0.55 25.0 0.034 1.6 0.13

99 C

WHITTIER\A-FAR000 0.55 25.0 0.048 2.2 0.26

WHITTIER\A-FAR090 0.40 25.0 0.053 3.0 0.29

USC 90032 LA - N Figueroa St #

WHITTIER\A-FIG-UP 0.55 25.0 0.169 5.7 0.47

99 B

WHITTIER\A-FIG058 0.30 25.0 0.151 7.9 1.10

WHITTIER\A-FIG328 0.20 25.0 0.166 13.1 1.82

CDMG 24400 LA - Obregon Park 13.9

AQD WHITTIER\A-OBR-UP 0.50 35.0 0.144 5.2 0.59

99

WHITTIER\A-OBR270 0.40 35.0 0.450 16.1 2.18

WHITTIER\A-OBR360 0.40 35.0 0.400 22.9 2.53

USC 90022 LA - S Grand Ave #

WHITTIER\A-GR2-UP 0.30 25.0 0.122 3.5 0.29

99 C

WHITTIER\A-GR2090 0.35 25.0 0.191 8.6 0.75

WHITTIER\A-GR2180 0.28 25.0 0.149 8.0 1.19

USC 90091 LA - Saturn St #

WHITTIER\A-SAT-UP 0.28 25.0 0.041 2.0 0.59

99 C

WHITTIER\A-SAT020 0.25 25.0 0.099 6.1 0.68

WHITTIER\A-SAT110 0.23 25.0 0.141 4.5 0.58

USC 90023 LA - W 70th St #

WHITTIER\A-70S-UP 0.30 25.0 0.077 2.8 0.45

99 C

WHITTIER\A-70S000 0.30 25.0 0.198 19.5 2.49

WHITTIER\A-70S270 0.20 25.0 0.151 8.7 1.51

USC 90021 LA - N Westmoreland #

WHITTIER\A-WST-UP 0.35 25.0 0.084 3.1 0.43

99 B

WHITTIER\A-WST000 0.30 25.0 0.214 9.7 0.98

WHITTIER\A-WST270 0.30 25.0 0.199 6.2 0.72

USC 90017 LA - Wonderland Ave #

WHITTIER\A-WON-UP 0.55 25.0 0.024 0.9 0.10

99 A

WHITTIER\A-WON075 0.53 25.0 0.039 1.7 0.17

WHITTIER\A-WON165 0.70 25.0 0.047 1.5 0.16

USC 90060 La Crescenta - New York #

WHITTIER\A-NYA-UP 0.38 25.0 0.090 2.8 0.40

99 C

WHITTIER\A-NYA090 0.40 25.0 0.134 11.7 1.18

WHITTIER\A-NYA180 0.30 25.0 0.141 10.9 1.69

USC 90074 La Habra - Briarcliff #

WHITTIER\A-BRC-UP 0.50 25.0 0.064 2.6 0.31

				99		C		
WHITTIER\A-BRC000	0.25	25.0	0.183	9.9	2.23			
WHITTIER\A-BRC090	0.25	25.0	0.131	7.3	1.10			
				USC	90072 La Puente - Rimgrove Av #			
WHITTIER\A-RIM-UP	0.45	25.0	0.076	2.5	0.19			
				99		C		
WHITTIER\A-RIM015	0.18	25.0	0.143	6.2	1.04			
WHITTIER\A-RIM105	0.50	21.5	0.118	5.9	0.42			
				CDMG	24271 Lake Hughes #1		74.7	APC
WHITTIER\A-HG1000	0.90	20.0	0.035	2.5	0.19			
				99				
WHITTIER\A-HG1090	0.80	20.0	0.029	1.6	0.18			
				USC	90084 Lakewood - Del Amo Blvd #			
WHITTIER\A-DEL-UP	0.30	25.0	0.126	3.4	0.55			
				99		C		
WHITTIER\A-DEL000	0.30	25.0	0.277	28.5	4.52			
WHITTIER\A-DEL090	0.30	25.0	0.178	11.8	2.13			
				CDMG	24526 Lancaster - Med Off FF		69.5	
IQC WHITTIER\A-LAN-UP	1.30	35.0	0.027	0.8	0.03			
				99				
WHITTIER\A-LAN010	0.80	25.0	0.067	2.5	0.16			
WHITTIER\A-LAN100	0.60	25.0	0.071	2.8	0.17			
				USC	90045 Lawndale - Osage Ave #			
WHITTIER\A-OSA-UP	0.33	25.0	0.031	2.0	0.26			
				99		C		
WHITTIER\A-OSA092	0.35	25.0	0.066	5.3	0.89			
WHITTIER\A-OSA182	0.38	25.0	0.053	5.3	0.71			
				CDMG	14395 LB - Harbor Admin FF		34.2	
IQD WHITTIER\A-HAR-UP	0.20	25.0	0.028	1.6	0.40			
				99				
WHITTIER\A-HAR000	0.60	30.0	0.058	4.1	0.63			
WHITTIER\A-HAR090	0.25	25.0	0.071	7.3	0.85			
				USC	90080 LB - Orange Ave #			
WHITTIER\A-OR2-UP	0.55	25.0	0.136	3.4	0.38			
				99				
WHITTIER\A-OR2010	0.12	25.0	0.255	32.9	4.83			
WHITTIER\A-OR2280	0.28	25.0	0.149	10.3	1.36			
				CDMG	14242 LB - R. Los Cerritos		26.0	IQD

WHITTIER\A-CER-UP 0.70 35.0 0.084 2.8 0.21
99
WHITTIER\A-CER000 0.25 40.0 0.159 16.9 2.90
WHITTIER\A-CER090 0.50 35.0 0.194 17.2 2.21
CDMG 14241 LB - Recreation Park 30.5 IQD
WHITTIER\A-REC-UP 0.60 20.0 0.038 1.6 0.23
02
WHITTIER\A-REC090 0.20 30.0 0.058 3.1 0.80
WHITTIER\A-REC180 0.30 25.0 0.051 6.8 1.64
CDMG 24055 Leona Valley #5 - Ritter 61.3 IQC
WHITTIER\A-LN5-UP 1.00 25.0 0.029 1.0 0.07
99
WHITTIER\A-LN5000 0.80 25.0 0.047 2.1 0.14
WHITTIER\A-LN5090 0.80 30.0 0.056 2.7 0.19
CDMG 24309 Leona Valley #6 64.8 I-D
WHITTIER\A-LN6-UP 1.00 25.0 0.024 1.0 0.10
99
WHITTIER\A-LN6000 1.00 25.0 0.036 1.6 0.10
WHITTIER\A-LN6090 0.80 25.0 0.053 1.9 0.11
USC 90050 Malibu - Las Flores Canyon #
WHITTIER\A-LAS-UP 0.65 25.0 0.015 1.0 0.13
99 B
WHITTIER\A-LAS160 0.65 25.0 0.065 2.3 0.14
WHITTIER\A-LAS250 0.65 25.0 0.055 2.2 0.32
CDMG 24396 Malibu - Point Dume Sch 65.3
AMB WHITTIER\A-MAL-UP 0.35 30.0 0.029 1.9 0.15
99
WHITTIER\A-MAL180 0.35 25.0 0.048 2.4 0.32
WHITTIER\A-MAL270 0.60 20.0 0.040 2.0 0.18
USC 90051 Malibu - W Pacific Cst Hwy #
WHITTIER\A-WPA-UP 0.38 25.0 0.029 1.6 0.24
99 B
WHITTIER\A-WPA060 0.40 25.0 0.038 2.5 0.28
WHITTIER\A-WPA150 0.70 25.0 0.032 2.3 0.22
USC 90046 Manhattan Beach #
WHITTIER\A-MAN090 0.40 25.0 0.054 5.8 0.85
99 C
USC 90062 Mill Creek, Angeles Nat For #

WHITTIER\A-ANG-UP 0.70 25.0 0.040 1.6 0.10
99
WHITTIER\A-ANG000 0.40 25.0 0.089 4.0 0.52

WHITTIER\A-ANG090 0.63 25.0 0.071 3.3 0.32
CDMG 24283 Moorpark - Fire Sta 27.1 AQD
WHITTIER\A-MRP-UP 1.00 25.0 0.019 1.0 0.08
99
WHITTIER\A-MRP090 0.80 15.0 0.039 3.1 0.26

WHITTIER\A-MRP180 0.50 15.0 0.042 2.5 0.26
CDMG 24399 Mt Wilson - CIT Seis Sta 21.2
IGA WHITTIER\A-MTW-UP 0.40 40.0 0.119 3.3 0.25
01
WHITTIER\A-MTW000 0.60 40.0 0.123 3.3 0.37

WHITTIER\A-MTW090 0.70 40.0 0.186 4.6 0.21
USC 90009 N Hollywood - Coldwater Can #
WHITTIER\A-COL-UP 0.20 25.0 0.059 2.7 0.49
99 C
WHITTIER\A-COL180 0.20 25.0 0.116 6.2 0.97

WHITTIER\A-COL270 0.30 25.0 0.250 14.3 1.11
CDMG 24279 Newhall - Fire Sta 55.2 AQD
WHITTIER\A-NWH-UP 1.00 25.0 0.038 1.0 0.09
99
WHITTIER\A-NWH180 0.50 15.0 0.044 2.9 0.31

WHITTIER\A-NWH270 0.60 15.0 0.060 2.9 0.41
USC 90056 Newhall - W Pico Canyon #
WHITTIER\A-PIC-UP 0.30 25.0 0.035 1.7 0.17
99
WHITTIER\A-PIC046 0.28 25.0 0.088 5.6 0.47

WHITTIER\A-PIC316 0.38 25.0 0.055 3.9 0.32
USC 90003 Northridge - Saticoy St #
WHITTIER\A-STA-UP 0.25 25.0 0.084 2.4 0.41
99 C
WHITTIER\A-STA090 0.23 25.0 0.161 8.5 0.72

WHITTIER\A-STA180 0.20 25.0 0.118 5.1 0.83
USGS 634 Norwalk - Imp Hwy, S Grnd 17.2
IHD WHITTIER\A-NOR-UP 0.60 45.0 0.096 2.9 0.30
02
WHITTIER\A-NOR090 0.15 40.0 0.107 8.4 1.40

WHITTIER\A-NOR360 0.15 45.0 0.248 20.7 4.21
USGS 697 Orange Co. Reservoir 23.0 APB
WHITTIER\A-ORN-UP 1.00 35.0 0.126 2.7 0.19
99
WHITTIER\A-ORN006 0.40 30.0 0.185 10.2 0.96

WHITTIER\A-ORN096 0.30 30.0 0.198 6.1 0.74
USC 90049 Pacific Palisades - Sunset #
WHITTIER\A-SUN-UP 0.28 25.0 0.035 1.3 0.25
99 C
WHITTIER\A-SUN190 0.45 25.0 0.063 2.0 0.28

WHITTIER\A-SUN280 0.50 25.0 0.038 2.0 0.33
CDMG 24088 Pacoima Kagel Canyon 37.9
AMB WHITTIER\A-PAC-UP 0.50 35.0 0.055 2.7 0.30
99
WHITTIER\A-PAC000 0.35 20.0 0.166 6.2 0.68

WHITTIER\A-PAC090 0.45 20.0 0.164 6.8 0.87
USC 90005 Pacoima Kagel Canyon USC #
WHITTIER\A-KAG-UP 0.53 25.0 0.076 4.0 0.57
99 B
WHITTIER\A-KAG045 0.30 25.0 0.119 7.9 1.07

WHITTIER\A-KAG315 0.23 25.0 0.133 5.5 0.60
USC 90007 Panorama City - Roscoe #
WHITTIER\A-RO2-UP 0.25 25.0 0.079 2.8 0.50
99 B
WHITTIER\A-RO2090 0.25 23.5 0.105 7.2 0.81

WHITTIER\A-RO2180 0.20 25.0 0.108 7.2 1.48
CDMG 80046 Pasadena - Brown Gym 15.5
-QD WHITTIER\A-BRN-UP 0.50 40.0 0.161 3.7 0.48
99
WHITTIER\A-BRN180 0.35 30.0 0.165 13.2 2.09

WHITTIER\A-BRN270 0.35 30.0 0.149 9.1 1.24
CDMG 80053 Pasadena - CIT Athenaeum 15.4
CQD WHITTIER\A-ATH-UP 0.50 30.0 0.125 4.8 0.44
99 B
WHITTIER\A-ATH180 0.30 40.0 0.174 11.5 1.68

WHITTIER\A-ATH270 0.30 35.0 0.101 6.0 0.74
CDMG 80052 Pasadena - CIT Bridge Lab 15.5

-QD WHITTIER\A-BRI-UP 0.70 40.0 0.132 3.6 0.28
99
WHITTIER\A-BRI090 0.40 35.0 0.184 10.3 1.13

WHITTIER\A-BRI360 0.25 35.0 0.147 15.0 2.72
CDMG 80047 Pasadena - CIT Calif Blvd 15.5
AQD WHITTIER\A-CAL-UP 0.30 40.0 0.171 7.0 0.58
99
WHITTIER\A-CAL270 0.30 40.0 0.177 8.1 0.96

WHITTIER\A-CAL360 0.30 35.0 0.271 15.4 2.33
CDMG 80051 Pasadena - CIT Indust. Rel 15.5
BQD WHITTIER\A-IND-UP 0.50 40.0 0.184 5.5 0.45
99
WHITTIER\A-IND090 0.30 25.0 0.239 8.4 0.99

WHITTIER\A-IND180 0.30 30.0 0.228 13.8 1.95
CDMG 80049 Pasadena - CIT Keck Lab 15.5
-QD WHITTIER\A-KEC-UP 0.60 60.0 0.096 4.0 0.41
99
WHITTIER\A-KEC270 0.40 35.0 0.152 5.1 0.60

WHITTIER\A-KEC360 0.25 35.0 0.188 14.1 2.63
CDMG 80054 Pasadena - CIT Kresge Lab 17.4
-QD WHITTIER\A-KRE-UP 0.50 45.0 0.081 3.3 0.37
99
WHITTIER\A-KRE090 0.40 40.0 0.112 8.0 0.99

WHITTIER\A-KRE360 0.60 40.0 0.089 3.8 0.28
CDMG 80048 Pasadena - CIT Lura St 15.5
AQD WHITTIER\A-LUR-UP 0.43 50.0 0.236 5.0 0.61
99
WHITTIER\A-LUR090 0.40 40.0 0.360 9.8 0.92

WHITTIER\A-LUR180 0.30 40.0 0.352 18.1 2.35
CDMG 80050 Pasadena - CIT Mudd Lab 15.5
-QD WHITTIER\A-MUD-UP 0.70 30.0 0.134 3.9 0.36
99
WHITTIER\A-MUD090 0.40 30.0 0.137 9.4 1.30

WHITTIER\A-MUD360 0.30 35.0 0.163 15.1 2.23
USC 90095 Pasadena - Old House Rd #
WHITTIER\A-OLD-UP 0.25 25.0 0.102 3.5 0.89
99 C
WHITTIER\A-OLD000 0.28 25.0 0.231 10.6 1.58

WHITTIER\A-OLD090 0.23 25.0 0.258 8.0 1.23
USC 90047 Playa Del Rey #
WHITTIER\A-SAR-UP 0.35 25.0 0.018 1.2 0.22
99
WHITTIER\A-SAR000 0.40 25.0 0.025 2.5 0.47
WHITTIER\A-SAR270 0.38 25.0 0.034 2.5 0.32
CDMG 23525 Pomona - 4th & Locust FF 28.8
IQD WHITTIER\A-PMN-UP 0.80 40.0 0.055 1.3 0.13
99 C
WHITTIER\A-PMN012 0.50 30.0 0.067 3.4 0.35
WHITTIER\A-PMN102 0.55 30.0 0.056 2.5 0.22
CDMG 23497 Rancho Cucamonga - Law & J 44.3
IHD WHITTIER\A-CUC-UP 0.70 40.0 0.044 0.9 0.09
99 B
WHITTIER\A-CUC090 0.60 50.0 0.060 1.5 0.18
WHITTIER\A-CUC360 0.60 50.0 0.050 1.4 0.16
USC 90044 Rancho Palos Verdes #
WHITTIER\A-LUC-UP 0.55 21.5 0.017 0.9 0.11
99 C
WHITTIER\A-LUC186 0.45 21.5 0.021 2.0 0.28
WHITTIER\A-LUC276 0.53 25.0 0.021 1.6 0.24
CDMG 13123 Riverside Airport 56.8 AQB
WHITTIER\A-RIV-UP 3.00 50.0 0.044 0.7 0.01
99 B
WHITTIER\A-RIV180 1.70 35.0 0.050 1.4 0.05
WHITTIER\A-RIV270 2.00 45.0 0.047 1.4 0.04
CDMG 24274 Rosamond - Goode Ranch 86.0
IQC WHITTIER\A-ROS-UP 0.40 30.0 0.021 1.2 0.11
99
WHITTIER\A-ROS000 0.40 20.0 0.070 3.8 0.39
WHITTIER\A-ROS090 0.50 20.0 0.065 3.2 0.31
USC 90019 San Gabriel - E Grand Av #
WHITTIER\A-GRN-UP 0.35 25.0 0.227 5.5 0.44
99 A
WHITTIER\A-GRN180 0.35 25.0 0.304 23.0 3.34
WHITTIER\A-GRN270 0.35 25.0 0.199 11.0 1.04
CDMG 24401 San Marino, SW Academy 14.7

AQD WHITTIER\A-SMA-UP 0.60 40.0 0.142 5.4 0.74
99
WHITTIER\A-SMA270 0.40 40.0 0.128 5.6 0.58

WHITTIER\A-SMA360 0.40 40.0 0.204 12.8 2.60
USC 90077 Santa Fe Springs - E Joslin #
WHITTIER\A-JOS-UP 0.25 25.0 0.206 6.7 1.03
99 C
WHITTIER\A-JOS048 0.35 25.0 0.426 38.1 3.54

WHITTIER\A-JOS318 0.35 25.0 0.443 21.7 3.00
USC 90048 Santa Monica - Second St #
WHITTIER\A-SEC-UP 0.53 25.0 0.021 0.8 0.13
99 B
WHITTIER\A-SEC205 0.53 25.0 0.033 2.7 0.28

WHITTIER\A-SEC295 0.28 25.0 0.034 4.1 0.60
USC 90010 Studio City - Coldwater Can #
WHITTIER\A-CO2-UP 0.35 25.0 0.073 2.8 0.37
99 C
WHITTIER\A-CO2092 0.28 25.0 0.177 14.2 1.15

WHITTIER\A-CO2182 0.30 25.0 0.231 13.7 1.14
USC 90006 Sun Valley - Roscoe #
WHITTIER\A-RO3-UP 0.25 25.0 0.093 3.9 0.43
99 B
WHITTIER\A-RO3000 0.25 25.0 0.202 8.5 0.87

WHITTIER\A-RO3090 0.28 25.0 0.223 13.3 1.05
USC 90008 Sun Valley - Sunland #
WHITTIER\A-SUL-UP 0.35 25.0 0.043 2.3 0.41
99 B
WHITTIER\A-SUL220 0.30 25.0 0.075 3.4 0.73

WHITTIER\A-SUL310 0.38 25.0 0.074 3.2 0.30
USC 90058 Sunland - Mt Gleason Ave #
WHITTIER\A-GLE-UP 0.30 25.0 0.072 3.5 0.50
99 B
WHITTIER\A-GLE180 0.28 25.0 0.089 4.5 0.73

WHITTIER\A-GLE270 0.28 25.0 0.072 4.0 0.59
CDMG 24514 Sylmar - Olive View Med FF 47.7
AQD WHITTIER\A-SYL-UP 0.50 25.0 0.042 1.7 0.18
99 C
WHITTIER\A-SYL000 0.35 20.0 0.065 4.4 0.67

WHITTIER\A-SYL090 0.40 20.0 0.055 3.2 0.46

USC 90001 Sylmar - Sayre St #

WHITTIER\A-SAY-UP 0.33 25.0 0.033 1.2 0.20

99 B

WHITTIER\A-SAY045 0.25 25.0 0.051 4.2 0.65

WHITTIER\A-SAY315 0.28 25.0 0.046 2.7 0.41

CDMG 24436 Tarzana, Cedar Hill 43.0 A-B

WHITTIER\A-TAR-UP 0.70 40.0 0.248 5.9 0.31

99

WHITTIER\A-TAR000 0.60 40.0 0.449 20.1 1.29

WHITTIER\A-TAR090 0.60 40.0 0.644 22.9 1.68

USC 90082 Terminal Island - S Seaside #

WHITTIER\A-SEA-UP 0.28 25.0 0.021 1.2 0.32

99 C

WHITTIER\A-SEA252 0.20 25.0 0.042 3.9 0.97

WHITTIER\A-SEA342 0.28 25.0 0.041 3.1 0.97

USC 90038 Torrance - W 226th St #

WHITTIER\A-TOR-UP 0.40 25.0 0.025 1.2 0.26

99

WHITTIER\A-TOR090 0.23 25.0 0.031 2.6 0.65

WHITTIER\A-TOR180 0.28 25.0 0.051 2.4 0.48

CDMG 24047 Vasquez Rocks Park 52.4

IBA WHITTIER\A-VAS-UP 0.90 35.0 0.039 1.1 0.09

99

WHITTIER\A-VAS000 1.00 25.0 0.060 2.1 0.12

WHITTIER\A-VAS090 1.00 25.0 0.060 2.3 0.11

USC 90090 Villa Park - Serrano Av #

WHITTIER\A-SER-UP 0.50 25.0 0.033 1.3 0.11

99 B

WHITTIER\A-SER000 0.70 25.0 0.046 1.4 0.13

WHITTIER\A-SER270 0.55 25.0 0.072 2.6 0.27

USC 90071 West Covina - S Orange #

WHITTIER\A-SOR-UP 0.50 25.0 0.131 3.7 0.23

99 C

WHITTIER\A-SOR225 0.23 25.0 0.137 10.6 1.84

WHITTIER\A-SOR315 0.23 25.0 0.179 7.0 1.79

USGS 289 Whittier N. Dam upstream 12.3 IHD

WHITTIER\A-WHD-UP 0.55 50.0 0.505 7.1 0.31
01
WHITTIER\A-WHD062 0.20 50.0 0.229 17.8 2.62

WHITTIER\A-WHD152 0.40 40.0 0.316 12.0 1.36

0090 Whittier Narrows 1987 1004 1059 5.3 5.3 CDMG 24461 Alhambra - Fremont
Sch 12.6* AMD WHITTIER\B-ALH-UP 0.50 40.0 0.082 2.9 0.26
03 00 B
WHITTIER\B-ALH180 0.60 30.0 0.174 10.8 0.91

WHITTIER\B-ALH270 0.50 40.0 0.178 8.9 0.87
CDMG 24402 Altadena - Eaton Canyon 16.1*
AQD WHITTIER\B-ALT-UP 0.50 30.0 0.122 3.4 0.28
00
WHITTIER\B-ALT000 0.45 30.0 0.264 9.5 0.78

WHITTIER\B-ALT090 0.30 30.0 0.199 10.2 0.81
CDMG 14368 Downey - Co Maint Bldg 20.5*
AQD WHITTIER\B-DWN-UP 0.80 40.0 0.048 1.2 0.14
00
WHITTIER\B-DWN180 0.40 25.0 0.073 4.7 0.55

WHITTIER\B-DWN270 0.60 30.0 0.065 5.4 0.58
CMDG 14196 Inglewood - Union Oil 27.3*
IQD WHITTIER\B-ING-UP 1.00 30.0 0.031 1.9 0.12
00
WHITTIER\B-ING000 0.40 30.0 0.110 6.9 0.93

WHITTIER\B-ING090 0.40 30.0 0.157 9.2 0.98
CDMG 14403 LA - 116th St School 24.6*
AQD WHITTIER\B-116-UP 0.70 30.0 0.036 1.4 0.12
00
WHITTIER\B-116270 0.40 30.0 0.166 10.6 1.13

WHITTIER\B-116360 0.15 30.0 0.151 10.1 1.06
CDMG 24157 LA - Baldwin Hills 27.6* IPD
WHITTIER\B-BLD-UP 0.80 35.0 0.040 2.5 0.19
00
WHITTIER\B-BLD000 0.30 30.0 0.065 6.2 1.08

WHITTIER\B-BLD090 0.30 30.0 0.134 11.2 1.07
CDMG 24303 LA - Hollywood Stor FF 24.5*
IPD WHITTIER\B-HOL-UP 0.60 25.0 0.027 1.0 0.13
00 C

WHITTIER\B-HOL090 0.50 20.0 0.056 2.6 0.31

WHITTIER\B-HOL360 0.50 25.0 0.079 3.8 0.45

CDMG 24400 LA - Obregon Park 14.9*

AQD WHITTIER\B-OBR-UP 0.45 35.0 0.098 3.7 0.35

00

WHITTIER\B-OBR270 0.55 25.0 0.374 14.5 0.98

WHITTIER\B-OBR360 0.30 30.0 0.261 24.0 2.57

CDMG 24399 Mt Wilson - CIT Seis Sta 20.4*

IGA WHITTIER\B-MTW-UP 0.50 35.0 0.086 2.2 0.16

00

WHITTIER\B-MTW000 0.70 35.0 0.158 5.7 0.25

WHITTIER\B-MTW090 0.70 40.0 0.142 4.6 0.20

CDMG 24401 San Marino - SW Academy 12.8*

AQD WHITTIER\B-SMA-UP 0.60 40.0 0.079 2.7 0.26

00

WHITTIER\B-SMA270 0.50 40.0 0.156 7.8 1.02

WHITTIER\B-SMA360 0.30 50.0 0.212 12.9 1.51

CDMG 24436 Tarzana - Cedar Hill 42.7* A-B

WHITTIER\B-TAR-UP 1.00 35.0 0.037 1.4 0.09

00

WHITTIER\B-TAR000 0.50 30.0 0.074 2.8 0.23

WHITTIER\B-TAR090 1.00 25.0 0.113 4.5 0.31

0091 Superstitn Hills(A)1987 1124 0514 6.3 5.8 6.2 USGS 5210 Wildlife Liquef. Array
24.7 IQD SUPERST\A-IVW-UP 0.20 50.0 0.186 4.6 2.2
00 00

SUPERST\A-IVW090 0.20 50.0 0.132 12.7 7.3

SUPERST\A-IVW360 0.20 50.0 0.134 13.4 5.2

0092 Superstitn Hills(B)1987 1124 1316 6.7 6.6 CDMG 01335 El Centro Imp. Co. Cent
13.9 AQD SUPERST\B-ICC-UP 0.10 47.0 0.128 8.4 4.9
00 00 C

SUPERST\B-ICC000 0.10 40.0 0.358 46.4 17.5

SUPERST\B-ICC090 0.10 38.0 0.258 40.9 20.2

CDMG 11369 Westmorland Fire Sta 13.3

ADD SUPERST\B-WSM-UP 0.10 50.0 0.249 8.7 4.2

00 C

SUPERST\B-WSM090 0.10 35.0 0.172 23.5 13.0

SUPERST\B-WSM180 0.10 40.0 0.211 31.0 20.3
USGS 5210 Wildlife Liquef. Array 24.4 IQD
SUPERST\B-IVW-UP 0.10 50.0 0.408 6.0 3.9
00
SUPERST\B-IVW090 0.10 50.0 0.181 29.9 19.9
SUPERST\B-IVW360 0.10 40.0 0.207 34.5 21.0
0093 Spitak, Armenia 1988 1207 6.8 7.0 12 Gukasian 30.0
A-A SPITAK\GUKVRT 0.50 25.0 0.119 8.8 4.3
99
03
SPITAK\GUK000 0.50 25.0 0.199 28.6 9.8
SPITAK\GUK090
0.50 25.0 0.175 15.1 4.3
0094 Loma Prieta 1989 1018 0005 6.9 7.1 CDMG 57066 Agnews State Hospital
28.2 AQD LOMAP\AGW-UP 0.20 42.0 0.093 8.3 4.43
99 C
03
LOMAP\AGW000 0.20 30.0 0.172 26.0 12.64
LOMAP\AGW090 0.20 30.0 0.159 17.6 9.75
USGS 1652 Anderson Dam (Downstream) 21.4
AFA LOMAP\AND-UP 0.20 48.0 0.151 9.9 3.17
99 B
LOMAP\AND270 0.20 41.0 0.244 20.3 7.73
LOMAP\AND360
0.20 40.0 0.240 18.4 6.73
USGS 1652 Anderson Dam (L Abut) 21.4
AQD LOMAP\ANA-UP 0.10 41.0 0.053 9.3 4.07
99 B
LOMAP\ANA250 0.10 32.0 0.064 12.2 11.87
LOMAP\ANA340
0.10 41.0 0.077 10.0 5.54
USGS 1002 APEEL 2 - Redwood City 47.9
IQD LOMAP\A02-UP 0.10 40.0 0.083 9.5 3.15
99 D
LOMAP\A02043 0.10 27.0 0.274 53.6 12.68
LOMAP\A02133
0.10 22.0 0.220 34.3 6.87
CDMG 58393 APEEL 2E Hayward Muir Sch 57.4
ABD LOMAP\A2E-UP 0.20 40.0 0.095 3.8 2.40
99 C
LOMAP\A2E000 0.20 30.0 0.171 13.7 3.89
LOMAP\A2E090

0.20 25.0 0.139 11.5 5.65

CDMG 58219 APEEL 3E Hayward CSUH 57.1

ABA LOMAP\A3E-UP 0.20 38.0 0.047 4.2 3.33
99 B

LOMAP\A3E000 0.20 30.0 0.078 5.6 3.93

LOMAP\A3E090

0.20 30.0 0.084 6.4 3.57

CDMG 58378 APEEL 7 - Pulgas 47.7 IEC

LOMAP\A07-UP 0.10 30.0 0.061 6.2 3.08
99 B

LOMAP\A07000 0.10 30.0 0.156 16.1 7.75

LOMAP\A07090

0.10 22.0 0.088 15.7 8.41

USGS 1161 APEEL 9 - Crystal Springs Res 46.9

IQC LOMAP\A09-UP 0.20 40.0 0.049 7.2 2.11
99 B

LOMAP\A09137 0.20 40.0 0.113 15.6 5.78

LOMAP\A09227

0.20 40.0 0.104 18.1 8.11

CDMG 58373 APEEL 10 - Skyline 47.8 I-A

LOMAP\A10-UP 0.10 30.0 0.037 8.0 3.71
99 B

LOMAP\A10000 0.10 25.0 0.103 13.9 8.55

LOMAP\A10090

0.10 20.0 0.088 24.0 7.35

CDMG 58262 Belmont - Envirotech 49.9

BFA LOMAP\BES-UP 0.20 38.0 0.041 4.5 2.46
99 B

LOMAP\BES000 0.20 22.0 0.108 11.8 3.30

LOMAP\BES090

0.20 30.0 0.110 16.2 5.71

CDMG 58471 Berkeley LBL 83.6 --B

LOMAP\BRK-UP 0.20 20.0 0.039 3.9 1.40
99 B

LOMAP\BRK000 0.20 20.0 0.057 9.2 1.78

LOMAP\BRK090

0.20 18.0 0.117 20.9 4.44

UCSC 13 BRAN 10.3 --A

LOMAP\BRNVRT 0.10 0.507 17.9 4.17
99

LOMAP\BRN000 0.10 0.453 51.3 8.37

LOMAP\BRN090

0.10 0.501 44.6 4.86

CDMG 47125 Capitola 14.5 AQD

LOMAP\CAP-UP 0.20 50.0 0.541 19.4 2.60

99 C
LOMAP\CAP000 0.20 48.0 0.529 36.5 9.11
LOMAP\CAP090
0.20 40.0 0.443 29.3 5.50
CDMG 57007 Corralitos 5.1 APD
LOMAP\CLS-UP 0.20 32.0 0.455 17.7 7.11
02 B
LOMAP\CLS000 0.20 40.0 0.644 55.2 10.88
LOMAP\CLS090
0.20 40.0 0.479 45.2 11.37
CDMG 57504 Coyote Lake Dam (Downst) 22.3
IHD LOMAP\CLD-UP 0.10 30.0 0.095 9.9 4.51
02 B
LOMAP\CLD195 0.10 30.0 0.160 13.0 6.11
LOMAP\CLD285
0.10 29.0 0.179 22.6 13.20
CDMG 57217 Coyote Lake Dam (SW Abut) 21.8
IFA LOMAP\CYC-UP 0.10 50.0 0.076 8.6 3.21
02
LOMAP\CYC195 0.10 31.0 0.151 16.2 7.37
LOMAP\CYC285
0.10 33.0 0.484 39.7 15.17
USGS 1001 Foster City - 355 Menhaden 51.2
LOMAP\A01-UP 0.10 50.0 0.075 5.8 2.70
99 LOMAP\A01270
0.10 28.0 0.107 20.6 8.05
LOMAP\A01360
0.10 30.0 0.116 20.4 3.94
USGS 1686 Fremont - Emerson Court 43.4
AQD LOMAP\FMS-UP 0.10 38.0 0.067 8.6 6.37
99
LOMAP\FMS090 0.10 31.0 0.192 12.7 5.50
LOMAP\FMS180
0.10 32.0 0.141 12.9 8.37
CDMG 57064 Fremont - Mission San Jose 43.0
AMB LOMAP\MSJ-UP 0.20 32.0 0.080 8.5 5.30
99 B
LOMAP\MSJ000 0.20 24.0 0.124 11.5 5.43
LOMAP\MSJ090
0.20 28.0 0.106 8.8 4.36
CDMG 47006 Gilroy - Gavilan Coll. 11.6 AFB
LOMAP\GIL-UP 0.20 50.0 0.191 12.0 5.77
99 B
LOMAP\GIL067 0.20 45.0 0.357 28.6 6.35
LOMAP\GIL337

0.20 35.0 0.325 22.3 4.59

CDMG 57476 Gilroy - Historic Bldg. 12.7 BQD

LOMAP\GOF-UP 0.20 52.0 0.149 11.1 6.03

02

LOMAP\GOF090 0.20 38.0 0.284 42.0 11.10

LOMAP\GOF180

0.20 40.0 0.241 24.0 3.66

CDMG 47379 Gilroy Array #1 11.2 IFA

LOMAP\G01-UP 0.20 52.0 0.209 14.0 5.59

99 A

LOMAP\G01000 0.20 50.0 0.411 31.6 6.38

LOMAP\G01090

0.20 50.0 0.473 33.9 8.03

CDMG 47380 Gilroy Array #2 12.7 IQD

LOMAP\G02-UP 0.20 40.0 0.294 14.6 4.66

99 C

LOMAP\G02000 0.20 40.0 0.367 32.9 7.15

LOMAP\G02090

0.20 31.0 0.322 39.1 12.07

CDMG 47381 Gilroy Array #3 14.4 IHD

LOMAP\G03-UP 0.10 50.0 0.338 15.5 7.03

99 C

LOMAP\G03000 0.10 33.0 0.555 35.7 8.21

LOMAP\G03090

0.10 40.0 0.367 44.7 19.25

CDMG 57382 Gilroy Array #4 16.1 AHD

LOMAP\G04-UP 0.20 42.0 0.159 14.6 5.10

99 C

LOMAP\G04000 0.20 28.0 0.417 38.8 7.09

LOMAP\G04090

0.20 30.0 0.212 37.9 10.08

CDMG 57383 Gilroy Array #6 19.9 IKA

LOMAP\G06-UP 0.20 32.0 0.101 9.5 4.10

99 B

LOMAP\G06000 0.20 38.0 0.126 12.8 4.74

LOMAP\G06090

0.20 31.0 0.170 14.2 3.79

CDMG 57425 Gilroy Array #7 24.2 AHB

LOMAP\GMR-UP 0.20 48.0 0.115 5.6 2.87

99 C

LOMAP\GMR000 0.20 40.0 0.226 16.4 2.52

LOMAP\GMR090

0.20 35.0 0.323 16.6 3.26

USGS 1678 Golden Gate Bridge 85.1 --A

LOMAP\GGB-UP 0.20 30.0 0.056 11.3 3.81

99 B
LOMAP\GGB270 0.20 22.0 0.233 38.1 11.45
LOMAP\GGB360
0.20 27.0 0.123 17.8 2.92
CDMG 57191 Halls Valley 31.6 IFB
LOMAP\HVR-UP 0.20 28.0 0.056 8.4 4.07
02 C
LOMAP\HVR000 0.20 22.0 0.134 15.4 3.30
LOMAP\HVR090
0.20 22.0 0.103 13.5 5.46
CDMG 58498 Hayward - BART Sta 58.9
I-D LOMAP\HWB-UP 0.20 40.0 0.082 4.7 2.76
99 B
LOMAP\HWB220 0.20 31.0 0.159 15.1 3.72
LOMAP\HWB310
0.20 36.0 0.156 10.6 3.33
USGS 1028 Hollister City Hall 28.2 CHD
LOMAP\HCA-UP 0.10 32.0 0.216 14.9 7.11
99 C
LOMAP\HCA090 0.10 29.0 0.247 38.5 17.83
LOMAP\HCA180
0.10 30.0 0.215 45.0 26.10
USGS 1656 Hollister Diff. Array 25.8 IQD
LOMAP\HDA-UP 0.10 38.0 0.154 8.4 4.19
99
LOMAP\HDA165 0.10 40.0 0.269 43.9 18.48
LOMAP\HDA255
0.10 33.0 0.279 35.6 13.05
USGS 1032 Hollister - SAGO Vault 30.6 FGA
LOMAP\SGI-UP 0.10 40.0 0.042 5.0 3.95
99 A
LOMAP\SGI270 0.10 32.0 0.036 7.1 4.55
LOMAP\SGI360
0.10 31.0 0.060 8.4 4.89
CDMG 47524 Hollister - South & Pine 28.8 IQD
LOMAP\HSP-UP 0.10 31.0 0.197 15.1 7.06
99
LOMAP\HSP000 0.10 29.0 0.371 62.4 30.28
LOMAP\HSP090
0.10 23.0 0.177 29.1 18.13
UCSC 16 LGPC 6.1 --A
LOMAP\LGPVRT 0.10 0.890 54.9 17.56
99
LOMAP\LGP000 0.10 0.563 94.8 41.18
LOMAP\LGP090

0.10 0.605 51.0 11.50

CDMG 47377 Monterey City Hall 44.8 CGA

LOMAP\MCH-UP 0.20 32.0 0.032 2.7 0.92

99 A

LOMAP\MCH000 0.20 28.0 0.073 3.5 1.41

LOMAP\MCH090

0.20 22.0 0.063 5.8 2.89

CDMG 58224 Oakland - Title & Trust 77.4

BBD LOMAP\TIB-UP 0.20 49.0 0.148 6.8 1.81

99 C

LOMAP\TIB180 0.20 38.0 0.195 19.9 3.54

LOMAP\TIB270

0.20 44.0 0.244 36.1 7.20

CDMG 58264 Palo Alto - 1900 Embarc. 36.1

BQD LOMAP\PAE-UP 0.20 50.0 0.080 7.3 3.33

99

LOMAP\PAE000 0.20 32.0 0.204 22.0 11.67

LOMAP\PAE090

0.20 30.0 0.213 39.6 17.13

USGS 1601 Palo Alto - SLAC Lab 36.3

AMD LOMAP\SLC-UP 0.20 40.0 0.090 10.2 2.82

99 C

LOMAP\SLC270 0.20 33.0 0.194 37.5 9.96

LOMAP\SLC360

0.20 28.0 0.278 29.3 9.72

CDMG 58338 Piedmont Jr High 78.3 I-A

LOMAP\PJH-UP 0.20 32.0 0.026 2.5 1.91

99 A

LOMAP\PJH045 0.20 27.0 0.084 8.2 2.94

LOMAP\PJH315

0.20 28.0 0.071 9.1 3.35

CDMG 58043 Point Bonita 88.6 AFA

LOMAP\PTB-UP 0.20 21.0 0.034 7.2 2.67

99 A

LOMAP\PTB207 0.20 22.0 0.071 11.4 3.98

LOMAP\PTB297

0.20 20.0 0.072 12.9 3.93

CDMG 58505 Richmond City Hall 93.1 I-D

LOMAP\RCH-UP 0.20 30.0 0.032 4.4 1.27

99 C

LOMAP\RCH190 0.20 25.0 0.124 17.3 2.59

LOMAP\RCH280

0.20 29.0 0.106 14.2 3.91

CDMG 47189 SAGO South - Surface 34.7

IGA LOMAP\SG3-UP 0.10 29.0 0.060 7.8 5.86

99 B

LOMAP\SG3261 0.10 25.0 0.073 10.5 6.40

LOMAP\SG3351

0.10 30.0 0.067 9.6 6.42

CDMG 47179 Salinas - John & Work 32.6

AHD LOMAP\SAL-UP 0.10 42.0 0.101 6.7 2.38

99 C

LOMAP\SAL160 0.10 30.0 0.091 10.7 8.56

LOMAP\SAL250

0.10 28.0 0.112 15.7 7.87

CDMG 58065 Saratoga - Aloha Ave 13.0

AQD LOMAP\STG-UP 0.10 58.0 0.389 26.9 15.15

99 B

LOMAP\STG000 0.10 38.0 0.512 41.2 16.21

LOMAP\STG090

0.10 50.0 0.324 42.6 27.53

CDMG 58235 Saratoga - W Valley Coll. 13.7

AQD LOMAP\WVC000 0.10 38.0 0.255 42.4 19.55

99 B

LOMAP\WVC270 0.10 49.0 0.332 61.5 36.40

CDMG 58132 SF - Cliff House 84.4 CFA

LOMAP\CFH-UP 0.20 29.0 0.062 7.7 2.38

99

LOMAP\CFH000 0.20 22.0 0.075 10.8 4.35

LOMAP\CFH090

0.20 28.0 0.108 19.8 5.06

CDMG 58130 SF - Diamond Heights 77.0

BBA LOMAP\DMH-UP 0.20 30.0 0.043 6.7 2.07

99 B

LOMAP\DMH000 0.20 30.0 0.098 10.0 2.10

LOMAP\DMH090 0.20 22.0 0.113 13.1 3.36

CDMG 58131 SF - Pacific Heights 81.6 BFA

LOMAP\PHT-UP 0.20 24.0 0.031 6.0 2.87

99 A

LOMAP\PHT270 0.20 22.0 0.061 12.8 3.45

LOMAP\PHT360

0.20 20.0 0.047 9.2 2.92

CDMG 58222 SF - Presidio 83.1 IFA

LOMAP\PRS-UP 0.10 31.0 0.058 11.7 4.07

99 LOMAP\PRS000

0.10 32.0 0.099 12.9 4.32

LOMAP\PRS090

0.10 32.0 0.200 32.4 5.86

CDMG 58151 SF - Rincon Hill 79.7 IFA

LOMAP\RIN-UP 0.20 39.0 0.029 3.6 2.38
99 A
LOMAP\RIN000 0.20 41.0 0.078 6.7 2.58
LOMAP\RIN090
0.20 40.0 0.092 10.4 3.91
CDMG 58133 SF - Telegraph Hill 82.0 CFA
LOMAP\TLH-UP 0.10 22.0 0.026 3.0 1.55
99
LOMAP\TLH000 0.10 29.0 0.036 3.3 1.40
LOMAP\TLH090
0.10 28.0 0.077 6.7 4.45
CDMG 58223 SF Intern. Airport 64.4 AHD
LOMAP\SFO-UP 0.20 38.0 0.065 5.2 2.47
99 C
LOMAP\SFO000 0.20 31.0 0.236 25.5 4.20
LOMAP\SFO090
0.20 30.0 0.329 27.9 6.03
CDMG 58539 So. San Francisco, Sierra Pt. 68.2
AFA LOMAP\SSF-UP 0.06 30.0 0.034 4.7 3.35
99 A
LOMAP\SSF115 0.06 35.0 0.056 7.1 5.18
LOMAP\SSF205
0.06 30.0 0.105 8.8 4.59
USGS 17 Stanford Park. Garage 36.3
LOMAP\SPG360 0.10 70.0 0.254 38.5 15.89
99
USGS 1695 Sunnyvale - Colton Ave. 28.8
AHD LOMAP\SVL-UP 0.10 50.0 0.104 8.6 4.06
99 C
LOMAP\SVL270 0.10 40.0 0.207 37.3 19.11
LOMAP\SVL360
0.10 32.0 0.209 36.0 16.90
CDMG 58117 Treasure Island 82.9 B-D
LOMAP\TRI-UP 0.10 21.0 0.016 1.2 1.44
99 D
LOMAP\TRI000 0.10 28.0 0.100 15.6 4.41
LOMAP\TRI090
0.10 30.0 0.159 32.8 11.52
UCSC 15 UCSC 18.1 --A
LOMAP\UC2VRT 0.10 0.223 6.7 1.77
01
LOMAP\UC2000 0.10 0.309 10.3 2.80
LOMAP\UC2090
0.10 0.396 13.2 2.32
CDMG 58135 UCSC Lick Observatory 17.9

AKB LOMAP\LOB-UP 0.20 50.0 0.367 10.6 5.39
01 E
LOMAP\LOB000 0.20 40.0 0.450 18.7 3.84
LOMAP\LOB090
0.20 40.0 0.395 17.6 5.00
UCSC 14 WAHO 16.9 AQD
LOMAP\WAHVRT 0.10 0.267 12.0 2.01
99
LOMAP\WAH000 0.10 0.370 27.2 3.84
LOMAP\WAH090 0.10 0.638 38.0 5.85
CDMG 58127 Woodside 39.9 APB
LOMAP\WDS-UP 0.10 31.0 0.050 6.2 2.80
99 B
LOMAP\WDS000 0.10 25.0 0.080 13.7 8.47
LOMAP\WDS090
0.10 25.0 0.082 16.7 8.89
CDMG 58163 Yerba Buena Island 80.6 AFA
LOMAP\YBI-UP 0.20 32.0 0.028 3.8 1.82
99 A
LOMAP\YBI000 0.20 22.0 0.029 4.2 1.45
LOMAP\YBI090
0.20 31.0 0.068 13.4 3.26

0095 Georgia, USSR 1991 0615 0059 6.2 18 Ambralauri
73.7* A-A GEORGIA\AMBZ 0.10 0.007 1.0 0.31
99 99
GEORGIA\AMBX 0.10 0.018 1.8 0.54
GEORGIA\AMBY 0.10 0.016 1.3 0.39
21 Baz 49.0* A-D
GEORGIA\BAZZ 0.10 0.016 1.4 0.39
99
GEORGIA\BAZX 0.10 0.033 2.2 0.40
GEORGIA\BAZY
0.10 0.038 2.0 0.35
19 Iri 36.4* A-D
GEORGIA\IRIZ 0.20 0.045 2.9 0.59
99 GEORGIA\IRIX
0.20 0.117 7.4 0.96
GEORGIA\IRIY
0.20 0.111 7.9 0.81
20 Oni 52.0* A-D
GEORGIA\ONIZ 0.20 0.018 1.2 0.32
99

GEORGIA\ONIX 0.20 0.075 3.1 0.40

GEORGIA\ONIY

0.20 0.046 2.6 0.44

22 Zem 56.9* A-D

GEORGIA\ZEMZ 0.20 0.026 2.1 0.62

99

GEORGIA\ZEMX 0.20 0.061 4.7 0.83

GEORGIA\ZEMY 0.20 0.065 4.0 0.49

0096 Erzican, Turkey 1992 0313 95 Erzinican

ERZIKAN\ERZIUP 0.20 0.248 18.3 7.86

ERZIKAN\ERZINS 0.10 0.515 83.9 27.35

ERZIKAN\ERZIEW 0.10 0.496 64.3 22.78

0096 Cape Mendocino 1992 0425 1806 7.1 7.1 CDMG 89005 Cape Mendocino #
8.5 IFA CAPEMEND\CPM-UP 0.07 23.0 0.754 63.0 109.48

02 01

CAPEMEND\CPM000 0.07 23.0 1.497 127.4 41.01

CAPEMEND\CPM090 0.07 23.0 1.039 42.0 12.39

CDMG 89509 Eureka - Myrtle & West # 44.6

IHD CAPEMEND\EUR-UP 0.16 23.0 0.042 7.5 2.92

99 B

CAPEMEND\EUR000 0.16 23.0 0.154 20.2 5.89

CAPEMEND\EUR090 0.16 23.0 0.178 28.3 11.41

CDMG 89486 Fortuna - Fortuna Blvd # 23.6

IQD CAPEMEND\FOR-UP 0.07 23.0 0.049 5.8 3.72

99 B

CAPEMEND\FOR000 0.07 23.0 0.116 30.0 27.59

CAPEMEND\FOR090 0.07 23.0 0.114 21.7 12.79

CDMG 89156 Petrolia # 9.5 IMD

CAPEMEND\PET-UP 0.07 23.0 0.163 24.5 31.78

01 B

CAPEMEND\PET000 0.07 23.0 0.590 48.4 21.74

CAPEMEND\PET090 0.07 23.0 0.662 89.7 29.55

CDMG 89324 Rio Dell Overpass - FF # 18.5

APC CAPEMEND\RIO-UP 0.07 23.0 0.195 10.6 7.07

01 B

CAPEMEND\RIO270 0.07 23.0 0.385 43.9 22.03

CAPEMEND\RIO360 0.07 23.0 0.549 42.1 18.62

CDMG 89530 Shelter Cove Airport # 33.8 IFB

CAPEMEND\SHL-UP 0.50 23.0 0.054 2.0 0.33

99 B

CAPEMEND\SHL000 0.50 23.0 0.229 7.1 0.39

CAPEMEND\SHL090 0.50 23.0 0.189 6.6 0.57

0097 Landers 1992 0628 1158 7.3 7.4 CDMG 21081 Amboy #

69.2 AAD LANDERS\AMB-UP 0.10 23.0 0.090 11.0 3.75

00 99 A

LANDERS\AMB000 0.10 23.0 0.115 18.3 11.16

LANDERS\AMB090 0.10 23.0 0.146 20.0 7.38

USC 90088 Anaheim - W Ball # 134.0

LANDERS\BAL-UP 0.20 25.0 0.017 3.0 1.27

99 C

LANDERS\BAL000 0.13 25.0 0.047 10.8 5.91

LANDERS\BAL090 0.12 25.0 0.035 10.5 4.01

USC 90099 Arcadia - Arcadia Av # 137.1

LANDERS\ARC-UP 0.53 25.0 0.015 2.1 0.48

99 C

LANDERS\ARC172 0.20 25.0 0.031 6.1 2.91

LANDERS\ARC262 0.10 25.0 0.027 10.2 6.77

USC 90093 Arcadia - Campus Dr # 135.5

LANDERS\CAM-UP 0.25 25.0 0.023 3.4 1.26

99 C

LANDERS\CAM009 0.18 25.0 0.046 9.8 3.66

LANDERS\CAM279 0.12 25.0 0.051 12.6 7.27

CDMG 32075 Baker Fire Station # 88.5 A-D

LANDERS\BAK-UP 0.10 23.0 0.056 4.9 3.52

99 B

LANDERS\BAK050 0.10 23.0 0.108 9.4 6.35

LANDERS\BAK140 0.10 23.0 0.106 11.0 7.96

USC 90069 Baldwin Park - N Holly # 131.6

LANDERS\HOL-UP 0.28 25.0 0.020 4.2 1.25

99 B

LANDERS\HOL180 0.15 25.0 0.028 8.7 5.03

LANDERS\HOL270 0.12 25.0 0.026 7.4 5.04

CDMG 23559 Barstow # 36.1 IQD

LANDERS\BAR-UP	0.07	23.0	0.066	7.7	4.38		
				99			
LANDERS\BAR000	0.07	23.0	0.132	21.9	20.59		
LANDERS\BAR090	0.07	23.0	0.135	25.8	18.67		

USC 90094 Bell Gardens - Jaboneria # 153.9

LANDERS\JAB-UP	0.65	25.0	0.016	1.1	0.18		
				99		C	
LANDERS\JAB220	0.30	25.0	0.036	4.7	1.48		
LANDERS\JAB310	0.18	25.0	0.044	10.5	4.74		

USC 90061 Big Tujunga, Angeles Nat F # 144.3

LANDERS\TUJ-UP	0.30	25.0	0.015	2.8	0.98		
				99		B	
LANDERS\TUJ262	0.33	25.0	0.025	3.2	0.65		
LANDERS\TUJ352	0.30	25.0	0.025	3.4	0.69		

CDMG 33083 Boron Fire Station # 90.6 A-D

LANDERS\BOR-UP	0.07	23.0	0.054	5.1	3.15		
				99		B	
LANDERS\BOR000	0.07	23.0	0.119	12.9	9.14		
LANDERS\BOR090	0.07	23.0	0.090	9.6	3.70		

USC 90087 Brea - S Flower Av # 136.5

LANDERS\FLO-UP	0.20	25.0	0.018	3.7	1.30		
				99		C	
LANDERS\FLO020	0.13	25.0	0.036	11.0	6.15		
LANDERS\FLO290	0.12	25.0	0.045	11.3	7.55		

USC 90086 Buena Park - La Palma # 148.6

LANDERS\PLM-UP	0.55	25.0	0.009	0.9	0.18		
				99		C	
LANDERS\PLM090	0.18	25.0	0.045	11.5	4.81		
LANDERS\PLM180	0.15	25.0	0.052	8.8	5.64		

USC 90012 Burbank - N Buena Vista #

LANDERS\BUE-UP	0.33	25.0	0.023	4.7	1.03		
				99		C	
LANDERS\BUE250	0.25	25.0	0.049	7.2	2.18		
LANDERS\BUE340	0.28	25.0	0.068	10.4	2.86		

USC 90052 Calabasas - N Las Virg #

LANDERS\VIR-UP	0.50	25.0	0.013	1.4	0.31		
				99		B	

LANDERS\VIR200 0.28 25.0 0.018 2.8 0.81

LANDERS\VIR290 0.20 22.5 0.012 2.5 0.95

USC 90004 Chatsworth - Devonshire #

LANDERS\DEV-UP 0.20 25.0 0.018 3.8 1.31

99 C

LANDERS\DEV000 0.23 25.0 0.031 4.2 1.50

LANDERS\DEV090 0.07 25.0 0.033 6.5 5.97

USC 90078 Compton - Castlegate # 161.2

LANDERS\CAS-UP 1.25 25.0 0.020 0.8 0.07

99

LANDERS\CAS000 0.15 22.5 0.065 12.2 4.99

LANDERS\CAS270 0.15 25.0 0.063 13.1 4.05

SCE 23 Coolwater 21.2 --D

LANDERS\CLWVRT 0.10 30.0 0.174 9.9 4.01

99 B

LANDERS\CLW-LN 0.10 30.0 0.283 25.6 13.74

LANDERS\CLW-TR 0.10 30.0 0.417 42.3 13.76

USC 90070 Covina - W Badillo # 128.3

LANDERS\BAD-UP 0.15 25.0 0.029 6.1 2.42

99 C

LANDERS\BAD000 0.13 25.0 0.057 15.8 9.60

LANDERS\BAD270 0.28 25.0 0.046 7.5 2.09

CDMG 12149 Desert Hot Springs # 23.2

AQD LANDERS\DES-UP 0.07 23.0 0.167 9.9 4.71

99 B

LANDERS\DES000 0.07 23.0 0.171 20.2 13.86

LANDERS\DES090 0.07 23.0 0.154 20.9 7.77

CDMG 14368 Downey - Co Maint Bldg # 157.0

AQD LANDERS\DWN-UP 0.07 23.0 0.016 6.4 4.46

99

LANDERS\DWN000 0.07 23.0 0.051 18.3 24.03

LANDERS\DWN090 0.07 23.0 0.039 11.3 10.32

USC 90067 Duarte - Mel Canyon Rd # 126.4

LANDERS\MEL-UP 0.28 25.0 0.019 4.0 1.14

99 B

LANDERS\MEL090 0.28 25.0 0.026 3.5 0.86

LANDERS\MEL180 0.30 25.0 0.017 2.8 1.05

USC 90066 El Monte - Fairview Av # 136.1

LANDERS\FAI-UP	0.25	25.0	0.021	3.8	1.30		
				99		C	
LANDERS\FAI095	0.09	25.0	0.037	11.8	9.40		
LANDERS\FAI185	0.23	25.0	0.038	7.4	2.58		

CDMG 13122 Featherly Park # 121.9 AMC

LANDERS\FEA-UP	0.16	23.0	0.026	2.2	1.74		
				99			
LANDERS\FEA000	0.16	23.0	0.051	7.0	3.35		
LANDERS\FEA090	0.16	23.0	0.052	4.6	2.53		

CDMG 24577 Fort Irwin # 64.2 --D

LANDERS\FTI-UP	0.07	23.0	0.056	5.6	3.90		
				99		B	
LANDERS\FTI000	0.07	23.0	0.114	9.7	3.66		
LANDERS\FTI090	0.07	23.0	0.122	16.4	21.81		

USC 90002 Fountain Valley - Euclid #

LANDERS\EUC-UP	0.90	25.0	0.014	1.0	0.11		
				99		C	
LANDERS\EUC022	0.13	25.0	0.069	14.7	7.87		
LANDERS\EUC292	0.13	25.0	0.058	10.3	4.70		

USC 90063 Glendale - Las Palmas # 147.9

LANDERS\LPL-UP	1.10	25.0	0.027	1.0	0.07		
				99		C	
LANDERS\LPL177	0.30	25.0	0.044	6.4	1.07		
LANDERS\LPL267	0.28	25.0	0.071	4.1	0.74		

USC 90065 Glendora - N Oakbank # 122.2

LANDERS\OAK-UP	0.38	25.0	0.030	2.8	0.60		
				99		B	
LANDERS\OAK080	0.30	25.0	0.039	5.1	1.36		
LANDERS\OAK170	0.28	25.0	0.063	9.9	2.79		

USC 90073 Hacienda Heights - Colima # 136.0

LANDERS\COL-UP	0.20	25.0	0.027	2.9	1.11		
				99		C	
LANDERS\COL140	0.28	25.0	0.058	8.5	2.63		
LANDERS\COL230	0.25	25.0	0.046	5.7	1.31		

CDMG 12331 Hemet Fire Station # 69.5

AQD	LANDERS\HEM-UP	0.16	23.0	0.063	3.0	1.64		
					99		C	

LANDERS\HEM000 0.16 23.0 0.081 5.6 1.36

LANDERS\HEM090 0.16 23.0 0.097 5.7 2.27

USC 90083 Huntington Bch - Waikiki # 153.3

LANDERS\WAI-UP 0.63 25.0 0.012 1.0 0.15

99 C

LANDERS\WAI200 0.14 25.0 0.056 9.5 5.09

LANDERS\WAI290 0.12 25.0 0.059 10.8 4.07

CDMG 12026 Indio - Coachella Canal # 55.7

IQD LANDERS\IND-UP 0.10 23.0 0.042 6.6 3.99

99 C

LANDERS\IND000 0.10 23.0 0.104 9.6 5.05

LANDERS\IND090 0.10 23.0 0.109 15.2 9.69

CDMG 14196 Inglewood - Union Oil # 166.9

IQD LANDERS\ING-UP 0.07 23.0 0.015 4.8 5.52

99

LANDERS\ING000 0.07 23.0 0.043 15.7 19.03

LANDERS\ING090 0.07 23.0 0.035 10.5 9.99

CDMG 22170 Joshua Tree # 11.6 AGC

LANDERS\JOS-UP 0.07 23.0 0.181 15.0 9.39

99 B

LANDERS\JOS000 0.07 23.0 0.274 27.5 9.82

LANDERS\JOS090 0.07 23.0 0.284 43.2 14.51

CDMG 14403 LA - 116th St School # 164.0

AQD LANDERS\116-UP 0.07 23.0 0.013 5.2 4.36

99

LANDERS\116000 0.07 23.0 0.042 14.1 17.91

LANDERS\116090 0.07 23.0 0.042 12.1 13.75

USC 90025 LA - E Vernon Av # 157.7

LANDERS\VER-UP 0.38 25.0 0.019 2.2 0.61

99 C

LANDERS\VER090 0.13 25.0 0.034 7.7 4.64

LANDERS\VER180 0.18 25.0 0.039 8.9 4.24

USC 90034 LA - Fletcher Dr # 152.3

LANDERS\FLE-UP 0.20 22.5 0.024 3.1 0.62

99 C

LANDERS\FLE144 0.28 25.0 0.045 6.2 1.48

LANDERS\FLE234 0.28 25.0 0.040 4.0 1.10

USC 90032 LA - N Figueroa St # 148.7

LANDERS\FIG-UP 0.40 25.0 0.016 2.3 0.52
99 B

LANDERS\FIG058 0.35 25.0 0.030 3.6 1.09

LANDERS\FIG328 0.38 25.0 0.037 4.3 1.09

USC 90021 LA - N Westmoreland 159.2

LANDERS\WES-UP 0.53 25.0 0.016 1.9 0.38
99 B

LANDERS\WES000 0.38 25.0 0.044 3.7 0.81

LANDERS\WES270 0.25 25.0 0.036 3.9 1.31

CDMG 24400 LA - Obregon Park # 151.4

AQD LANDERS\OBR-UP 0.07 23.0 0.020 4.1 3.72
99

LANDERS\OBR000 0.07 23.0 0.043 15.5 16.38

LANDERS\OBR090 0.07 23.0 0.065 7.6 5.83

USC 90022 LA - S Grand Ave # 161.1

LANDERS\SGR-UP 0.40 25.0 0.014 1.9 0.51
99 C

LANDERS\SGR090 0.28 25.0 0.028 4.7 1.64

LANDERS\SGR180 0.18 25.0 0.035 6.6 2.88

USC 90020 LA - W 15th St # 161.2

LANDERS\W15-UP 0.30 25.0 0.015 3.3 1.02
99 C

LANDERS\W15090 0.09 25.0 0.029 7.8 5.44

LANDERS\W15180 0.30 25.0 0.036 6.3 1.89

USC 90023 LA - W 70th St #

LANDERS\W70-UP 0.35 25.0 0.014 1.8 0.56
99 C

LANDERS\W70000 0.18 25.0 0.055 9.6 3.06

LANDERS\W70270 0.20 25.0 0.049 11.3 3.93

USC 90060 La Crescenta - New York # 147.9

LANDERS\NYK-UP 0.50 25.0 0.014 1.9 0.32
99 C

LANDERS\NYK090 0.40 25.0 0.024 2.7 0.56

LANDERS\NYK180 0.30 25.0 0.030 4.3 1.11

USC 90074 La Habra - Briarcliff # 142.8

LANDERS\BRI-UP 0.53 25.0 0.026 2.2 0.44
99 C

LANDERS\HEM000 0.16 23.0 0.081 5.6 1.36

LANDERS\HEM090 0.16 23.0 0.097 5.7 2.27

USC 90083 Huntington Bch - Waikiki # 153.3

LANDERS\WAI-UP 0.63 25.0 0.012 1.0 0.15

99 C

LANDERS\WAI200 0.14 25.0 0.056 9.5 5.09

LANDERS\WAI290 0.12 25.0 0.059 10.8 4.07

CDMG 12026 Indio - Coachella Canal # 55.7

IQD LANDERS\IND-UP 0.10 23.0 0.042 6.6 3.99

99 C

LANDERS\IND000 0.10 23.0 0.104 9.6 5.05

LANDERS\IND090 0.10 23.0 0.109 15.2 9.69

CDMG 14196 Inglewood - Union Oil # 166.9

IQD LANDERS\ING-UP 0.07 23.0 0.015 4.8 5.52

99

LANDERS\ING000 0.07 23.0 0.043 15.7 19.03

LANDERS\ING090 0.07 23.0 0.035 10.5 9.99

CDMG 22170 Joshua Tree # 11.6 AGC

LANDERS\JOS-UP 0.07 23.0 0.181 15.0 9.39

99 B

LANDERS\JOS000 0.07 23.0 0.274 27.5 9.82

LANDERS\JOS090 0.07 23.0 0.284 43.2 14.51

CDMG 14403 LA - 116th St School # 164.0

AQD LANDERS\116-UP 0.07 23.0 0.013 5.2 4.36

99

LANDERS\116000 0.07 23.0 0.042 14.1 17.91

LANDERS\116090 0.07 23.0 0.042 12.1 13.75

USC 90025 LA - E Vernon Av # 157.7

LANDERS\VER-UP 0.38 25.0 0.019 2.2 0.61

99 C

LANDERS\VER090 0.13 25.0 0.034 7.7 4.64

LANDERS\VER180 0.18 25.0 0.039 8.9 4.24

USC 90034 LA - Fletcher Dr # 152.3

LANDERS\FLE-UP 0.20 22.5 0.024 3.1 0.62

99 C

LANDERS\FLE144 0.28 25.0 0.045 6.2 1.48

LANDERS\FLE234 0.28 25.0 0.040 4.0 1.10

USC 90003 Northridge - Saticoy St #

LANDERS\STC-UP	0.20	25.0	0.017	4.5	1.69			
				99		C		
LANDERS\STC090	0.08	25.0	0.036	12.2	8.82			
LANDERS\STC180	0.07	25.0	0.036	15.9	17.06			

CDMG 12025 Palm Springs Airport # 37.5

IQD LANDERS\PAL-UP	0.07	23.0	0.108	6.8	3.08			
				99		C		
LANDERS\PAL000	0.07	23.0	0.076	10.9	6.95			
LANDERS\PAL090	0.07	23.0	0.089	13.8	5.29			

CDMG 23525 Pomona - 4th & Locust # 117.0

IQD LANDERS\POM-UP	0.12	23.0	0.035	2.8	1.52			
				99		C		
LANDERS\POM000	0.12	23.0	0.067	12.8	6.92			
LANDERS\POM090	0.12	23.0	0.044	8.6	3.50			

CDMG 12168 Puerta La Cruz # 95.9 AQB

LANDERS\PUE-UP	0.30	23.0	0.038	1.7	0.45			
				99		B		
LANDERS\PUE000	0.30	23.0	0.047	2.0	0.39			
LANDERS\PUE090	0.30	23.0	0.044	2.0	0.55			

CDMG 13123 Riverside Airport # 96.1 AQB

LANDERS\RIV-UP	0.16	23.0	0.040	1.7	1.64			
				99		B		
LANDERS\RIV180	0.16	23.0	0.043	3.0	1.76			
LANDERS\RIV270	0.16	23.0	0.041	3.2	1.36			

USC 90019 San Gabriel - E Grand Av # 141.6

LANDERS\GRN-UP	0.16	22.5	0.022	6.3	2.97			
				99		A		
LANDERS\GRN180	0.07	25.0	0.041	14.1	15.03			
LANDERS\GRN270	0.13	25.0	0.036	9.6	6.03			

USC 90077 Santa Fe Springs - E Joslin # 150.4

LANDERS\EJS-UP	0.35	25.0	0.024	1.5	0.47			
				99		C		
LANDERS\EJS030	0.18	25.0	0.060	5.9	2.67			
LANDERS\EJS120	0.15	25.0	0.047	9.2	4.23			

CDMG 12206 Silent Valley - Poppet Flat # 51.7

IGA LANDERS\SIL-UP	0.12	23.0	0.038	3.2	2.02			
				99		A		

LANDERS\SIL000 0.12 23.0 0.050 3.8 2.02

LANDERS\SIL090 0.12 23.0 0.040 5.1 3.89

USC 90008 Sun Valley - Glenoaks #

LANDERS\GLN-UP 1.00 25.0 0.012 0.9 0.08

99 B

LANDERS\GLN230 0.33 25.0 0.027 2.6 0.71

LANDERS\GLN320 0.45 25.0 0.021 2.9 0.60

USC 90006 Sun Valley - Roscoe #

LANDERS\ROS-UP 0.12 25.0 0.021 4.4 2.48

99 B

LANDERS\ROS000 0.07 25.0 0.039 18.1 18.27

LANDERS\ROS090 0.18 25.0 0.028 7.0 2.62

USC 90058 Sunland - Mt Gleason Av # 151.1

LANDERS\GLE-UP 0.20 25.0 0.021 2.8 0.91

99 B

LANDERS\GLE170 0.33 25.0 0.029 5.3 1.40

LANDERS\GLE260 0.25 25.0 0.031 6.0 1.70

CDMG 24436 Tarzana - Cedar Hill # 175.6 IPD

LANDERS\TAR-UP 0.12 23.0 0.026 2.5 1.15

99

LANDERS\TAR000 0.12 23.0 0.066 9.5 6.18

LANDERS\TAR090 0.12 23.0 0.043 5.4 2.75

USC 90089 Tustin - E Sycamore # 134.0

LANDERS\SYC-UP 0.28 25.0 0.017 3.3 0.97

99 C

LANDERS\SYC135 0.13 25.0 0.044 14.2 5.90

LANDERS\SYC225 0.23 25.0 0.046 6.6 2.11

CDMG 22161 Twentynine Palms # 42.2

AGA LANDERS\29P-UP 0.12 23.0 0.040 3.3 2.62

99 A

LANDERS\29P000 0.12 23.0 0.080 3.7 2.36

LANDERS\29P090 0.12 23.0 0.060 4.9 4.06

USC 90090 Villa Park - Serrano Av # 131.4

LANDERS\SER-UP 0.20 25.0 0.021 2.8 0.93

99 B

LANDERS\SER000 0.11 25.0 0.028 8.0 5.32

LANDERS\SER270 0.18 25.0 0.035 7.0 3.51

USC 90071 West Covina - S Orange # 132.4

LANDERS\ORA-UP 0.25 25.0 0.023 5.7 2.38
99 C

LANDERS\ORA225 0.28 25.0 0.048 8.7 2.30

LANDERS\ORA315 0.13 25.0 0.048 15.1 12.06

CDMG 22074 Yermo Fire Station # 24.9

AQD LANDERS\YER-UP 0.07 23.0 0.136 12.9 4.82
99 C

LANDERS\YER270 0.07 23.0 0.245 51.5 43.81

LANDERS\YER360 0.07 23.0 0.152 29.7 24.69

0098 Northridge 1994 0117 1231 6.7 6.6 6.7 CDMG 24576 Anaverde Valley - City R # 38.4 NORTHR\ANA-UP 0.20 46.0 0.044 4.7 1.70
02 99

NORTHR\ANA090 0.20 46.0 0.044 3.9 1.09

NORTHR\ANA180 0.20 46.0 0.060 5.5 1.54

CDMG 24087 Arleta - Nordhoff Fire Sta # 9.2

AQD NORTHR\ARL-UP 0.12 23.0 0.552 18.4 8.83
99

NORTHR\ARL090 0.12 23.0 0.344 40.6 15.04

NORTHR\ARL360 0.12 23.0 0.308 23.2 10.75

USC 90053 Canoga Park - Topanga Can # 15.5

NORTHR\CNP-UP 0.20 0.408 14.0 3.20
99 C

NORTHR\CNP106 0.13 0.377 36.2 7.56

NORTHR\CNP196 0.08 0.427 57.8 15.85

CDMG 24278 Castaic - Old Ridge Route # 22.6

A-B NORTHR\ORR-UP 0.12 23.0 0.217 12.4 1.94
99 B

NORTHR\ORR090 0.12 23.0 0.568 52.1 4.21

NORTHR\ORR360 0.12 23.0 0.514 52.2 2.41

CDMG 14368 Downey - Co Maint Bldg # 47.6

AQD NORTHR\DWN-UP 0.80 23.0 0.146 3.9 0.27
99

NORTHR\DWN090 0.20 23.0 0.177 9.9 2.11

NORTHR\DWN360 0.20 23.0 0.223 12.9 2.01

CDMG 24575 Elizabeth Lake # 37.2

NORTHR\ELI-UP 0.16 46.0 0.049 4.7 2.35

99

NORTHR\ELI090 0.16 46.0 0.155 7.3 2.70

NORTHR\ELI180 0.16 46.0 0.114 8.1 2.08

CDMG 13660 Hemet - Ryan Airfield # 144.1

NORTHR\HEM-UP 0.30 46.0 0.027 2.0 0.18

99

NORTHR\HEM000 0.30 46.0 0.064 4.5 0.66

NORTHR\HEM090 0.30 46.0 0.046 4.7 0.51

USGS 0655 Jensen Filter Plant # 6.2

NORTHR\JENVER 0.08 0.400 34.1 8.89

99

NORTHR\JEN022 0.20 0.424 106.2 43.06

NORTHR\JEN292 0.30 0.593 99.3 24.00

CDMG 14403 LA - 116th St School # 41.9

AQD NORTHR\116-UP 0.70 23.0 0.061 2.8 0.30

99

NORTHR\116090 0.16 23.0 0.198 15.9 3.01

NORTHR\116360 0.16 23.0 0.142 13.4 2.73

CDMG 24157 LA - Baldwin Hills # 31.3 IPD

NORTHR\BLD-UP 0.16 23.0 0.091 8.4 3.29

99

NORTHR\BLD090 0.16 23.0 0.239 14.9 6.17

NORTHR\BLD360 0.16 23.0 0.168 17.6 4.79

CDMG 24389 LA - Century City CC North # 25.7

IQD NORTHR\CCN-UP 0.14 23.0 0.116 8.7 3.47

99

NORTHR\CCN090 0.14 23.0 0.256 21.1 6.68

NORTHR\CCN360 0.14 23.0 0.222 25.2 5.70

CDMG 24592 LA - City Terrace # 37.0

NORTHR\LAC-UP 0.20 46.0 0.135 7.6 1.84

99

NORTHR\LAC090 0.20 46.0 0.263 12.8 2.89

NORTHR\LAC180 0.20 46.0 0.316 14.1 2.42

CDMG 24303 LA - Hollywood Stor FF # 25.5

IPD NORTHR\HOL-UP 0.20 23.0 0.139 9.2 2.30

C

99

NORTHR\HOL090 0.20 23.0 0.231 18.3 4.81

NORTHR\HOL360 0.20 23.0 0.358 27.5 3.04

CDMG 24400 LA - Obregon Park # 37.9

AQD NORTHR\OBR-UP 0.20 23.0 0.115 3.7 1.27

99

NORTHR\OBR090 0.60 23.0 0.355 16.7 1.43

NORTHR\OBR360 0.90 23.0 0.563 24.5 2.79

CDMG 24612 LA - Pico & Sentous # 32.7

NORTHR\PIC-UP 0.20 46.0 0.065 5.3 1.69

99

NORTHR\PIC090 0.20 46.0 0.103 12.2 3.71

NORTHR\PIC180

0.20 46.0 0.186 14.3 2.38

CDMG 24611 LA - Temple & Hope # 32.3

NORTHR\TEM-UP 0.20 46.0 0.097 4.6 1.34

99

NORTHR\TEM090 0.20 46.0 0.126 13.9 3.15

NORTHR\TEM180 0.20 46.0 0.184 20.0 2.74

CDMG 24605 LA - Univ. Hospital # 34.6

NORTHR\UNI-UP 0.20 46.0 0.119 6.4 1.37

99

NORTHR\UNI005 0.20 46.0 0.493 31.1 2.39

NORTHR\UNI095 0.20 46.0 0.214 10.8 2.37

USGS 127 Lake Hughes #9 # 26.8 AGA

NORTHR\LH9-UP 0.08 0.079 3.6 3.56

99

NORTHR\LH9000 0.08 0.165 8.4 4.54

NORTHR\LH9090 0.08 0.217 10.1 2.77

CDMG 24607 Lake Hughes #12A # 22.8

NORTHR\H12-UP 0.13 46.0 0.121 4.0 2.59

99

NORTHR\H12090 0.12 46.0 0.174 11.8 4.64

NORTHR\H12180 0.12 46.0 0.258 11.9 6.24

CDMG 14560 LB - City Hall # 58.2 ---

NORTHR\LBC-UP 1.20 23.0 0.021 1.2 0.11

99

NORTHR\LBC090 0.30 23.0 0.036 5.0 1.65

NORTHR\LBC360 0.30 23.0 0.051 4.0 1.09

CDMG 23595 Littlerock - Brainard Can # 46.9

NORTHR\LIT-UP 0.25 46.0 0.034 2.4 0.50

99
NORTHR\LIT090 0.20 46.0 0.072 6.0 1.35

NORTHR\LIT180
0.20 46.0 0.060 6.3 1.25

CDMG 24396 Malibu - Point Dume Sch # 35.2
AMB NORTHR\MAL-UP 0.30 23.0 0.087 4.4 1.09
99
NORTHR\MAL090 0.30 23.0 0.130 8.5 2.11

NORTHR\MAL360 0.30 23.0 0.084 8.9 1.79

CDMG 24283 Moorpark - Fire Sta # 28.0
AQD NORTHR\MRP-UP 0.45 23.0 0.159 7.9 0.90
99
NORTHR\MRP090 0.16 23.0 0.193 20.2 4.79

NORTHR\MRP180 0.16 23.0 0.292 20.7 4.24

CDMG 23572 Mt Baldy - Elementary Sch # 71.5
NORTHR\BAL-UP 0.30 46.0 0.037 2.2 0.39
99
NORTHR\BAL090 0.30 46.0 0.080 3.8 0.56

NORTHR\BAL180 0.30 46.0 0.070 4.3 0.39

CDMG 24399 Mt Wilson - CIT Seis Sta # 36.1
IGA NORTHR\MTW-UP 0.08 0.087 3.6 0.58
99
NORTHR\MTW000 0.08 0.234 7.4 0.70

NORTHR\MTW090 0.08 0.134 5.8 0.45

CDMG 24586 Neenach - Sacatara Ck # 53.2
NORTHR\NEE-UP 0.12 46.0 0.047 7.2 3.10
99
NORTHR\NEE090 0.12 46.0 0.056 10.0 6.48

NORTHR\NEE180 0.12 46.0 0.069 13.1 8.22

CDMG 24279 Newhall - Fire Sta # 7.1 AQD
NORTHR\NWH-UP 0.12 23.0 0.548 31.5 16.27
99
NORTHR\NWH090 0.12 23.0 0.583 75.5 17.57

NORTHR\NWH360 0.12 23.0 0.590 97.2 38.05

CDMG 13610 Newport Bch - Newp & Coast # 84.6
NORTHR\NEW-UP 0.17 46.0 0.021 2.2 0.66
99
NORTHR\NEW090 0.12 46.0 0.106 7.1 1.76

NORTHR\NEW180 0.12 46.0 0.081 7.4 1.79

USC 90003 Northridge - Saticoy St # 12.8

NORTHR\SAT-UP 0.08 0.785 32.5 6.65

99

NORTHR\SAT090 0.13 0.364 29.5 8.36

NORTHR\SAT180 0.00 0.452 62.0 16.99

CDMG 24207 Pacoima Dam (downstr) # 8.0

AMB NORTHR\PAC-UP 0.75 23.0 0.190 14.2 1.35

99

NORTHR\PAC175 0.16 23.0 0.415 45.6 5.06

NORTHR\PAC265 0.16 23.0 0.434 31.3 4.80

CDMG 24207 Pacoima Dam (upper left) # 8.0

NORTHR\PUL-UP 0.16 23.0 1.229 49.6 11.75

99

NORTHR\PUL104 0.16 23.0 1.585 55.7 6.06

NORTHR\PUL194 0.16 23.0 1.285 103.9 23.80

CDMG 24088 Pacoima Kagel Canyon # 8.2

AMB NORTHR\KAG-UP 0.20 23.0 0.169 15.1 4.14

99

NORTHR\KAG090 0.14 23.0 0.301 31.4 10.87

NORTHR\KAG360 0.14 23.0 0.433 51.5 7.21

CDMG 23597 Phelan - Wilson Ranch # 86.1

NORTHR\PHE-UP 0.20 46.0 0.036 2.3 0.48

99

NORTHR\PHE090 0.20 46.0 0.047 5.0 1.00

NORTHR\PHE180 0.20 46.0 0.057 4.0 1.23

76 Point Mugu - Laguna Pk # 44.3

NORTHR\MUG-UP 0.08 0.065 3.7 0.96

99

NORTHR\MUG000 0.20 0.198 13.2 1.83

NORTHR\MUG090 0.20 0.156 16.0 3.08

CDMG 23598 Rancho Cucamonga - Deer Can # 80.0

NORTHR\CUC-UP 0.30 46.0 0.025 2.2 0.40

99

NORTHR\CUC090 0.30 46.0 0.071 4.2 0.56

NORTHR\CUC180 0.30 46.0 0.051 5.9 0.78

DWP 77 Rinaldi Receiving Sta # 7.1

NORTHR\RRS-UP 0.00 0.852 50.7 11.65

99

NORTHR\RRS228 0.00 0.838 166.1 28.78

NORTHR\RRS318 0.00 0.472 73.0 19.76

CDMG 23672 San Bernardino - CSUSB Gr # 103.1

NORTHR\BER-UP 0.30 46.0 0.021 1.5 0.25

99

NORTHR\BER000 0.30 46.0 0.034 2.8 0.31

NORTHR\BER090 0.30 46.0 0.069 4.0 0.77

CDMG 23542 San Bernardino - E & Hosp # 108.1

NORTHR\SBE-UP 0.20 46.0 0.044 2.6 0.51

99

NORTHR\SBE090 0.20 46.0 0.085 5.9 0.97

NORTHR\SBE180 0.20 46.0 0.096 6.5 1.34

CDMG 12673 San Jacinto - CDF Fire Sta # 146.5

NORTHR\CDF-UP 0.16 46.0 0.022 3.7 1.27

99

NORTHR\CDF000 0.16 46.0 0.081 8.1 1.62

NORTHR\CDF090 0.16 46.0 0.099 7.7 1.56

CDMG 24401 San Marino, SW Academy # 35.1

AQD NORTHR\SMR-UP 0.60 23.0 0.083 3.7 0.41

99

NORTHR\SMR090 0.30 23.0 0.116 7.3 1.10

NORTHR\SMR360 0.60 23.0 0.150 7.4 0.75

CDMG 24644 Sandberg - Bald Mtn # 43.4

NORTHR\SAN-UP 0.12 46.0 0.044 6.4 3.66

99

NORTHR\SAN090 0.12 46.0 0.091 12.2 4.73

NORTHR\SAN180 0.12 46.0 0.098 8.9 4.61

CDMG 24538 Santa Monica City Hall # 27.6 ---

NORTHR\STM-UP 0.14 23.0 0.230 14.3 4.17

99

NORTHR\STM090 0.14 23.0 0.883 41.7 15.09

NORTHR\STM360 0.14 23.0 0.370 25.1 7.16

USGS 5108 Santa Susana Ground # 19.3

NORTHR\SSU000 0.20 0.279 19.4 4.11

99

NORTHR\SSU090 0.00 0.290 19.7 7.45

CDMG 14578 Seal Beach - Office Bldg # 64.9

NORTHR\SEA-UP	0.16	46.0	0.037	2.1	1.45				
				99					
NORTHR\SEA000	0.16	46.0	0.061	5.8	1.87				
NORTHR\SEA090	0.16	46.0	0.084	6.9	1.99				
				USGS	0637	Sepulveda VA #		8.9	
NORTHR\SPVVER	0.10		0.467	33.2	9.58				
				99					
NORTHR\SPV270	0.10		0.753	84.8	18.68				
NORTHR\SPV360	0.00		0.939	76.6	14.95				
				MWD	78	Stone Canyon #		22.2	
NORTHR\SCRVER	0.08		0.181	6.1	2.42				
				99					
NORTHR\SCR000	0.03		0.252	28.0	3.14				
NORTHR\SCR090	0.03		0.388	38.0	4.60				
				USC	90006	Sun Valley - Roscoe #		10.7	
NORTHR\ROS-UP	0.17		0.282	12.3	5.27				
				99			B		
NORTHR\ROS000	0.00		0.267	23.3	6.20				
NORTHR\ROS090	0.10		0.440	38.2	9.95				
				DWP	74	Sylmar - Converter Sta #		6.2	
NORTHR\SCS-UP	0.00		0.586	34.6	25.44				
				99					
NORTHR\SCS052	0.00		0.612	117.4	53.47				
NORTHR\SCS142	0.00		0.897	102.8	46.99				
				DWP	75	Sylmar - Converter Sta East #		6.1	
NORTHR\SCE-UP	0.00		0.377	24.3	7.30				
				99					
NORTHR\SCE018	0.00		0.828	117.5	34.22				
NORTHR\SCE288	0.00		0.493	74.6	28.69				
				CDMG	24514	Sylmar - Olive View Med FF #		6.4	
AQD NORTHR\SYL-UP	0.12	23.0	0.535	19.1	8.54				
				99			C		
NORTHR\SYL090	0.12	23.0	0.604	78.2	16.05				
NORTHR\SYL360	0.12	23.0	0.843	129.6	32.68				
				CDMG	24436	Tarzana, Cedar Hill #		17.5	A-B
NORTHR\CHA-UP	0.10	23.0	1.048	75.4	19.56				
				99					
NORTHR\CHA090	0.10	23.0	1.779	113.5	32.71				

NORTHR\CHA360	0.10	23.0	0.990	77.4	32.65
			USGS 5081 Topanga - Fire Sta #		23.4
NORTHR\TPFVER	0.10		0.199	10.5	3.10
				99	
NORTHR\TPF000	0.20		0.364	17.6	2.87
NORTHR\TPF090	0.30		0.266	12.9	1.34
			CDMG 24047 Vasquez Rocks Park #		24.2
IBA NORTHR\VAS-UP	0.10		0.091	6.1	1.61
				99	
NORTHR\VAS000	0.00		0.151	18.5	2.92
NORTHR\VAS090	0.08		0.139	11.2	2.89
			CDMG 23574 Wrightwood - Swarthout #		71.9
NORTHR\WRI-UP	0.30	46.0	0.034	2.0	0.25
				99	
NORTHR\WRI090	0.30	46.0	0.047	3.7	0.49
NORTHR\WRI180	0.30	46.0	0.060	3.7	0.52

****
****
****

Notes:

(1) Source mechanism: 00 = strike slip, 01 = normal, 02 = reverse, 03 = reverse-oblique, 04 = normal-oblique, 99 = unknown.

Dip is the dip of rupture surface.

(2) M is moment magnitude, UNK = Magnitude type unknown.

(3) Station numbers were assigned where not available, using numbers 1-33 and 60-100.

Records marked with a # were corrected by CDMG or other agency because the uncorrected records are not available yet.

Records marked with a @ did not have Fourier spectra computed because the noise levels were high.

H/F is the designation for the site being on the hanging wall (01) or foot wall (02), or unknown/not applicable (99).

(4) Distances marked with a * are hypocentral instead of closest distances.

(5) Site codes are from two sources: 1) Geomatrix (3 letter), 2) USGS (1 letter), described below.

GEOMATRIX 3-LETTER SITE CLASSIFICATIONS

FIRST LETTER: Instrument housing

I = Free-field instrument or instrument shelter. Instrument is located at or within several feet of the ground surface.

A = One-story structure of lightweight construction. Instrument is located at the lowest level and within several feet of the ground surface.

B = Two- to four-story structure of lightweight construction. Instrument is located at the lowest level and within several feet of the ground surface.

C = Two- to four-story structure of lightweight construction. Instrument is located at the lowest level in a basement and below the ground surface.

D = Five or more story structure of heavy construction. Instrument is located at the lowest level and within several feet of the ground surface.

E = Five or more story structure of heavy construction. Instrument is located at the lowest level in a basement and below the ground surface.

F = Structure housing instrument is buried below the ground surface, eg. tunnel.

G = Structure of light or heavyweight construction, instrument not at lowest level.

H = Earth dam.

I = Concrete Dam.

SECOND LETTER: Mapped local geology

Sedimentary or metasedimentary:

H = Holocene (Recent) Quaternary (< 15000y bp).

Q = Pleistocene Quaternary (< 2my bp).

P = Pliocene Tertiary (< 6my bp).

M = Miocene Tertiary (< 22my bp).

O = Oligicene Tertiary (< 36my bp).

E = Eocene Tertiary (< 58my bp).

L = Paleocene Tertiary (< 63my bp).

K = Cretaceous (< 145my bp).

F = Franciscan Formation (Cretaceous/Late Jurrassic).

J = Jurassic (< 210my bp).

T = Triassic (<255my bp).

Z = Permian or older (> 255my bp).

Igneous or meta-igneous:

V = Volcanic (extrusive).

N = Intrusive.

G = Granitic.

THIRD LETTER: Geotechnical subsurface characteristics

A = Rock. Instrument on rock (Vs > 600 mps) or < 5m of soil over rock.

B = Shallow (stiff) soil. Instrument on/in soil profile up to 20m thick overlying rock.

C = Deep narrow soil. Instrument on/in soil profile at least 20m thick overlying rock, in a narrow canyon or valley no more than several km wide.

D = Deep broad soil. Instrument on/in soil profile at least 20m thick overlying rock, in a broad valley.

E = Soft deep soil. Instrument on/in deep soil profile with average Vs < 150 mps.

USGS 1-LETTER SITE CLASSIFICATIONS

Average shear-wave velocity to a depth of 30m is:

A = > 750 m/s

B = 360 - 750 m/s

C = 180 - 360 m/s

D = < 180 m/s

APPENDIX C

Probabilistic Models of Site Velocity Profiles for Generic and Site-Specific Ground-Motion Amplification Studies

APPENDIX D

Recommendations for Uncertainty Estimates in Shear Modulus Reduction and Hysteretic Damping Relationships

RECOMMENDATIONS FOR UNCERTAINTY ESTIMATES IN SHEAR MODULUS REDUCTION AND HYSTERETIC DAMPING RELATIONSHIPS

Prepared By
Carl J. Costantino
Department of Civil Engineering
City University of New York

for
Brookhaven National Laboratory
Upton, New York

October, 1996

1.0 INTRODUCTION

This report summarizes some recent efforts made to generate estimates of potential variability in shear modulus degradation and hysteretic damping data typically used for site seismic response analyses. These degradation properties are of interest for both rock-like and soil-like materials. The variability in these parameters plays a significant role in ascertaining the uncertainty in free-field site responses computed at the ground surface which typically serves as input to structural response evaluations. Although much data are usually available in the open literature to estimate appropriate "best estimate" properties, comparable information on the uncertainty in this information is not usually specifically evaluated.

2.0 ESTIMATES APPROPRIATE FOR ROCK MATERIALS

To address the issue of uncertainty in degradation properties appropriate for rock materials, data available from twenty (20) resonant column (RC) tests conducted on rock samples were analyzed. Seventeen (17) of the RC tests were conducted on samples analyzed for the Comanche Peak NPP (Ref. 8). These data were generated from samples taken from three separate rock formations which were labeled as claystones, limestones and sandstones. Three RC tests were performed on samples taken from Los Alamos National Laboratory (Ref. 9), two on tuff rocks and one from a basalt rock sample. The low strain shear moduli for these samples are listed in Table 1, together with an estimate of the low strain shear wave velocity. This latter parameter was estimated by assuming a rock unit weight of 150 pcf. As may be noted, the shear wave velocities for the rock samples varies from about 1,000 fps to over 7,000 fps. The low value of shear wave velocities for some of these rock samples is in the range typically considered appropriate for sandy soils and indicate that significant levels of shear strain (nonlinearity) may occur during seismic shaking. In such cases, the issue of degradation properties and their uncertainty becomes important.

From each RC test, values of G/G_{max} and D were obtained from plots of data presented in the reports at various values of cyclic shear strain from low strain levels ($1*10^{-4}$ percent) to intermediate levels (about $3*10^{-2}$ percent). Where available, data were selected at percent shear strain levels [specified in terms of log to the base 10] of -4, -3.5, -3, -2.5, -2 and -1.5. It should be noted that not all tests spanned this entire strain range. For example, only 7 experiments extended to the strain level of $\log_{10}$ (% strain) of (-1.5). Plots of G/G_{max} and D from these experiments are shown in Figure 1. It is clear that since the shear modulus data is scaled to its low strain value, the scatter in G/G_{max} is much lower at all strain levels than that in hysteretic damping (D) data.

The summary of the statistics computed from this data set at each strain level is listed in Table 2. Plots of the corresponding median values and ± sigma values in G/G_{max} and D from all

the test data are listed in Figure 2. Again, the much larger scatter in hysteretic damping data is obvious. In addition, the scatter in shear modulus ratio increases with shear strain while the scatter in hysteretic damping data reduces with strain level.

In addition to using the data set from all of the rock tests available, a subset of the data for a single rock formation was selected and analyzed. This was done to address the issue of potential scatter in data which may occur over the footprint of a critical facility. In this case, the claystone data from the Comanche Peak site was selected as being appropriate. The same calculations were then performed for this reduced data set and these are summarized in Table 3 and plotted in Figure 3. The scatter in the data is obviously much lower than that obtained from the whole data set , as indicated by comparing Figures 2 and 3.

Following the evaluation of the rock test data available, a comparison of the degradation data was made with the recommendations on degradation properties for rock materials contained in the EPRI study (Ref. 10). These recommendations contain degradation curves which are functions of depth or confining pressures, but do not contain estimates of variability. In Figure 4, the data from all the rock tests is compared with the EPRI recommendations for rocks at a shallow depth (0' to 20' depth) or rocks at a deep depth (2,000' to 5,000'). As may be noted, the median test damping data at low strain matches the EPRI recommendation and tends to follow the deep rock curve. However, the variability in the measured damping ratio is much greater at low strain than the EPRI low strain estimate for either shallow or deep rocks. The comparison of shear modulus degradation data falls within the bounds for the EPRI rock curves, but again tracks closer to the recommendation for the deeper rocks.

3.0 ESTIMATES APPROPRIATE FOR SOIL MATERIALS

A similar effort was undertaken to estimate appropriate values of variability (or sigma) for soil moduli curves. Figure 5 presents estimates of sigma as a function of cyclic strain for sandy soils. After reviewing typical test results presented in the literature, the envelope functions for shear modulus ratio and damping modulus from the original Seed-Idriss plots (Ref. 1, 2) were used. It should be noted that these bounding curves are similar to the recent recommendations of Pyke, et al (Ref. 5) for sands. If the bounding curves are assumed to be appropriate definitions of the 5th and 95th percentile cases, the sigma computation is straight forward and these are indicated in Figure 5. Again, it may be noted that the same trend in the data exists as mentioned above for the rock data; that is, the sigma in the hysteretic damping modulus is greatest at low strain and decreases with strain, whereas the opposite is true with the shear modulus reduction data.

Figure 6 presents similar information available for gravelly soils. In this case the Seed-Idriss and Pyke recommendations are similar for G/G_{max} but not for damping. The Seed-Idriss

data was taken from tests on four different gravel types. In addition, some recent test data for gravels presented by the Japanese (CRIEPI) for the Taiwan project are shown on the plots which, as may be noted, are significantly different from either of the Seed-Idriss or Pyke recommendations. Again using the definition of the 5th and 95th percentiles from the upper bound Pyke and lower bound Seed-Idriss data, the values of sigma can be calculated at each strain level of interest, and these are shown in Figure 7. Once again, the same trends in sigma for both hysteretic damping and shear modulus reduction can be noted.

In addition to this generic data available in the literature, the recently developed data from the Savannah River Site (Ref. 11) were also analyzed for its variability, some of which are shown in Figure 8. These data were developed by K. Stokoe from torsional shear (TS) tests conducted on undisturbed samples taken at the site under very careful scrutiny and control. The variability in the measured hysteretic damping data is shown in Figure 8 and again are found to be similar to the estimates previously presented for the generic sand and gravel materials.

A comparison of these various estimates of strain dependent sigma are presented in Figure 9 for both soil and rock materials. As may be noted, the values of sigma are very similar in magnitude for both shear modulus reduction and hysteretic damping and follow the same general trends previously mentioned; that is, the variability in damping decreases with strain level, while the variability in shear modulus ratio increases with strain level. The plots also indicate that the recommendations from the EPRI study may not be appropriate for generic application, particularly when estimating values of hysteretic damping at the lower strain levels.

4.0 References

1. H. B. Seed, I. M. Idriss, "Soil Moduli and Damping Factors for Dynamic Response Analyses", Report No. EERC-70-10, University of California, Berkeley, CA, December, 1970

2. H. B. Seed, R. T. Wong, I. M. Idriss, K. Tokimatsu, "Moduli and Damping Factors for Dynamic Analyses of Cohesionless Soils", Earthquake Engineering Research Center Report No. EERC-84/14, September, 1984

3. J. I. Sun, R. Golesorkhi, H. B. Seed, "Dynamic Moduli and Damping Ratios for Cohesive Soils", Earthquake Engineering Research Center Report No. EERC-88/15, August, 1988

4. I. M. Idriss, "Response of Soft Soil Sites During Earthquakes", Proceedings of the H. B. Seed Memorial Symposium, Berkeley, CA, May 1990

5. R. Pyke, K. H. Stokoe, D. G. Anderson, I. M. Idriss, "Development of Generic Modulus Reduction and Damping Curves, ...

6. A. J. Bolognesi, O. A. Varde, F. L. Giuliani, "Shear Wave Velocity in Gravels", Proc. Specialty Conference on Earthquake Engineering and Soil Dynamics, edited by L. Von Thun, ASCE Special Publication No. 20, June, 1988

7. T. Kokusho, Y. Tanaka, "Dynamic Properties of Gravel Layers Investigated by Insitu Freezing Sampling", ...

8. "Geotechnical Laboratory Testing, Comanche Peak Steam Electric Station, Glen Rose, Texas", Dames and Moore for Texas Utilities Generating Company, October, 1986

9. "Seismic Hazard Evaluation of the Los Alamos National Laboratory", Woodward-Clyde Federal Services, Oakland, CA, February, 1995

10. "Guidelines for Determining Design Basis Ground Motions", EPRI TR-102293, November 1993

11. "Investigations of Nonlinear Dynamic Soil Properties at the Savannah River Site", Westinghouse Savannah River Site, WSRC-TR-96-0062, Rev. 0, March, 1996

TABLE 1
LOW STRAIN SHEAR MODULUS DATA

Sample No.	Rock Descriptor	Shear Modulus (ksf)	Estimated Shear Wave Velocity (fps)
1	Claystone	4,188	948
2	Claystone	4,120	940
3	Claystone	19,100	2,025
4	Claystone	24,300	2,284
5	Claystone	8,160	1,324
6	Claystone	12,900	1,664
7	Limestone	69,000	3,849
8	Limestone	47,000	3,176
9	Limestone	181,000	6,233
10	Limestone	122,000	5,118
11	Limestone	104,000	4,725
12	Sandstone	5,344	1,071
13	Sandstone	43,100	3,042
14	Sandstone	5,270	1,064
15	Sandstone	41,400	2,981
16	Sandstone	37,900	2,852
17	Sandstone	10,800	1,523
18	Tuff	12,000	1,605
19	Tuff	17,000	1,910
20	Basalt	280,000	7,753

TABLE 2
STATISTICS FOR ALL ROCK DATA

	LOG(%Strain)	SAMPLES	Log10(G/Gmax)	Log10(D)	Ln(G/Gmax)	Ln(D)
MEAN	-1.5	7	-1.241E-1	9.187E-1	-2.857E-1	2.114E+0
MEDIAN			-1.327E-1	9.184E-1	-3.056E-1	2.115E+0
STD DEV			4.693E-2	1.608E-1	1.081E-1	3.704E-1
VARIANCE			2.202E-3	2.587E-2	1.168E-2	1.372E-1
COEF OF VARIATION			-3.782E-1	1.752E-1	-3.782E-1	1.752E-1
MINIMUM			-1.831E-1	6.868E-1	-4.216E-1	1.581E+0
MAXIMUM			-7.049E-2	1.099	-1.623E-1	2.530E+0
MEAN	-2	16	-5.616E-2	6.131E-1	-1.293E-1	1.412E+0
MEDIAN			-5.914E-2	6.899E-1	-1.362E-1	1.589E+0
STD DEV			3.122E-2	3.746E-1	7.188E-2	8.625E-1
STD ERROR			7.804E-3	9.365E-2	1.797E-2	2.156E-1
VARIANCE			9.745E-4	1.403E-1	5.167E-3	7.439E-1
COEF OF VARIATION			-5.558E-1	6.110E-1	-5.558E-1	6.110E-1
MINIMUM			-1.024E-1	-5.229E-1	-2.357E-1	-1.204E+0
MAXIMUM			-8.774E-3	9.542E-1	-2.020E-2	2.197E+0
MEAN	-2.5	20	-2.868E-2	5.028E-1	-6.605E-2	1.158E+0
MEDIAN			-2.781E-2	5.543E-1	-6.403E-2	1.276E+0
STD DEV			1.956E-2	3.879E-1	4.504E-2	8.932E-1
STD ERROR			4.374E-3	8.674E-2	1.007E-2	1.997E-1
VARIANCE			3.827E-4	1.505E-1	2.029E-3	7.978E-1
COEF OF VARIATION			-6.820E-1	7.715E-1	-6.820E-1	7.715E-1
MINIMUM			-7.465E-2	-6.990E-1	-1.719E-1	-1.609E+0
MAXIMUM			-2.785E-3	9.468E-1	-6.413E-3	2.180E+0
MEAN	-3.000	20	-8.729E-3	4.146E-1	-2.010E-2	9.546E-1
MEDIAN			-7.450E-3	4.645E-1	-1.715E-2	1.070E+0
STD DEV			6.583E-3	4.187E-1	1.516E-2	9.641E-1
STD ERROR			1.472E-3	9.363E-2	3.389E-3	2.156E-1
VARIANCE			4.334E-5	1.753E-1	2.298E-4	9.296E-1
COEF OF VARIATION			-7.541E-1	1.010	-7.541E-1	1.010E+0
MINIMUM			-2.012E-2	-6.990E-1	-4.632E-2	-1.609E+0
MAXIMUM			0.000E+0	8.779E-1	0.000E+0	2.022E+0
MEAN	-3.5	20	-4.048E-3	3.937E-1	-9.320E-3	9.066E-1
MEDIAN			-2.617E-3	4.195E-1	-6.025E-3	1.035E+0
STD DEV			4.491E-3	4.130E-1	1.034E-2	1.020E+0
STD ERROR			1.004E-3	9.906E-2	2.312E-3	2.281E-1
VARIANCE			2.017E-5	1.962E-1	1.069E-4	1.040E+0
COEF OF VARIATION			-1.110E+0	1.125E+0	-1.110E+0	1.125E+0
MINIMUM			-1.639E-2	-6.990E-1	-3.774E-2	-1.609E+0
MAXIMUM			0.000E+0	9.214E-1	0.000E+0	2.122E+0
MEAN	-4.000	20	-2.416E-3	3.701E-1	-5.564E-3	8.522E-1
MEDIAN			-1.364E-3	4.284E-1	-3.140E-3	9.865E-1
STD DEV			3.748E-3	4.410E-1	8.630E-3	1.015
STD ERROR			8.381E-4	9.861E-2	1.930E-3	2.271E-1
VARIANCE			1.405E-5	1.945E-1	7.448E-5	1.031E+0
COEF OF VARIATION			-1.551E+0	1.191E+0	-1.551E+0	1.191E+0
MINIMUM			-1.639E-2	-6.990E-1	-3.774E-2	-1.609E+0
MAXIMUM			0.000E+0	8.762E-1	0.000E+0	2.018E+0

TABLE 3
STATISTICS FOR CLAYSTONE ROCK SAMPLES

	LOG(%STRAIN)	SAMPLES	Log10(G/Gmax)	Log10(D)	Ln(G/Gmax)	Ln(D)
MEAN	-1.5	4	-9.129E-2	8.015E-1	-2.102E-1	1.846E+0
MEDIAN			-8.097E-2	8.005E-1	-1.864E-1	1.843E+0
STD DEV			2.851E-2	9.461E-2	6.565E-2	2.179E-1
VARIANCE			8.129E-4	8.952E-3	4.310E-3	4.746E-2
COEF OF VARIATION			-3.123E-1	1.180E-1	-3.123E-1	1.180E-1
MINIMUM			-1.327E-1	6.868E-1	-3.056E-1	1.581
MAXIMUM			-7.049E-2	9.184E-1	-1.623E-1	2.115
MEAN	-2	5	-3.875E-2	7.175E-1	-8.923E-2	1.652E+0
MEDIAN			-8.097E-2	8.005E-1	-1.864E-1	1.845E+0
STD DEV			2.554E-2	1.470E-1	5.882E-2	3.270E-1
VARIANCE			6.525E-4	2.017E-2	3.459E-3	1.069E-1
COEF OF VARIATION			-6.592E-1	1.979E-1	-6.592E-1	1.979E-1
MINIMUM			-8.198E-2	5.250E-1	-1.888E-1	1.209E+0
MAXIMUM			-2.216E-2	9.117E-1	-5.102E-2	2.099E+0
MEAN	-2.5	6	-1.970E-2	7.011E-1	-4.537E-2	1.614
MEDIAN			-8.097E-2	8.005E-1	-1.864E-1	1.652E+0
STD DEV			1.397E-2	1.375E-1	3.218E-2	3.166E-1
VARIANCE			1.953E-4	1.891E-2	1.035E-3	1.003E-1
COEF OF VARIATION			-7.093E-1	1.962E-1	-7.093E-1	1.962E-1
MINIMUM			-3.943E-2	4.737E-1	-9.079E-2	1.091
MAXIMUM			-6.998E-3	8.603E-1	-1.611E-2	1.981
MEAN	-3	6	-7.021E-3	6.738E-1	-1.617E-2	1.551
MEDIAN			-8.097E-2	8.005E-1	-1.864E-1	1.652E+0
STD DEV			7.271E-3	1.291E-1	1.674E-2	2.972E-1
VARIANCE			5.287E-5	1.666E-2	2.803E-4	8.831E-2
COEF OF VARIATION			-1.036	1.915E-1	-1.036	1.915E-1
MINIMUM			-2.012E-2	4.667E-1	-4.632E-2	1.075
MAXIMUM			0	8.410E-1	0	1.936
MEAN	-3.5	6	-4.456E-3	6.613E-1	-1.026E-2	1.523
MEDIAN			-8.097E-2	8.005E-1	-1.864E-1	1.652E+0
STD DEV			5.981E-3	1.369E-1	1.377E-2	3.152E-1
VARIANCE			3.577E-5	1.874E-2	1.897E-4	9.935E-2
COEF OF VARIATION			-1.342	2.070E-1	-1.342	2.070E-1
MINIMUM			-1.639E-2	4.624E-1	-3.774E-2	1.065
MAXIMUM			0	8.231E-1	0	1.895
MEAN	-4	6	-4.255E-3	6.452E-1	-9.797E-3	1.486
MEDIAN			-8.097E-2	8.005E-1	-1.864E-1	1.652E+0
STD DEV			6.189E-3	1.374E-1	1.425E-2	3.165E-1
VARIANCE			3.831E-5	1.889E-2	2.031E-4	1.002E-1
COEF OF VARIATION			-1.455	2.130E-1	-1.455	2.130E-1
MINIMUM			-1.639E-2	4.399E-1	-3.774E-2	1.013
MAXIMUM			0	8.062E-1	0	1.856

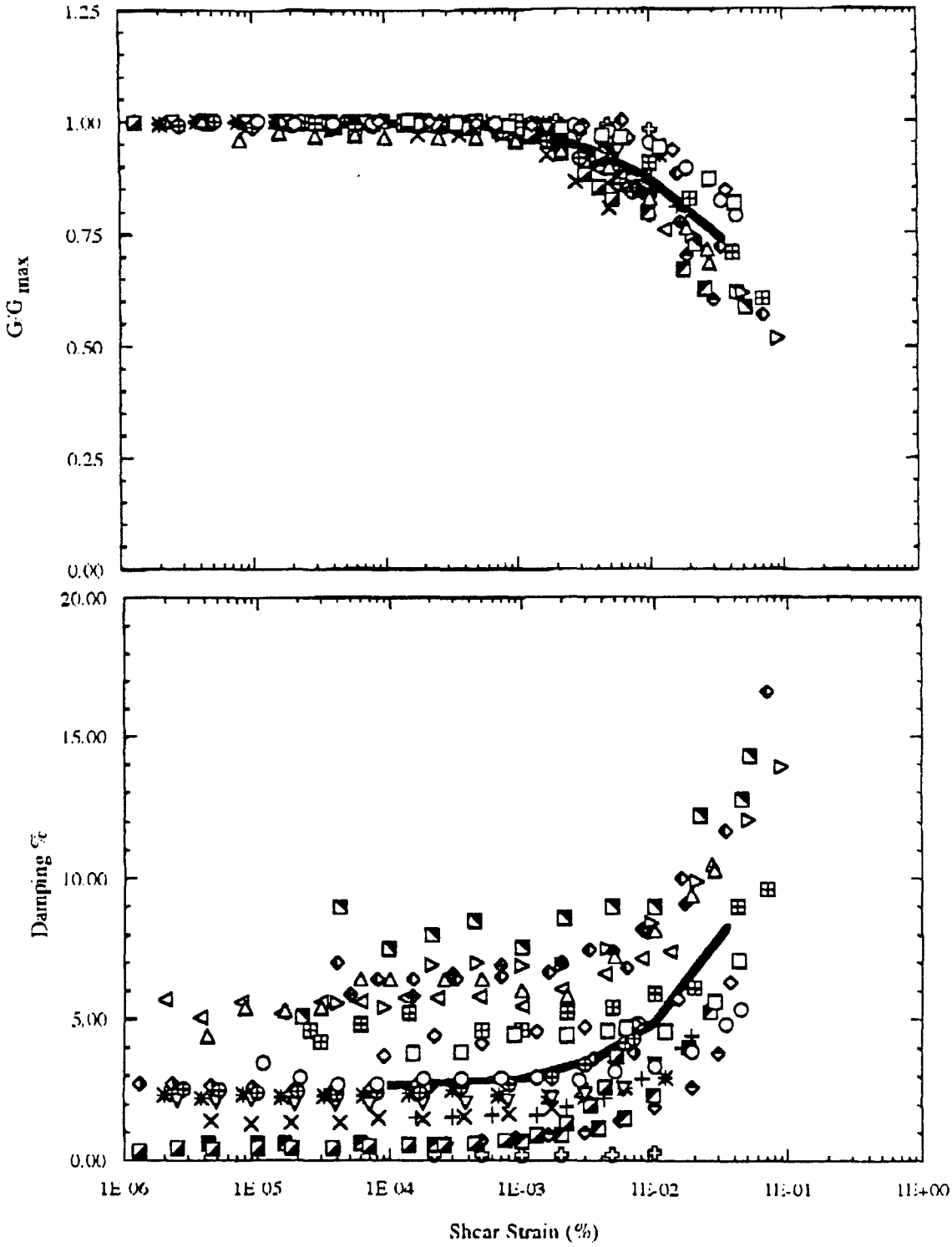

Figure 1 Measured G/Gmax and Hysteretic Damping Data for All Rock Resonant Column Tests

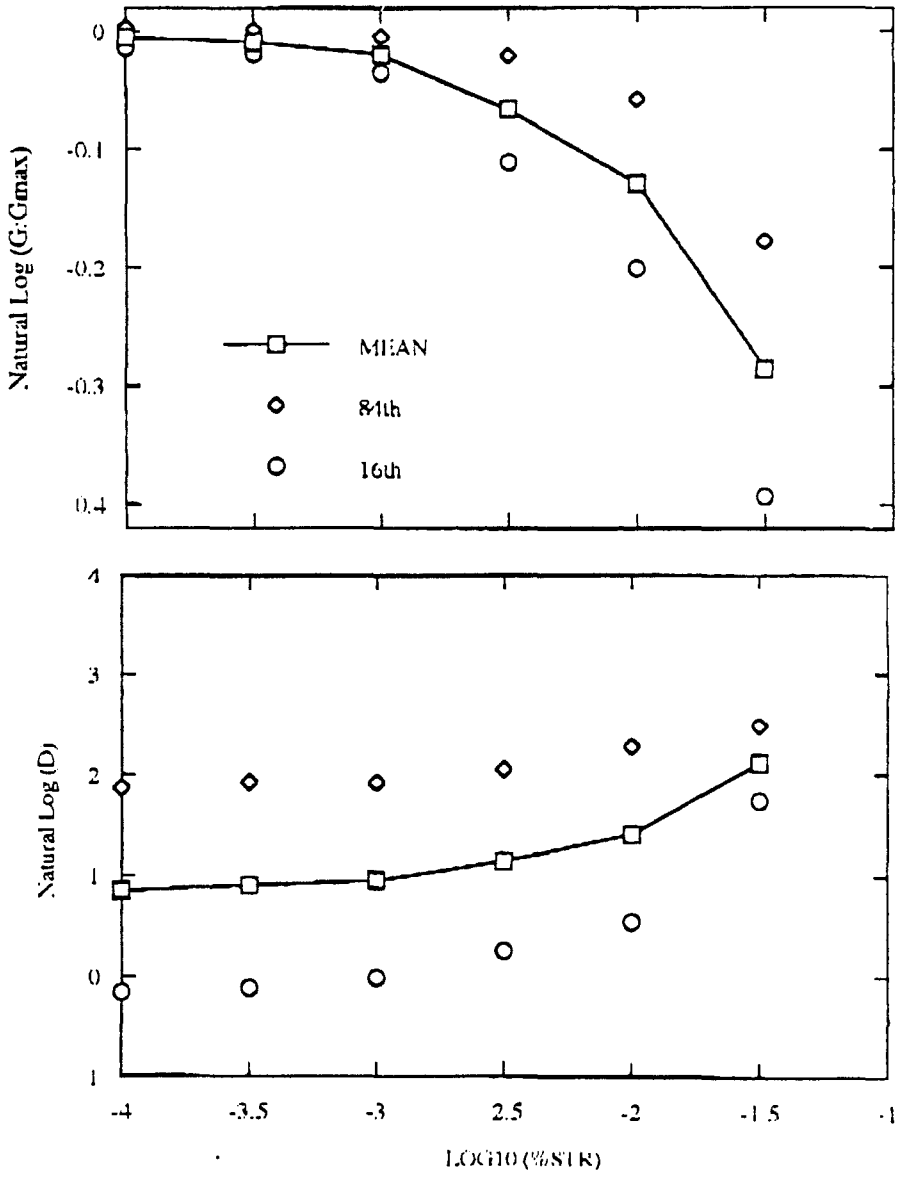

Figure 2 Statistics for All Rock Data

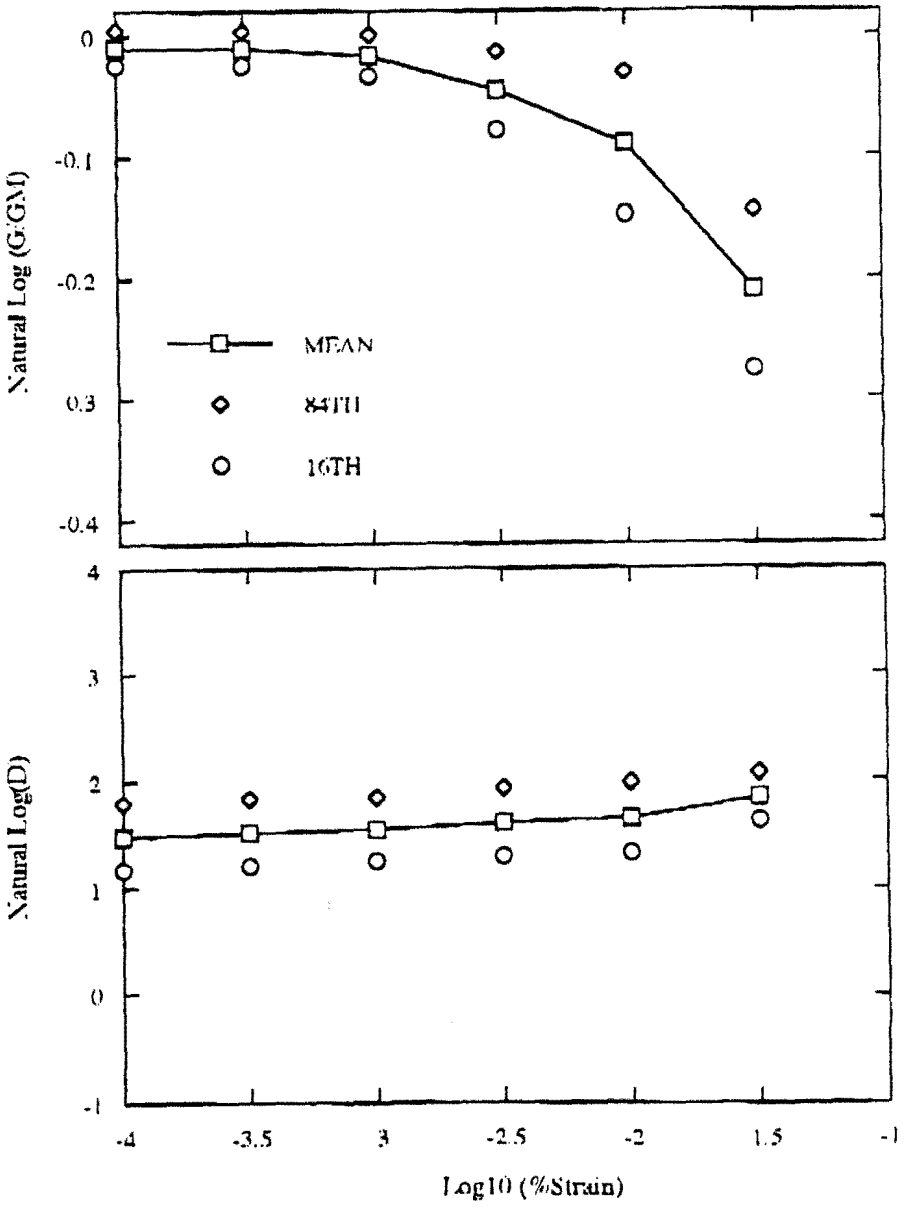

Figure 3 Statistics of Claystone Rock Samples

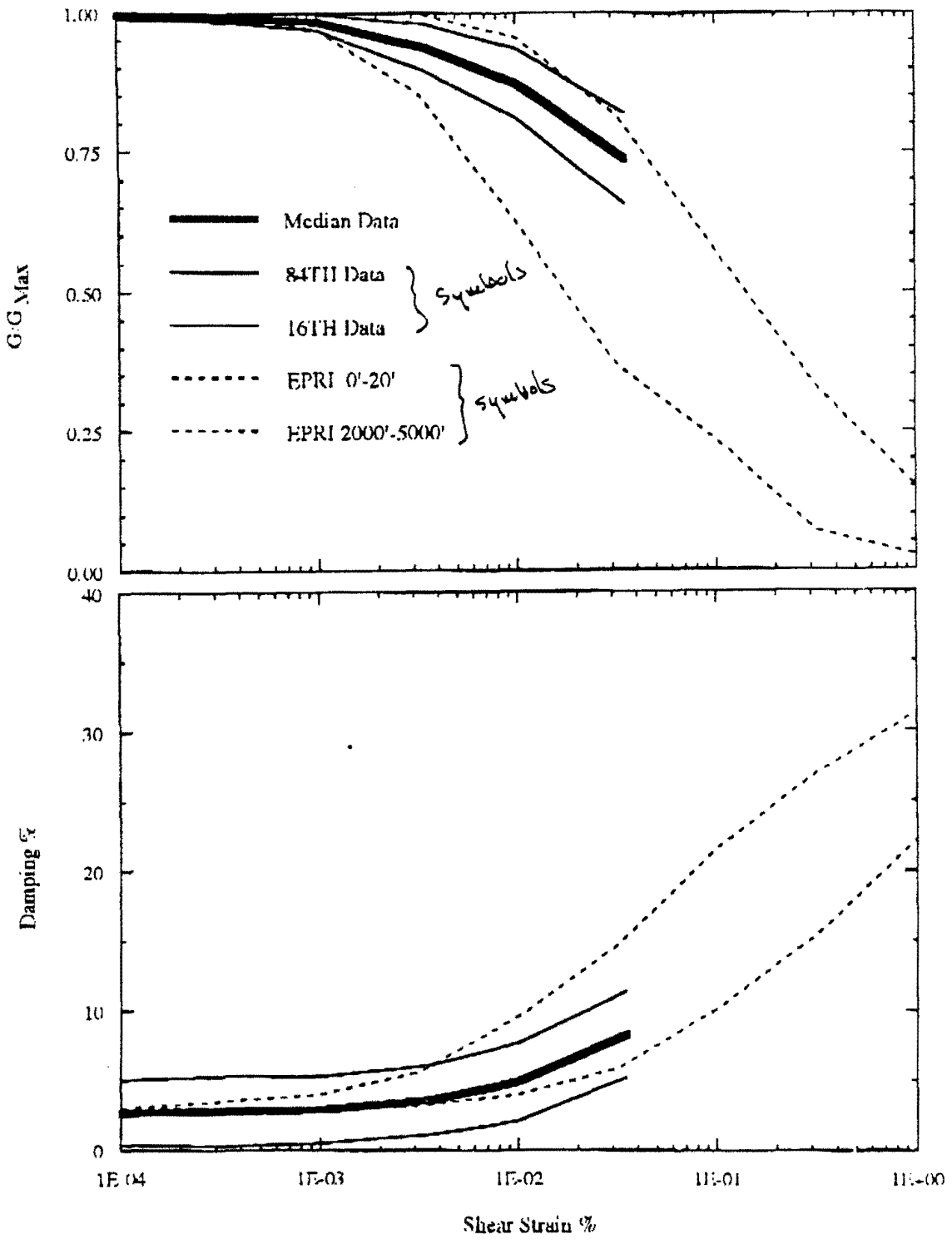

Figure 4 Comparison of RC Rock Data with EPRI Recommendations

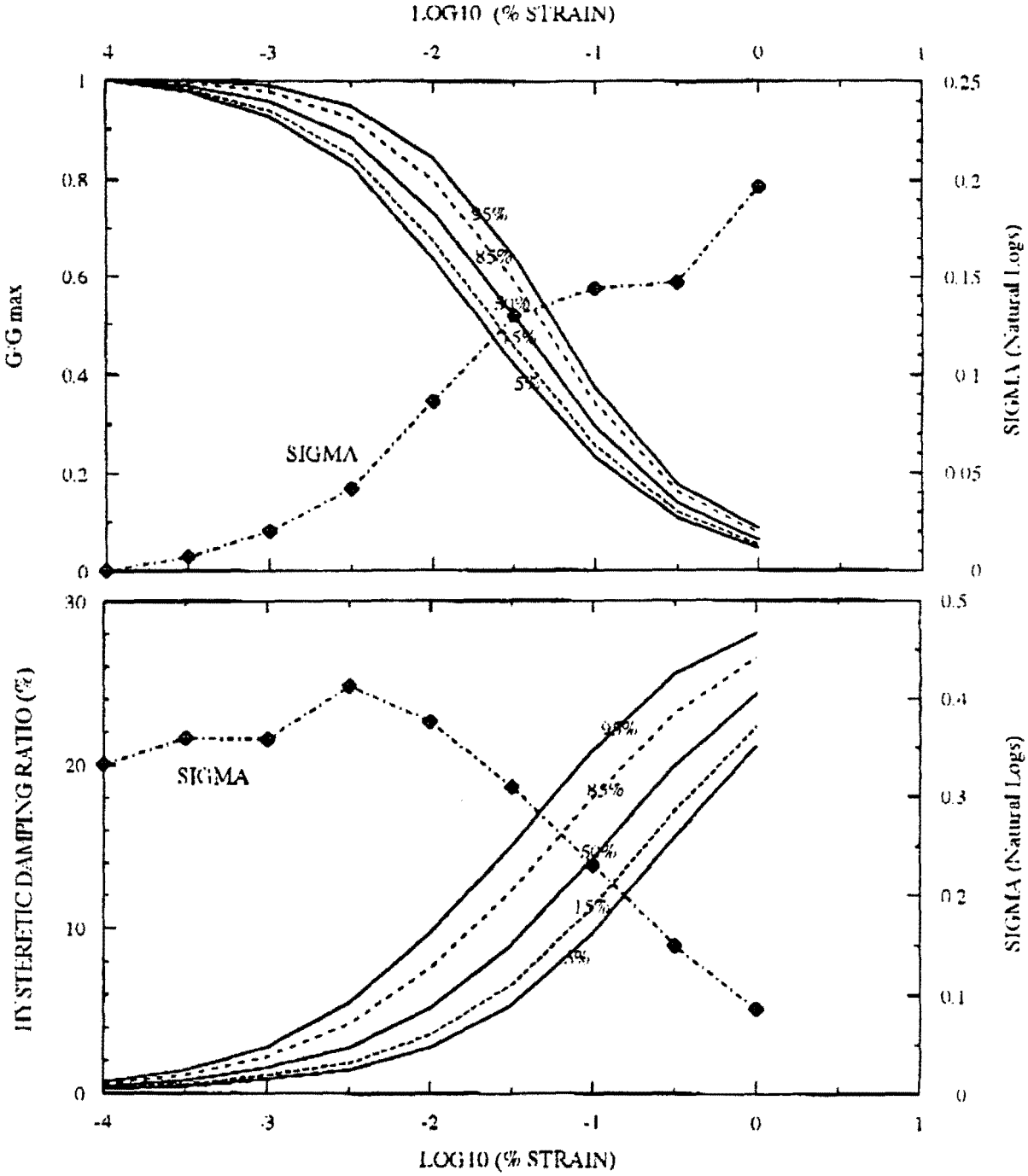

Figure 5 Seed-Idriss (1970) Sand Data

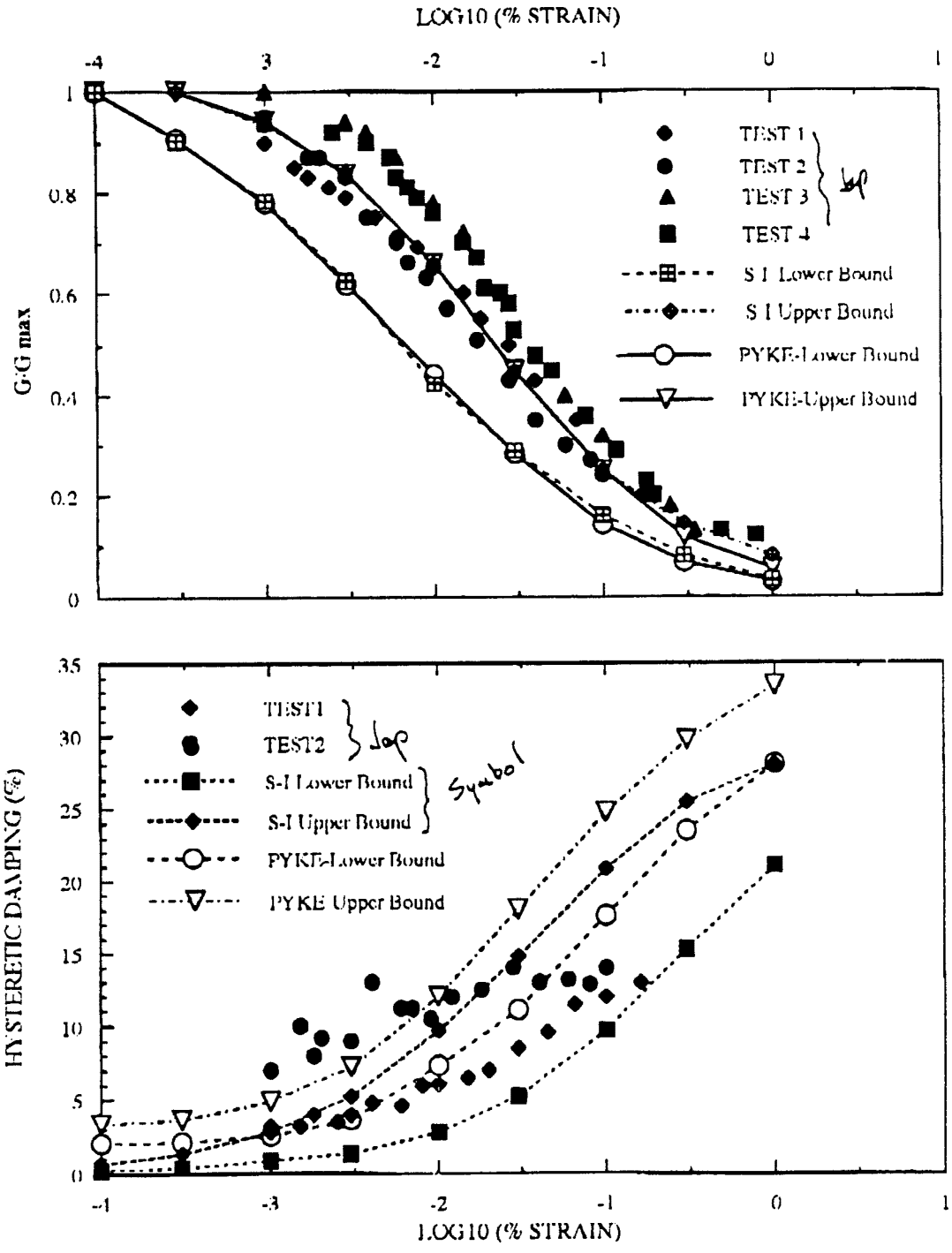

Figure 6 Degradation Properties for Gravels

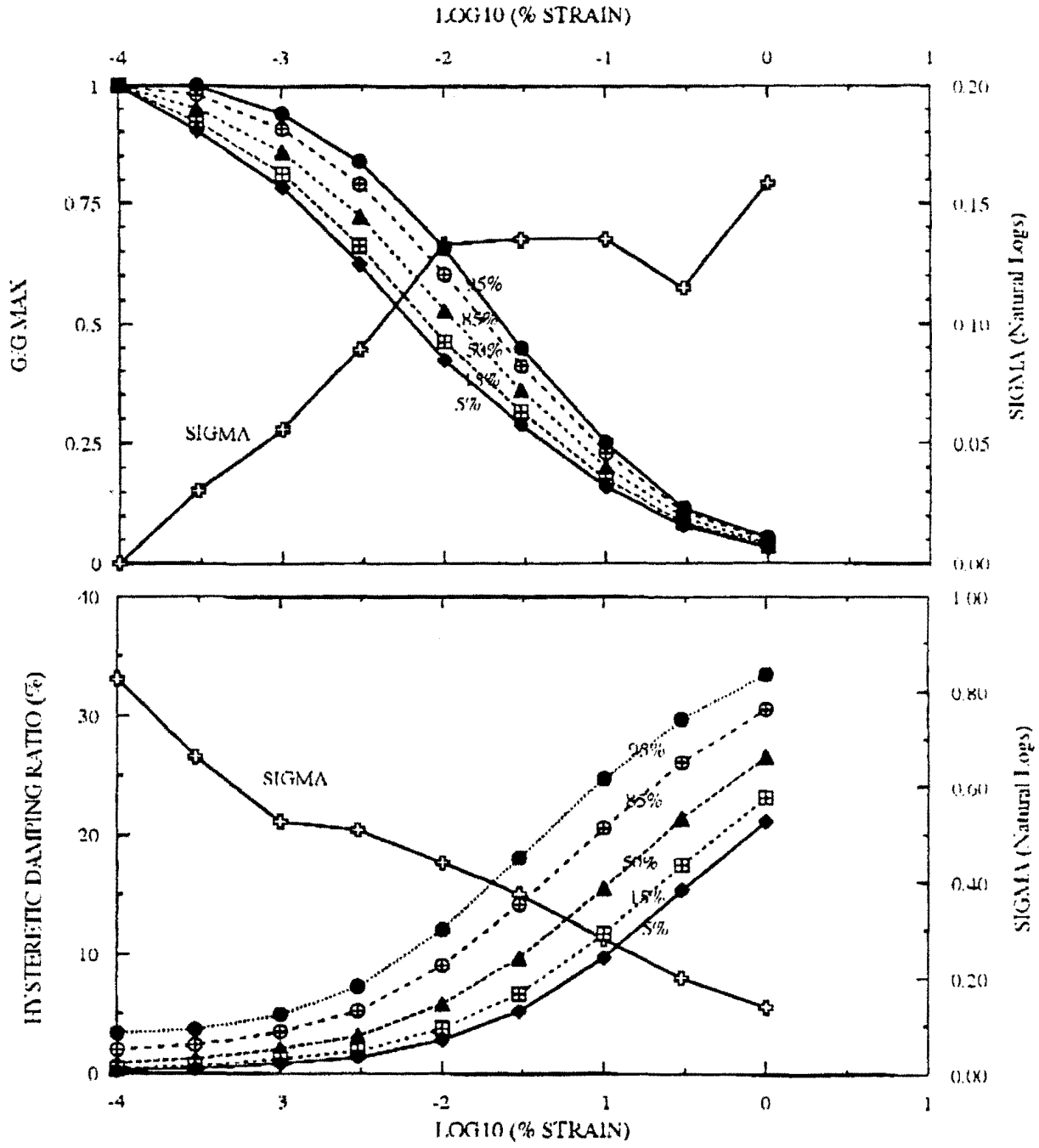

Figure 7 Statistical Properties for Gravelly Soils

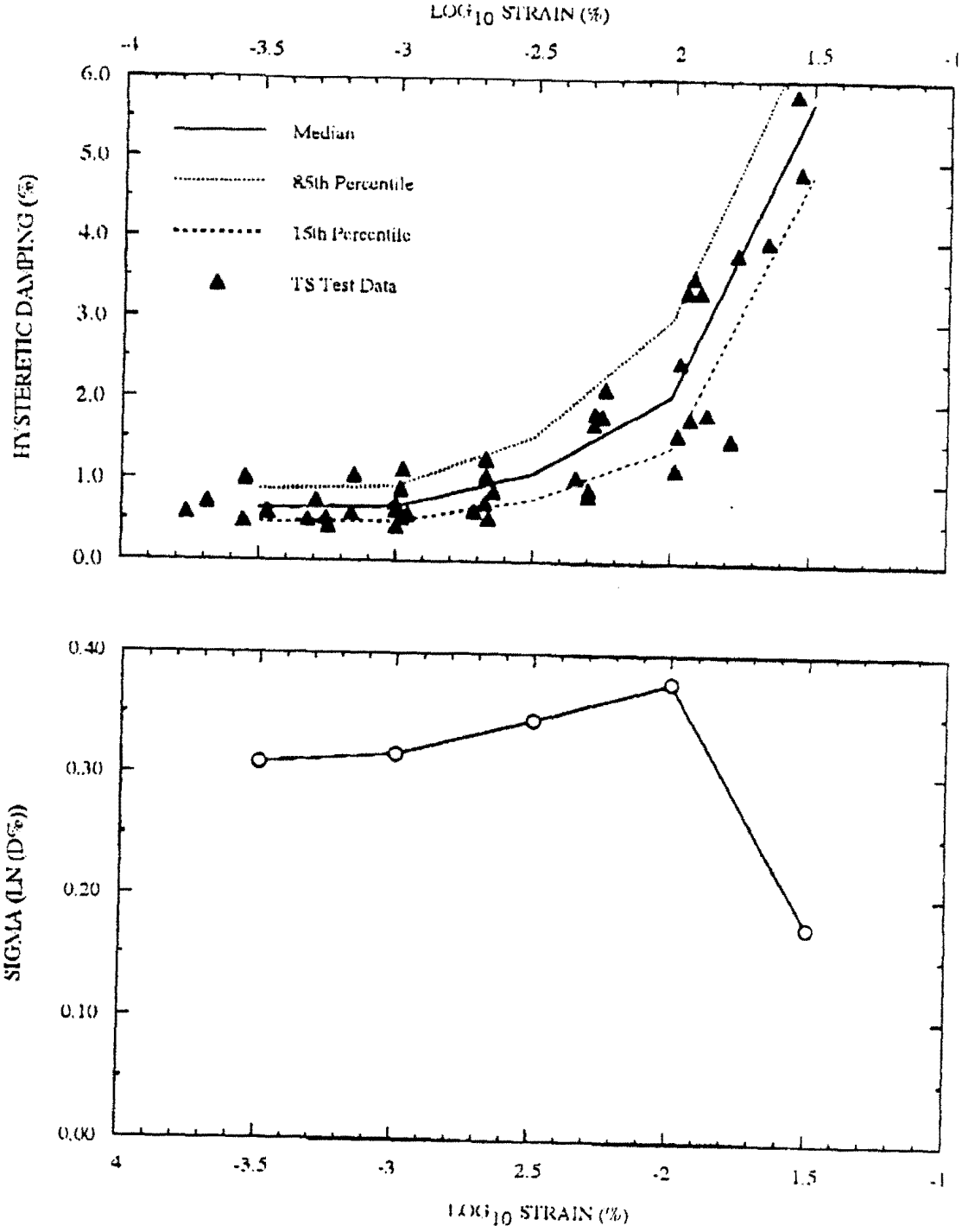

Figure 8 Statistics for Torsional Shear Hysteretic Damping Data for Savannah River Site (from Stokoe 1995)

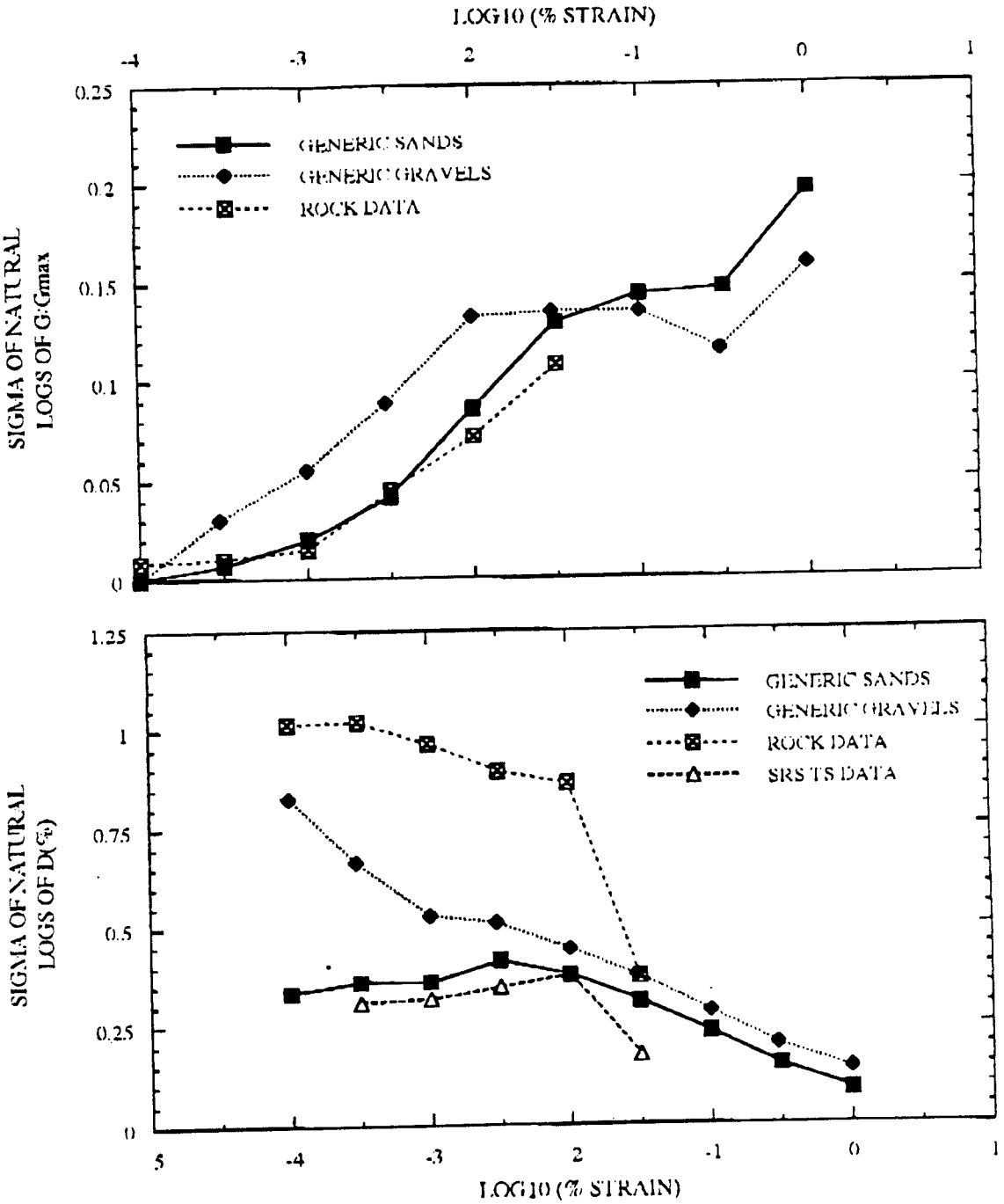

Figure 9 Comparison of Variability in Degradation Data for Various Soil/Rock Types

PROBABILISTIC MODELS OF SITE VELOCITY PROFILES FOR GENERIC AND SITE-SPECIFIC GROUND-MOTION AMPLIFICATION STUDIES

(Second Draft, November 17, 1995)

Prepared by

Gabriel R. Toro

Risk Engineering, Inc.

4155 Darley Avenue, Suite A

Boulder, CO 80303

for

Brookhaven National Laboratory

Upton, New York

Under Contract 779574

ABSTRACT

A probabilistic model is constructed for the variation of shear-wave velocity in soil and rock sites, for the purpose of calculating site-amplification factors at generic soil or rock sites (and their associated uncertainties). The data used for constructing and calibrating the model consists of 557 profiles, coming mostly from California sites. The probabilistic model consists of three parts, as follows: (1) a model that describes the random stratigraphy at the site, (2) a median site-velocity profile, and (3) a model that describes the deviations of the velocity in each layer from the median and its correlation with the velocity in the layer above. Sample artificial profiles are generated and shown in graphical form.

The model is extended to situations where site-specific velocity measurements are available, but these measurements are not sufficient for deriving an entirely new model. By considering the lateral correlation between velocities in multiple boreholes in the site vicinity, one can simulate profiles using a weighted combination of the generic model and the velocities observed at the site. Site-specific applications are illustrated by investigating the lateral correlation of velocities at 10 sites and simulating artificial profiles for three of these sites.

1. INTRODUCTION

This report presents models for the probabilistic characterization of the shear-wave velocity profiles at soil and rock sites. These models can be used to generate a suite of artificial velocity profiles for a site whose velocity characteristics are known only in terms of broad site categories. These artificial profiles can then be used to calculate the median and uncertainty of ground-motion amplification at that site (see Roblee et al., 1995). These models can also be used for a site where some velocity profiles are available, in order to generate artificial profiles that are probabilistically consistent with the available profiles. This requires consideration of the horizontal correlation of shear-wave velocity.

The work presented here constitutes an extension of the work of Toro et al. (1995; see also Appendix 6A of EPRI, 1993). This study utilized a much larger soil-velocity database, which allowed the fitting of a more refined model. Also, we are able to calculate model parameters for multiple site categories, using two of the common site characterizations in current engineering use. Also, we utilize site-specific velocity data in order to refine the site-specific version of the model, which was proposed in EPRI (1993) but was never applied.

Two other approaches have been used in the past to calculate the effect of soil-profile variability on ground-motion amplification. The first approach varies the velocities at all depths assuming perfect correlation, by either multiplying the median velocities at all depths by a random factor (e.g., McGuire et al., 1988), or by adding a random quantity to the median velocities at all depths (Toro et al., 1992). The second approach assumes probabilistic independence between the velocities in adjacent layers (Costantino et al., 1991; Field and Jacob, 1993). Both approaches represent extreme, albeit convenient, assumptions about the correlation structure of layer velocities of real soil profiles. The model developed here represents a mid-point between the two extreme models described above. In addition, a probabilistic model of layer thickness as a function of depth is developed for generic sites where the stratigraphy is not known.

A third type of approach was used by Vanmarcke (1977). Unlike the models discussed above, this model does not explicitly consider the soil stratigraphy. It does, however, consider the vertical correlation structure of velocity by means of an auto-correlation function. Another related model is used by Rouhani et al. (1993), who consider only the horizontal correlation (at a given depth) between profiles at the same site and use the technique known as Kriging to estimate this correlation structure.

Section 2 of this report presents a summary of the data used for this study and the site categorizations employed. Section 3 describes the probabilistic models of layering and velocity, the procedure used to derive model parameters for the various site categories, and presents samples of the artificial profiles generated with the model. Section 4 describes an

extension of the above model to situations where site-specific velocity data are available and the application of this model to several sites. We refer to the model in Section 3 (where profiles within each category are considered probabilistically independent) as the generic model, and to the model in Section 4 (where correlation between nearby profiles is considered) as the site-specific model.

2. DATA

At the time of this study, the soil-profile database assembled by Pacific Engineering and Analysis contained information on 745 soil profiles.

For the purposes of this analysis, we utilized only those profiles that satisfied the following conditions:

- The profile contains shear-wave velocity information based on field measurements.
- The profile contains interpreted velocities (as opposed to raw velocities).
- The velocity measurements were made during or after 1974. Many site investigations made after 1974 followed the guidelines for site investigation contained in the "Appendix A" reactor-siting criteria (Atomic Energy Commission, 1973), making them more reliable.

A total of 557 profiles meet these requirements. Most of these profiles come from California sites. A list of these profiles is contained in Table 1.

Some profiles in the database contain well-log entries describing the material type as a function of depth, but many others do not. Thus, it was not practical to identify where the profile reaches material that should be considered as bedrock. Instead of attempting to

identify the depth to rock in each profile, as was done in Toro et al. (1995), we modified the analysis procedure in order to allow for the possibility that some of the deeper layers in a profile may represent rock (see Section 3).

There are 11 clusters of profiles, with all profiles in each cluster located within a radius of several hundred meters to a few kilometers. Seven of these clusters contain accurate location information, which may be used to investigate the horizontal correlation structure of shear-wave velocity. Table 2 contains a list of the clusters.

Two site characterizations were considered in this study. The first characterization, which we call the Geomatrix characterization, is based on a qualitative description of the site and is reproduced in Table 3. The second characterization, which we call the USGS characterization, is based on the harmonic or time-weighted average velocity over the top 30 meters of the profile and is defined in Table 4.

The USGS characterization has been employed by Borcherdt (1993) and Boore et al., (1993, 1994) and has been adopted in the 1994 NEHRP model seismic-design provisions. The Geomatrix characterization has the following important advantages: it is available for more strong-motion sites, and it can be applied to sites where no velocity measurements are available. Of the 557 profiles selected above, 541 profiles have USGS classification[1] and only 164 have Geomatrix classification.

Sometimes these characterizations are collapsed into grouped categories AB (rock or firm soil) and CD (soft soil). We will develop model parameters for these grouped categories and for the individual USGS categories. Limitations in the data do not allow us to develop model parameters for the individual Geomatrix categories.

[1]Some profiles are too shallow or are missing data near the surface, making it impossible to calculate the harmonic-average velocity over the top 30 m.

3. GENERIC MODEL: DATA ANALYSIS, MODEL FITTING, AND RESULTS

Figures 1 through 4 show the profiles for the Geomatrix and USGS grouped categories. These figures give an indication of the variability in velocities. Figures 5 through 12 show the median ± logarithmic σ and the logarithmic σ as a function of depth for the same categories. Similar results, but with smaller σ, are obtained for the individual USGS categories. These figures suggest models where the standard deviation of ln-velocity is constant as a function of depth, as used in Toro et al. (1994). Figure 13 shows eight Geomatrix Category D profiles and shows the presence of correlation between layer velocities, in the sense that a profile that starts with above-average velocity has a tendency to remain above average. Another way to think of this correlation is that if the velocity in one layer is higher than average, the velocity in the layer immediately below also tends to be higher than average.

3.1 Elements of Probabilistic Model

The probabilistic model to characterize these profiles attempts to capture the main features observed in Figures 1 through 13; namely, random layering, velocities with a constant COV, and correlated velocities. Figure 14 illustrates the various elements of the soil-profile model. The layering model describes the thicknesses of the layers (or the location of layer boundaries). The velocity model describes the velocity at the mid-point of each layer and its relationship to the velocity in other layers.

Bedrock is represented separately from the soil layers in the simulations. The depth to bedrock is specified as having a uniform distribution within a pre-specified range and the bedrock shear-wave velocity has its own median velocity and logarithmic standard deviation (which have been estimated separately).

The general structure of this probabilistic model, as illustrated in Figure 14, is the same used in Toro et al. (1995). The parameter values, detailed model parameterization, and details analysis procedure are different.

3.2 Layering Model

Regarding the layering, we note that layers tend to be thinner near the surface and thicker at depth (see Figures 1 through 4 and 13). A simple probabilistic model to characterize the layering is a Poisson process with depth-dependent rate (i.e., a non-homogeneous Poisson process; see Parzen, 1962). In this model, the mean layer thickness is depth-dependent, but the thickness of layer i is probabilistically independent of the thickness of layer $i-1$. In a Poisson model with constant rate, the layer thicknesses follow an exponential distribution. Because we utilize a depth-dependent rate, the distribution of layer thickness is no longer exponential, but this causes no problems in the analysis or in the generation of artificial profiles.

We adopt a modified power-law model to characterize the depth-dependent rate of layer boundaries, i.e.,

$$\lambda(h)=c_3[h+c_1]^{-c_2} \tag{1}$$

where λ is the rate of layer boundaries (m^{-1}) and h denotes depth in meters. Coefficients c_1 through c_3 are estimated from the data, using the method of maximum likelihood (Benjamin and Cornell, 1971). The following result is obtained

$$\lambda(h)=1.98[h+10.86]^{-0.89} \tag{2}$$

Figure 15 compares the rate function in Equation 2 to the observed rate of layer boundaries[2] (or transition rate). The observed rates (thin line) are shown as running averages over a 10 m window (i.e., the quantity shown for a depth of 50 m is the number of layer boundaries between 40 and 60 m, divided by the number of profiles with depths greater than or equal to 50 m). This figure shows a good agreement between the data and the fitted model. In

[2]It is useful to think of the rate of layer boundaries as the reciprocal of the mean layer thickness. This is strictly applicable only if the rate varies slowly.

addition, a statistical goodness-of-fit test for Poisson (Parzen, 1962) performed by Toro et al. (1995) indicates no significant deviation from the assumption of a Poisson process.

Equation 2 predicts mean layer thicknesses of 4.5 m near the surface, in agreement with the value suggested by Idriss (personal communication, 1992). Thus, the judgmental modifications to Equation 1 that were introduced in Toro et al. (1995) are not required.

3.3 Velocity Model

As shown in Figure 14, the velocity model operates on the velocities at the layer midpoints. One can think of these velocities, for a given profile, as a sequence of velocity values (i.e., V_1, V_2, V_3, ...). The velocity model defines the probability distribution of $\ln[V_i]$, and its correlation with the ln-velocities in adjacent layers. More precisely, the model operates with the normalized quantity

$$Z_i = \frac{\ln(V_i) - \ln[V_{median}(h_i)]}{\sigma_{\ln V}} \tag{3}$$

Normal probability plots in Toro et al. (1995) indicate that Z_i is well approximated by a normal distribution (or, equivalently, that V_i is well approximated by a log-normal distribution).

We characterize the lognormal distribution of velocities and the correlation among layers by means of a first-order auto-regressive model; i.e.,

$$\begin{aligned} Z_1 &= \varepsilon_1 \\ Z_i &= \rho Z_{i-1} + \sqrt{1-\rho^2}\ \varepsilon_i, \qquad i>1 \end{aligned} \tag{4}$$

where ρ is the serial auto-correlation coefficient of Z, and ε_1, ε_2, ε_3, ... are independent normal random variables with zero mean and unit standard deviation. Toro et al. (1995)

assumed constant ρ, obtaining $\sigma_{ln(Vel.)}$ and ρ, obtaining $\sigma_{ln(Vel.)}$=0.39 (corresponding to a velocity COV of 41 %), and ρ=0.577.

We investigated a number of variations to this model, including higher-order auto-regressive models, ARMA models, mixtures of auto-regressive and equicorrelated models, and first-order auto-regressive models in which ρ depends on various quantities such as depth, or the distance or travel time between the mid-points of layers *i* and *i-1*.

As mentioned earlier, the Z_i are intended to represent soil, not bedrock. The unavoidable presence of some bedrock velocities in the data, if not considered explicitly, has the following effects on the calculated parameters: (1) the median soil velocity will be over-estimated and the plot of median velocity vs. depth will exhibit bulges at depths where many profiles reach bedrock, (2) the standard deviation of soil ln-velocity will be over-estimated because the data will contain a mixture of rock and soil velocities, and (3) correlation will be under-estimated because of the large step that often occurs at the point where the profile reaches bedrock. Ideally, one should remove all bedrock velocities from the data prior to the analysis. This is not practical, however, given the number of profiles and the information currently available in the database.

In order to allow for the more general model forms, and to remove the effect of bedrock velocities, we use a maximum-likelihood formulation to estimate model parameters. This formulation may be thought of as an extension of the regression procedure used by Toro et al. (1995). The basic assumption used to remove the effect of bedrock velocities is that $\ln[V_i]$ comes from a mixture of probability distributions for soil and bedrock. The parameters of the distribution for soil (i.e, mean, standard deviation, and correlation structure) are unknowns to be determined. The parameters and distribution for bedrock are considered known (lognormal

with median=1020 m/s and $\sigma_{\ln V}$=0.30)[3]. The proportion p_R of bedrock velocities is another unknown to be determined as part of the maximum-likelihood estimation.

Based on the above considerations, the likelihood function for layers i, i+1, ... n may be written as follows:

$$L_{i,\ldots.n}=(1-p_R)\,f_S(\ln V_i|\ln V_1,\ln V_2\ldots\ln V_{i-1})\,L_{i,\ldots.n-1}+p_R\,f_R(\ln V_i) \tag{5}$$

where $f_S(\ln V_i|\ln V_1,\ln V_2\ldots\ln V_{i-1})$ represents the probability density function of soil ln-velocity for layer i (conditional on the ln-velocities in the layers above) and $f_R(\ln V_i)$ is the probability density function of bedrock ln-velocity. In the common case of a first-order auto-regressive model, the density function for soil reduces to

$$f_S(\ln V_i|\ln V_{i-1})=\frac{1}{\sqrt{2\pi(1-\rho^2)}\;\sigma_{\ln V}}\exp\left[-\frac{1}{2}\left(\frac{Z_i-\rho Z_{i-1}}{\sqrt{1-\rho^2}}\right)^2\right] \tag{6}$$

The recursive relationship in Equation 5 is used to compute the likelihood function of all the layers in a profile, starting at the bottom (layer n)[4]. The likelihood function for all profiles in a category is the product of the layer likelihood functions. The value of the likelihood function (given the data) depends on the median velocity (as a function of depth), on $\sigma_{\ln V_i}$, and on ρ (which may be constant or may depend on depth, etc). The median velocity vs.

[3]These values are appropriate for the Western United States (Silva, personal communication, 1995).

[4]Actually, depths for which there are fewer than five profiles in the category being analyzed are not included in the calculations.

depth function is represented in terms of the median velocities at several control depths (typically 25) and is made smooth by applying a penalty function.

The optimal parameter values for a given model formulation (i.e., for given assumptions about correlation and about the dependence of ρ on depth, etc.) were obtained numerically by finding the parameter values that maximize the likelihood function. Comparisons among model formulations were made using the AIC criterion (Akaike, 1971, 1974; this criterion considers the maximum value of the likelihood function and the number of free parameters) and by visual examination of artificial profiles generated using the candidate models. In addition, the final model was required to fit well across all site categories.

The best fit was obtained by a first-order auto-regressive model (Equation 5) with a correlation coefficient ρ that depends on depth and on the distance between the mid-points of layers i-1 and i. Inter-layer correlation tends to be higher at greater depths and between thin layers. The expression used for ρ is as follows:

$$\rho(h,t) = \left(1-\rho_d(h)\right)\rho_t(t) + \rho_d(h) \tag{7}$$

where ρ_d represents depth-dependent correlation (higher at greater depths) and ρ_t thickness-dependent correlation (higher for shallow layers, which tend to occur at shallow depths) and are of the form

$$\rho_d(h) = \begin{cases} \rho_{200}\left[\dfrac{h+h_0}{200+h_0}\right]^b & \text{for } h \le 200 \\ \rho_{200} & \text{for } h > 200 \end{cases} \tag{8}$$

$$\rho_t(t)=\rho_0 \exp\left[-\frac{t}{\Delta}\right] \tag{9}$$

where h is the average of the midpoint depths of layers i and i-1 and t is the difference between these midpoint depths. ρ_{200}, h_0, b, ρ_0, and Δ are model parameters to be determined.

The maximum-likelihood procedure solves for $\sigma_{\ln v}$, ρ_{200}, h_0, b, ρ_0, Δ, p_R, and the median velocity at the control depths. Table 5 lists the parameter values estimated for all categories considered. Table 6 and Figures 16 through 23 show the median velocities versus depth obtained as part of the estimation process. These median velocities differ somewhat from those calculated from the raw profiles (e.g., Figures 5, 7, 9, and 1) in that the effect of bedrock-velocity data has been removed and in the effect of smoothing[5]. Similarly, the σ values in Table 5 are smaller than the values in Figures 6, 8, 10, and 12. The median velocities extend to a depth where fewer than five profiles are available in the corresponding category. Data at greater depths were not used in the calculations.

The un-combined USGS categories have significantly lower standard deviations than the combined categories, as anticipated.

The median velocity for USGS category D (Figure 23) shows a reversal in the upper 7 m of the profile. We interpret this as due to the presence of artificial fill material. Most of the category D profiles come from the Bay Area and may not be representative of other category D sites.

Figures 24 through 31 show the variation of ρ_d and ρ_t as a function of depth for the various categories. Because ρ_t depends on thickness (which is random) rather than on depth h, we plot ρ_t as a function of $\lambda(h)^{-1}$, which is approximately the average layer thickness at depth h.

---

[5]The smoothing has a slight tendency to bias the velocities at depth towards higher values, as one can notice by comparing Figures 9 and 18.

We note that the un-combined USGS categories, which have lower values of $\sigma_{ln\ V}$ than the combined categories, also have lower correlations. USGS Category D also shows unusual correlation results: it shows no thickness-dependent correlation (Figure 31).

We obtain ρ_{200}=1 for several of the site categories analyzed. This result implies perfect correlation between Z_i and Z_{i-1} values at depths greater than 200 m. This result is believed to be an artifact of having limited data at depths near 200 m and greater, and of the functional form used in Equation 8. It is expected that the correlation $\rho(h)$ is high, but not unity, at those depths.

3.4 Simulation Results

Figures 32 through 34 show samples of the artificial profiles generated using the model and parameters developed here. In the generation of artificial profiles, the truncation of ln-velocities and residuals at $\pm 2\sigma$ (see Toro et al., 1995) is still used although it may no longer be necessary. The present model appears to have less of a tendency than the earlier model to generate profiles with large low-velocity "notches" at depth, due to the lower sigma and higher correlation in the deep profiles.

Artificial profiles generated using this procedure may be used to perform site-response calculations in order to obtain the amplification factors corresponding to the various site categories, and the associated uncertainty.

4. SITE-SPECIFIC MODEL

4.1 Introduction

A site-specific velocity model could be developed by collecting site-specific profile data and repeating the analysis procedure followed in Section 3 above. This approach is generally not practical because it requires a large number of site-specific profiles. The procedure

developed here uses the site-specific velocity measurements and stratigraphy to modify the generic model. The relative weights given to the site-specific data and to the generic parameters depend on the amount of data and its (profile-to-profile) variability. If the correlation between two profiles in the same cluster depends on the horizontal distance between the borings, then profiles closer to the target site are given more weight in modifying the generic results.

The site-specific model is based on the idea that if one applies the model in Section 3 to a narrow class of sites (assuming there are sufficient data to obtain stable results), one would obtain a lower $\sigma_{\ln V}$ (and usually a different median profile) than for the broader class of sites. This is exemplified by the comparing the narrower USGS category A or B results to the broader A+B results. This lower value of $\sigma_{\ln V}$ arises because there are some characteristics in common among the profiles in the narrow class, which are not shared with all other profiles in the broader class. Therefore, there is less variability among the profiles in the narrow class. This lower variability relative, to the variability in the broader class of profiles, may be interpreted as positive correlation among the profiles in the narrow class. In this analysis, the narrow class corresponds to a cluster of sites with distances of a few hundred to a thousand meters.

It is also expected that there will be less variability between two nearby profiles than between two more distant profiles in the same cluster. Thus, one expects higher correlation among nearby profiles in the same cluster.

The information provided by the measured profiles at the site is treated as additional information, which is combined with the information contained in the generic model to produce a site-specific model. Because there is correlation between sites in the cluster, the site-specific data are more relevant than the generic data. The advantage of not discarding the generic data is that we obtain more stable results in cases where the number of available site-specific profiles is small.

The key to applying the site-specific model is the horizontal (more precisely, profile-to-profile) correlation between profiles in the same cluster and its possible dependence on distance. This correlation is investigated in Section 4.2, using data for all the clusters available to this study.

Section 4.3 present the formulation for a site-specific velocity model, which includes horizontal correlation, vertical correlation, and the generic model (an early version of this model was presented in Appendix 6A of EPRI,1993). Section 4.4 presents a preliminary site-specific model for the stratigraphy. Section 4.5 presents the simulation of site-specific profiles for several clusters.

4.2 Analysis of Cluster Velocity Data

The velocity data for the site clusters and their summary statistics are contained in Figures 35 through 69. The following information is shown for each cluster: relative borehole locations (if available), individual velocity profiles, median$\pm\sigma$ profiles, and σ vs. depth plots. Velocity data that were clearly associated with bedrock were removed prior to plotting and analysis. The plots of σ vs. depth also show the statistical uncertainty in σ (roughly the $\pm$one standard deviation interval for σ, shown as dashed lines). Most clusters show less variability than the generic plots in Figures 1 through 12.

We want to determine the horizontal correlation between ln-velocities within each cluster and its possible dependence on distance between boreholes. If we view the horizontal variation of ln-velocity at a given depth as a stationary, isotropic random function[6], the covariance between the values at any two points $\underline{X}_1$ and $\underline{X}_2$ is given by

[6]These two assumptions are required given the small number of boreholes per site, in order to keep the number of parameters to a minimum. The isotropic assumption was examined and is not grossly violated.

$$E\left[\left(lnV(\underline{X}_1)-\ln V_{median}\right)\times\left(lnV(\underline{X}_2)-\ln V_{median}\right)\right]=R\left(|\underline{X}_1-\underline{X}_2|\right) \tag{10}$$

where E denotes mathematical expectation. Equation 10 indicates that the covariance between ln-velocity at two points depends only on the distance between the points. $R(\tau)$ is known as the auto-covariance function; it takes its maximum value (equal to the variance of the function) at $\tau=0$. $R(\tau)$ is often estimated by means of the semivariogram

$$\gamma(\tau)=R(0)-R(\tau)=\frac{1}{2}E\left[\ln V(\underline{X})-\ln V(\underline{X}+\underline{\tau})\right]^2 \tag{11}$$

where $\underline{\tau}$ is a vector of length τ and any arbitrary direction. Figure 69 shows a typical semivariogram. By definition, $\gamma(0)=0$. If samples of the random function are continuous, $R(\tau)$ and $\gamma(\tau)$ are continuous at $\tau=0$. If samples of the random function are discontinuous, $R(\tau)$ and $\gamma(\tau)$ are discontinuous at $\tau=0$ (the so-called nugget effect). If samples of the random function are differentiable, $R(\tau)$ and $\gamma(\tau)$ are also differentiable at $\tau=0$. In practice, the semivariogram is estimated from a finite number of observations by means of the experimental semivariogram:

$$\gamma_e(\tau)=\frac{1}{2N}\sum_{\tau-\varepsilon<|\underline{X}_i-\underline{X}_j|<\tau+\varepsilon}\left[\ln V(\underline{X}_i)-\ln V(\underline{X}_j)\right]^2 \tag{12}$$

where ε is typically one-half the distance between consecutive values of τ and N is the number of terms in the summation. In the discussion that follow, we will refer almost exclusively to the experimental semivariogram. For the sake of brevity, we will omit the subscript e and the "experimental" prefix.

In the EPRI(1993), we suggest that horizontal correlation be investigated as a function of layer number (i.e., one would compare the ln-velocities in the first layers of the various profiles and compute their variances, then do the same for the second layers, etc.). This would be appropriate if most layers (with their particular properties) could be traced across the various profiles in a cluster. The profile plots in figures 35 through 68 suggest that this is

generally not the case. Thus, we will parameterize horizontal correlation as a function of depth.

One could calculate semivariograms at multiple depths, as done by Rouhani et al. (1993). For the sake of simplicity (i.e., a model with fewer parameters), and in order to obtain more stable estimates, we "pool" data from multiple depths to obtain one semivariogram. This is also justified by the earlier observation that the standard deviation of ln-velocity is roughly independent of depth. If a cluster shows large depth-wise variations in its standard deviation, we sub-divide the cluster into depth ranges with roughly constant standard deviation and perform separate calculations for each depth range. The sampling over depth is equally spaced (every meter) down to 10 m and logarithmically spaced at greater depths (i.e., at depths of 11, 12.1, 13.3, 14.6m, etc.)[7].

Figures 70 through 73 show the experimental semivariograms for the three Savannah River clusters (cpt, K, and NPR). Two depth ranges are considered for cpt; namely 0-50 m and 50m+. The dashed horizontal line in each figure shows the variance for the generic category that includes the site[8]. The small numbers indicate the number of points used to compute each point in the semivariogram. The results for cpt (0-50 m) and the K-site show that γ is weakly dependent of distance. The results for cpt (50m+) are erratic, possibly because they are based on a much smaller number of profiles. Results for NPR show a stronger dependence on distance. All Savannah River results show a strong correlation among the profiles in each cluster (as manifested by the low ratio of the semivariogram to the generic variance).

---

[7]If the cluster has a fairly simple dipping stratigraphy, one could offset the profiles prior to these calculations in order to obtain higher correlations. This should only be done if the stratigraphy is simple enough, and well-known enough, that one can easily determine the offset to apply to any hypothetical location within the cluster.

[8]Because we know the variance of ln-velocity for this soil category, we assume that the semivariogram would converge to this dashed line if we had data extending to large distances.

It is also interesting to combine the data from the three Savannah River clusters. This information might be used to obtain preliminary estimates of velocities at a site located outside of the clusters but not too far from them. Figures 74 and 75 shows the resulting semivariograms at small and large scales, respectively. Figure 76 shows a combination of both. Figure 76 shows more significant dependence on distance, with γ values ranging from 0.02 to 0.50. Even at distances of 10 km, there is significant correlation among sites (relative to the generic model).

Figures 77 through 79 show the semivariograms for the other sites with relative-location information (Highways 5 and 14 Intersection, Bayshore Viaduct, and Highway 118; all in California). The semivariograms for the first two are much higher than the generic variance, indicating that there is more variability in ln-velocity in each of these two clusters than in the generic dataset. The semivariogram for the Highway 118 cluster, on the other hand, shows significant correlation beyond 1000m distances.

The Bay Bridge and Dumbarton Bridge clusters have no relative-location information. The calculated variances for each of these clusters, and for the clusters described above, are shown in Table 7. Except for their top 20 m, these two clusters show very high correlation, even though they extend over distances of more than 1000 m.

In summary, certain sites (mainly deep-soil sites) exhibit high within-cluster correlation over distances of several hundred to a few thousand meters. Other sites, have within-cluster variances higher than the generic variances. In most of the former cases, the correlation is only moderately dependent on distance. The model to be presented below is applicable only to the sites that exhibit inter-cluster correlation.

Because correlation is moderately dependent on distance, the model will be formulated in terms of a general atocovariance function but then it will be specialized to the simpler case where the correlation is independent of distance.

4.3 Site-Specific Velocity Model

Consider a cluster of sites that exhibits inter-cluster correlation (i.e., where the semivariogram is smaller than or equal to the generic variance) and assume that we have fit a variogram model that allows us to calculate $\gamma(\tau)$ or $R(\tau)$ for any value of τ. From $R(\tau)$, we can calculate the autocorrelation function $\rho_h(\tau) = R(\tau) / \sigma_{\ln v}^2$ (we use the subscript h to emphasize that this quantity represents horizontal correlation). This model provides information about the horizontal correlation between the ln-velocities of the various profiles, at a given depth.

Let $Z_{0,j}$ denote the normalized ln-velocity (see eq. 3) at location 0 (the location at which we wish to generate an artificial profile) and at depth h_j. Let $Z_{i,j}$, i=1,n be the normalized ln-velocities at depth h_j in the n profiles measured in the cluster. We do not know $Z_{0,j}$, but we know $Z_{i,j}$, i=1,n. We also know that the random vector $\mathbf{Z}_j=[Z_{0,j},Z_{1j},Z_{2j},...Z_{nj}]^T$ follows a multi-normal distribution with mean zero and with an autocorrelation matrix that is given in terms of $\rho_h(\tau)$, the distances between the various boreholes, and the distance from site 0 to the various boreholes. This correlation matrix may be written as

$$R_{Z_j}=\begin{bmatrix} 1 & R_{0,i}^T \\ R_{0,i} & R_{i,i} \end{bmatrix} \tag{13}$$

where $\boldsymbol{R}_{i,i}$ is the n×n correlation matrix of the cluster ln-velocities and $\boldsymbol{R}_{0,i}$ is an n×1 column vector containing the correlations between Z_0 and the clustered ln-velocities.

In addition, the generic velocity model specifies the vertical correlation (within a profile) between the ln-velocity of a layer and that of the layer immediately above (i.e., the correlation between $Z_{0,j}$ and $Z_{0,j-1}$, where the latter is also assumed to be known if we are generating artificial velocities from the top to the bottom of the profile. This correlation is given by equation 7 (we will call this correlation ρ_v.

The normalized ln-velocities at depth h_{j-1} (i.e., $\mathbf{Z}_{j-1}=[Z_{0,j-1},Z_{1,j-1},Z_{2,j-1},...Z_{n,j-1}]^T$) also have the correlation matrix given by equation 13.

We have no information, however, about the correlation between the values of Z in two different profiles and at different depths (this correlation cannot be zero). A reasonable assumptions is that the correlation between the the ln-velocity at depth j in one profile and depth j-1 in another profile is given by $\rho_v \times \rho_h(\tau)$, where τ is the horizontal distance between the two profiles (this assumption is analogous to a Markov assumption). Thus, one can construct the joint covariance matrix of the Z's at depths j and j-1 in terms of the quantities in eq. 13 and of ρ_v. Using this correlation matrix, one can determine the conditional distribution of $Z_{0,j}$ (the only unknown quantity), given the values of the other quantities, using the properties of the multi-normal distribution[9]. In the special case where the horizontal correlation is independent of distance (horizontal equicorrelation), one obtains the following expression for the conditional mean of ln $V_{0,i}$:

$$\ln V_{0,j,\text{cond.median}} = \frac{n\rho_h}{1+(n-1)\rho_h}\overline{\ln V}_j + \left[1-\frac{n\rho_h}{1+(n-1)\rho_h}\right]\ln V_{j,\text{median}} + \rho_v\left(\ln V_{0,j-1} - \ln V_{j-1,\text{median}}\right) - \frac{n\rho_h\rho_v}{1+(n-1)\rho_h}\left(\overline{\ln V}_{j-1} - \ln V_{j-1,\text{median}}\right) \quad (14)$$

where n is the number of profiles in the cluster (at depth h_j), ρ_h is the correlation between profiles in the clusters (i.e., the quantity in the last column of Table 7), $\overline{\ln V}_j$ and $\overline{\ln V}_{j-1}$ are the mean ln-velocities from all profiles in the cluster at depths h_j and h_{j-1}, and $V_{0,j-1}$ is the (previously calculated) artificial velocity in the layer above. The quantity

[9]This process is equivalent to linear regression or to the determination of weights in geostatistical "Kriging."

$$\frac{n\rho_h}{1+(n-1)\rho_h} \tag{15}$$

in the first term represents the weight given to the site-specific mean ln-velocity. This weight approaches 1 (and the weight given to the generic data in the second term approaches 0) if $n\rho_h >> 1$. For instance, the weight given to the site-specific data is 0.964 for the K site at shallow and moderate depths (n=18, ρ_h=0.6). The third term represents vertical correlation between adjacent layers in the same profile (coming from the generic model). The final term (which has a lower weight than the first and third terms) is required because the correlation between the correlation between ln-velocities at different depths and in different profiles cannot be zero. In the case where the horizontal correlation depends on distance, one would obtain a similar expression in terms of weighted averages of the ln-velocities in the cluster at depths h_j and h_{j-1}.

Similarly, one obtains the following expression for the conditional variance of ln $V_{0,i}$:

$$\sigma^2_{\ln V_{0,j},\,\text{cond.}} = \sigma^2_{\ln V}(1-\rho_v^2)\left(1-\rho_h^2\frac{n}{1+(n-1)\rho_h}\right) \tag{16}$$

The equation above indicates that the conditional variance is reduced by both the vertical correlation and the horizontal correlation. The reduction factor for horizontal correlation is $(1-\rho_h^2)$ for n=1 and $(1-\rho_h)$ for $n\rho_h >> 1$.

This site-specific model is not applicable to cases where the cluster variance is greater than the generic variance. This is not an uncommon situation, as demonstrated in Table 7. The current implementation of the simulation code assumes ρ_h=0 in these cases, thereby ignoring the site-specific data and using the generic model alone. Another, perhaps preferable, approach is to ignore the generic median and $\sigma_{\ln V}$ and use the site-specific median and $\sigma_{\ln V}$ as if they were the generic ones (one might still use the generic ρ_v model, unless a site-specific ρ_v model were available).

4.4 Site-specific Layering Model

If the profiles in a cluster tend to have layer boundaries concentrated at certain depths, one would like the artificial profiles to also have layer boundaries concentrated at those depths. On the other hand, one should not preclude all artificial profiles from having layer boundaries at depths different from those occurring in the observed profiles, especially if the number of site-specific profiles is small. In a manner analogous to that used for the velocity data, one can construct a rate function $\lambda(h)$ that is a combination of the generic rate function in Equation 2 and the observed rate of layer boundaries in the site-specific profiles. The resulting expression for the rate of layer boundaries between depths h_1 and h_2 is given by

$$\Lambda(h_1,h_2)=\frac{m\int_{h_1}^{h_2}\lambda(t)dt+N(h_1,h_2)}{m+n} \tag{17}$$

where m is the "equivalent number of site-specific profiles" represented by the generic data, $N(h_1,h_2)$ is the number of observed layer boundaries between depths h_1 and h_2 in the cluster data, and n is the number of site-specific profiles that extend down to depth h_2 or greater. We do not have a quantitative procedure to estimate m, but simulations suggest that a value m=1 is appropriate. Note that if n is large, equation 17 will be dominated by the depth-wise distribution of layer boundaries in the cluster data. The calculation of layer boundaries in the artificial profiles uses Equation 17 but maintains the Poisson assumption.

One of the benefits of using this model for the simulation of the layering (as opposed to the generic model) is that the median of the artificial profiles is closer to the site-specific median when n is large and the site-specific median profile has sharp changes in velocity. If one uses the generic layering model, the median of the artificial profiles tends to be smooth, even if the cluster median has sharp changes in velocity.

4.5 Examples of Artificial Site-Specific Profiles

Figures 80 through 87 show artificial profiles for the K and NPR clusters of Savannah River and for the Highway 118 site in California, as well as the respective medians and standard deviations calculated from 100 artificial profiles. Site K is an interesting site because one of the profiles in this cluster extends to much greater depth. Thus, we can see the effect of the number of profiles on the site-specific results.

Comparing the median $\pm\sigma$ plot for the artificial profiles (Fig. 81) to that for the cluster data (Fig. 41), we see that they match closely in the upper 50 m, for which there are a large number of profiles. Beyond 60 m, there is only one profile (profile 736) in the cluster and the resulting median profile is clearly a weighted combination of the generic category-B profile and profile 736. The results for h> 60 m depend significantly on the value of ρ_h used for this depth range, which depends on the corresponding value of $\sigma_{\ln V}$. Obviously, one cannot compute the cluster $\sigma_{\ln V}$ for h> 60 m using this one profile. In these simulations, we use the $\sigma_{\ln V}$ obtained by pooling data at all depths. If one has reason to expect greater horizontal homogeneity at these depths, one may choose to use a higher ρ_h, thereby down-weighting the generic profile.

The site-specific layering model increases the probability of layer boundaries occurring at depths near 80 and 120 m. This helps preserve the sharp steps in the median profile at these depths.

The artificial profiles for the NPR site are similar in appearance to the measured profiles. The median of the artificial profiles does not conserve the mild velocity variations in the median of the measured profiles. This is not unexpected because ρ_h is lower for NPR.

The artificial profiles for Highway 118 show the effect of even lower values of n and ρ_h. In cases like this, one gains considerable statistical stability by using a combination of the site-specific measurements and the generic model.

5. SUMMARY AND CONCLUSIONS

to be added later

6. ACKNOWLEDGMENTS

This work was performed under contract 779574 between Brookhaven National Laboratory and Risk Engineering, Inc, under the technical supervision of Kamal Bandyopadhyay. This work has benefited from discussions with Walt Silva, Richard Lee, Cliff Roblee, S.C. Wu, Carl Costantino, John Schneider, I. Idriss, and others. The soil-profile database used in this study was developed by Walt Silva, Kathy Stark, and Sylvia Li of Pacific Engineering and Analysis.

7. REFERENCES

Atomic Energy Commission (1973). "Reactor Siting Criteria: Seismic and Geologic Siting Criteria." *Federal Register* - 10 CFR Part 100, Vol. 38, No. 218, November.

Benjamin, Jack R., and C. Allin Cornell (1971). *Probability, Statistics and Decisions for Civil Engineers*. McGraw Hill, New York.

Costantino, Carl J., E. Heymsfield, and Y. T. Gu (1991). *Site Specific Estimates of Surface Ground Motions for the K-Reactor Site, Savannah River Plant.* Report CEERC-91-003, Structural Analysis Division, Nuclear Energy Department, Brookhaven National Laboratory, Upton, N.Y.

McGuire, R. K., Gabriel R. Toro, Thomas P. O'Hara, John P. Jacobson, and Walter J. Silva (1989). *Probabilistic Seismic Hazard Evaluations at Nuclear Plant Sites in the Central and Eastern United States: Resolution of the Charleston Earthquake Issue.* Palo Alto, California: Electric Power Research Institute, April 1989. NP-6395-D.

Parzen, E. (1962). *Stochastic Processes*. Holden Day.

Rouhani, S., Y.-P. Lin, and A. Majid (1993). *Velocity Model Database, Statistical Models of Soil Columns Velocity, and Maps of Model Layers*. Georgia Institute of Technology, Final technical report to Westinghouse Savannah River Company, August.

Silva, W. J., et al. (1994). "Generic Soil Amplification Factors for Application to Ground Motion in Eastern North America," submitted to Earthquake Spectra.

Toro, Gabriel R., Walter J. Silva, Robin K. McGuire, and Robert B. Herrmann (1992). "Probabilistic Seismic Hazard Mapping of the Mississippi Embayment," *Seismological Research Letters*, Vol. 63, No. 3, July-September.

Vanmarcke, E. H. (1977). "Probabilistic Modeling of Soil Profiles," *J. Geo. Eng. Div., ASCE*, Vol. 103, No. GT11, pp. 1227-1246.

TABLE 1
PROFILES USED IN THIS STUDY

Profile No.	Name	Lat. (N)	Long. (W)	USGS Site Class.	Geomatrix Site Class.	Profile Depth (m)
1	Gilroy 1 -Gavilan Water Tank	36.97	121.57	A		20.30
2	Gilroy 2 -Misn. Trails Motel	36.98	121.56	C		33.40
3	Gilroy 3 -Sewage Treat Plant	36.99	121.54	C		60.50
4	Gilroy 4 -San Ysidro School	37.01	121.52	C		30.50
5	Gilroy 6 -Canada Road	37.03	121.48			25.00
6	Cholome 5 -Cockrum's garage	35.70	120.33	C	IHC	55.50
7	Cholome 8 -Shandon Pump Sta	35.67	120.36	C	ABB	30.40
8	Cholome 12 -Shandon Vineyards	35.65	120.40	B	IBB	26.70
9	Cholome 11 -Temblor II	35.71	120.17	B		27.70
10	Lincoln School	35.15	119.46	B		60.00
11	Purisma	37.46	122.42	C		30.00
12	Cozzolino's	37.48	122.39	C		29.00
13	MaryKnoll	37.33	122.08	B		28.30
14	El Granada	37.52	122.45	A		30.00
15	Black Mountain	37.34	122.16	B		29.00
16	Digges Canyon	37.50	122.42	B		31.00
17	Pise Lookout	37.46	122.34	B		28.00
18	Pulgas Water Temple	37.48	122.32	B		28.00
19	Spring Valley Ridge	37.57	122.45	B		29.20
20	Vista Point	37.49	122.30	B		29.00
21	North Peak	37.56	122.47	B		20.00
22	Sawyer Ridge	37.57	122.42	B		26.60
23	Bonds Corner	32.69	115.34	C	AQD	55.00
24	Calexico Fire Station	32.67	115.49	C	AQD	75.60
25	Holtville Post Office	32.81	115.38	C	AQD	75.00
26	El Centro Array #2	32.92	115.37	C	IQD	75.40
27	El Centro Array #3	32.89	115.38	D	AQD	67.80
28	El Centro Array #4	32.86	115.43	C	IQD	73.80
29	El Centro Array #5	32.86	115.47	C	IQD	68.70
30	El Centro Array #6	32.84	115.49	C	IQD	70.00
31	El Centro Array #7	32.83	115.50	C	AQD	57.70
32	El Centro Array #8	32.81	115.53	C	AQD	72.60
33	El Centro Array #9	32.79	115.55	C	EQD	244.40
34	El Centro Array #10	32.78	115.57	C	AQD	71.10
35	El Centro Array #11	32.75	115.59	C	AQD	62.60
36	El Centro Array #12	32.72	115.64	C	IQD	27.50
37	El Centro Array #13	32.71	115.68	C	AQD	71.80
38	El Centro Differential G.M.A.	32.80	115.54	C	IQD	118.90
39	Savannah River SSW-1	33.19	81.67	B		137.16
40	Savannah River P-25	33.19	81.67	B		121.92
81	Forgaria, Italy			B		34.90
82	Southern Pacific Bldg	37.79	122.40	C		86.80
83	Lotung LSST			C		60.00
85	Anza - PFO rock	33.50	116.65	B		255.00
86	Anza - KNW rock	33.50	116.65	B		290.00
89	Richmond Field Station	37.90	122.30	C		45.00
90	Richmond Landfill -Hole GT1			C		15.30
91	Richmond Landfil-Hole GT 1&2			D		41.10
93	Alhambra	34.09	118.15	B		27.50

TABLE 1 (continued)
PROFILES USED IN THIS STUDY

Profile No.	Name	Lat. (N)	Long. (W)	USGS Site Class.	Geomatrix Site Class.	Profile Depth (m)
94	Vernon	34.00	118.19	C		28.70
95	LA - Olive	34.05	118.25	C		27.50
96	LA - Hill	34.05	118.25	B		29.80
97	Hollywood Storage	34.09	118.34	C	IPD	30.00
98	Santa Monica-Wilshire	34.01	118.48	B		30.00
99	Tishman Airport Center	33.96	118.38	B		30.00
100	Hyperion	33.93	118.43	C		30.00
101	Devonshire Police Station	33.26	118.53	B		29.00
102	Olive View	34.32	118.45	C	AQD	27.50
103	Mullholland Jr. H.S.	34.19	118.51	C		30.00
104	Camp Munz	34.65	118.48	B		30.00
105	Rosamond Dry Lake	34.76	118.10	C		46.00
106	Lake Hughes F.S.	34.67	118.43	B	APC	26.70
107	Leona Valley F.S.	34.61	118.28	C	I-D	20.70
108	Llano North	34.53	117.81	B		30.00
109	Littlerock Post Office	34.52	117.98	B		25.00
110	Llano South	34.51	117.82	B		27.50
111	Pearblossom Pump Plant	34.51	117.92	B	AGB	25.00
112	Holiday Inn Palmdale	34.58	118.12	B		30.00
113	Palmdale F.S.	34.58	118.10	B		30.00
114	Castaic Dam	34.52	118.60	C		24.00
116	Lexington Dam	37.20	121.95	A		22.50
117	Hollister, SAGO South	36.75	121.40	B		19.51
118	Diamond Heights, San Francisco	37.74	122.43	B	BBA	29.91
119	Pacific Heights, San Francisco	37.79	122.43	A	BFA	34.02
120	Sierra Point, South SF	37.66	122.44	A		27.20
121	Haviland Hall, U.C. Berkeley	37.87	122.26	A		21.33
122	Point Bonita	37.82	122.53	A	AFA	29.91
123	Martinez VA Hospital	37.99	122.11	B		36.01
124	Patterson Pass			B		29.91
125	Memorial Stadium, U.C.B.	37.87	122.25	B		70.03
126	San Francisco VA Hospital	37.78	122.50	B		83.82
127	Capitola Fire Station	36.97	121.95	C		30.12
128	Monterey City Hall	36.60	121.90	A		19.51
129	Piedmont Jr. High School	37.82	122.23	A	I-A	28.01
130	Rincon Hill, San Francisco	37.79	122.39	A	IFA	24.11
131	Belmont, Davis Drive	37.51	122.31	B		34.99
132	Site 300, Lawrence Liv. Lab			B		31.00
133	Halls Valley	37.34	121.71	C	IFB	30.51
135	Wheeler Ridge	35.03	119.99	C	IBD	30.00
136	Edmonston Pumping Plant	34.94	118.82	B		29.60
137	OSO Pumping Plant	34.54	118.72	C		26.80
138	Castaic Old Ridge Route	34.56	118.65	B	A-B	28.00
139	Elizabeth Lake Fire Station	34.57	118.56	B		30.00
140	Warm Springs Camp	34.61	118.56	A		20.70
141	Wrightwood	34.36	117.63	B	BAB	30.00
142	Allen Ranch	34.28	117.33	A		22.20
143	Cedar Springs Dam	34.31	117.31	B		30.00
144	Colton SCE	34.06	117.31	C	ACD	30.00

TABLE 1 (continued)
PROFILES USED IN THIS STUDY

Profile No.	Name	Lat. (N)	Long. (W)	USGS Site Class.	Geomatrix Site Class.	Profile Depth (m)
145	CIT Athenaeum	34.14	118.12	B	CQD	24.00
146	CIT Old Seismological Lab	34.15	118.17	A		30.00
147	Griffith Observatory	34.12	118.30	A		30.00
148	Palos Verdes	33.88	118.39	C		27.00
149	Santa Barbara Cnty Courthse	34.42	119.70	B	CQD	26.00
150	El Centro Differential G.M.A.	32.80	115.54	C	IQD	73.10
151	Imperial Co. Serv. Bldg.	32.79	115.56	C		33.50
152	Brawley Airport	32.99	115.51	C	AQD	38.40
153	Westmorland Fire Station	33.04	115.62	C	ADD	30.00
154	Parachute Test Site	32.93	115.70	B	AQD	28.70
155	Calipatria Fire Station	33.13	115.52	C	BQD	24.10
156	Salton Sea Wildlife Ref.	33.18	115.62	D		27.70
164	Big Rock			A		128.00
165	Big Rock			A		54.86
166	Hope Creek	39.46	75.54	D		60.96
167	Hope Creek	39.46	75.54			548.64
168	Millstone	41.31	72.17	A		9.75
169	South Texas	28.79	96.05	C		91.44
170	Susquehanna	41.09	76.15	A		9.14
171	Susquehanna BH 1102	41.09	76.15	B		27.43
174	Susquehanna	41.09	76.15	B		24.38
176	Oyster Creek	39.81	74.21	C		548.64
177	River Bend	30.76	91.33	C		64.01
179	Beaver Valley	40.62	80.43	C		30.48
180	Beaver Valley	40.62	80.43	C		35.05
181	La Salle	41.25	88.67	D		1341.10
184	Hatch	31.93	82.34	B		40.50
185	Yankee Rowe,c	42.73	72:92	B		30.49
186	Alameda Naval Air Station			C		140.00
187	Gilroy 2 EPRI hole-USGS	36.98	121.56	C	IQD	70.00
189	Gilroy 2 USGS hole	36.98	121.56	C	IQD	120.00
190	Oakland Outer Harbor Wharf	37.82	122.31	C		168.00
191	S.F. International Airport SFO	37.62	122.39	C		145.00
192	Treasure Island	37.83	122.37	D		103.00
193	Palo Alto Veterans hospital			C		147.50
194	Yerba Buena Island	37.81	122.36	A	AFA	24.50
196	Alviso Raceway	37.43	121.97	C		29.70
197	Blackberry Farm	37.32	122.06	B		25.00
198	John Muir School	37.66	122.08	C		29.40
199	Lowry Road	37.57	122.07	C		24.40
200	Hayward Sink	37.61	122.09	C		27.50
201	Parkway Towers	37.54	121.97	C		29.00
202	Palo Alto Square	37.42	122.14	C		25.00
203	Mission Peak	37.52	121.87	A		30.00
204	Montgomery School	37.34	121.98	C		30.00
205	Stevens Creek Quarry	37.30	122.08	A		30.00
206	Cal State Hayward	37.66	122.06	B		30.00
207	Miller School	37.30	122.01	B		26.50
208	Oliver's Salt Works	37.62	122.13	E		12.80

TABLE 1 (continued)
PROFILES USED IN THIS STUDY

Profile No.	Name	Lat. (N)	Long. (W)	USGS Site Class.	Geomatrix Site Class.	Profile Depth (m)
209	Corte Madera	37.36	122.22	B		30.50
210	Mitchell Park	37.42	122.11	C		30.00
211	Foothills Park	37.35	122.17	B		29.00
212	Sierra Morena	37.41	122.31	B		30.00
213	Pulgas Tunnel	37.18	122.31	B		30.00
214	Frenchman's Creek	37.49	122.43	B		20.60
215	Half Moon Bay Terrace	37.52	122.50	C		30.00
216	Vista Grande	37.70	122.46	B		30.00
217	Morrison Canyon	37.58	122.92	B		30.00
218	Lake Merced Country Club	37.70	122.47	B		30.00
219	Agnews State Hosp-Agbab DH	37.40	121.95	C	AQD	50.00
221	Capitola-Agbab DH	36.97	121.95	C	AQD	30.10
223	Martinez-Agbab DH	37.99	122.11	B		36.00
225	Menlo Park VA-Agbab DH	37.47	122.16	C		60.00
227	Fremont Mission SJ-Agbab DH	37.53	121.92	B	AMB	72.00
230	Patterson Pass(rock)-Agbab DH	37.70	121.68	B		29.90
232	Richmond City Hall-Agbab DH	37.94	122.34	C	I-D	72.00
234	UCSC Lick Observ-Agbab DH	37.00	122.06	E	AKB	13.70
235	Oakland 1700 Webster	37.81	122.27	C		113.99
242	Redwood City-Bridgeway Prk	37.53	122.25	D		29.60
243	Wind Mill	37.77	122.51	C		29.80
244	Chain of Lakes	37.77	122.50	E		21.50
245	Prayer Book Cross	37.77	122.48	E		19.00
246	Page Mill	34.40	122.17	B		16.00
247	Southern Pacific	37.78	122.39	C		27.70
248	Avalon	37.68	122.49	C		30.00
250	Quintara (Sunset District)	37.76	122.50	C		29.80
251	Hillview	37.69	122.50	B		26.60
252	Twin Peaks	37.75	122.45	A		30.40
253	San Bruno Mountain	37.70	122.43	A		28.00
254	Skyline	37.69	122.49	C		28.00
255	Westmoor	37.68	122.49	C		27.50
256	Peninsula Country Club	37.54	122.32	A		11.20
257	Merritt College	37.79	122.16	A		28.70
258	KGEI	37.54	122.24	D		28.80
259	Crest Road	37.45	122.25	B		30.00
260	Audubon School	37.57	122.26	D		27.50
261	Santa Clara County Fairgrounds	37.30	122.85	C		25.00
262	College of San Mateo	37.59	122.33	B		16.30
263	Carmichael School	37.78	122.40	C		27.00
264	Oak Avenue School	37.36	122.07	B		30.00
265	Merrit Sand	37.81	122.28	C		26.70
269	Gilroy 2 EPRI hole-Agb interp	36.98	121.56	C	IQD	213.35
271	Gilroy 2 EPRI hole-USGS	36.98	121.56	C	IQD	70.00
289	Gilroy 2 EPRI hole-Redp interp	36.98	121.56	C	IQD	167.60
310	Savannah River NPR M12A-17	33.25	81.64	B		78.96
311	Savannah River NPR M12A-18	33.25	81.64	C		42.99
312	Savannah River NPR M12A-19	33.25	81.64	B		63.14
313	Savannah River NPR M12A-20	33.25	81.64	B		68.62

TABLE 1 (continued)
PROFILES USED IN THIS STUDY

Profile No.	Name	Lat. (N)	Long. (W)	USGS Site Class.	Geomatrix Site Class.	Profile Depth (m)
314	Savannah River NPR M12A-21	33.25	81.64	B		70.41
315	Savannah River NPR M12A-22	33.25	81.64	B		79.69
316	Savannah River NPR M12A-25	33.25	81.64	B		53.05
317	Savannah River NPR M12A-26	33.25	81.64	B		41.15
318	Savannah River NPR M12A-27	33.25	81.64	B		44.81
319	Savannah River NPR M12A-28	33.25	81.64	B		66.82
320	Savannah River NPR M12A-29	33.25	81.64	C		59.44
321	Savannah River NPR M12A-30	33.25	81.64	C		64.95
349	Treasure Isl.-EPRI Hole Redpa	37.83	122.37	D	B-D	85.30
350	Treasure Isl.-EPRI Hole U.NH	37.83	122.37	D	B-D	42.50
351	Treasure Isl.-EPRI Hole USGS	37.83	122.37	D	B-D	100.00
353	Treasure Isl.-EPRI Hole U.MI	37.83	122.37	D	B-D	27.40
361	Yerba Buena Isl. -Redpath	37.81	122.36	A	AFA	23.80
363	Oakland Bay Bridge Toll, intrp	37.81	122.32	C		156.00
364	Cypress Structure hole B-2	37.80	122.25	C		170.69
365	Cypress Structure hole B-8	37.80	122.25	C		173.74
366	Islais Creek -Hole 15	37.80	122.40	A		13.72
367	Embarcadero B1	37.75	122.40	C		64.01
368	Islais Creek -Hole 16	37.80	122.40	D		35.05
369	Islais Creek -Hole 19	37.80	122.40	C		33.53
370	Islais Creek -Hole 21	37.80	122.40	D		22.86
371	Islais Creek -Hole 4	37.80	122.40	D		33.53
372	Islais Creek -Hole 5	37.80	122.40	D		33.53
373	LLNL -NE Corner EW-Poleriz	37.70	121.80	C		60.96
374	LLNL -NE Corner NS-Poleriz	37.70	121.80	B		60.96
375	Oakland Harbor -Redpath	37.82	122.31	C		146.30
377	Olmsted Dam-KY side	37.15	89.07	C		46.63
378	Olmsted Dam-KY side	37.15	89.07	C		21.34
381	Olmsted Dam-IL side general	37.15	89.07	C		52.73
382	Port of Stockton-hole 17	37.95	121.30	E		13.72
383	Port of Stockton-hole 5	37.95	121.30	E		14.63
384	Richmond Dump-averaged	33.00	81.00	D		39.62
385	Richmond Dump- GT-1	33.00	81.00	D		36.58
386	Richmond Dump-GT-2	33.00	81.00	D		39.62
387	Richmond Dump-GT-3	33.00	81.00	E		13.72
388	SF Airport -Redpath	37.62	122.40	C	AHD	152.40
389	Vineyard Canyon	35.80	120.40	C		190.00
391	Port of Stockton-hole 10	37.95	121.30	E		9.14
392	Camarillo State Hospital 2	34.16	119.04	C		29.00
393	Marina Del Rey	33.97	118.46	C		39.00
394	Westminster H.S	33.75	118.01	C		29.20
395	Burbank Fire Station	34.18	118.30	B		24.00
396	Shellmaker Island	33.62	117.89	C		29.00
397	Cypress College	33.83	118.02	C		24.00
398	Ventura Pistol Range	34.29	119.29	B		29.00
399	Sierra Linda School	34.23	119.19	C		28.00
400	San Miguel School	34.18	119.18	C		29.50
401	Alta Vista Park	33.49	118.38	E		25.00
402	Seal Beach Weapons Station	33.75	118.09	C		26.00

TABLE 1 (continued)
PROFILES USED IN THIS STUDY

Profile No.	Name	Lat. (N)	Long. (W)	USGS Site Class.	Geomatrix Site Class.	Profile Depth (m)
403	Ridgeline Water Tank	33.99	117.82	B		27.00
404	Diamond Bar	33.98	117.82	B		20.00
405	Sky Terrace	34.29	118.40	B		28.00
406	Sylmar Nursery	34.32	118.43	B		29.00
407	Sylmar Park	34.31	118.45	C		28.00
408	Hilltop House	34.33	118.45	B		28.50
409	Cedar Hills Nursery	34.16	118.54	B		29.00
410	Cal State Northridge	34.24	118.52	C		29.00
411	Magnolia	33.77	118.20	C		28.00
412	1st Lutheran Church	33.78	118.18	B		26.00
413	Terminal Island	33.75	118.25	C	CCD	21.20
414	Lakewood Golf Course	33.83	118.15	E		18.10
415	F.S. 105	33.86	118.22	C		28.00
416	Compton Airport	33.89	118.24	E		15.00
417	Compton Civic Center	33.89	118.22	C		31.00
418	Holiday Inn	34.21	118.47	B		29.00
419	Veterans Hospital	33.78	118.12	B		29.00
420	Newport Beach SDP 2	33.63	118.96	C		46.00
421	Katella School	33.83	117.83	B		20.00
422	St. Jude's Hospital	33.90	117.93	B		29.00
423	Rowland Heights	33.99	117.89	C		28.00
424	El Monte Courthouse	34.70	118.03	C		29.00
425	Verdugo Park	34.17	118.23	B		25.00
426	20th Century	34.05	118.41	C		29.50
427	Upper Van Norman Dam	34.53	118.49	C		27.00
428	Pacoima Memorial Hospital	34.28	118.38	C		29.00
430	Sylmar High School	34.31	118.44	B		29.00
431	Mission Hills P.O.	34.26	118.46	B		29.00
432	Eton School	34.19	118.60	C		30.00
433	Camarillo State Hospital	34.19	119.04	C		30.50
434	Pacific Missle Test Center	34.11	119.11	C		30.00
435	Ventura Co. Airport	34.20	119.20	C		28.50
436	Mandalay Beach	34.20	119.25	C		30.00
437	Ventura Co. General Hospital	34.28	119.25	C		30.50
438	Bard Sanitarium	34.28	119.25	C		29.00
440	Gilroy 1 -Gavilan Water Tank	36.97	121.57	A	IFA	20.30
441	Gilroy 6 -Canada Road	37.03	121.48	B	IKA	30.00
442	APEEL 9-Crystal Springs	37.48	122.32	B	IQC	30.00
443	APEEL 7-Pulgas Water	37.48	122.31	B	IEC	30.00
444	APEEL 10-Skyline	37.47	122.34	B	I-A	30.00
445	APEEL 3E-Hayward CSUH	37.66	122.06	B	ABA	30.00
446	Gilroy Gavilon College	36.97	121.57	B	AFB	30.00
447	APEEL 2E-John Muir School	37.66	122.08	C	ABD	30.00
448	Gilroy 2 -Misn. Trails Motel	36.98	121.56	C		32.80
449	Gilroy 3 -Sewage Treat Plant	36.99	121.54	C	IHD	60.00
450	Gilroy 4 -San Ysidro School	37.01	121.52	C	AHD	30.00
451	Hollister City Hall	36.85	121.40	C	CHD	105.00
452	APEEL 2-Redwood City	37.52	122.25	D	IQD	30.00
453	APEEL 1-Foster City	37.54	122.21	D	IQE	30.00

TABLE 1 (continued)
PROFILES USED IN THIS STUDY

Profile No.	Name	Lat. (N)	Long. (W)	USGS Site Class.	Geomatrix Site Class.	Profile Depth (m)
454	Corralitos	37.05	121.80	B	APD	30.00
455	San Francisco - generic	37.79	122.43	A		30.00
456	UC Santa Cruz	37.00	122.06	B	--A	30.00
457	Cherry Flat Reservoir	37.40	121.76	B		30.00
458	Stanford Linear Accelerator	37.42	122.21	C		30.00
459	Woodside Fire Station	37.43	122.26	B	APB	30.00
460	Golden Gate Bridge -Toll Plaza	37.81	122.47	B		30.00
461	Patterson Pass Road	37.70	121.20	B		30.00
462	Sierra Point	37.70	121.20	A		30.00
463	Bear Valley 7 -Pinnacles	36.48	121.18	A		30.00
464	Strawberry Canyon -UCB	37.87	122.24	B		30.00
465	Memorial Stadium -UCB	37.87	122.25	B		30.00
466	Lawrence Berkeley Lab	37.88	122.25	B	--B	30.00
467	Hayward City Hall FF-N	37.68	122.08	B		30.00
468	Hayward City Hall FF-S	37.68	122.08	B		30.00
471	Public Utilities Bldg, LB	33.77	118.19	C		2529.80
473	1800 Century Pk E,Century City	34.06	118.42	C		122.20
474	3345 Wilshire Blvd, LA	34.06	118.30	B		71.90
475	8244 Orion Blvd (Holiday Inn)	34.22	118.47	C		304.80
476	15910 Ventura Blvd, LA	34.16	118.48	C		97.50
477	CIT Miliken Library, Pasadena	34.14	118.13	B		115.20
478	Orange Co. Engr. Bldg, S Ana	33.75	117.87	D		2436.90
479	LA Chamber of Commerce	34.03	118.27	C		2499.40
480	Cholame-Shandon Array 2	35.73	120.29	C		64.00
481	Cholame-Shandon Array 5	35.70	120.33	C		55.70
482	Taft, Lincoln School Tunnel	35.15	119.46	B		92.00
483	Melendy Ranch Barn, Hollister	36.59	121.19	B		103.70
484	Esso Refinery, Managua	11.90	86.30	C		50.00
485	633 E. Broadway, Glendale	34.15	118.25	B		18.30
486	Hum. Bldg, LB State Univ.	33.78	118.11	B		15.20
487	2011 Zonal Ave., LA	34.06	118.21	B		42.70
488	3440 Univ. (USC), LA	34.02	118.28	B		10.70
489	3710 Wilshire Blvd., LA	34.06	118.31	B		15.20
490	4680 Wilshire Blvd., LA	34.06	118.33	B		7.60
491	8639 Lincoln Blvd., LA	33.96	118.42	B		15.20
492	JPL at CIT, Pasadena	34.20	118.17	B		125.00
493	San Onofre Nuclear Gen. Stn.	33.37	117.56	B		35.10
494	LA Westwood	34.07	118.45	B		1554.50
495	9100 Wilshire Blvd., Bev. Hill	34.07	118.39	B		15.20
496	1625 W. Olympic Blvd., LA	34.05	118.27	B		15.20
499	445 Figueroa St., LA	34.05	118.26	C		121.91
539	Savannah River 200-S					152.39
543	Light & Life Christian School	34.31	118.44	B	--D	46.70
544	Mile Square Regional School	33.72	117.94	C	--D	27.50
545	White Oak Covenant Church	34.21	118.52	C	--D	35.20
546	St. Stephen Presbyt. Church	34.36	118.57	C	--D	41.20
547	Evangelical Methodist Church	34.25	118.42	B	--D	32.00
548	Grace Community Church	34.22	118.42	B	--D	31.40
549	Panaroma Presbyterian Church	34.22	118.43	C	--D	33.20

TABLE 1 (continued)
PROFILES USED IN THIS STUDY

Profile No.	Name	Lat. (N)	Long. (W)	USGS Site Class.	Geomatrix Site Class.	Profile Depth (m)
550	Sun Valley Church of Nazarene	34.24	118.37	B	--B	23.90
551	Colwater Canyon Ave. School	34.19	118.41	B	--C	31.10
552	Los Angeles City Fire Sta. #78	34.15	118.41	C	--D	41.40
553	St. Vincent's Seminary	34.22	118.42	D	--D	21.60
554	Westminster Presbyt. Church	34.17	118.33	C	--D	45.90
555	Los Angeles City Fire Sta. #99	34.13	118.44	C	--C	35.20
556	Los Angeles City Fire Sta.#108	34.13	118.41	B	--C	40.30
557	Mount St. Mary's College	34.09	118.48	B	--B	19.70
558	Westlake School	34.09	118.43	C	--B	28.90
559	Wonderland Ave. Elem. School	34.11	118.38	A	--A	31.50
560	Laurel Children's Center	34.09	118.37	B	--D	35.60
561	Lincoln School	34.09	118.09	A		11.80
562	St. Thomas School	34.05	118.30	C	--C	15.60
563	Dayton Heights Elem. School	34.08	118.30	B	--D	33.70
564	West Vernon Ave. School	34.01	118.28	C	--D	24.50
565	St. Raphael School	33.98	118.29	C	--D	24.40
566	Vernon City School	34.00	118.23	C	--D	31.70
567	Los Angeles City Fire Sta. #12	34.11	118.19	B	--C	34.60
568	Divine Savior School	34.09	118.22	B	--C	31.40
569	Los Angeles City Fire Sta. #50	34.12	118.24	C	--D	23.20
570	Redondo First Ward LDS Church	33.82	118.36	E	--E	20.60
571	Catskill Avenue School	33.81	118.27	C	--D	21.90
572	Margate School	33.78	118.41	C	--C	31.80
573	Mira Catalina School	33.74	118.33	C	--C	27.40
574	Hawthorne Ward LDS Church	33.90	118.35	C	--D	18.40
575	Los Angeles City Fire Sta. #2	33.89	118.39	C	--C	22.20
576	Del Rey Hills Evang. Church	33.96	118.43	E		4.00
577	Santa Monica 1st Ward LDS Chur	34.01	118.49	B	--B	42.50
578	Los Angeles City Fire Sta.#23	34.04	118.55	C	--B	30.60
579	Garden Malibu C6 School	34.05	118.64	B	--B	15.20
580	St. Aidams Episcopal Church	34.02	118.79	B	--B	34.60
581	L.A. County Fire Sta. #125	34.15	118.70	B	--B	13.00
582	Epiphany Lutheran Church	34.21	118.61	C	--D	40.70
583	McBridge School	34.00	118.43	C	--D	57.00
584	Knolls Elementary School	34.26	118.67	E		8.90
585	Sulphur Spring School	34.42	118.43	C	--D	24.40
586	Mt. Gleason Jr. High School	34.27	118.30	B	--C	45.40
587	Castaways Restaurant	34.20	118.30	A	--B	44.30
588	Anderson W. Clark J.H.S.	34.24	118.25	C	--C	31.20
589	Condor Peak Forest Station	34.29	118.23	B	--C	22.60
590	Fremont Elementary School	34.20	118.23	C	--C	33.90
591	Azuza Ward LDS Church	34.14	117.88	B	--D	42.30
592	Azuza Ward LDS Church	34.14	117.88	B	--D	20.00
593	El Monte 1st Ward LDS Church	34.09	118.02	C	--D	32.40
594	Valley View Elementary School	34.15	117.94	B	--B	25.70
595	Covina State Ward LDS Church	34.08	117.87	C	--C	41.80
596	Olive Jr. High School	34.10	117.97	B	--B	31.40
597	Baldwin Park Ward LDS Church	34.09	117.92	C	--D	42.60
598	Baldwin Park 1st Ward LDS Chur	34.06	117.95	C	--B	23.60

TABLE 1 (continued)
PROFILES USED IN THIS STUDY

Profile No.	Name	Lat. (N)	Long. (W)	USGS Site Class.	Geomatrix Site Class.	Profile Depth (m)
599	W. Covina 3rd Ward LDS Church	34.03	117.92	C	--D	43.90
600	Hacienda Hts.1st Ward LDS Chur	33.99	117.94	C	--C	35.10
601	Olita School	33.92	117.97	C	--C	25.10
602	Lou Henry Hoover School	34.02	118.03	B	--B	32.70
603	Lakeview School	33.94	118.09	C	--B	26.40
605	Del Amo Elementary School	33.84	118.24	C	--D	26.50
606	Los Angeles City Fire Sta.#111	33.74	118.27	C	--D	17.10
607	Haven View School	33.71	118.60	C	--D	18.60
608	Mae Bayer Park	33.85	118.10	C	--D	24.70
609	Patton School, Los Alamitos	33.79	118.01	C	--D	32.80
610	Centeralia Sch Dist Adm Office	33.85	118.02	C	--D	29.40
611	Brea Laurel School	33.92	117.90	C	--D	35.20
612	Brea Laurel School	33.92	117.90	C	--D	20.70
613	Francis Scott Key School	33.82	117.95	C	--D	23.70
614	St. Cecilia's School	33.73	117.82	C	--D	25.10
615	Cerro Villa Jr. High School	33.82	117.82	B	--B	11.10
616	Saturn Street School	34.05	118.36	C	--D	22.80
617	Arcadia High School	34.13	118.04	C	--D	27.80
618	Grant Ward LDS Church	33.97	118.16	C	--D	28.90
619	Eaton Canyon Golf Course	34.17	118.08	C	--C	35.20
620	USC, Kaprielian Hall	34.02	118.29	C	--D	16.10
621	855 Arcadia Ave Residentia Bld	34.13	118.06	C	--D	40.00
622	Jefferson Blvd,Vermont Ave Pk	34.24	118.29	B	--B	34.00
623	USC, Dedeaux Field	34.02	118.29	B	--D	21.80
624	USC, Jeff. Blvd,Orchard Ave Pk	34.24	118.29	C		23.70
625	USC, Dental School Parking	34.02	118.29	B		16.70
626	USC, Univ Religious Ctr Prking	34.24	118.29	C		24.10
627	USC, Jefferson Blvd,Royal St	34.02	118.29	B		18.50
628	USC,Mark Taper Hall, Las Bldg2	34.24	118.29	C		28.80
629	USC, Doheny Library	34.02	118.29	B		22.20
630	USC, Alumni House	34.24	118.29	B		18.70
631	USC, Faculty Ctr, Pk Lot E	34.02	118.29	B		28.90
632	USC, Doheney&Hancock Found Bl	34.24	118.29	B		24.40
633	USC, Gerontology Bldg	34.02	118.29	C		28.50
634	USC, Parkside Apts Pk.	34.24	118.29	C		17.90
635	USC, Vermont&Exposition Blvd	34.02	118.29	C		28.10
636	USC, Exposition Blvd,Hoover St	34.24	118.29	C		25.20
637	USC, Exposition Blvd,Bridge Hl	34.02	118.29	C		23.80
638	USC, John Stauffer Hall	34.24	118.29	B		17.70
639	USC, Bovard	34.02	118.29	C		23.20
640	USC, Bing Theater&Heritage Hl	34.24	118.29	C		17.00
641	USC, Cromwell Athletic Field	34.02	118.29	C		29.60
642	USC, McKlintock&Intramural Fld	34.24	118.29	C		18.90
643	USC, Drama Ctr&John Brooks Mer	34.02	118.29	B		15.70
644	USC, McKlintock&Intramural Fld	34.24	118.29	B		31.50
645	USC, The Hedco Fndtion&Olin Hl	34.02	118.29	C		19.80
646	USC, Childs Way&Vermont Ave	34.24	118.29	B		18.30
647	USC, Vermont Ave. Post Office	34.02	118.29	C		25.60
648	St. Mark Lutheran Church	34.24	118.29	B		13.80

TABLE 1 (continued)
PROFILES USED IN THIS STUDY

Profile No.	Name	Lat. (N)	Long. (W)	USGS Site Class.	Geomatrix Site Class.	Profile Depth (m)
649	USC, East of Prking Struct D	34.02	118.29	C		21.60
650	USC, West of Prking Struct X	34.24	118.29	C		16.10
651	USC, East of Prking Struct X	34.02	118.29	B		27.20
652	USC, Lot K2, Neurol. Sci Bldg	34.24	118.29	C		36.20
653	USC, Vermont Ave&Entrance 7 Pk	34.02	118.29	C		38.60
654	Stone Canyon Res. Left Abut.	34.18	118.08	B		58.90
655	Stone Canyon Res. Right Abut.	34.18	118.08	B		35.70
656	Alhambra Fremont School	34.02	118.03	B	AMD	16.10
657	Garvey Reservoir Control Bldg	34.00	118.00	B	APB	25.90
658	Whittier Narrow Dam, Crest	34.00	118.00	C		38.20
659	Whittier Narrow Dam, Base	34.00	118.00	B		45.70
660	7215 Bright Ave. Whittier Bldg	33.17	118.01	C		32.00
661	Fort Tejon	34.87	118.90	B	AAB	35.00
662	Pacific Co. Airport	34.12	119.11	C		29.50
663	APEEL #1 (KGEI)	37.54	122.21	D		185.00
664	APEEL #2 (Portside Park)	37.52	122.25	D		70.00
665	Corralitos	37.05	121.80	B	APD	37.50
666	Gilroy 7 - Mantelli Ranch	37.03	121.43	C	AHB	32.50
667	Oakland 2-story (Snow Park)	37.81	122.27	C		60.00
668	Palo Alto 2-story Office Bldg	37.45	122.11	C		50.00
669	Presidio	37.79	122.46	B		54.00
670	Woodside Fire Station	37.43	122.26	B	APB	41.50
671	Beach Park Blvd.	37.56	122.24	D		90.00
672	Fremont	37.54	121.92	C		45.00
673	Hayward City Hall	37.69	122.09	B		29.50
674	Larkspur Ferry	37.95	122.52	D		38.50
675	Pacific Park Plaza	37.85	122.30	C		60.00
676	SLAC	37.42	122.20	B		60.00
677	Sunnyvale Colton Avenue	37.40	122.03	C	AHD	60.00
678	Savannah River K-1003	33.21	81.66	B		58.21
679	Savannah River K-1008	33.21	81.66	C		57.91
680	Savannah River K-1012	33.21	81.67	B		57.91
681	Savannah River KC-2	33.21	81.66	B		37.49
682	Savannah River KC-9	33.21	81.66	B		37.49
683	Savannah River KC-10	33.21	81.66	C		41.45
684	Savannah River KC-15	33.21	81.66	C		49.68
685	Savannah River KC-18	33.21	81.66	B		28.35
686	Savannah River KC-20	33.21	81.66	C		39.01
687	Savannah River KC-RT3	33.21	81.66	B		36.57
688	Savannah River KR-1	33.21	81.66	B		31.09
689	Savannah River KR-2A	33.21	81.66	C		27.13
690	Savannah River KR-3	33.21	81.66	C		29.87
691	Savannah River KR-5	33.21	81.67	B		17.37
692	Savannah River KR-6	33.21	81.67	B		38.71
693	Savannah River KR-9	33.21	81.66	C		38.71
694	Savannah River KR-12B	33.21	81.67	B		22.55
695	1901 Avenue of the Stars			C		3962.21
696	Mill Creek Summit Ranger Sta	34.39	118.08	C	--B	28.70
697	Compton 1st Ward LDS Church	33.90	118.20	C	--D	15.90

TABLE 1 (continued)
PROFILES USED IN THIS STUDY

Profile No.	Name	Lat. (N)	Long. (W)	USGS Site Class.	Geomatrix Site Class.	Profile Depth (m)
698	South Junior High School	33.92	118.74	C	--D	23.90
699	Long Beach 6th Ward LDS Church	33.88	118.18	C	--D	24.60
700	5/14 Intrchng-Gavin Canyon Rd			C		21.80
701	5/14 Intrchng-Boring 94B23R	34.33	118.50	B		10.40
702	5/14 Intrchng-Boring 94B21R	34.33	118.50	C		23.50
703	5/14 Intrchng-Boring 94B22R	34.33	118.50	B		54.90
704	5/14 Intrchng-Boring 94B30R	34.33	118.51	C		39.60
705	5/14 Intrchng-Boring 94B32R	34.33	118.51	C		27.40
706	5/14 Intrchng-Boring 94B33R	34.33	118.50	C		36.57
707	5/14 Intrchng-Boring 94B34R	34.33	118.51	C		36.57
708	Bayshore Viaduct-Hole P1	37.78	122.40	C		82.00
709	Bayshore Viaduct-Hole P2	37.77	122.41	C		75.00
710	Bayshore Viaduct-Hole P3	37.78	122.40	D		70.00
711	Bayshore Viaduct-Hole P4	37.78	122.40	C		30.00
712	Bayshore Viaduct-Hole 94B5R	37.77	122.41	C		67.00
713	Bayshore Viaduct-Hole 94B4R	37.77	122.40	C		54.00
714	Bayshore Viaduct-Hole 94B3R	37.77	122.40	B		24.00
715	Bayshore Viaduct-Hole 94B2R	37.77	122.40	C		37.60
716	Bayshore Viaduct-Hole 94B1R	37.77	122.40	C		26.00
717	HWY 210/I5, SW Conn O.C.	34.31	118.49	C		29.20
718	HWY 405/118 Intrchng	34.27	118.47	C		70.50
719	HWY 118 at Mission Gothic U.C.	34.27	118.49	C		58.00
720	HWY 118 at Bull Ck Cany O.C.	34.27	118.49	C		49.00
721	I10 at Fairfax/Washington U.C.	34.04	118.37	C		38.10
722	I10 at La Cienega/Venice O.C.	34.04	118.38	C		87.00
723	Bay Bridge Approach-Hole B28			D		148.74
724	Bay Bridge Approach-Hole B3			C		156.00
725	Bay Bridge Approach-Hole B20			D		56.00
726	Bay Bridge Approach-Hole B9			D		163.70
727	Bay Bridge Approach-Hole B30			D		57.00
728	Dumbarton Bridge-Hole 93B11R			D		160.00
729	Dumbarton Bridge, west end			D		228.60
730	Dumbarton Bridge, mid-crossing			C		219.40
732	Sav.River,A-Area,MMP-4-SB,intr	33.34	81.71	C		246.90
734	Sav.River,H-Area,MMP-2-SB,intr	33.28	81.64	C		304.80
736	Sav.River,K-Area,MMP-3-SB,intr	33.21	81.66	C		335.30
756	Yerba Buena,Boring B8,Pier E2			A		57.91
757	Treasure Island Borehole USN-1			D		121.91
758	Savannah River CPT-5 interp	33.28	81.60	C		59.43
759	Savannah River CPT-6B interp	33.28	81.60	C		44.50
760	Savannah River CPT-7 interp	33.28	81.60	C		60.96
761	Savannah River CPT-10 interp	33.28	81.60	C		40.84
762	Savannah River CPT-11 interp	33.28	81.60	C		60.96
763	Savannah River CPT-14 interp	33.28	81.60	C		48.77
764	Savannah River CPT-16 interp	33.28	81.60	C		32.92
765	Savannah River CPT-18 interp	33.28	81.60	B		52.42
766	Savannah River CPT-25 interp	33.28	81.60	C		46.94
767	Savannah River CPT-26 interp	33.28	81.60	C		52.42
769	Savannah River CPT-29 interp	33.28	81.60	C		60.96

TABLE 1 (continued)
PROFILES USED IN THIS STUDY

Profile No.	Name	Lat. (N)	Long. (W)	USGS Site Class.	Geomatrix Site Class.	Profile Depth (m)
770	Savannah River CPT-30 interp	33.28	81.60	C		62.18
771	Savannah River CPT-31 interp	33.28	81.60	C		40.23
772	Bessie Carmichael School	37.78	122.41	D		87.00
773	Embarcadero Plaza	37.80	122.39	D		80.00
774	Levi Plaza	37.80	122.40	C		42.00
775	Savannah River L13					56.69
776	Savannah River L201					47.85
777	Savannah River L202					51.05
778	Savannah River L203					38.71
779	Savannah River L204					51.20
780	Savannah River L205					51.81
781	Savannah River L206					48.16
782	Savannah River L8					46.33
783	Savannah River L10					37.03
784	Savannah River L11					40.23
785	Savannah River L12					33.53
786	Savannah River L6					44.19
787	Savannah River L7					55.47

TABLE 2

CLUSTER DATA

Savannah River CPT cluster (interpreted)

Profile No.	Profile Name	Latitude (N)	Longitude (W)
758	Savannah River CPT-5 interp	33.2799	81.6021
759	Savannah River CPT-6B interp	33.2803	81.6021
760	Savannah River CPT-7 interp	33.2801	81.6014
761	Savannah River CPT-10 interp	33.2800	81.6014
762	Savannah River CPT-11 interp	33.2802	81.6021
763	Savannah River CPT-14 interp	33.2795	81.6012
764	Savannah River CPT-16 interp	33.2792	81.6018
765	Savannah River CPT-18 interp	33.2795	81.6026
766	Savannah River CPT-25 interp	33.2813	81.6017
767	Savannah River CPT-26 interp	33.2801	81.6025
768	Savannah River CPT-28.2 interp	33.2801	81.6031
769	Savannah River CPT-29 interp	33.2804	81.6013
770	Savannah River CPT-30 interp	33.2805	81.6019
771	Savannah River CPT-31 interp	33.2796	81.6019

Savannah River K-area cluster (interpreted)

Profile No.	Profile Name	Latitude (N)	Longitude (W)
41	Savannah River KC-10	33.2112	81.6626
42	Savannah River KC-9	33.2119	81.6617
43	Savannah River KC-RT3	33.2130	81.6626
44	Savannah River KC-2	33.2133	81.6629
678	Savannah River K-1003	33.2132	81.6628
679	Savannah River K-1008	33.2108	81.6642
680	Savannah River K-1012	33.2118	81.6657
681	Savannah River KC-2	33.2133	81.6629
682	Savannah River KC-9	33.2119	81.6617
683	Savannah River KC-10	33.2112	81.6626
684	Savannah River KC-15	33.2125	81.6639
685	Savannah River KC-18	33.2133	81.6638
686	Savannah River KC-20	33.2112	81.6626
687	Savannah River KC-RT3	33.2130	81.6626
688	Savannah River KR-1	33.2104	81.6647
689	Savannah River KR-2A	33.2109	81.6642
690	Savannah River KR-3	33.2108	81.6640
691	Savannah River KR-5	33.2113	81.6657
692	Savannah River KR-6	33.2109	81.6660
693	Savannah River KR-9	33.2121	81.6645
694	Savannah River KR-12B	33.2118	81.6657
736	Sav.River,K-Area,MMP-3-SB,intr	33.2110	81.6574

TABLE 2 (continued)

CLUSTER DATA

Savannah River NPR cluster (interpreted)

Profile No.	Profile Name	Latitude (N)	Longitude (W)
310	Savannah River NPR M12A-17	33.2525	81.6378
311	Savannah River NPR M12A-18	33.2522	81.6369
312	Savannah River NPR M12A-19	33.2528	81.6372
313	Savannah River NPR M12A-20	33.2520	81.6375
314	Savannah River NPR M12A-21	33.2533	81.6374
315	Savannah River NPR M12A-22	33.2529	81.6365
316	Savannah River NPR M12A-25	33.2535	81.6367
317	Savannah River NPR M12A-26	33.2513	81.6379
318	Savannah River NPR M12A-27	33.2528	81.6387
319	Savannah River NPR M12A-28	33.2543	81.6364
320	Savannah River NPR M12A-29	33.2519	81.6361
321	Savannah River NPR M12A-30	33.2515	81.6351

5/14 Interchange cluster (interpreted)

Profile No.	Profile Name	Latitude (N)	Longitude (W)
700	5/14 Intrchng-Gavin Canyon Rd		
701	5/14 Intrchng-Boring 94B23R	34.3324	118.5043
702	5/14 Intrchng-Boring 94B21R	34.3333	118.5044
703	5/14 Intrchng-Boring 94B22R	34.3337	118.5047
704	5/14 Intrchng-Boring 94B30R	34.3349	118.5057
705	5/14 Intrchng-Boring 94B32R	34.3333	118.5056
706	5/14 Intrchng-Boring 94B33R	34.3341	118.5046
707	5/14 Intrchng-Boring 94B34R	34.3332	118.5067

Bayshore Viaduct cluster (interpreted)

Profile No.	Profile Name	Latitude (N)	Longitude (W)
708	Bayshore Viaduct-Hole P1	37.7764	122.4033
709	Bayshore Viaduct-Hole P2	37.7736	122.4061
710	Bayshore Viaduct-Hole P3	37.7778	122.4008
711	Bayshore Viaduct-Hole P4	37.7786	122.3997
712	Bayshore Viaduct-Hole 94B5R	37.7719	122.4050
713	Bayshore Viaduct-Hole 94B4R	37.7708	122.4044
714	Bayshore Viaduct-Hole 94B3R	37.7689	122.4039
715	Bayshore Viaduct-Hole 94B2R	37.7678	122.4039
716	Bayshore Viaduct-Hole 94B1R	37.7661	122.4036

TABLE 2 (continued)

CLUSTER DATA

HWY 118 cluster (interpreted)

Profile No.	Profile Name	Latitude (N)	Longitude (W)
717	HWY 210/I5, SW Conn O.C.	34.3083	118.4889
718	HWY 405/118 Intrchng	34.2667	118.4708
719	HWY 118 at Mission Gothic U.C.	34.2722	118.4889
720	HWY 118 at Bull Ck Cany O.C.	34.2697	118.4861

I10 cluster (interpreted)

Profile No.	Profile Name	Latitude (N)	Longitude (W)
721	I10 at Fairfax/Washington U.C.	34.0350	118.3681
722	I10 at La Cienega/Venice O.C.	34.0367	118.3769

Bay Bridge cluster (interpreted)

Profile No.	Profile Name	Latitude (N)	Longitude (W)
723	Bay Bridge Approach-Hole B28		
724	Bay Bridge Approach-Hole B3		
725	Bay Bridge Approach-Hole B20		
726	Bay Bridge Approach-Hole B9		
727	Bay Bridge Approach-Hole B30		

Dumbarton Bridge cluster (interpreted)

Profile No.	Profile Name	Latitude (N)	Longitude (W)
728	Dumbarton Bridge-Hole 93B11R		
729	Dumbarton Bridge, west end		
730	Dumbarton Bridge, mid-crossing		

Gilroy 2 cluster (interpreted)

Profile No.	Profile Name	Latitude (N)	Longitude (W)
2	Gilroy 2 -Misn. Trails Motel	36.9820	121.5560
187	Gilroy 2 EPRI hole-USGS	36.9820	121.5560
188	Gilroy 2 EPRI hole-USGS	36.9820	121.5560
189	Gilroy 2 USGS hole	36.9820	121.5560
269	Gilroy 2 EPRI hole-Agb interp	36.9820	121.5560
271	Gilroy 2 EPRI hole-USGS	36.9820	121.5560
289	Gilroy 2 EPRI hole-Redp interp	36.9820	121.5560
448	Gilroy 2 -Misn. Trails Motel	36.9820	121.5560

TABLE 2 (continued)

CLUSTER DATA

Treasure Island cluster (interpreted)

Profile No.	Profile Name	Latitude (N)	Longitude (W)
192	Treasure Island	37.8250	122.3730
349	Treasure Isl.-EPRI Hole Redpa	37.8250	122.3730
350	Treasure Isl.-EPRI Hole U.NH	37.8250	122.3730
351	Treasure Isl.-EPRI Hole USGS	37.8250	122.3730
353	Treasure Isl.-EPRI Hole U.MI	37.8250	122.3730

TABLE 3

GEOMATRIX SITE CATEGORIES

Third Letter*	
Designation	**Description**
A	Rock. Instrument is founded on rock material (Vs > 600 m/s) or a very thin veneer (less than 5m) of soil overlying rock material.
B	Shallow (Stiff) Soil. Instrument is founded in/on a soil profile up to 20m thick overlying rock material, typically in a narrow canyon, near a valley edge, or on a hillside.
C	Deep Narrow Soil. Instrument is founded in/on a soil profile at least 20m thick overlying rock material in a narrow canyon or valley no more than several kilometers wide.
D	Deep Broad Soil. Instrument is founded in/on a soil profile at least 20m thick overlaying rock material in a broad canyon or valley.
E	Soft Deep Soil. Instrument is founded in/on a deep soil profile that exhibits low average shear wave velocity (Vs < 150 m/s).

* The first two letters in the Geomatrix site characterization are not used in this study.

TABLE 4

USGS SITE CATEGORIES

Designation	Average Shear-Wave Velocity (30 m)*
A	greater than 750 m/s
B	360 to 750 m/s
C	180 to 360 m/s
D	less than 180 m/s

* This is actually the geometric or time-weighted average velocity; i.e., 30 m divided by the travel time through the top 30 m of the profile.

TABLE 5

CALCULATED PARAMETER VALUES: GENERIC MODEL

	Category							
Parameter	Geomatrix A+B	Geomatrix C+D	USGS A+B	USGS C+D	USGS A	USGS B	USGS C	USGS D
sigma	0.46	0.38	0.35	0.36	0.36	0.27	0.31	0.37
rho0	0.96	0.99	0.95	0.99	0.95	0.97	0.99	0.00
Delta	13.1	8.0	4.2	3.9	3.4	3.8	3.9	5.0
rho200	0.96	1.00	1.00	1.00	0.42	1.00	0.98	0.50
h0	0.0	0.0	0.0	0.0	0.0	0.0	0.0	0.0
b	0.095	0.160	0.138	0.293	0.063	0.293	0.344	0.744
No. Profiles	45	109	204	253	35	169	226	27
No. Layers	243	692	280	1487	129	750	1349	136

TABLE 6

CALCULATED MEDIAN VELOCITIES: GENERIC MODEL

Depth (m)	Category							
	Geomatrix A+B	Geomatrix C+D	USGS A+B	USGS C+D	USGS A	USGS B	USGS C	USGS D
0.00	192	144	182	147	314	159	145	176
1.00	209	159	221	164	346	200	163	165
2.00	230	178	262	178	384	241	179	154
3.00	253	193	297	188	430	275	191	142
4.00	278	204	330	193	485	308	200	129
5.00	303	211	362	196	550	337	208	117
6.00	329	217	390	200	624	361	215	109
7.20	357	228	412	209	703	382	226	106
8.64	395	240	437	218	789	404	237	109
10.37	443	253	468	228	880	433	250	117
12.44	502	270	504	248	973	467	269	130
14.93	575	291	540	273	1070	501	291	148
17.92	657	319	578	296	1160	535	314	170
21.50	748	357	615	317	1260	567	336	192
25.80	825	402	653	347	1330	605	372	210
30.96	886	444	702	374	1380	654	391	229
37.15	942	474	734	386	1420	687	401	246
44.58	998	495	759	394	1460	711	408	266
53.50	1060	516	782	403	1500	732	413	289
64.20		541	805	427		749	433	318
77.04		566	834	459		772	459	353
92.44		593	870	488		802	486	392
110.93			922	515		847	513	435
133.12			983	550		900	550	
159.74				604			604	
191.69				682			676	
230.03				770			756	

Table 7

Summary of Cluster Variances

Cluster	USGS Site Cat.	No. Prof's	Min. Dist. (m)	Max. Dist. (m)	Depth Range (m)	Cluster Variance	Generic Variance	Cluster Correl.
SR "CPT"	C, B	14	11	218	0-50	0.015	0.094	0.84
					50+	0.052	0.094	0.45
SR K site	B, C	18	2	795	0-30	0.037	0.094	0.60
SR NPR	B	12	59	363	0-74	0.025	0.072	0.65
5-14 Interchange	B	7	46	307	0-18	0.121	0.072	--
Bayshore Viaduct	C	9	124	1444	0-74	0.292	0.094	--
Hy. 118	C	4	379	4945	0-67	0.060	0.094	0.36
Bay Bridge	D, C	5	-	-	0-20	0.366	0.154	--
					20+	0.029	0.154	0.81
Dumbarton Br.	D, C	3	-	-	0-20	0.431	0.092	--
					20+	0.029	0.154	0.82

FIGURE CAPTIONS

Figure 1. Geomatrix category A+B profiles used in this study.

Figure 2. Geomatrix category C+D profiles used in this study.

Figure 3. USGS category A+B profiles used in this study.

Figure 4. USGS category C+D profiles used in this study.

Figure 5. Median±σ of ln-velocity: Geomatrix category A+B profiles.

Figure 6. Median±σ of ln-velocity: Geomatrix category C+D profiles.

Figure 7. Median±σ of ln-velocity: USGS category A+B profiles.

Figure 8. Median±σ of ln-velocity: USGS category C+D profiles.

Figure 9. Standard deviation (σ) of ln-velocity and its $\pm 1\sigma_\sigma$ statistical uncertainty: Geomatrix category A+B profiles.

Figure 10. Standard deviation (σ) of ln-velocity and its $\pm 1\sigma_\sigma$ statistical uncertainty: Geomatrix category C+D profiles.

Figure 11. Standard deviation (σ) of ln-velocity and its $\pm 1\sigma_\sigma$ statistical uncertainty: USGS category A+B profiles.

Figure 12. Standard deviation (σ) of ln-velocity and its $\pm 1\sigma_\sigma$ statistical uncertainty: USGS category C+D profiles.

Figure 13. Sample Geomatrix category C+D profiles.

Figure 14. Elements of the probabilistic model of soil-velocity profiles.

Figure 15. Probabilistic layering model: Transition rate $\lambda(h)$ as a function of depth.

Figure 16. Model results for Geomatrix category A+B. Solid: median velocity; dots: statistical uncertainty in the median; dashes: median±σ.

Figure 17. Model results for Geomatrix category C+D. Solid: median velocity; dots: statistical uncertainty in the median; dashes: median±σ.

Figure 18. Model results for USGS category A+B. Solid: median velocity; dots: statistical uncertainty in the median; dashes: median±σ.

Figure 19. Model results for USGS category C+D. Solid: median velocity; dots: statistical uncertainty in the median; dashes: median±σ.

Figure 20. Model results for USGS category A. Solid: median velocity; dots: statistical uncertainty in the median; dashes: median±σ.

Figure 21. Model results for USGS category B. Solid: median velocity; dots: statistical uncertainty in the median; dashes: median±σ.

Figure 22. Model results for USGS category C. Solid: median velocity; dots: statistical uncertainty in the median; dashes: median±σ.

Figure 23. Model results for USGS category D. Solid: median velocity; dots: statistical uncertainty in the median; dashes: median±σ.

Figure 24. Model results for Geomatrix category A+B. Solid: depth-dependent correlation coefficient $\rho_d(h)$; dashes: thickness-dependent correlation coefficient $\rho_t(t)$. corresponding to the mean layer thickness $\lambda^{-1}(h)$.

Figure 25. Model results for Geomatrix category C+D. Solid: depth-dependent correlation coefficient $\rho_d(h)$; dashes: thickness-dependent correlation coefficient $\rho_t(t)$. corresponding to the mean layer thickness $\lambda^{-1}(h)$.

Figure 26. Model results for USGS category A+B. Solid: depth-dependent correlation coefficient $\rho_d(h)$; dashes: thickness-dependent correlation coefficient $\rho_t(t)$. corresponding to the mean layer thickness $\lambda^{-1}(h)$.

Figure 27. Model results for USGS category C+D. Solid: depth-dependent correlation coefficient $\rho_d(h)$; dashes: thickness-dependent correlation coefficient $\rho_t(t)$. corresponding to the mean layer thickness $\lambda^{-1}(h)$.

Figure 28. Model results for USGS category A. Solid: depth-dependent correlation coefficient $\rho_d(h)$; dashes: thickness-dependent correlation coefficient $\rho_t(t)$. corresponding to the mean layer thickness $\lambda^{-1}(h)$.

Figure 29. Model results for USGS category B. Solid: depth-dependent correlation coefficient $\rho_d(h)$; dashes: thickness-dependent correlation coefficient $\rho_t(t)$. corresponding to the mean layer thickness $\lambda^{-1}(h)$.

Figure 30. Model results for USGS category C. Solid: depth-dependent correlation coefficient $\rho_d(h)$; dashes: thickness-dependent correlation coefficient $\rho_t(t)$. corresponding to the mean layer thickness $\lambda^{-1}(h)$.

Figure 31. Model results for USGS category D. Solid: depth-dependent correlation coefficient $\rho_d(h)$; dashes: thickness-dependent correlation coefficient $\rho_t(t)$. corresponding to the mean layer thickness $\lambda^{-1}(h)$.

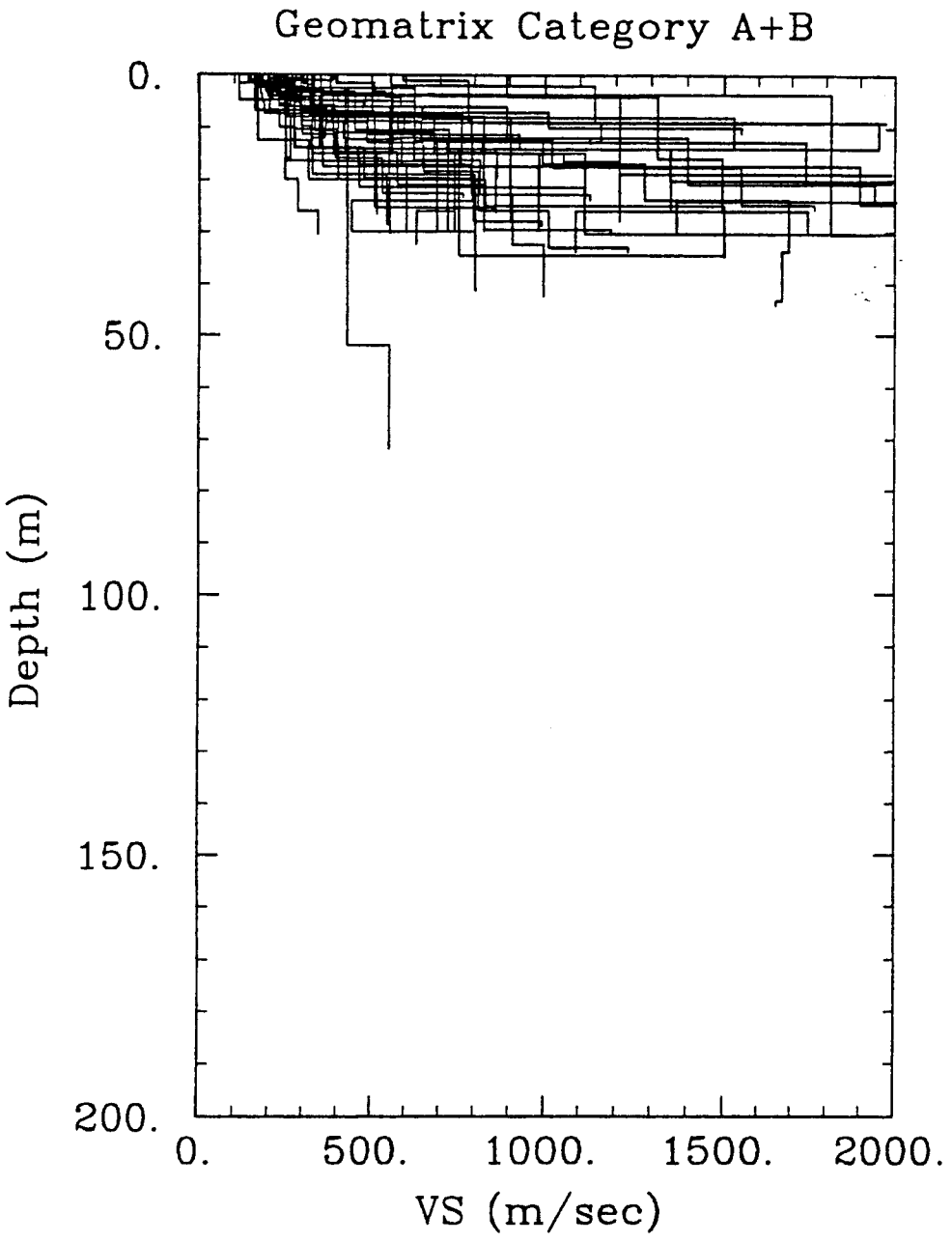
Geomatrix Category A+B
0.
50.
100.
150.
200.
Depth (m)
0.
500.
1000.
1500.
2000.
VS (m/sec)

FIGURE 1

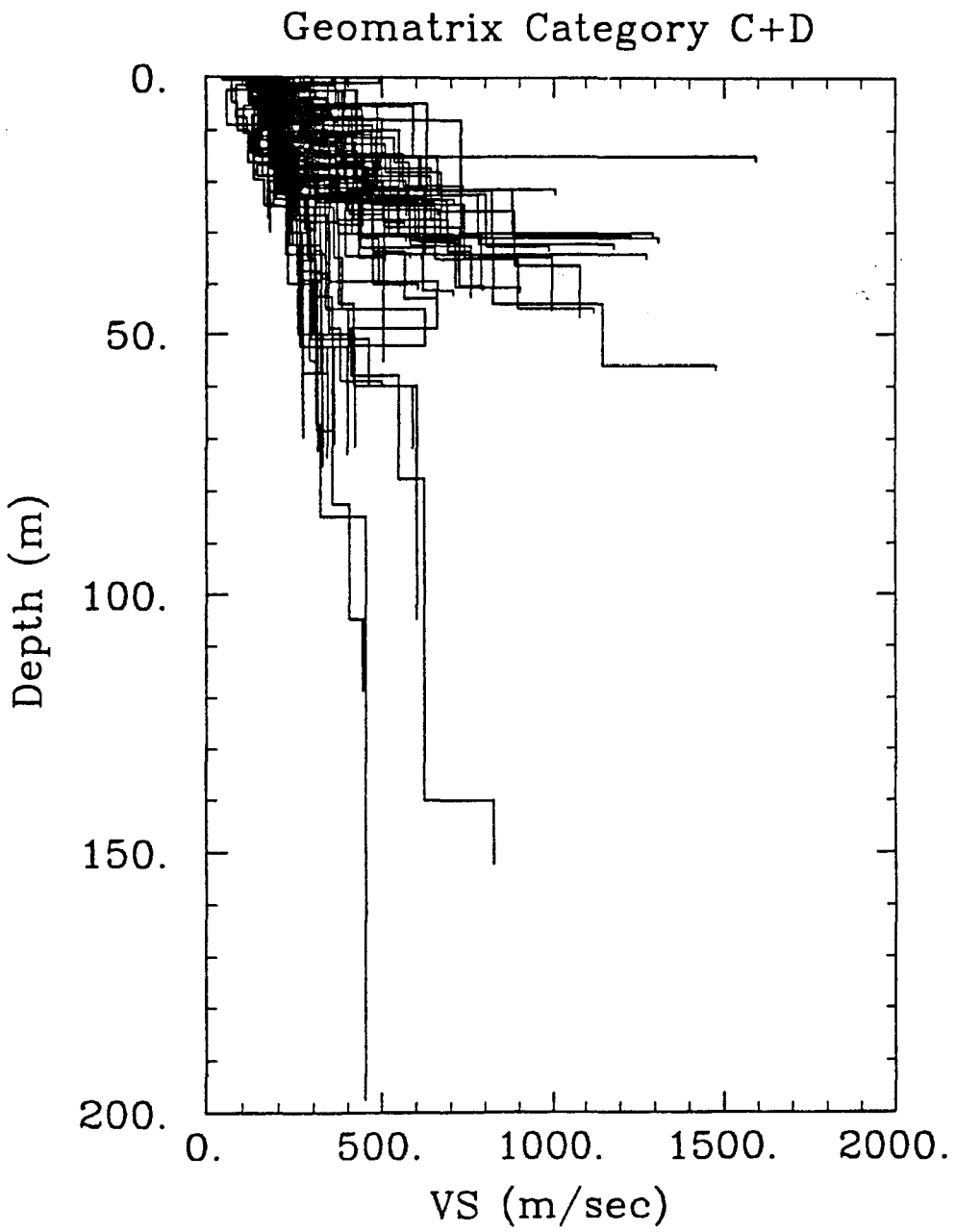
Geomatrix Category C+D
0.
50.
100.
150.
200.
Depth (m)
0.
500.
1000.
1500.
2000.
VS (m/sec)

FIGURE 2.

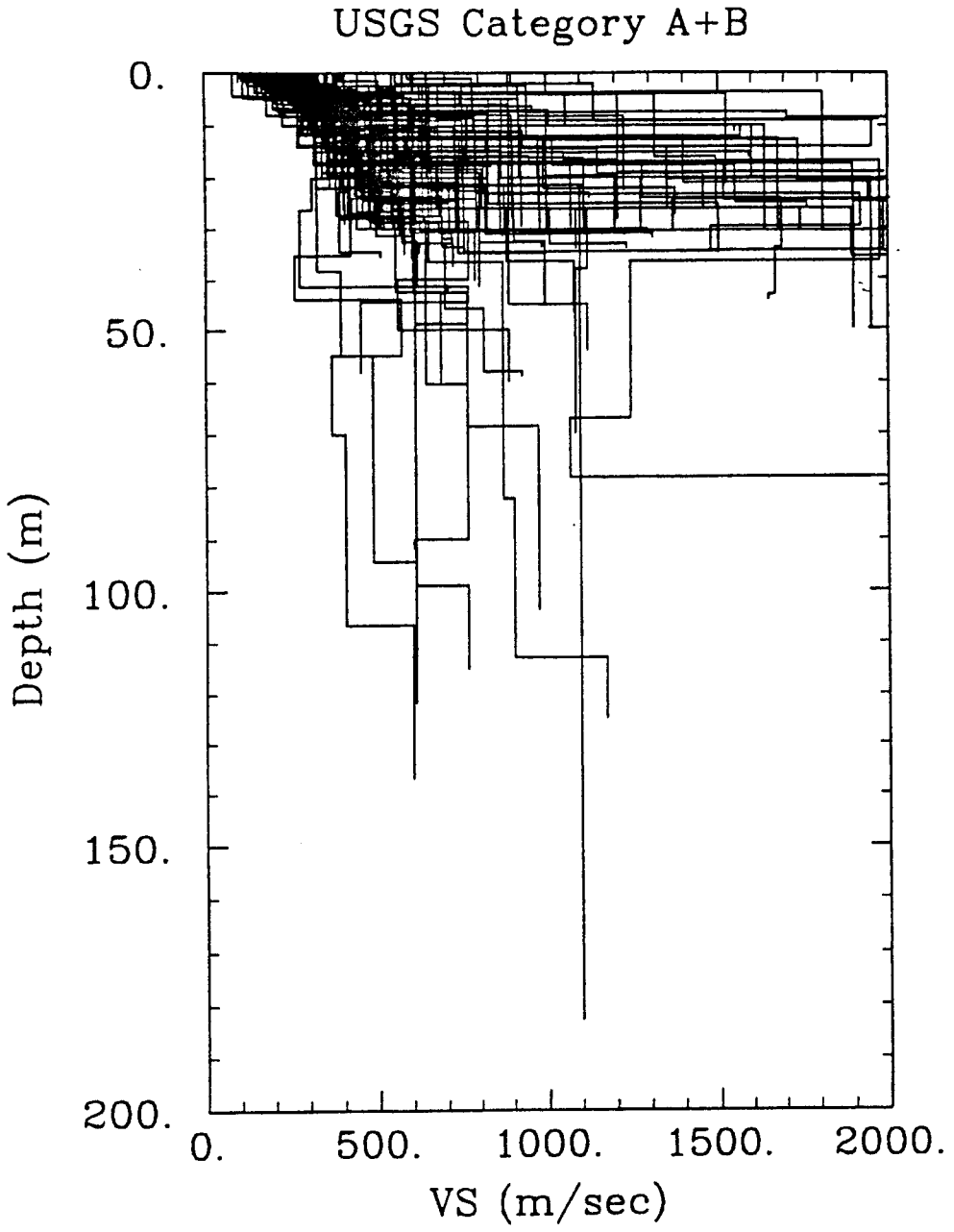
USGS Category A+B
0.
50.
100.
150.
200.
Depth (m)
0.
500.
1000.
1500.
2000.
VS (m/sec)

FIGURE 3.

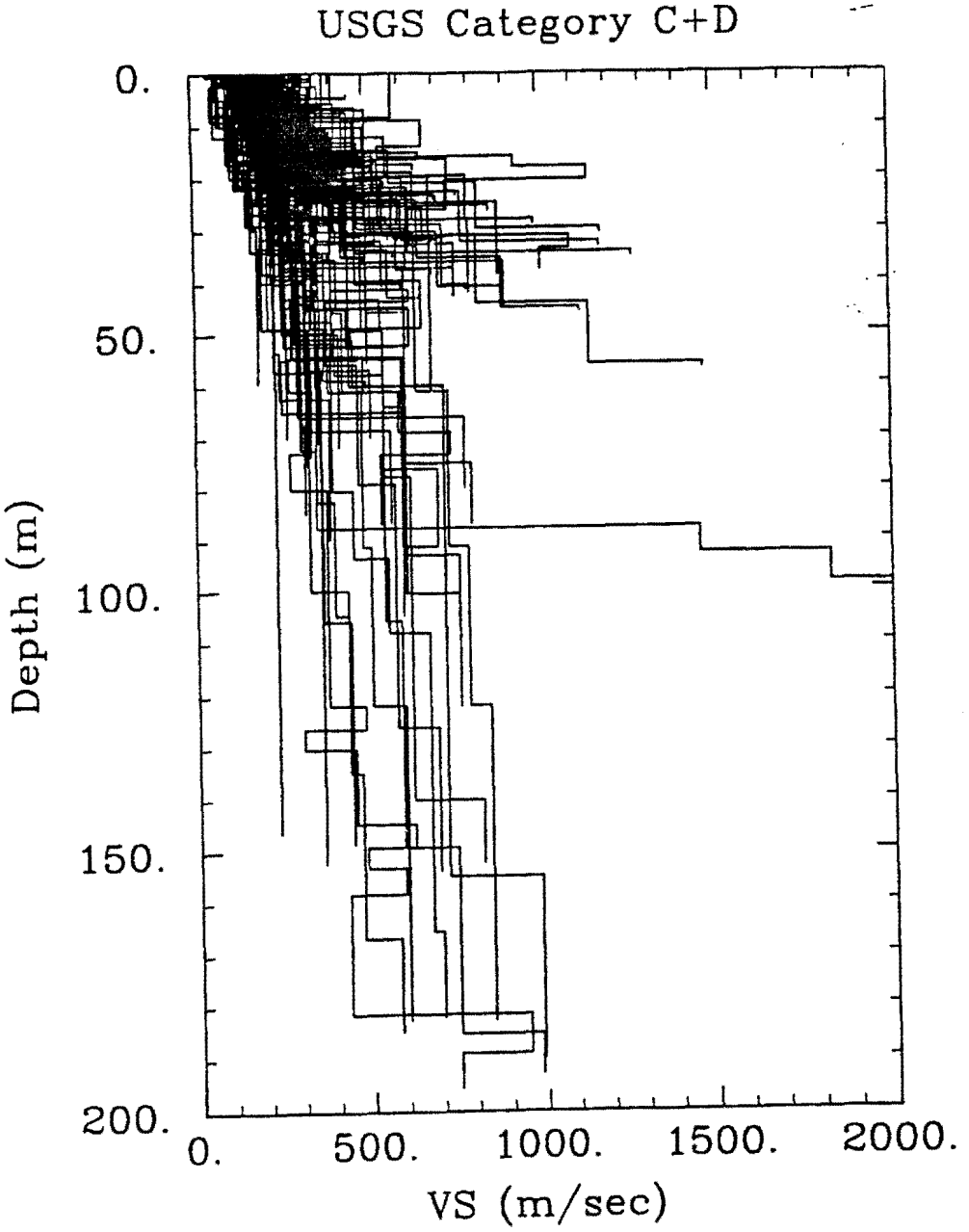
USGS Category C+D
Depth (m)
0.
50.
100.
150.
200.
0.
500.
1000.
1500.
2000.
VS (m/sec)

FIGURE 4.

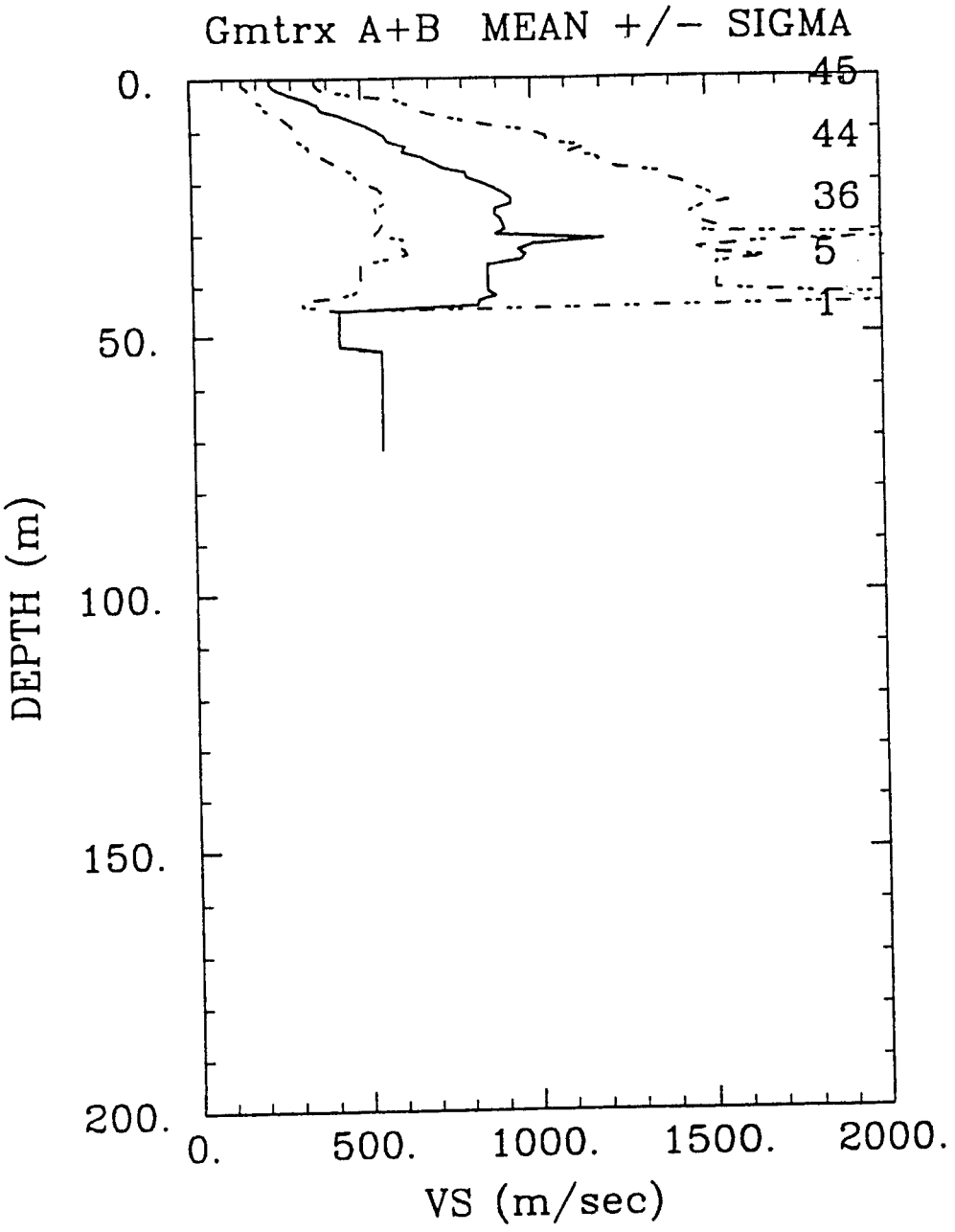
Gmtrx A+B MEAN +/- SIGMA
45
44
36
5
1
0.
50.
100.
150.
200.
DEPTH (m)
0.
500.
1000.
1500.
2000.
VS (m/sec)

FIGURE 5.

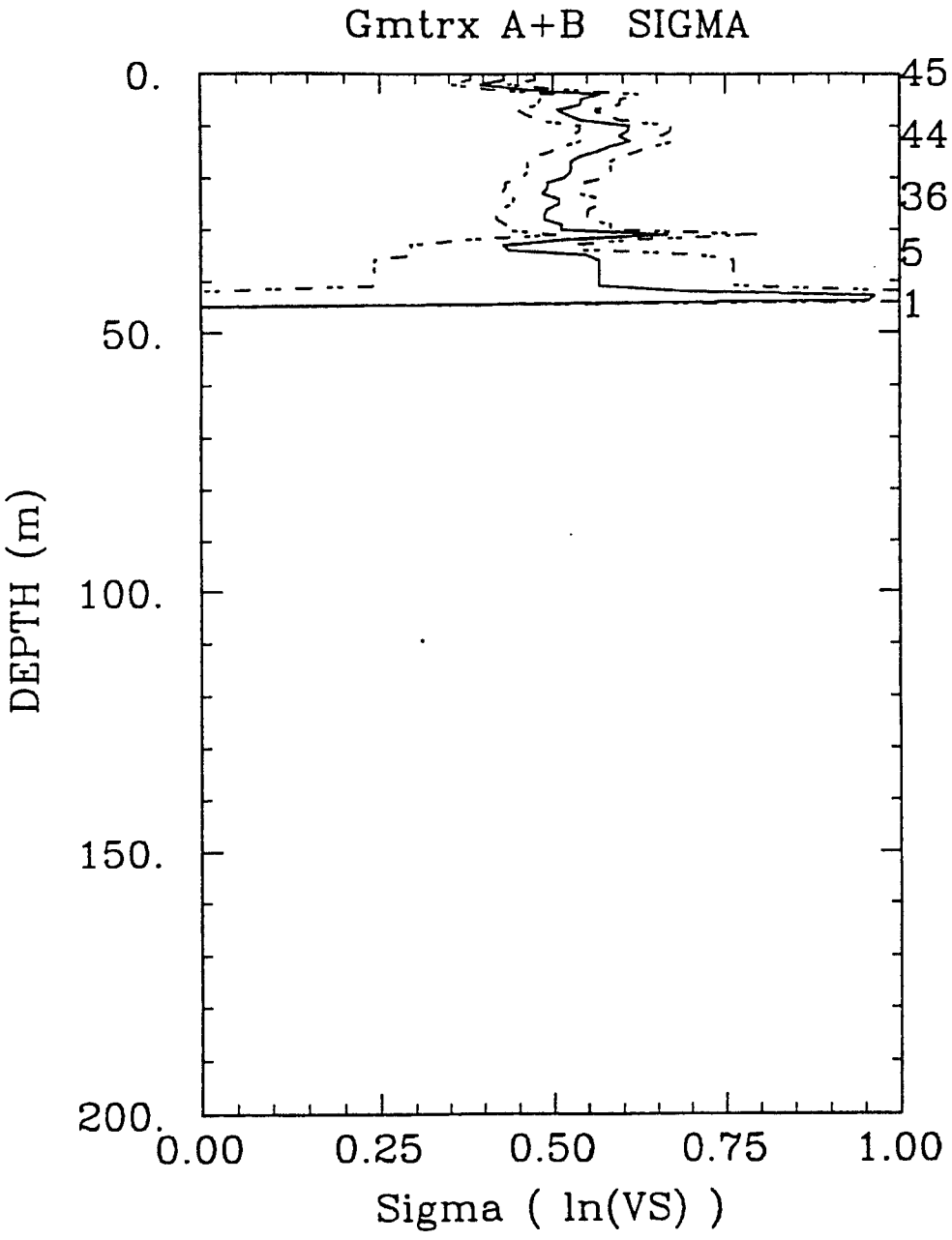
Gmtrx A+B SIGMA
0.
50.
100.
150.
200.
DEPTH (m)
45
44
36
5
1
0.00
0.25
0.50
0.75
1.00
Sigma (ln(VS))

FIGURE 6.

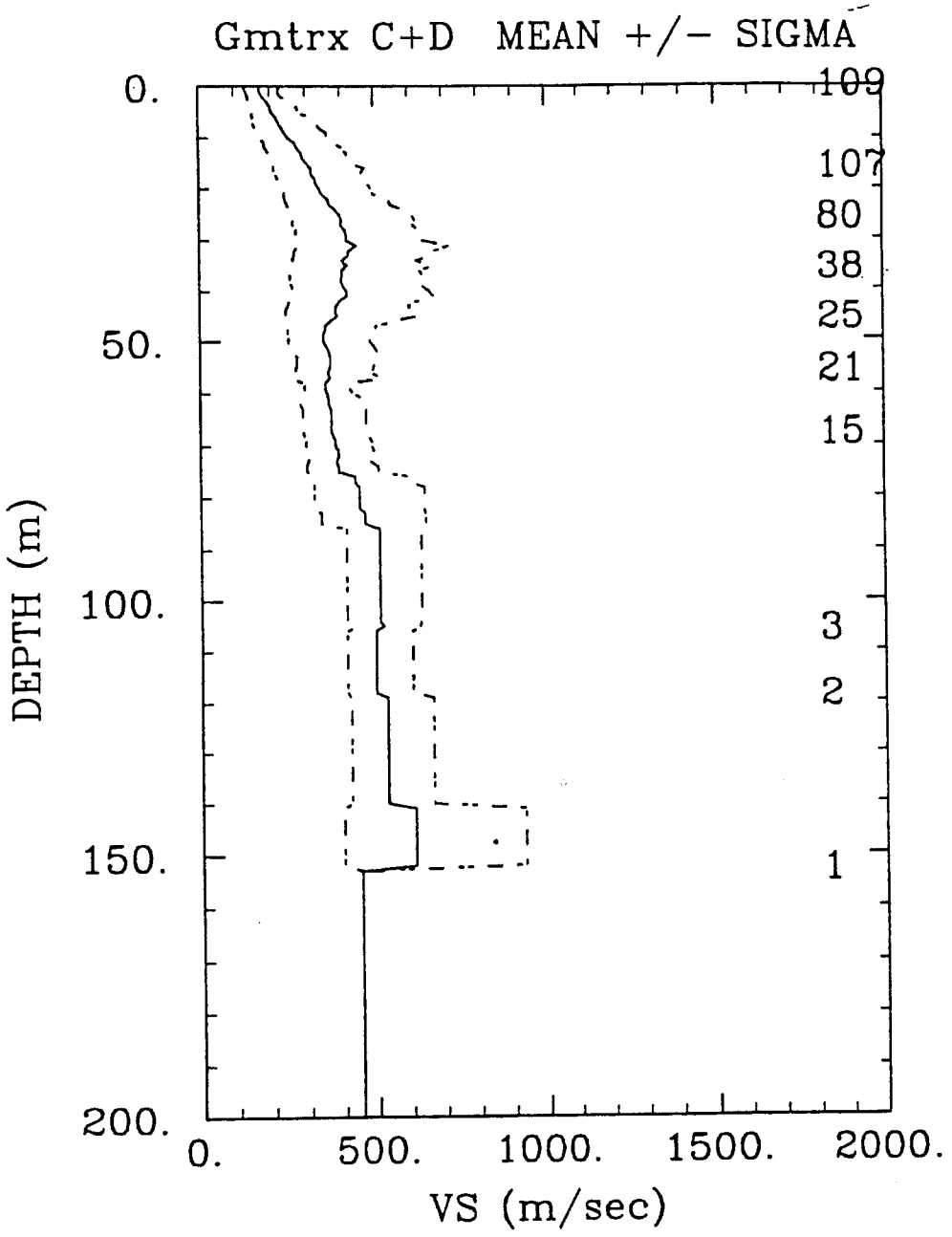
Gmtrx C+D MEAN +/- SIGMA
0.
50.
100.
150.
200.
DEPTH (m)
109
107
80
38
25
21
15
3
2
1
0.
500.
1000.
1500.
2000.
VS (m/sec)

FIGURE 7.

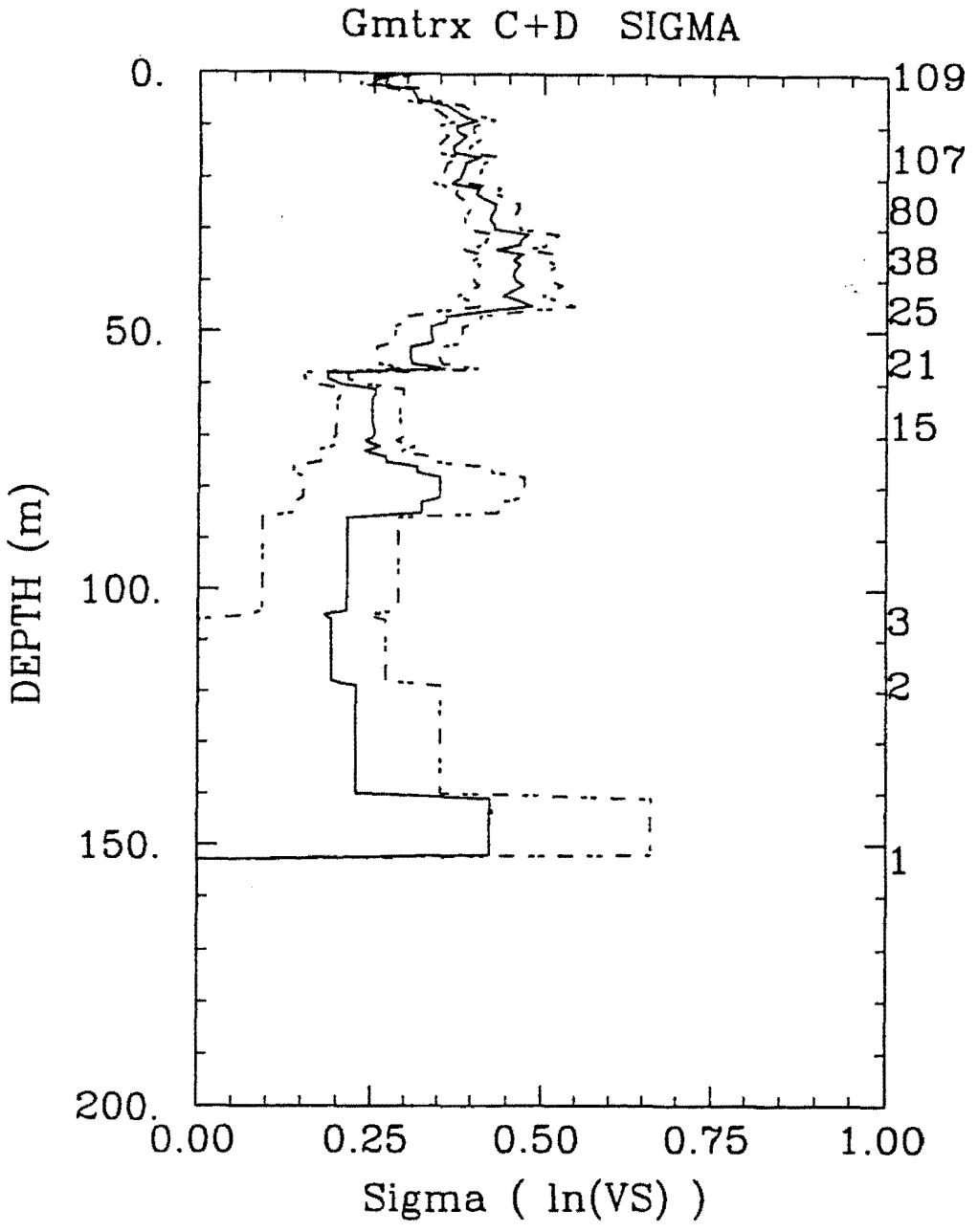
Gmtrx C+D SIGMA
0.
50.
100.
150.
200.
DEPTH (m)
109
107
80
38
25
21
15
3
2
1
0.00
0.25
0.50
0.75
1.00
Sigma (ln(VS))

Figure 8.

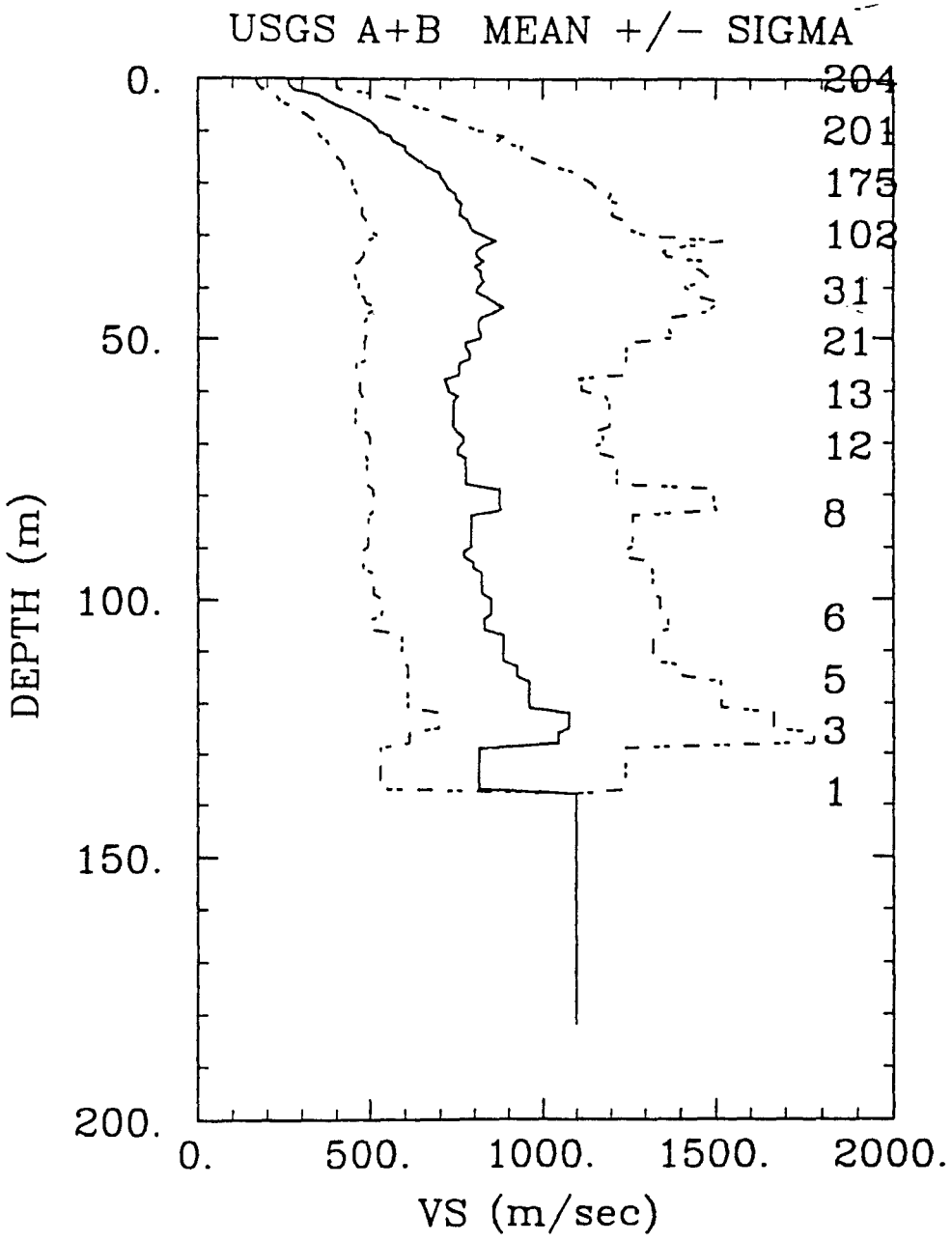
USGS A+B MEAN +/- SIGMA
DEPTH (m)
0.
50.
100.
150.
200.
204
201
175
102
31
21
13
12
8
6
5
3
1
0.
500.
1000.
1500.
2000.
VS (m/sec)

FIGURE 9.

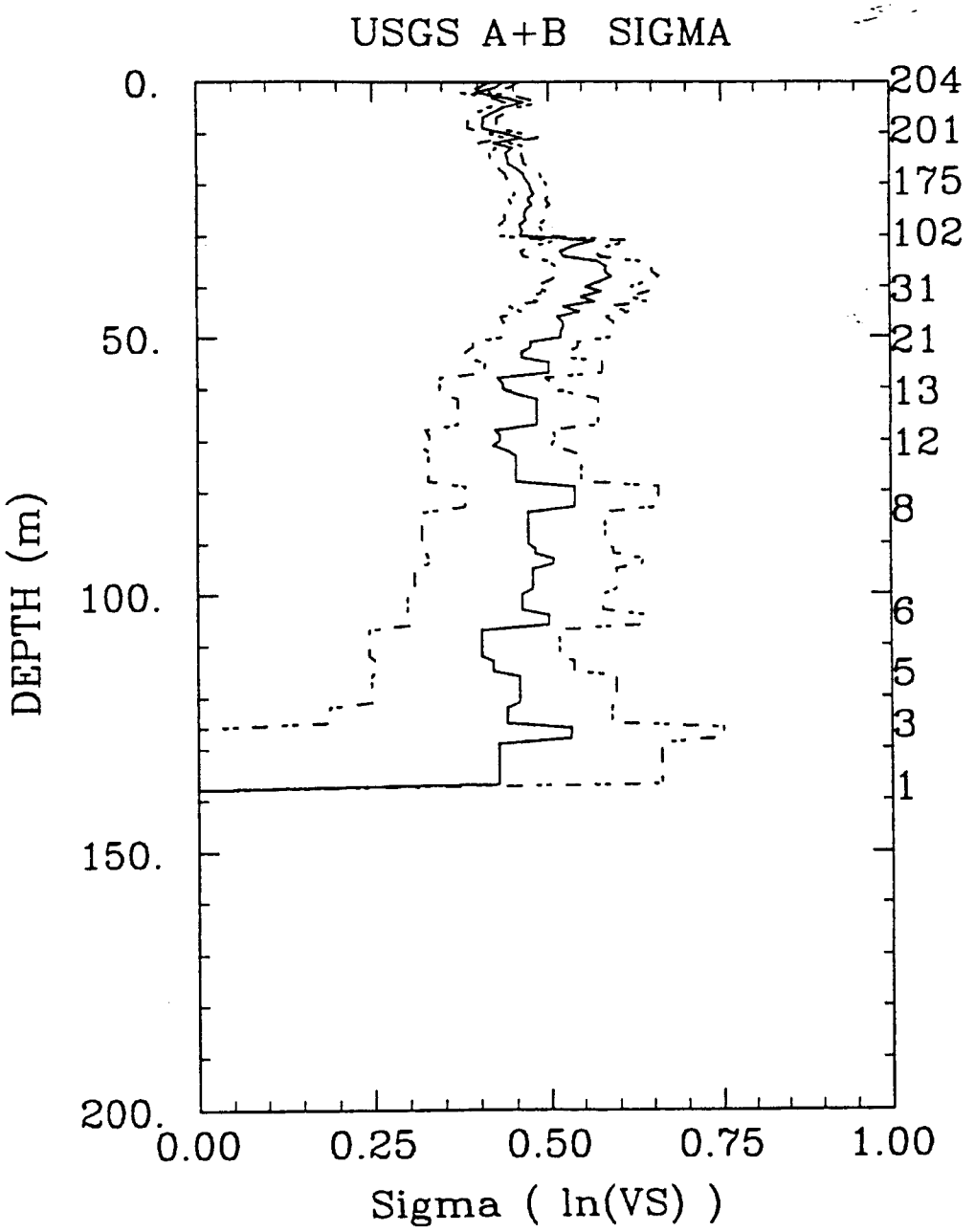
USGS A+B SIGMA
0.
50.
100.
150.
200.
DEPTH (m)
204
201
175
102
31
21
13
12
8
6
5
3
1
0.00
0.25
0.50
0.75
1.00
Sigma (ln(VS))

FIGURE 10.

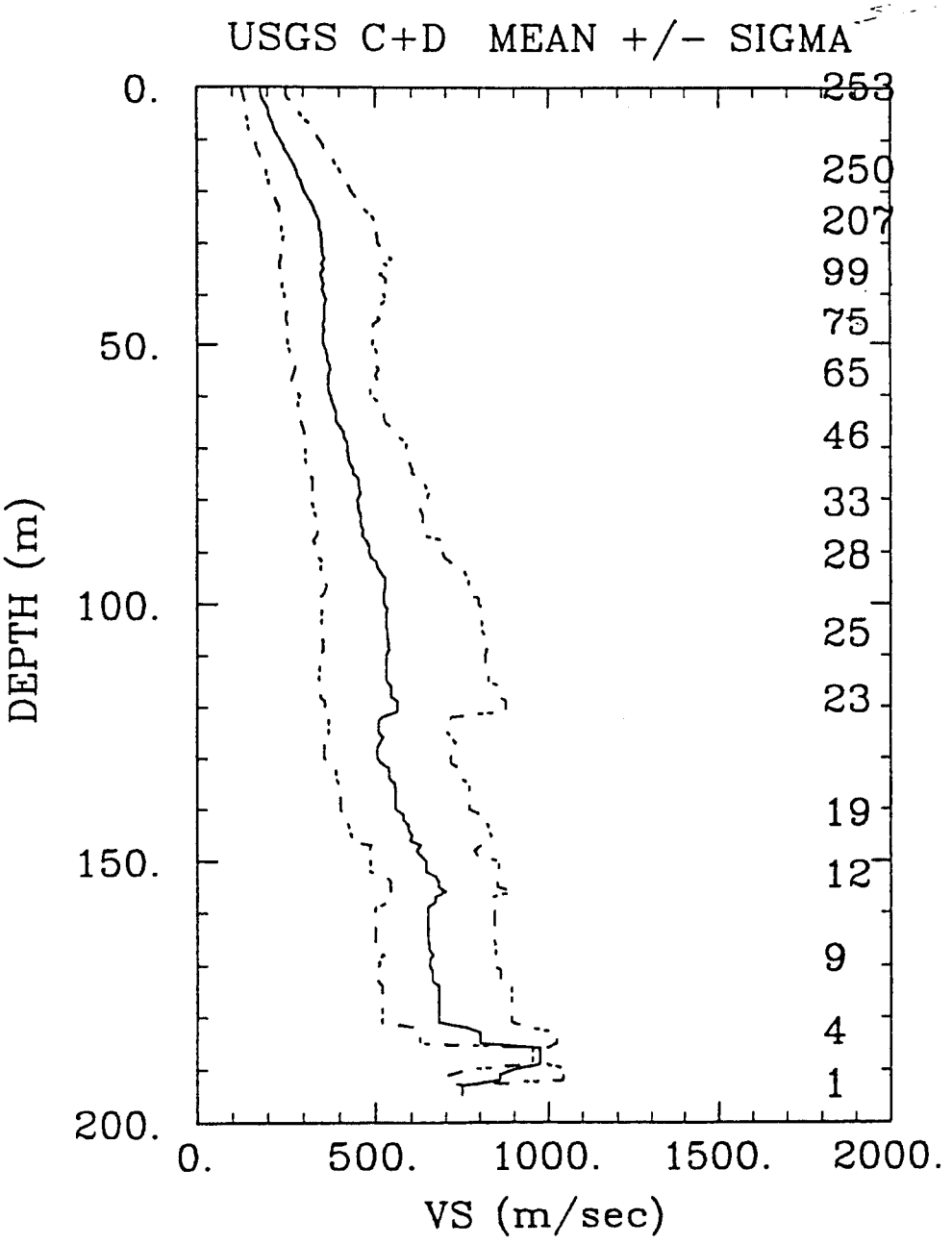
USGS C+D MEAN +/- SIGMA
DEPTH (m)
0.
50.
100.
150.
200.
253
250
207
99
75
65
46
33
28
25
23
19
12
9
4
1
0.
500.
1000.
1500.
2000.
VS (m/sec)

FIGURE 11.

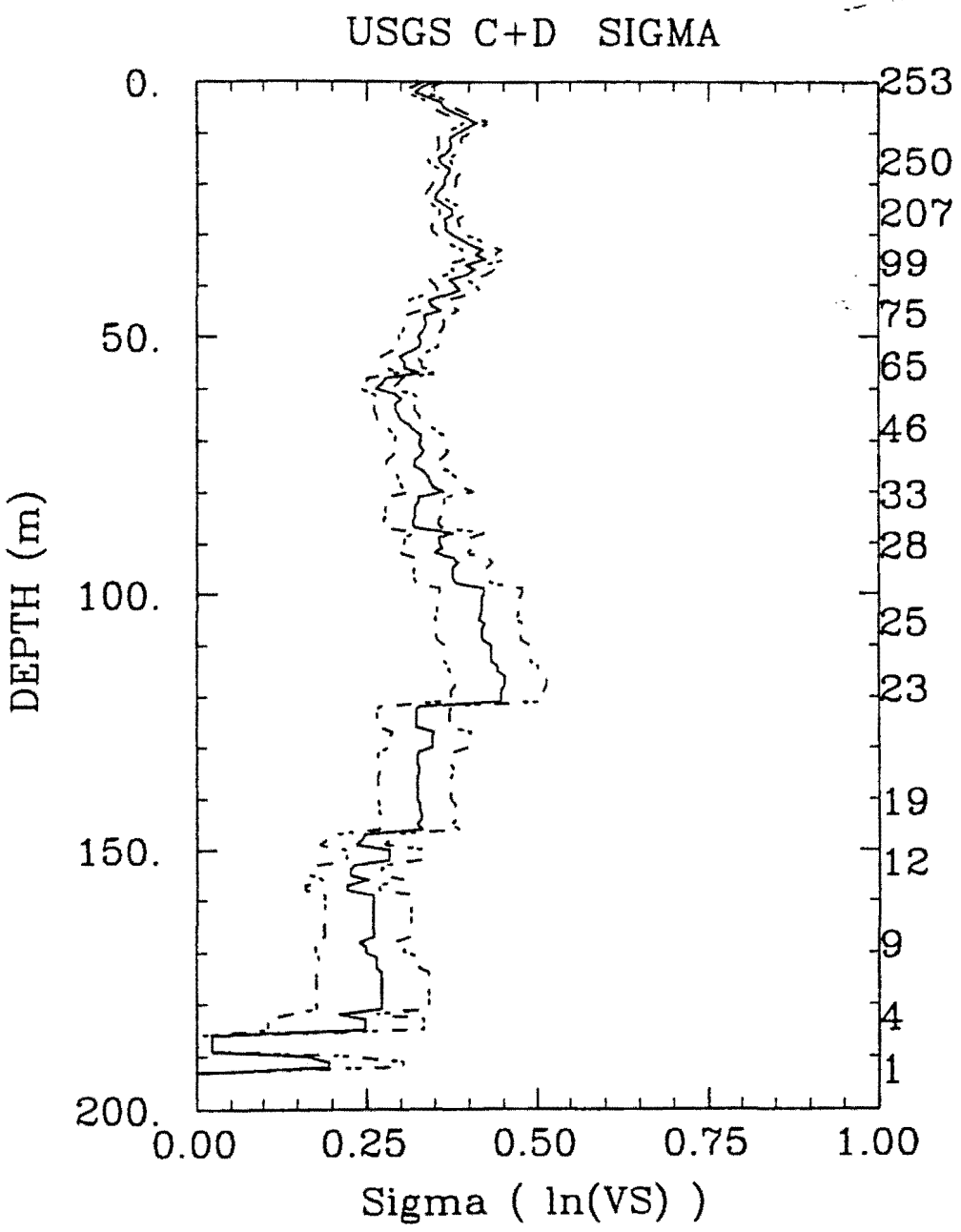
USGS C+D SIGMA
DEPTH (m)
0.
50.
100.
150.
200.
0.00
0.25
0.50
0.75
1.00
Sigma (ln(VS))
253
250
207
99
75
65
46
33
28
25
23
19
12
9
4
1

FIGURE 12.

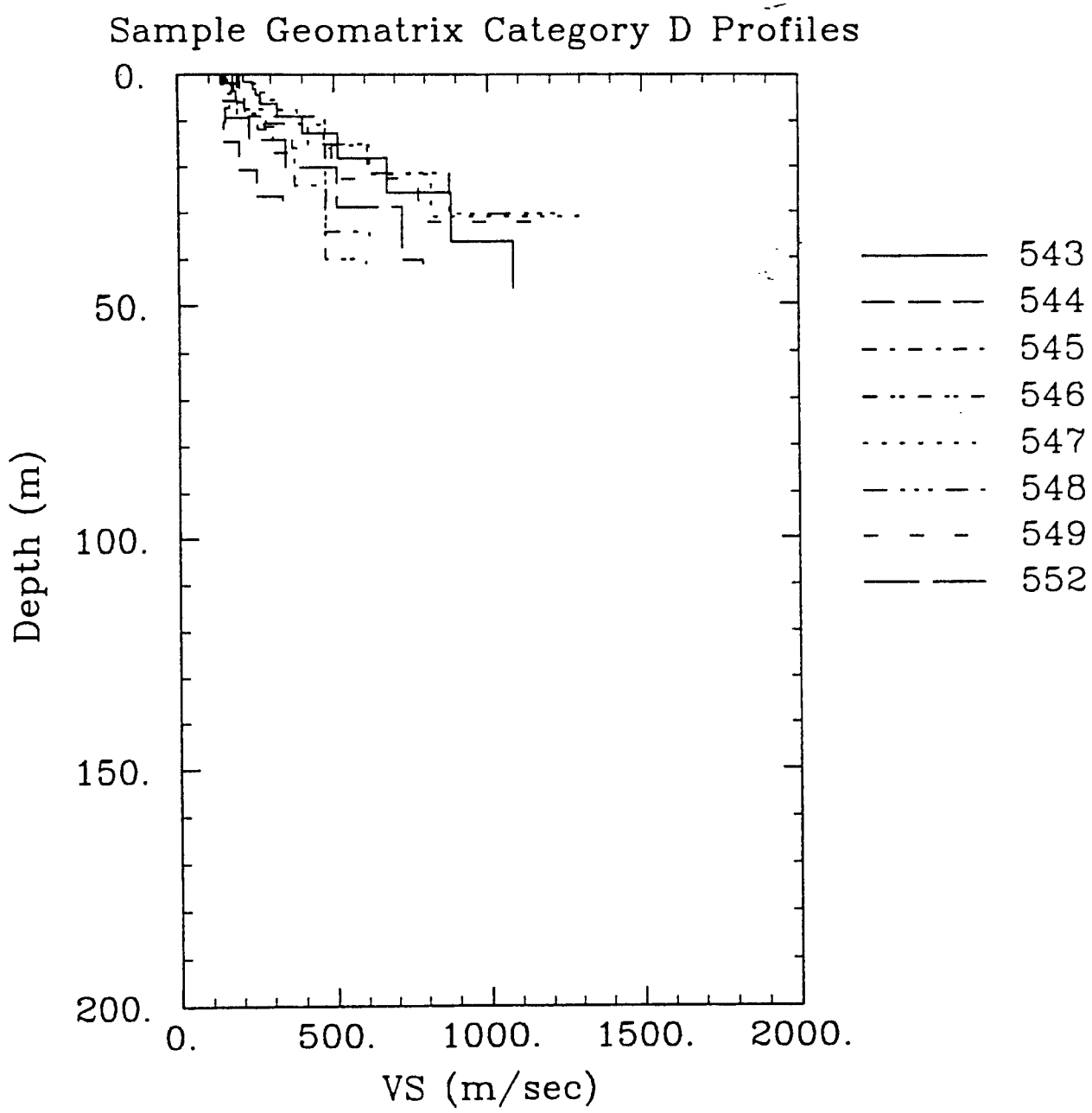
Sample Geomatrix Category D Profiles
0.
50.
100.
150.
200.
Depth (m)
0.
500.
1000.
1500.
2000.
VS (m/sec)
543
544
545
546
547
548
549
552

FIGURE 13.

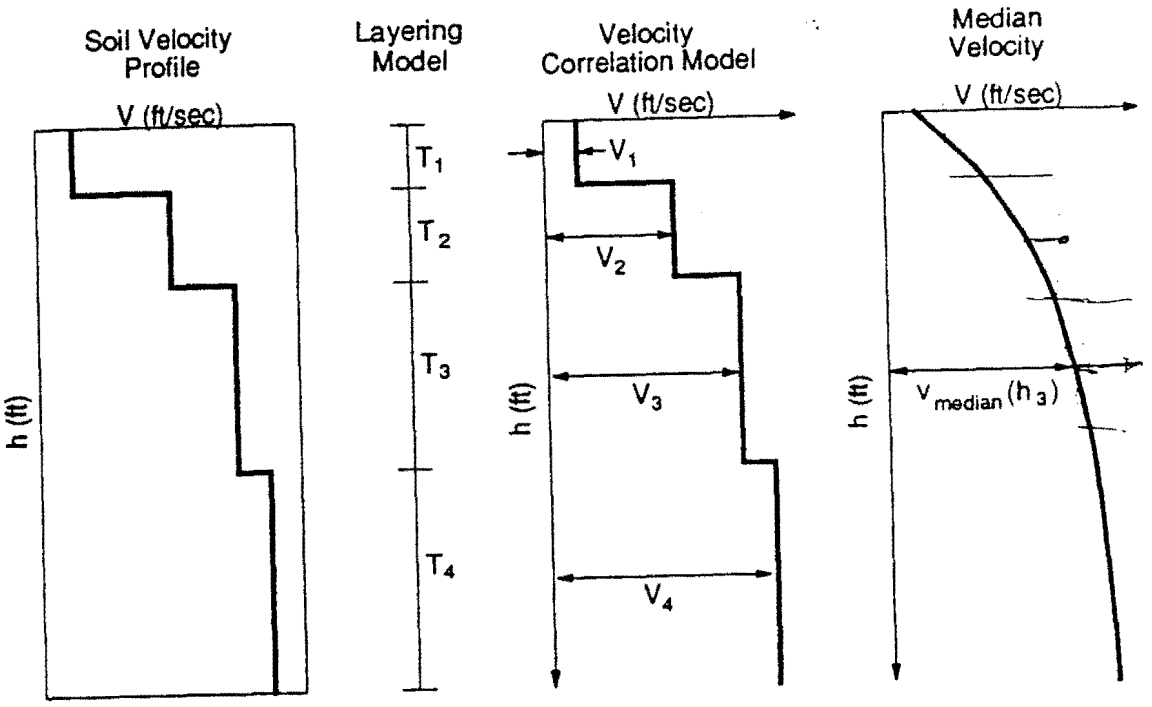

14

Figure 1. Elements of the probabilistic model for soil velocity profiles.

FIGURE 14.

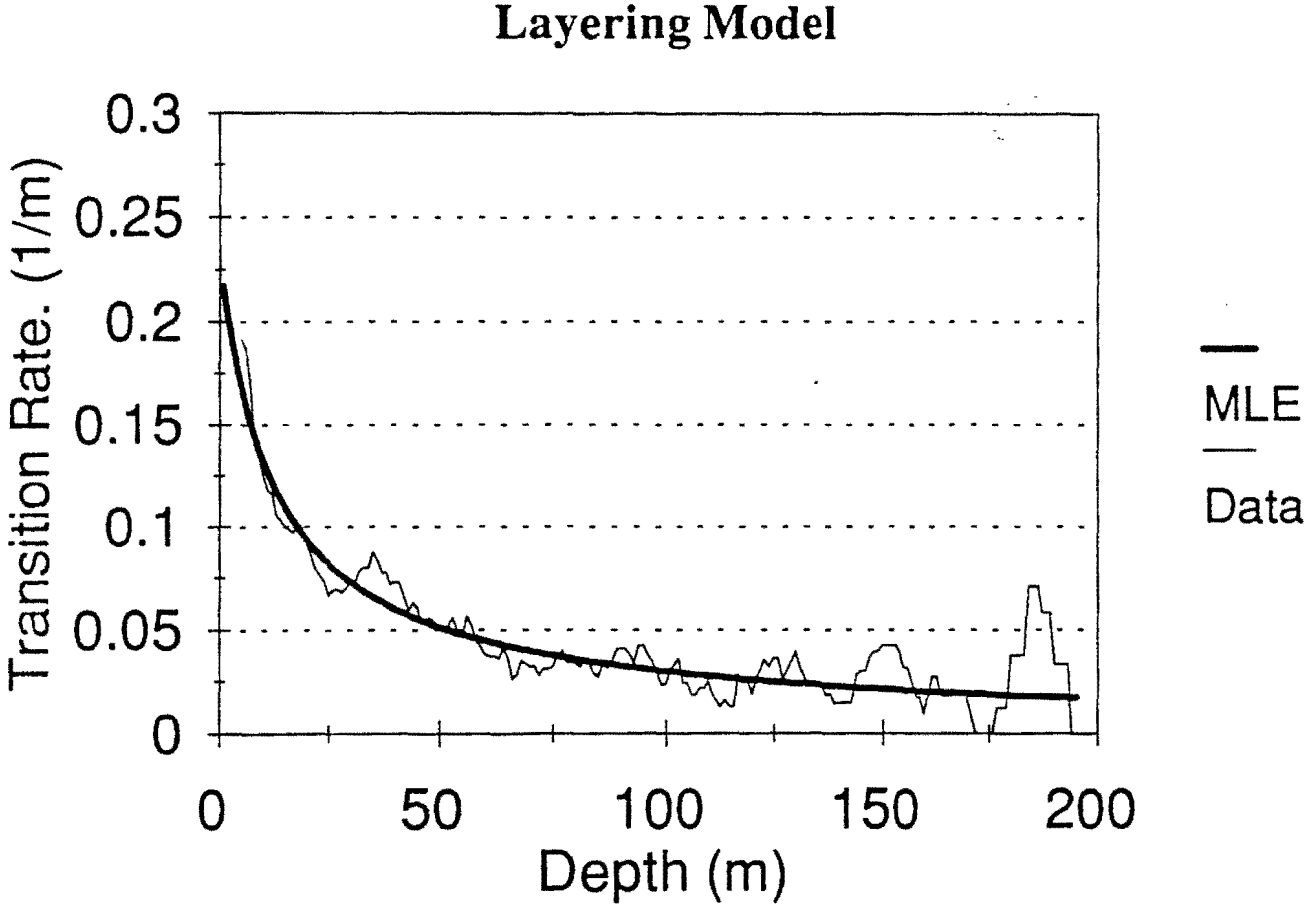
Layering Model
Transition Rate. (1/m)
0.3
0.25
0.2
0.15
0.1
0.05
0
0
50
100
150
200
Depth (m)
MLE
Data

FIGURE 15.

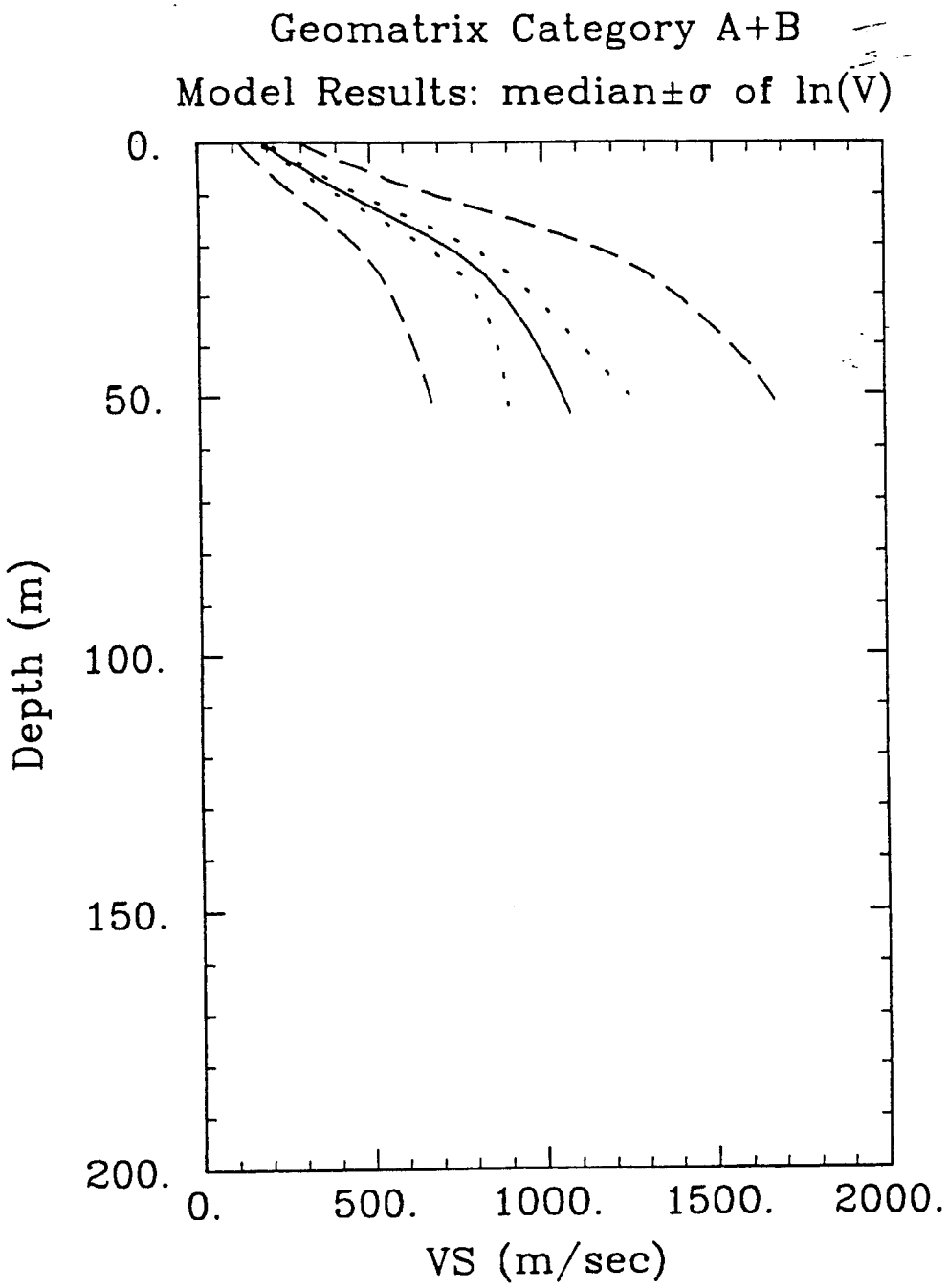
Geomatrix Category A+B
Model Results: median±σ of ln(V)
Depth (m)
0.
50.
100.
150.
200.
0.
500.
1000.
1500.
2000.
VS (m/sec)

FIGURE 16.

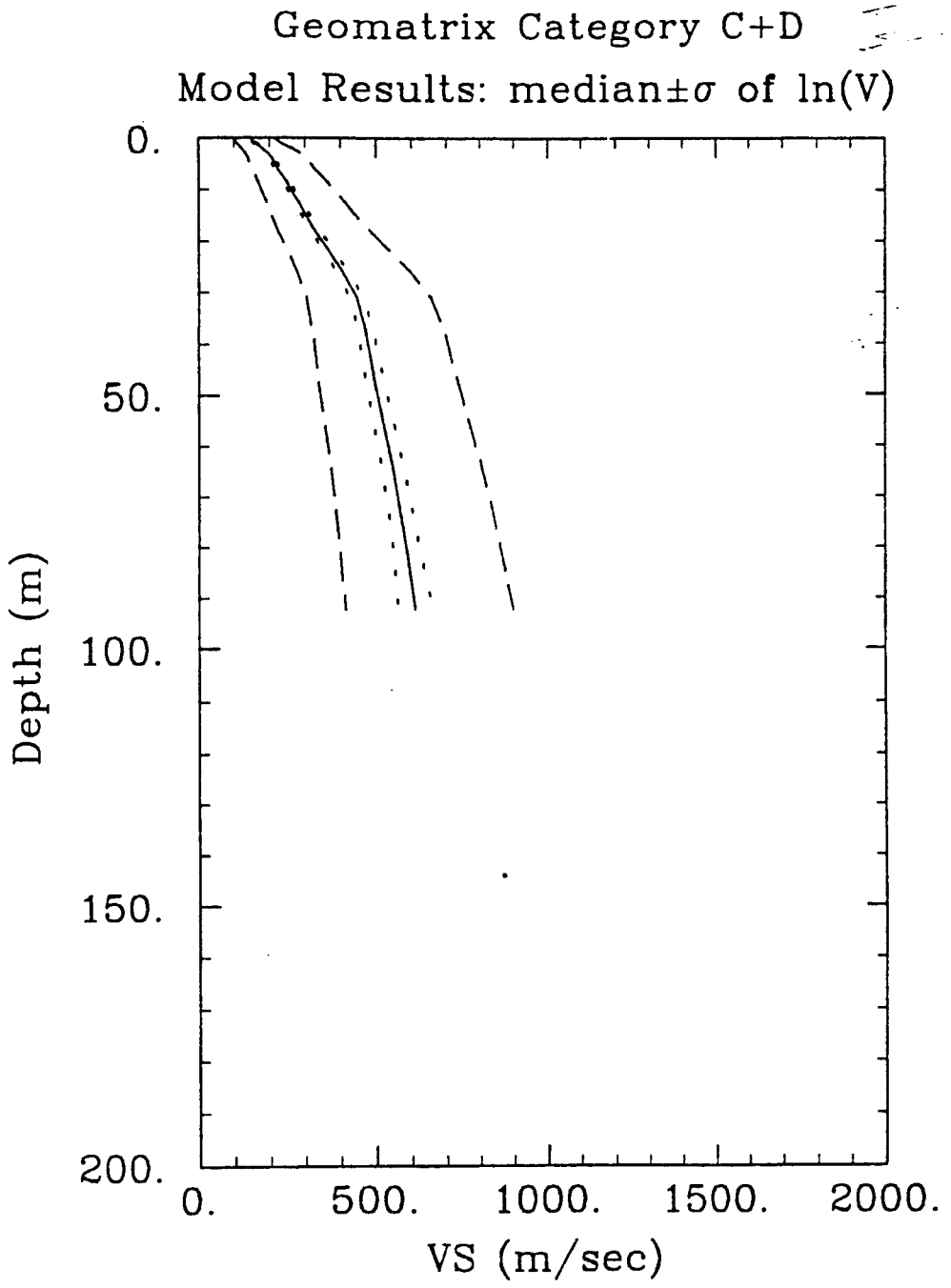
Geomatrix Category C+D
Model Results: median±σ of ln(V)
Depth (m)
0.
50.
100.
150.
200.
0.
500.
1000.
1500.
2000.
VS (m/sec)

FIGURE 17.

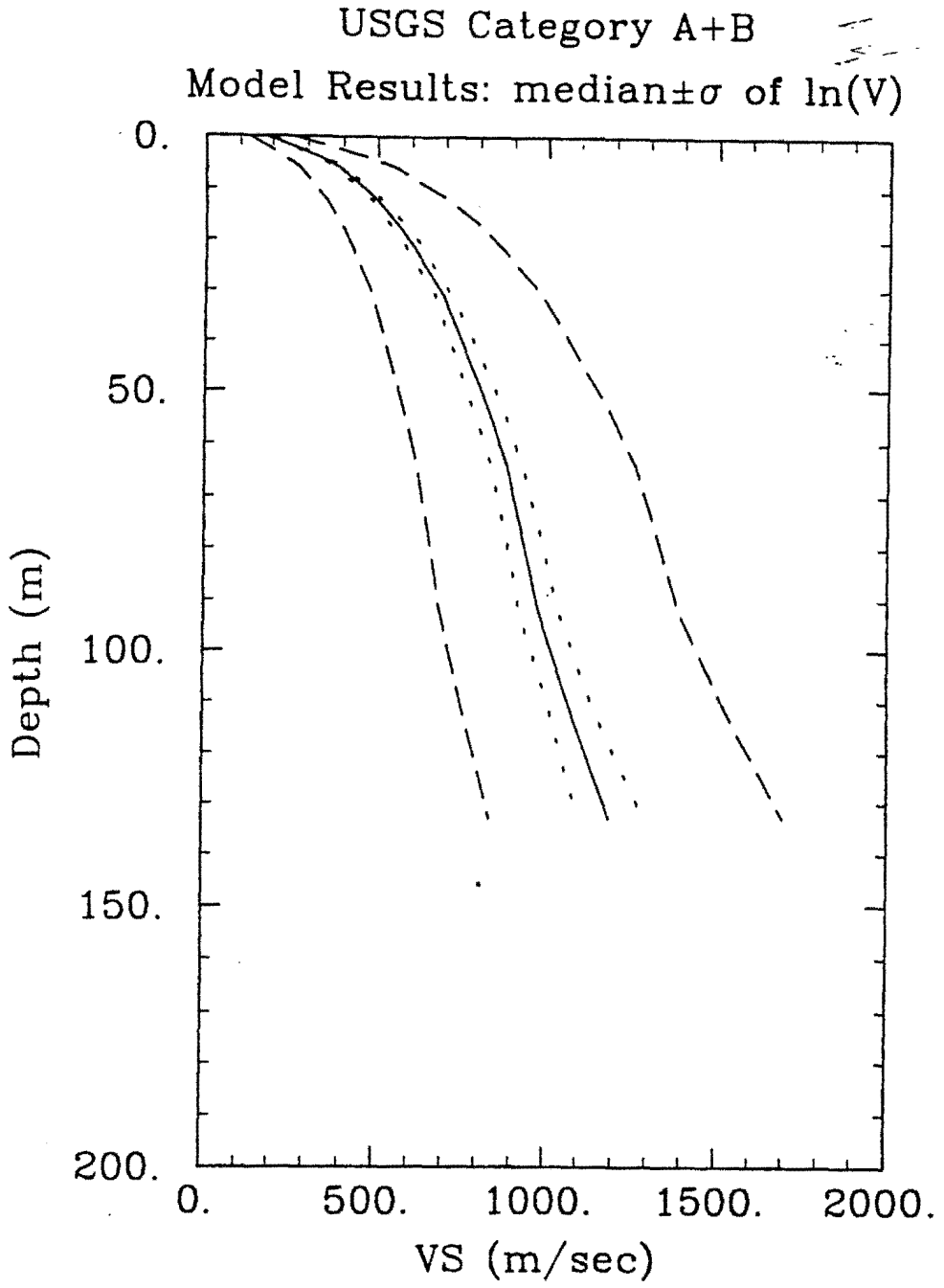
USGS Category A+B
Model Results: median±σ of ln(V)
0.
50.
100.
150.
200.
Depth (m)
0.
500.
1000.
1500.
2000.
VS (m/sec)

FIGURE 18

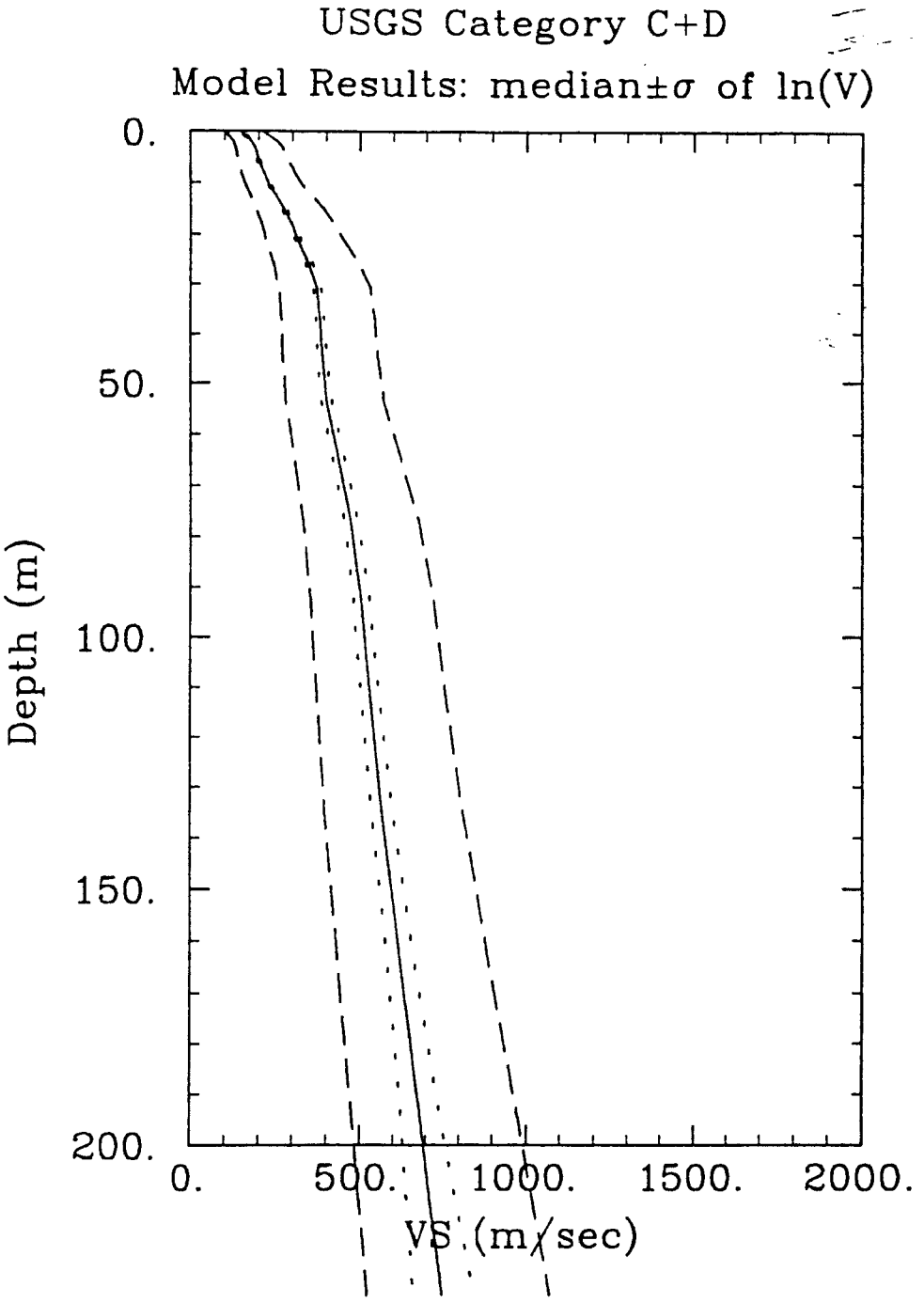
USGS Category C+D
Model Results: median±σ of ln(V)
Depth (m)
0.
50.
100.
150.
200.
0.
500.
1000.
1500.
2000.
VS (m/sec)

FIGURE 19.

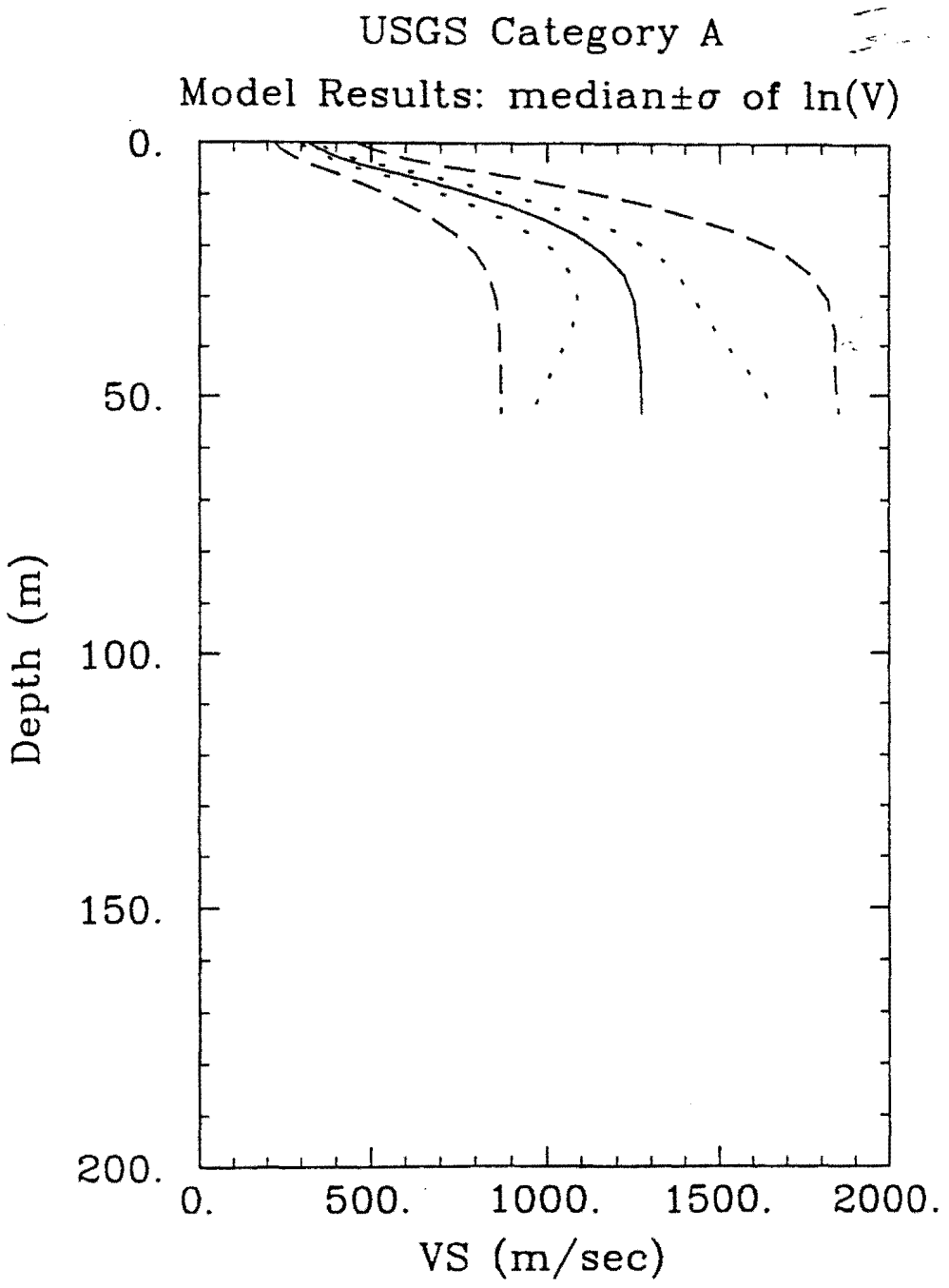
USGS Category A
Model Results: median±σ of ln(V)
0.
50.
100.
150.
200.
Depth (m)
0.
500.
1000.
1500.
2000.
VS (m/sec)

FIGURE 20.

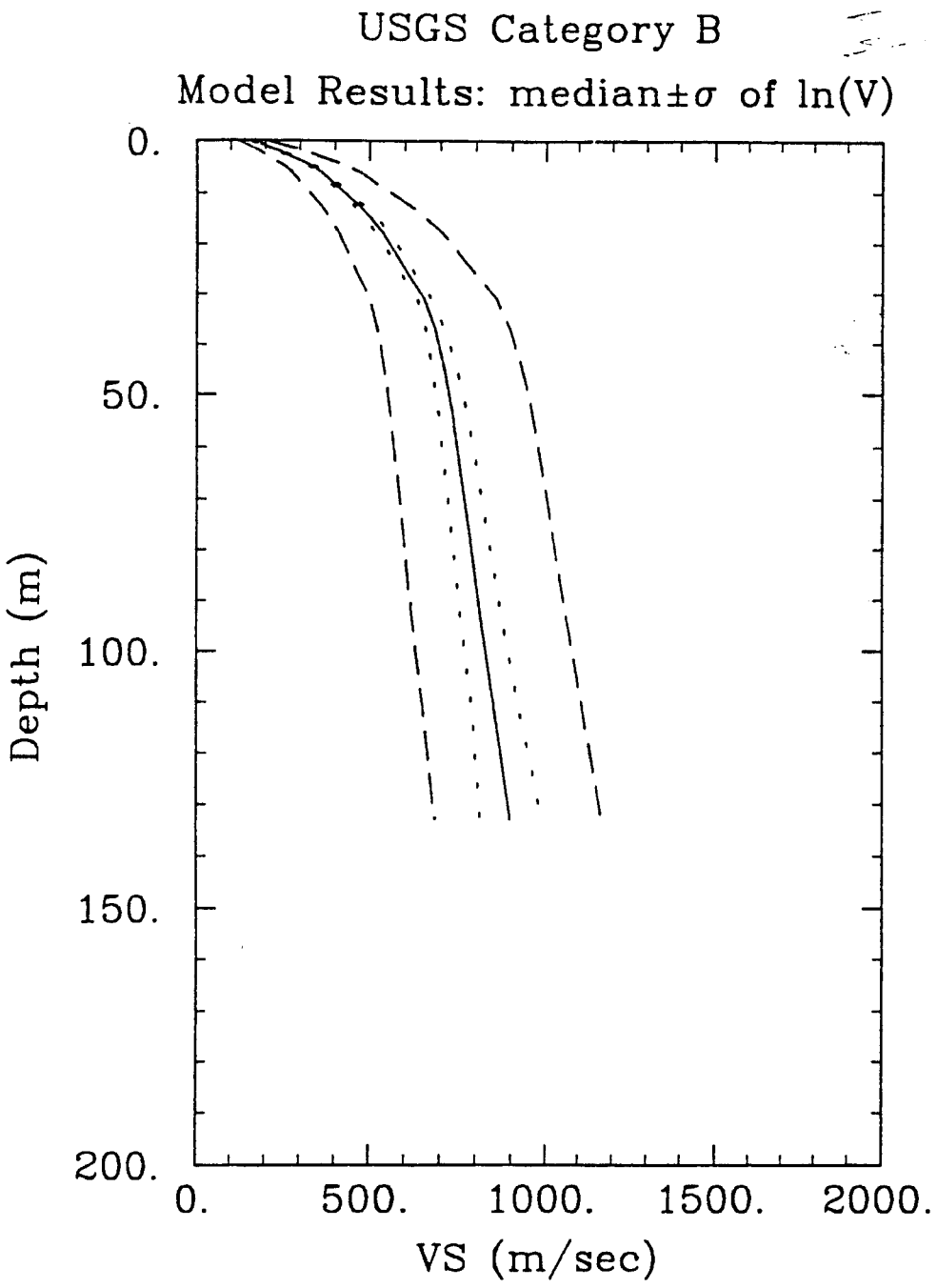
USGS Category B
Model Results: median±σ of ln(V)
0.
50.
100.
150.
200.
Depth (m)
0.
500.
1000.
1500.
2000.
VS (m/sec)

FIGURE 21.

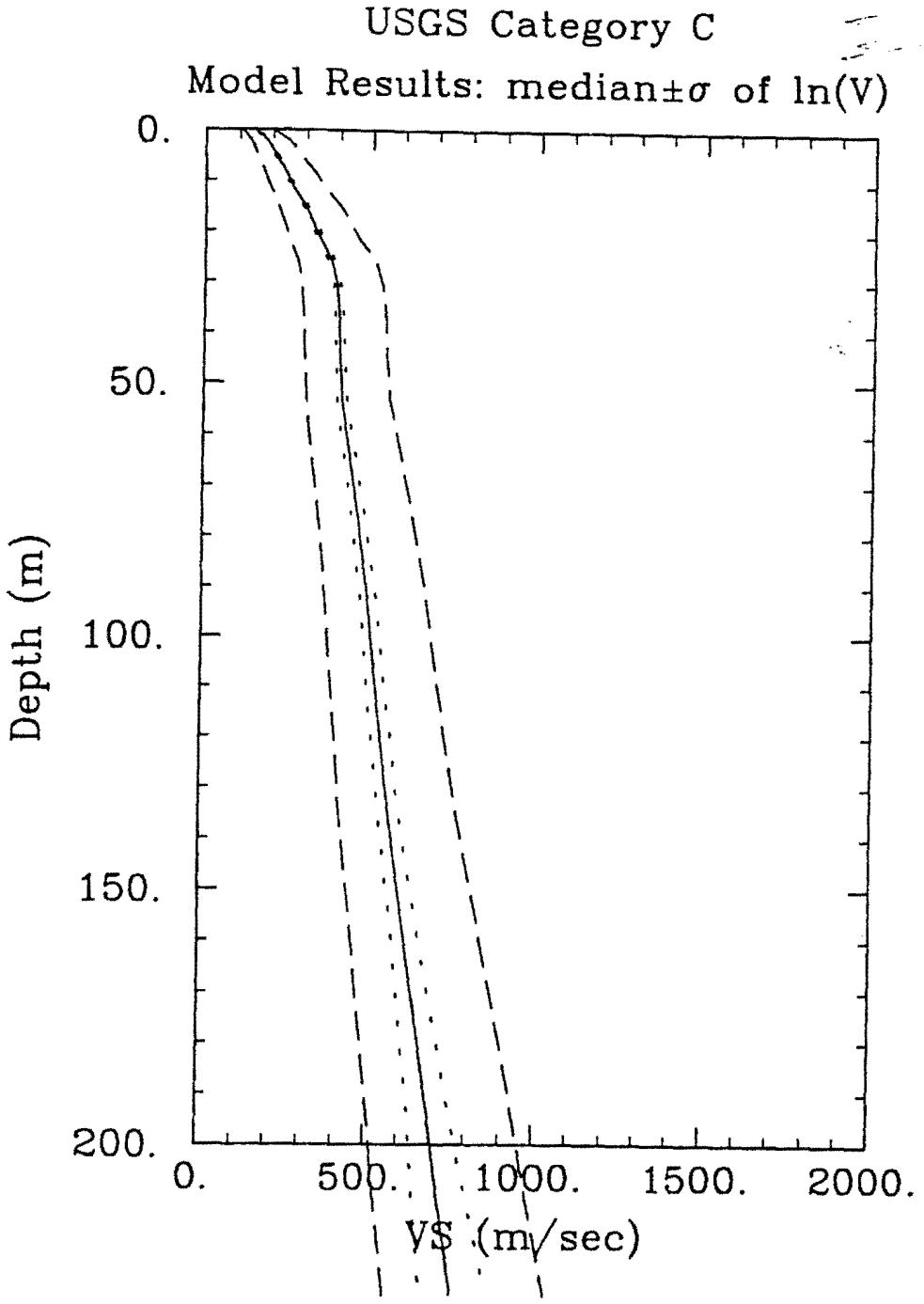
USGS Category C
Model Results: median±σ of ln(V)
0.
50.
100.
150.
200.
Depth (m)
0.
500.
1000.
1500.
2000.
VS (m/sec)

FIGURE 22.

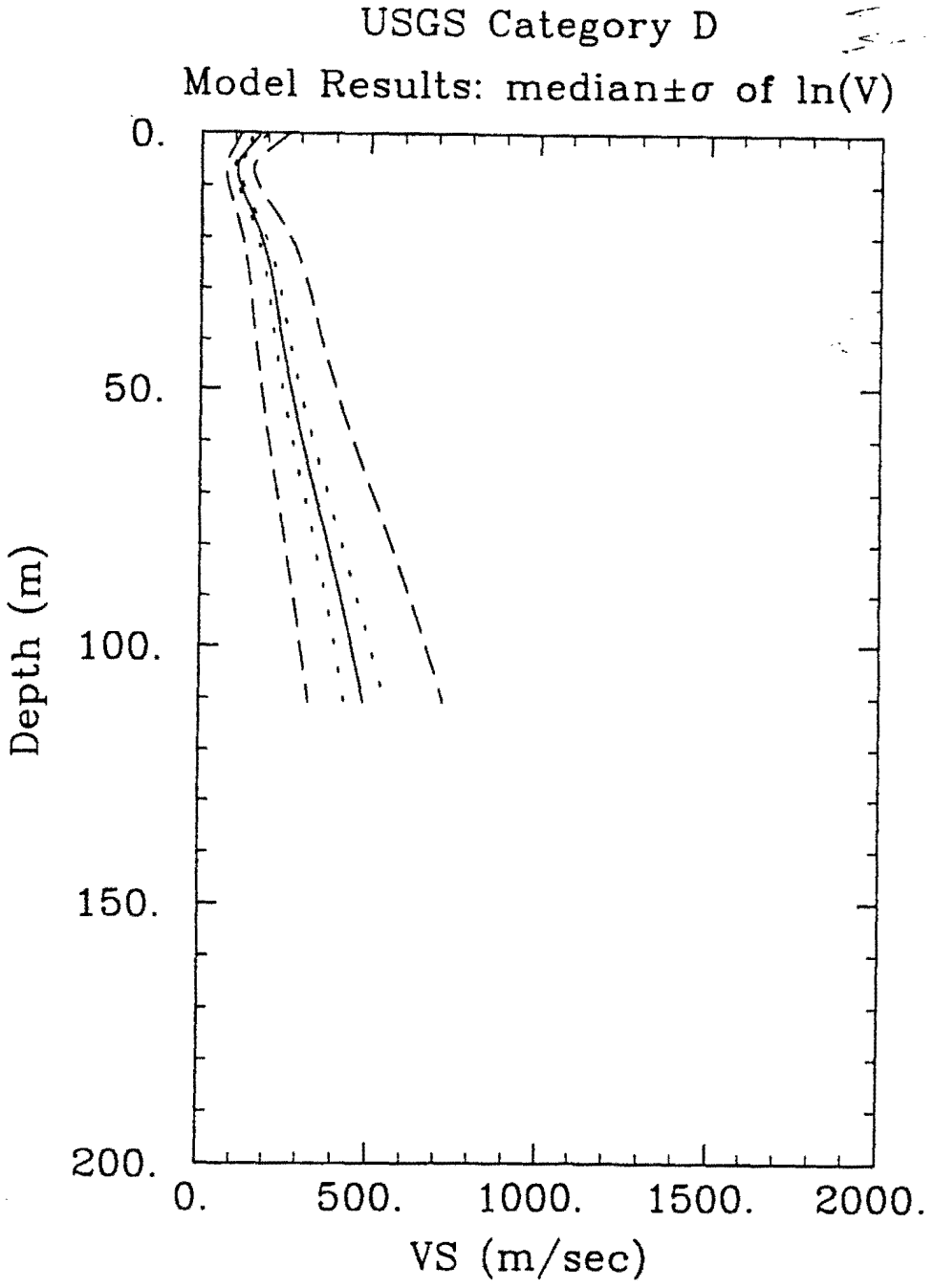
USGS Category D
Model Results: median±σ of ln(V)
0.
50.
100.
150.
200.
Depth (m)
0.
500.
1000.
1500.
2000.
VS (m/sec)

FIGURE 23.

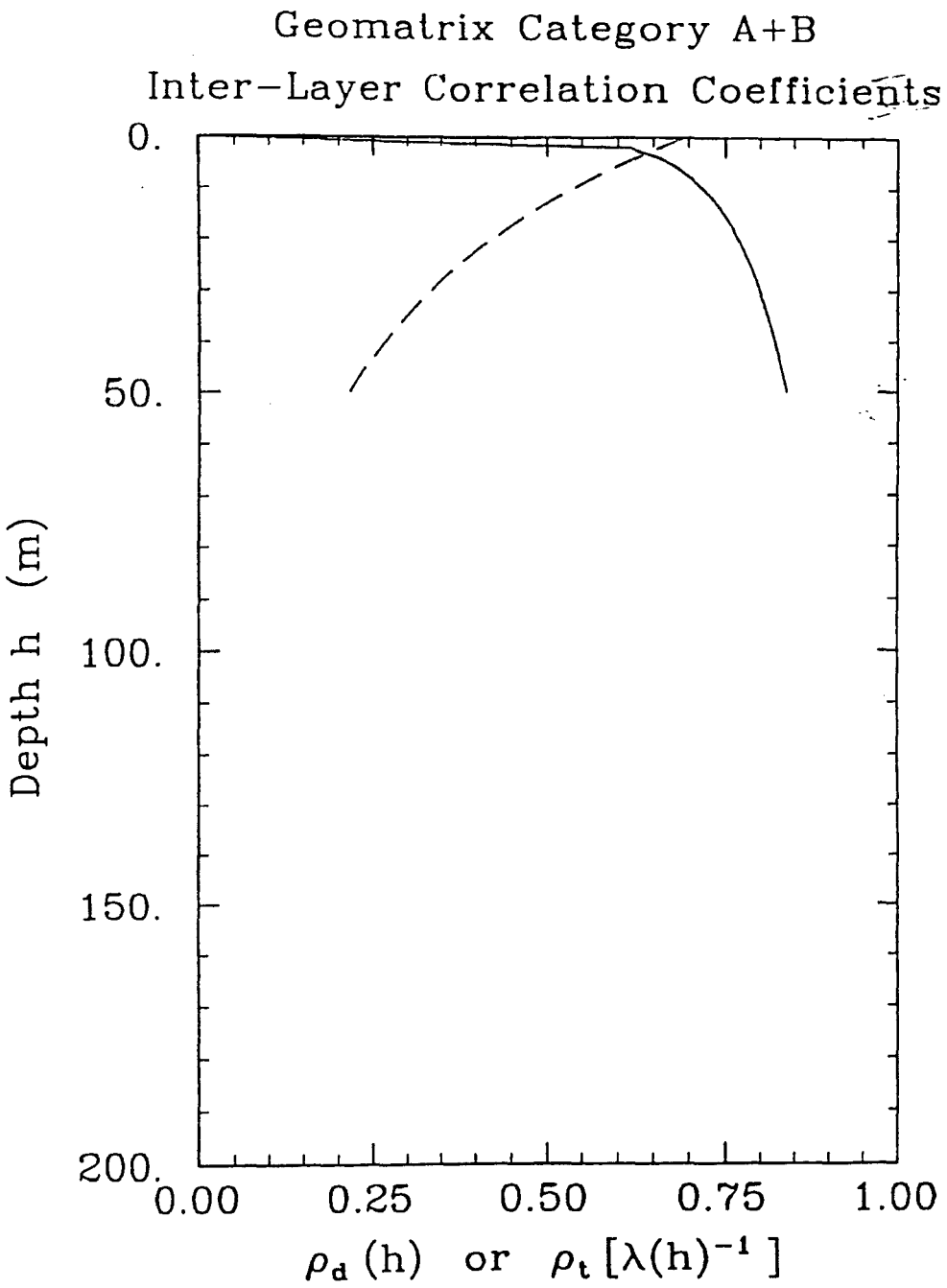
Geomatrix Category A+B
Inter-Layer Correlation Coefficients
0.
50.
100.
150.
200.
Depth h (m)
0.00
0.25
0.50
0.75
1.00
ρ_d (h) or ρ_t [λ(h)$^{-1}$]

FIGURE 24.

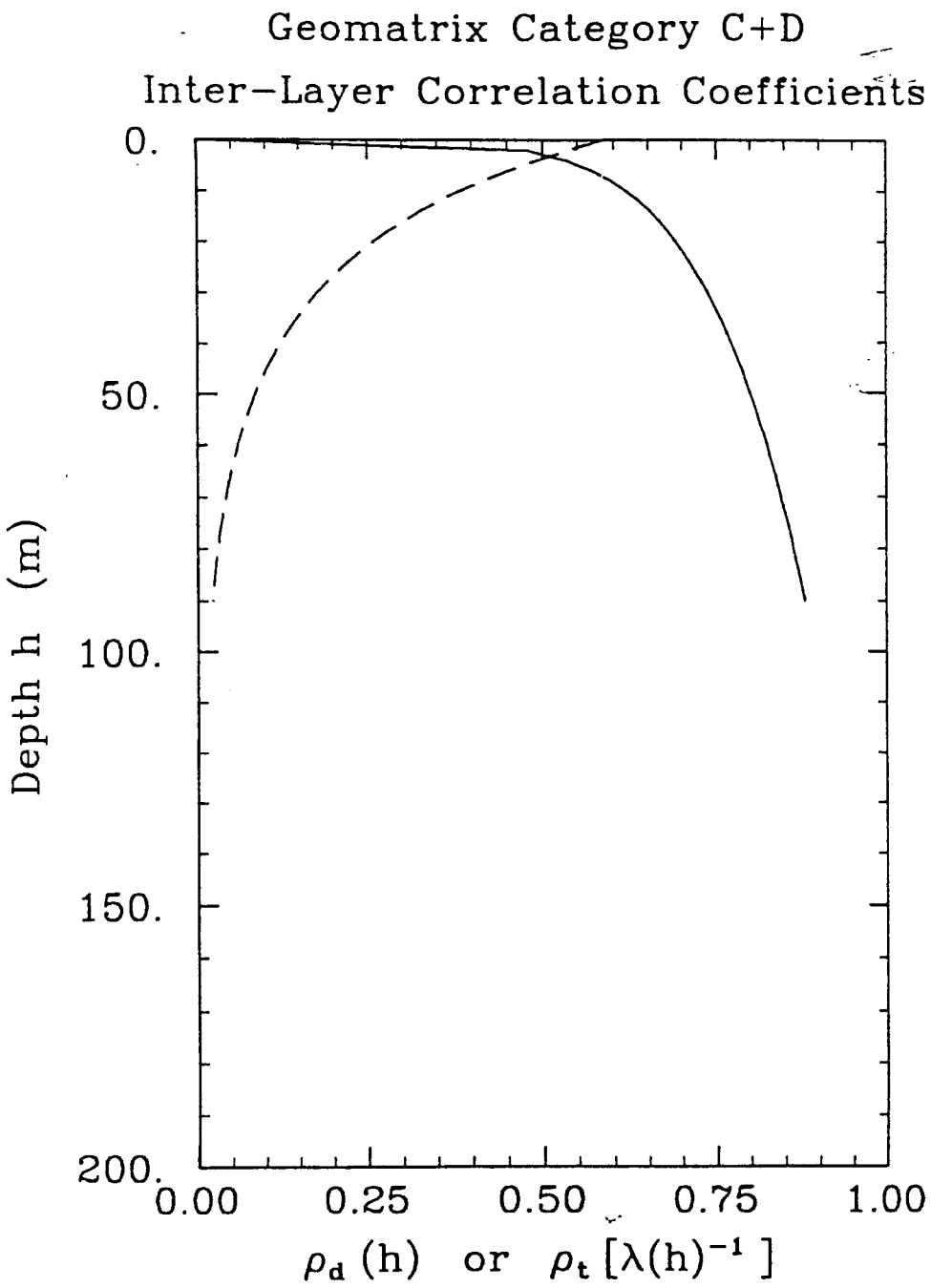
Geomatrix Category C+D
Inter-Layer Correlation Coefficients
0.
50.
100.
150.
200.
Depth h (m)
0.00
0.25
0.50
0.75
1.00
ρ_d (h) or ρ_t [λ(h)$^{-1}$]

FIGURE 25.

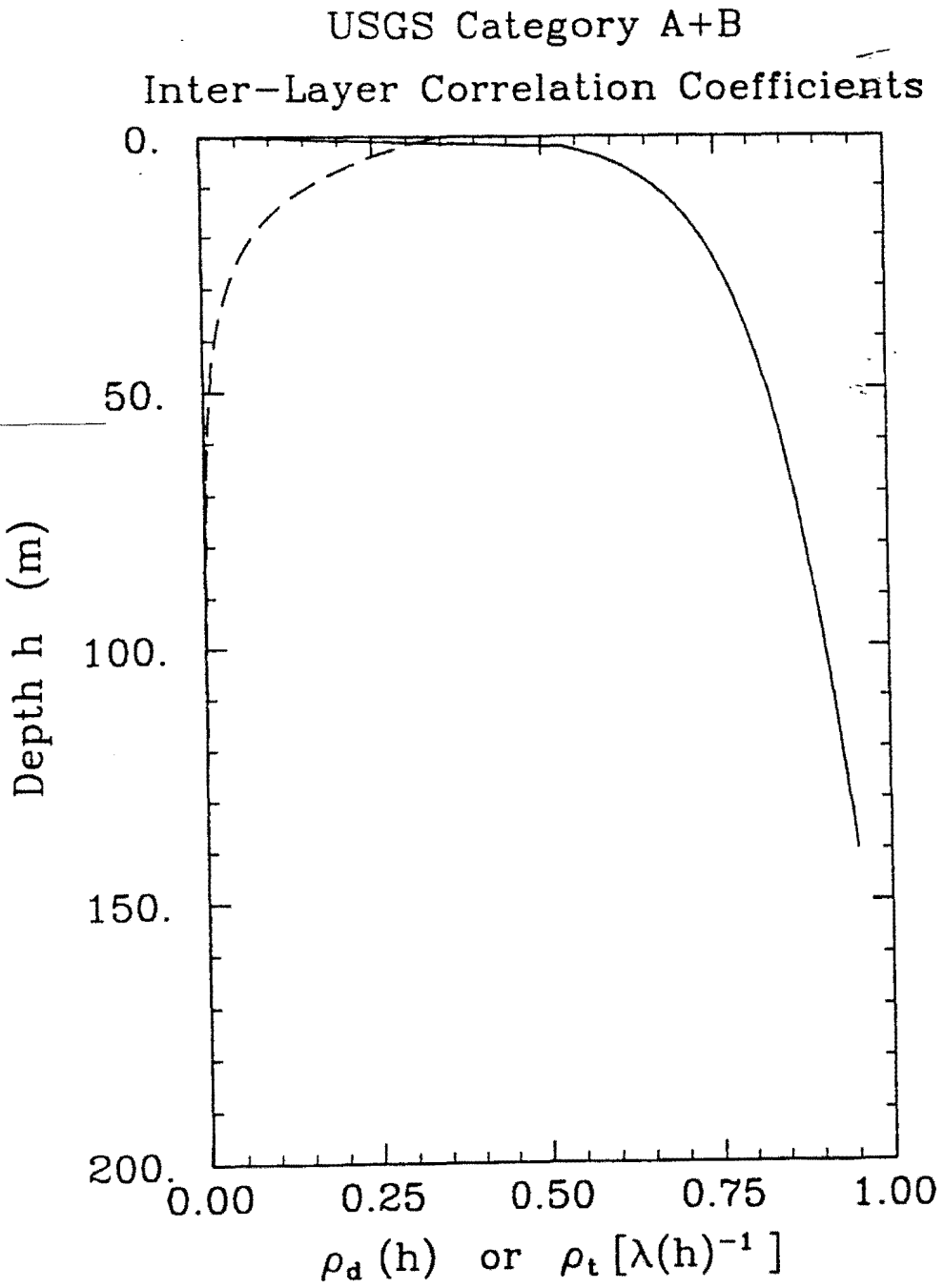
USGS Category A+B
Inter-Layer Correlation Coefficients
0.
50.
100.
150.
200.
Depth h (m)
0.00
0.25
0.50
0.75
1.00
ρ_d (h) or ρ_t [λ(h)$^{-1}$]

FIGURE 26.

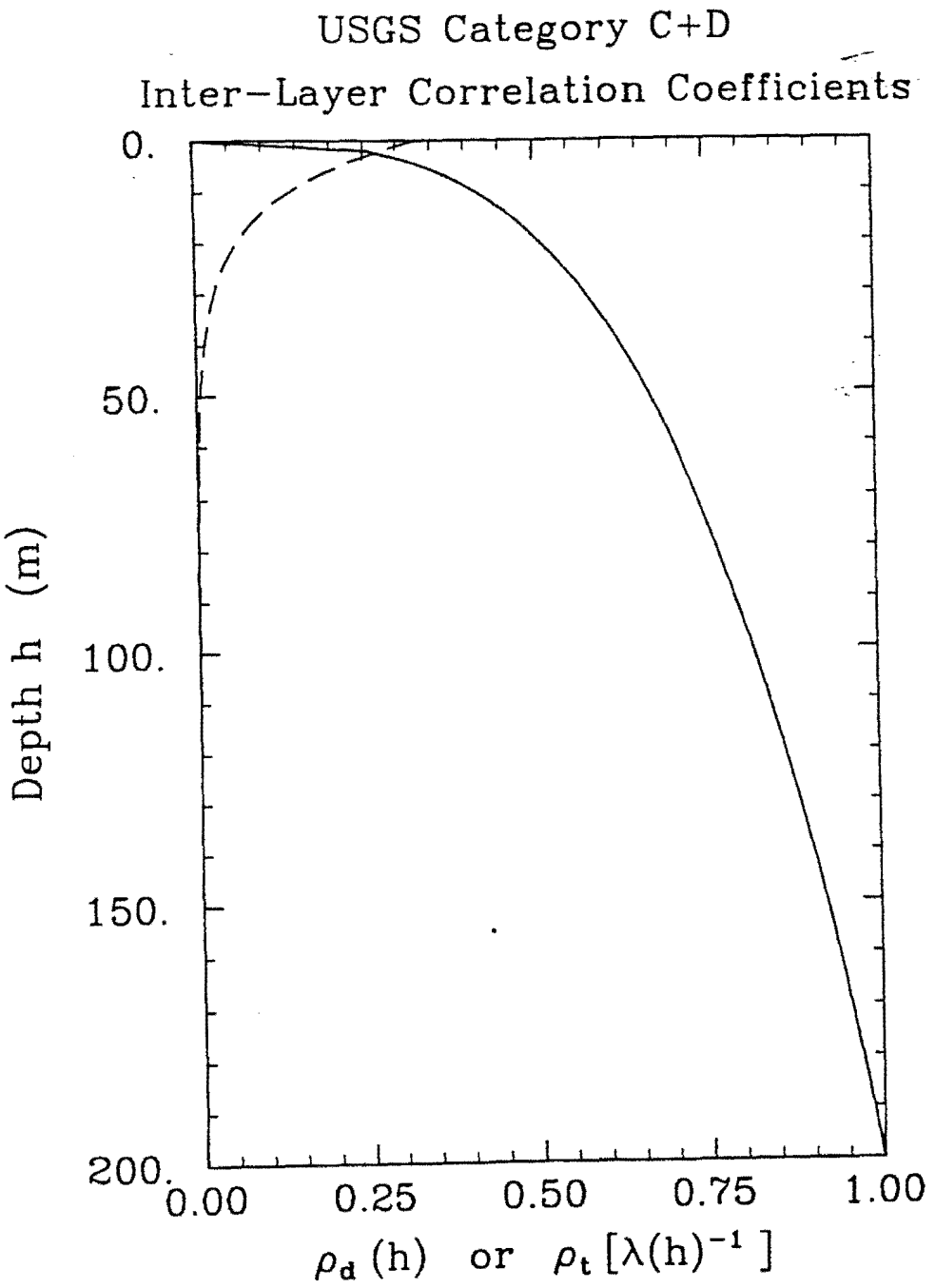
USGS Category C+D
Inter-Layer Correlation Coefficients
0.
50.
100.
150.
200.
Depth h (m)
0.00
0.25
0.50
0.75
1.00
ρ_d (h) or ρ_t [λ(h)$^{-1}$]

FIGURE 27.

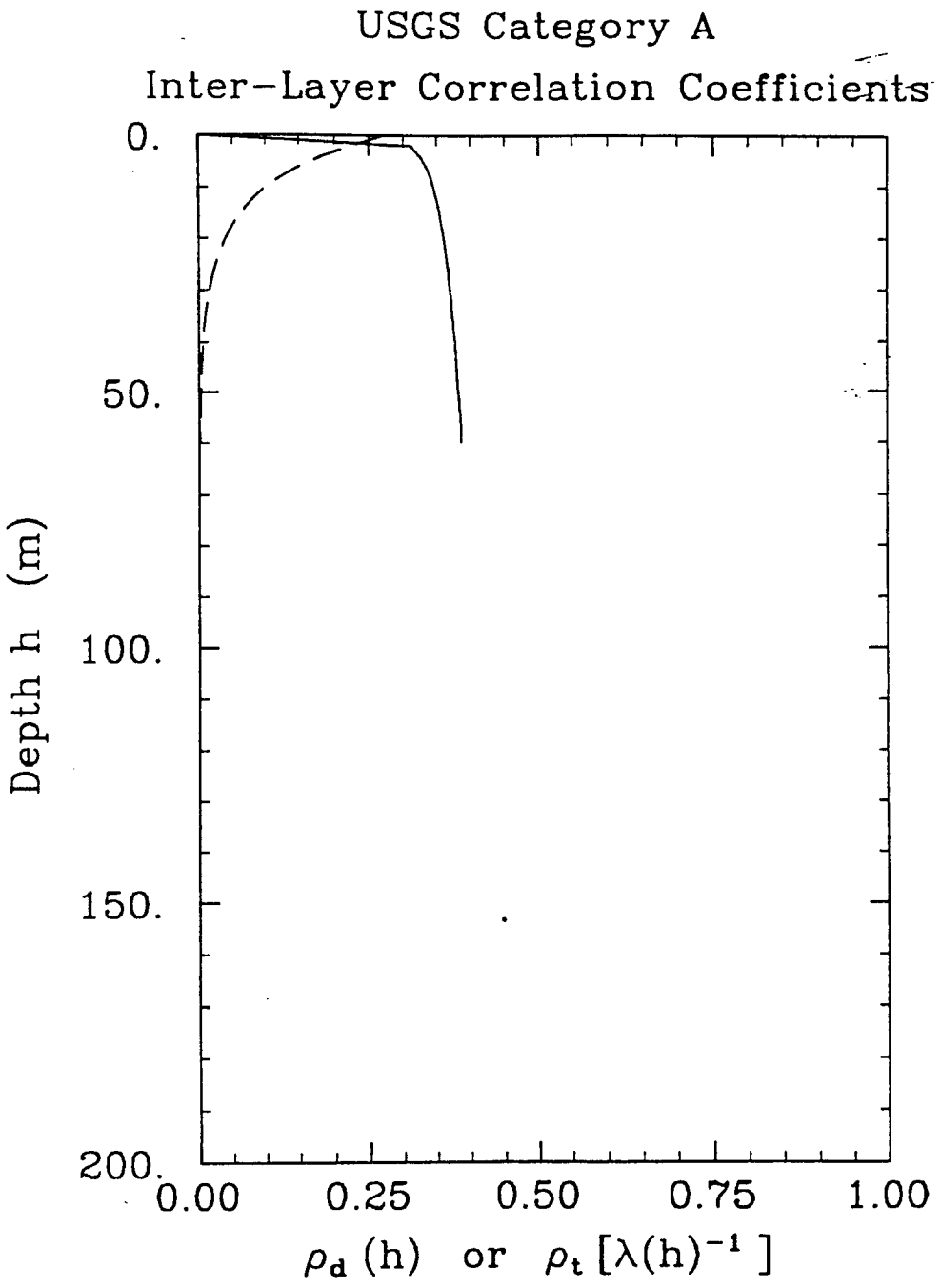
USGS Category A
Inter-Layer Correlation Coefficients
0.
50.
100.
150.
200.
Depth h (m)
0.00
0.25
0.50
0.75
1.00
ρ_d (h) or ρ_t [λ(h)$^{-1}$]

FIGURE 28.

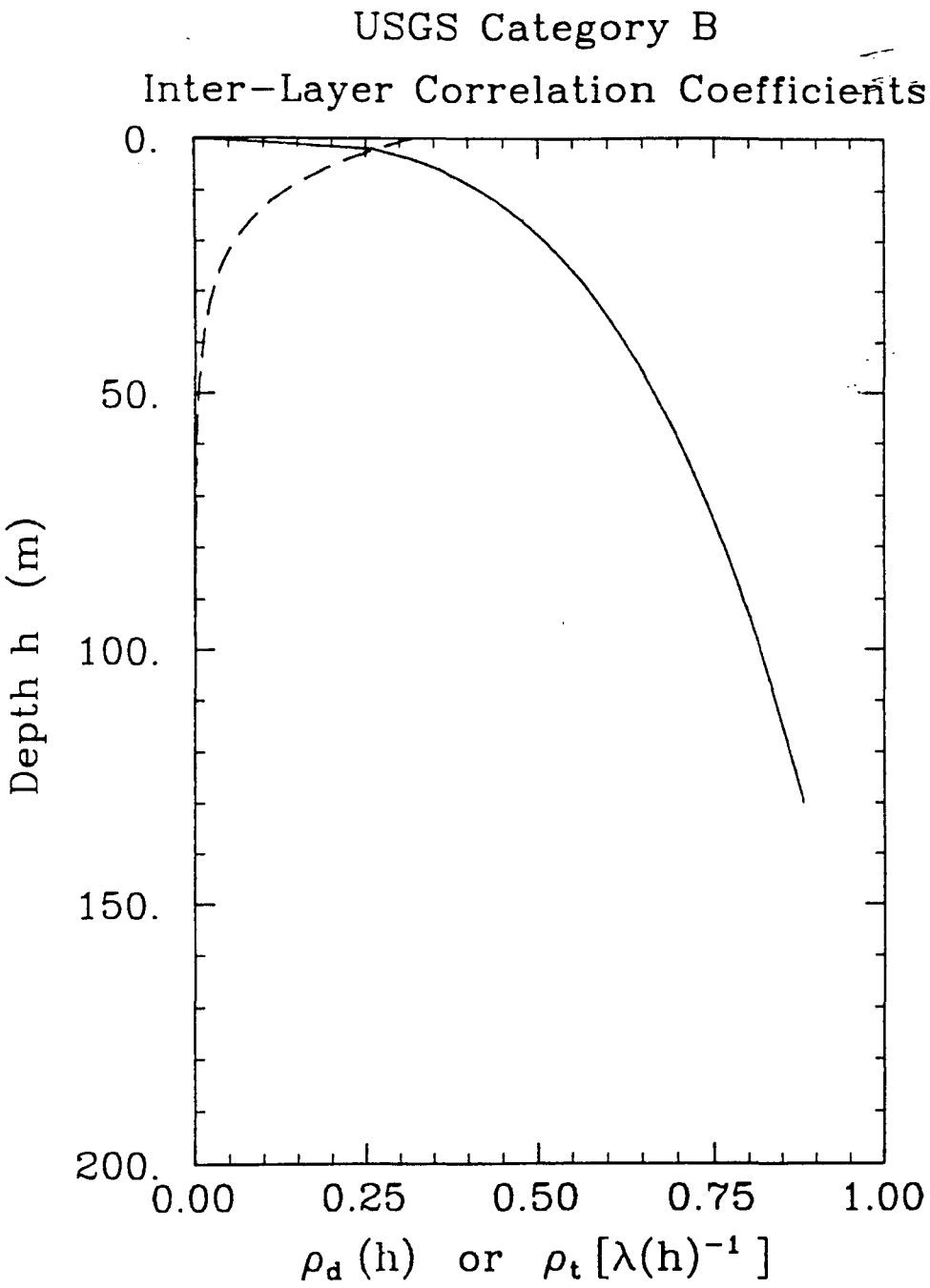
USGS Category B
Inter-Layer Correlation Coefficients
0.
50.
100.
150.
200.
Depth h (m)
0.00
0.25
0.50
0.75
1.00
ρ_d (h) or ρ_t [$\lambda(h)^{-1}$]

FIGURE 29.

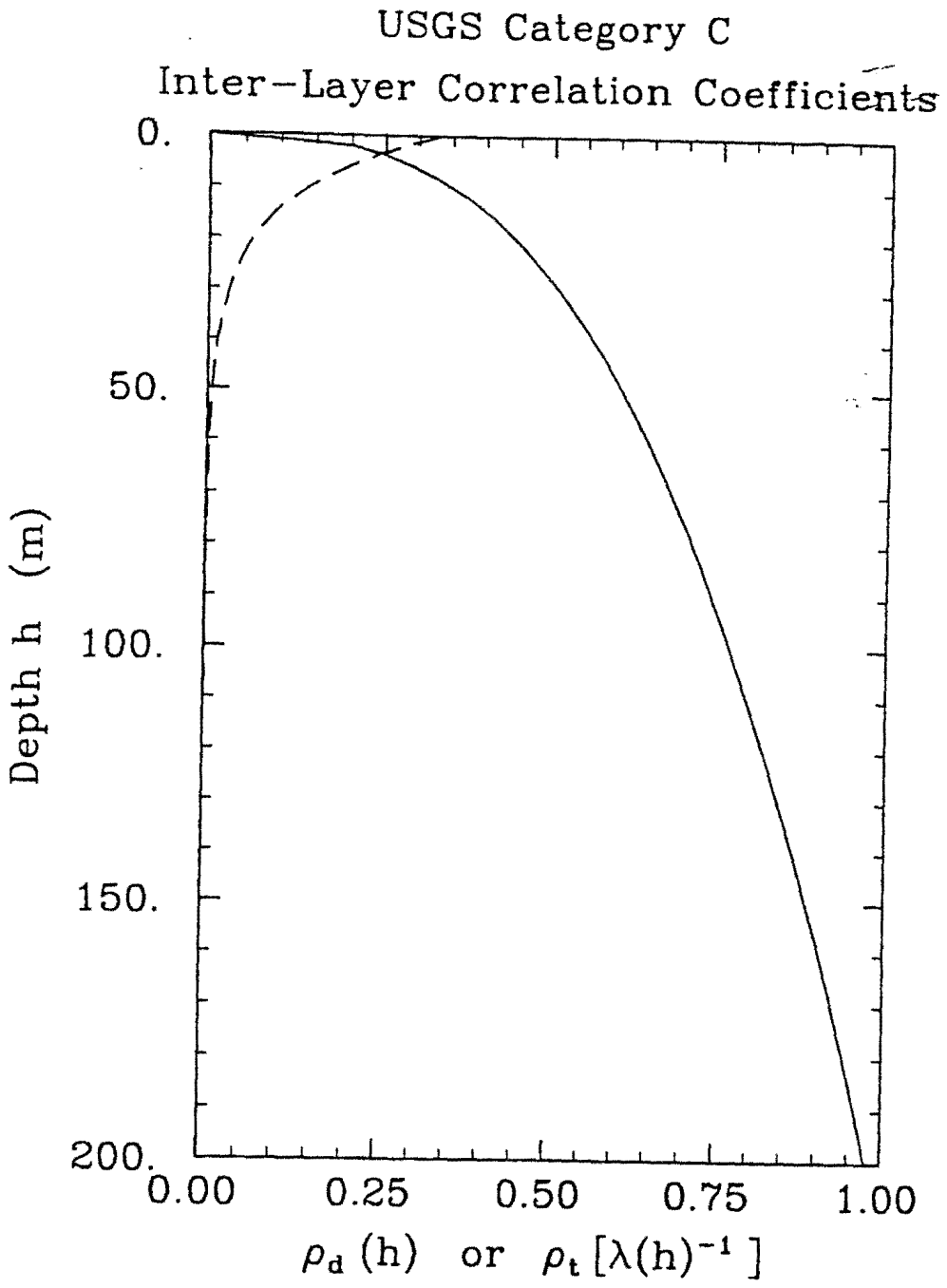
USGS Category C
Inter-Layer Correlation Coefficients
0.
50.
100.
150.
200.
Depth h (m)
0.00
0.25
0.50
0.75
1.00
ρ_d (h) or ρ_t [λ(h)$^{-1}$]

FIGURE 30.

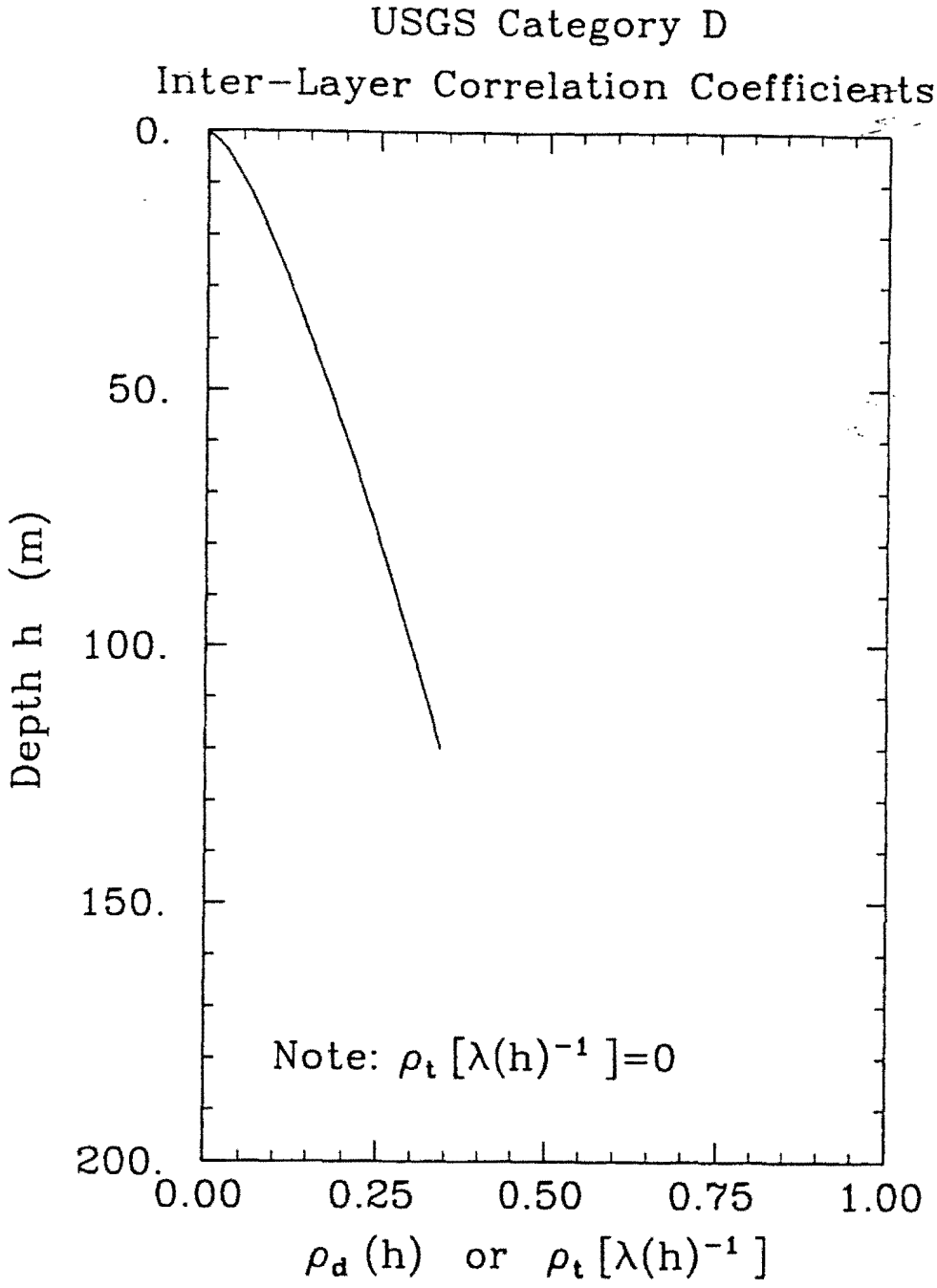
USGS Category D
Inter-Layer Correlation Coefficients
0.
50.
100.
150.
200.
Depth h (m)
Note: $\rho_t [\lambda(h)^{-1}]=0$
0.00
0.25
0.50
0.75
1.00
ρ_d (h) or $\rho_t [\lambda(h)^{-1}]$

FIGURE 31.

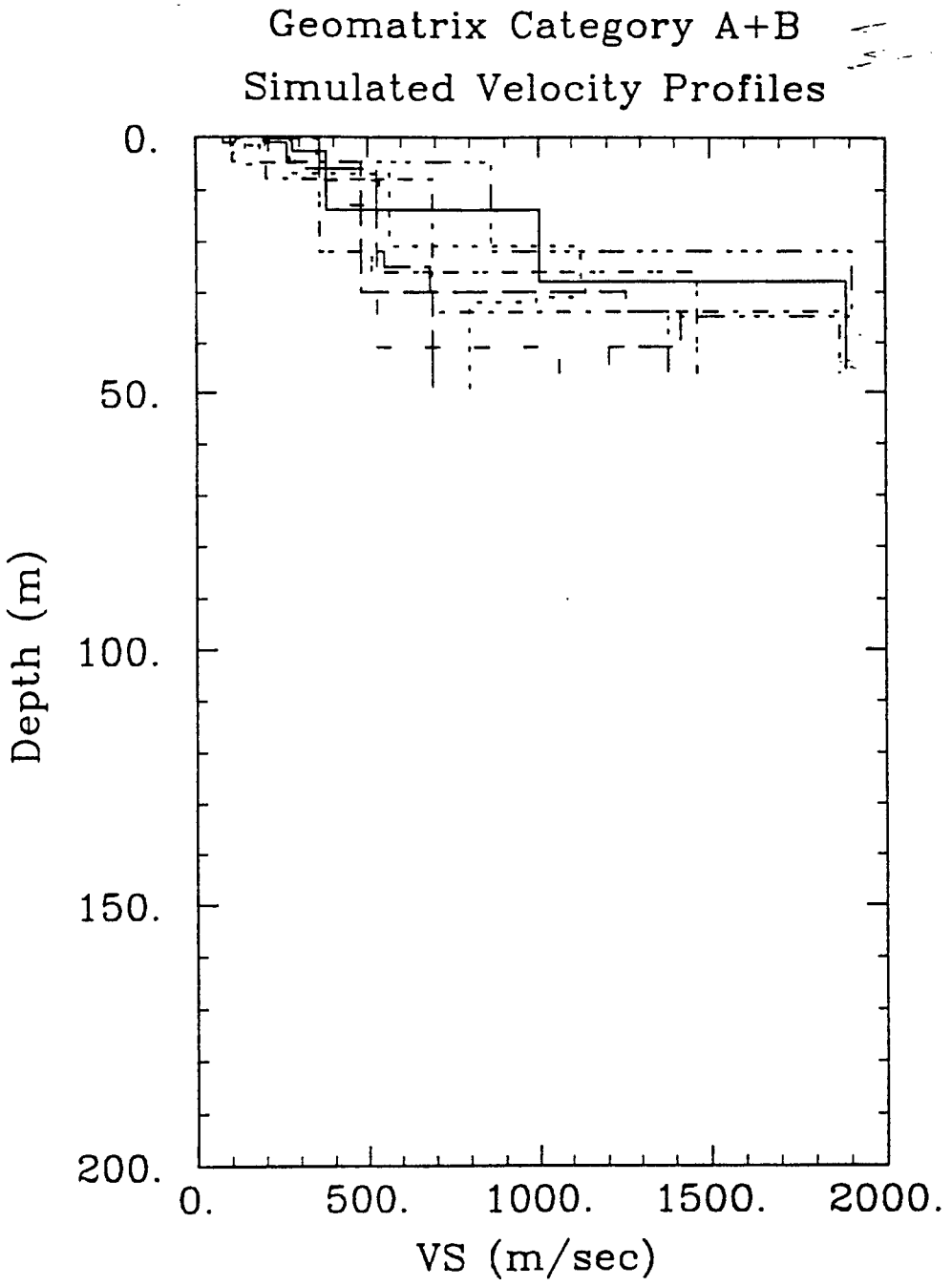
Geomatrix Category A+B
Simulated Velocity Profiles
Depth (m)
0.
50.
100.
150.
200.
0.
500.
1000.
1500.
2000.
VS (m/sec)

FIGURE 32.

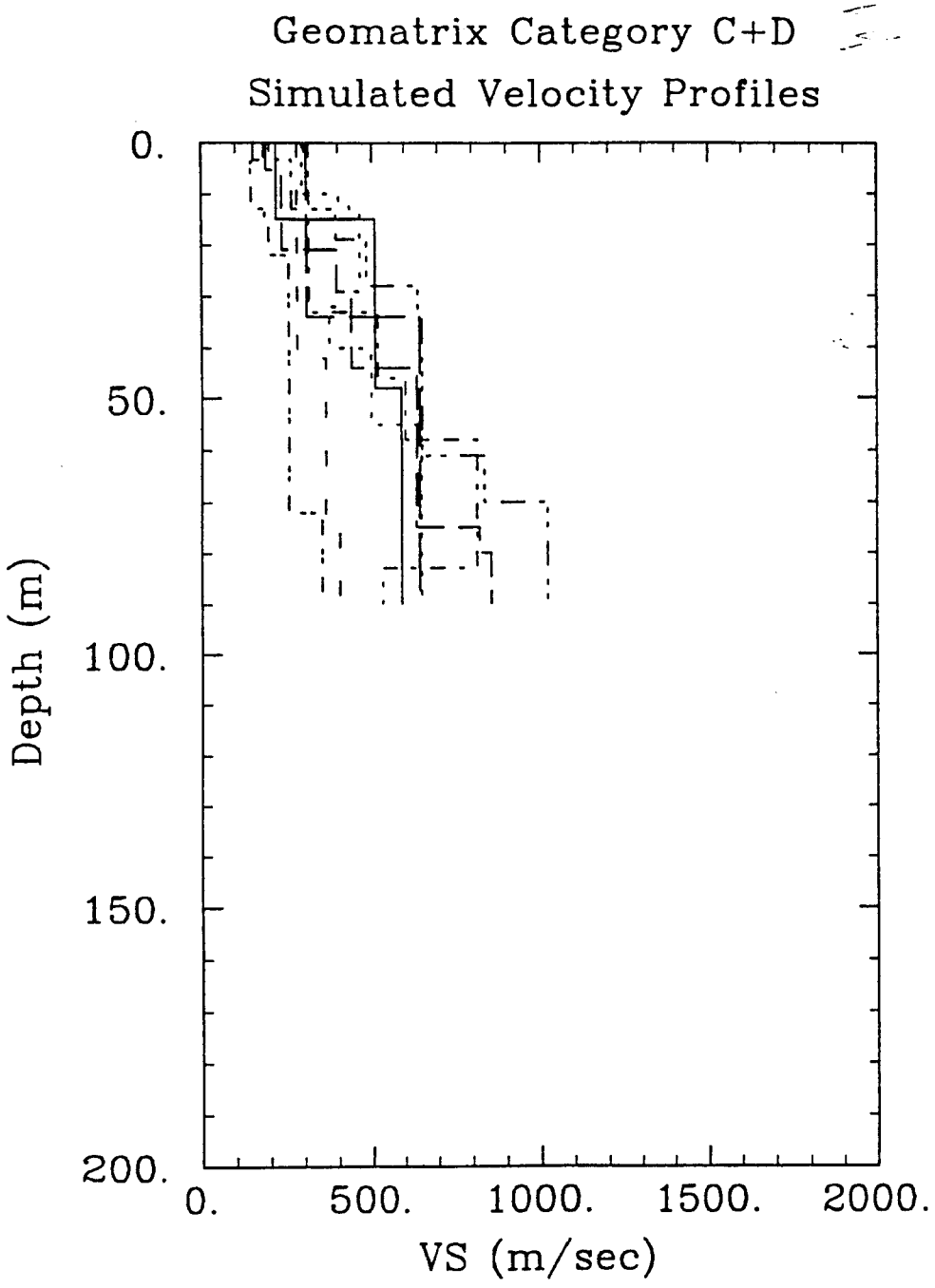
Geomatrix Category C+D
Simulated Velocity Profiles
Depth (m)
0.
50.
100.
150.
200.
0.
500.
1000.
1500.
2000.
VS (m/sec)

FIGURE 33.

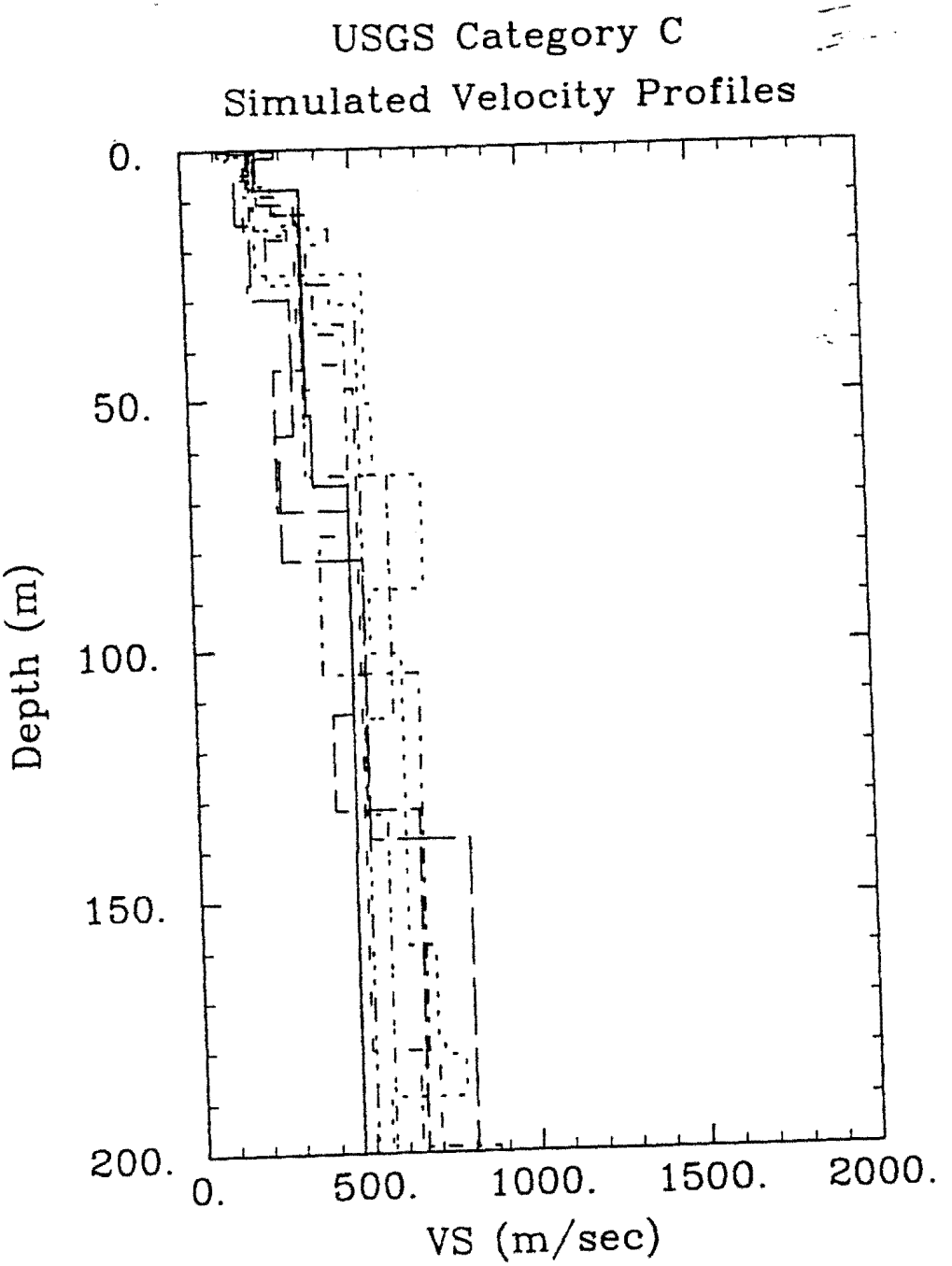
USGS Category C
Simulated Velocity Profiles
Depth (m)
0.
50.
100.
150.
200.
0.
500.
1000.
1500.
2000.
VS (m/sec)

FIGURE 34.

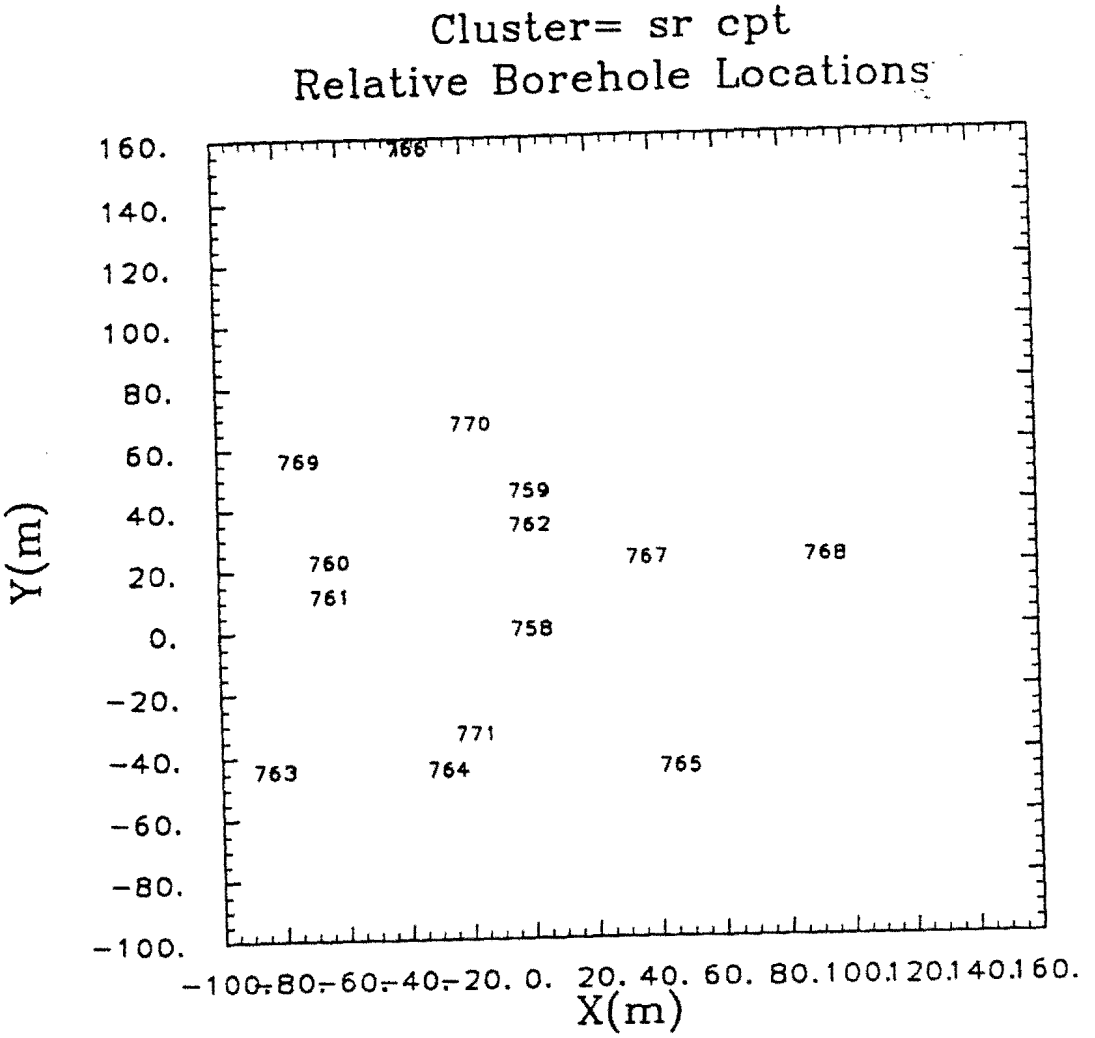
Cluster= sr cpt
Relative Borehole Locations
160.
140.
120.
100.
80.
60.
40.
20.
0.
-20.
-40.
-60.
-80.
-100.
Y(m)
766
770
769
759
762
767
768
760
761
758
771
763
764
765
-100.-80.-60.-40.-20. 0. 20. 40. 60. 80.100.120.140.160.
X(m)

FIGURE 35.

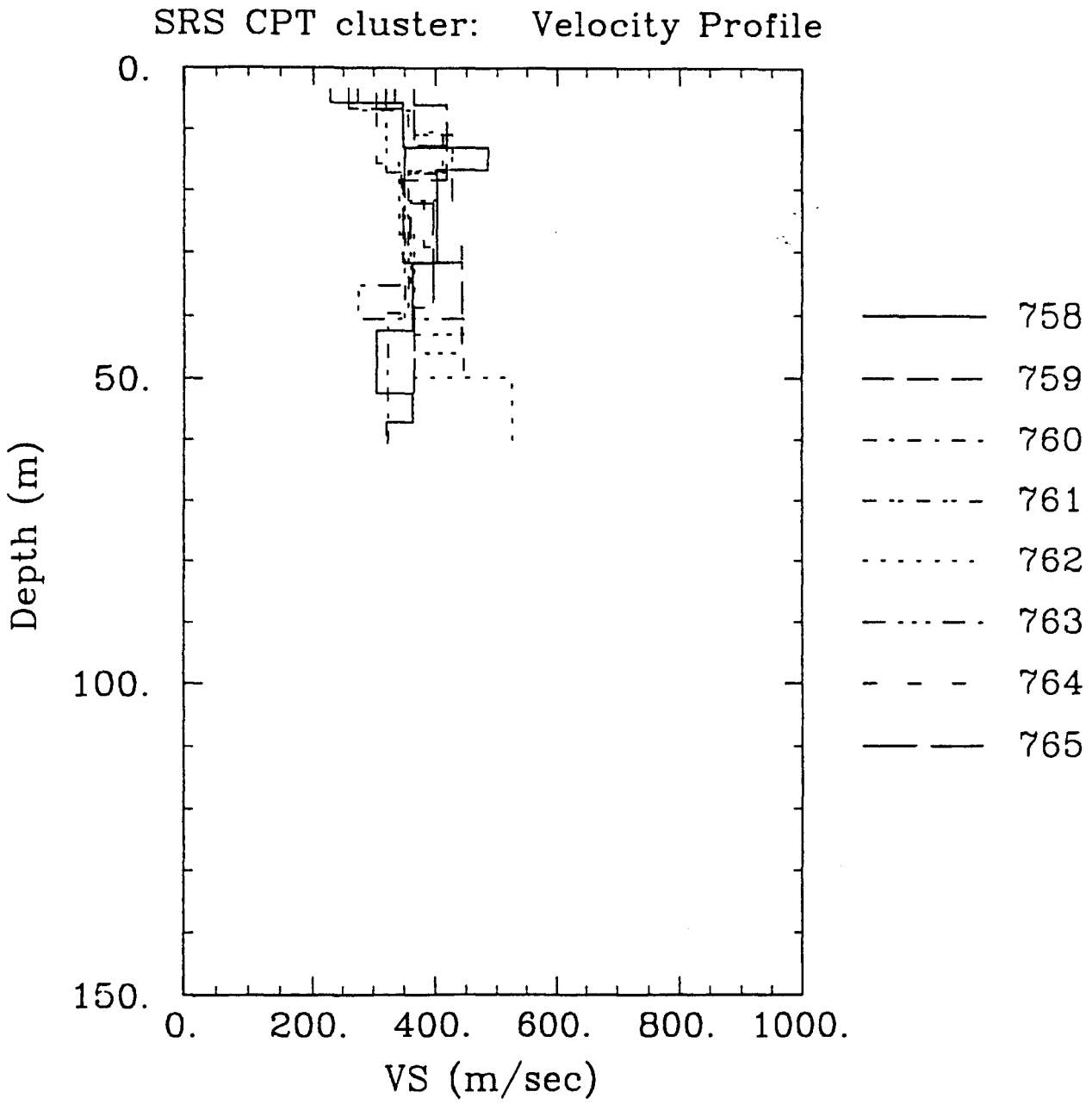
SRS CPT cluster: Velocity Profile
0.
50.
100.
150.
Depth (m)
0.
200.
400.
600.
800.
1000.
VS (m/sec)
758
759
760
761
762
763
764
765

FIGURE 36.A.

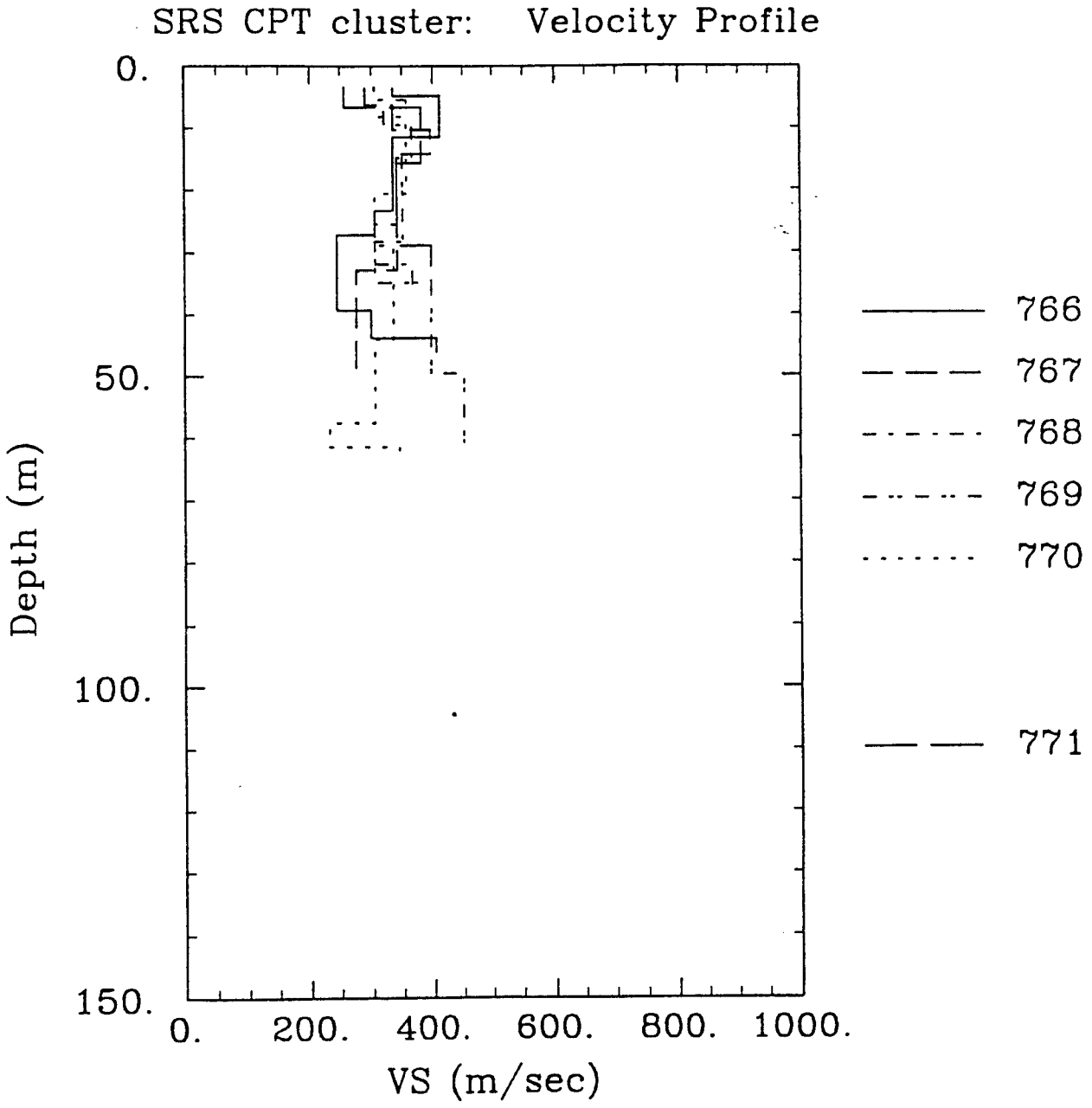
SRS CPT cluster: Velocity Profile
0.
50.
100.
150.
Depth (m)
0.
200.
400.
600.
800.
1000.
VS (m/sec)
766
767
768
769
770
771

FIGURE 36.B.

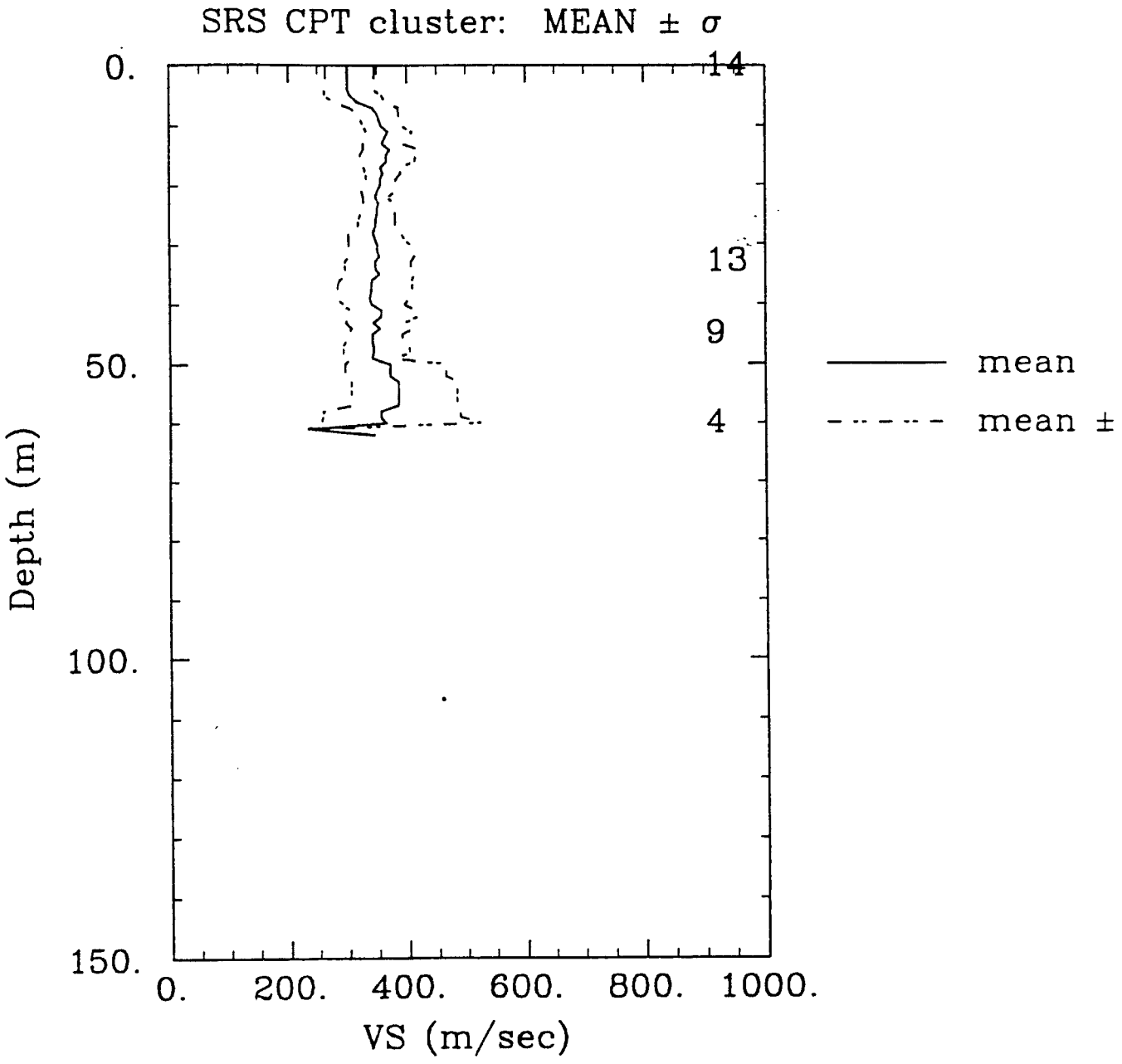
SRS CPT cluster: MEAN ± σ
0.
50.
100.
150.
Depth (m)
14
13
9
4
mean
mean ±
0.
200.
400.
600.
800.
1000.
VS (m/sec)

FIGURE 37.

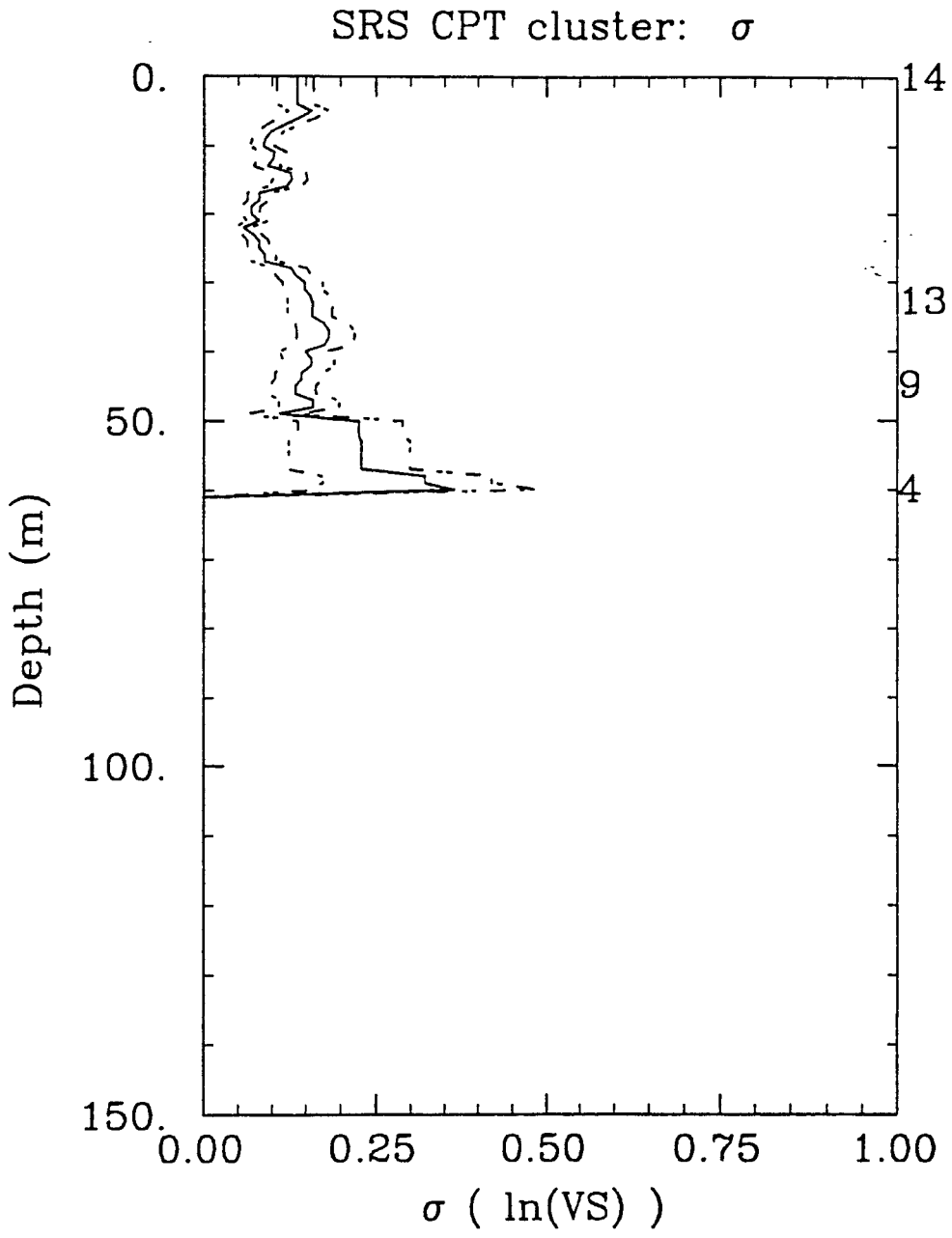
SRS CPT cluster: σ
0.
50.
100.
150.
Depth (m)
14
13
9
4
0.00
0.25
0.50
0.75
1.00
σ (ln(VS))

FIGURE 38

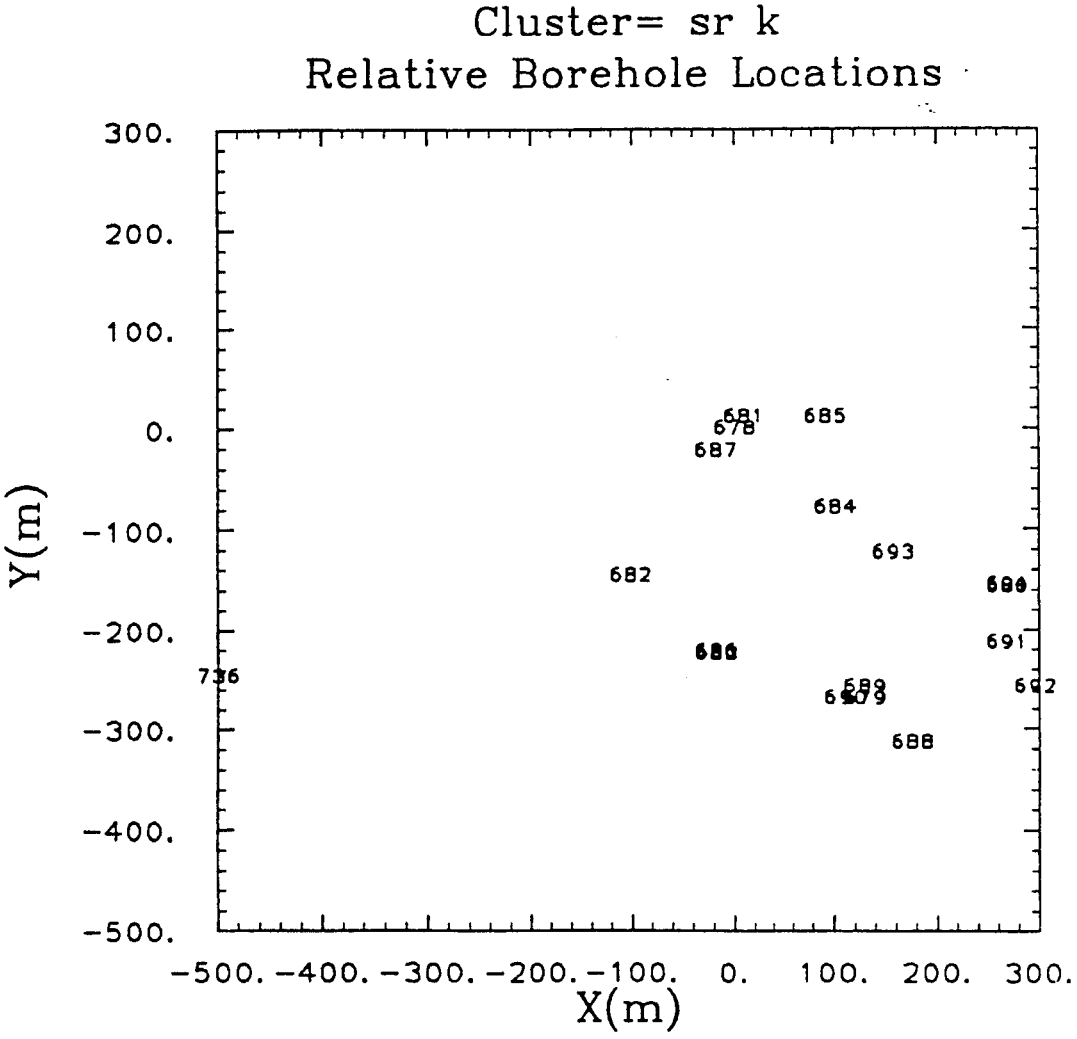
Cluster= sr k
Relative Borehole Locations
300.
200.
100.
0.
-100.
-200.
-300.
-400.
-500.
Y(m)
-500. -400. -300. -200. -100. 0. 100. 200. 300.
X(m)
681
678
685
687
684
693
682
691
688

FIGURE 39.

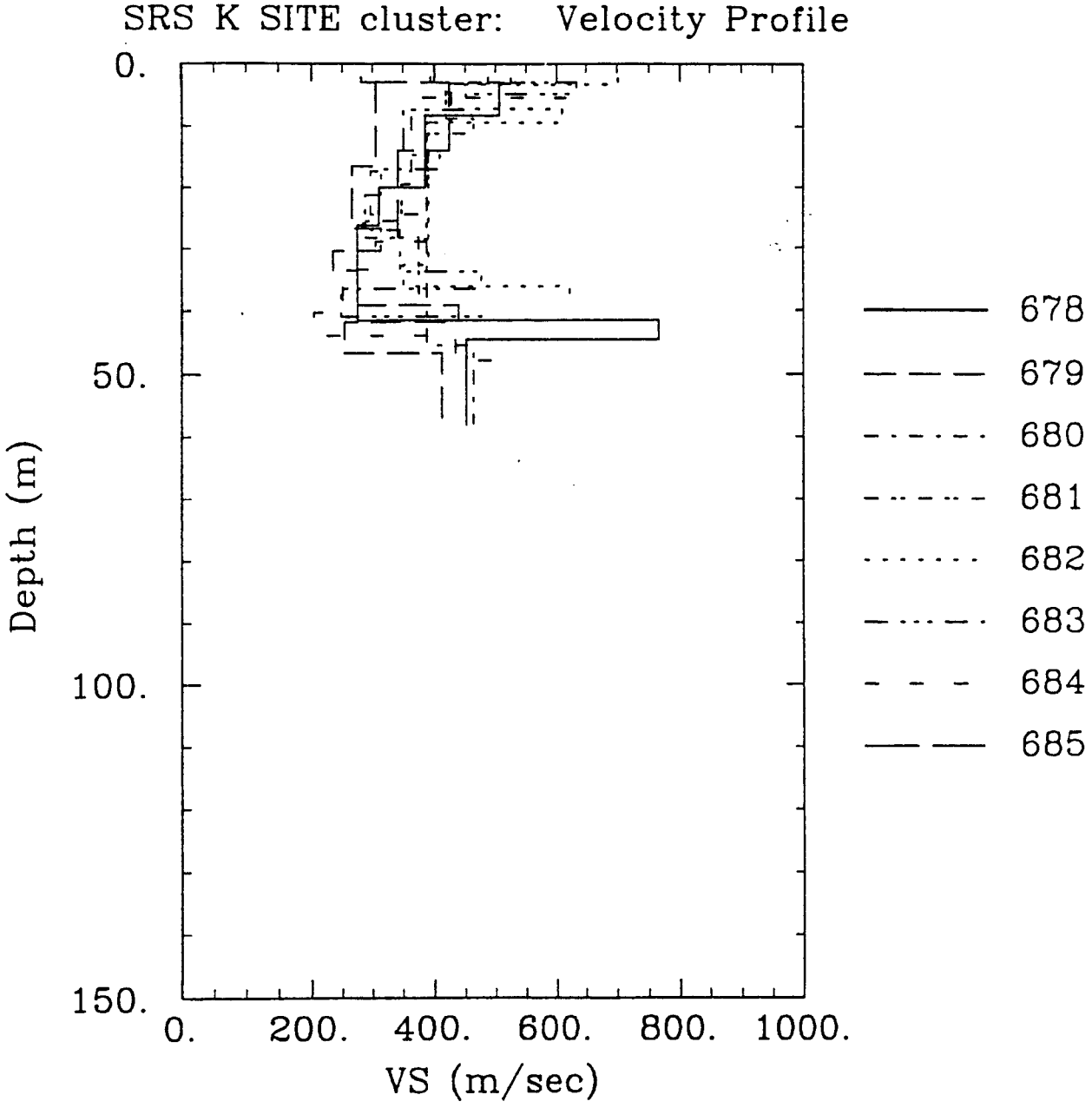
SRS K SITE cluster: Velocity Profile
0.
50.
100.
150.
Depth (m)
0.
200.
400.
600.
800.
1000.
VS (m/sec)
678
679
680
681
682
683
684
685

FIGURE 40-A.

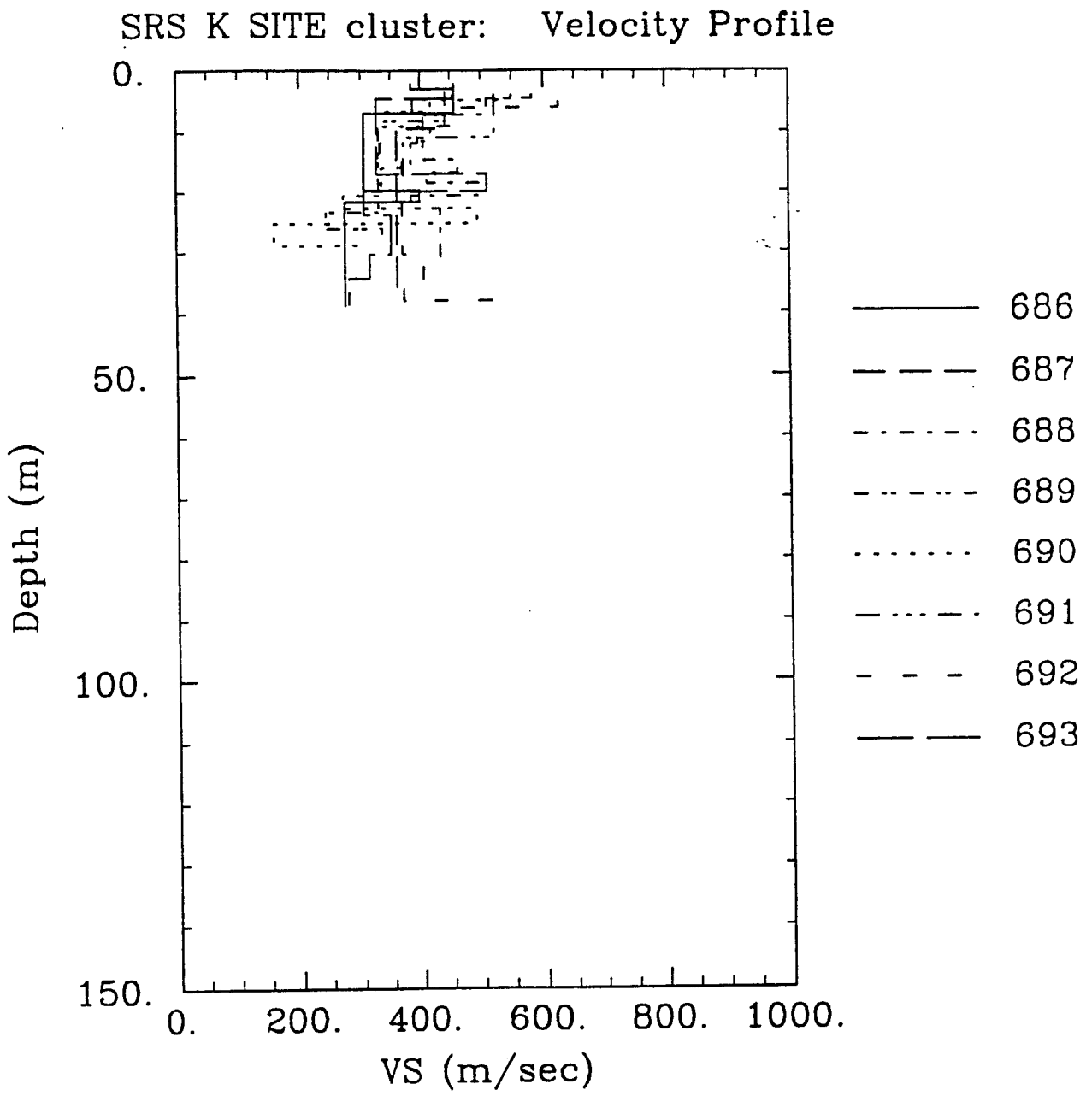
SRS K SITE cluster: Velocity Profile
0.
50.
100.
150.
Depth (m)
0.
200.
400.
600.
800.
1000.
VS (m/sec)
686
687
688
689
690
691
692
693

FIGURE 40-B.

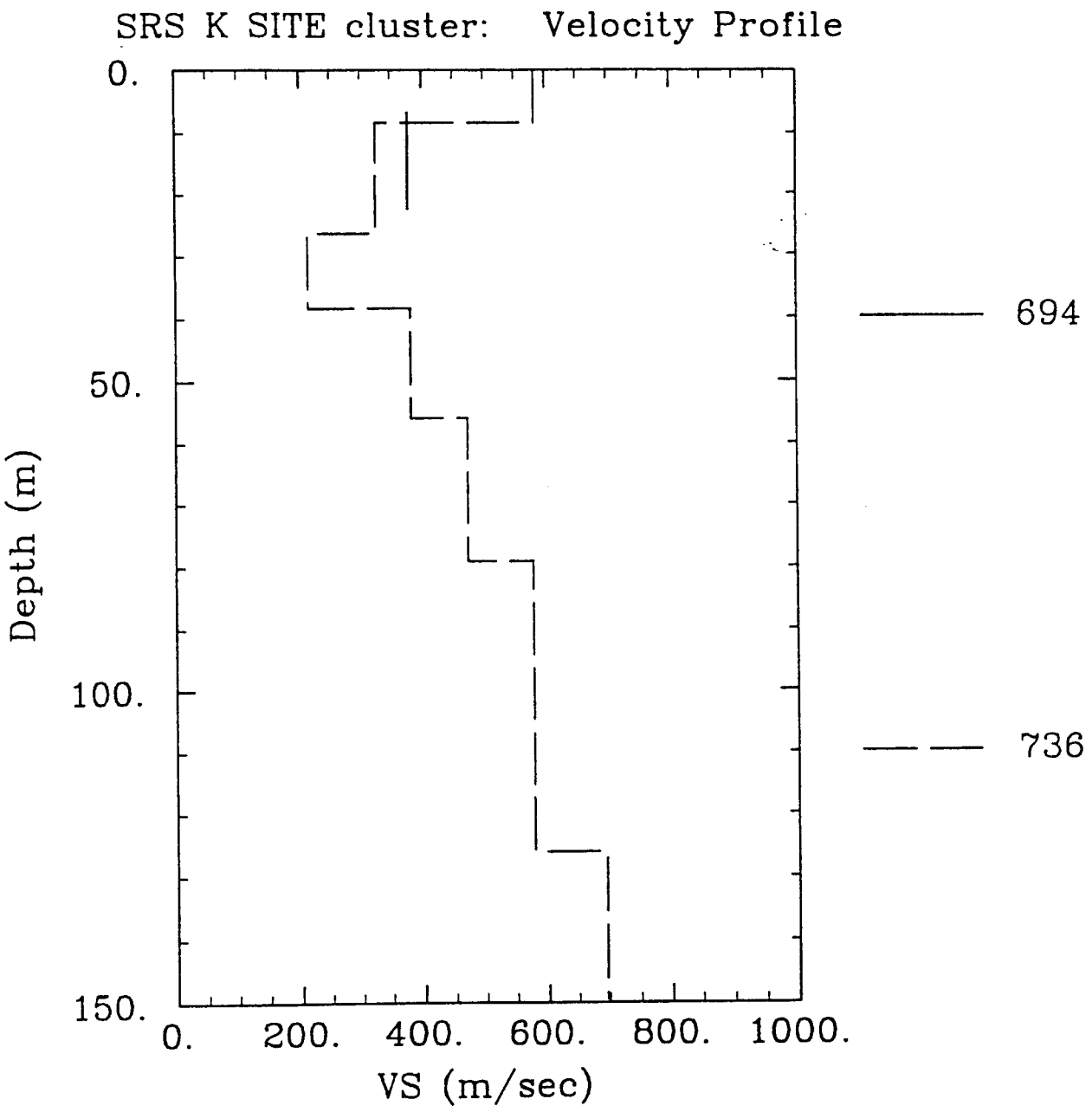
SRS K SITE cluster: Velocity Profile
0.
50.
100.
150.
Depth (m)
0.
200.
400.
600.
800.
1000.
VS (m/sec)
694
736

FIGURE 40-C.

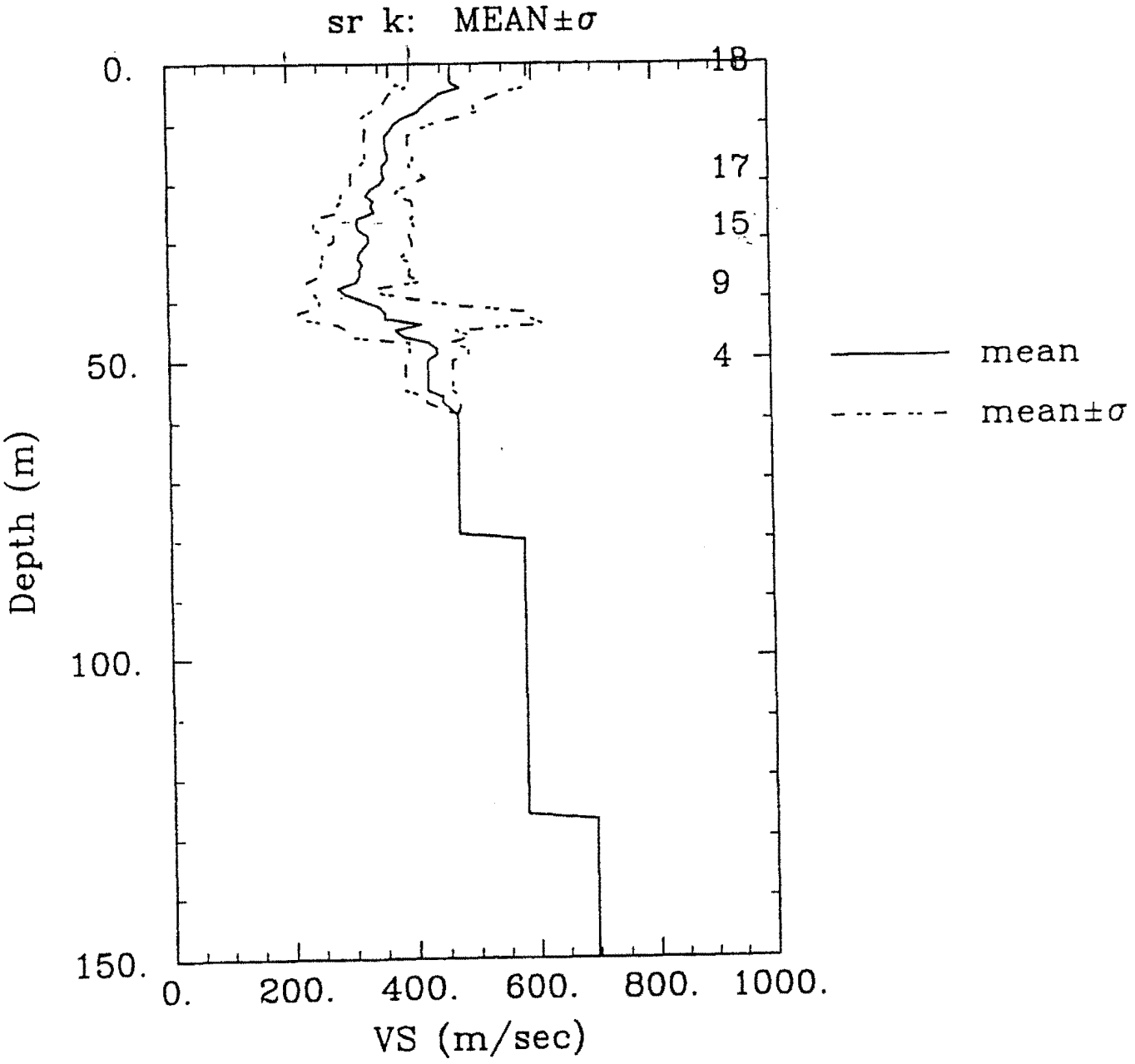
sr k: MEAN±σ
0.
50.
100.
150.
Depth (m)
18
17
15
9
4
0.
200.
400.
600.
800.
1000.
VS (m/sec)
mean
mean±σ

FIGURE 41.

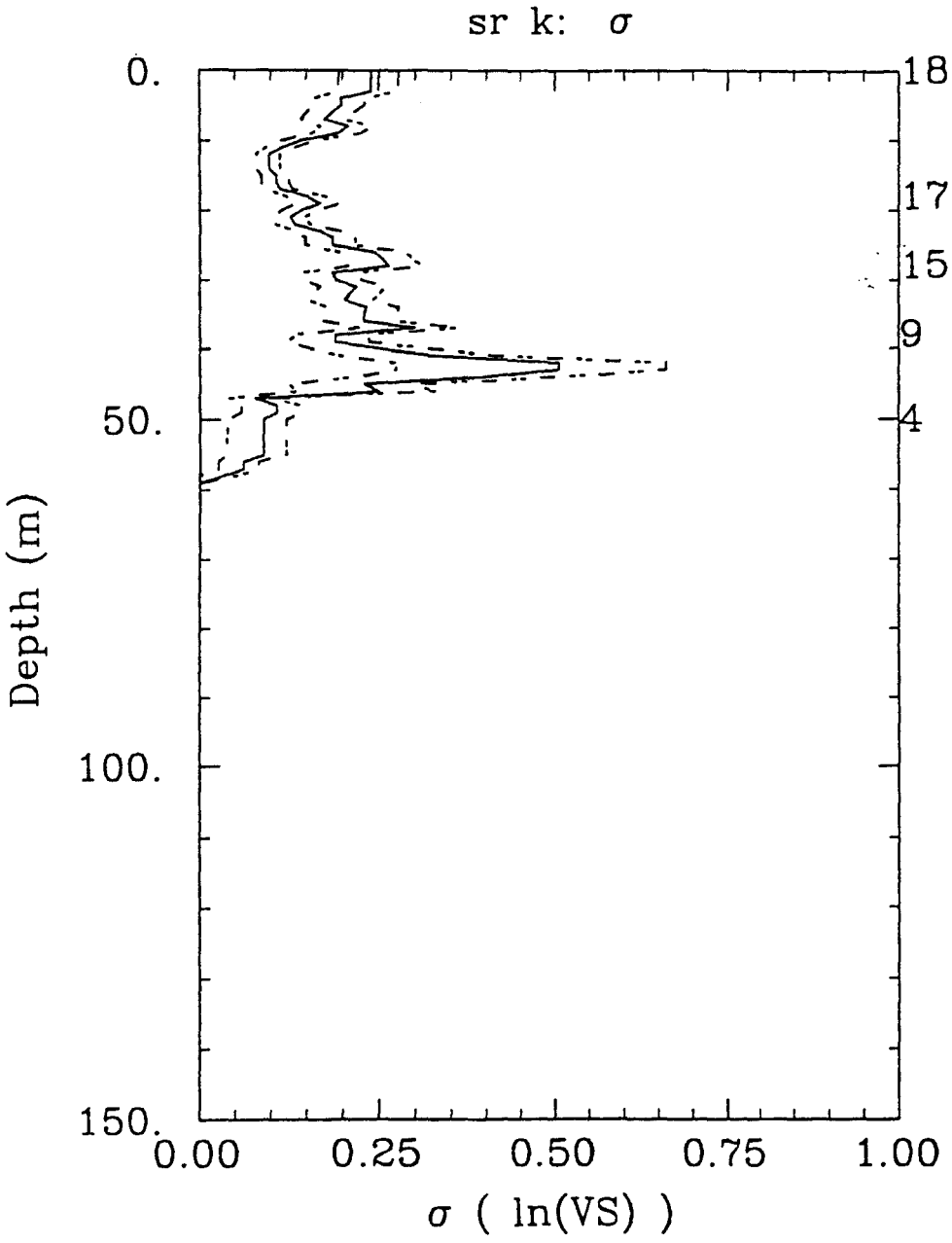

FIGURE 42.

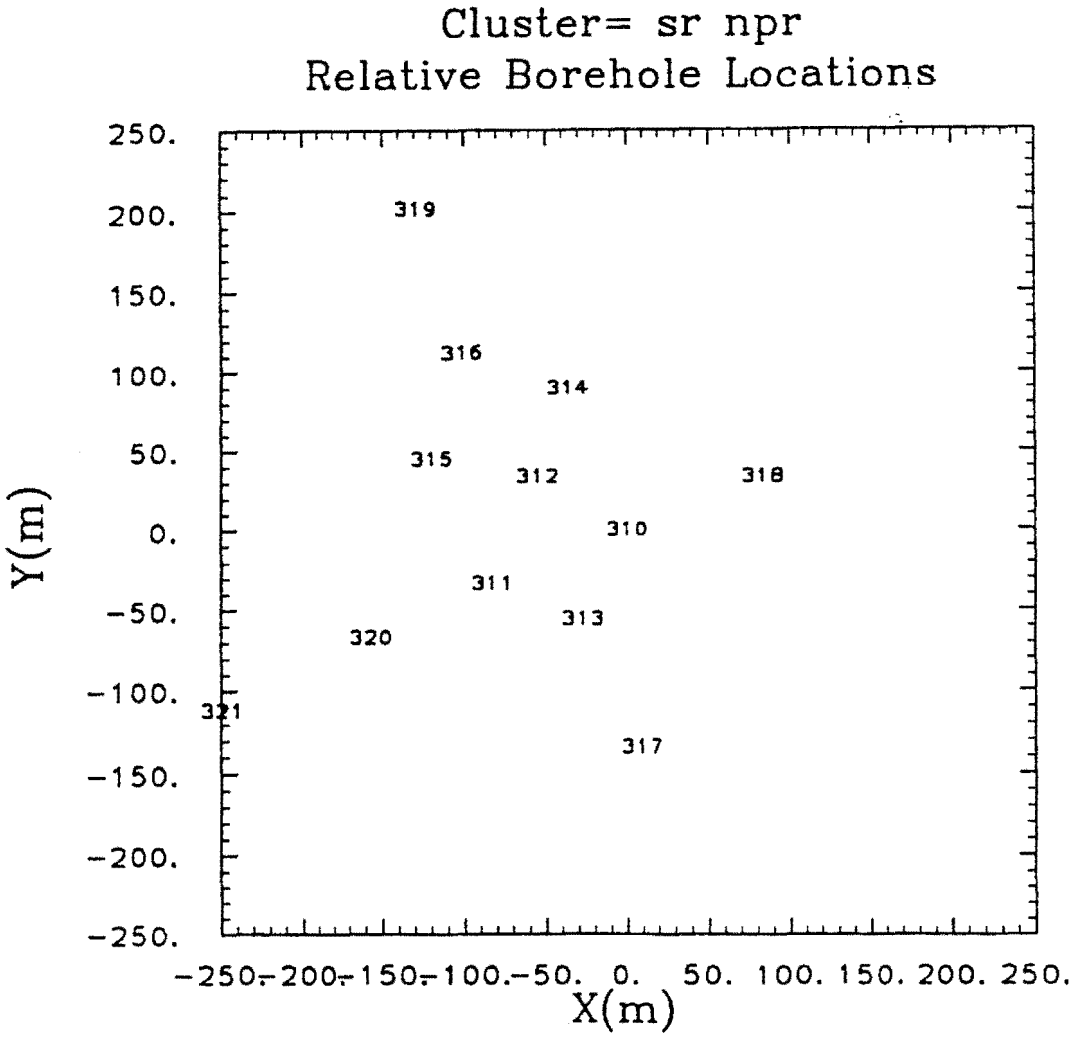
Cluster= sr npr
Relative Borehole Locations
250.
200.
150.
100.
50.
0.
-50.
-100.
-150.
-200.
-250.
Y(m)
319
316
314
315
312
318
310
311
313
320
321
317
-250.-200.-150.-100.-50. 0. 50. 100. 150. 200. 250.
X(m)

FIGURE 43.

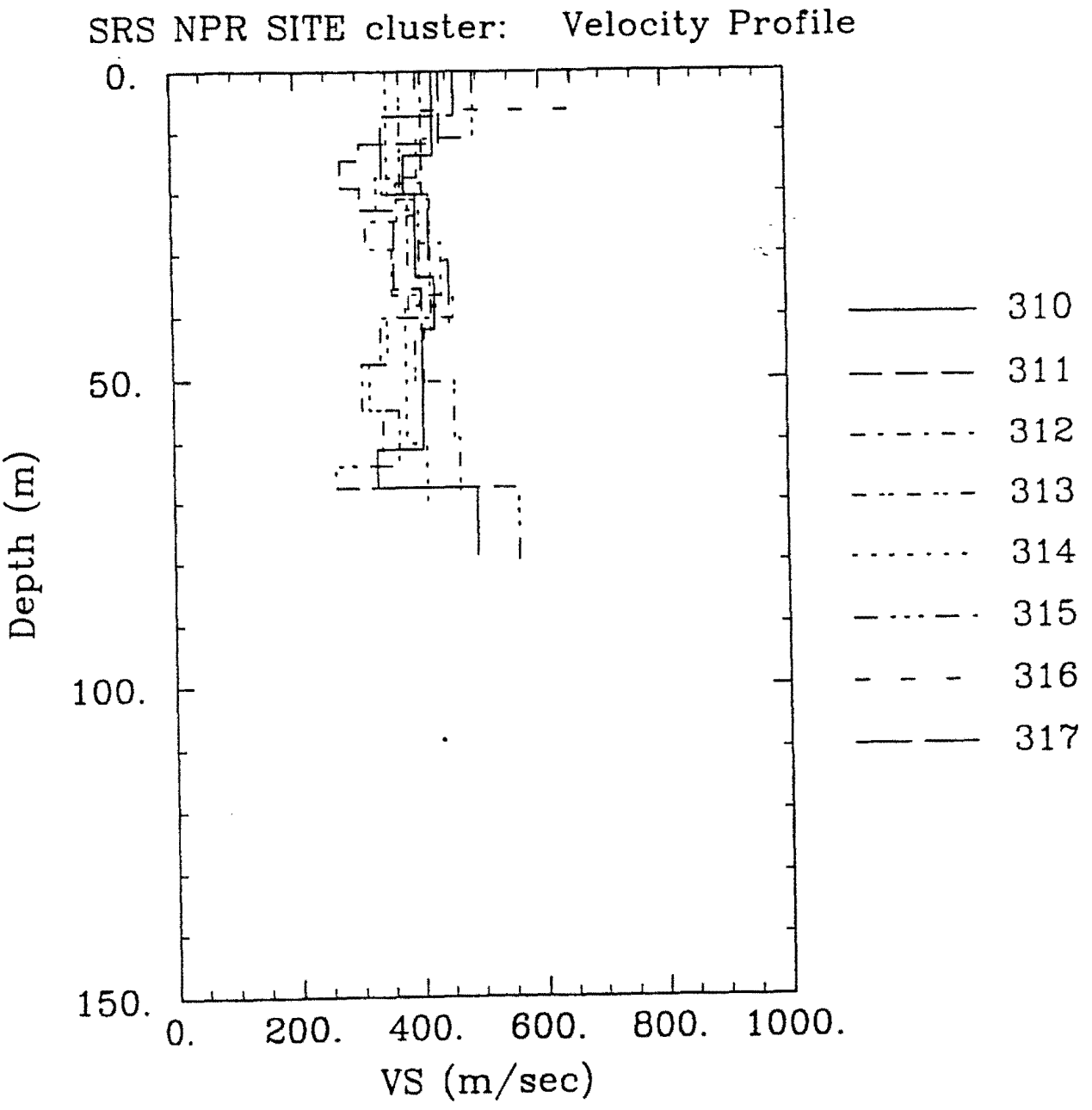
SRS NPR SITE cluster: Velocity Profile
0.
50.
100.
150.
Depth (m)
0.
200.
400.
600.
800.
1000.
VS (m/sec)
310
311
312
313
314
315
316
317

FIGURE 44-A.

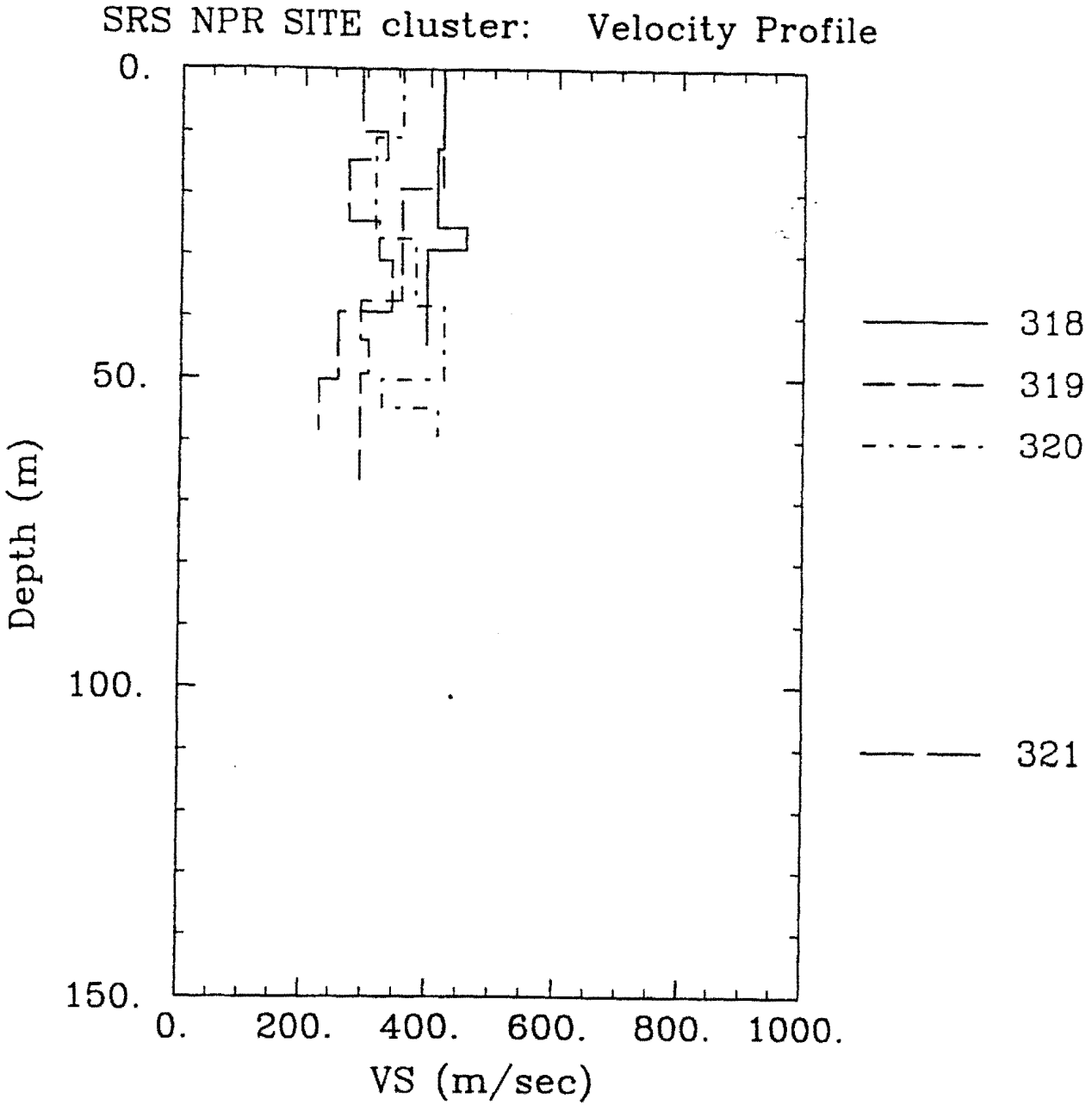
SRS NPR SITE cluster: Velocity Profile
0.
50.
100.
150.
Depth (m)
0.
200.
400.
600.
800.
1000.
VS (m/sec)
318
319
320
321

FIGURE 44-B.

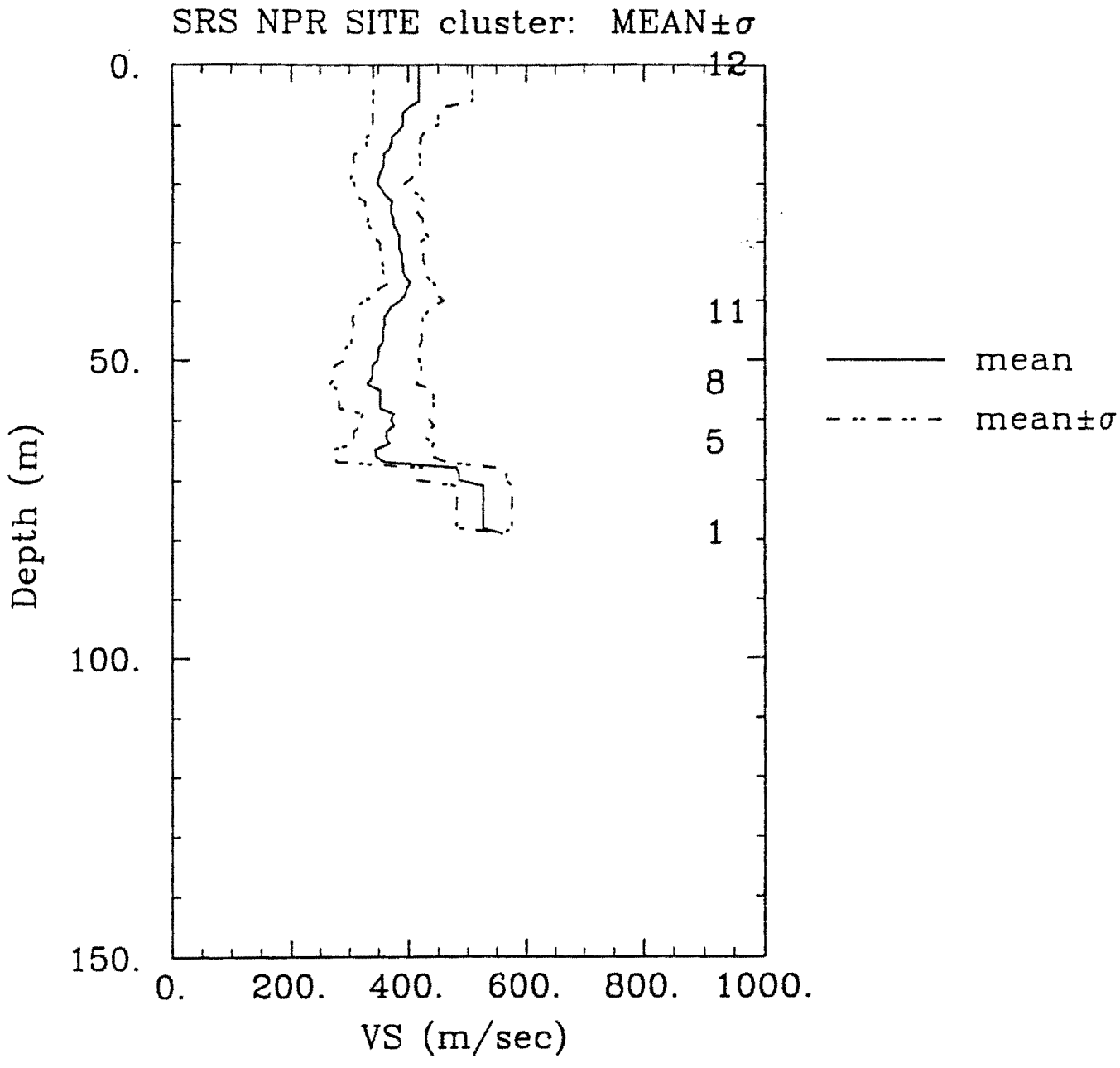
SRS NPR SITE cluster: MEAN±σ
0.
50.
100.
150.
Depth (m)
0.
200.
400.
600.
800.
1000.
VS (m/sec)
12
11
8
5
1
mean
mean±σ

FIGURE 45.

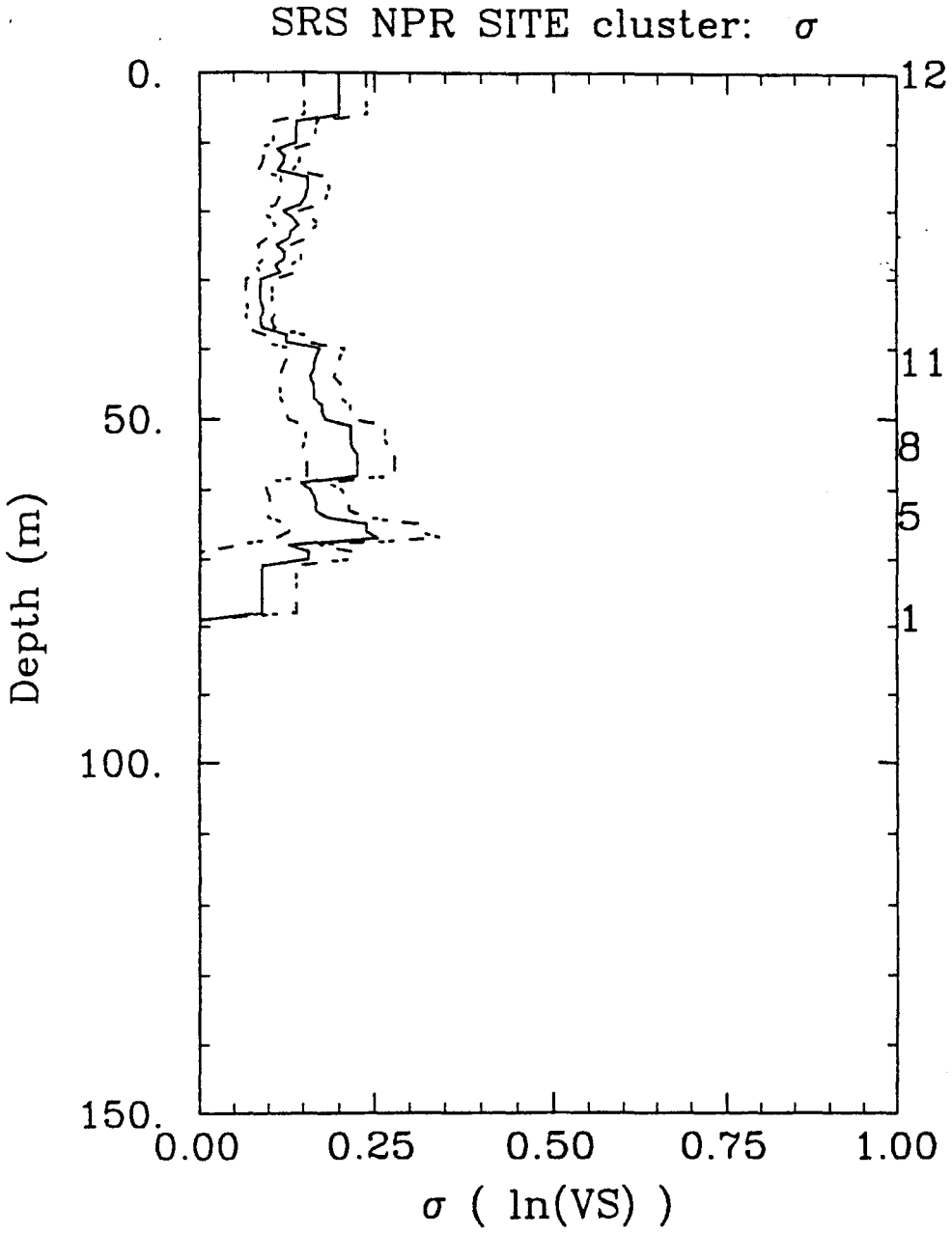
SRS NPR SITE cluster: σ
0.
50.
100.
150.
Depth (m)
12
11
8
5
1
0.00
0.25
0.50
0.75
1.00
σ (ln(VS))

FIGURE 46.

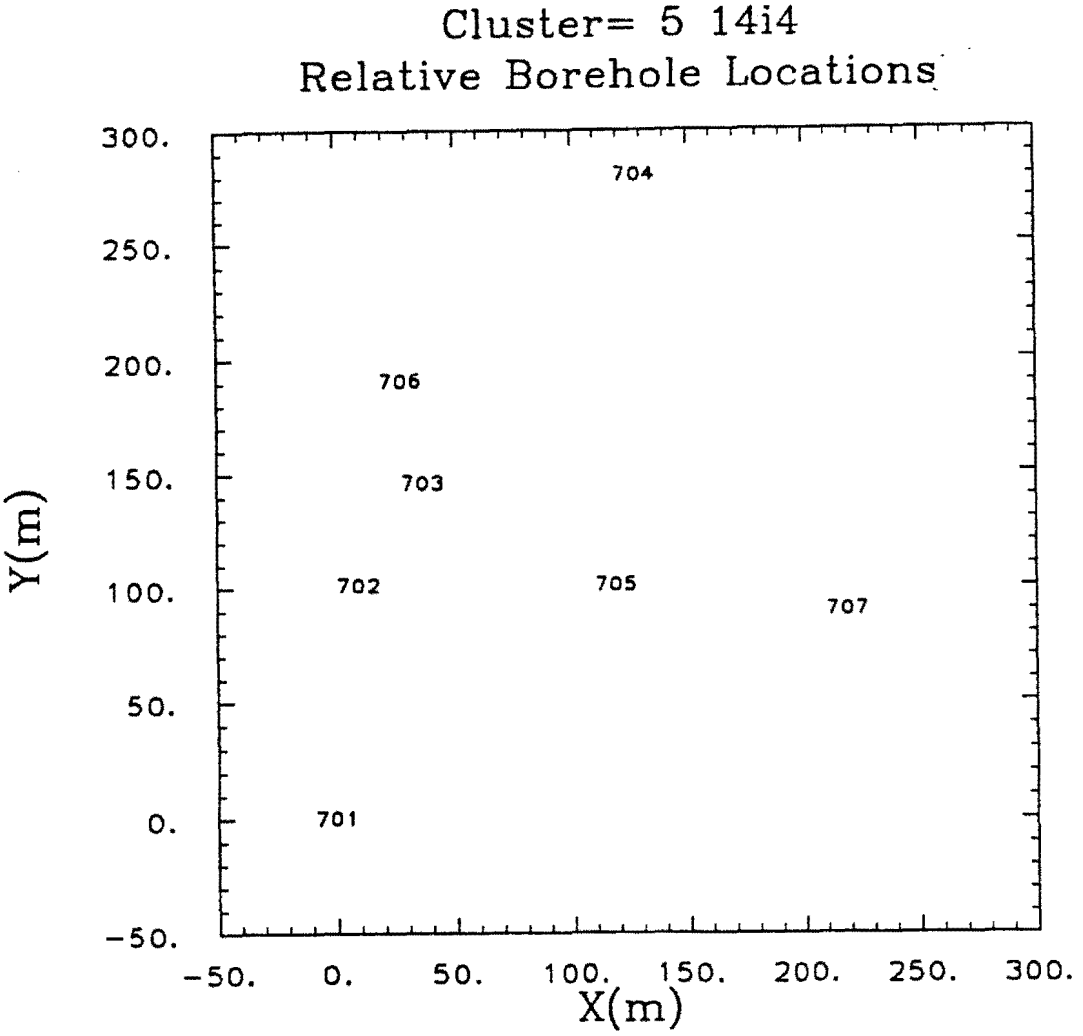
Cluster= 5 14i4
Relative Borehole Locations
300.
250.
200.
150.
100.
50.
0.
-50.
Y(m)
704
706
703
702
705
707
701
-50.
0.
50.
100.
150.
200.
250.
300.
X(m)

FIGURE 47.

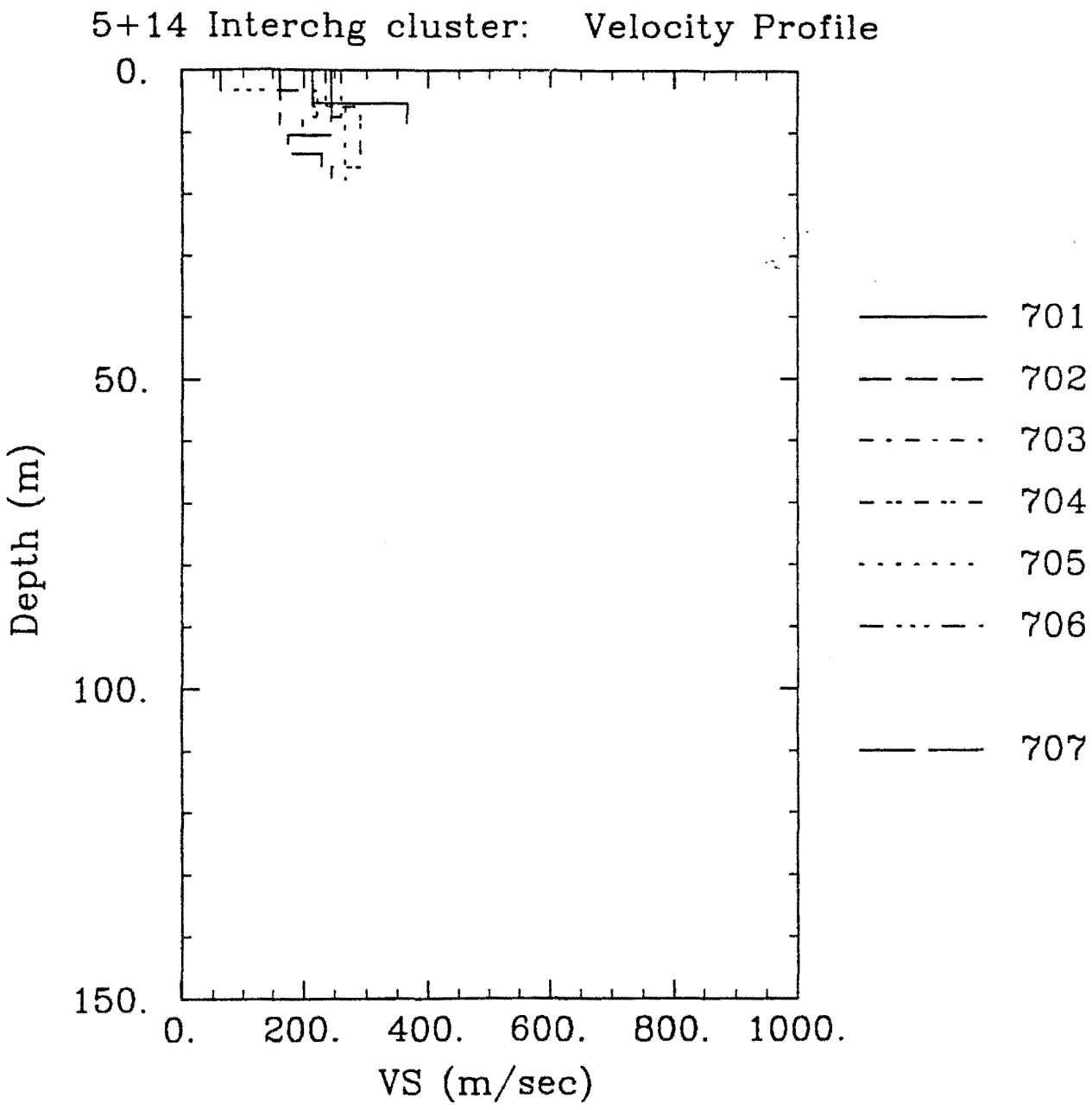
5+14 Interchg cluster: Velocity Profile
0.
50.
100.
150.
Depth (m)
0.
200.
400.
600.
800.
1000.
VS (m/sec)
701
702
703
704
705
706
707

FIGURE 48.

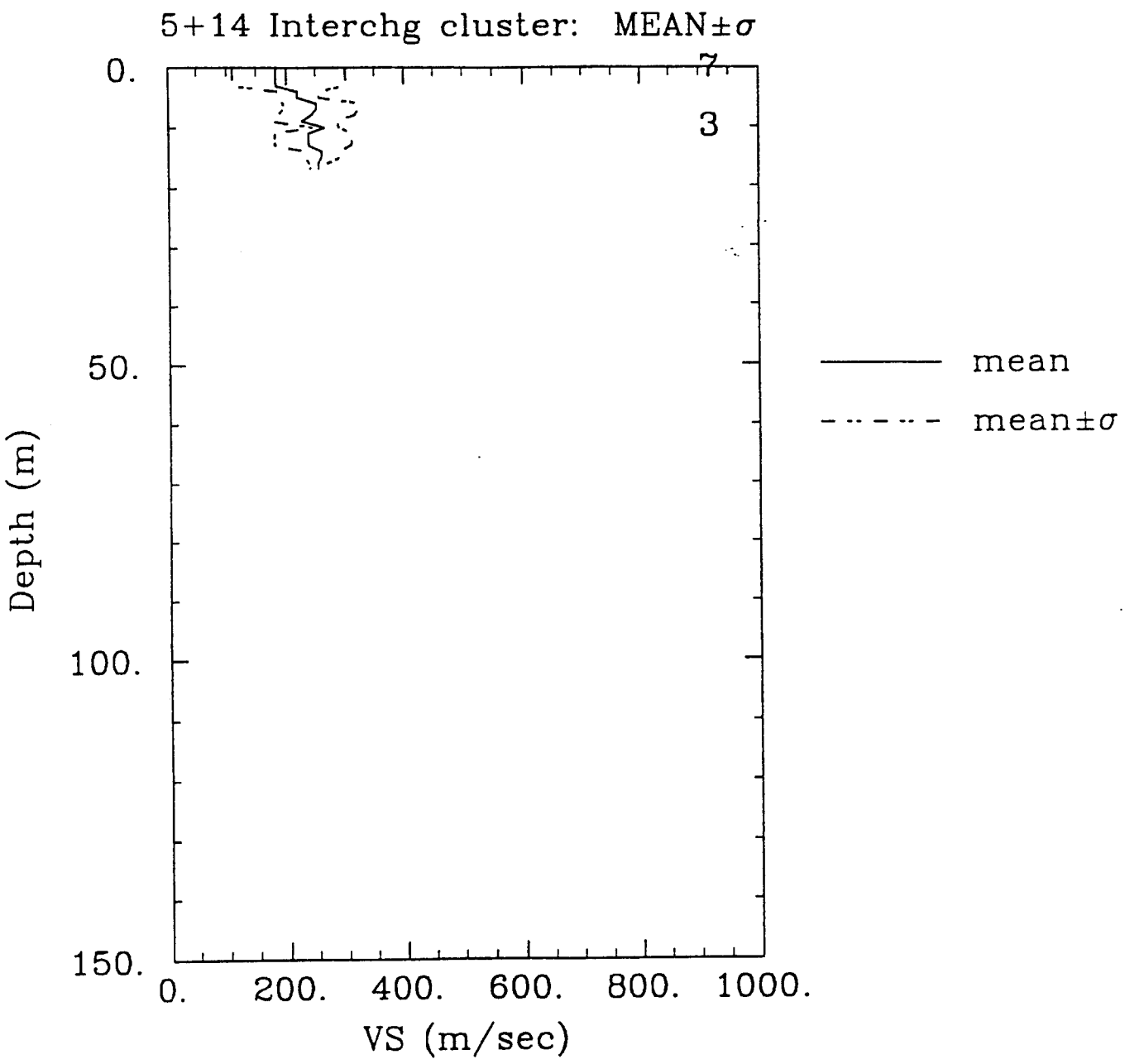
5+14 Interchg cluster: MEAN±σ
0.
50.
100.
150.
Depth (m)
0.
200.
400.
600.
800.
1000.
VS (m/sec)
7
3
mean
mean±σ

FIGURE 49.

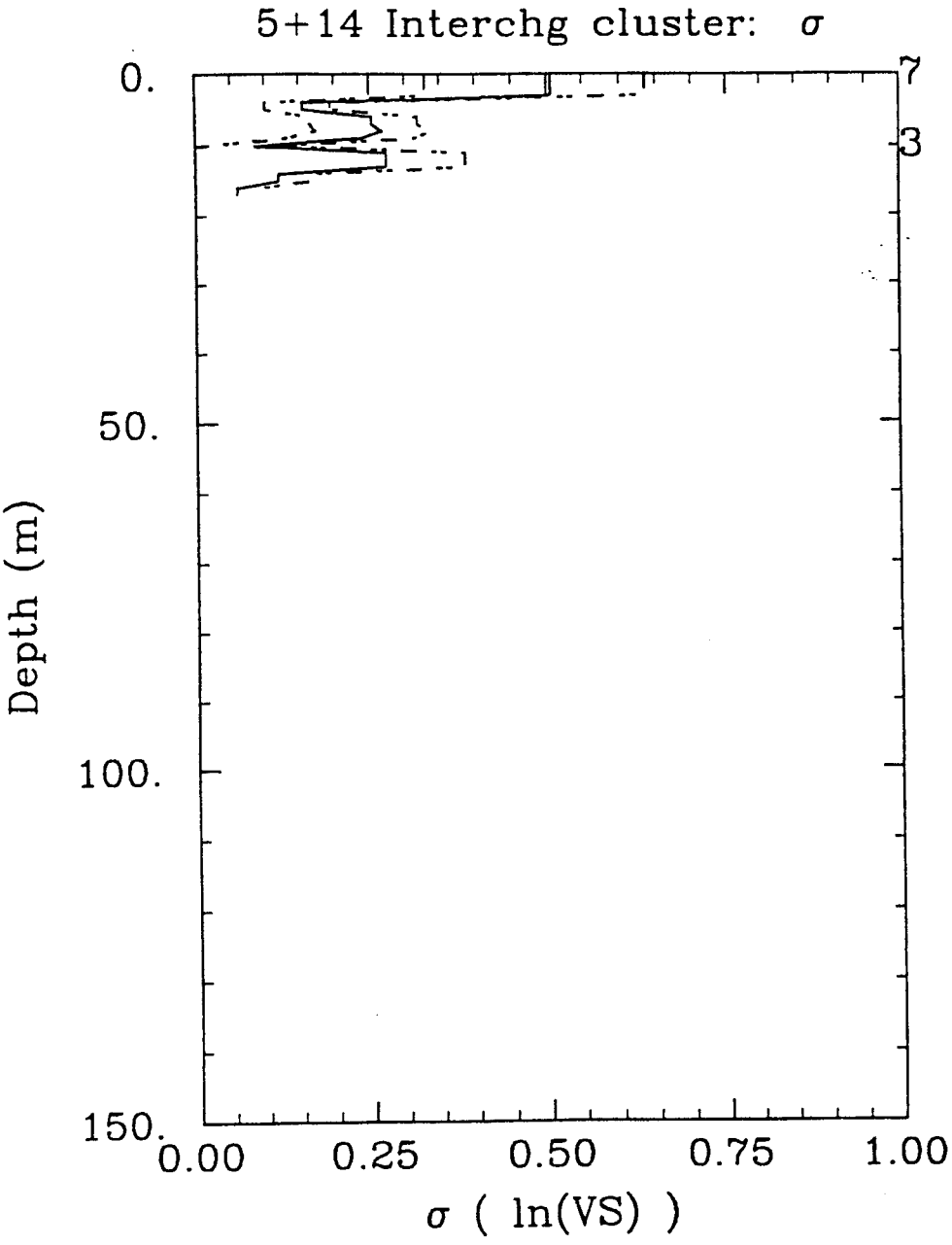
5+14 Interchg cluster: σ
0.
50.
100.
150.
Depth (m)
7
3
0.00
0.25
0.50
0.75
1.00
σ (ln(VS))

FIGURE 50.

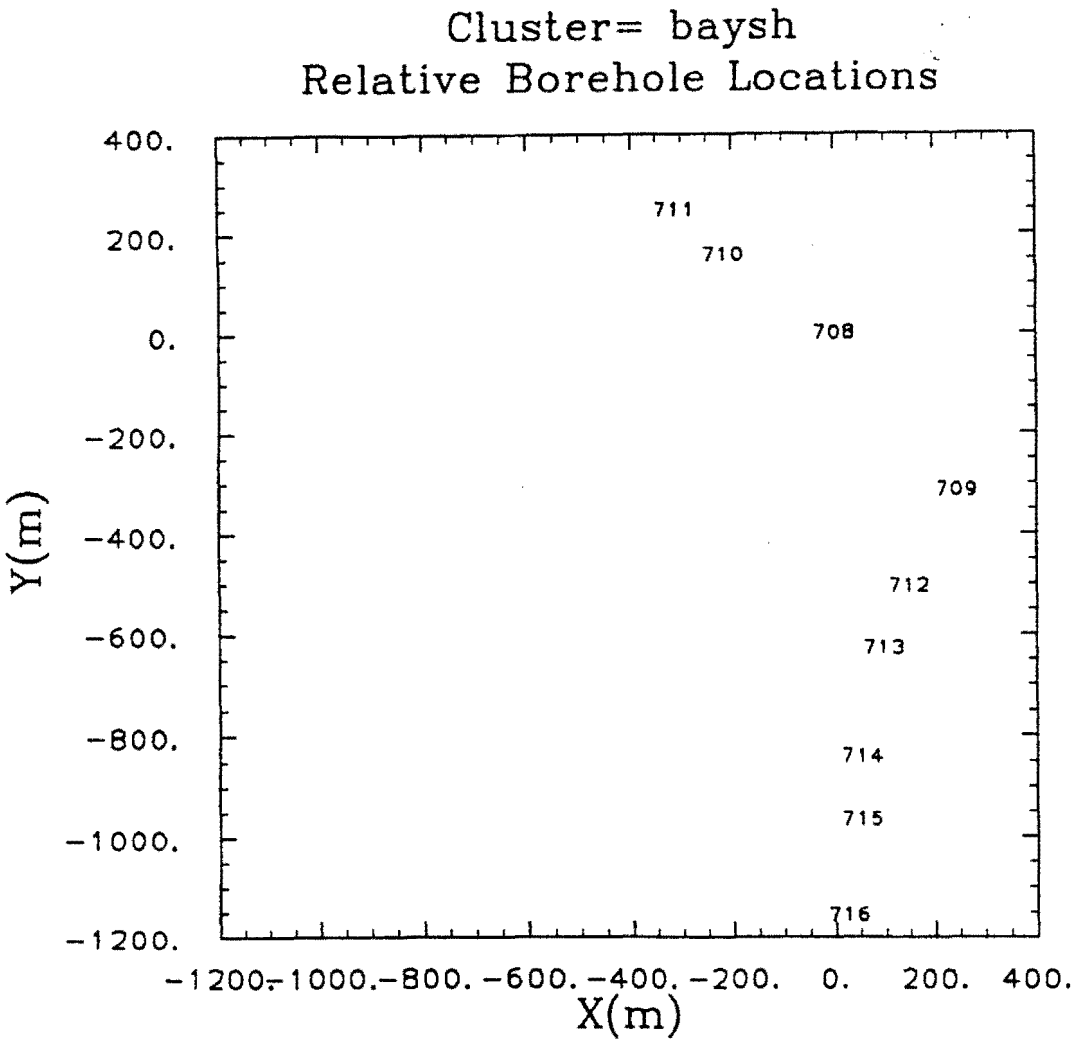
Cluster= baysh
Relative Borehole Locations
400.
200.
0.
-200.
-400.
-600.
-800.
-1000.
-1200.
Y(m)
711
710
708
709
712
713
714
715
716
-1200.-1000.-800.-600.-400.-200.
0.
200.
400.
X(m)

FIGURE 51.

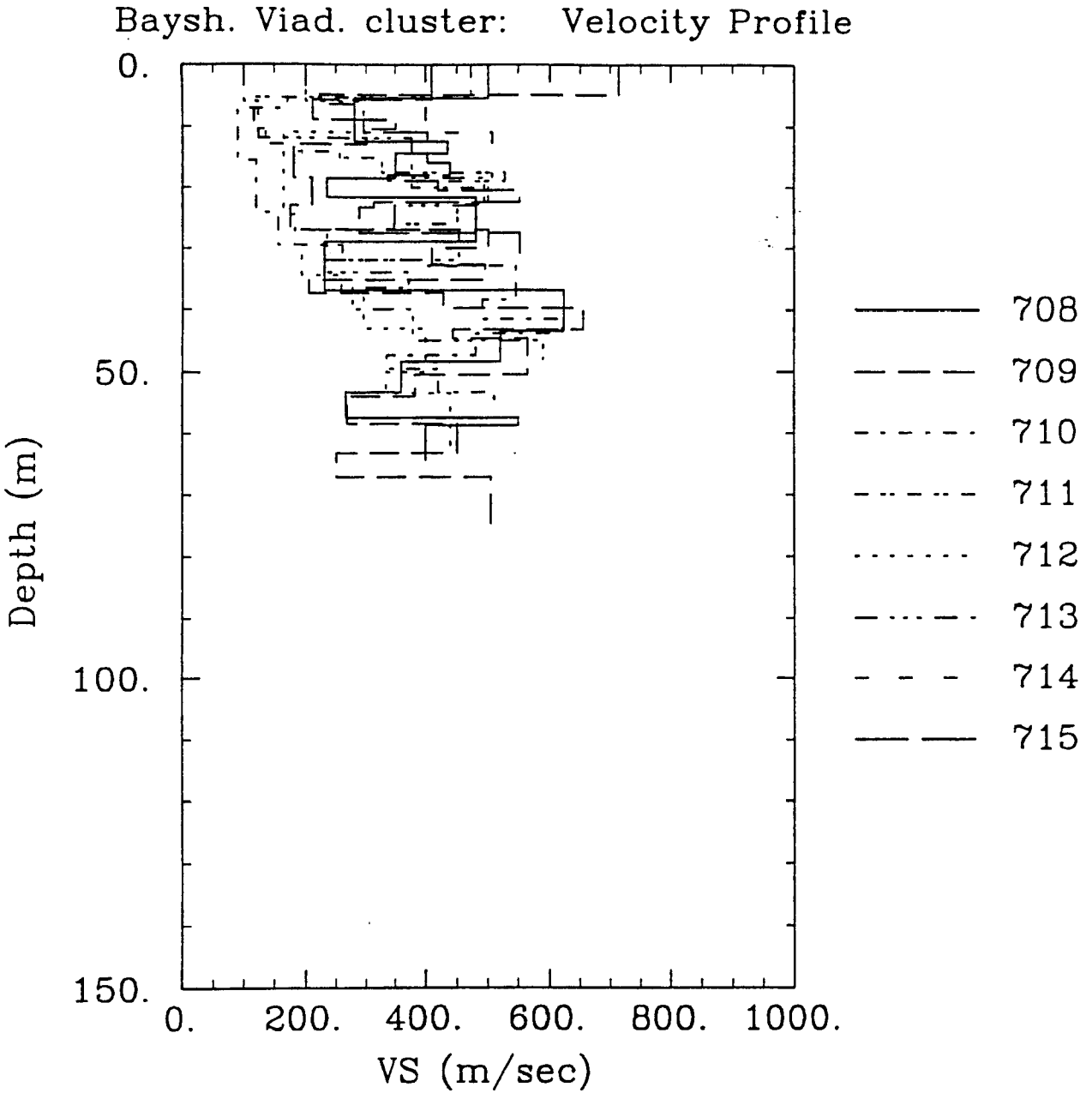
Baysh. Viad. cluster: Velocity Profile
0.
50.
100.
150.
Depth (m)
0.
200.
400.
600.
800.
1000.
VS (m/sec)
708
709
710
711
712
713
714
715

FIGURE 52-A.

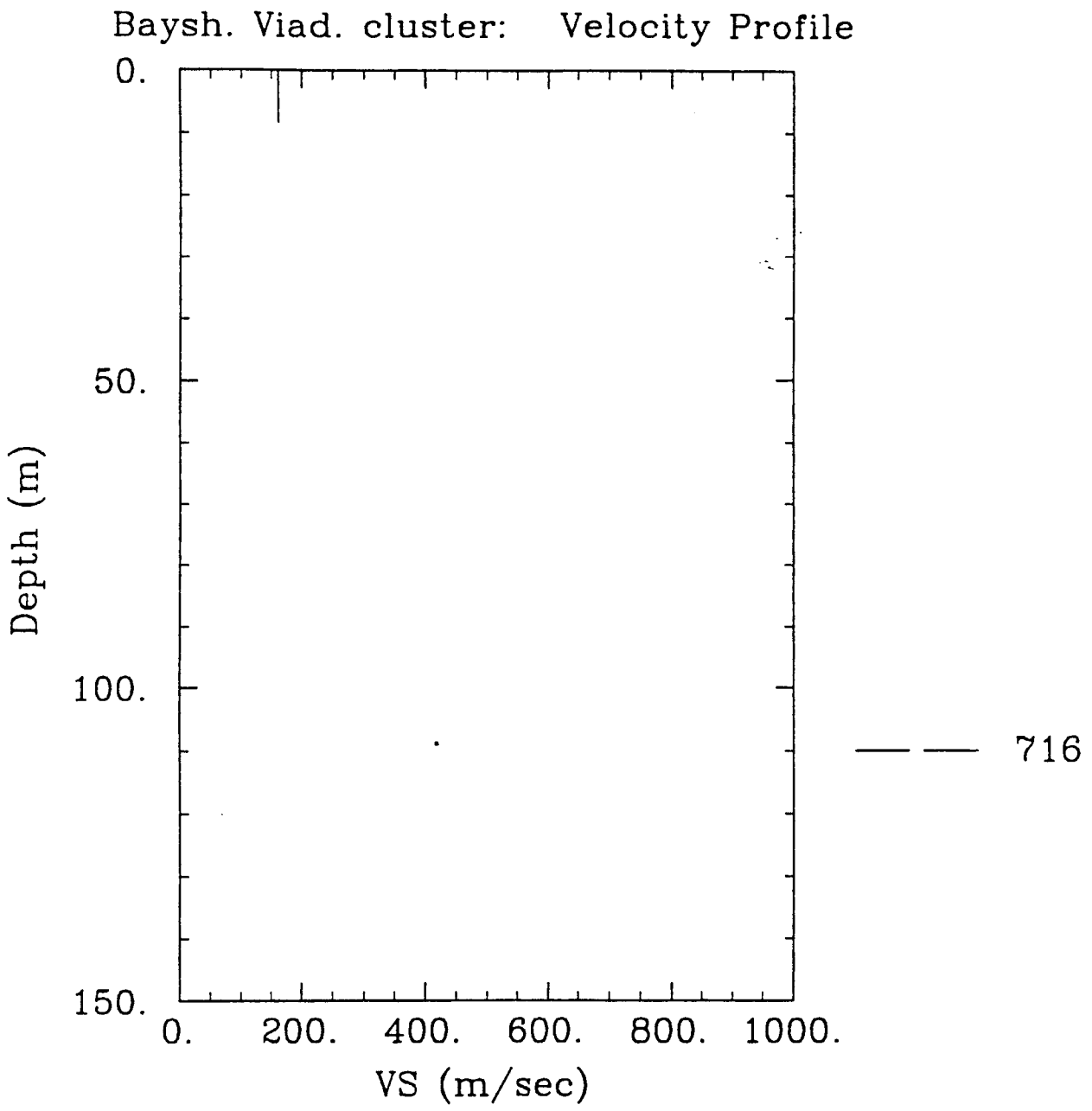
Baysh. Viad. cluster: Velocity Profile
0.
50.
100.
150.
Depth (m)
0.
200.
400.
600.
800.
1000.
VS (m/sec)
716

FIGURE 52-B.

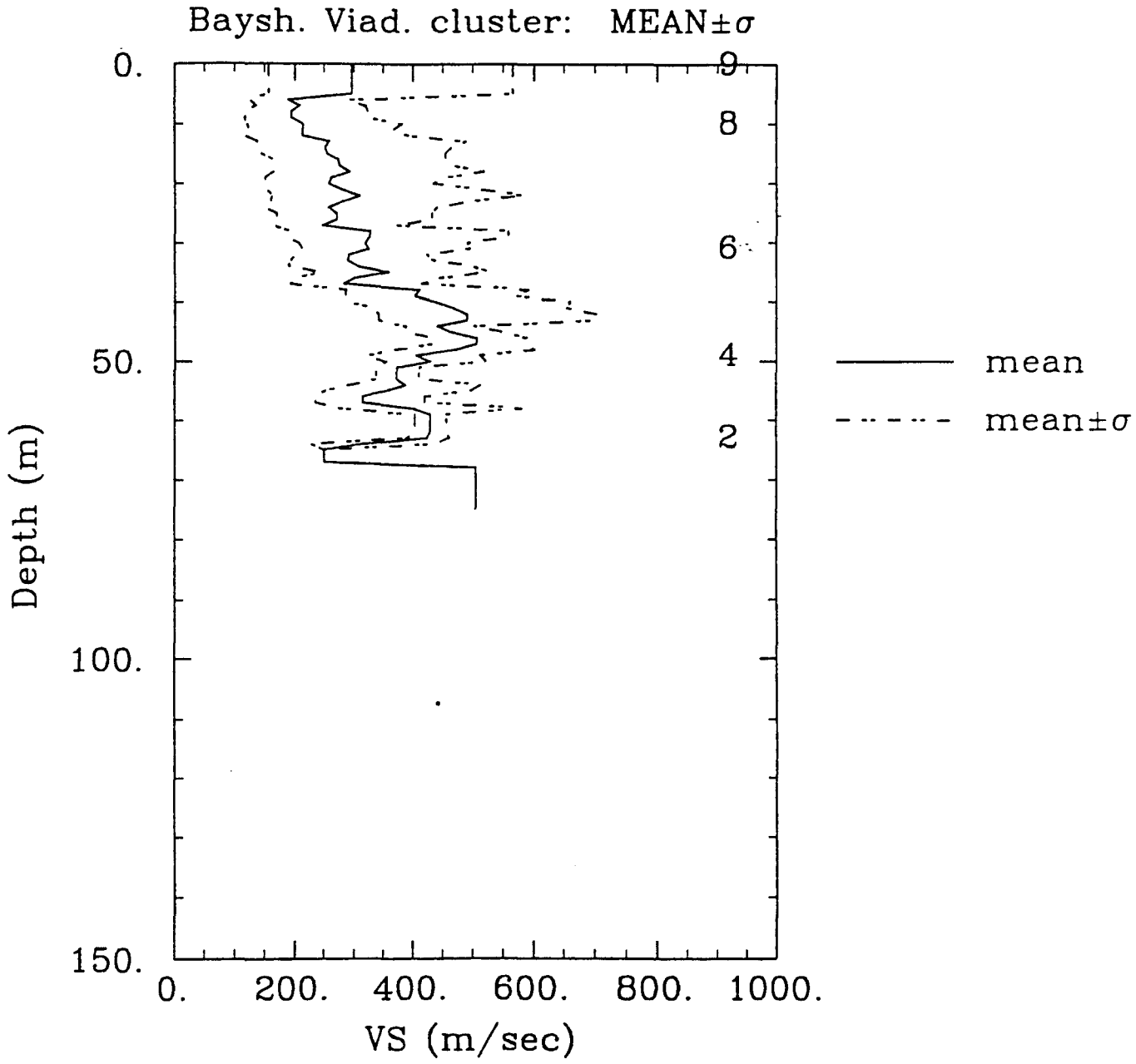
Baysh. Viad. cluster: MEAN±σ
0.
50.
100.
150.
Depth (m)
0.
200.
400.
600.
800.
1000.
VS (m/sec)
10
8
6
4
2
mean
mean±σ

FIGURE 53.

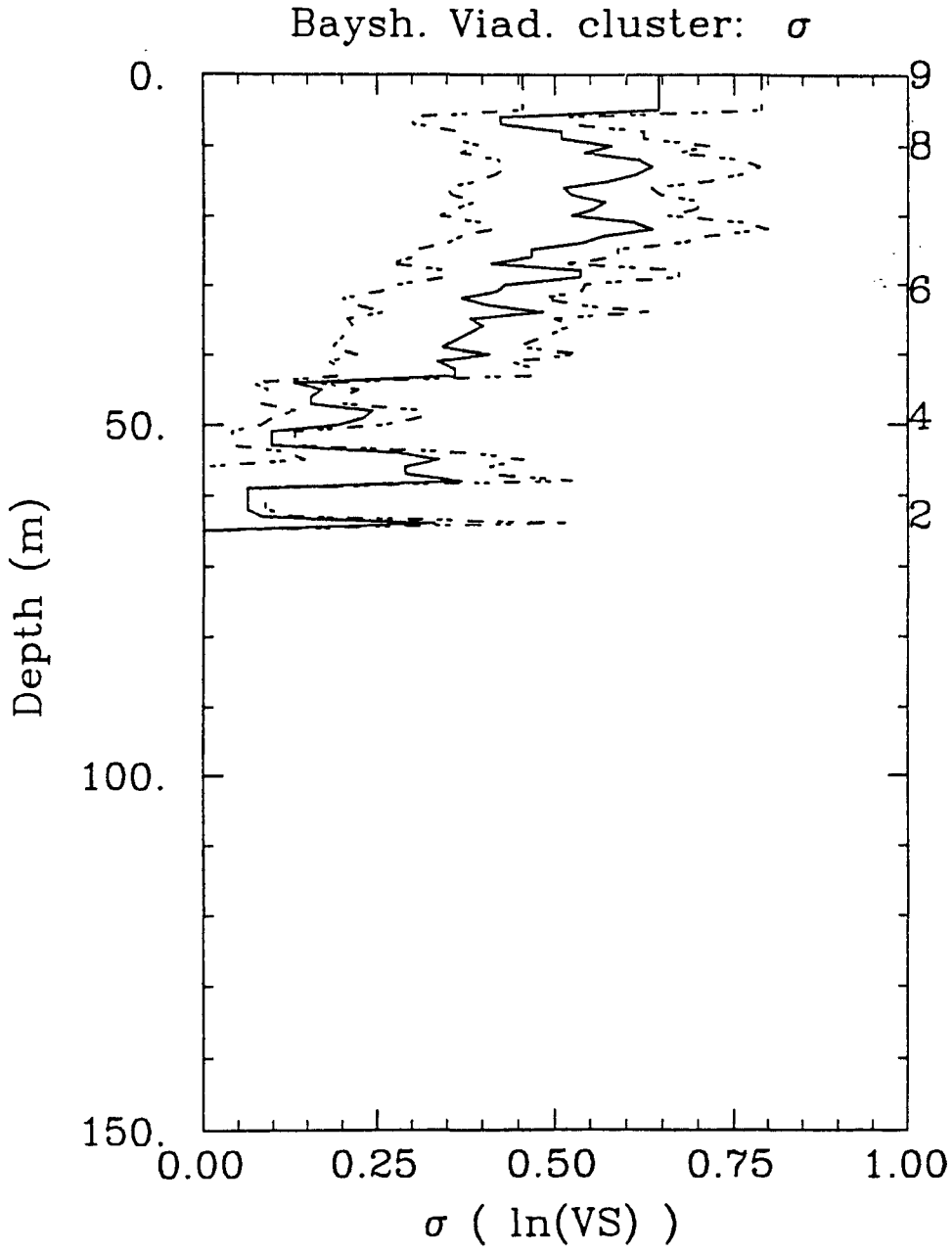
Baysh. Viad. cluster: σ
0.
50.
100.
150.
Depth (m)
9
8
6
4
2
0.00
0.25
0.50
0.75
1.00
σ (ln(VS))

FIGURE 54.

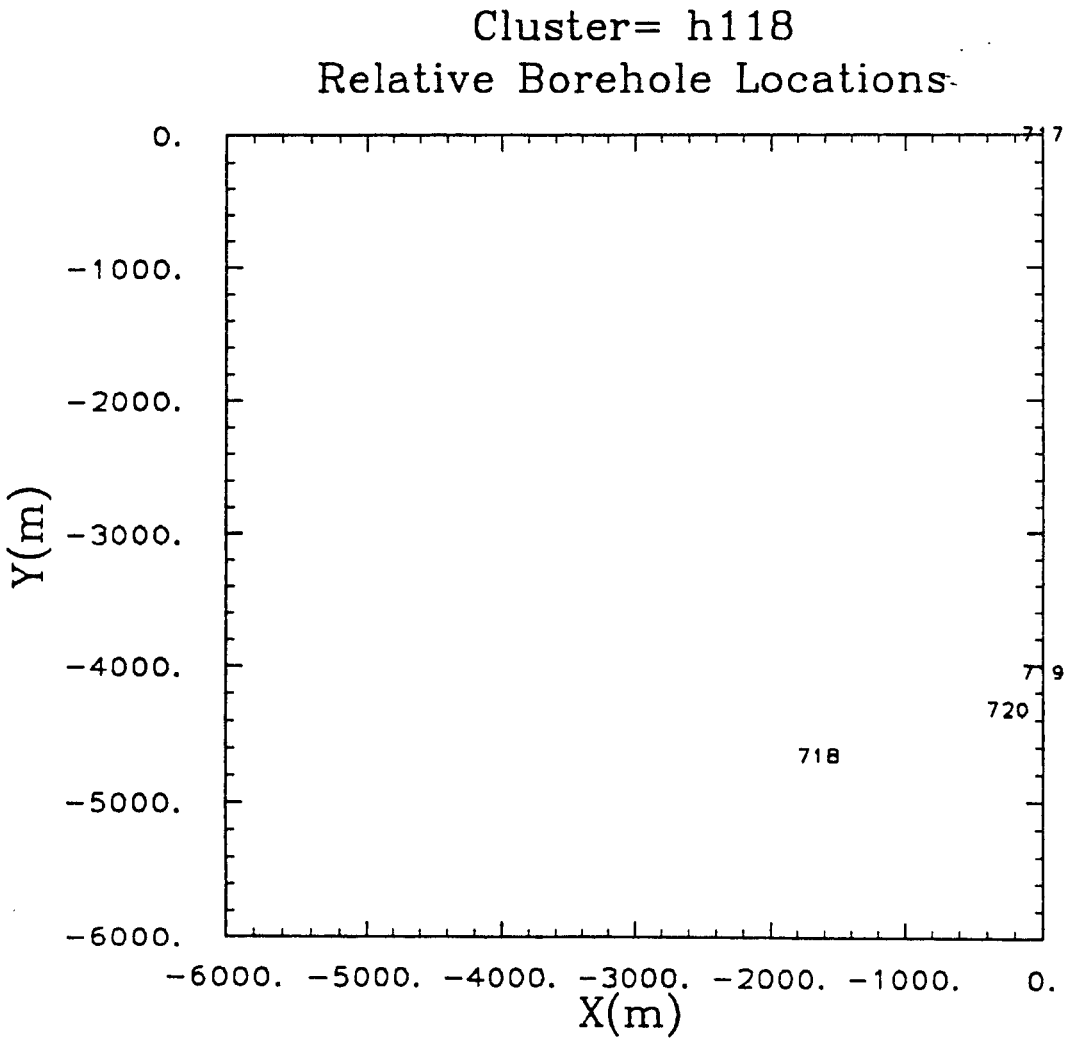
Cluster= h118
Relative Borehole Locations
0.
-1000.
-2000.
-3000.
-4000.
-5000.
-6000.
Y(m)
-6000. -5000. -4000. -3000. -2000. -1000. 0.
X(m)
717
719
720
718

FIGURE 55.

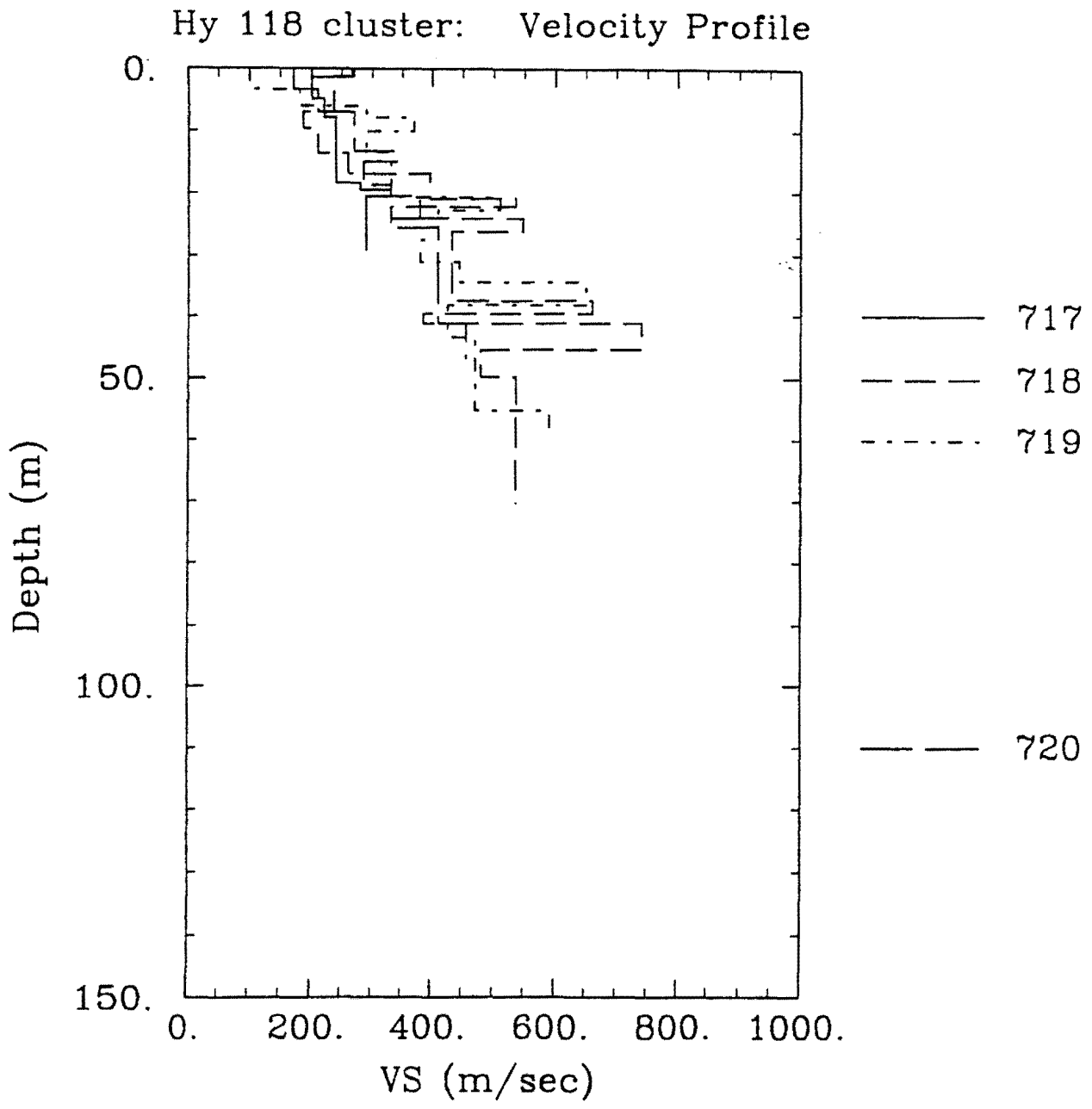
Hy 118 cluster: Velocity Profile
0.
50.
100.
150.
Depth (m)
0.
200.
400.
600.
800.
1000.
VS (m/sec)
717
718
719
720

FIGURE 56.

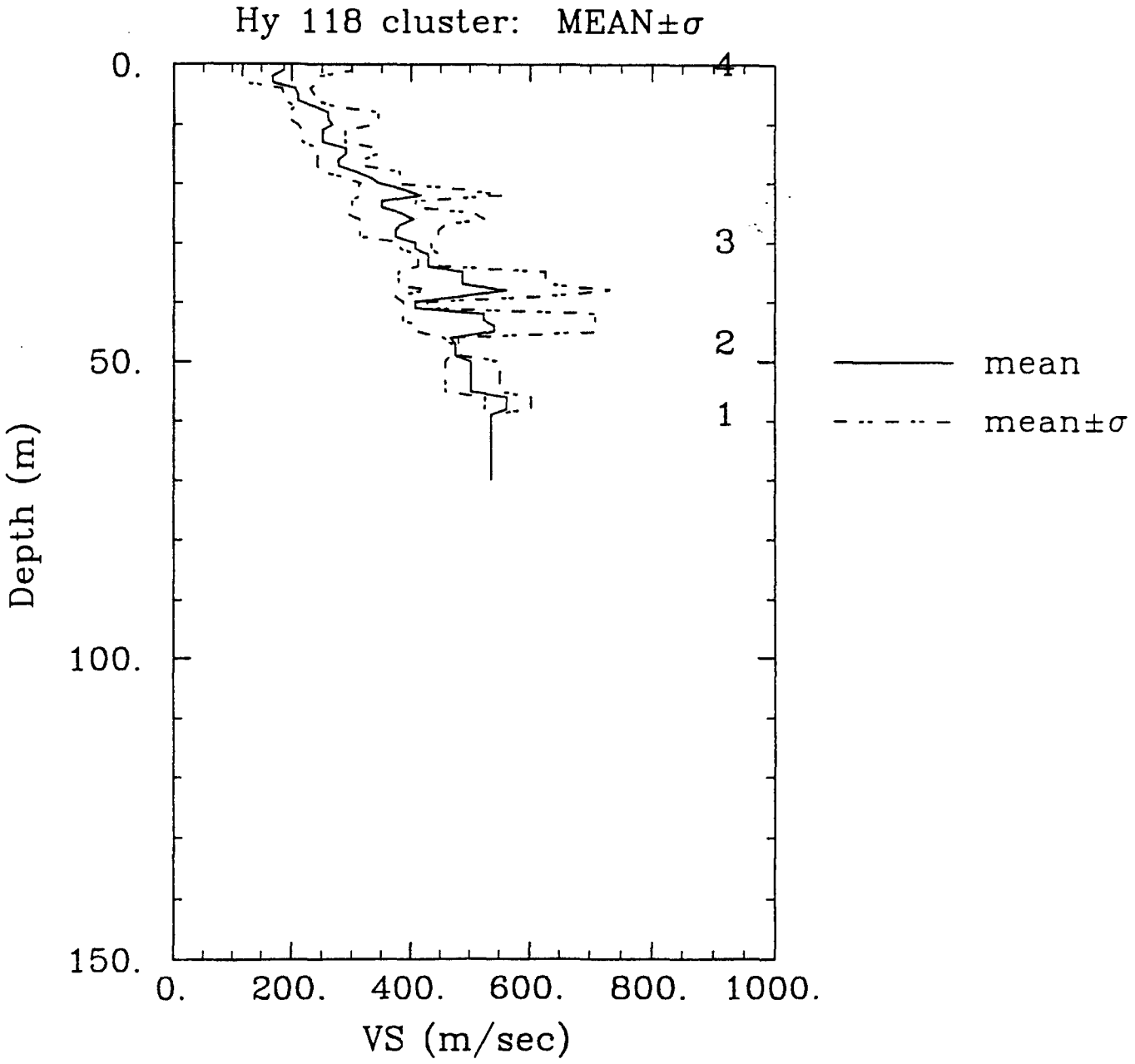
Hy 118 cluster: MEAN±σ
0.
50.
100.
150.
Depth (m)
0.
200.
400.
600.
800.
1000.
VS (m/sec)
4
3
2
1
mean
mean±σ

FIGURE 57.

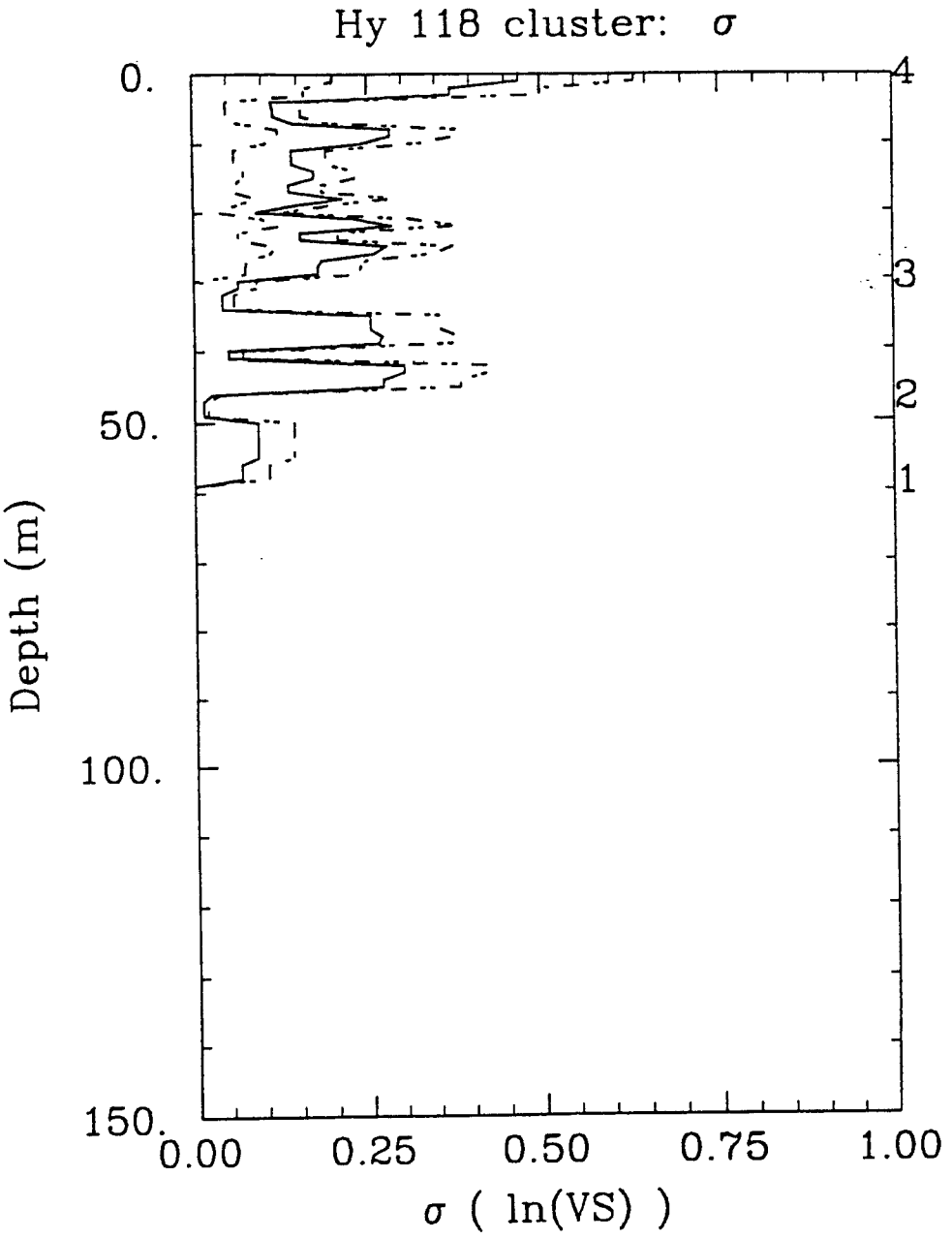
Hy 118 cluster: σ
0.
50.
100.
150.
Depth (m)
0.00
0.25
0.50
0.75
1.00
σ (ln(VS))
4
3
2
1

FIGURE 58.

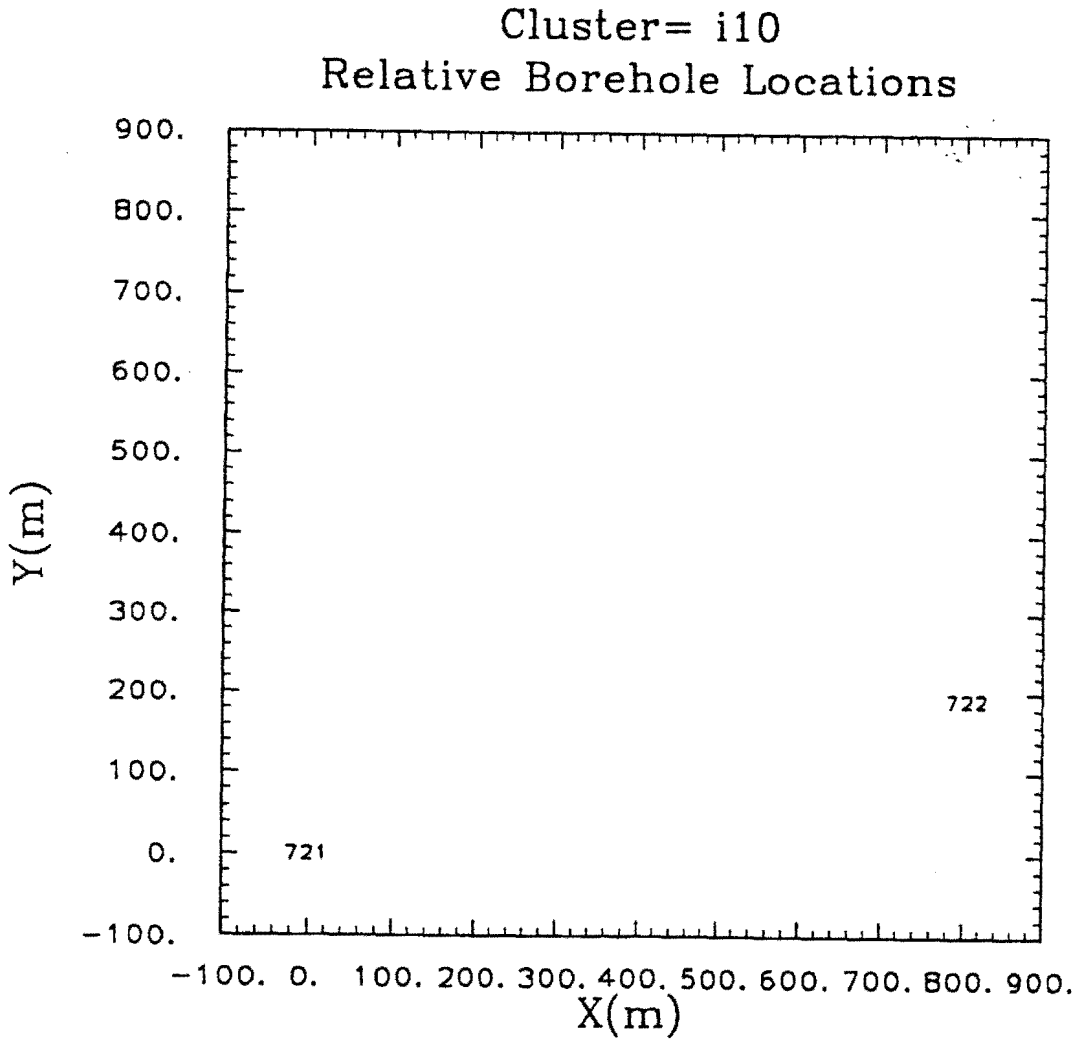
Cluster= i10
Relative Borehole Locations
900.
800.
700.
600.
500.
400.
300.
200.
100.
0.
-100.
Y(m)
721
722
-100. 0. 100. 200. 300. 400. 500. 600. 700. 800. 900.
X(m)

FIGURE 59.

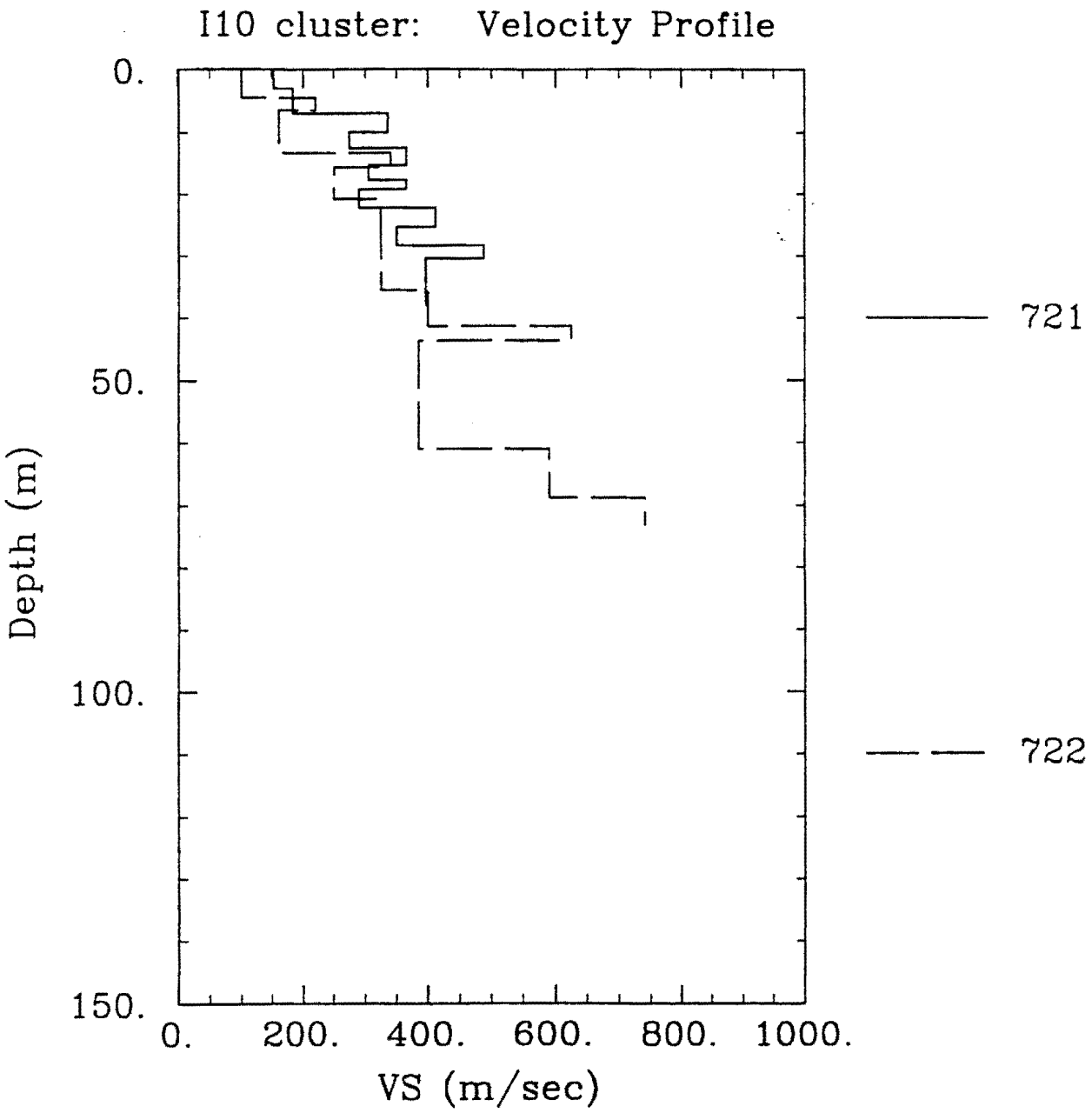
I10 cluster: Velocity Profile
0.
50.
100.
150.
Depth (m)
0.
200.
400.
600.
800.
1000.
VS (m/sec)
721
722

FIGURE 60.

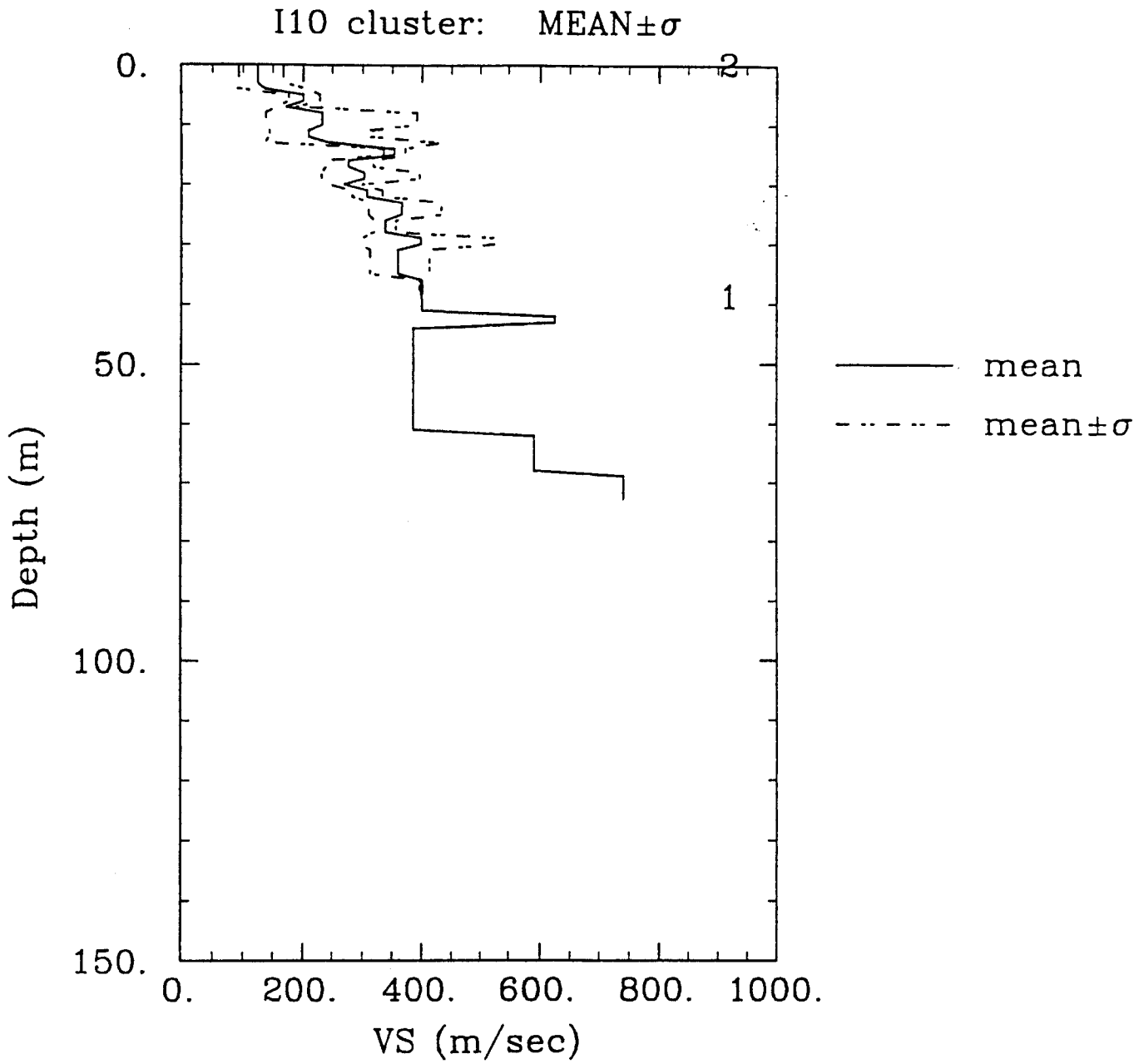
I10 cluster: MEAN±σ
0.
50.
100.
150.
Depth (m)
0.
200.
400.
600.
800.
1000.
VS (m/sec)
2
1
mean
mean±σ

FIGURE 61.

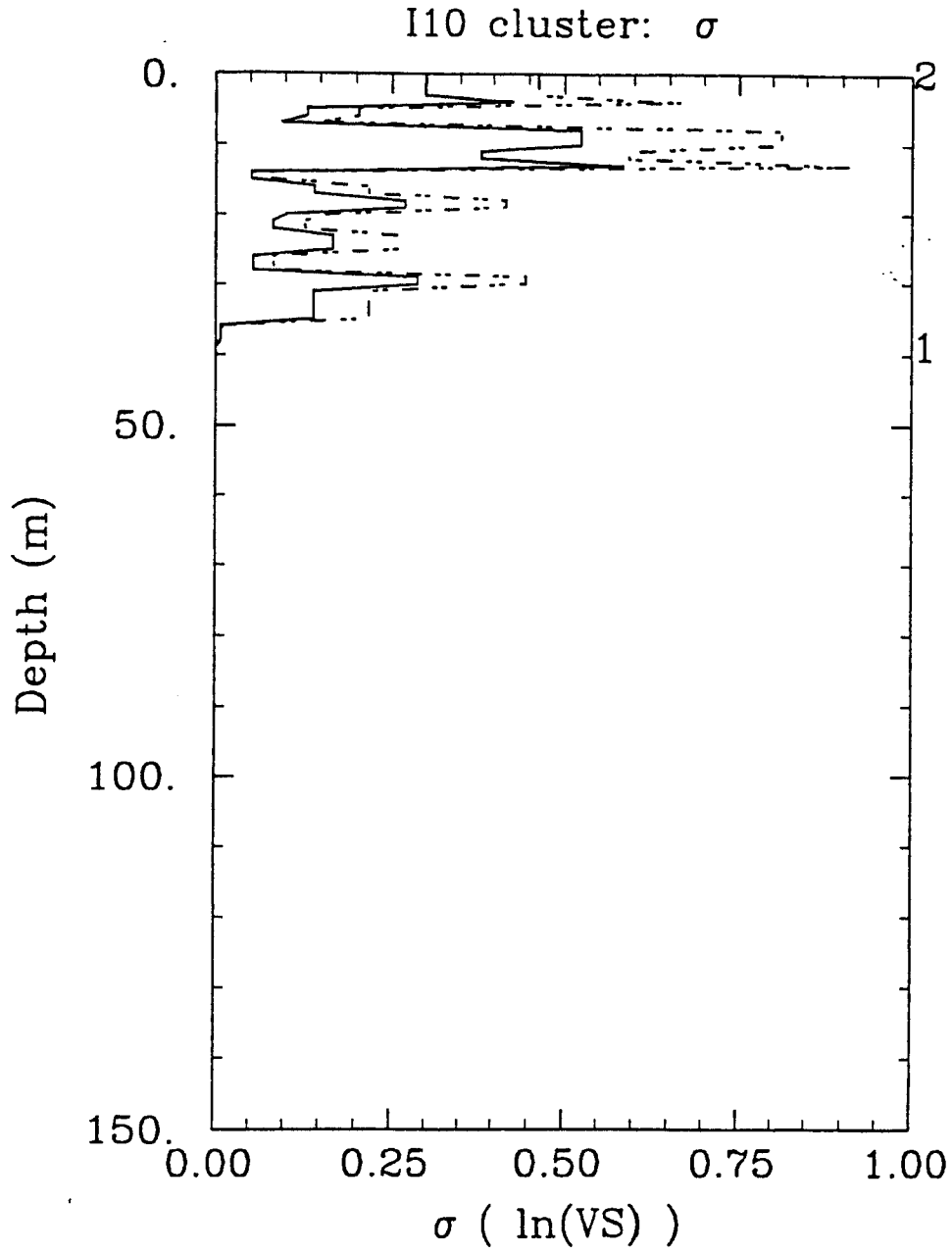

FIGURE 62.

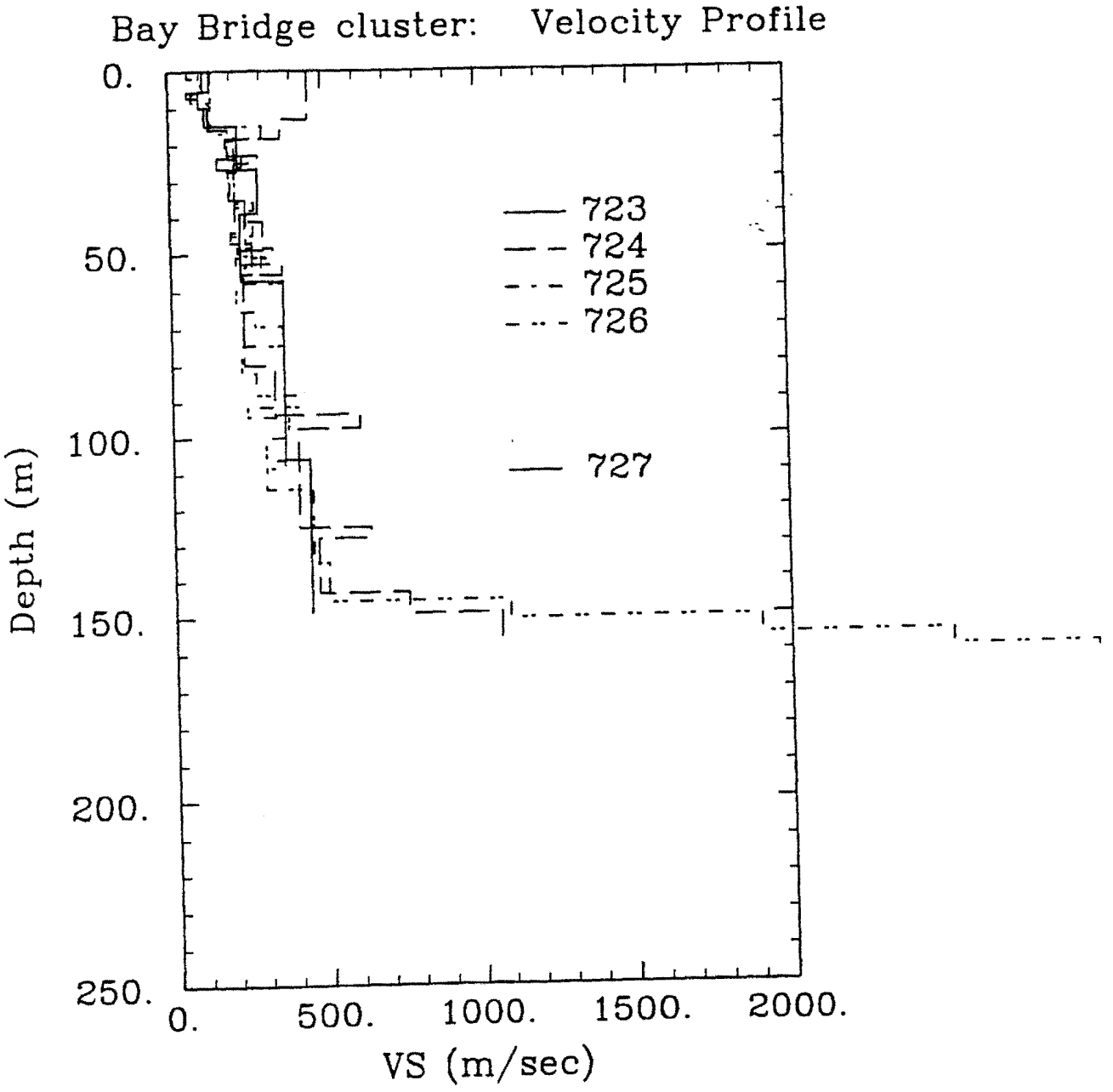
Bay Bridge cluster: Velocity Profile
0.
50.
100.
150.
200.
250.
Depth (m)
0.
500.
1000.
1500.
2000.
VS (m/sec)
723
724
725
726
727

FIGURE 63.

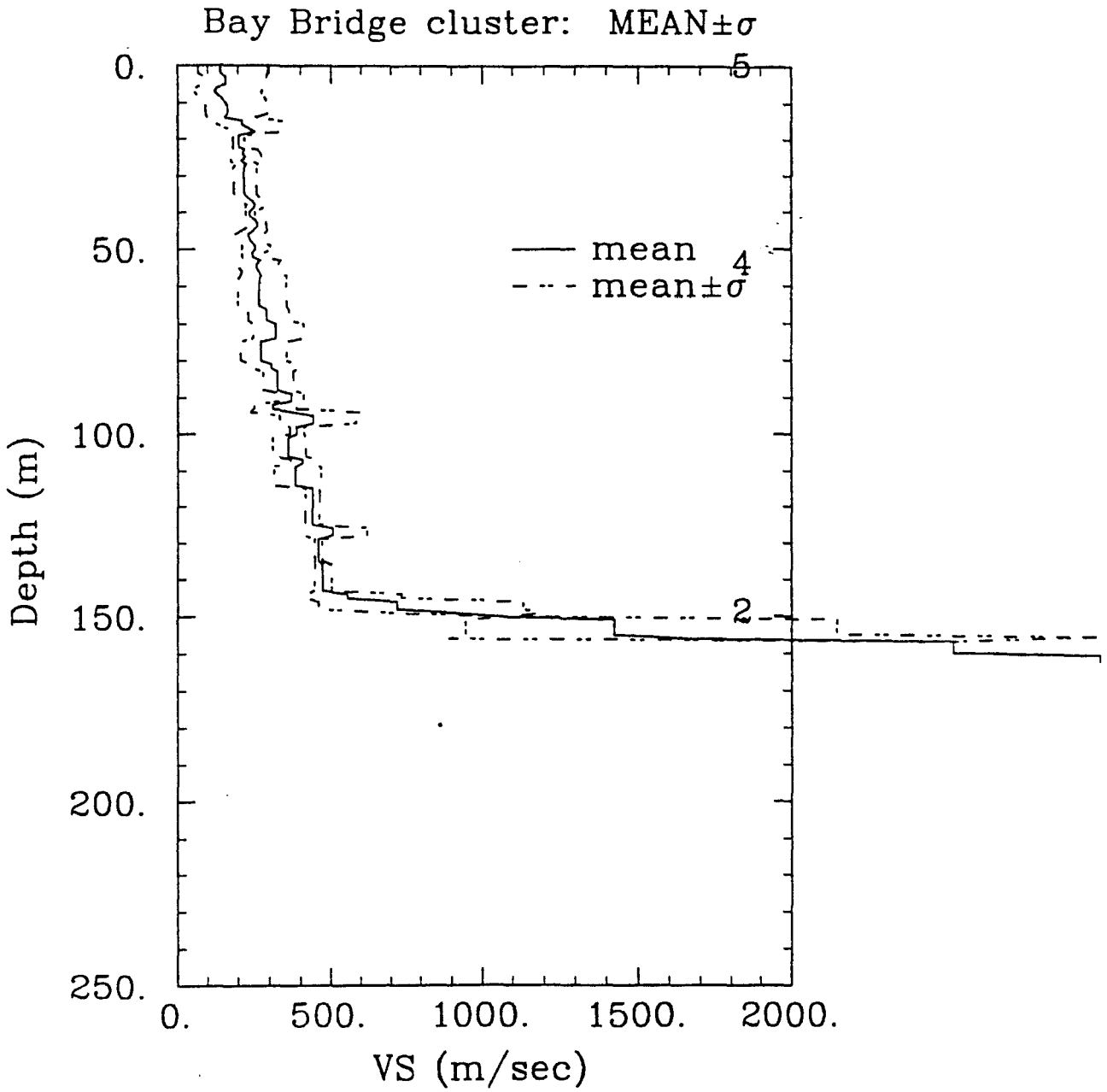
Bay Bridge cluster: MEAN±σ
0.
50.
100.
150.
200.
250.
Depth (m)
0.
500.
1000.
1500.
2000.
VS (m/sec)
mean
mean±σ
5
4
2

FIGURE 64.

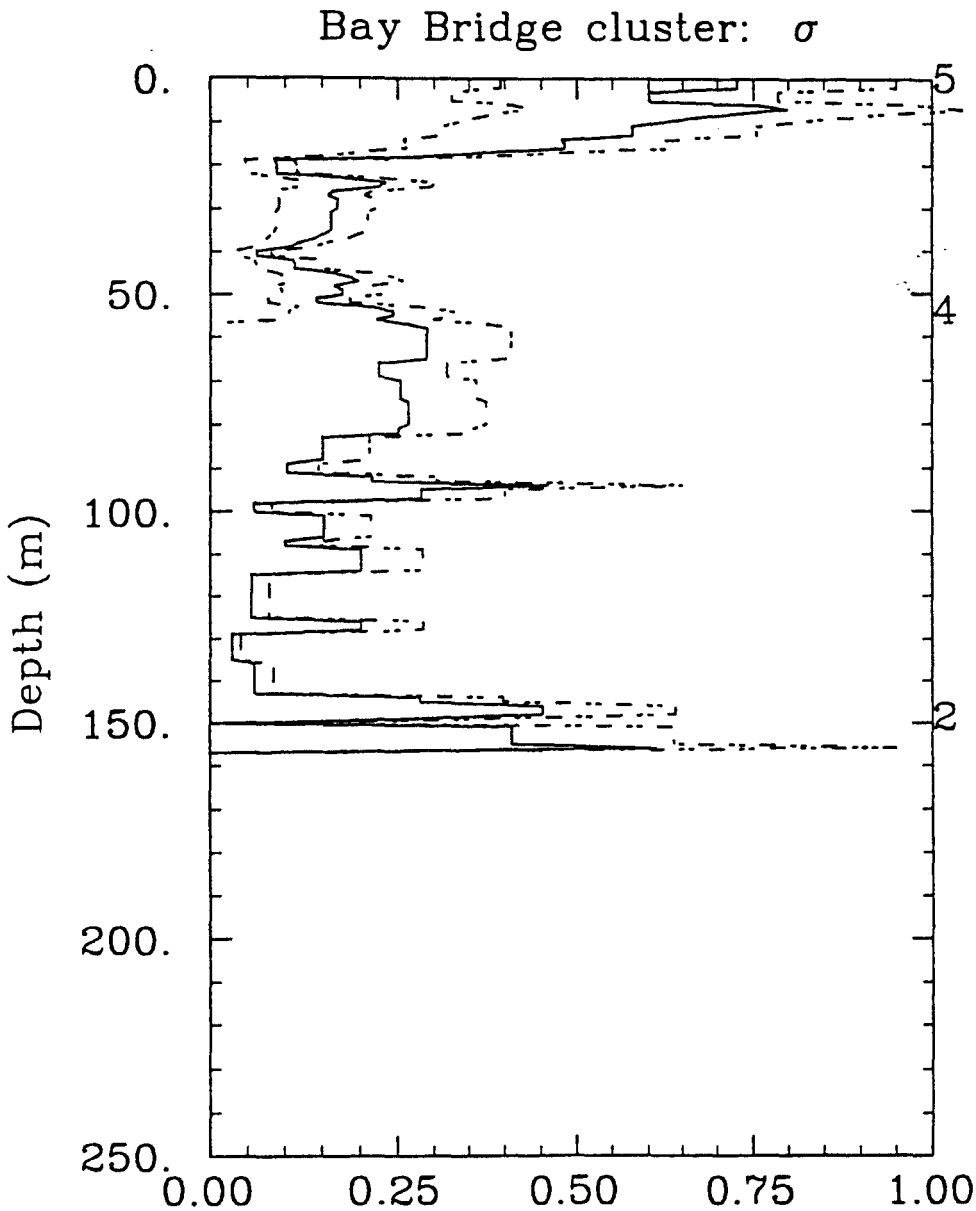
Bay Bridge cluster: σ
0.
50.
100.
150.
200.
250.
Depth (m)
5
4
2
0.00
0.25
0.50
0.75
1.00
σ (ln(VS))

FIGURE 65.

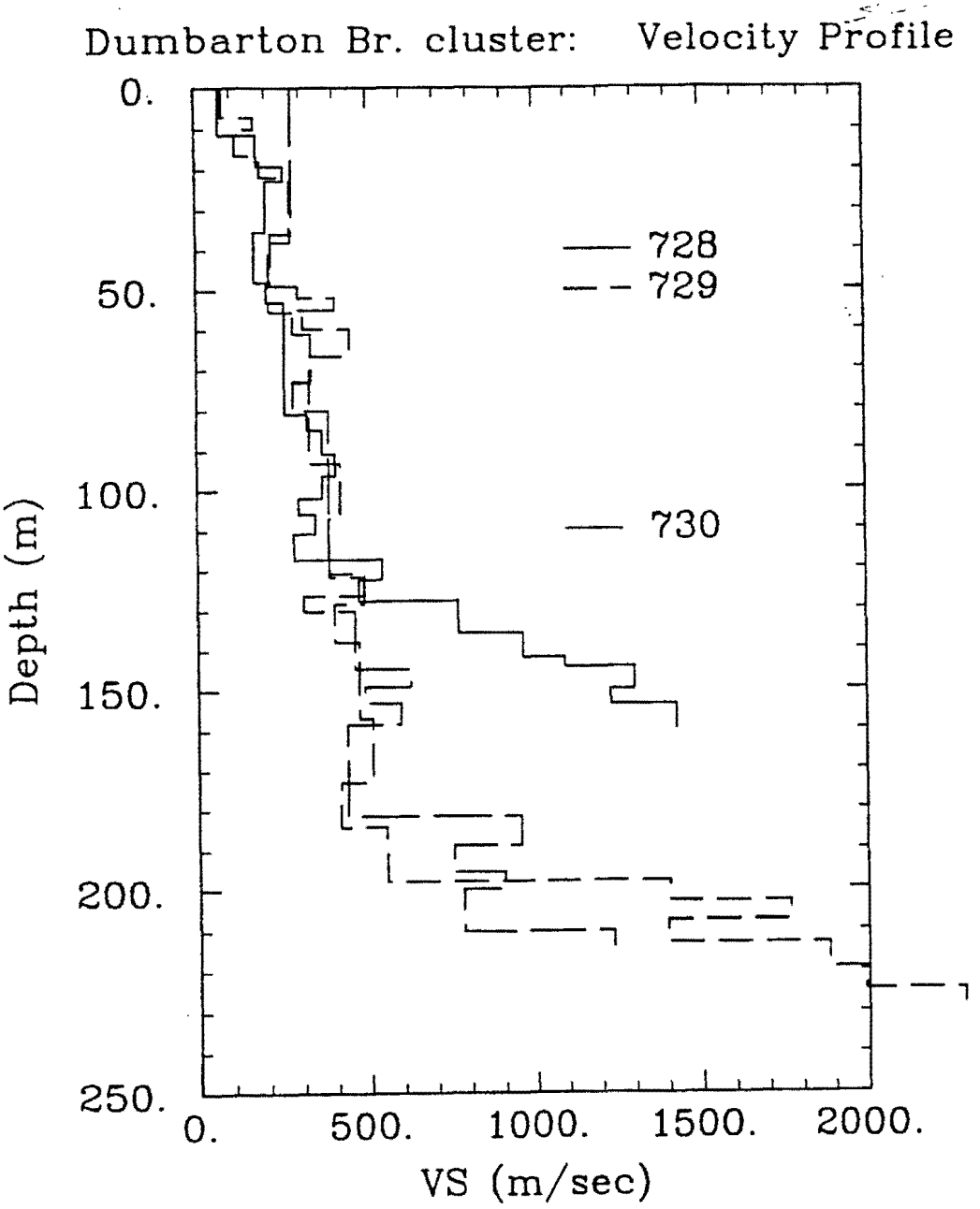
Dumbarton Br. cluster: Velocity Profile
0.
50.
100.
150.
200.
250.
Depth (m)
728
729
730
0.
500.
1000.
1500.
2000.
VS (m/sec)

FIGURE 66.

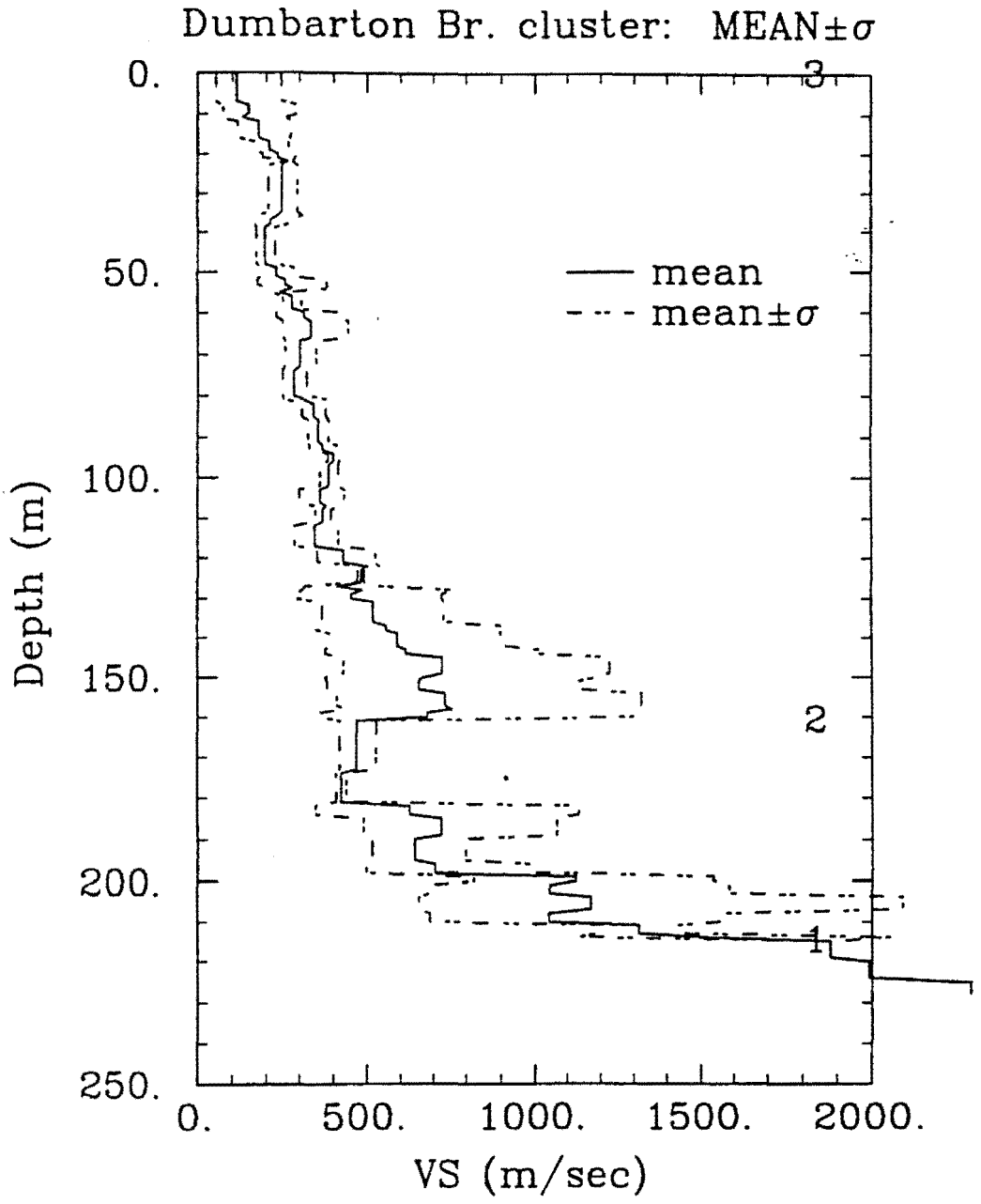
Dumbarton Br. cluster: MEAN±σ
0.
50.
100.
150.
200.
250.
Depth (m)
0.
500.
1000.
1500.
2000.
VS (m/sec)
mean
mean±σ
3
2
1

FIGURE 67.

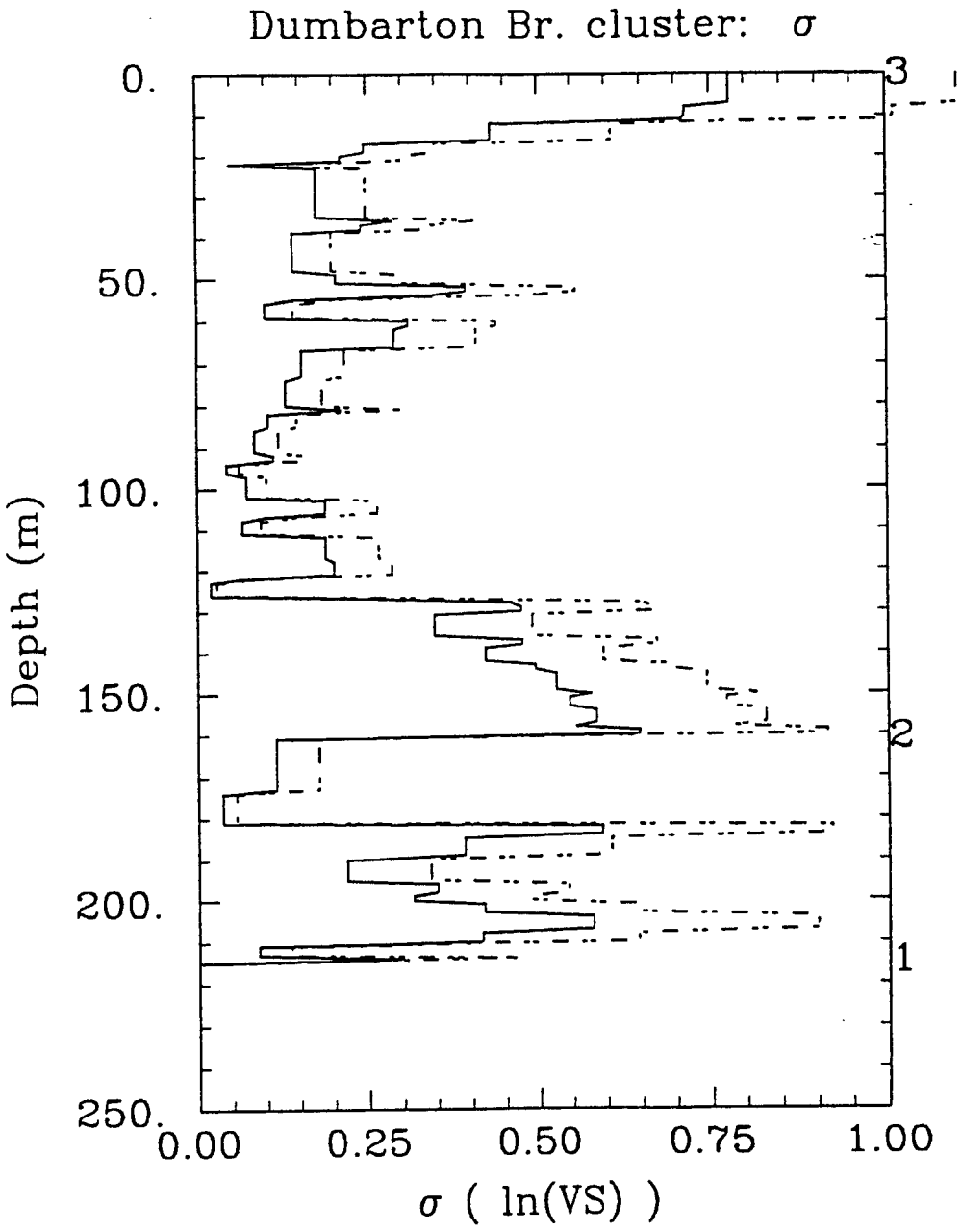
Dumbarton Br. cluster: σ
Depth (m)
0.
50.
100.
150.
200.
250.
0.00
0.25
0.50
0.75
1.00
σ (ln(VS))
1
2
3

FIGURE 68.

$$\gamma_{ij} = \frac{1}{2}E[Z_i - Z_j]^2$$

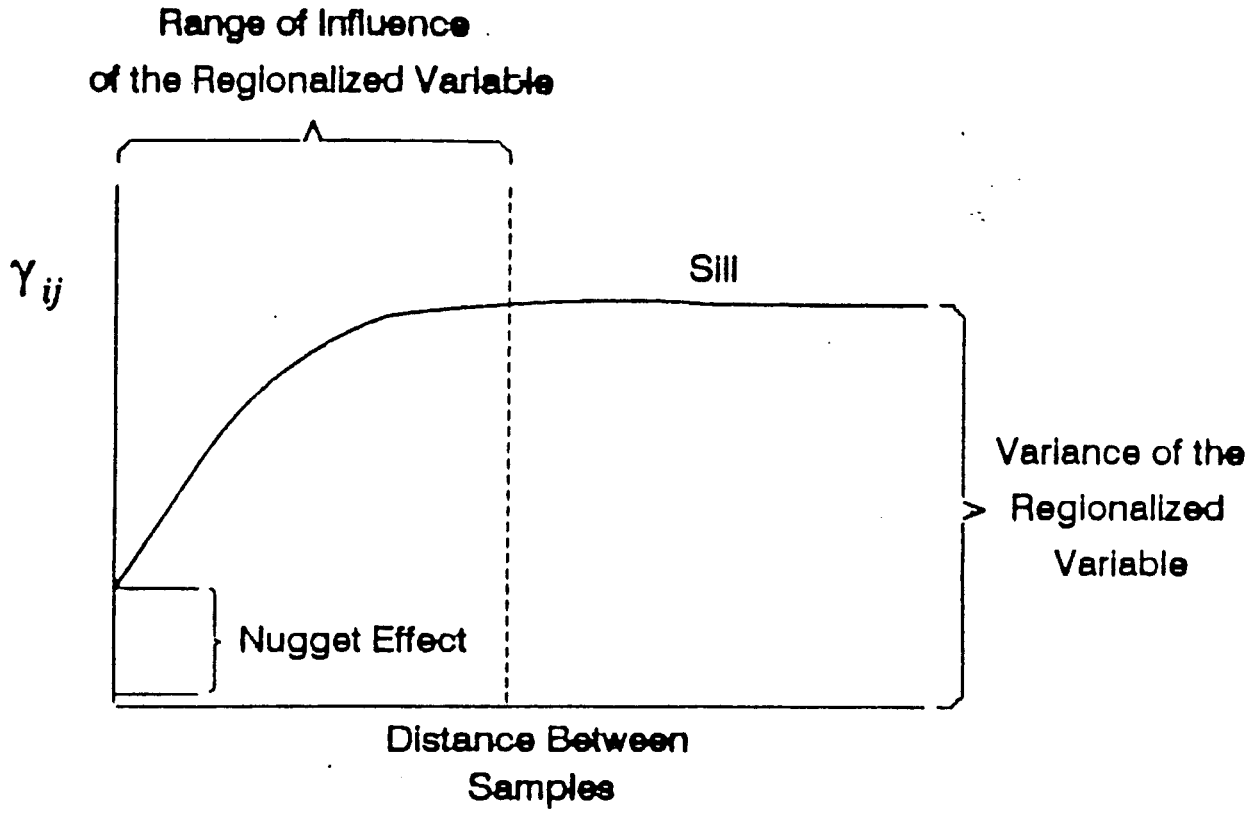

Figure ~~1.1~~ 69 General Features of a Typical Variogram
(Source: Rouhani et al.)

FIGURE 69.

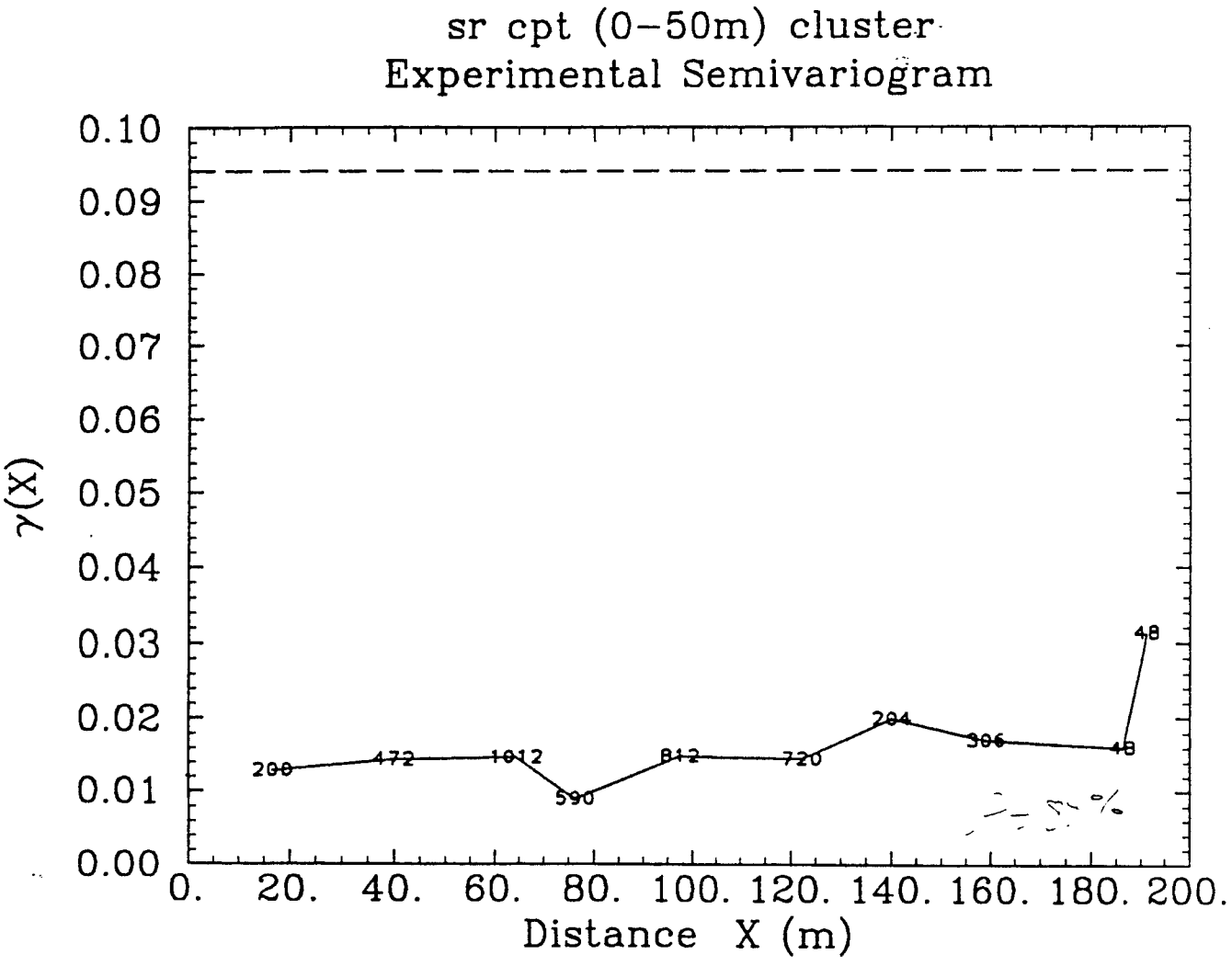
sr cpt (0-50m) cluster
Experimental Semivariogram
0.10
0.09
0.08
0.07
0.06
0.05
0.04
0.03
0.02
0.01
0.00
γ(X)
200
472
1012
590
812
720
204
306
48
48
0.
20.
40.
60.
80.
100.
120.
140.
160.
180.
200.
Distance X (m)

FIGURE 70.

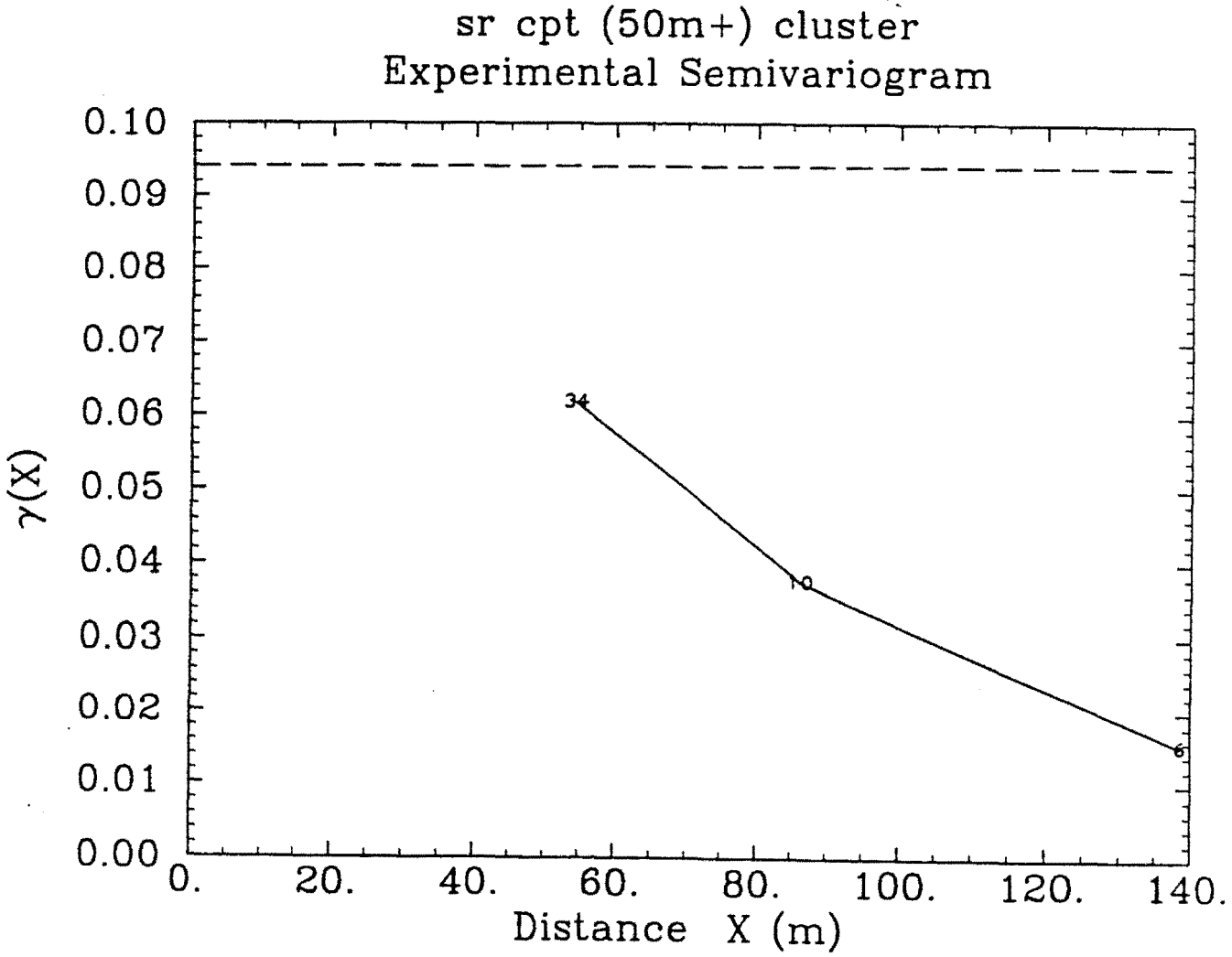
sr cpt (50m+) cluster
Experimental Semivariogram
0.10
0.09
0.08
0.07
0.06
0.05
0.04
0.03
0.02
0.01
0.00
γ(X)
34
10
6
0.
20.
40.
60.
80.
100.
120.
140.
Distance X (m)

FIGURE 71.

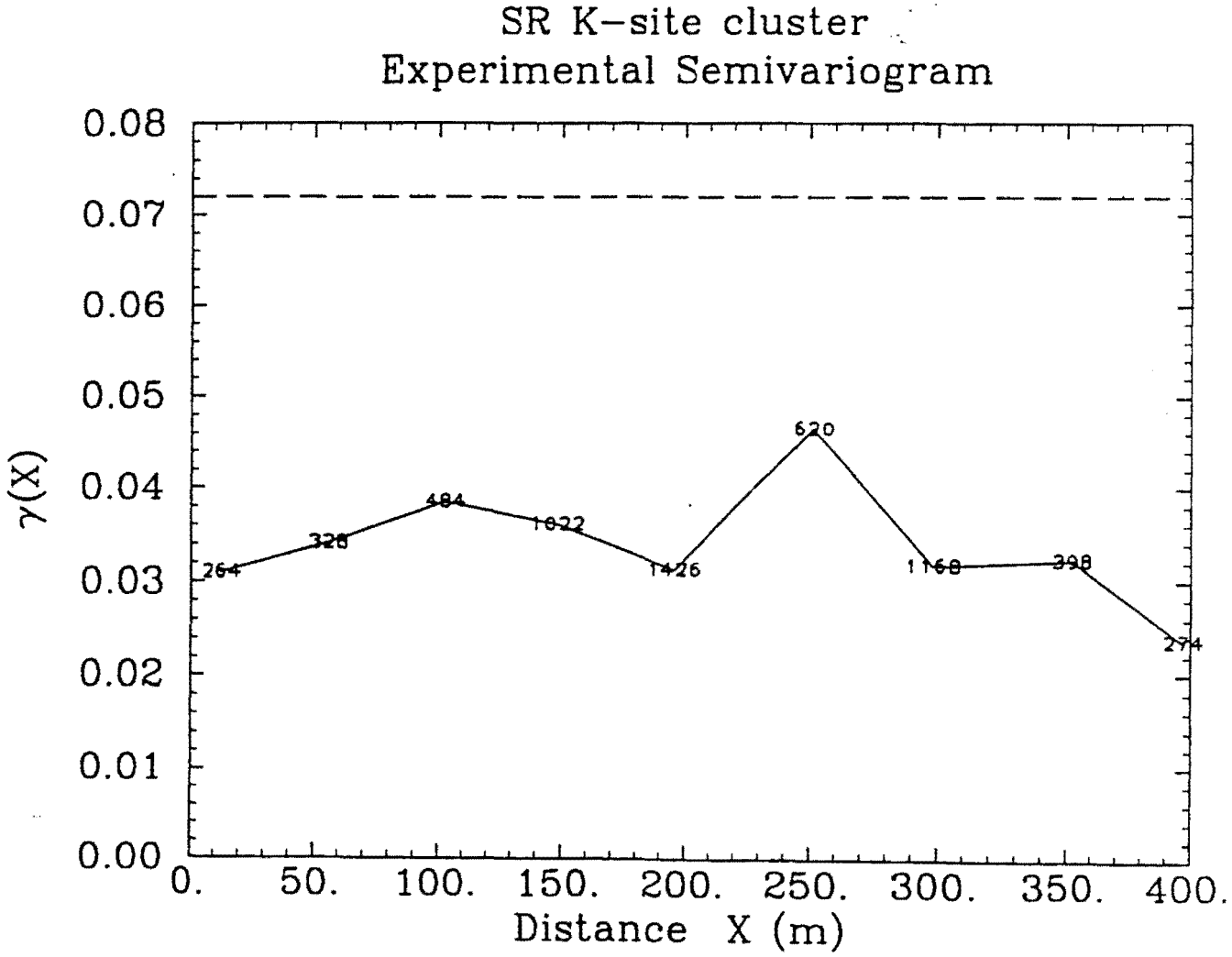
SR K-site cluster
Experimental Semivariogram
0.08
0.07
0.06
0.05
0.04
0.03
0.02
0.01
0.00
γ(X)
264
328
484
1022
1426
620
1168
398
274
0.
50.
100.
150.
200.
250.
300.
350.
400.
Distance X (m)

FIGURE 72.

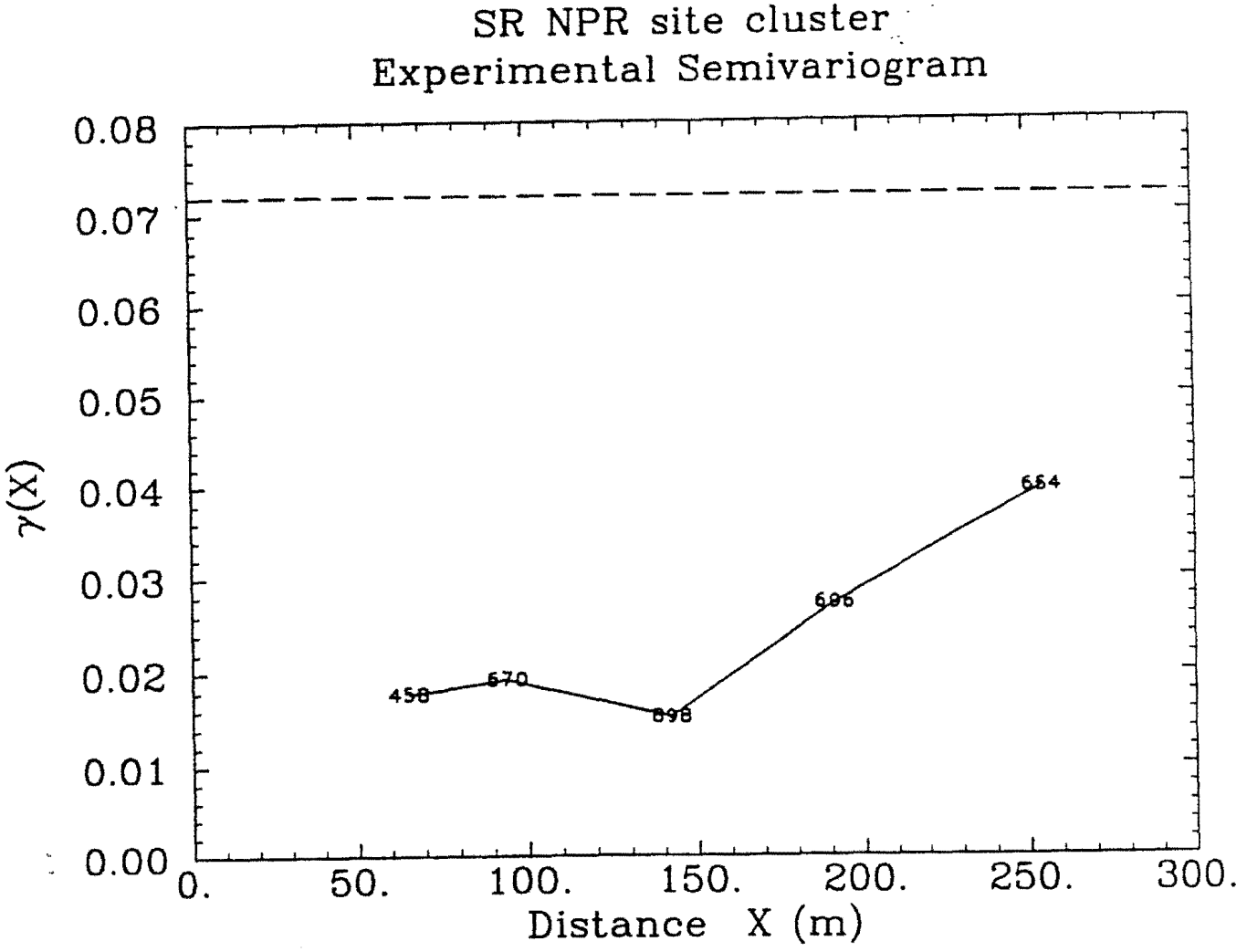
SR NPR site cluster
Experimental Semivariogram
0.08
0.07
0.06
0.05
0.04
0.03
0.02
0.01
0.00
γ(X)
458
670
698
696
654
0.
50.
100.
150.
200.
250.
300.
Distance X (m)

FIGURE 73.

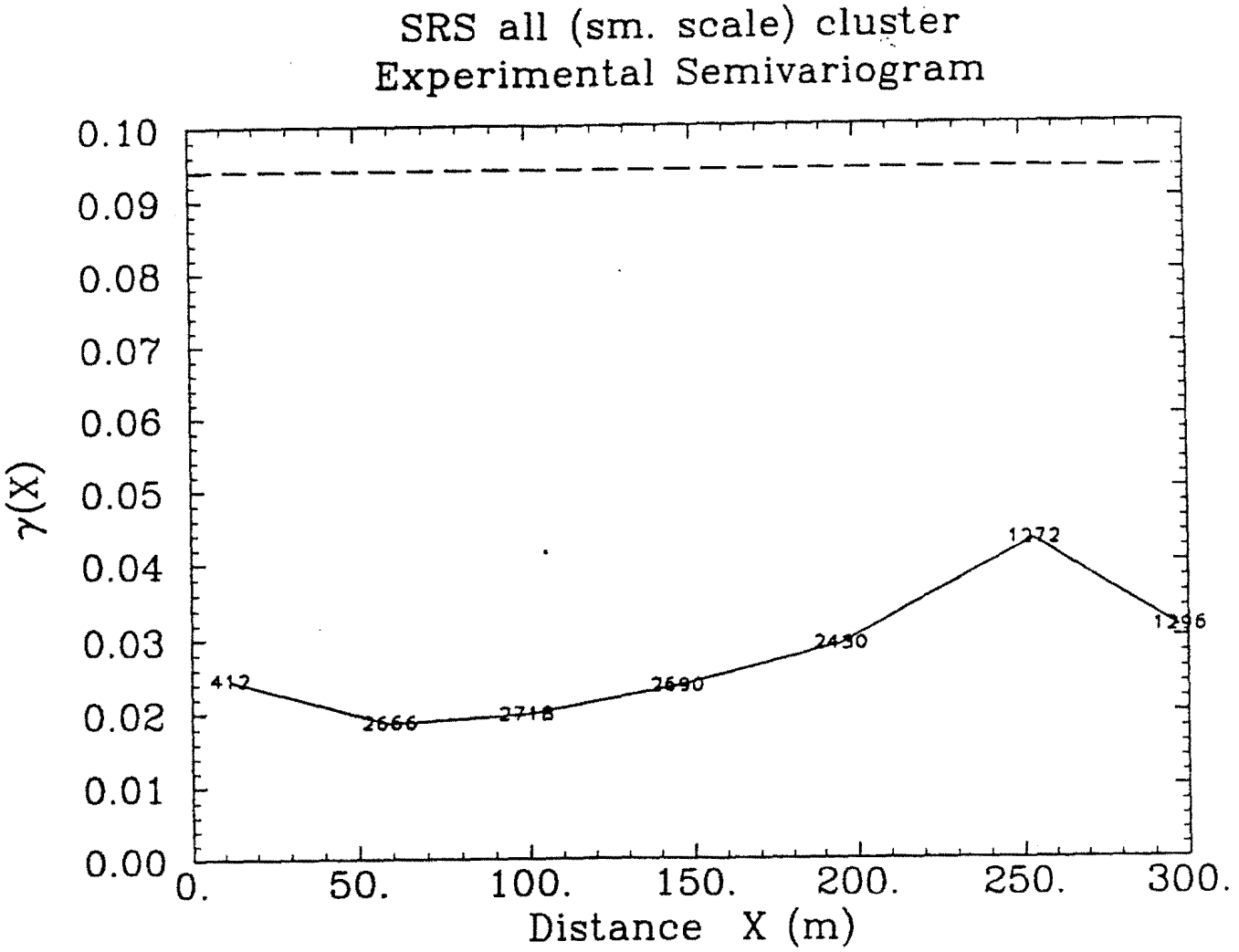
SRS all (sm. scale) cluster
Experimental Semivariogram
0.10
0.09
0.08
0.07
0.06
0.05
0.04
0.03
0.02
0.01
0.00
γ(X)
412
2666
2718
2690
2450
1272
1296
0.
50.
100.
150.
200.
250.
300.
Distance X (m)

FIGURE 74.

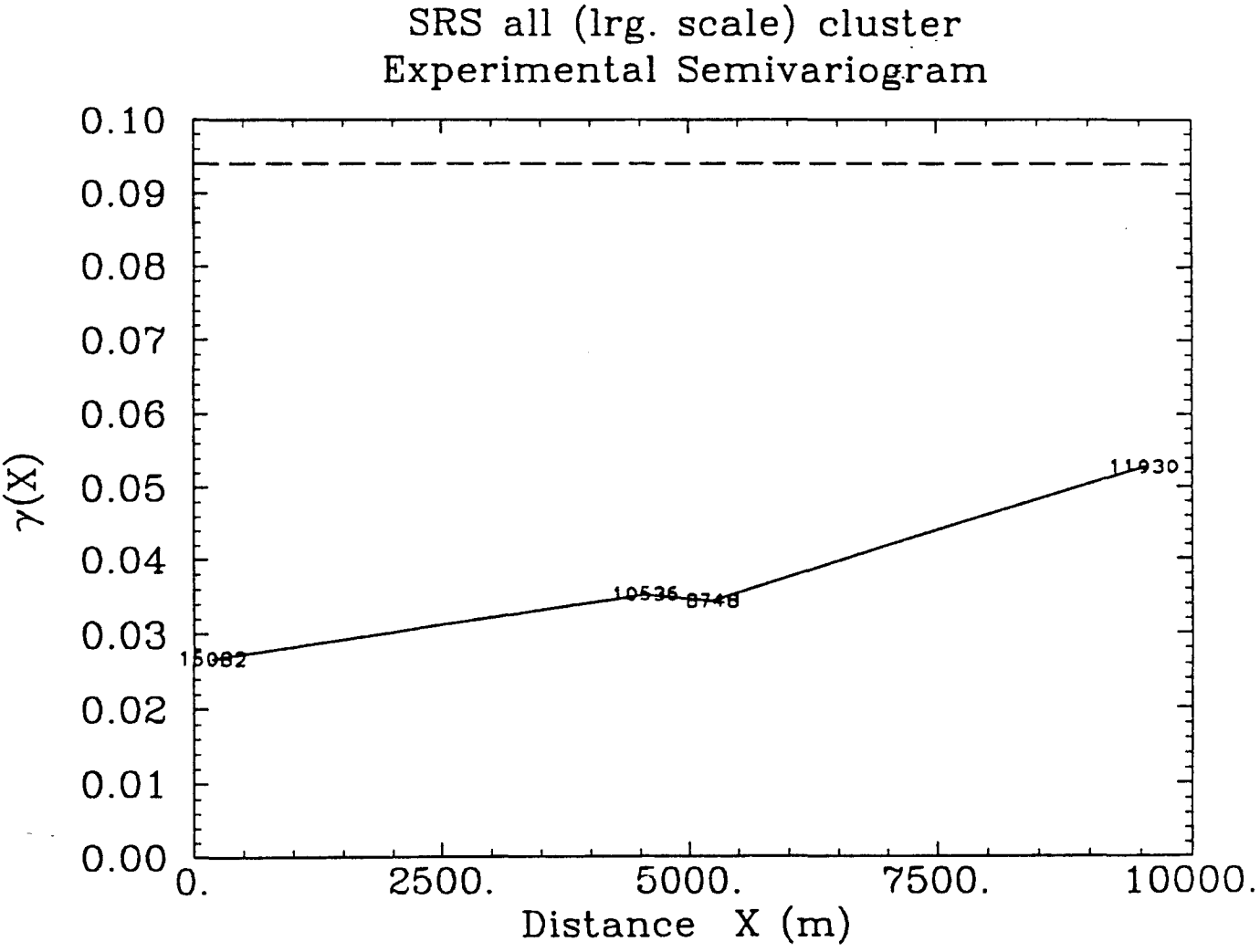
SRS all (lrg. scale) cluster
Experimental Semivariogram
0.10
0.09
0.08
0.07
0.06
0.05
0.04
0.03
0.02
0.01
0.00
γ(X)
0.
2500.
5000.
7500.
10000.
Distance X (m)
11930
10536
8748
15082

FIGURE 75.

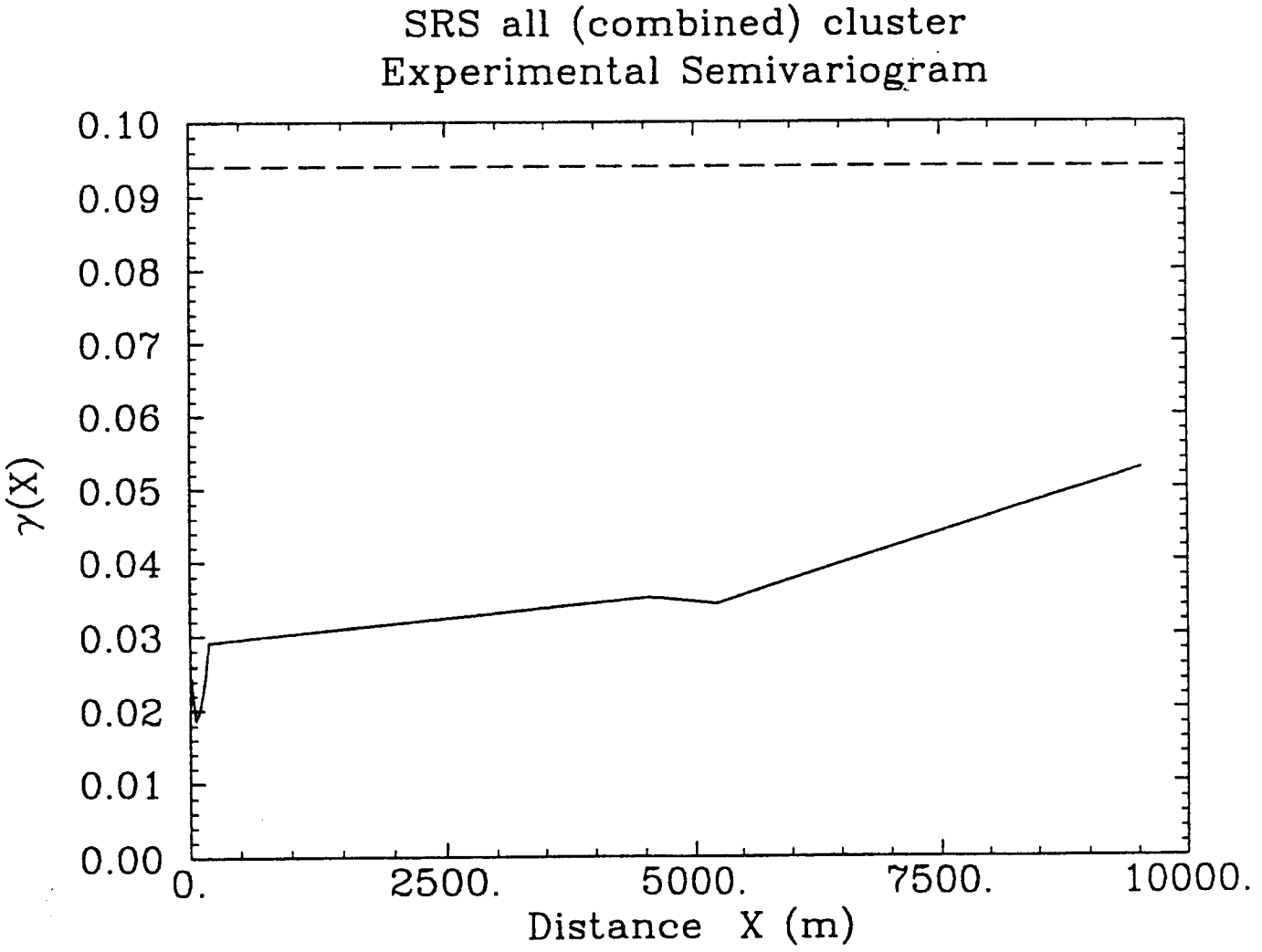
SRS all (combined) cluster
Experimental Semivariogram
0.10
0.09
0.08
0.07
0.06
0.05
0.04
0.03
0.02
0.01
0.00
γ(X)
0.
2500.
5000.
7500.
10000.
Distance X (m)

FIGURE 76.

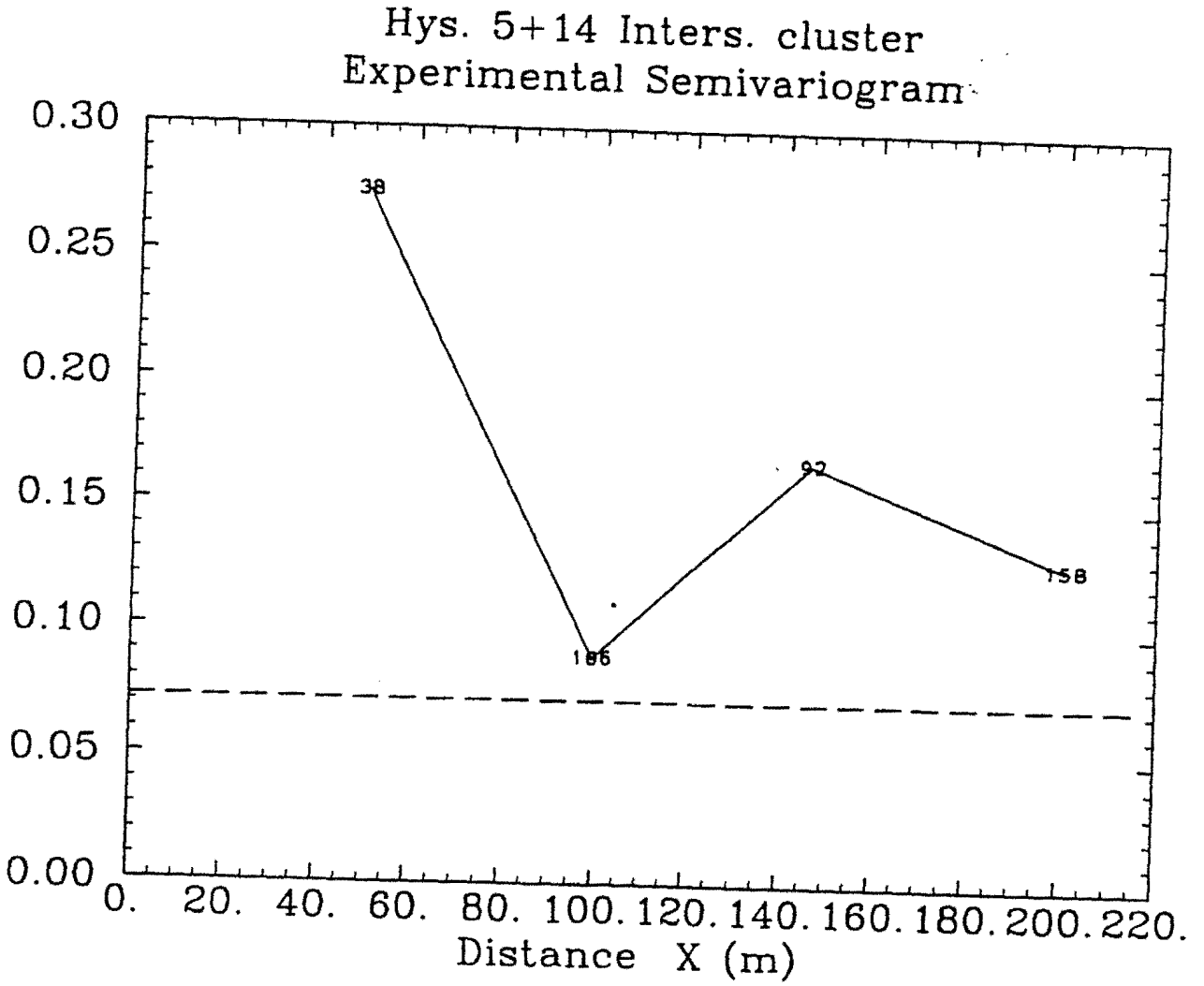
Hys. 5+14 Inters. cluster
Experimental Semivariogram
0.30
0.25
0.20
0.15
0.10
0.05
0.00
38
92
158
186
0. 20. 40. 60. 80. 100. 120. 140. 160. 180. 200. 220.
Distance X (m)

FIGURE 77.

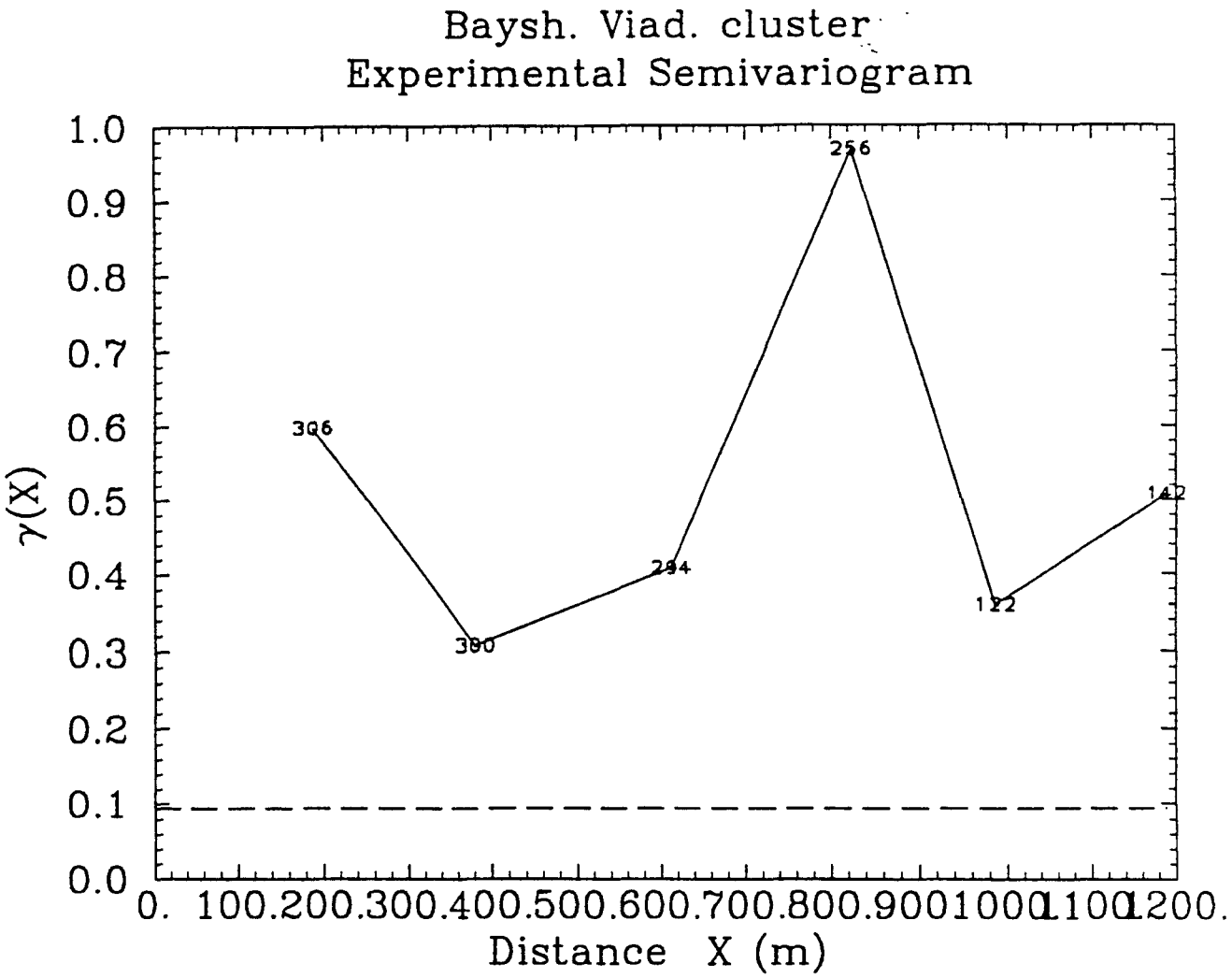
Baysh. Viad. cluster
Experimental Semivariogram
1.0
0.9
0.8
0.7
0.6
0.5
0.4
0.3
0.2
0.1
0.0
γ(X)
306
380
294
256
122
142
0. 100.200.300.400.500.600.700.800.900100011001200.
Distance X (m)

FIGURE 78.

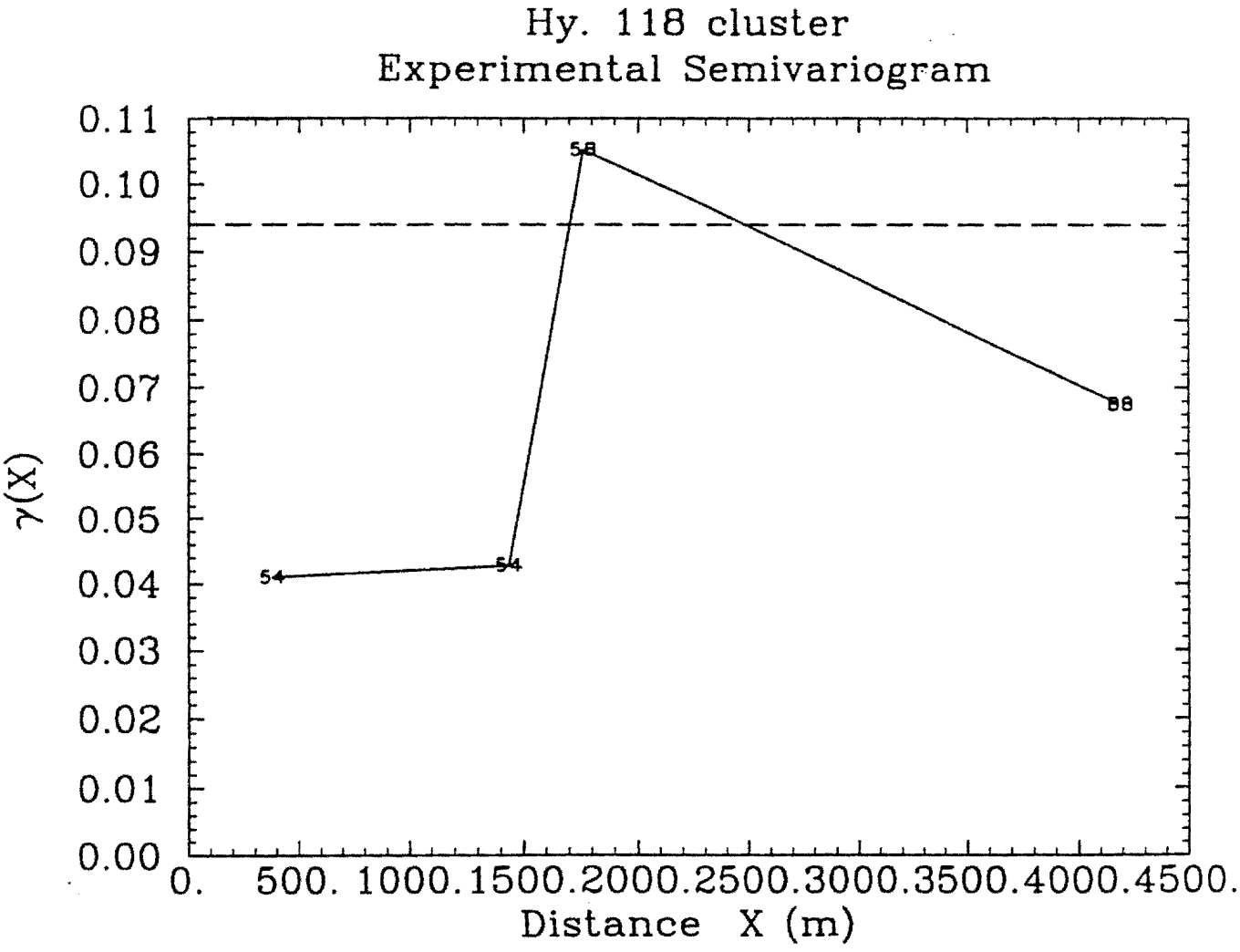
Hy. 118 cluster
Experimental Semivariogram
0.11
0.10
0.09
0.08
0.07
0.06
0.05
0.04
0.03
0.02
0.01
0.00
γ(X)
58
54
54
88
0. 500. 1000. 1500. 2000. 2500. 3000. 3500. 4000. 4500.
Distance X (m)

FIGURE 79.

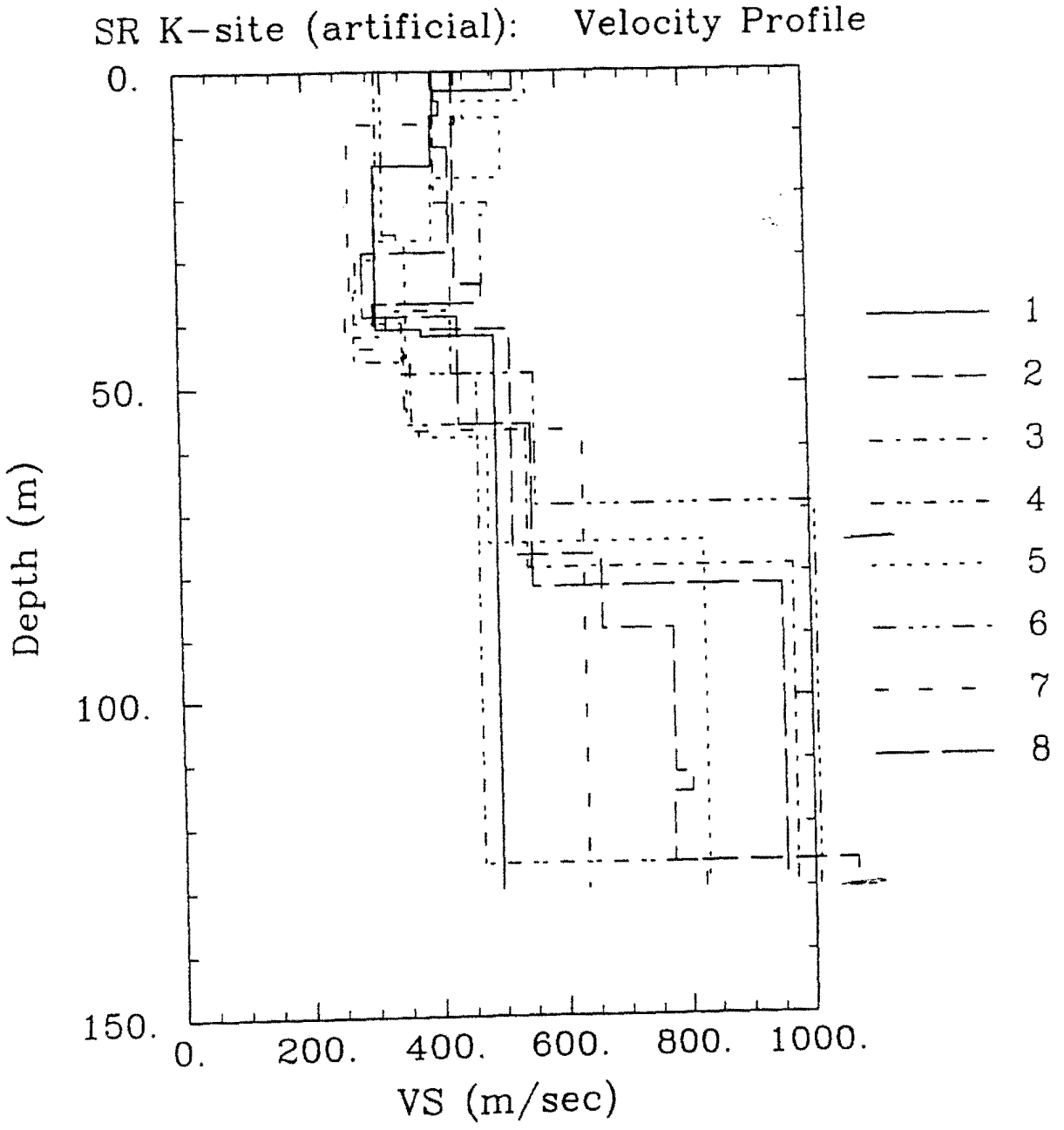
SR K-site (artificial): Velocity Profile
0.
50.
100.
150.
Depth (m)
0.
200.
400.
600.
800.
1000.
VS (m/sec)
1
2
3
4
5
6
7
8

FIGURE 80-A.

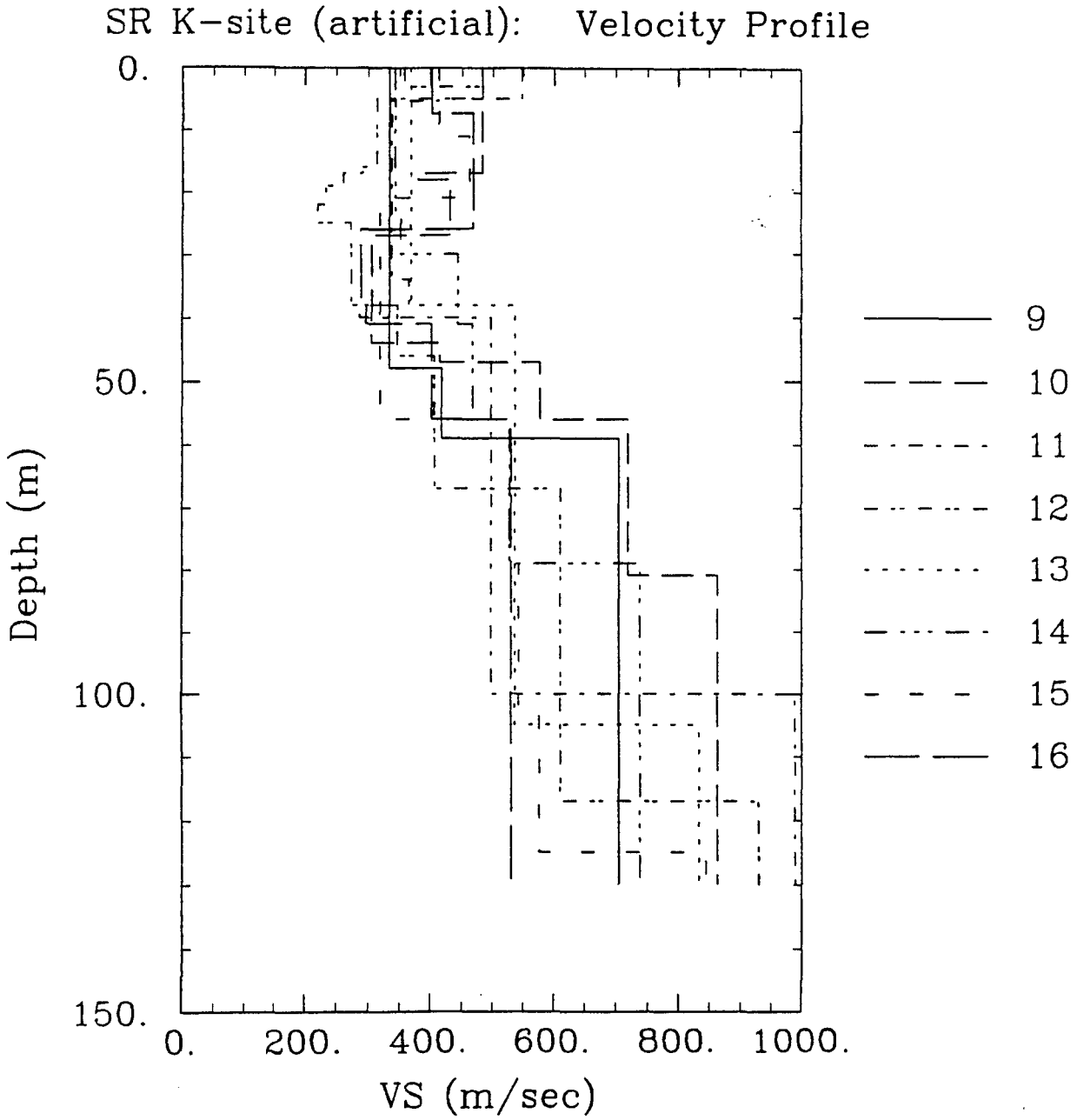
SR K-site (artificial): Velocity Profile
0.
50.
100.
150.
Depth (m)
0.
200.
400.
600.
800.
1000.
VS (m/sec)
9
10
11
12
13
14
15
16

FIGURE 80-B.

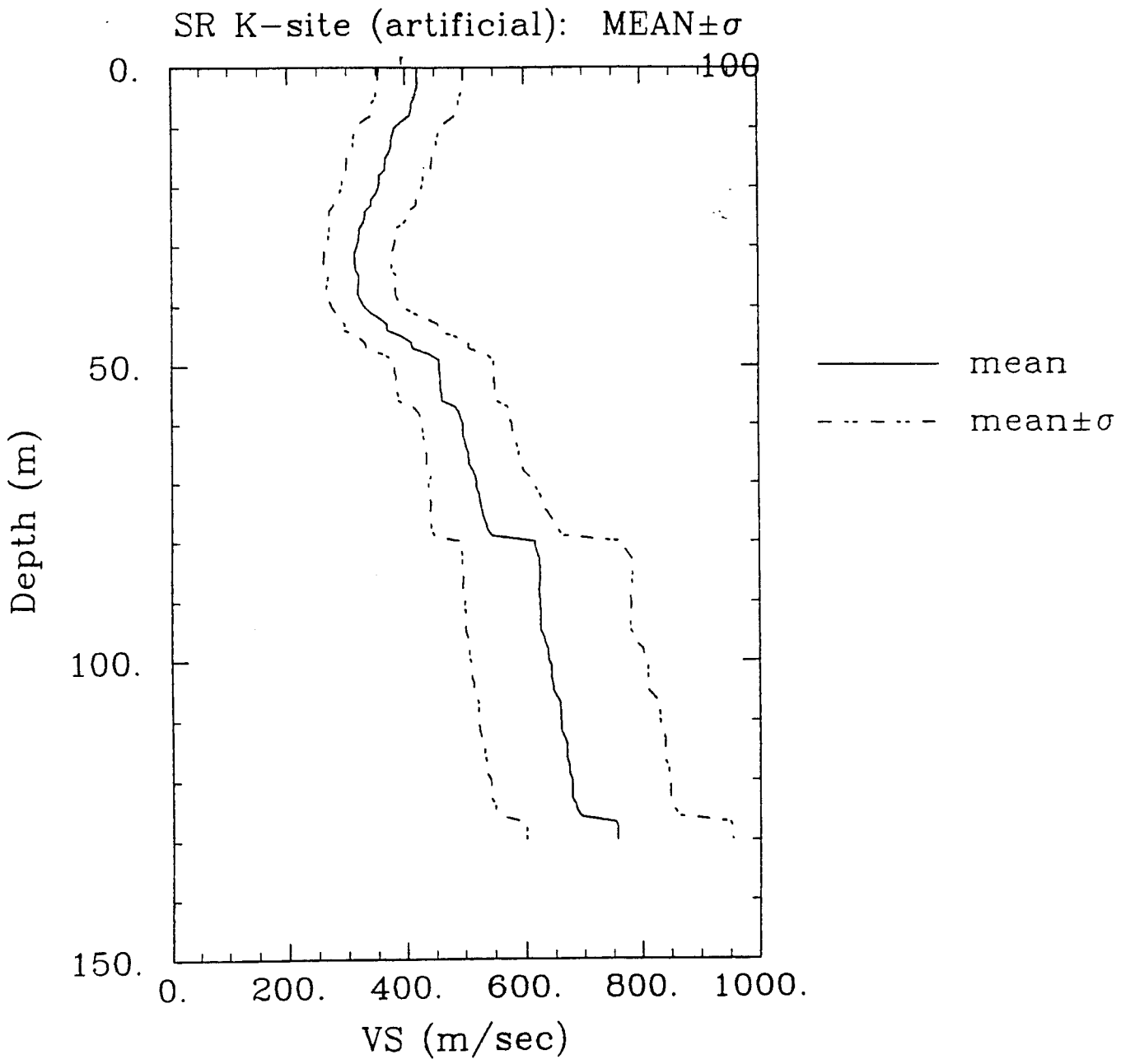
SR K-site (artificial): MEAN±σ
0.
100
50.
100.
150.
Depth (m)
0.
200.
400.
600.
800.
1000.
VS (m/sec)
mean
mean±σ

FIGURE 81

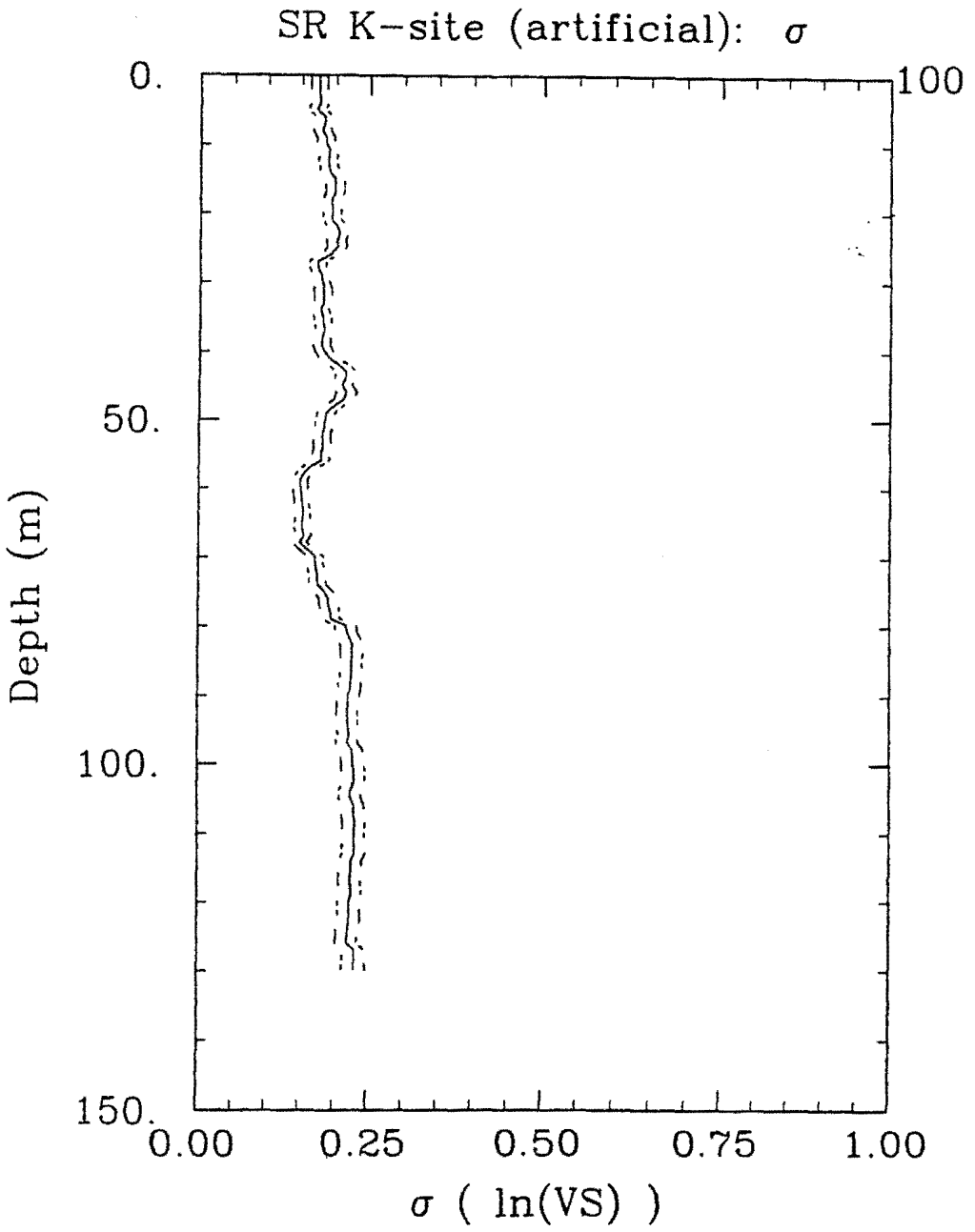
SR K-site (artificial): σ
0.
100
50.
100.
150.
Depth (m)
0.00
0.25
0.50
0.75
1.00
σ (ln(VS))

FIGURE 82.

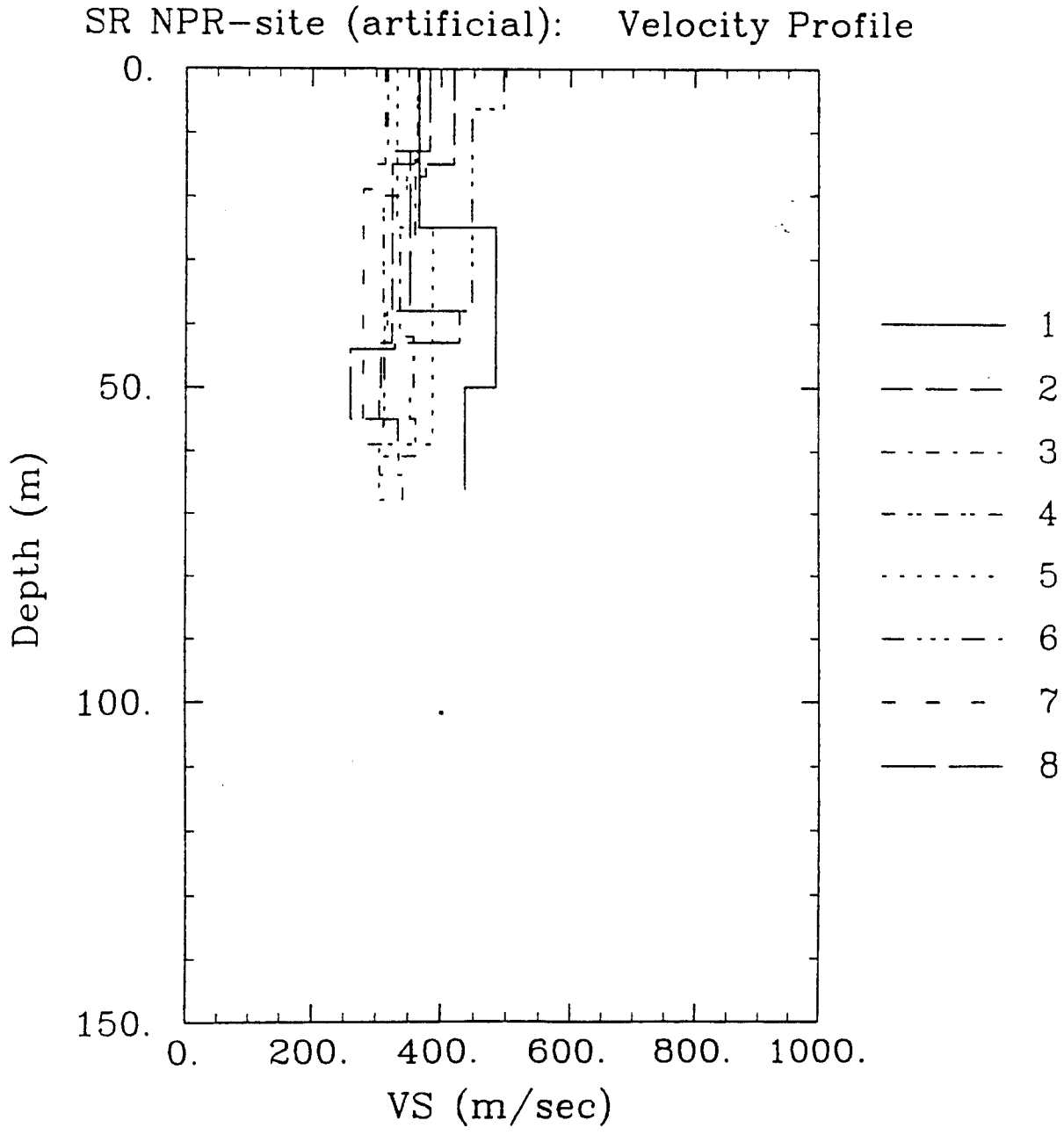
SR NPR-site (artificial): Velocity Profile
0.
50.
100.
150.
Depth (m)
0.
200.
400.
600.
800.
1000.
VS (m/sec)
1
2
3
4
5
6
7
8

FIGURE 83-A.

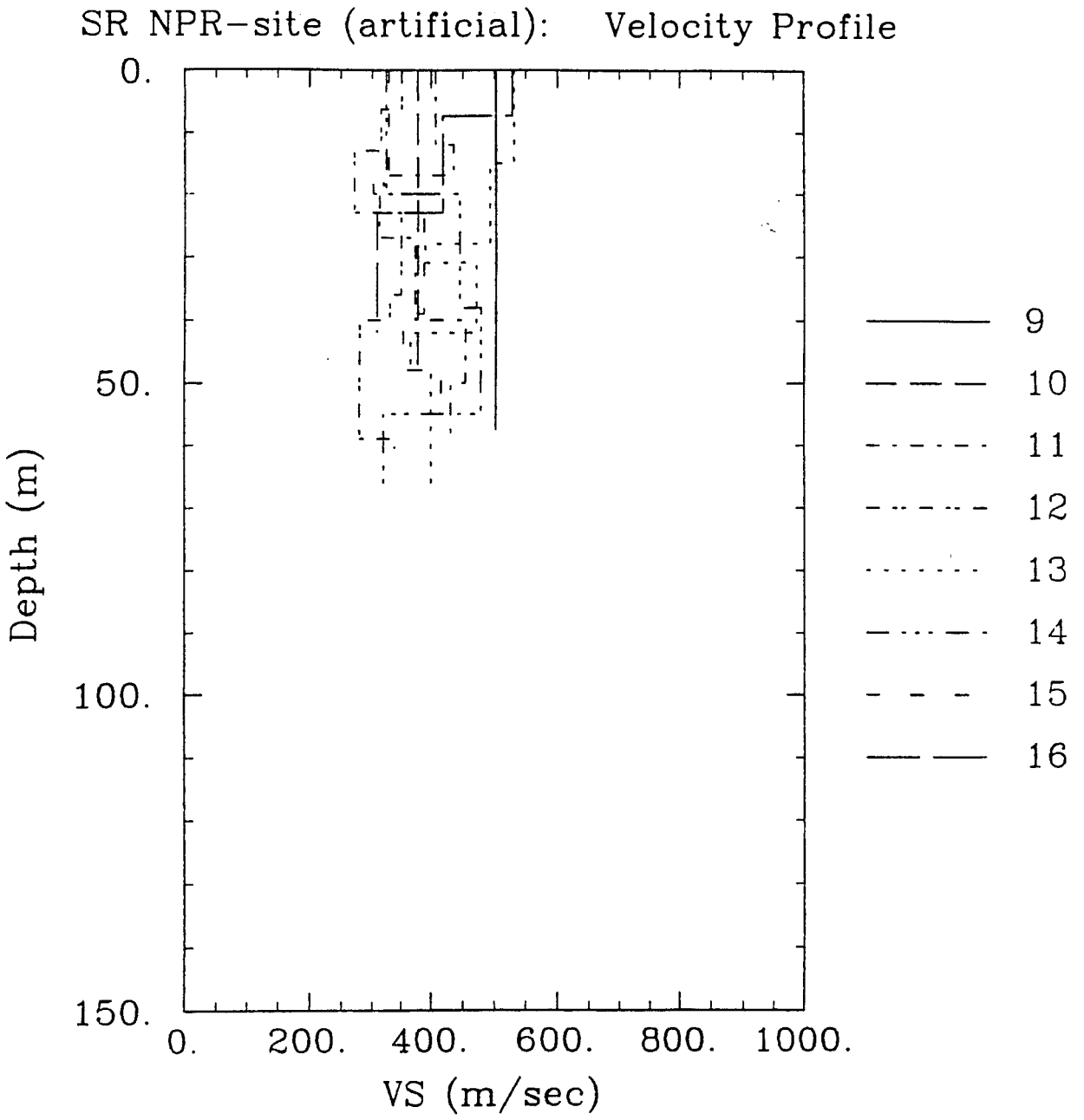
SR NPR-site (artificial): Velocity Profile
0.
50.
100.
150.
Depth (m)
0.
200.
400.
600.
800.
1000.
VS (m/sec)
9
10
11
12
13
14
15
16

FIGURE 83B.

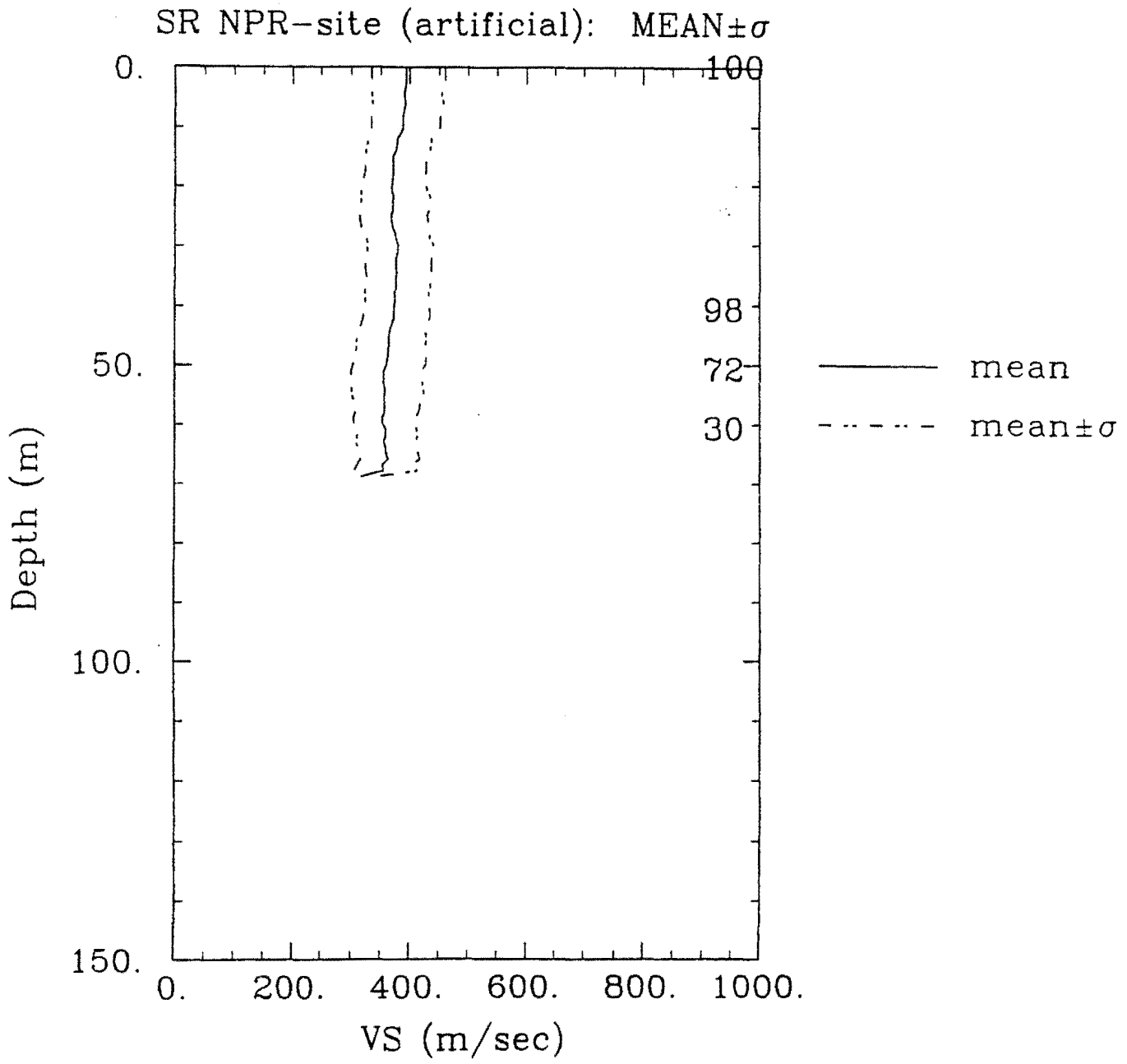
SR NPR-site (artificial): MEAN±σ
0.
50.
100.
150.
Depth (m)
100
98
72
30
mean
mean±σ
0.
200.
400.
600.
800.
1000.
VS (m/sec)

FIGURE 84.

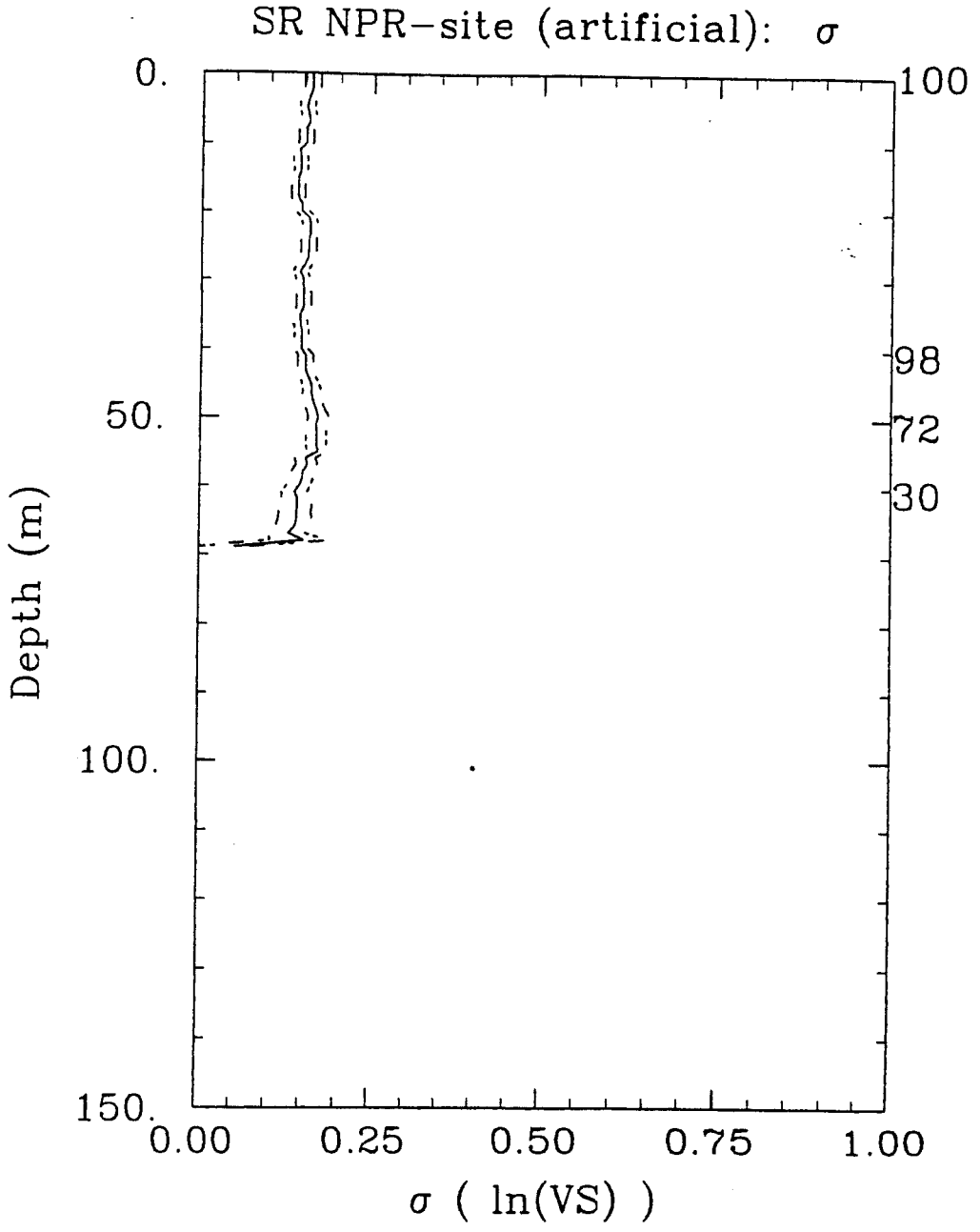
SR NPR-site (artificial): σ
0.
50.
100.
150.
Depth (m)
100
98
72
30
0.00
0.25
0.50
0.75
1.00
σ (ln(VS))

FIGURE 85.

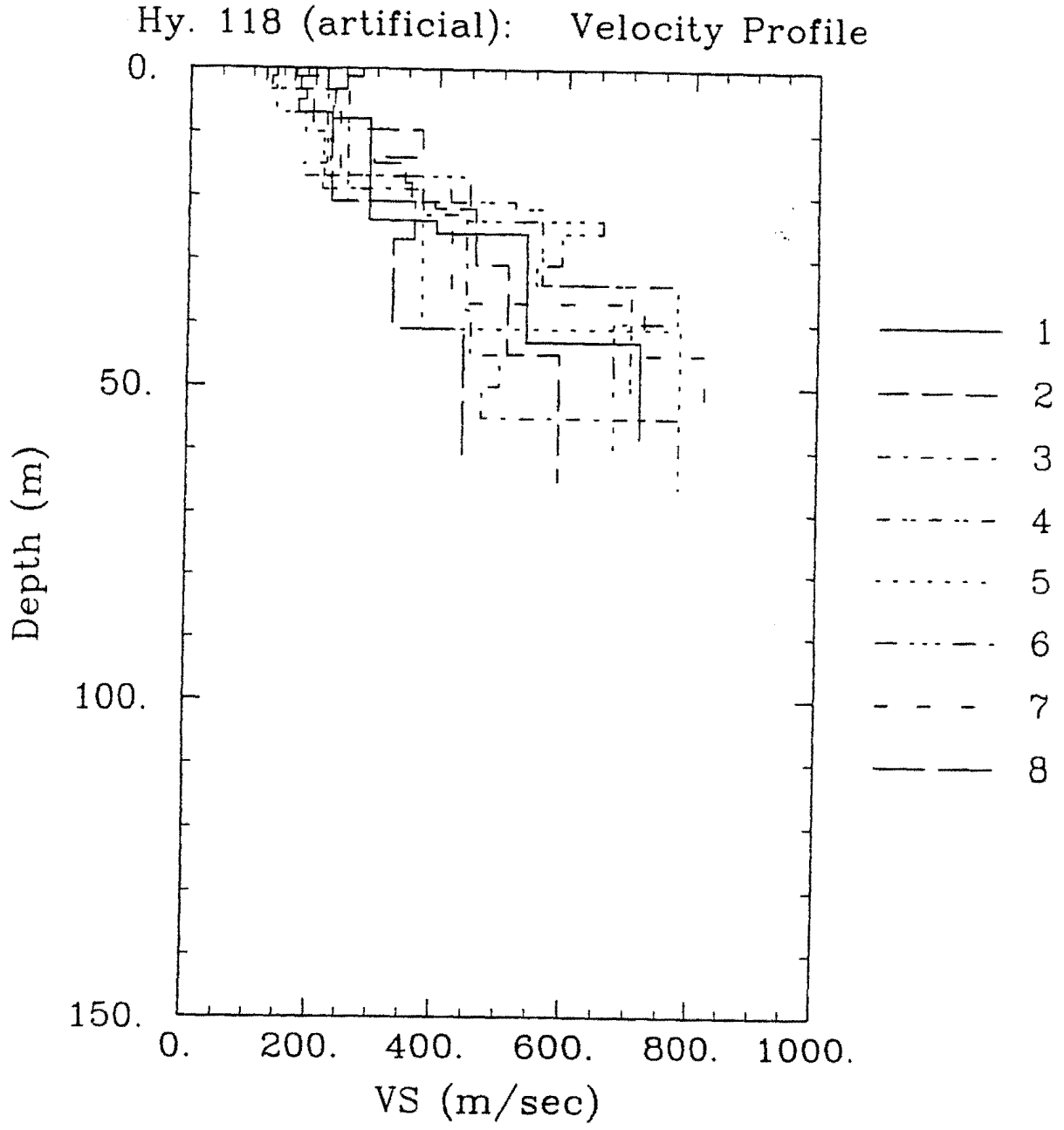
Hy. 118 (artificial): Velocity Profile
0.
50.
100.
150.
Depth (m)
0.
200.
400.
600.
800.
1000.
VS (m/sec)
1
2
3
4
5
6
7
8

FIGURE 86-A.

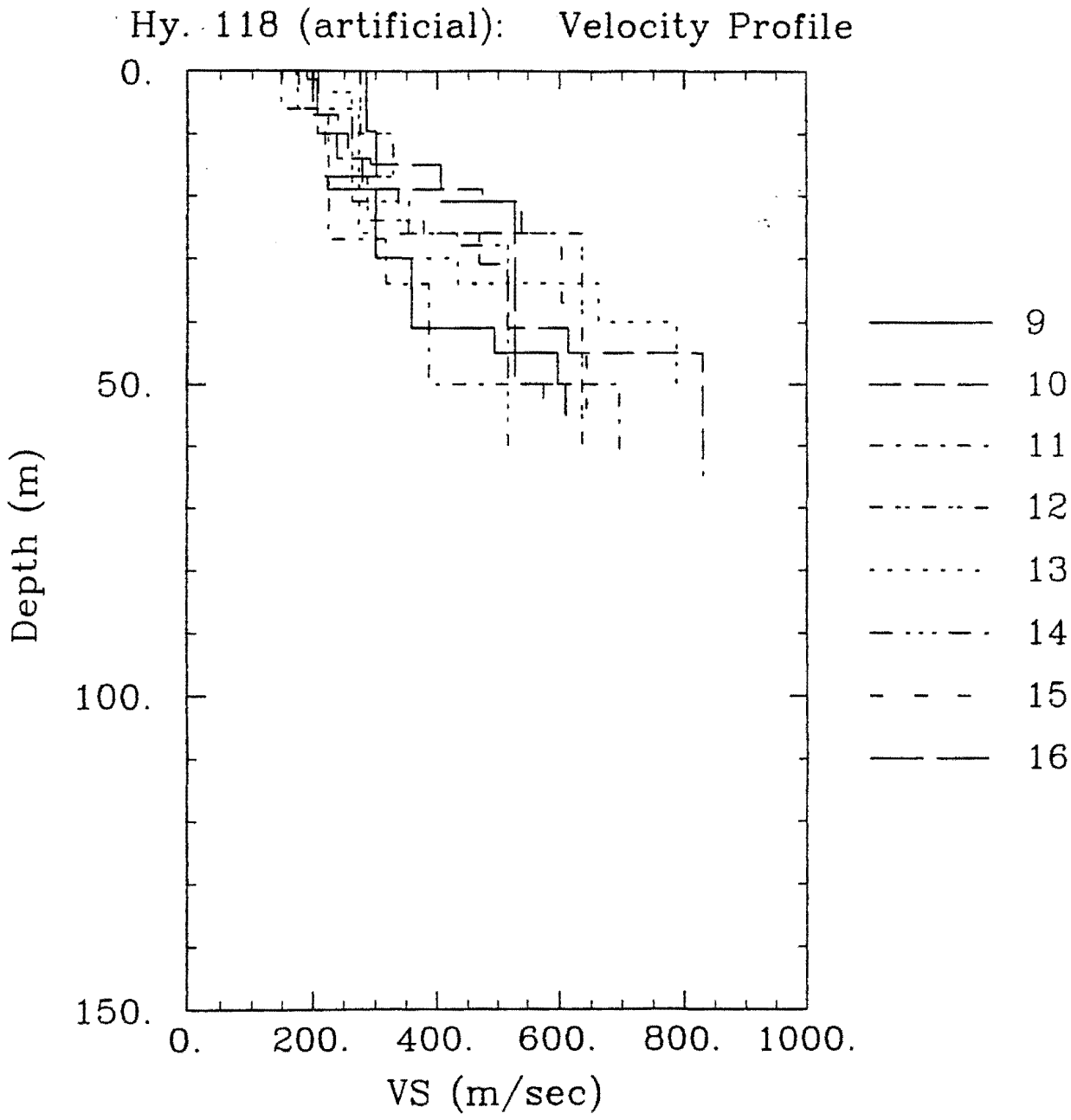
Hy. 118 (artificial): Velocity Profile
0.
50.
100.
150.
Depth (m)
0.
200.
400.
600.
800.
1000.
VS (m/sec)
9
10
11
12
13
14
15
16

FIGURE 86-B.

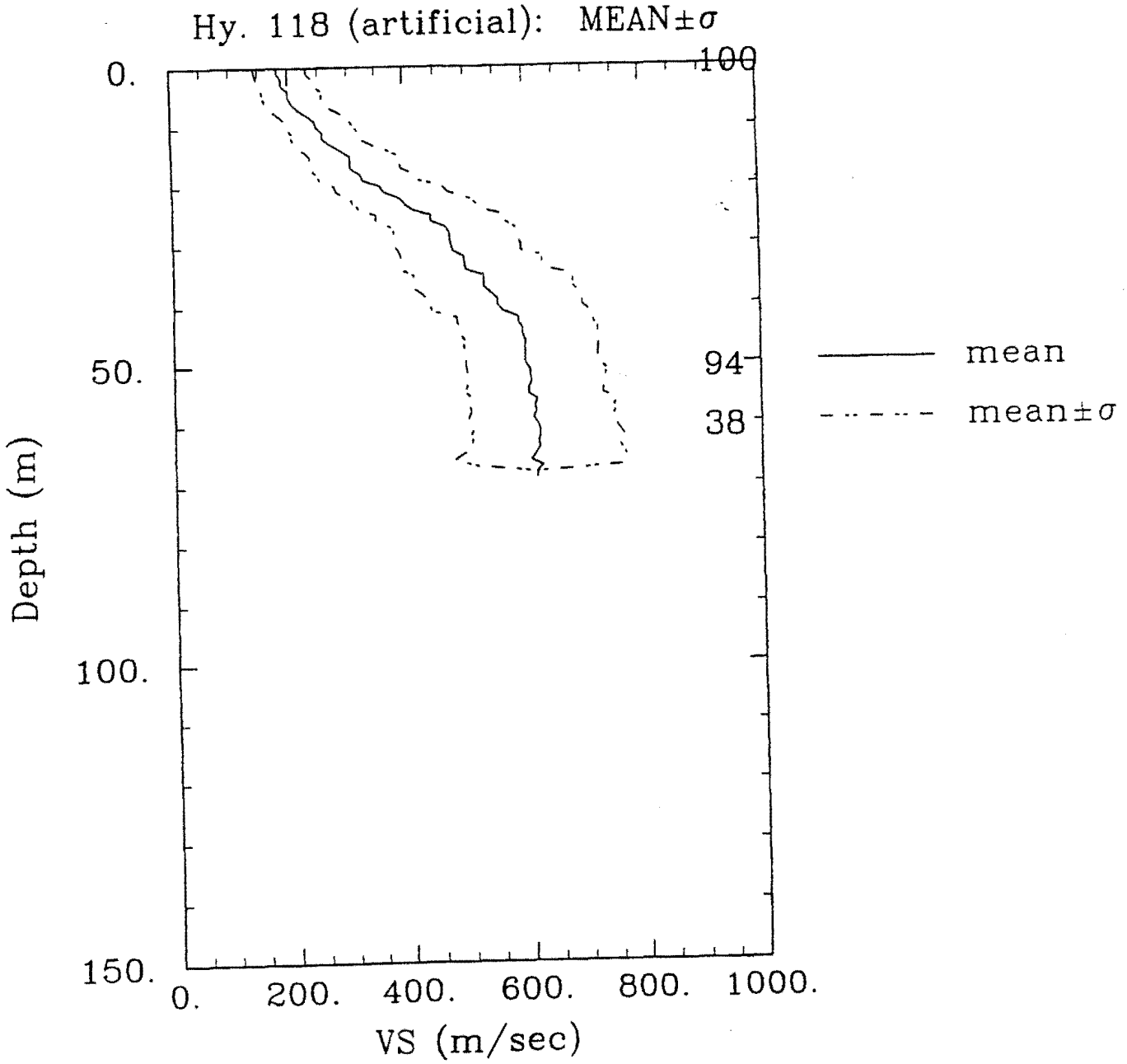
Hy. 118 (artificial): MEAN±σ
0.
50.
100.
150.
100
94
38
Depth (m)
0.
200.
400.
600.
800.
1000.
VS (m/sec)
mean
mean±σ

FIGURE 87.

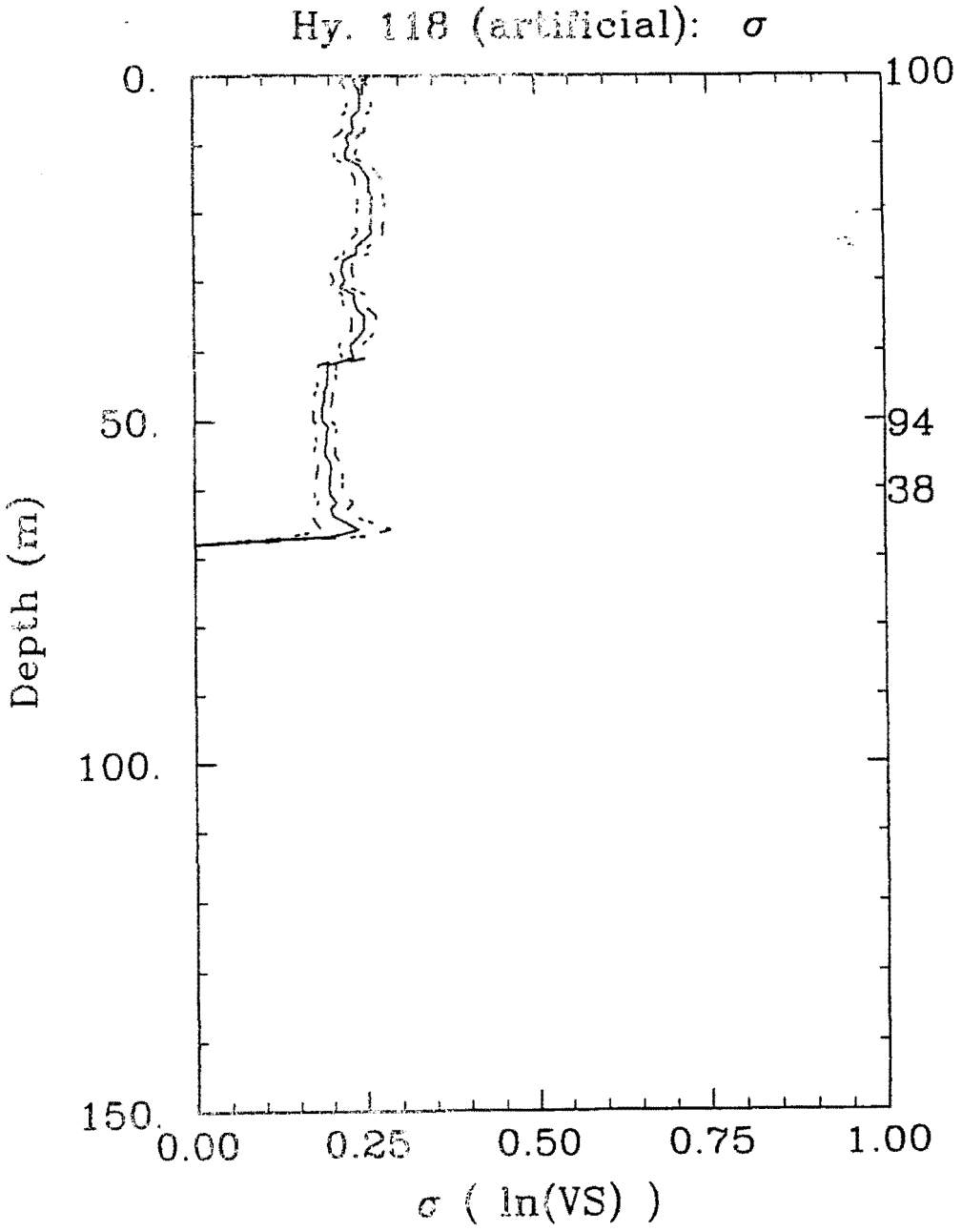
Hy. 118 (artificial): σ
0.
50.
100.
150.
Depth (m)
100
94
38
0.00
0.25
0.50
0.75
1.00
σ (ln(VS))

FIGURE 88.